Proceedings of:

The Twenty-third Annual Meeting of The American Society for Precision Engineering and the Twelfth ICPE

October 19-24, 2008
Marriott Portland Downtown Waterfront Hotel
Portland, Oregon

The American Society for Precision Engineering (ASPE) is a multidisciplinary professional and technical society concerned with research and development, design, manufacture and measurement of high accuracy components and systems. ASPE activities encompass relevant aspects of mechanical, electronic, optical and production engineering, physics, chemistry, and computer and materials science. Membership is open to anyone interested in any aspect of precision engineering.

Founded in 1986, ASPE provides a new focus for a diverse but important community. Other professional organizations have covered aspects of precision engineering, always as a sideline to their principal goals. ASPE is based on the core of generic concepts necessary to achieve precision in any application; independent of discipline, ASPE intends to be the focus for precision technology — and to represent all facets from research to application.

ASPE — The American Society for Precision Engineering
301 Glenwood Avenue, Suite 205, Raleigh, NC 27603
P.O. Box 10826, Raleigh, NC 27605
Telephone: (919) 839-8444 Fax (919) 839-8039
http://www.spe.net

Preface

This book comprises the proceedings of the 23rd ASPE Annual Meeting and the 12th ICPE. The contributions reflect the authors' opinions and are published as presented to ASPE, without change. Their inclusion in this publication does not necessarily constitute endorsement by the ASPE, or its editorial staff.

individual readers of this book and nonprofit libraries acting for them are permitted to make fair use of the material contained in this book to be used in teaching or research; provided they copy said paper in total, as written by the author. Permission is granted to quote excerpts from the scientific or technical works in this book with proper acknowledgment of the source to include: The author's name, the book name, and the ASPE tag line. Reproduction of figures and tables is likewise permitted from the contents of this book, provided that the same acknowledgment of the same source and content is permitted.

Any other type reproduction, systematic copying or multiple reproduction of any material in this book is expressly prohibited except with the written permission of the ASPE editorial staff, addressed to the Society's headquarters.

ISBN 978-1-887706-47-6

2008

American Society for Precision Engineering
301 Glenwood Avenue, Suite 205
Raleigh, NC 27603

Printed in the United States of America

Welcome Note

Welcome to Portland and the Twenty-third Annual Meeting of The American Society for Precision Engineering. Over the past two decades, the Annual Meeting of the ASPE has evolved into a premier international forum for the exchange of ideas and presentation of research results relating to precision engineering, metrology, controls, and system integration. Precision engineers and scientists from private industry, government laboratories, and universities meet to learn about the latest developments and to share ideas about the future directions of these technologies.

*But this year's Meeting is especially exciting because it is the beginning of bi-annual series of International Meetings jointly organized by ASPE, the Japan Society for Precision Engineering (JSPE) and the European Society for Precision Engineering and Nanotechnology (eu**spen**). These meetings — called the International Conference on Precision Engineering (ICPE) — have been held for many years but this year marks the beginning of a new collaboration that will see each Society host the ICPE on a rotating basis. This year it is part of the ASPE Annual Meeting, in 2010 it will be at the eu**spen** Annual Meeting and in 2012 it will hosted by the JSPE. The growth and success of each Society reflects the increasing importance of precision engineering in fields ranging from manufacturing to microelectronics to basic science. These International Meetings will serve to strengthen the international community and provide a forum for precision engineers from across the globe.*

The 2008 ASPE Annual Meeting continues the tradition of offering two full days of tutorials presented by some of the foremost precision engineers and scientists in the world. The technical sessions and poster presentations offer the latest research results in the areas of ultraprecision machining, metrology, controls, precision grinding, micro-positioning, material processing, design, precision transducers, surface profilometry, and error compensation. Special sessions will be organized by the collaborating Societies to provide a more international flavor to the talks. The commercial exhibits will provide attendees with the opportunity to view and discuss the latest precision engineering equipment, products, and services.

The conference organizing committee is proud to present the program for the Twenty-third Annual Meeting of the ASPE and the Twelfth ICPE. We welcome your participation and your feedback on how to make future meetings even better.

2008 Organizing & Technical Program Committee

Hans-Jochen Trost
MicroFab Technologies, Inc., Conference Chair

Eric S. Buice, Delft University of Technology
Keith Carlisle, Lawrence Livermore National Laboratory
Thomas A. Dow, North Carolina State University
Jonathan D. Ellis, Delft University of Technology
Kenneth P. Garrard, North Carolina State University
David D. Gill, Sandia National Laboratories
Robert D. Grejda, Corning Tropel Corporation
Bradley H. Jared, Sandia National Laboratories
Mark T. Kosmowski, Electro Scientific Industries, Inc. (ESI)
Jeremy J. Kroll, Lawrence Livermore National Laboratory
Don A. Lucca, Oklahoma State University
Reg R. Maas, CoorsTek, Inc. - Oregon Operations
Brian P. O'Connor, Aerotech, Inc.
Stefan Rakuff, General Electric Global Research
Jeffrey W. Roblee, AMETEK Precitech, Inc.
Deming Shu, Argonne National Laboratory
Alex Sohn, North Carolina State University
Henny A.M. Spaan, IBS Precision Engineering BV
Mark A. Stocker, Cranfield Precision
David R. Stussi, Gardner Stussi Tool & DieStussi
Pradeep K. Subrahmanyan, RAPT Industries, Inc.
Steven C. Williams, QED Technologies, International
Allen Y. Yi, The Ohio State University

2008 Scholarship Recipients

Vijay Shilpiekandula, Massachusetts Institute of Technology
R.V. Jones Memorial Scholarship

Jonathan D. Ellis, Delft University of Technology
Hyo Soo Kim, University of Florida
Bartosz K. Nowakowski, University of North Carolina at Charlotte
Amit Ravindra Suratkar, University of North Carolina at Charlotte
Wesley B. Williams, University of North Carolina at Charlotte

2008 Corporate Scholarship Sponsors

Cranfield Precision, Division of Cinetic Landis Ltd., UK
Corning Inc., Corning, NY
DTL Corporation, West Sacramento, CA
Moore Tool Company, Inc., Bridgeport, CT
New Way Air Bearings, Aston, PA
Lion Precision, St. Paul, MN

2008 Annual Meeting
Contents

Preface . . . . . *ii*

Welcome Note . . . . . *iii*

Organizing Committee – 2008 Scholarship Recipients and Sponsors . . . . . *iv*

Table of Contents . . . . . *v*

Program . . . . . *vi*

Keynote Address . . . . . *vii*

Technical Exhibitors . . . . . *viii*

Lifetime Achievement Award . . . . . *ix*

Sustaining Corporate Sponsors . . . . . *x-xi*

Corporate Sponsors . . . . . *xii*

Technical Paper Index *1-11*

Technical Papers *15-647*

Author Index. *649-653*

Program

2008 ASPE/ICPE Annual Meeting

Time	Sun., Oct. 19	Mon., Oct. 20	Tues., Oct. 21	Wed., Oct. 22	Thurs., Oct. 23	Fri., Oct. 24
8:00	Registration		Registration and Early Coffee			
9:00	Tutorials	Tutorials	Technical Session I	Technical Session III JSPE	Technical Session VII	Technical Tours
10:00			Break	Break	Break	
11:00			Technical Session II	Technical Session IV euspen	Technical Session VIII	
12:00	Lunch on your own	Lunch on your own	Lunch and Committee Meetings	Awards Lunch and Business Meeting	Lunch and Open Forum	
1:00						
2:00	Tutorials	Tutorials	Commercial Session	Technical Session V	Technical Session VIII	
3:00			Break	Break		
4:00			Poster Session	Poster Session		
5:00			Hospitality Hour on Bus	Hospitality Hour		
6:00		Welcome Reception	Dinner Banquet at Evergreen Aviation Museum	Technical Session VI		
7:00		Keynote Address				
8:00						
9:00						

☐ Exhibit Open Hours

Keynote Address

W. Bruce Banerdt, Ph.D
Jet Propulsion Laboratory

Monday, October 20, 7:00 p.m.
Session Chair: Hans-Jochen Trost, MicroFab Technologies, Inc.

Bruce Banerdt is a planetary geophysicist who has been working in the Earth and Space Sciences Division at JPL since 1977. He earned a BS in Physics ('75) and a PhD in Geophysics ('83) at USC (with a 2-year detour through Penn State).

He has participated in numerous planetary flight instrument teams, including the Mars Orbiter Laser Altimeter on Mars Global Surveyor, the Synthetic Aperture Radar on the Magellan mission to Venus, the Seismometer on the NetLander mission to Mars (unfortunately canceled before launch), and the SESME Acoustic Sounder on the European Rosetta comet mission. He helped develop a miniature MEMS seismometer and has been working for the past 18 years to send seismometers to Mars. He is currently heading a NASA project to develop a Mars seismic network mission, and is working on several projects relating to seismic stations on the Moon.

Dr. Banerdt has served on several NASA and National Academy of Sciences advisory panels on space science, and is currently a member of COMPLEX (the Committee for Planetary Exploration). He has been the Project Scientist for the Mars Exploration Rovers for the past two years.

Prospecting for Water in the Deserts of Mars

NASA launched two robotic geologists, Spirit and Opportunity, toward Mars in June and July of 2003, reaching the planet Mars the following January. Although they were designed for a 90-day mission, both rovers have lasted more than four years on the surface of this inhospitable planet and each has covered more than four miles while gathering evidence on ancient environmental conditions on Mars.

The science objectives for this mission are focused on delineating the geologic history for two locations on Mars using geological and geochemical techniques. There is an emphasis on the ancient history of Mars, as there is much evidence that conditions may have been much more clement than today. A common focus of the various investigations is the role of water, as it is a unique ingredient in a broad variety of processes, and leaves its fingerprints in the chemistry and configuration of rocks. Instruments include high-resolution cameras (both panoramic and close-up), a thermal infrared spectrometer, an alpha particle/X-ray spectrometer, and a Mössbauer spectrometer.

Cooperating Sponsors

Elsevier Science, Inc.

Technical Exhibitors

4D Technology Corporation

Aerotech, Inc.

ALIO Industries, Inc.

Ambios Technology, Inc.

AMETEK - Precitech, Inc.

Bal-tec

Center for Precision Metrology—
University of North Carolina at Charlotte

Chardon Tool

Contour Fine Tooling, Inc.

CoorsTek, Inc.

Engineered Surface Finishes, a Group of CMC

Fabreeka International, Inc.

Heidenhain Corporation

Kugler of America Ltd.

Lion Precision

Machine Dynamics Research Laboratory —
The Pennsylvania State University

Makino

Moore Nanotechnology Systems, LLC

Moore Tool Company, Inc.

New Way Air Bearings, Inc.

Philips Applied Technologies

Precision Engineering Center—
North Carolina State University

Precision MicroDynamics, Inc.

Professional Instruments Company, Inc.

TAC Americas, Inc.

Third Wave Systems, Inc.

Trust Automation

Veeco Instruments, Inc.

Zygo Corporation

Commercial Session

Tuesday, October 21, 1:30 - 3:00 p.m.

Session Co-Chairs: Reg Maas (CoorsTek, Inc.)
and Daniel C. Thompson (Olympic Precision, Inc.)

The Commercial Session will take place early in the week on Tuesday afternoon. This is a special session where companies and participants are free to open discussions on a less-formal basis and to promote interaction on a variety of topics. In the first part of this session, company representatives are invited to make brief presentations (five minutes) on new products associated with precision engineering. This provides participants with the opportunity to receive timely information on new technologies that have been commercialized into products and services, as well as information on advances that can be expected in the near future.

2008 ASPE Lifetime Achievement Award

Toshimichi Moriwaki

Toshimichi Moriwaki has been selected for the 2008 ASPE Lifetime Achievement Award. This selection is based on his significant published research, which has led to a better understanding of materials, facilities, principles, operations, and their application to improve manufacturing processes. Dr. Moriwaki is widely regarded as one of the leading researchers in the international manufacturing community, where he has addressed audiences in Japan, the US, Germany, Australia, Canada, and Singapore, among other countries.

Some of his most significant research includes such manufacturing processes as ultraprecision machining and machine tools and sensor technology and he has been credited with being among the first in the world to perform ultraprecision machining with diamond cutting tools. His research work has covered a wide range of topics from intelligent production system, dynamic stiffness and thermal deformation analysis of machine tools and studies of the cutting process. He has been active in JSPE and CIRP as well as ASPE.

A prolific scholar, Moriwaki is the author or coauthor of hundreds of papers and presentations. A committed educator and academic administrator, Dr. Moriwaki was on the faculty of Japan's prestigious Kobe University for 33 years beginning in 1974. In 2007, he moved to Setsunan University, and is currently a Dean and Professor of the Department of Industrial and Management Systems Engineering. He also works on the development of the local economy and industry as the chief director of the Kobe City Industrial Promotion Foundation.

ASPE 2008 Sustaining Corporate Sponsors

3M Company
St. Paul, MN 55144
Phone: (651) 737-3790
www.mmm.com

ADCOLE Corporation
669 Forest Street
Marlborough, MA 01752
Phone: (508) 485-9100
Fax: (508) 481-6142
www.adcole.com

Aerotech, Inc.
101 Zeta Drive
Pittsburgh, PA 15238-2897
Phone: (412) 963-7470
Fax: (412) 963-7459
www.aerotech.com

Ametek Precitech, Inc.
44 Blackbrook Road
Keene, NH 03431
Phone: (603) 357-2511
Fax: (603) 358-6174
www.precitech.com

Center for Precision Metrology
University of North Carolina-Charlotte
9201 University Blvd.
Charlotte, NC 28223
Phone: (704)-687-8499
www.cpm.uncc.edu

Chardon Tool
115 Parker Court
Chardon, OH 44024
Phone: (440) 286-6440
Fax: (440) 286-7165
www.ChardonTool.com

Corning Tropel Corporation
60 O'Connor Road
Fairport, NY 14450
Phone: (585) 388-3500
Toll-free: (888) 4-TROPEL
www.tropel.com

Equilibria
472 Amherst Street
Unit 25
Nashua, NH 03063
Phone: (603) 880-7722
www.eqlib.com

Fabreeka International, Inc.
P.O. Box 210
1023 Turnpike Street
Stoughton, MA 02072
Phone: (781) 341-3655
Toll-free: (800) 322-7352
www.fabreeka.com

Lion Precision
563 Shoreview Park Road
St. Paul, MN 55126-7014
(651) 484-6544
(651) 484-6824
www.lionprecision.com

ASPE 2008 Sustaining Corporate Sponsors

Makino
7680 Innovation Way
Mason, OH 45040
Phone: (513) 573-7200
Fax: (513) 573-7360
www.makino.com

Mitutoyo America Corporation
945 Corporate Boulevard
Aurora, IL 60504-9102
Phone: (630) 723-3619
Fax: (630) 978-6471
www.mitutoyo.com

Moore Tool Company, Inc.
800 Union Avenue
Bridgeport, CT 06607-0088
Phone: (203) 366-3224
Fax: (203) 366-5694
www.mooretool.com

New Way Precision, Inc.
4009-I Market Street
Aston, PA 19014
Phone: (610) 494-6700
Fax: (610) 494-0911
Toll-Free: (800) 394-1046
www.newwaybearings.com

Philips Applied Technologies
1140 Ringwood Court
MS16
San Jose, CA 95131-1706
Phone: (408) 991-2261
www.apptech.philips.com

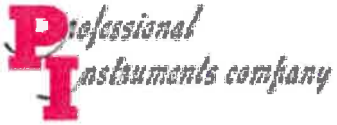

Professional Instruments Company
7800 Powell Road
Hopkins, MN 55343
Phone: (952) 933-1222
Fax: (952) 933-3315
www.airbearings.com

Queensgate Instruments, Ltd.
Woodland Road
Torquay Devon TQ2 7AY
United Kingdom
Phone: 44-1803-407710
Fax: 44-1803-4076
www.nanopositioning.com

StarragHeckert, Incorporated
Skyport Business Park
2379 Progress Drive
Hebron, KY 41048
Phone: 859-534-5201
Fax: 859-534-5212
www.starragheckertus.com

Trust Automation, Inc.
143 Suburban Road
San Luis Obispo, CA 93401
Phone: (805) 544-0761
Fax: (805) 544-4621
www.trustautomation.com

Zygo Corporation
Laurel Brook Road
Middlefield, CT 06455-0448
Phone: (860) 347-8506
Fax: (860) 347-8372
Toll-free: (800) ZYGO-NOW
www.zygo.com

ASPE 2008 Corporate Sponsors

Contour Fine Tooling, Inc.
Marlborough, NH 03455
Contact: Jeffrey Tomlin
(603) 876-4908

Corning Inc.
Corning, NY 14831
Contact: John Thomas
(607) 974-3842

Cranfield Precision, Div. of Landis Lund
Division of Cinetic Landis Grinding, Ltd.
Cranfield, Bedford MK43 OJR, U.K.
Contact: Edric M. E. Brown
+44-1234-754222

euspen
Cranfield University
Cranfield, Bedford, MK43 OAL, U.K.
Contact: Theresa Burke
+44-1234-754024

Nano Corporation
Tokyo 144-0042, Japan
Contact: Akira Hayashi
+81-3-5735-6631

Reflexite Precision Technology Ctr.
West Henrietta, NY 14586
Contact: Mr. Steven M. Scott
(585) 272-0290

Seagate Technology
Scotts Valley, CA 95066
Contact: Robert M. Pelstring
(831) 439-3697

Singulus Mastering, B. V.
5657 EN Eindhoven, The Netherlands
Contact: Jelm Franse
+31-40-7501-400

Veeco
Tucson, AZ 85706-7123
Contact: Geoffrey Anderson
(520) 741-1044

Technical and Poster Sessions Index

The technical program of the 2008 ASPE/ICPE Meeting contains 162 papers on precision engineering advances. Papers that lent themselves to significant verbal interaction, concise but important discoveries, or strongly visual or tactile subjects have been selected for the poster presentation. Authors will be in attendance to discuss their work on Tuesday, October 21, and Wednesday, October 22, from 3:30 to 5:00 p.m.

Session I
Machine Design I

Tuesday, October 21, 2008, 8:30 am - 10:00 am

Session Chair: Keith Carlisle (Lawrence Livermore National Laboratory) and Hans-Jochen Trost (MicroFab Technologies, Inc.)

1. ***Robotic System for Precision Assembly of NIF Ignition Targets***
   Montesanti, R. C.; Seugling, R. M.; Klingmann, J. L.; Dzenitis, E. G.; Miller, G. L.; Kent, R. A.; Castro, C.; Reynolds, J. L.; Carrillo, M. A. (Lawrence Livermore National Laboratory); and Alger, E. T. (General Atomics) 15
2. ***Rotary-axial Spindles for Precision Manufacturing***
   Lu, X.; Paone, M.; Usman, I. (The University of British Columbia); Slocum, A. H. (Massachusetts Institute of Technology); and Yui, A. (The National Defense Academy of Japan) 19
3. ***Design and Test of a 2-D Precision Weak-link Stage System with Sub-centimeter Travel Range and Sub-nanometer Resolution***
   Shu, D.; Maser, J. (Argonne National Laboratory) 23
4. ***Design, Realization and Testing of the NANOMEFOS Non-contact Measurement Machine for Freeform Optics***
   Henselmans, R.; Rosielle, P. C. J. N.; Steinbuch, M. (Eindhoven University of Technology); and Cacace, L. (AC Optomechanix) 27

Session II
Novel Systems

Tuesday, October 21, 2008, 10:30 am - 12:00 pm

Session Chair: Pradeep K. Subrahmanyan (RAPT Industries, Inc.) and Mark Kosmowski (Electro Scientific Industries, Inc.)

1. ***The Thirty Meter Telescope Project: Designing and Building the World's Largest Telescope (Invited Paper)*****
   Nelson, J. E. (Center for Adaptive Optics, University of California)
2. ***Precision Material Removal Using the Electrokinetic Phenomenon***
   Leo, C. S.; Yang, C.; Butler, D. L. (Nanyang Technological University); Blackburn, T. L.; Danyluk, S. (Georgia Institute of Technology); and Ng, S. H. (Singapore Institute of Manufacturing Technology) 31
3. ***Open Loop Fast Tool Servo with Nanometer Accuracy for Diamond Machining of Diffractive Structures***
   Brinksmeier, E.; Lünemann, B.; Gläbe, R. (Bremen University); and von Kopylow, C.; Falldorf, C.; Dankwart, C. (Bremer Institut für Angewandte Strahltechnik (BIAS)) 35

***No Abstract available*

4. ***Pneumatic Servo Bearing Actuator for Ultraprecise Positioning — Part 1: Principle and Basic Performance***
Hirayama, T.; Kitagawa, T.; Kadotani, M.; Danjyo, H.; Matsuoka, T. (Doshisha University); Sasaki, K. (Pneumatic Servo Controls, Ltd.); and Yabe, H. (Kyoto University) 39

5. ***Grinding of Microstructured Functional Surfaces – A Novel Strategy for Dressing of Microprofiles on Vitrified Grinding Wheels***
Denkena, B.; Boehnke, D.; Wang, B. (Leibniz Universität Hannover) 43

Session III
State of the Art Precision and Ultra-Precision Machining

Wednesday, October 22, 2008, 8:30 am - 10:00 am

Session Chair: Toshiyuki Enomoto (Osaka University) and Hideo Takino (Nikon Corporation)

1. ***The Current State of Art in Ultraprecision Cutting Technology in Japan***
Takeuchi, Y. (Osaka University) 49

2. ***The Current State of Art in Nano-precision Micro/Meso Mechanical Manufacturing (M^4) Processes***
Kuriyagawa, T.; Yoshihara, N. (Tohoku University) 51

3. ***Challenges to Miniaturization in Micro EDM***
Kunieda, M. (Tokyo University of Agriculture & Technology) 55

4. ***Microfactory — Novel Manufacturing Systems for Precision Machining —***
Mishima, N.; Kondoh, S.; Nakano, S.; Ashida, K.; Masui, K. (Advanced Manufacturing Research Institute (AIST)) 61

Session IV
Highlights from the European Precision Engineering Field

Wednesday, October 22, 2008, 10:30 am - 12:00 pm

Session Chair: Theresa Burke (euspen) and Henny Spaan (IBS Precision Engineering BV)

1. ***Precision Engineering: The European Way***
Van Brussel, H. (Katholieke Universiteit Leuven); van Eijk, J. (Technical University Delft); Spaan, H. A. M. (IBS Precision Engineering BV); and Brinksmeier, E. (Bremen University) 65

2. ***Advancements in Displacement Metrology Based on Encoder Systems***
Holzapfel, W. (Dr. Johannes Heidenhain GmbH) 71

3. ***Ultra Precision Surfaces***
Shore, P. (Optic Technium and Cranfield University Precision Engineering Centre) 75

4. ***Manufacturing Better Chips at Lower Cost****
Loopstra, E. R.; Ockwell, D C.; Butler, H.; Levasier, L. (ASML) 79

Session V
Machining

Wednesday, October 22, 2008, 1:30 pm - 3:00 pm

Session Chair: David D. Gill (Sandia National Laboratories) and Allen Y. Yi (The Ohio State University)

1. ***The Milling Dynamics "Super Diagram": Combining Stability and Surface Location Error***
Zapata, R. E.; DeMarco, C.; Schmitz, T. L. (University of Florida) 80

2. ***Sub-surface Damage Evaluation in Grinding of Large Optics***
Tonnellier, X.; Shore, P.; Morantz, P. (Optic Technium and Cranfield University Precision Engineering Centre) 84

3. ***Ultrasonic Assisted Turning of Hardened Steel with Mono-crystalline Diamond***
Klocke, F.; Dambon, O.; Bulla, B.(Fraunhofer Institute for Production Technology - IPT); and Heselhaus, M. (ZF Friedrichshafen AG) 88

**Extended Abstract unavailable at press time*

Technical Papers

ASPE

2. ***Performance Improvements in the Measurements of a Large Range Scanning Probe Microscope****
Rachakonda, P. K.; Kramar, J. A. (National Institute of Standards and Technology) 586

SURFACE METROLOGY

1. ***Characterization of Microstructure Freeform Surfaces Using a Pattern Matching Analysis***
Cheung, C. F.; Kong, L. B.; Lee, W. B.; To, S. (The Hong Kong Polytechnic University) 587

2. ***Analysis of Surface Accuracy by End Milling***
Ikeda, N.; Kobayashi, Y.; Shirai, K. (Nihon University); and Tozawa, K. (Nissan Motor Co., Ltd.) 591

3. ***Modeling of Cylinder Surface Topography***
Pawlus, P. (Rzeszów University of Technology); and Reizer, R. (University of Rzeszów) 595

4. ***Optimizing a Gaussian Filter Long Wavelength Cutoff for Improving 3D Ballistics Signature Correlations***
Song, J.-F.; Ma, L.; Vorburger, T. V., Ballou, S. (National Institute of Standards and Technology) 599

5. ***Study of an Interpolation of Flatness Data Measured by Successive Differential Laser Auto-collimation***
Uda, Y.; Shimada, S. (Osaka Electro-Communication University); and Go, Y. (Nagase Integrex Co., Ltd.) 603

ULTRAPRECISION MACHINING

1. ***Ultra Fine Tool Servo System***
Gan, S. W.; Rahman, M. (National University of Singapore); and Lim, H. S. (Mikrotools Pte. Ltd.) 607

2. ***Machining Technology of Micro Waved V-Pattern Using Shaping Process***
Je, T.-J.; Choi, D.-S.; Lee, K.-W.; Park, K.-T.; Whang, K. H. (Korea Institute of Machinery & Materials (KIMM)) 611

3. ***Factors Affecting Changes in Removal Rate of Elastic Emission Machining***
Kanaoka, M.; Takino, H.; Nomura, K. (Nikon Corporation); and Mimura, H.; Yamauchi, K., Mori, Y. (Osaka University) 615

4. ***Ultra Precision Machine Integrated Measurement of Spheres and Aspheres with a Twyman-Green Interferometer***
Uhlmann, E.; Kurz, M.; Oberschmidt, D. (Technical University Berlin); and Bluemel, T.; Neubert, R. (FISBA OPTIK GmbH) 619

5. ***Ultra Precision Machining Disturbance Frequency Extraction from Finished Surface Metrology***
Meyer, P. A.; Veldhuis, S. C.; Elbestawi, M. A. (McMaster University) 622

6. ***Development of CAPP/CAM System for Ultraprecision Micromachining***
Oba, T.; Ishida, T.; Takeuchi, Y. (Osaka University) 626

7. ***Historical Note on Dynamic Strain Measurements***
Rhorer, R. L. (National Institute of Standards and Technology) 630

8. ***Application of Magnetorheological Jet (MR JET®) in Precision Finishing***
Shorey, A. B.; Tracey, J. P.; Kordonski, W. I. (QED Technologies Inc.) 632

9. ***Surface Generation in Ultra Precision Single Point Diamond Turning of Aluminum***
Tauhiduzzaman, M.; Veldhuis, S. C. (McMaster University) 636

10. ***Machining of Glass Lens Mold with Minute Structures by Grinding and Cutting***
Yamamoto, S.; Fujii, T.; Ishida, T.; Takeuchi, Y. (Osaka University); Hirano, M. (JTEKT Corporation); and Shibukawa, T. (Mitsui Seiki Kogyo Co., Ltd.) 640

11. ***Influence of Cutting Speed on Ultra-precision Cutting Characteristics of Stainless Steel with Coated-cemented-carbide Tool***
Yasui, H.; Kawabayashi, T.; Toyama, A.; Hayashi, H. (Kumamoto University); and Shinozaki, A. (Ariake National College of Technology) 644

**Extended Abstract unavailable at press time*

5. ***Development of a Precise and Quick Response Pneumatic Pressure Regulator and its Application to Pneumatic Vibration Isolator***
Kato, T. (Tokyo Metropolitan College of Industrial Technology); Tadano, K.; Kawashima, K.; Kagawa,T. (Tokyo Institute of Technology); and Yamamoto, N. (Tokyo Meter Co., Ltd.) 518

6. ***Multisectional Synthesis of Tungsten Oxide Nanowires Using Micropatterned Layer for Field-emission Displays***
Moritani, H.; Nagato, K.; Kojima, Y.; Furubayashi, M.; Hamaguchi, T.; Nakao, M. (The University of Tokyo); and Kasuya, K. (Hitachi, Ltd.) 522

7. ***Micro and Nano Assembly Tools Utilizing Standing Wave Technology***
Nowakowski, B. K.; Smith, S. T. (University of North Carolina at Charlotte); and Woody, S. C. (InsituTec, Inc.) 526

8. ***Development of Multi-wire EDM Slicing Method for Silicon Ingot***
Okamoto, Y.; Uno, Y.; Okada, A.; Ohshita, S. (Okayama University); Hirano, T. (Toyo Advanced Technologies Corporation); and Takata, S. (Makino Milling Machine Corporation) 530

9. ***A Cutting Tool with Nano/Micro-textured Surface for High Anti-adhesive Effects***
Sugihara, T.; Enomoto, T. (Osaka University) 534

10. ***Improvement of Thickness Uniformity of Silicon and SOI Wafer by Numerically Controlled Local Wet Etching***
Yamamura, K.; Mitani, T.; Zettsu, N. (Osaka University) 538

OPTICS AND INTERFEROMETRY

1. ***Manufacture and Measurement of a Precision Milli-scale Germanium Optical Array for Novel Thermal Imaging Systems***
Davies, M. A.; Dutterer, B. S.; Suleski, T. J.; Barkman, M. L. (University of North Carolina at Charlotte) 542

2. ***Manufacture of Large Optics: Materials and Processes***
Brooks, D.; Gee, A. E. (University College London) 546

3. ***A Two-degree-of-freedom Linear Encoder for Measurement of Position and Straightness***
Kimura, A.; Arai, Y.; Gao, W. (Tohoku University) 550

4. ***Development of a Sensitive 3-Axis Angle Sensor Based on Laser Autocollimation***
Saito, Y.; Arai, Y.; Gao, W. (Tohoku University) 554

5. ***Design, Fabrication and Testing of Kinoform Lenses***
Garrard, K. P.; Sohn, A.; Dow, T. A. (North Carolina State University) 558

6. ***The Development of an Offset-locked Frequency Stabilized Heterodyne Laser Source for Precision Metrology***
Stroup Jr., C. G.; Overcash, J. L.; Hocken, R. J. (University of North Carolina at Charlotte) 562

PRECISION FABRICATION AND ASSEMBLY

1. ***Automated Part Centering Through Impulse Actuation***
Furst, S. J.; Dow, T. A.; Sohn, A.; Garrard, K. P. (North Carolina State University) 566

2. ***Fabrication of Micro Aspherical Lens Array Using Fast Tool Servo with Tool Path Compensation***
Hsu, W.-Y.; Chen, F.-Z.; Kuo, C.-H.; Cheng, Y.-C.; Lin, W.-L. (Instrument Technology Research Center, National Applied Research Laboratories) 570

3. ***Experimental Study on Microassembly by Using Liquid Surface Tension***
Kato, Y.; Mizuno, T.; Takagi, H.; Ishino, Y.; Takasaki, M. (Saitama University) 574

4. ***Rapid Shape Comparison Method for 3D Virtual Manufacturing Systems***
Song, I.-H.; Lee, W.-S.; Chung, S.-C. (Hanyang University) 578

SCANNING PROBE MICROSCOPY

1. ***High-scan Rate Positioner for Scanned Probe Microscopy***
MacKenzie, R. I.; Gawlik, A. J.; Trumper, D. L. (Massachusetts Institute of Technology) 582

2. ***Measurement and Compensation of a 4 Axis Ultra-precision Machine Tool for Generating Micro Patterns on the Large Surfaces***
Hwang, J.; Song, Y.-C.; Song, C.-K.; Park, C.-H. (Korea Institute of Machinery and Materials (KIMM)) 460

3. ***Detection of Orientation-dependent, Single-crystal Diamond Tool Edge Wear Using Cutting Force Sensors, While Spin-turning Silicon***
Marsh, E. R. (The Pennsylvania State University); and Kim, G. A.; Simonson, J. A. (Edge Technologies, Inc.) 464

MEASUREMENT UNCERTAINTY

1. ***Thermistor Bridge Performance in the 10^{-4} to 1 Hz Range and its Applications in Gravitational Wave Detection Projects***
Higuchi, S.; Clark, D. E.; Lantz, B. T.; DeBra, D. B. (Stanford University) 468

2. ***Test Uncertainty & Test Uncertainty Ratio (TUR)***
Khanam, S. A.; Morse, E. P. (University of North Carolina at Charlotte) 472

3. ***Bayesian Updating of Stability Beliefs***
Zapata, R. E.; Schmitz, T. L. (University of Florida); and Traverso, M. G.; Abbas, A. E (Univerisity of Illinois at Urbana-Champagne) 476

MICRO-ELECTROMECHANICAL DEVICES

1. ***The Design and Optimization of Cascaded Chevron Flexures and Actuators for Precision Motion Guidance***
Chen, S.-C. (Massachusetts General Hospital-Harvard Medical School); and Culpepper, M. L. (Massachusetts Institute of Technology) 480

2. ***Design and Fabrication of a Microrobot Movable in Human's Large Intestine Model***
Kato, S.; Goto, Y.; Hamano, T. (Nippon Institute of Technology); and Ono, M. (Tokyo Metropolitan College of Industrial Technology) 484

3. ***Comparisons of Anchor Designs for MEMS Resonant Mass Sensors***
Li, C.; Miller, M. H. (Michigan Technological University) 488

4. ***Investigation of Air Damping and Q in a MEMS Resonant Mass Sensor***
Li, C.; Miller, M. H. (Michigan Technological University) 492

NANOTECHNOLOGY

1. ***Nanometer-scale Ultrasonic Cutter Using an Atomic Force Microscope Controlled by a Haptic Device***
Iwata, F.; Ohara, K.; Kawanishi, S. (Shizuoka University); Aoyama, H. (University of Electro-Communications); and Ushiki, T. (Niigata University) 496

2. ***The Discrete Polystyrene-gold Core-shell Nanoparticles Array and their Surface Plasmonic Properties***
Zettsu, N.; Uchida, S.; Yamamura, K. (Osaka University) 500

NOVEL EQUIPMENT AND PROCESSES

1. ***Experimental Study of Micro Ultrasonic Machining Process***
Cheruku, S.; Sundaram, M. M.; Rajurkar, K. P. (University of Nebraska-Lincoln) 502

2. ***Combination Machining of Wire-sawing with Electro-chemical Discharge Machining***
Furutani, K. (Toyota Technological Institute); and Tomoto, M. (Toray Engineering Co., Ltd.) 506

3. ***New Approaches of Bevel Shape Generation for Quartz Crystal***
Horio, K.; Kaneko, J.; Yamazaki, T. (Saitama University) 510

4. ***Local Synthesis of Cabon Nanotubes by Electron Beam-heating Chemical Vapor Deposition***
Kaito, H.; Nagato, K.; Tsuchiya, K.; Hamaguchi, T.; Nakao, M. (The University of Tokyo); and Kasuya, K. (Hitachi, Ltd.) 514

5. ***Mechanochemical Diamond Stone Containing $BaSO_4$ Abrasive***
Higuchi, M.; Furushiro, N.; Yamaguchi, T.; Sugimoto, T. (Kansai University); Matsumori, N.; Ogura, H. (Mizuho Co., Ltd.); and Shimada, S. (Osaka Electro-Communication University) 392

6. ***Achievement of High Flatness of Large Diameter Silicon Wafer in Double-sided Polishing — Optimization of Polishing Conditions Based on Kinematical Analysis —***
Hirose, K.; Enomoto, T. (Osaka University) 396

7. ***Optimization of Quality of the Cylindrical Superfinished Surfaces***
Ionescu, R.; Amarandei, D. (University Stefan cel Mare) 400

8. ***Corrective Polishing of Complex Ceramics Geometries***
Klocke, F.; Brecher, C.; Zunke, R.; Tuecks, R. (Fraunhofer Institute for Production Technology – IPT) 404

9. ***Polishing-grinding – An Innovation for Manufacturing of High Precision Optics***
Klocke, F.; Grüntzig, A.; Hollstegge, D.; Völker, C.; Dambon, O.; Herben, M.; Bulla, B.; Czarlay, D.; Riegel, J. (Fraunhofer Institute for Production Technology – IPT) 408

10. ***Characterisation on the Surface Quality and Removal of Wafer with Variable Machining Conditions in the Wafer Polishing System***
Lee, J. T.; Won, J. K.; Lee, E. S. (INHA University) 412

11. ***Influence of Polisher Surface Structure on Ultra-smoothness Polishing Characteristic of Magnetic Disk Substrate***
Takagi, M.; Yasui, H.; Kusaba, K.; Fukakusa, N. (Kumamoto University) 416

12. ***Development of Nano-precision Synergistic Finishing Process Integrated ELID-grinding and MRF***
Ohmori , H.; Uehara, Y. (RIKEN (The Institute of Physical and Chemical Research)); Yin, S. (Hunan University); and Ishida, S. (The Nexsys Corporation) 420

13. ***Engineering a Next Generation Water-based Grinding Fluid***
Hug, P. (Recombinant Innovation, LLC); Nelson, A. R. (ARN Engineering Ltd.); and Salmon, S. C (Next Generation Technology Group, Inc.) 424

14. ***Characterization of Pad Materials in Abrasive Profile Polishing***
Schulte, H.; Riemer, O.; Gläbe, R.; Brinksmeier, E. (University of Bremen) 428

15. ***A Metrological Study on Hardened Steel Surface Finishing Using a Diamond Burnishing Tool***
Tanaka, H.; Yanagi, K. (Nagaoka University of Technology); and Tabuto, H. (Fuji Heavy Industries Ltd.) 432

16. ***Continuous Phase Plate Polishing Using Magnetorheological Finishing***
Tricard, M.; Dumas, P. R. (QED Technologies, Inc.); and Menapace, J. (Lawrence Livermore National Laboratories) 436

17. ***Characterizing Quantum Dots for Use in Detecting Subsurface Damage***
Williams, W. B.; Mullany, B. A.; Moyer, P. J.; Parker, W. C. (University of North Carolina at Charlotte); and Randles, M. H. (Northrop Grumman Synoptics) 440

18. ***Contact Stiffness of Vitrified and Resinoid Grinding Wheels Taking Into Account of the Dressing Condition***
Yamada, T.; Lee, H.-S.; Takemoto, K. (Nihon University) 444

19. ***Influence of Normal Feed on Surface Roughness in Newly Developed Ultra-smoothness Grinding Method***
Yasui, H.; Sakamoto, R.; Tanaka, Y.; Yoshimura, T. (Kumamoto University) 448

20. ***An Investigation on In-process Dressing Method Developed for New Ultra-smoothness Grinding Method Using Super Abrasive Wheel***
Yasui, H.; Tanaka, Y.; Sakamoto, R.; Matsuda, K. (Kumamoto University) 452

MACHINE TOOL METROLOGY

1. ***Machine Vision with Spindle Metrology Using a CCD Camera***
Deakyne, T. R.; Marsh, E. R. (The Pennsylvania State University); and Lehman, J.; Bartlett, B. (Confero Solutions) 456

9. ***Updating the Sub-atomic Measuring Machine***
Overcash, J. L.; Stroup Jr., C. G.; Hocken, R. J. (University of North Carolina at Charlotte) . . . 320

10. ***Multi-scale Alignment Positioning System for NIL***
Ozturk, O.; Caskey, G. W.; Hocken, R. J. (University of North Carolina at Charlotte); and Fesperman Jr., R. R. (Moore Tool Company, Inc.) . . . 324

11. ***Pneumatic Servo Bearing Actuator for Ultraprecise Positioning — Part 2: A New Approach to Ultra-precision Motion Control***
Sasaki, K; (Pneumatic Servo Controls, Ltd.); Hirayama, T. (Doshisha University); and Yabe, H. (Kyoto University) . . . 328

12. ***Design of a High Frequency MEMS Scanning Mirror***
Soemers, H.; van Lierop, D. (Philips Applied Technologies); and Krastev, K. (Yacht) . . . 332

13. ***Efficient Evaluation of Early Machine Concepts in the Frequency Domain Including Control Issues***
Weikert, S.; Jäger, C.; Bossoni, S.; Wegener, K. (Swiss Federal Institute of Technology (ETHZ)) . . . 336

DIMENSIONAL METROLOGY

1. ***Microscale Metrology Using Standing Wave Probes***
Bauza, M. B.; Woody, S. C. (InsituTec, Inc.); Smith, S. T. (University of North Carolina at Charlotte); and Seugling, R. M.; Darnell, I. M.; Florando, J. N. (Lawrence Livermore National Laboratory) . . . 340

2. ***Field-of-view Distortion Calibration and Compensation for Ultra-high Accuracy Video-based Metrology Systems***
Ding, Y.; Tobiason, J. D. (Micro Encoder, Inc.) . . . 344

3. ***Performance of a 2D Speckle Displacement Sensor with Various Measurement Surfaces***
Harsila, S. A.; Jones, B. K.; Masreliez, K. (Micro Encoder, Inc.) . . . 348

4. ***Comparison of Fringe Pattern Obtained by Scanning Polished Metal Cylinders and Sharp-edged Objects with Laser Beam***
Jablonski, R. T.; Markowski, J. (Warsaw University of Technology) . . . 352

5. ***Development of the Primary Nanoparticle Measurement Standard by the Electro-gravitational Aerosol Balance***
Lin, C.-M.; Chen, C.-J.; Pan, S.-P.; Weng, H.-F.; Yu, T.-C. (Center for Measurement Standards/Industrial Technology Research Institute) . . . 356

6. ***Development of a Measuring System for a Micro Hole Using an Optical Fiber Probe***
Murakami, H. (Fukuoka Industrial Technology Center); and Katsuki, A.; Onikura, H.; Sajima, T. (Kyushu University) . . . 360

7. ***Precision Measurement of Motion Accuracy for Development of Micro Measurement Center***
Ogura, I.; Okazaki, Y. (National Institute of Advanced Industrial Science and Technology) . . . 364

8. ***Profile Measurement of Micro-aspheric Surface by a Small-scale Measuring Instrument***
Shibuya, A.; Arai, Y.; Yoshikawa Y.; Gao, W. (Tohoku University) . . . 368

9. ***Subnanometer Displacement Measurement Using Common-path Grating Interferometry***
Wu, C.-C.; Hsu, C.-C.; Chen, C.-J. (Center for Measurement Standards/Industrial Technology Research Institute); and Lee, J.-Y. (National Central University) . . . 372

GRINDING, POLISHING, AND LAPPING

1. ***Precision Grinding of Silicon***
Konneh, M.; Alao, A.-R. (International Islamic University) . . . 376

2. ***Dicing Process for the Device Separation of a Slider with an Integrated Microactuator (SLIM)***
Cvetkovic, S.; Saalfeld, H.; Gatzen, H. H. (University of Hannover) . . . 380

3. ***Ultrasonic Assisted Grinding of Brittle Materials – Surface Topography and Process Forces***
Denkena, B.; de Leon, L.; Hahmann, D. (University of Hannover) . . . 384

4. ***Nano-indentation and Scratch Tests on Optical Fiber Material to Determine Ductile Mode Critical Depth of Cut***
Gharbia, Y. A. (Dhofar University); Katupitiya, J. (University of New South Wales) . . . 388

4. ***Piezo Driven XY Stage with Nano-manipulators for SEM Operation***
Kanegae, S.; Hiroyuki, C.; Aoyama, H.; Irie, Y. (University of Electro-Communications); Iwata, F. (Shizuoka University); and Ushiki, T (Niigata University) . . . 249

5. ***Novel Switching Control of the Ball-screw Driven Stage for Nano Positioning***
Kim, G-H.; Kim, W.-S.; Lee, S.-K. (Gwangju Institute of Science and Technology (GIST)); and Cho, S.-G. (Hyundai Steel Company) . . . 253

6. ***Development of Intelligent Encoder***
Kitawaki, J.; Kanamori, C. (The University of Electro-Communications) . . . 257

7. ***Optimized Production of Complex Shaped Optical Components via Precision Glass Molding***
Klocke, F.; Dambon, O.; Sarikaya, H.; Wang, F. (Fraunhofer Institute for Production Technology – IPT) . . . 261

8. ***Detection of Micro Tool Wear in Diamond Turning of Large Area Micro-lens Array by In-process Cutting Force Measurement***
Noh, Y. J.; Arai, Y.; Gao, W. (Tohoku University) . . . 264

9. ***Motion Control and Optimization for Nano Lithography***
Ruben, S.; Tsao, T.-C. (University of California - Los Angeles) . . . 268

10. ***Characteristics of PVAJT Trajectory Generator and its Implementation***
Shin, D. (Kumoh National University of Technology); and Choi, S.-H. (Ajinextek Co. Ltd.) . . . 272

11. ***Control Strategies for a Dynamic Positioning Machine at Nanometer Level***
Yang, R. H.; Smith, S. T. (University of North Carolina at Charlotte); Teo, C. S. (Singapore Institute of Manufacturing Technology); Buice, E. S. (Delft University of Technology); and Liu, X. P.; Wang, W. L. (University of Warwick) . . . 276

DESIGN AND FABRICATION OF STRUCTURED SURFACES

1. ***Improvement of Adhesive Strength of Ti-doped DLC Films by Heat Treatment in Vacuum***
Kohzaki, M. (Tokai University) . . . 280

2. ***Investigation on Laser Interaction in Annealing of Amorphous Silicon Films by Pulsed Nd^{3+}: Yag Laser***
Palani, A. I.; Vasa, N. J.; Singaperumal, M. (Indian Institute of Technology Madras) . . . 284

DESIGN OF PRECISION MACHINES AND INSTRUMENTS

1. ***Selection of Precision Actuators by Novel Function-structure-correspondences***
Erbe, T.; Król, J.; Ströhla, T.; Theska, R. (Technical University of Ilmenau) . . . 288

2. ***Mineral Casting as Material for Machine Base-frames of Precision Machines***
Erbe, T.; Król, J.; Theska, R. (Technical University of Ilmenau) . . . 292

3. ***Micro-positioning for Precise Ink Jet Delivery***
Gatica, A. W. (M3 Design Inc.) . . . 296

4. ***Application of Planar Air Bearing Concept for Precision Machine Tool Design***
Gorniak, J.; Erkorkmaz, K. (University of Waterloo) . . . 300

5. ***Fabrication of a Green Caterpillar Type In-pipe Mobile Inspection Microrobot Driven by Pneumatic and Vacuum Pressures***
Goto, Y.; Kato, S.; Hamano, T. (Nippon Institute of Technology); and Ono, M. (Tokyo Metropolitan College of Industrial Technology) . . . 304

6. ***A Platform for Observing the Behavior of AFM Cantilevers During Quasi-static Loading***
Kumanchik, L. M.; Schmitz, T. L. (University of Florida); and Pratt, J. R. (National Institute of Standards and Technology) . . . 308

7. ***A Compact, Compound Actuator for the Molecular Measuring Machine***
Li, J.; Shen, Y.-L. (The George Washington University); Jeong, J. (Korea University & National Institute of Standards and Technology); and Scire, F. E.; Kramar, J. A. (National Institute of Standards and Technology) . . . 312

8. ***Fabrication of a Snake Type In-pipe Mobile Robot Passable T-junction***
Ono, M.; Ito, S. (Tokyo Metropolitan College of Industrial Technology); and Goto, Y.; Hamano, T.; Kato, S. (Nippon Institute of Technology) . . . 316

2. ***Three-dimensional Internal Information Acquisition System Based on Consecutive Precision Machining and Cross-sectional Observation — Development of the System and its Applications —***
Furushiro, N. (Kansai University); Yokota, H.; Yamagata, Y.; Himeno, R.; Makinouchi, A. (RIKEN (The Institute of Physical and Chemical Research)); Fujisaki, K. (Hokkaido University); Kokubo, M. (Toshiba Machine Co., Ltd.); and Higuchi, T. (The University of Tokyo) 180

3. ***Fabrication of a New Three Dimensional Position Surveying System for the Underground Pipes Using Four Rotary Encoders***
Hamano, T.; Kato, S. (Nippon Institute of Technology); and Ono, M. (Tokyo Metropolitan College of Industrial Technology) 184

4. ***Synthesis of Semi-solid Casting Processes for Optimal Fabrication of Thin-walled Parts***
Hong, S.-H.; Lee, K.-J.; Chung, S.-C. (Hanyang University) 188

5. ***Optical Closed Loop Control for the Precision Grinding of Micro-EDM Electrodes***
Howe, M.; Bamberg, E. (University of Utah) 192

6. ***The Lubricant Applying Effect in Ti Alloy Ti-6Al-4V Cutting***
Kaneeda, T.; Kinugawa, K. (Okayama University of Science) 196

7. ***Storing Period Effects on Wear Properties in UHMWPE Inserts for Artificial Joints***
Kaneeda, T.; Miyata, Y. (Okayama University of Science); and Fujiwara, K. (Nakashima Propeller Co., Ltd.) 200

8. ***Deviated-deep-hole Boring for Avoiding an Existing Reinforcing Member***
Katsuki, A.; Onikura, H. (Kyushu University); and Horita, K.; Horiuchi, T. (Japan Fine Tech Co., Ltd.) 204

9. ***Generating Method of Micro Grooves by Micro EDM***
Lee, H. S.; Mikami, H.; Yamada, T. (Nihon University) 208

10. ***3D Reconstruction for the 3D Engraving System From 2D Images***
Lee, W.-S.; Song, I.-H.; Chung, S.-C. (Hanyang University) 212

11. ***Fabrication of Fused Silica Optical Quality Pin Chuck Using a Wet Etching Process***
Lemmons, T. D.; Ozturk, O.; Hocken, R. J. (University of North Carolina at Charlotte and Center for Scalable and Integrated Nanomanufacturing (SINAM)); and Fesperman Jr., R. R. (Moore Tool Company, Inc.) 216

12. ***The Zeeko Corrective Polishing Techniques as Applied to the Finishing of Semiconductor Thin Films****
Morton, R. K. (Zeeko Ltd.) 220

13. ***Minimum Quantity Lubrication Turning Using Tools with Oil Holes***
Ozawa, M.; Hosokawa, A.; Tanaka, R.; Furumoto, T.; Ueda, T. (Kanazawa University) 221

14. ***Flexure-based Mechanisms for Precision Guidance and Angular Alignment Under Large Loads***
Shilpiekandula, V.; Youcef-Toumi, K. (Massachusetts Institute of Technology) 225

15. ***Improvement of Chip Controllability of Carbon Steel in Turning by Laser Heat Treatment***
Tanaka, R.; Hosokawa, A.; Ueda, T.; Furumoto, T.; Kusano, T.; Lin, Y. (Kanazawa University) 229

16. ***Intelligent-speed-increasing Spindle Using Traction Drive***
Yamanaka, M.; Inoue, K. (Tohoku University); and Sugimoto, K. (Sony Corporation) 233

CONTROL OF PRECISION MACHINES AND PROCESSES

1. ***High Resolution, High Speed Real-time Digital Control System For Precision Applications***
Gawlik, A.; MacKenzie, R. I.; Otten, D.; Trumper, D. L. (Massachusetts Institute of Technology) 237

2. ***Integrated Tuning of a Robust Controller for Linear Servomechanisms***
Hong, S.-H.; Kim, S.-C.; Chung, S.-C. (Hanyang University) 241

3. ***Precision-limit Positioning of an Ultra Precision Table Using HSMC***
Hsieh, C.; Yang, C.-C. (National Cheng Kung University) 245

**Extended Abstract unavailable at press time*

Session VIII
Interferometry

Thursday, October 23, 2008, 10:30 am - 12:00 pm

Session Chair: Robert D. Grejda (Corning Tropel Corporation) and Byron R. Knapp (Olympic Precision, Inc.)

1. ***A New Heterodyne Interferometer with Zero Periodic Error and Tunable Beat Frequency***
   Kim, H. S.; Schmitz, T. L.; Rueff, M. C. (University of Florida); and Beckwith, J. F. (Lawrence Livermore National Laboratory) 136
2. ***Uncertainty Considerations for Interferometric Stability Testing***
   Ellis, J. D.; Joo, K.-N.; Spronck, J. W.; Munnig Schmidt, R.-H. (Delft University of Technology); and Verlaan, A. (TNO Science and Industry) 140
3. ***Measurement of the Absolute Distance Between Two Partially Reflective Surfaces***
   Badami, V. G.; Deck, L. L.; Selberg, L. A. (Zygo Corporation) 144
4. ***Measuring Machines with Interferometrical Stylus for Form Measurement of Precise Mechanical Parts***
   Drabarek, P.; Gnausch, T.; Fleischer, M. (Robert Bosch GmbH) 148
5. ***Absolute Length (Thickness) Measurements Using Wavelength Scanning Interferometry***
   Suratkar, A. R.; Davies, A. D.; Farahi, F. (University of North Carolina at Charlotte) 152

Session IX
Machine Design II

Thursday, October 23, 2008, 1:30 pm - 3:00 pm

Session Chair: Deming Shu (Argonne National Laboratory) and Mark A. Stocker (Cranfield Precision, Division of Cinetic Landis Grinding, Ltd.)

1. ***Parallel-kinematics MEMS Stages for High Precision Nanopositioning and Manipulation***
   Dong, J.; Mukhopadhyay, D.; Pengwang, E.; Ferreira, P. M. (University of Illinois Urbana-Champaign) 156
2. ***Novel Split Stage Architecture***
   Kosmowski, M. T. (Electro Scientific Industries, Inc. (ESI)) 160
3. ***Design of a Fast Long Range Actuator - FLORA II***
   Zdanowicz, E. M.; Eischen, J. W.; Dow, T. A. (North Carolina State University) 164
4. ***Simulation and Prediction of the Thermally Induced Deformations on Machine Tools Caused by Moving Linear Axis Using the FDEM Simulation Approach***
   Mayr, J.; Ess, M.; Weikert, S.; Wegener, K. (Swiss Federal Institute of Technology (ETHZ)) 168
5. ***Component Placement Robot with Wireless Energy and Data Transfer***
   Jansen, G. L. M.; Sahin Nomaler, F. (Philips Applied Technologies) 172

Poster Sessions

Tuesday, October 21, 2008, 3:30 pm - 4:30 pm

Wednesday, October 22, 2008, 3:30 pm - 5:00 pm

Session Chair: Bradley H. Jared (Sandia National Laboratories) and Eric S. Buice (Delft University of Technology)

APPLICATIONS OF PRECISION ENGINEERING IN MANUFACTURING

1. ***Model for Cutting Edge Tools in Order to Evaluate Plastic Deformation and Friction Forces at High Speed Machining***
   Amarandei, D.; Ionescu, R.; Petrariu, V. (University Stefan cel Mare) 176

4. ***Diamond Micro Chiseling of Molding Inserts for Optical Micro Structures***
Flucke, C.; Gläbe, R.; Brinksmeier, E. (Bremen University) 92

5. ***Machining Behaviour of Monocrystalline Diamond End Mills***
Uhlmann, E.; Oberschmidt, D. (Fraunhofer Institute for Production Systems and Design Technology) 96

Session VI

Sensors and Controls

Wednesday, October 22, 2008, 5:30 pm - 6:30 pm

Session Chair: Jeffrey W. Roblee (AMETEK-Precitech, Inc.) and Steven Williams (QED Technologies, International)

1. ***Control of a Fast Long Range Actuator (FLORA)***
Chen, Q.; Dow, T. A.; Garrard, K. P.; Sohn, A. (North Carolina State University); and Richardson, D. (Precision MicroDynamics, Inc.) 100

2. ***Evaluation of Harmonic Distortions in Precision Inertial Sensors***
Spiewak, S. A. (University of Calgary); Hauer, G. (ARAM Systems, Ltd.); and Ludwick, S. J. (Aerotech, Inc.) 104

3. ***High Accuracy Atomic Force Microscope for Dimensional Metrology***
Ljubicic, D. M.; Trumper, D. L. (Massachusetts Institute of Technology); and Hocken, R. J.; Overcash, J. L. (University of North Carolina at Charlotte) 108

4. ***Error Motions of a Non-orthogonal Rotary Axis***
McGlauflin, M. L.; Moylan, S. P. (National Institute of Standards and Technology) 112

Session VII

Metrology

Thursday, October 23, 2008, 8:30 am - 10:30 am

Session Chair: Byron R. Knapp (Olympic Precision, Inc.) and Henny A. M. Spaan (ISB Precision Engineering BV)

1. ***Comparison of NIST Si Force Scale to NPL Si Mass Scale***
Jones, C. W.; Davidson, S.; Leach, R. K. (National Physical Laboratory); and Kramar, J. A.; Pratt, J. R. (National Institute of Standards and Technology) 116

2. ***Investigating Scaling Limits of a Fiber Based Resonant Probe for Metrology Applications***
Seugling, R. M.; Darnell, I.; Florando, J. (Lawrence Livermore National Laboratory); Woody, S. C.; Bauza, M. B. (InsituTec, Inc.); and Smith, S. T. (University of North Carolina at Charlotte) 120

3. ***A Comparison of Optical Sensing Methods for the High Precision 3D Surface Profile Measurement of Grooved Surfaces***
McBride, J. W.; Zhao, Z.; Boltryk, P. (University of Southampton) 124

4. ***Design and Fabrication of a Multifunctional Scanning Probe with Integrated Tip Changer for Fully Automated Nanofabrication***
Leang, K. (University of Nevada-Reno); and Taylor, C. R. (University of Florida) 128

5. ***Two-dimensional Displacement Measurement Using the Six-point Atomic Encoder Technique***
Chaikool, P.; Aketagawa, M. (Nagaoka University of Technology); and Okuyama, E. (Akita University) 132

ROBOTIC SYSTEM FOR PRECISION ASSEMBLY OF NIF IGNITION TARGETS

Richard C. Montesanti[1], Richard M. Seugling[1], Jeffrey L. Klingmann[1], Elizabeth G. Dzenitis[1], Ethan T. Alger[2], George L. Miller[1], Robert A. Kent[1], Carlos Castro[1], Jack L. Reynolds[1], Manuel A. Carrillo[1]
[1]Lawrence Livermore National Laboratory, Livermore, CA, USA
[2]General Atomics, San Diego, CA, USA

INTRODUCTION

This paper provides an overview of the design and testing of a robotic system developed for assembling the inertial confinement fusion ignition targets (depicted in Figures 1 and 2) that will be fielded on the National Ignition Facility (NIF) laser [1]. The system, referred to as the Final Assembly Machine and shown in Figure 3, consists of six groups of stacked axes that allow manipulating millimeter-sized components with submicron precision, integrated with an optical coordinate measuring machine (OCMM) that provides in-situ metrology. Nineteen motorized axes and ten manual axes are used to control the position and orientation of five objects that are predominantly assembled together in a cubic centimeter work zone. An operator-in-the-loop provides top-level control of the system, making it more similar to a surgical robot than to a programmed computer-controlled machine tool. The operator is provided visual feedback by the vision system of the OCMM, and tactile feedback by force and torque sensors embedded in the tooling that holds the major components being assembled. The vision system is augmented with auxiliary mirrors providing multiple viewing directions, and is used to guide the approach and alignment of the components, and to measure the relative position and orientation of the components. The force and torque sensors are used to guide the final approach, alignment, and mating of the components that are designed to slip–fit together, and to monitor that mating while adhesively bonding those components and attaching the target base.

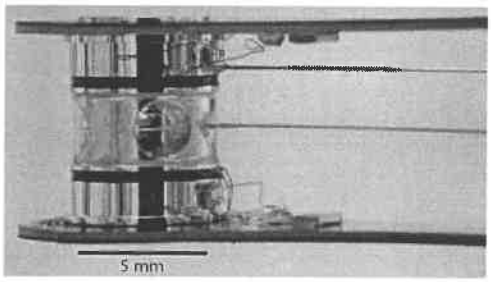

FIGURE 1. A prototype NIF ignition target.

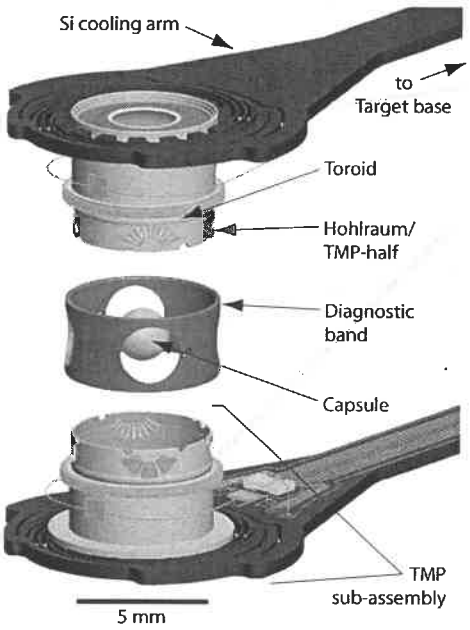

FIGURE 2. Model of a NIF target (exploded).

MOTIVATION FOR DEVELOPING THE FINAL ASSEMBLY MACHINE

The National Ignition Campaign [2] goal of achieving thermonuclear fusion burn and gain with the NIF laser requires building at least one target per day while maintaining flexibility to accommodate changes in target parameters governed by the evolving physics requirements expected during the campaign. Referring to Figure 2, the target is designed so that the physics package (hohlraum inner-liner, fuel-filled capsule, and the gas between them) can be tailored somewhat independently of the thermal–mechanical package that holds it (the TMP-halves, diagnostic band, and cooling arms). The required position accuracy of the assembled target components is in the range of $\pm$ 2–20 μm. Historically, building

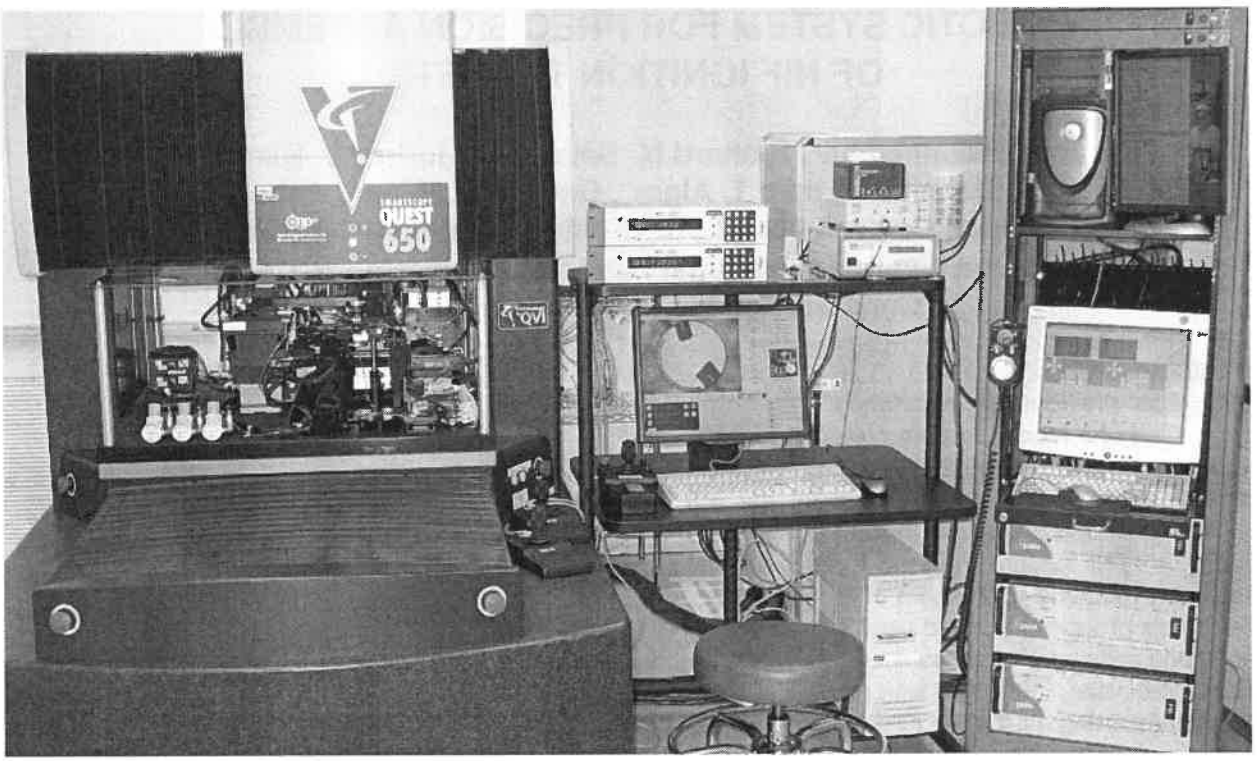

FIGURE 3. The NIF Ignition Target Final Assembly Machine: Manipulation System integrated with an optical coordinate measuring machine (left); operator console and display for the OCMM (center); and operator console and displays for the Manipulation System (right).

inertial confinement fusion targets depends on a significant amount of hand-crafting skill and technique involving manually-driven fixtures for guiding components together. Using that method, building a target like the one shown in Figure 1 used to require a one week effort by a team of two to three people; increases in efficiency and incremental gains in equipment roughly halved that time. The Final Assembly Machine provides the needed transformation in how the targets are assembled: the motorized slides in the Manipulation System provide the precise and repeatable motion needed for assembling a target, the force and torque feedback allows an operator to more deterministically engage the components being assembled, and the in-situ metrology enables the requisite alignment of components during the assembly process and provides an immediate verification of the accuracy of the as-assembled target. The Final Assembly Machine is on track for meeting its major goal of allowing one person to build a target in one day while improving the quality of the target and the repeatability of that quality.

OVERVIEW OF THE SYSTEM

Designed to operate in a class 1000 clean room, the Final Assembly Machine (Figure 3) consists of an LLNL-developed Manipulation System, a commercial optical coordinate measuring machine (OCMM), and an operator station comprising controllers, displays, joysticks, and a handwheel-pendant. A close-up view of the Manipulation System is shown in Figure 4. Each stage–stack provides its target component with the requisite translational and rotational degrees of freedom. Target components are held by a vacuum chuck at the distal end of the tooling that attaches that component to its stage–stack. Incorporated in the proximal ends of the tooling are kinematic or semi–kinematic mounts that provide accurate remove–and–replace orientation of the tooling. One of the more significant challenges during the design phase for the Manipulation System was maintaining a relatively open assembly arena (the zone where the target components come together) while providing the total of twenty-nine degrees of freedom for the five objects being assembled (nineteen motorized and ten manual).

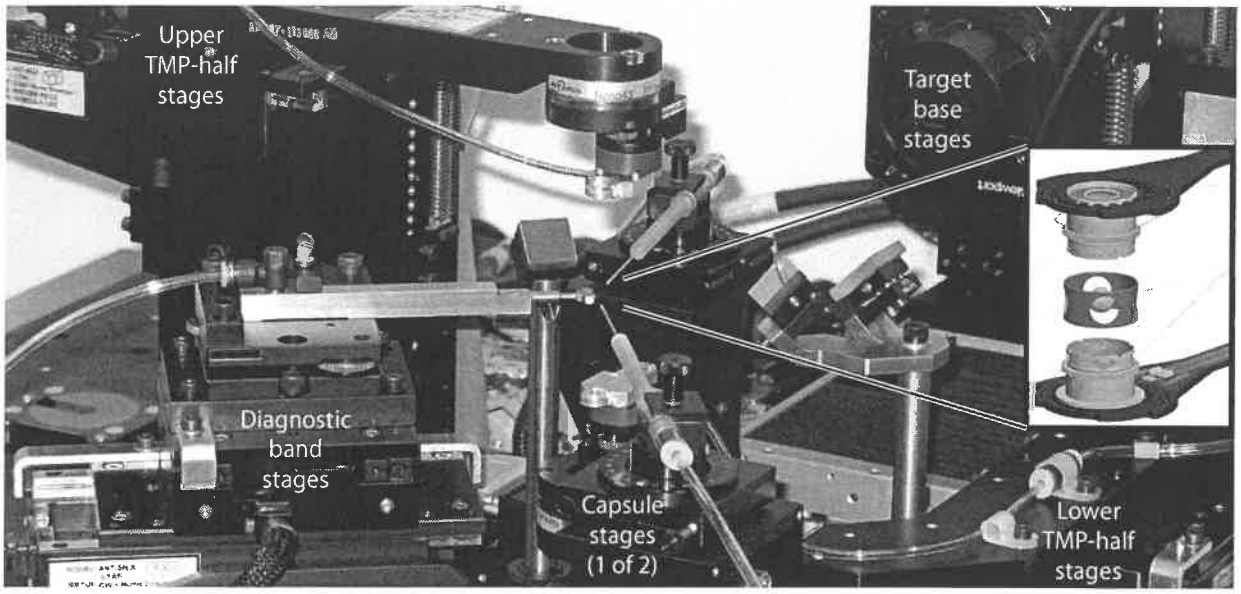

FIGURE 4. Manipulation System for assembling the NIF ignition targets, with model of a target.

Kinematic mounts allow accurate remove–and–replace of the auxiliary mirrors that provide the OCMM with multiple viewing directions into the assembly arena, and of the capsule stage–stacks that occupy the same region as some of those mirrors and the target base, albeit during different times during the assembly process. Commercial linear motor–driven crossed–roller bearing slides were selected for the majority of the actuated degrees of freedom because their compactness allowed integrating them into tightly–packed stage–stacks, and their repeatable motion and positioning resolution of 25 nm and 1 μrad met our requirements. Figure 5 shows how closely the lens of the OCMM approaches the Manipulation System when positioned for a side–view of the assembly arena. Because the control systems for the Manipulation System and the commercial OCMM are independent of each other, significant operator vigilance is required to avoid a collision between the two systems. Errors in this regard are initially accommodated by a pressure-activated emergency–stop switch in the OCMM, setting low over-current limits on the linear motor-driven stages so that they have low break-away forces, and the addition of an operator's dead-man enable switch for driving the OCMM optics assembly below the top of the Manipulation system. We plan to transfer the Manipulation System to a similar OCMM having a higher bridge and longer working–distance lens, eliminating the possible interference between the two systems.

FUTURE WORK

Ideally, all of the degrees of freedom needed for manipulating the target components during the assembly process would be motorized. For instance, when an operator reaches into the assembly arena to align the orientation of one component with respect to another, the tooling deflects due to the pressure of the operator's hand, and target components, tooling, and fixtures in the area are at risk of being bumped. One trade-off during the design phase was to retain the TMP-half tooling and manual pitch/roll/yaw stage

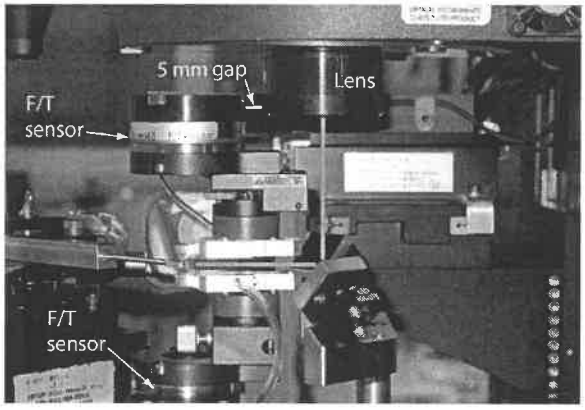

FIGURE 5. Side-view of the assembly arena, with the lens of the OCMM positioned over a mirror that provides a horizontal-direction view of the components being assembled. The force/torque sensors are centered on the TMP-halves.

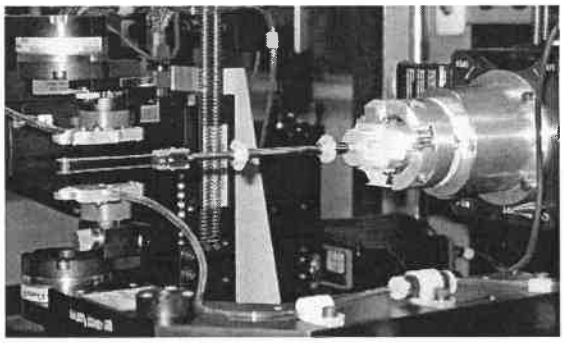

FIGURE 6. A prototype NIF ignition target that was assembled and mounted to its base using the Final Assembly Machine.

used in previous target assembly stations, instead of developing a compact motorized pitch/roll/yaw stage and new tooling that would fit into the space available. This choice allowed a shorter development path to fielding a system that provides an early proof-of-principle demonstration of other, more critical aspects of the Final Assembly Machine. A significant drawback of that choice is that the rotation axes of the manual pitch/roll/yaw stages do not pass through the desired pivot points on the TMP-halves. This results in unwanted translations of a TMP-half when adjusting its orientation, which precludes adjusting the orientation of a TMP-half after it engages the diagnostic band. Moreover, those manual stages require that an operator reach into the assembly arena to adjust them. If these issues unacceptably limit the target assembly process or quality of the targets, we have a contingency plan to replace those stages with custom motorized stages and new tooling. In this case, all six degrees of freedom of each TMP-half would be motorized. A possible follow-on is to add a haptic interface consisting of two force/torque reflecting joy sticks; providing the operator with a more intuitive feedback of the forces and torques developed between the TMP-halves and diagnostic band. Currently, all of the feedback to an operator is visual: displacements of the components being assembled and the forces and torques between the major components are displayed in graphical user interfaces. Controlling sub-micron machine motion of multiple objects with only visual feedback requires a high level of operator skill and sustained vigilance. By allowing the operator to feel amplified representations of the critical forces and torques, the aggregate feedback information (displacements, forces, and torques) can be split between two functionally parallel processing paths in the operator's mind. Compared to a visual-only feedback system, being able to see the relative position of the components in a vision system while feeling an amplified representation of their contact via a haptic interface will enhance an operator's skill level while reducing fatigue, leading to quality and productivity gains in the assembled NIF ignition targets.

CONCLUSION

The Manipulation System has been used to assemble prototype NIF ignition targets, both off of the OCMM (with the use of a microscope) and after it was integrated with the OCMM to form the Final Assembly Machine. Figure 6 shows one of these targets, assembled in one day by one person on the Final Assembly Machine, fourteen months after starting this project. The combination of the deterministic motor-driven motion, force and torque feedback, in-situ metrology, accurate remove–and–replace tooling and fixtures, and relatively open assembly arena present in Final Assembly Machine successfully demonstrated that it provides the needed transformation in how inertial confinement fusion targets are assembled.

ACKNOWLEDGEMENTS

In accomplishing this work, we acknowledge the helpful contributions and support of Jeff Atherton, Evan Mapoles, Abbas Nikroo, John Taylor, Robert Bates, Jim Ferguson, Carolyn Vargas, Steve Gross, Daniel Stefanescu, Jim Sater, Joe Florio, Jim Peterson, Suhas Bhandarkar, Michael Stadermann, Monica Witte, Ray Sadre, John Noriega, Robert Bickel, James Pryatel, John Burmann, Russell Jones, John Metz (Aerotech, Inc.), John Hammond (Indicate Tenconlogies, Inc.), Sam Skuce (ATI Industrial Automation), and Keith Blanchet (Quanser, Inc.).

This work performed under the auspices of the U.S. Department of Energy by Lawrence Livermore National Laboratory under Contract DE-AC52-07NA27344 and by General Atomics under Contract DE-AC52-06NA27279.

REFERENCES

[1] National Ignition Facility Programs. http://www.llnl.gov/nif/.

[2] National Ignition Campaign. https://lasers.llnl.gov/programs/nic/icf/.

ROTARY-AXIAL SPINDLES FOR PRECISION MANUFACTURING

Xiaodong Lu[1], Matthew Paone[1], Irfan Usman[1], Alexander Slocum[2], Akinori Yui[3]
[1]The University of British Columbia, Vancouver, British Columbia, Canada
[2]Massachusetts Institute of Technology, Cambridge, Massachusetts, USA
[3]National Defense Academy of Japan, Yokosuka, Kanagawa, Japan

INTRODUCTION

In manufacturing processes such as turning, milling, and grinding, machine tool spindles are usually supported by a Z axis. This requires the spindle to have its own thrust and radial bearings and the Z axis to have an actuator with secondary thrust and lateral support, as shown in Figure 1(a). The serial duplication of bearings reduces stiffness, degrades precision, and increases heat generation. Our novel solution is to construct a spindle that combines rotary motion and axial in-feed motion on a single moving rotor to achieve stiffer structural loops with fewer components, negating the need for a separate Z axis support. In the literature, there exist a number of spindle designs capable of both axial and rotary motions [1][2][3], and typically voice-coil or moving-magnet motors are used as thrust actuators. In this paper, we present a rotary-axial spindle, in which the Z axis position is controlled by a new magnetic bearing with millimeter range stroke and several thousand Hz bandwidth.

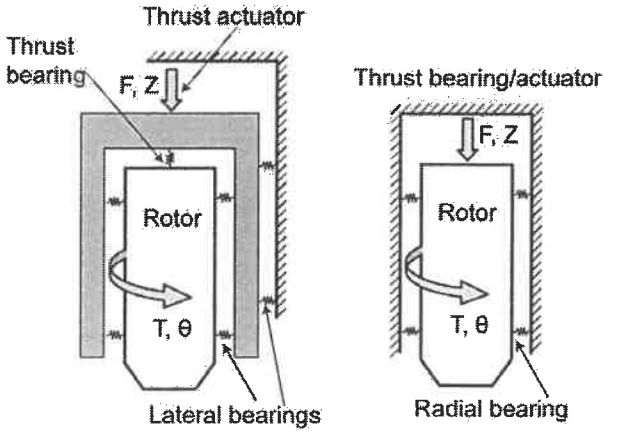

(a) Spindle on a linear slide (b) Rotary-axial spindle

FIGURE 1.Layout of Z-axis spindle.

ROTARY-AXIAL SPINDLE CONCEPT

Figure 1(b) shows the rotary-axial spindle concept: the rotor is radially supported with pressurized fluid journal bearings, axially with a thrust bearing/actuator, and azimuthally driven by a brushless rotary motor. As a result, the floating rotor mass can be independently actuated in the rotary (θ) or axial (Z) directions. This layout eliminates serially-connected redundant bearings, reduces machine component numbers, shortens the structure loop, and results in higher stiffness, better precision, and simultaneously lower cost.

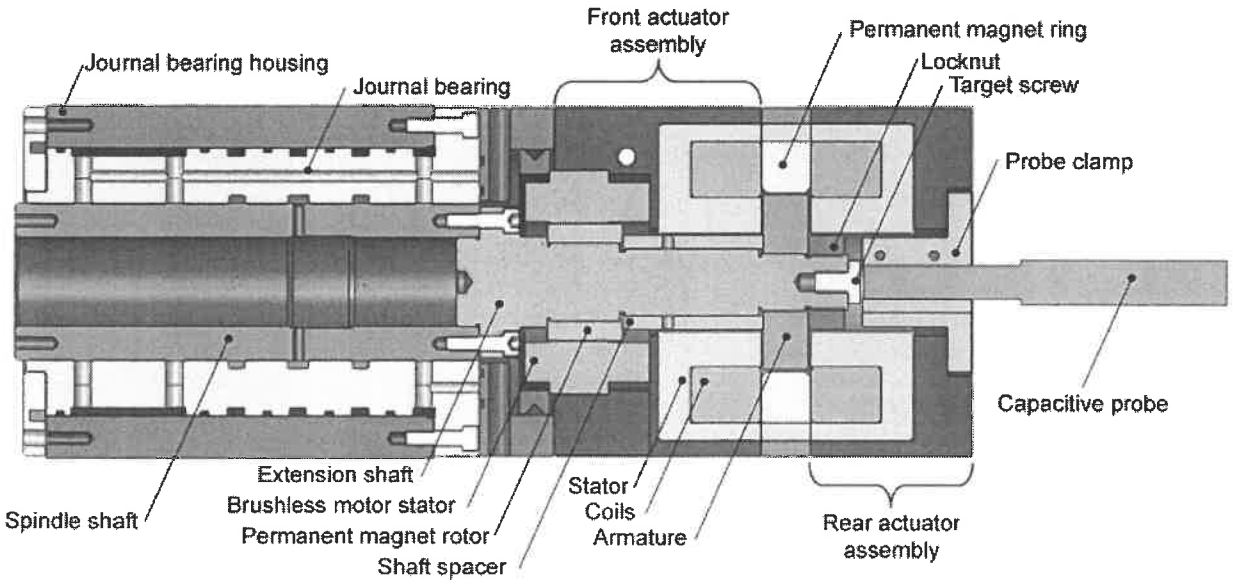

FIGURE 2. Sectioned view of the rotary-axial spindle prototype.

ROTARY-AXIAL SPINDLE DESIGN

Figure 2 shows a sectioned view of our first rotary-axial spindle prototype, which is modified from a commercial aerostatic spindle (Precitech SP-75) by replacing the aerostatic thrust plate (3" OD and 0.5" thick) with an magnetic bearing armature (2" OD and 0.5" thick). From the left to the right, the spindle includes an aerostatic journal bearing, a brushless rotary motor and a magnetic thrust bearing. Figure 3 shows a solid model of the shaft assembly, including a journal bearing surface, a rotary motor magnet, a thrust magnetic bearing armature, and a target screw for axial position sensing. The actuator stator is composed of front coils, stator cores, rear coils, and a ring-shaped permanent magnet for providing bias flux radially into the armature circumference. Finally, a probe holder clamps a capacitance probe into the rear end of the spindle. The capacitance probe axially looks at the sensing surface of the target screw. Figure 4 shows the fully assembled rotary-axial spindle prototype.

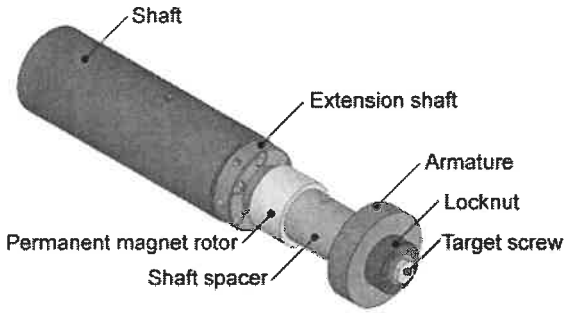

FIGURE 3. Moving assembly.

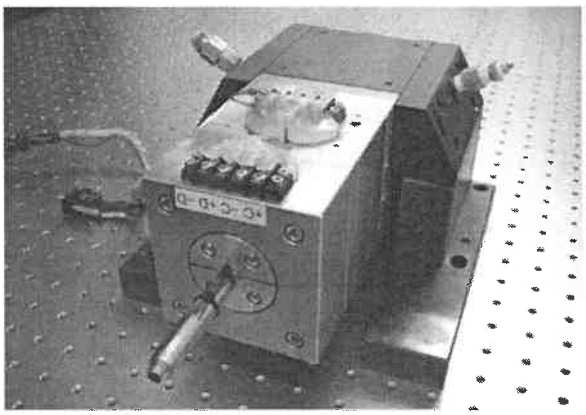

FIGURE 4. Rotary-axial spindle prototype.

The thrust actuator design is an axis-symmetric version of the normal-stress actuator used for the ultra-fast tool servo [4]. The permanent magnet ring is composed of 12 pieces of linearly magnetized permanent magnet arcs. Two excitation coils work together to deliver a steering flux, which controls the force applied to the armature. Two 0.5 mm gaps on each side of the armature combine for a 1 mm working stroke. The armature and stator are made of powdered iron to reduce eddy current effects. A 1 kW linear current amplifier with 60 kHz bandwidth controls the actuator current. The experiment results demonstrate that this rotary-axial spindle prototype has 600 N axial load capacity, 1 mm stroke, 5 nm axial positioning error, infinite static stiffness, and 9000 rpm rotary speed.

ROTARY-AXIAL SPINDLE CONTROL

Rotary and axial motions are designed independently. The rotary control loop runs at 10 kHz sampling rate and the axial loop at 100 kHz.

Rotary Control

Conventional optical encoders typically require 100 um fixed gap between its read heads and disk. Due to the large axial motion of the rotary-axial spindle, the optical encoder in the original spindle has to be abandoned. Instead, the three Hall-effect sensors used for commutating the motor are used to provide rotary position information. As the rotary motor has eight poles, 24 rotary positions in each revolution can be generated directly from the Hall-effect signal rising/falling. By appropriate interpolation, a final resolution of 6144 counts/rev is achieved. Figure 5 shows the block diagram for the rotary control loop. When the spindle rotary position θ is measured by the Hall-effect sensor, both quantization error θ_q and nonlinear error θ_n are introduced. Through a differential operation scaled by sampling time T_s, we can get speed measurement ω_1.

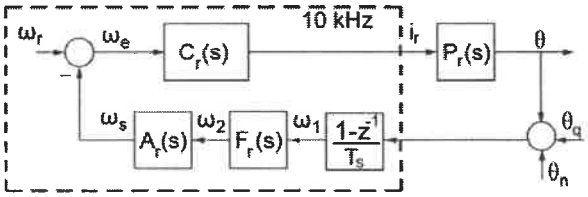

FIGURE 5. Rotary block diagram.

Figure 6 shows the measured plant frequency response from the motor current command i_r to the rotational speed ω_1, using swept sine waves. The response below 40 Hz behaves like a free mass, but the magnitude slope changes to 20dB/decade at higher frequencies. In fact, the Hall-effect sensor measures the rotary displacement between the rotor and the Hall

sensor. The reaction torque applied on the motor coil can reversely rotate the Hall-effect sensor due to the finite torsional stiffness of its underlying coil. As a result, at high frequencies the Hall effect sensor measures the motion of itself rather than the rotor motion. The zeros at 40Hz limit the achievable bandwidth of the rotary speed control.

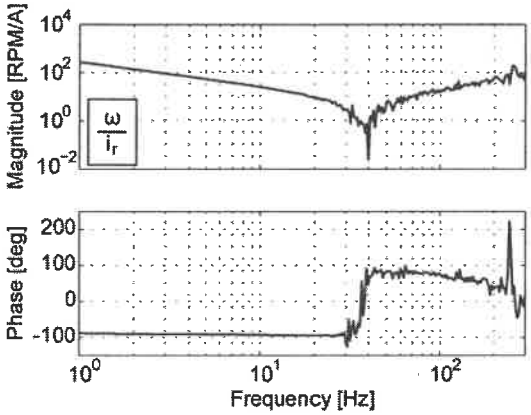

FIGURE 6. Rotary plant frequency response

In order to eliminate the quantization error and roll off the high-frequency response, a 4-th order low pass filter $F_r(s)$ with 100 Hz cutoff is placed in the feedback loop:

$$F_r(s)=\left(\frac{1}{2.5\times10^{-6}s^2+3.2\times10^{-3}s+1}\right)^2 \quad (2)$$

Further to remove the nonlinear error, which is harmonic of the spindle rotation frequency, a notch filter $A_r(s)$ with zeros at these frequencies is included as shown in Figure 5:

$$A_r(s)=\frac{T_s}{T_a}\frac{1-e^{-sT_a}}{1-e^{-sT_s}}, \quad (3)$$

where T_a is the period of spindle rotation and T_s is the sampling time. The speed regulation is performed by a proportional-integral controller $C_r(s)$, which results in 10 Hz of the unity gain loop transmission crossover frequency (Figure 7) and 17.5 Hz of the closed-loop bandwidth. Figure 8 shows the 100-rpm step response of the rotary speed control loop, and the peak time is 0.05 sec which corresponds with half of the period at the crossover frequency. The RMS speed regulation error is 0.194 RPM as shown in Figure 9. This result is as good as that of using 1000 line optical encoders when testing on the original aerostatic spindle.

Axial Control

The axial actuating force F [N] is proportional to both the excitation current i_a [A] and the axial displacement Z [μm]: $F(z,i_a)=1.01z+118i_a$.

Figure 10 shows the frequency response $P_a(s)$ from the excitation current i_a to Z.

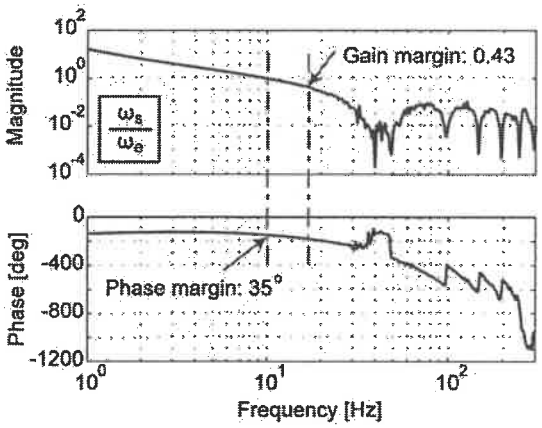

FIGURE 7. Negative loop transmission of the rotary control system

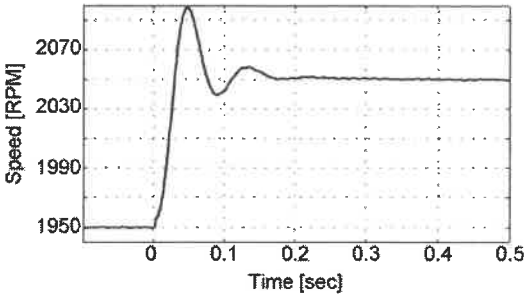

FIGURE 8. 100 RPM step response of the closed rotary control loop

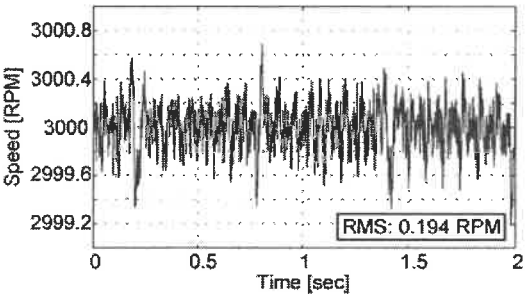

FIGURE 9. Speed regulation noise

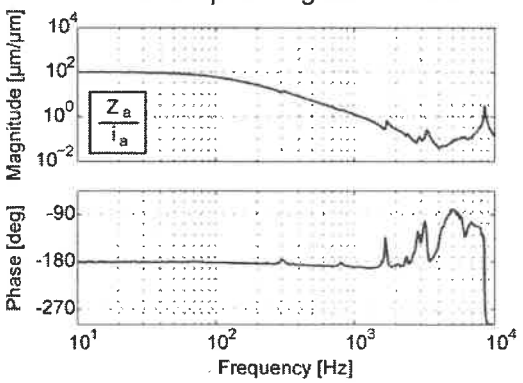

FIGURE 10. Axial plant frequency response

The region from DC to 120 Hz is dominated by the destabilizing negative spring effect of the magnetic actuator. From 120 Hz to 1 kHz, the frequency response shows a free moving mass with the magnitude slope of -40 dB/decade. Higher than 1 kHz, several vibration modes are excited. Two collocated modes occur at 1730 Hz and 3300 Hz, and a non-collocated mode occurs at 8500 Hz. These resonances are the shaft bending modes.

A block diagram of the axial control loop is shown in Figure 11 .Our controller consists of a loop-shaping term $C_a(s)$ and an integrator to eliminate steady state error. $C_a(s)$ contains two notch filters at 3300 Hz and 8500 Hz for resonance attenuation, a double lead-lag compensator to increase phase margin from 1 kHz to 3 kHz, and a series of low pass filters to roll off the high frequency response. Figure 12 shows the experimentally measured frequency response of the compensated negative loop transmission. The resulting -3dB closed-loop bandwidth is around 2 kHz. A 400 nm step response is shown in Figure 13. The frequency spectrum of the closed-loop position noise is shown in Figure 14. The RMS position noise is only 4.78 nm, which is mainly the electrical noise of the capacitive probe.

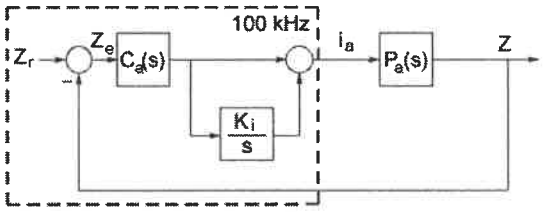

FIGURE 11. Axial system block diagram

CONCLUSIONS

A rotary-axial spindle prototype has been built and tested. Both the axial and rotary motions can be actuated independently and with a high degree of precision. Investigating machining performance is in the future research plan.

ACKNOWLEDGEMENTS

The authors would like to thank Precitech for providing the spindle and Aerotech for providing the motor and amplifier.

REFERENCES

[1] Liebman, M. K., Rotary-Linear Axes for High Speed Machining, MIT PhD Thesis, 2001.

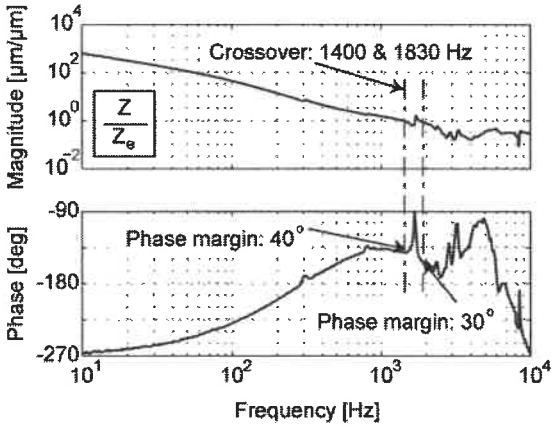

FIGURE 12. Axial negative loop transmission

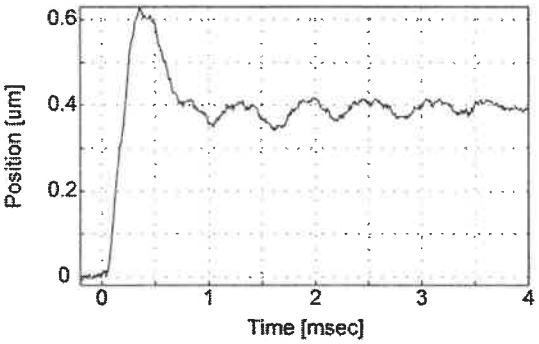

FIGURE 13. Step response of the axial loop.

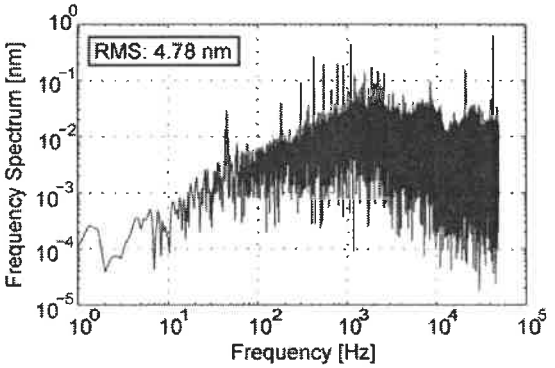

FIGURE 14. FFT of closed-loop position noise.

[2] Zhang, X., *et al*, Micro Electrical Discharge Machining Using a 5-DOF Controlled Maglev Actuator, Proc. of ASPE 2007 Annual Meeting, 36-39, 2007.

[3] Shinshi, T., *et al*, A Compact Aerostatic Spindle Integrated with an Axial Positioning Actuator for Micro and Ultra-Precision Machine Tools, Int. Journal of Automation Technology, Vol. 2, No. 1, 56-63, 2007.

[4] Lu, X.-D., Trumper, D. L., Ultra Fast Tool Servos for Diamond Turning, Annals of the CIRP, Vol. 54, No. 1, pp. 383-388, 2005.

DESIGN AND TEST OF A 2-D PRECISION WEAK-LINK STAGE SYSTEM WITH SUB-CENTIMETER TRAVEL RANGE AND SUB-NANOMETER RESOLUTION

Deming Shu[1] and Jorg Maser[2,1]

[1]Advanced Photon Source
[2]Center for Nanoscale Materials
Argonne National Laboratory
Argonne, IL 60439, U.S.A.

INTRODUCTION

Recent developments in hard x-ray focusing at the nanometer scale with linear multilayer Laue lenses (MLLs), as reported by H. C. Kang et al. [1], have demonstrated promising new x-ray optics for focusing hard x-rays to a spot of a few nanometers. To use x-ray optics with a nanometer-scale resolution limit, scanning x-ray nanoprobes with corresponding mechanical positioning capability need to be designed. In particular, positioning stages with both sub-nanometer resolution and a positioning/scanning range of several millimeters is required.

Based on our design of precision weak-link stages with interferometric encoders for the Center for Nanoscale Materials (CNM) /Advanced Photon Source (APS) hard x-ray nanoprobe at APS Sector 26 [2,3], we have developed a new two-dimensional (2-D) weak-link stage system for nanopositioning of a specimen holder. This system provides sub-nanometer resolution, coupled to sub-nanometer metrology, and a travel range of several millimeters. The 2-D weak-link stage system is designed with high structure stiffness using laminar overconstrained weak-link mechanisms [4,5].

Unlike traditional kinematic linear spring mechanisms, the overconstrained laminar weak-link mechanism provides much higher structure stiffness and stability. Using laminar structures configured and manufactured by chemical etching and lithography techniques, we were able to design and build planar-shape, high-precision weak-link modules. The precision of modern photochemical machining processes using lithography techniques makes it possible to construct a strain-limited overconstrained structure from thin metal sheets. By stacking these thin-metal weak-link sheets with alignment fixtures, we can construct a solid, complex, thick, weak-link module at a reasonable cost [6].

More than 40 sets of laminar weak-link mechanisms have been made for APS users to apply in synchrotron radiation precision-instrumentation applications, such as rotary stages for high-energy-resolution monochromators with 10-nrad-level angular resolution and linear scanning stages for x-ray nanoprobes with sub-100-pm level resolution [7]. In this paper we present a novel precision linear weak-link stage system using laminar weak-link mechanisms with sub-centimeter travel range and sub-nanometer positioning resolution. Finite-element analyses and test results with a laser Doppler displacement meter are also presented.

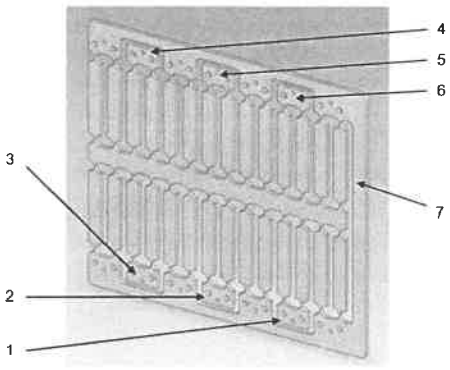

FIGURE 1. A 3-D model of the fishbone-shaped multiple parallelogram weak-link structure. Items (1) to (6) are terminals mounted to the fixed base. Item (7) is the moving part.

THE LAMINAR WEAK-LINK STRUCTURE

Figure 1 shows a three-dimensional (3-D) model of a "fishbone"-shaped multiple parallelogram weak-link structure [8]. The 2-mm-thick 118 mm

x 116 mm weak-link module is a bounded laminar structure with eight thin-metal weak-link sheets. There are two groups of mounting terminals on the weak-link module: terminals 1-6 are terminals for a mounting base and terminals on frame 7 are mounted on a carriage. Figure 2 shows a finite-element simulation for a 1.61-mm displacement of the carriage. In this simulation, a 17-N force is applied on the carriage and the maximum Von Mises stress is 974 MPa, which is about 81% of the tensile yield strength of the stainless steel 17-7 PH, as shown in Fig. 3. The simulation shows that, if the carriage is driven by the same level of push-pull force, the weak-link linear stage will have a travel range of 3.22 mm.

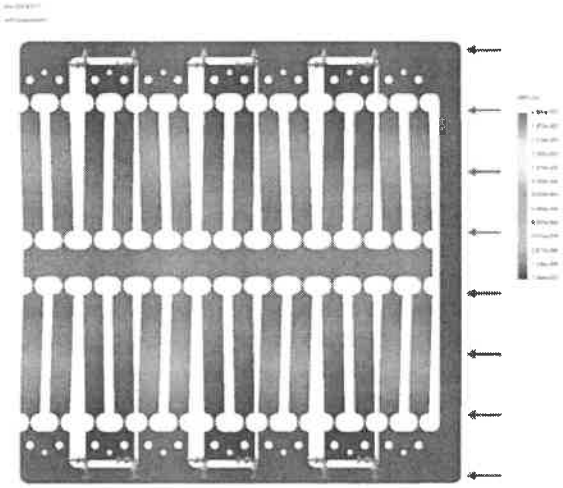

FIGURE 2. A finite element analysis result for displacement of the multiple parallelogram weak-link structure.

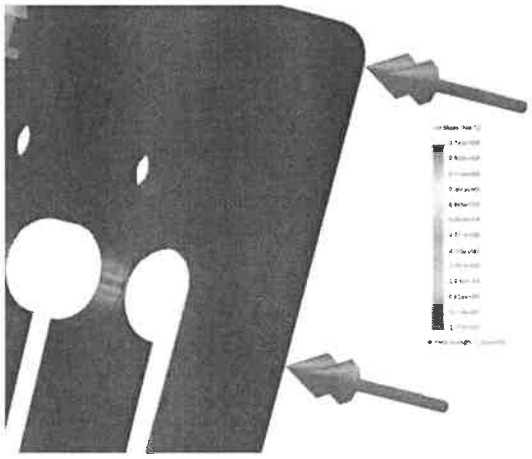

FIGURE 3. Maximum Von Mises stress result from a finite element analysis for the multiple parallelogram weak-link structure.

STRAIGHTNESS OF THE TRAJECTORY TEST

To test the straightness of trajectory for the new weak-link module, a test stage for the single weak-link module has been constructed as shown in Fig. 4. The test was performed with a commercial dual-beam laser Doppler displacement meter with a 0.9-μrad resolution. A 3-mm travel range is demonstrated in the test with 3- to 4-μrad tilt errors in the middle of the 2.4-mm travel range.

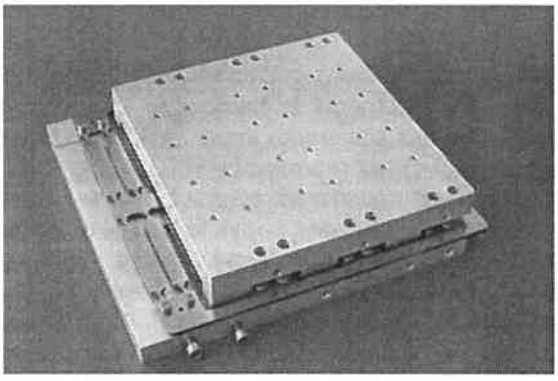

FIGURE 4. Photograph of a test stage for the single weak-link module with a 3-mm travel range, sub-nanometer resolution, and μrad-level straightness of trajectory.

DRIVING FORCE AND STIFFNESS TEST

Figure 5 shows a driving force test result for the single weak-link module stage. The test result shows that a 3.19-mm displacement was achieved when a ±18-N force is applied on the carriage. This result is in close agreement with the finite-element simulation. Lateral stiffness is also tested with centered and offset forces.

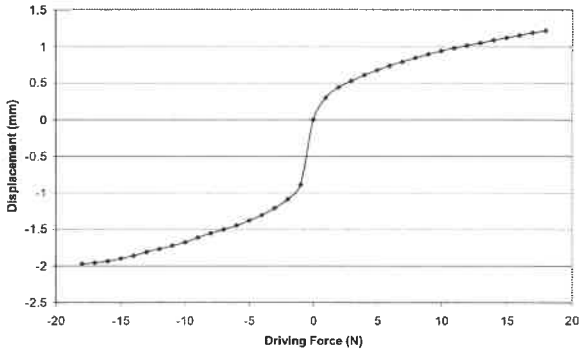

FIGURE 5. Test result of the driving force for the single weak-link module stage.

2-D PRECISION WEAK-LINK STAGE

For scanning microscope instrumentation developers, it is always a dream to have a compact single stage to cover large travel range with very high positioning resolution. Based on the fishbone-shaped laminar weak-link structure design, we are exploring the feasibility to build a weak-link-based precision linear guiding system with sub-nanometer resolution and sub-centimeter travel range with a reasonably compact size.

Design of the Vertical Stage

Using four fishbone-shaped laminar weak-link modules, we have designed a vertical weak-link stage, APS T8-31, for a scanning sample stage system as shown in Figures 6 and 7. It is part of a hard x-ray nanoprobe test setup for MLLs to be tested at APS Sector 26.

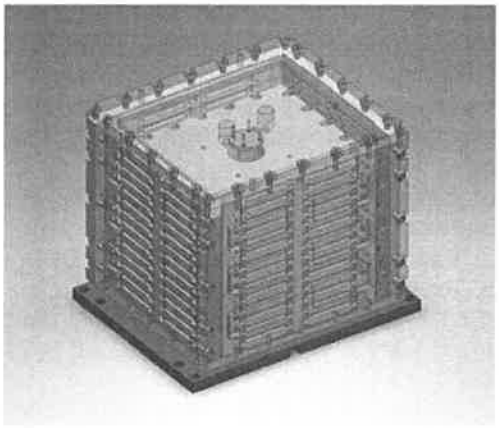

FIGURE 6. A 3-D model of the vertical weak-link stage APS T8-31.

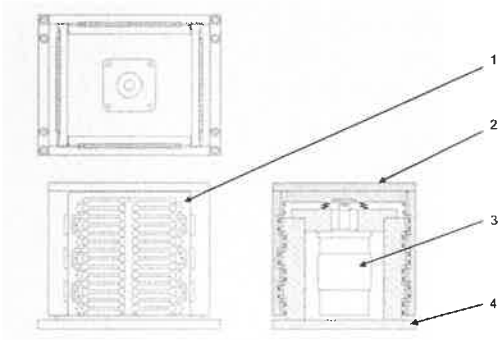

FIGURE 7. Design of a vertical ultra-precision stage with 4-mm travel range and sub-nanometer positioning resolution. (1) Fishbone-shaped multiple parallelogram weak-link structure. (2) Moving parts. (3) Commercial linear actuator. (4) Fixed base.

We have two choices for the vertical stage driver. Figure 7 shows the option to use a commercial PZT-based nanopositioning motor, such as the N-214 NEXLINE motor provided by PI GmbH and Co. [9]. With an N-214 driver, the T8-31 weak-link stage has a 10-kg load capacity, 3-mm travel range with 10-nm closed-loop resolution, and sub-nanometer resolution within a 3-μm step. For applications that needs long scanning range with sub-nanometer resolution, a laser Doppler displacement meter (LDDM)-based encoder with sub-nanometer resolution [10,11] will be equipped for the stage positioning closed-loop feedback system. A customized stepping-motor-driven linear driver combined with a PZT actuator will provide the driving force for sub-nanometer-level closed-loop resolution in the entire 3-mm travel range.

Design of the Horizontal Stage

As shown in Figure 8, the horizontal-stage APS T8-32 consists of three laminar weak-link modules with an inverse "U" configuration for a 5-kg load capacity. As for the vertical stage, there are two options for the stage's driver. Figure 9 shows the use of a N111 NEXLINE motor provided by PI GmbH and Co. [9]. It drives the T8-32 with 5 nm closed-loop resolution for a 3-mm travel range and sub-nanometer resolution within a 0.8-μm step. With a LDDM encoder system and a customized motor/PZT combined linear driver, the T8-32 stage has sub-nanometer level resolution for the entire 3-mm travel range.

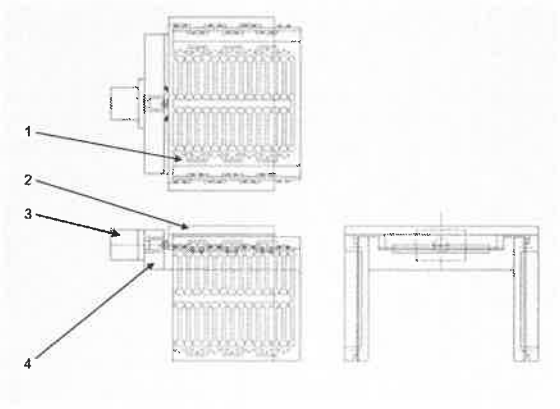

FIGURE 8. Design of a horizontal ultra-precision stage with 4 mm travel range and sub-nanometer positioning resolution. (1) Fishbone-shaped multiple parallelogram weak-link structure. (2) Moving parts. (3) Commercial linear actuator. (4) Fixed base.

Combination for a 2-D stage

The T8-32 horizontal stage is designed to fit on top of the T8-31 vertical stage to perform a 2-D sub-nanometer resolution scanning function in a 3 mm x 3 mm range for a nanoprobe sample holder with a maximum weight of 5 kg. Figure 9 shows the combined 2-D stage design.

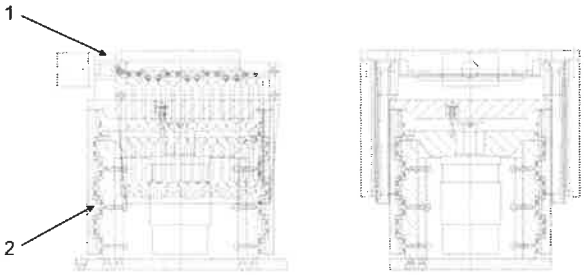

FIGURE 9. Design of a 2-D scanning stages assembly for x-ray nanoprobe applications. (1) Horizontal stage. (2) Vertical stage.

DISCUSSION

We present a novel mechanical design for laminar weak-link mechanisms with centimeter-level travel range and sub-nanometer positioning resolution. This design is a new development in applications of the redundantly constrained laminar structures as weak-link mechanisms. The novelty of this new mechanical design is its fishbone-shaped multiple parallelogram structure, which performs the function of a high-stiffness, high-precision linear motion guider with sub-centimeter level travel range and sub-nanometer positioning resolution.

Based on the results of finite-element simulation, it is feasible to scale up or scale down the overall dimension of the fishbone-shaped multiple parallelogram weak-link structure for variant nanopositioning applications. For instance, with the same 17-7 PH stainless steel material, a scaled-up laminar weak-link structure with an overall dimension of 350 mm x 350 mm x 6 mm will have a 1-cm travel range with sub-nanometer resolution. As an example for scale down applications, a weak-link structure with 18 mm x 18 mm x 0.3 mm overall size will have a 0.5-mm travel range for a Micro-Electro-Mechanical Systems device. This weak-link structure will provide a larger travel range if advanced structure material is used.

We continue to optimize the capabilities and explore the potential of this new weak-link design. Its potential applications could be in advanced developments of ultra-precision positioning stages for scanning x-ray nanoprobes, long-range scanning atomic force microscopes, and equipment for nanotechnology and the semiconductor industry.

ACKNOWLEDGEMENTS

This work is supported by the U.S. Department of Energy, Office of Science, Office of Basic Energy Sciences under Contract No. DE-AC02-06CH11357.

REFERENCES

[1] H. C. Kang et al., Phys. Rev. Lett. 96, 127401 (2006).
[2] J. Maser et al., Proc. 8th Int. Conf. X-ray Microscopy, IPAP Conf. Series 7 (July 2006) 26-29.
[3] D. Shu et al., Proc. 8th Int. Conf. X-ray Microscopy, IPAP Conf. Series 7 (July 2006) 56-58.
[4] U.S. Patent granted No. 6,607,840, D. Shu, T. S. Toellner, and E. E. Alp, 2003.
[5] U.S. Patent granted No. 6,984,335, D. Shu, T. S. Toellner, and E. E. Alp, 2006.
[6] D. Shu, T. S. Toellner, and E. E. Alp, Nucl. Instrum. Methods A 467-468, 771-774 (2001).
[7] D. Shu et al, SRI 2006, AIP CP879, (2007) 1073-1076.
[8] D. Shu and J. Maser, U.S. Patent application in progress for ANL-IN-08-013.
[9] Physik Instrumente (PI) is a trademark of the Physik Instrumente GmbH & Co. Germany.
[10] LDDM is a trademark of the Optodyne Inc., 1180 Mahalo Place, Compton, CA 90220, U.S.A.
[11] D. Shu, Y. Han, T. S. Toellner, and E. E. Alp, Proc. SPIE Vol. 4771 (2002) 78-90.

DESIGN, REALIZATION AND TESTING OF THE NANOMEFOS NON-CONTACT MEASUREMENT MACHINE FOR FREEFORM OPTICS

Rens Henselmans[1,2], Lennino Cacace[3], Nick Rosielle[1] and Maarten Steinbuch[1]
[1]Control Systems Technology, Mechanical Engineering faculty, Technische Universiteit Eindhoven, the Netherlands
[2]Precision Mechanics department, Advanced Precision and Production Equipment, TNO Science & Industry, Delft, the Netherlands
[3]AC Optomechanix, Eindhoven, the Netherlands

INTRODUCTION

By applying freeform optics (figure 1) in high-end optical systems such as used in space, science and lithography applications, system performance can be improved while decreasing the system mass, size and number of required components (for instance [1]). The applicability of classical metrology methods is limited for freeform surfaces, which is currently holding back their widespread application. TNO, TU/e and NMi VSL therefore initiated the NANOMEFOS project in 2004 [2]. The development of this universal non-contact and fast measurement machine with 30 nm uncertainty (2σ) for freeform optics up to ∅500 mm is now nearing completion.

FIGURE 1: Freeform surface example

CONCEPT

Freeform optics usually have up to a few mm departure from rotational symmetry. An optical probe is developed to enable high scanning speeds. While the optic is mounted on a continuously rotating air bearing spindle, the optical probe is positioned over it by a motion system (figure 2).

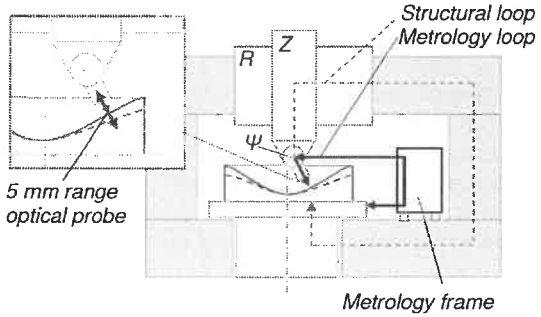

FIGURE 2: Schematic machine concept

The developed optical probe has 5 mm range to capture the departure from rotational symmetry of the surface, allowing the R,Z and ψ stages to be stationary when measuring a track. Such a circular track is measured several times to acquire sufficient data for averaging and drift compensation. This way, a surface can be measured in minutes. The position of probe and product is measured relative to a metrology frame in a separate metrology loop.

MOTION SYSTEM

The machine is shown in figure 3. An air bearing motion system positions the probe relative to the product, with sub-micron uncertainty in the out-of-plane directions. Here, an accurate plane of motion is provided by directly aligning the vertical stage to a vertical base plane on the granite base. Separate preload and position frames are applied throughout to minimize distortion and hysteresis, and the motors and brakes are aligned with the centers of gravity of the stages.

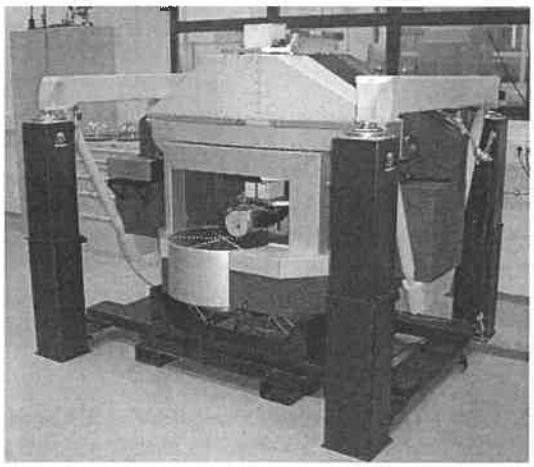

FIGURE 3: NANOMEFOS machine

For optimal positioning stability when measuring a track, the stages are braked by mechanical clamps, to exclude encoder, amplifier and EMC

noise. To test this stability, 3 orthogonal reference capacitive probes are mounted on the (stationary) spindle and measure to a target that is mounted to the ψ-axis, such that the measurement point coincides with the focal point of the later to be mounted optical probe. Figure 4 shows the measured relative displacement between spindle and probe tip in radial (R), out-of-plane (Y) and vertical (Z) direction. This is an indication of the stability of the structural loop.

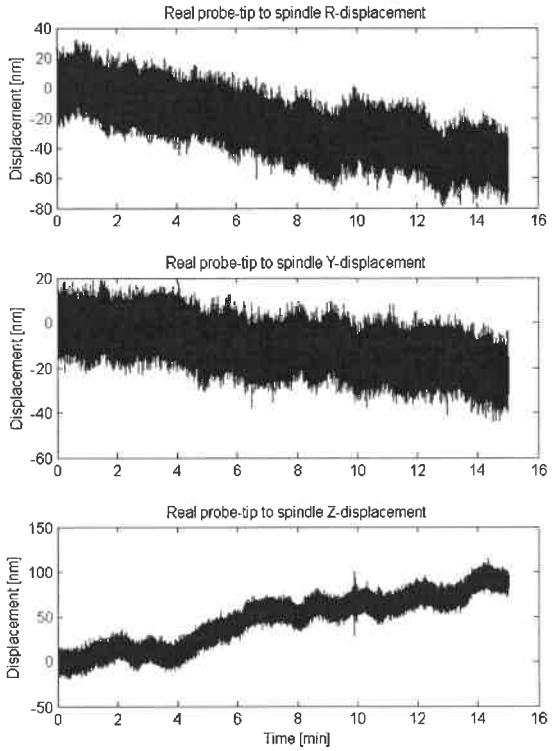

FIGURE 4: Displacement at the probe tip relative to the spindle, measured by reference capacitive probes

As can be seen, the position of the probe tip relative to the product has a noise level of 45 nm, 35 nm and 25 nm PV in R,Y,Z respectively. It is suspected that this is mainly caused by acoustic disturbances due to turbulent flow in the air-supply system. The drift over 15 minutes is typically 50 nm, 20 nm and 85 nm. A shock in the nearby workshop can further be seen at t = 10 minutes.

METROLOGY SYSTEM

As explained, the position of the probe is measured by a separate metrology system. A short metrology loop for the critical in-plane directions is obtained by directly measuring the probe rotation axis position interferometrically, relative to a metrology frame. A vertical and horizontal interferometer beam (Z IF and R IF in figure 5) measure the displacement of a cylindrical mirror on the face of the Ψ-axis, relative to mirrors on the metrology frame. This frame is mounted inside an Aluminum box that serves as a thermal shield. An angle encoder measures the ψ rotation of the probe.

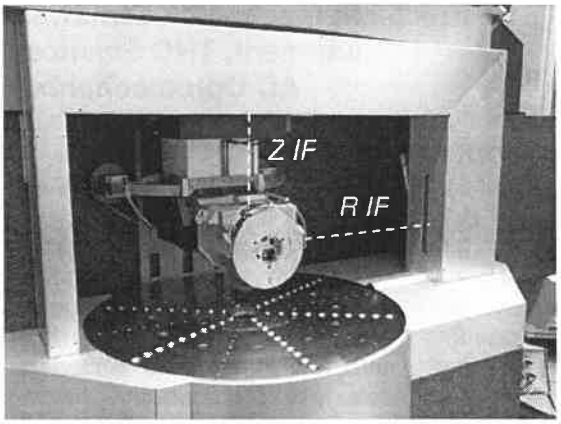

FIGURE 5: Interferometers of the metrology loop

Mechanical and thermal simulations resulted in Silicon Carbide as the preferred material for the metrology frame. The reference mirrors are polished directly onto the beams of this frame (figure 6), and it is mounted statically determined on SuperInvar struts. The thermal stability is simulated to be about 2 nm, and the first resonance occurs at 620 Hz.

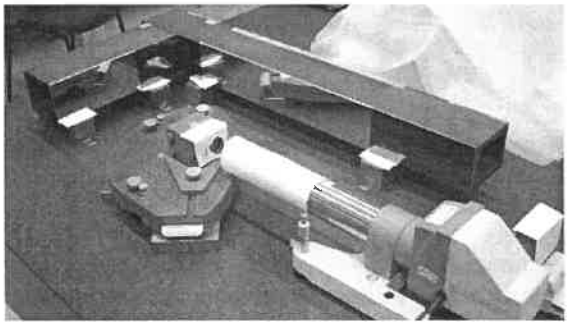

FIGURE 6: Silicon Carbide metrology frame during alignment

The product position is measured relative to this same frame with capacitive probes which measure the spindle error motion. The multi-probe method [3] is applied to separate roundness error of the reference edge and the spindle error motion in five degrees of freedom by Fourier decomposition. Simulations show nanometer level uncertainties. The method is currently being tested.

Figure 7 shows the real displacement in Z-direction during 0.1 s, as measured by the three reference capacitive probes as explained in the previous section (*Real*), and the displacement as calculated by combined results of the capacitive probes around the spindle and the interferometers in the metrology system (*Measured*).

As can be seen, most of the mechanical vibrations as shown in figure 4, are also measured by the metrology loop and thus cancel out. The 17 nm PV displacement is herewith reduced to 4 nm PV or 0.6 nm rms over 0.1 s.

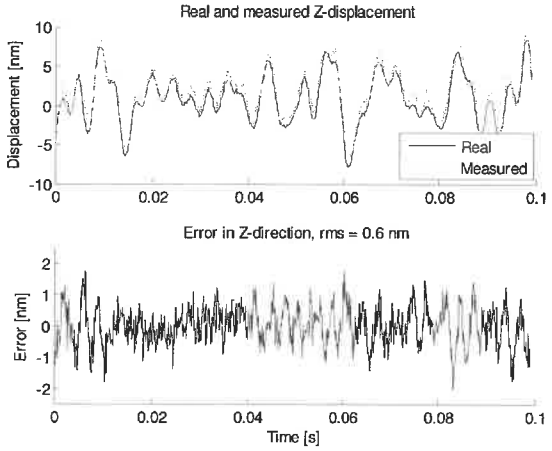

FIGURE 7: Short term measurement error in Z-direction

Similarly, the error in R,Y and Z-direction over the 15 minute measurement of figure 4 is shown in figure 8. Including the remaining drift, the error is 8.2 nm rms in R, 8.2 nm rms in Y and 2.3 nm rms in the (most critical) Z-direction. Five consecutive measurements show consistent results of 2.0 – 3.2 nm rms error in Z.

Almost all drift in the in-plane directions (R and Z) that was present in figure 4, has been eliminated by the metrology system. This also holds for the shock at 10 minutes. Refractive index changes of air are compensated with a pressure, temperature and humidity sensor. What remains is mainly air turbulence in the interferometer beams, since they operate in open air. The vibration levels in the R-directions are higher compared to the Z-direction due to the Abbe offset in this direction. Since the Z-direction would be normal to the surface to be measured in this case, this has most influence on the final shape measurement uncertainty that can be achieved.

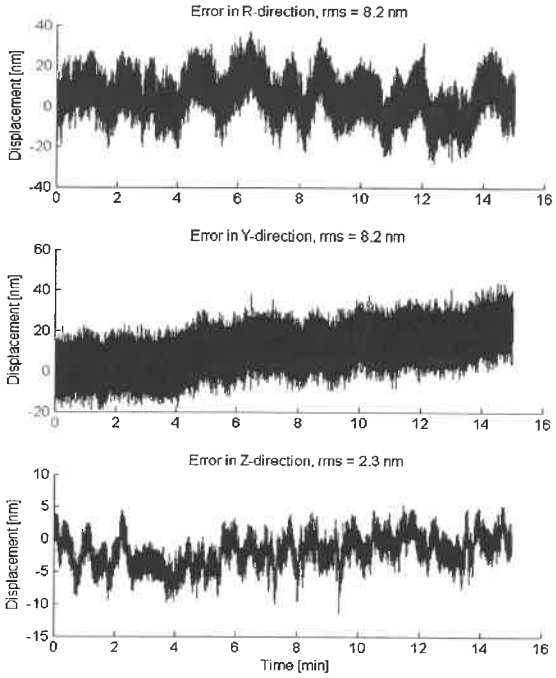
Error in R-direction, rms = 8.2 nm
Displacement [nm]
Error in Y-direction, rms = 8.2 nm
Displacement [nm]
Error in Z-direction, rms = 2.3 nm
Displacement [nm]
Time [min]

FIGURE 8: Resulting measurement error

OPTICAL PROBE

The optical probe concept is based on the differential confocal method, which has been optimized by analytical modeling and experiments with a test setup. The range is increased with an interferometer compactly integrated in series [4]. The focusing objective and interferometer mirror are guided by a flexure guidance and actuated by a voice coil. The interferometer measures the displacement of the objective, which results in a short metrology loop with minimal sensitivity to thermomechanic effects in the actuator. By FEM analysis the guidance was optimized to obtain a first resonance of 2 kHz and about 50 g of moving mass, resulting in an expected closed loop bandwidth of 700 Hz.

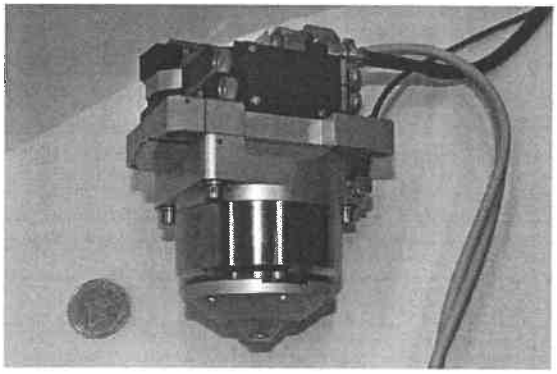

FIGURE 9: Optical probe

Figure 9 shows the developed optical probe. The differential confocal system was tested by scanning a mirror mounted on a piezo through the focus of the probe. The Focus Error Signal (FES) is shown in figure 10, which shows 55 consecutive measurements. The sensitivity at the zero-crossing is 5.5 V/µm. The measurement range is approximately 4 µm.

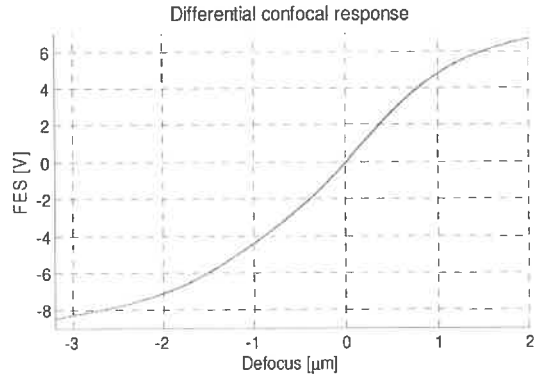

FIGURE 10: Focus error signal (FES)

The noise level is 0.15 nm rms at the zero crossing and 0.8 nm rms at the ends of the measurement range. The achievable measurement uncertainty was estimated by fitting a curve to the average of similar FES measurements 5 days earlier, as if it were a calibration result. Figure 11 shows the variation of the above 55 curves to this fit. It should be noted that the temperature was 0.7°C warmer at that time. A ghost interference determines most of the deviation, giving an rms error of 4.1 nm.

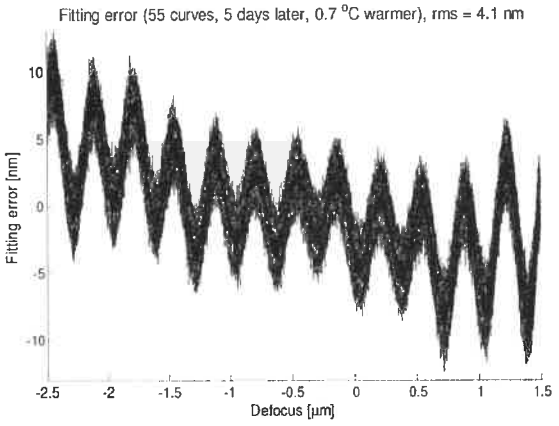

FIGURE 11: FES error relative to measurement of 5 days earlier

The extension of the range to 5 mm by scanning the objective and measuring its displacement with the interferometer has been tested separately, and full functionality of the probe will be tested when mounted onto the machine.

CONCLUSION

The realization and testing of the prototype, including the custom control software and electronics is now almost complete. After the optical probe is mounted, the stability and repeatability of the instrument will be further tested and traceable calibrations are performed by NMi VSL. Full surface measurements will follow to demonstrate the suitability of the new instrument for measuring freeform optics.

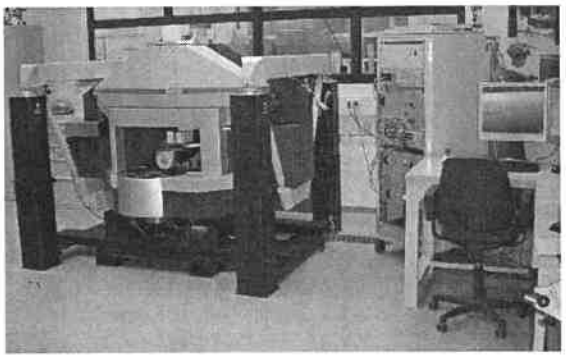

FIGURE 12: Current realization status

ACKNOWLEDGEMENT

This research is partially funded by the SenterNovem IOP Precision Technology program of the Dutch Ministry of Economic Affairs. It would not have been possible without the valuable contribution of many people from TU/e, TU/e GTD workshop, TNO and NMi VSL.

REFERENCES

[1] Winsor, R., et.al., *Optical design of an Infrared Multi-object spectrometer utilizing freeform optical surface, ASPE winter topical meeting, 2004*

[2] Henselmans, R., et.al., *NANOMEFOS – Nanometer Accuracy Non-contact Measurement of freeform optical surfaces,* ASPE winter topical meeting, 2004

[3] Whitehouse, D.J., *Some theoretical aspects of error separation techniques in surface metrology*, J. of Physics E, Vol. 9, 1976

[4] Cacace, L.A., et.al., Development of a new differential confocal probe with nanometer accuracy at large acceptance angles for measurement of freeform surfaces, Proc. of Euspen Annual meeting, 2007

PRECISION MATERIAL REMOVAL USING THE ELECTROKINETIC PHENOMENON

C. S. Leo[1], T. L. Blackburn[3], S. H. Ng[2], C. Yang[1], D. L. Butler[1,2,*] and S. Danyluk[3]
[1]School of Mechanical and Aerospace Engineering, Nanyang Technological University, Singapore, 639798
[2]Singapore Institute of Manufacturing Technology, 71 Nanyang Drive, Singapore, 638075
[3]George W. Woodruff, School of Mechanical Engineering, Georgia Institute of Technology, 801 Ferst Drive, Atlanta, Georgia, USA, 30332-0405

INTRODUCTION

Non-contact material removal processes offer numerous advantages over traditional machining approaches and no where is this more apparent than in the fabrication of micro devices. Current micromachining techniques such as microgrinding and micromilling have limitations with respect to their positioning accuracy and tool deflections. Electro thermal processes such as microEDM and laser machining usually result in a heat affected zone being produced. Other approaches such as etching and non-contact ultraprecision polishing are either costly or are not suitable for high throughput. In order to address these limitations, alternative micromachining techniques are required.

In this paper, a non-contact material removal technique based on the electrokinetic phenomenon is proposed for precise material removal at rates in the order of nanometers/min. The aim of this research is to have a better understanding of the electrokinetic material removal technique by studying the trajectory of the particles and the influence of the frequency of the electric field on the material removal rate.

CONCEPT OF PROPOSED TECHNIQUE

The two primary mechanisms that are involved in the material removal technique are the electrokinetic and hydrodynamic effects. Electrokinetic effect on the particles is based on the movement of suspended colloids under an electric field while the hydrodynamic effect is based on the movement of the particles under a fluidic flow.

When a particle is submerged in an aqueous solution, it is charged as the solid interfaces of the particles carry electrostatic charges where a difference in potential is developed across the interface between the two phases. The charged interface of the particle will attract counter-ions and repel co-ions to form an electric double layer. The surface charge of the particles is related to the particles' zeta potential, size and dielectric constant which can be determined by [1]:

$$Q_E = 4\pi a \varepsilon \varepsilon_o \varsigma \tag{1}$$

where Q_E is the surface charge of the particle, a is the radius of the particle, ε is the dielectric constant, ε_o is the permittivity of vacuum, and ς is the zeta potential of the particle.

As mentioned earlier, one of the primary forces that acts on the particles (normal to surface of the workpiece) to cause surface wear is the electrokinetic force which is mainly governed by electrostatics, given by equation (2) [1].

$$F_E = Q_E E_{AC+DC\,Bias} = 4\pi a \varepsilon \varepsilon_o \varsigma \left[\left(\frac{V_{AC} \sin(2\pi f t)}{d} + \frac{V_{DC\_Bias}}{d} \right) \right] \tag{2}$$

where V_{AC} is the AC voltage of the electric field, $V_{DC\text{-}Bias}$ is the DC voltage of the electric field, d is the distance between the two electrodes through which an AC electric field with DC bias is applied and f is the frequency of the AC electric field.

Besides the influence of the electrokinetic effect on the material removal, the other determining factor that acts on the particles (along the surface of the workpiece) to cause surface wear is the hydrodynamic effect of the fluidic flow that is mainly given by the expression:

$$u = 6U \left[\frac{1}{4} - \left(\frac{y'}{H} \right)^2 \right] \tag{3}$$

where u is the localized fluid velocity, U is the general fluid velocity, y' is the height of the localised element of the fluid at the centre of the channel and H is the height of the microchannel.

In addition, the horizontal component of the particle motion exerted by the flowing fluid was

used to ensure constant, uniform material removal during the material removal process. Figures 1(a) and 1(b) show the idealized movement of the particles when they are under the influence of the fluidic flow with no electric field and an AC electric field respectively. With an AC electric field applied to the particles only, the particles are expected to have relatively few collisions and interactions with the workpiece. Figure 1(c) shows the movement of the particles when they are subjected to DC electric field only where the particles are expected to move towards the workpiece and deposit on the surface of it. It is suggested that the particles would experience cyclic collisions with the surface of the workpiece only under the influence of a combination of AC and DC electric field coupled with the effect of the hydrodynamic flow. During the experiments conducted, dielectrophoresis was considered negligible as there were no electric gradients between the electrodes. Electroosmotic flow was also considered to be negligible as the fluid was a non-electrolyte.

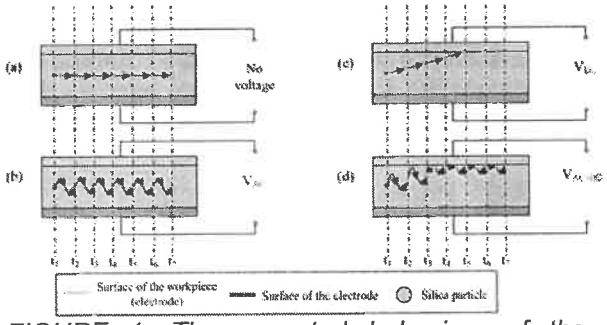

FIGURE 1. The expected behaviour of the particles when they are under the influence of fluid flow velocity and (a) no electric field (b) AC electric field only (c) DC electric field only (d) AC electric field with a DC biased.

EXPERIMENTAL PROCEDURES

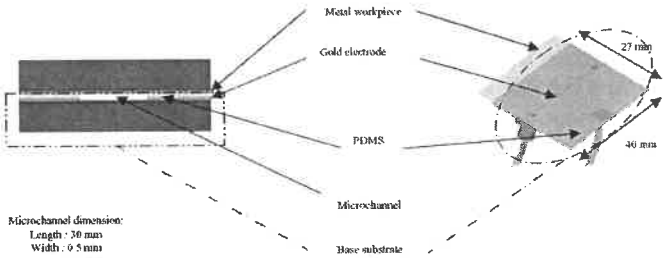

FIGURE 2. A schematic on the experimental setup for electrokinetic material removal.

The schematic of the experimental setup is illustrated in Figure 2. A base substrate consisting of a channel for fluid flow that was made of polydimethylsiloxane (PDMS) was fabricated. The base substrate was attached to a gold workpiece with a metallic clamp. The channel in the PDMS was 500 µm wide and 25 µm deep (20 µm after compression during clamping). A voltage potential was subsequently introduced to the electrodes via voltage probes and wires that were soldered onto them. An AC electric field with a DC offset was supplied to the electrodes in such a manner that the workpiece was positively biased while the electrode was negatively biased with the DC electric field. The workpiece then underwent the material removal process for one hour with a syringe pump regulating the flow of the particle (1.5 µm diameter silica particles from Alfa Aesar) suspended fluid (ethanol from Sino Chemical) across the micro-channel. Experiments were carried out to study the influence of the frequency of the electric field on the material removal rate. Throughout the experimental processes, an oscilloscope was used to monitor the voltage that was supplied across the electrodes to ensure that the electric field was of the prescribed amount. Table 1 lists the experimental conditions which were varied and the values selected.

TABLE 1. Experiments carried out to study the influence of frequency on material removal rate.

DC electric field (kV/cm)	AC electric field (kV/cm)	AC electric field frequency (Hz)	Fluid velocity (m/s)
12.5	50	100 ~ 500	0.4

Material removal was determined by using a combination of white light interferometry (Wyko NT2000 from Veeco), stylus profilometry (Dektak^{3}ST from KLA-Tencor) and scanning electron microscopy (Hitachi S-3500) to determine the depth of material removal. The material removal rate was calculated by dividing the depth of the material removed from the workpiece by the span of time (usually one hour) taken during the material removal process. For each data point on the graph, a total of 10 measurements were made. Outliers from each set of measurements were removed such that a more robust and accurate account on the material removal rate could be reflected. The sample mean and standard deviation of the wear depth for each data point was then calculated and plotted along with a best fit line.

RESULTS AND DISCUSSION

Preliminary results seemed to be promising as initial results showed that the electrokinetic

phenomenon was capable of creating nano-metric material removal. This is demonstrated by the results as shown in Figure 3. From Figure 3 (c), it was observed that there was greater material removal at the edges of the channel. This was due to the non-homogeneities of the electric field in the channel where the electric field lines are more concentrated at the edges as the electrical resistivity of the PDMS (4×10^{13} Ω m) is much greater than that of the ethanol (1.8×10^{8} Ω m) [2]. This observation corroborated with the profiles that were taken from the workpieces that underwent the process.

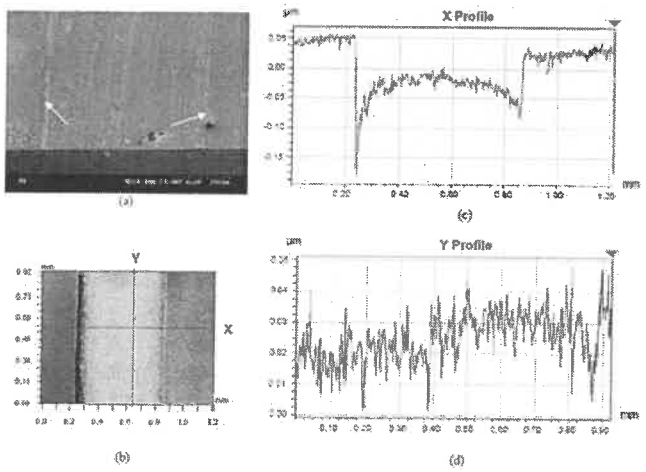

FIGURE 3. (a) SEM picture with white arrows pointing to the channel walls (b) WYKO top view image of the material removed from a gold workpiece (c) 2-D profile on the material removed from the gold workpiece in the X direction (direction perpendicular to the channel) (d) 2-D profile on the material removed from the workpiece in the Y direction (along the channel).

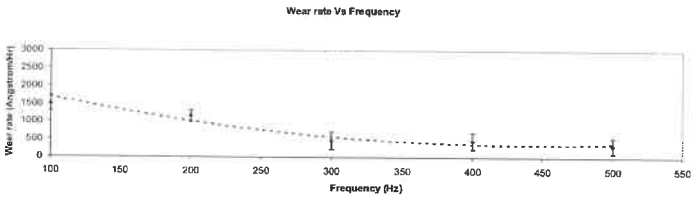

FIGURE 4. The influence of the frequency of AC electric field on the wear rate of the workpiece.

Figure 4 shows the experimental results that relate the influence of the AC electric field frequency on the material removal rate of the workpiece. It is observed that there is a clear trend in decreasing material removal rate with increasing electric field frequency. At higher frequency, more particles were expected to collide with the workpiece within a fixed amount of time. However, when the frequency was too high, the particles were unable to react with the electrokinetic force fast enough to collide with the surface of the workpiece. Fagan *et al* noted this behaviour as well where they reported that the height levitation of the particles decreased with increasing frequency in a similar setup [3]. It was also observed that the particles were not able to create material removal beyond a frequency of 300Hz. This is likely due to the effect of inertia where the particles' mass on the electrokinetic response was not great enough to create an impact for the removal of the material from the surface of the workpiece before being pulled in the opposite direction.

A Matlab mathematical model for the vertical trajectory of the particle by solving Nnewton's second law under the electrokinetic effect and a multiphysics (COMSOL) simulation based on the fluid velocity acting on the particles were made. The trajectory of the particles obtained mathematically appeared to follow the same trend as the predicted and observed motion of the abrasive particles during the experimentation as shown in Figure 5. Modelling results showed that the velocities in the vertical direction of the particles, when they were in close proximity to the surface of the workpiece, were in the range of around 1 mm/s to 20 mm/s during the experimental processes. On the other hand from the COMSOLI simulation, the horizontal velocity of the fluid that exerts on the centre of the particle, when it is in close proximity with the surface of the workpiece, is approximately fifteen percent of the fluidic velocity at the centre of the channel (which is approximately twenty percent of the general flow velocity) as shown in Figure 6. With the resultant velocity of the two components, the particle has sufficient energy to break the metallic bonds of the atoms on the workpiece to create material removal with a relatively similar mechanism as the elastic emission machining where the minimum velocity required for a 1.5 µm diameter particle to break the metallic bond is about 16 mm/s. During the experiments, the influence of the temperature due to the electric field may have an effect on the viscosity and may affect the material removal rate. However, at this stage of the experiment it was not considered.

During characterization of the material removal from the workpiece, the observations obtained suggested that the primary material removal mechanism was a mechanical one. Any other material removal mechanisms were

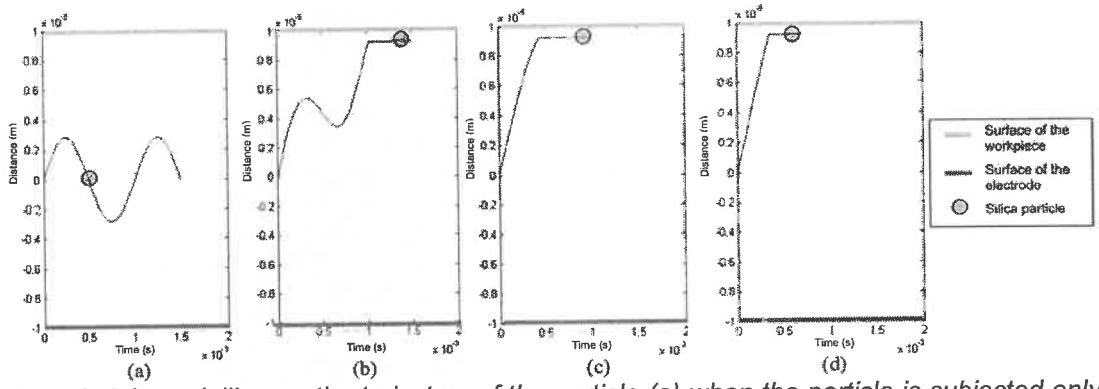

FIGURE 5. Matlab modelling on the trajectory of the particle (a) when the particle is subjected only to AC electric field strength at 1000 Hz (b) when the particle is subjected to AC electric field at 1000 Hz with a DC bias (c) when the particle is subjected to a lower AC electric field frequency of 500Hz with a DC bias (d) when the particle is subjected to a even lower AC electric field frequency of 100Hz with a DC bias.

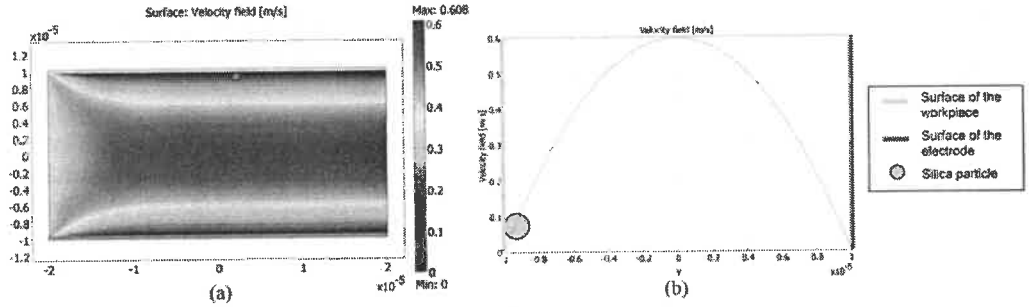

FIGURE 6. COMSOL simulation on the velocity profile of the particle (a) a 2-D simulation plot of the fluid velocity (b) a 1-D simulation of the velocity profile. Both simulations were done with the general internal flow velocity of 0.4 m/s.

regarded insignificant as there were insufficient evidence. Some of the possible material removal mechanisms include electro discharge machining (EDM) and galvanic corrosion. However, EDM could not be identified as the material removal mechanism as there is insufficient presence of craters to suggest so. Galvanic corrosion could not be the main mechanism also as the fluid that was utilized during the process was a dielectric one. This consequently led us to suggest the mechanical mechanism to be the most prevalent method for the material removal as the net resultant velocity of the particles far exceeds the energy to break the metallic bonds of the workpiece.

CONCLUSIONS

In this paper, the novel technique of using electrokinetic phenomenon for precise material removal was presented. The work demonstrated the influence of the electric field frequency on the material removal rates. By varying the frequency of the electric field, it provided a degree of control over the electrokinetic material removal process. The technique allows precise material removal without the limitations of most traditional approaches.

ACKNOWLEDGEMENTS

The authors would like to acknowledge the support of the Agency for Science Technology & Research provided by Public Sector Fund Grant # 042 101 0018.

REFERENCES

[1] Hunter, R.J., Zeta Potential in Colloid Science: Principle and Applications. Academic Press. London: 1980.

[2] Prego, M., O. Cabeza, E. Carballo, C.F. Franjo, and E. Jimenez. Measurement and interpretation of the electrical conductivity of 1-alcohols from 273 K to 333 K, Journal of Molecular Liquids. 2000; 89: 233-238.

[3] Fagan, J.A., P.J. Sides, and D.C. Prieve. Vertical motion of a charged colloidal particle near an AC polarized electrode with a nonuniform potential distribution: Theory and experimental evidence, Langmuir. 2004; 20: 4823-4834.

OPEN LOOP FAST TOOL SERVO WITH NANOMETER ACCURACY FOR DIAMOND MACHINING OF DIFFRACTIVE STRUCTURES

Ekkard Brinksmeier[1], Christoph von Kopylow[2], Claas Falldorf[2], Colin Dankwart[2], Björn Lünemann[1], Ralf Gläbe[1]
[1]LFM – Laboratory for Precision Machining, University of Bremen, Germany
[2]BIAS – Bremer Institut für Angewandte Strahltechnik, Germany

INTRODUCTION

Many security applications use diffractive optical elements (DOE) for the proof of the genuineness of products e.g. software licenses or Euro-banknotes. They are mostly made in long, time-consuming and expensive process chains. Since it is a mass product the individual DOE or hologram is inexpensive. However, there are almost no technologies known for making cost efficient individual DOEs for highly sophisticated products. To fill this gap, a diamond turning process was developed for machining individual arbitrary diffractive patterns. The key component is the developed nano fast tool servo (nFTS). It enables the fabrication of DOEs with any step height between 0 and halve of the wavelength that can not easily achieved by common structuring methods like gray-scale lithography or laser ablating technologies. [1]

The application of fast tool servo systems is a common way to enable the generation of freeform surfaces and non rotational structures using a turning process [2,3]. It is possible to manufacture microstructures with optical surface finish. However, the commonly achievable structure density and accuracy is not sufficient for the generation of diffractive optical elements with arbitrary pattern. The main reasons are limitations regarding the system bandwidth and positioning accuracy [4,5].

In the following a new fast tool servo technology is presented, that will enable the generation of individual DOEs for security applications.

EXPERIMENTAL SETUP & MACHINING PROCESS

The diamond machining process for machining energy efficient DOEs using a fast tool servo requires a well tuned combination of all participating components as well as the process itself. The major components of this system are the type of DOE structure, the nFTS and the positioning system, the shape of the diamond tools cutting edge, the workpiece material and the machining process. All components have requirements to others. The following description of the major components will give an overview of the setup as well as the most important requirements.

DOE Design

The data density of a diffractive optical element (DOE) depends mainly on the dimension of structure elements and the number of machinable height levels. The dimension has to be small for high data density. By individual modification of the height levels it is possible to modify the phase of light to make the step from a binary to a full modulated DOE with increased functionality. It was found that a blaze structure will fulfill these requirements taking the system components discussed below into account. In Figure 1 the topography of the blazed structure is depicted.

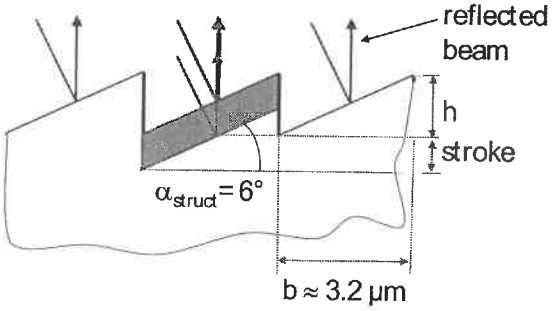

Figure 1. Blaze DOE-structure with h = 316.4 nm and height modification of the middle element.

nFTS Setup

The key component of the developed nano fast tool servo (nFTS) is a custom piezoelectric actuator. This ceramic has high linearity, nearly zero hysteresis and therefore negligible heat dissipation.

The nFTS is designed for the generation of discontinuous DOEs with a diameter up to 20 mm on flats (spheres and aspheres are also conceivable). The current nFTS has a bandwidth

of approx. 5 kHz with a stroke of up to 500 nm. Systematic deviations can be determined pre-process and superimposed to the nFTS control signal for calibration reasons. Therefore, it can be used in an open loop control mode while maintaining a nanometer positioning accuracy. This is the most important characteristic and the biggest advantage of this system.
Figure 2 shows the setup of the nFTS. The dimension is 40x40 mm^2, therefore, this system can easily integrated in ultra-precision machine tools.

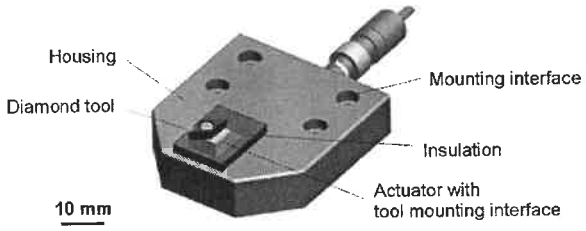

Figure 2. nFTS setup.

Workpiece Material & Cutting Process

Surface defects that remain on the DOE after the machining process like burr, roughness and effects of the grain structure will affect the efficiency of the DOE to be machined. Therefore, electroless nickel, nano-crystalline aluminum, OFHC-copper and several nickel silver alloys are investigated in cutting experiments for determining an appropriate workpiece material. A straight edge mono-crystalline diamond tool with tool nose angle of 84°, a clearance angle of 6°, a rake angle of 0° and an additional minor cutting edge was used. Due to the limited bandwidth of the nFTS and the required data density of up to 3000 height levels (data) per revolution, the spindle speed has to be reduced down to 50 ... 150 rpm ($v_c \leq 3.1$ ... 9.3 m/min). Figure 3 shows the AFM images of four machined structures. Nano-crystalline aluminum suffers from low inter-crystalline bonding strength and shows a disrupted topography and high roughness values. Electroless nickel and OFHC-copper achieves low surface roughness but suffers from high tool wear and plastic deformation of the structure respectively. The nickel silver alloy (49% Cu, 39% Zn, 7% Ni, 3% Pb, 2% Mn) shows low surface roughness at low tool wear. Interestingly, the crystalline structure of the material does not effect the surface topography.

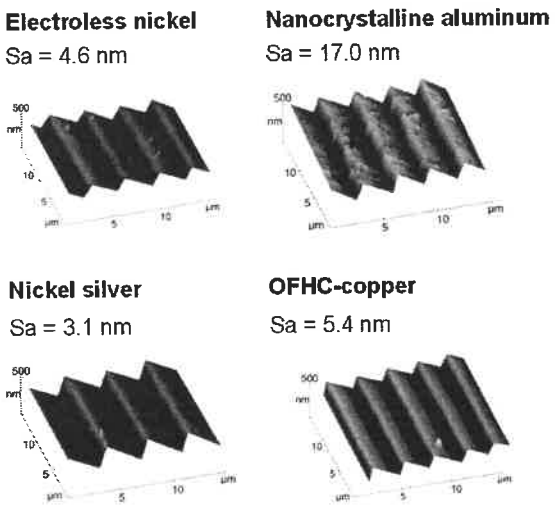

Figure 3. AFM images of continues blaze structures for testing the material properties (20x20 mm^2).

Figure 4 shows the nFTS setup integrated in an ultra-precision machine tool. It was installed upside down for better chip removal and some aspects of the machine tool structure. The data flow to the nFTS is synchronized with the rotational angle of the workpiece by triggering the data flow with the rotational glass scale signal of the spindle-axis (C-axis). Figure 5 gives an overview of the signal flow.

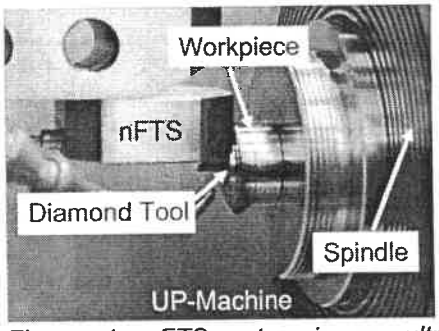

Figure 4. nFTS setup in an ultra-precision machine tool.

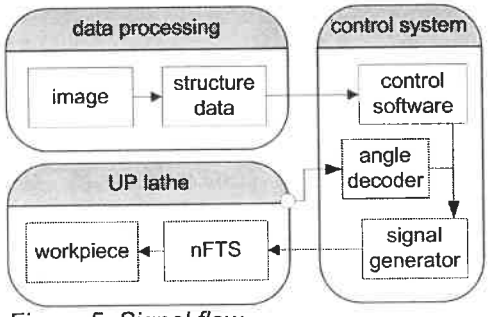

Figure 5. Signal flow.

RESULTS

Using the system several diffractive structures have been machined and the quality of the machining process and the system design was tested. Moreover, the optical properties of the machined DOEs were evaluated by analyzing holographic images reproduced in a propagation plane.

For assessing the positioning accuracy several systems tests have been performed. Figure 6 shows an AFM image of the center of a sample with two step heights. The height difference between the rear and the front part of the structure is 400 nm. The concentric rings correspond to the structure width b (= tool feed, cf. Figure 1). The result of this experiment was that no deviation of the angular position of the height step could be measured. This demonstrates the accuracy of triggering the signal generator (cf. Figure 5) by using the angle encoder signal.

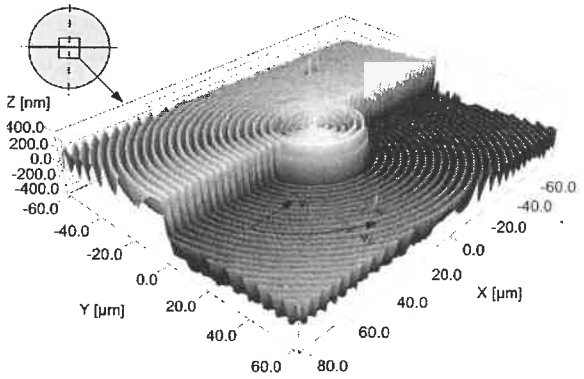

Figure 6. AFM image of a structure for testing the quality of the data trigger for the signal generator.

For determining the deviation in step height in the described open loop system a sample with 10 height levels in 50 nm steps and 10 reference levels was machined (cf. Figure 7 - top). For this experiment a radius diamond tool with a tool nose radius of 50 µm was used. Figure 7 - bottom shows the achieved height profile on a diameter of approx. 200 µm. The mean accuracy of the stroke using this un-calibrated system is achieved to approx. 10 nm.

It was found, that the uncontrolled open loop system has a tendency to oscillate after performing a height step. It is called 'over shoot' effect. For reducing this effect in an open loop system, the signal for the step jump was divided in two parts which one could refer to as "input shaping". At the nominal trigger for the step only a share of the step height signal is sent to the piezo of the nFTS. After a time period that is halve of the oscillation time of the natural frequency of the nFTS the full step is performed. By this method, the amplitude of the tool oscillation after performing a step can be reduced by a factor 4 at minimum (cf. Figure 8).

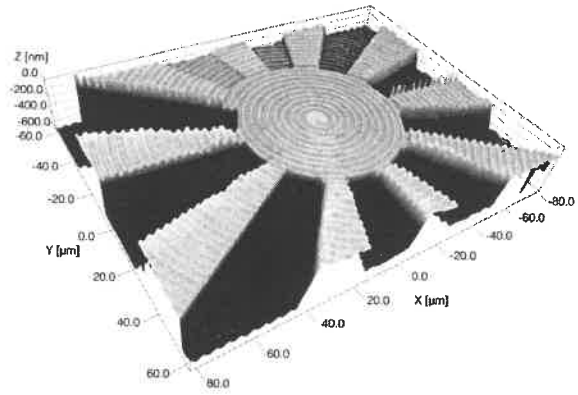

Figure 7. WLI image of a 120x160 µm² structure (top) for testing the step height deviation.

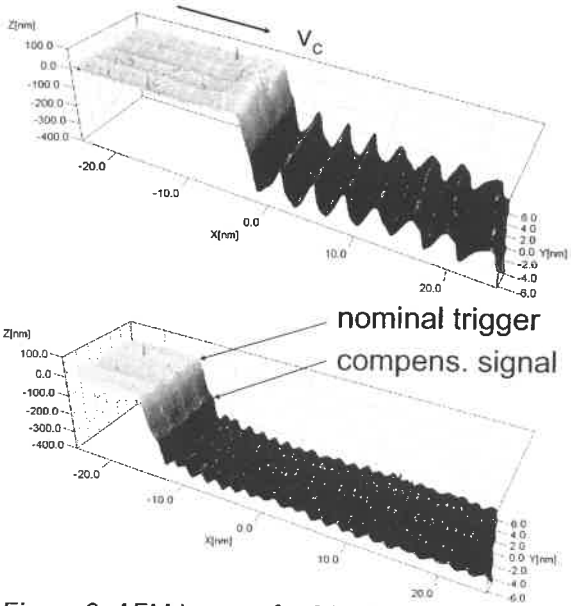

Figure 8. AFM image of a 316.4 nm step without compensation (top) and with compensation.

Figure 9 shows an example of a DOE machined with nFTS. The white light interferometer image shows the topography of the center of a flat DOE with a diameter of 20 mm. The maximum step height is 316.4 nm. In contrast to DOEs machined by lithography, any step height between 0 nm and 316.4 nm can be achieved and therefore any kind of phase modulation can be obtained. The optical reproduction of the DOE in Figure 9 in the far field is depicted in Figure 10. It derives from the DOE if illuminated using a coherent light source with a wavelength of 632.8 nm. The non-uniform distribution of the intensity is assumed to be a consequence of the not fully calibrated nFTS system and the DOE calculation algorithm. A model for suppressing the systematic deviations for a calibration process and an advanced DOE calculating algorithm are under development.

The advantage of the technology described will be the short manufacturing time of almost less than one hour including the design of the image to be depicted, calculating the DOE-structure and machining of the DOE. Therefore, it is applicable to a single piece production of individual DOEs at a relatively low price and it is easy applicable to industrial processes.

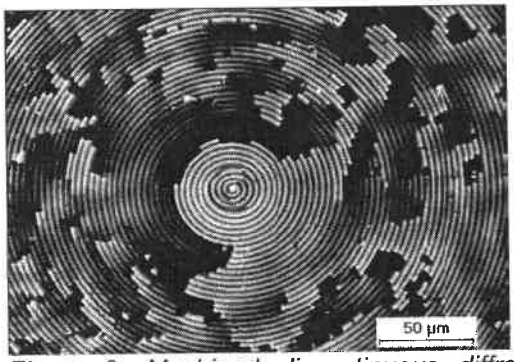

Figure 9. Machined discontinuous diffractive structure (WLI image).

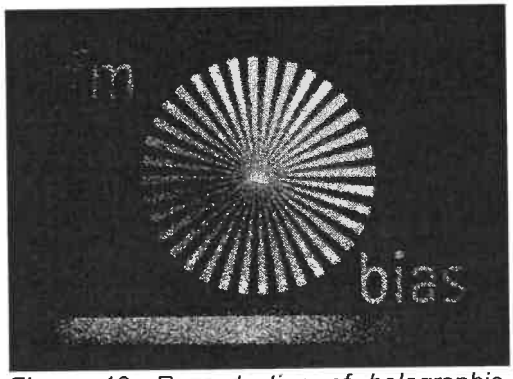

Figure 10. Reproduction of holographic data (40 x 30 mm^2).

CONCLUSION

A novel diamond turning process has been realized enabling the fast and efficient generation of discontinuous diffractive patterns on metal substrates. It is based on a developed nano fast tool servo. The current system is designed for generating saw-tooth- (blaze) structures with a maximum step height of 500 nm. It exhibits an accuracy of approx. 10 nm in an un-calibrated system. It has been successfully shown, that this technology can be used to generate holograms by a diamond turning process. In contrast to typical FTS the developed nFTS has a simple system architecture and can be easily adapted to several ultra-precision machine tools.

It was found that nFTS technology can act as a new key technology for several DOE applications. Further work will focus on advanced DOE calculation methods and machining technologies for multilayered DOEs that will be manufactured in several process steps. Those DOEs cannot be copied with justifiable means. Therefore, they are ideal for security applications.

ACKNOWLEDGEMENT

The work is funded within the initiative "Innovative Methods for Manufacturing of Multifunctional Surfaces" of the Volkswagen Foundation.

The authors also like to thank Physik Instrumente GmbH & Co. KG for their cooperation in design and setup of the nFTS.

REFERENCES

[1] Driggers, R.G.: Encyclopedia of optical engineering: Vol 1, CRC Press, 2003.

[2] Lu, X.: Electromagnetically-Driven Fast Tool Servos For Diamond Turning. P.h.D.-thesis, MIT, Cambridge, USA, 2005.

[3] Herzig, H.P.: Micro-Optics – Elements, systems and applications, Institute of Microtechnology, Switzerland, Taylor & Francis, 1997.

[4] Brinksmeier, E.; Gläbe, R.; Lünemann, B.: Manufacturing of diffractive microstructures using an open loop nanometerstroke Fast Tool Servo system. Proc. of the 10th **euspen** Conference, Zurich, May 2008, pp. 125 – 128.

[5] Brinksmeier, E.; Gläbe, R.; Lünemann, B.: Diamond machining of diffractive optical patterns using a nanometer-stroke Fast Tool Servo. Proc. of the 8th International Lamdamap Conference, Cardiff, GB, 25.06.-28.06.2007, pp. 232 – 242.

PNEUMATIC SERVO BEARING ACTUATOR FOR ULTRAPRECISE POSITIONING – PART 1: PRINCIPLE AND BASIC PERFORMANCE

Tomoko Hirayama[1], Takakazu Kitagawa[1], Masato Kadotani[1], Hiroki Danjyo[1], Takashi Matsuoka[1], Katsumi Sasaki[2] and Hiroshi Yabe[3]

[1]Department of Mechanical Engineering, Doshisha University
1-3 Miyakodani, Tatara, Kyotanabe, Kyoto, Japan
[2]Pneumatic Servo Controls Ltd.
2266-22 Anagahora, Shimo-Shidami, Moriyama-ku, Nagoya, Aichi, Japan
[3]Department of Mechanical Engineering, Kyoto University (former affiliation)
Yoshida-honmachi, Sakyo-ku, Kyoto, Japan

INTRODUCTION

Advances in various areas of precision mechanics, such as semi-conductor exposure apparatus, MEMS/NEMS, nano-imprint lithography devices, and other nano-technology applications, have required ultraprecise positioning techniques with nanometer-scale accuracy to be developed. To meet such specific needs, many different kinds of actuators capable of ultraprecise motions have been developed. However, the needs for ultraprecise positioning system continue to expand – for example, for higher load and for circumstances free from electromagnetic fields. Therefore, new actuators with higher accuracy and better reliability are strongly required.

In this paper, we have developed a 'Pneumatic Servo Bearing Actuator (PSBA)' as a new actuator that uses pneumatic servo technology for ultraprecise positioning. The actuator mainly consists of an aerostatic thrust bearing and a pneumatic servo valve. In this first report, we describe its operation principle, prototype construction, and basic performance of the prototype PSBA under open- and closed-loop controls.

PRINCIPLE OF OPERATION

A schematic diagram of the PSBA is shown in Figure 1. The actuated part is the output spool, as shown in the figure. Its position is set by balancing two forces; force f_s is generated in the aerostatic thrust bearing and acts to the left, and force f_b $(=a_b \cdot p_b)$ is a constant preload force and acts to the right. The inlet pressure of air, p_c, from the compressor to the bearing clearance is controlled with a servo valve. After the air works as the fluid of the aerostatic bearing in the bearing clearance, it passes out into the atmosphere. Force f_s is the integrated value of the pressure distribution in the bearing clearance. Because aerostatic bearings have innately stiffness, a change in inlet pressure alters the bearing clearance, which directly corresponds to a change in the displacement of the actuated spool. The spool is capable of frictionless movement because it is supported by an aerostatic journal bearing.

The flow diagram of physical quantities in the PSBA is expressed using a four-terminal network, as shown in Figure 2. The figure illustrates the relationship between input and output, which can be expressed as a matrix:

$$\begin{pmatrix} q_c \\ f_s \end{pmatrix} = \begin{pmatrix} Y_{11} & Y_{12} \\ Y_{21} & -Y_{22} \end{pmatrix} \begin{pmatrix} p_c \\ h \end{pmatrix} + \begin{pmatrix} 0 \\ -f_b \end{pmatrix} \qquad (1)$$

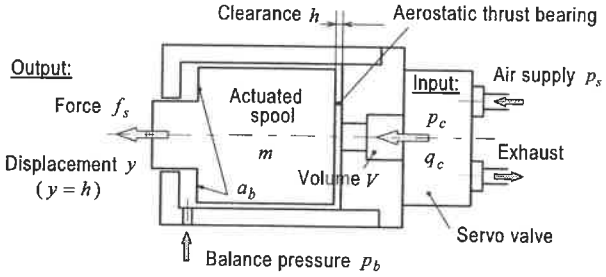

FIGURE 1. Schematic diagram of pneumatic servo bearing actuator (PSBA).

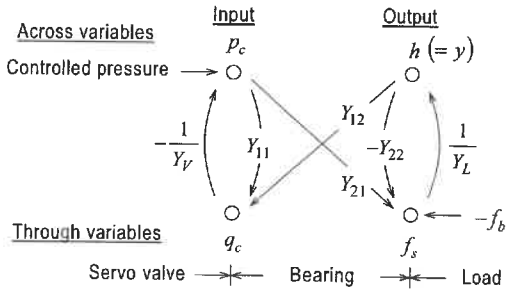

FIGURE 2. Four-terminal network flow diagram of physical quantities in PSBA.

In the PSBA, an aerostatic thrust bearing with groove compensation was used. General design of the bearing is illustrated in Figure 3 (left). According to some previous researches [1], the performance of a bearing with a groove compensation can be approximately estimated using a simple shallow-recessed bearing model with equivalent recess depth (Figure 3, right). Applying the lumped parameter model proposed by Mori [2] enables the admittances in Figure 2, from Y_{11} to Y_{22}, to be expressed as follows:

$$Y_{11} = \frac{\Delta q_c}{\Delta p_c} = \frac{\beta\eta}{\alpha+\beta} \cdot \frac{1+\tau_4 s}{1+\tau_2 s} \tag{2}$$

$$Y_{12} = \frac{\Delta q_c}{\Delta h} = \alpha \frac{\theta-\psi}{\alpha+\beta} \cdot \frac{1+\tau_1 s}{1+\tau_2 s} + \psi \tag{3}$$

$$Y_{21} = \frac{\Delta f_s}{\Delta p_c} = A_e \cdot \frac{\eta}{\alpha+\beta} \cdot \frac{1}{1+\tau_2 s} + A_c = A_p \cdot \frac{1+\tau_3 s}{1+\tau_2 s} \tag{4}$$

$$Y_{22} = -\frac{\Delta f_s}{\Delta h} = A_e \cdot \frac{\theta-\psi}{\alpha+\beta} \cdot \frac{1+\tau_1 s}{1+\tau_2 s} \tag{5}$$

where the linearized parameters are:

$$\alpha = -(\partial q_{in}/\partial p_r)_0,\ \psi = (\partial q_{in}/\partial h)_0,$$
$$\beta = (\partial q_{out}/\partial p_r)_0,\ \theta = (\partial q_{out}/\partial h)_0, \tag{6}$$
$$\chi = (\partial \overline{q}/\partial p_r)_0,\ \varphi = (\partial \overline{q}/\partial h)_0$$

* q_{in}: inlet mass rate of flow to bearing

q_{out}: outlet mass rate of flow from bearing

$\overline{q}$: mass rate of flow in bearing clearance

p_r: pressure at recess edge in bearing clearance

0: operating point

and

A_e: effective bearing area ($=\partial f_s/\partial p_r$)

A_c: $=\partial f_s/\partial p_c$

A_p: equivalent bearing area ($=df_s/dp_c$)

time constant:

$\tau_1 = \varphi/(\theta-\psi)$, $\tau_2 = \chi/(\alpha+\beta)$,

$\tau_3 = A_c/A_p \cdot \tau_2$, $\tau_4 = \chi/\beta$

Therefore, the bearing stiffness and damping coefficient are given by:

$$k = A_e \cdot \frac{\theta-\psi}{\alpha+\beta} \tag{7}$$

$$b = k(\tau_1 - \tau_2) \tag{8}$$

The damping coefficient estimated using Eq. (8) is innately positive, so the operation of the bearing should be stable, free from the inherent pneumatic self-excited oscillation.

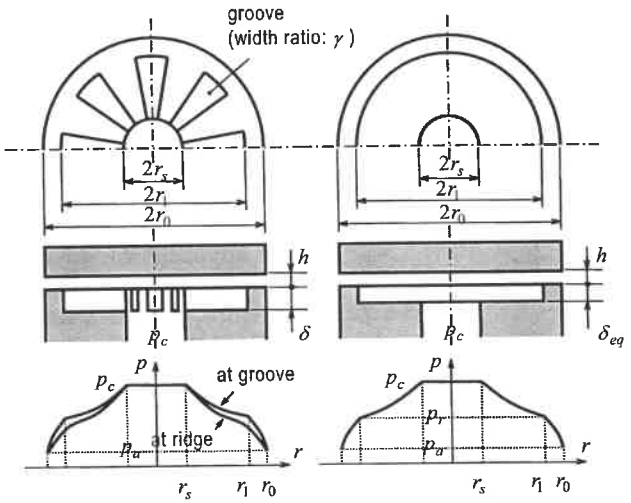

FIGURE 3. Illustration of aerostatic thrust bearing with groove compensation (left) and equivalent shallow-recessed bearing (right).

PROTOTYPE ACTUATOR

The dimensions of the prototype PSBA are listed in Table 1. The servo valve is a nozzle-flapper type valve with an axial torque motor (Pneumatic Servo Controls Ltd.). The displacement of the spool was measured with a high-resolution capacitance-type non-contact displacement sensor (Microsense, ADE Ltd.). Its minimum resolution is 0.3 nm.

TABLE 1. Dimensions of prototype PSBA.

Outer radius of bearing	13.5 mm
Radius of inlet port	2.5 mm
Number of grooves	16
Average depth of grooves	19 μm
Spool mass m	260 g
Volume V	1574 mm^3

BASIC PERFORMANCES OF PSBA UNDER OPEN-LOOP CONTROLS

The repetition accuracy of the actuator's positioning was tested by continuously changing the signal input to the servo valve. The pressure of the air supplied to the servo valve, p_s, was a constant 0.3 MPa and the zero position (= base clearance) was 7 μm. As shown by the typical results in Figure 4, the repetition error of the prototype was less than 20 nm, meaning that the actuator exhibited almost no hysteresis even under open-loop control. The level of fluctuation of the actuated spool depended on the bearing clearance and inlet air pressure. When the bearing clearance was less than 20 μm and the inlet air pressure p_c was less than 0.1 MPa, the

fluctuation was less than 1 nm under any condition.

The step response of the prototype PSBA under open-loop control with a 5 nm-high step is shown in Figure 5. The zero position was set to 7 μm. Even though there were some small fluctuations (including electric noise), the actuator performed sharp switching. This means that the developed actuator has a high potential for ultraprecise positioning with nanometer-scale accuracy.

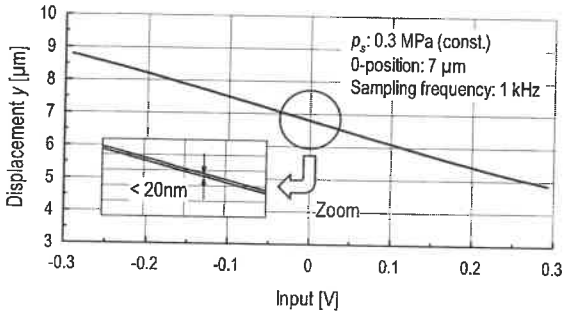

FIGURE 4. Repetition accuracy of prototype PSBA under open-loop control.

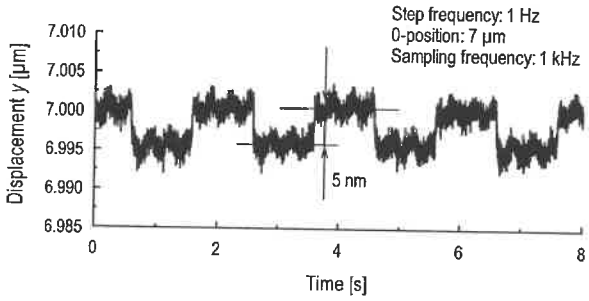

FIGURE 5. 5 nm-high step response of prototype PSBA under open-loop control.

IMPROVED PERFORMANCES OF PBSA UNDER CLOSED-LOOP CONTROLS

The performance of the PBSA was improved by applying closed-loop control to the system. Simple position feedback was added, as illustrated by the block diagram in Figure 6. The only control parameter was loop gain, K_p.

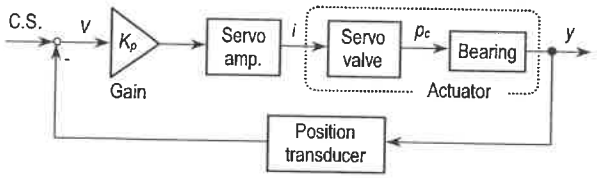

FIGURE 6. Block diagram of PSBA system with position feedback.

The controllability of the axial force of PSBA with this simple position feedback was examined. The results are shown in Figure 7. The black circles show the axial force of the PSBA when the servo valve was kept full-open under constant air supply pressure into the valve (p_s =0.3 MPa), and the white circles in the figure show the axial force controlled by the feedback for maximum stiffness. The actuator's stiffness was increased about 12-fold by applying the feedback control. Reducing the loop gain reduced the stiffness. This means that the axial force can be perfectly controlled for the area under the curve (dotted area), so the stiffness appropriate for each device can be obtained.

Bode diagrams for open- and closed-loop control of the PSBA are shown in Figure 8. The black circles show the gain and phase for the PSBA under open-loop control, while the white ones show them for under closed-loop control where the loop gain was set for maximum stiffness.

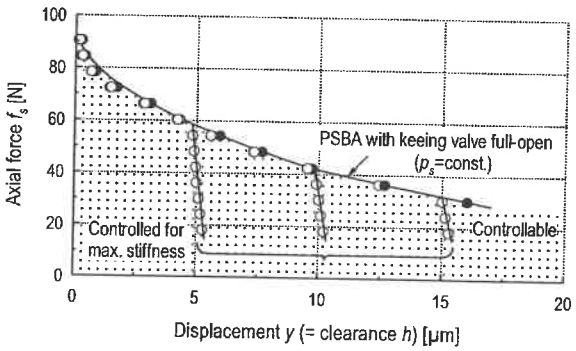
PSBA with keeing valve full-open (p_s=const.)
Controlled for max. stiffness
Controllable
Axial force f_s [N]
Displacement y (= clearance h) [μm]

FIGURE 7. Axial force of the PSBA with a closed-loop control for maximum stiffness.

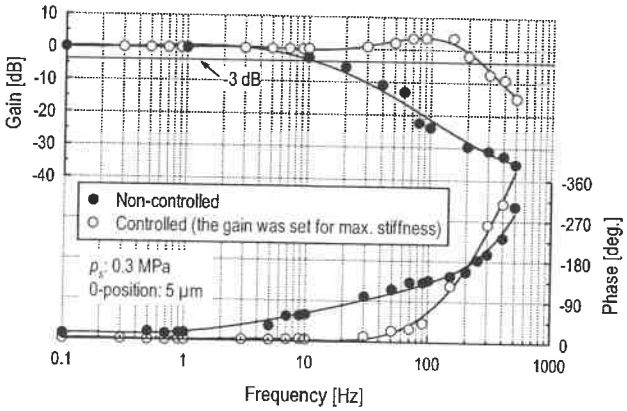

FIGURE 8. Bode diagrams of PSBA under open- and closed-loop control.

These diagrams demonstrate that the PSBA is an inherently stable system. The closed-loop control expanded its bandwidth from 10 Hz to 115 Hz. Note that the break frequency, at about 10 Hz, in the gain diagram under the non-controlled condition is determined by the volume V of air arranged prior to the inlet port to the aerostatic bearing (see Figure 1).

The step responses of the PSBA under the non-controlled and the position feedback control are shown in Figure 9. The zero position was 5 μm, and the step height was 40 nm. The controlled PSBA performed sharper switching without any drift or hysteresis than the non-controlled one. Position feedback is thus effective for achieving stable ultraprecise motion of the PSBA. In the experiments with feedback control, the gain was set for maximum stiffness, resulting in a damping ratio of about 0.2. By selecting the appropriate loop gain, we can obtain the optimal damping ratio for each device.

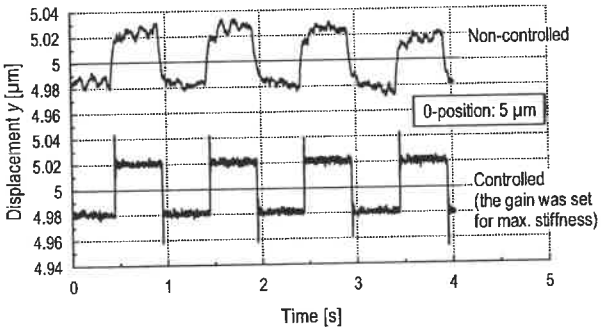

FIGURE 9. Step response of PSBA under open- and closed-loop control (40 nm-high steps).

The step responses of the PSBA with a 10 nm-, 5 nm- and 2 nm-high steps without noise filtering are shown in Figure 10 for a sampling frequency of 1 kHz and with a loop gain for maximum stiffness. The zero position was 5 μm. The PSBA performed sharp switching and the minimum positioning resolution of the prototype PSBA was about 2 nm. Application of another feedback control such as velocity feedback, acceleration feedback, or disturbance observer, or use of another displacement sensor with higher resolution would result in even more precise motion of the PSBA. In addition, a new approach to ultraprecise positioning that uses PSBAs with multiple bearing pads in a tandem arrangement has been examined; the results are described in the following Part 2 report.

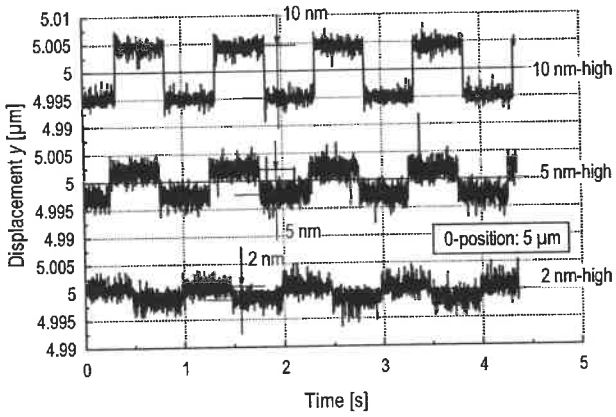

FIGURE 10. Ultraprecise step responses of prototype PSBA under closed-loop control.

TABLE 2. Specifications of prototype PSBA.

Stroke	< 20 μm
Resolution	< 2 nm
Load capacity (= axial force)	< 90 N @p_s=0.3 MPa
Stiffness: non-controlled : controlled	2-5 N/μm 50-70 N/μm
Band width: non-controlled : controlled	10 Hz 115 Hz
Fluctuation level	< 1 nm

CONCLUSION

A pneumatic servo bearing actuator (PSBA) has been developed as a potential new actuator to meet the needs for ultraprecise positioning brought about by advances in ultraprecision mechanics. The specifications of the prototype PSBA are enumerated in Table 2. Even under open-loop control, the PSBA had good repetition accuracy and a sharp step response. Applying simple closed-loop control increased the stiffness 12-fold and sharpened the step response without any drift or hysteresis. The PBSA will thus succeed in breaking new technology for the development of ultraprecision positioning system in the immediate future.

REFERENCES

[1] H. Yabe et al., Trans. Japan Society of Mechanical Eng., Ser. C, 45, 389 (1979) 100-107, in Japanese.

[2] A. Mori, Text of Gas Bearing Workshop, Japanese Society of Tribologists (1991), in Japanese.

GRINDING OF MICROSTRUCTURED FUNCTIONAL SURFACES – A NOVEL STRATEGY FOR DRESSING OF MICROPROFILES ON VITRIFIED GRINDING WHEELS

Berend Denkena[1], David Boehnke[1], Bo Wang[1]
[1]Institute of Production Engineering and Machine Tools
Leibniz Universität Hannover
Hannover, Germany

INTRODUCTION

Surface relief structures at micro and nanoscales are currently focused in different engineering areas. These structures enable special optical, mechanical or chemical properties of the workpiece surfaces. One example is the riblet surface, on which microgrooves are distributed in flow direction. Compared to smooth surfaces ideal riblet structures have been proven to reduce skin friction and wall shear stresses in turbulent flow up to 10% [1]. For most technical applications of riblets, microgroove structures with a width of less than 100 µm and a depth of the half of the width are required on extensive surfaces. The purpose of the present study is to apply profile grinding for the manufacturing of riblets on compressor blades of gas turbines directly (FIGURE 1). For this application, microgrooves with a width of 40 µm and a depth 20 µm are required. Grinding wheel profiles with microscopic profile peak geometries have to be generated by a dressing process to grind such microgrooves. In this paper, a novel profile dressing method using special profile shift kinematics is introduced. This method enables the generating of the required wheel profile geometries.

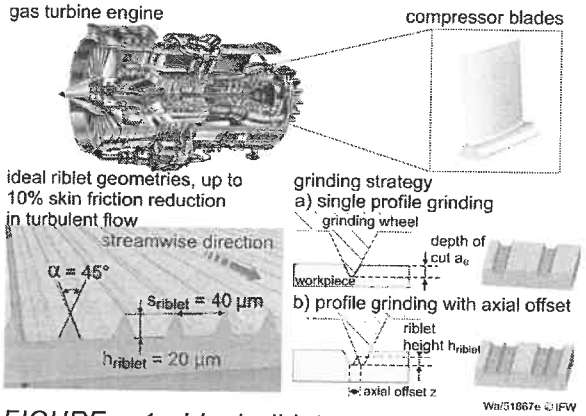

FIGURE 1. Ideal riblet geometries for the application on compressor blades

DRESSING STRATEGIES

For the dressing of multiprofiled vitrified grinding wheels, two main dressing methods are possible (FIGURE 2). The first method is form dressing using a diamond form roller. The contour of the wheel is generated by NC-programs and dressed by the dressing tool along the axial direction. The whole wheel profile is generated layer by layer. Due to the axial dressing path over all of the profiles to be dressed, dressing using a form roller is a highly time consuming process. Furthermore, the actual geometry of the dressing tool is required for the dressing tool correction in the NC-program. Due to the ongoing wear of the dressing tool, this actual geometry is difficult to determine. Besides that, the stability of the machine axis control system can be influenced negatively by temperature effects due to the long dressing time. The second method is profile dressing using a diamond profile roller. The negative profile of the grinding wheel is mapped on the dressing roller. The whole wheel profile is generated within a plunge movement of the dressing tool toward the grinding wheel. Compared to the form dressing process, profile dressing offers a higher dressing efficiency and process stability. On the other hand, the dressing force could be higher due to the longer tool contact width, which has to be considered to achieve a stable dressing process.

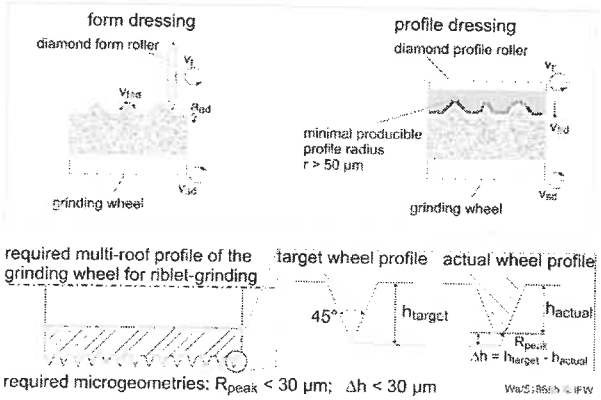

FIGURE 2. Dressing kinematics for form dressing and profile dressing

In the current riblet grinding studies, multiroof profiles with a micro tip geometry on the grinding wheel (R_{peak} < 30 µm, FIGURE 2) are required. However, it is currently not possible to produce microprofiles on grinding wheels with a profile tip radius smaller than 50 µm directly by profile dressing. This is due to the limited minimal profile geometry on the diamond profile dressing roller, which can be produced [3]. Hence a novel dressing strategy using profile rollers is introduced in the following (FIGURE 3). With the new dressing strategy, roof profiles with an ideal sharp profile tip can be produced, if the breakout behavior of the grinding layer is not being considered. In the first plunge movement, one flank of the profiles is dressed. The second plunge movement is carried out with an axial offset of the dressing roller, whereby the other flank of the profiles is dressed. Due to the special process kinematics, all roof profiles on the grinding wheel can be produced within two plunge movements. Furthermore, generally the tip areas of the dressing roller profile undertake a higher load than the flank areas. Using the new dressing kinematics, the flank areas of the dressing roller profile are responsible for the generation of the tips of the roof profiles and enable a higher wear resistance.

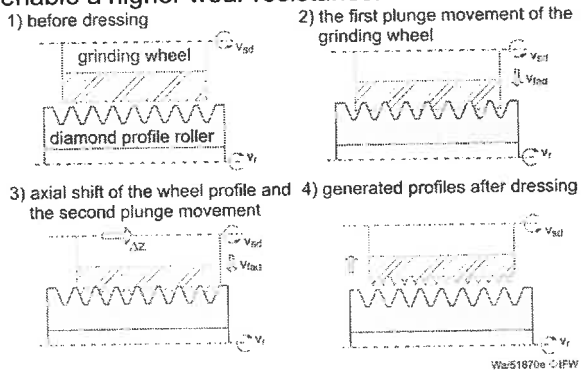
1) before dressing
grinding wheel
diamond profile roller
2) the first plunge movement of the grinding wheel
3) axial shift of the wheel profile and the second plunge movement
4) generated profiles after dressing

FIGURE 3. Novel dressing strategy for profile dressing of microprofiles

EXPERIMENTAL SETUP

The dressing and grinding experiments were carried out on a high precision surface grinding machine (Blohm, type profimat 407). The dressing system using a diamond profile roller has been integrated in the machine (FIGURE 4). Vitrified bonded SiC-wheels with a variable average grain size from d_G = 9 µm to d_G = 60 µm were investigated at form dressing experiments [2]. The results show that the SiC-wheel SiC400 with a grain size of d_G = 17 µm has achieved the best results concerning the profile breakout behavior. Furthermore, a vitrified bonded CBN-wheel with a grain size of 16 µm was investigated. By means of increasing the target profile angle from 45° to 90°, the desired profile peak geometries could be achieved. Thus, in this study the same wheel specification was selected for the following profile dressing experiments. The topography of the used diamond dressing roller is shown in the lower right side of FIGURE 4. Different profile flank angles have been designed on the dressing roller. In this way it is possible to achieve three profile angles from 45°, 60° to 90° on the grinding wheel. Furthermore, for the evaluation the peripheral wheel profiles were plunged in graphite plates and measured by a high precision contour measuring machine (Mahr, Pethometer). For the following riblet grinding tests, a typical steel material for compressor blades, X20Cr13 (St1.4021) was machined.

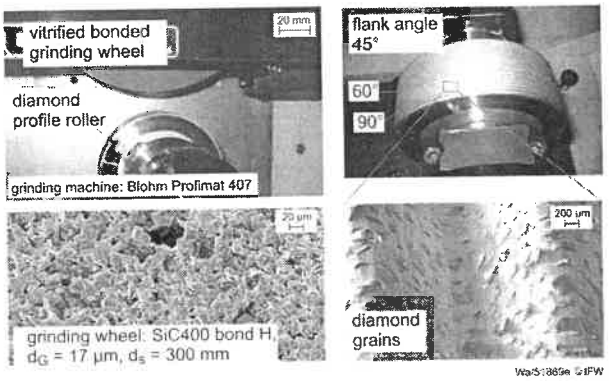

FIGURE 4. Experimental setup

DRESSING OF SIC-WHEELS

The influence of the profile dressing parameters on the grinding wheel topography has been described in [4]. The actual surface roughness of the grinding wheel after dressing R_t increases with rising radial feed in dressing f_{rd}. Considering the ratio of the dressing speed q_d the up dressing modus generates smoother wheel topography as the down dressing modus. However, in the current application of grinding riblets, microscopic wheel profiles are required. The main issue of the dressing experiments is to investigate the minimal achievable wheel profile geometry. At the profile tip, the structure strength of the grinding layer is quite low. Due to the mechanical loads at dressing, breakouts occur at the profile tip. To evaluate the dressing results, the difference Δh between the target profile height with ideal sharp profile tip h_{target} and the actual achieved profile height h_{actual} after dressing has been used (FIGURE 2).

FIGURE 5 gives an overview of the executed variations of the dressing parameters. At a profile angle of 45° both the radial feed f_{rd} and the ratio of dressing speed q_d have been varied. The dressing results show a significant influence of the dressing parameters on the profile height difference Δh. With increasing dressing infeed f_{rd} the dressing force and loading on the wheel layer turns higher. This causes larger breakouts of the profile tip. On the other hand, the profile accuracy gets better with decreasing dressing speed ratio from down dressing to up dressing modus. Under the different variations the best result (Δh = 20 µm) has been achieved at a dressing speed ratio q_d = -0.7 and a radial infeed f_{rd} = 0.1 µm/rev.

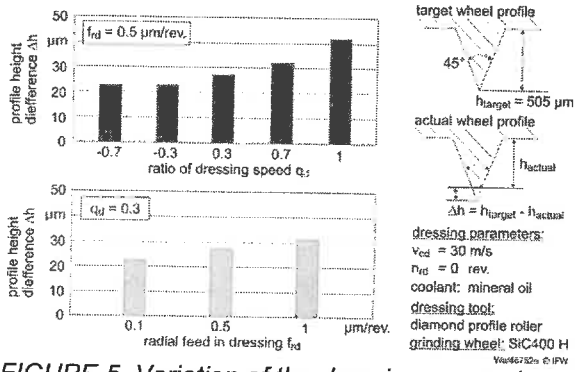

FIGURE 5. Variation of the dressing parameters

DRESSING OF CBN-WHEELS

Besides the SiC400 wheel, a vitrified bonded CBN-wheel with a grain size of 16 µm (MB16) has been applied for the following dressing experiments. In comparison to conventional wheels, CBN wheels offer a large potential regarding tool wear resistance. However, the bonding system of CBN wheels is generally much harder than that of conventional grinding wheels. The pictures on the right in FIGURE 6 show SEM pictures of the topography of the SiC400 H (on top) and those of the CBN wheel (below). The SiC grains and the pores are distributed uniformly troughout the bond. The bonding bridges are very short shaped. At the CBN wheel, the grains build lots of clusters which are surrounded by the bond material. Profile dressing experiments have been done at the CBN wheel with a target profile angle of 45° firstly. Sidewise profile breakouts could be observed at large areas. This leads to a blunt profile tip geometry (Δh = 45 µm).

INFLUENCE OF TARGET PROFILE ANGLE

At the CBN-wheel the target profile angle was increased from 45° to 90° at dressing. The profile holding performance improves and the achieved tip geometry dimension decreases. The difference Δh is about 7 µm at a profile angle of 90°. The required profile tip geometry for grinding riblets can be achieved. The same trend can also be proved at the SiC wheel during the dressing experiments (FIGURE 6). However the skip is not as significant as with the CBN wheel with a more closed bonding structure. This behavior can be explained by higher structure stability and bonding force, which are due to the sidewise bonding support at the profile tip. To analyze the structure stability at the profile tip, FE-modeling has been carried out at a varied profile angle from 45°, 60° to 90°. The wheel profile was modeled as a homogenous body. A constant dressing load is applied on the wheel tip. The results show that at the smaller angle of 45° the maximal von Mises stress in the grinding layer is about four times higher than at a 90° profile angle. To compare the real geometry for different profile angles, the profile tip height at a fixed profile width should be used for the evaluation. Furthermore, the resulting profile stability at grinding should also be taken into account.

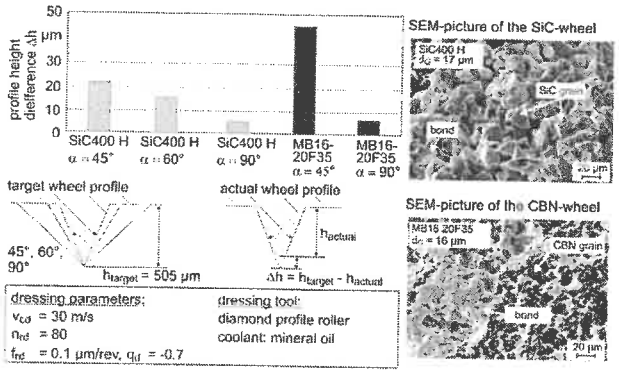

FIGURE 6. Influences of the profile angle on the profile dressing process

GRINDING OF RIBLETS

After the microprofiles were generated on the grinding wheels via profile dressing, grinding experiments have been carried out. The aim of the grinding tests is to investigate the producible micro profiles on workpieces as well as the tool wear behavior. Since the distance between two profile tips on the grinding wheel is larger than the riblet width, grinding strategy with profile overlapping has been applied to achieve continuous riblets (FIGURE 1, lower right). The desired riblet profiles could be machined through axial overlapping of the single profiles. FIGURE

7 shows the SEM images and the micrograph section pictures of the ground microgrooves.
The measured micrograph section profile shows a profile height of 20 µm and a profile width of 50 µm, which is determined by the set axial offset of the wheel profiles at grinding. Noticeable are the asymmetric profile flanks and the roll-in effect at the profile tips due to the plastic material deformation.

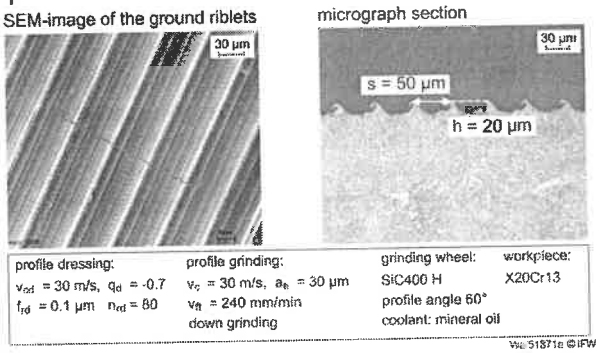

FIGURE 7. Grinding of riblets

In grinding of microstructures the grinding wheel profile wear is to investigate. Since the structure stability of the microscopic wheel profile is relatively low, the radial wear increases directly with higher material removal rate. This results from the increasing single grain chip thickness and the higher loads on the wheel profile. To compare the wheel profile geometry concerning the aspect ratio at different profile angles, the residual profile height at a profile width of h_r = 60 µm was used to evaluate the wear behavior (FIGURE 8). For each parameter variation the grinding wheel was redressed and a groove with a length of 100 mm was ground. The residual profile height was then measured and plotted in the diagram.

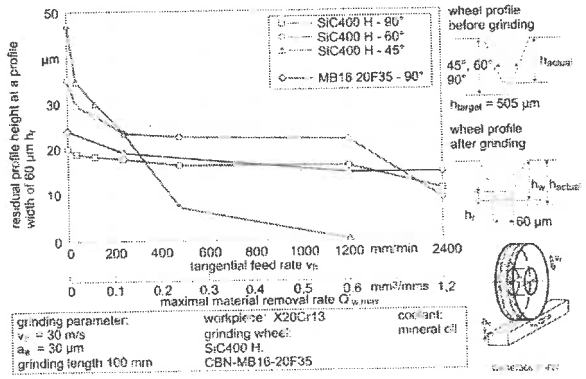

FIGURE 8. Profile wear behavior at different profile angles

A high increase in wear can be seen at increasing tangential feed rate v_{ft} for all of the wheel profiles. However, the wear rate is different at different profile angles at the SiC400 wheel. The CBN-wheel shows a higher wear resistance at a high cutting rate. The SiC400 wheel with a profile angle of 45° has achieved the highest aspect ratio of the ground microgroove structures, if the cutting rate Q'_w is lower than 0.12 mm³/mm min. The SiC-wheel with a profile angle of 60° should be chosen at cutting rates Q'_w from 0.12 mm³/mm min to 0.6 mm³/mm min. The CBN-wheel with a profile angle of 90° should be used at even higher cutting rates.

SUMMARY

For grinding of microstructures like riblets a novel dressing strategy using a profile roller was applied to vitrified bonded grinding wheels. Through the dressing kinematic using a profile shift kinematic the limit of the smallest dressable wheel profile tip geometry could be reduced significantly. To achieve smaller profile breakouts and higher profile accuracy, small dressing infeed and the up dressing modus should be chosen. Furthermore, the angle of the roof profile has a high impact on the profile stability at dressing as well as the tool wear behavior at grinding. To achieve optimal grinding results concerning the geometrical aspect ratio of the ground microstructure, both the profile angle and the cutting rate at grinding should be taken into account.

ACKNOWLEDGEMENTS

The investigations presented in this paper are kindly supported by the German Research Foundation (DFG) within the project "Riblets on Compressor Blades".

REFERENCES

[1] Hage, W.: Zur Widerstandsverminderung von dreidimensionalen Riblet-Strukturen und anderen Oberflächen. Dr.-Ing. Diss., Technical University Berlin, Germany, 2005

[2] Denkena, B.; Reichstein, M.; Wang, B.: Manufacturing of Functional Micro-structured Surfaces by Grinding. International Symposium on Advances in Abrasive Technology (ISAAT), September 2007, Dearborn, USA

[3] Product information, Dr. Kaiser Diamantwerkzeuge GmbH, Germany, 2008

[4] Minke, E.: Handbuch zur Abrichttechnik. Riegger Diamantwerkzeuge GmbH, 1999

THE CURRENT STATE OF ART IN ULTRAPRECISION CUTTING TECHNOLOGY IN JAPAN

Yoshimi Takeuchi
Department of Mechanical Engineering
Osaka University
Suita, Osaka, Japan

INTRODUCTION

Ultraprecision machining, especially micromachining is a key technology to realize the fabrication of small parts, small mechanisms and small robots with extremely high accuracy. Until now, etching and lithography based technologies are well known in the microfabrication fields, where such a material as silicon oxide is generally utilized. A problem of these technologies is the difficulty of producing 3-dimensional shapes with inclined and sculptured surfaces, which are inevitably required to construct a variety of microproducts.

Ultraprecision mechanical machining/ micromachining technology can meet the requirement, using a diamond cutting tool and an ultraprecision machine tool such as a turning lathe or a milling machine with multi-axis control machining function. Multi-axis control ultraprecision machine tools are one solution for improving productivity and accuracy, however, it is difficult to actually implement due to several problems, for example, the interference problem between a cutting tool and a workpiece. Thus, the study presents the current state of 5-axis control ultraprecision machine tools in Japan and a machined example of small workpieces with a complicated shape by making use of 5-axis control machining function.

5-AXIS CONTROL ULTRAPRECISION MACHINE TOOLS

In order to set a cutting tool at an arbitrary position with an arbitrary tool attitude and cutting edge direction, 6 degrees of freedom are required, that is, 3 translational positioning functions, X, Y, and Z, and 3 rotational positioning functions, A, B, and C around each translational axis. Usually, conventional machine tools consist of 3 translational axes. On the contrary, multi-axis control machine tools stand for machine tools having more than 3 control axes. 5-axis control machine tools, the representative of multi-axis control ones, are usually equipped with 3 translational axes and 2 rotational axes, for example, X, Y, Z, A, and B. The axis C is used as the main spindle to rotate a diamond cutting tool or a workpiece so that high cutting speed can be realized. In case of 6-axis control machining, non-rotational diamond cutting tools are used, which enable the characteristic machining in spite of

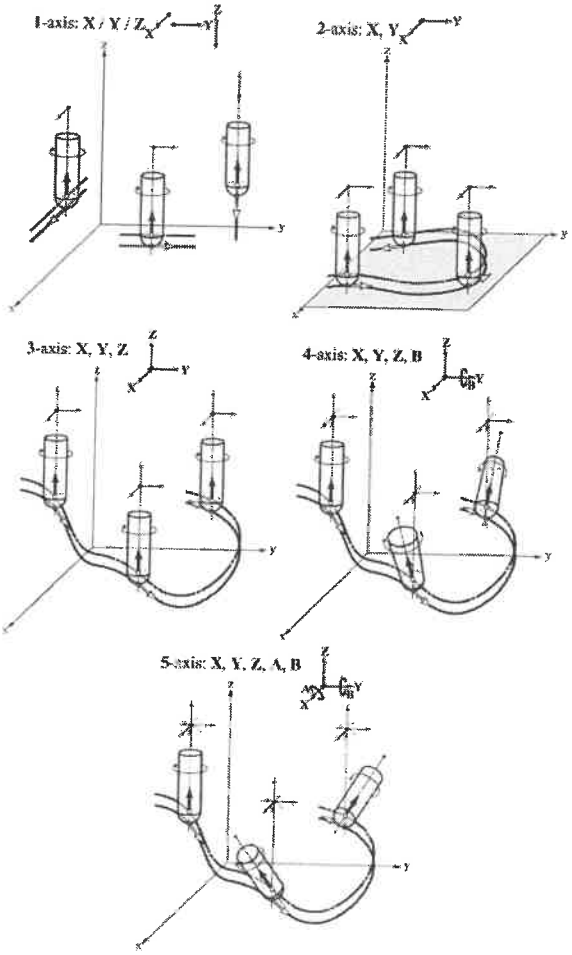

FIGURE 1. Relationship between the axis number and shape to be created.

FIGURE 2. ULC100 (Toshiba Machine Co., Ltd).

FIGURE 3. ASP30X (NACHI-FUJIKOSHI Co.).

extremely low cutting speed. The relationship between the number of axes and the shape to be created is illustrated in Figure 1.

In general, ultraprecision machine tools have the translational positioning accuracy of 1 nm and the rotational one of 0.0001 to 0.00001 degree. In Japan, there are currently more than 5 ultraprecision machine tool builders. Ultraprecision machine tools can be classified into several types in terms of driving mechanism of movement axes such as ball-screw, pneumatic/hydrostatic screw or linear drive, and supporting mechanism/bearing such as ball/roller bearing or pneumatic/hydrostatic bearing.

Let's introduce 5-axis control ultraprecision machining centers produced in Japan. Figure 2 shows ULC100 (Toshiba Machine Co., Ltd) with ball-screw driving and needle bearing. Figure 3 and Figure 4 show ASP30X (NACHI-FUJIKOSHI Co.) and AHN15 (JTEKT Co.) with hydrostatic screw/linear motor and bearing respectively. Figure 5 and Figure 6 show Ultra NANO100

FIGURE 4. AHN15 (JTEKT Co.).

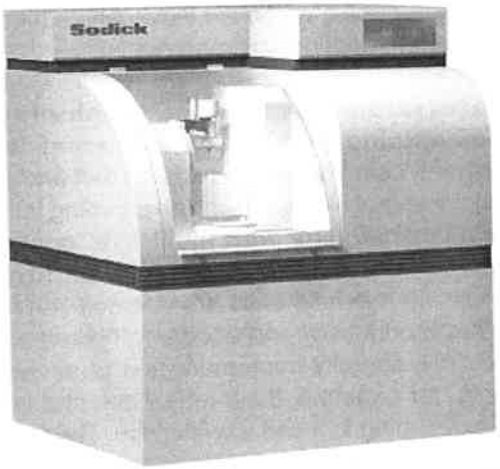

FIGURE 5. Ultra NANO100 (Sodick Co. Ltd.).

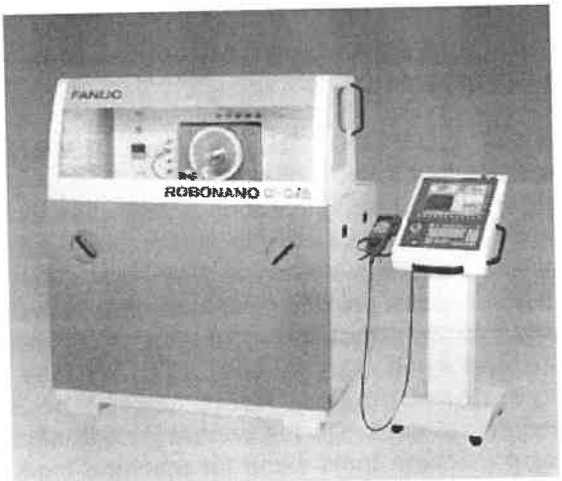

FIGURE 6. ROBONANO α0iB (FANUC Ltd.).

(Sodick Co. Ltd.) and ROBONANO α0iB (FANUC Ltd.) with linear driving and pneumatic bearing. These machine tools are equipped with a high speed air spindle.

MANUFACTURE OF ULTRAPRECISION MICROINDUCER OF MICROPUMP

As a representative of micromachines, there is a miropump useful for water-cooling of heat generation from CPU, fuel-supplying to fuel cells, blood circulation and so on. Let us explain the machining of an inducer of axial flow type micropump for blood circulation [1].

Figure 7 shows an inducer consisting of 3 equally arranged blades and hubs of 5 mm in diameter. Each blade is composed of a ruled surface, a kind of free-form surface. Figure 8 is the configuration of the designed inducer. Based on the defined shape of the inducer by use of 3D-CAD system,

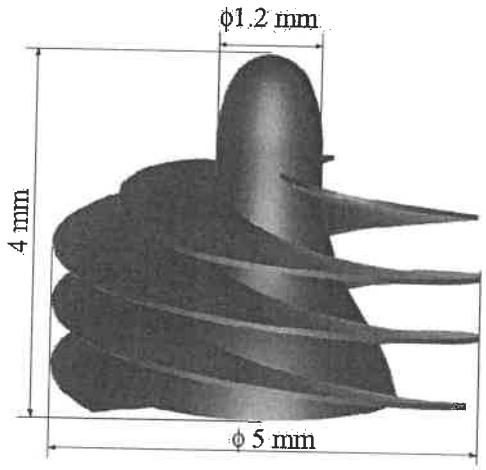

FIGURE 7. Inducer to be machined.

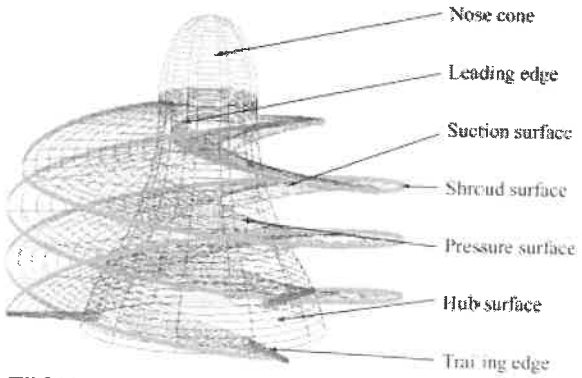

FIGURE 8. Configuration of the inducer.

the developed CAM system finally generates interference-free NC data for 5-axis control ultraprecision milling, taking account of collision between a diamond milling cutter and a workpiece, as illustrated in Figure 9.

Figure 10 illustrates the tool setting in performing 5-axis control machining. The center of a diamond cutting tool is set so that it can coincide with the

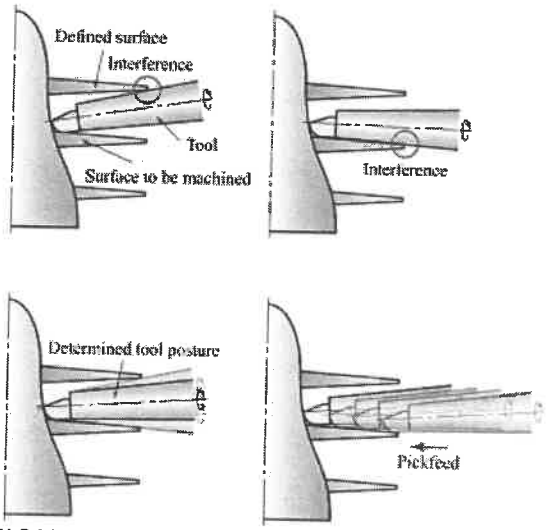

FIGURE 9. Collision avoidance between a diamond milling cutter and a workpiece.

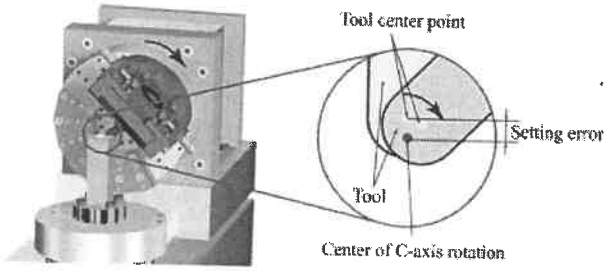

FIGURE 10. Tool setting in performing 5-axis control machining.

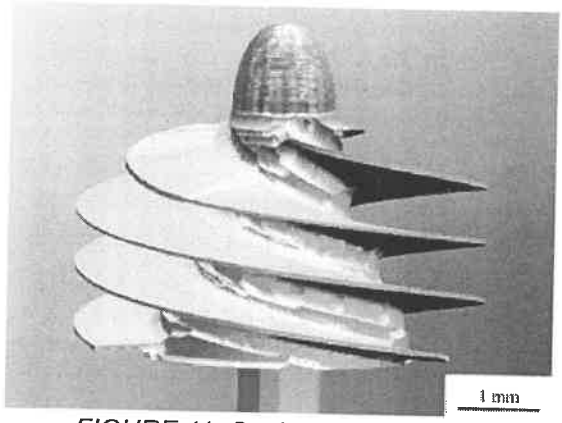

FIGURE 11. Cutting simulation.

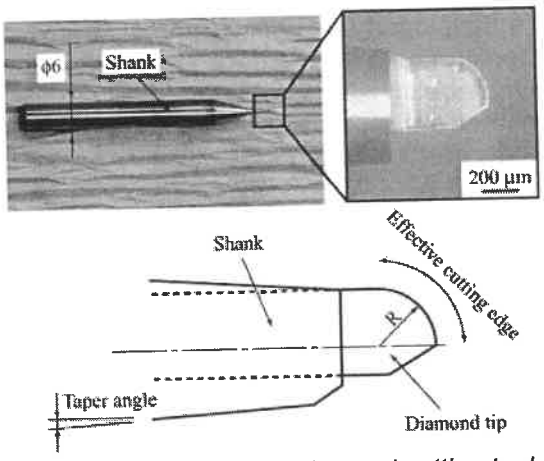

FIGURE 12. Single crystal diamond cutting tool.

rotational center of C axis. Before machining, cutting simulation is performed on the basis of generated NC data, whose result is shown in Figure 11. From the simulation, it is confirmed that the generated NC data can manufacture the inducer.

Machining is carried out, using a diamond cutting tool of 0.2 mm in radius, as shown in Figure 12, under the cutting condition of 20 μm in depth of cut, 10 mm/min in feed rate, 20 μm in pick feed and 35000 rpm in spindle rotation. Figure 13 shows the machined inducer. It is seen that the inducer has a good shape and surface. The total cutting time is 42 hours.

The performance as a micropump is subjected to test, putting it together with a motor and a casing, as shown in Figure 14. As a result, it is found that the micropump can exhibit its performance.

CONCLUSION

With regard to 5-axis control ultraprecision machine tools, the current state of art in Japan is introduced, together with a machined result of a small inducer as an example of a very complicated shape. From now on, the ultraprecision mechanical micromachining technology is actively engaged in this field.

REFERENCES

[1] N. Kitamura, Y. Tsujimoto, Y. Takeuchi, Y. Sakaida, T. Kawai: 5-Axis Control Ultraprecision Micromachining of Axial-Flow Pump as a 3-D Micropart, Proc. of ASPE2005 Annual Meeting, Norfolk, Virginia (2005) 419-422

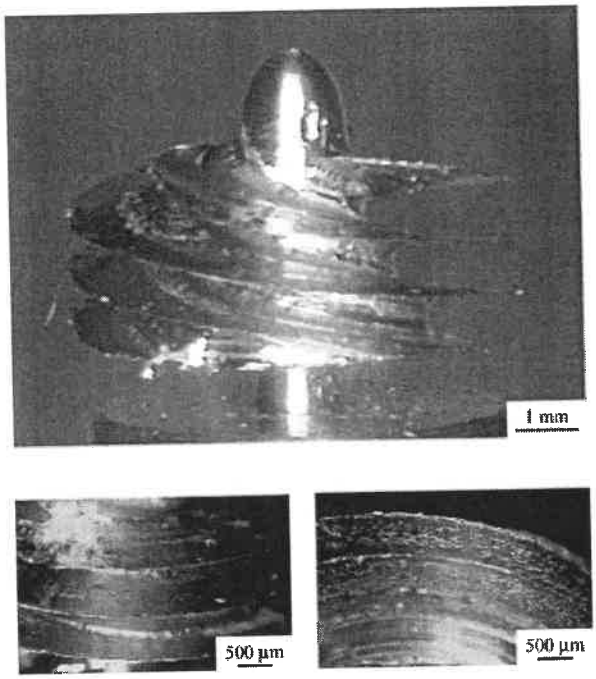

FIGURE 13. Actual machined inducer.

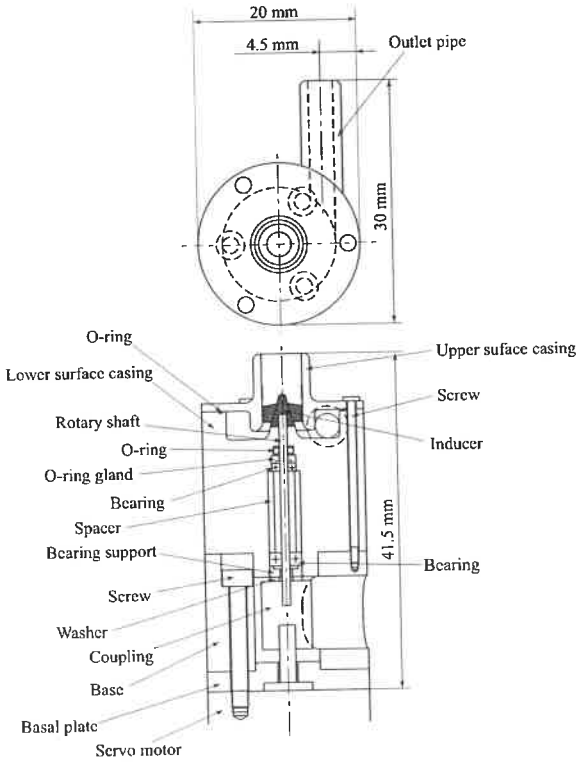

FIGURE 14. Configuration of micropump.

THE CURRENT STATE OF ART IN NANO-PRECISION MICRO/MESO MECHANICAL MANUFACTURING (M^4) PROCESSES

Tsunemoto Kuriyagawa and Nobuhito Yoshihara
Department of Nanomechanics
Tohoku University, Sendai 980-8579, Japan.

INTRODUCTION

The 21st century is said to be the century of the aging society which will require increasingly more advanced devices and systems to ensure comfort, safety and a high quality of life. There is no doubt that devices will become more complicated and more compact. The technologies used for manufacturing such devices must also be improved. Therefore, it will be important to develop infrastructure technologies such as nanotechnology (NT), information technology (IT), bio-technology (BT), and manufacturing technology (MT) from their fundamentals and then combine them organically. To ensure our position at the frontier of the MT field, we are conducting research to achieve nano-precision mechanical MT and micro/meso mechanical MT (M^4 process). This research involves both scientific investigations and practical applications.

NANO-PRECISION FLUCTUATION-FREE ASPHERICAL GRINDING

It is essential that aspheric surface lenses and mirrors have high precision, definition, and reliability for application in optical digital devices, optical information and communication systems, and advanced medical equipment such as endoscopes. Aspheric resin lenses currently make up the largest proportion of aspheric lenses produced in Japan. In this study, however, they will be replaced with glass lenses and the fluctuation in the form error will be suppressed by developing both a technique that greatly enhances the form precision of aspheric glass lenses and a mechanical manufacturing system. So far, we have been developing an arc envelope grinding method to improve the form precision of lenses, a parallel grinding method to improve their finished surface roughness, and a computer simulation of the nano-topographic surface production mechanism for mirror-finished surfaces. On the basis of these studies, we developed the world's first fluctuation-free ultra-precise aspheric grinding system as shown in Figure 1(a). Using this system, we succeeded in achieving ultra-precision grinding of aspheric glass lenses and WC glass molding dies shown in Figure 1(b). As a result, the machining accuracy of the aspheric surface was greatly enhanced (form precision: ±25 nm, surface roughness: 18 nmRy) and we could produce aspheric optical components that were free of form error patterns on machined surfaces without polishing.

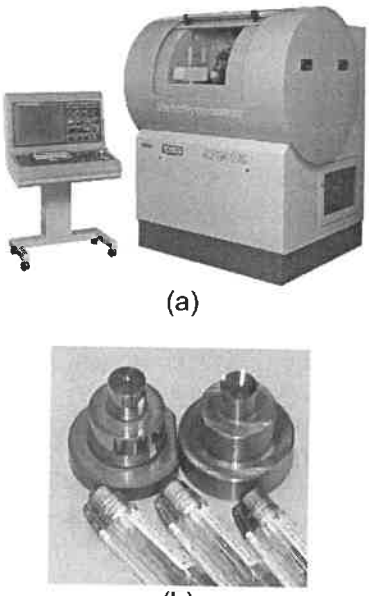

(a)

(b)

FIGURE 1. Developed manufacturing system and aspherical molding dies. (a) Fluctuation-free ultra-precision aspherical generator. (b) WC aspherical molding dies.

M^4 PROCESS TECHNOLOGY

In recent years, there has been an increasing demand for micro-components, such as microlens arrays, holographic optical components, and optical waveguides, to be composed of materials besides silicon. These components include those which have sub-millimeter dimensions and have complex shapes. In addition, the materials themselves are difficult to process, not only by the aforementioned lithographic technique but also by thermal

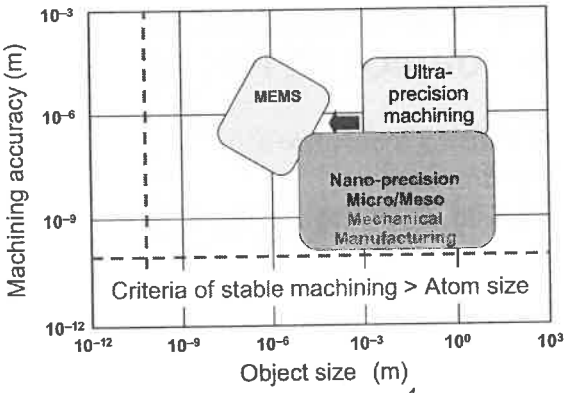

FIGURE 2. Machining size of M^4 processes.

treatment using a laser or electron beam. This is because many of them are very hard and brittle and have high melting points. Also, a micro mechanical manufacturing method of low processing costs and high processing efficiency is required. There is, however, still no established technology for mechanical manufacturing in the 10-micron to sub-millimeter range. The future development of such a technology is considered to be a critical area of investigation (see Figure 2). We are developing a new principle of mechanical manufacturing termed micro/meso mechanical manufacturing (abbreviated hereafter as the M^4 process) for micro mechanical manufacturing.

Micro-Aspheric Polishing Using an ER Fluid

Aspheric surfaces used to be predominantly polished manually by experienced workers or by using NC-driven small polishing pads. For micro aspheric surfaces, however, it is difficult to fabricate small polishing pads and to limit polishing to micro regions. To enhance the efficiency of polishing using loose abrasives, it is important to ensure that as many abrasives as possible remain in the polishing area and that this situation continues over a long time. For a micro aspheric surface, it is difficult to concentrate abrasives at the interface between the tool and the workpiece.

Therefore, we developed the world's first polishing method that concentrates polishing grains in a micro area by using an electrorheological (ER) fluid whose viscosity increases in proportion with the applied electric field intensity (see Figure 3). This has enabled micro aspheric surfaces to be polished, which previously was impossible.

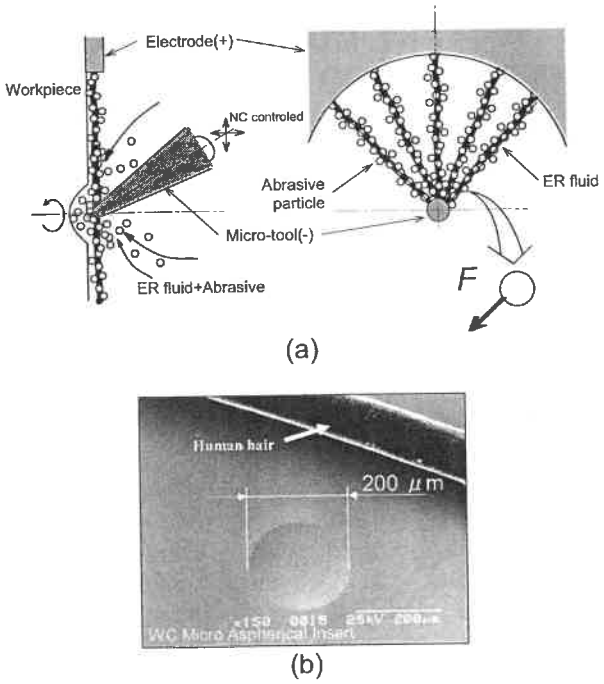

FIGURE 3. Electrorheological fluid assisted polishing. (a) Principle of electrorheological fluid assisted polishing. (b) WC micro-aspherical dies.

Ultrasonic Micro Machining with ER Fluid

We developed an ultrasonic micro machining system to produce submillimeter-sized (tens to hundreds of microns) holes and grooves and 3D microstructures in glass, ceramics, and other brittle materials using ultrasonic machining with grains. We used the electrorheological fluid method to ensure that as many abrasives possible were used for producing high-grade forms. By scanning micro tools, we can create holes, grooves, and 3D-structures.

CREATION OF FUNCTIONAL INTERFACES

We are strongly promoting the application of particle jet technologies for machining. More specifically, we are striving for a breakthrough in the ultra-precision machining field by making the best use of the particle jet technologies. These particle jet technologies are expected to have wide application not only to material removal in ultra-precision machining but also to powder jet deposition and even such diverse fields as medical treatment and biological applications.

Powder Jet Deposition

We have developed a digital powder jet deposition system capable of accurately streaming particles. Using this system we have succeeded in depositing thick ceramic films at

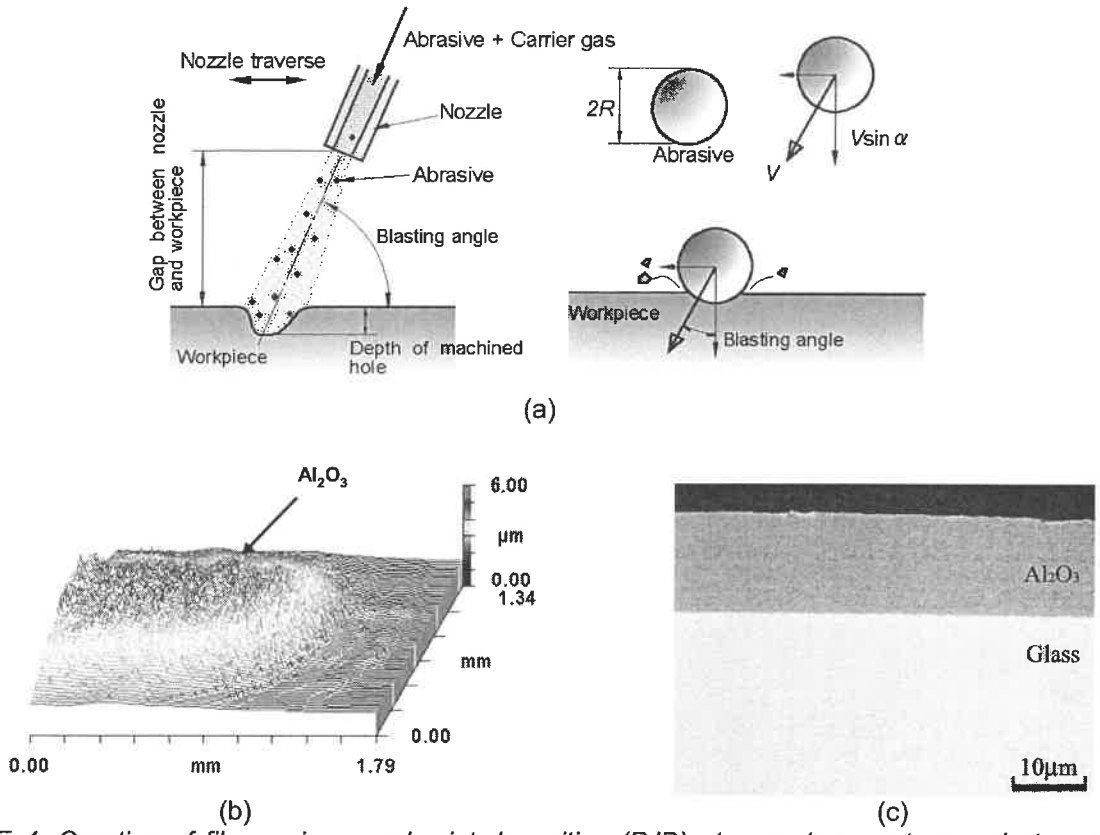

FIGURE 4. Creation of films using powder jet deposition (PJD) at room temperature and atmospheric pressure. (a) Principle of PJD. (b) Deposited Al_2O_3 film. (c) Cross section of deposited film.

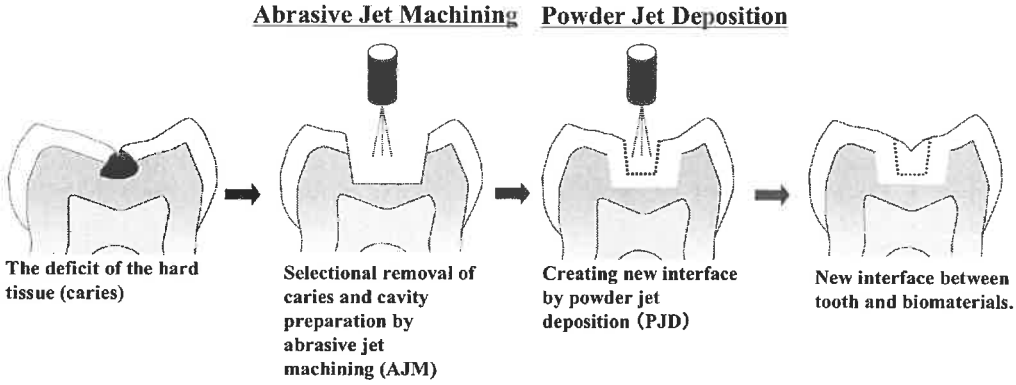
Abrasive Jet Machining
Powder Jet Deposition
The deficit of the hard tissue (caries)
Selectional removal of caries and cavity preparation by abrasive jet machining (AJM)
Creating new interface by powder jet deposition (PJD)
New interface between tooth and biomaterials.

FIGURE 5. Creation of new interface between tooth and biomaterials (Creation of Hydroxyapatite Film on Human Tooth).

room temperature and atmospheric pressure shown in Figure 4. This technology enables inexpensive production and integration of nano-ceramics at room temperature. Powder jet deposition is expected to have wide application to the manufacture of functional components such as high-frequency (GHz and THz) chips, which combine integrated circuits and high-frequency components, the next-generation of high-speed response actuators and ultrahigh-speed optical switches and also to the creation of new functional composite materials such as transparent insulating films having large voltage resistances and dielectric films for communication components, thick films for secondary batteries, and surface-modified films.

For Future Dental Treatment

We have developed a digital abrasive jet system which is capable of accurately controlling the

streaming of dental particles and is expected to have applications in dental treatment. The digital abrasive jet system has begun to be applied to non-contact painless treatment for the selective removal of carious dentin (i.e. a tooth cavity) without affecting healthy dentin. It has also been applied to oral cleaning as a non-contact method for the effective removal of plaque from teeth surfaces without damaging the dentine.

With deposition by particle streaming in mind, we bombarded the surface of a human tooth (enamel) with hydroxyl-apatite (HA) particles at high speed at room temperature and atmospheric pressure and succeeded in depositing a thick film of HA for the first time. This method enables dentine to be reconstructed and is attracting attention in the areas of treatment and prevention of teeth cavities as a technology that has the potential to revolutionize dental treatment (see Figure 5).

SUMMARY

New technologies for ultra-precision aspherical grinding and polishing of aspherical optical lenses and molding dies were introduced. Also, new powder jet technology, which will be widely applied to the creation and control of functional interface near future, was introduced.

REFERENCES

[1] M.Saeki, T.Kuriyagawa and K.Syoji, *Machining of Aspherical molding Dies Utilizing Parallel Grinding Method*, J. of JSPE, 68, 8, (2002) 1067-1071. [in Japanese]

[2] M.Saeki, T.Kuriyagawa, N.Yoshihara, W.K.Chen and K.Syoji, *Study of Parallel Grinding Method for Aspheric Optical Elements*, Proc. of Int. Conf. on Leading Edge Manufacturing in 21st Century (JSME), (2003) 49-54.

[3] T.Kuriyagawa, N.Yoshihara, M.Saeki and K.Syoji, *Nano-Topography Characterization of Axisymmetric Aspherical Ground Surfaces*, Key Engineering Materials, 238, (2003) 125-130.

[4] N.Yoshihara, T.Kuriyagawa and K.Syoji, *Effect of Wheel Revolutional Speed on Striped Pattern on Surfaces Finished by High-Speed Reciprocation Grinding*, Proc. of the 10th International Conference on Precision Engineering, (2001) 446-450.

[5] N.Yoshihara, T.Kuriyagawa, H.Ono and K.Syoji, *Nano-Topography on Axisymmetric Aspherical Ground Surface*, 7th International Symposium on Advances in Abrasive Technology, (2004) 525-529.

[6] J.Yan, K.Syoji and T.Kuriyagawa, *A New Diamond Turning Method for Fabrication of Convex aspheric Surface on Hard Brittle Material*, Proc. of the 10th Int. Conference on Precision Engineering, (2001) 254-258.

[7] J.Yan, J.Tamaki, K.Syoji, T.Kuriyagawa, *Single-point diamond turning of CaF_2 for nanometric surface*, Int. Journal of Advanced Manufacturing Technology, 24, (2004) 640-646.

[8] J.Yan, M.Yoshino, T.Kuriyagawa, T.Shirakashi, K.Syoji and R.Komanduri, *On the Ductile Machining of Silicon for Micro Electro-Mechanical Systems (MEMS), Opto-electronic and Optical Applications*, Materials Science and Engineering A, 297 (1-2), (2001) 230-234.

[9] T.Kuriyagawa, K.Syoji, *Development of electrorheological fluid assisted machining for 3-dimensional parts*, J. of JSPE, 65, (1999) 1145-1149. [in Japanese]

[10] T.Kuriyagawa, M.Saeki and K.Syoji, *Electrorheological Fluid-Assisted Ultra-Precision Polishing for Small Three-Dimensional Parts*, J. of the Int. Societies for Precision Engineering and Nanotechnology, 26, 4, (2002) 370-380.

[11] T.Kaku, T.Kuriyagawa and N.Yoshihara, *Electrorheological Fluid-Assisted Polishing of WC Micro Aspherical Glass Molding Dies*, 7th International Symposium on Advances in Abrasive Technology, (2004) 417-421.

[12] T.Kuriyagawa, T.Shirosawa, O.Saitoh and K.Syoji, *Development of Micro Ultrasonic Abrasive Machining System (Studies in Micro Ultrasonic Abrasive Machining, 1st Report)*, JSME International Journal Series C, 45 (2), (2002) 593-600.

[13] T.Kuriyagawa, T.Sakuyama, K.Syoji and H.Onodera, *A New Device of Abrasive Jet Machining and Application to Abrasive Jet Printer*, Key Engineering Materials, 196, (2001) 103-110.

[14] N.Yoshihara, T.Kuriyagawa, Y.Yasutomi, K.Ogawa, *Powder Jet Deposition of Ceramic Films*, Proc. of the 3rd Int. Conf. on Leading Edge Manufacturing in 21st Century, (2005) 833-838.

[15] M.Noji, K.Sasaki, T.Kuriyagawa, O.Suzuki, K.Ogawa, M.Kanehira, *Creating new interface between tooth and biomaterials using powder jet technology*, International Congress Series 1284 (2005) 302-304.

CHALLENGES TO MINIATURIZATION IN MICRO EDM

Masanori Kunieda
Department of Mechanical Systems Engineering
Tokyo University of Agriculture and Technology
Koganei, Tokyo, Japan

INTRODUCTION

In electrical discharge machining (EDM), the process force is negligibly small and removal occurs regardless of workpiece material hardness because EDM is a thermal process. For this reason, EDM processes are widely used for the micro-machining of fuel injection nozzles, spinneret holes for synthetic fibers, electronics and optical devices, and micro-tools for the mass-production of these parts. However, the minimum machinable size is no smaller than several micrometers. This paper discusses some reasons for the limit of miniaturization in EDM and introduces the latest technologies for reducing the minimum size obtainable by EDM.

MINIMUM SIZE

The minimum machinable diameter of micro rods was investigated [1] using the Wire Electro-Discharge Grinding (WEDG) method which was developed by Prof. Masuzawa [2]. Using a wire electrode traveling along the groove of a wire guide, a micro rod can be machined like a turning process. Tool electrode wear is not a problem because a renewable wire is used as the tool electrode. In addition, since the wire is supported by the wire guide, machining accuracy is not deteriorated by wire vibration unlike the WEDM process.

At present, however, the minimum machinable diameter of micro rods is about 2 μm at best even using WEDG. Figure 1 shows the relationship between the target rod diameter and machined rod diameter [1]. Cemented tungsten carbide rods of 0.3 mm in diameter with a WC particle size of 0.4 μm were used as the workpiece. It was found that with decreasing target diameter, the machined diameter decreases. However, micro rods smaller than 2.3 μm in diameter were not obtained even with the minimum discharge energy. Red dots indicate failure in machining due to breakage of the micro rod. Deviation in the machined rod diameter from the target rod diameter was obviously caused by the positioning error, thermal deformation of the equipment, and inaccuracy of wire electrode diameter. However, these are not the reasons for why rod diameter under 2.3 μm was not obtained. If they were, we would have obtained successful results in the vacant zone since machining was repeated many number of times. Therefore, in this case, the plausible reasons would be the minimum limit of discharge energy, residual stress inside the workpiece, and microstructure of the workpiece material.

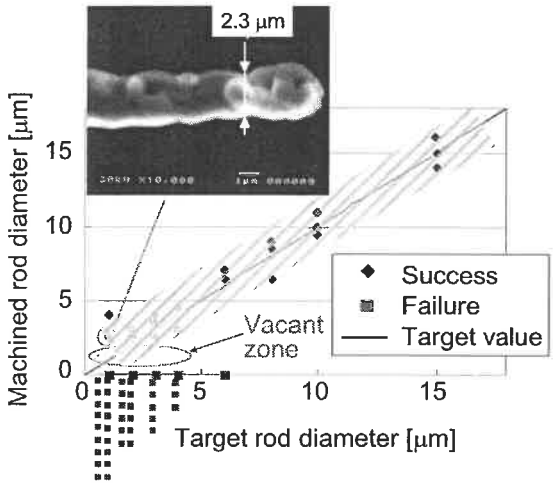

FIGURE 1. Relationship between target rod diameter and machined rod diameter (WC grain size : 0.4 μm) [1].

MINIMUM DISCHARGE ENERGY

Pulse Generator used in Micro EDM

Early EDM equipment used relaxation type pulse generators with capacitor discharges as shown in Figure 2. With improved capability of power transistors which can handle large currents with high response, the relaxation type was replaced by the transistor type. This is because, on the outbreak of short circuit in the discharge gap, electric current continues flowing through the gap. This leak current does not allow the capacitance to be charged, resulting in interruption of pulse discharge. Furthermore,

since the leak current generates Joule heat at the short circuiting spot, the recovery of dielectric strength of the gap is hindered even if the mechanical contact is released due to generation of high temperature plasma, resulting in machining instability.

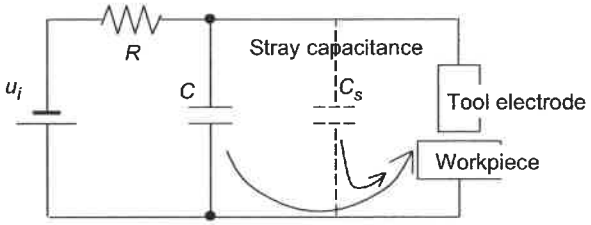

FIGURE 2. Relaxation type pulse generator.

Nevertheless, in micro EDM, the relaxation type pulse generator is still being used because it is difficult to obtain significantly short pulse duration with constant pulse energy using the transistor type pulse generator. With the transistor type, there is a delay in the circuit for detecting the discharge occurrence, in the circuit for generating a signal to switch off the power transistor, and also in the power transistor itself. Hence it is difficult to keep the discharge duration constant, shorter than several tens of nanoseconds.

With the relaxation type pulse generator, electric charge in the capacitance can be discharged in a short period of time even shorter than ten nanoseconds followed by recovery of dielectric strength of the gap. Thus charging and discharging of the capacitance can be repeated autonomously. The discharge duration can be very short because the resistance and inductance in the circuit loop on the right side of the circuit shown in Figure 2 are negligibly small.

Influence of Stray Capacitance

In order to obtain smaller discharge energy per pulse, the capacitance should be decreased as much as possible. However, in an actual EDM machine, there exists stray capacitance C_s in the circuit between the electric feeders, between the tool electrode holder and work table, and between the tool electrode and workpiece. Hence all the charge stored in C_s is discharged to the working gap together with the charge stored in the capacitor C wired to the circuit. For this reason, shortening of electric feeders and use of electrical insulator for the tool electrode holder and work table materials are effective for reducing discharge energy. In the final finishing, when minimum discharge energy is necessary, the capacitor is not wired and machining is conducted with C_s only. However, the discharge energy smaller than $1/2(C_s u_i^2)$, where u_i is voltage of the power source, cannot be obtained, limiting miniaturization in micro EDM [3].

Egashira et al. [4] thus decreased the voltage of the power source u_i, usually 40 to 100 V, to 20 V and obtained the minimum rod diameter of 1μm. However, decrease in the open voltage normally results in machining instability because the gap width becomes narrow, leading to the frequent occurrence of short circuiting.

Figure 3 shows the influence of gap voltage measurement on the discharge energy. An oscilloscope of 1 GHz band width, and voltage probe of 10 MΩ input resistance and 8 pF input capacitance were used. Since the probe input capacitance was not negligibly small compared to the stray capacitance of roughly 10 pF, the discharge current i_1+i_2 measured at point B was greater than i_1 measured at point A. This indicates that even gap voltage measurement may deteriorate the miniaturization limit.

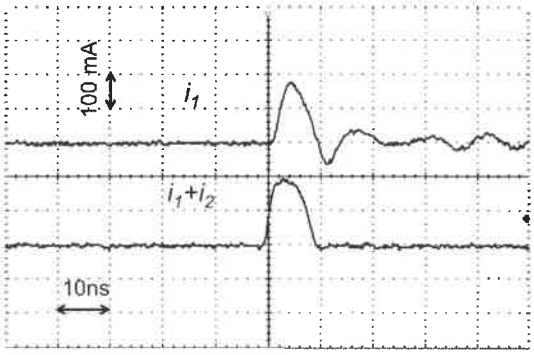

(a) Current waveforms

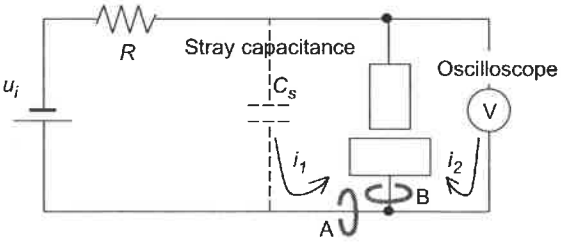

(b) Current measurement points

FIGURE 3. Influence of voltage measurement.

To minimize the influence of the stray capacitance, resistances may be wired to the discharge gap as close as possible, as shown in Figure 4. Thus discharge current pulse of 80 mA in peak and 4 ns in duration was obtained. Using the minimum discharge energy, however, the material removal rate of the relaxation type pulse generator is significantly low. This is because the frequency of discharge per second is not high due to the occurrence of short circuiting described in the previous section.

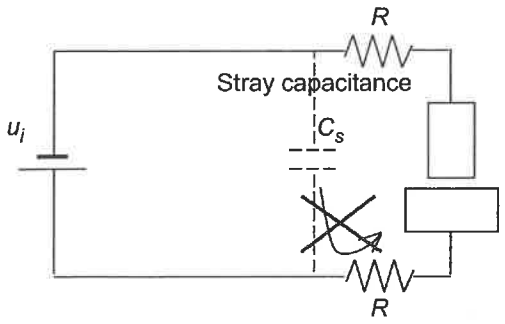

FIGURE 4. Minimizing influence of stray capacitance.

Electrostatic Induction Feeding Method

To obtain the minimum discharge energy with a significantly high material removal rate, a new pulse generator was developed using electrostatic induction feeding [5] as shown in Figure 5. To apply pulse voltage to the discharge gap, a pulse power source was used in place of the direct current power supply. Then the pulse voltage was coupled with the tool electrode by capacitance *C*. Since the polarity of the working gap is reversed at both the rising and falling of the pulse voltage, discharge is bipolar. Moreover, because the pulse power source is coupled by capacity, discharge can occur only once for each half cycle of the pulse. Leak current does not flow even when short circuiting occurs, therefore guaranteeing the recovery of the dielectric strength of the gap after every discharge if at least the mechanical contact is released.

Figure 6 shows the discharge current measured for the relaxation type and the electrostatic induction feeding pulse generator. It was found that, in the case of electrostatic induction method, discharge is bipolar and occurs regularly synchronized with the pulse voltage. In contrast, discharge frequency is not uniform with the relaxation type pulse generator.

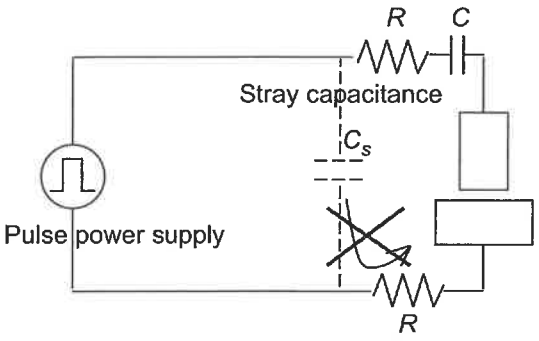

FIGURE 5. Electrostatic induction feeding method.

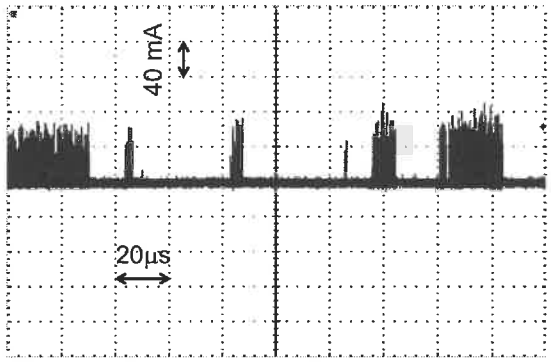

(a) Relaxation type

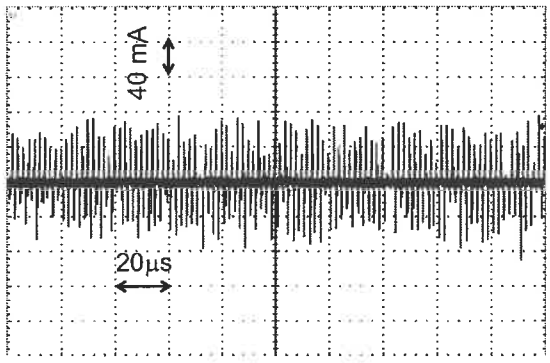

(b) Electrostatic induction feeding method

FIGURE 6. Comparison of machining stability between relaxation type pulse generator and electrostatic induction feeding method (R=15 kΩ, C=15 pF, open voltage: 40 V).

Capacitance C can be replaced by a gap between the cylindrical feeding electrode and coaxially rotating spindle as shown in Figure 7. Since non-contact electric feeding is possible, this method enables feeding electricity to high speed rotating spindles, air bearing spindles and magnetic bearing spindles without causing runout of the spindles.

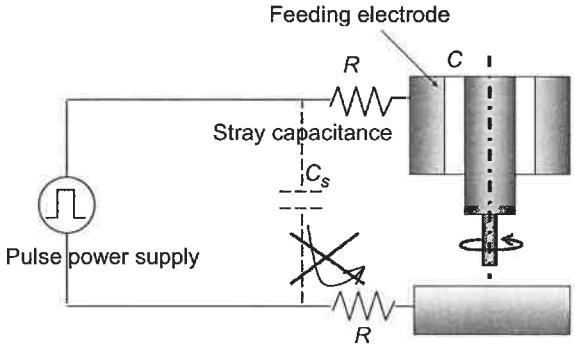

FIGURE 7. Non-contact electric feeding.

Using the electrostatic induction feeding method with minimum discharge energy, a tungsten carbide micro rod of 1.3 μm in diameter was obtained successfully as shown in Figure 8. It took about 18 min to reduce the diameter from ϕ5 μm to ϕ1.3 μm. Finish-cut with a depth of cut of 0.3 μm was repeated six times.

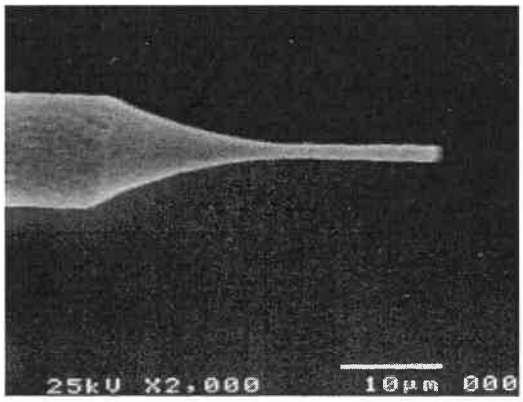

FIGURE 8. Micro rod machined by electrostatic induction feeding method.

INFLUENCE OF RESIDUAL STRESS

Residual Stress Generated by Discharge

There are two kinds of residual stress which may influence on miniaturization; one is generated by EDM itself on the machined surface, and the other is already present inside workpiece materials prior to machining.

Since EDM is a thermal process, tensile residual stress is generated in the re-solidified layer. Spur et al. [6] reported that thin fins cut by wire EDM may bend due to the residual stress caused by the EDM process when fin thickness is smaller than 0.1 mm in rough cutting. Figure 9 shows results of cutting micro fins using micro WEDM [7]. Gauge steel sheets of 90 μm in thickness were cut by a tungsten wire electrode of 30 μm in diameter using oil as the working fluid. Fins cut by the relaxation type pulse generator were bent, while those cut by the electrostatic induction feeding method were straight. In the electrostatic induction feeding method, since recovery of dielectric strength of the gap is guaranteed after every discharge, thermal load on the workpiece surface is constant and uniform, resulting in thinner heat affected zones compared to the relaxation type.

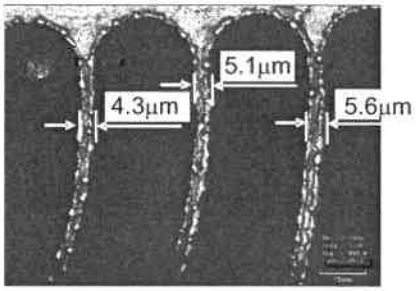

(a) Relaxation type

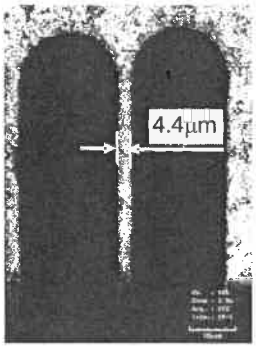

(b) Electrostatic induction feeding

FIGURE 9. Effect of residual stress generated by micro WEDM [7].

Grooves were cut serially from the right to the left. Tensile stress generated on the right side surface of a fin was released when the left side surface was being formed followed by the generation of tensile residual stress on the left side.

Residual Stress Present in Raw Materials

Residual stress already present prior to machining can be found in tungsten rods which are produced by the wire drawing process. The residual stress in the axial direction is not distributed uniformly in the radial direction. On the other hand, the center of rotation does not always coincide with the center of the material rod when the material rod is held by the chuck of the spindle of the WEDG machine. Therefore the micro rod is generally formed off-centered from the center of the material rod as shown in Figure 10.

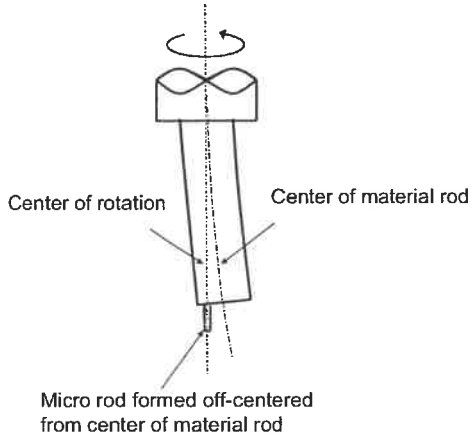

FIGURE 10. Micro rod formed off-centered from center of material rod.

Hence, when the micro rod is formed in the area where the residual stress increases with the distance from the center of the material rod, the machined micro rod will bend outward, while in the area where the residual stress decreases with increasing distance from the center of the material, it will bend inward as shown in Figure 11. The same test was carried out using tungsten rods whose axial residual stress was released by annealing. In comparison with un-annealed tungsten rods, the bending deformation was small regardless of eccentricity [1].

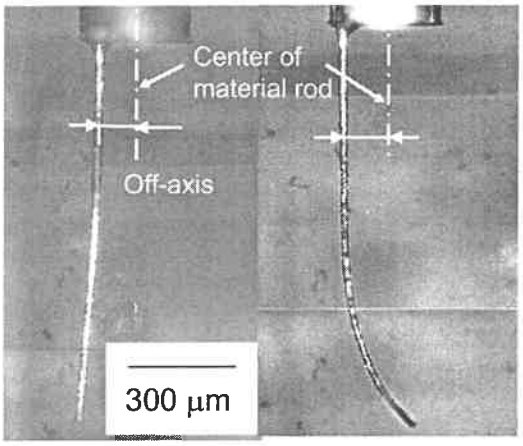

Off-axis 90μm Off-axis 120μm

FIGURE 11. Effect of residual stress present in tungsten rod prior to machining [1].

INFLUENCE OF MICRO-STRUCTURE OF WORKPIECE

Influence of grain size of tungsten carbide (WC) in cemented tungsten carbide material on the limit of miniaturization was examined. Since the minimum diameter machinable using cemented tungsten carbide with WC grain size of 0.4 μm was 2.3 μm as shown in Figure 1, change in the limit was examined using grain sizes larger than 0.4 μm. Figure 12 shows the relationship between the target rod diameter and machined rod diameter with the grain size of 2 μm [1]. The vacant zone area was wider and the minimum machinable rod diameter increased to 3 μm. The photo demonstrates that grain size may influence the limit because of the difference in the melting point between the WC grain and Co binder.

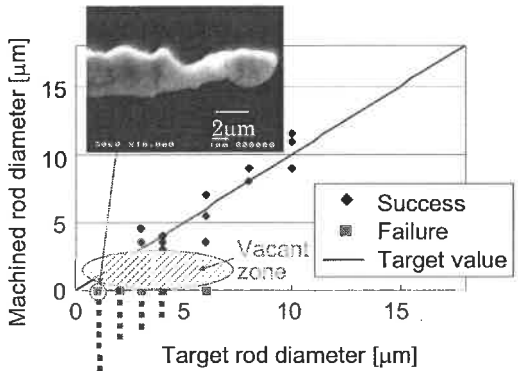

FIGURE 12. Influence of microstructure of workpiece on miniaturization (WC grain size : 2 μm) [1].

CONCLUSIONS

Factors which influence on the limit of miniaturization in micro EDM were discussed. To minimize the discharge energy maintaining machining stability, the electrostatic induction feeding method was developed. A tungsten carbide micro rod of 1.3 μm in diameter was obtained. Under the influence of the tensile residual stress generated by EDM, the micro beam machined is bent to the side where EDM is performed. When the center of the micro rod machined is off-centered from the center of the material rod in which residual stress is generated by the wire-drawing process prior to electrical discharge machining, this residual stress causes deformation of the micro rod after machining. Releasing the residual stress by annealing is effective for avoiding the deformation. WC grain size influences the minimum machinable diameter of cemented tungsten carbide rods.

REFERENCES

[1] Kawakami T, Kunieda M. Study on Factors Determining Limits of Minimum Machinable Size in Micro EDM. Annals of the CIRP. 2005; 54 (1): 167-170.

[2] Masuzawa T, Fujino M, Kobayashi K. Wire Electro-Discharge Grinding for Micro-Machining. Annals of the CIRP. 1985; 34 (1): 431-434.

[3] Masuzawa T. State-of-the-art on Micromachining. Annals of the CIRP. 2000; 49 (2): 473-488.

[4] Egashira K, Mizutani K. EDM at Low Open-Circuit Voltage. IJEM. 2005; 10: 21-26.

[5] Kunieda M, Hayasaka A, Yang X, Sano S, and Araie I. Study on Nano EDM Using Capacity Coupled Pulse Generator. Annals of the CIRP. 2007; 56 (1): 213-216.

[6] Spur G, Uhlmann E, Doll U, Daus N. WEDM of Microstructured Component Parts – Heat Conduction Model. IJEM. 1999; 4: 41-46.

[7] Yang X, Xu C, Kunieda M. Miniaturization of WEDM Using Electrostatic Induction Feeding Method. Proc. of JSPE Autumn Meeting. 2008: to be presented.

MICROFACTORY
-NOVEL MANUFACTURING SYSTEMS FOR PRECISION MACHINING-

Nozomu Mishima[1], Shinsuke Kondoh[1], Shizuka Nakano[1], Kiwamu Ashida[1] and Keijiro Masui[1]
[1]Advanced Manufacturing Research Institute
National Institute for Advanced Industrial Science and Technology
Tsukuba, Ibaraki, Japan

1. FIRST PROPOSAL; MICROFACTORY

"Microfactory" was a concept of a future manufacturing system, which was proposed in the Japanese national R&D project named "Micro Machine Project [1]." The original concept of the microfactory was a super-miniature manufacturing system that consists of miniature machine tools and manipulators. In 1999, AIST developed the first prototype of a microfactory. (Figure1) The result of the test production [2] showed that the microfactory-like miniature manufacturing system could be an option for precision machining. We also insisted that the advantage of the microfactory would be low environmental impact and costs of manufacturing. In addition, the smallness of the machines enables flexible layout changes when the product designs have been modified. However, since there have been no study on evaluating the microfactory quantitatively, the advantage of the system to reduce environmental impact and enhance production flexibility of micro mechanical fabrication is still uncertain. So, the authors have been trying to propose a method to support system configuration design of a microfactory-like system. Then, we are trying to show its merits on diverse-types-and-small-quantity production.

FIGURE 1. Overview of the microfactory

2. PRECISION MACHINING BY THE MICROFACTORY

2.1 Miniature Machine Tools

The microfactory shown in Figure 1 consisted of five miniature components. The five components were a lathe, a milling machine and a press machine for precision machining, and a transfer arm and a micro-hand for assembly. Every component was designed rather specifically and extremely small. In the aspect of machining, key components of the microfactory were the micro lathe (Figure 2) and micro milling machine (Figure 3).

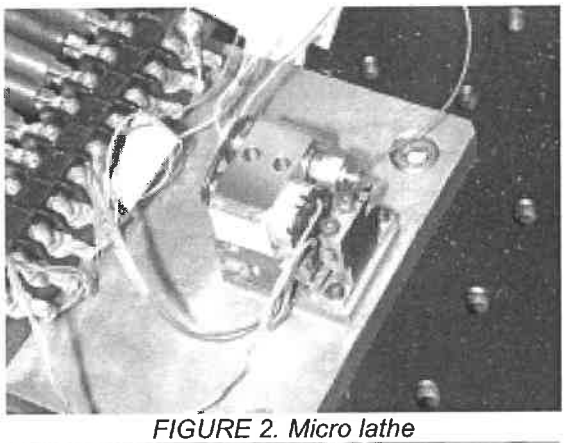

FIGURE 2. Micro lathe

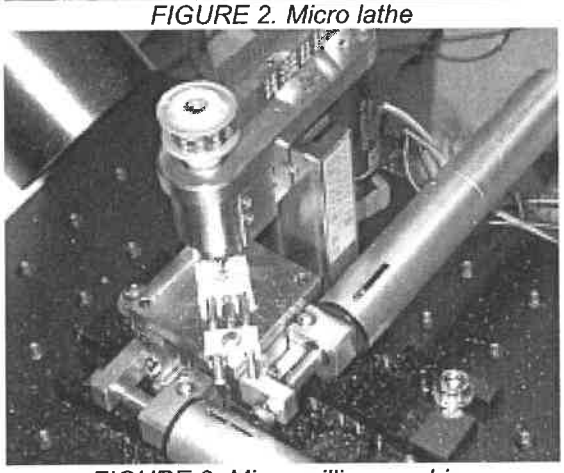

FIGURE 3. Micro milling machine

2.2 Machining capability of miniature machine tools

Form-shaping theory [3] is a well-known method to analyze cutting motions of machine tools. Based on the theory, relative positioning error between the cutting tool and the workpiece called form-shaping error function is calculated. Form-shaping error function includes many design parameters and error factors, and the function varies with structures of machine tools. By applying robust design technique to the form-shaping error function, it is possible to identify how design parameters, error factors, sizes and structures affect the error [4]. Figure 4 shows the average positioning error, when the machine size changes proportionally. The size of a standard machine tool is normalized as 1. Considering scale effects of error sources, it can be calculated that a miniature machine tool having about 1/10 size of a normal machine tool has the smallest error. In the aspect of accuracy, miniature machine tool can be an option.

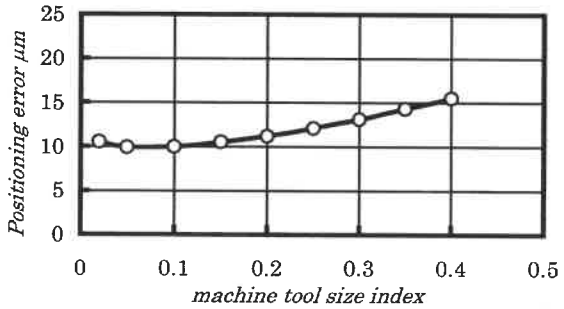

FIGURE 4. Optimum size of machine tool for micro mechanical fabrication

2.3 Test machining by the microfactory

In order to show the machining capability of the microfactory, a test product which was a miniature ball bearing shown in Figure 5 having 900 microns diameter was made.

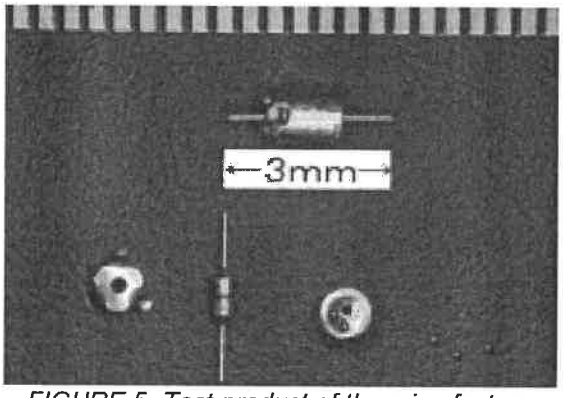

FIGURE 5. Test product of the microfactory

Since the machining of each part except the steel ball and assembly of the ball bearing was done by the microfactory, it can be said that the microfactory had enough capability for precision machining.

3. EFFICIENCY OF THE MICROFACTORY

3.1 What are the advantages?

We insisted the "Microfactory" is a hopeful system for precision machining. And downsizing of the manufacturing system can be an option to reduce environmental impact of manufacturing. In addition, since the smallness of each machine enables changeable factory layout, downsizing of machines will enhance production flexibility, too. However, whether the system is really environmentally conscious and flexible has not been examined quantitatively. An appropriate index to evaluate manufacturing systems will help the microfactory concept to become more practical.

3.2 Proposal of a system efficiency index

The authors proposed an efficiency index named "total performance indicator (TPI) [5]." Although the index was proposed to evaluate product efficiency, the same idea can be applied to evaluate the efficiencies of manufacturing systems. The index is defined by (1).

$$Ef = \frac{F}{\sqrt{C}\sqrt{E}} \tag{1}$$

Ef: total performance indicator (TPI)
F: system throughput
C: cost of the system (yen/hour)
E: environmental impact (kg-CO2/hour)

By defining the throughput by number of products assembled in an hour, the efficiency index for the microfactory can be calculated. "C" can be calculated as a sum total of machine costs, labor costs and electricity cost during the corresponding time. Labor cost is assumed to be 5.0 (million yen) per person per year. For "E", since the microfactory does not generate any special waste, equivalent CO2 emission will be a good index to estimate the environmental impact. So, "E" can be expressed by the sum of CO2 emission caused by electricity consumption (1kwh =0.38kg-CO2) and machine material.

3.3 Analysis of the manufacturing process

As the result of the test production, the microfactory was capable of precision machining. Therefore, it can be said that the microfactory

has possibility as a future manufacturing system to produce many varieties of micro mechanical products. However, it still has some problems, such as low productivity. To improve the productivity, an appropriate system configuration should be considered. To fabricate the miniature ball bearing shown in Figure 5, manufacturing process in Figure 6 was applied. Every part starts from the material shown in the upper side, passes through some segment-processes shown in the block and reaches the assembly processes in the lower side. From the figure it is easily imaginable that the assembly processes are very time-consuming, because the processes should be done sequentially under a microscopic vision using the micro-hand.

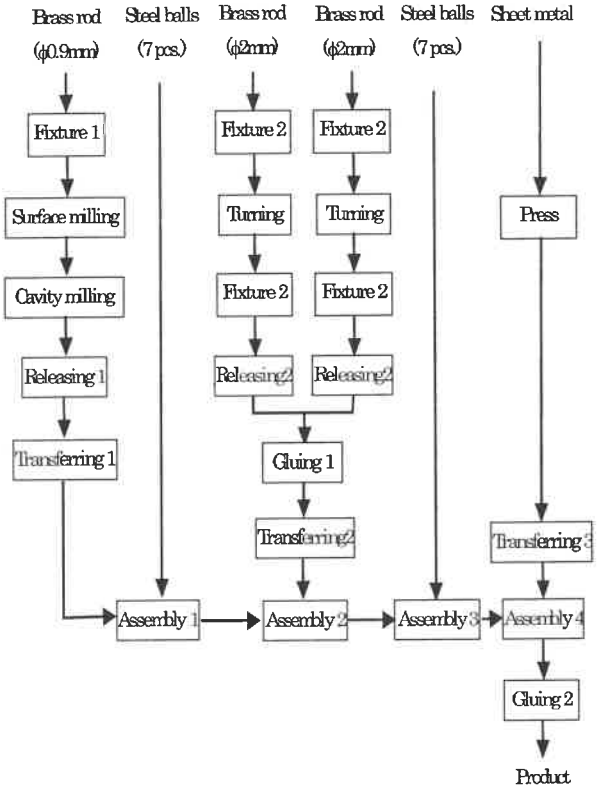

FIGURE 6. Process diagram

Table 1 indicates the average process time of the corresponding processes in Figure 6, after operators had been skilled enough. Number of operators required for each process is also shown in the table. According to Table 1, it is evident that the assembly operations done by the micro hand were the bottlenecks for the throughput. Machine and labor costs, and the energy consumption of each machine are important factors to consider system efficiencies.

TABLE 1. Average process time

Process name	Process time	No. of operators
Fixture 1	10 sec.	1
Fixture 2	5 sec.	1
Surface milling	1 min.	1
Cavity milling	2 min.	1
Turning	2 min.	1
Press	0.2 sec.	0
Releasing 1	10 sec.	1
Releasing 2	5 sec.	1
Transferring 1	1 sec.	0
Transferring 2	1 sec.	0
Transferring 3	1 sec.	0
Assembly 1	3 min. (per ball)	1
Assembly 2	3 min.	1
Assembly 3	3 min. (per ball)	1
Assembly 4	3 min.	1
Gluing 1	1 min.	1
Gluing 2	2 min.	1

3.4 System configuration redesign

Based on equation (1), system efficiency of the microfactory can be calculated using the actual data. Figure 7 shows the behavior of the system efficiency (TPI) calculated by the equation. From the figure it can be said that there is a peak value of TPI in each configuration. It means that system configuration can be redesigned based on the analysis.

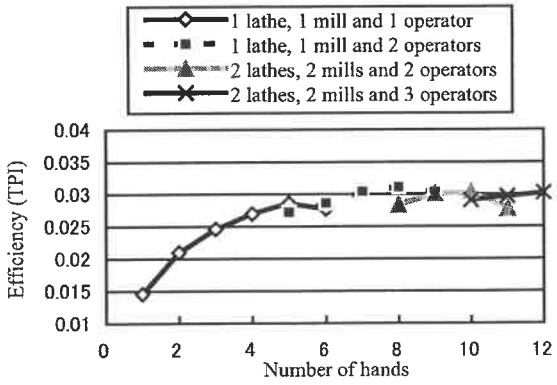

FIGURE 7. System efficiency of the microfactory

3.5 Comparison with a conventional system

Figure 8 shows a comparison of TPI of the mass production system with that of the microfactory, corresponding to average throughput. The TPI of the mass production system decreases with the decrease of the throughput, because the system should be designed to satisfy maximum throughput. TPI of microfactory does not change remarkably. It is because the mass production system meets the low demand by stop-and-go of the system. On the other hand, microfactory can do that by changing the number of the installed systems.

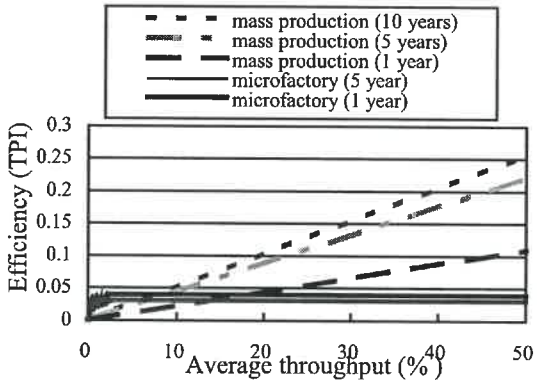

FIGURE 8. Comparison of TPI

4. A NEW PROPOSAL; ON-DEMAND FACTORY

In the former section, the idea of redesigning the system configuration has been considered. However, since the Microfactory was a conceptual proposal, it was difficult to produce real products. To apply the idea to practical manufacturing system, a new development was necessary. The next generation microfactory should be a system that enhances the original concept such as miniature, flexible, environmentally conscious and lean, to practical levels. Figure 9 shows a new prototype of a microfactory, named on-demand factory [6].

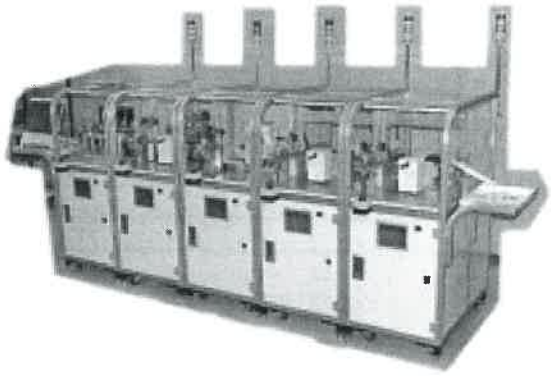

FIGURE 9. On-demand factory

The system has five modularized units connected in-line. The size of each unit is 500* 800*1200mm. It is a highly modularized system for MEMS devices. MEMS devices are usually fabricated on silicon base structures, using silicon processing technologies such as chemical vapor deposition or photolithography. Silicon is a good base material for MEMS devices, but the concept of metal-based MEMS has been proposed. By changing the base material, low-cost, environmentally benign and efficient micro mechanical press can be used. Our estimation shows that TPI of the on-demand factory is higher than that of the conventional silicon-based system. Basically, it can be said that the on-demand factory has a great capability for diverse-types-and-small-quantity production of precise mechanical products.

5. CONCLUSIONS AND MORE

Machining capability of each miniature machine tool was supported by theoretical analysis based on the form-shaping theory. The capability of the overall system was proved through the test production. A simple index (TPI) to evaluate the efficiency of a microfactory-like system was proposed. It was able to re-design system configuration. AIST has proposed the next generation microfactory named on-demand factory. TPI of the on-demand factory seems higher than that of a conventional facility.

As future work, more precise comparisons with mass production systems are required in order to prove microfactory-like systems are effective for precise mechanical products.

REFERENCES

[1] Kawahara N, Suto T, Hirano T, Ishikawa Y, Ooyama N and Ataka T, Microfactories; New Applications of micro machine technology to the manufacture of small products, Microsystem Technologies, 1997; 3-2, 37-41.

[2] Mishima N, Ashida K, Tanikawa T and Maekawa H, Design of a Microfactory, Proc. of ASME/DETC 2002, Montreal, Canada, Sept. 2002, DFM-34164.

[3] Reshtov D N and Portman V T, Accuracy of Machine Tools, ASME Press, New York; 1988.

[4] Mishima N, Design evaluation method for miniature machine tools utilizing form-shaping theory, Proc. of ASME/DETC 2003, Chicago, IL, Sept. 2003, DAC-48787.

[5] Kondoh S, Masui K, Hattori M, Mishima N and Matsumoto M, Total Performance Analysis of Product Life-cycle Considering the Deterioration and Obsolescence of Product Value, Proc. of CARE INNOVATION 2006, Vienna, Austria, 2006, 2.10.1.

[6] Nakano S, Ashida K, Park J and Akedo J, On-demand MEMS factory system consists of metal forming and aerosol deposition, Proc. of the 24th International Japan-Korea Seminar on Ceramics, Shizuoka, Japan, Nov. 2007, 735-738.

PRECISION ENGINEERING: THE EUROPEAN WAY

Hendrik Van Brussel[1], Jan van Eijk[2], Henny Spaan[3], and Ekkard Brinksmeier[4]
[1]Division PMA
Katholieke Universiteit Leuven, Belgium
[2] Dep. Precision and Microsystems Engineering
Technical University Delft, the Netherlands
[3]IBS Precision Engineering BV
Eindhoven, the Netherlands
[4]Laboratory of Precision Machining
University of Bremen, Germany

INTRODUCTION

In Europe, precision engineering, as an engineering discipline, is historically rooted in the need for accurate instruments and machines for astronomy, horology, navigation, surveying, weaponry, metrology (standards), manufacturing (machine tools), and dates back to Renaissance times.

Names as Gemma Frisius (1508-1555, Leuven School, astronomic and navigation instruments), and his brilliant pupil Mercator [1], even James Clerk Maxwell (1831-1879, who formulated the principles of kinematic design), Carl Zeiss (1816-1888, optical instruments), Ernst Abbe (1840-1905, instruments), Robert Willis (1800-1875, air bearings (!), gears, machine design), to name only a few giants, are connected with the early development of precision engineering in Europe.

Pioneering European companies, producing metrology instruments and high-precision machine tools, were Zeiss and Mahr in Germany (metrology instruments and microscopes), Dixi and SIP in Switzerland (jig borers, co-ordinate measuring machines). The extensive and longstanding research in precision engineering at Philips Research Labs and at Philips CFT has been instrumental in spinning out several world-leading precision engineering companies, like ASML (wafer steppers), FEI (electron microscopes), Singulus (disc mastering equipment), turning the Eindhoven region into a world centre of precision engineering.

The emergence of precision engineering as a fully-fledged academic discipline came only some 40 years ago, with pioneering work of the group around Prof. P. McKeown at Cranfield, with the establishment of CUPE (Cranfield Unit for Precision Engineering) and with one of the first academic programmes in precision engineering in Europe. The technical universities in the Netherlands have a longstanding tradition of teaching and research in precision engineering (originally called 'fine mechanics'). While German academic research in precision engineering was for a long time primarily orientated towards machine tools, more recently an impressive activity in precision and microsystems engineering has emerged at universities (RWTH, Aachen, University of Bremen) and research institutes (Fraunhofer IPT, PTB).

This paper is meant to highlight a few salient developments in precision engineering in Europe. This will be done by revisiting some precision engineering principles, thereby indicating some innovative solutions and their application in new products and processes resulting from European research and development programmes.

PRINCIPLES OF PRECISION ENGINEERING REVISITED

Design for stiffness

In precision engineering applications, design for stiffness, rather than design for strength, is the ruling paradigm. Classical passive solutions soon hit an upper bound due to stacked slideways, Hertzian contact deformations in roller guideways and bearings, elastic deformations in machine elements, etc. The mechatronics design approach provides active solutions by which extremely high (or extremely low) active stiffnesses can be obtained. Too often the importance of dynamic stiffness is overlooked. High dynamic stiffness means a high lowest natural frequency and sufficient – preferably viscous- damping. This has consequences for the obtainable bandwidth of the positioning loops. Indeed, one important rule of thumb states that the positioning servo loop

bandwidth must be lower than half of the lowest natural frequency of the machine structure. The lowest resonance frequency can be increased by increasing the stiffness, but equally well, and less understood, by lowering the mass. The use of parallel kinematic configurations is an important step for increasing the dynamic stiffness and is increasingly applied in European machine tools and measuring machines. Also linear motor drives allow to increase the position loop bandwidth dramatically, thanks to the absence of low-frequency resonances.

In Figure 1, a high-speed electrospindle for mould-and-die milling is shown. It has an active front radial air bearing, with an infinite static stiffness and an active stiffness control bandwidth of 700 Hz. The active behaviour is obtained by a compliant bearing surface (10) that is supported by four piezo-actuator pairs (11). Air gap changes are measured by radially mounted capacitive transducers and fed back to a PID-controller that generates voltages to the piezos. Consequently, the bearing surface is deformed by which a radial force in the air film is generated acting on the shaft and increasing the bearing stiffness [2].

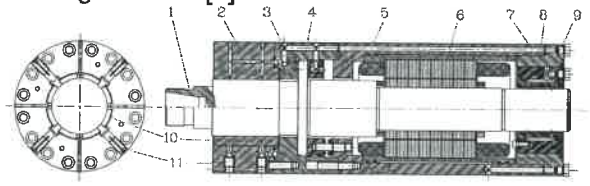

FIGURE 1. High-speed milling spindle with active front air bearings, providing dramatically increased stiffness over passive designs.

Metrology frames

Abbe's principle requires that the line of action of the displacement measurement system be collinear with the displacement to be measured. Special efforts must be made to satisfy Abbe's principle in high- and ultra-precision measuring equipment and machine tools, often giving rise to very complicated setups and hence expensive machines. Figure 2 shows the high-precision measuring machine ISARA, developed at Eindhoven Technical University [4] and presently marketed by IBS [12]. The measuring range is 100x100x40mm, and the measuring uncertainties are 15nm (X&Y), 25nm (Z) and 30nm (3D). Abbe's principle is satisfied in 3D using a metrology frame and a plane-mirror block and by keeping the probe stationary while the workpiece table is moving in 3D using an original motion system with linear motors [12].

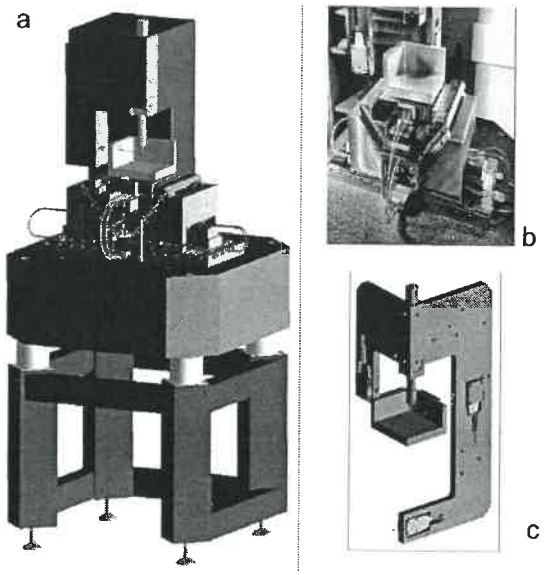

FIGURE 2. The ISARA 3D nano measuring machine: (a) the machine setup, (b) the special stage layout, (c) satisfying the Abbe principle.

Another example is the Nanogrind machine, shown in Figure 3, a five-axis ELID grinding machine for free-form optical components, developed in FP6 EU-project NanoGrind [7].

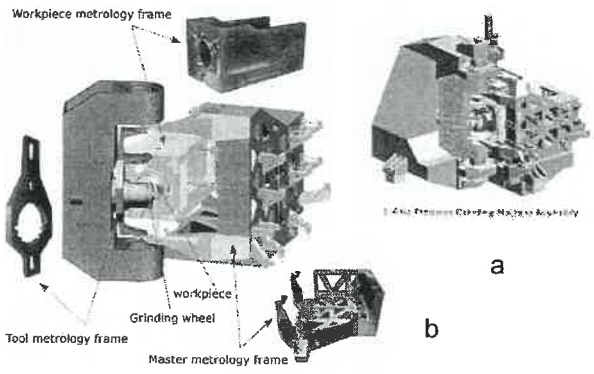

FIGURE 3. The 5 dof Nanogrind ELID grinding machine, (a) the global machine setup, (b) the three metrology frames.

The machine is designed to machine (optical) components with maximal a diameter of 100 mm and a height of 70 mm. Required form accuracy is 0.3 micron. This high accuracy can only be achieved by using metrology frames. The machine incorporates a unique measurement system consisting of three metrology frames to satisfy Abbe's principle. Laser interferometers,

together with auxiliary capacitive sensors are utilized to determine directly the position of the grinding wheel with respect to the workpiece. The metrology loop is made up of three dedicated frames, kinematically connected to the relevant machine components. The tool metrology frame is connected to the grinding spindle, and the workpiece metrology frame is fixed to the slide close to the workpiece. A separate master metrology frame is kinematically connected to the machine frame.
The workpiece moves in three translational directions. The grinding wheel is mounted on a yoke structure providing the two additional degrees of freedom.
It should be mentioned that also the ISARA nanoCMM of IBS, shown in Figure 2, has a separate metrology frame, unlike most 'traditional' nanoCMMs.

Thermal design

Two thermal compensation schemes, or a combination of both, can be applied. A first (feedback) approach to active compensation of thermal deformation is the use of thermal actuators or compensation heat sources so as to counteract certain types of deformation in the machine. The goal of this approach is (i) to compensate deformation in non-actuated degrees of freedom, and (ii) to obtain a more symmetric temperature distribution which then allows a better compensation with the second approach.
A second (feedforward) approach is to measure the temperature at a series of discrete locations, use these measurements to predict the deformation, based on a thermal model, and send appropriate tool trajectory correction signals to the NC-controller.
Recently, thermal modal analysis has been put forward as a powerful method to model and predict thermal compensation signals [9,10]. It provides qualitative insight into the dominant thermal deformation modes, and from this a qualitative method to determine optimal positions for the thermal sensors.

Mechatronic design

The mechatronic design methodology aims at achieving optimal system designs by simultaneously taking all system aspects (mechanical, control, programming) and their interactions in consideration from the very beginning of the design process.

Disturbance rejection

Robustness against disturbances (process forces, nonlinear friction, time-varying machine configuration) is of primary concern in position control of ultra-precision machines. The increasing use of linear motor drives makes the problem even more acute. Although linear motors allow high positioning bandwidths, high drive stiffness and low tracking errors, they are more affected by disturbances. Advanced control strategies are needed to effectively eliminate these disturbances.
In Figure 4, some contouring results are shown obtained on a two-axis high-speed milling machine tool XY-table driven by linear motors [6].

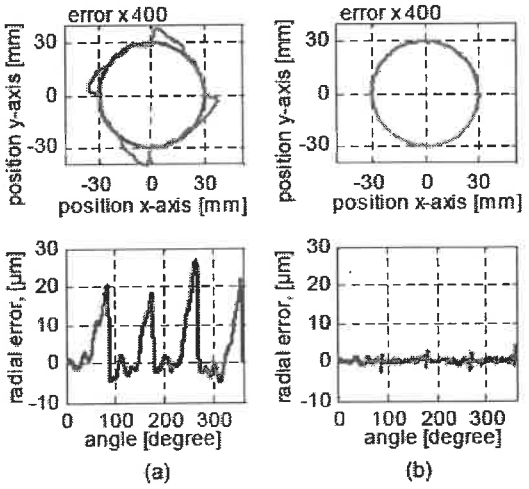

FIGURE 4. Quadrant glitch removal by disturbance observer feedback and GMS friction model feedforward

The control scheme consists of a traditional cascade control with an internal velocity loop enclosed by an external position loop. Cutting force estimation by an inverse-model based disturbance observer and friction compensation through a Generalised Maxwell Slip (GMS) friction model feedforward results in a complete removal of the quadrant glitch error and very low tracking errors.
The use of balancing masses to eliminate the forces to the outside world at high stage accelerations in wafer steppers is another way to increase robustness, and is presently common practice in ASML machines.
Singulus [8] developed a voice-coil focus actuator with integrated counter mass by which they achieved a dynamic decoupling of the actuator from the machine structure at high

frequencies. By applying learning feedforward, the tracking error could be drastically reduced.

Error budgetting

In the design of precision machines, dynamic error budgetting (DEB) is a method used to determine how much each component is allowed to contribute to the total (position) error. Disturbances are modelled as stochastic processes. Common mechatronic disturbances are: ground vibrations, electronic noise, quantisation noise, acoustic noise, Brownian noise, air turbulence. DEB provides useful information on how to improve the controller or plant design, by indicating which disturbances are dominant, in which frequency range, and how they propagate through the closed loop system. It has been successfully applied for the design and optimization of a magnetically suspended rotating platform in [3]. Singulus has applied error budgetting for designing their third-generation high-density inline mastering systems CRYSTALLINE [8]. They consider following error sources: floor vibrations, acoustic noise, spindle error motions, frame vibrations, EMC noise, substrate roughness, substrate form errors, thermal effects, optical path tolerances. After design optimisation they arrive at a total track pitch error of less than 2nm and a total focus error of less than 20nm.

Multi-dimensional drives

Combined multi-axis drives enable to reach very high stage stiffnesses by avoiding the stacking of motion axes, as is customary in traditional machine designs, and to arrive at compact designs. As an example, a nanometer-resolution piezostepper [5], shown in Figure 5, is briefly described.

The challenge of this project was to design an XY-stage with very high stiffness (typically 300 N/μm), with a resolution of a few nanometres, at linear velocities of a few mm/s. Such stages could for instance be used in ELID grinding machines.

A piezostepping technology has been adopted, mainly to satisfy the stiffness requirement. The design eliminates the main sources of compliance found in traditional designs: stacking of single-degree-of-freedom motion modules resulting in long force loops, compliance in guideways, ball screws, bearings, etc. of traditional drive systems. The design features a walking stage able to move in three degrees of freedom (X, Y, and C). It combines the 'guiding' and 'driving' functions into one unit, in three directions, thereby eliminating all sources of compliance. Moreover, the actuators built into the feet of the piezostepper enable the realisation of an infinite active static stiffness in all six degrees of freedom (dofs).

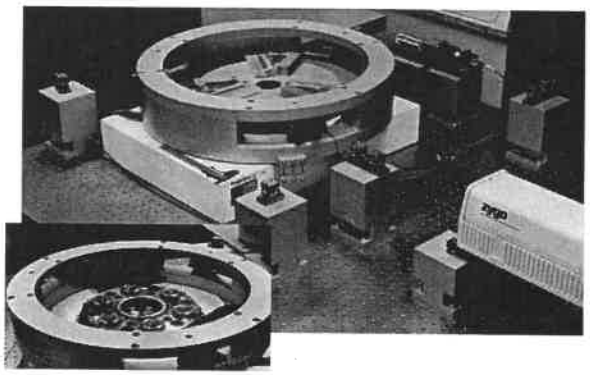

FIGURE 5. Nanometre-resolution piezostepper.

To satisfy the smooth-motion requirement, the 'hammering' effect, typical for stepping drives, has to be avoided. This is achieved by 'gently' putting down the feet on the ground through control of the contact force build-up. Several mechatronic features have been introduced: (i) infinite active stiffness is obtained in six degrees of freedom, (ii) smooth stepping and traction control is introduced through force measurement in three directions in the feet, and (iii) compensation of hysteresis in the piezos and of the nonlinear Hertzian contacts has been introduced.

Worth mentioning here is the longstanding research by Philips Applied Technologies on magnetic levitation multi-dof drive systems. The platforms are either based on variable reluctance actuators or on voice coil actuators for levitation purposes. The result is a planar motor, of which Figure 6 shows an example, with correction possibilities in all six dofs down to nanometer level, with application potential in lithography and laser machining [11].

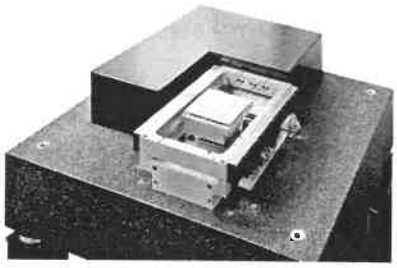

FIGURE 6. The Philips 2D linear motor Nforcer technology [11].

Other examples of a multi-dof actuators are the magnetically rotating platform, developed at TU Delft [3] and shown in Figure 7, to be used for disc mastering applications, and the HF-spindle with active air bearings already discussed earlier in this paper [2].

Where for the spindle the purpose is to maximize the stiffness, for the rotating platform the aim is to achieve zero stiffness so as to isolate the rotating platform from external disturbances. Using nonlinear compensation, the stiffness of the magnetic bearings could be made extremely low (typically less than 1N/m).

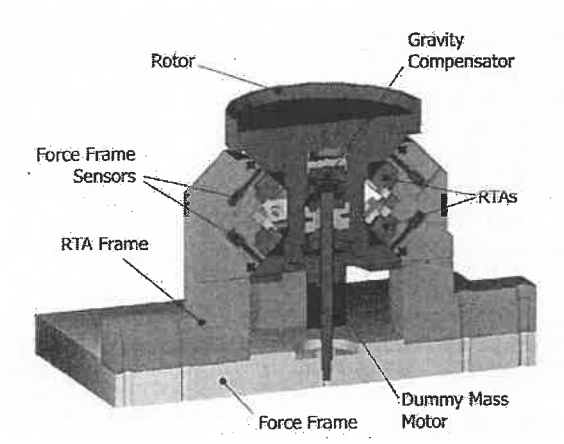

FIGURE 7. Magnetically suspended rotating platform using active magnetic bearings with Reluctance Type Actuators (RTAs) [3].

Measuring systems

To facilitate the simultaneous measurement of two perpendicular displacements when using planar actuators (see above), Heidenhain has developed a two-dimensional incremental encoder. Both measuring range (68x68mm) and accuracy level (2 micron) are still limited but the potential use of this type of encoder is tremendous. See also the presentation by Heidenhain in this session.

An important element in nanotechnology with nanoCMMs, still needing considerable research, is the nanometer probe. Several developments, of Technical University Eindhoven, NPL, METAS, ... are being compared. On ISARA, the NPL probe is being used. It has a capacitive measurement system, and a parallel kinematic structure with an isotropic stiffness of 10N/m, a resolution of 1nm, and a tip radius of 150nm (Figure 8).

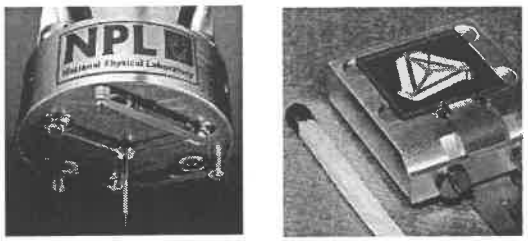

a b

FIGURE 8. Nanometre probes, (a) developed by NPL, (b) developed by Technical University Eindhoven.

HIGH-PRECISION MACHINING

Ultra-precision machining of macro components has become a well-established discipline. Key applications are the manufacture of optical components. See the presentation by Paul Shore in this session for details.

Precision engineering also has a major role to play in providing appropriate manufacturing technology for micro- and nanostructured surfaces. In Europe, Fraunhofer IPT in Aachen takes a leading position in developing microstructuring technology, both processes and machines. They develop innovative compact high-precision machine tools (MiniMill, MiniGrind, UltraOptik lathe with voice-coil driven fast tool) [13].

At the Laboratory of Precision Machining (LFM), University of Bremen, a very interesting nanometre-stroke fast tool servo (nFTS) has been developed to generate discontinuous diffraction optical elements [14]. It consists of a low-hysteresis $LiNbO_3$ piezostack driving the diamond cutting tool in the feed rate direction. It is used in open loop so that a 5kHz bandwidth can be obtained. Very steep diffractive step features of 316 nm depth and 20 µm length could be optained, as shown in Figure 9. The remaining waviness on the machined surfaces can be removed by 'input shaping'.

A third area were high-precision machining can make a difference is that of microsystems technology (MST). It is full of issues waiting for an answer: micromanufacturing processes, mass production of microproducts (replication techniques), micro-fixturing techniques, microassembly. The EU has launched several research projects to find solutions for these problems, such as 4M, MasMicro, Production for Micro, LaunchMicro, Eupass, MicroSapient, nanoCMM, MINAM, ...

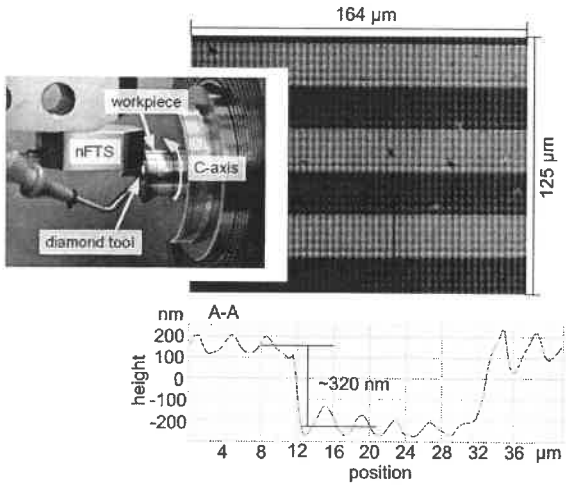

FIGURE 9. Discontinuous diffractive step structure machined with diamond tool driven by a nanometre-stroke fast tool servo (nFTS).

Also euspen has realized the importance of the field of microsystems technology and recently launched a special interest group (SIG) on Integration of Microfabrication Technologies into SMEs. It is coordinated by LFM, University of Bremen (Prof. E. Brinksmeier) and by KUGLER GmbH, a leading German company active in many aspects of high-precision and microsystems technology.

CONCLUDING REMARKS

Precision engineering has evolved into a multidisciplinary fully-fledged engineering and academic discipline. It is an extremely powerful enabling technology, without which the new high-tech products of micro- and nano-electronics, micro-and nanosystems technology (MST/NST) could never be realized. Moore's and Taniguchi's laws go hand-in-hand.

Euspen (ww.euspen.org) considers it its main mission to increase the awareness of European scientific policy makers, funding agencies and academic authorities of the importance of precision engineering for our future world, and to assist the European precision engineering industry in their development of innovative products.

REFERENCES

[1] http://www.mhs.ox.ac.uk/epact/

[2] Al-Bender F, Van Brussel H. Development of high-frequency (HF) electrospindles with passive and active air bearings. Proceedings of International Seminar on Improving Machine Tool Performance, San Sebastian, 1998; Vol. I, 175-184.

[3] Jabben L. Mechatronic Design of a Magnetically Suspended Rotating Platform. PhD Thesis Technical University of Delft, 2007; ISBN978-90-9022523-4

[4] Ruijl T.A.M. Ultra Precision Coordinate Measuring Machine, Design, Calibration and Error Compensation. PhD Thesis Technical University of Delft, Philips Centre for Industrial Technology Eindhoven, The Netherlands, 2001; ISBN 90-6464-287-7

[5] Van Brussel H, Reynaerts D, Vanherck P, Versteyhe M, Devos S. A nanometre-precision, ultra-stiff piezostepper stage for ELID-grinding. CIRP Annals, 2003; Vol. 52/1, 317-322.

[6] Jamaludin Z, Van Brussel H, Swevers J. Design of a Disturbance Observer and Model-Based Friction Feedforward to Compensate Quadrant Glitches. Proc. 9th International Conference on Motion and Vibration Control (MOVIC), Munich, 2008.

[7] Hemschoote D, Qian J, Van Brussel H, Reynaerts D. The use of metrology frames in an ultra-precision 5-axis machine for elid-grinding. Proc. 6th Euspen International Conference, Baden bei Wien, 2006; 249-252.

[8] http://www.singulus.nl/3_products/frameset_products.htm

[9] Ruijl Th. Development of compensation method based on thermal mode shapes. Proc. SIG meeting on Thermal Issues in Precision Engineering, Eindhoven 2006; http://euspen.org .

[10] Uriarte L. Thermal Modal Analysis. Proc. SIG meeting on Thermal Issues in Precision Engineering, Eindhoven 2006; http://euspen.org.

[11] http://www.apptech.philips.com/html/press_center/philips_nforcer_technology_nl.htm.

[12] http://www.ibspe.com/ibs_precision_engineering_uk/downloads_special_machines.html.

[13] Brecher C, Klar R, Wenzel C. Development and Design of Compact High Precision Machine Tools. Proc. COMA'07, 2007.

[14] Brinksmeier E, Schönemann L, Lünemann B, Gläbe R, Falldorf C, Kopylow C. Design and application of an open loop nanometerstroke Fast Tool Servo system for the generation of diffractive optical elements. Proceedings of the Adaptronic Congress 2008, Berlin, 173-177

ADVANCEMENTS IN DISPLACEMENT METROLOGY BASED ON ENCODER SYSTEMS

Wolfgang Holzapfel
Holzapfel@Heidenhain.de
Dr. Johannes Heidenhain GmbH
P.O. Box 1260, 83292 Traunreut, Germany

1 ABSTRACT

Production equipment for semiconductors and optical components most often contain stages with high demands on positioning or scanning. Dedicated optical feedback sensors such as laser interferometers or interferential grating encoders [1] with sub-nanometer resolutions are applied there. In most applications critical measurements are performed over small distances within short time intervals. This article highlights the current status of interferential grating encoder technology.

High-resolution optical encoders contain small grating interferometers with equal and short optical path lengths in both interferometer arms. Thus they are almost not affected by air turbulences and can show noise levels below 100 pm. By using proper materials and designs also the temporal and thermal drift can be reduced to sub-nanometer levels at appropriate environmental conditions. Position dependant errors in the whole spatial frequency range must be kept at a minimum. High-frequency interpolation errors can be limited to below ±10 pm in specific applications by using sophisticated scales and interpolation electronics. Low-frequency scale deviations are normally calibrated out. Mid-frequency scale deviations can become visible between calibration points and must be minimized through appropriate scale manufacturing equipment. For the calibration of encoder scales the measuring equipment must be traceable to the meter definition.

2 INTRODUCTION

For production and qualification of semiconductors or optical components there exist many different machines like wafersteppers, e-beam or laser writers, various kinds of inspection machines and diamond cutting machines, all requiring high-precision stages for one, two or more degrees of freedom. Since structure sizes and form tolerances are getting smaller and smaller the demands on such stages are increased accordingly. Depending on the application the critical specifications can comprise position stability, position repeatability, accuracy of scanning trajectories, speed ripple, accuracy of length measurements over small distances and also absolute position accuracy. Typical measuring times are seconds to several hours. High accurate stages are usually calibrated by referencing to sophisticated transfer standards. Calibration data must stay valid over reasonable times to avoid frequent recalibration cycles.

High-resolution optical encoders are grating interferometers with equal path lengths of both interferometer arms and are called interferential encoders [2][3]. Mutual phase shifts are not introduced by changing the propagation paths but by using the opposite phase shifts of both first diffraction orders when moving the scale grating (see figure 1). The signal period is thus not related to the wavelength of the light source but to the grating pitch of the scale. If the light beams are only diffracted once by the scale the signal period is half the grating pitch. In case of two scale reflections or transmissions it is reduced to a quarter. Signal periods of interferential encoders range from 5 µm down to below 130 nm.

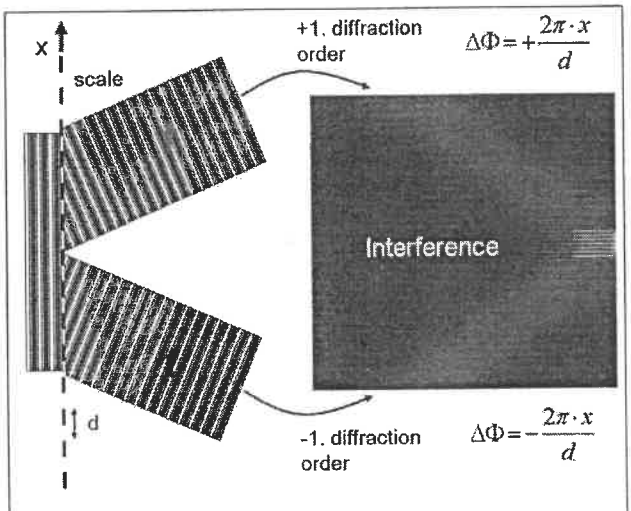

Figure 1: basic principle of an interferential encoder

Interpolation electronics is necessary to subdivide signal periods SP into smaller measuring steps. Current interpolation factors are between 2^{12} and 2^{16} (12-16 Bit) resulting in smallest measuring steps of $SP/2^{16}$ = 2 pm. In practice the achievable resolution of encoders is limited not by the size of measuring steps but by noise levels (see below).

There exist many different designs of high-resolution encoders optimized for different applications. The adaptations are for example related to specific environments (vacuum encoders), materials and thermal expansion (steel, Invar, Zerodur®) and allowed heat dissipation (encoders with fiber coupling, see figure 2).

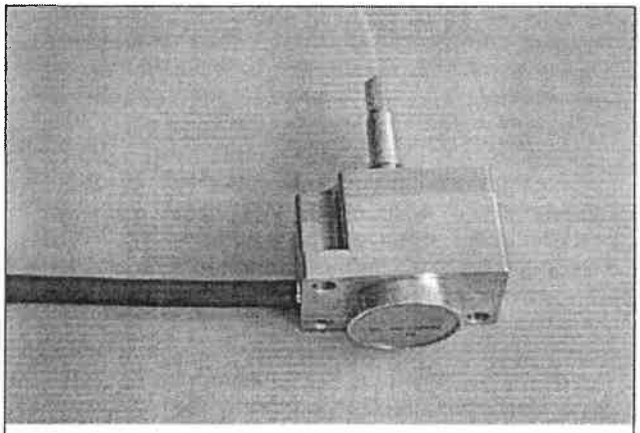

Figure 2: encoder fiber-coupled to an external light source

According to Abbe's principle [4] the measured point on the object and the effective measuring point of the encoder should be aligned along the measuring direction. Although there are several concepts for reducing Abbe offsets like phantom scale arrangements, cross-grid scales, split-axes kinematics with linear scales and 1Dplus scales [5], in most cases they are only reduced to a practical minimum.

3 PROPERTIES OF INTERFERENTIAL ENCODER

Position noise of encoders determines the achievable resolution and is therefore an important parameter in nearly all applications. Figure 3 shows the noise performance of a high-resolution encoder evaluated with two different interpolation electronics. The version with 500 kHz analogue bandwidth has a RMS noise of 28 pm whereas the version with 20 kHz has only 4.2 pm. This indicates a spectral noise density of 0.03...0.04 pm/√Hz. There is still some room for further improvements to come down to the shot noise limitation.

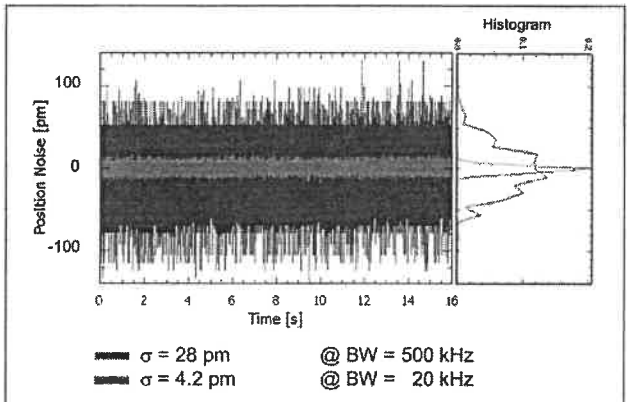

Figure 3: noise of an encoder with 128 nm signal period evaluated by electronics with two different bandwidths

Drift properties of encoders are critical in applications where objects have to be adjusted and positioned over long times. Both temporal and thermal drift is determined by the selection of materials and proper designs of joints. Figure 4 shows the temporal drift an encoder made of Zerodur® indicating values below 10 pm/h after initial relaxation. Similar drift performance is also achievable when using materials with thermal expansion coefficient around $10 \cdot 10^{-6}$ K^{-1}.

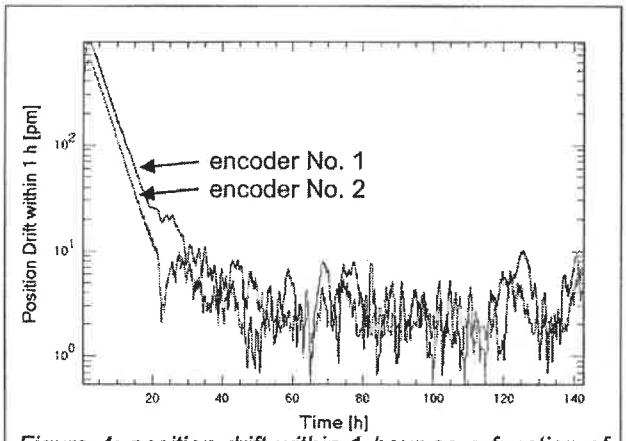

Figure 4: position drift within 1 hour as a function of time after installation in a test chamber for two encoder samples made of Zerodur®

In many applications small dimensions have to be measured with high accuracy. Also very common are high-accurate scanning operations demanding small speed ripples. Both require encoders with small errors over short distances or low errors at high spatial frequencies. Especially interpolation errors can affect the performance. Interpolation errors can be minimized by improving the homogeneity of scale gratings, optimizing the

scanning optics and using compensating interpolation electronics. Figure 5 shows a result of an encoder with 128 nm signal period. In scans across 10 signal periods (top graph) no periodic error contribution is visible. In the accumulated PSD spectrum (bottom graph) the RMS values of the interpolation error frequencies at f = 1/SP and 2/SP can be estimated to 3.2 pm and 3.5 pm respectively indicating a total interpolation error below ±10 pm.

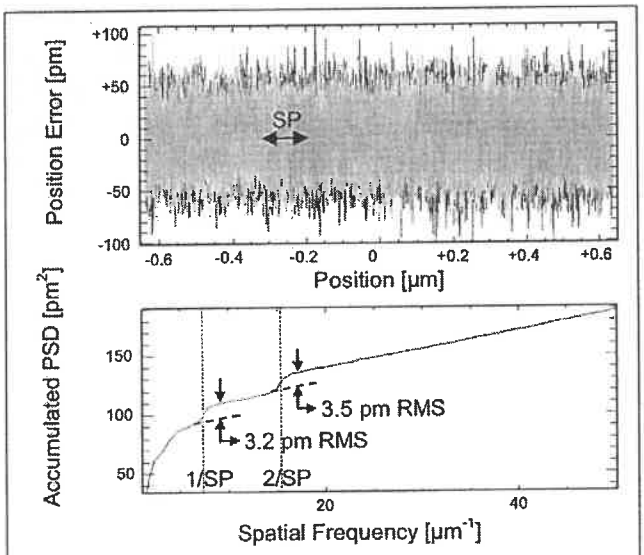

Figure 5: Interpolation error of an encoder with 128 nm signal period (SP); top graph: measured error curve, only noise contributions are visible, bottom graph: accumulated PSD spectrum, interpolation error visible as steps at f=1/SP and f=2/SP.

Low-spatial frequency errors of encoders are usually eliminated when machines are calibrated. The stability of these calibrations depends mostly on the stability of the mechanics of the machine itself and requires a very careful design. Calibrations are normally performed at a set of calibration points at distances of a few millimetres. To limit the errors in-between calibration points, the mid-spatial frequency scale errors must be minimized. Figure 6 shows results for a high-accurate scale. In the graph the residual scale error after calibration is plotted as a function of the calibration point spacing neglecting error contributions from the calibration reference itself. For a residual scale error of 1 nm RMS the scale has to be calibrated with calibration points every 3 mm.

4 MEASURING EQUIPMENT AND TRACABILITY

The improvements in encoder technology leading to more and more reduced errors have to be accompanied by sophisticated measuring equipment. As a rule of thumb it should provide a 10-fold higher repeatability and accuracy as the investigated encoder itself. In addition the measurement must be traceable to the meter definition. Both requirements can be fulfilled by using a length comparator with interferometers in vacuum where the stabilized laser source is linked via a frequency comb to an atomic clock. The comparator of such measuring equipment is shown in Figure 7 and described elsewhere [6].

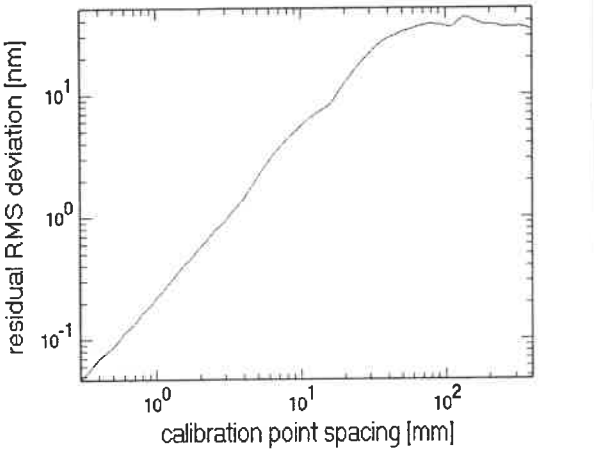

Figure 6: residual scale error after piecewise-linear correction as a function of calibration point spacing

Typical results of a high-resolution encoder measured on that comparator are plotted in figure 8. A high-resolution scale was measured over 280 mm (top curve). To visualize the mid-spatial frequency content the error curve was filtered by a high-pass filter at f = 0.1 mm^{-1} (middle curve) showing a residual RMS error of 0.28 nm. The repeatability of that measurement is demonstrated by taking the difference of two subsequent measurements (bottom curve). The RMS value of this difference is 0.016 nm.

5 CONCLUSIONS

High-resolution interferential optical encoders are available with signal periods between 5 µm and below 130 nm and interpolation factors of 12 – 16 Bit. They contain small grating interferometers with inherently low sensivities to air turbulences. The resulting spectral noise densities can reach 0.03...0.04 pm/√Hz. A proper mechanical design including a careful selection of materials reduces temporal and thermal drifts. Values around 10 pm/h have been demonstrated. High-frequency errors of encoders are dominated by interpolation errors. It was shown that amplitudes of 10 pm are achievable by using high-quality scales and compensating interpolation electronics.

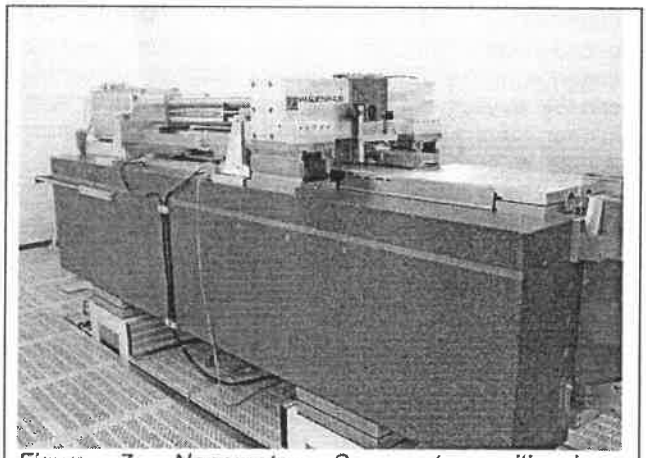

Figure 7: Nanometer Comparator with laser interferometers in vacuum

For verifying those levels of repeatability and accuracy improved measuring tools are needed. Here a measuring machine with laser interferometers in vacuum and a stabilized laser source is used which is traceable to the meter definition through a frequency comb and an atomic clock. It allows measurements of scale deviations in the nanometer range over a length of several 100 mm and in addition small deviations below 0.1 nm over shorter distances of some millimetres.

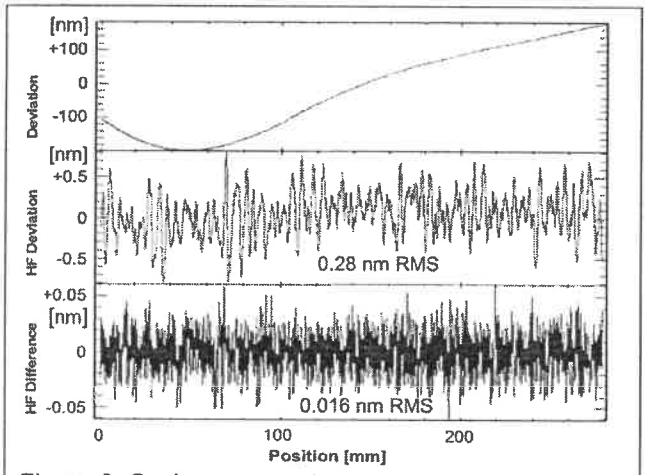

Figure 8: Scale measured on nanometer comparator: top: measured position deviation, centre: position deviation after high-pass filtering (f>0.1mm^{-1}), bottom: position deviation difference of two subsequent measurements after high-pass filtering (f>0.1mm^{-1})

REFERENCES

[1] H. Kunzmann, T. Pfeifer, J. Flügge, Scales vs Laserinterferometers – Performance and comparision of two measuring systems, Annals CIRP 42 (2) 1993, p 753-767

[2] A. Spies, Längen in der Ultrapräzisionstechnik messen, Feinwerktechnik & Messtechnik 98, Vol. 10, 1990, p 404 – 410

[3] J. Thiel, E. Spanner, Interferential linear encoder with 270mm measuring length for nanometrology, http://www.auto-met.com/heidenhain/techdata/thiel.html

[4] G. X. Zhang, A study on the Abbe principle and Abbe error, Annals CIRP 38 (1) 1989, p 525 - 528

[5] W. Holzapfel, Using High-resolution encoders in Nanometre Applications, Proceedings of the 6th euspen International Conference, Baden 2006

[6] J. Flügge, R. Köning, Status of the nanometer comparator at the PTB, In J.E. Decker, N. Brown, editors, Proceedings of SPIE Vol. 4401, 2001, p 275 -283

ULTRA PRECISION SURFACES

Paul Shore[1, 2]
[1]Ultra Precision and Structured Surfaces Centre
Optic Technium
Denbighshire, Wales, UK
[2]Cranfield University Precision Engineering
Cranfield, Bedfordshire, England, UK

SUMMARY
Ultra precision surfaces (UPS) are pivotal. They enable many high technology processes that realize numerous consumer products and they add value, function and life time to many advanced products themselves. Fundamental for many astronomy missions, large scale UPS are fundamental to enable clean energy production. Nevermore so are we as reliant on our ability to produce and apply ultra precision surfaces.

This paper provides an overview of important topics demanding UPS and details a UK research initiative to establish a leading capability for their effective production.

INTRODUCTION
Large scale ultra precision surfaces are pivotal to a number of strategically important industrial sectors, defence initiatives and science programmes [1]. Ultra Precision Surfaces can be considered as those surfaces having a relative ratio of size to form accuracy in the range 1 part in 10^7 to 1 part in 10^8. At a level of 1 part in 10^8, a 1 metre surface would have a 10nm form error.

High Technology Industry
Surfaces of this extreme quality are demanded within high technology components such as the lenses employed within the optical towers used within IC lithography systems. It is these optical surfaces which significantly influence the achievable transistor density packing and adherence to Moore's law. It is clear significant research has been undertaken to ensure lithography lenses are manufactured to the highest quality level possible.

Astronomy programmes
Surfaces of this extreme quality are also employed in ground and space-based optics (mirrors).

A number of next generation astronomy programmes will demand many hundreds of large scale ultra precision surfaces. These programmes include the US led Thirty Metre Telescope (TMT) project and the 42 metre European Extra Large Telescope (EELT) – led by the European Organisation for Astronomical Research in the Southern Hemisphere. These ground-based telescopes will, amongst addressing other science issues, provide the capabilities for detecting earth-like planets of far away stars. The mirror technology of these ELT designs will follow that set out by the KECK telescopes whereby hundreds of hexagonal mirror segments of 1 – 1.5 metres will be employed.

Nuclear Fusion Science
Near metre scale UPS are demanded, and pivotal, within the high power laser systems such as the US National Ignition Facility and the French Laser Mega Joule project. These major projects have helped establish large scale optical fabrication capacity within their respective domestic industries. Future planned fusion energy study programmes, such as the European HiPER project, also demand complex shape large scale UPS. These large optics can be considered as potential "wear" components of a future sustainable energy source.

Earth observation
Large UPS are demanded within space-based systems for earth observation. Earth orbiters provide essential information for studies into crop development, weather monitoring, flood avoidance, ice cap melting rate, drought awareness, together with issues linked to security and defence.

Consideration
In summary, UPS are strategically important across advanced industry, defence, future energy sources, astronomy programmes and earth monitoring. Ensuring a credible national

capability is consequently an important issue. In 2003 a UK initiative was instigated to develop a UK capability for the fabrication of large scale UPS. This paper describes the development and progress of this programme.

UK'S ULTRA PRECISION INITIATIVE

Large Optics Manufacturing Study

In 2003 a six month manufacturing study, LOMS, was part funded by the UK's Department of Trade and Industry [2]. LOMS investigated the potential importance of large scale UPS and considered the UK's international standing and inherent industrial capability. LOMS identified a number of UK strengths regarding the fabrication of large scale UPS fabrication equipment but also highlighted a highly fragmented situation regarding funded research programmes and industrial capability.

LOMS highlighted the UK's ability to produce ultra precision machines [3,4, 5] and to develop novel processes [6] but it clearly showed such capabilities were "not joined up" within the UK to form any notable national UPS capability. LOMS therefore recommended a UK research project dealing with a number of key processing stages in the production of large scale UPS, namely grinding, polishing and final figuring.

Ultra Precision Surfaces Project

In April 2004, a £3.6 million 4 year RCUK Basic Technologies project was started through a collaboration between UCL and Cranfield University together with selected industrial partners: Cranfield Precision, Optropreneurs Ltd, RAPT Industries Inc. and Zeeko Ltd. The objective of the UPS project was to establish a processing chain capable of producing 1 metre scale surfaces having 10nm RMS form accuracy and 1 nm RMS roughness using a number of optimised yet discrete processing stages, each having a maximum 10 hour duration, see Figure 1.

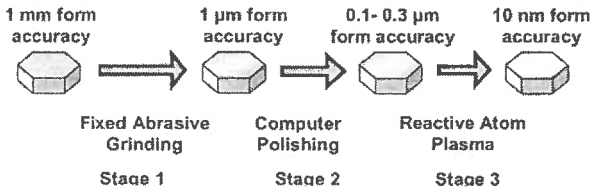

FIGURE 1. UPS project process chain.

In selecting the specific processes a major consideration was given to the material removal capacity of the individual processes such that a 10 hour processing stage could be achieved. Figure 3 shows the considered material removal capacity of potential processes against achievable material removal rate.

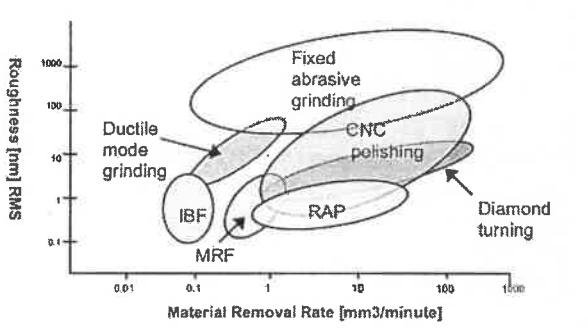

FIGURE 2. Material removal capability of optical machining processes.

The UPS project developed three new large scale surface processing stages. The basis of each stage and the developed systems are introduced below:

Cranfield Box®

This machine has been developed by Cranfield University in partnership with Cranfield Precision. Conceptually it is based around research of low damage grinding using highly stiff machine tools and the approach of employing an in-situ metrology frame to permit error correction against measured surface errors.

The Box® machine, see Figure 4, is an ultra precision grinding machine whose design employs high power density sub-systems of minimal moving mass allowing a high dynamic stiffness to be achieved. The high dynamic stiffness allows high material removal rates (up to 200mm^3/sec) to be employed without inducing significant levels of sub-surface damage (SSD). Excessive SSD would demand long polishing times for its removal. Thermal stabilisation techniques are employed within Box® to gain high levels of machine dimensional stability prior to a post grinding in-situ measurement operation referenced to an in-situ metrology frame. Surface measurement data is used to generate error correcting part programmes for finishing cuts allowing Box® to achieve a 1 um form accuracy on 1 metre scale free form shape

surfaces. A surface roughness of 150nm RMS and 5 um SSD levels can be achieved when removing 1 mm depth in a 10 hour processing time. The ouput quality achieved from the BoX system permits interferometric measurement to be employed.

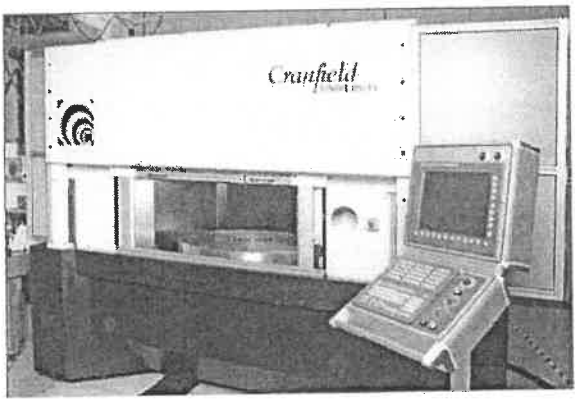

FIGURE 3. BoX® precision grinding machine.

Zeeko IRP1200

A computer controlled polishing stage was established by the partnership of University College London and Zeeko Ltd. The developed IRP1200 is a 7 axes robotic polishing system that employs inflated bonnets of differing types and sizes, see Figure 4. This free abrasive polishing system uses a sub-aperture process which employs a 'time-dwell approach'. The tool dwells on the high point regions layer in comparison to relatively low regions. The calculation of pseudo randomised tool path motions minimises potential for mid spatial tool path "in print".

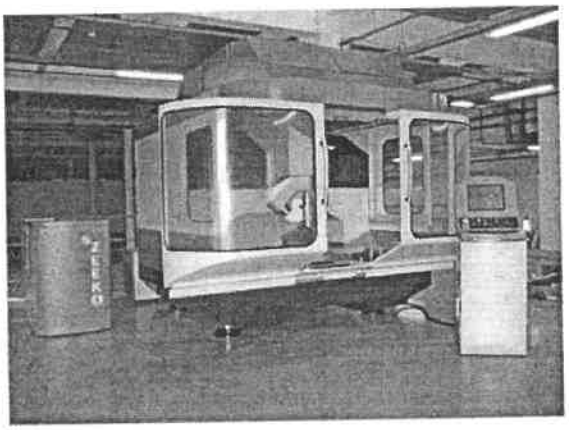

FIGURE 4. ZEEKO IRP1200 polishing machine.

Positioned over the Zeeko IRP1200 is an optical test tower. This measurement system employs a full aperture laser interferometer to collect measurement data from which to drive the form convergence process. From these surface error maps, tool path motions are calculated which figure the input quality to the desired surface shape. This polishing stage improves the form accuracy from 1 part in 10^6 to better than 1 part in 10^7 (from 1um to better than 100 nm on a 1 metre surface). This polishing stage also improves the surface texture from ~150 nm RMS to less than 1nm RMS roughness.

RAPT Helios

The third system developed for the UPS process chain is based on Reactive Atom Plasma (RAP). The RAP process emerged from the Lawrence Livermore National Laboratory and has been commercialised through RAPT Industries Inc. RAP is a control etching process driven by a stable inductively coupled plasma into which active gas species are introduced to a central region, see Figure 5.

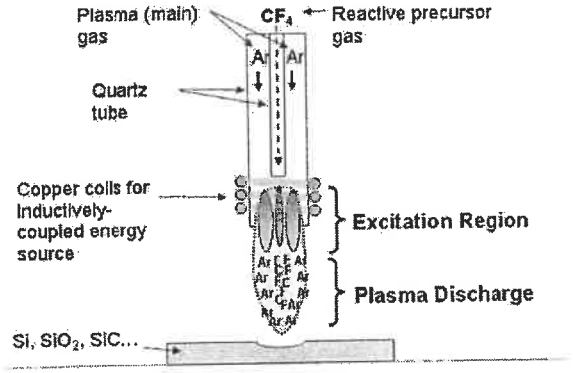

FIGURE 5. Schematic of RAP process.
(Courtesy of J W Carr)

The Helios 1200 shown in Figure 6 has been jointly developed by RAPT Industries and Cranfield University. It is the first industrialised CNC RAP machine for rapidly figuring large scale optics. The Helios RAP process operates using the same convergence principles as established for ion beam figuring. However, RAP has a wider material removal rate capability, faster but with the same fine control. Importantly the RAP process operates at atmospheric pressure, making it even more cost effective than ion beam figuring.

FIGURE 6. Helios 1200 RAP machine.

Total Process Chain Optimisation

Optimisation of the input and output qualities across the three processing stages is on-going. Encouraging initial results have already demonstrated rapid material removal and surface finishing rates within each of the discrete process steps. Attention to issues such as mid spatial surface qualities are now underway.

Ultra Precision & Structured Surfaces Centre

At the beginning of 2007 the machine systems developed under the UPS project were firmly established as a UK National Facility under a new EPSRC knowledge and wealth generation initiative entitled, UPS^2[7].

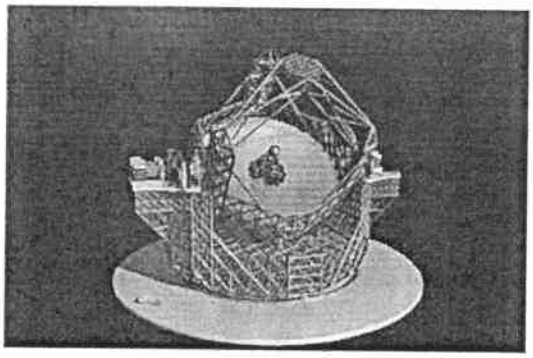

FIGURE 7. Conceptual Design of the E-ELT.

By the end of 2007 the business partner of UPS^2, Optropreneurs Ltd, signed a contract with the European Southern Observatory (ESO) worth €5 million to produce an initial batch of 7 mirror segments for the European Extremely Large Telescope (E-ELT). The order is one of several that ESO is placing to provide organisations with the opportunity to demonstrate their ability to produce the necessary mirror segments and to provide a clear description of the production route for fabricating these ultra precision surfaces. The E-ELT is an optical and infrared telescope with an estimated cost of €800 million that is due to go into service in 2017, see Figure 7. The core of the E-ELT will be a 42m diameter mirror composed of 906 hexagonal segments each of which will be 1.45m in size and will have a form accuracy of ~ 75 nanometres.

The order from ESO, secured by Optropreneurs Ltd, is the first large optics fabrication order to be secured in the UK for over 30 years.

CONCLUSIONS

A new process chain for the effective fabrication of large scale ultra precision has been developed. The previously "fragmented" UK expertise in ultra precision surface generation has been collated into a new facility covering specific manufacturing steps. The facility is strengthened by additional US inspired technologies helping to ensure a leading large optics fabrication facility within the UK.

ACKNOWLEDGMENTS

The author gratefully acknowledges funding from the McKeown Precision Engineering and Nanotechnology Foundation, UK Dept. of Trade and Industry, Welsh Assembly Government MNT programme, Qioptiq Ltd, RCUK Basic Technology programme, Cranfield Precision, Optropreneurs Ltd, RAPT Industries Inc., Zeeko Ltd and the UK's EPSRC funded Integrated Knowledge Centre for Ultra Precision and Structured Surfaces.

REFERENCES

[1] Shore P, Fabrication and Uses of Ultra Precision Surfaces. Royal Academy Eng, Ingenia, 2008, 35; 33-38.

[2] Shore P, Parr-Burman P, LOMS report to UK DTI, October 2003.

[3] Shore P, May-Miller R. Production Challenge of Optical Segments for ELT's. Proc.Progress on Adv. Optics, 2003; 25-30.

[4] Carlisle K, Shore P, et al. Review of an Ultra Precision Research Facility. Proc. UME 3, 1994; 89–95

[5] Wills-Moren W J, et al. Unique machine for grinding large off-axis optical components. Precision Eng. 1989; 11/4:191-196.

[6] Bingham R G, Walker D, et al. Novel automated process for aspheric surfaces. Proc SPIE 2000; 4093: 445-448.

[7] IKC. http://www.ups2.co.uk – 08/2008.

MANUFACTURING BETTER CHIPS AT LOWER COST

Erik Loopstra, David C. Ockwell, Hans Butler, and Leon Levasier
ASML
Veldhoven, The Netherlands

ABSTRACT
There is a continuing drive for Integrated Circuits ('chips') to be manufactured with higher performance and at lower cost. This paper introduces how a chip is made and how its performance is affected by the mechanical aspects of the lithography exposure tool. The paper proceeds with an explanation of measures taken within the exposure tool to enhance its performance.

THE MILLING DYNAMICS "SUPER DIAGRAM": COMBINING STABILITY AND SURFACE LOCATION ERROR

Raúl E. Zapata, Christopher DeMarco, and Tony L. Schmitz
Department of Mechanical and Aerospace Engineering
University of Florida
Gainesville, FL, USA

INTRODUCTION

Well known limitations to milling productivity include tool wear, quasi-static and dynamic positioning errors of the tool relative to the workpiece, spindle error motions, fixturing concerns, programming challenges, and the process dynamics. Many research studies have been completed to address these issues. In this work, we are concerned with the limits imposed by the process dynamics. For a particular machine-spindle-holder-tool-workpiece-fixture system, the assembly frequency response function and force model establish the variation in the stability limit and location of the machined surface (due to forced vibrations) as a function of spindle speed. Frequency domain solutions for the stability limit have been available for many years [e.g., 1,2]. The data is presented graphically in the form of stability lobe diagrams, which separate stable spindle speed-axial depth combinations from unstable pairs. Recently, a frequency domain solution to surface location error, SLE, was also demonstrated in the literature [3]. In this paper, we augment the stability limit with the user selected maximum allowable SLE to produce a new "super diagram" which identifies stable zones that also meet accuracy requirements.

NUMERICAL DEMONSTRATION

The "super diagram" is a combination of the information in a stability lobe diagram and the information obtained from surface location error (SLE) predictions. The predicted stability limit is at a fixed location given the dynamics of the system and the cutting conditions. However, the threshold for the acceptable levels of surface location error is user defined; therefore, user dependent accuracy requirements are incorporated with stability limitations. The parameters for the system selected for a numerical demonstration are shown in Table 1. These include the tool geometry, the system dynamics, and the cutting parameters.

TABLE 1. System parameters used in the numerical example.

Parameter	Value	Units
Stiffness	$5x10^6$	N/m
Damping ratio	0.05	
Natural frequency	2400	Hz
Tool Diameter	6.35	mm
Helix angle	45	degrees
Number of teeth	4	teeth
Tangential cutting coefficient	700	N/mm^2
Normal cutting coefficient	210	N/mm^2
	0.15	
Feed per tooth	0.075	mm/tooth
Radial depth of cut	3.175	mm

The limits of surface location error used in this example are based on the absolute value of the calculated positive or negative SLE. However, this is not a generic requirement. For example, the user may only care if a part is overcut (too much material removed) because the part is then tool small and cannot be corrected by a "finishing pass". However, if the part is undercut then finishing operations can be performed to obtain accurate dimensions.

In order to complete the combined stability and SLE diagram, we first calculate the stability boundary using the method in [2]. We then compare a grid of test points (within the preselected domain) to the stability boundary to determine their feasibility. Next, we calculate SLE using the frequency domain method defined in [3] for each of the grid points. Penalties are finally applied to

the points as necessary. For example, an unstable point receives a penalty of two, whereas a point that is stable but outside the SLE limit gets a penalty of 1, while points that are stable and within the user's SLE preference receive no penalty. Example diagrams are shown in Fig. 1 with varying SLE limits, but the same dynamic system and cutting conditions (see Table 1). This helps illustrate the effects of user preferences or requirements on the usable machining parameter space. In this figure, the black regions are unstable, the grey regions violate the SLE limit, and the white areas are the preferred zones for operation. Note that the grey areas are smaller in Fig. 1B due to the relaxed SLE limit.

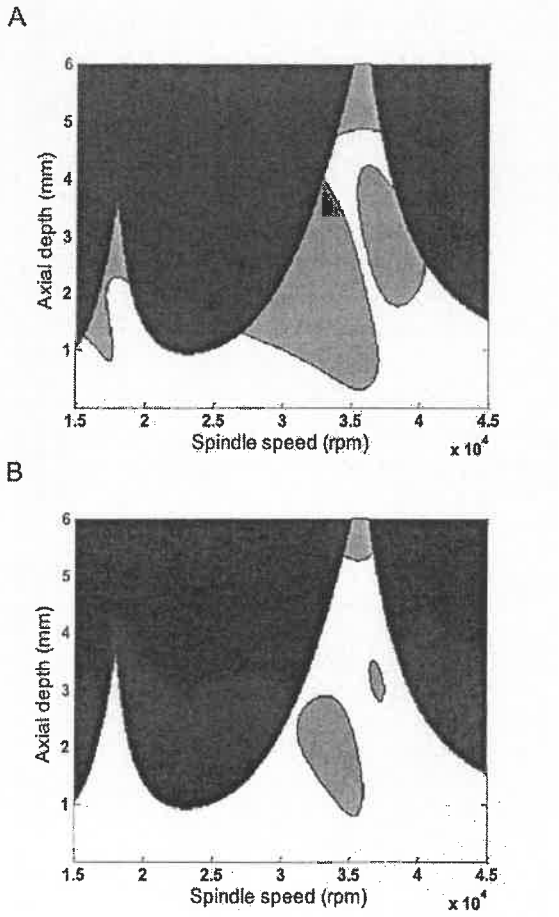

FIGURE 1. Effects of the user's SLE limits on the feasible machining domain for errors A) greater than 30 μm and B) greater than 70 μm at a 0.15 mm/tooth feed rate.

The feed rate during the machining process also affects the diagram. Although feed rate has only a second order affect on stability, it is an important parameter in the SLE calculations. For a linear force model, the force amplitude scales proportionally with feed rate. In other words, doubling the feed rate doubles the force amplitude. This, in turn, doubles the forced vibration amplitude, which doubles the surface location error as well. Figure 2 displays the same SLE limits as Fig. 1, but with half the feed rate. Note that Figure 2B shows no SLE in excess of the user's limit of 70 μm.

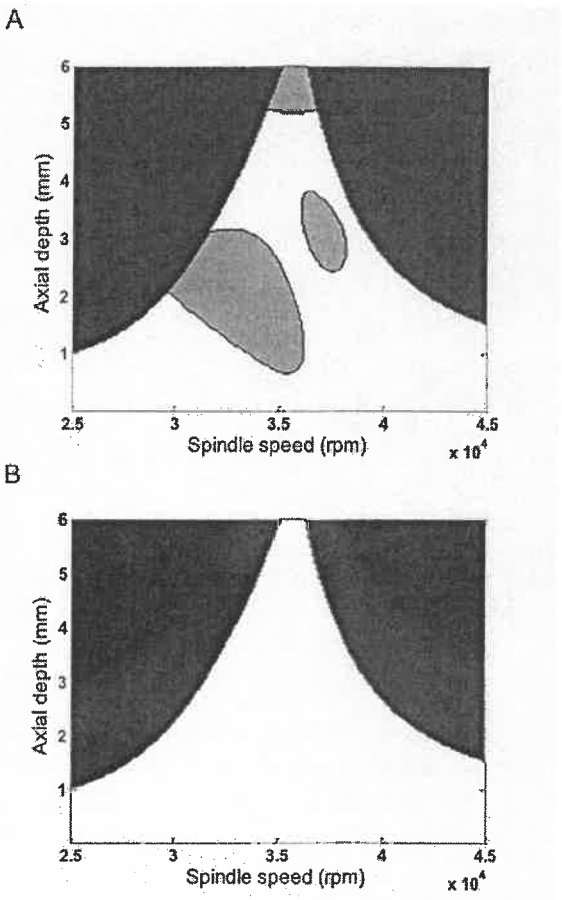

FIGURE 2. Effects of the user's SLE limits on the feasible machining domain for errors A) greater than 30 μm and B) greater than 70 μm at a 0.075 mm/tooth feed rate.

We note that, in general, the SLE varies with spindle speed for a particular axial depth of cut. The source of this SLE behavior is the system frequency response function magnitude and phase with the forcing frequency. Due to the change in phase with tooth passing frequency (spindle speed), the time lag between the force and vibration

varies. Therefore, the location of the cutter in its vibration cycle when leaving the surface depends on the selected spindle speed. The dependence of SLE on the phase lag between the forcing function and displacement causes significant variation near the natural frequency (considering a single degree of freedom system for simplicity) because, for the lowly damped tool point frequency responses typically observed in practice, the phase changes rapidly in this frequency range.

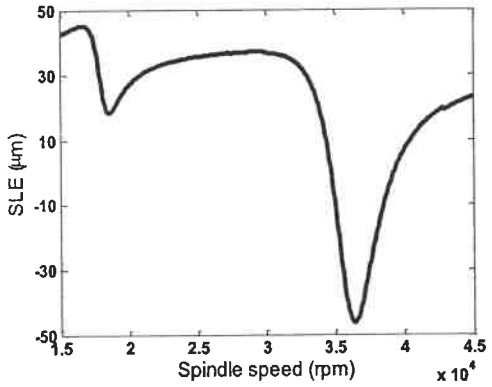

FIGURE 3. SLE variation with respect to spindle speed at an axial depth of 4 mm and a feed per tooth of 0.15 mm/tooth . Note the correspondence between sharp changes in SLE with the location of the stable zone peaks in Fig. 1.

The variation in SLE with spindle speed for an axial depth of 4 mm is demonstrated in Fig. 3. Here we see significant variation in SLE for spindle speeds near 36000 rpm. This corresponds to a tooth passing frequency of $\frac{36000 \cdot 4}{60} = 2400$ Hz, which is equal to the selected natural frequency for the system dynamics (Table 1). This spindle speed is the "best speed" normally selected for high-speed milling applications due to the increased stability limit. However, there is clearly a tradeoff between accuracy and the increased material removal rate. We also see local SLE variation at integer fractions of this best speed; specifically, 18000 rpm (1200 Hz tooth passing frequency).

Another condition we consider here is when the combination of system parameters and helical endmill geometry leads to a constant (or nearly constant) cutting force condition. Depending on the user's SLE limits, this may expose a feasible zone that would not be present on a straight flute cutter under the same conditions. The location and viability of this parameter space depends on the helix angle and number of teeth on the cutter (the tool geometry determines the axial depth at which the phenomenon occurs), as well as the system dynamics (these determine if the axial depth is feasible or not at any given spindle speed). This phenomenon is demonstrated in Fig. 4 using the parameters described in Table 1. The user's SLE limit is 42 μm.

The axial depth, b, at which constant force occurs is determined using Eq. 1, where d is the tool diameter, ϕ_p is the angular tooth spacing, and γ is the helix angle of the cutter. The resulting constant force depth occurs at approximately 4.98 mm, and its multiples, using the selected cutter geometry.

$$b = \frac{d \cdot \phi_p}{2\tan(\gamma)} \qquad (1)$$

This results in a horizontal "step" in the SLE behavior at an axial depth of 4.98 mm. For constant force, the deflection calculation reduces to the force divided by the static stiffness and the SLE reduces substantially (Fig. 4).

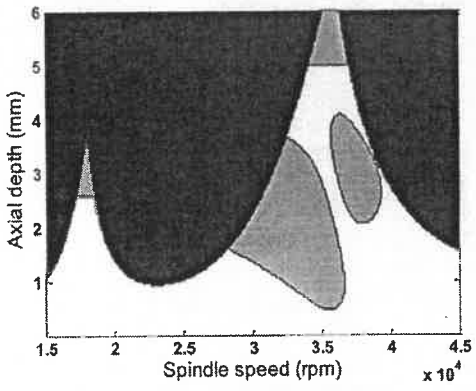

FIGURE 4. Demonstration of the constant force phenomenon. The "step" behavior is observed at an axial depth of 4.98 mm with a 42 μm SLE limit (0.15 mm feed/tooth).

Because the force behavior depends on the selected axial depth for helical endmills, SLE also varies strongly with axial depth (rather than increasing monotonically as we might expect). This is shown in Fig. 5 for a fixed spindle speed of 36000 rpm. Here we see that the SLE increases with axial depth up to about 1.25 mm, where it begins to decrease as we experience the combined effect of a phase change and the approach towards the 4.98 mm constant force depth. The "slope" of sinusoidal variation is caused by the linearly scaling of force (and deflection) with axial depth of cut.

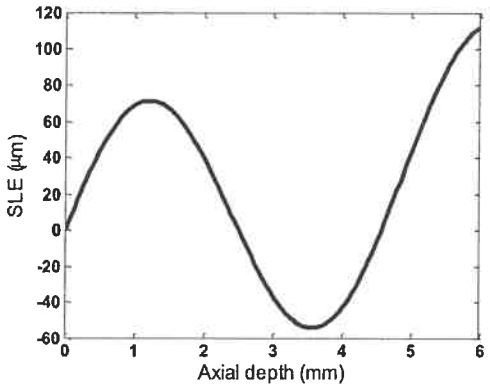

FIGURE 5. SLE variation with respect to axial depth at 36000 rpm and a feed per tooth of 0.15 mm/tooth.

Figure 6 shows the effect of the interaction between these two phenomenon at the first constant force axial depth. Note that despite the fact the SLE still varies with spindle speed the variation is much less than in Fig. 3. These small variations may be a result of the discretization of the tool and parameter space in the SLE algorithm as well as truncation errors of the axial depth at which these were calculated.

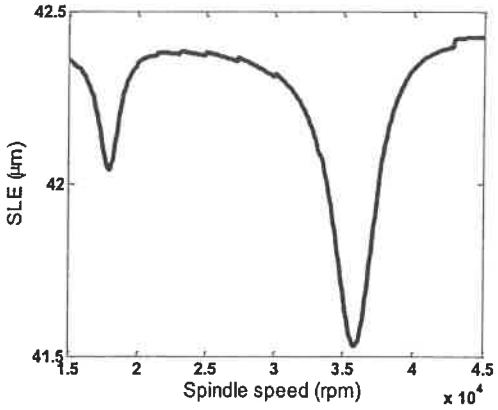

FIGURE 6. Variation of SLE with respect to spindle speed at an axial depth of 4.98 micrometers and a feed per tooth of 0.15 mm/tooth.

CONCLUSION

This paper presented a method of combining surface location error and stability information in a new "super diagram". When applied at the process planning stage, this diagram will enable users to make machining parameter decisions that respect the system dynamics.

ACKNOWLEDGEMENTS

The authors gratefully acknowledge financial support for this work from the National Science Foundation (DMI-0642569 and DMI-0238019). Any opinions, findings, conclusions or recommendations expressed in this material are those of the authors and do not necessarily reflect the views of this agency.

REFERENCES

[1] Tlusty J, Zaton W, Ismail F. Stability Lobes in Milling. Annals of the CIRP. 1983; 32/1: 309-313.

[2] Altintas Y, Budak E. Analytical Prediction of Stability Lobes in Milling. Annals of the CIRP. 1995; 44/1: 357-362.

[3] Schmitz T, Mann B. Closed Form Solutions for Surface Location Error in Milling. International Journal of Machine Tools and Manufacture. 2006; 46: 1369-1377.

SUB-SURFACE DAMAGE EVALUATION IN GRINDING OF LARGE OPTICS

Xavier Tonnellier[1, 2], Paul Shore[1, 2], and Paul Morantz[1, 2]
[1]Ultra Precision and Structured Surfaces Centre
Optic Technium
Denbighshire, North Wales, UK
[2]Precision Engineering Centre
Cranfield University
Bedfordshire, England, UK

INTRODUCTION

A number of projects are studying the possibility of making next generation Extremely Large Telescopes (ELT). The European Extremely Large Telescope (E-ELT) is one such project. The E-ELT will have a 42 m primary mirror made from 906 hexagonal shape segments of 1.45 m size acroos corners. Two potential materials for these mirror segments are ULE® and Zerodur® [1].

Manufacturing processes examples for making >1 metre hexagonal mirrors have been reported by both Sagem and Kodak.
First, the blank is ground to the desired shape. Then, the mirror is lapped and polished to get the correct form geometry and to remove any subsurface damage induced by previous machining process [2].

A possible production improvement is to achieve an effective grinding process that can produce better shaped surfaces with less subsurface damage. This will reduced subsequent polishing operations. To achieve this effective grinding capability, a new ultra precision large optics grinder - BoX® - has been developed at Cranfield University (Figure 1).
This grinding machine now forms part of an Ultra Precision and Structured Surfaces (UPS^2) facility, at the Technium OpTIC, St Asaph, North Wales [3].

The purpose of the work described in this paper has been to establish the induced level of subsurface damage (SSD) in ULE® and Zerodur® when grinding at differing levels of material removal rate.

SUBSURFACE DAMAGE MECHANISMS OF BRITTLE MATERIALS

Ductile or brittle fracture mode grinding can be used to machine brittle materials [4] such as Zerodur® and ULE®. Ductile mode grinding has been reported to give low subsurface damage (SSD). However, achievable material removal rate is low, as for example the critical depth of cut is ~50 nm [5] on Zerodur®.

Higher manufacturing rates are supported using micro brittle fracture grinding. However, the brittle mode leaves surface and subsurface damage.
Micro fracture mechanisms that lead to SSD in brittle materials have been extensively investigated by Lawn [6].
An efficient grinding process requires optimisation of the grinding parameters to reduce the penetration depths of the micro fractures.

In order to measure the extent of subsurface cracks, different non-destructive and destructive measurement methods have been developed. [7, 8] Destructive methods have proved, and remain, more successful for detecting micron and sub-micron scale fractures.
Repetitive polish, etch and optical microscopy have been widely employed to observe SSD in ground glasses [9, 10].

Two terms have been employed to describe the subsurface damage observed.
The majority of subsurface cracks cluster together near the surface and finish at a characteristic 'cluster depth'.
A small minority of cracks propagate deeper beneath the surface the so-called 'single last fracture depth' which is often much deeper than the cluster [11-12].

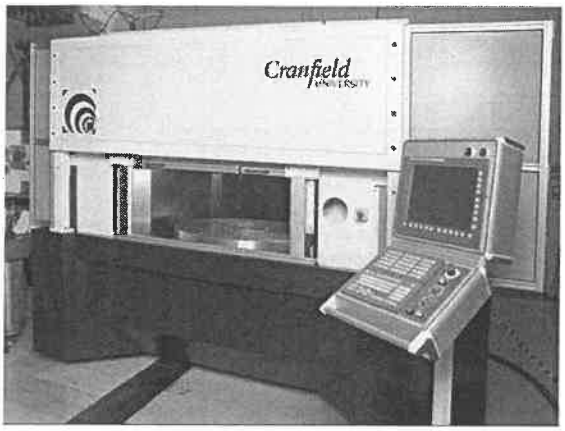

FIGURE 1. BoX® precision grinding machine

EXPERIMENTAL DETAILS

Grinding parameters

The grinding parameters controlled are the depth of cut (a_e), the feed per revolution (f_r), the surface speed (v_w). They are shown in Table 1. The grinding wheel cutting speed (v_c) is kept constant at 30m/s.

TABLE 1. Grinding parameters.

Grinding Conditions	Depth of cut a_e (µm)	Feed Rate f_r (mm/rev)	Surface speed v_w (mm/s)
Rough cut	500	15	25
Semi Finish cut	200	10	20
Finish cut	50	1.5	25

The rough cut removes the bulk material. A semi finish cut eliminates the amount of damage induced by the rough grinding. A first finish cut takes out the previous grinding damage which is followed by a second finish cut which creates the desired form accuracy, surface roughness and minimal level of induced subsurface damage.

Grinding wheels

'Toric' shaped resin bonded diamond cup grinding wheels have been employed. Three abrasive grit sizes were chosen for this grinding process, 76 µm, 46 µm and 25 µm.

Material

Two materials were tested (see Table 2). A glass material, ULE® (Ultra Low Expansion), produced by Corning and a glass ceramic material, Zerodur®, made by Schott.

TABLE 2. Zerodur® and ULE® parameters.

	ULE	*Zerodur*
Elastic modulus E (GPa)	70	91
Hardness H (GPa)	4.6	6.2
Fracture toughness K_c ($MPa.m^{1/2}$)	1.8	0.9
Brittleness H/K_c ($m^{1/2}$)	2560	6890

Both ULE® and Zerodur® have low thermal expansion coefficients.
The difference of fracture toughness and hardness between those two materials means that Zerodur® has brittleness three times higher than ULE®.

Test specimen size was 100 mm x 100 mm and 20 mm thick.

Sub-surface damage evaluation

Using a 'wedge' polishing and surface etching approach, the SSD was evaluated using an optical microscope.
Grooves were polished using a Zeeko IRP polishing machine. They were placed in line with the grinding direction and at bottom of the 'cusping'. The wedge depth was measured using a profilometer.
The number of defects per mm^2 relative to the depth below the ground surface has been analysed using optical microscopy. Identification of defects for counting was based on judgment.

EXPERIMENTS RESULTS

Surface roughness

The surface roughness along the grinding direction, (R_a), changes with the grinding wheel grit size. Typically larger grit size results in an increase of the surface roughness for ULE® and Zerodur®.

TABLE 3. Grinding results

Grinding Conditions	Wheel type	Surface roughness Ra (nm)	
		ULE	*Zerodur*
Rough cut	D76	303	394
Semi Finish cut	D76	266	265
	D46	186	186
	D25	165	165
Finish cut	D76	231	287
	D46	172	248
	D25	191	247

Overall, Zerodur® has higher roughness than ULE® for equivalent grinding conditions.
Interestedly, during a finish cut on ULE®, the D46 grinding wheel gives better results than the D25 grinding wheel. On Zerodur®, under those same grinding conditions, the two grinding wheels leave equivalent surface roughness.

Subsurface damage

Figure 2 and 3 show different microscope pictures taken of Zerodur® and ULE® cracks for each grinding conditions employed.

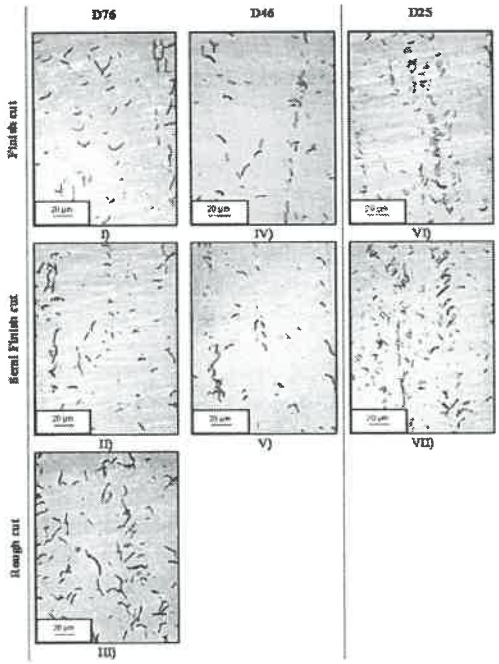

FIGURE 2. Different Zerodur® cracks

For each material, the shape of the cracks is similar for each grinding conditions. However, larger grit size tents to induce longer cracks.
The Zerodur® cracks are small and slightly curved in comparison to ULE® where observed cracks are longer. They also overlap each other and have a more 'fork type' shape. The cracks length to thickness ratio is also larger for ULE® than Zerodur®.

'cluster' and 'single last fracture' depth results were measured and are shown in Figure 4.

The cluster depth results in ULE® are larger than in Zerodur®. However, this depth difference is typically within 1-2 μm. Interestingly, the semi finish cut (D25) leaves deeper cluster damages in Zerodur® than ULE®.

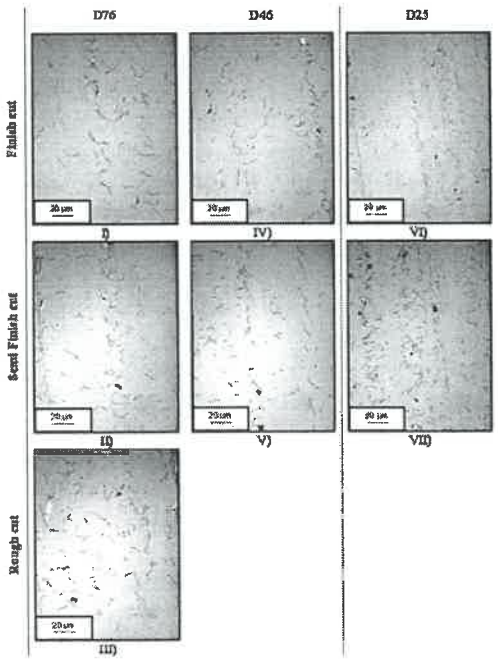

FIGURE 3 Different ULE® cracks

Overall, the single last fracture depths follow the same trend as cluster depths. The subsurface damage depths in ULE® are larger than in Zerodur®. During the rough cut (D76), the single last fracture depth is more than twice the depth in ULE® compared to Zerodur®. This can be explained by a lower brittleness value for ULE® leading to larger cracks using higher grinding forces. However, the finish cut (D46) and semi finish cut (D76) give more damage in Zerodur®.

Those results are in accordance with the consideration that the single last fracture depth is highly associated with machine dynamics whilst the cluster depth is related to material mechanics. [10] A previously reported correlation between surface roughness and subsurface damage is not observed in these results.

The important subsurface damage values are those created during the finish cuts. Importantly, the finish cut using a D25 grinding wheel leaves 8 μm in ULE® and 4 μm in Zerodur®. Using the same grinding parameters, the subsurface damage depth increases with the grit sizes. The finish cuts using 25 μm grit size reach the target value for Zerodur® (< 5μm) but not for ULE®.

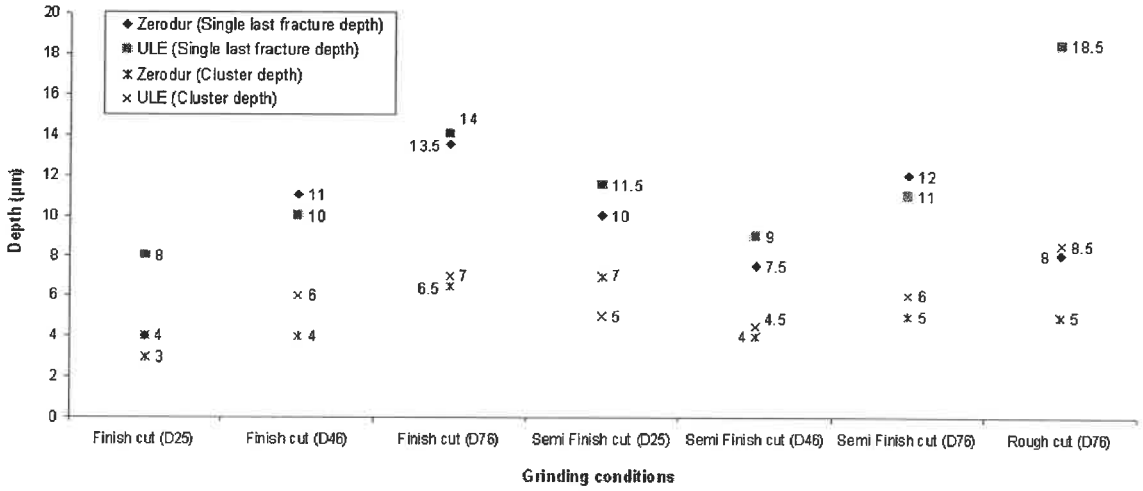

FIGURE 4. 'Cluster' and 'single last fracture' depths *results – ULE® and Zerodur®*

CONCLUSIONS

This paper shows results obtained when grinding optical materials using the BoX® grinding system. An efficient process has been developed for precision grinding large optics. Total grinding process time to remove 0.5 mm from a pre-shaped 1 metre optical blank is 10 hours.

On Zerodur®, the surface roughness (R_a) and subsurface damage level obtained are 247 nm and 4 μm respectively. On ULE®, R_a and SSD level obtained are 191 nm and 8 μm respectively. The difference of subsurface damage can be related to relative material brittleness. No significant connection was seen between surface roughness and subsurface damage using the BoX® grinding mode. Further work will be carried out regarding the influence of grinding machine dynamics and induced subsurface damage levels in optical surfaces.

ACKNOWLEDGMENTS

The authors gratefully acknowledge funding from the McKeown Precision Engineering and Nanotechnology Foundation at Cranfield and project funding through the UK's Joint Research Councils' - Basic Technologies programme and EPSRC funded Integrated Knowledge Centre for UPS[2].

REFERENCES

[1] Gilmozzi R, Spyromilio J. The European Extremely Large Telescope (E-ELT). ESO Messenger. 2007; 127: 11–19.

[2] Shore P, May-Miller R. Production Challenge of Optical Segments for ELT's. EOS Proceeding. 2003; 40: 25.

[3] IKC. http://www.ups2.co.uk – 08/2008.

[4] Inasaki I. Grinding of hard and brittle materials. CIRP annals. 1987; 36: 463–471.

[5] Shore P, McKeown P, et al. Surface and near surface conditions of 'ductile' mode ground Zerodur. IPES Proc. 1995; 365–368.

[6] Lawn B R, Wilshaw T R. Fracture of brittle solids. Cambridge university press. 1975.

[7] Tonshoff H K, Brinksmeier E, Hetz F, Detection of microcracks. CIRP annals. 1987; 36(2): 545–552.

[8] Puttick K E, Jeynes C, Whitmore L, Rudman M R, Yamasaka M, Shore P, Gee A E. Surface damage in nanoground silicon. IMECH Proc. 1992; 49–51.

[9] Ball M J, Murphy N A, Shore P. Electrolytically assisted "ductile" mode diamond grinding of BK7 and SF10 optical glasses. SPIE Proceeding. 1991; 1573: 30.

[10] Tonnellier X, Morantz P, Shore P, Baldwin A, Evans R, Walker D, Subsurface damage caused during rapid grinding of Zerodur. Advance in Abrasive Technology. 2007; 10.

[11] Lambropoulos J C. From abrasive size to subsurface damage in grinding. OSA Technical Digest. 2000; 8: 17–18.

[12] Menapace J A, Davis P J, Steele W A, Wong L L, Suratwala T I, Miller P E. MRF Applications: Measurement of Process-dependent Subsurface Damage in Optical Materials using the MRF Wedge Technique. SPIE Proc. 2005; 5991: 39.

ULTRASONIC ASSISTED TURNING OF HARDENED STEEL WITH MONO-CRYSTALLINE DIAMOND

Fritz Klocke[1], Olaf Dambon[1], Benjamin Bulla[1] and Michael Heselhaus[2]
[1]Department of Process Technology
Fraunhofer Institute for Production Technology IPT
Aachen, Germany
[2]Corporate Production Engineering
ZF Friedrichshafen AG
Friedrichshafen, Germany

INTRODUCTION

The demand for ultra-precise steel parts with optical surface qualities and complex shaped geometries is increasing and could be applied for plastic injection molding or precision glass molding processes. Nowadays optical molds for injection molding are coated with a nickel layer, in order to be able to machine the surface with diamond tools. Directly machined steel parts would decrease manufacturing time, making the coating process step unnecessary. Additionally, the life time of the mold is increased dramatically. Uncoated steel tools have a higher scratch resistance and no risk of delamination. Therefore the potential of directly machining steel with monocrystalline diamond is exceptionally high.

Though ultra-precision machining with mono-crystalline diamonds is limited to non-ferrous, a few crystalline and plastic materials. Due to excessive tool wear in case of machining ferrous materials caused by the affinity between the carbon (diamond) and the iron (workpiece), mono-crystalline diamonds are unsuitable for this application. Diverse trials to solve the mentioned problem have been undertaken, e.g. turning with cryogenic or carbon saturated atmospheres [1]. Unfortunately these methods failed due to their tremendous efforts and relatively poor results.

Ultrasonic assisted diamond tools have the ability to bridge this gap and thus to reduce the diamond tool wear significantly by factor 100 or higher. The lower tool wear is caused by a discontinuous contact between the diamond and the substrate material during the manufacturing process. This leads to improved cooling conditions and thus to a reduced tool tip temperature. Furthermore, a reduction of the average cutting forces can be detected [2].

This paper describes the latest results in ultrasonic assisted diamond turning at the Fraunhofer IPT. Experiments were conducted with 40 kHz and 60 kHz ultrasonic transducers in order to understand the influence of the vibration frequency

THEORETICAL CONSIDERATIONS

The ultrasonic assisted turning technology works with a fixed transducer. On top of the mounted sonotrode and booster system a mono-crystalline diamond tool tip is clamped. As written before the aim is to utilize mono-crystalline diamond tools to manufacture ultra-precise hardened steel parts.

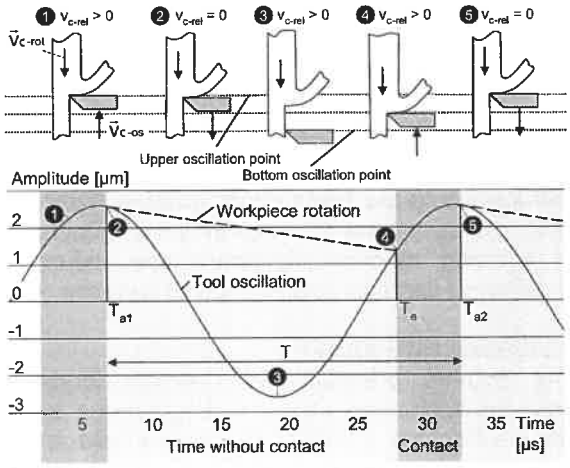

FIGURE 1. Kinematics of ultrasonic assisted process

It was shown in several publications, that the diamond tool wear can be reduced by a superimposed vibration. This was applied for the first time by Moriwaki for ultra-precision machining purposes in 1991 [2].

In literature two different types of oscillation movements appear, uniaxial and elliptical. In this

paper the tool movement occurs exclusively in the cutting direction.

It is essential for the transition from the conventional to the vibration-assisted process, that the maximum oscillation speed reached in the zero-crossing, is bigger than the constant workpiece speed (FIGURE 1 between point 2 and 3). Only when this condition is met the tool does detach itself from the chip during the oscillation (point 2, relative speed $v_{rel} = 0$). The contact occurs again (point 4) during the upward motion after the vibrational direction changes at the bottom oscillation point (point 3).

Accordingly, the effective contact time between the part and the cutting edge is reduced significantly by the high frequency excitation of the tool. As previously demonstrated, this modification in the kinematics of the turning process has a considerable impact on the efficiency of ultra-precision operations conducted on critical materials such as steel or glass [3,4,5].

The relationships shown, permit mathematical interrelationships to be derived for the exact calculation of time, position and speed of the workpiece (s_{rot}, $v_{c\text{-}rot}$) and of the tool (s_{os}, $v_{c\text{-}os}$) as well as of the associated relative values (v_{rel}). The derivation of the mathematical relationships illustrates the complex kinematics correlations involved in vibration-assisted machining.

In accordance with the description of the operating cycle, the cutting speed in the machining zone $v_{c\text{-}rel}$, is dependent not only on the workpiece motion caused by the spindle rotation, but also on the oscillation of the tool (FIGURE 1):

$$v_{c\text{-}rel}(t) = v_c = v_{c-rot} + v_{c\text{-}os} \qquad (1)$$

Rübenach could derive the parameters which have the greatest influence on the vibration assisted turning process [4]:

- entrance duration ED: percentaged contact time between workpiece and tool within one vibration cycle and
- entrance speed v_{in}: relative velocity between workpiece and tool in the moment of contact $v_{c,rel}$ ($t = T_e$).

However, these parameters have to be transformed into set-up parameters for the workpiece speed $v_{c,rot}$ and amplitude A of the ultrasonic transducer. The relationship between parameters was derived numerically.

Exemplarily a point is shown with an entrance duration of ED = 20% and a entrance speed v_{in} = 600 mm/s at both, 40 kHz and 60 kHz. By increasing the frequency from 40 kHz to 60 kHz equal working points regarding ED an v_{in} are generated with a decrease of the amplitude by 33%. This leads to a stabilized vibration and theoretically to better surface qualities. Furthermore the ultrasonic device used for 60 kHz has better vibration properties than the one used for 40 kHz, due to the optimization of the system for the application.

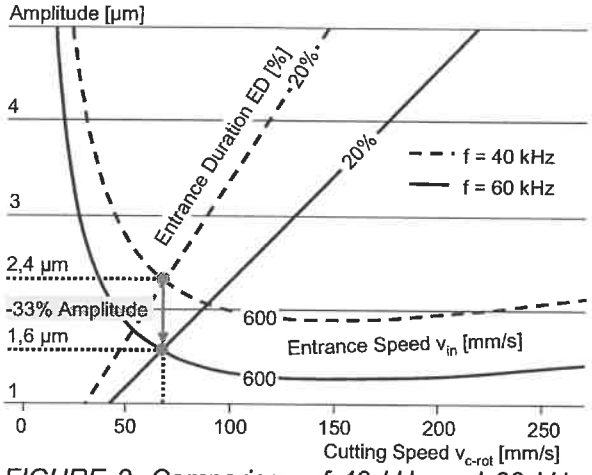

FIGURE 2. Comparison of 40 kHz and 60 kHz parameter field for equal working points.

This paper will point out the influence of different working frequencies on the generated results during ultrasonic assisted diamond turning of hardened steel.

EXPERIMENTAL RESULTS

The results shown here are related to the ultrasonic assisted turning of plane hardened steel cylinders with a diameter of D = 22 mm. The ultrasonic tool system was mount on an ultra-precision lathe from the company Precitech. The applied steel material is the commonly known mold and die steel 1.2083 (STAVAX® ESU, X42Cr13) which was hardened and annealed in four discrete configurations (35, 40, 45, 53 HRC).

The results obtained by machining this material using a vibration assisted diamond tool with

40 kHz and 60 kHz and different feed rates are shown in FIGURE 3. Parameters such as cutting depth, entrance duration and entrance speed are kept constant and equal throughout the presented tests.

The graphs verify the theoretical supposition placed in the first part of this paper, that a frequency increment leads to a process stabilization. This means, that the process reacts much more sensitive towards parameter variation (e.g. feed rate), using a frequency of 40 kHz, than using a frequency of 60 kHz. The variation of the results using 40 kHz, specially at very low and very high feed rates, is much higher than using 60 kHz as a working frequency. Furthermore the absolute surface roughness (Ra) is better at almost every point using a frequency of 60 kHz.

With a feed rate between 5 µm and 10 µm surfaces with optical qualities can be generated with both frequencies (Ra < 10 nm). However the results with 60 kHz are more stable and do not show any dependence on the machined material hardness. Using 60 kHz as good results are obtained when turning STAVAX® ESU with a hardness of 35 HRC, as with a hardness of 53 HRC. The question, whether there is a limitation due to the machined hardness is very interesting regarding the application and will be analyzed in the near future. Effects such as the »size effect« or the kinematical roughness $R_{t,theo}$ have less influence on the surface roughness using the higher frequency of 60 kHz.

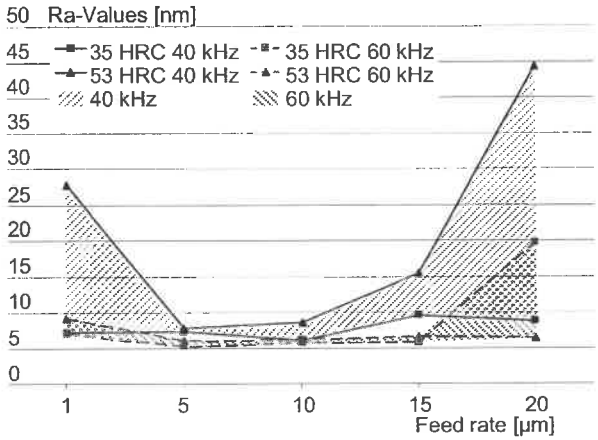

FIGURE 3. Surface roughness (Ra) depending on the frequency, the steel hardness and the feed rate.

The process stability with 60 kHz can not only be reflected in the generated surfaces, but also in the chip formation during the cutting process (FIGURE 4).

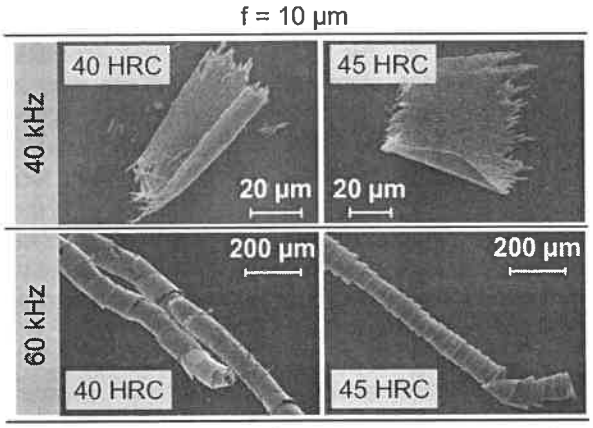

FIGURE 4. Steel chips generated during ultrasonic assisted turning with 40 and 60 kHz

When the process is running at optimal parameters, the chips generated during the cutting process differ depending on the used working frequency. While using a frequency of 40 kHz, the chips have a length of averaged 50 µm and a curly form (FIGURE 4 top). The hardness of the material has no considerable influence on the form and the length of the chips. When the process is conducted with the same parameters (ED, v_{in}, f, a_p) and a frequency of 60 kHz, smaller amplitudes are used (FIGURE 2). This leads to a stabilized chipping process and therefore to endless flow chips (FIGURE 4 bottom). All chips show a classical sawtooth geometry. which are commonly known from the high precision hard turning process with cubic boron nitride (cBN) tools. Usually this chip form is generated for a material hardness above 50 HRC and is caused by the low material deformation capability – at lower material hardness a continuous chip is generated. Due to the intermitting cut of the ultrasonic tool vibration the sawtooth chip is generated at lower material hardness. The backside of the chips look smooth which indicates the ductile cut.

After the machining tests, the diamonds, as well as the chips, were investigated in a scanning electron microscope. Whether with 40 kHz, neither with 60 kHz there could be detected any tool wear on the diamond tips (FIGURE 5). The process was conducted at optimal parameters with a cutting distance of 100 m. This implicates no loss of form accuracy during the manufacturing process of a hardened steel component with a hardness of 53 HRC and a

diameter of 22 mm. Even with lower feed rates, leading to higher cutting distances of 400 m, there could not be detected any tool wear at both frequencies.

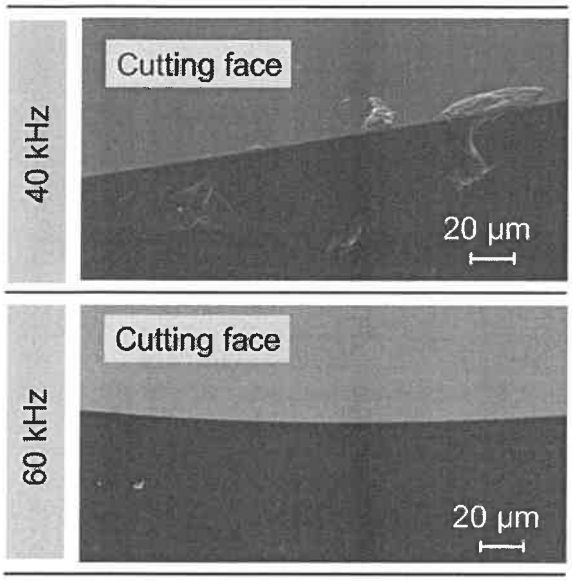

FIGURE 5. Diamond tools after ultrasonic assisted turning of hardened steel (53 HRC)

SUMMARY AND CONCLUSION

The potential of ultrasonic assisted diamond turning is shown in this paper. The kinematical consideration of the vibration assisted process is the key to achieve appropriate surface conditions as well as reduced tool wear. Furthermore the high influence of the vibration frequency was pointed out.

The investigations show, that optical surfaces (Ra < 10 nm) can be generated on hardened steel parts applying ultrasonic assisted machining. The machined steel (STAVAX ESU®, 1.2083, X40Cr14) was hardened to 35, 40, 45 and 53 HRC. The conventional parameters such as feed rate f lead to similar results compared to conventional ultra-precision machining. However the used frequency is a main factor regarding the achievable surface qualities and the process stability.

By increasing the frequency from 40 kHz to 60 kHz, smaller amplitudes can be applied for the same process conditions. This leads to surfaces of higher qualities and the cutting process is stabilized. The stability of the process is reflected in the sensitivity of the process towards effect such as the »size effect« or the kinematical roughness $R_{t,theo}$. Furthermore the chip formation changes from short curly chips to endless flow chips by increasing the frequency and maintaining the process conditions.

Further investigations using 60 kHz and even higher frequencies will be undertaken in the future.

REFERENCES

[1] J. Casstevens, Precision Engineering, Vol. 5, No. 1 (Jan 1983), 9-15

[2] Moriwaki, T.; Shamoto, E.: Ultraprecision Diamond Turning of Stainless Steel by Applying Ultrasonic Vibration, Annals of the CIRP Volume 40/1/1991, Page 559-562

[3] Klocke, F.; Heselhaus, M.; Puellen, J.: Vibration Assisted Diamond Tools for Ultra-precision Turning of Hardened Steel Alloys, Euspen Conference Proceedings, 2005

[4] Rübenach, R.: Schwingungsunterstützte Ultrapräzisionsbearbeitung optischer Gläser mit monokristallinen Diamant-werkzeugen, PhD Thesis, RWTH Aachen, 2001, Page 42-54

[5] Vibration-Assisted Machining Research at Fraunhofer IPT – Diamond Turning and Precision Grinding, Olaf Dambon, Fritz Klocke, Michael Heselhaus, Benjamin Bulla, Andreas Weber, Ralf Schug, Bernd Bresseler, Proceedings of the 23rd Annual Meeting of the American Society for Precision Engineering, 2006

DIAMOND MICRO CHISELING OF MOLDING INSERTS FOR OPTICAL MICRO STRUCTURES

Christian Flucke, Ralf Gläbe, and Ekkard Brinksmeier
Laboratory for Precision Machining
University Bremen
Bremen, Germany

INTRODUCTION

Diamond Micro Chiseling (DMC) is a new diamond cutting process developed for the fabrication of micro structured precision optics. It is designed to machine prismatic micro structures onto surfaces of molding inserts for the replication of polymer optics. The lateral dimension of the structures ranges from 50 µm to 500 µm with a structure depth from 5 µm to 500 µm. Of particular significance is that any arbitrary geometry of V-grooves or pyramidal cavities can be machined as the process is much less limited by kinematics of the machine tool or the diamond tool geometry in comparison to other ultra precision cutting processes like diamond milling, turning or planing [1]. This feature gives the optic designer new degrees of freedom for the design of micro structured optic components. The range of possible applications lies in components for micro spectroscopy devices, bio-chemical photometry and fluorescence assays, optics for measuring devices in production engineering, integrated micro optics for LEDs, and micro structured optics for illumination technologies e.g. in the automotive industry.

This paper gives a brief introduction into the kinematics of the DMC cutting process and focuses then on the main developments which are crucial to lead DMC to a future industrial employment. The goal was to achieve sufficient machining accuracy, tool life and acceptable machining time for manufacturing of micro optic arrays with macroscopic lateral extension.

KINEMATICS OF DMC

In DMC a CVD monocrystal diamond with an opening angle of 50°, rake angle of 18° and flank angle of 2° is utilized for the tool (cf. fig. 1). The applied ultra precision machine tool is comprised of three linear and two rotational axes. A camera provides a resolution of 1.25 µm/pixel and is used to monitor the tool positioning and cutting process [2]. The alignment of the tool to the workpiece and the workspace coordinate system is performed by cutting test structures, measuring these in-situ with a digital video microscope and generating correcting summands for the coordinates. Applying this method a setup deviation in [XYZ] of less than one micrometer is achieved.

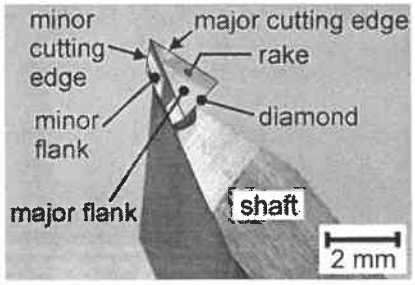

FIGURE 1. DMC tool geometry with DMC specific location of faces and edges.

The cutting principle is illustrated in fig. 2 for a three sided cavity. In combined movements of axes X, Y and Z the tool enters the workpiece and a sloped mirror edge is cut (cf. fig. 2a).

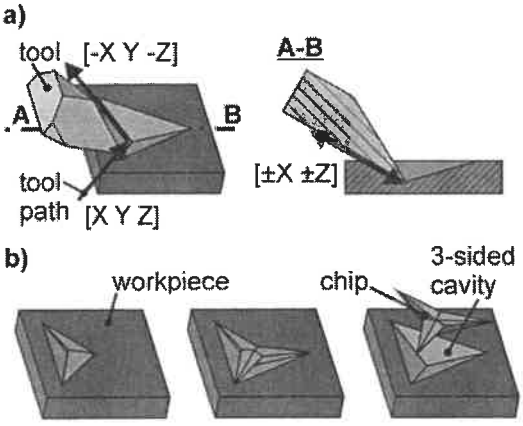

FIGURE 2. Cutting kinematics of DMC demonstrated by cutting a three-sided cavity.

Then the tool is retracted in [-X Y -Z]-direction cutting the second half of the micro mirror. By rotating the workpiece two times and repeating the process, three sided cavities can be generated by aligning the generated micro

mirrors (cf. fig. 2b). A precise alignment within the mentioned set-up accuracy is crucial - otherwise the chip material does not come off.
Following this principle, cavities with up to six sides and four-sided V-grooves are combined to larger arrays such as cubic micro hexagon retro reflectors (cf. fig 6 and 7, also [2]).

PARTITION OF UNDEFORMED CHIP CROSS-SECTION

In practice, a structure cannot be machined with only a single cut per side as depicted in fig. 2, because the maximum thickness of cut, bearable by the tool, would be exceeded. Therefore, the cross-section of undeformed chip has to be partitioned vertically or both, vertically and laterally.

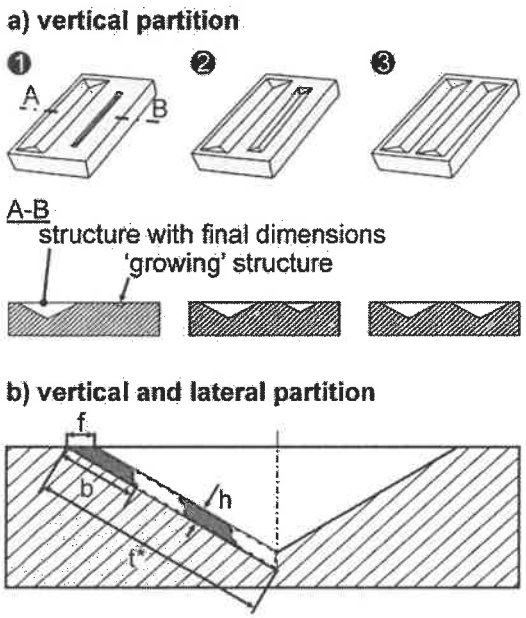

FIGURE 3. Vertical and lateral partition of undeformed chip cross-section.

When only vertical partition of the cross-section is applied the structure grows in depth and lateral dimension (cf. fig. 3a). The thickness of cut is constant but the cross-section increases due to the increasing length t* = b, which is one side of the V-groove. If the cross-section is still beyond the acceptable maximum the length t* is divided in n = t*/b segments which are cut one after another. Here the cross-section is (approximately) constant for each cut.
Cutting experiments with variation of b and h were performed and the cutting force was measured with a dynamometer (Kistler MiniDyn) to quantify and characterize the load of the tool.

One set of experiments was performed under normal conditions, with both, major and minor cutting edge engaged. For the other set the same cutting parameters were applied but the contact of the minor cutting edge was avoided by a modification of the V-groove design. As workpiece materials electroless nickel and OFHC copper were investigated to characterize the influence of material strength.

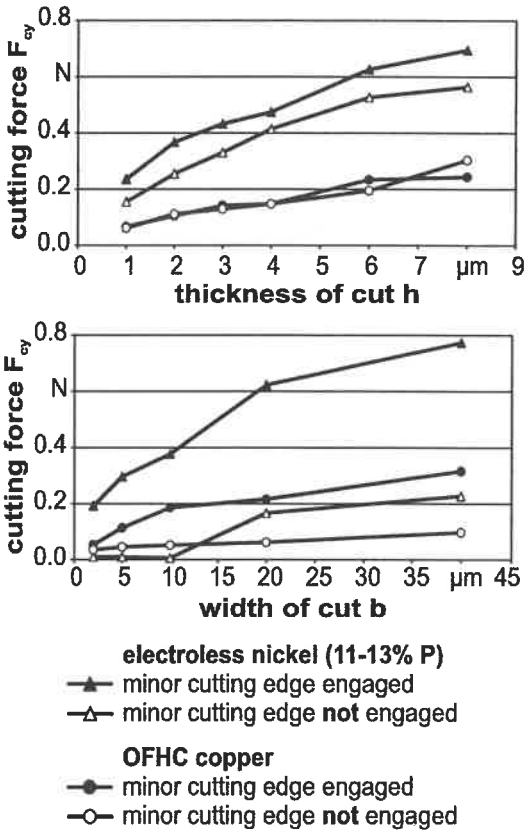

FIGURE 4. Cutting forces dependent on engagement of minor cutting edge. Cutting parameters: v_c = 750 µm/s, γ = 16°, b = 40 µm, h = 4 µm (if not stated otherwise in the diagram). Sample size of five, standard deviation Ø 0.02N.

Fig. 4 shows the data of the forces measured. If h or b is raised, the cutting force increases for both materials. As expected the material with the higher strength, electroless nickel, shows generally higher cutting forces. The increase of the cutting force is due to the raised cross-section of undeformed chip nearly identical for tool engagement with and without minor cutting edge, but there is an offset between the curves showing the amount of force generated at the minor cutting edge. In the variation of b the offset appears much stronger for both materials.

Considering these facts it is concluded that a significant share of the cutting force is generated at the minor cutting edge, even if the contact length is small. This is plausible as the minor rake angle is negative and the cutting edge radius is considerably larger at the minor cutting edge because the adjacent tool faces are not polished.

A strategy for the design of cutting parameters can be derived from these results to minimize the cutting force per cross-sectional area and, therefore, also the load of the tool. When h is increased, the contact length of the major cutting edge stays constant but the contact length of the minor cutting edge increases proportional to h. An increase of b represents directly the increase of the main cutting edge contact length while the contact length of the minor cutting edge remains constant. The thickness of cut should be as low as possible to minimize minor cutting edge contact length, as long as the minimum thickness of cut dependent on the cutting edge radius is regarded (excellent overview in [3]). To achieve a feasible cross-section of undeformed chip the width of cut may be as large as possible, ideally being t*. In this case the micro mirror is finished with a single cut and there is no effect of kinematic roughness. The surface texture is only dependent on the cutting edge quality and the accuracy of the ultra precision machine tool.

COMPENSATION OF TOOL TIP RADIUS

The ideal tool geometry for DMC is a sharp point tool, which is in theory capable of cutting cavities with infinitely sharp concave corners. In reality a sharp point tool is too fragile and breaks upon first use. Therefore, a radius of several micrometer size is ground at the tip of the tool. When cutting with a radius tool the utmost point of the radius in contact with the workpiece, which is defining the generated geometry of the cavity, changes with the engagement parameters and the structure geometry. When generating the CNC-code for DMC machining this point has to be determined and considered when calculating the tool path.

Fig. 5 demonstrates the function of the radius compensation at the example of a four-sided V-groove machined with an 8 µm radius tool. None or an insufficient compensation leads to overlapping edges of the mirror facets as visible in the SEM picture at top. In the middle picture the edges are repositioned in [XYZ] such as they meet with a deviation in position of less than one micrometer. The values for the reposition are calculated in dependency of the tool radius, the inclination of the micro mirror to the workpiece surface and the angles between the mirror facet edges. A surplus of compensation leads to a bar between the mirror facets (cf. bottom SEM picture).

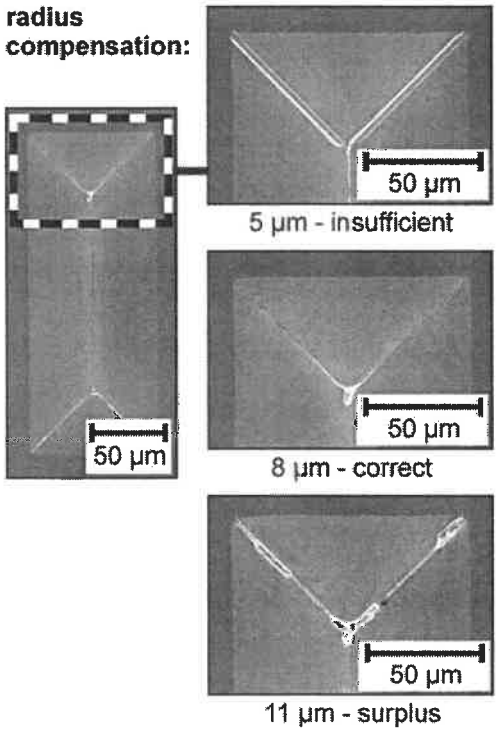

FIGURE 5. Tool radius compensation for an 8 µm radius DMC tool at the example of a four-sided V-groove.

Applying the radius compensation sharp mirror facet edges are generated while keeping the overall geometry at nominal dimensions. Only a very small area (less than 0.1% of the total mirror surface for a 3 µm radius finish machining tool) in the concave corners of the cavities remains undefined, as it cannot be reached by the tool. Accordingly, with DMC machining nearly 100% yield of efficient micro mirror surface can be generated.

PRE- AND FINISH MACHINING WITH TOOL EXCHANGE

For reducing the machining time and increasing surface quality and dimensional accuracy DMC machining is performed in three steps. During pre-machining a robust DMC tool with a radius of 8 - 12 µm is applied for high chip load ($h > 8$ µm, $b = t^*$) at high cutting speeds $v_c \geq 2000$ µm/s. The first of two finish-machining

steps is done with the same tool at $v_c < 500$ µm/s and $h = 4$ µm to achieve dimensional deviations below 1 µm of the structures, which is a necessary preparation for the final cut to be placed accurately in the pre-machined structure. Finally, the tool is exchanged applying a 3 µm radius tool and second step finish machining is performed with $h = 1.5$ µm and $v_c \leq 500$ µm/s for optimized surface quality. Mandatory for the tool exchange is the precise setting-up described above. For an array of 2,500 cubic hexagon retro reflectors (cf. fig. 7) of 200 µm structure size (area approx. 8.84 x 10.3 mm²) the machining time (simulated applying an analytical model) can be reduced about 72% from impossible 437 hours to 79 hours, which is still very much, but feasible, if the value of a micro structured master mold is considered.

Conclusion

The process strategies described above were tested by machining an electroless nickel coating molding insert with several arrays of optical micro structures. Fig. 6 shows an example how V-grooves and four-sided small cavities can be combined to form a riblet structure. The second example (fig. 7) is an array of cubic retro reflectors with hexagonal aperture [2]. The surfaces are of optical quality with a roughness $Ra < 10$ nm, flatness $PV < 50$ nm and are free of artifacts. The effect of tool radius compensation is clearly visible as the edges and corners are sharp and only an insignificant small area in concave corners remains undefined.

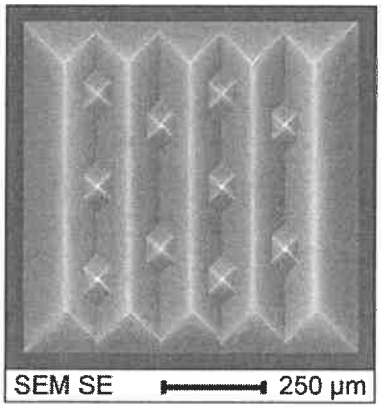

FIGURE 6. Riblet structure of overlapping V-grooves with cavities at the protruding ridges.

By reducing the contact length of the minor cutting edge the better understanding of the mechanism of cutting force generation was used when machining these samples to decrease the amount of cutting force per cross-sectional area of uncut chip. This allows lager cross-sections, shorter machining time and increased tool life. Better surface quality is gained as no effect of kinematic roughness occurs when finish machining micro mirror facets with a single cut cutting width being $b = t^*$. Also the concept of pre and finish machining by utilizing two dedicated tools reduces machining time and quality, as the main load is taken by the robust pre-machining tool: Nevertheless, the machining time is quite high and future work will deal with further reduction. The maximum cutting speeds are not limited by the DMC process itself, but by the dynamics of the machine tool and stiffness of the DMC diamond tool. Here lies a large potential for further optimization.

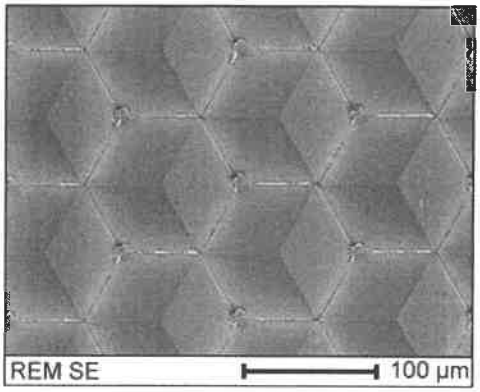

FIGURE 7. 100 µm cube corner retroreflectors with hexagonal, 100%-effective aperture.

ACKNOWLEDGEMENTS

The authors like to thank the German Research Foundation (DFG) for funding this work as a part of the Transregional Collaborative Research Center SFB/TR4.

REFERENCES

[1] E. Brinksmeier, O. Riemer: Metal cutting of microstructures. Proc. of First International Conference on Multi-Material Micro Manufacture. Elsevier, 2005.

[2] E. Brinksmeier, R. Gläbe, C. Flucke: Manufacturing of molds for replication of micro cube corner retroreflectors. Production Engineering. 2008; Vol. 2/1: 33-38.

[3] D. Dornfeld, S. Min, Y. Takeuchi: Recent Advances in Mechanical Micromachining. Annals of the CIRP. 2006; Vol. 55/2: pp. 745-768.

MACHINING BEHAVIOUR OF MONOCRYSTALLINE DIAMOND END MILLS

Eckart Uhlmann, Dirk Oberschmidt
Production Systems
Fraunhofer Institute for Production Systems and Design Technology
Berlin, Germany

INTRODUCTION

Monocrystalline diamonds are used as cutting parts for milling tools to produce structures with a geometric accuracy less than 1 µm and of a surface quality with roughness values of less than Ra = 5 nm. Three types of monocrystalline diamond are available on the market. These are natural diamond (ND), high pressure synthetic diamond (HSD), and monocrystalline CVD-diamond (MCCVDD). The paper shows results for milling tools with a diameter of D = 0.25 mm and D = 0.5 mm. For all experimental results, presented in this paper, brass work pieces with a Vickers Hardness of 145 HV are used.

CUTTING PART GEOMETRY

As a prerequisite for the machining tests the geometry of the cutting part has to be defined. For this purpose different geometries of diamond cutting parts are evaluated by simulation with the software tool ANSYS. The cutting corner and the cross section of the cutting part are varied.

Cutting Corner

Sharp corners and chamfered corners are analyzed by experiment on an ultra precision machining system Nanotech® 350 FG by Moore Nanotechnology Systems and by simulation. The process forces are measured with a dynamometer Kistler 9265A. As cutting parameters a cutting depth $a_p = 5$ µm and an infeed $f = 5$ µm were used. The value of the cutting force $F_c = 0.2$ N was calculated as maximum value from the force components feed force F_f, feed normal force F_{fN}, and thrust force F_p, measured during experiments. This F_c value is used in the simulation as normal force on the face $F_{\gamma n}$ at a section of 5 µm times 5 µm. Figure 1 illustrates the results of the simulation in comparison to results of cutting experiments, where the cutting corner wear occurred as fracture. Simulation and experiment are of good conformity. The fracture lines of the diamonds correspond with the regions of the cutting part with the highest values for the comparison stress by Huber/von Mises. It is also clear that a chamfered corner is of no advantage. Therefore, sharp corners are used for the further experiments.

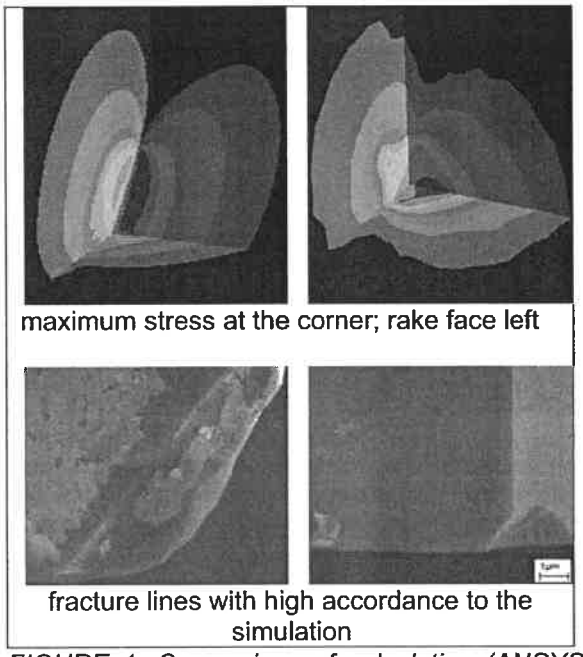

FIGURE 1. Comparison of calculation (ANSYS simulation, top) and experiment (SEM images, bottom) for a chamfered cutting corner (10 µm x 10 µm, left) and a sharp corner (right)

Cutting Part Macroscopic Geometry

The macroscopic geometry of a diamond cutting part used in a milling tool is mostly shaped according to the structure of the diamond. For a successfull use of a milling tool, it has to fulfill the following requirements:

- geometrical accuracy regarding milling diameter and effective tool length,
- cutting edge roundness of less than $r_s = 50$ nm, and
- sufficient bending stiffness.

Two general principles are common at manufacturers. The first one is to machine the basic geometry of the cutting part on the whole length of the diamond. At second a big diamond is used and the cutting part geometry is a

section of the whole diamond. In both cases the diamond is fixed at a metallic bracket. The geometric accuracy regarding milling diameter and effective tool length depends on the assembly process. It is of high importance for the milling process, because the excentricity of the rake face determines the rake angle.
To estimate the bending stiffness, different cross section geometries of the cutting part are simulated and calculated in the software tool ANSYS. Table 1 shows the calculations for two different cross sections for a milling diameter D = 0.25 mm. Tool No 1 has a trapezoid cross section; tool No 2 has a semicircle cross section. These geometries possess the lowest values for tool tip deflection and bending stress within a row of cutting part geometries from different manufacturers. The effective tool length here is l = 0.5 mm and the normal force on the face is $F_{\gamma n}$ = 0.25 N on a section of 5 µm times 5 µm.

TABLE 1. Simulation results of tool deflection and bending stress at two different macroscopic cutting part geometries

Cutting part geometry	tool tip deflection δ /µm	bending stress σ_B /Nmm^{-2}
No 1 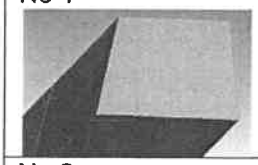	0.6	10,980
No 2 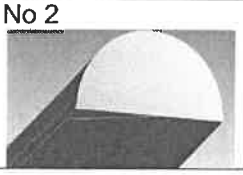	2.0	5,205

For the tool life a minimum bending stress is of more importance than the tool tip deflection. According to this a semicircle cross section for the milling tools is used for the further research work.

MACHINING BEHAVIOUR

The evaluation of the machining behaviour of the tools is scrutinized by experiments to ascertain the process forces and the process temperatures. The results of these experiments are used to determine the temperature at the cutting zone by simulation. Thermo gravimetry and contact angle measurements characterize the diamond thermal properties.

Process Forces

The maximum values for feed force F_f, feed normal force F_{fN}, and thrust force F_p are determined by an analog process with fixed milling tool. For the experiments the Nanotech® 350 FG and the Kistler 9265A are used. Rail-turning-tests are scrutinized to model the conditions of full section cuts (figure 2).

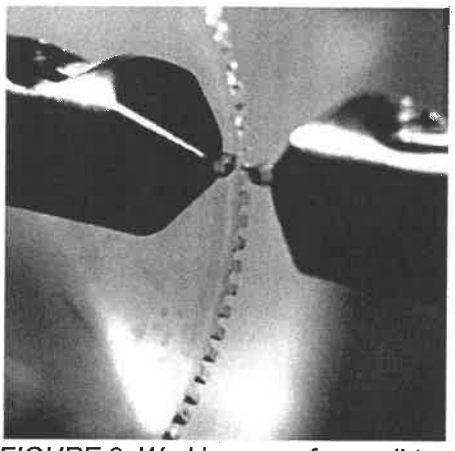

FIGURE 2. Working zone for a rail-turning-test

On the circumference of a cylinder with a diameter of 20 mm alternate rails and grooves with a width of the half circumference according to the nominal milling tool diameter D. The rotational speed of the cylinder is adjusted to ensure an analog rotational speed of the milling tool of n = 75,000 min^{-1}, that means a rotational frequency of f = 1,250 Hz. In these experiments the cutting conditions are different from a real milling process. But it is reasonable, because the maximum values for the three force components are orthogonal to each other [1].
The evaluation is done with the software tool ORIGIN. The determined force signals of the dynamometer are filtered with a band pass FFT filter. The frequency band for the evaluation is from 500 Hz to 1,300 Hz. Thus, the critical value regarding the natural frequency of the dynamometer and the low frequent oscillation coming from the experimental set-up are filtered out. In table 2 the maximum force levels as results of cutting experiments with milling tools from the different types of diamond are shown. The tool diameter is D = 0.5 mm each. In this case correspond F_x to F_f, F_y to F_{fN}, and F_z to F_p. From the three components the cutting force F_c is calculated. The cutting depth is a_p = 5 µm. The feed is varied as f_1 = 1 µm, f_2 = 2 µm, f_3 = 5 µm. The rake angle is γ = 0°.

TABLE 2. Determined maximum force levels and calculated cutting force

a_p /µm	f /µm	F_{Xmax} /N	F_{Ymax} /N	F_{Zmax} /N	F_c /N
Natural diamond - ND					
5	1	0.04	0.05	0.02	0.07
5	2	0.04	0.08	0.04	0.10
5	5	0.04	0.17	0.06	0.19
High pressure synthetic diamond - HSD					
5	1	0.05	0.05	0.02	0.07
5	2	0.06	0.06	0.03	0.09
5	5	0.04	0.13	0.05	0.15
Monocrystalline CVD-diamond - MCCVDD					
5	1	0.10	0.05	0.02	0.11
5	2	0.10	0.09	0.03	0.14
5	5	0.08	0.16	0.07	0.19

The level of F_{Xmax} is in a narrow range for each tool and only depends on a_p. F_{Ymax} and F_{Zmax} are depending on f and increasing. Inspite of the different diamond types the F_c values are similar for same parameters.
Further experiments are carried out with an additional variation of the cutting depth as a_{p1} = 5 µm, a_{p2} = 7.5 µm, a_{p3} = 10 µm. The correlation of F_c and area of chip section $A_c = f \cdot a_p$ as well as active cutting edge length $l_k = f+a_p$ do not show a clear relationship. Figure 4 illustrates the correlation of F_c and A_c.

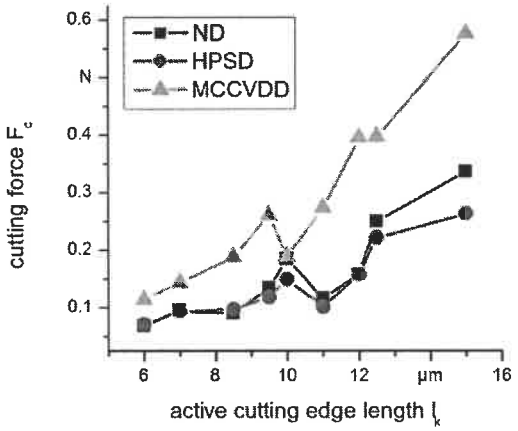

FIGURE 3. Correlation of cutting force and active cutting edge lentgh at rail-turning-tests

The results of the analog experiments are very similar to the results of real milling experiments, carried out on a high precision milling machine WISSNER Gamma 303.

Cutting Part Temperature

The process force measurements are combined with temperature measurements. Here thermocouples of type K are mounted on the cutting edge. The temperature signals, like the force signals, are collected with a data-logger by National Instruments and the software tool LabView®. There is to observe a stationary temperature in the thermocouple after a few seconds. In contrast to the cutting force, the detected cutting edge temperature difference Δt_{ce} is clearly to correlate to the area of chip section A_c (figure 4). Thus, for simulations of the temperature in the working zone, the area of chip section can be used as load zone.

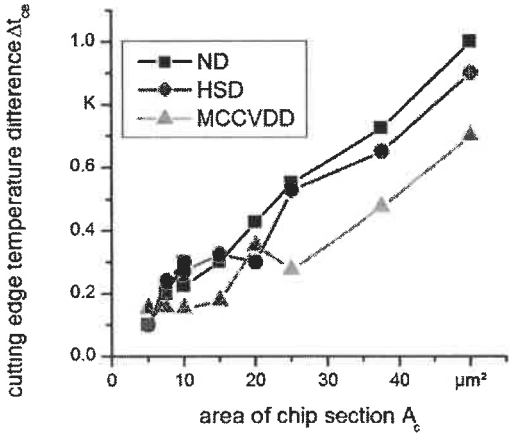

FIGURE 4. Correlation of cutting edge temperature difference and area of chip section at rail-turning-tests

The backward projection of the temperature under consideration of the thermocouple position leads to calculated maximum temperatures of no more than 200°C in the cutting zone.

Diamond Temperature Behaviour

In several experiments it was figured out, that chipping and abrasive wear occur at natural diamonds most. Artificial diamonds often show additional chemical and adhesive wear. One reason can be the change of the boundary layer of the diamond. By Differential Scanning Calorimetry with a NETZSCH STA 449 C is found out, that artificial diamonds are reacting between 100°C and 600°C without changing the mass. From 100°C to about 250°C there is to observe an endothermic reaction. It is followed by an exothermic reaction from 250°C (figure 5). Contact angle measurements with Pentandiol and Methyleniodid show a decrease from nearly 90° at 20°C to about 35° for MCCVDD's and about 40° for HSD's at 300°C. It can be assumed that the free bonds on the boundary of

the diamond lattice are used by reactive components like the hydroxyl group, that causes increasing chemical wear.

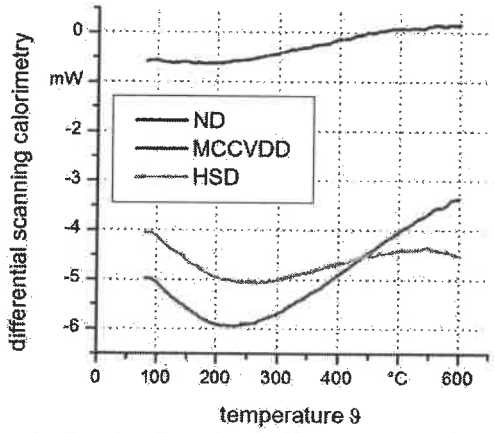

FIGURE 5. Temperature behavior of different diamond types related to differential scanning calorimetry

CUTTING PART WEAR

The wear of diamond mills occurs as tool fracture and as cutting edge wear.

Tool Fracture

The tool fracture is to observe in two variants. Breakage of the whole cutting part is a result of non-adequate handling. The forces to break a diamond cutting part are measured by nano indentation on a Zwick z005 as appr. F = 3 N for tools with D = 0.25 mm and appr. F = 10 N for tools with D = 0.5 mm.

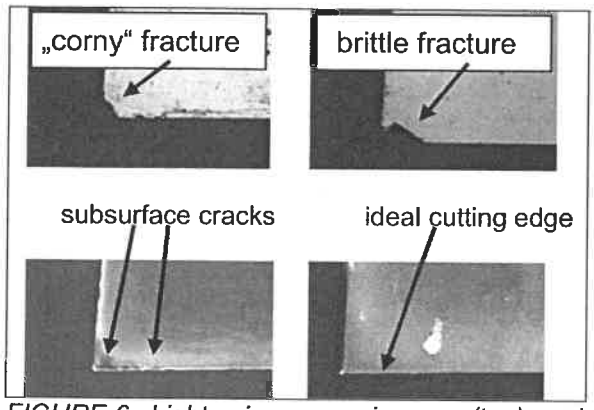

FIGURE 6. Light microscopy images (top) and SEM images (bottom) of tool fracture and initial condition of diamond cutting corners

Figure 6 illustrates the second appearance is the fracture of the cutting corner. Here is to observe a relation of subsurface damages of the diamond with the fracture characteristic. Subsurface cracks, visible in low-voltage scanning electron microscopy, give a hint on the fracture behavior of the tool cutting corner.

Cutting Edge Wear

During the experiments cutting edge rounding, corner wear, chipping, displacement of the cutting edge, and adhesive wear occured. Especially adhesive wear was more often to observe at HSD's. Figure 7 illustrates on atomic force microscope (AFM) images the topology of cutting edge wear on the example of MCCVDD's with D = 0.5 mm after different path lengths due to primary motion l_c.

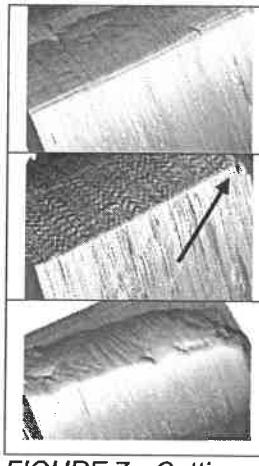

	l_c = 50 m; cutting edge still onworn
	l_c = 400 m; slight corner wear
	l_c = 1,200 m; corner wear, cutting edge rounding, displacement of the cutting edge

FIGURE 7. Cutting edge wear topology at a MCCVDD cutting part, measured with AFM (image source: Fraunhofer IZM)

CONCLUSIONS AND OUTLOOK

It is shown, that the three types of monocrystalline diamond have different properties in details. It seems, that MCCVDD is of the highest potential for the use as cutting part of milling tools. Further investigations have to be done to investigate especially the temperature influence and the wear mechanisms.

REFERENCES

[1] Schauer K. Entwicklung von Hartmetallwerkzeugen für die Mikrozerspanung mit definierter Schneide. Berlin, Univ. Diss, Fraunhofer IRB Verlag; 2006

CONTROL OF A FAST LONG RANGE ACTUATOR (FLORA)

Qunyi Chen[1], Thomas A. Dow[1], Kenneth Garrard[1], Alex Sohn[1] and Derek Richardson[2]
[1]Precision Engineering Center, NC State University, Raleigh, NC
[2]Precision MicroDynamics, Inc Victoria, BC, Canada

INTRODUCTION

The development of a Fast LOng Range Actuator (FLORA) is driven by the need to create non-rotationally symmetric (NRS) optical surface with millimeters of sag at high production rates on diamond turning machines. The existing technology on tool positioning with the PZT FTS is limited by stroke or the slow slide servo is limited by speed. The actuator proposed in this paper is supported by an air bearing, driven by a linear motor, measured by a high-resolution linear encoder and controlled by a high-speed DSP based controller [1] as shown in Figure 1. The goal is to retain the surface quality (form error and surface finish) of existing diamond turning machines while moving the tool over a range of 4 mm at a frequency of 20 Hz.

To meet the ultraprecision tool positioning requirement in the machining process, the actuator has been optimized from both physical design and control design.

(1) Have a system easy to control. The physical construction of this actuator is free of major nonlinearities such as hysteresis, backlash and friction commonly seen in other motion systems.
(2) Develop an effective control approach to minimize the influence of error, noise and disturbance on the system performance.

More specifically, there are four critical tasks to be addressed in the development of the actuator.

(1) The reaction force in the linear actuation process shall be cancelled out by a symmetric dual motor design.
(2) The heat generated in motor coil shall be removed for continuous high-speed operation.
(3) The air bearing and supporting structure shall be designed as stiff as possible
(4) The tool motion command shall be accurately generated and closely followed.

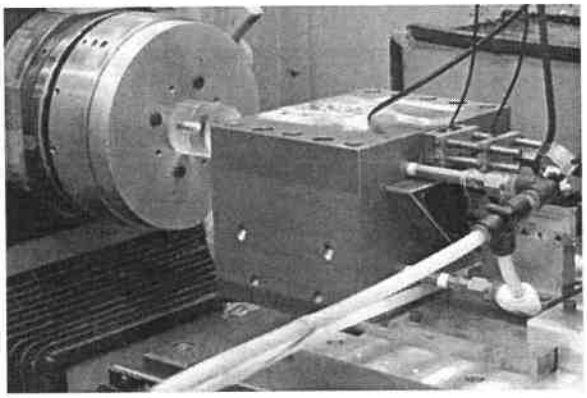

FIGURE 1. Photograph of the FLORA system mounted on the ASG 2500 DTM.

Motion sensing, feedforward and feedback controller design and the system performance are described in the following sections.

MOTION SENSING

To create a freeform surface, the position of the tool is synchronized to the position of the DTM axes by generating its motion command (Z) as a function of the spindle angular position (θ), z-slide position (Z_s) and cross-feed slide position (X). All the position measurement in the four motion axes will be involved. It is desirable to have any measurement induced tool positioning errors to be less than a few nanometers. Laser interferometers installed on the ASG-2500 can provide measurement resolution and errors below 2 nm for z-slide and x-slide position. However, there are measurement errors in the other two motion axes discussed later.

The ability to follow the trajectory command within tens of nanometer is first dependent on the tool position measurement. The laser-scale encoder (Sony BH25) generates two differential sinusoidal signals with 250 nm pitch. The encoder interpolator sub-resolves the analog signal pitch by a factor of 256 for 1 nm resolution. To maintain the position measurement resolution up to 250 mm/s tool

speed, a signal processing and interpolation algorithm is implemented in the firmware of the PMDi interpolator, so that interpolation frequency limit is increased to above 1 MHz.

The quality of motion synchronization depends not only on the profile tracking performance of the actuator but also on the real-time generation of tool motion commands. For the 20,000 count/rev Heidenhain rotary encoder used for spindle angular position measurement, the effective measurement resolution is increased by filtering the raw encoder reading without introducing phase distortion in the estimation process. With this technique, the maximum contribution of quantization error in the command due to the limited encoder resolution is reduced to 20 nm. Furthermore, a small amount of runout in the rotary encoder disk will appear as a non-uniform pitch of the angular steps when read by the stationary read head. This pitch error repeats each revolution and since the spindle speed is constant over a single revolution, it can be determined and compensated at the servo sampling rate.

CONTROL SYSTEM DESIGN AND TESTING

The functional requirement for the FLORA is to follow the tool motion profile as closely as possible while minimizing the effects of measurement errors and disturbances. The disturbance force to the tool motion could be from the errors in motor actuation force generation process, or from the tool-workpiece interaction process which largely depends on the tool wear condition, and the material properties of the workpiece.

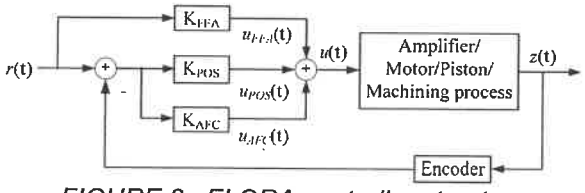

FIGURE 2. FLORA controller structure

Figure 2 shows a block diagram of the proposed controller structure to achieve the control task. A position feedback controller (K_{POS}) is designed to establish the basic closed-loop control system. An acceleration feedforward controller (K_{FFA}) is applied to improve profile tracking. An adaptive feedforward controller (K_{AFC}) is designed to further improve trajectory tracking and disturbances rejection at selected frequencies.

Position feedback controller (K_{POS})

Based on the measured open loop system frequency response characteristic, the position feedback controller with different lead-lag designs [1] are applied to obtain three loop gain crossover frequency at 100 Hz, 600 Hz, and 1000 Hz. Figure 3 shows the Bode diagram for each controller. The system with 100 Hz crossover frequency has much lower peak magnitude but it has the slowest response and lowest stiffness. The system with 1000 Hz crossover frequency has the highest servo stiffness but it caused saturation of the amplifier during the tracking experiments.

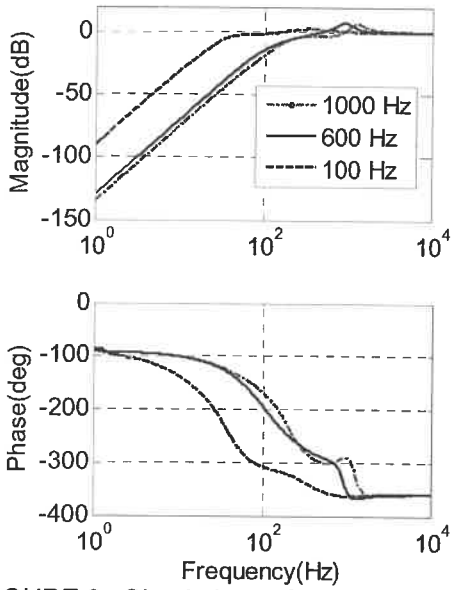

FIGURE 3. Simulations of system sensitivity function frequency response with PID and Lag-lead controllers

Acceleration feedforward controller (K_{FFA})

An acceleration feedforward controller generates most of the current for the desired acceleration and reduces the phase lag in profile tracking. Equation (1) shows the form of the feedforward algorithm:

$$K_{FFA}(s) = \frac{\hat{m}}{\hat{K}_f} s^2 \qquad (1)$$

where $\hat{K}_f$ is the estimated motor force constant, $\hat{m}$ is the estimated moving mass, the term s^2 is to take double-derivative of the desired position motion path $r(t)$.

Adaptive feedforward controller (K_{AFC})

Because of the speed and resolution demands in ultraprecision machining, a control system with position feedback and acceleration

feedforward may not be sufficient. To improve the profile tracking and disturbance rejection, an adaptive feedforward control (AFC) approach [2] has been explored. The basic principle of this control approach is to estimate the magnitudes and phases of the position error at selected frequencies and to generate the control effort needed to remove the error at these frequencies. Functionally, it is equivalent to putting a model of the disturbance signal into the feedback control to create larger feedback gains at these selected frequencies.

The transfer function *Gc* from the basic position feedback controller (K_{POS}) for the open loop system *G* in Equation (3) is used to find the parameters for the adaptive algorithm in Equation (4) at the selected frequency, ω.

$$G_{cn}(i\omega) = A_C e^{i\varphi};\quad G_C(s) = \frac{G(s)}{1 + K_{POS}G(s)} \tag{3}$$

$$K_{AFC}(z) = \frac{2\alpha}{A_C}\frac{z^2\cos(\varphi) - z\cos(\omega T_s - \varphi)}{z^2 - 2z\cos(\omega T_s) + 1} \tag{4}$$

where T_s is the sampling interval, the parameter α is a convergence coefficient, A_C and ϕ are nominal magnitude and phase derived from the frequency response of the transfer function *Gc* from $u_{AFC}(t)$ to $z(t)$. The controller parameter α is selected to maximize the convergence rate of the adaptive controller (shorten the transient response) while maintaining the stability (robustness) of closed-loop controller.

Figure 3 shows the positioning error in a test of sinusoidal profile tracking at the amplitude of 2 mm and the frequency of 20 Hz. A combination of PID, AFC and acceleration feedforward controller is used in this test. The frequency ω in Equation (4) was the sine wave excitation frequency (20 Hz) and the parameter α was selected as 0.001. The tracking error in Figure 3(a) is ±70 nm (only 0.0035% of the positions command) compared to ±170 nm a similar experiment without the AFC. The frequency spectrum in Figure 3(b) shows the tracking error has negligible magnitude at the fundamental frequency (20 Hz) but has peaks at 2 and 3 times this frequency. For the tool motion path in the machining of typical freeform surface, only the first few harmonics of the spindle rotational frequency have significant magnitudes. The position error at these frequencies can be eliminated by putting the basic element of AFC in Equation (2) in parallel with the closed loop controller.

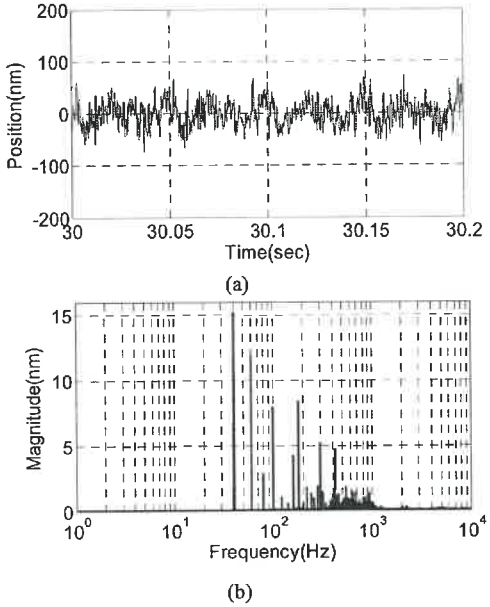

FIGURE 4. 2mm 20 Hz sinusoidal tracking test (a) Tracking error for four motion cycles (b) Frequency spectrum of tracking error

CUTTING PERFORMANCE

A flat surface was machined to test the ability of the FLORA piston to hold position while excited by the forces of machining. The flat was machined on a hard-plated copper substrate with a 0.53 mm radius diamond tool at 500 rpm with a 1 mm/min feedrate (2 µm/rev) and 2 µm depth of cut on the finish pass. The theoretical finish is 1 nm PP. The Zygo NewView measurement in Figure 4 shows a 144×108 µm patch that represents approximately 72 tool passes and has an RMS surface finish of 7.4 nm.

Table 1 compares the RMS of flat surface finish when the tool is locked or positioned by the control system. For the locked case, the air was removed from the lower sides of the triangular piston. Comparing to the case of the locked tool, the three controllers increased the surface roughness. The active closed-loop control adds 3.7 nm RMS error for the 100 Hz lag-lead controller, but a larger error for higher crossover frequency controller designs. The results indicate that it is desirable to remove the major peaks in the 600 Hz and 1000 Hz controller design (Figure 3). To maintain the speed of response and servo stiffness, it is necessary to

have an amplifier with faster current loop dynamics.

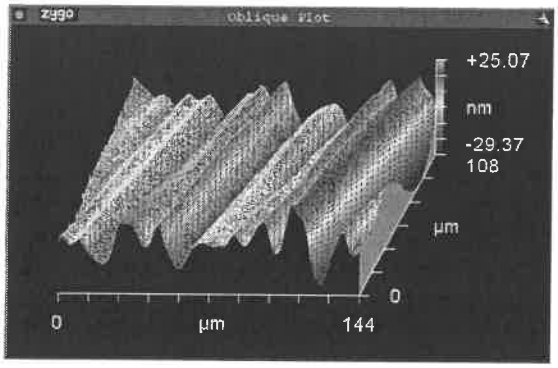

FIGURE 4. ZYGO image of surface finish (RMS=7.4 nm) on a plated copper flat

TABLE 1. Comparison of RMS error with a locked and position controlled tool holder

RMS (nm)	Tool holding method			
	Locked	LL* (100Hz)	LL* (600Hz)	LL* (1kHz)
Piston Motion	1	14.4	16.0	14.3
Surface finish	3.7	7.4	11.4	10.5

Note: LL stands for lag-lead controller

A tilted flat was machined to evaluate the ability of the servo to create NRS optical surfaces. The tilted flat requires a sine wave motion of the tool with the amplitude changing linearly with the radius. This part is a good test of the linearity of the actuator as the amplitude changes but the frequency remains constant. However, the machined surface should be a flat and thus easy to measure in a laser interferometer. Only a combination of acceleration feedforward controller and PID controller is used for the tool motion control in tilted flat machining. Acrylic tilted flats with 50.8 mm diameter and 4 mm sag were created at spindle speeds from 300-1200 rpm. The measurement of flatness by the Zygo GPI laser interferometer for the tilting surface shows the surface residual error with the best-fit tilted flat removed. The flatness error is 1 µm in Figure 6. The measured average surface finish is 22 nm (RMS) or twice the holding position value.

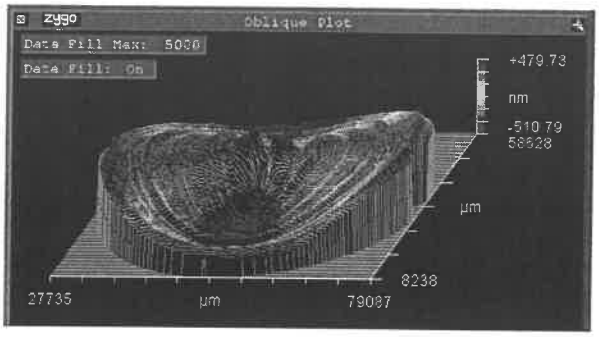

FIGURE 5. Measured flatness error of the 50 mm diameter tilted flat using laser interferometer

CONCLUSIONS

When the FLORA is used to cut freeform surface with two millimeters of motion at high spindle speed (1200 rpm), it is critical to reduce the tool positioning error to retain the surface quality possible for symmetric diamond turned parts. The performance of the FLORA has been significantly improved as a result of upgraded hardware and control algorithms over the original prototype [3]. Further improvement will involve an amplifier with higher current loop bandwidth, implementation of faster and/or more advanced control approaches, a faster DSP processor and stiffer mechanical components.

ACKNOWLEDGEMENT

Principal funding for this research is through the NSF Grant DMI-0556209 monitored by G. Hazelrigg. PMDi provided software support to implement the control system and increase the interpolation speed of the linear encoder.

REFERENCES

[1] Q. Chen, T. Dow, K. Garrard and A. Sohn, 2007. "A Fast Long Range Actuator", Proc. of ASPE, Vol 42, pg 287-290, 2007.

[2] Messner, and Bodson, Design of adaptive feedforward algorithms using internal model equivalence, International Journal of Adaptive Control and Signal Processing, Vol.9, p199-212, 1995.

[3] Buescher, N., "Live Axis Turning", MS Thesis, Mech Engr., North Carolina State University, Raleigh, NC 2005.

EVALUATION OF HARMONIC DISTORTIONS IN PRECISION INERTIAL SENSORS

Swavik Spiewak [1], Glenn Hauer [2], and Stephen J. Ludwick [3]
[1]University of Calgary
Calgary, AB, Canada
[2]ARAM Systems, Ltd.
Calgary, AB, Canada
[3]Aerotech, Inc.
Pittsburgh, PA, USA

INTRODUCTION

Inertial sensors do not require physical reference bases and relevant fixtures. Their unique property is the ability to measure 6-degrees-of-freedom (6-DOF) displacements relative to the inertial coordinates of the Earth, an ideal reference frame. Other sensors for measuring linear or angular displacement, including laser and lidar trackers, need reference bases such as tripods and measure displacements with reference to these bases [1]. Since reliable reference frames and low-invasiveness of fixtures are critical in precision engineering, inertial sensors have the potential to enable qualitative changes in this field. However, to be a viable element of precision engineering solutions, the accuracy of inertial sensors has to be in the range of at least "parts-per-million" (ppm).

The introduction of Global Positioning System (GPS) greatly diminished the importance of high performance accelerometers, indispensable in Inertial Navigation Systems (INS). This has shifted the focus of research towards small, inexpensive and reliable Microsystems Technology (MST) based designs [1]. A rapid progress in miniaturization and cost reduction that followed has not been matched by an increased accuracy and resolution of the new generation of sensors.

INVESTIGATED SENSORS

Commercially available accelerometers fall short of the requirements of precision engineering. In particular their distortions are high, typically above 0.1%, i.e, 1,000 ppm. However, this level is a result of technological imperfections in fabrication. Simulations of the best accelerometers available today suggest nonlinear distortions well below 1 ppm [2]. There is also an experimental evidence of distortions below 50 ppm. It is therefore justified to investigate, detect, model and attenuate an impact of phenomena that degrade the achievable accuracy of sensors below the level predicted by the relevant physical laws.

A challenging consequence of size scaling in MST based devices is, from the viewpoint of precision engineering, the need for extremely high resolution of motion measurement. Movements of components in MST based inertial sensors are typically in the sub-micron range. Consequently, investigating phenomena occurring in these sensors with a "part-per-million" precision implies femto-meter (10^{-15} m) resolution. Such resolution is feasible in some currently available accelerometers employing capacitive transducers. For example, the digital SiFlex accelerometer [2] features 24 bit "word length". This is equivalent to the resolution of 0.05 ppm. Its noise floor, although relatively low, limits at present the resolution to 10 pm/$\sqrt{Hz}$ at 25 Hz and 700 fm/$\sqrt{Hz}$ at 100 Hz. However, with narrow band digital filters reaching the needed femto-meter resolution is possible.

In this research we consider a representative pendulous servo accelerometer. Its mechanical design, shown in Figure 1, limits the total displacements of the seismic mass to about ±1 μm. Furthermore, the servo system keeps this mass at a nearly constant distance from the enclosing plates. This is necessary to minimize nonlinear distortions of the capacitive readout system as discussed below.

The seismic mass suspended on flexures exhibits complex spatial dynamics which has to be accounted for in the design and tuning of the servo. Since imperfections of fabrication affect this dynamics, there is a need to identify it for the purpose of monitoring and correcting the fabrication process. Furthermore, if an accurate model of the sensor is identified, such a model can be used for the cancellation of distortions occurring in this sensor.

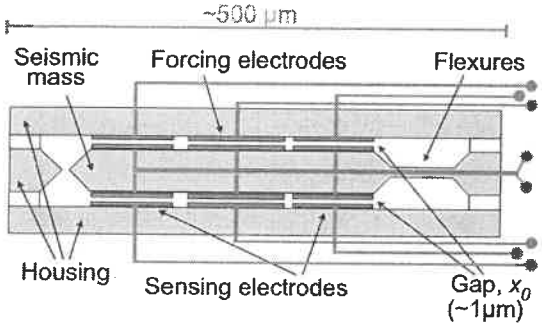

FIGURE 1. Schematic cross-section of the investigated capacitive, servo accelerometers.

DISTORTIONS OF READOUT

A representative accelerometer considered here employs four "parallel plate", capacitive transducers in a differential, "voltage mode" arrangement shown in Figure 2.

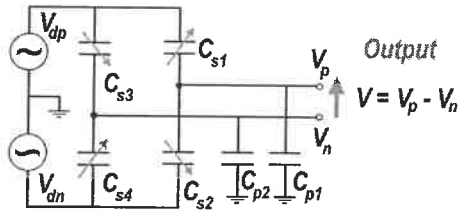

FIGURE 2. Schematic diagram of the differential capacitive transducer.

Two symmetric pairs of capacitors designated C_{s1}, C_{s2} and C_{s3}, C_{s4} are driven by the voltage sources V_{dp} and V_{dn} applied symmetrically with reference to the electrical ground. As the gaps between sensing electrodes on the mass and the housing change, a voltage is generated between the terminals V_p and V_n. It is a function of several variables, such as the nominal gap, x_0, nominal capacitances of individual sensors, and parasitic capacitances C_{p1} and C_{p2}. This voltage designated $V_x[\mathbf{C}, x_0, x(t)]$ is, in particular, a nonlinear function of the gap variation $x(t)$. The capacitances are designated collectively as $\mathbf{C} = \{C_{s1}, C_{s2}, C_{s3}, C_{s4}, C_{p1}, C_{p2}\}$. In this extended abstract we do not show the exact expression for $V_x[\mathbf{C}, x_0, x(t)]$, which is long and complicated. Instead we focus on a case when $C_{p1} = C_{p2} = \beta\, C_s$, $V_{dp} = V_{dn} = V_d$, and $C_{s1} = C_{s2} = C_{s3} = C_{s4} = C_s$, and obtain

$$V_x[\beta, x_0, x(t)] = \frac{4\, V_d\, x_0\, x(t)}{(\beta+2)\, x_0^2 - \beta\, x(t)^2} \qquad (1)$$

We further observe that if $x(t) << x_0(t)$, which is common in servo accelerometers, the output signal becomes a nearly linear function of the mass displacement

$$V_{xL}[\beta, x_0, x(t)] \approx \frac{4\, V_d\, x(t)}{(\beta+2)\, x_0} \qquad (2)$$

The gap variation $x(t)$ is a function of the acceleration $a(t)$ acting on the sensor. In general this relationship is dynamic and nonlinear (e.g., asymmetric gain for the positive/negative accelerations, insensitivity at small signals, hysteresis, etc.). In this abbreviated analysis we neglect the dynamics and use an asymmetric gain to express the acceleration-gap relationship as follows

$$x(t) = \Psi[a(t)]\, K_a\, a(t); \quad \Psi[\vartheta] = \begin{cases} 1 & \text{for } \vartheta \geq 0 \\ \gamma & \text{for } \vartheta < 0 \end{cases} \qquad (3)$$

This leads to the acceleration-voltage formula

$$V_a[\beta, \gamma, x_0, a(t)] = \frac{4\, V_d\, x_0\, \Psi[a(t)]\, K_a\, a(t)}{(\beta+2)\, x_0^2 - \beta\, \{\Psi[a(t)]\, K_a\, a(t)\}^2} \qquad (4)$$

To facilitate a systematic characterization of the investigated nonlinearity we employ the Taylor series expansion. Assuming a small ratio $\Psi[a(t)]\, K_a\, a(t) / x_0$ (i.e., small variations $x(t)$ of the gap) we expand the above expression around 0 and keep the first 5 terms

$$V_{aL}[\beta, x_0, a(t)] = \alpha_1 \frac{a(t)}{x_0} + \alpha_3 \frac{a(t)^3}{x_0^3} + \alpha_5 \frac{a(t)^5}{x_0^5}$$

where (5a-d)

$$\alpha_1 = \frac{2\, V_m\, K_g\, [1 + \gamma + (1-\gamma)\, \mathrm{sgn}(x)]}{(\beta+2)}$$

$$\alpha_3 = \frac{V_m\, K_g^3\, \beta\, [1 + \gamma^3 + (1-\gamma^3)\, \mathrm{sgn}(x)]}{(\beta+2)^2}$$

$$\alpha_5 = \frac{V_m\, K_g^5\, \beta^2\, [1 + \gamma^5 + (1-\gamma^5)\, \mathrm{sgn}(x)]}{(\beta+2)^3}$$

An absence of the even terms in the expansion is a consequence of the simplifications made above. In general, all terms are present and their analytical form can be derived using, for example, software capable of symbolic computations.

Equations (4) and (5) show that the level of nonlinear distortions in the considered capacitive transducer depends upon:

1. a relative input strength coefficient, η, defined as $\eta = K_a\, a(t) / x_0$,
2. coefficient γ, i.e., a nonlinearity of the acceleration-gap relationship,
3. coefficient β, *i.e., an* impact of the parasitic capacitance C_p

A knowledge of these quantities facilitates correction of the inherent nonlinearities of the considered transducer. The following section illustrates the estimation of x_0 and γ.

PARAMETER ESTIMATION

To assure the needed accuracy, the above coefficients should be estimated in the conditions closely resembling the actual operation of the sensors. In particular, the tested sensors should be subjected to dynamic excitations. In this research we use precisely guided, servo controlled translational air bearing stages ABL1500 and ABL2000 with brushless DC motors (Aerotech, Inc.). One of the tests setups is shown in Figure 3.

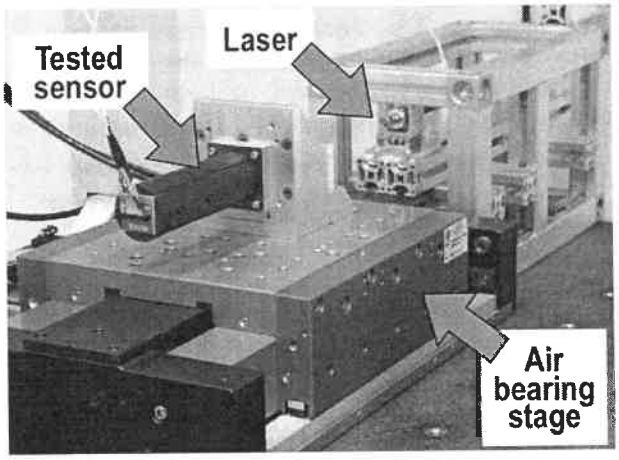

FIGURE 3. Experimental setup.

To maximize the accuracy, identification is conducted in a very narrow frequency bandwidth and repeated over the entire frequency range of interest. The stages are driven such that the tested sensor is subjected to sinusoidal acceleration $a(t) = A_0 \sin(n\, \omega_i\, t)$. Furthermore, rather than using the time domain relationships, Eqs. (4, 5), we employ the trigonometric Fourier series and formulate expressions involving the sought coefficients in the frequency domain as

$$a_0(\beta,\gamma,\eta) = \frac{\omega}{\pi} \int_{-\pi/\omega}^{\pi/\omega} V_a[\beta,\gamma,x_0,a(t)]\, dt$$

$$a_n(\beta,\gamma,\eta) = \frac{\omega}{\pi} \int_{-\pi/\omega}^{\pi/\omega} V_a[\beta,\gamma,x_0,a(t)] \cos(n\,\omega\, t)\, dt$$

$$b_n(\beta,\gamma,\eta) = \frac{\omega}{\pi} \int_{-\pi/\omega}^{\pi/\omega} V_a[\beta,\gamma,x_0,a(t)] \sin(n\,\omega\, t)\, dt$$

$$n = 1, 2, 3, \ldots \qquad \text{(6a-c)}$$

Performing the above integrations yields relationships needed for the parameter estimation. In particular

$$a_1(\cdot) = b_2(\cdot) = a_3(\cdot) = 0, \text{ etc.}$$

$$b_1(\cdot) = \lambda \left(\sqrt{\frac{2+\beta}{2+\beta-\beta\,\eta^2}} + \sqrt{\frac{2+\beta}{2+\beta-\beta^2\gamma^2\eta^2}} - \gamma - 1 \right)$$

$$\text{where } \lambda = \frac{4\, V_d}{\beta\, \gamma\, \eta} \qquad (7)$$

Expressions for other coefficients are too long to be shown here. Nonetheless it becomes clear that, if we experimentally estimate the coefficients on the left hand side of the obtained analytical expressions, we can then compute the sought parameters γ, and x_0 (provided that K_a is known). To illustrate this we plot in Figure 4 a relative deviation of the coefficient $b_1(\cdot)$ from unity, which is its ideal value. The deviation is in terms of γ with η as a parameter. The value of β is set to 2, which is reasonable for the accelerometers under consideration. If we choose, for example, an estimate $b_1(\cdot) = 0.04\%$ and $\eta = 0.4$, we find out γ as -0.04 % (i.e., $\gamma = 0.96$). In the actual assessment we solve a relevant set of nonlinear equations to simultaneously find all the needed quantities.

EXPERIMENTAL RESULTS

Successful application of the proposed approach to improving precision of inertial sensors hinges upon:

1. the fidelity of employed models of investigated nonlinearities, and
2. the accuracy of experimentally estimated values of Fourier coefficients.

The latter item is of utmost importance, since reliable identification of model coefficients aids a refinement of these models.

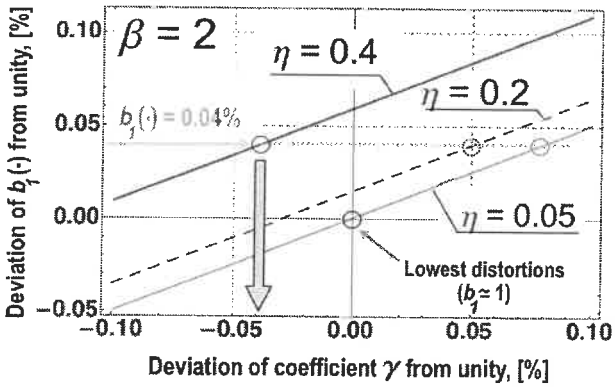

FIGURE 4. Fourier coefficient $b_1(\cdot)$ as a function of γ at representative values of η and β.

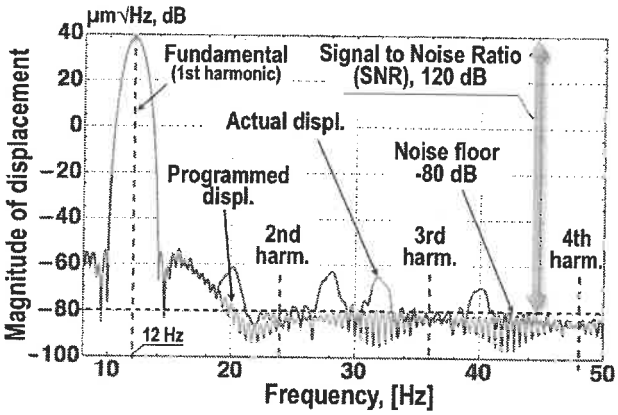

FIGURE 5. Power spectral density of sinusoidal motion with fundamental frequency 12 Hz.

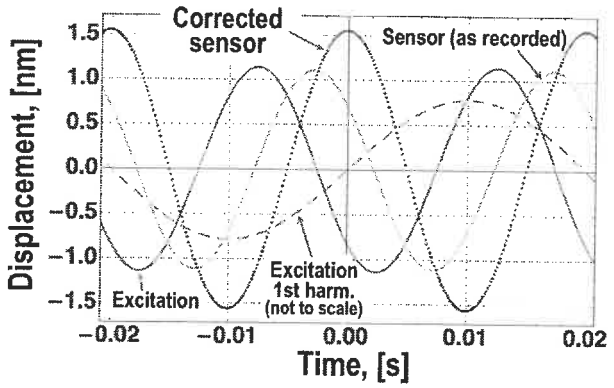

FIGURE 6. Representative plots of the second harmonic distortions in the investigated signals.

Accurate assessment of the Fourier coefficients depends upon (1) the ability of generating precise sinusoidal translational motion, and (2) suppression the impact of unavoidable, residual imperfections of motion on the recorded sensor signals [3]. These imperfections interact with distortions caused by the nonlinearity of investigated sensors and can greatly deteriorate the accuracy of results.

The quality of sinusoidal excitations generated in this research is characterized in Figure 5 by the magnitude spectrum of displacement obtained for 12 Hz oscillations with the amplitude of 120 μm. Of particular interest in an absence of the 2nd, 3rd or 4th harmonics. Figure 6 shows a representative plot versus time of the second harmonic of the excitation which remains in the generated signal when the motion controller can not provide a desirable quality of excitation, e.g. for oscillations with amplitudes below 10 nm. The same figure shows a signal from the output of the tested accelerometer. This latter signal has nearly the same amplitude but a significant phase shift, which indicates a strong interference between distortions introduced by the tested sensor and the impurity of the generated motion. A "true" distorted signal, computed according to the method proposed in [3] is also plotted.

CONCLUSIONS

Model based suppression of distortions is a convenient way for improving precision of MST based inertial sensors. Needed models can be developed by analyzing responses of these sensors to precisely controlled excitations. Robust mechanical integration of guidance, actuation and measurement functions in the air bearing stages used in this research facilitates achieving the quality of motion that is necessary to develop models for the best currently available accelerometers.

REFERENCES

[1] Barbour N. Inertial Components - Past, Present and Future. Proc. AIAA Guidance, Navigation and Control Conf. 2001; AIAA-2001-429

[2] Speller K, Yu D. A low-noise MEMS accelerometer for unattended ground sensor applications. Proc. SPIE. 2004; 5417: 63-72.

[3] Spiewak S, Hauer G, Lawrence E. Identification of Nonlinear Distortions in MST Based Inertial Sensors. Proc. euspen Int'l Conf. 2008.

HIGH ACCURACY ATOMIC FORCE MIRCOSCOPE FOR DIMENSIONAL METROLOGY

Dean M. Ljubicic[1], David L. Trumper[1], Robert Hocken[2] and Jerald Overcash[2]
[1]Mechanical Engineering Department
Massachusetts Institute of Technology
Cambridge, MA 02139
[2]Mechanical Engineering Department
University of North Carolina at Charlotte
Charlotte, NC 28223

INTRODUCTION

The purpose of this work was to develop a high accuracy atomic force microscope. An AFM tip was mounted to a one degree of freedom actuator capable of 20 microns of linear travel. The project focused on limiting positioning errors due to mechanical, electrical, and thermal noise to 1 nm. A new self-sensing, self-actuating probe developed by Dr. T. Akiyama was used in our instrument [1].

The high accuracy AFM detailed in this abstract was tailored to interface with the Sub Atomic Measuring Machine (SAMM)[2], a metrology device developed at the University of North Carolina at Charottle. The SAMM uses Halback motor arrays to control the position of a neutrally buoyant stage in six degees of freedom. The SAMM stage has demonstrated 0.1 nm resolution, 1 nm repeatability, and 25 nm accuracy. Together these two instruments will be used to generate a high accuracy contour plot of given samples whereby the SAMM stage will raster scan a sample while the AFM reads its height. The AFM was made to achieve compatible performance as the SAMM stage.

OVERALL ARCHITETURE

The high accuracy AFM is a classic mechantronic device. All of the following features are shown in a cross sectional sketch in Figure 2. A moving Invar mass is constrained to move in one degree of freedom by a monolithic steel flexure. Its displacement is measured by three low thermal expansion capacitance sensors. The stage is actuated by a tubular piezoelectric actuator which engages the stage through a second steel decoupling flexure. The atomic force microscope sits in a kinematic mount which allows for coarse movement and calibration along the measurement axis. The center axis of the instrument is reserved for a borescope which gives a top down coarse view of the target to identify micron sized features.

MECHANICAL NOISE

The atomic force microscope was designed to reject mechanical noise input by the piezoelectric actuator. Although the actuator extends primarily along its axial dimension, it has undesirable second order motions that cause it to tip, tilt, shear, and twist. Only a fraction of these second order motions from the actuator propagate into the moving stage by using a flexure to decouple the two components. The decoupling flexure is axially stiff to transmit forces and weak in the remaining five degrees of freedom to attenuate error motions. Conversely, the guide flexure is axially weak and stiff in the remaining five degrees of freedom. Figure 1 shows these components side by side.

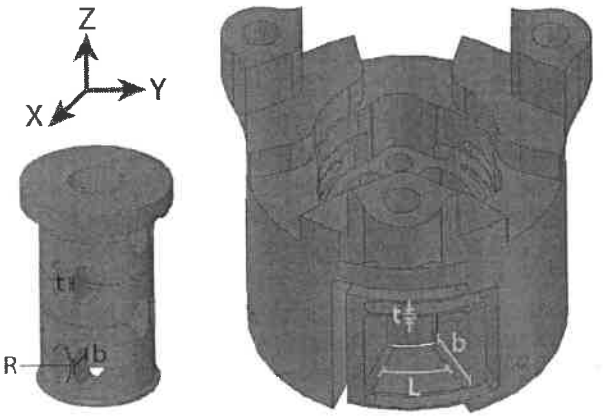

FIGURE 1. *Decoupling and guide flexures used in the AFM in relative proportion.*

Table 1 holds the stiffness of both flexures as defined by the coordinate system presented in Figure 1. Table 2 gives the worst case estimate of the second order error motions and their effect on the Invar stage. We find that the error motions that are translated through into the stage are less than one nanometer and therefore within our mechanical error budget.

TABLE 1. *Lateral and Rotational stiffnesses of the Decoupling and Guide Flexures.*

Direction	Decoupling	Guide	Ratio
Z	$18\ \frac{N}{\mu m}$	$1.0\ \frac{N}{\mu m}$	18
X	$0.033\ \frac{N}{\mu m}$	$56\ \frac{N}{\mu m}$	1690
Y	$0.033\ \frac{N}{\mu m}$	$56\ \frac{N}{\mu m}$	1690
θ_x	$0.75\ \frac{Nm}{rad}$	$2.0\ \frac{kNm}{rad}$	2670
θ_y	$0.75\ \frac{Nm}{rad}$	$2.0\ \frac{kNm}{rad}$	2670
θ_z	$23.6\ \frac{Nm}{rad}$	$1.8\ \frac{kNm}{rad}$	77.2

TABLE 2. *Estimated error motions transmitted into the moving stage from the actuator.*

Direction	Error Piezo	Error Stage
X or Y	$1.0\ \mu m$	0.59nm
θ_x or θ_y	$100\ \mu$rad	37.5 nrad
θ_z	$1\ \mu$rad	13.0 nrad

FORCE AND METROLOGY LOOPS

The high accuracy AFM was designed to have non intersecting force and metrology loops. The piezoelectric actuator imparts a force onto the moving platform and a reactionary force upon a bridge as denoted in Figure 2. Preliminary designs placed a singular capacitance sensor concentric with the tubular actuator and affixed to the AFM by this bridge. A 20 Newton reactionary force upon the bridge would deflect it vertically by 5.8 nanometers. Had the sensor been affixed the bridge, this deflection would feed directly into the capacitance measurement and remain indistinguishable from the desired measurement of the displacement of the moving mass. The capacitance sensors were then moved to the bottom of the Invar base where reactionary forces from the piezoelectric actuator would not inject noise into the measurement.

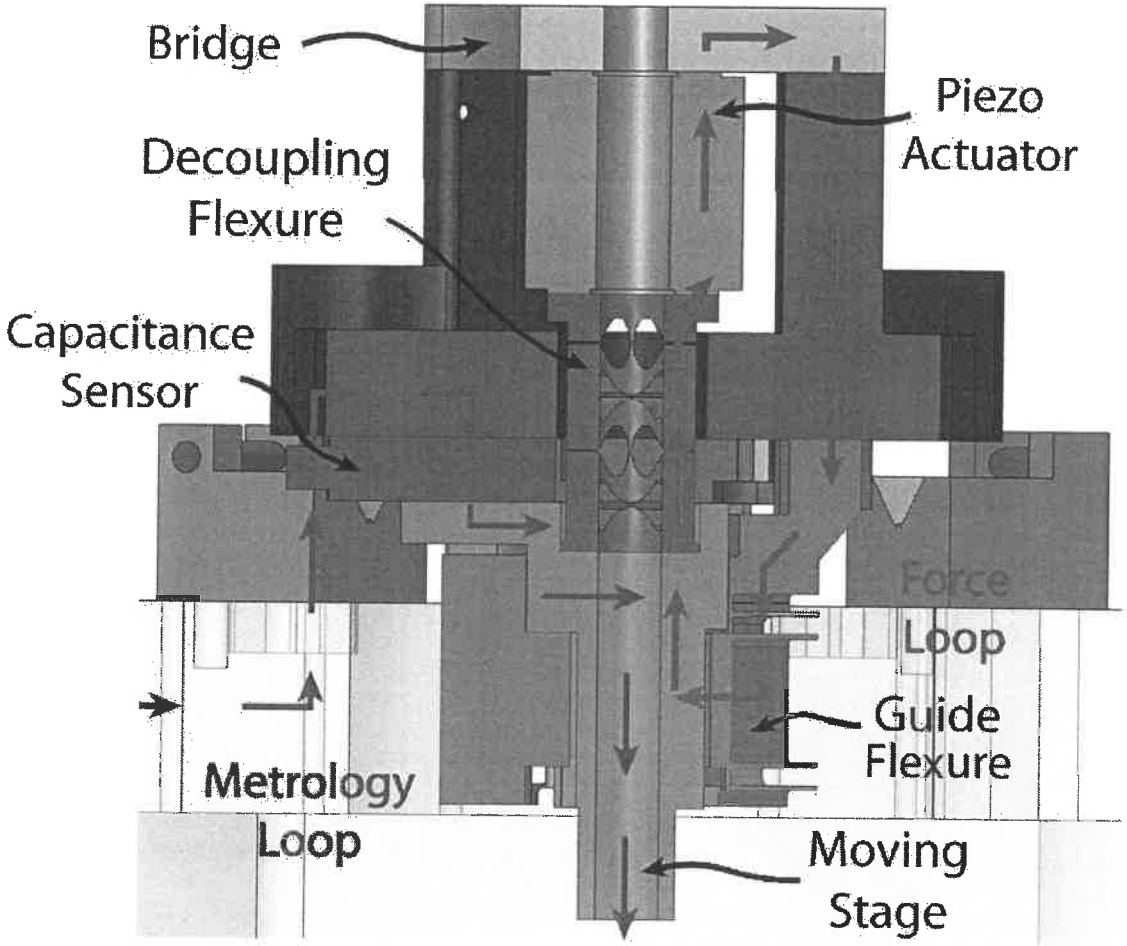

FIGURE 2. *Cross-sectional view of the AFM with overlayed force and metrology loops.*

MANUFUACTURING OF THE FLEXURE

The atomic force microscope utilizes a monolithic one degree of freedom flexure to guide the movement of the tip sensing stage. The long faces of the flexures seen in Figure 3 were cut in a pocketing operation with a high speed mill. In a final operation, the back of the flexure was cut loose with force free wire EDM cutting. The area removed by this operation is denoted in green in the Figure 3, which shows two generations of flexure development. All faces on the figure not highlighted in green were cut by high speed milling. The back end of the flexure was not cut free until the high speed milling was completed. This avoided excitement of the vibratory modes of the thin flexures. This order of operations safeguards the flexures against chatter which can lead to bad surface finish and tolerancing of the thickness which greatly affects the flexure's stiffness.

ELECTRICAL NOISE

The electrical system that measures the position of the moving stage required 0.1 nanometer resolution to achieve 1.0 nanometer accuracy. The capacitance sensors were selected to have 0.12 nanometer RMS noise at 1000 Hz bandwidth over a 50 micron range. This noise floor was further reduced by a factor of 1.73 by averaging the outputs of three capacitance sensors that were all measuring the same target. The three analog voltage outputs from the capacitance sensors were fed into a dSpace system through a 20 effective bit high resolution analog to digital converter. These high resolution converters were developed in the Precision Motion Control Laboratory. The standard dSpace 16 bit analog to digital converters output a 0.1nm resolution over a 50 micron range thereby requiring us to improve the A/D converters to reach our 1 nanometer accuracy goal.

THERMAL NOISE

To attain nanometer scale accuracy, the atomic force microscope must be protected against errors due to thermal expansion. The microscope will work in an environment that is temperature controlled to 0.01 degrees Celsius over which temperature range a length of steel one inch long will expand three nanometers. Thus, in order to reach the target accuracy low thermal expansion materials Zerodur and Invar had to be used along the entirety of the metrology loop which included the Invar base and moving mass. Concurrently, we used stainless steel for the flexure material due to its long life and good machining properties. Because both guide and decoupling flexures are not in the metrology path, their thermal expansion is simply measured and accounted for in the capacitance measurement, as seen in Figure 2.

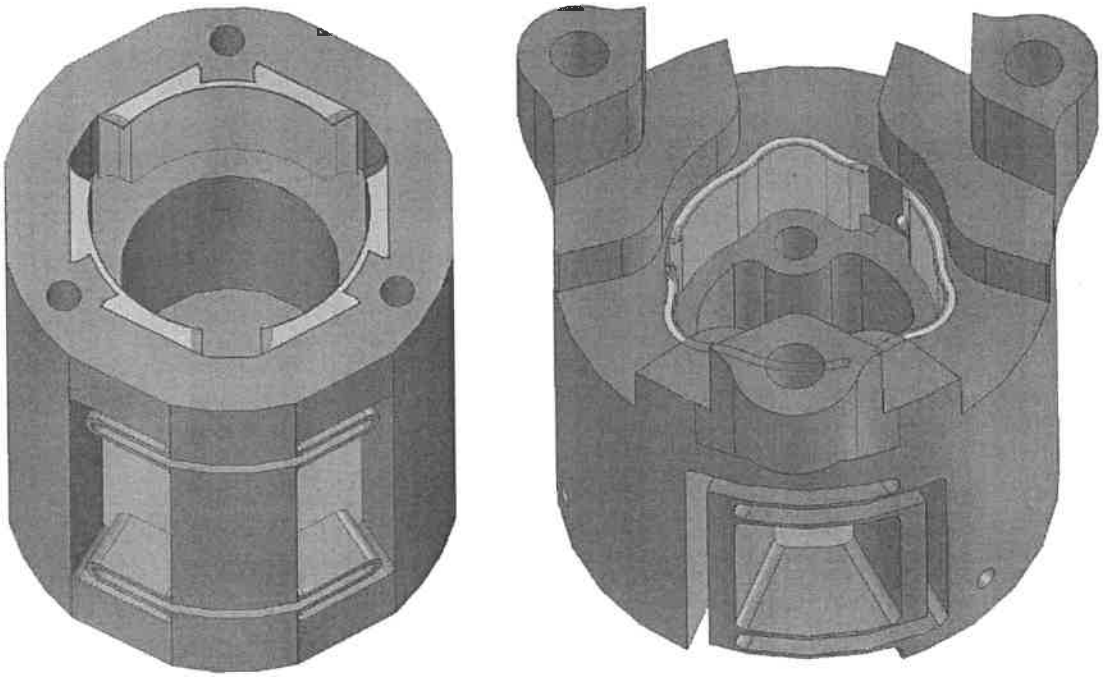

FIGURE 3. *CAD representation of two generations of guide flexures highlighting in green areas removed by the wire EDM process.*

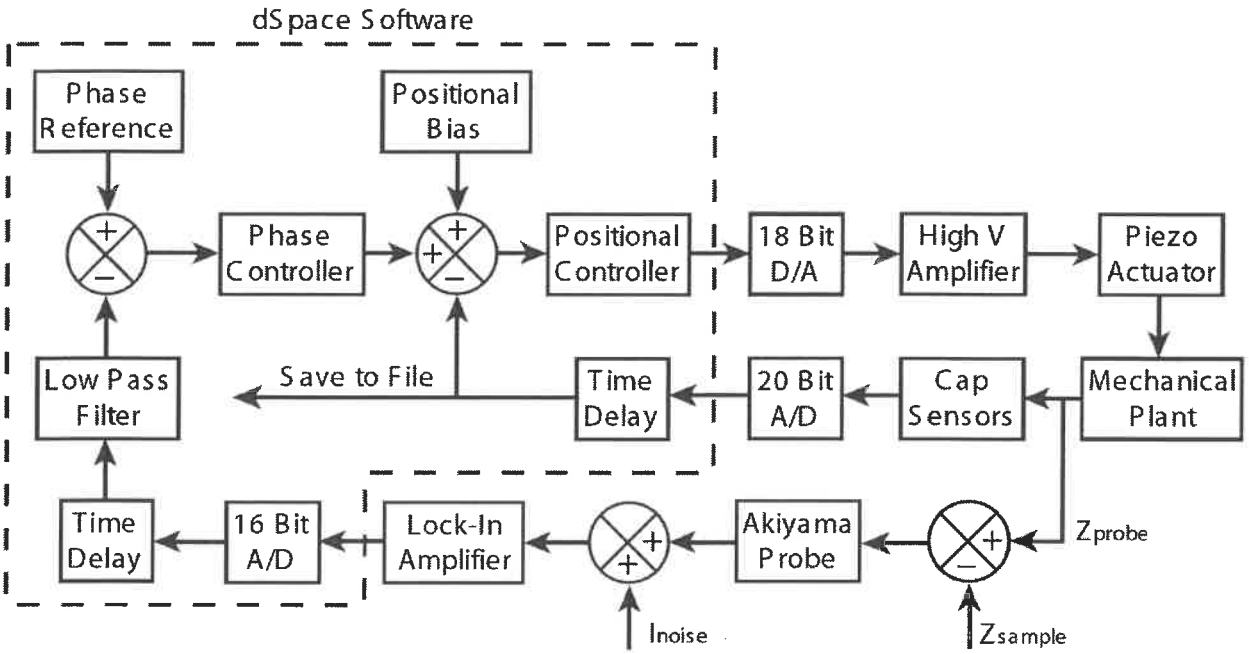

FIGURE 4. *Block diagram of the tracking system. The positional control feedback system has been integrated into the system as a minor loop.*

POSITION CONTROL

We first demonstrated position control of the moving mass whose position was measured by the capacitance sensors and actuated by the piezoelectric actuator. This position feedback control loop demonstrated 0.25 nanometer RMS noise at an open loop crossover frequency of 200 Hz. As seen in Figure 4, the position control was a minor loop in the overall control scheme of the atomic force microscope. Closing the minor loop at a significantly higher bandwidth than the major loop hides the phase loss and hysteresis associated with the actuator and capacitance sensors.

To track the surface of a target we measured the phase between the sinusoidal drive voltage across the Akiyama probe versus the current running through the probe. At a fixed frequency of oscillation a few Hz below the natural frequency of the probe, the phase between these two signals decreases as the probe engages the surface. Thus, by keeping a constant phase the instrument keeps a constant probe to sample gap. Unfortunately, the overall noise of the surface tracking system did not meet our 1.0 nanometer target. While the Akiyama probe engaged a stationary target, we measured 8.3 nanometer RMS noise with a 27 Hz crossover frequency.

CONCLUSION

The high accuracy atomic force microscope demonstrated its ability to control the position of a moving stage to 0.25 nm RMS noise. Although we can not directly measure the lateral position of the stage, our calculations show that the microscope is capable of achieving 1 nanometer accuracy positioning amidst all mechanical, thermal, and electrical noise sources. Further research is required to demonstrate 1 nanometer surface tracking with the Akiyama probe. The variation between the Akiyama probes as well as their hysteretic behavior will have to be addressed in the future in order to ultimately reach this goal.

REFERENCES

[1] N. F. de Rooij, T. Akiyama, K. Suter. Novel dynamic scanning microscope probe and its application to local electrical measurement in an ion sensitive field effect transistor. *Mater. Res. Soc. Symp. Proc.*, 838, 2005.

[2] Michael L. Holmes and David L. Trumper. Design and three dimensional calibration of a meaching scanning tunneling microscope for metrological applications. *Precision Engineering,* 18:38-49, 1996.

ERROR MOTIONS OF A NON-ORTHOGONAL ROTARY AXIS

Michael L. McGlauflin[1], Shawn P. Moylan[1]
[1]Machine Tool Metrology Group
Manufacturing Metrology Division
Manufacturing Engineering Laboratory
National Institute of Standards and Technology
Gaithersburg, Maryland, USA

INTRODUCTION

Error motions of rotary axes are among many sources of imprecision in machining. International and U.S. national standards on machine tool performance contain parameters and procedures to quantify these error motions [1, 2].

The National Institute of Standards and Technology employs a 5-axis machining center that utilizes a "B-axis" which is oriented in the YZ plane at a -45° angle to the Y-axis. This unusual configuration creates a challenge when attempting to measure axis of rotation error motions. A non-orthogonal orientation introduces considerations regarding location, alignment, and coverage area of the measurement artifact as they relate to standoff distances, indicator range, and fixture interference. Subsequent consideration must also be given to the proper analysis of the resultant data to correctly orient the error-motions to the machine coordinate system.

This paper describes a method for determining rotating sensitive direction [1] error-motions of a rotary axis whose axis of rotation is -45° to the X/Y plane. The method is based on a spindle-mounted touch-trigger probe and simple table-mounted spherical artifact. The method was compared to more traditional non-contact measurements (capacitance sensors) to validate the results. The paper also describes the analysis procedures and an evaluation of the measurement uncertainty [3].

DESCRIPTION OF THE TEST MACHINE AND SIGN CONVENTIONS

The machine tool used in this research is a vertical five-axis high-speed machining center with an integrated strain-gage type, touch-trigger probe.

The machine is comprised of stacked slides (Z on Y on X) that move the tool and separately stacked rotary axes (C on B) that move the work-piece (Figure 1). For purposes of clarity, the manufacturer's nomenclature will be used regarding the B-axis although its axis of rotation is not parallel to the Y-axis. Position feedback is provided by linear and rotary glass scales.

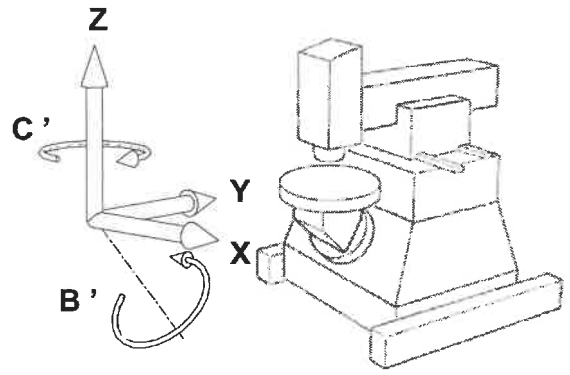

FIGURE 1. Machine-tool structure and sign convention.

MEASUREMENT AND ANALYSIS PROCEDURES

A 25.4 mm, grade 5 gage sphere (0.13 µm sphericity) was mounted on the rotary table in two different measurement locations (Locations I and II) and probed every 5 degrees of the B-axis rotation from 0° to 180° (the maximum travel of the axis) for a total of 37 data sets per run. Location I was aligned to the C-axis of rotation 100 mm below the Point of Rotation (POR), so named because its position in the machining volume does not change as the B-axis rotates. Location II was also aligned to the C-axis 50 mm above the POR. Thirty test runs were performed at each location. Figure 2 illustrates how the sphere center locations vary as the B-axis rotates. With a feedrate of 300 mm/min for probing and a B-axis positioning feedrate of 1575 °/min (10 % of rapid rate), the total time per test was five hours.

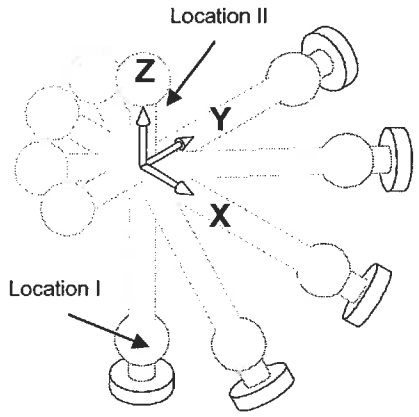

FIGURE 2. Artifact orientation as B-axis rotates

The position of the center of the spherical artifact at each B-axis position was determined by probing nine points on the surface using vector-normal probing and least squares fitting. The locations obtained by probing, and thus the center location estimated by the sphere fitting algorithm, are in the machine coordinate frame. To align them in a plane perpendicular to the B-axis, the center positions are multiplied by a coordinate transformation matrix, a simple -45° rotation around the machine's X-axis.

Following procedures outlined in the standards, a least-squares circle is fit to the 37 sphere center positions [1, 2]. The distances from the sphere center locations to the best-fit circle represent the radial error-motion of the B-axis. The probing and analysis procedure is repeated for thirty data sets, allowing synchronous and asynchronous error motion to be determined. Figures 3 and 4 show the radial error motion. Figure 5 shows the synchronous radial error-motion at sphere locations I and II.

The synchronous tilt error motion is the difference in the synchronous error motion components divided by the distance between them (150 mm * cos 45°) at each B-axis position (Figure 6). The asynchronous tilt error motion value at Locations I and II was 17.9 µrad. It is important to note that the asynchronous value stated here was calculated from data gathered sequentially. While the data was collected at the same nominal positions of the B-axis, the actual positions vary.

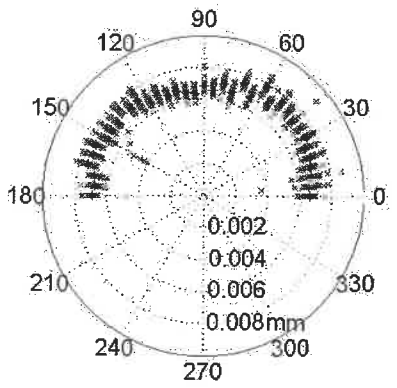

FIGURE 3. Radial error motion at Location I Asynchronous error motion (4.2 µm)

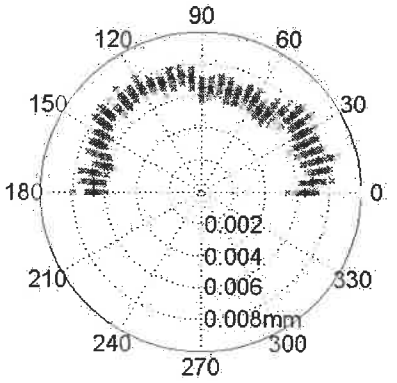

FIGURE 4. Radial error motion at Location II Asynchronous error motion (2.3 µm)

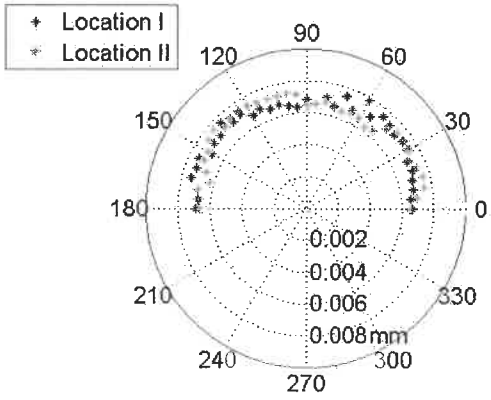

FIGURE 5. Synchronous radial error motions; Location I (1.4 µm) Location II (1.4 µm).

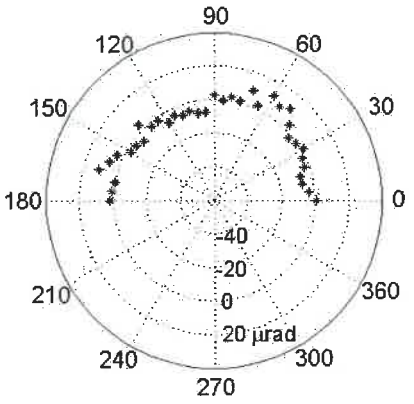

FIGURE 6. Synchronous tilt error motion value (17.9 µrad)

Face error motion at Location I was calculated using the Z component of the sphere center points after the coordinate transformation. Figure 7 shows the synchronous face error motion. Asynchronous face error motion was 6.7 µm.

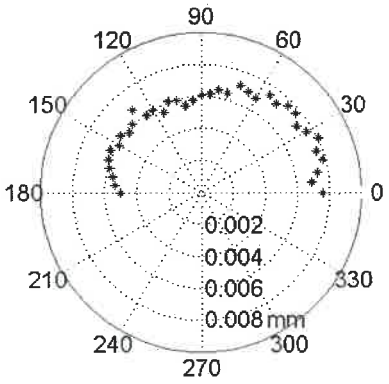

FIGURE 7. Synchronous face error motion at Location I (3.1 µm)

VERIFICATION TESTS AND RESULTS

Verification tests were executed by conducting probing and capacitance sensor tests on the C-axis of the machining center. The C-axis is oriented parallel to the machine's Z-axis, making axis of rotation testing more straightforward and therefore more suitable for verification. Probing data was taken every 10° as the axis rotated through 360° for a total of 37 data points.

Capacitance sensor data were gathered as the axis continuously rotated through 360° at a speed of 1575 °/min. To maintain the rotating sensitive direction orientation, the spherical artifact was fixtured in the machine spindle, which remained stationary, and a capacitance sensor was attached to the work table in a radial direction and rotated with the C-axis. The sensor was oriented in the negative X direction (when C = 0).

Analysis of both probing and capacitance sensor data was similar to the analysis of the B-axis data. However, because the C-axis is an orthogonal axis, the coordinate transformation is not necessary. A least squares circle fit was applied to the raw capacitance sensor data, and the deviation from the best fit circle was calculated.

Figure 8 shows a comparison of the measurement results for synchronous radial error motion determined by the two methods.

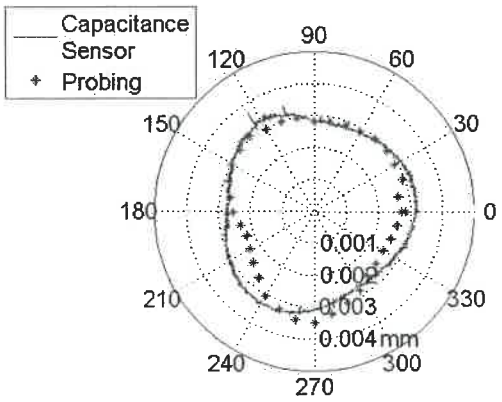

FIGURE 8. Synchronous radial error-motion of the C-axis; capacitance sensor vs. probing. Synchronous error value probing (1.2 µm); capacitance sensor (1.1 µm); asynchronous error value probing (1.6 µm); capacitance sensor (1.0 µm).

UNCERTAINTY ANALYSIS

The main contributors to the uncertainty of measurements by probing are probing repeatability, positioning accuracy of the linear axes, and thermal growth.

The machine has a well documented thermal behavior due to machine startup sources such as electrical and mechanical systems and lubrication. To minimize this influence, a simple procedure was followed at the beginning of each day's data collection. The machine was initialized, homed, left to stabilize for a minimum of 2 hours, and then run through a short 5-axis

lubrication program to ensure the axes were properly lubricated.

Because the linear axes are moving during probing and stationary during capacitance sensor tests, the influence of motion-induced thermal growth and the large amount of time required to collect probing data as compared to that required for capacitance data are the largest sources of uncertainty in the comparison. The value for this uncertainty came from previously compiled data of the entire work volume. Since the probing occurred in a small portion of the volume, we estimated the drift corresponding to that portion as X = 1 µm, Y = 13 µm, and Z = 3 µm.

For the purposes of this discussion, probing repeatability for 3 dimensional probing systems is the ability of the machine/probe system to locate the center of a stationary spherical artifact by touching the surface of the sphere at multiple locations. We determined this error by repeatedly probing a spherical artifact at nine uniformly distributed points. Thirty measurement cycles were performed with no rotation of the rotary axes and no interruption between cycles. A least squares spherical fit was applied to each data set and the standard deviation of the 30 center X, Y, and Z positions calculated. Probe lobing was included in this determination.

The location of the target sphere changes as the B-axis rotates. Therefore the geometric errors of the machine can result in uncertainty in probing data due to the volumetric accuracy of the machine. However, as explained previously, the probing head moves through a small portion of the work volume so this contribution to the combined standard uncertainty is small (0.3 µm).

Thermal growth of the artifact was not significant due to the minimal contribution from the sphere and the invar material for the support column for the sphere.

The combined standard uncertainty estimation is given in Table 1.

TABLE 1. Estimated uncertainty for the probing method.

Source	Std.Uncertainty (µm)
Thermal Growth	13.4
Probing Repeatability	0.5
Volumetric Accuracy	0.3
Combined Std. Uncertainty	13.4
Expanded Uncertainty (k=2)	26.8

CONCLUSIONS

Probing appears to be a viable option for characterizing axis of rotation error motions of non-orthogonal rotary axes. The comparison data in Figure 8 show a good correlation in form and magnitude. The uncertainty related to thermal growth overshadows the surprisingly small uncertainties related to probing error and volumetric accuracy.

The test is easy to set up and align, and doesn't require expensive equipment. The extreme difficulty in aligning an artifact to a non-orthogonal axis of rotation makes traditional methods of eliminating artifact alignment error prohibitively complicated and time consuming.

A thorough understanding of the sources of uncertainty could allow probing to provide a cost- and time-effective alternative to traditional axis of rotation measurements of complicated machine designs. The uncertainty related to thermal growth could be reduced by a modified warm-up procedure. Previous thermal expansion tests [4] indicate a three hour 5-axis motion period prior to testing could potentially reduce this uncertainty to less than 8 µm.

REFERENCES

[1] ISO 230-7, Geometric Accuracy of axes of rotation.

[2] ANSI/ASME B89.3.4M, Axes of Rotation Methods for Specifying and Testing, 1985.

[3] NIST TN1297, Guidelines for Evaluating and Expressing the Uncertainty of NIST Measurement Results, 1994.

[4] ISO 230-3, Test code for machine tools—Part 3: Determination of thermal effects, 2001.

This Publication was prepared by a United States Government employee as part of official duties and is, therefore, a work of the U.S. Government and not subject to copyright.

COMPARISON OF NIST SI FORCE SCALE TO NPL SI MASS SCALE

Christopher W. Jones[1], John A. Kramar[2], Stuart Davidson[1], Richard K. Leach[1], and Jon R. Pratt[2]
[1]National Physical Laboratory, Teddington TW11 0LW, UK
[2]National Institute of Standards and Technology, Gaithersburg, MD 20899, USA

INTRODUCTION

Recent advances in device manufacture and object manipulation at the micro- and nanometre level have intensified the need for quantitative understanding of forces acting at this scale. Impacted industries include automotives, pharmaceuticals and communications. To meet this need, several major national metrology institutes (NMIs) have developed specialist balances to measure low forces traceable to the International System of Units (SI). These include efforts at the National Institute of Standards and Technology (NIST) [1], National Physical Laboratory (NPL) [2], Physikalisch-Technische Bundesanstalt (PTB) [3] and Korea Research Institute of Standards and Science (KRISS) [4]. Forces measured by the first three are ultimately traceable through electrical and length units, as opposed to the International Prototype Kilogram (IPK).

Well-characterised MEMS artefacts can be used to transfer force calibrations to users in industry [5]. The traditional choice for transferring a well-defined force, the weight of a known mass, is not suitable in the low force regime. Small masses are cheap but difficult to manipulate and easily contaminated in the typical industrial environment, invalidating associated calibration data. At the nanonewton level relative uncertainties typically approach and exceed unity.

Nevertheless, small masses are still very relevant for pharmaceutical dosing applications, where the infrastructure for the clean handling of small objects is already in place and uncertainty in mass measurement is not the limiting factor. Further, in the specialist facilities at the larger NMIs, small deadweights remain a suitable artifact for the validation of electrostatic force balances. Repeated weighings highlight systematic discrepancies, which, if explained in terms of base principles and verified independently of the weighings, lower the uncertainties on the traceability route through electrical units. These comparisons require an investment of time and equipment only practicable as a one-off.

This international comparison, funded by the UK National Measurement System Engineering Metrology Programme, is validated by the CIPM Mutual Recognition Agreement that allows quantitative comparability of work at different NMIs.

OVERVIEW

Small masses in the 1.0 mg to 0.1 mg range were developed and calibrated at NPL with traceability to the IPK. These masses were transported to NIST at Gaithersburg and used as deadweights on the NIST electrostatic force balance, to facilitate a mass-force scale comparison.

As a result of the experimentation a Type B uncertainty leading to a 10 nN under-read in weighing was highlighted. Subsequent work has fully identified and confirmed this systematic uncertainty and work is underway to eliminate it.

NPL MASS SCALE

Calibrated mass measurements at NPL are traceable to the IPK *via* kilogram 18. In order to minimise traceability uncertainties, small masses are calibrated by subdivision from the kilogram using an overconstrained matrix of equations. This standardised procedure permits estimates of the departure of the masses from nominal values and facilitates calculation of type A uncertainties. Comparisons are carried out on a suite of balances from several manufacturers. In this approach, only the repeatabilities of the balances are important; absolute values are not. Mass balances remain an acceptable tool for traceable milli- to micronewton force measurement, but care must be taken to understand the uncertainties behind the apparent ease of operation.

NIST FORCE SCALE

Traceability in the micro- to nanonewton range is realised at NIST using the Electrostatic Force Balance (EFB) in which studied forces are traceable via calibrated displacement, voltage and capacitance transducers. The balance consists of a nested cylindrical capacitor on a counter-balanced flexure system and interfer-

ometrically measured displacement is used to null the balance position to an appropriate set-point. The development of the EFB was particularly motivated by the need for traceable force measurement in MEMS devices and AFM, and has been successfully employed in this way [6].

In practice, the EFB performance is usually not limited by the uncertainties in the realisation of the electrical force, but rather by the ability to accurately compare this force to other mechanical forces using the balance mechanism. For example, for weighings at the level of tens of micronewtons, Type A uncertainty sources due to seismic and servo control noise have dominated the uncertainty budget. Similarly, for calibration of stiffness artefacts or force transducers, the uncertainty budget is dominated by contact mechanics, not by the EFB realization of force.

MASS ARTEFACTS, HANDLING

The NPL-developed small mass artefacts were formed manually from small-gauge aluminium wire and shaped to suit. Aluminium was chosen for increased mass size through low density and its non-magnetic properties. A number of small masses were prepared to allow optimised calibration with the NPL comparator balance and to allow for a range of experimentation. The masses ranged from 1.0 mg to 0.05 mg.

The repeated loading and unloading of the test mass on the EFB represents the greatest challenge to success. Considerable dexterity and patience is required for manual placement where the mass artefacts, as tiny springs, are easily ejected and lost. The EFB is equipped with a three-axis sample-stage micro-positioning system, the sample stage adapted to suit each experiment. The repeated exchange cycles, required to statistically reduce measurement uncertainties on the EFB, demand an extremely reliable exchange mechanism. A 'safely' dropped mass requires a full vacuum cycle to re-seat, which is costly in terms of time.

Two successful lifting mechanisms were developed for this work. Small wire masses were folded into a free-standing shape with a lifting point over the centre of gravity (Figure 1a, b). This latter specification prevents rotation on exchange that can cause the mass to 'walk off' the lift hook. Longer masses were straightened and exchanged between fixed and moving hook pairs (Figures 1c, 3). It is important to note that reshaping to suit a given set-up represents a significant risk to the test mass due to work hardening and subsequent failure.

For small objects at this scale surface interaction forces tend to dominate over gravitational weight and introduce considerable difficulties to otherwise straightforward mechanical operations. In air, humidity-dependent capillary forces adhere otherwise clean surfaces and suggest the need to reduce the interacting surface area. In vacuum these forces are removed, but electrostatic charge may perturb the measured force unless controlled through adequate grounding.

Under correct EFB displacement servo operation, the force output difference measures the applied weight. Figure 3 shows typical mass exchange force curves. Slight asymmetries in the hand-shaped masses result in two-stage exchanges. In the mass touch-down exchange in air, capillary hook-mass adhesion causes the still-lowering hook to pull the landed mass downwards such that the EFB registers a significant additional force. When the adhesion fails, the sudden force imbalance causes the platen to ring back to zero displacement. The size of the resultant error is not negligible due to otherwise insignificant effects such as flexure hysteresis. On air liftoff, and in vacuum, this adhesion is not observed.

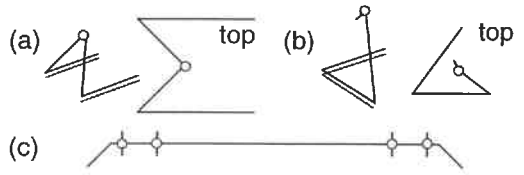

FIGURE 1. Masses reshaped for exchange (lifting points labeled red, mass touch-down points green). (a, b) are single hook systems, (a) the most stable; (c) is a two-hook system. Note end turndowns on (c) to prevent mass walk-off.

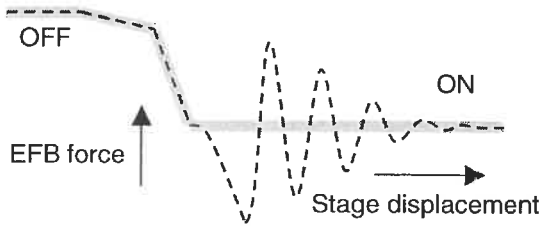

FIGURE 2. Mass exchange force curves. Black dashed is air touchdown curve, with adhesion and ringing on hook release; yellow solid is air liftoff and both transitions in vacuum.

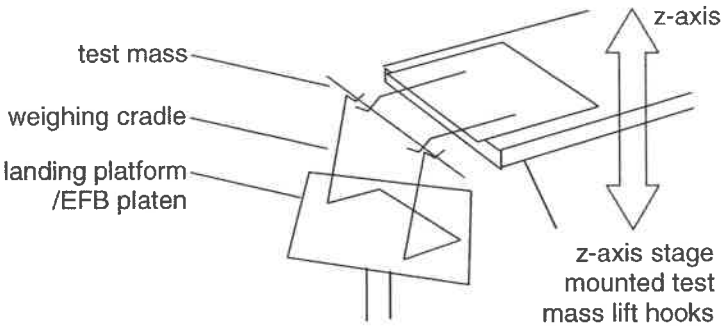

FIGURE 3. Mass exchange system. A Au/Pd coated thin glass square of side approximately 7 mm forms the landing platform. This accepts the mass directly, for single-hook experiments, or supports a weighing cradle as shown for two-hook experiments. The mass lift hook plate is floated on vacuum grease to attenuate stage mechanical noise; the lifter system is also Au/Pd coated to conduct away electrostatic charge in the exchanger.

For larger small masses (0.5 mg to 1.0 mg), denser metals were later found to be acceptable due to resultant smaller wire diameters and in turn smaller hook-mass interaction areas. This was verified qualitatively using 2.0 mg and 1.5 mg PtW alloy test masses. A smaller interaction area reduces capillary forces acting at the interface.

The vacuum-compatible precision stages used for the mass exchange were found to be a significant heat source when in closed-loop mode. Three energised axes produced a peak temperature as much as 20 ºC above ambient in sections of the metrology loop; for a single axis energised, the peak was 10 ºC above ambient. To overcome this rise, open-loop operation was used, with intelligent force-curve monitoring to detect lift-off and reset the encoder scales on each cycle. This was an acceptable approach because the exact position of the stage motion endpoints was not critical for the application, and errors scaled well with distance traversed.

RESULTS

Mass calibration

The full small mass artifact set was calibrated at NPL prior to experimentation at NIST. Values for the artifact subset used to obtain the reported results, specifically 1.0 mg, 0.8 mg and 0.1 mg, are given in Table 1. As per standard comparison procedures the masses were re-calibrated on their return to NPL; this data is also reported. The calculated changes in mass across the calibration transfer for the 0.1 mg, 0.8 mg masses are within the $k = 2$ uncertainty for each calibration, suggesting the same for the 1.0 mg mass, which was lost before recalibration could take place. Thus the reshaping required between use at NPL and NIST appears to have had an insignificant effect on the total mass. Air calibrated values were buoyancy corrected using the known mass volumes and an estimate for air density at the NPL site.

Force calibration

After initial trial weighings with locally produced PtW alloy test masses, formal weighings of the mass subset were carried out in vacuum and air on the EFB using repeated mass exchange cycles. The vertical stage motion required to effect the exchange was minimised to increase cycling speed and was typically around 100 µm to 500 µm. Statistical analysis of the results of typically around fifty load cycles gave a Type A uncertainty in the final weight estimate of about 1 nN. A previously determined local gravitational acceleration value was used to convert weight to mass to enable comparison. The results are presented in Figure 4. The 'force-scale' error bars show the measurement set repeatability but neglect further unknown, possibly significant, systematic errors. The discrepancy of the 0.8 mg vacuum value against the other force-scale data is likely due to non-optimum conditions such as a thermal or mechanical non-equilibrium state.

Systematic error: sample stage magnetic crosstalk

In Figure 4, a systematic discrepancy in the measured weights of the calibrated masses inconsistent with the measurement uncertainties was highlighted.

TABLE 1. NPL calibrated masses, with values from before and after NIST experiments. k=2 uncertainties are 0.3 µg on each calibration and 0.4 µg on the combined average.

	NPL Calibration (µg)		
Nominal mass (µg)	Initial (June 07)	Repeat (May 08)	Change
1000	1002.3	*lost*	*n/a*
800	801.6	801.4	-0.2
100	105.8	105.9	0.1

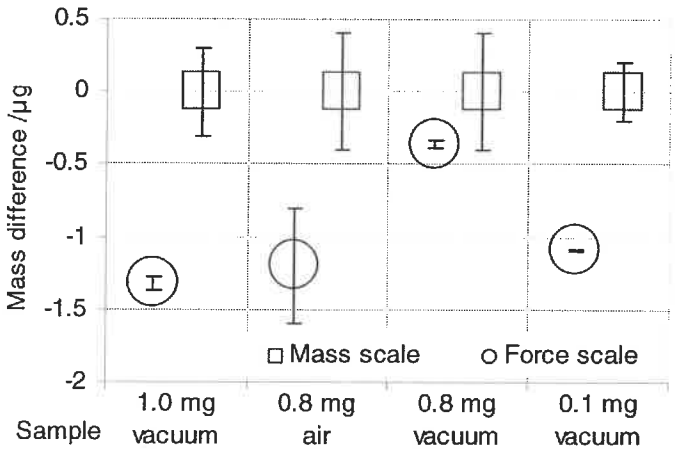

FIGURE 4. Key results of comparison between NPL mass and NIST force scales. Values are offset by the NPL mass calibration for each sample to give a 'mass difference'. An under-read in mass calculated from the NIST weighing was observed in each case. The values compare via a local gravitational acceleration, previously determined for the NIST laboratory, and a buoyancy factor determined from standard environmental factor values based on NPL laboratory specifications. The gravitational acceleration and buoyancy adjustments have uncertainties at the 5×10^{-6} and 1×10^{-6} level respectively.

Further experimentation identified the observed under-read as a product of an interaction between the EFB and the sample stage. Empty weighings, where the empty lifting stage was moved repeatedly between 'on' and 'off' park positions, recreated a fictitious negative weight with a dependence on the stroke (Table 2). The magnitude of the fictitious negative weight for the strokes used for the actual weighings is consistent with the weighing force discrepancies. It is suspected that the weak magnetism in the vertical stage used for mass exchange exerts a small force on the EFB's flexures, which are made from a ferromagnetic material.

A discrepancy of this magnitude had appeared in previous EFB-mass comparisons with larger masses [7]. In that case, the difference was 13 nN relative to a 20 mg test mass and was within the $k = 2$ uncertainty bounds. Note that this error is not a systematic in the force measurement itself, but is only due to the mass exchange stage motion. Therefore, it would not have influenced cantilever stiffness measurements or piezoresistive force transducer measurements previously made.

TABLE 2. "Empty weighing" forces.

On-off position stage stroke (10^3 actuator steps)	Apparent force (nN)
20	-5.0
40	-7.3
50	-11.9
100	-16.3

CONCLUSIONS

In this work the newly emerged independent force traceability route has been verified against the mature traceable mass scale at a level not previously attempted. The use of sub-milligram test masses on the NIST EFB has successfully led to the identification of a systematic error of nanonewton size that may now be removed or corrected for. This work exemplifies the benefits of international cooperation between NMIs to bring added value to their individual stakeholders.

REFERENCES

[1] Pratt J R, Kramar J A, Newell D B, Smith D T, 2005 *Meas. Sci. Technol.* **16** 2129-2137.

[2] Leach R K, Oldfield S, Georgakopoulos D 2006 *Proc. 6th euspen Int. Conf., Baden, Austria, 28th May – 1st June* 414–417

[3] Nesterov, V., 2007 *Meas. Sci. Technol.* **18** 360-366.

[4] Kim, M-S., Choi, J-H., Park, Y-K, Kim, J-H, 2006 *Metrologia* **43** 389-395

[5] Jones C W and Leach R K 2008 *NPL Report ENG 5*, March 2008

[6] Gates, RS and Pratt JR, 2006 Meas. Sci. Technol. 17 2852-2860

[7] Pratt J R and Kramar J A 2006 *XVIII IMEKO World Congress, Rio de Janeiro, Brazil*

INVESTIGATING SCALING LIMITS OF A FIBER BASED RESONANT PROBE FOR METROLOGY APPLICATIONS

Richard M. Seugling[1], Ian M. Darnell [1], Jeffery N. Florando[1], Shane C. Woody[2], Marcin Bauza[2] and Stuart T. Smith[3]
[1]Lawrence Livermore National Laboratory
Livermore, CA
[2]InsituTec Inc.
Charlotte, NC
[3]University of North Carolina at Charlotte
Charlotte, NC

INTRODUCTION

Currently, Inertial Confinement Fusion (ICF) and High Energy Density Science (HEDS) targets comprise components with dimensions in the millimeter range, while having micrometer-scale, high aspect ratio functional features, including fill-tube holes and counterbores, slotted patterns, and step-joint geometry on hemispherical targets. Representative geometry is shown in Figure 1. Future target designs will likely have additional challenging features. The dimensional metrology of these features is important for a number of reasons, including quantifying geometrical tolerances of as-built components prior to delivery, qualification of sub-components prior to assembly, and as a feedback mechanism for fabrication process development. Variations in geometry from part to part can lead to functional limitations, such as limited flow rates during target filling, unpredictable instabilities during an experiment, and the inability to assemble a target from poorly matched sub-components. Adding to the complexity are the large number and variety of materials, components, and shapes that render any single metrology technique difficult to use with low uncertainty.

Adapting standing wave probe technology [i] for micrometer sized features requires the understanding of the physical interaction between the oscillating, slender rod (probe) and the sample as a means of transferring information about the surface, such as topography and material properties, analogous to tapping mode atomic force microscopy (AFM) and/or instrumented indentation machines. By utilizing the variation in dynamic response of the probe as the tip interacts with a surface, information about the sample may be obtained and used for mapping surface topography, and potentially characterizing material properties. The novel long aspect ratio geometry of the probe enables the characterization of features such as small holes, slots, and corners, which typically cannot be accessed using AFM and instrumented indentation technology.

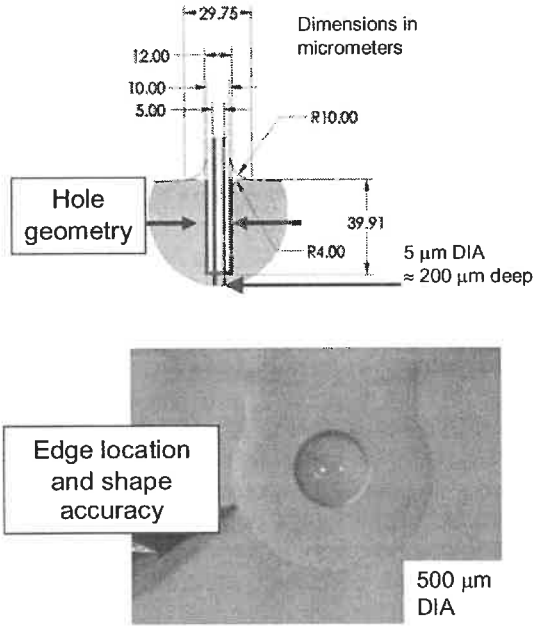

FIGURE 1. a) Fill tube assembly for NIC target designs. High aspect ratio, micrometer sized holes required for assembly. b) HEDS capsule assembly of silica bead molded in aerogel (50 mg/cc SiO_2). Target geometry requires micrometer concentricity and low density materials are difficult to profile without fracture.

Uncertainty of the surface location is a combination of near surface effects such as van der Waals and electrostatic forces combined with contact force such adhesion and meniscus contributions. In addition, environmental effects, such as thermal gradients and air turbulence, will influence probe performance and

repeatability. A combination of complex nonlinear models of the tuning fork driver/sensor mechanics, fiber dynamics, circuit response and contact interactions have been developed for the current scale system in an effort to predict scaling limitations of this technology for characterizing micrometer sized features with nanometer sensitivity.

THEORY

To address the potential application of this technology for use on micrometer-scale, high aspect ratio features, a detailed understanding of the probe dynamics coupled with the nonlinear contact interactions is required. A set of complex numerical models have been derived to incorporate the drive/sensor piezoelectric effect, [ii,iii] dynamics of the probe fiber and surface interactions between the probe tip and surface. Modeling of the complete system has been a combination of finite element analysis and numerical integration to account for the complex nonlinear surface contact effects. This system has been broken down into four subsystems including the piezoelectric tuning fork driver/sensor, electronic sensing/drive circuits, beam dynamics and surface force interactions. Nonlinearities of the system are primarily dictated by the surface interaction of the probe tip as it comes into contact with the workpiece. Integrated within the model boundary conditions at the probe are elastic and inelastic impact [iv,v], meniscus, air damping, electrostatic, and Van der Waals and adhesion forces [vi,vii].

Because of the complexity of the dynamic interaction between the oscillating fiber (probe) and the surface, the system was modeled numerically in FORTRAN using Euler –Bernoulli beams for the fiber, piezoelectric beams for the tuning fork tines. Included in the numerical model are the drive electronics and the nonlinear boundary conditions. A schematic illustration of the model is shown in Figure 2. In addition, COMSOL multiphysics finite element analysis (FEA) package was used to verify modes and sensitivity of the tuning fork.

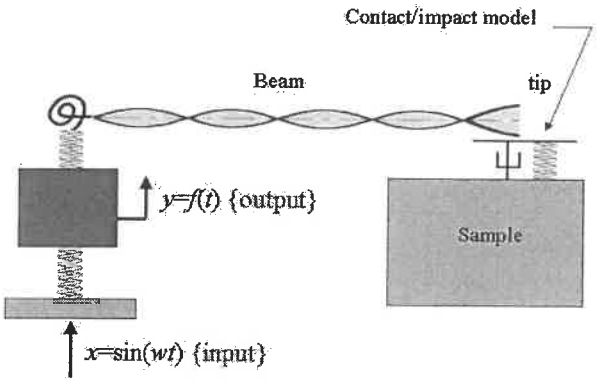

FIGURE 2. Schematic illustration of the numerical model derived representing the probe system dynamics and contact with a surface.

To verify that the model represents our system, the first task was to compare the frequency response of the model in the free-state (i.e. noncontact) with the experimental data, results of which are shown in Figure 3. In this case, material properties, geometry and electronics parameters are quantitatively measured and included in the calculation. However, damping of both the material and viscous effects of operating in air are "tuned" to properly represent probe dynamics in an air environment.

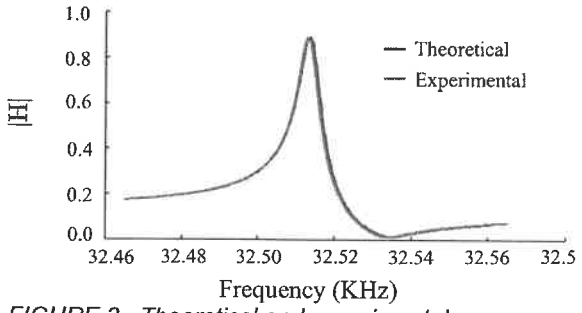

FIGURE 3. Theoretical and experimental frequency response of the probe system.

To validate the sensitivity of the tuning fork to applied voltage a nanoindentor was used to simultaneously measure load and displacement, see Figure 4. The results were compared to the COMSOL FEA model with an agreement of better than 10% and a strain sensitivity of 0.3 $nm \cdot V^{-1}$.

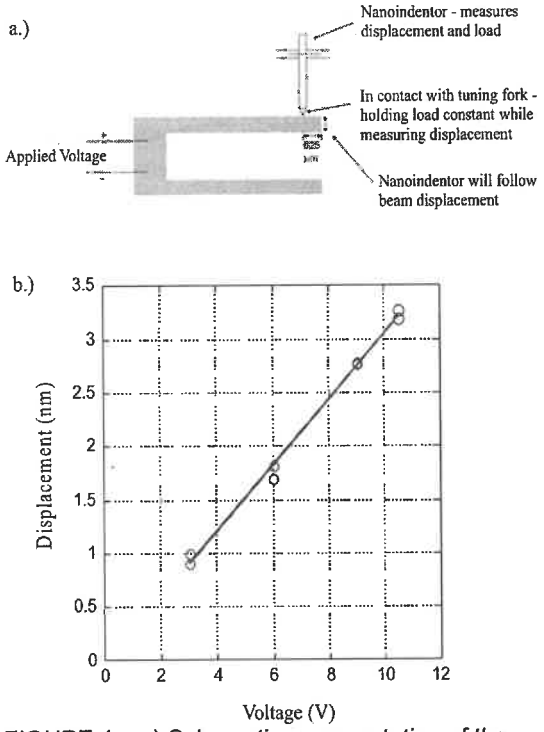

FIGURE 4. a.) Schematic representation of the nanoindentor test set-up. b.) Displacement as a function of applied voltage.

With the static and dynamic data well represented by the numerical model, the nonlinear boundary conditions of the probe tip contacting a surface were added. These include surface force effects, as mentioned earlier and an elastic and/or inelastic contact model. In general, the surface forces are dominated by meniscus effects at this probe scale. Figure 5b shows the complete model output as the probe tip comes into contact with a surface. Figure 5a are snap-shots in time of the mode shape of the beam and tuning fork as the surface is brought into contact. It is clear that energy imparted to the probe during initial contact excites lower order modes, however the amplitude only reaches ~40 μm with a ± 10 μm initial oscillation amplitude This effect can be observed experimentally and has proven to damp out due partially to air drag damping. The low mode oscillations tend to decrease in amplitude as the surface is continually stepped into contact as can be seen in the step #3 (0.72 μm) mode shape. Figure 5b is the RMS signal amplitude variation as the probe is stepped into contact with a surface as predicted by the model.

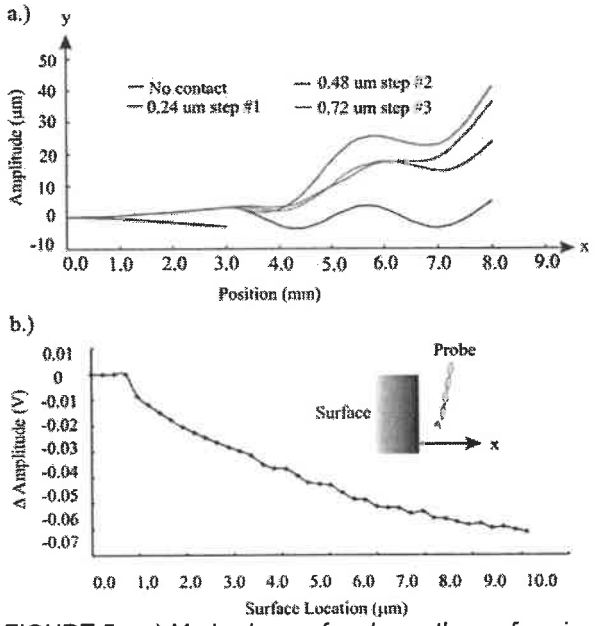

FIGURE 5. a.) Mode shape of probe as the surface is brought into contact with the probe tip. b.) Model predicted amplitude variation as the surface is brought into contact with the surface.

In general, the combination of the numerical model and the COMSOL FEA model predict the response of the system to better than 10% for the "free" and static cases. Introducing the nonlinear boundary conditions add uncertainty to model in that quantification of the relative surface force and material contributions is a bounded estimate. Surface forces were quantified experimentally using an atomic force microscope (AFM) by attaching a probe fiber tip to an AFM cantilever and measuring the forces of materials of interest, such as steel gage block and a gold foil. It has been found both analytically and experimentally that for a nominally 5.0 mm long fiber an adhesion force of ~ 100 μN will stick the fiber to the surface. Both the theoretical and measured surface forces for this scale system are ~ 10 μN, an order of magnitude smaller than the restoring force in the prestrained fiber allowing the probe tip to disengage from the surface.

Scaling the standing wave probe an order of magnitude, as illustrated in Figure 6 and using a similar analysis, the restoring force in the prestrained fiber is ~ 2 μN, while the adhesion force can be as much as 0.5 μN. In this case the nonlinear adhesion force is substantially more comparable to the restoring force at this scale. However, by either increasing the drive frequency and subsequently the strain energy in

the fiber, and/or shortening the fiber length, more restoring force can be derived mediating the additional influence of the surface forces. An approximately 0.1 scale probe system has been designed and is currently being fabricated. The system will incorporate a ~400 kHz tuning fork driver/sensor and a Si etched fiber for the probe operating in nominally the 4th resonant mode.

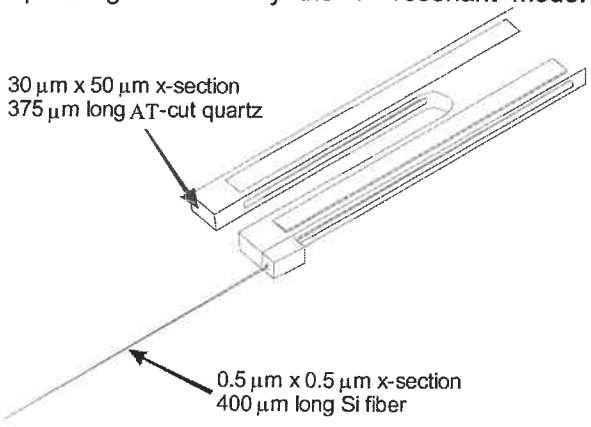

FIGURE 6. Scaled probe system design incorporating a ~0.1 scale AT- cut quartz tuning fork driver/sensor and a 0.5 μm × 0.5 μm x-section 400 μm long fiber.

CONCLUSIONS

A combination of numerical modeling, finite element analysis and experimental results developed for standing wave probes at the tens of micrometer scale has been derived and used to design a scaled version of the probe system. By increasing the frequency and/or mode of the oscillating fiber, adhesion forces at the probe/surface interface can be overcome even though they are more dominant at the smaller scale. A prototype scaled probe is currently being fabricated using microfabrication techniques commonly used for MEMS devices.

ACKKNWOLEDGEMENTS

This work performed under the auspices of the U.S. Department of Energy by Lawrence Livermore National Laboratory under Contract DE-AC52-07NA27344. The authors would like to also thank Dr. Wendelin Wright from Santa Clara University for the use of her nanoindenter.

REFERENCES

[i] Bauza M.B., Hocken R.J., Smith S.T., Woody S.C., "Development of a virtual probe tip with an application to high aspect ratio microscale features," *Rev. Sci. Instrum.* 76, 095112 (2005).

[ii] Lee, S, Moon, Y, Yoon, J and Chung, H, "Analytical and finite element method design of quartz tuning fork resonators and experimental test of samples manufactured using photolithography 1- significant design parameters affecting static capacitance C_0" *Vacuum*, 75, (2004).

[iii] Wang, J and Momosaki, E, "The Piezoelectrically Forced Vibrations of AT-Cut Quartz Strip Resonators" *1996 IEEE International Frequency Control Symposium*, (1996).

[iv] Stronge, W J, "Impact Mechanics" *Cambridge University Press*, (2004).

[v] Maugis D., "Contact, Adhesion and Rupture of Elastic Solids", *Springer*, (2000).

[vi] Adamson A.W. and Gast, A.P., "Physical Chemistry of Surfaces, 6th Ed.", *Wiley-Interscience*, (1997).

[vii] Israelachvili J.N., "Intermolecular and Surface Forces, 2nd Ed." *Academic Press*, (1992).

A COMPARISON OF OPTICAL SENSING METHODS FOR THE HIGH PRECISION 3D SURFACE PROFILE MEASUREMENT OF GROOVED SURFACES

J. W. McBride, Z. Zhao, P. J. Boltryk
School of Engineering Science
University of Southampton
Southampton, UK

ABSTRACT

A non-contact method has been shown to be the preferred solution for the scanning of valuable early sound recordings, such as wax cylinders and flat discs for the purpose of cultural preservation [1]. This paper describes the operating principles and compares the performances of four different sensing techniques, including scanning white light interferometer (SWLI), con-focal laser (CL), con-focal white light sensor (WL), and atomic force microscope (AFM), in a range of measurement tasks. The con-focal systems described in this paper are used in a 3 dimensional (3D) cylinder scanning system for the measurement of wax cylinder recordings, where the 3D data is used to create a map of the measured surface. The generation of the map allows the sound recorded on the surface to be decoded without physical contact to the surface. The main advantage of the con-focal system is the scanning speed. Reference samples with sinusoidal and rectangular profiles are used to investigate the effects of surface inclination angle and the interaction between the sensor head and the measured surface. The effects of precision mode, grid spacing and spot size on surface height measurements are investigated.

INTRODUCTION

The 3D measurement of complex surface profiles is a rapidly developing technique with a wide range of applications. Of the instruments used to obtain 3D surface profiles, the non-contact optical methods are desirable in circumstances where high speed measurement are required and where there is a requirement to avoid potential surface damage. The work presented here is part of the Sound Archive Project, where the focus is on sound extraction from early mechanical recordings, [1-5]. It has been shown that early recorded media can be damaged by repeated playing using the traditional stylus playback, [1]. The aim of the Sound Archive Project is therefore to investigate non-contact optical surface sensing technology to map the surfaces of the early sound recordings in 3D and to save the surface into a digital format for the purpose of cultural preservation. Sound extraction can be undertaken using a number of methods. [5]. For the surface measurement process it has been shown that an angular tolerance of approximately 30° and an axial resolution of 10nm are required to map a cylinder sound recording [2]. A con-focal chromatic aberration sensor (WL) was found to be the most appropriate for this application with the potential for high speed scanning and with a 27° angular tolerance and 10nm axial resolution, [2]. Previous studies have shown that different types of optical sensors are affected to varying degrees by surface reflectivity, surface inclination angle, spot size and axial resolution [6]. The aim in the current work is to determine the lower envelope for these sensing technologies. To achieve this, a set of reference samples have been used, to investigate the limits of the con-focal systems. A critical aspect of the sound archive project is that the recorded surfaces should be scanned to a precision sufficient for archival purposes. This requires the surfaces to be scanned at high speed to minimize scan times. With typical grid resolutions of 10µm x 5µm, over typical areas of 100mm x 150mm, corresponding to 150 million data points, the measurement time should be of the order of 24 hours; requiring sampling at 4kHz. This is currently beyond the capabilities of commercial sensors, [2].

In this paper, the WL and the CL sensor types will be reviewed and compared with the SWLI and the AFM methods. This follows a study [7] where

the same samples where used to compare a number of commercial SWLI systems. In a parallel study investigations were considered on a reference artifact with groove profiles similar to those used in the early sound recordings, where it was shown that the WL system provided the best surface representations in the shortest time, [2]. The reference artifacts are two sets of grooves with sinusoidal profiles with 25µm and 8µm periods, and another groove with rectangular profiles with 8µm period. Each set of the sinusoidal artifacts consists of four samples with different peak-to-valley distance (PV), as shown in Table 1. The nominal PV distances used as reference values in this paper were measured by AFM [7]. For all the reference samples, the PV distance is used to compare the difference between surface height measurements by different systems. The interaction between the sensor heads of different systems and the measured surfaces is studied by investigating the 2D cross sections of the surface profiles.

TABLE 1. Specification of the sinusoidal artifacts

Pitch (µm)	PV distance (µm)	Maximum gradient (°)
25*	2.720	37.20
25	0.654	5.30
25	0.531	3.90
25	0.134	1.10
8	0.496	17.10
8*	0.124	3.00
8	0.068	1.50
8	0.020	0.50

DESCRIPTION OF THE CON-FOCAL SENSING METHODS

The WL sensor characterizes the surface height of the measured surface by making use of a lens system's chromatic aberration, whereby the focal length of a dispersive lens varies with wavelength. A polychromatic light source is focused onto the measured surface passing through a series of lenses. The objective lens has a large chromatic aberration making different wavelengths focus at different depths. The reflected light path is diverted towards the spectrometer by the beam splitter. The wavelength representing the peak of the spectrum corresponds to the wavelength most in focus on the surface. The distance to the surface can then be calculated based on the known specific focal length of the focused light. Typical sampling rates are 1kHz with a spot size of 7µm.

The Con-focal laser is based on the same con-focal principle as the WL sensor. The laser beam passes through a collimator lens followed by an objective lens which is oscillating at high frequency using a tuning fork arrangement to move the focal point relative to the objective lens position. The reflected light passes back through the lenses and is then diverted towards a pinhole by a beam splitter. As the focal point on the measured surface varies as a function of the objective lens position, surface height can be measured by detecting the position of the lens corresponding to the maximum received light intensity detected by the CCD array. Typical sample rates are 1.4kHz with a spot size of 2µm.

EXPERIMENT RESULTS

In this paper results are presented on two sinusoidal samples highlighted (*) in table 1. The 25µm sample with the steepest gradient is beyond the limits of both con-focal sensor types, but is representative of groove structures in recorded surfaces. The 8µm sample with 124nm PV is used to test resolution limitations. The influence of precision mode, grid spacing and spot size are considered. The main emphasis of the study is to use the low precision mode consistent with high speed scanning.

The instruments used are commercially available. The software used to control the measurement of the WL and the CL systems is supplied by TaiCaan Technologies Ltd. The control software provides three operating precision modes, namely low, medium and high precision, corresponding to the high, medium and low scanning speed respectively [8]. The software used to analyse the data is BODDIES™, which provides both 3D and 2D cross section analysis. The measurements using the WL sensor and the CL were taken in an uncontrolled environment, while the measurements using the SWLI and the AFM were taken in temperature controlled environments. All the systems performed the measurements with approximately 0.2µm grid spacing in the scanning axis.

Measurements of the 25µm pitch sinusoidal artifacts

The 2D cross section figures of the measured profiles of the 25µm pitch, 2.72µm PV distance sinusoidal sample obtained from the con-focal systems are shown in Figure 1. Both the CL and

the WL sensor have an angular tolerance smaller than the maximum gradient of the surface. Therefore, only the top and the bottom of the groove structure were defined by these two sensors, and no valid measurements were achieved on the side walls. Similar results were reported by the SWLI on this sample with large data loss on the side walls and serious distortion of the surface profile, consistent with the results in [7]. The AFM used in the tapping mode provided the most representative surface profile. For the other 25µm pitch samples all the instruments provided better profiles with valid measurements on the side walls of the surface waveform. The PV distance was measured as an evaluation of the system performances. The CL, the SWLI and the AFM all reported PV distances within acceptable error range (< 0.3µm). The WL sensor failed to achieve valid PV distance measurements for all the samples.

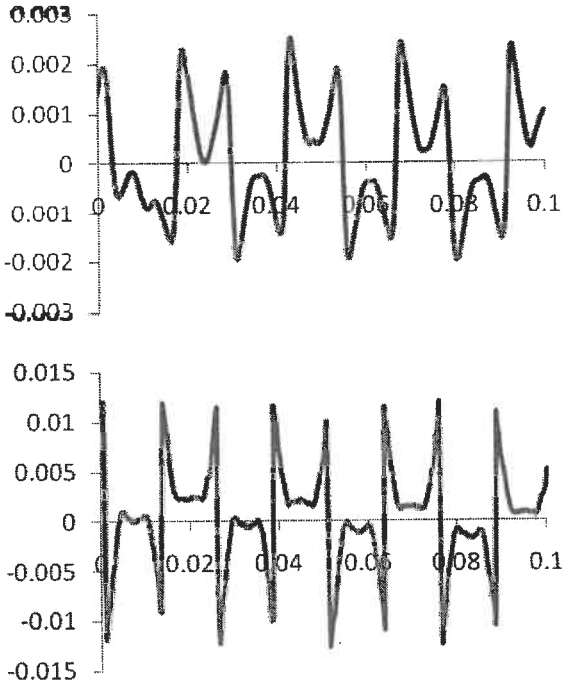

FIGURE 1. 2D cross section of the 25µm pitch, 2.72µm PV distance sinusoidal sample measured in low precision mode. Top: WL sensor; bottom CL. 501x101 data points, area 0.1mm x 0.1mm.

Measurements of the 8µm pitch sinusoidal artifacts

Only the CL, the AFM and the WL sensor were considered in this comparison. As the maximum gradient of the sample is smaller than the angular tolerance of the con-focal systems, both the CL and the WL sensor provided improved profiles. However, a high level of noise is shown in the low precision CL measurement. This results from noise in the analogue data collection prior to digital conversion. To overcome this, the lower 2D section in Figure 2 shows the digital high precision mode. The profiles obtained from the AFM are consistent with the 25µm samples. The PV distances measured by the CL and the AFM are within acceptable error range (<0.1µm); the WL sensor failed to achieve valid PV distance.

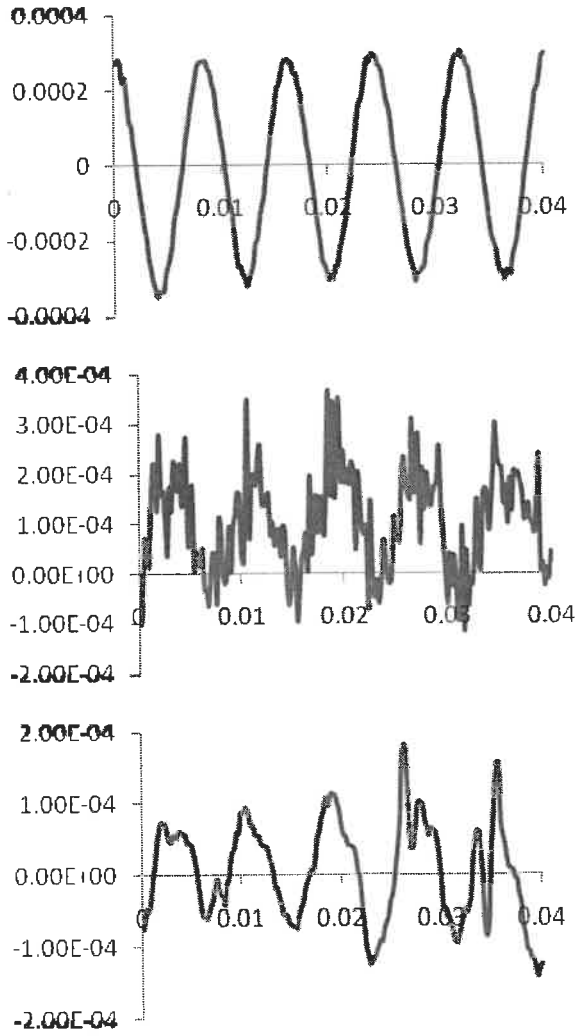

FIGURE 2. 2D cross section of the 8µm pitch, 0.496µm Top: WL sensor low precision mode; middle CL low precision mode; lower CL high precision mode. 501x101 data points, area 0.04mmx0.04mm.

Measurements of the 8µm pitch groove channel artifact

To investigate the response of the con-focal sensors to step sections, an 8µm pitch, 0.184µm amplitude groove channel sample with rectangular profile was measured by the CL, the

WL sensor and the AFM. Both the con-focal methods failed to report valid profiles of the sample, as shown in Figure 3.

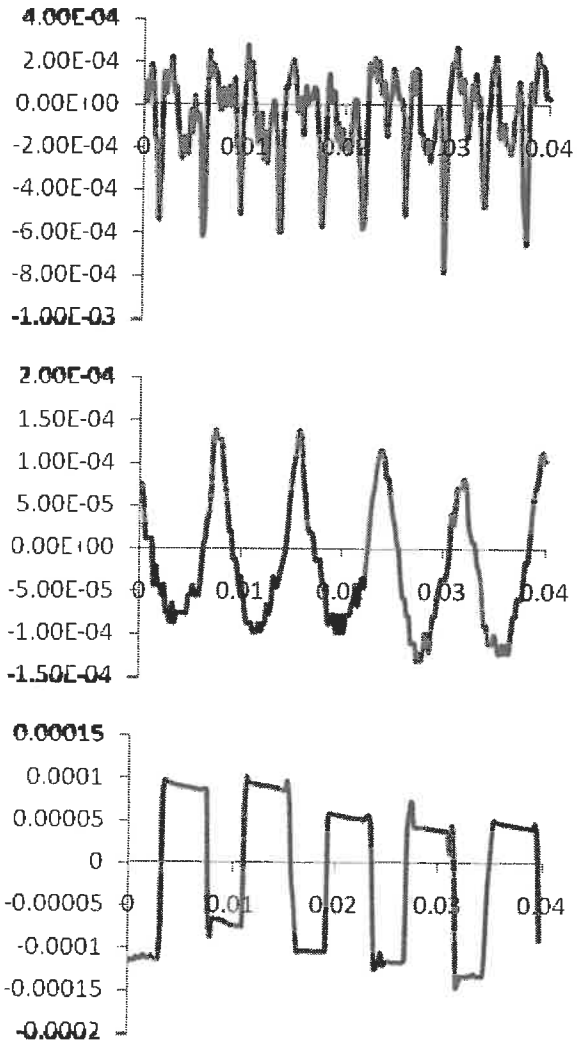

FIGURE3. 2D section of 8μm, 0.184μm amplitude groove channel sample. Top: CL; middle: WL sensor; bottom: AFM. CL and WL 201x101 data points, area, 0.04mmx0.04mm. AFM, 192x128 data points, area 0.04mmx0.02mm.

In the low precision mode shown in Figure 3, neither the valleys nor the side walls were faithfully measured by the CL. As a result, the CL failed to measure the PV distance of the sample. The WL sensor achieved valid measurements at the top and the bottom, but rounded off the rest of the surface due to its large spot size of 7μm. The WL sensor provided a PV distance of 0.17μm, comparable to the nominal value. The AFM provides the reference surface profile with a PV distance of 0.17μm.

CONCLUSIONS

Small scale reference samples with sinusoidal waveforms and rectangular profiles have been measured to compare three different optical sensing methods The emphasis of the study has been to determine the limits of high speed measurements to reflect the requirements of the sound archive project. The CL, the WL sensor and the SWLI all exhibited poor performances when measuring highly sloped or near vertical surfaces. For the con-focal systems, the angular tolerance, the spot size, the resolution limit and the dispersion of the reflected light have been shown to be the crucial parameters which caused the distortion of the measured profile and the invalid PV distance measurements. Another observation is the noise level of the measured profile could be reduced by using the high precision mode due to its point scanning process (the scanning system stops at each measurement point). For the WL system, sensor drift was found to be a systematic error source. There was a sensor drift of 0.2μm over 180s time. Although the AFM provided the highest quality profiles and the PV distances, the method is only practical as a reference of the con-focal systems. The results show that the con-focal systems although providing the highest measurement speed, are unable to define surfaces beyond the angular tolerance of the optical system, and that step features can introduce errors.

REFERENCES

[1] P. J. Boltryk, et al., Non-contact surface metrology for preservation and sound recovery from mechanical sound recordings, JAES 2008, in press.

[2] P. J. Boltryk, Martyn Hill, J. W. McBride, A. Nasce, Sensors and Actuators A: Physical, 142, (1), 2-11, 2007.

[3] www.sesnet.soton.ac.uk/archivesound/home

[4] V. Fadeyev, C. Haber, C. Maul, J. W. McBride, M. Golden, J. Audio Eng. Soc. 53 (6) (2005) 485-508.

[5] Nasce et al. A quantitative analysis of signal reproduction from cylinder recordings measured via non-contact, full surface mapping. JASA, in press.

[6] J. W. McBride, C. Maul, IEICE Trans. E87 (8) (2004) 1261-1267.

[7] F. Gao, R. K. Leach, J. Petzing, J. M. Coupland, Meas. Sci. Technol. 18 (2007), 1-12.

[8] XYRIS User Manual Edition 4.0, TaiCaan Technologies, 2007.

DESIGN AND FABRICATION OF A MULTIFUNCTIONAL SCANNING PROBE WITH INTEGRATED TIP CHANGER FOR FULLY AUTOMATED NANOFABRICATION

Kam K. Leang[1] and Curtis R. Taylor[2]
[1]Dept. of Mechanical Engineering, Univ. of Nevada-Reno, Reno, NV
[2]Dept. of Mechanical and Aerospace Engineering, Univ. of Florida, Gainesville, FL

INTRODUCTION

The use of scanning probe microscope (SPM) tips as manufacturing tools for the fabrication of integrated microsystems, nanoelectromechanical (NEMS) systems, and nanoelectronic devices have been widely proposed and progress towards these goals was recently demonstrated, for example, by nanopatterning of 88 million nanofeatures in less than 20 minutes over 1 cm^2 using dip pen nanolithography [1]. However, in order to enable practical nanofabrication with probe tips for such applications as: (1) handheld replicators for nano rapid prototyping of nanoelectronics and NEMS, (2) printing and nanomachining of unique hybrid organic and inorganic material [2], (3) 3-D nanofabrication and assembly, and (4) complete desktop nanofactories [3]; it will be critical to address the issues of throughput, tip wear effects, chemical cross contamination, and scalability – all of which act to decrease the quality, reliability, and efficiency of probe-based fabrication.

To address these critical issues, a novel active cantilever probe is proposed with an automated ability to interchange probe tips (tools); for example, from nanotube tips for high resolution metrology to dynamic tips for nanomachining to chemically functionalized tips for cell biology, without the need for an operator to physically replace the cantilever as in traditional atomic force microscopy (AFM). The concept of the active cantilever system is shown in Figure 1. This novel design models macroscale computer numerical control (CNC) manufacturing in which CNC machines are fully automated allowing for rapid tool changes without operator interruption. Located at the distal end of an SPM cantilever is an electrically activated microgripper, which is designed to automatically load and unload tips from an array of available tools. Automation is achieved by exploiting the thermal properties of the microgripper to create a thermal-proximity sensor to determine the relative location between the microgripper and tool tip, similar to thermally activated cantilevers for AFM thermal imaging [4].

The ability to provide fully automated on-demand probe tip changes will improve the overall efficiency of a fabrication process, allow for multifunctional probe capabilities, and improve process reliability and quality by enabling the ability to replenish worn or chemically fouled tips in an efficient manner. This paper addresses the design aspects of the active cantilever probe and system automation, with preliminary experimental results to justify the design.

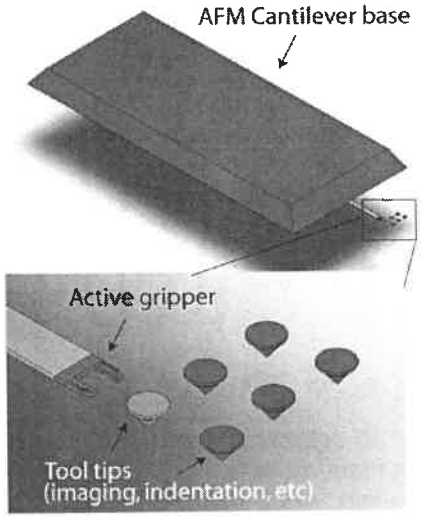

FIGURE 1. Concept drawing showing active cantilever probe and modular tool tips.

CANTILEVER PROBE AND MODULAR-TIP DESIGN

The active cantilever probe design is based upon a thermally actuated microgripper that offers several advantages over other actuation techniques. In general, the available actuation mechanisms consist of: (1) electrostatic actuation [5], (2) thermal actuation [6], and (3) piezoelectric actuation, to name a few. Although piezoelectric actuators are the workhorse for positioning an SPM probe tip relative to a

sample surface, their use as microgrippers is rather limited because of their low percent strain (<0.5%). Micron-size electrostatic actuators have been developed to manipulate objects, such as a nanowire [7], with relatively large strain; however, they require large electric fields (as large as 100 V). A thermal-based actuator was developed that consumed 75 mW of power with an expansion of 35 μm [8]. Thermal actuators can provide a significant amount of force for gripping and holding a modular tool tip. Second, the fabrication process to create a micron-size thermal gripper is well established [9]. Thirdly, they occupy a relatively small foot print. Finally, the thermal behavior of the gripper can be exploited to create a sensor to detect the location of modular tips for loading/unloading. Therefore, no additional sensing mechanism is needed to determine the relative locations between the thermal gripper and tool tips for automated exchange.

A schematic of the active cantilever probe design is shown in Figure 2. Cantilevers with different geometries and dimensions were designed; in particular, the design in Figure 2 has approximate dimensions of 400 μm x 35 μm x 3 μm (*length;width;thickness*). The probe was designed to be compatible with existing commercial AFM systems; therefore the dimensions and mechanical performance were optimized within ranges of commercially available contact-mode probes. A 2 x 4 mm base (not shown) allows the probe to be handled relatively easy using tweezers. The chip base has metallic electrodes for electrically activating the microgripper at the distal end of the cantilever. The probe and modular tips (when attached) will function as a conventional AFM system using the optical lever mechanism for detection of tip deflection. A significant advantage of this design is that since only the modular tip is exchanged and not the entire cantilever, recalibration and alignment of the laser to the probe, as in replacement of conventional probes, is not needed. Additionally, the cantilever can be designed with integrated piezoelectric sensors for sensing of tip deflection thereby eliminating the need and associated complexities of an optical lever system.

Thermal actuation of the gripper is achieved by differential thermal expansion of the inner and outer arms of the gripper as shown in Figure 2. The current path through the gripper results in resistive Joule heating with higher temperature occurring in regions of smaller cross-sectional area. The smaller (hot) inner arm expands more than the (cold) outer arm resulting in bending or actuation of the gripper (Huang and Lee, 1999). The dimension and geometry of the gripping arms were designed to provide adequate gripping force to ensure a no slip condition of the secured modular tip and to ensure dynamic robustness during imaging and other functions. Thus the gripping force (> 17 μN) is passively maintained by making the modular tip dimensions greater than the equilibrium gripping dimensions—a compression fit is formed and is always maintained unless the gripping arms are actuated (opened). The U-shaped wedge design of the grips allows for mechanical interlocking and ensures non-rotation of the modular tip. The modular tips (not shown) are designed with a reverse geometry that locks into the gripper. The tips have a top gold coating to allow deflection of laser light as in conventional probes and will be stored for retrieval in a specially designed storage cassette. At present, modular tips are to be mass fabricated on a silicon wafer and attached via tabs similar to commercially fabricated cantilever probes.

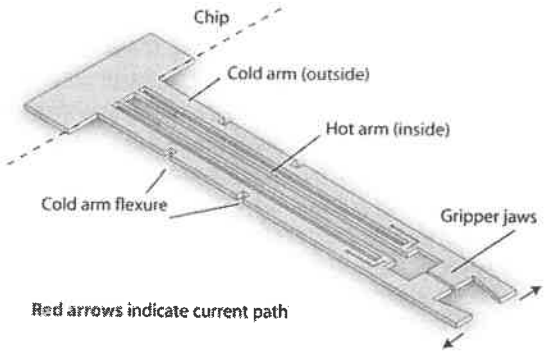

FIGURE 2. Prototype design of cantilever probe with integrated thermally actuated gripper (electrodes and chip base not shown).

The mechanical behavior of the cantilever probe was analyzed using finite element software (ANSYS FEA, Canonsburg, PA, USA). The cantilever material is polysilicon, with Young's modulus of 150 GPa, density of 2330 kg/m^3, Poisson's ratio of 0.28, and thermal expansion of 2.6×10^{-6} °C^{-1}. Using the temperature distribution given in [10], with low temperature value of 25 °C and maximum of 775 °C, the maximum gripper opening, measured at the distal end of the gripper, was 7.08 μm. Assuming a boundary condition in which the base of the cantilever was fixed, the resonant

frequency of the first bending mode, without modular tool tip, was approximately 28 kHz.

FABRICATION PROCESS

The active cantilever probe will be mass fabricated on a silicon-on-insulator (SOI) wafer. Si is widely used in conventional probe designs and offers flexibility in processing and tuning of mechanical and electrical properties. The fabrication process is shown in Figure 3. A n-type SOI wafer with a 3 μm Si device layer, 1 μm oxide (SiO_2) layer, and 350 μm Si handle layer is used. First, three Cr etch masks are made to transfer the top/bottom probe and electrode patterns to the SOI wafer for etching. A 25 nm Cr adhesion layer followed by a 150 nm Au layer is deposited on the Si device layer by electron beam evaporation. Next, photoresist is spun on top of the Au layer and patterned by photolithography to etch and form the Au electrode pads. After removal of the resist for the electrodes; a new layer of photoresist is deposited and patterned to form the probe and gripper geometries. The Au and Cr layers are etched through to the Si and the Si selectively etched using reactive ion etching (RIE) down to the SiO_2 layer. This completes the top-side (device layer) processing and the wafer is oriented for backside processing. Next, a 300 nm Al metal mask layer is deposited on the backside of the wafer by electron beam evaporation and a photoresist layer is deposited and patterned by photolithography to define the gripper and probe support chip. The Si handle layer is etched using reactive ion etching (RIE). Finally, the substrate is etched in a buffered oxide etch solution until the wafer has been completely etched through from the backside thereby releasing the cantilever. Modular tool tips are to be fabricated on Si using a similar microfabrication process.

PROXIMITY SENSING AND AUTOMATION

Sensing the relative location (*x,y,z coordinates*) between the distal end of the gripper (jaws) and a tool tip will be achieved using an integrated thermal-proximity sensor [11]. This sensing scheme avoids the complexity of adding additional sensors to the cantilever probe. The junction will then be heated to a specific temperature and positioned relative to a calibration zone or tool tips until a noticeable change in thermal behavior is observed to indicate proximity (without physically touching the surface).

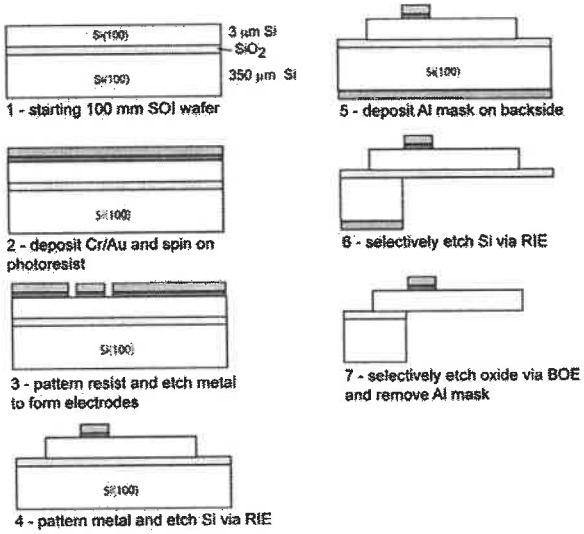
Si(100)
3 μm Si
SiO2
350 μm Si
Si(100)
1 - starting 100 mm SOI wafer
Si(100)
2 - deposit Cr/Au and spin on photoresist
Si(100)
3 - pattern resist and etch metal to form electrodes
Si(100)
4 - pattern metal and etch Si via RIE
Si(100)
5 - deposit Al mask on backside
6 - selectively etch Si via RIE
7 - selectivsly etch oxide via BOE and remove Al mask

FIGURE 3. Fabrication process of active cantilever probe.

Figure 4 shows the layout of the envisioned workspace as well as the thermal-proximity concept. In particular, the heated gripper will be positioned over the calibration zone and slowly lowered until there is a noticeable change in thermal response due to conduction of thermal energy between the calibration feature and integrated sensor. By using the heated gripper as a thermal-proximity sensor, it can be rastered at constant height above the tool-tip array (x and y) to determine the approximate location of the tool tips relative to the jaws of the gripper. This information will be used to automatically position the AFM active cantilever at the correct location (x, y, and z) to enable loading/unloading of tips.

One significant design challenge is to ensure adequate resolution of the sensor within the framework of the three thermal resistances in series (i.e. the cold arm--sensor--hot arm). A coupled electro-thermo-mechanical model will be used to address this issue along with possibly tuning the resistivity via electrical doping of the gripper arms in order to achieve an adequate sensor signal.

CONCLUSION

A novel system for automated exchange of multiple probe tip tools for nanoscale fabrication, metrology, and characterization has been presented. An active cantilever probe with a thermally actuated microgripper is used to sense and secure tool tips. The probe is compatible with commercially available AFM systems. A

working prototype of the active cantilever is currently being fabricated and tested.

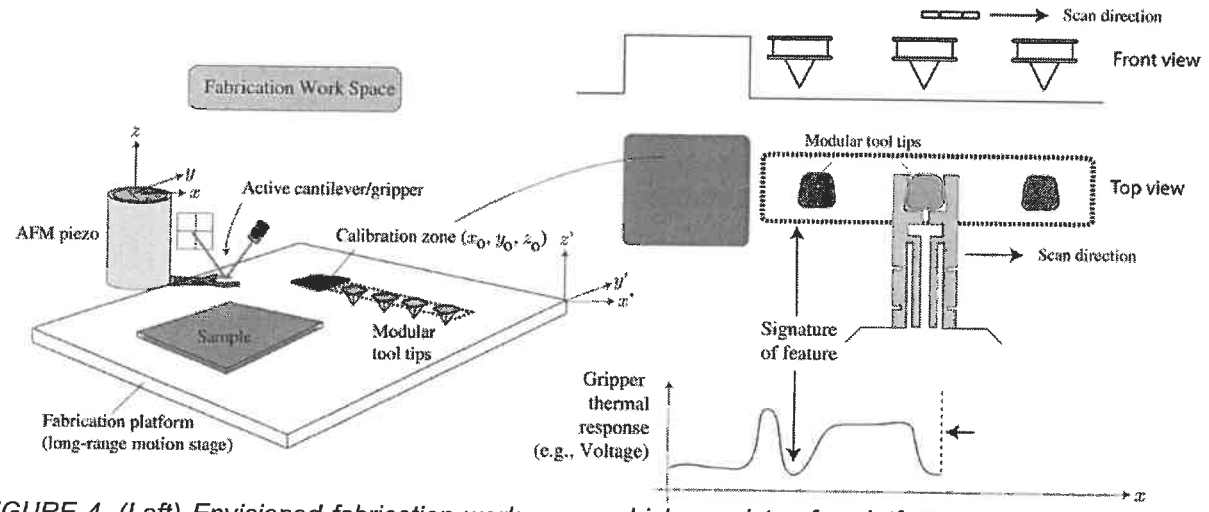

FIGURE 4. (Left) Envisioned fabrication workspace, which consists of a platform containing sample and modular tool tips with a calibration zone (home position). The gripper is actuated by the AFM piezoactuator for scanning. (Right) Front and top view of thermal gripper hovering over tool tips. The relative location between gripper and tool tip is determined using thermal proximity sensing: monitoring the thermal behavior of the gripper as it moves over the calibration zone and tool tips.

REFERENCES

[1] Salaita, K., Y. Wang, J. Fragala, R.A. Vega, C. Liu, and C.A. Mirkin. Massively parallel dip-pen nanolithography with 55000-pen two-dimensional arrays. *Angew. Chem. Int. Ed.* 2006; 45: 7220-7223.

[2] Kentsch, J., M. D.urr, T. Schnelle, G. Gradl, T. Muller, M. Jager, A. Normann, and M. Stelzle. 2003. Microdevices for separation, accumulation, and analysis of biological micro- and nanoparticles. IEE Proceedings Nanobiotechnology. 150:82 -- 89.

[3] Johansson, S. 1995. Micromanipulation for micro- and nana- manufacturing. In INRIA/IEEE Symposium on Emerging Technologies and Factory Automation. 3-8.

[4] Lee, J., T. Beechem, T.L. Wright, B.A. Nelson, S. Graham, and W.P. King. 2006. Electrical, thermal, and mechanical characterization of silicon microcantilever heaters. Journal of Microelectromechanical Systems. 15:1644 -- 1655.

[5] Kim, C.-J., A.P. Pisano, and R.S. Muller. 1992. Silicon-processed overhanging microgripper. IEEE/ASME J. Microelectromechanical Systems. 1:31 -- 36.

[6] Jonsmann, J., O. Sigmund, and S. Bouwstra. 1999. Compliant electro-thermal microactuators. In 12th IEEE International Conference on Micro Electro Mechanical Systems. 588 -- 593.

[7] Molhave, K., T. Wich, A. Kortschack, and P. Boggled. 2006. Pick-and-place nanomanipulation using microfabricated grippers. Nanotechnology. 17:2434 -- 2441.

[8] Keller, C.G., and R.T. Howe. 1997. Hexsil tweezers for teleoperated micro-assembly. In IEEE 10th Annual International Workshop on Micro Electro Mechanical Systems. 72 -- 77.

[9] Liu, C. 2006. Foundations of MEMS. Prentice Hall, Upper Saddle River, New Jersey.

[10] Huang, Q-A. and Lee, N. K. S. Analysis and design of polysilicon thermal flexure actuator, J. Micromech. Micron.; 1999; 9; 64-70.

[11] Abraham, D.W., T.J. Chainer, K.F. Etzold, and H.K. Wickramasinghe. 2000. Thermal proximity imaging of hard-disk substrates. IEEE Trans. on Mathematics. 36:3997 -- 4004.

TWO-DIMENSIONAL DISPLACEMENT MEASUREMENT USING THE SIX-POINT ATOMIC ENCODER TECHNIQUE

Patamaporn Chaikool[1], Masato Aketagawa[1], and Eiki Okuyama[2]
[1]Department of Mechanical Engineering
Nagaoka University of Technology
Nagaoka, Niigata, JAPAN
[2]Department of Mechanical Engineering
Akita University
Akita, JAPAN

INTRODUCTION

Since rapid progresses in nanotechnology and ultra precision engineering, several research activities and applications in fabrication process and metrology require an accuracy of sub-nanometer or less. For example, the precision *X-Y* stage used in the semiconductor lithography needs to be positioned and controlled accurately. A measurement of the two-dimensional (2-D) displacement is important for evaluating the stage's performance and the feedback control. In the previous research, the 2-D displacement measurement technique with 10-picometer resolution using a combination of the scanning tunneling microscope (STM) and the highly oriented pyrolytic graphite (HOPG) crystal was proposed [1]. The STM is the instrument wildly used in the surface engineering which can observe an image of atoms on the crystalline surface. And, a lattice spacing of approximately 0.246 nm of the HOPG crystal [2] is uniform and stable over a long range when the crystals are stress free. In the technique, the HOPG crystal is utilized as the atomic reference scale and observed by the multi-tunneling-probe STM (MTP-STM). However, a requirement of two STM tips to perform this technique introduces a complicacy of the technique for applications and design. In this article, a new 2-D displacement measurement technique based on the MTP-STM technique using only one STM tip is proposed. The measurement principle and result are discussed in the article.

PRINCIPLE OF SIX-POINT ATOMIC ENCODER

In the MTP-STM technique, two sinusoidal signals with a 90° phase difference and the desired amplitudes are applied to the *XY* tip scanner to achieve a lateral-circular dither motion. *FIGURE 1* shows an ideal surface of the HOPG crystal. In the figure, $\vec{a}_i$ and $\vec{k}_j$ are the unit lattice vector and reciprocal vector, respectively. The relationships

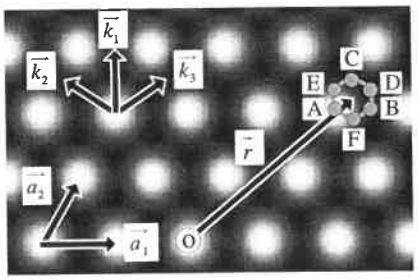

FIGURE 1. Ideal surface of the HOPG crystal and the specific points for six-points atomic encoder technique. o : origin

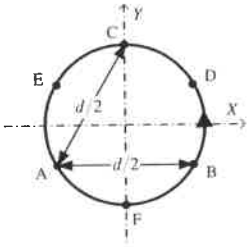

FIGURE 2. Trajectory of high-speed lateral dither modulation applied to the STM tip

between $\vec{a}_i$ and $\vec{k}_j$ are

$$\vec{a}_i \cdot \vec{k}_j = \delta_{ij} \begin{cases} 1 & (i=j) \\ 0 & (i \neq j) \end{cases} , \quad (1)$$

$$\vec{k}_3 = \vec{k}_1 - \vec{k}_2 , \quad (2)$$

where δ_{ij} is Kronecker's δ. $|\vec{a}_1|$ and $|\vec{a}_2|$ (= lattice spacing of the HOPG crystal) is 0.246 nm [2], and the intersectional angle between $\vec{a}_1$ and $\vec{a}_2$ is 60°. As shown in *FIGURE 1*, the arbitrary 2-D displacement vector $\vec{r}$ can be represented by the linear sum of the unit vectors $\vec{a}_1$ and $\vec{a}_2$. Therefore, we can obtain

$$\vec{r} = m\vec{a}_1 + n\vec{a}_2 , \quad (3)$$

where m and n is the number of atom in the direction of $\vec{a}_1$ and $\vec{a}_2$, respectively. The topographical

height $Z(\vec{r})$ of the HOPG crystal can be approximately represented using the next equation.

$$Z(\vec{r}) = \sum_{i=1}^{3} A_i \cos\left(2\pi \vec{k}_j \cdot \vec{r}\right) \quad (4)$$

By applying a properly amplitude of the circular dither modulation, the STM tip is located at 6 specific points *A-F* on the crystalline surface, as shown in *FIGURE 1* and *FIGURE 2*. The displacement vectors $\vec{r}$ at each point can be represented using the following equations.

$$\vec{r}_A = \left(m - \frac{1}{6}\right)\vec{a}_1 + \left(n - \frac{1}{6}\right)\vec{a}_2 \quad (5)$$

$$\vec{r}_B = \left(m + \frac{1}{3}\right)\vec{a}_1 + \left(n - \frac{1}{6}\right)\vec{a}_2 \quad (6)$$

$$\vec{r}_C = \left(m - \frac{1}{6}\right)\vec{a}_1 + \left(n + \frac{1}{3}\right)\vec{a}_2 \quad (7)$$

$$\vec{r}_D = \left(m + \frac{1}{6}\right)\vec{a}_1 + \left(n + \frac{1}{6}\right)\vec{a}_2 \quad (8)$$

$$\vec{r}_E = \left(m - \frac{1}{3}\right)\vec{a}_1 + \left(n + \frac{1}{6}\right)\vec{a}_2 \quad (9)$$

$$\vec{r}_F = \left(m + \frac{1}{6}\right)\vec{a}_1 + \left(n - \frac{1}{3}\right)\vec{a}_2 \quad (10)$$

From (4)-(10), the following equations are obtained.

$$I_{AB} = Z(\vec{r}_A) + Z(\vec{r}_B) = 2A_2 \cos\left\{2\pi\left(n - \frac{1}{6}\right)\right\} \quad (11)$$

$$I_{DE} = Z(\vec{r}_D) + Z(\vec{r}_E) = 2A_2 \cos\left\{2\pi\left(n + \frac{1}{6}\right)\right\} \quad (12)$$

$$I_{AC} = Z(\vec{r}_A) + Z(\vec{r}_C) = 2A_1 \cos\left\{2\pi\left(m - \frac{1}{6}\right)\right\} \quad (13)$$

$$I_{DF} = Z(\vec{r}_D) + Z(\vec{r}_F) = 2A_1 \cos\left\{2\pi\left(m + \frac{1}{6}\right)\right\} \quad (14)$$

In the calculation, we assume the non-linearity between the tunneling current and the height *Z* is calibrated. These equations lead to

$$I_{AB} + I_{DE} = 2A_2 \cos 2\pi n\,, \quad (15)$$

$$I_{AB} - I_{DE} = 2\sqrt{3}A_2 \sin 2\pi n\,, \quad (16)$$

$$I_{AC} + I_{DF} = 2A_1 \cos 2\pi m\,, \quad (17)$$

$$I_{AC} - I_{DF} = 2\sqrt{3}A_1 \sin 2\pi m\,. \quad (18)$$

Equations (15)-(18) show the possibility to determine m and n with an integer and fractional parts from $(\cos 2\pi m, \sin 2\pi m)$ and $(\cos 2\pi n, \sin 2\pi n)$ by using the interpolation method. The lateral displacement vector $\vec{r}$ can be represented formally as the next equation.

$$\vec{r} = \frac{1}{2\pi}\tan^{-1}\left[\frac{1}{\sqrt{3}}\left(\frac{I_{AC} - I_{DF}}{I_{AC} + I_{DF}}\right)\right]\vec{a}_1 + \frac{1}{2\pi}\tan^{-1}\left[\frac{1}{\sqrt{3}}\left(\frac{I_{AB} - I_{DE}}{I_{AB} + I_{DE}}\right)\right]\vec{a}_2 \quad (19)$$

Using this technique, the lateral displacement vector $\vec{r}$ can be measured using the tunneling currents at points *A* to *F*.

MEASUREMENT SYSTEM

The measurement system shown in *FIGURE 3* contains the *XYZ* tip scanner, the STM tip, the HOPG crystal, the *XY* sample stage, the *Z* servo controller, the digital signal processor (DSP) with the 16 bit A/D and D/A converter, the piezoelectric (PZT) amplifier and 2 capacitive displacement sensors (only 1 sensor is shown in this figure). In the experiment, the *XY* raster (or *XY* driving motion) and dither signals produced by the DSP/DA with proper amplitude are amplified by the PZT amplifier, and fed into the sample stage and tip scanner, respectively. Suitable and high-speed dither signals allow the dither motion at the STM tip so that the tunneling current signals at the 6 specific points (point *A* to *F*) are correctly obtained, as mentioned in the previous section. The tunneling current signals detected by the STM tip are converted to voltage signal using the I/V converter, and collected with the A/D converter. These signals are simultaneously used as the input of the *Z* servo controller in order to keep the height of the STM tip constantly. On the other hand, raster (or driving motion) signals applied to the *XY* sample stage enable the stage moves in the *XY*-plane. The *XY*-axes reference plate is

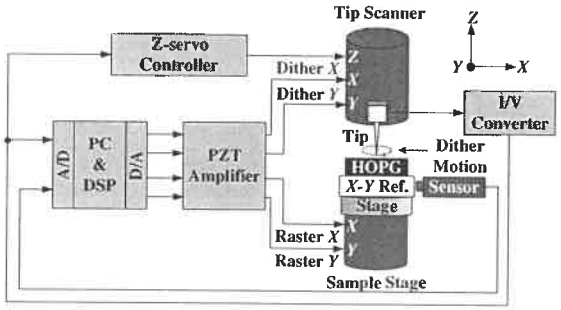

FIGURE 3. Measurement system

installed on the top of the stage, and utilized as the *XY*-axes reference of stage's movement measured by 2 capacitive displacement sensors. This result of 2-D displacement of the stage is compared with the proposed technique.

SEPARATION OF THE CRYSTALLINE ORIENTATION

Before measuring the 2-D displacement using the six-point atomic encoder, the separation of the crystalline orientations was performed to confirm positions of point *A* to *F* on the HOPG crystal. The parameters used in this experiment are listed in *TABLE 1*. *FIGURE 4* illustrates the results of the separation of crystalline orientations which were properly obtained. *FIGURE 4*(a)-(f) are the atomic images of the HOPG crystal based on the tunneling current signals from points *A* to *F*, respectively. *FIGURE 4*(g) and (h) are the summed images of *4*(a)+(b) (I_{AB}) and *4*(a)+(c) (I_{AC}) given

TABLE 1. Experimental conditions

Material	Sample Tip	HOPG Pt-Ir
STM	Bias voltage Set point current	50 mV 2 nA
Raster	Scan size Frequency	2 nm 10.2 Hz
Dither	Amplitude Frequency	0.13 nm 5 kHz
AD/DA board	Sampling freq.	210 kHz

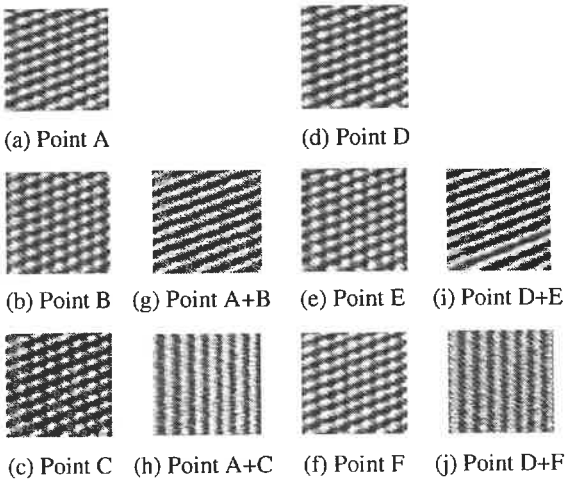

FIGURE 4. Separation of the crystalline orientations of HOPG crystal using six-point atomic encoder

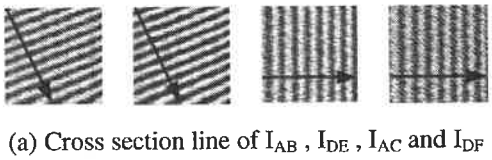

(a) Cross section line of I_{AB} , I_{DE} , I_{AC} and I_{DF}

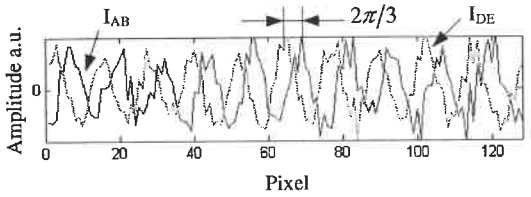

(b) Comparison between I_{AB} and I_{DE}

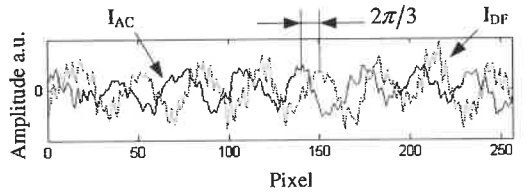

(c) Comparison between I_{AC} and I_{DF}

FIGURE 5. Cross section comparison between figure 4(g), 4(i), 4(h) and 4(j)

by equations (11) and (13), respectively. Similarly, *FIGURE 4*(i) and (j) are the summed images of *4*(d)+(e) (I_{DE}) and *4*(d)+(f) (I_{DF}) given by equations (12) and (14), respectively. In addition, *FIGURE 4*(g) and (i) represent the $\vec{k}_1$'s sinusoidal wave signals, while the $\vec{k}_2$'s sinusoidal wave signals are shown in *4*(h) and (j), respectively. The cross-sections in *FIGURE 4*(g) and (i), and *4*(h) and (j) were investigated to determine the phase difference between equations (11) and (12), and between (13) and (14), respectively. *FIGURE 5*(a) shows the cross-sections line of *4*(g), (i), (h) and (j). *FIGURE 5*(b) shows the difference between *4*(g) and (i), while *5*(c) also shows the difference between *4*(h) and (j). *FIGURE 5*(b) and (c) indicate that the phase differences between *4*(g) and (i), and *4*(h) and (j)) are almost $\frac{2\pi}{3}$ radian, which confirms a validity of equations (11)-(14).

2-D DISPLACEMENT MEASUREMENT

After verifying the STM tip's position, the 2-D displacement was measured and compared with 2 capacitive displacement sensors. The sensors were installed at both sides of the *XY*-axes reference plate located on the top of the stage. The sample scanner was driven by driving signals so that the stage moved 20 times repeatedly in bidirection with expected amplitude of approximately 39 nm along approximately 0° direction from *X*-

axis. The results of the 10th measurement are shown in *FIGURE 6*. Signals obtained by 2 displacement sensors shown in *FIGURE 6* indicate that the stage was moved with the displacement of 39.25 nm and 1.72 nm in *X*- and *Y*-axis, respectively, and the amplitude of the 2-D displacement vector $\vec{r}$ is calculated to be 39.29 nm. From the results, the value of m and n are measured to be 182.5 and -82, respectively. The angle of $\vec{a}_1$ and $\vec{a}_2$ are shown as 29° and 89°, respectively. Using equation (3), the 2-D displacement is determined to be 38.91 nm and 1.60 nm in *X*- and *Y*-axis, respectively. Therefore, the amplitude of the 2-D displacement vector $\vec{r}$ can be calculated as 38.95 nm, which is different from that measured by the displacement sensors within 0.34 nm. The comparison of the displacement measured by displacement sensors and the proposed technique is shown in *FIGURE 7*. The displacement vector measured by the capacitive displacement sensors and six-point atomic encoder has some difference in both *X*- and *Y*-axis. It might be caused by the thermal drift, the cosine error and non-perpendicularity of the *XY*-axes reference plate.

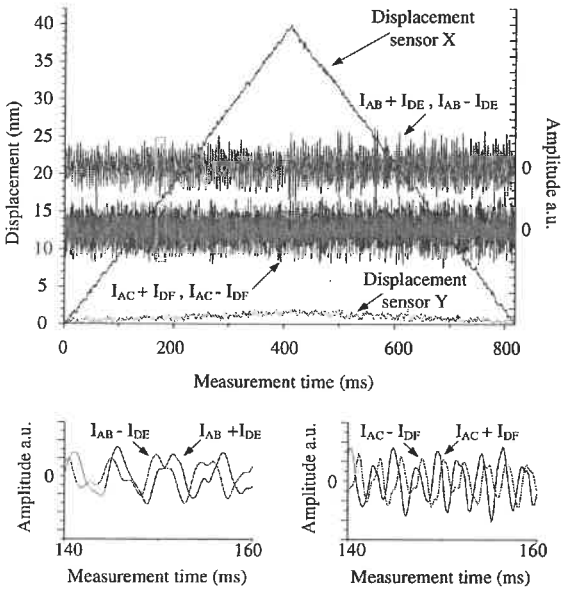

FIGURE 6. Two-dimensional displacement measurement using six-point atomic encoder

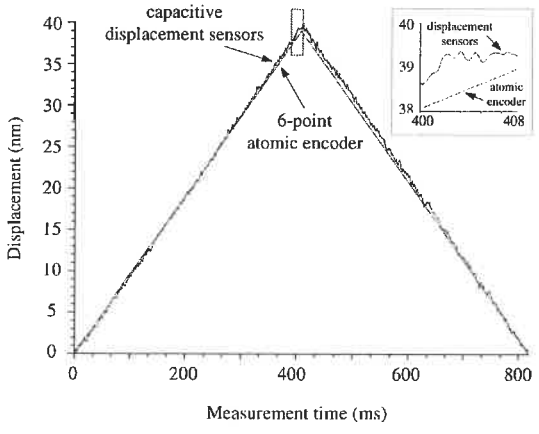

FIGURE 7. Comparison of the displacement measured by displacement sensors and six-point atomic encoder

CONCLUSION AND FURTHER STUDY

A new method for measuring the 2-D displacement based on the MTP-STM technique with one STM tip was proposed. Although the comparison of the 2-D displacement measured by the six-point atomic encoder and the capacitive displacement sensors showed an error of 0.34 nm for measurement range of approximately 39 nm, the measurement with a resolution of sub-nanometer or less can be performed. We expect that the proposed technique is available for the direct measuring the spindle radial motion error [3].

REFERENCES

[1] Aketagawa M, Honda H, Ishige M, Chaikool P. Two-Dimensional Encoder with Picometer Resolution using Lattice Spacing on Regular Crystalline Surface as Standard. Measurement Science and Technology. 2007;18:342–349.

[2] Rerkkumsup P, Aketagawa M, Takada K, Watanabe T, Sadakata S. Direct Measurement Instrument for Lattice Spacing on Regular Crystalline Surfaces Using a Scanning Tunneling Microscope and Laser Interferometry. Review of Scientific Instrument. 2003;74:1205–1210.

[3] Aketagawa M, Chaikool P, Ishige M, Okuyama E. Direct Measurement of Spindle Error Motion with 10-Picometer Resolution Using Regular Crystalline Lattice and Scanning Tunneling Microscope. In: Proceeding of the 22th Annual Meeting of the American Society for Precision Engineering. American Society for Precision Engineering. Raleigh, NC, USA: ASPE; 2007. p. 52–55.

A NEW HETERODYNE INTERFREOMETER WITH ZERO PERIODIC ERROR AND TUNABLE BEAT FREQUENCY

Hyo Soo Kim[1], Tony L. Schmitz,[1] John F. Beckwith[2,*], and Matthew C. Rueff[1]
[1]Department of Mechanical and Aerospace Engineering
University of Florida, Gainesville, FL, USA
[2]Electronics Engineering Technologies Division
Lawrence Livermore National Laboratory, Livermore, CA 94550, USA
[*]Retired

INTRODUCTION

Since its introduction in the mid-1960s, displacement measuring interferometry has offered high accuracy, range, and resolution for non-contact displacement measurement applications, including position feedback for lithographic stepper stages, precision cutting machines, and coordinate measuring machines, as well as transducer calibration, for example. A common configuration choice in these situations is the heterodyne (or two frequency) Michelson-type interferometer with single, double, or multiple passes of the optical paths. These systems infer changes in displacement of a selected optical path by monitoring the optically induced variation in the photodetector current, which is generated from the optical interference signal.

Periodic error remains an intrinsic error source that prevents traditional configurations from achieving sub-nanometer level accuracy. The purpose of this research is to validate the absence of periodic error in a new interferometer design that does not rely on polarization coding, where the two (heterodyne) optical frequencies are carried on coincident, linearly polarized, mutually orthogonal laser beams and separated/recombined using polarization dependent optics. Rather, the two frequencies are carried on spatially separate beams in a polarization independent optical configuration that also enables the user to select the beat (or split) frequency. By eliminating the potential for mixing between the two heterodyne frequencies, the periodic error source is removed.

PERIODIC ERROR BACKGROUND

Imperfect separation of the two light frequencies into the moving and fixed paths in polarization coded heterodyne interferometers has been shown to produce first and second order periodic errors, or errors of one and two cycles per wavelength of optical path change, respectively. In a perfect system, a single frequency would travel to the fixed target, while a second, single frequency traveled to the moving target. Interference of the combined signals would yield a perfectly sinusoidal trace with phase that varied, relative to a reference phase signal, in response to motion of the moving target. However, the inherent frequency leakage in actual implementations produces an interference signal which is not purely sinusoidal (i.e., contains unintended spectral content) and leads to a periodic error in the measured displacement.

Quenelle [1] performed an early investigation of periodic error in heterodyne interferometers. Subsequent areas of research have included efforts to measure periodic error using frequency domain analysis [2], analytical modeling techniques [3], Jones calculus modeling [4], and reduction of periodic error [5-7].

Schmitz and Beckwith [8] summarized the potential periodic error contributors using a Frequency-Path model, which identified all possible paths for each light frequency from the source to detector and predicted the number of interference terms that may be expected at the detector output. For the single pass, polarization-coded heterodyne interferometer, it was demonstrated that 10 distinct interference terms exist in a fully leaking interferometer (i.e., each frequency is present in both the moving and fixed paths). These interference terms may be grouped by optical path change dependency into only four categories: 1) o*ptical power* which contributes a constant intensity to the photodetector current independent of optical path changes; 2) *AC reference* terms with phase that varies by one full cycle over the synthetic wavelength; 3) *DC interference*, which are Doppler shifted up from zero frequency during

target motion; and 4) *AC interference* terms which produce a time harmonic variation in the detector current at the beat frequency (f_b) and are Doppler shifted (f_d) up or down during target motion depending on direction. The corresponding frequency content during constant velocity motion is depicted in Fig. 1.

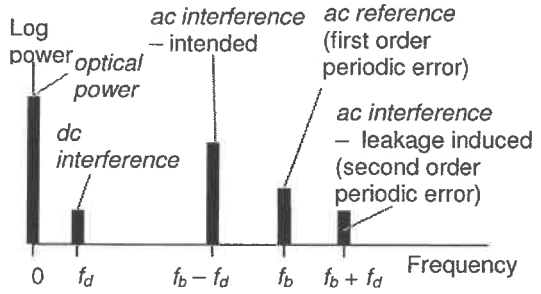

FIGURE 1. Frequency spectrum for constant velocity motion in fully leaking heterodyne interferometer.

EXPERIMENTAL SETUP

In the AOM DMI design, a pair of AOMs is used to generate, and keep spatially separate, the heterodyne frequencies. The basic elements of an AOM are a glass body with a piezoelectric transducer (PZT) attached at one end and a frequency source (stable quartz oscillator) to drive the PZT.

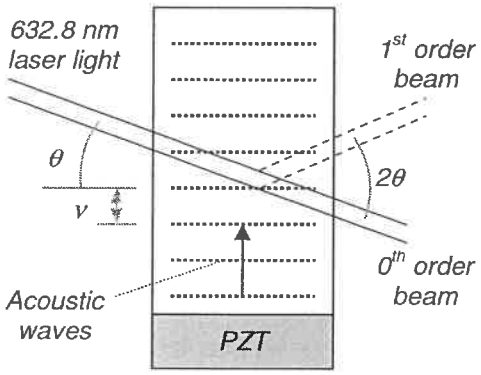

FIGURE 2. Acousto-optic modulator schematic. The incident beam is diffracted into the 0^{th} and 1^{st} order beams.

Actuation of the PZT at the oscillator driving frequency generates acoustic waves within the glass which leads to periodic spatial variations in the glass refractive index due to the changes in density (i.e., a moving diffraction grating is produced). When laser light is incident on the moving diffraction grating, it is diffracted into multiple separate beams (or orders). The diffraction angles, θ, are given by Eq. 1, where m = 0, ±1, ±2, ... is the order number, λ is the light wavelength (633 nm), and v is the acoustic wavelength. Under high driving frequencies and by proper design, a portion of the light is diffracted into the 1^{st} order (m = 1) beam while the rest (0^{th} order beam) passes through the glass; see Fig. 2.

$$\sin\theta = \frac{m\lambda}{2v} \qquad (1)$$

A photograph and schematic diagram of the AOM DMI setup are provided in Fig. 3. In Fig 3(b), a single frequency laser is used as the light source rather than the two frequency source applied in polarization dependent configurations. The beam passes through the first acousto-optic modulator (AOM1). Setting the angle of AOM1 (f_1 driving frequency) to the incident beam as shown in Eq. 1 produces the 0^{th} order and 1^{st} order beams. The frequency of the 0^{th} order beam is simply the optical frequency, f_o, while the 1^{st} order beam frequency is $f_o + f_1$. The 0^{th} order beam continues toward the second acousto-optic modulator (AOM2), which is driven at frequency f_2, while the 1^{st} order beam is directed toward the fixed retroreflector for the measurement signal and one of the two retroreflectors for the reference signal. The 0^{th} order beam from AOM1 passes through AOM2. The 1^{st} order (diffracted) beam from AOM2 with a frequency of $f_o + f_2$ is directed toward the moving retroreflector and the second retroreflector for the reference signal. Both the 1^{st} order beams from AOM1 and AOM2 are retroreflected and recombined at AOM1 (i.e., it functions essentially as a beamsplitter). The reference and measurement interference signals, with a beat frequency equal to two times the difference between the two AOM (user selected) driving frequencies, are collected using two photodetectors with fiber optic pickups. The reader may note that the angle of 1^{st} order diffracted beam in Fig. 3(b) is exaggerated. Sufficient distance is needed for the beams from the AOMs to be separated and directed onto each retroreflector due to the small diffraction angle from the AOMs (approximately 7 mrad or 0.4 deg).

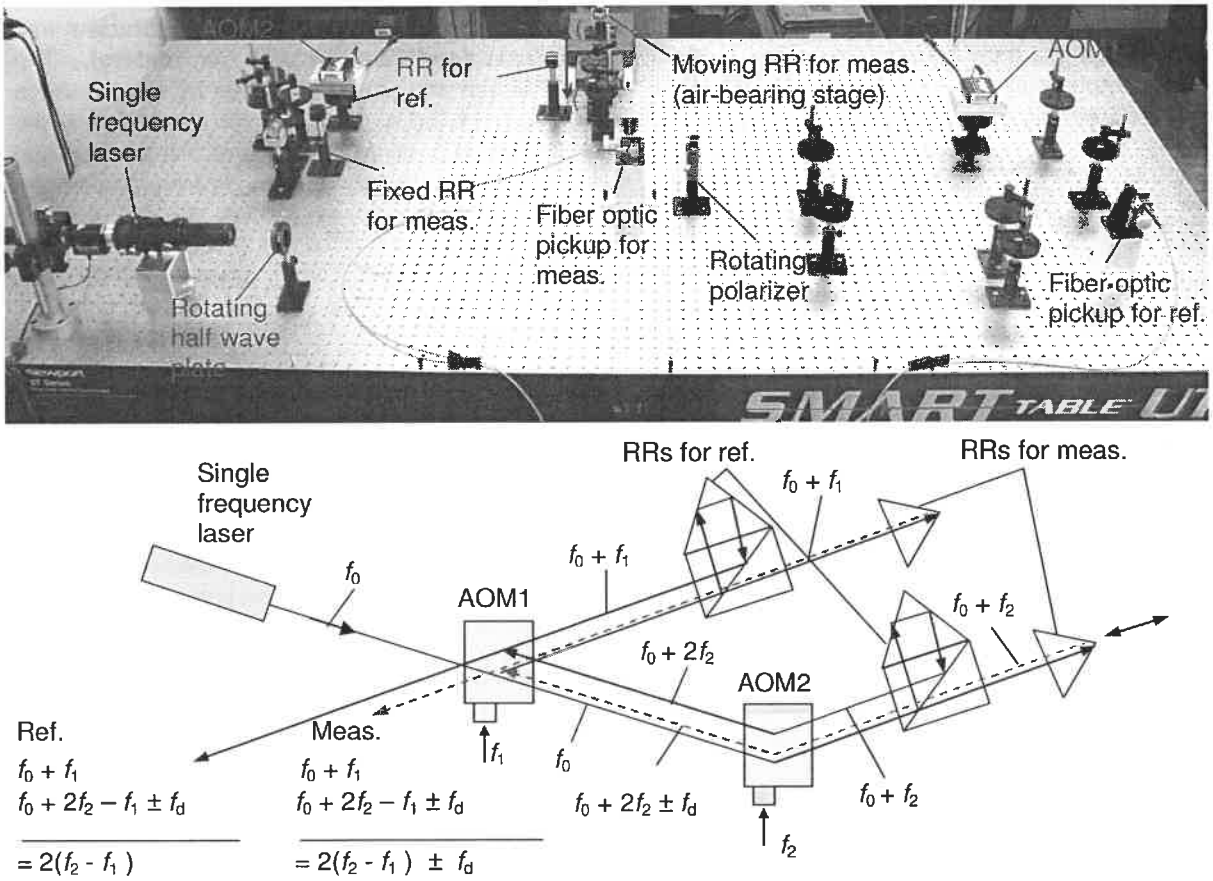

FIGURE 3. (a) Experimental setup of heterodyne interferometer using acousto-optic modulators to spatially separate the beams. (b) Schematic of acousto-optic modulator based interferometer showing the beam separation and combination at each AOM.(RR is used to abbreviate retroreflector.)

EXPERIMENTAL RESULTS

In this section, the frequency content of interference signals from the AOM DMI (collected using a spectrum analyzer) is presented. The undesired interference terms, which cause periodic error, are not observed in the spectrum. Data was collected while the target displaced in the +x direction (see Fig. 3(a)). The beat frequency for a first alignment was 3.64 MHz; it was obtained by setting f_1 to 40 MHz and f_2 to 41.82 MHz. Figures 4 shows the frequency content for the velocities of 10,000 mm/min. The corresponding Doppler shift is 0.53 MHz. It is seen that only the desired *ac interference* signal (3.64 + 0.53) MHz and *dc power* peak are present with no content at the *ac reference* signal (first order periodic error) frequency of 3.64 MHz or the leakage induced *ac interference* signal (second order periodic error) frequency of (3.64 – 0.53) MHz.

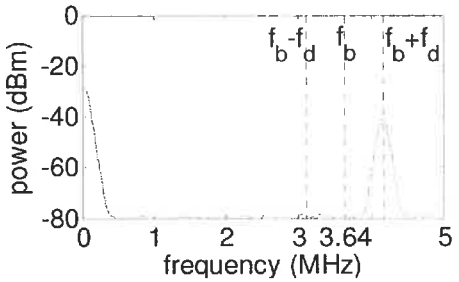

FIGURE 4. Desired ac interference term and dc peak for 10,000 mm/min (f_d = 0.53 MHz). No other content is present.

In Fig. 5(a), spectra for a single target velocity (10,000 mm/min) for various linear polarizer angles are shown. Again, unwanted interference signals are not present for any angular orientation. The test results from a polarization-coded interferometer for the same test conditions are provided in Fig. 5(b) for comparison purposes. It is seen that both first and second order periodic error are present.

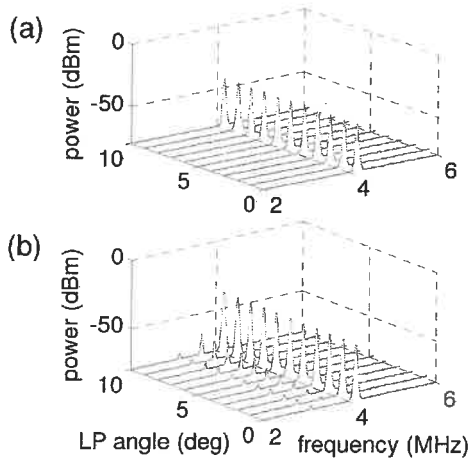

FIGURE 5. (a) No undesired frequency content for the AOM DMI with linear polarizer (LP) angle variation. (b) The leakage induced interference terms accompany the desired ac interference signal for the traditional DMI with the same test setup as the AOM DMI.

One of the advantages in the new design of the interferometer is the ability to tune the beat frequency by adjusting the driving frequency for the two acousto-optic modulators. This makes the new design compatible with existing phase measuring hardware/software independent of the system specific beat frequency. To demonstrate the variable beat frequency capability, the driving frequency for AOM2 was modified to f_2 = 42.5 MHz, while f_1 was maintained at 40 MHz. This gave a new beat frequency of f_b = 5 MHz. Figure 6 shows the spectra for this new configuration at target velocities of 10,000 mm/min. No periodic error content is observed.

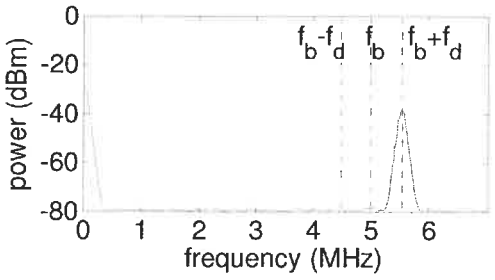

FIGURE 6. Result for new beat frequency of 5 MHz. No periodic error frequency content is observed for target velocity of 10,000 mm/min (f_d = 0.53 MHz).

CONCLUSIONS

This study demonstrated a new displacement measuring interferometer configuration that exhibits no periodic error. Experimental results were presented for two arrangements of the new design, which showed the capability to arbitrarily set the beat frequency. Spectral content was collected using a spectrum analyzer to verify zero periodic error. These results were compared to data obtained from a traditional polarization-coded heterodyne interferometer.

ACKNOWLEGEMENTS

This work was supported by the National Science Foundation (DMI-0555645) and Agilent Technologies, Inc. Any opinions, findings, and conclusions or recommendations expressed in this material are those of the authors and do not necessarily reflect the views of these agencies.

REFERENCES

[1] Quenelle R. Nonlinearity in interferometric measurements. Hewlett-Packard Journal 1983; 34(4):10.

[2] Badami V, Patterson S. A frequency domain method for the measurement of nonlinearity in heterodyne interferometry. Precision Engineering 2000; 24(1):41-49.

[3] Cosijns S, Haitjema H, Schellekens P. Modeling and verifying non-linearities in heterodyne displacement interferometry. Precision Engineering 2002; 26:448-455.

[4] Stone J, Howard L. A simple technique for observing periodic nonlinearities in Michelson interferometers. Precision Engineering 1998; 22(4):220-232.

[5] Patterson S, Beckwith J. Reduction of systematic errors in heterodyne interferometric displacement measurement, In: Proceedings of the 8th International Precision Engineering Seminar (IPES), Compiegne, France, 1995. pp. 101-104.

[6] Tanaka M, Yamagami T, Nakayama K. Linear interpolation of periodic error in a heterodyne laser interferometer at subnanometer levels. IEEE Transactions on Instrumentation and Measurement 1989; 38(2):552-554.

[7] Wu C, Lawall J, Deslattes R. Heterodyne interferometer with subatomic periodic nonlinearity. Applied Optics 1999; 38(19):4089-4094.

[8] Schmitz T, Beckwith J. An investigation of two unexplored periodic error sources in differential-path interferometry. Precision Engineering 2002; 27(3):311-322.

UNCERTAINTY CONSIDERATIONS FOR INTERFEROMETRIC STABILITY TESTING

Jonathan Ellis[1], Ki-Nam Joo[1], Ad Verlaan[2], Jo Spronck[1], and Rob Munnig Schmidt[1]
[1]PME: Mechatronics, Delft University of Technology, Delft, The Netherlands
[2]Optics Division, TNO Science and Industry, Delft, The Netherlands

BACKGROUND

Material stability is an important parameter for EUV lithography, space instrumentation, and metrology in general. In both EUV lithography and space, more information is needed about material stability during an atmospheric to vacuum transition. For metrology instruments in general, determining the causes of drift, as well as the most stable materials is becoming more critical as uncertainty decreases. A measurement system with high resolution and low measurement uncertainty is required for the investigation into material stability. We are investigating an instrument that can measure the length change of a 50 mm long sample with a 10 pm (k=2) measurement uncertainty for 10 minute measurements and 100 pm (k=2) uncertainty for four week measurements. Here, we present an investigation of the uncertainty contributors of this instrument and design considerations for two balanced interferometers to measure material stability.

DOUBLE PASS INTERFEROMETER

For this research, we are focused on interferometers which measure both sides of the sample. There are several instruments that measure from one side (e.g., [1],[2]), but these designs introduce additional uncertainty sources from mounting and reference plate characterization. The first interferometer that was investigated during this research was a double-pass, double-sided design [3]. Improvements to this interferometer were made, specifically placing the reference beam inside the interferometer, as shown in Figure 1. For a description of the unmodified interferometer, see Ref. 3.

There are a total of four beams in this interferometer, where one pair measures the sample and the other pair measures the deadpath. This interferometer has an optical resolution of $\lambda/4$ and the only optical path difference is the sample. By measuring the deadpath, it is possible to compensate some errors common to both the sample measurement and the deadpath measurement.

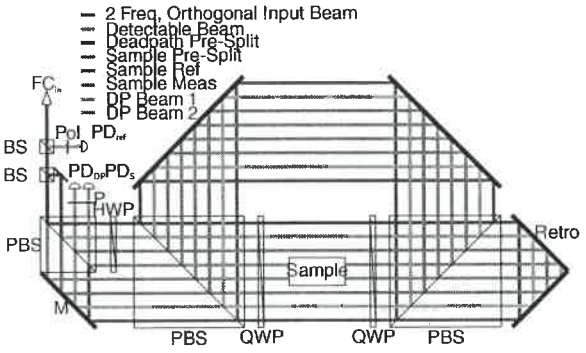

FIGURE 1. Double-pass, double sided interferometer for measuring sample length changes.

A Jones matrix analysis of the double-pass interferometer showed that the effects of polarization mixing are approximately 50 pm because the sample-measuring reference beam polarization effects are completely compensated by the deadpath measurement. This is a significant improvement over standard Michelson interferometer designs because the sample drift is not predictable, and thus, cannot be corrected using a signal processing technique [4]. For a full fringe cycle (158 nm), the periodic nonlinearity is estimated to be 50 pm, which means the sample length change due to temperature must be kept under 3 nm, for a 1 pm error. For a 50 mm long aluminum sample with a high CTE, the resulting temperature control would need to be less than 3 mK to reach this target.

In addition to reducing the errors of polarization mixing, referencing with respect to the deadpath also reduces some of the geometrical instability effects. For instance, when using an external reference, the sensitivity of the first polarizing beam splitter (left side in Figure 1) for measurement error is 45 nm per μrad. However, by measuring the deadpath, this sensitivity is lowered to 30 nm per μrad. The reason for these large sensitivities is due to the long optical path length in the interferometer which magnifies small errors. Additionally, a tilt of 1 μrad of one side of the sample results in a 30 nm error at the detector. However, for a

5 mm beam separation, a 1 μrad tilt is the same as a translation of 5 nm. Therefore, a sample tilting effect is not only indistinguishable from a sample length change, but the effect is magnified six times as well.

SINGLE PASS INTERFEROMETER

Distinguishing sample tilting from sample length change is an important aspect in determining material stability. For instance, one single crystal material may drift differently along one axis than another due to its crystalline orientation. Additionally, some of the manufacturing and stability tolerances for the double-pass interferometer described above were deemed unattainable. Therefore, a more compact interferometer was sought which would be able to distinguish between sample tilt and sample length change, have lower sensitivity to geometrical errors and remain optically balanced.

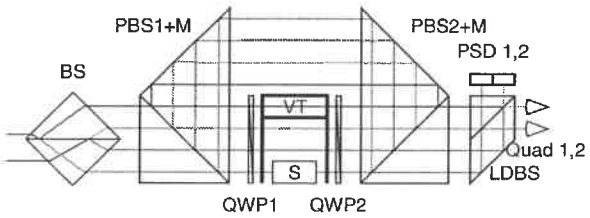

FIGURE 2. Single-pass, double sided interferometer for measuring sample (S) length changes. The input beams have a frequency offset but are the same polarization state. The vacuum tube (VT) has extended flanges to keep the paths comman between all 4 beams. The beams are combined on a lateral displacement beam splitter (LDBS). Measurement is done by 2 position sensing detectors (PSD) and 2 quadrant detectors (Quad).

Figure 2 shows a schematic of the new balanced, single pass interferometer for measuring both sides of a sample. Two input beams with a frequency offset and vertically polarized are passed through a beam splitter turned 45°. The middle two beams pass through PBS1, both QWPs, and then reflect off of PBS2. Both beams then reflect off of the two top mirrors and PBS1, pass through the QWPs a second time and then transmit through PBS2. Both signals then traverse to a lateral displacment beam splitter (LDBS) where they are combined with the sample and vacuum tube signals. These two signals are the reference signals for the deadpath and sample measurements. The top input beam follows the same exact path as the reference signals except it passes through a vacuum tube twice, creating an OPD as a function of refractive index difference between it and its reference.

The bottom signal passes through PBS1 and QWP1 to reflect off of the sample. It then passes through QWP1 again, reflects off PBS1, both top mirrors and then PBS2. It then passes through QWP2, reflects off the sample's right side, passes through QWP2 and PBS2, to be recombined on the NLBS.

This interferometer differs slightly from the double pass arrangement because the sample measuring interference signal has a beam that reflects off one extra mirror. However, this is symmetric between the sample interference signal and the reference interference signal, thus the beam paths are common between sample and reference beams. Another benefit of this layout is the addition of a vacuum tube in one arm of the reference signal which means the reference signal effectively tracks the refractive index changes.

The combining element in the single pass interferometer is a neutral beam splitter, which means it generates two equal signals for each measurement, 90° out of phase from each other. Two different types of detectors to are used measure not only the OPD, but also the angular and lateral changes, as well as the overlap change. A position sensing detector (PSD) can be used to measure the lateral displacements and the beam overlap, while the quadrant detector on the other beam can measure the OPD and the angular changes. By measuring these seven different aspects for both the sample and the deadpath signals, it should be possible to distinguish interferometer motions from sample changes. For instance, if one sample surface tilts, it not only causes a change in OPD, but also changes the lateral, overlap, and angular errors at the detectors. A decoupling algorithm is needed to distinguish sample motions from interferometer motion which needs to be investigated further.

PRELIMINARY UNCERTAINTY ANALYSIS

Because the interferometer is balanced, the sample measurement phase difference is

$$\phi_s = \frac{2\pi N x \eta f}{c}, \qquad (1)$$

where ϕ_s is the sample measurement phase, N is the interferometer constant, x is the length difference between the sample measurement and reference beams, η is the refractive index, f is the frequency of the light used, and c is the speed of light [299792458 m·s^{-1}]. After taking the time derivative, $d\phi/dt$, and assuming a constant, discrete sampling interval, the length change between sample measurement and reference beams is

$$\Delta x = \frac{c\Delta\phi}{2\pi N\eta f} - \frac{x\Delta f}{f} - \frac{x\Delta\eta}{\eta}. \quad (2)$$

The measured length change is a sum of correctable effects and drift. The correctable effects are dominated by thermal effects, and to a lesser extent, pressure fluctuations. The length change is corrected by

$$\Delta x_c = \alpha x\Delta T - \frac{3x\left(1-2\nu\right)\Delta P}{E}, \quad (3)$$

where α is the material thermal expansion coefficient, x is the nominal sample length, ΔT is the temperature change, ν is Poisson's ratio, ΔP is the pressure change, and E is the material elastic modulus. Equation 3 assumes a first-order correction for both temperature and pressure fluctuations. Therefore, Equations 2 and 3 can be combined to determine the sample drift by

$$\begin{aligned}\Delta x_{\text{drift}} &= \frac{c\Delta\phi}{2\pi N\eta f} - \frac{x\Delta f}{f} - \frac{x\Delta\eta}{\eta} \\ &\quad -\alpha x\Delta T + \frac{3x\left(1-2\nu\right)\Delta P}{E}.\end{aligned} \quad (4)$$

A first order, expanded uncertainty was used to determine the measured length change uncertainty. This assumption is somewhat incorrect because temperature and pressure changes couple with the refractive index uncertainty, but the refractive index is measured using the reference signal, separately from the temperature and pressure measurements. This can reduce the uncertainty in the measured refractive index changes because the systematic effects from the modified Edlén formula are removed [5]. Additionally, the refractive index measurement is directly coupled with the sample measurement, which eliminates the need for a correlation coefficient when expanding the uncertainty.

If a stabilized laser is used, the largest uncertainty contributors are from the refractive index and temperature change uncertainties. The refractive index uncertainty needs to be better than 2×10^{-11} for a 1 pm uncertainty, while the temperature change needs to be less than 5 mK for most samples. Both uncertainties are a function of sample length, which means larger samples will have a higher uncertainty and certain materials may have a higher uncertainty because their CTE is higher.

The phase measurement and thermal expansion coefficient are the next two largest uncertainty sources. For materials used in precision instruments, the material properties are often known with a much lower uncertainty than with standard materials. Typically a CTE uncertainty of 0.01% is needed and the phase uncertainty must be lower 0.001° for 1 pm of uncertainty.

Essentially, the entire measurement uncertainty is dependent on the measurement environment, where the material properties of the sample and interferometer are scaling factors. Even the measured phase uncertainty is dependent on the environmental conditions because less environmental control will lead to higher gradients, which reduces the stability of the individual interferometer components. Also, higher rates of thermal and pressure fluctuations lead to faster rates of sample length changes, which sets the required measurement bandwidth.

REFRACTIVE INDEX MEASUREMENT

As stated previously, the reference signal effectively measures the refractive index changes, eliminating the systematic uncertainties from using the modified Edlén equation. Also, it is beneficial to have the refractive index changes measured concurrently with the sample in the same interferometer because the sample and reference measurements are directly correlated. The phase from the reference signal is

$$\phi_r = \frac{2\pi NL\left(\eta-1\right)f}{c} \quad (5)$$

where ϕ_r is the measured reference phase, and L is the vacuum tube length. Provided the walls on the vacuum tube are extended through the three other beams, the interferometer still remains balanced. After taking the time derivative, assuming a constant sampling interval, and correcting for thermal and pressure fluctuations, the measured refractive index change is

$$\begin{aligned}\Delta\eta &= \frac{c\Delta\phi}{2\pi NLf} - \frac{\left(\eta-1\right)\Delta f}{f} \\ &\quad -\left(\eta-1\right)\left(\alpha\Delta T - \frac{3\left(1-2\nu\right)\Delta P}{E}\right)\end{aligned} \quad (6)$$

After performing a first-order uncertainty expansion, the two largest uncertainty contributors are from the phase measurement (1.8×10^{-12}) and from the temperature measurement (1.6×10^{-12}). This assumes a phase uncertainty of 3.5 μrad, and a temperature uncertainty of 0.5 mK for a 75 mm long, glass vacuum tube. This is almost a factor of 10 better than the required 2×10^{-11} refractive index change uncertainty.

PRELIMINARY MEASUREMENTS

The interferometer was setup on a standard optical bench using a Zygo 2/20 Axiom laser head with a 20 MHz split frequency. The two different frequencies were separated using a PBS, half wave plate, and two mirrors. The optical layout is then similar to Figure 2 where the two input beams have a frequency offset and the same polarization state. The measured sample is a 1 mm thick glass sheet with an 86 nm thick aluminum coating on one surface which is reflective on both sides. This coating only partially covers the glass sheet, allowing the other three beams to pass through unobstructed. The 20 MHz measurement and reference signals were detected using 150 MHz detectors, which were then mixed with a common, 19.9995 MHz source to produce a 500 Hz beat frequency. Both signals are then filtered through 1 kHz, 4-pole Butterworth filter and then amplified. An analog lock-in amplifier (1 Hz time constant) was then used to detect the relative phase between the two signals. Figure 3 shows a 16 hour measurement of the "zero"-length sample, sampling at 20 Hz using a 12-bit data acquisition board.

The system was partially shielded from air currents and the temperature near the "zero"-length sample was also measured (right axis in Fig. 3). The results showed the temperature was nominally constant (75 mK, 1σ) within a range of 0.5 K, while the measured signal drifted approximately 80 nm at a fairly constant rate. From this measurement, it is unclear whether the sample signal or the deadpath signal is causing the drift. However, the air pressure and humidity were not monitored and may contribute to some of this error. Additional sources of error also include the drift in the electronics from mixing, filtering, and amplifying.

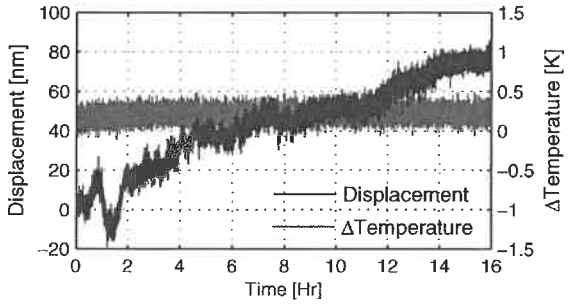

FIGURE 3. Measurement of a 86 nm thin film aluminum sample for 16 hours.

ADDITIONAL WORK

From Figure 3, it is clear that the sample signal and deadpath signal should be measured with respect to an external reference, to isolate the source of the drift. Additionally, the system will be housed in an environmental chamber which will keep the temperature and pressure much more constant than in the current laboratory environment. Lastly, the multi-attribute detection needs to be investigated further to determine a decoupling algorithm for interferometer errors versus sample drift.

ACKNOWLEDGEMENTS

The authors would like to thank the Dutch IOP (project IPT06104) for supporting this research. The authors would like to thank Dr. Eric Buice for valuable discussions regarding this research.

REFERENCES

[1] Okaji M, Yamada N, Nara K, Kato H. Laser interferometric dilatometer at low temperatures: application to fused silica SRM 739. Cryogenics. 1995;35:887–891.

[2] Schödel R, Bönsch G. Highest-Accuracy Interferometer Alignment by Retroreflection Scanning. Appl Opt. 2004;43(31):5738–5743.

[3] Ren D, Lawton K, Miller J. A double-pass interferometer for measurement of dimensional changes. Meas Sci Technol. 2008;19:1–4.

[4] Schmitz T, Chu D, Houck III L. First-order periodic error correction: validation for constant and non-constant velocities with variable error magnitudes. Meas Sci Technol. 2006;17:31953203.

[5] Birch KP, Downs MJ. An Updated Edlén Equation for the Refractive Index of Air. Metrologia. 1993;30:155–162.

MEASUREMENT OF THE ABSOLUTE DISTANCE BETWEEN TWO PARTIALLY REFLECTIVE SURFACES

Vivek G. Badami, Leslie L. Deck, and Lars A. Selberg
Zygo Corporation
Middlefield, CT, USA

INTRODUCTION

The absolute distance between two surfaces is a parameter of interest in many applications. Examples include wavelength standards, etalons, gage block calibrations, the measurement of sphere diameters, etc. Many interferometric techniques exist for making such a measurement. Of these, the highest precision methods that do not involve modifications to the surfaces are based on the method of exact fractions [1] and wavelength tuning [2]. The former method is limited due to the phase resolution attainable from analysis of a static fringe pattern, while the latter technique requires a wide tuning range to measure relatively small separations (of the order of a few mm).

This paper describes an interferometric technique for measuring the separation between two plane-parallel, uncoated, dielectric surfaces with separations of a few mm. This technique is similar to the one described by Coppola et al [3], but differs from it in some significant respects. A description of the method is provided along with an uncertainty analysis that supports the techniques' potential to perform measurements with sub-nm uncertainty. Preliminary experimental results are also included.

THE MEASURAND

The objective of the measurement is to determine the absolute separation between two plane surfaces. An assembly of the type used in the measurements described here is shown in Figure 1, and is comprised of two wedged optical flats assembled with an intervening annular spacer to form a rigid assembly. The measurand is the separation between the two inner surfaces denoted by d in the figure and is hereafter referred to as the gap.

MEASUREMENT PRINCIPLE

The method is based on the change in the optical path difference (OPD) between the beams reflected from the two surfaces of the sample due to physical rotation (in the direction shown in Figure 1), which for a given rotation angle is a function of d.

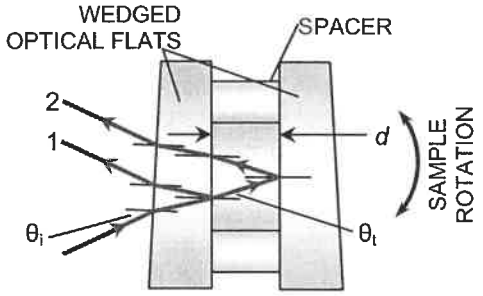

FIGURE 1. Interference between reflections from the two surfaces of the sample.

This dependence of the OPD between the beams (beams 1 & 2) reflected from the two surfaces of the plane-parallel transparent region (bounded by the wedged optical flats and depicted in Figure 1) on the transmitted angle θ_t is given by $2ndcos\theta_t$, where n is the refractive index of the medium and θ_t is in turn a function of the angle of incidence θ_i. The change in OPD causes an intensity variation due to interference between the reflected beams. Therefore, the gap may be extracted from knowledge of the rotation angle and the corresponding intensity variation.

EXPERIMENTAL SETUP & PROCEDURE

A schematic of the experimental setup is shown in Figure 2. All adjustments and motions are relative to the coordinate system shown. The axis of rotation is assumed to be coincident with the z axis, while the y axis is coincident with the input beam from the laser.

The artifact or sample to be measured is mounted via a six degree-of-freedom (6DOF) adjustment (not shown) to a high-accuracy rotary stage, positioned so the gap is over the center of rotation. The laser beam used to interrogate the sample originates from a frequency stabilized laser of known wavelength. The beam passes through an uncoated wedged plate beamsplitter (B/S) before entering the

artifact. The surface of the B/S closest to the sample serves as the splitting surface. The

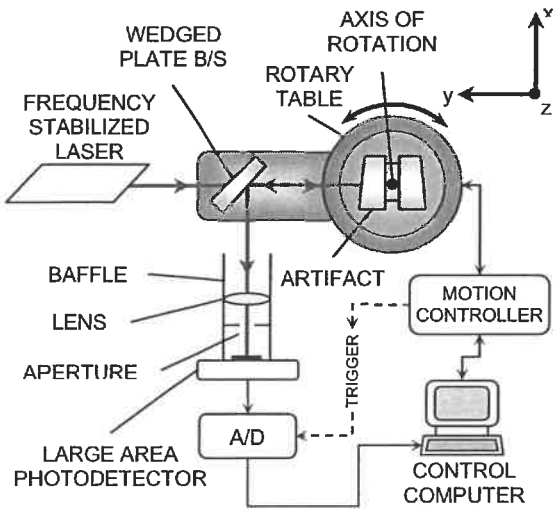

FIGURE 2. Schematic of experimental setup.

wedge in the B/S and the wedged optical flats of the sample prevent spurious reflections. The reflected beams from the two surfaces of interest of the artifact are reflected by the B/S and enter the detector assembly. The beam passes through a baffle and is then incident on a lens, the focus of which is located in the plane of a variable aperture (iris diaphragm). The beam passes through the aperture and strikes a large-area photodetector. The aperture and the baffle work to minimize stray light. Note that the signal from the artifact is monitored in reflection, rather than in transmission as in the technique described by Coppola et al [3]. The arrangement described here provides a much higher S/N ratio as there is no DC light intensity in the measured signal.

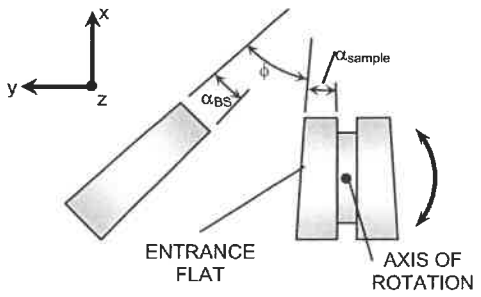

FIGURE 3. Wedge and relative orientation angles.

Alignments

Several critical alignments & measurements are performed during setup. These include aligning the plane of the wedge of the entrance flat of the sample and B/S to the plane of rotation, positioning the center of the spacer over the center of rotation and establishing the nominal 'zero' position of the rotary stage. The latter corresponds to the situation where the input beam is normal to the surface(s) of interest. Several angles are required as inputs to the mathematical model of the system in addition to the rotary stage angle. The wedge angles of the B/S and the entrance flat of the sample (α_{BS} and α_{sample} in Figure 3) are measured along with the angle that establishes the relationship between the B/S and the entrance flat of the sample (ϕ in Figure 3). These angles are used to compute the angle of incidence at the gap as a function of stage rotation.

The sample is rotated about the z axis by the rotary stage under computer control. The output of the detector is digitized and the data acquisition is triggered by pulses from the rotary stage encoder, thus rendering data collection immune to variations in stage velocity. This also permits registration of successive runs.

A typical measurement commences by driving the stage to one end of the desired travel. The stage is then rotated through the desired travel while the voltage from the detector is recorded simultaneously and synchronously with the stage position. This is designated as one scan. The stage then returns to its start position before starting the next scan. Any given measurement is comprised of five such scans which are then averaged. Typical rotations are ±5° about the zero position at a scan speed of 1°/sec.

UNCERTAINTY ANALYSIS

This uncertainty analysis is based on a Monte Carlo simulation and is performed in accordance with the methodology outlined in Supplement 1 [4] to the ISO Guide to the Expression of Uncertainty in Measurement (GUM) [5]. The influence quantities, their respective uncertainties and their contributions are listed in Table 1. All contributing distributions are assumed to be uniform distributions. The analysis generates a simulated intensity trace as a function of angle. This simulated data is then subjected to the same fitting procedure used to process the real data while the input parameters to the fitting function are varied in accordance with the distributions assigned to each parameter.

The significant contributors are the uncertainties in index of air in the gap, the measurement of the rotation angle, measurement of α_{BS} and the

wavelength. The uncertainty in the index of air in the gap is derived from uncertainties in measuring temperature and pressure of 0.1°C and 1 mm Hg respectively. The uncertainty in the measurement of rotation angle is derived from the stage manufacturer's specification. The wavelength is measured by beating the laser against an iodine stabilized laser (measurement uncertainty of 2.5×10^{-11}) and the uncertainty is derived from the specification on the tolerances on the components of the control loop used to stabilize the frequency. Uncertainties in the index of the various fused silica optical flats are based on the variability in the index as reported by Malitson [6]. Uncertainty estimates for angle measurements are based on what is easily achievable with the equipment at hand.

TABLE 1. Influence quantities and contributions for a 1.5 mm gap. Uncertainties values listed are the half-widths of uniform distributions.

Influence Quantity	Uncertainty	Contribution (pm)
Index of air in gap	0.18 ppm	155
Rotation angle	3.6 arcsec	60.4
α_{BS}	10 arc sec	52.4
Wavelength	0.05 ppm	43.3
α_{sample}	10 arcsec	31.4
Measured intensity	1%	11
ϕ	10 arcsec	2.65
Index of B/S	10 ppm	0.45
Ambient air index	5 ppm	0.24
Index of entrance flat	10 ppm	0.03
Expanded uncertainty (k=2)		353.9

The contribution from the uncertainty associated with the index of air in the gap dominates the resulting expanded uncertainty (k=2) of ~354 pm.

DATA PROCESSING

The data reduction process consists of performing a nonlinear least-squares fit to the measured intensity, with the rotation angle as an independent parameter and the gap as a free parameter. The model function for the fit requires the critical angles shown in Figure 3, the vacuum wavelength, the refractive indices of the entrance flat of the sample and B/S, and the polarization direction. Snell's law and Fresnel's equations are then used to calculate the optical paths lengths and reflection coefficients, respectively, of the two reflected beams to compute the expected interference pattern as a function of beam launch angle at the B/S and the gap. The square of the residual to the fit is used as a merit function for the fitting routine. Excellent agreement was observed between the data and the fit (Figure 4).

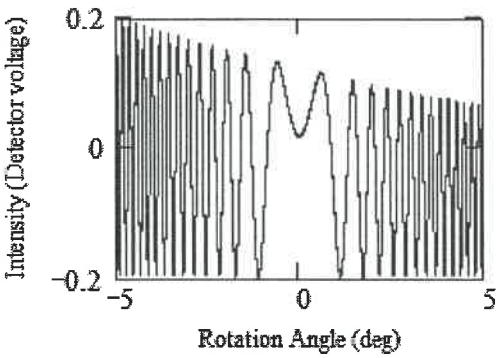

FIGURE 4. Comparison of measured and fit intensities.

The fringe order is calculated from an *a priori* estimate of the gap (uncertainty ~50 nm) based on measurements of the gage blocks used as spacers in the artifact (see next section), and the method is used to determine only the fringe fraction. The merit function has a well defined minimum which is used to compute the fringe fraction. This fringe fraction and fringe order values are combined to calculate the gap. The technique has the potential to also determine the fringe order. This will be validated in future work.

TABLE 2. Measurement results.

Gap	Cal. Value	Meas. Value.	Δ	σ
	(μm)	(μm)	(nm)	(nm)
R1	1270.0121	1270.0216	9.55	0.22
R2	1778.0254	1778.0461	20.65	0.36
RN	1500.0000	1500.1058	105.82	0.10

EXPERIMENTAL RESULTS

The method was tested on three samples, two of which were constructed with Starrett® square croblox® gage blocks (0.050" & 0.070") as spacers, while the third one was constructed with two closely matched rectangular gage blocks of the same nominal size (1.5 mm) as spacers. The three gaps are designated R1, R2 and RN respectively. In the case of the first two samples, the gap is formed by the space enclosed by the hole in the block and the optical flats and is nominally sealed. In the third case, the two blocks are placed parallel to one another with a space between them. The gap of interest is the separation between the flats in the region between the blocks. The samples are

assembled by a procedure similar to optical contacting and then mounted in spring loaded cells for ease of handling.

The results of the measurements of the physical gap are shown in Table 2. The table lists the calibrated value of the gage block used as the spacer (the average value of the two blocks is listed for RN), the mean measured value of the gap, the deviation of the measured value from the calibrated value Δ, and the standard deviation σ of the five measurements used to compute the mean measured value. The measurements must be compared to the reference values in the context of the uncertainties of the measured values and the calibrated values. The expanded uncertainty (k=2) of the measured value is estimated in an earlier section to be ~0.35 nm. The uncertainty in the reference value of the gap is derived from the uncertainty in the calibrated value of the gage block (~30 nm), and uncertainties associated with the 'film' between the two contacting faces of the block and the flats, and the correction of the calibrated length to the measurement temperature (~2 nm). While the films are assumed to have zero thickness, the uncertainty in this value is assumed to be 25 nm [7] each, which when added in quadrature to the uncertainty in block length results in an expanded uncertainty (k=2) of ~46.5 nm. When viewed in the context of these uncertainties, it can be seen that the measurements for R1 and R2 agree to within this uncertainty. It is also evident that the deviation in the case of RN exceeds the uncertainty in the calibrated value. The discrepancy is believed to arise as consequence of the method of construction of the artifact. This artifact is constructed by sandwiching two rectangular gage blocks placed parallel to one another. Due to the slight difference in the dimensions of the blocks and lack of coplanarity of the contacting faces, it is quite likely that the contact between the flats and the blocks is not as intimate as in the case of the other cavities. It is also possible that the flats are distorted due to the same reasons, with the result that the gap produced does not agree with the dimensions of the spacers. For these reasons, it is probably inappropriate to use the calibrated values of the gage blocks as reference values for RN. The measurements have also proved to be stable over time and a sense for the reproducibility of the measurement can be derived from measurements of the gaps almost six months apart under similar (but not identical) conditions. R1 and R2 show values that agree to within 2 nm over this period. RN, however shows a difference of 12 nm. This instability is probably an indication of lack of stability and marginal quality of the assembly.

CONCLUSION

A method for making absolute distance measurements between two partially reflective, uncoated, plane-parallel surfaces separated by a few mm has been described. The supporting uncertainty analysis suggests that the technique is capable of sub-nm uncertainties. Results of preliminary experiments with well constructed samples show that the results agree to within the uncertainty of the calibrated references. It is also clear that the uncertainties of the reference values used in these measurements is large compared to the estimated uncertainty of the technique and another technique with commensurate uncertainty is required to completely test this technique.

ACKNOWLEDGEMENTS

The authors would like to acknowledge the input and assistance of Dr. Xavier Colonna de Lega, Andrew Stein and Andrew Carlson.

REFERENCES

[1] Tilford CR. Analytical procedure for determining lengths from fractional fringes. Applied Optics. 1977; 16(7): 1857-1860.

[2] Deck L. Absolute distance measurements using FTPSI with a widely tunable IR laser. Proc SPIE. 2002; 4778: 218-226.

[3] Coppola G, Ferraro P, Iodice M, and De Nicola S, inventors; Consiglio Nazionale Delle Ricerche, assignee; Interferometric system for the simultaneous measurement of the index of refraction and of the thickness of transparent materials, and related procedure. United States patent US 7046373, 2006 May 16.

[4] BIPM. Evaluation of measurement data – Supplement 1 to the "Guide to the expression of uncertainty in measurement" – Propagation of distributions using a Monte Carlo method. JCGM 101:2008.

[5] ISO. Guide to the expression of uncertainty in measurement. 1st ed. Geneva: ISO, 1995.

[6] Malitson IH. Interspecimen comparison of the refractive index of fused silica. JOSA. 1965; 55(10): 1205-1209.

[7] Doiron T and Beers JS. Gage Block Handbook. NIST Monograph 180, 2005.

MEASURING MACHINES WITH INTERFEROMETRICAL STYLUS FOR FORM MEASUREMENT OF PRECISE MECHANICAL PARTS

Pawel Drabarek, Tobias Gnausch, Matthias Fleischer
Manufacturing Measurement Systems
Robert Bosch GmbH
Stuttgart, Germany

INTRODUCTION

Today, more than ever, small, precise, mechanical parts such as automotive components containing flat, cylindrical or conical surfaces with form tolerances of less than 1 micrometer are being manufactured in high volumes. Frequently, the 3-D information on entire surfaces is needed to evaluate the correct function of these parts. Tactile systems are usually insufficient for these types of measurements due to the probing force or lengthy measurement times

Figure 1 shows an example of a parallelism measurement on a pin with a 4mm diameter performed with a tactile and non contact optical stylus. The 0.5 gram tactile force caused a parallelism error of 0.8 µm.

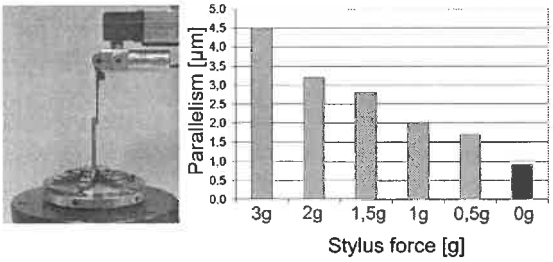

FIGURE 1. This is a typical tactile parallelism measurement of a pin and the resulting measurement error due to the stylus force.

INTERFEROMETRICAL STYLUS SYSTEM

An interferometrical stylus system for form measuring machines which allows form and diameter measurements on precision mechanical parts with tolerances of less than 1µm has been developed, built, tested and already used under shop floor conditions.

The optical system is based on a novel concept of short coherence heterodyne interferometry working with two wavelengths [1]. It is divided into two subsystems: a modulation interferometer and a small, robust optical probe connected through a single monomode optical fiber [2].

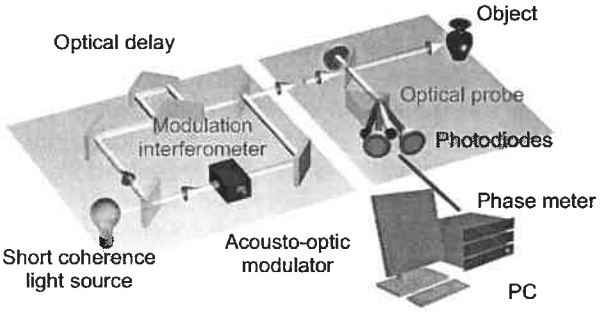

FIGURE 2. Optical scheme of an interferometrical stylus and the technical realization WhitePoint.

The interferometer employs a broadband fiber-optic light source and works at an optical wavelength of 1,55µm and a synthetic wavelength of 36µm.

Under laboratory conditions we achieved distance equivalent noise level of $1\sigma < 1$nm at a sampling frequency of 10kHz. Fig. 3 presents measurement of the distance equivalent noise of an interferometrical stylus and Fig. 4 shows compared distance measurements between an interferometrical stylus and a Polytec Vibrometer.

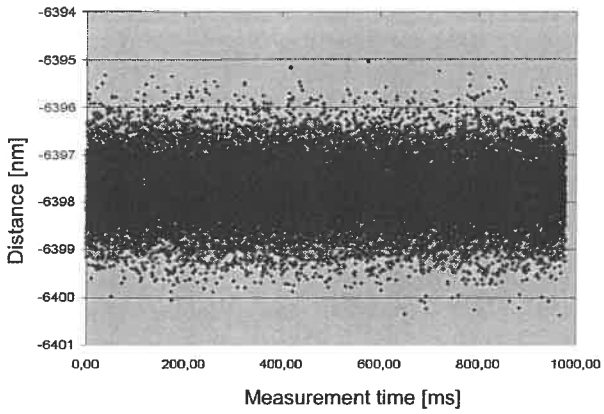

FIGURE 3. Measurement of the distance equivalent noise of an interferometrical stylus.

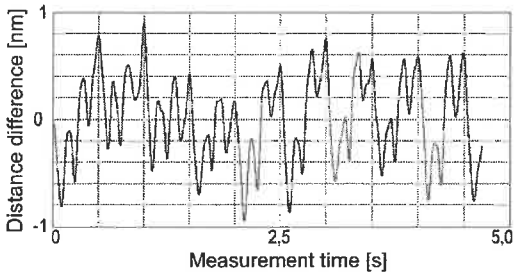

FIGURE 4. Compared distance difference measurement between an interferometrical stylus and a Polytec Vibrometer.

Currently, several custom, application specific, non-contact probes have been developed and built. Fig. 5 shows a fiber probe (microstylus) with a diameter of 35µm and optical probe with a diameter of 1.2mm and two optical outputs for cylinder and cone measurements.

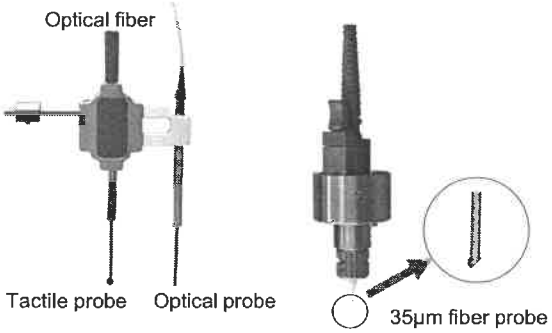

FIGURE 5. Non-contact interferometrical probes. Tactile and interferometrical probe for the MFU110WP form measuring machine, Mahr Company and a fiber probe with a diameter of 35µm for the Altera Nano optical coordinate measuring machine, Mycrona Company.

Furthermore, custom software for post measurement processing and visualization of 3-D interferometrical data has been developed.

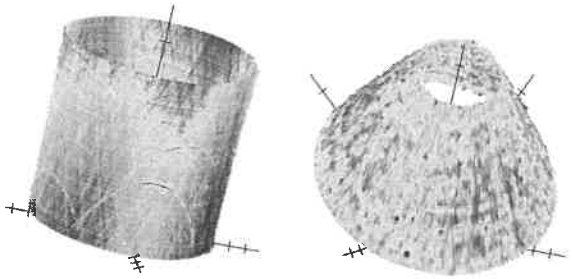

FIGURE 6. Example of 3-D measurements on a very precise cylinder and cone.

MEASURING MACHINES

For fast measurement of high volumes of precision parts, such as automotive parts close to the production line, we have integrated the interferometrical stylus system on to an unrivaled, high speed, rotational measuring machine.

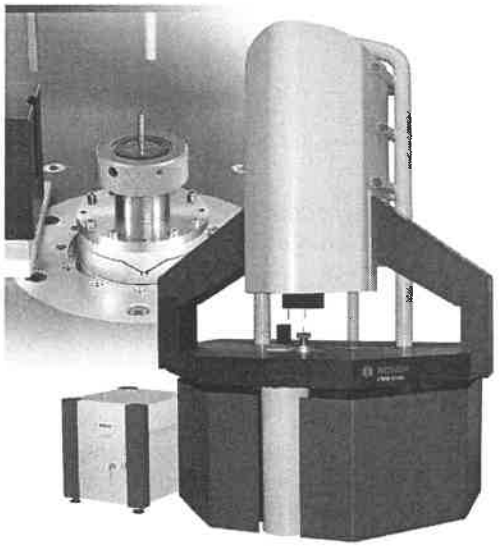

FIGURE 7. High speed rotational measuring machine FMS 1000 from Bosch Company.

The machine uses air bearings for the rotary table (C axis) and translation stage (Z axis). The maximum rotation speed for high precision measurements is 1000 RPM with a maximum error of both axis (roundness and straightness)

of less than 50nm. A typical measurement of a 20mm high cylinder including part fixturing, data acquisition of approximately 300,000 points and calculation of roundness, straightness, parallelism and diameter can be achieved in less than 2 minutes.

For universal applications we have used the form measuring machine type Mahr MFU100 and combined the interferometrical probe with a tactile probe [3].

FIGURE 8. Universal form measuring machine MFU110WP, Mahr Company.

Thus this measuring machine is used for both tactile and optical measurements during one measurement cycle. In order to examine the measuring capability of the system for tolerances smaller than 1µm we developed dedicated processing algorithms and performed a substantial amount of test measurements. A cylinder gage certified by the German National Metrology Institute (PTB) and production parts served as test objects for a %GRR and Cg capability study.

For form and diameter measurement of small, microscopic structures, such as holes with a diameter of 100µm, we have integrated the 35µm fiber probe on to a Mycrona ALTERA Nano optical coordinate measuring machine.

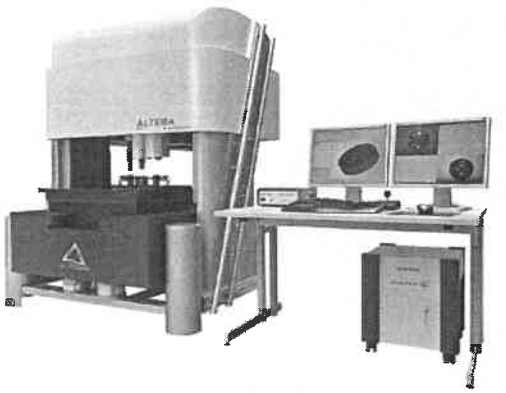

FIGURE 9. Commercial machine Altera Nano, Mycrona Company.

This machine was used to evaluate and create traceability of the patented micro-hole gage developed by the PTB. Results of this measurements are shown on Figs. 10 and 11.

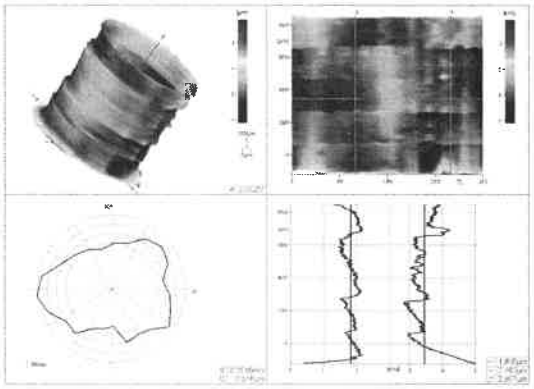

FIGURE 10. Form measurement of micro-hole gage developed by the PTB.

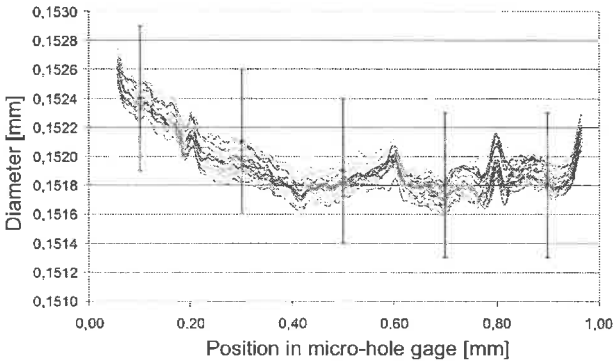

FIGURE 11. Repeatability of a diameter measurement of a PTB micro-hole gage.

CONCL USION

An interferometrical stylus system for form measuring machines which allows form and diameter measurements on precision mechanical parts with tolerances of less than 1µm has been developed, built, tested and already used under shop floor conditions.

The optical system is based on a novel concept of short coherence heterodyne interferometry and achieved distance equivalent noise level of $1\sigma < 1$nm with a sampling frequency of 10kHz.

In order to examine the measuring capability of the system for tolerances smaller than 1µm we developed dedicated process algorithms and performed a substantial amount of test measurements.

The interferometrical stylus is already working in following machines:

- Mahr *MFU100WP* for universal measurements
- Bosch *FMS 1000* for fast measurements near the production line
- Mycrona *ALTERA Nano* for measuring of small structures

Further a special software for post measurement visualization and processing of 3D interfrometrical data has been developed.

REFERENCES

[1] Drabarek P. Interferometric measuring device for determining the profile or the pitch of especially rough surfaces. WO 99/44009 (1999).

[2] Drabarek P, Duvoisin M-H, Marchal D, Thominet V. Modulation Interferometer and fiberoptically divided measuring probe with light guided.

[3] Jusko O, Neugebauer M, Reimann H, Drabarek P, Fleischer M, Gnausch T. Form Measurements by Optical and Tactile Scanning. To be published in Proc. 5th International Symposium on Instrumentation Science and Technology, Shenyang (Mukden), China, 2008.

ABSOLUTE LENGTH (THICKNESS) MEASUREMENTS USING WAVELENGTH SCANNING INTERFEROMETRY

Amit R. Suratkar, Angela D. Davies, and Faramarz Farahi
Department of Physics and Optical Science
Center for Optoelectronics and Optical Communications
Center for Precision Metrology
The University of North Carolina at Charlotte
Charlotte, North Carolina, USA

OVERVIEW

Wavelength scanning interferometry offers a new dimension in precision metrology by measuring the cavity length (thickness), the cavity length variation over the cavity area (flatness), and the optical homogeneity within a transparent cavity; without any mechanical movement by implementing a tunable laser. This property is useful when the physical movement of a large optic is not feasible using traditional phase shifting methods and for characterizing solid optical cavities. The use of Fourier analysis on the intensity (interference) time history as a post processing step enables the measurement of cavity lengths without any 2π phase ambiguity [1,2].

We propose to demonstrate absolute length (thickness) measurements of a transparent planar cavity (thickness of a fused silica window), transparent spherical cavity (diameter of a ball lens), and opaque planar cavity such as the length of a gauge block on a commercial wavelength scanning Fizeau interferometer from Zygo Corporation; the MST (Multiple Surface Transform). A mathematical model of the measurement process is demonstrated along with uncertainty contributions to understand the limits in the system and the technique in general. This is complimented with a software simulation to understand the impact of dynamic parameters such as the tuning rate of the laser on the final measurement [3].

MEASUREMENT TECHNIQUE

The technique of wavelength scanning interferometry for characterizing an optical cavity (Figure 1) involves a) using a tunable source to sweep around a given wavelength range continuously or in stepped mode and b) recording the intensity (interference) pattern on the detector at any pixel.

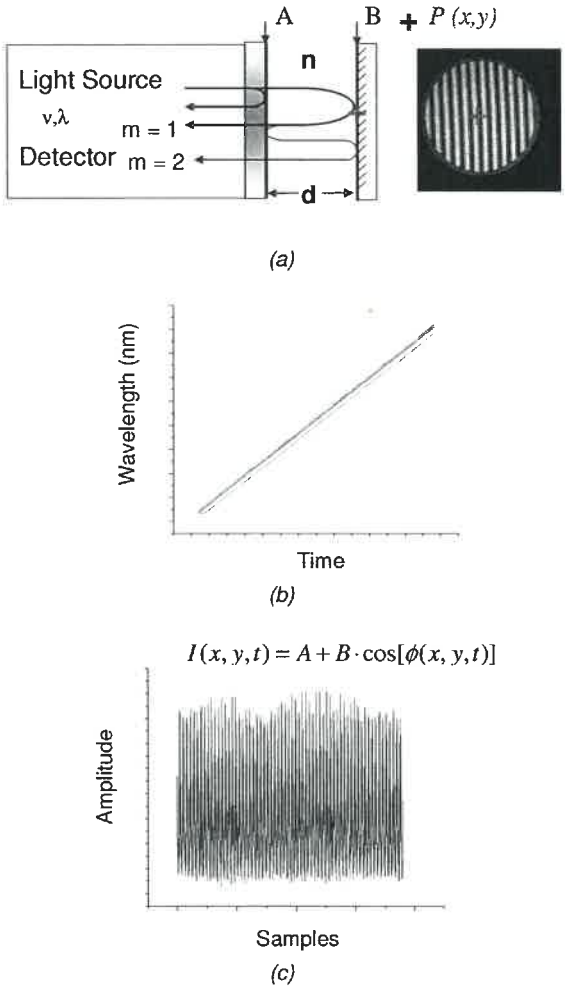

FIGURE 1.a) Interferometric cavity in a Fizeau setup. b) Tuning the laser over a given range. c) Intensity at any point P(x,y) during the laser tune.

As a post processing step, a Fourier transform is implemented which yields the frequencies of the cavities, as given by Figure 2.

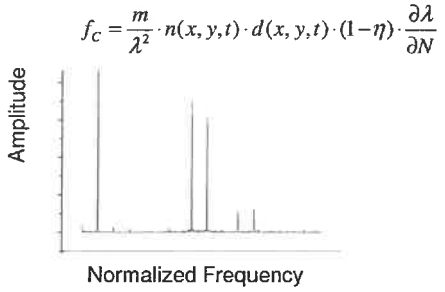

FIGURE 2. A Fourier transform on the intensity yields frequencies corresponding to each cavity length.

During the tune, each cavity resonates with its own frequency, which is characteristic of its optical length, as given by Equation 1.

$$f_C = \frac{m}{\lambda^2} \cdot n(x,y,t) \cdot d(x,y,t) \cdot (1-\eta) \cdot \frac{\partial \lambda}{\partial N} \quad (1)$$

where $\eta = \frac{\lambda}{n} \cdot \frac{\partial n}{\partial \lambda}$ (2)

is the dispersion in the cavity. In order to reduce the non linear effect of tuning, a reference cavity is incorporated so that a given cavity length is measured as a fraction of the reference optical length, the fraction being the ratio of the frequency of the cavity to be measured with the frequency of the reference cavity. The optical path length (OPL) can be measured either using a frequency ratio, using the phase ratio, or a combination of both. In this paper, we discuss the measurements on the MST, which use the frequency of the cavity and the phase of the reference in determining optical cavity lengths, as given by Equation 3 where *C and R* represent cavity and reference, respectively, and *R_calib* represents the calibrated value of the reference cavity.

$$OPL_C = \frac{2 \cdot \pi \cdot f_C}{[\frac{\partial \phi}{\partial N}]_R} \cdot OPL_{R\_calib} \quad (3)$$

The OPL of each cavity in the MST is computed as per Equation 3 and is displayed as the OPL spectrum result, as shown in Figure 3.

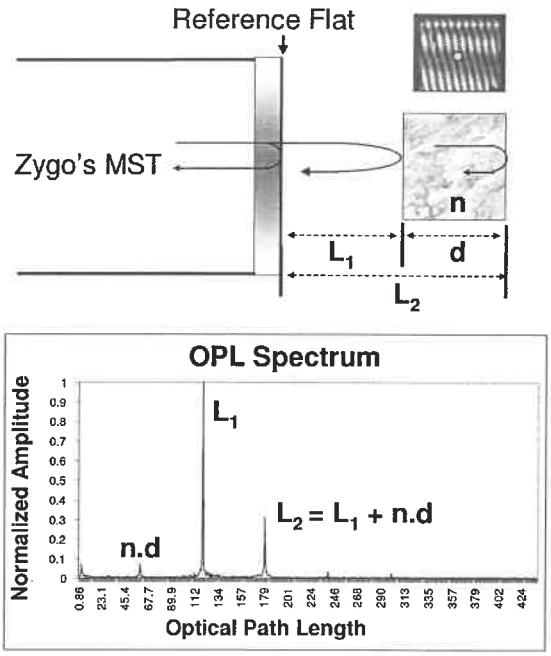

FIGURE 3. OPL Spectrum in the MST.

MODELING

In order to estimate the uncertainty sources, a mathematical model is investigated to understand the effect of different parameters on the length of the test cavity (L_c),

$$L_C = FN(n_C(T), L_C(T), n_R(T), L_R(T), N, \frac{\partial \lambda}{\partial N}) \quad (4)$$

where *T* represents temperature.

In addition to an analytical approach, a simulation of the wavelength scanning process is also performed using the equations for intensity and wavelength in MATLAB®. The wavelength sweeps are modeled by fitting experimental data for wavelength slopes obtained using a wavelength meter. The simulation enables a detailed understanding of the effect of different wavelength sweeps on the repeatability in the measurement.

MEASURING A TRANSPARENT PLANAR CAVITY

A half inch fused silica cavity polished on both sides was measured similar to the setup in Figure 3 for a set of 40 measurements. The estimated value and combined uncertainty for the optical thickness of the cavity is found to be 19.415 mm ± 0.033 mm [3]. The refractive index and dispersion value for fused silica was obtained using Malitson's equation [4]. The

physical thickness of the fused silica cavity was computed to be 13.275 mm ± 0.023 mm which was within the manufacturer's specification of 12.7 mm ± 1.5 mm.

MEASURING A TRANSPARENT SPHERICAL CAVITY

In order to measure the diameter of a fused silica ball lens, we replaced the reference flat, as shown in Figure 3, with a transmission sphere and aligned the spherical ball lens in a confocal position with respect to the transmission sphere.

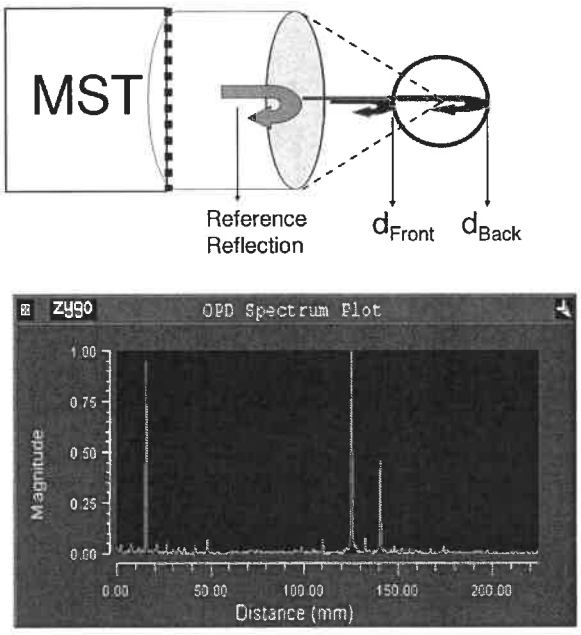

FIGURE 4. Measuring a spherical ball lens using the MST.

The confocal position was realized by minimizing the defocus term in the OPD plot for the first surface of the ball. With this confocal arrangement, the measurement is analogous to Figure 3 where a planar cavity is measured using a planar reference flat, and this is confirmed from the OPD spectrum. The average diameter of the ball lens for ten readings was measured to be 10.001 ± 0.0009 mm and was within the manufacturer's specification of 10.000 mm ± 0.005 mm. The dispersion and refractive index values were computed from Malitson's equation similar to the previous example.

MEASURING AN OPAQUE PLANAR CAVITY

We used a two mirror Sagnac configuration in conjunction with the existing interferometer to measure the length of a gauge block. This is done by measuring cavity lengths at both ends of the gauge block and measuring the length of the empty cavity. The length of the gauge block is then given by a difference between these measurements, as shown in Equation 5.

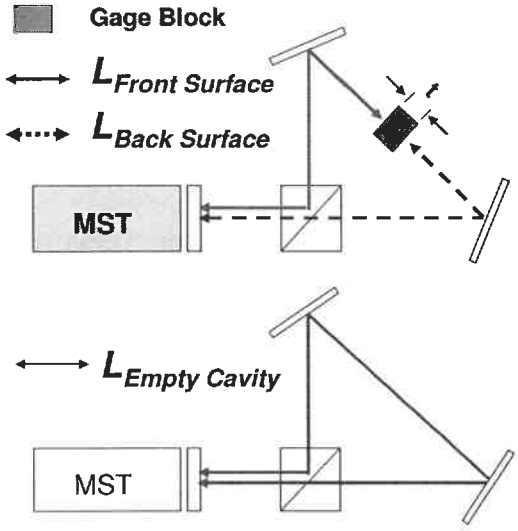

FIGURE 5. Measuring the thickness of a gauge block using the MST and a two mirror Sagnac configuration.

$$t = L_{\text{EmptyCavity}} - (L_{\text{FrontSurface}} + L_{\text{BackSurface}}) \quad (5)$$

Most gauge block measurements are relative; meaning an absolute value estimate of the gauge block is needed a priori to compare with a reference [5-7]. Current techniques include static and multiple wavelength interferometry measurements, phase shifting techniques, and the more recent femtosecond technique. Multiple wavelength interferometry which is the standard technique for measuring relative gauge block lengths has been used to measure the absolute length (thickness) by increasing the number of wavelengths to four instead of the standard three. The uncertainty in the absolute value of a 100 mm gauge block was around 138 microns [8]. The measurement also required a different optics setup for the fourth wavelength, thereby increasing measurement time and uncertainty. By using wavelength scanning on the MST, we approach the measurement of the gauge block by measuring the lengths of the front and back surface of the gauge block in one set of measurements and an empty cavity measurement in another set. For a set of ten measurements, we report the length (thickness)

of a one inch gauge block to 25.40 mm ± 0.01 mm [9].

ACKNOWLEDGEMENTS

This material is based on work supported by the Center for Precision Metrology at UNC Charlotte. The Center for Precision Metrology is a NSF-funded Industry University Cooperative Research Center. Any opinions, findings, and conclusions or recommendations expressed in this material are those of the authors and do not necessarily reflect the views of the National Science Foundation. The authors would like to thank Leslie Deck from Zygo Corporation for helpful insights in the measurement.

REFERENCES

[1] Deck L. Fourier-transform phase-shifting interferometry. Applied Optics. 2003; 42: 2354-2365.

[2] Deck L. Absolute distance measurements using FTPSI with a widely tunable IR laser. Interferometry XI: Applications, Proceedings SPIE. 2002; 4778:218-226.

[3] Suratkar A, Ghim Y, Davies A. Uncertainty analysis on the absolute thickness of a cavity using a commercial wavelength scanning interferometer. Interferometry XIV: Techniques and Analysis, Proceedings SPIE. 2008. (Accepted for publication).

[4] Malitson I. Interspecimen Comparison of the Refractive Index of Fused Silica. Journal of the Optical Society of America. 1965; 55: 1205-1209.

[5] Tsai M, Huang H, Itoh M, Yatagai T. Fractional Fringe Order method using Fourier Analysis for Absolute Measurement of Block Gauge Thickness. Optical Review. 1999; 6: 449-454.

[6] Jin J, Kim Y, Kim Y, Kang C, Kim S. Absolute length calibration of gauge blocks using optical comb of a femtosecond pulse laser, Interferometry XIII: Techniques and Analysis, Proceedings SPIE. 2006; 6292: 1-8.

[7] Kuriyama Y, Yokoyama Y, Ishii Y, Ishikawa J. Development of a New Interferometric Measurement System for Determining the Main Characteristics of Gauge Blocks. Annals of the CIRP. 2006; 55:563- 566.

[8] Decker J, Miles J, Madej A, Siemsen R, Siemsen K, Bonth S, Bustraan K, Temple S, Pekelsky J. Increasing the range of unambiguity in step-height measurement with multiple wavelength interferometry - application to absolute long gauge block measurement. Applied Optics. 2003; 42: 5670-5678.

[9] Suratkar A, Davies A, Farahi F. New interferometric technique to measure the length (thickness) of opaque objects using a commercial interferometer. Optical Manufacturing and Testing VII, Proceedings SPIE. 2007; 6671: 1-10.

PARALLEL-KINEMATICS MEMS STAGES FOR HIGH PRECISION NANOPOSITIONING AND MANIPULATION

Jingyan Dong, Deepkishore Mukhopadhyay, Eakkachai Pengwang, Placid M Ferreira
Department of Mechanical Science and Engineering
University of Illinois at Urbana-Champaign
Urbana, IL 61801, USA

INTRODUCTION

Micro Electro Mechanical Systems (MEMS) based micro-positioning stages are critically important in many micro/nano manipulation and manufacturing applications. Such stages have been extensively used in micro-force sensors, scanning probe microscopy and micro optical lens scanners [1-4]. While there is no unique definition for a micro-positioning stage, it generally refers to a system which can automatically move an end effector with certain degrees of freedom (DOF) in its work zone and maintain submicron positioning resolution. For a micropositioning stage, it is desirable to have a large work zone, high resolution, and high bandwidth simultaneously.

Parallel Kinematics Mechanism (PKM) use in-parallel actuation to produce multi-axis motion at the end effector of the machine. With careful design, PKMs have been successfully used in many different types of micro positioning stages. However, most designs are for stages with 3 or more DOF, for which SKMs are especially unsuitable due to the high inertia and low stiffness. Our motivation was to develop novel low DOF PKM stages with superior qualities to replace the existing SKM or PKM stages for increasingly challenging applications.

Planar low degree-of-freedom parallel kinematic mechanisms are well-suited for MEMS-based micro-positioning devices due to their simple and determinate kinematics, high bandwidth, and monolithic structure that conform well with micro fabrication technologies. In this paper, we described micro-scale stage system with novel parallel-kinematics mechanisms. The design, kinematics analysis and fabrication are discussed in the following sections.

KINEMATICS DESIGN OF PKM XY STAGES

Micro-scale XY stages have been fabricated on Silicon On Insulator (SOI) wafer by using MEMS fabrication techniques. The miniaturized MEMS stages enable seamless integration into many micro/nano manipulation and manufacturing applications that demand high resolution positioning capability in a relatively small footprint.

Figure 1 illustrates the design of a parallel kinematic micro positioning XY stage [5] with linear actuators. In this parallel kinematic mechanism design, there are two independent kinematics chains that connect the end effector to the base. Each of these kinematic chains includes two serially-connected degrees of freedom, a pure translation due to the prismatic joint and another translation along a circular

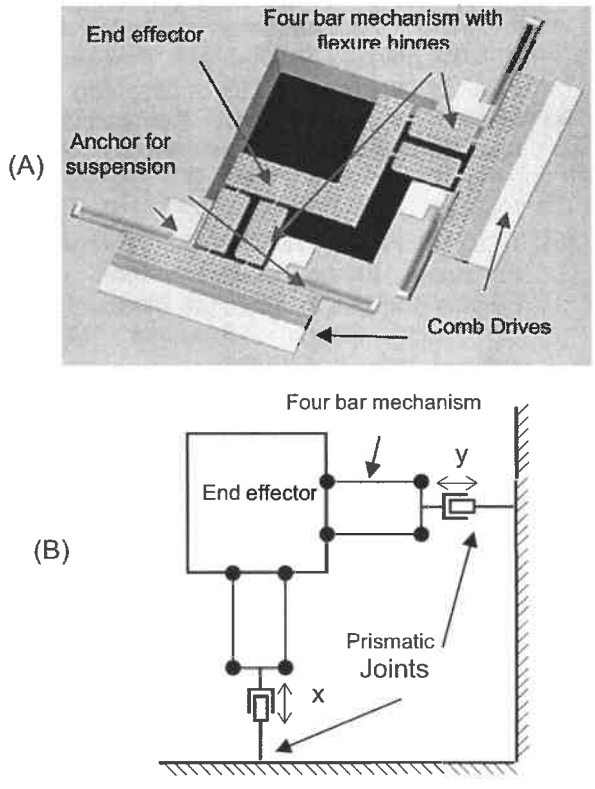

Figure 1: Schematic diagram of parallel kinematics XY stage. (A) XY stage with linear actuator. (B) Equivalent kinematic model

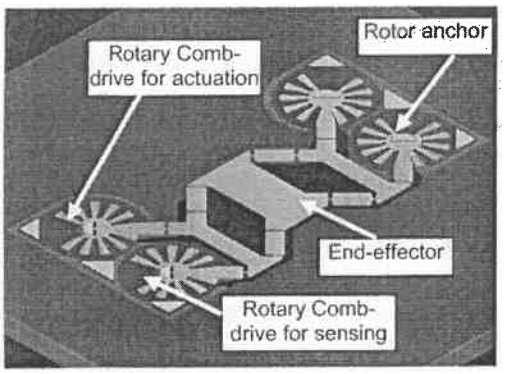

(A)

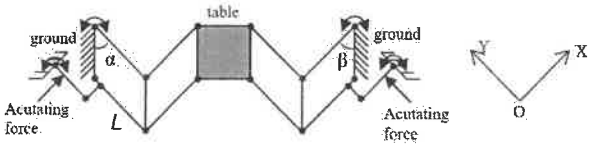

(B)

Figure 2: Schematic diagram of parallel kinematics XY stage. (A) XY stage with linear actuator. (B) Equivalent kinematic model

path due to the parallelogram 4-bar linkage system. The orientation of the two chains is such that the prismatic joints are perpendicular to each other, kinematically decoupling the two actuated joints to the maximum extent possible. A diagonal Jacobian matrix can be derived.

$$\begin{bmatrix}\Delta d_x\\ \Delta d_y\end{bmatrix}=\begin{bmatrix}-1 & 0\\ 0 & 1\end{bmatrix}\begin{bmatrix}\Delta x\\ \Delta y\end{bmatrix} \text{ and } \begin{bmatrix}\Delta x\\ \Delta y\end{bmatrix}=\begin{bmatrix}-1 & 0\\ 0 & 1\end{bmatrix}\begin{bmatrix}\Delta d_x\\ \Delta d_y\end{bmatrix}.$$

Here, Δd_x and Δd_y are joint displacements and x, y are end effector displacements.

The other kinematic design of XY stage is shown by Fig 2. It also has two independent kinematic chains that connect the end-effector to a fixed base. Each of its kinematic chains consists of two serially-connected parallelogram four-bar linkage mechanisms with an attached rotary actuator. By having two such kinematic chains connected to opposite ends of the end-effector, the scheme shown in Fig. 2(b) is obtained, where α and β are the two actuation angles and pivot points are represented by black dots. The orientations of the two chains are such that the four-bar linkages are perpendicular to each other thus kinematically decoupling the X and the Y axes. Additionally, due to the symmetric configuration of the kinematic chains, the stage mechanism has the same stiffness and bandwidth along any direction in the XY plane.

The relationship between the actuation at the rotary comb-drive and the displacement of the stage has been studied [6]. A diagonal Jacobian matrix (1) can be proven following the procedure developed in [7].

$$\begin{bmatrix}\Delta X\\ \Delta Y\end{bmatrix}=\begin{bmatrix}L & 0\\ 0 & L\end{bmatrix}\begin{bmatrix}\Delta\alpha\\ \Delta\beta\end{bmatrix}.$$

A specific advantage of this kinematic design is that the displacement of the end effector is not limited by the displacement from the actuator. By changing the length of link L, different achievable displacement at the end effector can be tuned.

KINEMATICS DESIGN OF PKM XYθ STAGES

A SOI MEMS-scale PKM based micro/nano positioning XYθ stage that integrates microfabrication techniques with the design of low DOF PKM stages is designed and fabricated. The device consists of three parallel linkages connecting the end-effector with the three linear comb drive actuators permitting all three possible degrees of freedom in a planar workspace, the two translations in XY plane and

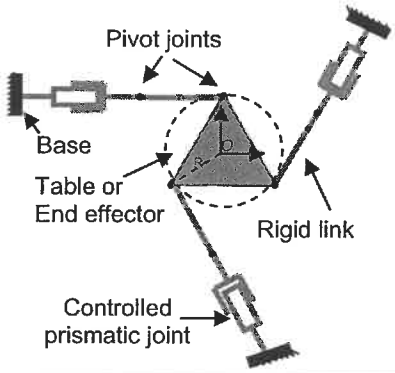

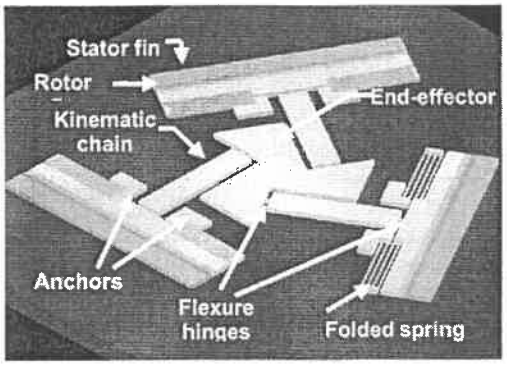

Figure 3: (a) Schematic of the PKM based 3 DOF, XYθ stage. (b) Model of the MEMS compatible PKM based 3 DOF, XYθ stage

rotation (θ) about the direction (Z) normal to the XY plane.

The schematic and solid model of such a PKM based MEMS XYθ stage is shown in Figure 3. It consists of an end-effector (or table) connected to the base by three in-parallel identical kinematic chains. Each chain consists of a prismatic joint connected to a fixed base on one end and to a rigid link on the other end, via a pivot joint. The rigid link is connected to the end-effector (the table) via a second pivot joint. Thus this mechanism is a planar 3-PRR (3-Prismatic-Revolute-Revolute) mechanism with the prismatic joint being the only controlled joint in the chain.

The kinematics is analyzed and the resulted Jacobian matrix is

$$J = \begin{bmatrix} \frac{2}{3} & -\frac{1}{3} & -\frac{1}{3} \\ 0 & \frac{1}{\sqrt{3}} & -\frac{1}{\sqrt{3}} \\ -\frac{1}{3R} & -\frac{1}{3R} & -\frac{1}{3R} \end{bmatrix}$$

STRUCTURE DESIGN AND FABRICATION

To implement parallel kinematics mechanisms at micro-scale with silicon micromachining technology, the prismatic joints in our kinematic model are replaced by linear comb drives with folded springs. The rotary/pivot joints around a four bar mechanism are implemented by flexure hinges. Rotary actuators are implemented by rotary comb drives. For the flexure hinges used in our design, we have a designed stiffness and maximum rotation range of *3.1e-6 N-m/radians* and *0.68 radians* respectively. Suppose the length of the four-bar structure is 1 mm, which indicates a maximum 630 μm displacement of the mechanical structure. However, factors such as the suspension structure and the limited actuating forces prevent us from reaching this limit. Generally the suspension structure is

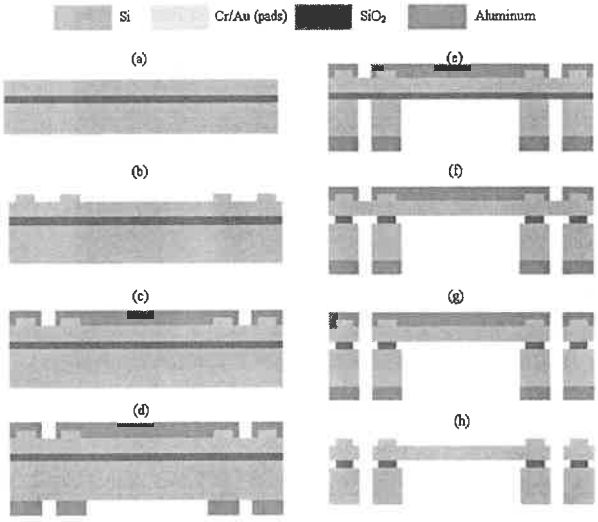

Figure 4: Fabrication Sequences. (a) Starting from a SOI die; (b) Conduction Pad layer patterning ; (c) Device patterning; (d) Handle layer patterning; (e) Handle layer etching; (f) BOX layer removal; (g) Device layer etching; (h) etch mask removal

required to have a large compliance in the actuation direction for possibly large displacements, and a high stiffness in the lateral direction so as to prevent side instabilities. In our linear actuator design, a folded spring is used to support the rotor as well as the table. The comb drive actuator is used to provide actuation force to overcome the stiffness from folded spring and flexure hinges. The force provided by a linear comb actuator is given by $F = n\frac{\varepsilon_0 h V^2}{g}$, and the torque provided by a rotary actuator is $\tau_{comb} = n\frac{\varepsilon_0 h}{g} V^2 \sum_i R_i$, where n is the number of fingers, h is the height of the fingers, g is the gap between two neighboring fingers. Our comb can thus generate a force of 5.5E-5 Newton at 50 V and 0.98 μNm torque under an actuation voltage

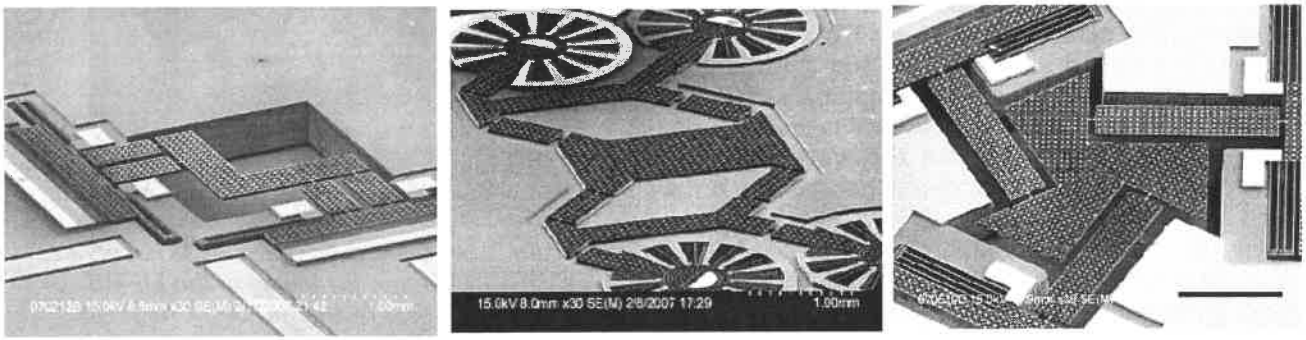

Figure 5: Fabricated PKM micro positioning XY stages and XYθ stage

of 200V.

The fabrication process for these micro positioning stages is depicted in Figure 4. The process includes three patterning and two DRIE etching steps. The fabricated devices are shown in Figure 5.

DEVICE CHARACTERIZATION AND DISPLACEMENT SENSING

Figure 6(a) shows the static displacement of the stage at different voltages. Experimental data overlays a second order curve fitted to the displacement. Within the resolution of the observations, no cross talk is observed even when the maximum displacement is achieved for both the X and Y axes at their maximum driving voltage. When a single axis is fully actuated, the generated motion in the other direction is not noticeable from a high resolution microscope. This is predicted by the kinematic analysis of the stage and accrues from the orthogonal design of the actuation. For the XY stage, a 20-30 micron displacement is achieved. For XYθ stage, the maximum displacements for XY and θ are 18 microns and 1.73 degree respectively.

To study the dynamic behavior of fabricated systems, a set of frequency response tests is performed. Sinusoid signals at different frequencies with small amplitude are applied to the stage. The amplitude of vibrations is observed at these frequencies. For our devices, a resonant frequencies in the range of 1kHz to 2kHz are achieved. The Q factors of these stages are derived from their frequency responses. The value of Q factor ranges from 60 to 150 for different designs. We attribute the relatively high Q factor to the high stiffness and good modal separation that results from the parallel kinematics stage design.

To precisely track the displacement of the comb drive actuated devices, a simultaneously actuation and displacement sensing scheme is developed [8]. Instead of using separate sensing capacitive structure, the sensing signal and actuation effect come from the same electrostatic actuator at the same time. A high frequency sensing signal is combined with the low frequency actuation voltage to drive the device. By detecting the phase or amplitude change at the sensing frequency from the resulting RC circuit, a high resolution sensing signal (about half nano meter) can be obtained (Fig 6(b)). Combining PKMs having determinate

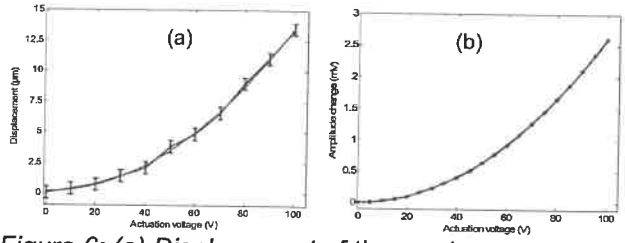

Figure 6: (a) Displacement of the comb actuator observed from microscope. (b) Sensed displacement

kinematics with high accurate position sensing at the actuator, allows us to sense the stage motion with high precision for many nano positioning and manipulation applications.

REFERENCES

[1] H.T.H. Chen, W. Ng, R.L. Engelstad, "Finite element analysis of a scanning x-ray microscope micropositioning stage", Review of Scientific Instruments 63 (1992) 591-594.

[2] K. Sugihara, I. Mori, T. Tojo, C. Ito, M. Tabata, T. Shinozaki, "Piezoelectrically driven XYθ table for submicron lithography systems", Review of Scientific Instruments 60 (1989) 3024-3029.

[3] A. Castaneda, L.M. Apatiga, R. Velazquez, V.M. Castano, "Micropositioning device for automatic alignment of substrates for industrial-scale thin films deposition", Assembly Automation, 21 (2001) 336-340.

[4] S. Stilson, A. McClellan, S. Devasia, "High-speed solution switching using piezo-based micropositioning stages", IEEE Transactions on Biomedical Engineering 48 (7) (2001) 806-814.

[5] J. Dong, D. Mukhopadhyay, P. M. Ferreira, "Design, Fabrication and Testing of Silicon-on-Insulator (SOI) MEMS Parallel Kinematics XY Stage", J. Micromech. Microeng, 17, 1154-1161 (2007)

[6] D. Mukhopadhyay, Jingyan Dong, Placid M. Ferreira, "Parallel Kinematic Mechanism based monolithic XY micro-positioning stage", *SPIE MOEMS-MEMS Conference,* San Jose, California, January 2008

[7] Q. Yao, J. Dong, P.M. Ferreira, "Design, Analysis, Fabrication and Testing of a Piezo-driven Parallel-Kinematics Micropositioning XY Stage", International Journal of Machine Tools & Manufacture, 47, 946–961 (2007).

[8] J. Dong, P. M. Ferreira, "Simultaneous Actuation and Displacement Sensing for Electrostatic Drives", J. Micromech. Microeng, 18(3), 035011 (10 pp) (2008).

NOVEL SPLIT STAGE ARCHITECTURE

Mark T. Kosmowski
Electro Scientific Industries
Portland, Oregon, USA

INTRODUCTION

This paper presents a new and unique split stage architecture that is used for processing wafers with a laser. The fundamental difference between traditional split stage designs and this new novel design is the elimination of the overhead beam. Traditional split stage architectures use a beam that spans over a major axis and supports the second minor axis. The elimination of the over head beam greatly improves many performance metrics of a split stage architecture, the most significant improvement is the first modal frequency of the split stage assembly and structure. Comparing Modal frequency data between a robust traditional split stage and the novel Beam-Less Split Stage (BLS Stage) shows that the first modal frequency increases from 105Hz to 319Hz. This frequency shift allows the major axis and minor axis to be driven harder from a speed and acceleration standpoint without sacrificing accuracy. Other performance metrics and design parameters are improved upon as well in the BLS Stage architecture.

The stage that positions the lens in the axis that is perpendicular to the wafer surface (Z axis) is also quite novel. The lens is guided and supported by a single cylindrical air bearing that utilizes the outer diameter of the lens as the inner race of the bearing. Motion of the lens is achieved through a voice coil motor that is connected to a slender "stinger" flexure. The stinger flexure isolates the mechanical guiding of the voice coil motor from influencing the guiding of the lens in the cylindrical air bearing, yet allows a very stiff connection along the axis of motion.

Light and stiff dynamic structures for the major axis (Y stage) and minor axis (X stage) are manufactured using a unique and economical fabrication method. These light and stiff structures allow higher natural frequencies on the stages and lower thermal loading on the drive motors.

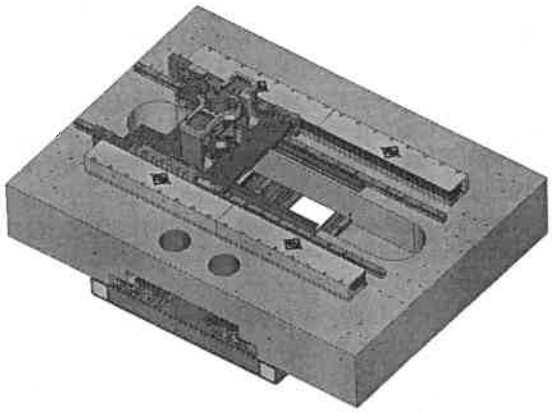

Figure #1 CAD image of the BLS Stage Minor axis (x stage) and lens focusing axis (Z stage) shown on top surface. Major axis (Y stage) is attached to lower granite surface.

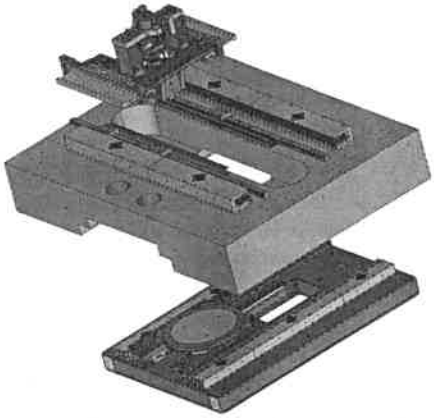

Figure #2 CAD exploded image of the BLS Stage, Minor axis (x stage) and lens focusing axis (Z stage) shown above granite slab. Major axis (Y stage) shown below granite slab.

DESIGN

Traditional split stage design typically incorporates a prismatic overhead beam that spans the major axis and supports the minor axis (see figure #3). Typically, the prismatic beam and the stage it supports greatly influence the first modal frequency that causes positional errors between the major axis and minor axis. The relative motion that this mode creates is usually not taken into consideration in the control system of the stages, thus errors in the

part processing occur from this motion. In order to increase this

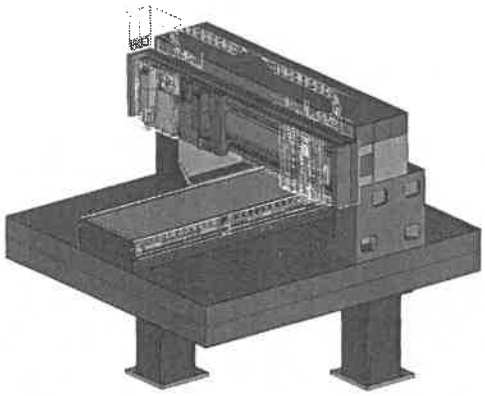

Figure #3 CAD image of a traditional split stage design. Minor axis (x stage) located on prismatic overhead beam. Major axis (Y stage) is attached to the main base structure

Modal frequency and decrease the positioning errors in the processed part, a fresh approach to the architecture of a split stage assembly was taken. This fresh approach is illustrated in Figures #1, #2 and #4. The main structure of the BLS Stage design is a granite slab; the granite slab is machined such that two slots are cut into it, one in the upper horizontal surface and one on the lower horizontal surface. The slots are mutually perpendicular and are deep enough that an opening is created in the granite slab were the two slots intersect. The major axis that carries the semiconductor wafer (Y stage) is attached to the lower surface of the granite slab and the silicon wafer is positioned in the lower slot. The minor axis that carries the laser focusing lens (X stage) for processing the wafer is attached to the upper surface of the granite and the laser focusing lens protrudes into the upper slot. Wafer processing occurs when the wafer and the laser focusing lens are in the opening were the upper and lower slots intersect. Placing the major axis and minor axis in the above mentioned arrangement, enables improvements in the design of the stage which are difficult to obtain in a traditional split stage design. These design improvements are listed below:

1) **Minor axis (x stage) symmetry is improved:** By arranging the minor axis (X stage) attachment to the top surface of the Slab structure, it is much easier to design the dynamic components of the stage such that the motors driving the stage are aligned with the centers of action (gravity, friction stiffness) of the stage.
2) **Driving the x stage with two motors:** By placing a motor on either side of the stage carriage and having encoder feedback on both sides of the stage carriage, it is possible to control Yaw error of the stage.
3) **Symmetrically mounting the motors on opposite sides of the carriage:** as shown in figures #1 and #2 allows good thermal management of the stage. The motors generate heat that can disturb thermally sensitive stage components such as encoders.
4) **Locating the cutting beam or cutting tool at the center of action of the stage carriage:** Locating the laser cutting beam at the center of action reduces errors caused by yaw of the stage carriage.
5) **Reduction of structural parts:** Allows the tolerance stack between stages to be reduced and reduces the cost of the stage assembly (i.e. less parts) and in this particular design, allows the Abbe error to be reduced via a shorter structural loop thus the raw accuracy of the stages are improved (see table #4)
6) **Improved rigidity of the entire stage structure (short structural loop).** By placing both stage assemblies on a single monolithic structure, the rigidity is improved from a structural element standpoint as well as the reduction of joints in the structure.

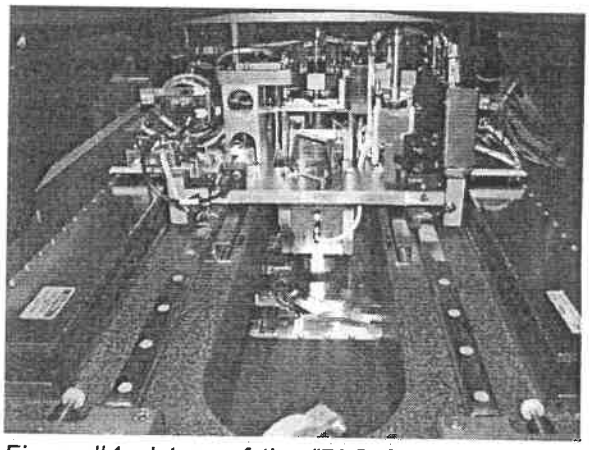

Figure #4 picture of the "BLS Stage" prototype close up of the major and minor axis in the processing area.

The performance requirements of the BLS stage are outlined in table #1.

Table #1
Performance specifications (BLS Stage):

Acceleration	2g (19.62m/sec^2)
Speed	2m/sec
Positioning accuracy	+/- 1.5 microns

Focusing lens stage design:

The third axis of this stage assembly is called the (Z axis). It controls the focal position of a 75mm diameter 2.5Kg lens that focuses the laser beam onto the wafer (See figure #4 and #5). This stage is driven by a voice coil motor and the 2.5Kg lens is guided and supported by a single 75mm diameter New Way™ air bushing. The outer diameter of the lens is used as inner race of the air bearing. This air bearing design allows the lens to have excellent stiffness in the minor axis (X stage) direction of motion.

The voice coil motor that drives this axis is connected to the lens via a stinger flexure (See figure #5) . The reason for using this flexure is to separate the mechanical guiding of voice coil from the air bearing guiding of the laser focusing lens. Separating these two guiding systems with a stinger flexure avoids an over constrained mechanical assembly, but allows the voice coil to have a stiff robust co-located guide and the lens to be properly guided and supported about its center of gravity via the air bushing. This stinger flexure is rigid in the axis of motion of the lens but is very flexible in motions that are perpendicular to the lens axis. Thus minimizing any parasitic forces from the voice coil mechanical guiding from influencing the motion of the lens in the air bushing.

The center of gravity of the Z axis assembly is located in the same plane as the motors that drive the Minor axis (X stage), thus reducing any offset moments between the force plane and the center of gravity of the stage assembly.

Stage carriage fabrication using replication techniques:

The stage carriages are fabricated using a replication technique that involves sheet metal, epoxy, thin wall structural tubing or a water jet cut structural metal web. This fabrication technique yields very light stiff structures that are economical to produce. The replication technique yields very flat surfaces on the carriage since the skins reference a granite surface plate during the replication process. This replication technique using a granite surface plate eliminates the need to surface grind the carriage face to obtain a flat surface, thus shortening the fabrication cycle and eliminating internal stresses caused by the grinding process.

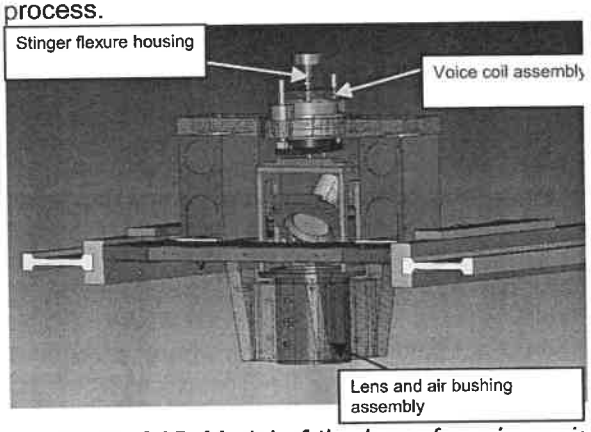

Figure #5 CAD Model of the laser focusing axis (Z stage)

TESTING RESULTS AND COMPARISONS

Testing of the BLS Stage and the traditional split stage consisted of the following:

- Loop transmission testing of the major (Y axis) Minor (X axis) and Z stage
- Modal testing of the entire stage assembly
- Raw accuracy mapping of the processing area

Table #2: Loop transmission testing of the BLS Stage resulted on the following frequency values:

Major axis (Y axis)	Minor Axis (X axis)	Lens axis (Z axis)
529 Hz	387 Hz	187 Hz

Table #3: Loop transmission testing of a traditional split stage resulted on the following frequency values

Major axis (Y axis)	Minor Axis (X axis)	Lens axis (Z axis)
180 Hz	140 Hz	N/A

Bode plots from the loop transmission testing are shown in figures #6 and #7. Both plots are from the major axis (Y stage) of the BLS Stage and the traditional split stage.

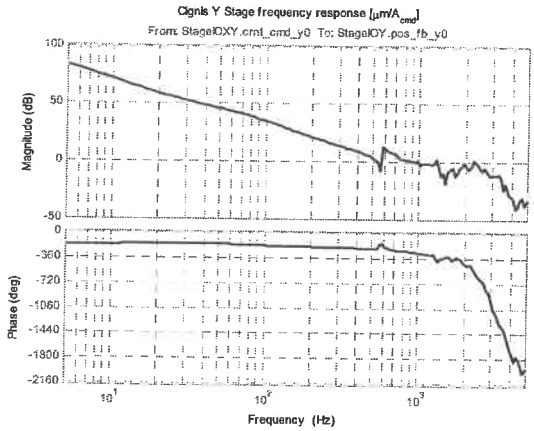

Figure #6 Major (Y-axis) Loop transmissions BLSStage

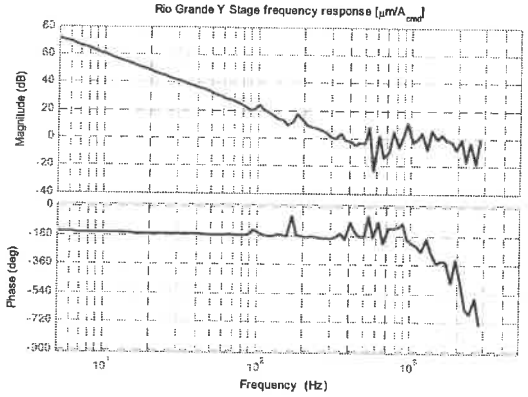

Figure #7 Major (Y-axis) loop transmission traditional split stage design

Modal testing:

Figures #9 and #10 are schematic representations of the BLS Stage and a traditional split stage. Using ME scope™ modal animation software, it is possible to identify the first structural mode shape that influences system accuracy in both assemblies.

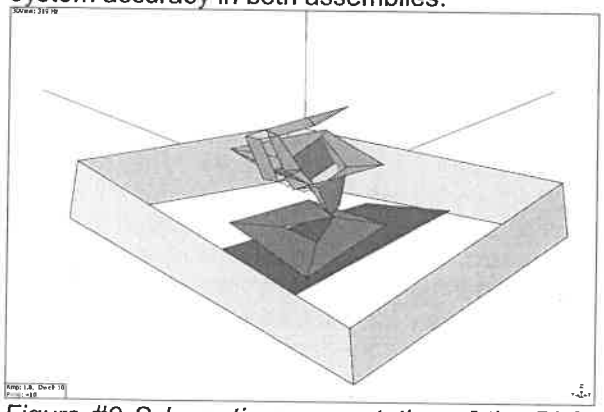

*Figure #9 Schematic representation of the BLS Stage assembly the first mode shape that influences stage accuracy at **319 Hz***

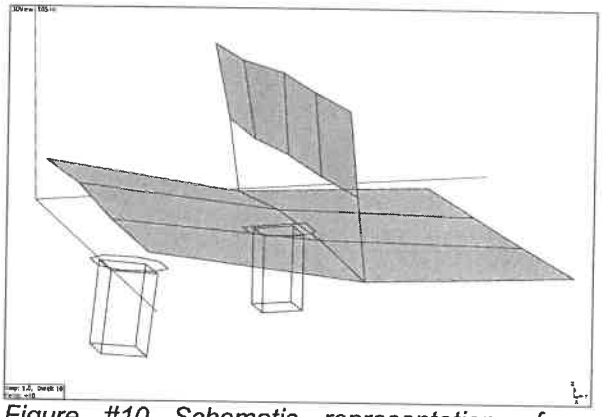

*Figure #10 Schematic representation of a traditional split stage assembly, the first mode shape that influences stage accuracy at **105 Hz***

Raw accuracy:

Raw mechanical accuracy comparisons of the traditional split stage and the BLS Stage are shown below. Both stages use mechanical guiding with comparable accuracy grades.

Table #4 Raw uncompensated mechanical accuracy of the "BLS Stage" and a traditional Split stage, both stage assemblies use mechanical bearings for guiding

Stage axis	Raw accuracy "Slab stage"	Raw accuracy Traditional split stage
Major (Y axis)	4 microns	25 microns
Minor (x axis)	7 microns	30 microns

FUTURE DESIGN IMPROVEMENTS:

In order to improve the accuracy and acceleration performance of the BLS stage assembly the following changes to the stages must be made:

1. All guide bearings must be changed from mechanical linear rail bearings to aerostatic bearings and vacuum preloaded aerostatic bearings
2. Balance reaction mass system must be implemented into the stage design.

ACKNOWLEDGEMENTS:

The author would like to thank:

Tim Nuckolls (ESI): For all of the modal testing and data reduction work

Joe Frankel (ESI): For the bode plots and loop transmission work.

DESIGN OF A FAST LONG RANGE ACTUATOR – FLORA II

Erik M. Zdanowicz, Jeffrey W. Eischen, and Thomas A. Dow
Precision Engineering Center
North Carolina State University
Raleigh, North Carolina, USA

INTRODUCTION

The objective of this NSF sponsored research is to develop machinery to fabricate Non-Rotationally Symmetric (NRS) optical surfaces. NRS surfaces have typically been machined using very slow spindle speeds or actuators with a limited range of several hundred μm. This means only limited surface features can be machine or the process takes a long time. A Fast LOng Range Actuator (FLORA) has been constructed [1] with a goal of machining NRS surfaces with a range of motion of ± 2 mm at 20 Hz. For the surface to have the same quality as conventional diamond turning machines the surface must have a form error of less than 150 nm peak-to-valley and a surface finish of 5 nm RMS.

The FLORA system consists of a triangular aluminum honeycomb piston supported by orifice type air bearings and driven by a linear motor. While machining with FLORA was successful, the system dimensions are large when compared with the range of motion and the size of the tool and the piston weighed 650 grams. In addition, the air bearing on the FLORA has 200 nm of vertical vibration which has an impact on the surface finish possible.

A new design, FLORA II, has been created to address the limitations of its predecessor. The FLORA II package is smaller and lighter than FLORA while maintaining bearing stiffness and improving system dynamics. This was accomplished through structural analysis supplemented with experimental testing. The design described in this paper will show how the FLORA II can produce high quality NRS optical surfaces from a small, lightweight system.

AIR BEARINGS

One of the main features in the FLORA design is the air bearing. This bearing eliminates friction, supports the tool with little or no deflection and moves piston in a straight line. The original FLORA design had orifice-type air bearings that consist of a number of small orifices along the bearing surface to create the pressurized air film that supports the piston. It is believed that these bearings are responsible for the 200 nm vertical vibration of FLORA [1]. For this reason, FLORA II was designed with porous-carbon air bearings. Porous air bearings are constructed with an aluminum backing that acts as a manifold to distribute air through a porous carbon material. This porous carbon material has millions of small holes for air distribution and creates a nearly uniform pressure distribution over the surface of the bearing. Orifice type bearings have more pressure variation over the face of the bearing.

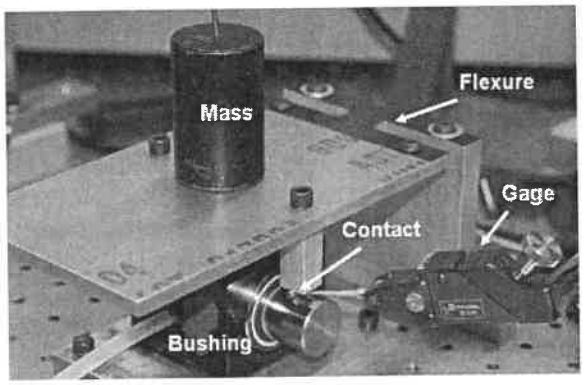

FIGURE 1. Radial stiffness test.

Finite Element Analysis (FEA) software is a powerful design tool that if used properly, can provide important information such as deformation of a complex body under load. The software ANSYS has an elastic foundation type of support which attaches a bed-of-springs from a moving part to a fixed support. This bed-of-springs foundation can be used to approximate the stiffness of the air bearing provided by the pressurized air. The company that makes the porous bearings, New Way [2], publishes an overall stiffness for their bearings at a certain pressure. To use the bed-of-springs approach, ANSYS requires specification of stiffness per unit area. Therefore, equivalent foundation stiffness had to be derived from the stiffness provided by New Way for use in the ANSYS

model. To verify the model, a 25 mm diameter air bushing shown in Figure 1 was purchased. The air bushing consists of a hollow aluminum tube with the carbon bearing material on the inside. A circular shaft rides in the bearing with a radial film thickness of about 5 μm. The aluminum tube is supported by 4 O-rings and an epoxy resin is injected between the tube and housing to rigidly support the bearing.

Air Bearing Experiment

Static and dynamic experiments were run on the test bushing in order to verify theoretical derivations. The tests consisted of the 25 mm bushing, a 110 mm long stainless steel shaft, a flexure loading device, and a mounting block. Epoxy adhesive applied between the bushing and support block eliminated any effect the O-rings had on the bearing stiffness.

Static Air Bearing Measurements

New Way provides two stiffness values for each bushing: radial and pitch. Radial stiffness is the load required to produce a unit value of radial translation of the shaft. Pitch is the moment required to produce a unit rotation of the shaft in the bushing. Figure 2 shows the radial and pitch directions.

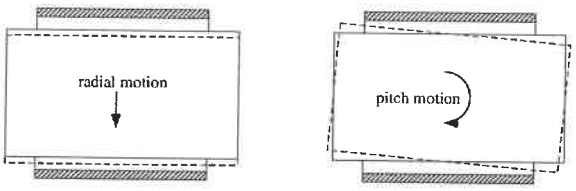

FIGURE 2. Radial motion is shown on the left while pitch motion is shown on the right.

The first static test was to verify the radial stiffness of the bushing. This is the stiffness of vertical translation of the shaft inside the bushing. The experiment was run as shown in Figure 1. The known mass was placed on the center of a load plate that was hinged to a vertical support by a thin flexure. The flexure had cut outs from the sides to allow the plate to twist so the contacts would apply equal loads to each end of the shaft. The contacts had small cylinders glued to the ends so as to apply a point contact. A lever-type gage head was used to measure the displacement under the contact. Three different known masses were placed on the load plate 10 times each and the displacements were recorded. From these experiments it was found that the radial stiffness was 25.8 N/μm. This value is close to the 27.9 N/μm predicted using the value (34 N/μm) [2] published by New Way reduced due to the bending stiffness of the steel shaft (156 N/μm).

To measure the pitch stiffness, the same equipment was used as in the radial test except one contact was removed to apply a moment to the bearing. The flexure shown in Figure 1 was thinned in the center to allow rotation of the loading plate. For the moment experiments, a new stiffer flexure with no cutouts was fabricated. In this experiment two gage heads, one on each side of the bushing, were used. This orientation allowed the rotation of the shaft to be determined. The measured pitch stiffness was 5.5 N-m/milli-radian which is close to stiffness quoted by New Way of 5.3 N-m/milli-radian [2].

Dynamic Air Bearing Measurements

The two factors that were the focus of the bushings dynamics experiments were natural frequencies and noise. Natural frequencies were obtained by measuring one end of the shaft with a capacitance gage while tapping the other end of the shaft. The signal analyzer then output the natural frequencies of the shaft on the pressurized air film. The first natural frequency, a rigid body pitch mode, was observed at about 700 Hz. The results are shown in Figure 3. The top plot is the time series of the shaft motion resulting from a single tap showing a peak spacing of 1.43 msec or 700 Hz. The lower plot is the frequency spectrum of the top plot that shows peaks at 590 and 690 Hz.

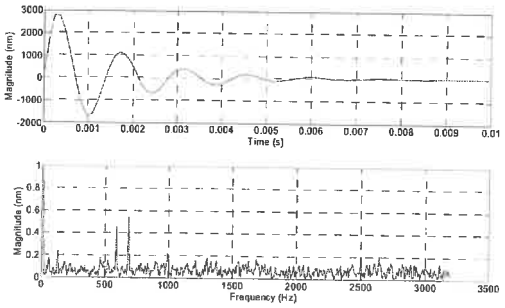

FIGURE 3. Radial motion of shaft when tapped in bushing measured by a capacitance gage.

The second reason for looking at the dynamics of the bushing was to determine the steady state vertical motion of the porous type bearing compared to the current FLORA. This experiment was the same as before except there was no excitation. A baseline recording of

the shaft sitting in the bearing is shown in Figure 4. Figure 4 shows that the bushing has a peak-to-peak motion of ± 4 nm. This is noise from the cap gage. Recall that FLORA had a motion of ± 100 nm which is significantly larger than the bushing. This finding reinforces the idea that porous air bearings are the right choice for use in FLORA I.

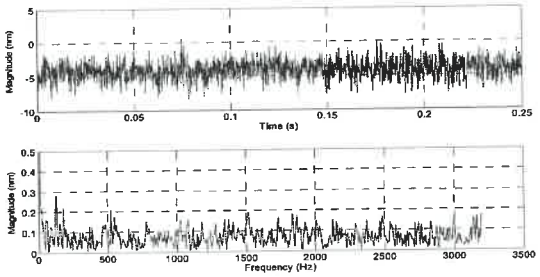

FIGURE 4. Steady-state vertical motion of shaft in bushing measured by a capacitance gage.

ANALYTICAL APPROACH

To compare the results of the experiments and ANSYS simulations of the bearing stiffness, equivalent radial and pitch stiffness are needed. The approach that was taken for both cases was to use a bed-of-springs approximation where the air bushing is modeled as a series of springs connected the shaft to the inside the bushing.

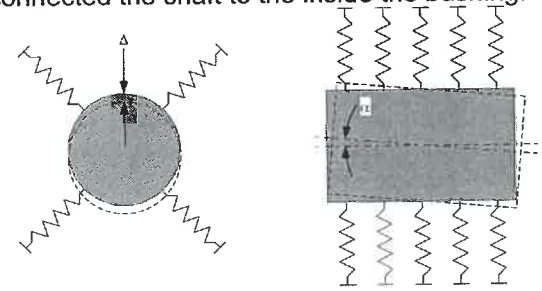

FIGURE 5. Bed of Springs approximation for radial stiffness (end view of shaft) and pitch stiffness (side view at right).

Equivalent Radial Stiffness

It is assumed that the equivalent radial stiffness will be a function of the radial stiffness provided by New Way. The equivalent stiffness was derived using an end view of the shaft as shown at left in Figure 5 to visualize the deflection of the springs. F_A is the applied force and Δ is the vertical translation of the shaft.

Using this model, the equivalent radial stiffness was derived as

$$k_A^r = \frac{2k_{NW}^r}{A_s} \quad (1)$$

The symbol k_A^r is the equivalent radial stiffness that is input into ANSYS and k_{NW}^r is the radial stiffness that is provided by New Way. The variable A_s is the surface area of the shaft inside the bushing. The equivalent radial stiffness is then used in a simulation of the shaft in FEA and the results is a stiffness of 34.1 N/um. FEA simulation with the derived stiffness behaves just like the physical bushing.

Equivalent Pitch Stiffness

As in the derivation of the equivalent radial stiffness, it was known that the equivalent pitch stiffness was going to be a function of the pitch stiffness that New Way provides. Figure 5 also shows a side view of the shaft that was used to derive a model of the equivalent pitch stiffness, which again must be done because the elastic foundation being used in ANSYS is stiffness per unit area. M is the applied moment and α is the pitch angle of the shaft. Using Figure 5, the following expression for the equivalent pitch stiffness is derived

$$k_A^p = \frac{24k_{NW}^p}{L^2 A_s} \quad (2)$$

k_A^p is the equivalent pitch stiffness for ANSYS and k_{NW}^p is the pitch stiffness provided by New Way. A_s is the surface area of the shaft inside the bushing and L is the length of the shaft. The equivalent pitch stiffness is simulated in FEA with a moment applied to the shaft. The rotation observed in the simulation replicates the behavior of the bushing.

A natural frequency simulation was also run in ANSYS using the equivalent stiffness which produced the bushing/shaft couplings first rigid body mode (pitch) at 700 Hz. This is the same value determined in the experiment shown in Figure 4.

PISTON CROSS SECTION

Three different piston cross sections were evaluated: box, triangle, and cross. ANSYS simulations were run to represent operating forces that the piston would encounter. Each cross section had equal length and mass to have as accurate a comparison as possible. After the simulations were run, each piston received a score based on performance to chose the superior cross section.

TABLE 1. Results from FEA simulations run on pistons with various cross sections

Scenario	Triangle	Box	Cross
End Load	3	1	2
Pressure	1	2	3
Bending	2	3	1
Rigid Body	2	2	1
Assembly	3	2	1
Total	**11**	**10**	**8**

A score of 3 was given to the cross section that performed the best while the worst received a 1. The end load test represented a vertical end load like the piston would see while machining. Pressure was the ability for a piston to withstand deformation from pressure applied by the bearings. Bending examined the first bending mode of the piston while rigid body was the first rigid body mode of the piston on the bed-of-springs approximation of the air bearing. Assembly refers to degree of difficulty in manufacturing each piston. The triangles ease of assembly is what made it more attractive than the box design.

PISTON MATERIAL

Choosing a material for the new piston will influence its mass and stiffness. Steel is a very stiff material but has a higher density, and potentially more mass, than competing materials for the application. A stiff, lightweight material is optimal. Aluminum was also considered which is 1/3 the density of steel but also 1/3 of the modulus. Aluminum is a good option, but to get a higher ratio of stiffness to density, composites were examined. After this study, one material that stood out was silicon carbide ceramic. Table 2 shows a comparison between steel, aluminum, and silicon carbide.

TABLE 2. Properties for piston material

Material	Modulus (Gpa)	Density (kg/m^3)	Modulus/Density (m^2/s^2)
Al	70	2700	26
Steel	200	7900	25
SiC	410	3150	130

It is clear that silicon carbide has a superior stiffness to mass ratio (5 times that of aluminum and steel) and that is why this material has been chosen for the FLORA II piston.

CONCLUSIONS

The analytical derivation, experimental verification, and FEA simulation that was described earlier in this section all lead to the new FLORA II design shown in Figure 6. The housing dimensions in mm are 90H x 110W x208L with motor. The piston is 70 mm in width across its top and 150 mm long with a moving mass of 250 g. Six porous air bearings provide stiffness for the piston which is driven by a voice coil motor. A linear encoder reads a glass scale attached to the piston for position feedback. As a comparison, the FLORA housing dimensions (mm) are 130H x 205W x 305L with motor and a moving mass of 650 g. The effort described in this section led into a new design for the FLORA II that will improve optical quality of NRS surfaces while reducing the size and mass of the actuator.

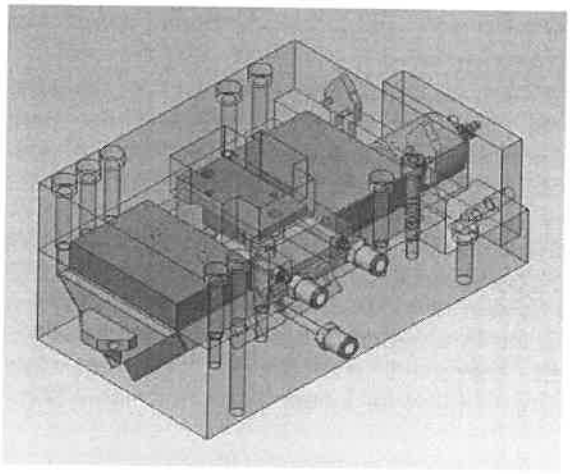

FIGURE 6. Isometric view of FLORA II with housing and base plate translucent.

ACKNOWLEDGEMENT

Principle funding for this research is through the NSF Grant DMI-0556209 monitored by G. Hazelrigg.

REFERENCES

[1] Q. Chen, T. Dow, K. Garrard and A. Sohn, 2007. "A Fast Long Range Actuator", Proc. of ASPE, Vol 42, pg 287-290, 2007.

[2] Newwayairbearings.com. Pennsylvania: New Way Air Bearings, Inc.;

SIMULATION AND PREDICTION OF THE THERMALLY INDUCED DEFORMATIONS ON MACHNIE TOOLS CAUSED BY MOVING LINEAR AXIS USING THE FDEM SIMULATION APPROACH

Josef Mayr[1], Markus Ess[1], Sascha Weikert[1], Konrad Wegener[1]
[1]Institute of Machine Tools and Manufacturing
Swiss Federal Institute of Technology (ETH)
Zurich, Switzerland

ABSTRACT
In this study the structure of a machine tool is analyzed using the Finite Difference Element Method (FDEM) simulation approach. This approach for the computation of thermally induced displacements of machine tools structures is characterized by using finite differences for the temperature field and based on that finite elements for the thermoelastic displacements. The simulation results are verified via measurements of displacement and temperatures in a test according to ISO 230-3.

INTRODUCTION
The thermo-elastic deformations of machine tools caused by internal and external heat sources largely contributes to the overall geometrical inaccuracies of the workpiece [2]. Machine tool manufacturers therefore deem thermal displacements as the the most important task towards better accuracy. Therefore thermal simulation of machine tools moved increasingly into the foreground of newer research activities. The "Thermal Effects Diagram" [1] knows six sources of thermal influences of machine tools:

- heat generated from the (cutting) process
- heat generated by the machine
- heating or cooling influence by the various cooling systems
- heating or cooling influence provided by the room
- the effect of people
- thermal memory from any previous environment

In this study an example is given to calculate effects of heat generated by the machine. The example describes a way to calculate the thermally induced deformations of machine tools by a moving linear axis. In standards like the ISO 230-3 or the ANSI/ASME B5.54 procedures to determine the thermo-mechanical behavior of machine tools under different thermal load cases [3,4] are described.
Due to the increase of computational power the Finite Element Method (FEM) becomes increasingly important for the simulation of the thermal behavior of machine tools. The Finite Differences Method (FDM) is often used to numerically solve temperature and flow field problems with the advantages that the models can easily be established and programmed, and the solving speed is high [10]. Using a Modified Lumped Capacitance Method (MLCM) the heat flow in a ball screw and a feed drive system has been solved [5,6]. Bearings have also been included into the simulation model of a ball screw system, as they influence the temperature distribution by producing frictional heat [7].

FDEM
The FDEM is an alternative way of simulating the transient thermal behavior of mechanical systems such as machine tools. The FDEM is a simulation approach that combines the advantages of FDM and FEM. In the first step the 3-D temperature distribution at discrete time points is calculate using FDM. In a second step the thermal deformations at the discrete time points are calculated using FEM. The temperature distribution at the discrete time points of the earlier FDM was used as temperature field for the FEM. Thus the FDEM can be seen as a serial simulation approach. The most advantage is that the method is very efficiently with short calculation time [8].

MACHNIE TOOL MODEL
A simplified model of a small three axes milling machine representing the thermal and mechanical behavior of the whole machine tool with less than 5'000 Elements was developed. FIGURE 1 shows the model of that milling machine. Material properties are an important factor in retrieving accurate simulation results. Values as Young's modulus (E), shear modulus (G) and

Poisson-ratio (ν) are important for describing the elastic behavior, while the coefficient of linear thermal expansion (α), the heat conductivity (λ) and the heat capacity (c_p) are important for the thermal behavior.

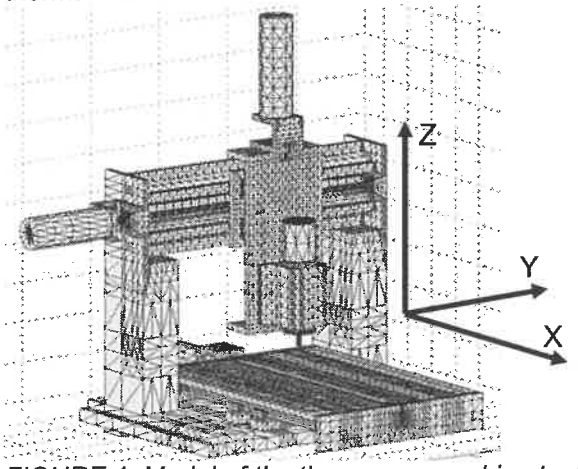

FIGURE 1. Model of the three axes machine tool with about 5'000 elements.

Bearings

The dimension of bearing models does not match with the bearings in detail. Therefore the material properties need to be adjusted. For example the density (ρ) can be adjusted to compensate the heat capacity of the whole bearing of mass m:

$$\Delta Q = \rho \cdot V \cdot c_p \cdot \Delta T = m \cdot c_p \cdot \Delta T \qquad (1)$$

Therefore if the volume of the components model is not equal to the real components volume we can change c_p or ρ to compensate for heat storage. In this study we changed ρ in the following way:

$$\rho = \frac{V_{model} \cdot \rho_{real}}{m_{real}} \cdot \rho_{real} \qquad (2)$$

m_{real}: mass of the real bearing

The mechanical material properties are also adjusted. For example the elastic coupling in axial direction of the floating bearings is modeled by setting the shear modules in the axial direction close to zero. FIGURE 2 illustrates the shear planes of the y-axis ball screw floating bearing. At this bearing the shear modules Gxy and Gyz are set close to zero. Similarly for the floating bearings of the x-axis ball screw the shear modules Gxy and Gxz and for the z-axis ball screw the shear modules Gyz and Gxz are set close to zero.

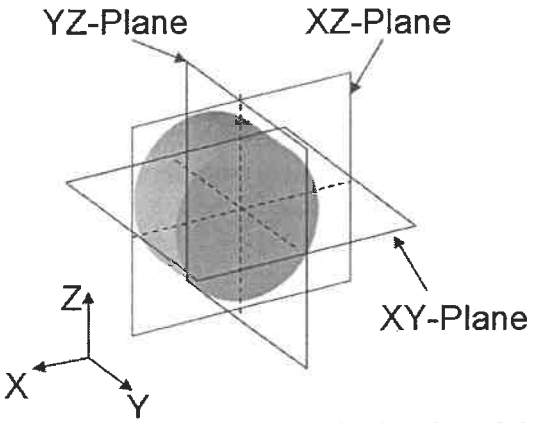

FIGURE 2. Shear planes of a bearing of the y-axis ball screw.

HEAT SOURCES

During a cyclic motion of a linear axis the actual forces are changing according to the actual state of motion. For example when the linear axes are moving with constant velocity only external forces caused by friction are acting. Other examples are forces acting because of increasing/decreasing velocity during acceleration/deceleration. The contribution of the different forces acting on the system during a cycle to the averaged force is proportional to their time duration.

$$F_{external} = \sum_i \frac{F_i \cdot t_i}{t_{cycle}} \qquad (3)$$

Ball Screw and Ball Screw Nut

The losses in a ball screw system are given by:

$$P_{ball\ screw\_tot} = \frac{F_{external}}{\cos^2(\varphi_{nut}) \cdot \sin(\alpha_{nut})} \cdot \mu_{nut} \cdot d_b \cdot \pi \cdot n + T_{no\_load} \cdot n \cdot 2 \cdot \pi \qquad (4)$$

d_b: ballscrew pitch diameter
μ_{nut}: friction coefficient of the ball screw nut
φ_{nut}: lead angle of the ball screw
α_{nut}: contact angle of the ball screw
T_{no_load}: idle torque

Equation 4 has two parts: The first part describes losses acting because of external forces. The second part describes losses due to idle torque of the ball screw system.
The heat distribution between the ball screw and ball screw nut is determined using the following procedure:

- measurement of the ball screw nut temperature during a given state of motion
- calculating the losses of the ball screw system using (4)
- calculating the heat stored in the ball screw nut using (1), assuming the heat losses form the balls to air are negligible
- find distribution factor $\xi_{ball\ screw}$

$$P_{ball\ screw} = \xi_{ball\ screw} \cdot P_{ball\ screw\_tot} \quad (5)$$

$$P_{nut} = \left(1 - \xi_{ball\ screw}\right) \cdot P_{ball\ screw\_tot} \quad (6)$$

NUMERICAL SIMULATION

To have a basis to compare simulations with measurements the load cases used in this study are load cases described in the ISO standards. Three different simulations according to the ISO 230-3 chapter 7: "Thermal distortion caused by moving linear axes" are done. The thermal distortions caused by moving the y-axis with constant velocity have been simulation. The feed rates chosen for simulation are:

- 2500 mm/min, 25% of fast motion
- 5000 mm/min, 50% of fast motion
- 7500 mm/min, 75% of fast motion

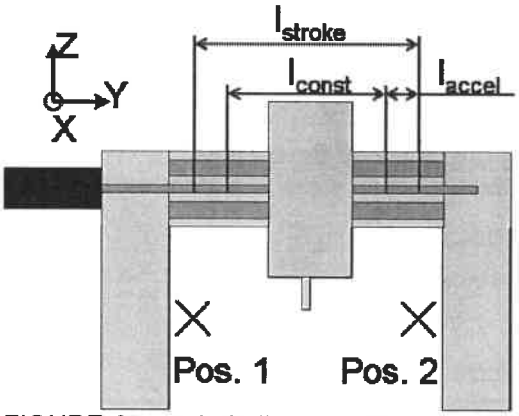

FIGURE 3. y-axis ball screw, Pos.1 and Pos.2: measurement positions.

Implementation of the Movement

In FIGURE 3 the configuration of the y-axis portal under investigation is shown. Pos.1 and Pos.2 are the measuring points. During the oscillating movement, between the measuring points, the y-axis ball screw nut travels along the ball screw over a distance l_{stroke}. During acceleration/deceleration the ball screw nut travels along the ball screw over a distance l_{accel}. Therefore the distance l_{stroke} is cut into three parts: l_{accel}, l_{const}, l_{accel}.

The boundary conditions and losses for the elements of the ball screw which are connected in l_{stroke} have to be modified.

$$P_{ele} = \left(\frac{P_{accel} * l_{accel} + P_{const} * l_{const}}{l_{ele}} \right) \cdot \frac{t_{ele\_tot}}{t_{cycle}} \quad (7)$$

l_{accel}, l_{const}: length described in FIGURE 3
t_{cycle}: time for a single cycle
t_{ele_tot}: contact time of nut and ball screw element

Equation 7 gives an example of the heat input into an element of the ball screws model which is part of l_{accel} and l_{const}. The convective boundary conditions of this element have been modified using equation 8.

$$\alpha_{ele} = \frac{t_{cycle} - t_{ele\_tot}}{t_{cycle}} \cdot \alpha_{cal} \quad (8)$$

α_{cal}: convective boundary coefficient

RESULTS AND DISCUSSION

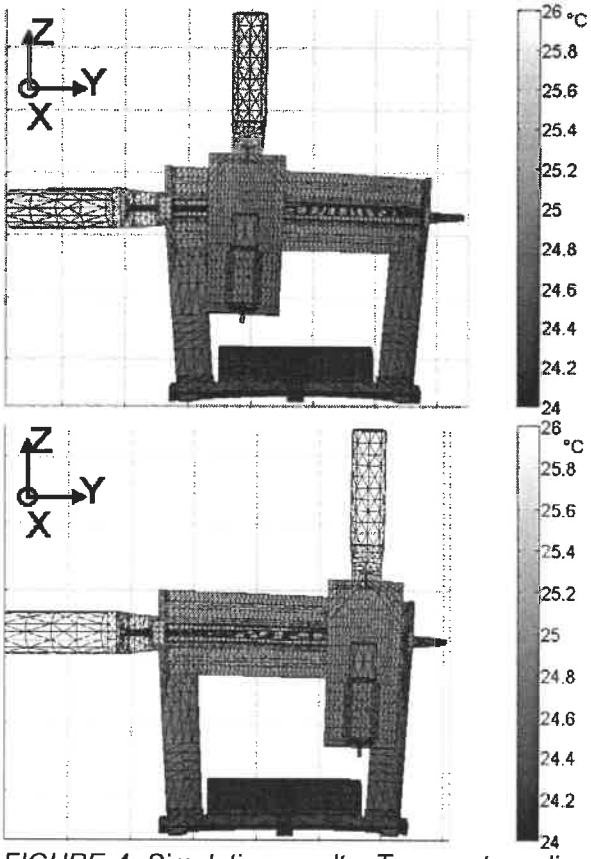

FIGURE 4. Simulation results: Temperature distribution and deformation, scale factor 10'000, steady state, top: Pos.1, bottom: Pos.2.

All diagrams in this chapter are taken from the load case of the y-axis oscillating with 5'000 mm/min over 265 mm. FIGURE 4 shows the calculated temperature distribution and deformation of the machine tool model in the measurement positions Pos.1 and Pos.2 in steady state. The colorbar shows the temperature values for the temperature distribution. Some parts of the machine tool are being heated to more than the maximum temperature in the colorbar, e.g. the y-axis ball screw and the motors.
The transient simulations help to understand the thermal behavior of machine tools in detail. FIGURE 5 shows for example the displacement in y-direction of the TCP(tool centre point). In the first two hours the TCP-displacement caused by deformation on the tool side dominates the overall TCP-displacement.

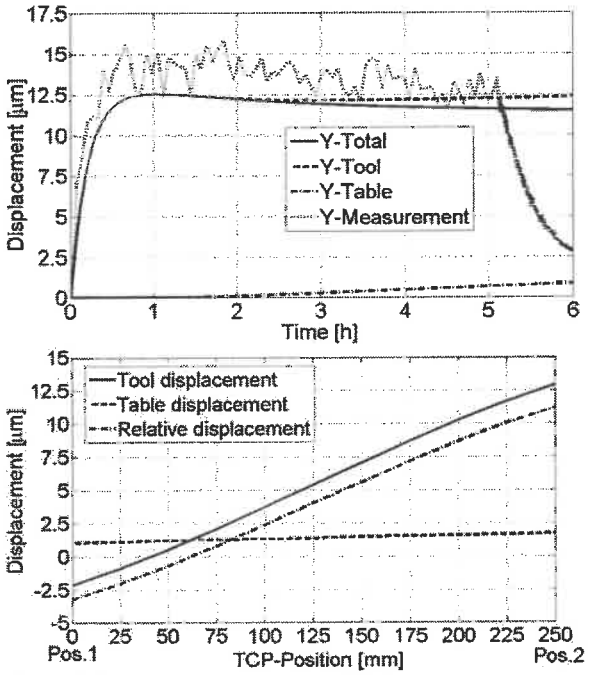

FIGURE 5. top: y-direction TCP-displacement in Pos.2, simulation and measurement, bottom: y-direction TCP-displacement for a virtual movement along the y-axis, Y-tool/YTable: TCP-displacement on the tool/table side.

Later, enough heat was flowing from the y-axis portal into the x-axis table. The table starts to grow and influences the TCP-displacements, shown in FIGURE 5, top as Y-Table.
In FIGURE 5, bottom the calculated y-direction TCP-displacement for a virtual movement cycle along the y-axis between Pos.1 and Pos.2 in steady state is shown. Because of warming the portal through oscillating y-axis the columns are bending outside. Therefore the TCP-displacements at Pos1 in y-direction are negative. The simulation results in FIGURE 5, bottom show that at about 30 mm the TCP-displacement turns into positive. The reason for this asymmetric behavior is the lengthening of the ball screw and portal.

ACKNOWLEDGEMENT

The Authors like to thank BBT for financial support.

REFERENCES

[1] Bryan J. International Status of thermal Error Research. Annals of the CIRP. 1990, 39/2. 645-656

[2] Weck M, McKeown P, Bonse R, Herbst U. Reduction and compensation of Thermal Errors in Machine Tools. Annals of the CIRP. 1995, 44/2. 589-598

[3] International Standard 230-3 2001: Test code for machine tools- Part 3: Determination of thermal effects

[4] ANSI/ASME B5.54 1991: Methodes for Performance Evaluation of Computer Numerical Controlled Machining Centres

[5] Kim S-K, Cho D-W. Real-time estimation of temperature distribution in a ball screw system. Int. Jour. of Machine Tools and Manufacturing. 1997, 37/4. 451-464

[6] Yun W-S, Kim S-K, Kung Y-T. Thermal error analysis for a CNC lathe feed drive system. Int. Jour. of Machine Tools and Manufacturing. 1999, 39/7. 1087-1101

[7] Horejs O. Thermo-mechanical model of the ball screw with non-steady heat sources. Int. Con. on Thermal Issues in Emerging Technologies: Theory and Application. 2007, 133-137

[8] Mayr J, Weikert S, Wegener K. Comparing the thermo-mechanical-behavior of machine tool frame designs using an FDM-FEM simulation approach. Proceedings ASPE 2007 Annual Meeting. 2007, 17-20

[9] VDI-Gesellschaft für Verfahrenstechnik und Chemieingenieurswesen. VDI-Wärmeatlas, 10. Auflage. Springer Verlag Berlin Heidelberg New York. 2006

[10] Xue X, Tian J, Xui G. Numerical Simulation of Thermal Stress in Castings Using FDM/FEM Integrated Method. Material Science Forum 2005, 490-491. 85-90

[11] Harris T-A. Roller Bearing Analysis, Second Edition. Wiley-Interscience New York Chichester Brisbane Toronto Singapore. 1984

COMPONENT PLACEMENT ROBOT WITH WIRELESS ENERGY AND DATA TRANSFER

Ger L.M. Jansen, and Funda Sahin
Philips Applied Technologies
Eindhoven, Netherlands

INTRODUCTION

This paper presents the results of a two years research project Wireless Interconnected Robot (WICOR). This project has been subsidized by the Dutch government and is conducted by a consortium of partners; Philips Applied Technologies, Assembleon, IMEC-NL, FMTC, NTS and Eindhoven University of Technology.

The pick and place machine AX-501 of Assembleon is shown in Figure 1. This machine is composed of up to twenty independently operating robots whose tasks is to place components on printed circuit boards, [1].

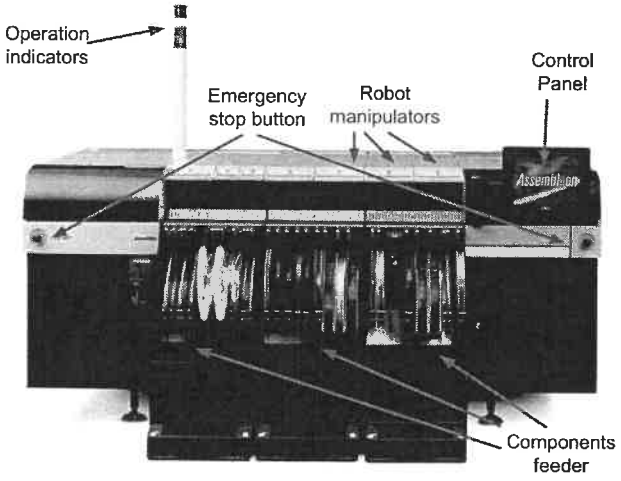

FIGURE 1. Assembleon AX-501 Component placement robot.

In the existing system, the existence of moving cables introduces reliability problems with regard to achieving higher acceleration rates and speeds. As schematically shown in Figure 2, linear motor based robots drawing wireless energy and data transfer is aimed at eliminating this hard wiring limitation. In this unit each robot is responsible for a 4-DOF movement. The X- and Y-movements are supplied by linear motors and a small φ-Z actuator on the head (Figure 2) that makes the movement in Z direction and a rotation around Z-axis. An image camera is connected to the head.

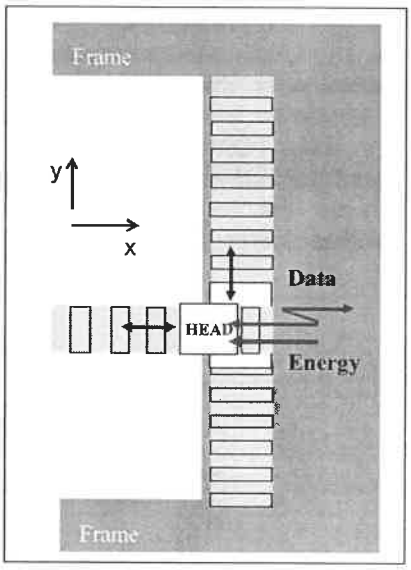

FIGURE 2. WICOR manipulator.

CONTROL ARCHITECTURE

Lower bandwidths, higher transmission delays and higher rates of packet losses all of which are typical to wireless networks are addresses by an Ethernet network topology. The real time requirement is imposed on several processes, such as motion synchronization, minimum latency in pneumatic valve control and by machine safety. This topology also dictates that the control hardware and software implementing servo control loops is located on the moving parts of the robot, [1]. The control architecture is shown in Figure 3.

WIRELESS DATA TRANSFER

The implementation of the machine control bus follows a hybrid approach that combines optical and radio frequency (RF) links. Image data is transferred via optical free-air interconnection. The light is collimated into a beam size of approximately 3 mm with a free air distance of 2 m. In order to connect the two translating axes, prisms are used as shown in Figure 4.

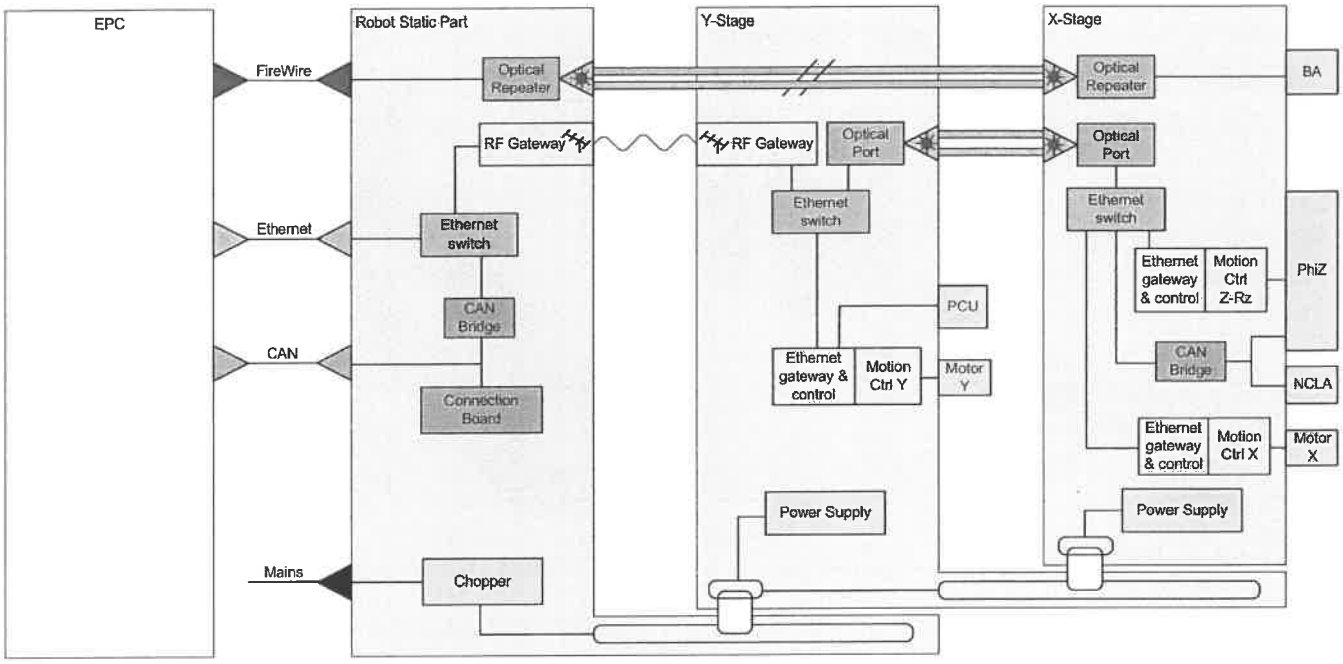

FIGURE 2. WICOR control architecture with distributed motion control and with wireless connections.

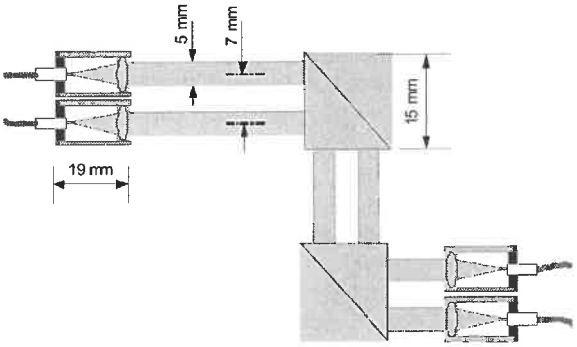

FIGURE 4.Optical free-air interconnection.

The distributed control architecture with hard real-time requirements makes the latency of the radio communication (RF) very critical, i.e. maximum of 1 ms. A comparative study of possible RF techniques (Bluetooth, Zigbee, Wi-Fi, WiMedia) showed that real time requirements can only be met by WiMedia, [2]. It has high data rate and a low latency. This standard is based on the ultra-wide band radio technology. During the project, there was no fully compliant WiMedia hardware has been available, thus a platform based on a Wisair radio chip is incorporated by IMEC-NL and FMTC [2]. The developed platform as shown in Figure 5 also includes a 32-bit ARM microcontroller, and different interfaces (Ethernet, USN, serial, etc) providing wide range of connectivity possibilities.

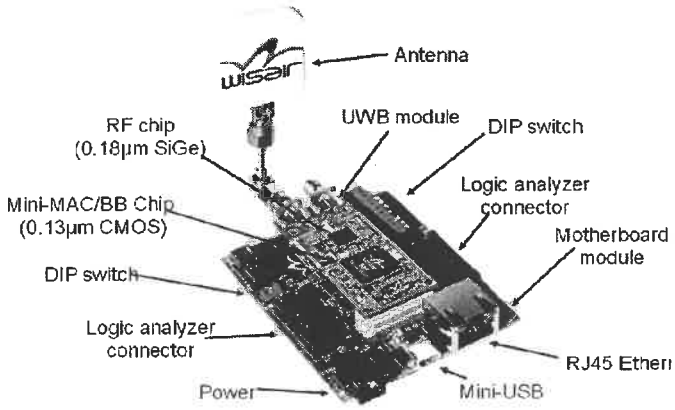

FIGURE 5. WiMedia based RF-link.

WIRELESS ENERGY TRANSFER

The two moving axes are energized by wireless energy transfer, [3]. The system is composed of a power converter, two magnetic couplers, and two power conditioners as shown in Figure 6. The details of the magnetic coupler are shown in Figure 7. The power conditioners energize the servo drive as well as the control circuitry. Due to the strict thermal specifications, extra attention is paid to limit the dissipation in the moving parts. One of the important properties studied during the project is the back delivery of the energy to the power boards during deceleration.

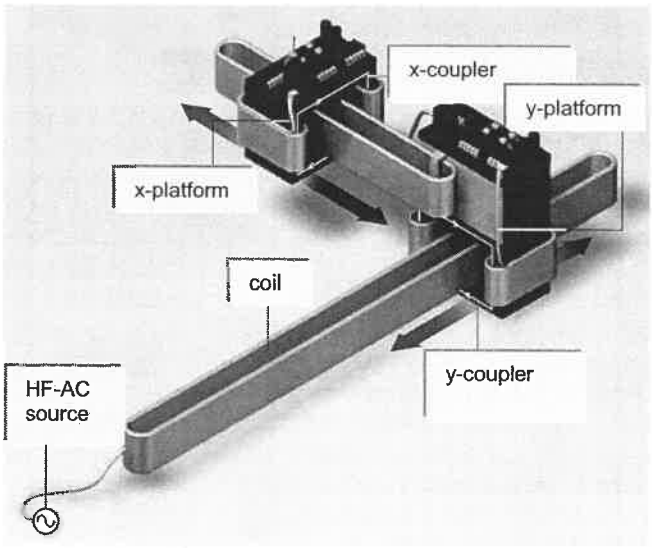

FIGURE 6. Wireless energy transfer overview.

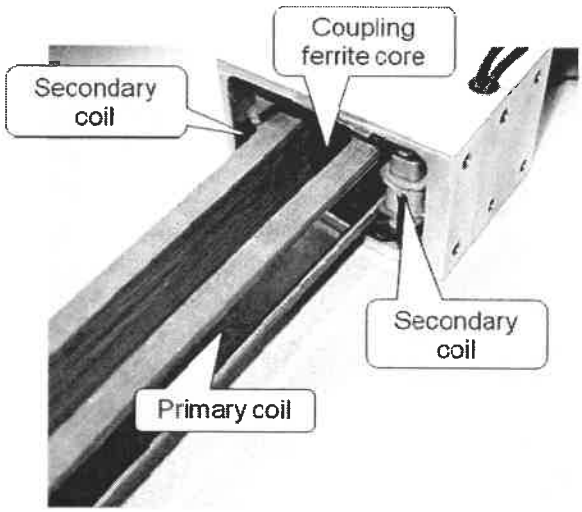

FIGURE 7. Inductive coupler.

The wireless power transfer system is shown in Figure 8 in detail. The input of the stationary power board is the 50/60 Hz mains. The output of this board generates a high-frequency (HF) AC voltage, which drives the y-coupler. Via the Y-coupler, this HF AC-voltage is contactlessly transferred to the Y-plateau. On the Y-plateau the voltage is rectified and conditioned in order to supply the controller and the motor amplifiers. Also on the Y-plateau this voltage is transferred to the X-coupler. Via the X-coupler this voltage is again contactless transferred to the X-plateau.

On the X-plateau the voltage is rectified and conditioned in order to supply the X-controller and the amplifier. The electronic circuitry of the placement head is located, and supplied here.
Due to safety requirements, standby mode of the electronics is required. Thus, the system has two modes of operation, one is standby, the other mode is full-power. In the full-power mode, the HF AC-voltage generated by the stationary power board peaks to the maximum amplitude. In case of standby this amplitude is halved.

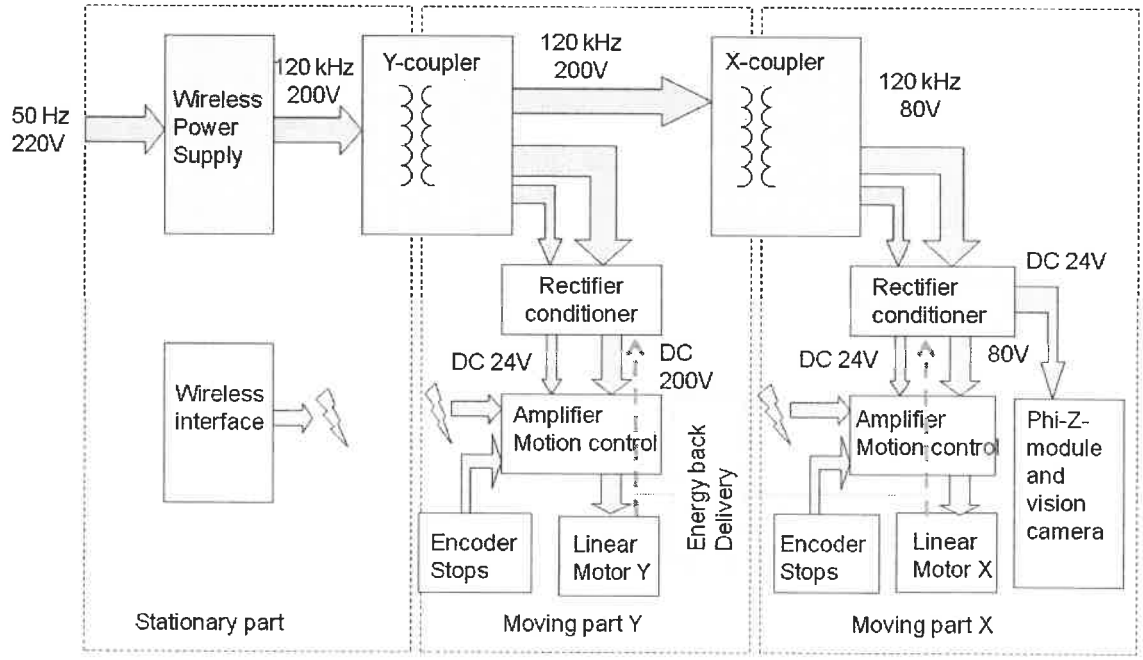

FIGURE 8. Wireless power interconnections.

During the standby mode the X and Y motors cannot be driven properly, only the control circuits on the X and Y-platform will be active. The various circuits have a status output, which are set when a certain amplitude or voltage is present.

The stationary power board incorporates mains filtering, inrush relay, pre-conditioner and the chopper. The mains filter not only prevents disturbances on the mains to enter into the supply circuitry but also prevents the disturbances generated by the supply to enter into the mains. The inrush relay limits the inrush current when the supply is turned on. This way the circuits and capacitor banks in the supply are protected against to high peak currents. With a control signal the supply can be turned off or on.

The pre-conditioner rectifies the low-frequency (LF) mains voltage and generates a constant 400 V DC voltage. The mains voltage can vary between 95 V and 265 V AC, the pre-conditioner converts this to a constant DC-voltage. The chopper consists of a halve bridge which chops the 400 V DC voltage from the pre-conditioner at a frequency of around 100 kHz. This is done with an LLC-converter. Due to the resonant operation of the LLC-converter, the AC output current is close to a sine and will generate less high harmonics which could cause EMC-problems in the system.

CONCLUSIONS

The finalized WICOR demonstrator is shown in Figure 9. It is shown that the peak power of 600 W and a continuous power of 300 W can be transferred to the moving stages without forced cooling with an overall efficiency of 80% during normal operation, excluding the power gain of the back delivered energy.

The tests conducted on WICOR demonstrator showed that the application of wireless energy and data transfer in component placement robots is feasible. Moreover, EMC tests showed no excessive radiation exceeding the legal limits. For the prospect of the industrialization of the prototype, a reduction of the total moving mass, simplification, optimized packaging and cost minimization is required.

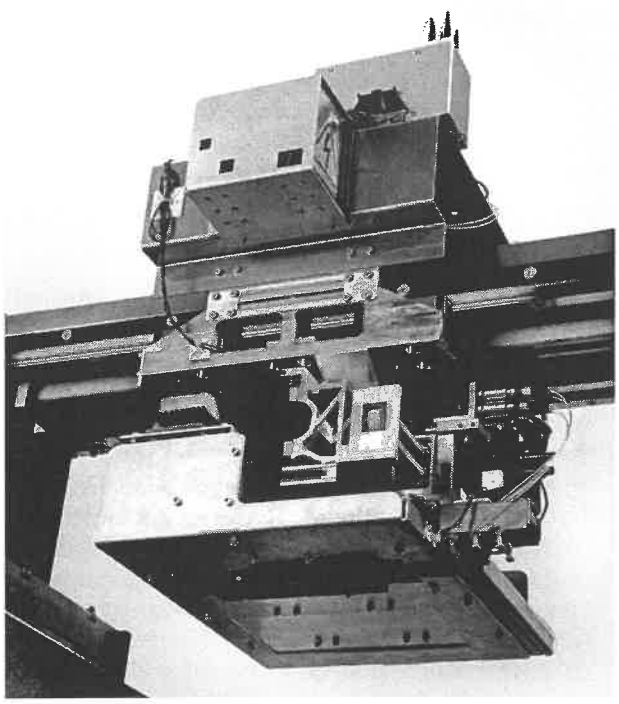

FIGURE 9. WICOR demonstrator.

ACKNOWLEDGMENTS

We would like to thank to Jef Horijon, Mark Sanders, Rik van der Brug, Milan van der Muyzenberg, Rob Hulseboos, Ray Brett and Jan van Dalfsen from Assembleon, Michelle Paselli, and Olivier Rousseau from IMEC-NL, Frederik Petre from FMTC, Jos Gunsing from NTS, Johan Paulides and Paul van den Bosch from Eindhoven University of Technology for their enthusiastic contributions to this project.

REFERENCES

[1] Horijon Jef L. Design of placement robot with wireless energy and data transfer. Philips Precision Technology Conference. 2008.

[2] Paselli, M. et al. A high-performance wireless sensor node for industrial control applications, International Conference on Systems. 2008.

[3] Jansen, G.L.M. 2-Dimensional positioning device, Patent WO2005013464A1, Koninlijke Philips Nederlands B.V. 10-02-2005.

MODEL FOR CUTTING EDGE TOOLS IN ORDER TO EVALUATE PLASTIC DEFORMATION AND FRICTION FORCES AT HIGH SPEED MACHINING

Amarandei D., Ionescu R., and Petrariu V.
Technology & Management Department
University „Stefan cel Mare"
Suceava, Romania

INTRODUCTION

The literature emphasizes that even though many calculation relations regarding the friction force are known, the plastic deformation force and the friction coefficient, are all based on the Ernst's and Merchant models, conceived for orthogonal or oblique cutting with normal speeds or derivated ones [7, 8, 9, 11, 12, 13]. For high speed cutting, Arndt [2, 3] proposes an improved model based on the spreading Merchant model for high speeds and on completing the cutting forces geometry with inertness force deducted by Ippolito, Tornincasa in [10]. According to this model, and to others, if the force's components along the feed's direction (F_c) and upon the normal direction to that (F_t), the rake angle, the flank angle are known, the friction force, the plastic deformation force and their ratio can by calculated. Also, it results that in establishing the method and devices for theoretical and experimental approach of the high speed cutting process it must refer to the problems connected to the dynamic process, to the difficult access in the research zone and to the safety of the experiment [4, 10, 13]. Referring to all these and to the working geometry of the tool, in order to investigate the aspects of the physical structure of the cutting forces, this paper proposes a spatial approach to the problem, based on the models of Ernst, Merchant and Arndt [9,12].

THE ORIGIN AND CHARACTERISTICS OF RESISTANCES TO CUTTING

Analyzing the plastic contortion mechanisms during the cutting and the mechanic characteristics of the materials one may say that considering the physical point of view, the cutting forces are made of plastic contortion force or of breakage and the friction force. The elastic force is in generally neglected. The size and especially the report between these components are influenced by the same factors that determine the cause of breakages. Therefore, the state of tensions/stress and their evolution historian, nature and properties of processes materials or of materials related to tools, the cutting conditions, respectively the speed, geometry of tool, the cutting environment and work temperature are the most important factors. The elastic deformation forces take effect within the exterior of loading area, preparing the final state of loading before the plastic deformation of the material. One may say that plastic deformation s depend upon this final state of loading (element enough for treating this problem within the elastic field) and of the way followed until achieving this state, respectively "the historian of loading" [1, 2, 3, 4]. References adequate to this part were not signaled yet by the specialty literature. The plastic deformation or instantaneous breakage is the basic parts of the cutting force. Depending of sliver's type, the forces that provoke the material's removing are of *plastic deformation or of instantaneous breakage. The plastic deformation forces* are characteristic to ductile slivers, determining the removal of material, exclusively as result of trans-crystalline breakages caused by the τ tensions. The process takes place mainly with maximal plastic deformations caused by the cutting forces on one side and the friction phenomena that take place on materials cutting, on the other side. *The instantaneous breakage forces* correspond to separating strength produced after a sudden trans-crystalline or inter-crystalline breakage under the action of normal σ tension. In this case, the process takes place without visible macroscopic plastic deformations. Practically, removing the material takes place both thanks to plastic deformation forces, and of those of instantaneous breakage, the report between them depending of processed material, the cutting speed and work temperature [1, 2, 3, 4]. The friction forces are given by external phenomena of friction, which are met on releasing areas and of placing the tool. The external friction on cutting is a complex phenomenon of molecular, mechanic and

energetic nature, being influenced by a complex of factors, among which the most important are normal forces, the speed of slipping of the sliver, the nature of contact and the hardness of materials in contact, the rigid or elastic character of contact surfaces, the temperature of the contact and the presence or absence of liquids of cutting. This complexity is amplified by the variable character of cutting conditions within the process, in report with which the contact temperature, the normal forces and nature of contact are modified. Depending of these variations, the friction can transit from dry friction on limit to mixed friction and reverse. Many of the authors that took care of the study of these phenomena reached to conclusion that friction force is made of more parts, which correspond to necessary efforts in the view of shearing the eventual micro-junctions, for producing the plastic and elastic local deformations, overcoming the shearing resistance on lubricating film or within layers of oxides on the tool's area or of processed material [4]

PHYSICAL MODEL FOR DETERMINING THE PLASTIC DEFORMATION (F_N) AND FRICTION (F) FORCES COMPONENTS

Theoretical considerations

The study of the cutting process mechanics is, quite often, assimilated with the study of the regular orthogonal cutting, which is a particular case, when the inclination edge angle is null. In the analysis of the orthogonal cutting we usually consider the process to be continuous and the chip to be the result of plastic deformation with no fissures in the deformed material and with no adherence to the edge [1]. Consequently, because of the complex of the phenomena considered, we had to adapt simplifying hypotheses, in order to resolve the issue of cutting. Time honoured models had been the standard for years, such as the Ernst and Merchant models. These are purely energetical models, which do not take into consideration the influence of deformation speed in the cutting area, the behaviour laws of the material, temperature, and so are only valid for the continuous chip formation. The bibliographical research on chip formation [4] has shown the great impact of speed on the chip formation mechanics, and on the chip shape, particularly at high speeds. Oxley and Stevenson drew up a cutting model that takes into consideration the influence of deformation speed as well as the temperature. We cannot help noticing, in Oxley's studies, identical hypotheses to be found in Merchant's studies, in particular the application of this model only in the case of formation for continuous splinter. But the laws of material behaviour, the instability that can occur, particularly in processing at high speed, are not taken into account by Oxley's model. In conclusion, in order to exploit the cutting models as well as the proposed calculation methods for cutting at high speed, we always need, as prerequisites, the characteristics of the cutting, the geometry of the tool, the mechanical characteristics of the material to be machined, and the refinement angle or the thickness of the chip. More to the point, we have to make the cutting experiments in order to obtain these data or to measure or calculate the cutting efforts.

Principle of model

The physical-mathematical model proposed in the paper [5] is here used to determine the normal force of plastic deformation and friction force on tool–chip contact surfaces, respectively on the tool–part in the case of orthogonal cutting at high speed. It consists of a cutting edge relative to the *Mxyz* system, regarding the tool; the origin of M is situated on the edge, while axis *Mz* defines the cutting speed (Vc)vector direction axis; *Mx* defines the vector of the main forward movement, and axis *My* completes the system (Figure 1).

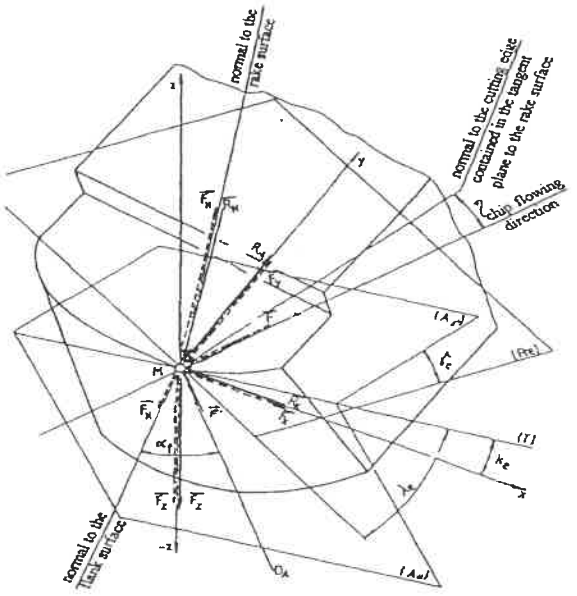
normal to the rake surface
normal to the cutting edge contained in the tangent plane to the rake surface
chip flowing direction
normal to the flank surface

FIGURE 1. Physical-geometrical model for a cutting tool.

For this model, we established linking relations between components F(t), F_N(t), R(t) and F_N(t)

components $F_x(t)$, $F_y(t)$ and $F_z(t)$, under experimental measurements.

$$\begin{bmatrix} -A_1 & B_1 & C_1 & N_1 \\ -A_2 & B_2 & C_2 & N_2 \\ -A_3 & B_3 & C_3 & N_3 \end{bmatrix} \cdot \begin{bmatrix} F(t) \\ F_N(t) \\ F'(t) \\ F'_N(t) \end{bmatrix} = \begin{bmatrix} +F_X(t) \\ -F_y(t) \\ +F_Z(t) \end{bmatrix} \quad (1)$$

The equation system (1) can be solved in two circumstances: considering the friction coefficient $\mu_\alpha = F'/F'_N$ as known or by experimentally measuring the friction force on the flank surface. Consequently, if coefficient A_i, B_i, C_i and N_i (i = 1, 2, 3) and the friction force on the flank surface, R(t) are known, we can find components F(t), $F_N(t)$ and F(t).

Method of evaluation for the friction force on the rake surface

The determination of friction forces at high speed machining was made taking into account that formation of the chips stops when the penetration into the material layer in contact with the tool is equal to the elastic deformation [4, 6]. At this moment, the experimentally obtained curves (Figure 2) for component, F_x, F_y, F_z of the cutting force have a corresponding landing.

We can observe that after an instant stop of the main feed the force is decreasing to a limit value and after that the variation is either on a circle arc or a stage.

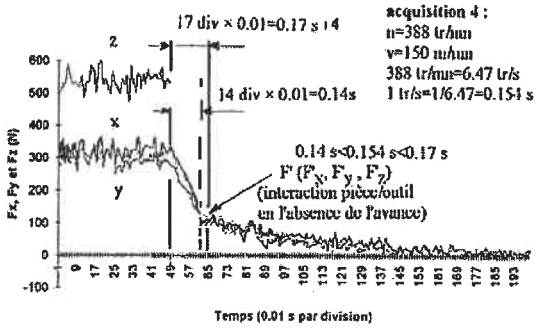

FIGURE 2. The values of the cutting force in oblique cutting of steel.

The value of the arc or the landing depends on the movement speed of the paper, but the landing appearance moment is corresponds to the feed stop. If we are consider that at the penetration (a_{min}) the cutting is stopped, it results that we can appreciate the friction force on the contact surface with the work part as the corresponding force on G point onto the experimental curves. These values are the friction forces values that correspond to the first rotation after stopping the main feed. We can also observe that the stage is present on all curves of the three components and in these conditions the resulting force can be calculated with relation (2).

$$F' = \sqrt{F_x'^2 + F_y'^2 + F_z'^2} \quad (2)$$

EXPERIMENTAL RESULTS

Condition of cutting

In order to obtain the variation curves for the cutting effort we are make the cutting tests in external cylindrical turning as indicated in (5).

The tests were done on a modified lathe, equipped with a 20 kw electrical engine and a cylindrical work piece. The work material was XC 48 and the tool was a mineral ceramic SiAlON CC 680E, SNUN type, with the following angles: $k=70^0$, $\gamma_{No} = 6^0$, $\alpha = 6^0$. Measurement of the forces was done using a piezo-electrical triple-axial dynamometer type 9257A (Kistler) in a measurement chain that also included an amplifier, a recording apparatus and a PC.

Experimental results and interpretation

The experimental results regarding the evolution of components F_x, F_y, F_z , conditioned by feed stopping time have made it possible in the given working circumstances, to obtain the values for the friction force on the flank surface, table 1. The values of components F_x, F_y, F_z inserted in model (1) led to the variation curves for components F_x, F_y, F_z .

TABLE 1. The experimental values and calculation with modelling (1).

Machining parameters		f=0.3 [mm/rot[, a=1.5 [mm[, k=70[°],γ=-6[°], λ=-6[°]						
		v, [m/min]						
		195.2	243.4	302.5	378.2	476.3	595.4	746.9
Measured forces	F_x	441	422	411	394	386	348	330
	F_y	539	514	491	467	454	415	338
	F_Z	964	955	945	939	938	935	915
	F	46.5	43.7	41.95	39.4	37.2	32.8	29.9
Calculated	F	361.0	338.2	314.6	314.6	278.4	245.3	221

forces	F_N	1007	996.1	984.2	976.5	984.6	969.3	947.8
	F_N	248.2	229.9	229.6	222.3	219.4	194.6	188.3
	μ_y	0.358	0.339	0.319	0.298	0.282	0.254	0.238

CONCLUSION

Taking into account the evolution of the cutting efforts F_x, F_y, F_z as functions of time and speed, for constant values of other cutting process parameters, with the proposed model we can determine the values for physical components of cutting force and friction coefficient. We can see that the values of these components and of the friction coefficient decrease with by the cutting speed increase.

The acquisition data system and the proposed model, for a variation law of the friction force on flank surface, make it possible determine and to study the variation of these components in dynamic.

Notations:

v - cutting speed; f.a - chip's cross section; μa - friction coefficient on the flank surface; μγ - friction coefficient on the rake surface; μγM - average friction coefficient, rake surface; τ, σ - tangential, normal stresses, rake surface; (P) - base plane; (Aα) - tangent plane to the flank surface, in M; (Aγ) - tangent plane to the rake surface, in M; (Pre) - pressure plane (normal to the effective speed vector ve-the resultant speed, at point M);T - tangent to the cutting edge, at point M; k, γ, α , λ - tool angles: tool cutting edge angle, tool rake angle, tool flank angle, tool cutting edge inclination angle respectively; ke, γe, αe , λe - working angles: working cutting edge angle, working minor cutting edge angle, working rake angle, working flank angle, working cutting edge inclination angle respectively; η - angle between the chip's flowing direction and the N vector measured in (A) plane; γN, αN - rake angle and flank angle in the secant plane No-No respectirely; No-No - secant plane; Fd - cutting force; FN -plastic deformation force; F - friction force; Fa - cutting force's component, normal to the cutting edge, in a plane parallel to the base plane; Ft - cutting force's component, along the cutting edge in plane orthogonal to rake surface; Fnt - cutting force's component, orthogonal to cutting edge in tangent plane with the rake surface.

REFERENCES

[1] Amarandei D., Des recherches concernant la grandeur des forces de déformation plastique et de frottement à la coupe avec grandes vitesses de l'acier, 1996, Thèse de doctorat, Université "Gh. Asachi" Iassy, Romania.

[2] Arndt G., Ultra-High-Speed Machining, 1972, Annals of the CIRP, vol 21/1.

[3] Arndt G., Ultra-High-Speed Machining: A review and an Analysis of Cutting Forces, 1973, Proc. Inst. Mech. Engrs., vol 187, 44/73, p625-634.

[4] Amarandei D., Méthodes expérimentales appliquées à la modélisation de l'usinage par outil coupant pour la détermination des forces de déformation plastique et de frottement pendant la coupe à grande vitesse, 1993, Mémoire du DEA de Mécanique, INSA Lyon, France.

[5] Amarandei D.,Alaci, S., Model pentru studiul influenței razei de racordare a tăişului asupra coeficientului de frecare la aşchiere, The[14th] International Conference Tehnomus, New Technologies And Products In Machine Manufacturing And Technologies, ed. a XIV-a, Suceava, 2007.

[6] Amarandei D., Researches and method concerning the experimental values of the average friction coefficient on the tool's flank in machining of carbon steels with speeds up to 1000 m/mn, 1997, 5-TH Yugoslav Conference of Tribology, Nice

[7] Elepin, A. P., Scorostnoe rezanie i ego effectihnostî pri obrabotke vleakik materialov, Sb. Nauki, TR/Gorki, In-t Inj. vod Transp., 1988, no. 233, pag. 55 – 62.

[8] Erdal, E., Elijah, K., Asibu, Jr.,"Acoustic emission and Force sensor Fusion for monitoring the Cutting Proces", Int. J. Mech. Vol. 31, No. 11/12, pag. 795, 1989.

[9] Ernst, H., Merchant, M.E., Chip Formation Friction and Hig Quality Machined Surface, Surface Treatment of Metals, Preprints, nr. 53, ASME, 1941.

[10] Ippolito, R., Tornincasa, S., Elepin, E. "Mecanica del taglio ad alta velocita, Ustensil, no.3, 1985, pag. 45–51.

[11] Merchant, M., Mechanics of the Metal Cutting process, Journal of Applied Physics, vol. 16, no. 5, 1946, pag. 267.

[12] Molinari, A., Dudzinski, D., Stationary shear band in high-speed machining, C.R. Acad. Sci., Paris-315, Seria II, 1992, pag. 399.

[13] Zorev, N.N., s.a., Razvitie nauki o rezanii metallov, Moskva, 1967.

THREE-DIMENSIONAL INTERNAL INFORMATION ACQUISITION SYSTEM BASED ON CONSECUTIVE PRECISION MACHINING AND CROSS-SECTIONAL OBSERVATION – DEVELOPMENT OF THE SYSTEM AND ITS APPLICATIONS –

Naomichi Furushiro[1], Hideo Yokota[2], Kazuhiro Fujisaki[3], Yutaka Yamagata[2], Mitsunori Kokubo[4], Ryutaro Himeno[2], Akitake Makinouchi[2], and Toshiro Higuchi[5]

[1]Department of Mechanical Engineering
Kansai University
Suita, Osaka 564-8680, Japan
[2]RIKEN (The Institute of Physical and Chemical Research)
Wako, Saitama 351-0198, Japan
[3]Division of Human Mechanical Systems and Design
Hokkaido University
Sapporo, Hokkaido 060-8628, Japan
[4]TOSHIBA MACHINE CO., LTD.
Numazu, Shizuoka 410-8610, Japan
[5]Department of Precision Engineering
The University of Tokyo
Bunkyo, Tokyo 113-8656, Japan

ABSTRACT

An automated system was developed to acquire three-dimensional information from metallurgical and biological specimens. The system is based on consecutive precision machining and cross-sectional image recording. In the system, face milling by a single crystal diamond tool is used for high precision machining, and an optical microscope is used for cross-sectional image recording.

The system enabled three-dimensional analyses of casting defects in a die casting alloy specimen, and three-dimensional microstructure observation of biological samples containing hard tissues.

INTRODUCTION

Recent advances in computer-aided engineering and diagnosis technologies need more accurate modeling techniques to acquire three-dimensional shapes and internal structures of manufactures and specimen. [1]

For years, we have developed three-dimensional internal structure microscopes (3D-ISM) to observe biological specimens. [2] [3] [4] [5] Those systems enabled us to obtain sub-micrometer volume data of specimens. But those systems cannot be applied to metallurgical samples because of their thin microtome, which chip during cutting.

In this paper, we propose a new system for acquiring internal information of both metallurgical and biological specimens.

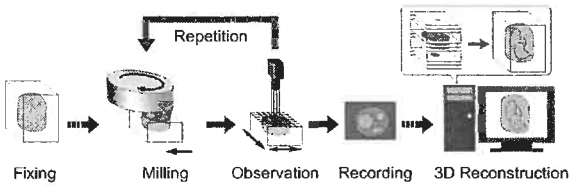

FIGURE 1. Outline of the RMSS-003

RMSS-003[6]

Figure 1 shows the outline of the system. Specimens are fixed on the system to following procedures. Precise milling and cross-sectional observations are repeated from top to bottom of the specimen. Cross-sectional information is recorded and three-dimensional information is reconstructed from that information. The system was named as RMSS-003 (Riken Micro-Slicer System 003).

Figure 2 shows the overview of the system. The system consists of a high-precision milling

machine (UVM-350(J):TOSHIBA MACHINE Co. Ltd.) and cross-sectional information recording devices. An optical microscope is used for cross-sectional image recording in this paper. Figure 3 shows the structural chart of the system. The specimen is moved to observation position after cutting. After recording all of cross-sectional images, we reconstruct three-dimensional volume of specimen with software (V-Cat[1]:RIKEN). Reconstructed volume can be segmented by the software to several parts for further analyses.

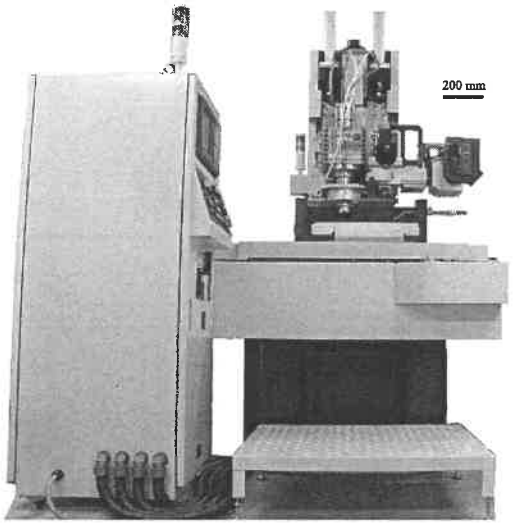

FIGURE 2. Overview of RMSS-003

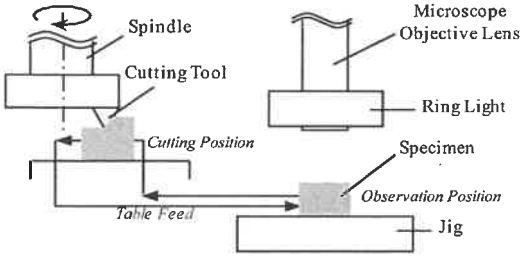

FIGURE 3. Structural chart of RMSS-003

RESULTS

System Verification

Resin Embedded Aluminum Specimen

We used a resin embedded aluminum specimen to verify the system. The specimen, 11.5 x 10.5 x 8.6 mm rectangular solid, was fixed on a jig. Then the specimen was milled and took its cross-sectional images in every 10 μm of its depth.

[1]V-Cat is a freeware developed at RIKEN and distributed at http://vcad-hpsv.riken.jp/en/release_software/V-Cat/

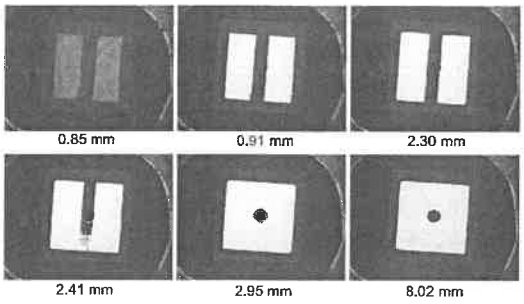

FIGURE 4. Cross-sectional images of a specimen

Figure 4 shows cross-sectional images of the specimen. Numbers below images indicate the depth from top of the specimen. We can distinguish aluminum regions in those images because they have higher pixel values than that of resin regions. We reconstructed three-dimensional images of aluminum regions and resin regions respectively.

Figure 5 shows the reconstructed images. Resin region images, upside, and aluminum region images, downside, indicate that this system can precisely acquire both internal and external shape of the specimen. The accuracy of external shape of aluminum region was approximately 0.3 %.

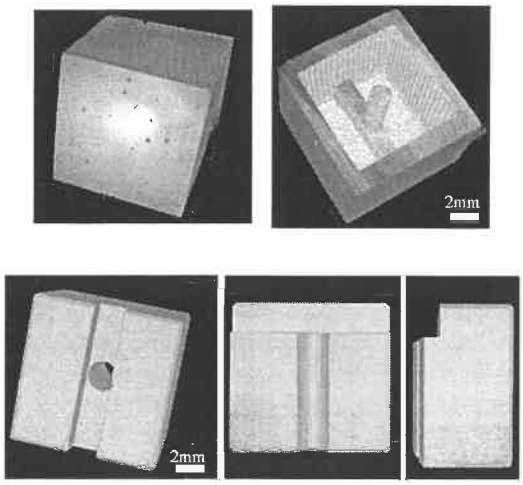

FIGURE 5. Three-dimensional images of a specimen (upside: resin, downside: aluminum)

Figure 6 shows comparison of cross-sectional images between this method and X-ray micro

computed-tomography. X-ray micro computed-tomography images were obtained by low tube voltage and high tube voltage. Figure 6 indicates that X-ray micro computed-tomography had difficulty in obtaining information of both relatively heavy and light specimen at one time. In contrast, our method can carry out that and has much less deformations and artifacts.

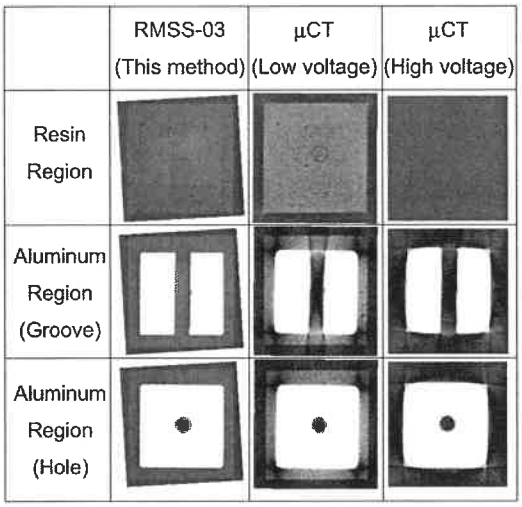

FIGURE 6. Comparison of cross-sectional images between this method and X-ray micro computed-tomography

Metallic Sample

Porosities inside Aluminum Die casts[7]

Casting defects in die casting materials are known as starting point of fatigue fractures. In this section, distributions, the sizes, and the shapes of casting defects inside aluminum die casting alloy were concerned.

Figure 7 shows X-ray transfer images of a die cast specimen (ADC12). Rectangle area between two dash lines was used as the specimen. The specimen, 20 x 14 x 37 mm rectangular solid, was fixed on a jig. Then the specimen was milled and recorded its cross-sectional images in every 5 μm of its depth.

Figure 8 shows the reconstructed image of casting defects and porosities inside the specimen. Over 5000 individual regions of casting defects and porosities were three-dimensionally reconstructed. Approximately 90% of those regions were near sphere and relatively small in diameter (smaller than 100 μm). The distribution and the size of the porosities were nonuniform inside the specimen.

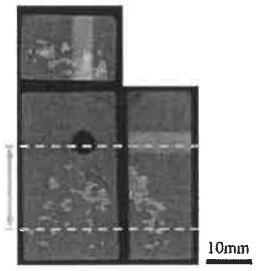

FIGURE 7. X-ray transfer image of the die cast specimen

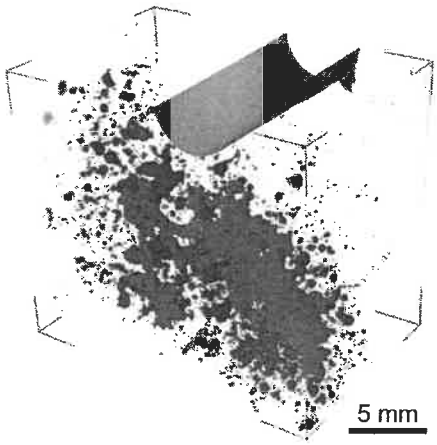

FIGURE 8. Three-dimensional reconstructed image of porosities in the die cast specimen

Biological Sample

Porcine Cortical Bone

To acquire biological samples' internal structure like lifelike shape, hard tissues and soft tissues should not be separated before cutting.

Hard tissues like bones were mirror-like finished by the system and internal structures of hard tissues were acquired. Three-dimensional internal structure of hard tissues were reconstructed and visualized by the system.

Figure 9 shows the reconstructed image of a porcine cortical bone specimen. We used a resin embedded porcine cortical bone as the specimen. The specimen was milled and recorded its cross-sectional images in every 10 μm of its depth.

Blood vessels inside bone were segmented from

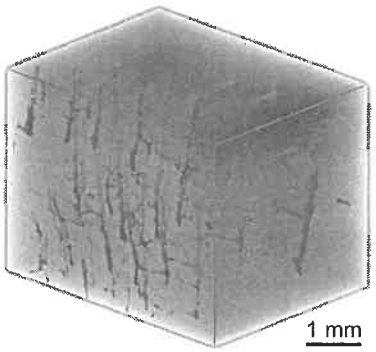

FIGURE 9. Three-dimensional reconstructed image of a bone specimen

cross-sectional images. The reconstructed image indicates that blood vessels run along the fibrous directions of the bone.

This system can be also applied to frozen specimens, which contains hard tissues and soft tissues. Both soft tissues and hard tissues of the specimen were able to be mirror-like finished. By the system, about 100 mm cube size specimen could be milled by every sub-micrometer depth. We plan to apply this system to larger biological and metallic specimens in near future.

CONCLUSIONS

An automated three-dimensional internal information acquisition system based on consecutive precision machining and high-resolution cross-section observation was developed. By the system, following results were obtained.

Cutting accuracy and information acquisition accuracy was tested and both of their errors, which are main cause of acquisition information errors, were below 1 μm. Surface roughness of a resin embedded aluminum specimen after cutting was approximately 100 nm p-v. Two-dimensional color cross-sectional images of the specimen were consecutively recorded from top to bottom. In those images, the aluminum was distinguishable from the surrounding resin, and the resin was also distinguishable from air. The aluminum and the resin were three-dimensionally reconstructed respectively from those images, and precise three-dimensional shapes and internal structures were acquired. In addition, compared to conventional nondestructive test, the information acquired by the system includes less skews, less artifacts, and has high spatial resolution.

Internal structures of over 10 mm cube size metallurgical specimen and biological sample were three-dimensionally reconstructed in less than 10 μm resolution.

ACKNOWLEDGEMENTS

This research was supported by computational biomechanics unit at RIKEN. The authors thank the unit members for their support.

REFERENCES

[1] Spowart JE. Automated serial sectioning for 3-D analysis of microstructure. Scripta Materialia. 2006;55:5–10.

[2] Kobayashi K, Higuchi T, Aoki I, Kudoh K. Development of Microslicer Implementation of 3-Dimensional Internal Structure Microscope. Journal of the Japan Society for Precision Engineering. 1995;61:100–106.

[3] Yokota H, Kudoh K, Higuchi T, Sato K. Development of 3-Dimensional Internal Structure Microscope (3D-ISM) for Observation of Expressed Gene. Japanese Journal of Medical Electronics and Biological Engineering. 1998;36:244–251.

[4] Kokubo M, Higuchi T, Kudoh K, Fukuda Y, Nanto H. The Automatic Thin Sectioning and Staining System for Light Microscopy : The Tests by Two Trial Products. Acta histochemica et cytochemica. 1999;32:223–228.

[5] Kudoh K, Kinoshita T, Do GS, Uchigasaki M, Sato K, Higuchi T. Development of an Internal Observation System for Biological Samples Using a Linear Micro-slicer. Transactions of the Japanese Society for Medical and Biological Engineering. 2005;43:103–108.

[6] Furushiro N, Yokota H, Fujisaki K, Yamagata Y, Kokubo M, Himeno R, et al. Development of Three-dimensional Internal Information Acquisition System based on Consecutive Precision Machining. Journal of the Japan Society for Precision Engineering. 2008;74:587–592.

[7] Furushiro N, Yokota H, Fujisaki K, Yamagata Y, Kokubo M, Himeno R, et al. Observation of Porosities inside Aluminum Diecasts using Three-dimensional Internal Information Acquisition System. Journal of the Japan Society for Precision Engineering. 2008;74:in press.

FABRICATION OF A NEW THREE DIMENSIONAL POSITION SURVEYING SYSTEM FOR THE UNDERGROUND PIPES USING FOUR ROTARY ENCODERS

Toshiaki HAMANO[1], Manabu ONO[2], Shigeo KATO[1]
[1]Nippon Institute of Technology, Saitama, Japan
[2]Tokyo Metropolitan College of Industrial Technology, Tokyo, Japan

INTRODUCTION

Optical fiber cable for broadband communication is usually covered by plastic pipe and buried under the ground. Then, we are required to grasp its real buried position before digging at the construction or the maintenance in order to prevent from the cutting of the optical fiber. However, once the optical fiber cable is buried under the ground, it is very difficult to confirm the buried position of the pipe, because the optical fiber cable and plastic cover pipe are not the metal.

A former way to confirm the buried position of the optical fiber cable is the ground penetrating radar method.[1], [2] The ground penetrating radar method is very useful for the metal. However, the optical fiber cable in plastic cover pipe is not metal. Another method is the elastic wave method.[3] In this method, a vibrator is put on the ground. The wave from the vibrator is detected by many in-lined receivers which are arrayed on the ground. However, the detection is only done at the place where the ground is covered by soil and the accuracy of the surveying is not good at the place where the position of the plastic cover pipe is so deep in the ground or in the different soils.

If we can detect directly the information of the buried three dimensional position of the pipe by a new position surveying system that can move itself in the pipe, the problem of the former way to confirm the buried position of the optical fiber cable is solved. This research aims to identify easily the buried position of the pipe, using the information of the buried position from the pipe. We use four rotary encoders that have pulleys contacting top, bottom, right and left walls of the buried pipe in order to detect directly the information of the buried position of the pipe.

It is confirmed that the new position surveying system can identify the buried position of a pipe that is 8 m long and has loose three-dimensional curvature in the error of 6 mm.

PRINCIPLE OF POSITION SURVEYING

Length of walls of both side of a pipe is same if the pipe is straight. If the pipe curves toward right, the length of the right wall is shorter than the length of the left wall. We use four rotary encoders that have pulleys contacting top, bottom, right and left walls of the buried pipe in order to detect directly the information of the buried position of the pipe. Output of rotary encoder contacting the wall shows the length of the wall. Average of summation of the outputs of the top, the bottom, the right and the left rotary encoder shows moving distance of a surveying mechanism of the position surveying system. The curvature of vertical direction of the buried pipe is obtained by difference of the outputs of the top and the bottom rotary encoder. The curvature of horizontal direction of the buried pipe is obtained by difference of the outputs of the right and the left rotary encoder. The three dimensional position of buried pipe is identified by the moving distance and the curvature of horizontal direction and the curvature of vertical

direction. The principle of position surveying of horizontal direction using the right and the left rotary encoders is shown in Fig. 1. Inner diameter of the pipe that has loose curvature is D. The original point is P_0. Present position of the surveying mechanism is P_n. Angle between the tangential line and the x-axis is θ_z. It is assumed that a difference ε is made by the both side rotary encoders when the surveying mechanism moves a small distance of s. This moved point is P_{n+1}. The normal lines that cross points P_n and P_{n+1} make an angle θ_z. The radius of the curvature is assumed as R. The difference ε of the right and left rotary encoders is shown as

$$\varepsilon=\left(s+\frac{\varepsilon}{2}\right)-\left(s-\frac{\varepsilon}{2}\right)=\left(R+\frac{D}{2}\right)\theta_z-\left(R-\frac{D}{2}\right)\theta_z=D\theta_z \quad (1)$$

Then, the small angle θ_z is obtained as

$$\theta_z=\frac{\varepsilon}{D} \quad (2)$$

Similarly, the curvature of vertical direction is obtained by difference of the outputs of the top and the bottom rotary encoder. The small angle of vertical direction is θ_y. The surveying mechanism may incline by some rolling force. The rolling angle is assumed as θ_x. The P_{n+1} $(x_{n+1},y_{n+1},z_{n+1})$ are calculated from the P_n (x_n,y_n,z_n), θ_x, θ_y, θ_z and s.

The coordinates of $P_{n+1}(x',y',z')$ after z rotation is

$$x'_{n+1}=s\cdot\cos(\Theta_z+\theta_z) \quad (3)$$
$$y'_{n+1}=s\cdot\sin(\Theta_z+\theta_z) \quad (4)$$
$$z'_{n+1}=0 \quad (5)$$

The coordinates of $P_{n+1}(x'',y'',z'')$ after y rotation is

$$x''_{n+1}=x'_{n+1}\cdot\cos(\Theta_y+\theta_y) \quad (6)$$
$$y''_{n+1}=y'_{n+1} \quad (7)$$
$$z''_{n+1}=x'_{n+1}\cdot\sin(\Theta_y+\theta_y) \quad (8)$$

The coordinates of $P_{n+1}(x,y,z)$ is what is added the coordinates after X rotation to the past coordinate of the point $P_n(x,y,z)$

$$x_{n+1}=x_n+x''_{n+1} \quad (9)$$
$$y_{n+1}=y_n+y''_{n+1}\cdot\cos(\Theta_x+\theta_x)-z''_{n+1}\cdot\sin(\Theta_x+\theta_x) \quad (10)$$
$$z_{n+1}=z_n+y''_{n+1}\cdot\sin(\Theta_x+\theta_x)+z''_{n+1}\cdot\cos(\Theta_x+\theta_x) \quad (11)$$

The tangential angle Θ is the summation of the small angle θ and shown as

$$\Theta_x=\Sigma\theta_x \quad (12)$$
$$\Theta_y=\Sigma\theta_y \quad (13)$$
$$\Theta_z=\Sigma\theta_z \quad (14)$$

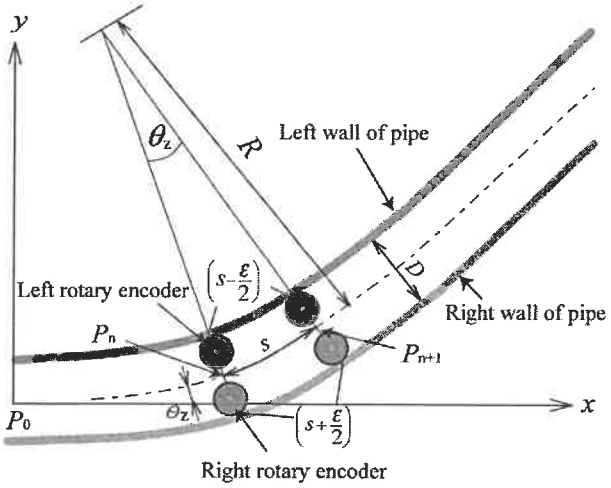

FIGURE 1. The principle of the position surveying in the underground pipe by in-pipe surveyor using rotary encoders

POSITION SURVEYING SYSTEM

A new position surveying system for underground pipes is shown in Fig. 2. The system consists of a surveying mechanism that carries the four rotary encoders, a signal processor, an I/O interface and a computer. The surveying mechanism that is 375 mm long is held to the inside of the pipe by eight small rollers and can move in the pipe. However, it is difficult to measure the length of the bottom inside pipe, because the cable exists in the pipe. Consequently, the rotary encoder is inclined 45 degrees and attached to the surveying mechanism. Small angle θ_{x0} is 45 degrees. A weight is attached under chassis in order to prevent rolling of the surveying mechanism. However, rolling of the mechanism can not be prevented perfectly. Therefore, rolling angle θ_x is

measured by another rotary encoder that is attached the chassis. The rotary encoders are held by arms that have pin joints and are attached the chassis of the surveying mechanism. The pulley is pushed to the wall of the pipe by force of 1 N and vibration of the rotary encoder is severely damped, because the arm is suspended by a spring and a dashpot. The circumference of a pulley is 64.7 mm. The signal processor consists of a detecting circuit of clockwise or counter clockwise and a mechanical chattering circuit. The rotary encoder makes 1440 pulses per one rotation. Resolution of the rotary encoder is 44 μm. The signal from the signal processor is introduced into the computer through the I/O interface. Software in the computer calculates locus of the surveying mechanism every 64.7 mm. This method decreases an error by the distortion of the pulley. Consequently, Small distance *s* is 64.7 mm of the same length as the circumference of a pulley. The result of the position surveying is displayed on the screen of the computer.

PIPE FOR SURVEYING EXPERIMENT

Coordinates of the pipe for surveying experiment

Pipe for surveying experiment is shown in Fig. 3 and Fig.4. The pipe consists of straight pipes and a curved pipe. The straight pipe and curved pipe is 4000 mm long. The curved pipe is curved of a vertical direction and horizontal direction. Distance from the original point that is the x-coordinates is measured by a tape measure. The y-coordinates is measured by steel measure from the standard line of the fishing line. The curved pipe has a curvature radius of horizontal direction 36860 mm and curvature radius of vertical direction 43930 mm and is 4000 mm long. The x-coordinates at 8000 mm of the x-axis is 186mm and z-axis is 127mm.

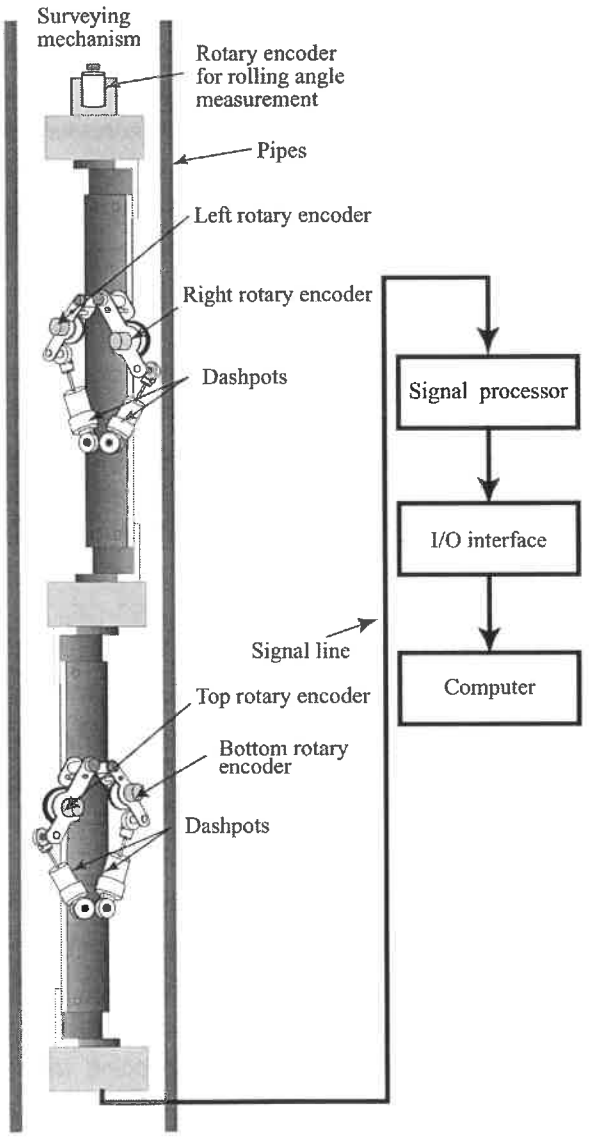

FIGURE 2. Structure of the position surveying system

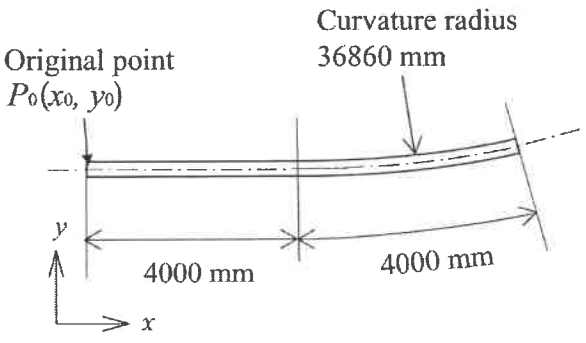

FIGURE 3. Pipe for surveying experiment of horizontal direction

Result of position surveying

The position coordinates of horizontal direction by the position surveying system and the position coordinate of horizontal direction by the steel measure are shown in Fig. 5. The position coordinates of vertical direction by the position surveying system and the position coordinate of vertical direction by the steel measure are shown in Fig. 6. The horizontal maximum of the difference occurs at the end of the pipe and is 6 mm. The vertical maximum of the difference occurs at the end of the pipe and is 5 mm.

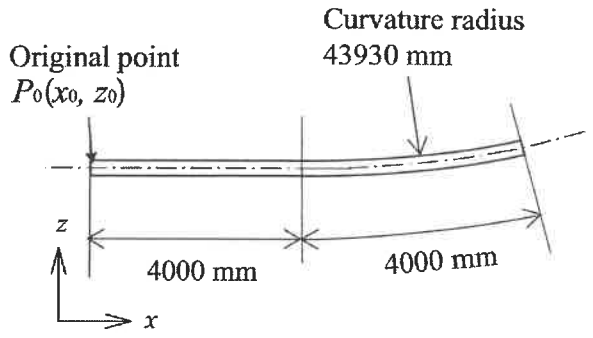

FIGURE 4. x-z Pipe for surveying of vertical direction

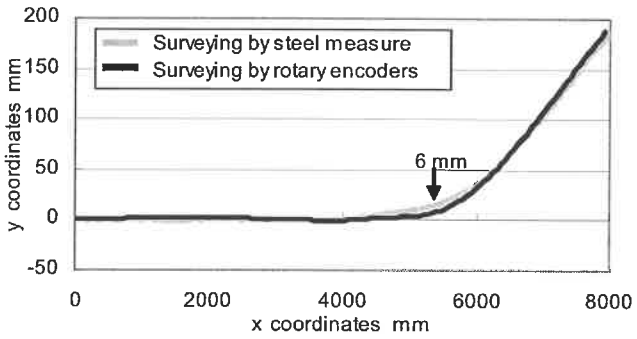

FIGURE 5. Measurement result of horizontal direction

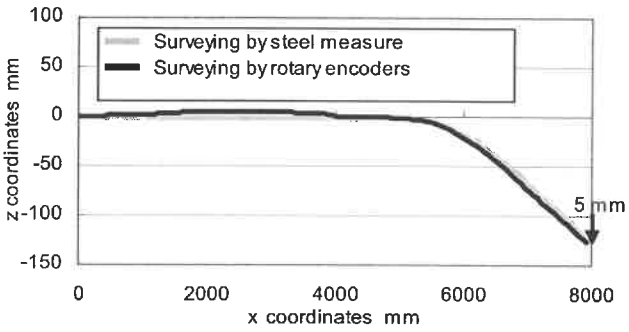

FIGURE 6. Measurement result of vertical direction

CONCLUSIONS

1. We fabrication of a new three dimensional position surveying system for the underground pipes using four rotary encoders. Four of rotary encoders measure distance of top, bottom, right and left walls of the pipe.
2. The curvature of vertical direction of the buried pipe is obtained by difference of the outputs of the top and the bottom rotary encoder. The curvature of horizontal direction of the buried pipe is obtained by difference of the outputs of the right and the left rotary encoder.
3. It confirmed that the fabricated position surveying system can survey the position of the experimental underground pipe that consists of 4000 mm straight pipes and 4000 mm curved pipe in the error of 6 mm.

REFERENCES

[1] M. Sato, Subsurface Imaging by Ground Penetrating Radar, Society of The Institute of Electronic Information and Communication Engineers Trans. , Vol. J85-C No. 7 (2002), pp. 520-530.

[2] M. Tanaka, J. Takayama, S. Ohyama Imaging Process Based on Bistatic Scanning for Subsurface Radar, Trans. on Society of Instrument and Control Engineering, Vol. 39 No. 4 (2003), pp. 325-331.

[3] Y. Kokubo, Y. Igarashi and K. Ozaki, Development of an Elastic Wave type Position Surveying System for Underground Pipe, EXTEC No. 64 pp. 57-60.

SYNTHESIS OF SEMI-SOLID CASTING PROCESSES FOR OPTIMAL FABRICATION OF THIN-WALLED PARTS

Seung-Hwan Hong[1], Kwang-Jo Lee[1] and Sung-Chong Chung[1]*
[1]Hybrid System Design & Control LABoratory
Department of Mechanical Engineering
Hanyang University, Sungdong-Gu, Seoul 133-791, KOREA

ABSTRACT
Thixomolding is one kind of semi-solid casting (SSC) processes. In this paper, to understand the thixomolding process to fabricate thin-walled Mg alloy parts, not only mechanical properties such as strength and ductility, but also dimensional accuracy of the thixomolding process are studied through experiments. To fabricate thin-walled magnesium (Mg) alloy parts, thixomolding parameters such as injection velocity, die temperature, barrel temperature, *etc.* on the quality of the finished products have been clearly studied through Taguchi methods. To expedite design processes of the warpage free parts, ANOVA is conducted to optimize the process parameters. Optimal conditions are suggested for optimal fabrication of thin-walled AZ91D alloy parts through thixomolding processes.

Key Words: ANOVA, Mg alloy, Optimal parameters, Semi-solid casting (SSC), Warpage, Thixomolding

INTRODUCTION
Magnesium (Mg) is 30% lighter than aluminum and the lightest metal. It has good damping, high specific strength, and excellent electromagnetic interference (EMI) shielding characteristics. Mg alloy is widely used for the IT, auto and consumer electronics industries [1]. Mg parts have been produced through the die casting process. Recently, they are being produced increasingly by SSC processes such as thixomolding and rheocasting processes. In this paper, thixomolding process is studied.

Microstructure of thixomolding products consists of spheroidal particles, compared with dendrites of conventional casting products. As the injected material into the die has laminar flow and the injection pressure is much greater than the die casting, SSC gives high-integrity and low-porosity products. It produces better mechanical property (dimensional accuracy, surface finish, strength, ductility, *etc.*) than what is achievable by the conventional liquid metal die casting process. However, there is difficulty for maintaining coexistence of liquid and solid in the thixomolding process. An inadequate set of process parameters causes a high porosity and unequal cooling in injection molding. Also, it causes deformation of products and nonhomogeneity [2]. Thus, optimal process parameters should be studied to meet the required characteristics of products.

Mg parts are mainly comprised of thin-wall parts. Using the thixomolding process, the high-precision fabrication of thin-walled components with large surface area is accomplished. To produce high quality parts, strength, dimensional accuracy and reduction of warpage are critical in the thixomolding of thin-walled magnesium alloy parts. They depend upon SSC parameters such as injection velocity, die temperature, barrel temperature, *etc.* In this paper, a cell-phone battery case made of AZ91D is studied through Taguchi method [3]. For the selection of optimal process conditions, the injection speed, barrel temperature and mold temperature affecting flow and cooling characteristics are selected as factors [4]. To understand the thixomolding process to fabricate thin-walled Mg alloy parts, not only mechanical properties such as strength and ductility, but also dimensional accuracy of the thixomolding process are studied through experiments.

THIXOMOLDING PROCESS
Fig. 1 shows a schematic diagram of the thixomolding process. It combines die casting with plastic injection molding and utilizes the thixotropy phenomenon [5], which primarily referred to the reversible changes from a flowable fluid to a solid-like elastic gel. First, billets are manufactured by using die casting without stirring at the liquid phase. Then the billets are made 4mm chips by cutting, and the

chips put into the hopper like the injection molding. To achieve the required solid to liquid ratio within the slurry, the temperature selected is to be based on the liquidus and solidus values of the equilibrium Mg-Al phase diagram [6] as shown in Fig. 2. When the temperature is reached at the prescribed point by reheating, the process is progressed as the high-pressure casting process. Thixomolding processes are able to obtain the uniform structure and the stabilized casting product with internal defect and porosity. The present effort is focused on a magnesium based family, mainly AZ91D, AM50 and AM60. In this paper, AZ91D Mg alloy is selected to fabricate a cell-phone battery cover.

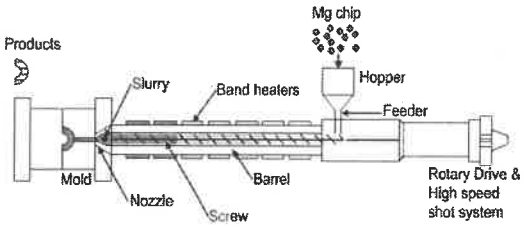

FIGURE 1. Schematic diagram of thixomolding process.

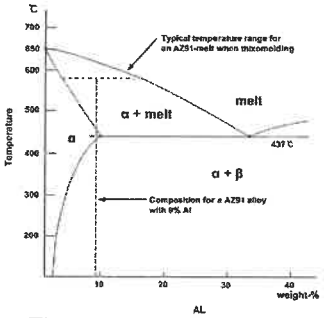

FIGURE 2. The Mg-Al phase diagram for the thixomolding process.

TAGUCHI METHOD

Taguchi method is used to develop an understanding of the individual and combined effects of various design parameters through minimum number of experiments. Objectives of the parameter design are to establish the optimal combination of design parameters and to reduce variation of product quality [4,7]. Taguchi method employs signal-to-noise(*SN*) ratio to quantify experimental variation. Depending on the particular type of characteristics involved, different *SN* ratios are applied such as 'smaller-the-better' (SB), 'nominal-is-best' (NB), and 'larger-the-better' (LB). In this paper, *SN* ratios for the LB and SB characteristics, given by Eqs.(1) and (2), related to the tensile strength and flatness are applied for the experiments, respectively.

$$SN = -10\log\left[\frac{1}{n_s}\sum_{i=1}^{n_s}\frac{1}{y_i^2}\right] \quad (1)$$

$$SN = -10\log\left[\frac{1}{n_s}\sum_{i=1}^{n_s} y_i^2\right] \quad (2)$$

where n_s is the total number of characteristic values in the orthogonal array(OA) table. y_i is the i th characteristic value, and subscript i means experimental number in the OA table. Mean statistical analysis is used to obtain optimal combination of design parameters. Eqs. (1) and (2) are applied to construct the factor response graph and to enable the robust design by using Eq. (3).

$$M_{Ai} = \frac{1}{n_A}\sum_{j=1}^{n_A}[(SN)_{Ai}]_j \quad (3)$$

where M_{Ai} is the mean *SN* ratio of the factor A at level i, n_A the number of appearances of the factor A in the OA table, $(SN)_{Ai}$ is the *SN* ratio of factor A at level i and subscript j indicates the level number.

Analysis of variance (ANOVA) is a collection of statistical models, and their associated procedures, in which the observed variance is partitioned into component due to different explanatory variables. Fundamental technique is a partitioning of the total sum of squares into components related to the effects used in the experiments [4]. *SN* ratios are derived from Eqs. (1) and (2). Variances of each factor are applied to analyze contribution of the factor in the thixomolding process.

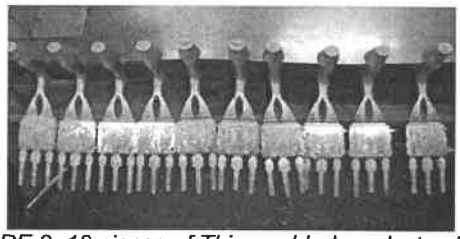

FIGURE 3. 10 pieces of Thixomolded products with the gate system and overflows.

TABLE 1. Experimental conditions for Thixomolding.

Level	A (m/s)	B (℃)	C (℃)
0	48	600	200
1	55	590	220
2	62	580	240

A: Injection velocity, B: Barrel temperature, C: Mold temperature

EXPERIMENTS

JLM220-MG thixomolding machine (JSW Inc.) is used to fabricate battery covers of a cell-phone. Mg alloy AZ91D with a nominal composition of 8.5% Al, 0.75% Zn, 0.3% Mn, Fe and Ni below 0.001%, and Mg as a balance is used for SSC. Fig. 3 shows thixomolded products. Experimental objectives are to derive optimal parameters to fabricate a battery case, which is located between a gate and overflows in the mold assembly, with good mechanical property and low warpage. Table 1 shows experimental conditions with three factors and 3 levels selected through prior experiments.

TABLE 2. OA Table, mechanical properties, and SN ratios.

No	Factors			T.S (MPa)	Y.S (MPa)	E_f (%) (gauge length 16mm)	*SN*
	A	B	C				
1	0	0	0	252.74	165	3.18	49.802
2	0	1	1	231.52	153	3.03	49.007
3	0	2	2	211.55	138	2.87	48.221
4	1	0	1	247.49	162	3.09	49.612
5	1	1	2	247.07	159	3.07	49.590
6	1	2	0	226.50	150	2.91	48.843
7	2	0	2	254.81	174	3.25	49.865
8	2	1	0	244.42	148	3.12	49.501
9	2	2	1	225.62	143	2.96	48.810

TABLE 3. ANOVA results for tensile strength.

Factor	SS	DOF	V	F0	P(%)
A	0.262	2	0.131	2.966	10.621
B	1.993	2	0.996	22.531	80.688
C	0.126	2	0.063	1.427	5.110
Error	0.088	2	0.044		3.581
Total	2.470	8	1.235		100

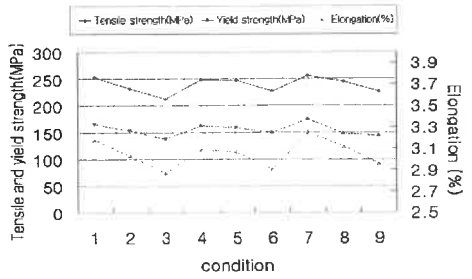

FIGURE. 4. Tensile strength, yield strength and elongation of the thixomolded AZ91D alloy.

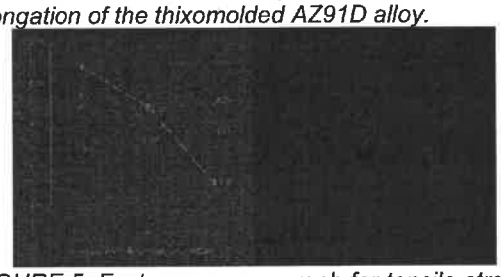

FIGURE 5. Factor response graph for tensile strength.

RESULTS AND DISCUSSION

Table 2 shows OA table with respect to experimental conditions selected in Table 1. 9 kinds of different thixomolding experiments were conducted on JLM220-MG machine with AZ91D Mg-alloy. To obtain stable and noise free results, 40 units were fabricated for each parameter combination through the thixomolding. Among the 40 units last 10 were selected for data acquisition. Fig. 3 shows them.

Mechanical properties

Table 2 and Fig. 4 show tensile strength (TS), yield strength (YS) and elongation (E_f) of the product according to experiment conditions. They were collected through the flat tension specimen (fabricated according to KS B 0801 standard) and the universal testing machine AG-10TE (Shimadzu LTD.). Tension tests were conducted according to KS B 0802 standard. 0.1 mm/min cross-head velocity was applied to reduce velocity effect in tension test.

Table 2 shows *SN* ratios of TS computed from Eq. (1) in LB characteristics. Using Eq.(3), corresponding factor response curve is obtained as shown in Fig. 5. According to the Taguchi method, maximum TS is obtained when the *SN* ratio is maximum. Fig. 5 reveals the optimal process conditions and corresponding factor values. They are 62m/s (A_2) injection speed, 600℃ (B_0) barrel temperature, and 200℃ (C_0) mold temperature. Elongation shows similar results as well.

ANOVA analysis [4] was performed using the corresponding *SN* ratios of TS. Table 3 shows ANOVA results. Barrel temperature, factor B, has contribution of over 80% about TS. YS and E_f show similar tendency as well. Taguchi experiments shows that barrel temperature should be carefully selected to obtain good mechanical properties in the SSC process.

Flatness (warpage)

SSC products have no porosity and excellent surface finish, they show better appearance than die casting products [1,2,6]. In addition to the surface quality, assessment of flatness is important to fabricate aesthetic and functional IT and digital appliance products. Warpage degrades flatness. This is generated due to residual stress occurred in cooling process. Fig 6 shows measurement regions and points of the cell-phone battery cover. 7 points are sampled in a region. As the back side does not have flaws and the thickness of the cover is 0.7mm, flatness measurements are collected from back side of 10 units by using Surfcom 1800A (Tokyo seimitsu Inc.).

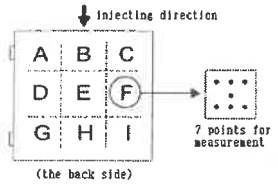

FIGURE 6. Flatness measurement regions and points.

TABLE 4. OA table, warpage values and SN ratios.

NO	A	B	C	wrapage(㎛) ave. of A~I	*SN*
1	0	0	0	20.6	-27.641
2	0	1	1	6.3	-16.305
3	0	2	2	3.4	-11.682
4	1	0	1	3.3	-10.795
5	1	1	2	4.7	-15.570
6	1	2	0	3.2	-12.770
7	2	0	2	6.6	-17.969
8	2	1	0	16.3	-27.657
9	2	2	1	3.2	-12.236

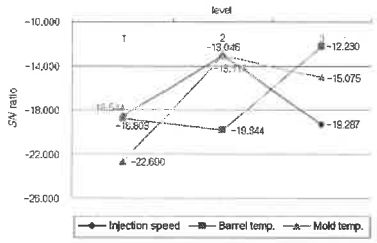

FIGURE 7. Factor response graph of warpage.

TABLE 5. ANOVA results for the warpage.

Factor	SS	DOF	V	F0	P(%)
A	66.93	2	33.46	5.088	19.87
B	104.38	2	52.19	7.936	31.00
C	152.22	2	76.11	11.573	45.21
Error	13.15	2	6.57		3.90
Total	336.69	8			100

In this paper, warpage is defined by the absolute maximum difference between concave and convex values of the battery cover. For collection of measurements, 9 regions are allocated and 7 points are measured in each region as shown in Fig. 6. To increase reliability of the data, flatness error is collected from the averaged 9 region values. Corresponding *SN* ratios with SB characteristics are computed by using Eq. (2). Table 4 shows average values of the warpage and *SN* ratios. Fig. 7 reveals the optimal process conditions and corresponding factor values to minimize the warpage. They are 55m/s (A_1) injection speed, 580℃ (B_2) barrel temperature, and 220℃ (C_1) mold temperature.

ANOVA analysis [4] was performed using the corresponding *SN* ratios of the warpage. Table 5 shows ANOVA results. Mold temperature, factor C, has significant contribution to the warpage (45.21%). Taguchi experiments confirms that mold temperature should be carefully selected to reduce warpage error in the SSC process.

CONCLUSIONS

AZ91D Mg alloy has been used to fabricate thin-walled battery cover of the cell-phone through the thixomolding process. $L_9(3^4)$ OA table and Taguchi method has been applied to select optimal process conditions and to understand the process. They have been selected to maximize mechanical properties and to minimize warpage. ANOVA has been also applied to quantize the contribution of 3 parameters. Following conclusions have been obtained:

1. Mechanical properties such as TS, YS, and E_f are reduced significantly according to decrement of barrel temperature.
2. ANOVA results show that TS is significantly governed by barrel temperature (80.688%), and warpage depends upon mold temperature dominantly (45.21%). They should be selected carefully in the SSC process.
3. 62m/s (A_2) injection speed, 600℃ (B_0) barrel temperature, and 200℃ (C_0) mold temperature are optimal values to obtain TS over 250 Mpa.
4. 55m/s (A_1) injection speed, 580℃ (B_2) barrel temperature, and 220℃ (C_1) mold temperature are optimal to reduce the warpage less than 4 ㎛.

REFERENCES

[1] Friedrich H. E., Mordike Barry L. Magnesium technology : metallurgy, design data, applications, Springer, 2006.
[2] F. Czerwinski, A. Zielinska-Lipiec, P. J. Pinet and J. Overbeeke, Correlating the microstructure and tensile properties of a thixomolded AZ91D magnesium alloy, Acta materialia Inc., 2001, Vol. 49, pp. 1225-1235.
[3] Park S.H., Modern Design of Experiments, Minyoungsa, 2001.
[4] Wang Y. C., Li D. Y., Peng Y. H. and Zeng X. Q., Numerical Simulation of Low Pressure Die Casting of Magnesium Wheel, International Journal of Advanced Manufacturing Technology, 2007, Vol. 32, pp. 257-264.
[5] Fan Z., Semi-solid Metal Processing, International Materials Reviews, 2002, Vol. 47, No. 2, pp.49-85.
[6] Avedesian M. M. and Baker H., Magnesium and Magnesium Alloys (ASM Specialty Handbook), ASM International, 1999.
[7] Wu D. H. and Chang M. S., Use of Taguchi Method to Develop a Robust Design for the Magnesium Alloy Die Casting Process, Materials Science and Engineering A, 2004, Vol. 379, pp. 366-371.

OPTICAL CLOSED LOOP CONTROL FOR THE PRECISION GRINDING OF MICRO-EDM ELECTRODES

Matthew Howe, Eberhard Bamberg
Precision Design Laboratory, Department of Mechanical Engineering
University of Utah
Salt Lake City, UT, USA

INTRODUCTION

When drilling micro holes or cutting features through the use of micro-electro discharge machining (EDM), an electrode is required that substantially matches the diameter of the feature being machined [1]. Micro-EDM electrodes are currently produced through either the mounting of standard EDM wires in precision collets or through the machining of larger electrode stock. When machined, electrodes can be manufactured through either conventional precision grinding or through reverse polarity wire electro discharge grinding (WEDG) [2]. While WEDG is known for excellent electrode quality down to extremely small diameters, it suffers from small material removal rates, which can result in several hours of grinding time for a single electrode. Conventional precision grinding, on the other hand, has much higher material removal rates, allowing electrodes to be ground much faster. However, variability in grinding parameters such as vibration, run out, electrode positioning, and electrode deflection at high length-to-diameter ratios and at small diameters can result in increased grinding time with reduced repeatability.

To mitigate this grinding variability and to provide both a faster and automated solution for conventional electrode grinding, a precision grinding machine was designed and built that incorporates a high resolution optical measurement system. The optical measurement feedback allows for automated compensation of electrode tip deflection and associated grinding variations, thereby substantially improving the repeatability and level of automation of the system.

MACHINE OPERATION OVERVIEW

The precision grinding machine shown in FIGURE 1. is comprised of an air spindle and x-y positioning stage as well as measurement feedback optics and laser light source. The electrode is located in a precision V-groove that is formed by four poly crystalline diamond (PCD) pads.

The electrode tip is fixed directly in the field of view of the optics objective. The optics and electrode as an assembly are mounted on top of a precision x-y air bearing stage, which provides the motion necessary for the grinding operation. Optical feedback is achieved by moving the stage to a retracted position at which the laser light source is focused and an image of the electrode is acquired. The image obtained by the optics is analyzed with a custom National Instruments LabVIEW Vision Virtual Instrument (VI). The VI identifies the contrast changes in the image and subsequently calculates the diameter using the mean average of over 400 separate diameter measurements spaced at 0.25 μm spacing along the length of the electrode. This data is then used as error feedback in the LabVIEW VI written for sequence automation and motion control. The flow chart for the system operation and image feedback is presented in FIGURE 2.

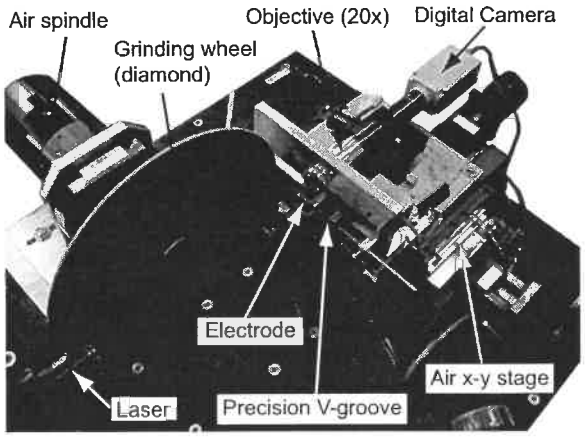

FIGURE 1. Overview of the precision grinding machine. The electrode is held in a precision V-groove that is actuated by an air x-y stage. The diamond grinding wheel is driven by an air spindle with an in-line motor.

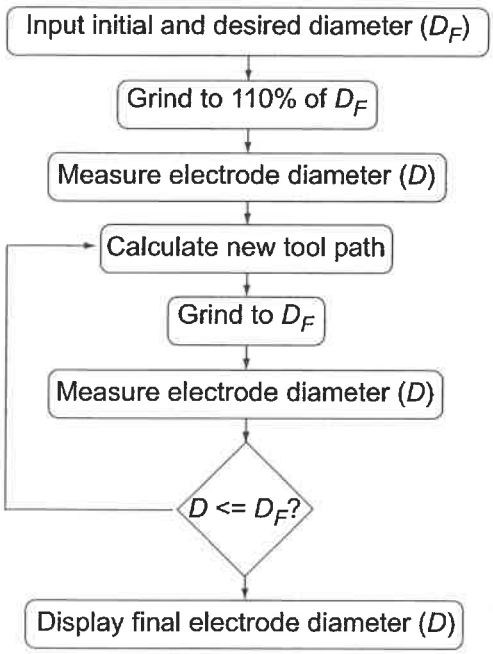
Input initial and desired diameter (D_F)
Grind to 110% of D_F
Measure electrode diameter (D)
Calculate new tool path
Grind to D_F
Measure electrode diameter (D)
$D <= D_F$?
Display final electrode diameter (D)

FIGURE 2. Flowchart of the grinder operation shows how optical measurements taken at intermediate diameters compensate for errors by adjusting the electrode position.

GRINDER DESIGN

In order to provide precise positional control for the electrode, the grinder was designed to compensate for three major sources of mechanical error inherent to the design of precision grinding equipment, which includes grinding spindle run out, vibration, and position control. To address this, the design focused on both the grinding spindle and x-y stages.

Grinding Spindle & Wheel

Electrodes are ground by means of a diamond grinding wheel mounted on a Dover Instruments precision air bearing spindle. The air bearing spindle was selected as an ideal component due its unique ability to average any run out error present while providing excellent stiffness and damping capabilities. Vibration is decreased significantly by dampening any of the imbalances present in the grinding wheel and eliminating the vibration associated with any mechanical bearings.

X-Y Air Bearing Stage

Precise positional control is necessary especially in the electrode's diametral axis (Y-axis) as this directly affects the final electrode diameter. Air bearing stages were chosen as an ideal candidate due to their extremely low friction, which eliminates position errors due to stick-slip effects. Both axes are controlled by means of closed loop control servo motors run with a National Instruments motion controller. The Y-axis position control was identified as a critical element of the design since the position of the axis defines the radius of the electrode. To mitigate this error, a Renishaw linear optical encoder with a resolution of 0.1 μm was mounted to the stage for position control. This enables 0.2 μm positional control over the diameter of the electrode.

OPTICS DESIGN

The optics for the imaging system was designed based on a resolution and field of view required to inspect typical micro-EDM electrodes. The design requirements were to achieve sub-micron measurements of the diameter with a field of view exceeding 250 μm. Measurements of the electrode diameter are based upon the detection of the two edges of an image that define the diameter of the electrode. This measurement method requires the optical resolution to be at least one half of the desired diameter resolution. In this system, the optical resolution was set to 0.5 μm with a field of view of more than 250 μm. TABLE 1. summarizes the optical results of the system that were achieved.

TABLE 1. Optics performance characteristics.

Optical Parameter	Value
Working distance	20 mm
Field of view	360 μm
Magnification	20x
Image resolve limit	0.4 μm
Camera pixel size	3.5 μm

A Mitutoyo 20x infinity corrected, long range objective was chosen as the primary optical element of the system due to its practical lens resolving limit of 0.4 μm. In order to complete the system, a mono chromatic machine vision camera was required that could handle the resolution of the objective and produce the desired field of view. A PixeLINK PL-B781U camera was chosen as being capable of providing a 0.4 μm minimum resolution at the objective magnification of 20x and a 360 μm maximum field of view. In addition

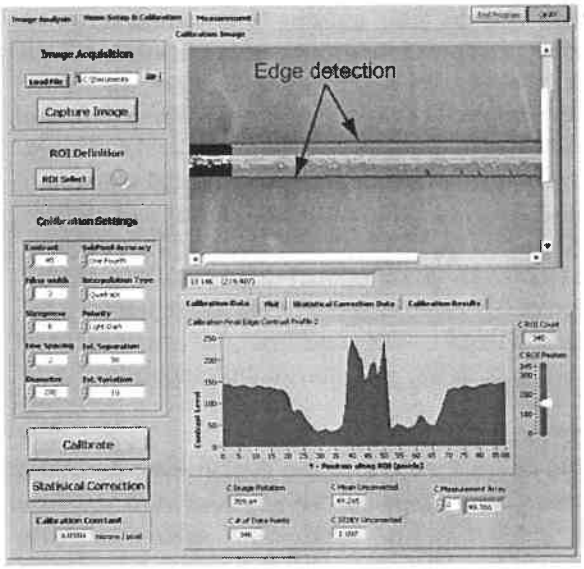

FIGURE 3. LabVIEW VI showing the edge detection technique used to measure electrode diameters from acquired images.

to the optical hardware, a machine vision software was created with LabVIEW to automatically acquire and inspect incoming images as shown in FIGURE 3.

Based on the user defined edge detection parameters, the program identifies the first and second edge of a single line crossing the imaged electrode. Next, the scaled distance between the two points is calculated as the diameter. This procedure is then iterated over the length of the image, providing a diameter data point for every pixel along the length of the electrode. Next, the data is analyzed and the mean diameter of the electrode is calculated. For the software to accurately detect the edge, the image analyzed must have a high degree of contrast at the edge transition. To achieve this, laser backlighting of the electrode is used for illuminating the image. FIGURE 4. shows the resulting contrast levels from laser backlighting of a 150 μm electrode. Note the sharp level of edge contrast.

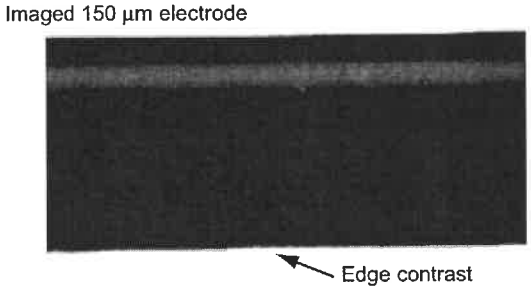

FIGURE 4. Imaged acquired from optical system illuminated using laser backlight for the production of high contrast edges.

CONTROL

System operation and control is provided by means of LabVIEW and is used to control the closed loop servo motors of the x-y axis as well as incorporating the machine vision software used for measurement of electrodes. Since the optic system is limited to a 360 μm field of view, the maximum electrode diameter that can be measured is 300 μm. For electrode stock larger than this value, a roughing program is run that initially machines the electrode without optical measurements until the diameter is smaller than the field of view. Once the electrode has been cut below the 300 μm limit, the optical feedback becomes available to provide the closed loop measurement control necessary to finish the electrode to its final dimension.

Machining parameters such as length of cut, feed rate, depth of cut, and final diameter are inputs provided by the operator. For the case where the initial electrode diameter is less than 300 μm, the program proceeds to grind automatically through completion and final measurement of the electrode. For every measurement taken, a correction factor is calculated and used to offset the actual position of the electrode by that factor. The program interface shown in FIGURE 5. is designed to provide a high level of automation and to minimize the required manual inputs from the operator.

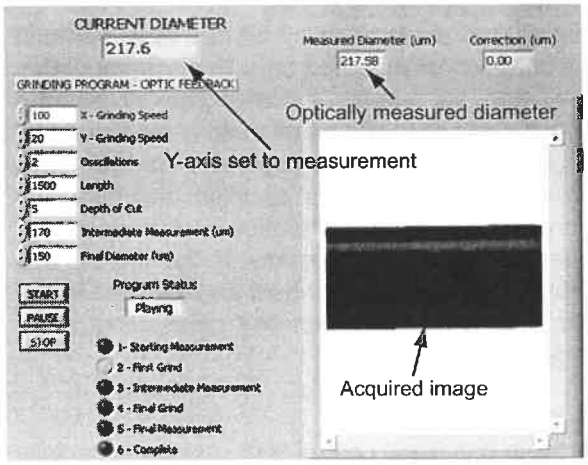

FIGURE 5. Software interface for the automated production of micro-EDM electrodes with optical measurement feedback (LabVIEW VI).

MACHINING EXPERIMENTS

To demonstrate the machining ability of the system, 3 electrodes with a diameter of 150 μm were machined. The electrodes were first machined using the software roughing program to bring approximately 500 μm electrode stock to a 200 μm starting point for the closed loop measurement system. From the rough starting value of 200 μm, the automated grinding program with optical feedback was run using the machining parameters listed in TABLE 2.

TABLE 2. Machining parameters used for the production of 3 electrodes with diameter 150 μm.

Machining parameters	Set point
Depth of cut per pass (μm)	5
Feed rate (μm/s)	100
Length of cut (μm)	1500
Final diameter (μm)	150

The results from the experiments are given in TABLE 3. The starting value in TABLE 3. indicates the measured diameter of the electrode after the rough ground without optical measurement feedback. This variation in starting value is attributed to the setup error between electrodes and the grinding variability that exists in the system. Also provided in TABLE 3. are the final measured electrode diameters along with the deviation from the actual set point. In each of the cases presented, the machining time was found to be approximately 6 minutes. To further verify the results, the electrode produced in trial #1 was measured using a separate calibrated microscope. As shown in FIGURE 6., the diameter was measured to be 148.1 μm compared to the value of 148.9 μm as reported by the grinder's measurement system.

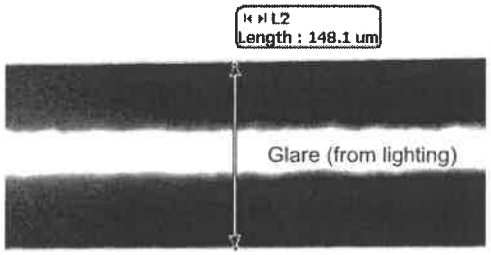

FIGURE 6. Electrode #1 measured with a calibrated microscope to verify the optical measurement of 148.9 μm from the grinder.

The deviations observed and presented in TABLE 3. allude to the current level of repeatability achieved in the system. It was observed that the electrode diameter exhibits a slight taper over the length of the electrode, which affects the measured diameter that is calculated by averaging 400 measurements along this length. Therefore, through additional calibration and better alignment of the motion elements, a reduction of these deviations is possible.

TABLE 3. Results of 3 electrodes with 150 μm set point using optical measurement feedback.

No	Starting value (μm)	Final value (μm)	Deviation (μm)
1	217.6	148.9	1.1
2	205.3	147.9	2.1
3	210.9	148.2	1.8

CONCLUSIONS

The design of a precision micro-EDM electrode grinder with air bearings, air spindle, and closed loop optical measurement feedback is presented in this paper. Three tungsten electrodes were machined with a length of 1.5 mm to a nominal diameter of 150 μm. The measured diameter deviated between 1.1 and 2.1 μm. The benefits of the optical measurement feedback can be seen by comparing the maximum tolerance of 17.6 μm achieved in grinding electrodes without optical feedback and the maximum of 2.1 μm deviation found in initial trials using the optical measurement feedback. Further tolerance improvements are expected from additional machine calibration and better component alignment, thereby reducing the presence of a slight grinding taper. Future experiments will focus on establishing and optimizing the necessary machining parameters to grind tungsten micro-EDM electrodes of given length and diameter.

REFERENCES

[1] Bamberg E, Heamawatanachai S. Orbital electrode actuation to improve efficiency of drilling micro holes by micro-EDM. J. Materials Processing Technology. In press: DOI: 10.1016/j.jmatprotec.2008.04.044.

[2] Ho KH, Newman ST. State of the art electrical discharge machining (EDM). Int. J. Machine Tools & Manufacture. 2003; 43: 1287-3000.

THE LUBRICANT APPLYING EFFECT IN Ti ALLOY Ti-6Al-4V CUTTING

Toshiaki Kaneeda and Kohei Kinugawa
Department of Mechanical System Engineering
Okayama University of Science
Okayama, Japan

INSTRUCTIONS

Large amounts of cutting oil are frequently used during cutting to improve lubrication, cooling, and chip disposal. However, the costs incurred when using and disposing of cutting oils, in addition to their negative impact on the environment, has led to increasingly strict work conditions and environmental legislation. One way to reduce the amount of cutting oil is to replace conventional oil supply methods with dry and near-dry cutting procedures. However, a detailed mechanism of near-dry lubrication has yet to be revealed.

Applying materials on the pre-cut surface in ductile metal cuttings can dramatically improve the machinability, due to a reduction in friction between the lamellas of the chip. This effect we define as the lubricant applying effect (called as LAE hereafter) [1]. Kaneeda et al. have already established that this improving machinability phenomenon is quite different from Rebinder effect. LAE have been already recognized in such ductile metals as pure aluminum, pure cupper, α-brass and mild steel by Kaneeda et al. [2], [3]. In recent years, LAE have been also recognized in SUS304 cutting by the authors [4]. Kaneeda et al. have also reported the mechanism of LAE. Under optimal conditions LAE can reduce the cutting forces by more than 90%. They determined the percentage of LAE in the lubrication by conducting the oil-submerged cutting [5] and the oil direct injection cutting. These experimental results indicated that the percentage is very high in most cutting conditions. The LAE plays a major role in lubrication in most cutting conditions, therefore, near dry machining could be performed by using the LAE.

The LAE in ductile metal cuttings have been already researched in detail. Ti alloy (Ti-6Al-4V), that is not a ductile metal, is one of the most useful materials for aircraft parts, artificial joints, etc.. In the Ti alloy cutting, it is known that cutting oil can reduce cutting forces by lubrication. Therefore, in this paper we have carried out three types of cutting experiments in order to investigate possibilities of near dry cutting and LAE.

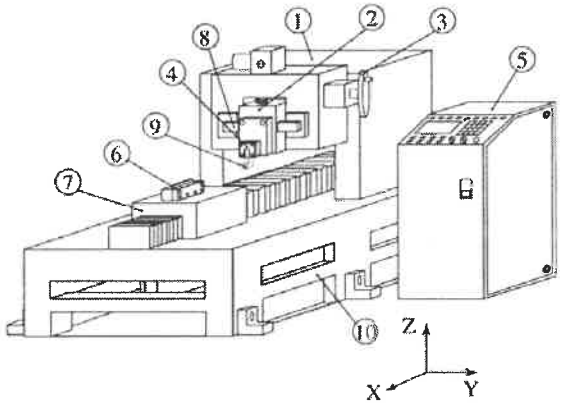

① Column ② Z axis slide ③ Y axis feed handle
④ Tool holder ⑤ Control panel ⑥ Work
⑦ X axis table ⑧ Z axis clamp ⑨ Tool
⑩ Base

FIGURE 1. NC orthogonal precision cutting apparatus

EXPERIMENTAL PROCEDURES

Three types of cutting experiments, that is to say, dry, LAE and oil-submerged (OS) cuttings were conducted on an NC orthogonal precision cutting apparatus as shown in Figure 1. Figure 2 shows the three types of cutting experiment.

TABLE 1. Cutting conditions

Work material		Ti alloy (Ti-6Al-4V)
Tool material		Cemented carbide K10
Tool geometry	Rake angle α°	0
	Relief angle ε°	7
Cutting form		Orthogonal cutting
Cutting speed V m/min		5.3, 25.7, 50.0
Depth of cut t_1 μm		10, 30, 50, 70, 100
Depth of cut at last pre-cutting t_L μm		10, 30, 50, 70, 100
Cutting oil		Oleic acid

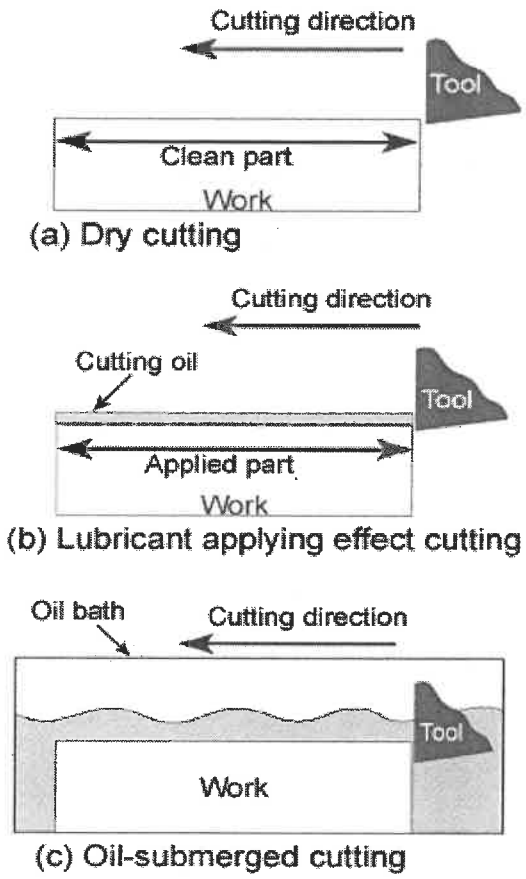

FIGURE 2. Cutting form

In LAE cutting as shown in Figure 2(b), the applied material, corresponding to cutting oil in conventional cutting, was coated on part of the pre-cut surface. The thickness of the applied material was estimated to be less than 1 μm, which led to a lusterless pre-cut surface [1]. Therefore, only minute quantity of the applied material was consumed in the experiments.

On the other hand, in the OS, both the workpiece and the nose of the tool were submerged into the cutting oil, which was in an oil bath, as shown in Figure 2(c). Any deviation in supply of the cutting oil could be eliminated.

Table 1 shows the cutting conditions.

Difficult-to-cut materials, Ti alloy (ASTEM Gr.5) Ti-6Al-4V was used as the workpiece material. Dimensions of the workpiece material was 80 × 35 × 3 mm. Cemented carbide K10 (WC + Co) was selected as the tool material. The rake angle was a constant 0 deg..

Cutting speeds are 5.3, 25.7 and 50.0 m/min. The depth of cut t_1 also ranged from 10 to 100 μm. The depth of cut at the last pre-cutting t_L, being able to control the rate of workpiece hardening in the region to be cut, ranged from 10 to 100 μm [1]. It is one of the most important factors in LAE cutting and controls the cutting forces [2]. Oleic acid was chosen as a cutting oil because of its high performance in LAE cutting of the ductile metal [6]. A quartz force transducer (Kistler Co. type 9251A) was employed to measure the cutting forces. The machined surface roughness was measured by a surface profilemeter.

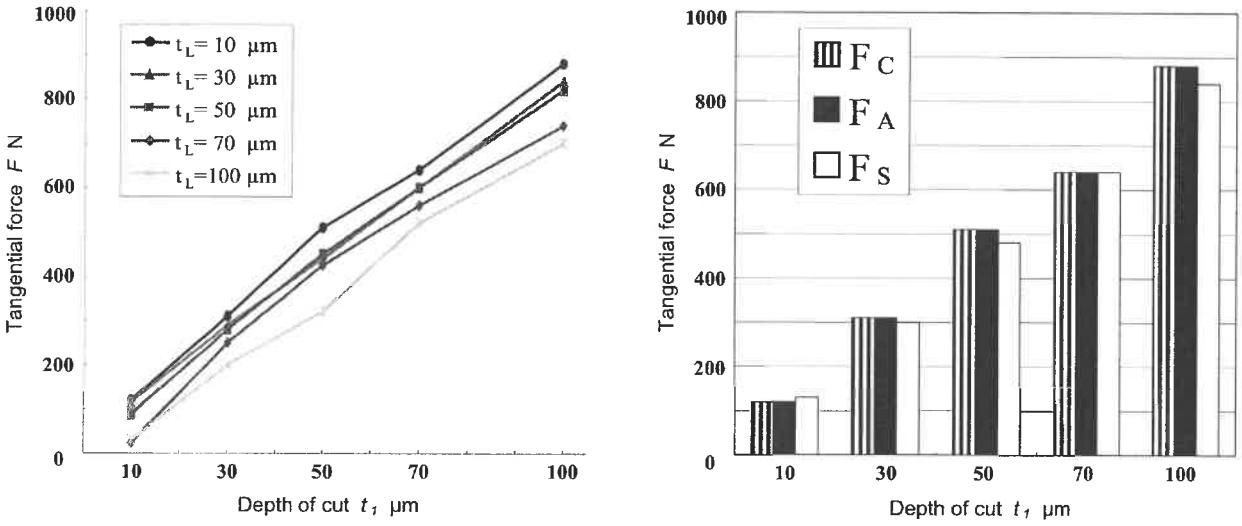

FIGURE 3. Depth of cut effects on tangential cutting forces

EXPERIMENTAL RESULTS

Figure 3a) shows the tangential cutting forces on the conditions as follows: t_L=10-100 μm, t_1=10-100 μm and V=5.3 m/min with oleic acid as the applied agent material. The tangential forces in dry cutting conditions were nearly the same values in LAE cutting in all cutting conditions. The tangential forces increased proportionally with an increase of t_1, then were affected by t_L to a great extent. This tendency is similar to in ductile material cutting such as pure Al.

Figure 3b) shows the tangential forces in the three types of cutting in t_L=10 μm constant. Other cutting conditions are the same as in Figure 3a). The symbol F_C, F_A, and F_S means the tangential forces in dry, LAE and OS conditions, respectively. Then marked differences between could be recognised. Similar results were also obtained for the other cutting conditions such as t_L=50 μm and t_L=100 μm. These results demonstrated that F_A could be identical F_C, which were only slightly higher than F_S. These results suggest that LAE could not be recognised in the Ti alloy cutting. One reason for this is due to continuous chip formation in the Ti alloy cutting under the conditions investigated, which is described later in detail.

Figure 4 shows micrographs of the machined surface in the three types of cutting. The surface profilemeter measurements presented Ra = 0.090, 0.093 and 0.089μm, respectively. These results indicated that neither the LAE nor the lubrication produced significant effects on cutting force reduction and surface roughness in Ti alloy cutting.

Figure 5 shows the tangential force, at cutting speed V=5.3, 25.7 and 50.0 m/min in dry and LAE conditions. The figure shows that the cutting forces in dry offered nearly the same value as in LAE conditions under all cutting speeds. This result dedicated no obvious LAE in Ti alloy cutting tested. The cutting forces at V=25.7, 50.0 m/min were much smaller than at V=5.3 m/min.

Figure 6 shows optical micrographs of the workpiece stopped during the cutting with t_L=50 μm, t_1=50 μm, V=5.3 m/min in the dry condition. The line AB in the Figure 6a) separated the chip and workpiece. The chip above this line has been deformed by severe shearing process. On the other hand the workpiece below the line was entirely undeformed. The chip was a continuous ribbon shape that is extremely homogeneous relative to shear strain and relatively smooth on the rake surface side [7]. The lamella on the free surface side in Figure 6 was similar to in the fan wiper type chip [1]. However, the slip lines started from the tool rake face side and ran parallel each other toward the free surface side

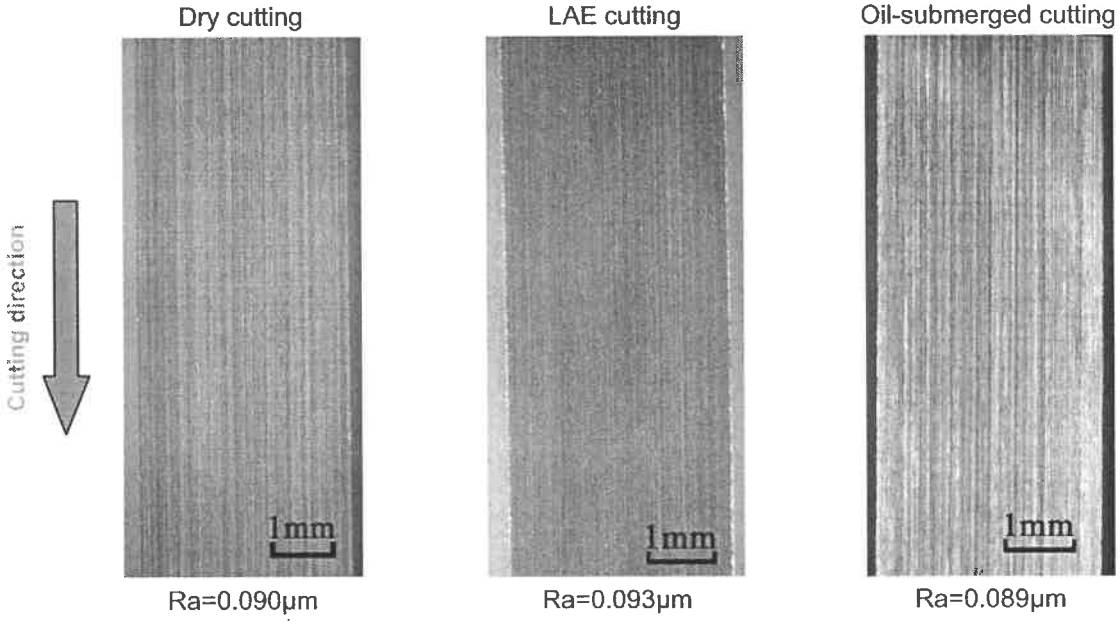

FIGURE 4. Micrographs of the machined surface and surface roughness

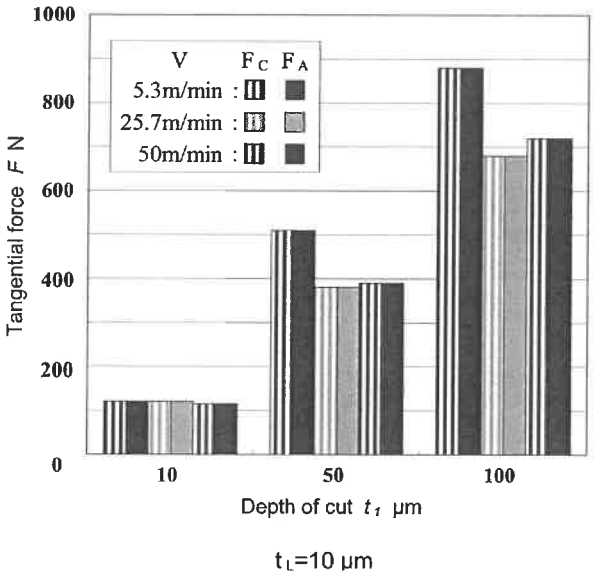

FIGURE 5. Cutting speed effects on cutting force

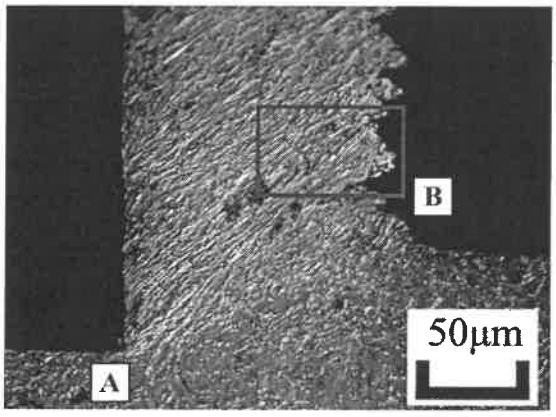

a) Deformed area

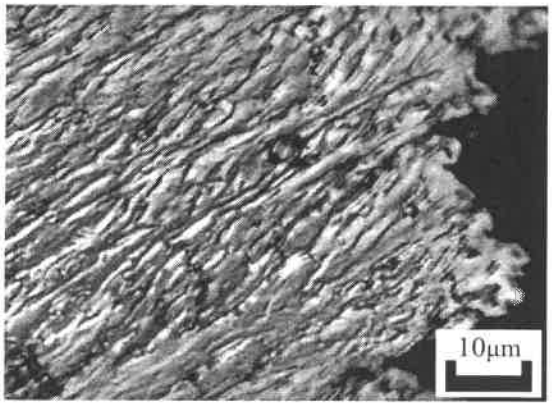

b) Lamella on the free surface side of the chip

FIGURE 6. Optical micrographs of chip

in the chip. The slip lines didn't have concave locus around the free surface, as shown in Figure 6b). This shape of slip line presented not severe friction condition between the lamella. The chip in Figure 6 was obtained in other cutting conditions tested. Therefore, it is concluded that lubrication by the cutting oil wasn't recognized in Ti alloy cutting.

CONCLUSIONS

1) Cutting forces and surface roughness in dry conditions presented almost the same value as in Lubricant applying effect (LAE).

2) LAE wasn't recognized in the conditions as follows: t_L=10-100 μm, t_1=10-100 μm.

3) LAE was not generated at various cutting speeds ranged from 5.3 ~ 50.0 m/min.

4) Shapes of chips were identified as the continuous type.

REFERENCES

[1] T. Kaneeda, Spreading Effect in Ductile Metal Cutting, Advancement of Intelligent Production, Elsevier Science B.V. (1994) 385.

[2] T. Kaneeda, et al., Lubricant Applying Effect in Ductile Metal Cutting (1st Report) - Generating Conditions and Boundary Lubrications Effects of Applied Material, J of JSPE (in Japanese). 61, 5 (1995) 702.

[3] T. Kaneeda, et al., Lubricant Applying Effect in Ductile Metal Cutting, Proc. of the 7th International Conference of ICAA7 (2000) 507.

[4] T. Kaneeda, et al., Lubricant Applying Effect in Stainless Steel Cutting, Proc. of ICPMT. (2004) 163-168.

[5] T. Kaneeda., et al., Lubricant Applying Effect in Ductile Metal Cutting (2nd Report)- Depth of Cut and Cutting Speed Effects and Mechanism, J of JSPE (in Japanese), 66, 1 (2000) 74

[6] S. Zaima, et al., A Few Consideration on Aluminum Cutting Mechanism, Trans of JSME (in Japanese), Ser.3, 35, 277 (1969) 1940.

[7] Milton C. Shaw, Metal Cutting Principles, Oxford Science Publications (1984) 411.

STORING PERIOD EFFECTS ON WEAR PROPERTIES IN UHMWPE INSERTS FOR ARTIFICIAL JOINTS

Toshiaki Kaneeda[1] , Yoshiaki Miyata[1] and Kunihiko Fujiwara[2]
[1]Department of Mechanical System Engineering
Okayama University of Science
Okayama, Japan
[2]Nakashima Propeller Co. Ltd.
Okayama, Japan

INTRODUCTION

Artificial joints have been increasingly used in treatment of physically disabled people who have severely damaged joints. In artificial joint, ultra high molecular weight polyethylene (UHMWPE) has been usually employed as a buffer because of its very low friction coefficient, high wear resistance, high impact strength, and bio-compatibility. [1].

When artificial joints were replaced, a number of best-fit sized inserts based on x-ray inspection would be chosen for the patients. Usually, more than 70 inserts would be prepared for the arthroplasties. Finally, one of them would be chosen, then rest of them would wait for the next arthroplasties as shelf-stored. If the shelf-stored inserts can be used, the manufacturing cost will reduce to a great extent. However, the shelf-storing period effects on wear properties in UHMWPE insert have not been investigated yet.

Then, storing period effects on wear properties in UHMWPE inserts were determined using a pin-on-disk wear testing machine.

EXPERIMENT

PIN-ON-DISK WEAR TEST

A pin-on-disk wear testing machine (JT-TOHSI INC., Japan) was used to investigate the tribological behavior of the UHMWPE disks against Co-Cr-Mo pins with distilled water as a lubricant. A contact stress 10Mpa, a constant sliding velocity of 196.5mm/sec (150rpm) and test durations up to 999999 revolutions (78.8km) were chosen. The friction force f was measured with a load cell.

The weight difference between before and after the tests was measured as a wear volume. Wear factor was employed to compare each data.

TABLE 1 shows wear test conditions.

MATERIALS

DISK

FIGURE 1 shows shape and dimensions of the pin and the disk. Three kinds of UHMWPE disk instead of the inserts have been prepared for the wear test.

TABLE 1. Wear test conditions

Experimental apparatus		Pin-on-disk wear testing machine
Disk	Material	UHMWPE (GUR1020)
	Molding	Machining
	Condition	Original disk (n=3) 4-year-stored disk (n=3) 8-year-stored disk (n=3)
Pin	Material	Co-Cr-Mo alloy
	Top of shape	Hemisphere(R17)
Normal load		98 N (30 MPa)
Sliding velocity		196.5mm/sec(150rpm)
Sliding distance		78.8km(1000000 revolutions)
Lubricant		Distilled water (37± 1 ℃)

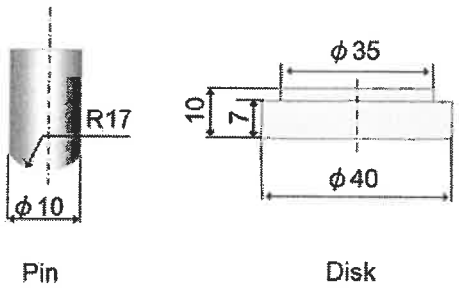

FIGURE 1. Shape of pin and disk

That is to say, they are (1) just after finished UHMWPE disks (called as original disk), (2) time passage-deteriorated UHMWPE disks (called as 4-year-stored disk) and (3) accelerated-aged UHMWPE disks (called as 8-year-stored disk).
All UHMWPE disk have 35 ϕ of sliding surface diameter. The thickness of the disk is 10mm. The disk samples were machined at Nakashima Propeller Co. Ltd. A 4-year-stored disk was extracted from actual artificial knee joint inserts. The accelerated oxidation was given to PE disk sample after it had molded, because it is difficult to obtain PE disks that passed eight years after molded,

ACCELERATED AGING OF PE DISKS

As oxidation rate is significantly slow, accelerated aging protocols have already been proposed by Sun et al. [2]. Disk samples were sterilized by gamma irradiation at a nominal 25KGy in air, then were placed in an oven at a constant temperature of 80 ℃ for 23days. The atmosphere was maintained at 1 atm in air.

PIN

The Co-Cr-Mo alloy pins have 10 ϕ . The top shape of the pin is hemisphere. The top has 17mm curvature radius corresponding to in femoral head of artificial knee joints. The surface is identified as a mirror surface (Ra<0.05μm) finished by buffing.

WEAR TEST RESULTS

FIGURE 2 shows wear volume of three kinds of disk sample. The result indicated that the original and the 4-year-stored disk sample produced greater wear volume. Wear volumes were 1.6mmg and 1.5mmg respectively. In comparison, the 8-year-stored disk sample presented the least wear volume.
FIGURE 3 shows friction forces during the wear test. At the beginning of the wear test, original and 8-year-stored disk sample indicated higher friction forces than the other. On the other hand, the friction force of 4-year-stored disk sample increased gradually during the test. However, it was found that there was little differences in the friction force between three kinds of disk sample.
An optical microscopy indicated that transfer film was formed on the pin counter face as shown in FIGURE 4.

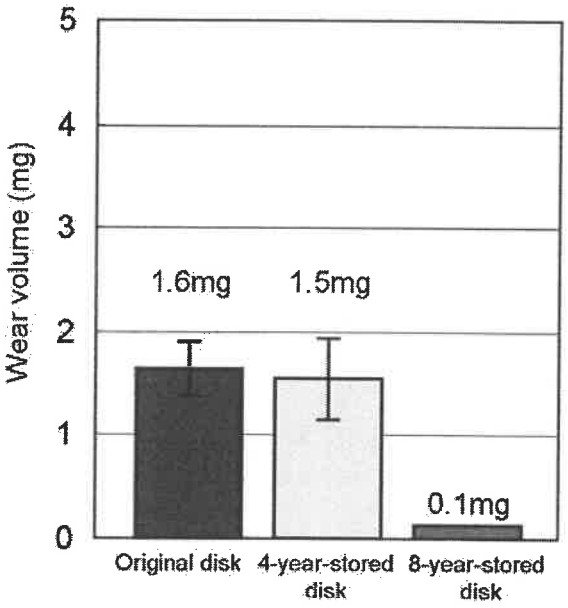

FIGURE 2. Wear volume

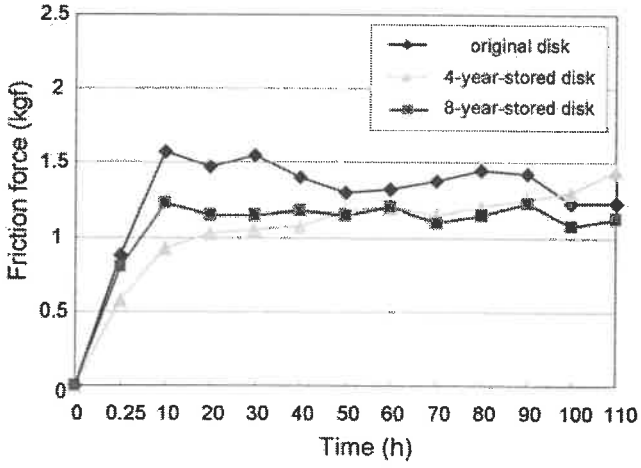

FIGURE 3. Friction forces throughout the testing

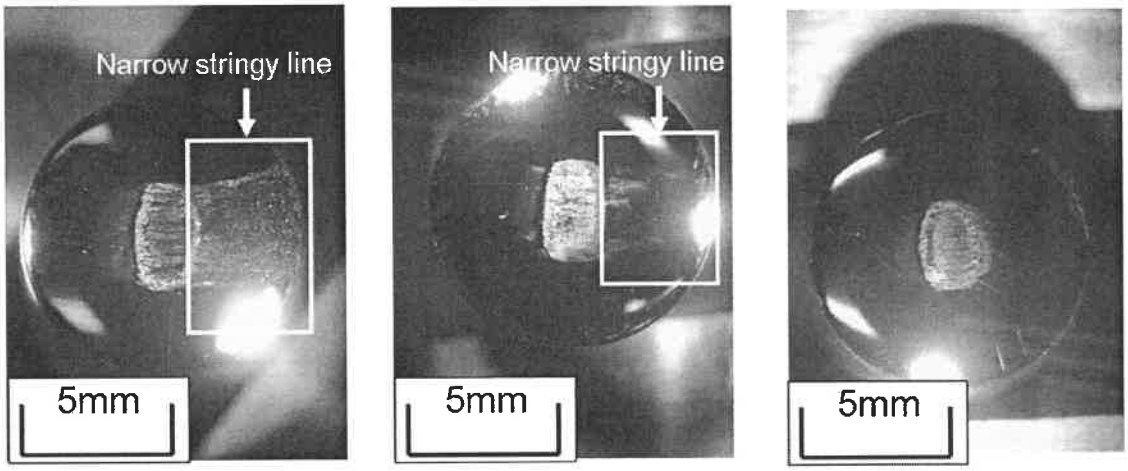

a) Original disk b) 4-year-stored disk c) 8-year-stored disk

Sliding direction is left to right.
FIGURE 4. Transfer film on pin counter face

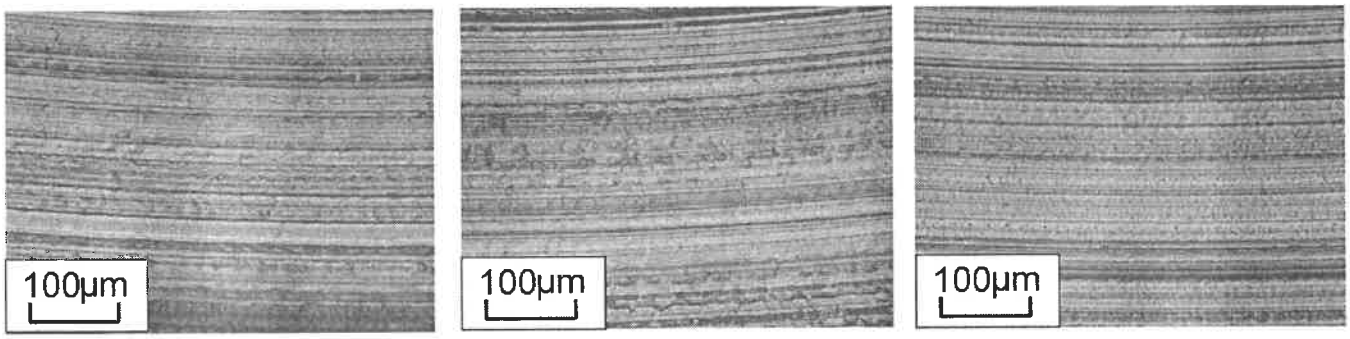

a) Original disk b) 4-year-stored disk c) 8-year-stored disk

Sliding direction is left to right.
FIGURE 5. Disk surface

Narrow stringy lines were observed at the end of the transfer film in FIGURE 4 a) and b). The line from the original disk sample was found to be larger than the others in FIGURE 4 a). On the other hand, the line from the 8-year-stored disk sample was not observed in FIGURE 4 c).
FIGURE 5 shows optical micrographs of disk sample surface. Small cracks were observed on the sliding surface of the original and the 4-year-stored disk sample. On the other hand, the 8-year-stored disk sample surface was smoother than the others. It is obvious that the smooth surface result in the least wear volume in FIGURE 2.
Hence, it is judged from FIGURE 4 and 5 that depth of settle down of the pin to the 8-year-stored disk should be small.

FT-IR ANALYSIS AND OXIDATION INDEX

It is said that time-dependent-deterioration is significantly controlled by oxidation. Then FT-IR analysis has been done to determine degree of oxidation. Using a poly cuts microtome (Reichert-Jung), we cut the specimens into approximately 40 μm-thickness horizontal sections from the disk surface to a depth of 7mm at 20 mm s^{-1} in air at room temperature. The extent of oxidation in each disk sample was measured by Fourier Transform Infrared Spectroscope (Perkin Elmer model 2000 FT-IR). All the spectral resolution were 4 cm^{-1}.

FT-IR RESULT

FIGURE 6 shows oxidation index in the three kinds of disk sample. The 8-year-stored disk sample

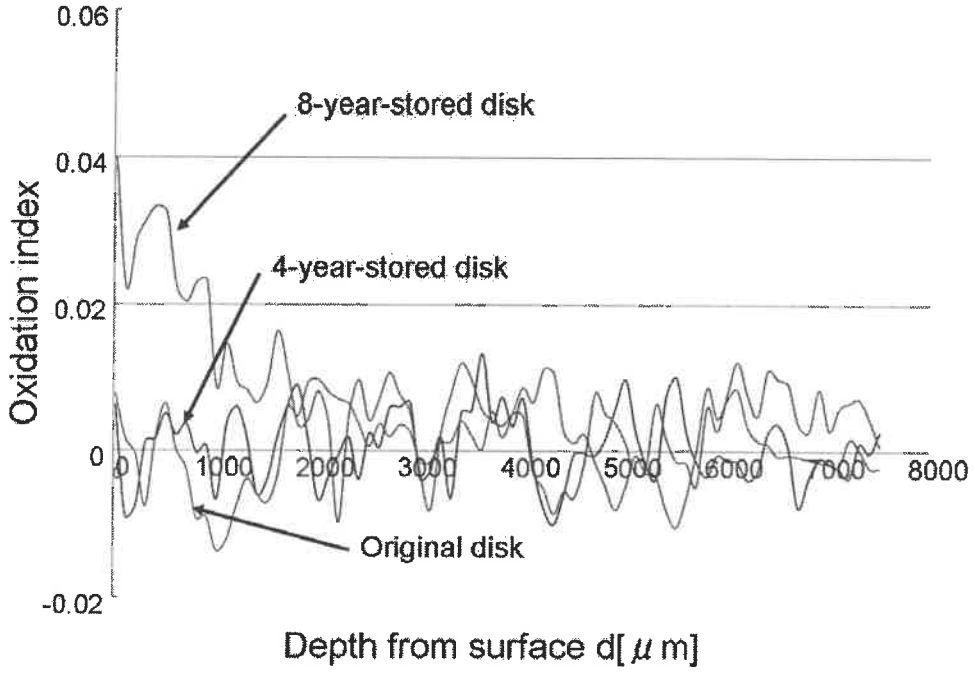

FIGURE 6. Oxidation index

offered greater oxidation index especially around the top surface, on the other hand oxidation index in the original disk sample provided similar tendency to the 4-year-stored disk sample. The 8-year-stored disk sample offered increasing degree of oxidation toward the top surface.

DISCUSSION

The wear test result demonstrated that the PE disk sample with a longer duration of storage and higher degree of oxidation absolutely presented greater anti-wear properties. This may indicate that oxidation progresses with prolonged storage of PE, which increases its hardness. [3, 4]. The evidence can be seen in FIGURE 4. It is said that that the increased hardness by oxidation results in greater anti-wear properties.

Finally, it must be noted that the same result may not be what occurs in human subjects. In a human body, additional factors of sliding and physical impact need to be considered.

CONCLUSIONS

1) UHMWPE disk sample with higher degree of oxidation presented greater anti-wear properties.
2) Little differences could be found in the friction force between three kinds of disk sample.
3) Narrow stringy line from the 8-year-stored disk sample was not observed.
4) The sliding surface of the 8-year-stored disk sample was smoother than the others.
5) FT-IR analysis demonstrated that the 8-year-stored disk sample offered greater oxidation index especially around the top surface.

REFERENCES

[1] S.M. Kurtz, et al., Advances in the Processing, Sterilization and Cross-Linking of Ultra-high-molecular-weight Polyethylene for Total Joint Arthroplasty, Biomaterials, 20 (1999) 1659-1688.

[2] D.C. Sun, et al., A Simple Accelerated Aging Method for Simulations of Long-Term Oxidative Effects in UHMWPE Implants, Proceedings of the Orthopaedic Research Society, 42nd Annual Meeting, Atlanta, Georgia, USA (1996) 493.

[3] J.P. Collier, et al., Overview of Polyethylene as a Bearing Material Comparison of Sterilization Methods, Clin. Orthop., 333 (1996) 76-86.

[4] C.J. Bell, et al., Effect of Oxidation on Delamination of Ultra-high-molecular-weight Polyethylene Tibial Components, J. Arthroplasty 13 (1998) 280-290.

DEVIATED-DEEP-HOLE BORING FOR AVOIDING AN EXISTING REINFORCING MEMBER

Akio Katsuki[1], Koichi Horita[2], T. Horiuchi[2] and Hiromichi Onikura[1]
[1]Department of Intelligent Machinery and Systems, Faculty of Engineering, Kyushu University 36,
744 Motooka, Nishi-ku, Fukuoka 812-8581, Japan
[2]Japan Fine Tech Co., Ltd.

INTRODUCTION

After the Hanshin-Awaji earthquake, reconstruction of highways, bridges, etc. are could be observed all over Japan. The Hanshin-Awaji earthquake occurred on January 17, 1995, in Japan. During the reconstruction, the following forty works are conducted, which constitute a social problem. Figure 1(a) shows a regular work that a regular anchor bolt is used after a long hole is bored between the reinforcing members. Figure 1(b) shows forty works. The left side shows the work that the short anchor bolt is used, while the right side shows the work that a reinforcing member is cut. In the former case, the pull-out resistance of the anchor bolt decreases, whereas in the latter case, the strength of the concrete decreases.

Irrespective of whether an earthquake occurred, reconstruction is necessary in all countries across the world because of the deterioration in existing construction.

The present paper introduces the technology that allows a person to drill without damaging a reinforcing member and to insert a special anchor bolt (Fig.2) [1]. Further, guidelines for efficient boring are given on the base of experiments.

MECHANISM OF BORING A BENT HOLE

Figure 3 shows the conditions of strain experienced by a boring bar during the process of boring. Figure 3(a) shows the strain experienced while boring a straight hole. The strain remains constant throughout a rotation of the boring bar. Figure 3(b) shows the strain experienced while boring a bent hole. When the tool progresses toward the direction of the inclination of the distal end, the marked (red) part of the boring bar extends (the largest tension) in **1**, remains neutral in **2**, contracts (the largest compression) in **3**, becomes neutral again in **4**, and in **5**, returns to the condition observed in **1**. The torque and thrust, which occur during boring, maintain constant. The

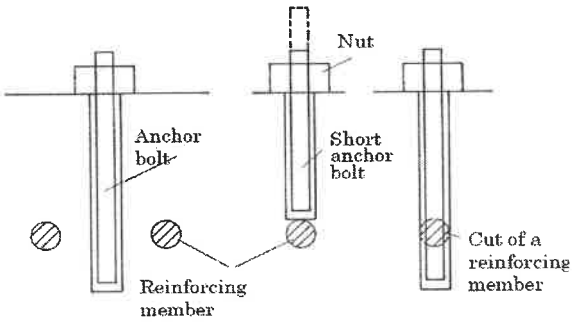

(a) Regular work (b) Forty works

FIGURE 1. Installation of anchor bolts.

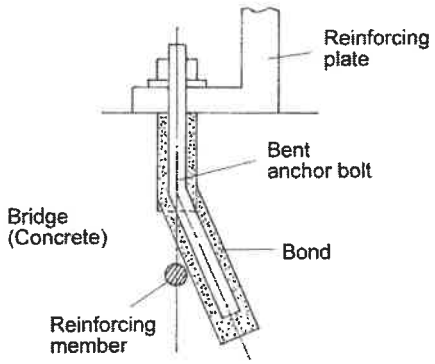

FIGURE 2. Reinforcement with a bent anchor bolt.

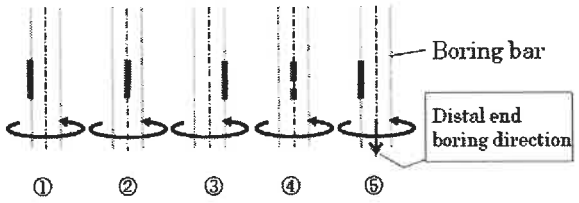

(a) While boring a straight hole

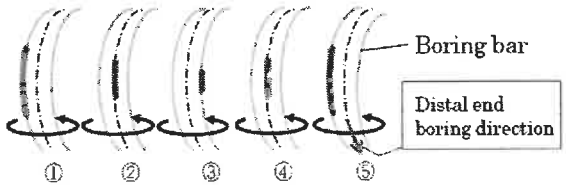

(b) While boring a bent hole

FIGURE 3. Condition of strain experienced by a boring bar while boring.

strain experienced by the boring bar remains constant while boring a straight hole, but changes in a rotation while boring a bent hole.

METHOD OF BORING A BENT HOLE

Figure 4 shows a drilling device, which is used to drill a bent hole, and an anchor bolt which is fixed in a branched hole. Two methods can be incorporated in order to install an anchor bolt in a fixing surface as follows:

Boring a Separate Hole on a Distal End Portion of the First Fixing Hole

Figure 4 (a) shows the boring of a branched hole. The first fixing hole for fitting the anchor bolt is bored in the fixing surface by a larger diamond core bit. Then the second fixing hole is bored from the distal end portion of the first fixing hole in an inclined state with a diamond core bit having a diameter smaller than that of the first diamond core bit. The boring bar of this core bit bends in order to bore a bent hole. Finally, an anchor bolt having several branched portions in the middle is fixed to the first fixing hole and the second fixing hole.

Boring a Bent Hole having a Diameter Equal to That of the First Fixing Hole

The first fixing hole for fitting the anchor bolt is bored in the fixing surface by using a larger diamond core bit. Then, the second fixing hole is bored from the distal end portion of the first fixing hole in an inclined state with a diamond core bit whose diameter is smaller than that of the first diamond core bit. The inclined state is achieved by inclining the diamond bit using a guide bush. Another diamond core bit with the same diameter as that of the first diamond core bit is moved along the prebored hole. In the last step, an anchor bolt bent at the middle is fixed to the first fixing hole and the second fixing hole.

EXPERIMENTAL METHODS

Experiments are conducted using the rotational diamond core bit - stationary concrete system. The core bit is manually fed in order to make an observation. The shape of a core bit with a diameter of 20 mm is shown in Fig.5. The photographs of the standard and guiding-type diamond core bits with a diameter of 40 mm are shown in Fig.6. As these photographs are taken after the experiments, powdered concrete is found adhered particularly to the guiding-type bit. The guiding-type bit has a guide with a diameter of 20mm on the front end of the core bit. The

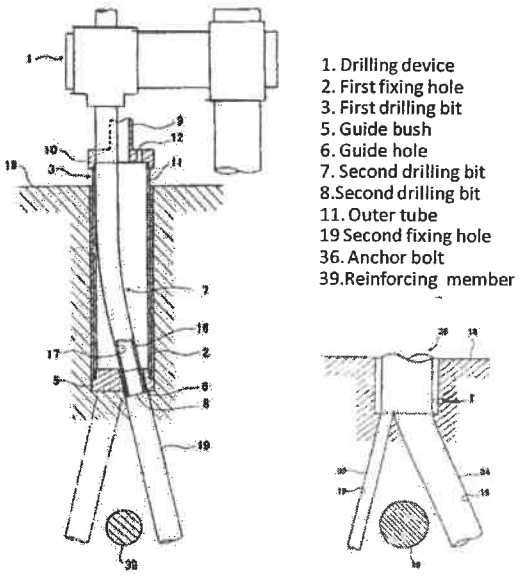

(a) Drilling device (b) Anchor bolt

Figure 4. Drilling device and a fixed anchor bolt.

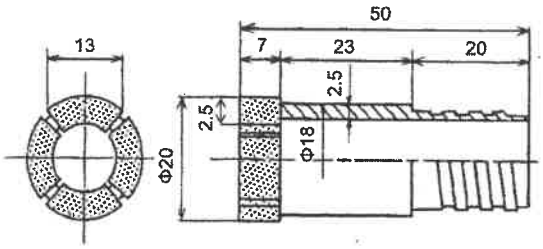

Figure 5. Shape of a 20-mm diamond core bit.

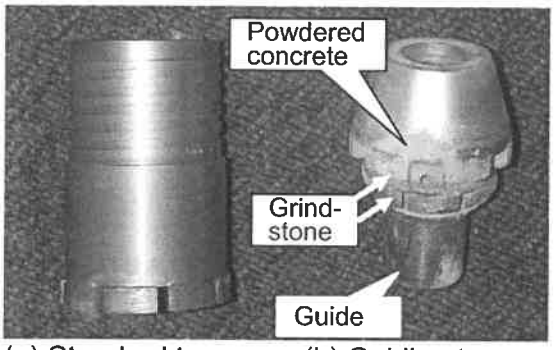

(a) Standard type (b) Guiding type

FIGURE 6 Diamond core bits with a 40-mm diameter.

guide supports the radial force acting on the core bit and guides the bit along the prebored hole. An easily available titan tube (referred to as E in Table 1) is used.

The two following types of experiments are performed in order to confirm that this technique

can be realized.

Boring of a Separate Hole on the Distal End Portion of the First Fixing Hole

Concrete made of strengthen mortar cement on the market is used. It composed of sands and cement. By using an excavator, we bore a hole having a diameter of 40 mm, up to a depth of 200 mm using a diamond core bit (SD40M) with a diameter of 40mm. The rotational speed *N* is 2000 rpm. By using a hand drill, we bore an inclined hole with a diameter of 20 mm using a diamond core bit (SD40M) with a diameter of 20 mm, up to a depth of 400 mm from the distal end portion of the first fixing hole. The rotational speed is 1000 rpm.

Boring a Bent Hole Having a Diameter Equal to That of the First Fixing Hole

The composition of the concrete used in the experiment is the same as that used in making the Hansin highway. The concrete is composed of sands, ballast, and cement.

Using an excavator, we bored a hole having a diameter of 40 mm, up to a depth of 200mm using a diamond core bit (SD40M) with a diameter of 40 mm. From the distal end portion of the first fixing hole, an inclined hole with a diameter of 20 mm is bored up to a depth of 400 mm by using the excavator under the machining condition shown in Fig.4. In order to insert the guide of the guiding-type core bit with a diameter of 40 mm, a hole wall on the inclination side and near the distal end portion is removed by a T-shape grinding tool. Then the diameter of hole is increased from 20 mm to 40 mm by using the guide-type bit shown in Fig.6 (b). City water is supplied at the rate of 7 L/min during the boring.

RESULTS

Boring a Separate Hole on the Distal End Portion of the First Fixing Hole

Figure 7 shows a bored hole with a diamond core bit fixed to the boring bar. In the case of boring the concrete without ballast, the bent hole can be easily bored with a little tool wear.

Boring a Bent Hole Having a Diameter Equal to That of the First Fixing Hole

Concrete is stronger than mortar cement; this implies that in the case of concrete, the boring torque and thrust are larger. However, it is not difficult to bore a straight hole in concrete (Fig.8). On the other hand, boring resistance increases significantly with decreasing curvature of the boring bar when a bent hole is bored. The

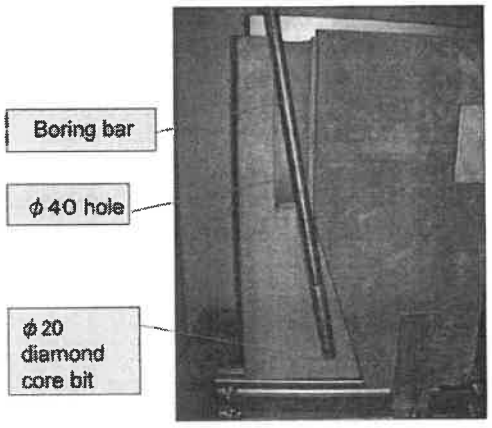

Figure 7. Boring an inclined hole with a 20mm diameter.

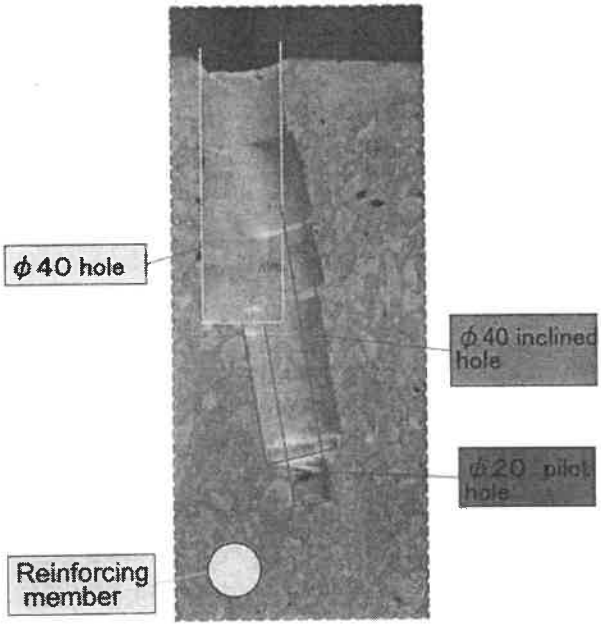

FIGURE 8. Boring an inclined hole having a 40-mm diameter after core boring up to a depth of 200 mm.

burden of the boring bar increases, which results in a large wear of the bit. It is also observed that the burden of the boring bar decreases when the shape of the guiding type bit is improved.

GUIDELINES FOR IMPROVING BENT-HOLE BORING

Material of the Boring Bar

While boring the bent hole, we observed that the boring torque increased; this resulted in damaging the boring bar. Hence, a material with a low Young's modulus, e.g., titan or aluminum, should be strengthened preferably by composite materials (CFRP).

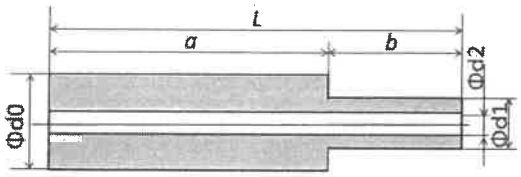

FIGURE 9.Shape of a boring bar

Shape of the Core Bit

The shape of the guiding-type core bit is important because of the low strength of the boring bar. This guide supports the radial force acting on the core bit. The front end of the guide should be changed so that it can enter a prepored hole easily. The shape of the diamond grindstones should also be designed such that they decrease the boring resistance.

Bending of a Boring Bar

Figures 9, 10 and 11 and Table 1 show the results of the examination of the relationship between the shapes and bending of the boring bars, carried out on a cantilever. The E-shaped boring bar is used in the abovementioned second experiment.

As shown in Figs. 4(a), 7, and 8, the boring bar is bent within a short range of depth in order to avoid the reinforcing member. The depth range is between 100 mm and 200mm. The short depth range is preferable, because the depth length of the hole wall, which is cut for repair work, decreases. However, when this range is shortened, the radial force increases in order to bend the boring bar. The F-shaped bar bends largely due to the application of a small force, as shown in Fig.10, while it cannot bear the torque. Therefore the D-shaped bar is preferable. If the forward part of the boring bar with a diameter of 8 mm cannot bear the torque, the part should be strengthened with some composite material in order to increase its torsional strength.

CONCLUSIONS

On the basis of these experiments, it can be concluded that this technology can be used to bore a bent hole. From now on, it is necessary to insert an anchor bolt and perform a pull-out test for this technology.

ACKNOWLEDGMENTS

We would like to express our sincere gratitude to Mr. Shinzo Wada (Ootomi Construction Co., Ltd.), Mr. Susumu Koyanagi (Noritake Super Abrasive Co., Ltd.) and Mr. Tsuyoshi Dotu for their cooperation. This research was supported by Japan Science and Technology Agency; the support is highly appreciated.

TABLE 1. Dimensions of boring bars.

Boring bar	L mm	d0 mm	d1 mm	d2 mm
A	a = 600, b = 0	14	—	4
B	a = 400, b = 200	14	8	4
C	a = 600, b = 0	14	—	6
D	a = 400, b = 200	14	8	6
E	a = 600, b = 0	12.7	—	10.7
F	a = 600, b = 0	8	—	6

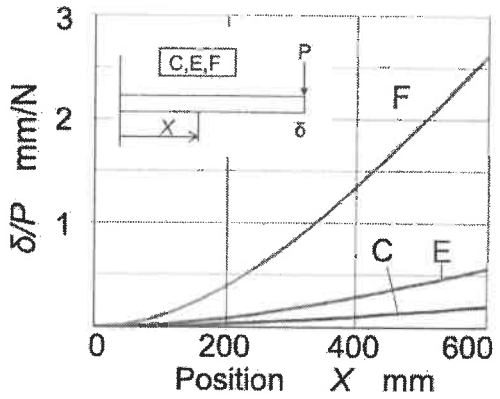

FIGURE 10. Relationship between the bending and the shape of the boring bar.

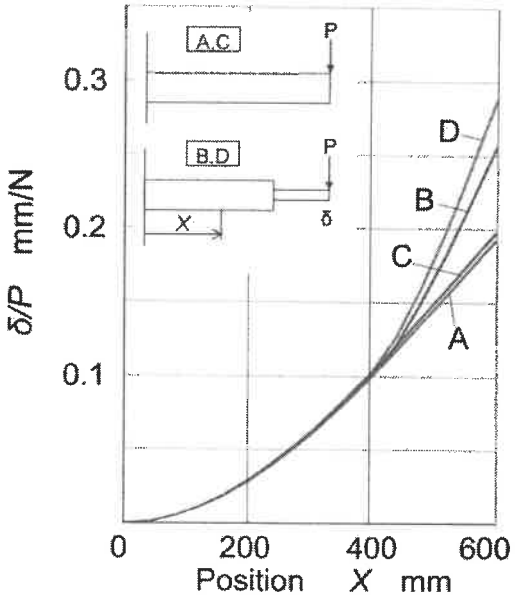

FIGURE 11. Relationship between the bending and the shape of the boring bar.

REFERENCES

[1] Japan Science and Technology Agency, PCT/JP2005/006165, United States Patent.

GENERATING METHOD OF MICRO GROOVES BY MICRO EDM

H. S. Lee[1], H. Mikami[1] and T. Yamada[1]
[1]Department of Mechanical Engineering,
College of Science and Technology,
Nihon University, Tokyo, JAPAN

INTRODUCTIONS

Micro total analysis system, that is micro TAS, is one of analyzing techniques in next generation used in medical and/or chemical fields. Substrates used in this technique are called to micro chips. In order to fabricate micro chips with micro grooves in their surfaces, mechanical machining, that is drilling, end-milling and/or grinding are applied conventionally. And then, in these fabricating processes, some problems depending on the tool wears and cracks of substrates had to be carefully taken into account so far.

On the other hand, photo-lithography used to fabricate integrated circuits is also applied to generate micro chips. In this case, however, another problem depending on the cost to generate negative plate has to be taken into account.

In this study, a new generating method of micro grooves which consists of micro electric discharge machining and etching is proposed. In this paper, as the first stage of the proposed method, a generating method of micro channels with their width is less than 0.1 mm by EDM is discussed.

GENERATING PROCEDURE OF MICRO GROOVES

A schematic diagram of the generating method proposed in this study is shown in figure 1 and its procedure is as follows.

STEP 1

A metal, in this case aluminum, is evaporated on the surface of a quartz glass substrate. This metal layer is removed by micro EDM in the next step.

STEP 2

Removing a part of evaporated metal layer by micro EDM, required micro patterns are generated in the surface of micro chips. By using servo controlled XY table, micro patterns can be easily generated only by controlling the path of XY movement. The sizes of patterns generated in this process can be controlled by setting thickness of evaporated metal layer, clearance between substrate and electrode, discharging voltage and/or amplifier. Therefore, the sizes of grove patterns can be set flexibly.

STEP 3

Etching the disclosed parts of the surfaces of glass substrates, required micro grooves are generated.

STEP 4

Removing the evaporated metal layer, micro chips with required patterns are completed.

As shown above, in this method, micro chips for micro TAS can be easily generated. In this study, as the steps 1 and 2 of the procedure written above are precisely discussed as the first stage of this study.

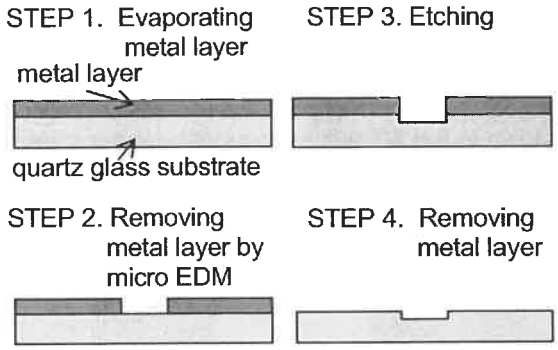
STEP 1. Evaporating metal layer
metal layer
quartz glass substrate
STEP 3. Etching
STEP 2. Removing metal layer by micro EDM
STEP 4. Removing metal layer

FIGURE 1. Generating procedure of micro grooves

SELECTION OF MATERIALS FOR ELECTRODES

In this experiment, aluminum is used for evaporated metal layer, which thickness is 0.20 micron. In order to select the electrode material, EDM tests are carried out under the condition shown in Table 1 and the consumption rates of electrodes are experimentally compared between two materials, that is copper tungsten and brass. The consumption rare of each material is evaluated as follows;

$$\text{Electrode consumption rate} = \frac{\text{Consumed volume of electrode}}{\text{Removed volume of metal layer}} \quad (1)$$

Experimental results are shown in figure 2. According to this figure, it is known that the consumption rate in case of copper tungsten 0.170 is smaller than of brass 0.259 and then copper tungsten, which is widely used as electrodes material for EDM, is selected as the material of electrode used in this study.

TABLE 1. Experimental condition

Material of tool electrode	Copper tungsten, Brass
Diameter of tool electrode	φ0.1 mm
Power supply	100 V, 5 A

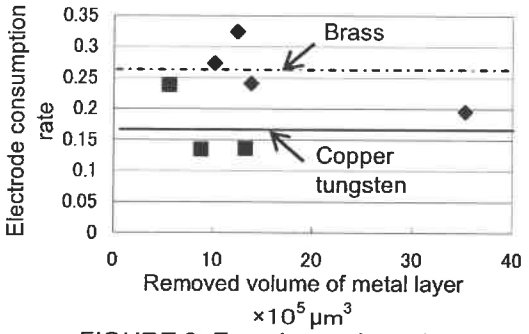

FIGURE 2. Experimental results

MICRO EDM TEST

In the step 2 shown in figure 1, micro EDM condition, under which required micro pattern can be generated stably, have to be selected. In this study, effects of following parameters on the micro EDM are discussed experimentally, which are electric voltage, diameter of electrode, clearance of electrode to the surface and feed rate of electrode. Table 2 shows the test results under which stable micro EDM can be carried out.

TABLE 2. Experimental condition

Material of electrode	Copper tungsten
Diameter of electrode	φ4 mm
Material of metal layer	Aluminum
Thickness of metal layer	0.20 micron
Voltage	15 V
Angle of electrode inclination	Applied angle
Feeding rate	3.0 mm/s
Clearance of electrode to the surface	10 micron

Furthermore, it is known that tilting the electrode to the surface of discharged material, the smaller width of discharged marks can be easily obtained, and smaller electric voltage makes narrower marks. Figure 3 shows an example of discharged mark obtained under the condition shown in table 2. The width of discharged mark in this case is about 10 micron.

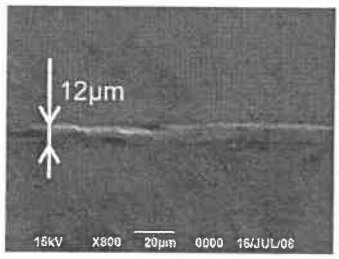

FIGURE 3. An example of discharged mark

FABRICATION OF STBSTRATES

Under the condition shown in table 2, a trial to fabricate substrates is carried out. At first, five patterns as shown in figure 4 is generated by micro EDM. Second, an etchant for quartz glass is applied to the discharged part. Ten hours later, removing the etchant from the substrate surface, micro groves are completed. Fabricated each part is shown in figure 5.

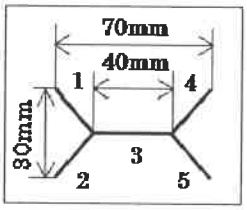

FIGURE 4. Tested groove patten

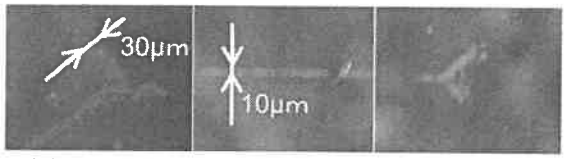

(a) 1 and 2 (b) 3 (c) 4 and 5

FIGURE 5. Obtained grooves by test

From figure 5, it is known that grooves 1 and 2 shown in figure (a) are generated well. It is clear, however, the grooves 3 to 5 shown in figure (b) and (c) are not generated continuously, that is, they are broken. It may depend on the unstable electric discharging due to the variation of clearance of electrode to the surface. This result show that the electrode consumption takes place locally under the condition that electrode is not rotating.

From these test results, it is known that electrode rotation is needed to discharge metal layer uniformly. Depending on this result, a driving device for electrode rotation is designed.

DISCHARGE TESTS WITH ROTATING ELECTRODES

A DESIGNED ELECTRODE ROTATING DEVICE

A designed electrode rotating device is shown in figure 6. Electrode is rotated by a direct current motor and the rotating speed is reduced 1:6.86 by a timing belt. An electrode is loaded to a chuck and it can be tilted around Y axis.

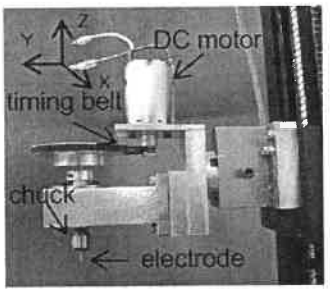

FIGURE 6. A designed electrode rotating device

EFFECT OF FEED RATE

In order to evaluate the effect of feed rate, electric discharging tests under two feed rate, that is 0.3 and 1.0 mm/s, are carried out. Other condition is same as shown in table 2. Where, the clearance of electrode to the surface is set to 12 micron and the rotation speed of electrode is 90 min^{-1}. Experimental results are shown in figure 7.

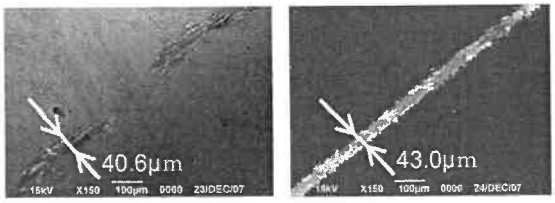

(a) 1.0mm/s (b)0.3mm/s

FIGURE 7. Obtained discharged marks

As shown in figure 7 (a), under the feed rate is 1.0 mm/s, continuous discharged mark cannot be obtained, and it may be caused by the unstable discharging due to the run-out of electrode. On the other hand, under the slow feed rate 0.3 mm/s as shown in figure (b), metal layer is removed continuously. As these test results, it is clarified that continuous discharged mark can be obtained by setting the feed rate appropriately.

EFFECT OF RUN-OUT OF ELECTRODE

Since the run-out of electrode affects on the stability of electric discharging, it must be set as small as possible. In order to do so, electrode is machined by EDM under rotating condition as shown in figure 8 before caring out micro EDM. In this case, stainless steel is used as the workpiece to consume the electrode.

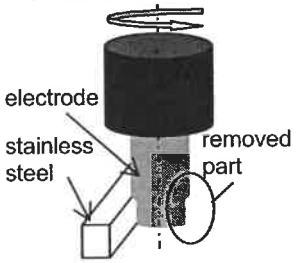

FIGURE 8. Schematic diagram to reduce the electrode run-out

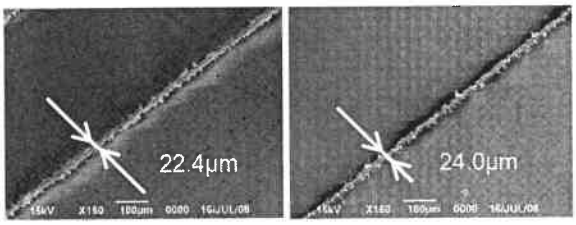

(a) 1.0mm/s (b)0.3mm/s

FIGURE 9. Obtained discharged marks

Examples of discharged marks with an electrode, which run-out is decreased in the method above, are shown in figure 9. In this case, it can be known that narrower discharged mark than in case of figure 7 can be obtained in high feed rate easily by decreasing the electrode run-out.

CONSUMED VOLUMES OF ELECTRODES

In order to evaluate the electrode rotation on the stability of electric discharge machining, discharging test under resting and rotating are carried out. In this test, rotating speed of electrode is set to 500 min^{-1}, in order to observe the consumed part clearly, and the electrodes which run-out are decreased in the method shown above.

Measured consumed volume of electrode and the variance of clearance of electrode to the surface are shown in figure 10 and 11 respectively. Figure 12 shows the consumed

parts of electrodes. It is clear that the consumed volume of static condition is less than rotating condition. It may be caused by that consumed area is narrow in this case. However, the variation of the clearance of electrode to the surface under rotating condition is smaller that of stable condition. It may be caused by as follows. That is, in case of stable condition, electrode consumption takes place locally, however, consumed volume is dispersed in wide area in rotating condition. Taking into account these test results, it is known that rotating condition is superior to generate long discharge marks stably.

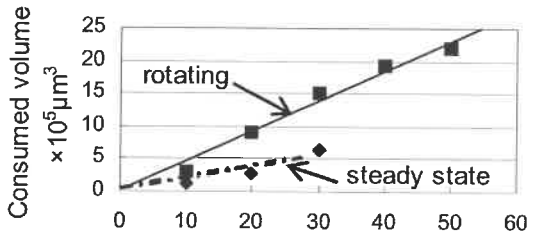

FIGURE 10. Consumed volume of electrode

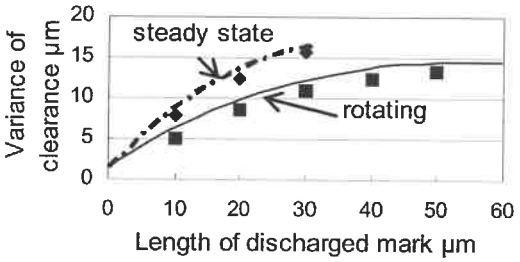

FIGURE 11. Variance of clearance

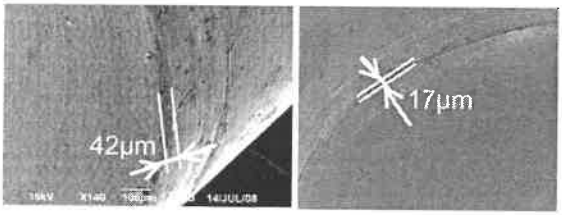

(a) steady state (b) rotating

FIGURE 12. Consumed electrodes

GENERATION OF LONG DISCHARGED MARKS FOR MICRO CHIP GROVES

Depending on the preliminary test results shown above, long discharged marks, length is 60 mm, are tried to be generated. In this test, the clearance is set to 6 micron, rotating speed is 500 min^{-1}. Other condition is same with table 2. Examples of test results are shown in figure 13. As shown in figure 13, continuous discharged mark can be obtained without any broken part in whole length 60 mm. And the width of discharged mark is almost 40 micron. As described above, the width of discharged marks depend on the electric discharge condition, for example clearance, voltage, feed rate and so on.

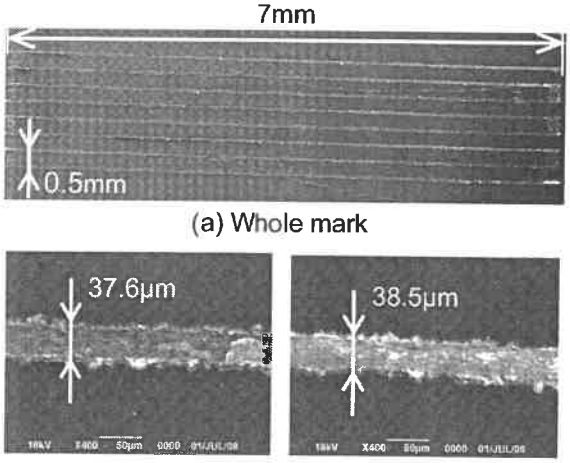

(a) Whole mark

(b) Part of marks

FIGURE 13. Discharged marks in length is 60 mm

Depending on these elemental test results, controlling method of the width of discharged mark will be discussed in future for generate smaller micro chips.

CONCLUSIONS

A new method to fabricate micro patterns for micro chips used in micro TAS is proposed. Results obtained this study are summarized as follows;

1) It is confirmed that micro groves for micro TAS can be easily generated by the combination of micro EDM and etching.
2) Rotating the electrode, continuous long discharged marks can be obtained stably.
3) Decreasing run-out of electrode, stable EDM can be carried out and then long micro grooves can be generated.

REFERENCES

[1] Masanori KUNIEDA: Present state and future of electric discharge machining technology. Science of Machine. 1999; 51: 634-640.

3D RECONSTRUCTION FOR THE 3D ENGRAVING SYSTEM FROM 2D IMAGES

Won-Seck Lee[1], In-Ho Song[1] and Sung-Chong Chung[1*]
[1]Hybrid System Design & Control LABoratory
Department of Mechanical Engineering
Hanyang University, Sungdong-Gu, Seoul 133-791, KOREA

ABSTRACT
Design is important in the IT, digital appliance, auto industries. Aesthetic and art images are being applied for better design satisfaction of the products. Various artistic image patterns are used to satisfy demand of design, but it takes much lead-time and effort to implement them for making dies and molds. In this paper, a hybrid reverse engineering method generating accurate 3D engraving models from 2D art images, which is called TechArt technology, is proposed through image processing, 3D reconstruction, and NURBS interpolation methods.
To realize a 3D art shape on the product from a 2D artistic image, an accurate 3D object model should be engraved on the dies or molds. In order to generate the 3D model from the 2D artistic image, cloud points with z-depth are extracted according to intensity values of the image. An adaptive median filter and low pass filter are used to obtain the intensity values accurately. NURBS surfaces are generated through the interpolation of the cloud points. Performance of the developed system is to be confirmed through the realization of Mona Lisa and Golden Gate Bridge.

KEYWORDS
3D Engraving, 3D Reconstruction, Adaptive Median Filter, Fourier Transform, IGES, Image Processing, NURBS, TechArt.

INTRODUCTION
Recently, quality and performance of the product is being equalized as the manufacturing industry develops rapidly. The trend makes design of the product important. This is generating TechArt technology. TechArt is based on aesthetic design. It is a rapidly growing trend in the IT, digital appliance and auto industries. Various aesthetic and artistic images are used to meet TechArt demand. However, it takes much lead-time and effort to implement the aesthetic design for making moulds and dies. To reduce the lead-time and to improve the process of making CAD design, an artistic CAD system generating 3D CAD models from 2D art images is required. In order to maximize the interfacing flexibility of the system, neutral CAD file for visualization and correction is also required.

In previous studies, the shape from silhouette [1] used 2D images for 3D reconstruction. But it requires many images and precise camera calibration to generate an accurate 3D model. Milan *et al.* [2] proposed a 3D engraving method from gray scale images. But this method is applicable to simple images without noise.

In this paper, a hybrid reverse engineering system is proposed to construct the TechArt technology, which generates 3D CAD model from 2D image. Generating procedure of 3D CAD model is as follows: First, an image is transformed to gray-scale and median filter is applied to reduce noise. Secondly, cloud points are extracted from the image according to image intensity. To remove high frequency spatial data from the image processed cloud points, Fourier transform is applied to the geometric data. NURBS surface is then generated through interpolation of the filtered cloud points. Finally, 3D CAD model is generated through a neutral data translator as a IGES file.

IMAGE PROCESSING
Invisible noise may exist on the 2D image. It deteriorates quality of the 3D reconstruction. In this paper, to reduce the noise, RGB image is transformed to gray image first. Then an adaptive median filter is applied to the image. Following adaptive median filter [3] with two levels is applied to filter out the image noise:

S_{xy} = rectangular window

z_{min} = minimum gray level in S_{xy}

z_{max} = maximum gray level in S_{xy}

z_{xy} = gray level at point (x,y)

S_{max} = maximum allowable size of S_{xy}

Level A:

A1 = $z_{med} - z_{\min}$, *A2* = $z_{\text{med}} - z_{\max}$

If A1>0 and A2<0, Go to level B

Else increase the window size

If window size $\leq S_{\max}$ *repeat level A*

Else output z_{xy}

Level B:

B1 = $z_{xy} - z_{\min}$, *B2* = $z_{xy} - z_{\max}$

If B1>0 and B2<0, output z_{xy}

Else output z_{med}

The adaptive median filter is effective to remove impulse noise and to reduce distortion. Fig. 1 shows the result of adaptive median filtering.

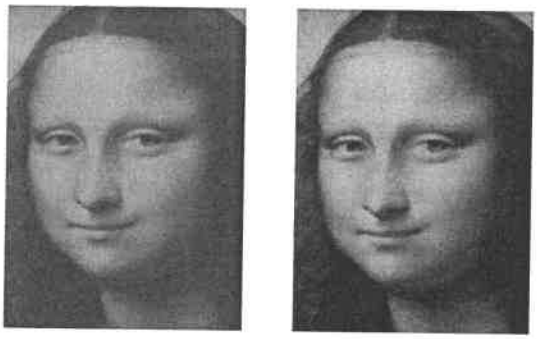

(a) Original image *(b) Filtered image*

FIGURE 1. Result of adaptive median filtering.

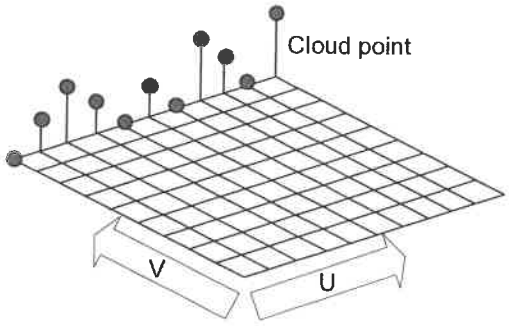

FIGURE 2. Extraction of cloud points.

EXTRACTION OF CLOUD POINTS

Cloud points are geometric elements representing shape of a 3D model. In this paper, cloud points are extracted according to intensity difference depending upon depth of a product, which is similar to the shape from shading [4]. As the gray image has the intensity range from 0 to 255, sampled z-depths of cloud points are extracted according to Eq. (1). Fig. 2 shows the extracted cloud points.

$$z-depth = \frac{Max\ Height}{255} \times Intensity\ value \qquad (1)$$

IMPROVEMENT OF FAIRNESS

Fig. 3(a) shows a high frequency spatial data of the cloud points along the direction u or v. They increase lead time to fabricate dies or moulds, and deteriorate quality of stamped or moulded products. To remove the high frequency spatial cloud points and smooth the 3D surface, following 2D Fourier transform pair are applied to design a harmonic filter:

$$F(k,l) = \frac{1}{\sqrt{MN}} \sum_{m=0}^{M-1} \sum_{n=0}^{N-1} f(m,n) \exp\left[-j2\pi(k\frac{m}{M} + l\frac{n}{N})\right]$$

$$f(m,n) = \frac{1}{\sqrt{MN}} \sum_{k=0}^{M-1} \sum_{l=0}^{N-1} F(k,l) \exp\left[j2\pi(k\frac{m}{M} + l\frac{n}{N})\right] \qquad (2)$$

In Eq. (2), $f(m,n)$ is a cloud point geometric value in spatial domain. $F(k,l)$ is Fourier transformed complex value in frequency domain. Its magnitude tells how much of a certain frequency component is present, and its phase tells where the frequency component is in the image. Smoothing of the original spatial data is performed through the following convolution:

$$G(u,v) = H(u,v) \cdot F(u,v)$$

$$H(u,v) = \begin{cases} 1 & if \quad F(u,v) \leq P_0 \\ 0 & if \quad F(u,v) > P_0 \end{cases} \qquad (3)$$

Where $H(u,v)$ is the harmonic filter to remove certain frequency of $F(u,v)$. P_0 is selected according to quality of smoothness. Then, harmonic filtered $G(u,v)$ is converted to real domain through the inverse Fourier transform given by Eq. (2). Fig.3 shows improved fairness through the devised harmonic filter.

GENERATION OF NURBS SURFACE

NURBS surface [5,6] is derived from the filtered cloud points according to Eq. (4).

$$P(u,v) = \frac{\sum_{i=0}^{n} \sum_{j=0}^{m} h_{i,j} P_{i,j} N_{i,k}(u) N_{j,l}(v)}{\sum_{i=0}^{n} \sum_{j=0}^{m} h_{i,j} N_{i,k}(u) N_{j,l}(v)} \qquad (4)$$

Where $P_{i,j}$ is xyz coordinates of control points and $h_{i,j}$ is homogeneous coordinates of the control points. $N_{i,k}(u)$ and $N_{j,l}(v)$ are blending functions given by

$$N_{i,1}(u)=\begin{cases}1 & u_i \le u < u_{i+1}\\ 0 & otherwise\end{cases}$$

$$N_{i,k}(u)=\frac{u-u_i}{u_{i+k-1}-u_i}N_{i,k-1}(u)+\frac{u_{i+k}-u}{u_{i+k}-u_{i+1}}N_{i+1,k-1}(u) \quad (5)$$

$$N_{i,1}(v)=\begin{cases}1 & v_j \le v < v_{j+1}\\ 0 & otherwise\end{cases}$$

$$N_{i,l}(v)=\frac{v-v_i}{v_{i+l-1}-v_i}N_{i,l-1}(v)+\frac{v_{i+l}-v}{v_{i+l}-v_{i+1}}N_{i+1,l-1}(v)$$

In Eq. (5), $u_i, v_j (i=0,...,n+k+1, j=0,...,m+l+1)$ are knots in u,v direction and k is the order of the surface. The control points, order of the surface and knots should be properly selected to derive a smooth 3D surface model.

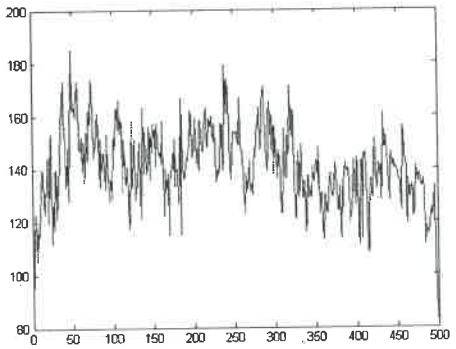

(a) High frequency spatial data

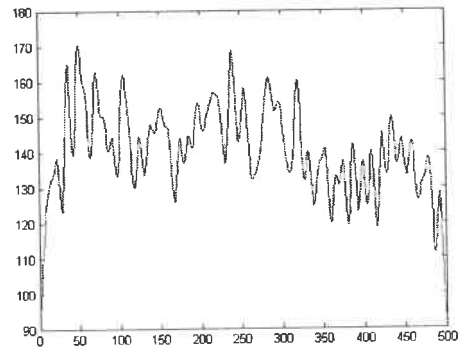

(b) Filtered spatial data

FIGURE 3. Enhancement of fairness through the harmonic filter.

INTERPOLATION OF NURBS SURFACE

In order to derive the control points of the NURBS surface given by Eq. (4), NURBS Interpolation [5,6] passing through the cloud points is required as follows:

$$Q_{p,q}=\sum_{i=0}^{n}\sum_{j=0}^{m}N_{i,k}(u_p)N_{j,l}(v_q)P_{i,j} \quad (a)$$

$$[Q]=[N_u][P][N_v]^T \quad (b) \quad (6)$$

$$[P]=([N_u])^{-1}[Q]([N_v]^T)^{-1} \quad (c)$$

Eq. (6)(b) is a matrix form of Eq. 6(a). u_p, v_q are parametric values of each cloud point. $Q_{p,q}$ are cloud points and $P_{i,j}$ are control points that let the fitted surface pass through all the cloud points, $Q_{p,q}$. $P_{i,j}$ is computed through Eq. 6(c). Knots are derived through averaging knot method [6] to compute blending functions given in Eq. (5). Average knots are derived from averaging of parameters, u_p and v_q as follows:

$$u_0=....=u_{k-1}=0$$
$$u_{n+1}=....=u_{n+k}=1$$
$$u_{i+k-1}=\frac{1}{k-1}\sum_{p=i}^{i+h-2}u_p, 1\le i\le n-l+1 \quad (7)$$
$$v_0=....=v_{l-1}=0$$
$$v_{m+1}=....=v_{m+l}=1$$
$$v_{j+l-1}=\frac{1}{l-1}\sum_{q=j}^{i+l-2}v_q, 1\le j\le m-l+1$$

EXPERIMENTS

In this paper, developed 3D hybrid reverse engineering system is verified through 3D reconstruction of two images, Mona-Liza and Golden-gate-bridge. Fitted 3D NURBS models are converted to IGES files [7], and visualized on CATIA. Fig. 6 shows 3D reconstruction results of Mona-Lisa and Golden-gate-bridge.

CONCLUSIONS

By designing a 3D hybrid reverse engineering system to generation 3D engraving models from 2D images, following conclusions have been obtained:

(1) 3D CAD model is reconstructed through IGES conversion and NURBS fitting of harmonic filtered cloud points obtained from 2D images.

(2) Fairness of NURBS surface is improved through the harmonic filter and the adaptive median filter.
(3) Validity and effectiveness of the developed system is verified through experiments.

(a) Original 2D image of Mona-Lisa

(b) 3D reconstructed result

(c) Original 2D image of Golden-gate-bridge

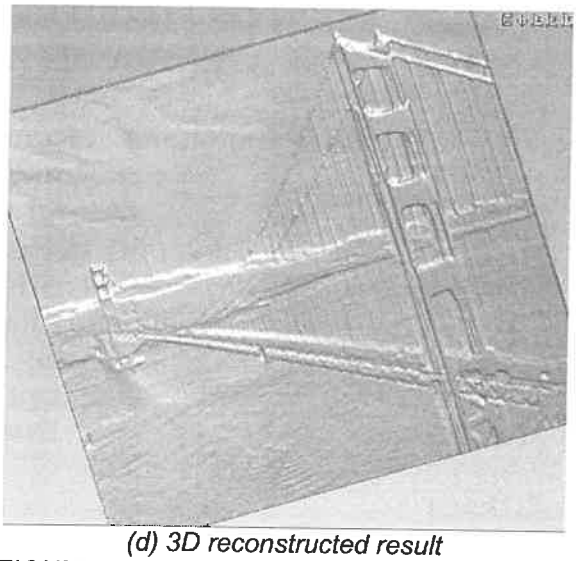

(d) 3D reconstructed result

FIGURE 6. Experiments of 3D reconstruction.

REFERENCES

[1] Cheung K M, Simon B, Takeo K. Shape-From-Silhouette Across Time Part 1:Theory and Algorithm. International Journal of Computer Vision. 2005; 62(3): 221-247.

[2] Milan S, Pavel N. Transformations between Pictures from 2D to 3D. Journal of Intelligent and Robotic Systems. 2000; 28: 69-84.

[3] Rafael C. Gonzalez, Richard E. Woods. Digital Image Processing. Prentice Hall: 2002.

[4] Courteille F, Crouzil A, Durou J D, Gurdjos P. 3D-spline reconstruction using shape from shading: Spline from shading. Image and Vision Computing. 2008; 26: 446-479.

[5] Lee K W. Priciples of CAD/CAM/CAE Systems. Addison-Wesley: 1999.

[6] Lee S B, Kim K D, Chung S C. Machined Surface Inspection Based on Surface Fairing on the Machine Tool. Transaction of the KSME(A). 2000; 24: 937-945.

[7] Lee S B, Chung S C. On-the-Machine Measuring and Inspection System for Freeform Surfaces based on IGES Format. Transaction of the KSME(A). 1999; 23: 590-607.

FABRICATION OF FUSED SILICA OPTICAL QUALITY PIN CHUCK USING A WET ETCHING PROCESS

Tiffany D. Lemmons[1,2], Ronnie R. Fesperman[3], Ozkan Ozturk[1,2], Robert J. Hocken[1,2]
[1]Center for Precision Metrology
University of North Carolina at Charlotte
Charlotte, NC
[2]Center for Scalable and Integrated Nanomanufacturing (SINAM)
Los Angeles, CA
[3]Moore Tool Company
Bridgeport, CT

ABSTRACT

The current work involves manufacturing an optical quality fused silica pin chuck, which will be employed as a template holder for a reconfigured nano-imprint lithography module. It is known that dust particle contamination between the back surface of a wafer and a chuck is a problem, so deep pins were incorporated into the pin chuck design. A wet etching process using hydrofluoric acid to dissolve fused silica was investigated to develop these pins. This wet etching process using a chrome-gold hard mask was very successful. According to Edmund Optics' specifications, the initial flatness of the fused silica window is λ/20 [1]. After the wet etching process, the pin chuck still retained this flatness on the individual pins. Also, the transmittance of UV light through the pin chuck was observed to be sufficient.

INTRODUCTION

Recent demands for economically viable tools that can generate structures at the nanometer scale have led to the development of a simple photo-curable nano-imprint lithography (NIL) module. The current work involves manufacturing a fused silica pin chuck, which functions as a template holder for a reconfigured NIL module designed and built at UNC Charlotte for use at UCLA. The pin chuck will be used in the Multi-Scale Alignment Positioning System (MAPS) [2].

In nanoimprinting a template is pressed into resist and the resist is exposed to UV light. The template will be held by the pin chuck which must transmit both visible, for moiré fringe alignment of the template to the wafer, and UV for resist exposure. For these reasons the chuck was manufactured from high purity UV grade synthetic silicon dioxide.

As the template feature size decreases so will the tolerance on template flatness. A known problem effecting flatness is the introduction of dust particles between the back surface of a wafer and a chuck. To reduce these effects and to achieve high template flatness the pin chuck surface contains many tiny pins. The template back-surface contacts only the tips of the pins significantly reducing the influence of dust. The channels created around the pins will not only provide a place for dust particles to go, but will also provide the passage way for vacuum and the pressurized imprinting gas. Each pin is be 0.2 mm (0.008 in) in diameter, ≥0.05 (0.002 in) mm tall and they are arrayed at a 1 mm (0.039 in) pitch across the chuck surface to reduce substrate deformation to less than 1 nm [2].

EXPERIMENTAL RESULTS

In order to fabricate the pins on the chuck, deep etching was required. Wet etching was explored. The lateral aspect of wet etching was accounted for by increasing the feature size of the pins on the mask. Hydrofluoric (HF) acid dissolves fused silica therefore it was an attractive process for investigating pin chuck fabrication.

Due to the inherent aggressiveness of HF, the photo resist patterned on top of the surface of the fused silica substrate cannot withstand the harsh chemical bath for the time period required to etch the deep pins, thus exposing the fused silica. It was essential to find a material with the capability of being patterned to use as a template for etching the pins in the fused silica. Since metal was used as this material it is being

referred to as a metal hard mask. Different hard masks were examined and the chrome-gold combination was found to be the most appropriate.

Three samples were prepared using the wet etching process developed. Sample 1 was etched longer and deeper than sample 2, however, the photo resist was stripped before the HF dip in sample 1 but was not removed prior to etch in sample 2. Sample 3 was subjected to the same etch time as sample 1 while retaining the photo resist prior to the HF etch.

Sample one's purpose was to develop a process protocol. It was prepared using an expensive mask used in UNC Charlotte's clean room to determine deposition and etch rates of different metals and substrates. The etch bath started with diluted HF and gradually increased to the concentration of pure HF. The Shipley's 1813 photo resist was stripped using acetone, methanol, and de-ionized water before the HF etch. The microscopic image of sample one is shown in Figure 1 one below.

FIGURE 1. Microscopic image of sample 1 using 20x objective. Etch time: 85mins; Depth: 82μm

Notice that the surface after the HF etch and metal strip where the Cr/Au was suppose to protect the fused silica was roughened. Sample two was prepared at the same time as sample one to develop an idea of the pinhole geometry by using a transparency that included a pattern that modeled the desired pins for the pin chuck. The microscopic image of Sample 2 is displayed in Figure 2.

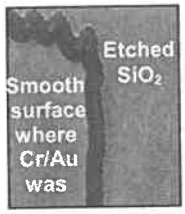

FIGURE 2. Microscopic image of sample 2 using 20x objective. Mask: transparency; Etch time: 65mins; Depth: ≈ 50μm

When trying to remove the Cr/Au mask, it was discovered that the photo resist was still on the wafer. Accidently, it was not stripped before the HF etch. As observed in Figure 2, the surface of the fused silica where the Cr/Au pattern was present, was much more smooth than the fused silica as shown in Figure 1. Sample 1 exhibited a roughened surface where the gold pattern had been suggesting the metal was porous instead of a smooth film allowing the HF to seep in and etch the substrate. Undercutting as a result of isotropic etching was not an issue due to the fact the feature size was too large and the metal would have been lifted off. Sample 3 was arranged using a transparency mask to determine if the photo resist provided a protective layer over the metal mask. It was exposed to HF the same time as Sample 1 but the photo resist was not stripped prior to the HF bath. Figure 3 shows the microscopic image of Sample 3.

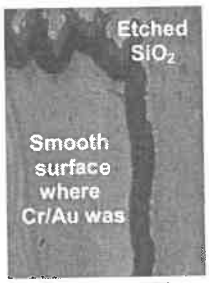

FIGURE 3. Microscopic image of sample 3 using 20x objective. Mask: transparency; Etch time: 85mins; Depth: ≈ 50μm

The concentrated HF bath yielded an etch rate of approximately 0.73 μm/minute.

This process realized high and controllable rates, which could be applicable for etching fused silica deeper than 0.05 mm. It was found that photo resist shielded the Cr-Au layer and prevented surface roughening. Smooth surfaces are required for high optical transmission. Wet etching using a chrome-gold hard mask was very successful.

The above experiments were done using a much thinner and higher quality piece of fused silica than the actual 5 mm (0.197 in) thick substrate, which is used for the MAPS stage. While etching the final piece adhesion failure occurred. It was found that the thicker wafer held moisture due to its permeable surface. A hard bake was added before metal deposition to assure dryness of the wafer. Also, it was established that the different fused silica substrate yielded a higher etch rate of 1.032 μm/minute.

FINAL PROCESS

The 5 mm (0.197 in) thick and ϕ 50.8 mm (2.000 in) substrate used was UV grade fused silica purchased from Edmunds Optics [1].

The 127 mm X 127 mm X 2.286 mm (5 in X 5 in X .090 in) chrome/soda lime mask used was purchased from Photo Sciences [3]. The template for the mask was drawn using Autocad and saved as a DXF file for Photo Sciences' use. Due to the lateral etching of the wet etch process; it was assumed that since the depth of the pins were required to be minimum 0.05 mm (0.002 in), the pins would etch that same amount from all sides. The pins were drawn as 0.3 mm (0.012 in) diameter circles because 0.2 mm (0.008 in) diameter pins were desired. The mask also incorporated two larger circles that remained un-etched during the fabrication process to allow for a smooth surface for the moiré patterns that will be used to test the MAPS alignment system.

The substrate was not the correct diameter upon arrival and the holes were not present, therefore, a surface grinder was used to grind the wafer to ϕ 43.94 mm (1.73 in) and to put a ring around the wafer for the seal. A vertical milling machine was used to drill holes in the substrate allowing for the placement of the vacuum/pressure tubes. Originally, the machining was done after the etching to prevent the contamination that was present from machining, affecting the etching process. It was evident that the glass was more likely to break while machining; therefore, it was decided that the machining should be done first to avoid damaging an etched piece.

After machining, the oils used during the process had to be removed by soaking the substrate in acetone for one hour, methanol for five minutes, and de-ionized (DI) water rinse for ten minutes. In order for metal to adhere to glass, the fused silica wafer was thoroughly cleaned prior to the metal deposition. The substrate was submerged in a 2:3 hydrogen peroxide/sulfuric acid bath for 20 minutes followed by a 5 minute DI water rinse. To ensure the substrate was free of all inorganic compounds and was completely dry the wafer was baked at 150° C for 12 hours in a Lindberg 3 zone tube furnace.

The wafer was immediately loaded into the CHA Mark 50 E-Beam Evaporator chamber. The metallization consisted of a 200 Å-Cr/3000 Å-Au film. Standard positive photolithography was used to pattern the substrate. Shipley's 1813 Positive PR was spun on the wafer at 3000 RPMs for 60 s. The substrate was then hard baked at 115 °C for 60 s. It was exposed at 175 mJ/cm^2 and immersed into Shipley's 354 positive developer for 30s. Submerging the wafer in gold etchant for 135 seconds and in chrome etchant for 25 seconds formed the pin template. The fused silica wafer was etched 0.0774 mm (0.003 in) deep by immersing the wafer in concentrated HF for 75 minutes. Dipping the wafer in acetone, methanol, and then DI water for 5 minutes each then stripped the photo resist. The Cr-Au was removed using Au and Cr etchants.

Figure 4 displays a microscopic image using an optical microscope of the pins on the final pin chuck.

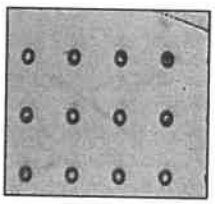

FIGURE 4. Microscopic image of pins 20x objective

TESTING

Since the pin chuck must be optical quality, to allow for the nano-imprint exposure, it was necessary to test the UV transmittance through the pin chuck. A series of experiments were performed in the clean room to assure that the etched substrate transmitted UV light appropriately. The experiments show that the final pin chuck will transmit light effectively, which is essential to the nano-imprinting process.

In order for the pin chuck to hold vacuum to a wafer, the top surface of the pins must be

exceptionally flat. The pins were observed using a white light interferometer made by Zygo. Figure 5 demonstrates the topography of one pin observed using the white light interferometer.

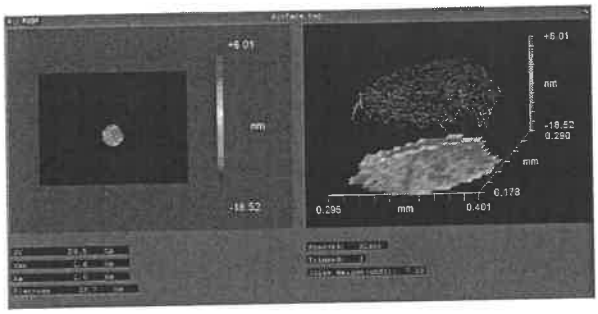

FIGURE 5. Pin image using the Zygo white light interferometer

The image was filtered to account for any particles on the surface of the fused silica.

This measurement revealed that the pin observed has an average roughness value of 1 nm and a flatness of 19.7 nm. This shows that the pin is very flat; it exceeds the flatness value, λ/20, which is the initial flatness of the un-etched UV grade fused silica. Also, other pins were observed and the flatness values were consistent with the pin examined in Figure 5.

APPLICATION

The pin chuck was connected to the imprint head of the MAPS stage with epoxy. Figure 6 displays the pin chuck acting as a template holder on the imprint head.

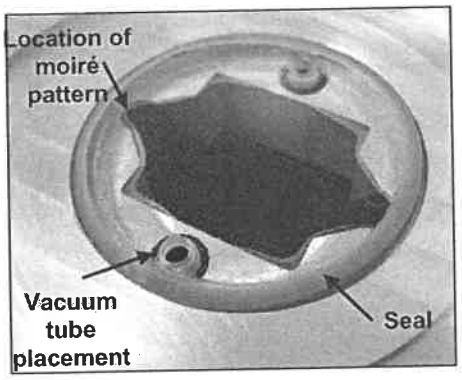

FIGURE 6: Final pin chuck attached to the imprint head of the MAPS stage

The original seal around the edge of the pin chuck was much higher than the top surface of the chuck. It was visible that when the pin chuck held vacuum on the wafer, the edge of the wafer was at a higher plane than the middle. The moiré pattern placement is on the edge, therefore, the alignment process would have been impossible to execute. Also, the imprinting process would be affected because the inconsistent plane would lead to non-uniform distribution of the photo resist.

CONCLUSION

Due to the deep etching required to fabricate this pin chuck, wet etching was the best alternative. Wet etching was more appropriate for this application because the pin hole geometry is not critical and most deep dry etch systems are not designed to etch wafers that are 5 mm (0.197 in) thick. Additionally a dry etch would require large RF-power, to facilitate high etch rates, whose ion bombardment would cause surface roughening and unrecoverable etch damage. The photo resist offered a protective barrier over the Cr/Au mask, which allowed for a smooth surface. This fabrication process of the pin chuck yielded controllable etch rates developed through multiple test runs. The fabrication procedure of the pin chuck could easily be replicated with the proper equipment in a clean room environment.

It was proven that the pin chuck transmitted UV light very well and the top surface of the pins were flat enough to hold vacuum to a wafer.

Although, the original seal of the pin chuck caused the plane of the wafer to be non-uniform, it was revised and a new seal was implemented. Successful imprints have been made with the pin chuck and a new seal.

ACKNOWLEDGEMENTS

The National Science Foundation under award number DMI-0327077 funds this research through SINAM. It is carried out in the Center for Precision Metrology. Also, special thanks to Stephen Bobbio, Bruce Dudley, John Hudak, and Roland Hege for their help with processing.

REFERENCES

[1] Edmund Optics. http://www.edmundoptics.com/onlinecatalog/displayproduct.cfm?productID=2076&search=1

[2] R.R. Fesperman, *Multi-scale alignment and positioning system*, Ph.D. Dissertation, UNC Charlotte, 2007.

[3] Photo Sciences. http://www.photo-sciences.com

THE ZEEKO CORRECTIVE POLISHING TECHNIQUES AS APPLIED TO THE FINISHING OF SEMICONDUCTOR THIN FILMS

Roger K. Morton
Zeeko Ltd.
Coalville, Leicestershire LE67 3FW
UNITED KINGDOM

Silicon On Insulator [SOI] technology utilises a thin layer of silicon (circa 500nm) deposited on an insulating material, in either single or multiple layers. Compared with bulk silicon, electrical current is constrained to flow in the thin layer, resulting in low power consumption – essential for mobile applications including displays. In order to improve performance further, the active silicon layer needs to be 'thinned' to approximately 80-150nm.

The quality of the thin film is critical, requiring control not only of surface-texture, but of thickness-uniformity as well. Chemical Mechanical Planarisation (CMP) polishing is the predominant technique used for traditional silicon wafers, where high pressures are applied over a large rigid tool. This not only gives high removal rates, but also tends to flatten the significant distortion each wafer exhibits. Nevertheless, there are residual variations in removal profile, which are irrelevant for a bulk silicon device, but a limiting factor where the active layer is thin. Clearly, there is potential for a method to control layer-thickness, using active sub-aperture polishing.

The Zeeko classic Precessions™ polishing process has been adapted to this application from its usual role of precision optical polishing. In this paper, we describe the technique, and report on results achieved in a pilot production plant. A film thickness of ~100nm ± 2nm (RMS) has been demonstrated, with Ra <3Å. Although sub-aperture polishing cannot approach the removal rates of CMP, the exquisite uniformity achieved provides a commercially viable balance between quality and overall process time. The two processes can be complimentary, CMP providing bulk removal, followed by corrective polishing using the Zeeko classic Precessions process.

Comparisons will also be made between the use of the Precessions process for SOI and the polishing of large scale precision optics planned for use on the European Southern Observatory – Extremely Large Telescope [ESO-ELT]. The ESO-ELT project plans to use in excess of 1000 hexagonal segments which are nominally 1.42metres across corners.

MINIMUM QUANTITY LUBRICATION TURNING USING TOOLS WITH OIL HOLES

Masahito Ozawa[1], Akira Hosokawa[1], Ryutaro Tanaka[1], Tatuaki Furumoto[1] and Takashi Ueda[1]
[1]Graduated School of Natural Science and Technology
Kanazawa University
Kanazawa, Ishikawa, Japan

INTRODUCTION

For ecological and economical reasons, the MQL (Minimum Quantity Lubrication) machining, in which a very small quantity of oil is supplied to the cutting point, attracts a great deal of attention, because it improves the cutting performance. Therefore several investigations on the effect of MQL have been performed, and most of them are focused on the reduction of tool wear and improvement of surface roughness of work materials [1-3].

In order to obtain the positive effect of MQL, it is very important to supply the oil mist to the cutting point correctly. In fact, our previous research revealed that the effect of oil mist is very sensitive and changes with mist diameter, nozzle orientation and flow rate [3]. Hence, it is important to establish the oil mist supplying method in which oil mist stably reaches to the cutting point at the first time. In intermittent cutting like end-milling, MQL seems to be effective because the oil droplets are easy to penetrate into cutting point. In contrast, it is rather difficult to supply the oil mist to the cutting point in turning, because continuous chips prevent the oil mist being supplied to the cutting point. Therefore the specified MQL turning tool having the duct lines of oil mist is used for turning experiments [4]. That is to say, stable supply of oil mist to the cutting point is expected.

In this study, tool temperature at the flank face is measured to discuss the cooling effect of MQL. Tool temperature in turning is measured using the newly constructed fiber-coupled two-color pyrometer [4]. And the effect of oil mist supplied to the flank face and rake face are investigated, respectively.

EXPERIMENTAL SETUP

MQL Turning System

Figure 1 indicates the oil mist supply system. Air is compressed and dried using a refrigerated air dryer, and it is sent to the atomizer to produce oil mist. As shown in Fig.1, generated oil mist passes inside of the tool and is supplied directly from two nozzles near the flank face and rake face of the tool tip. The supply conditions of the oil mist are summarized in Table 1. In this experiment, vegetable oil is used because it is harmless for operators and the people around. The actual oil flow rates from the flank nozzle and rake nozzle are 12cc/h and 13cc/h, respectively. Then total amount of oil mist is approximately 25cc/h.

Temperature Measurement System Using Fiber-coupled Two-color Pyrometer

As for the measurement of cutting temperature in turning, a tool-work thermocouple method is generally used but it is not applicable to the insulating materials such as ceramics or some coated tools. In this experiment, tool temperature at the flank face is measured using a fiber-coupled two-color pyrometer. The fundamental construction of this pyrometer is shown in Figure 2. In this method, chalcogenide glass 'Fiber-A' is embedded in the workpiece and the incidence face of the fiber is inserted into a small hole which extends to the outer surface of the cylindrical workpiece. Therefore Fiber-A rotates with the workpiece. The incidence surface of Fiber-A accepts the infrared rays radiated from the flank face of the tool tip when the fiber face passed under the tool tip. The thermal radiation accepted by Fiber -A is transmitted to the other fixed 'Fiber-B' in contactless and led to the two-color detectors. These two optical fibers are connected using the non-contact rotary fiber coupler which is attached to end-face of the workpiece.

The characteristics of fiber-coupled two-color pyrometer are summarized in Table 2. The two-color detector consists of InAs and InSb

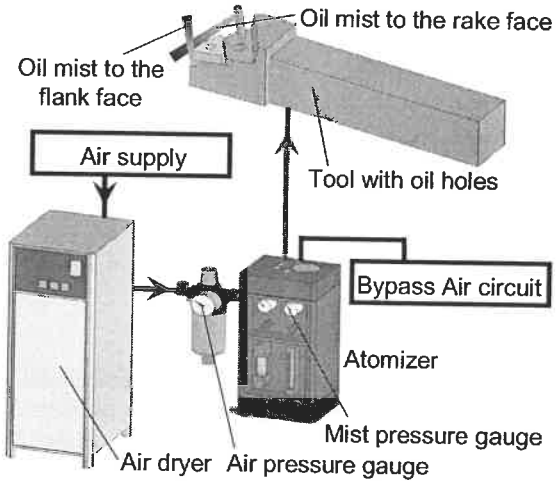

FIGURE 1. Schematic illustration of MQL turning system.

TABLE 1. Oil mist generating conditions.

Atomizer	Ebara Ecomist ZELLS MBM02
Air pressure	0.7 MPa
Mist pressure	0.6 MPa
Flow rate of oil mist	
Flank face	12 cc/h
Rake face	13 cc/h
Total	25 cc/h
Oil	Vegetable oil

photocells. The InAs detector is mounted over an InSb detector. The InAs detector responds to incident radiation from 1 to 3 μm and transmits waves larger than 3 μm, while the InSb detector responds to radiation from 3 to 5 μm. Taking the ratio of outputs from these two detectors, we can obtain the tool flank temperature using the calibration curve. Considering the transmission loss in the fiber coupler, the diameter of 400 μm is selected for rotary Fiber-A, and 500 μm for the fixed Fiber-B.

Experimental Conditions

The MQL turning is carried out with the rigid CNC turning center (OKUMA Co., Mac Turn 30). The experimental conditions are summarized in Table 3. Chromium–molybdenum steel (AISI 4140) is used as workpiece and TiCN-coated cermet as cutting tool. Principal force F_v, feed force F_f and thrust force F_p are measured using the elastic dynamometer, and the temperature of tool tip at the flank face is measured using fiber-coupled two-color pyrometer. After cutting test, surface roughness is measured and the effect of oil mist supplied to the rake face and

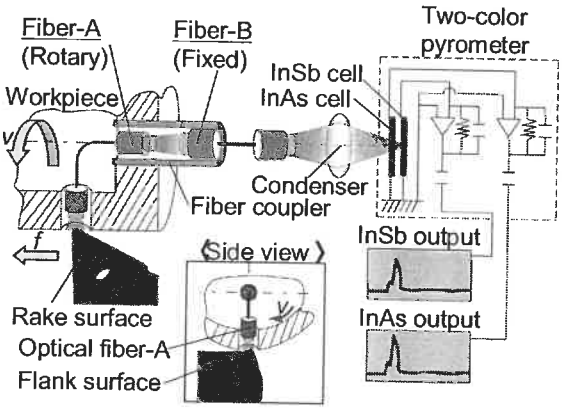

FIGURE 2. Fundamental construction of fiber-coupled two-color pyrometer.

TABLE 2. Characteristics of fiber-coupled two-color pyrometer.

Two-color detector	Photovoltaic InAs Photovoltaic InSb
Detectable wavelength	InAs: 1 - 3 μm InSb: 3 - 6 μm
Optical fiber	Chalcogenide glass
Core diameter	Fiber-A (Rotary) : 400 μm Fiber-B (Fixed) : 500 μm
Numerical aperture	NA=0.4
Frequency response	400 kHz

TABLE 3. Experimental conditions.

Workpiece	AISI 4140 (350HV0.5)
Cutting tool	TNGM 160408 Nose radius: 0.8 mm Rake angle: -6° Insert: TiCN-coated cermet
Cutting speed	v = 30 ~ 300 m/min
Depth of cut	a = 0.5 mm
Feed	f = 0.3 mm/rev
Cutting style	Dry, MQL(Flank face, Rake face, Both faces)

the flank face are investigated, respectively. In the experiments, cutting speed is changed in a wide range whereas feed rate and depth of cut are kept constant.

EXPERIMENTAL RESULTS

Lubrication Effect of MQL

Figure 3 indicates the effect of oil mist on cutting forces for three supplying styles when the cutting speed is 30 m/min. According to the previous study [4], the MQL is effective in low

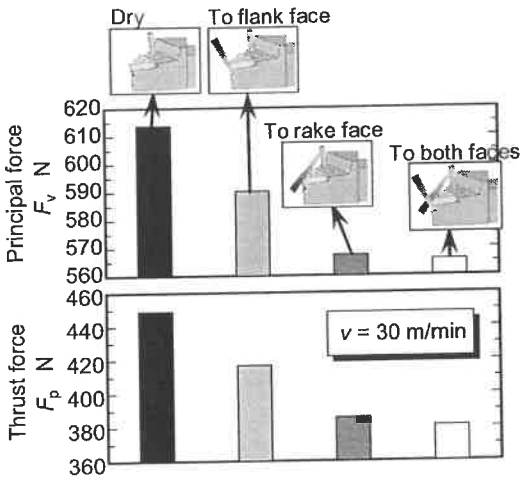

FIGURE 3. Cutting force of AISI 4140 in various cutting styles.

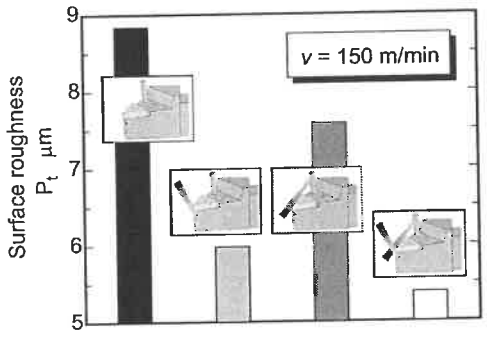

FIGURE 4. Surface roughness of AISI 4140 in various cutting manners.

cutting speed below 100 m/min. As for the effect of oil mist, it depends greatly on the position where the oil mist is supplied. Both principal force F_v and thrust force F_p are remarkably reduced when oil mist is supplied to the rake face, and the cutting forces are almost equal to those in the case oil mist is supplied to both rake and flank faces. In contrast, when the oil mist is supplied only to flank face, reduction of cutting force is smaller than that in the case oil mist is supplied to rake face. This result shows that the oil mist supplied to rake face has the effect to prevent the adhesion of chips on the tool face in low cutting temperature.

Figure 4 shows the lubrication effect of oil mist to improve the finished surface roughness. This result is obtained where the cutting speed is 150 m/min. Different from the result of cutting force, oil mist supplied to flank face is more effective to improve the finished surface. Same tendency is observed for all cutting speed.

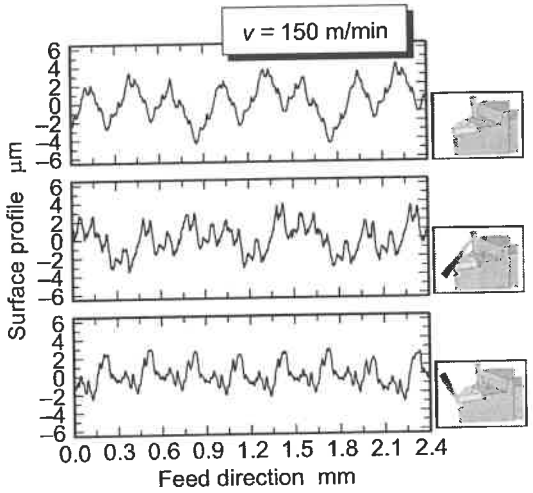

FIGURE 5. Comparison of surface profile in turning of AISI 4140.

Figure 5 indicates the comparison of surface profile after cutting experiments obtained where the cutting speed is 150 m/min. As shown in Fig.4 and Fig.5, surface condition seems favorable when the oil mist supplied to the tool flank face. Because of the lack of lubrication on the tool edge, finished surface becomes rough in dry and rake face MQL conditions. As for the lubrication effect to improve surface roughness, oil mist supplied to flank face is more effective in higher cutting speed where the adhesion of chip is little induced.

From the results of cutting force and surface roughness, it is considered that the oil mist supplied to rake face has the effect to prevent the adhesion of chip and the oil mist supplied to flank face has still lubrication effect to improve the finished surface roughness in higher cutting speed where the adhesion between chip and tool does not take place.

Cooling Effect of MQL

The tool temperature at the flank face as a function of cutting speed is shown in Figure 6. The temperature at the cutting speed of 300 m/min is 1090°C in dry turning and it drops to 1060°C by supplying the oil mist to the rake face. Tool temperature is still reduced when the oil mist is supplied to the flank face and then the temperature at the flank face is 1010° C. Additionally, when the oil mist is supplied to both rake face and flank face, the temperature drops to 980°C.

Based on the above results, the tool wear

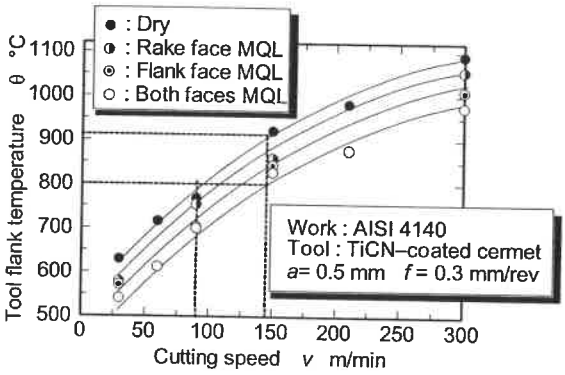
● : Dry
◑ : Rake face MQL
◉ : Flank face MQL
○ : Both faces MQL
Work : AISI 4140
Tool : TiCN–coated cermet
a= 0.5 mm f = 0.3 mm/rev
Tool flank temperature θ °C
Cutting speed v m/min

FIGURE 6. Effect of MQL on tool flank temperature in turning of AISI 4140.

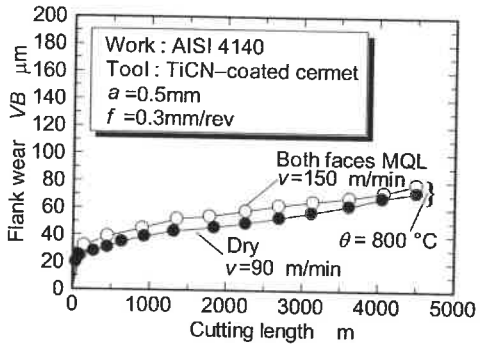

FIGURE 7. Effect of tool temperature on tool wear in turning of AISI 4140.

seems to be reduced in MQL cutting because of the reduction of tool temperature. To investigate the effect of oil mist to reduce tool wear, cutting tests are performed. Figure 7 indicates the effect of tool temperature on tool wear. As shown in Fig.7, dry cutting at the cutting speed of 90 m/min and MQL cutting at the cutting speed of 150 m/min are compared, in which the tool temperature is almost the same. Tool flank wear *VB* is almost same when the tool flank temperature is about 800°C. In contrast, when the tool temperature is approximately 900°C (*v*=150 m/min, Dry), *VB* reaches to 135 μm and then it is approximately 1.8 times larger than that at the temperature of 800°C. From Fig.6 and Fig.7, the different of tool temperature of 100°C is equivalent to a difference in cutting speed of 60 m/min, and then the MQL cutting can be performed 1.7 times faster than dry cutting.

CONCLUSIONS

The influence of oil mist supplied to tool rake face and flank face in turning are investigated. The turning experiments are carried out with the turning tool with oil holes. Tool temperature at the flank face is measured using fiber-coupled two-color pyrometer. And the effect of tool temperature on tool wear is examined. The main results obtained are as follows:

1. Oil mist supplied to rake face has the effect to prevent the adhesion of chip in low cutting temperature.

2. Oil mist supplied to flank face has still lubrication effect to improve surface roughness.

3. The tool temperature of AISI 4140 turning in which the oil mist is supplied from both nozzles is approximately 100°C lower than that in dry turning. If the oil mist is supplied only to rake face, the tool temperature is about 30°C lower than that in dry turning.

4. Tool wear is directly related to the tool temperature, and the effect of oil mist to reduce the tool temperature makes it possible to do the efficient cutting compared to dry cutting.

ACKNOWLEDGMENT

The authors are indebted to OKUMA Co., Ltd. for providing a turning center, and also would like to thank EBARA Ecomist Co., Ltd. for providing mist oil.

REFERENCES

[1] Dhar, N.R., Kamruzzaman, M., Ahmed, M. :Effect of minimum quantity lubrication (MQL) on tool wear and surface roughness in turning AISI-4340 steel, Journal of Materials Processing Technology, 172 (2006) 299

[2] Yatsuzaki, T., Onikura, H. : The Effect of Oil Mist on the Machinability in Turning of Super Heat-Resistant Alloy Inconel 718, Proc. 2nd Int. Conf. on LEM21, (2003) 1047.

[3] Ueda, T., Hosokawa, A., Yamada, K. : Effect of Oil Mist on Tool Temperature in Cutting, Trans. of the ASME, 128, 2 (2006) 130.

[4] Ozawa, M., Hosokawa, A., Tanaka, R., Furumoto, T., Ueda, T. : Minimum Quantity Lubrication Turning of Ferrous Metals – Measurement of Tool Temperature Using Fiber-Coupled Two-Color Pyrometer –, Proc. 4th Int. Conf. on LEM21, (2007) 339.

FLEXURE-BASED MECHANISMS FOR PRECISION GUIDANCE AND ANGULAR ALIGNMENT UNDER LARGE LOADS

Vijay Shilpiekandula, Kamal Youcef-Toumi
Mechatronics Research Laboratory, Department of Mechanical Engineering
Massachusetts Institute of Technology, Cambridge MA 02139 USA

INTRODUCTION

Flexure-based mechanisms have been extensively used in the design of positioning and alignment systems. Many performance requirements dictate the selection of flexures, examples being range, bandwidth, and load-capacity. In this research, we focus our interest on flexure-based mechanisms whose design is primarily driven by load-capacity requirements. Our target applications for such mechanisms include those requiring precise vertical guidance, and/or pitch and roll angular alignment. Examples are (i) positioning of large payloads and (ii) positioning under large externally applied load, such as in stamping for micro/nanomanufacturing applications.

In particular, this research addresses the following question: does the largest load-capacity design have to be the stiffest? Is it possible to design a large load-capacity flexural positioning system that meets the range requirement as well? This paper presents the design decisions and evolution of candidate designs for flexural positioning systems that meet that load capacity requirements while achieving sufficient range, without compromising significantly on bandwidth. A design methodology for load-capacity driven design is lacking currently in the literature. A systematic methodology provided in this paper is aimed at facilitating synthesis of new designs and comparison of candidate designs. Results from experimental testing of a prototype purely 1-DOF flexural stage designed for a desired load-capacity are presented. Further, a large load-capacity diaphragm flexure is also discussed.

MOTIVATION

Applications requiring large load-capacity include positioning of heavy payloads, and stamping in micro/nanomanufacturing applications. For example, micro-hot-embossing involves stamping a patterned tool into a polymer sample to form functional microfluidic channels. A typical stamping cycle involves applying large pressures on the order of $1-5\ MPa$ and heating of the polymer sample to high temperatures, in some cases, up to $200°C$. Pitch and roll angular misalignment between tool and sample can result in errors such as non-uniform depths of the transferred patterns, which can critically affect flow rates of biological samples. This application is discussed as part of the case studies in this paper.

Bandwidth and range are the commonly used design criteria for flexure-based mechanism design. For example, a high-speed atomic force microscope scanner with bandwidths on the order of $10\ kHz$, and range limited to an order of $15\ \mu m \times\ 15\ \mu m$ have been designed by Fantner et al in [1]. A large range (on the order of $5\ mm \times 5\ mm$) nanopositioning X-Y stage has been designed by Awtar et al in [2] using thin beam flexures that deflected more than their thickness. The use of serial kinematic configurations needed for reduced yaw motion of the stage, and decoupled $X-Y$ motions, results in relatively smaller bandwidths in this design. In both such state-of-the-art flexure designs, large load-capacity is not a critical requirement.

For the case of flexural beams subject to increasing bending stresses with increasing load, structural integrity of the flexures needs to be clearly addressed in the design. Load-capacity in this context is primarily dictated by the yield limit in the flexures reached by stresses developed under the applied load. This requirement is the focus of design approach presented in the next section.

DESIGN APPROACH

In this section, we present the design decisions and evolution of candidate designs that can meet large load-capacity requirements. First, consider the relations for load-capacity F_{max}, stiffness K, and range Δ_{max} for the fundamental flexural building blocks of Figure 1. The first four rows of Table 1 show the relations for these building blocks in terms of the parameters: maximum allowable stress σ_a and E_0 is: (i) E, the Young's Modulus for plane stress and (ii) $\frac{E}{1-\nu^2}$ for plane strain, ν being the poisson's ratio.

The relations given in Table 1 can be derived from

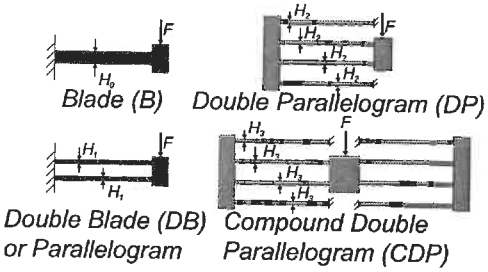

Figure 1: Flexural building blocks of length L, width (into the page) B, and beam thicknesses as shown.

simple linear beam bending lumped parameter models. For simplicity, we consider only small-deflection behavior, i.e. the beam deflections are an order of magnitude smaller than the beam thickness. While a detailed FEA can refine and be used in advanced design phases, the lumped models presented here enable closed-form solutions and allow for quick concept generation in the initial design phase.

Table 1: Comparison of flexural mechanisms

Block	F_{max}	K	Δ_{max}
B	$\frac{1}{6}\frac{BH_0^2}{L}\sigma_a$	$\frac{E_0 BH_0^3}{4L^3}$	$\frac{2}{3}\frac{L^2}{H_0}\frac{\sigma_a}{E_0}$
DB	$\frac{2}{3}\frac{BH_1^2}{L}\sigma_a$	$\frac{2E_0 BH_1^3}{L^3}$	$\frac{1}{3}\frac{L^2}{H_1}\frac{\sigma_a}{E_0}$
DP	$\frac{2}{3}\frac{BH_2^2}{L}\sigma_a$	$\frac{E_0 BH_2^3}{L^3}$	$\frac{2}{3}\frac{L^2}{H_2}\frac{\sigma_a}{E_0}$
CDP	$\frac{4}{3}\frac{BH_3^2}{L}\sigma_a$	$\frac{2E_0 BH_3^3}{L^3}$	$\frac{2}{3}\frac{L^2}{H_3}\frac{\sigma_a}{E_0}$
Proposed Concept	$pm\frac{2}{3}\frac{BH^2}{L}\sigma_a$	$\frac{pm}{n}\frac{2E_0 BH^3}{L^3}$	$n\frac{1}{3}\frac{L^2}{H}\frac{\sigma_a}{E_0}$

The same requirements for a generic design concept depicted in Figure 2 for large load-capacity are as indicated in the last row of Table 1. This concept is generated through parallel and series combination of flexural building blocks, as follows. First, load-sharing is introduced through multiple parallel beams supporting the central mass. A parallel combination of the flexural constraints can be obtained in two ways, one of which is by repeating the flexural units along a solid of revolution about the central axis. For m such combinations, as shown in the plan view of the Figure 2, the load transferred to each beam is reduced by a factor of m, and hence the maximum stress. The resulting configuration is that of a diaphragm flexure.

Another way to repeat the flexural units is by stacking one such solid of revolution vertically over the other. For p such stacked layers, the load

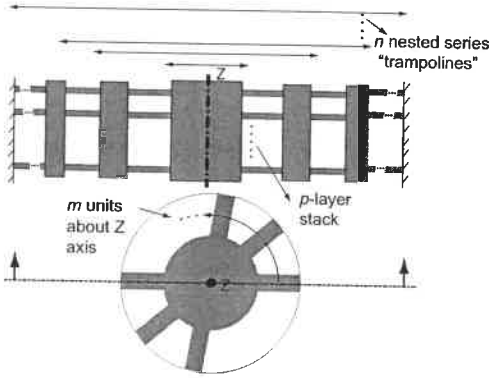

Figure 2: Proposed concept for large load-capacity. A plan view of the central ($n = 1$) trampoline is also shown. Serial combination of folded-back flexures is also possible, and is preferred for reducing over-constraint in the design.

is further reduced for each beam by a factor of p.

Table 2: Flexural mechanisms of Table 1 designed for the same load-capacity.

Block	H	K	Δ
B	H_0	K_0	Δ_0
DB	$\frac{1}{2}H_0$	K_0	Δ_0
DP	$\frac{1}{2}H_0$	$\frac{1}{2}K_0$	$2\Delta_0$
CDP	$\frac{1}{2\sqrt{2}}H_0$	$\frac{1}{2\sqrt{2}}K_0$	$2\sqrt{2}\Delta_0$
Proposed Concept	$\frac{1}{2\sqrt{pm}}H_0$	$\frac{1}{n\sqrt{pm}}K_0$	$n\sqrt{pm}\Delta_0$

However, these design changes aimed at an increase in load-capacity result in a over-constrained arrangement. In order to reduce the effect of the over-constraint, a series combination of the flexures is suggested. The resulting reduction in the stiffness allows for an increase in the range. Note that a series combination of diaphragm flexures results in a nested "trampoline" configuration. If n denotes the total number of trampolines, as shown in Figure 2, the overall stiffness and the range for the new design are as indicated in the last row of Table 1. The planar compound double parallelogram flexure is a special case of the generic design concept with values $m = 1$, $n = 2$, and $p = 2$. The spatial compliant translational joint presented in [5] is a special case of this generic design concept with $m = 2$, $n = 2$, and $p = 3$.

What distinguishes our approach from others is examining the range and stiffness performance space for two different designs meeting the same load-capacity requirement. Table 2 presents a

comparison for range and stiffness values when the flexural designs of Table 1 all have the same load-capacity. For simplicity, we assume length L and width B of the beams are kept the same. But their thickness H is varied such that the designs have the same load-capacity. In essence, for achieving large load-capacity, reinforcing flexural beam thickness is a poor choice, since an increase in thickness results also in an increase in stiffness and hence reduced range. As is evident from Table 2, the new proposed design has a range tunable by the parameters m, n, and p, and can be much larger than that of an equivalent thick beam configuration.

A point to be emphasized here is that it is not necessary that the largest load-capacity design has to be the stiffest. Sufficient range can be achieved by tuning n, which does not affect the load-capacity since series addition of beams does not result in load-sharing. The flexure building blocks used to populate the generic concept presented here is a choice dictated by various factors commonly encountered by designers. These include space constraints, thermal sensitivity, and parasitic and cross-axis error motions.

METHODOLOGY

In this section, we first present a non-dimensional approach to capturing design trade-offs all in one single graph. We use this graph to evaluate a design as well as compare different designs.

Using the normalization $f = \frac{F_{max}}{2BL\sigma_a/3}$, $k = \frac{K}{2E_0B}$, $\delta = \frac{\Delta_{max}}{\sigma_a L/(3E_0)}$, and $h = H/L$ the relations specified for the load-capacity, stiffness, and range of the proposed design concept reduce to the following nondimensional form:

$$f = pmh^2; \qquad k = \frac{pm}{n}h^3; \qquad \delta = \frac{n}{h} \qquad (1)$$

The f-k-δ design profiles for h varied in a typical range $0.05 \leq h \leq 0.1$ are shown in Figure 3 for a sample set of values for m, n, and p.

A design methodology for large load-capacity flexures is proposed with the following steps:
(i) Specify the desired performance requirements F_{max}, K, Δ_{max} for the application of interest. (ii) Is the material choice already made? If not, select a material with large σ_a/E, for e.g. Ti-6Al-4V alloy [2]. (iii) Assume a length L and width B for the beams. (Note that this step is assumed for simplicity. A more rigorous approach will iterate on these choices.) (iv) Find non-dimensional desired requirements: force f_d from F_{max}, δ_d from

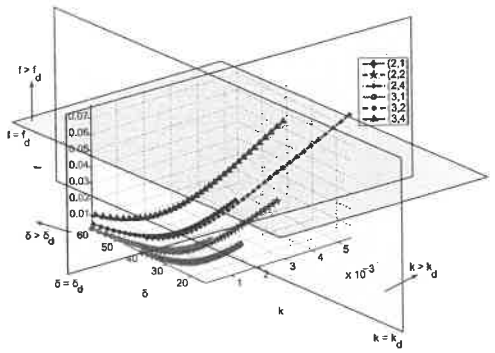

Figure 3: Non-dimensional performance space plotted as a function of non-dimensional thickness h for a sample set of $m = 1$, and (n,p) values as indicated.

Δ_{max}, and k_d from K using the normalization relations given above. (v) From the graph, view the $f = f_d$ planar section of the non-dimensional performance space. (vi) Select designs whose m, n, p values are such that the profile intersections in the $f = f_d$ plane have (δ, k) values in the quadrant $\delta > \delta_d, k > k_d$. (vii): If more than one design outcome is acceptable, use weighted criteria, or other criteria (such as thermal sensitivity, error motions), to obtain an optimal solution in the performance space. Using Eq. (1) estimate the corresponding parameter h in the input space. If no acceptable design exists, the steps need to be repeated for either a different L, B, or one of the stiffness or range constraints need to be relaxed. In order to compare two design concepts, we just need to examine the $f = f_d$ plane, and compare the δ and k values of the designs. Any series/parallel combination of flexures fits in this non-dimensional graph. Building on the treatment presented here, the performance space can be captured including the effects of other variables such as length and width of the beams, and material constants as well.

CASE STUDIES

Here, we present two case studies for large load-capacity flexure-based mechanism design.

Large Load-Capacity 1DOF Flexural Stage

A flexural motion stage for pure 1DOF vertical guidance for the following specifications is needed to meet the following requirements: vertical height ≤ 4 in, load-capacity of 100 N, range of atleast 50 μm, and minimal rotational errors. Al 6061 was chosen as a suitable material for this case due to its ease of machining with a conventional abrasive waterjet. For a maximum

allowable stress of 15 MPa, flexures of length $L = 1.25$", width $B \approx 0.8$", we find $f_d = 0.015$, $\delta_d = 31.5$. Of all the intersections of f_d plane with the performance space profiles of Figure 3, the design with $(m,\ n,\ p)$ values of $(1, 2, 4)$ is selected since it gives the largest K value for $\delta > \delta_d$.

A design embodiment for the above concept is shown in Figure 4, with the double beam units on the top and bottom spaced wide apart so as to reduce the rotational compliance. This design achieves purely 1DOF motion like the design of [4], and has the added benefit of design for adequate range at large loads. The collocated frequency response recorded for the system with a custom-built PRBS system identification program on a dSPACE DS1103 platform shows a fundamental resonance around about 650 Hz. This value is higher than expected, because of the mechanical stiffness of the piezoelectric stack actuator adding in parallel with the mechanism. An improvement on this design embodiment could be one which uses compound double parallelogram flexures to remove the over-constraint imposed in a fixed-fixed beam arrangement.

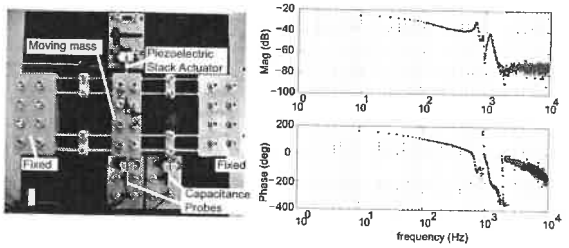

Figure 4: Large load-capacity purely 1DOF stage. Frequency response transfer function recorded between a piezoelectric actuator input and capacitance probe output is as plotted.

Large Load-capacity Diaphragm Flexure

In stamping applications such as micro-hot-embossing tool-sample angular alignment is critical for uniform channel depth. For example, for 10-micron deep channels to be formed over a 75 mm × 25 mm area, a 1 $mdeg$ (17.4 μrad) tool-sample misalignment can result in a 13% variation of depth across the 75 mm lateral span. Assuming other variations are held constant, this height variation corresponds to about a 39% variation in the flow rate across the polymer part, using a simplified Poiseuille flow approximation in the channels. Such a flow rate variation is unacceptable for many precise flow control applications, e.g. microfluidic devices designed for controlled drug delivery.

Diaphragm flexure stages are commonly used for 3DOF vertical guidance, tip and tilt alignment [3]. However, existing designs do not address the large load-capacity requirement. A design concept for a diaphragm flexure stage that can support the sample in micro-hot-embossing is shown in Figure 5. This design corresponds to $m = 3$, $n = 2$, and $p = 2$ and provides a vertical $\Delta \approx 5\Delta_0$, i.e. 5 times that of design using a conventional blade flexure. The angular range in pitch and roll is also improved, since we have the folded back double parallelogram flexure configuration. This design concept will be sized and built for a micro-hot-embossing stage for supporting the sample.

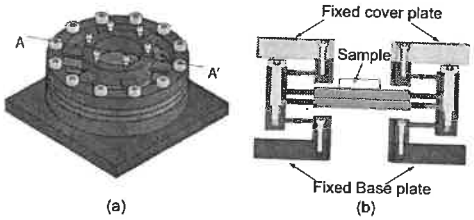

Figure 5: Design concept for a large load-capacity 3DOF diaphragm flexure stage for supporting sample in micro-hot-embossing.

SUMMARY

A methodology for designing large load-capacity flexural mechanisms is presented. A series and parallel combination of flexural constraints were appropriately chosen to increase load-sharing and also allow for large range. Two case studies, one for a purely 1DOF linear bearing and another for a diaphragm flexure are discussed.

ACKNOWLEDGEMENTS

This research has been supported by the Singapore MIT Alliance and the American Academy of Mechanics Robert and Mary Haythornthwaite foundation. We are thankful to the faculty and student collaborators in the Singapore MIT Alliance program for their feedback and suggestions. The first author would like to thank Prof. Shorya Awtar [2], University of Michigan, Ann Arbor, for his comments and suggestions.

REFERENCES

[1] Fantner GE, Schitter G, Kindt JH, et al, "Components for high speed atomic force microscopy," Ultramicroscopy, vol. 106, no. 8-9, pp. 881-887, Jun-July 2006.

[2] Awtar S, "Synthesis and Analysis of Parallel Kinematic XY Flexure Mechanisms," Ph.D. Thesis, Massachusetts Institute of Technology, Cambridge MA 02139.

[3] Kendale AM, "Automation of Soft Lithographic Microcontact Printing," SM thesis, Massachusetts Institute of Technology, Cambridge MA, 2002.

[4] Chen S, Golda D et al, "Design of an Ultra Precision Diaphragm Flexure Stage for Out-of-plane Motion Guidance," Proceedings of the ASME IDETC, Salt Lake City, UT, Sept,2004, pp. 1015-21.

[5] Trease BP, Moon Y, Kota S, "Design of Large Displacement Compliant Joints," Journal of Mechanical Design, vol. 127, pp 788-798, July 2005.

IMPROVEMENT OF CHIP CONTROLLABILITY OF CARBON STEEL IN TURNING BY LASER HEAT TREATMENT

Ryutaro Tanaka, Akira Hosokawa, Takashi Ueda, Tatsuaki Furumoto
Takahiko Kusano and Younchuan Lin
Institute of Science and Engineering
Kanazawa University
Kanazawa, Ishikawa, Japan

INTRODUCTION

This study deals with the influence of laser heat treatment for carbon steel AISI 1045 on chip controllability in turning. In turning at automated machining line, fine chip controllability is required. Irregular continuous chip gets caught in chuck and work material and causes damage of not only finished surface but also cutting tool and machine tool. To avoid these troubles, there are some methods such as adapting steels containing such as MnS and Pb[1], which has brittle as a work material and breaking chip by a breaker piece so on.

In this case, some problems still remain in degradation of mechanical strength and/or corrosion resistance of materials, deterioration of environment and such additives are often expensive. There have been ideas by surface treatment using electrical discharge and laser beam, but these ideas have no practical use. In this study, turning test was conducted for the purpose to clarify influence of heat treatment by laser beam scanning for work martial surface on chip controllability. Turning of hear treated carbon steel by a diode laser with carbide and ceramics insert is conducted in CNC lath and the influence of heat treatment for work material on chip form is investigated experimentally.

EXPERIMENTAL PROCEADURE

The work materials used in this study is a carbon steel AISI 1045 which is widely used in machine components and has good thermal processability. The work material is normalized after hot forging in such a way that it is heated to 850°C for 5 hours and allowed to cool freely in air to room temperature.

The conditions of laser heat treatment are shown in TABLE 1. The direct diode CW-laser (808 nm wavelength) is irradiated on the work surface having the rectangular spot of 2.5 x 0.1 mm. The average laser power and laser scan rate are 120 W and 126 mm/min, respectively. The optical absorbance of carbon steel at 808 nm is approximately 40%.

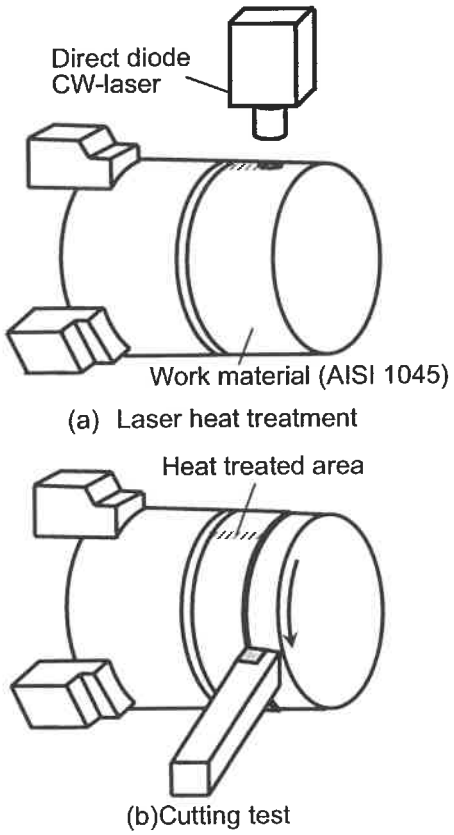

FIGURE 1. Experimental set up

A diode laser is irradiated linearly in the longitudinal direction on the cylindrical work material surface as shown in FIGURE 1(a), so that the in-situ selective laser heat treatment is carried out. Then the turning test is executed with the CNC lathe as shown in FIGURE 1 (b).

The cutting conditions are summarized in TABLE 2. The tools used in this experiment are cemented carbide P30 and ceramics insert.

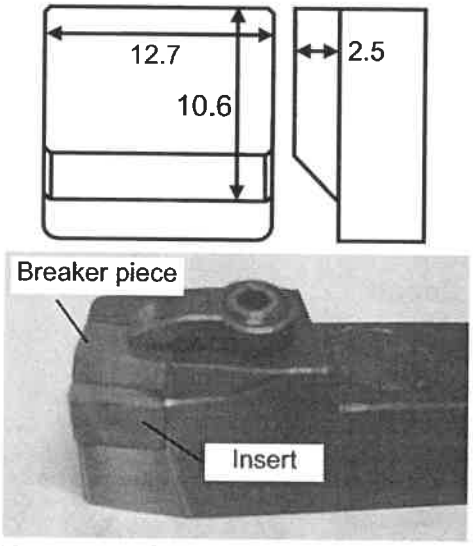

FIGURE 2. Appearance of the cutting tool and breaker piece

TABLE 1. Experimental conditions in laser hear treatment process

Semiconductor Laser (CW)		
Wave length :	λ	808 nm
Average power :	Q	120 W
Scan rate :		126 mm/min
Spot size :		0.1 mm×2.5mm

Table 2. Cutting conditions

Work :	AISI1045 (normalized) φ70mm (~60mm)	
Tool :	Carbide tool P30, TiC-Al_2O_3 ceramics insert (SNMN120408)	
Tool holder: CSMNR2020 (Mitsubishi material)		
Cutting speed :	v	100~250 m/min
Depth of cut :	d	0.4 mm
Feed rate :	f	0.1-0.2 mm/rev
Coolant :		dry

FIGURE 2 shows the appearance of the cutting tool and breaker piece. These tools have the same shape as ISO SNMN120408. The breaker piece is ISO CBS-4M. A carbide breaker-piece is fixed to an accurate position on the indexable insert for clamp type holder as shown in the figure. The thickness and wedge angle of the breaker-piece are 2.5 mm and 45°, respectively. The cutting speed is changed from 100 to 250 m/min and feed rate is changed from 0.10 to 0.20 mm/rev. Only the depth of cut is kept constant 0.4 mm.

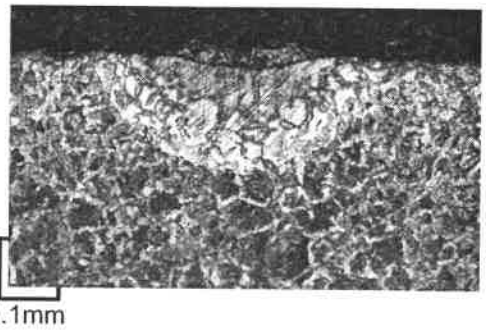

Power; 120W (λ: 808nm), Spot width; 0.1mm, Scan rate; 126mm/min
FIGURE 3. Cross section of AISI 1045 after laser heat treatment with direct diode CW-laser

RESULTS AND DISCUSSION

Heat-treatment characteristic of AISI 1045 steel by diode laser

FIGURE 3 shows the cross section of the AISI 1045 steel after linear laser heat treatment. The specimen is etched by a 3% Nital solution for 5 seconds at room temperature. As is obvious in the figure, a clear semicircle heat affected layer is observed, where the martensitic structure is formed in the ferrite-pearlite mother phase. The maximum hardness in this hardened layer is approximately 600HV.

The influence of laser power and scanning rate on the depth and width of heat affected zone are shown in Fig.3. The output laser power is 120 W and the laser scanning rate is 126 mm/min, the width of heat affected zone W is considerably larger than the laser spot width (0.1 mm). The heat affected area is approximately 0.5 mm width and 0.2 mm depth.

Effect of linear laser heat treatment of work material on chip breakability

FIGURE 4 shows the chip form generated in turning laser heat treated and non-laser heat treated carbon steel AISI 1045 with the carbide P30 insert. In the case of non-laser heat treaded carbon steel, the chip breakability is poor at the higher cutting speed and lower feed rare [2]. On the other hand, in the case of laser heat treated carbon steel, the chip is broken at any cutting condition.

FIGURE 5 shows the chip form generated in turning laser heat treated and non-laser heat treated carbon steel with the ceramic insert. Same as the case of turning non-laser heat

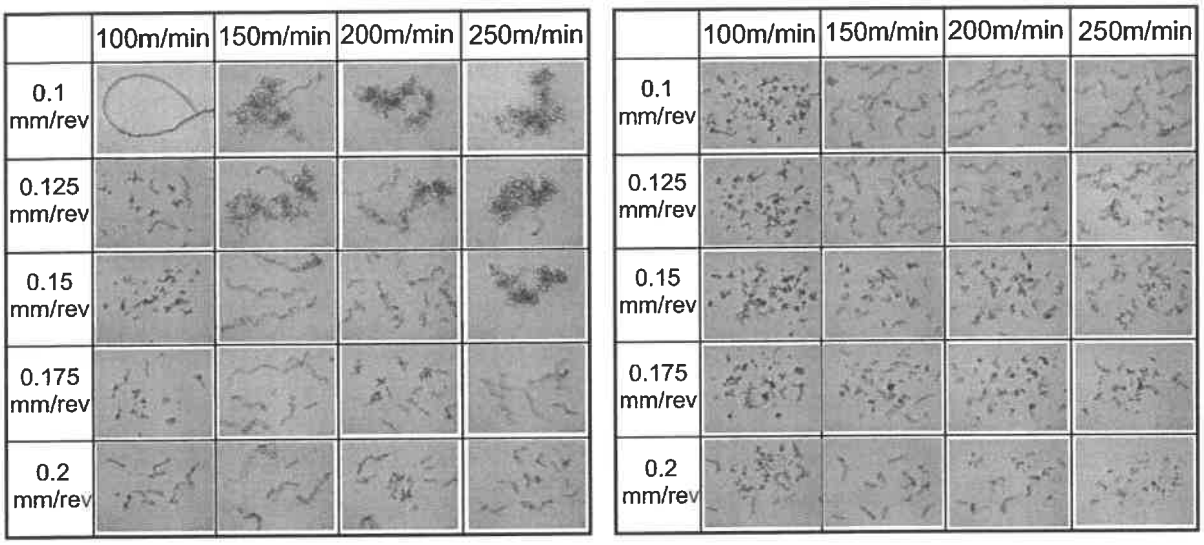

b) non-laser heat treated

b) laser heat treated

Work material; AISI 1045, V=100-250m/min, d=0.4mm, f=0.1-0.2mm/rev

FIGURE 4. Chip form generated in turning laser heat treated and non-laser heat treated carbon steel with the carbide P30 insert.

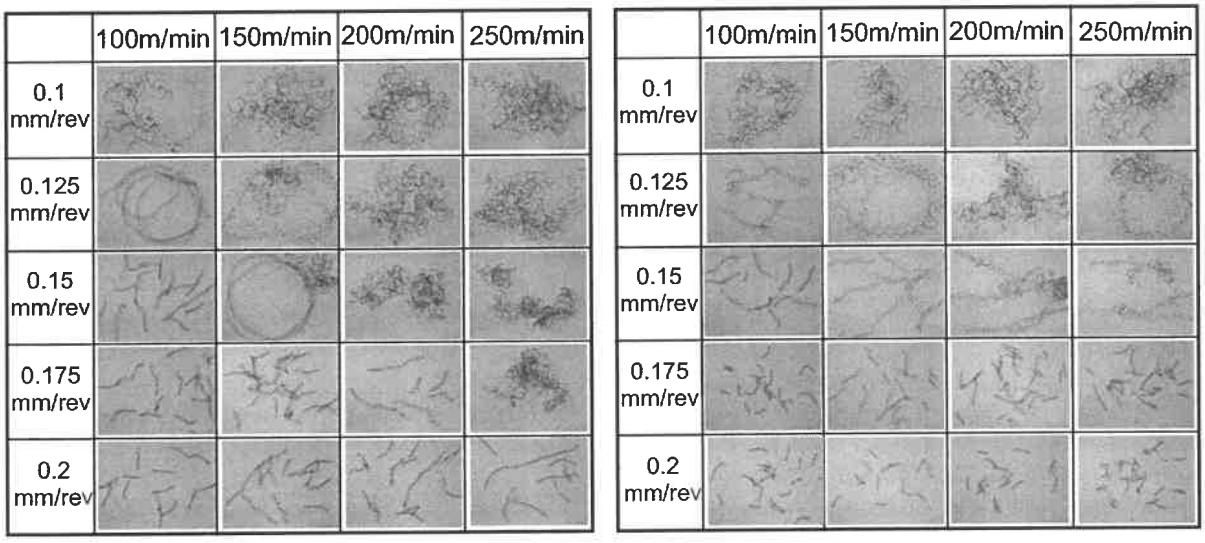

a) non-laser heat treated

b) laser heat treated

Work material; AISI 1045, V=100-250m/min, d=0.4mm, f=0.1-0.2mm/rev

FIGURE 5. Chip form generated in turning laser heat treated and non-laser heat treated carbon steel with the ceramic insert.

treated carbon steel with carbide P30 insert, the chip breakability is poor at the higher cutting speed and lower feed rare. In the case of laser heat treated carbon steel, the chip breakability is better than that in turning non-heat treated carbon steel with ceramic insert, but poorer than that in turning laser heat treated carbon steel with carbide P30 insert.

FIGURE 6 shows the cross section of chip generated in turning heat treated carbon steel AISI 1045 with the carbide P30 insert. In the

typical continuous chip structure, the deformed heat affected zone is observed. In turning, the bending moment is induced in the chip by chip flow and weight itself. Thus the local fracture occurs due to the higher brittleness and lower fracture strength of heat affected zone and the chip is broken easily.

FIGURE 7 shows the influence of cutting temperature on chip thickness. The cutting temperature is increasing with increase of cutting speed. The measured chip thickness is decreasing with increase of cutting temperature. As for chip thickness, the thinner chip is difficult to be broken. In turning with ceramics insert, the thickness is thinner than that in turning with carbide insert at the same cutting temperature. This indicates that the affinity of ceramics insert for carbon steel is lower than that of carbide insert. Then, the chip in turning with ceramics insert is more difficult to be broken than that in turning with carbide insert.

Consequently, the surface modification by selective laser heat treatment is one of the most effective methods in chip control in turning of carbon steel.

CONCLUSIONS

In this study, for the purpose of chip control in turning, a direct diode laser is irradiated linearly in the longitudinal direction on the cylindrical work material surface The influences of laser irradiation on the chip geometry. The main results obtained are as follows.

[1] A direct diode laser (DDL) is available for as an in-situ heat treatment device in turning of carbon steel. By selective laser irradiation, a clear semicircle heat affected layer having the hardness 600HV is formed, where the martensitic structure is observed in the ferrite-pearlite mother phase.

[2] The continuous chip is broken in the heat affected zone during cutting due to higher brittleness so that broken chips have spiral form and their length are approximately equal to those generated by less than 10 revolution cutting.

ACKNOULEDGEMENT

The authors would like to acknowledge the support of JFE BERS&SHAPES CO., LTD., which enabled this work to be carried out.

REFERENCES

[1] T.H.C. Childs, K. Maekawa, T. Obikawa and Y. Yamane "Metal Machining" 2000 John Willy & Sons Inc., New York.

[2] R.M.D. Mesquita, F.A.M. Soares, M.J.M. Barata Marques AN EXPERIMENTAL STUDY OF THE EFFECT OF CUTTING SPEED ON CHIP BREAKING. Journal of Materials Processing Technology 1996; 56: 313-320.

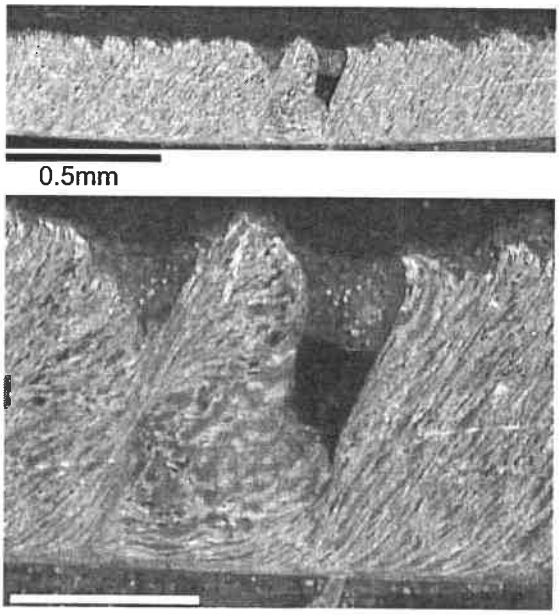

V=150m/min, d=0.4mm, f=0.15mm/rev

FIGURE 6. Cross section of chip in turning heat treated carbon steel AISI 1045 with the carbide tool P30.

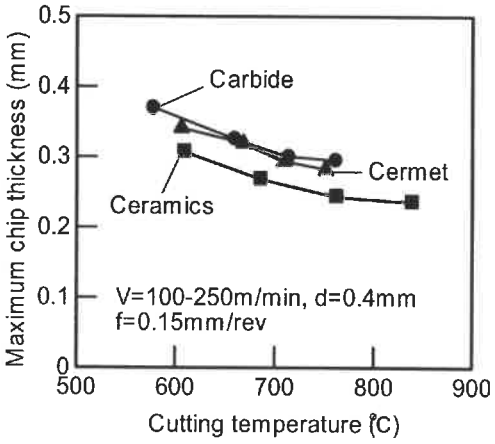

FIGURE 7. Influence of cutting temperature on chip thickness in turning AISI 1045

INTELLIGENT-SPEED-INCREASING SPINDLE USING TRACTION DRIVE

Masashi Yamanaka[1], Keigo Sugimoto[2], and Katsumi Inoue[1]
[1]Dept. Mechanical Systems and Design
School of Engineering, Tohoku University
Sendai, JAPAN
[2]Manufacturing Engineering Development Center
Sony Corporation
Atsugi, Kanagawa, JAPAN

INTRODUCTION

Recently, a milling for die using a small end mill of diameter less than 1 mm is increased, because sizes of plastic mold parts such as connectors for an IT and an electronics becomes micro extremely. In general, a tool life is long and a good cut surface is obtained as a cutting speed is high. A speed-increasing spindle, which is attached to a shank may be used to increase the cutting speed to achieve a high-speed cutting in an ordinary machining center (MC). Those using planetary gears [1] or a traction drive [2] that has a future of low vibration and high-accuracy power transmission comparing with a gear have already developed and marketed. In this research, the speed-increasing spindle using a traction drive applying a wedge action (WTD) different from the commercial type is developed to realize a high-accuracy milling, and its performance is evaluated by cutting tests.

Moreover, the function of measurement of cutting torque during end milling is added to make the spindle intelligent. It is effective for the optimization of cutting conditions, the prediction of tool life and the prevention of tool failure [3][4]. A cutting force can be detected by attaching a dynamometer to a spindle in the MC or a workpiece [5]. However, some problems remain; for example, the limitations of the milling range and the shape of the workpiece, and the high cost of equipment. We have proposed a new method of measuring cutting torque during milling using a small end mill, using a speed-increasing spindle. By attaching a few parts to the speed-increasing spindle, torque can be measured at a low cost [6]. Here, this method is applied to the developed WTD speed-increasing spindle and some experiments are carried out to show the viability of this measurement method..

COMPOSITION OF WTD SPEED-INCREASING SPINDLE

Traction drives transmit power using the shear force of an EHL film between two rolling elements [7]. It is necessary to apply a large contact force between rollers to generate the traction force. The WTD shown in Figure 1 is a kind of the planet roller variator. A ring and a sun rollers are concentric and diameters of all idler rollers are same in usual planet roller variator. The contact force is generated by a shrink fit of the ring roller. It becomes excessive and causes a heat generation in the range when the transmission torque is small.

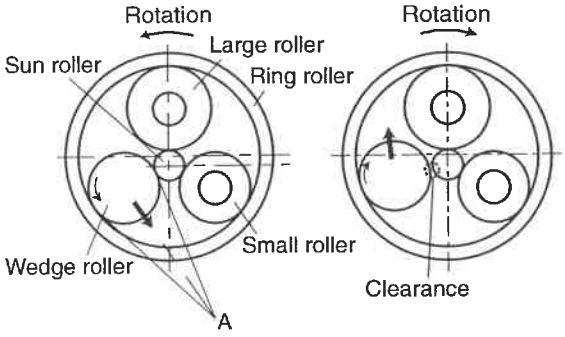

FIGURE 1. Mechanism of WTD

On the other hand, the ring and sun rollers are eccentric in the WTD. The small and the large rollers among three idler rollers are restrained by shafts, and can rotate along them. The wedge, the ring and the sun roller can move freely. The WTD is used an increaser here for the ring roller input and the sun roller output, respectively. The contact force does not generate between rollers without loads. The wedge roller digs into toward point A by the wedge action when the input ring roller rotates in CCW, and the contact force according to the load generate for the ring and the sun rollers. Because the small and large

rollers are fixed with the shafts, the contact force is applied between all rollers, and the input torque is transmitted to the sun roller through three idler rollers. A small heat generation is a feature of the WTD compared with the planet roller variator in fixed contact force. The contact force does not apply to the wedge roller when the input ring roller rotate in CW, and the torque is not transmitted. The WTD works like a one way clutch.

The traction coefficient and the Hertzian pressure between rollers in WTD change according to the arrangement and the diameter of idler rollers. These were designed under optimum conditions in this research, and the speed-increasing spindle was designed based on these results. The developed spindle is shown in Figure 2. The speed-increasing ratio is 5 and the shank is BT40. When the input shaft attached to the tool spindle of MC rotates, the end mill put to the output shaft rotates through the ring, the idler and sun rollers. The ring and sun rollers are slightly displaced when the wedge roller digs into by the wedge action during transmitting torque. Especially if the sun roller and the output shaft are in a body, the end mill will be eccentric and the cutting accuracy may become worse. Therefore, the output shaft and the sun roller were connected by an Oldham's coupling as shown in the figure, and the displacement was absorbed. The ring roller and the input shaft are coupled by a spline, and the ring roller can move in radial direction.

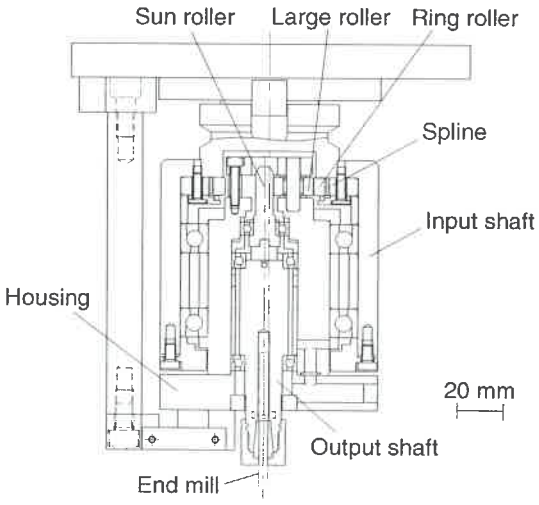

FIGURE 2. Composition of WTD speed-increasing spindle

The traction oil that is special oil for TD is used for traction contact and also lubricating bearings. The oil supply at the traction contact and bearings is an oil mist. It is confirmed by the experiment using the two-disk testing machine that the traction drive is achieved with a very small amount of traction oil [8].

EVALUATION OF PERFORMANCE

To evaluate the performance of the developed WTD spindle, the cutting tests were carried out using a vertical MC and end mills. The result is compared with that by a commercially available speed-increasing spindle using planetary gears.

An end milling was carried out with a variety of axial depth of cut, *Ad*, radial depth of cut, *Rd*, and feed speed, *C* in the range as shown in Table 1(a). Other conditions are also shown in the table. The measured surface roughness is shown in Figure 3. These of the WTD spindle are better in most cutting conditions. The main reason is considered that a vibration during transmission is smaller in the TD than the gear.

TABLE 1. Milling conditions

	(a)	(b)
End mill	ϕ2 square	ϕ0.5 square
Spindle rotary speed [min^{-1}]	3000	
Tool rotary speed [min^{-1}]	15000	
Cutting speed [m/min]	94.2	15.7
Axial depth of cut [mm]	0.5 - 2.0	0.125 - 0.5
Radial depth of cut [mm]	0.1 - 0.4	0.025 - 0.1
Feed speed [mm/min]	450 - 1800	75 - 300
Work piece	NAK55	
Coolant	Dry (Air blow)	
Type of milling	Up cut	

MEASUREMENT OF CUTTING TORQUE IN SMALL END MILLING

Principle of measurement

Depending on the transmission torque, a counter torque reacts in the fixed part. Therefore, the transmission torque can be calculated by measuring the magnitude of counter torque. In the case of the speed-increasing spindle with the WTD rollers, the ring roller and the sun roller are used as an input and an output, respectively, and the carrier is fixed. We devised a mechanism, in which the beam is fixed between the carrier and the stopper, and a strain gage is put on the beam, as shown in Figure 4. The magnitude of the strain changes according to the cutting torque applied on the sun roller during end milling.

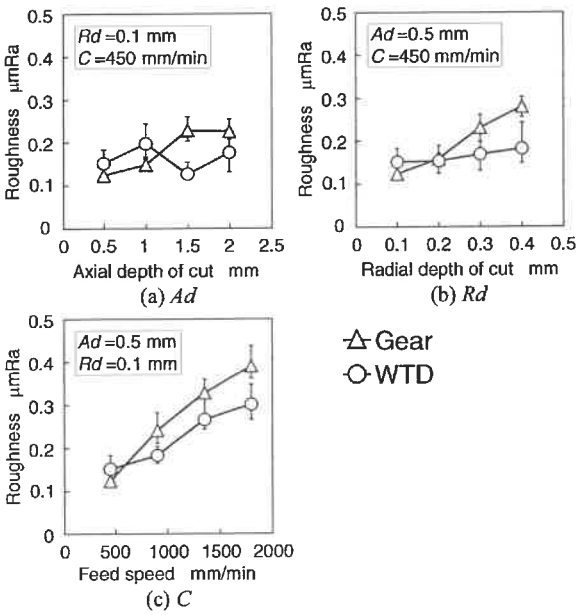

FIGURE 3. Measured surface roughness

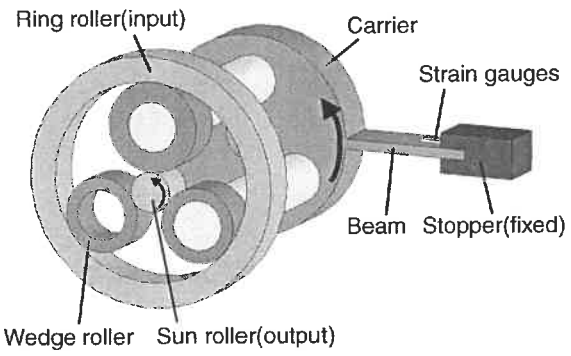

FIGURE 4. Principle of torque measurement

Measurement result

To verify that the cutting torque can be measured in the method proposed, the developed speed-increasing spindle was modified as shown in Figure 5. A beam was set between the carrier and stopper. The strain-gage output was input to a personal computer via a strain amplifier after A/D translation.

First, a static calibration was carried out in the following procedure. An L-shaped bar was fixed on the chuck, which is for grasping the end mill to be fixed. The bar was pulled with a spring scale in the rotational direction to give a torque. At that time, the strain-gage output was recorded. The output strain is proportional to the tensile force, and then the magnitude of torque is obtained by the magnitude of strain.

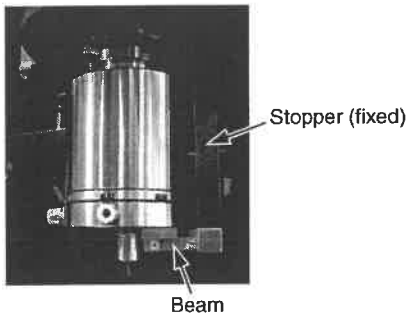

FIGURE 5. Spindle with torque measurement equipment

Next, the output time response at the strain-amplifier during milling using the ϕ0.5 2-flute end mill is shown in Figure 6. The spectrum is also shown to have the characteristics of frequency response. The vertical axis indicates the half amplitude of the time response for the frequency. A strong peak appears at 33.3 Hz. This is considered to be due to a torque irregularity occurring at the spindle motor because this frequency agrees with that of input rotary speed. In the spectrum, a very small peak was observed at 333 Hz. Because the speed increase ratio of the speed-increasing spindle is 5 and the end mill has two flutes, if the input ring roller rotates by one turn, the sun roller (output) rotates five times, resulting in a tenfold cutting rate. Accordingly, the peak caused by the milling was considered to appear at 333 Hz, which is the frequency tenfold that of the input waveform. This difference between the frequency component at milling and that at idling is considered to be the increase in frequency due to milling. This value is converted to the torque by using the calibration result.

An end milling was carried out under various cutting conditions using ϕ0.5 of carbide end mill shown in Table 1(b) and cutting torque was measured in the method explained above. The results of torque measurement during the end milling are shown in Figure 8. The cutting torque was measured five times under each *Ad* condition and the mean value and dispersion of five torques measured are shown. The measured cutting torque increased with *Ad*. The results of the torque measurement obtained by varying *Rd*, and *C*, are also shown in Figure 7.

Similarly to *Ad*, the values of cutting torque increased with *Rd* and *C*.

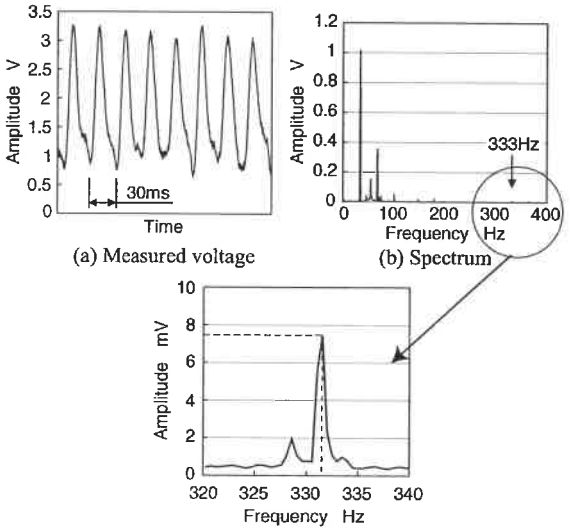

FIGURE 6. Output of strain amplifier during milling

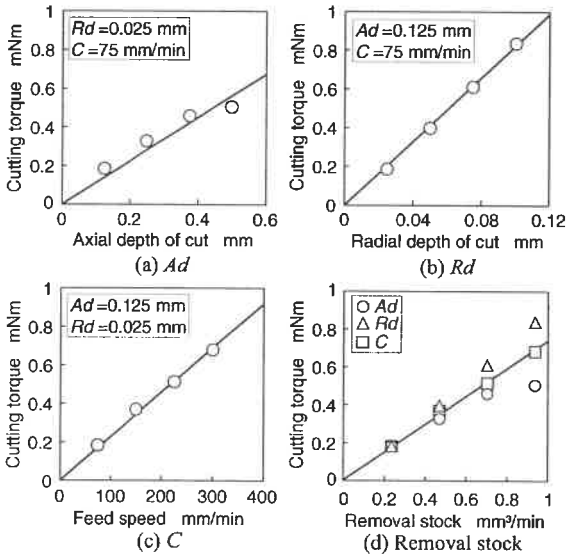

FIGURE 7. Relation between cutting torque and condition

Figure 7(d) shows the relationship between the removal stock rate and the cutting torque, which was obtained from the results shown in Figure 7(a) to (c). The increased rate of cutting torque owing to the increase in *Ad* is almost the same as that owing to the increase in *Rd* and C. Although calibration on the basis of the comparison using the dynamometer was not carried out, such a quantitative comparison is possible, showing the effectiveness of this measurement method.

CONCLUSIONS

- The WTD is applied to the speed-increasing spindle. The performance in the roughness of milled surface is better than the commercial type using planetary gears.
- Using the torque measurement method proposed, the cutting torque was measured quantitatively in small end milling.

ACKNOWLEDGMENT

This research is partly supported by the OSAWA Scientific Studies Grants Foundation in Japan. OSG Corporation offered the end mills used in the experiment. The authors wish to express thanks for their generous assistance.

REFERENCES

[1] NT TOOL CORPORATION, http://www.nttool.com/english/index.html

[2] SHOWA TOOL CO., LTD, http://www.showatool.com/en/traction/index.html

[3] Tansel IN, Arkan TT, Bao WY, Mahedrakar N, Shisler B, Smith D, McCool M. Tool wear estimation in micro-machining. Part I: tool usage-cutting force relationship. Int. J. Machine Tools & Manufacture. 2000; 40: 599-608

[4] Oketani T, Mase Y, Nishigaki Y, Sase N, Fujii H. Development of a force sensing drill holder for fine drilling. J. Materials Processing Technology. 1996; 56: 563-570

[5] Kistler corporation, http://www.kistler.com/

[6] Yamanaka, M., Miyamura, S., and INOUE, K. Measurement of cutting torque by speed increasing spindle. Proceedings of the 11th International Conference on Precision Engineering. 2006; 151-156.

[7] Hellich, F. W. and Shube, E. E. Traction Drive. Marcel Dekker New York: 1983.

[8] Yamanaka, M., Ida, M. and Inoue, K. E, Characteristics of Traction Drive in Minimum Oil Supply. Proceedings of ICMDT2007, JSME-KSME Joint International Conference on Macnufactuirng, Machine Design and Tribology. 2007; C12 (CD-ROM), 1-6.

HIGH RESOLUTION, HIGH SPEED REAL-TIME DIGITAL CONTROL SYSTEM FOR PRECISION APPLICATIONS

Aaron J. Gawlik, Ross I. MacKenzie, David Otten, and David L. Trumper
Department of Mechanical Engineering
Massachusetts Institute of Technology
Cambridge, MA

INTRODUCTION

We have designed, built, and tested a high sample rate, high resolution digital control system for precision engineering applications. The control system is based upon a field programmable gate array (FPGA) board commercially available from National Instruments. With the expanding capabilities of FPGAs such controllers will be of increasing interest. With this controller, we have demonstrated the capability for 625 kHz closed-loop control sample rate and 2.5 MHz data acquisition. Experimental results with custom analog interfaces demonstrated 0.1 nm RMS control over a 10μm mechanical range when filtered to the 1.5 kHz closed-loop bandwidth. The system architecture for a single channel is shown in Figure 2.

Design was completed to meet baseline specifications for an individual application, however flexibility was a key component for universal applicability to various control implementations. The particular application was a high-speed 2 DOF scanner with specifications to scan and digitally sample $2^{20} \approx$ 1M pixels at 1 Hz for a data acquisition rate of at least 1 million samples per second (MSPS). Each degree of freedom was specified to 113.7 dB signal-to-noise ratio (SNR), or 18.6 equivalent number of bits. The highest closed-loop bandwidth was set between 1 and 5 kHz, requiring a sample rate at least 100 kHz to limit discrete sampling and control effects.

The first proof-of-concept experiments used capacitive probes for position sensing, thus requiring high-resolution, high-speed analog-to-digital converters. Actuation was implemented with electromagnetic shear-mode actuators in a stacked-coil, moving-magnet configuration, driven with power amplifiers from digital-to-analog converters.

CONTROL PLATFORM HARDWARE

Following a product survey of available solutions, we decided to build a custom solution from individual commercial components. Numerous commercial control options exist, but become limited with regards to sample rate, precision, cost, design flexibility and support, and single-supplier dependence. An A/D PCB, shown in Figure 1, was designed and built around the Analog Devices AD7760 IC. This 24-bit, 2.5 MSPS sigma-delta converter has a 100 dB dynamic range but also introduces a 10.8 μs propagation delay.

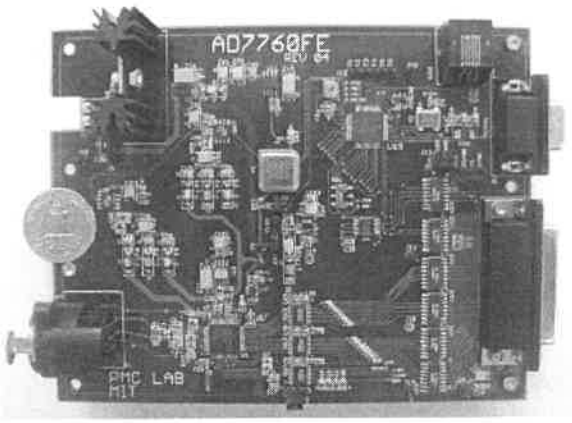

FIGURE 1. ADC PCB (quarter shown for scale).

Digital data acquisition and control can be implemented on either FPGAs or dedicated digital signal processors (DSP). As applications increase in bandwidth and digital hardware generates signals of faster sampling rates, dedicated logic circuits become more suited to specific data manipulation and high speed data routing tasks than a dedicated processor. The distinct advantage for FPGA processing is parallel execution capabilities. However, FPGA computations are limited because the logic architecture is suited for fixed-point simple bit operations, thus introducing more significant quantization whereas DSPs implement higher order computations more efficiently.

Numerous control platforms are based on DSPs, FPGAs, or a hybrid architecture to utilize the benefits of each device. An FPGA is required for the control platform as a digital front-end to inter-

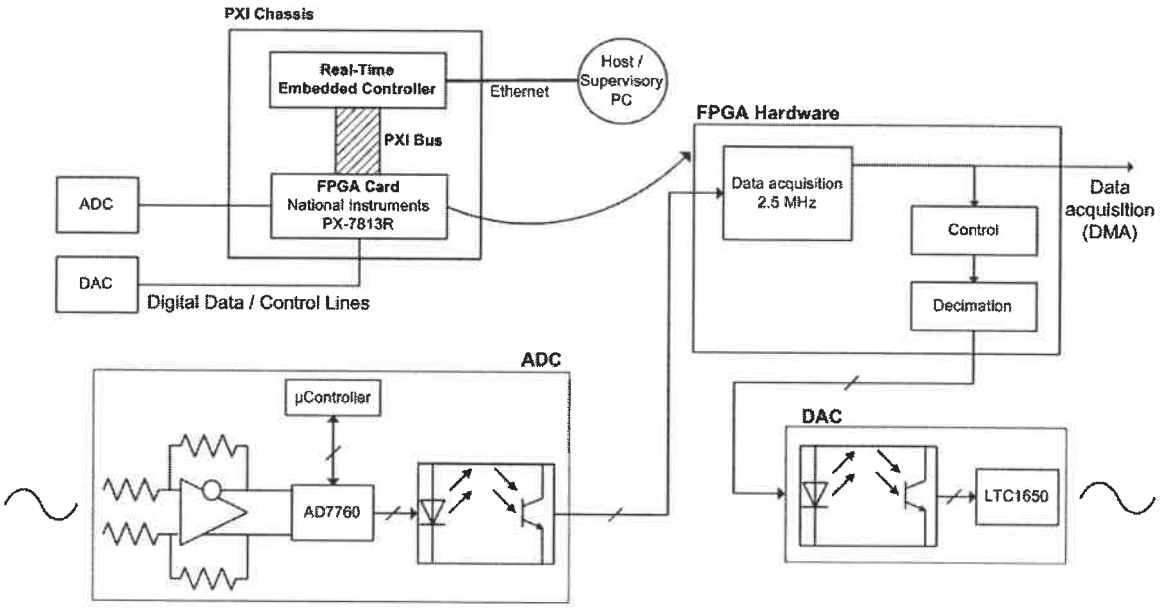

FIGURE 2. Control platform hardware functional block diagram.

face with the high A/D converter data rate, and this same FPGA is also capable of the control implementation. Thus an FPGA-based architecture was selected. The National Instruments (NI) FPGA product was selected because it incorporates a high performance Xilinx FPGA with the LabVIEW FPGA Module, allowing custom I/O and control without prior knowledge of traditional HDL languages or board-level hardware design. The NI LabVIEW FPGA Module uses the LabVIEW graphical development platform to directly compile applications onto FPGA hardware.

Custom PCB Design

Our analog interface PCB incorporates fully-differential inputs, complete power decoupling, digital galvanic opto-isolation, peer channel synchronization, a supervisory microcontroller, and signal input shifting, scaling, and filtering. The microcontroller was designed onto the PCB in order to provide the required A/D boot-up sequence, thus reducing the number of necessary galvanic isolators as well as dedicated FPGA resources to each A/D channel.

The control loop is closed with an output D/A to drive plant actuators. A 16-bit low glitch voltage output D/A with serial digital inputs from Linear Technology (LTC1650) was used. The D/A is built on a small PCB that can be located close to the signal sink. The D/A PCB also utilizes power supply decoupling and an isolated galvanic interface to eliminate ground loop issues.

DIGITAL PLATFORM SOFTWARE AND CONTROL IMPLEMENTATION

While the NI FPGA operations are scaled back from the general LabVIEW platform, additional advanced hardware interface features are available. These include a host interface and first in, first out (FIFO) buffers for communication between loops and sample rates, as well as direct memory access (DMA).

The A/D data acquisition and D/A data output for each sample is implemented with finite state control. A distinct advantage to the NI LabVIEW programming language is the ease of implementing sequential logic (opposed to combinational logic), which determines outputs based on inputs as well as past states.

Digital Control Implementation

The computation time for the implemented controllers and logic depends on the controller complexity. For the lag, triple-lead, and high-frequency low-pass controller implemented for the experimental results section, there are six shift registers at 2.5 MHz representing a controller computation time delay of 2.4 μs. A 4-point FIR filter averager is used to decimate the data stream from 2.5 MHz to 625 kHz. The total propagation/system delay, with the A/D delay, is 23.2 μs.

The expected negative phase loss for this time delay is 41.8 degrees for a 5 kHz closed-loop bandwidth. The phase loss is a limiting factor on the closed-loop bandwidth because it increases linearly with frequency.

PID Control

LabVIEW provides basic PID control functionality with the discrete PID FPGA block. This simplified block is limited to 16-bit precision and is intended for users with little experience in implementing linear controls. Simple PID also does not have the universality that arbitrary controller transfer functions are capable of and are generally designed from a qualitative approach. Standard benchmark tests on FPGA utilization are not provided for the PID block but the maximum operating frequency is 3.33 MHz whereas the IIR filter method described below can run a single lead controller at 5.7 MHz with 32-bit precision.

IIR Control from Arbitrary Discrete TF

An infinite impulse response (IIR) filter contains memory and has an infinite impulse response to an impulse input. The difference equations that describe an IIR filter can be represented in several ways, but a simplified canonical form is required when system performance is limited by the number and complexity of computations [1].

Filter design was completed with Matlab in continuous-time and then converted to discrete form and imported to a custom written LabVIEW VI that quantizes the discrete coefficients, simulates the filter response, and generates the FPGA code to be compiled in the end application as a canonical discrete form II cascaded subVI. A number of the subVI discrete filter tools are provided by National Instruments.

Addition and multiplication operations present unique challenges in fixed-point arithmetic. The multiplication subVI created by LabVIEW multiplies the signal and coefficient to 64 bits and then scales back the value to 32-bit precision. Also, the 32 by 32-bit multiplication is separated into parallel arithmetic paths and recombined to utilize dedicated multipliers of smaller widths built into the FPGA.

When implementing integral control, it is recommended to also implement anti-windup. This is completed by locating the integrator on its own data path with saturation limits. Boolean logic turns on/off the integrator term to the data stream and reinitializes the integrator when the integrator switch transitions true.

Parametric amplitude control was also designed for the 2 DOF scanner application to ensure that the system oscillates at its resonant frequency even as the resonant frequency shifts. While the concept is somewhat advanced [2], it is implemented with a series of parallel loops comprised of traditional IIR controllers and an amplitude measuring function, implemented with a custom peak-peak detector.

Lastly, a GUI was designed in order to view the system and interact with settings, variables, gains, and filters. This interface also provided a postprocessing platform to accept, process, and display the acquired data.

EXPERIMENTS AND RESULTS

The A/D PCB was characterized by supplying a grounded input between the differential inputs. This provided a measured unfiltered SNR of 66 μV RMS relative to a 20 V range at 2.5 MSPS. This is equivalent to 109.6 dB or 17.9 effective bits. When filtered to 100 kHz with a 25-point digital boxcar filter, the signal baseline noise then improves to 14.8 μV RMS, or 122.6 dB SNR.

The manufacturer characterization results for two separate ADE Technology capacitive probes and instrumentation measurements of the these probes are provided in Table 1 (probe model 6501, gauge electronics 6810, 100 kHz bandwidth). The probes were fixtured and offset from a stationary surface.

TABLE 1. Capacitive Probe Characterization Noise by Supplier and Instrumentation (RMS).

	40 μm Probe	50 μm Probe
Specified by Manufacturer	181 μV	309 μV
Measured by A/D	252 μV	298 μV
Measured by Diff Amp[1]	165 μV	260 μV

Sub-Nanometer Position Control Results

This section describes results for applying the designed digital platform to a single axis of the 2 DOF scanner described above. The plant is modeled as a spring-mass-damper system driven by a

[1] Low-pass filtered to 100 kHz on Tektronix AM502 differential amplifier

Lorentz force actuator which results in three poles all occurring near 400 Hz.

The z-axis controller for random access positioning with the 40 μm range capacitive probe was a lag, triple-lead controller designed for a 35 degree phase margin at a 1.5 kHz crossover frequency. This controller was first implemented on a dSPACE control platform with a 50 kHz closed-loop sampling rate. This system was capable of 50 kHz data sampling and 5.0 nm RMS unfiltered control positional noise with the native 16-bit ADCs and 14-bit DACs provided by dSPACE.

In order to implement the controller on the high-speed, high-resolution platform, the controller was redesigned to accommodate the additional phase loss due to the A/D and computational time delay, adding 23 degrees of positive phase. The controller was of the continuous form

$$H_Z(s) = \left(\frac{0.00229s+1}{0.00229s}\right)\left(\frac{0.00017s+0.75}{2.19\times10^{-5}s+1}\right) \times \left(\frac{0.000229s+1}{2.19\times10^{-5}s+1}\right)\left(\frac{0.000244s+1}{2.05\times10^{-5}s+1}\right) \quad (1)$$

Figure 3 shows the time and frequency response for a constant reference with 625 kHz sample rate closed-loop control. The unfiltered noise is 430 μV (0.86 nm RMS) and 51.9 μV (0.10 nm RMS) when filtered to the 1.5 kHz closed-loop frequency across a 10 μm mechanical range and a 40 μm sensor range. The filtered measurements correspond to 111.7 dB dynamic range and 18.3 effective bits.

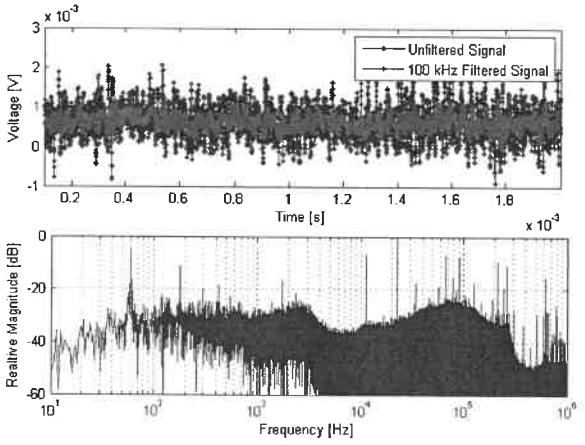

FIGURE 3. Controlled z-axis time response (top) and FFT (bottom).

CONCLUSIONS

In the effort to control systems of increasing bandwidth to finer resolutions, this control platform demonstrates the application of high sample rate, high resolution arbitrary control to universal systems. Results demonstrate a 111.7 dB dynamic range when filtered to the 1.5 kHz closed-loop bandwidth with 2.5 MHz data acquisition and 625 kHz closed-loop sample rate. This compares to control implemented on dSPACE with 78 dB dynamic range at 50 kHz data acquisition and closed-loop sample rate. Traditional controllers initially implemented with Matlab's Real-Time Workshop are converted and synthesized to the high-speed FPGA platform. The largest disadvantage to the FPGA control implementation is in flexibility, development, and debugging due to long synthesis and compilation times.

SUGGESTIONS FOR FUTURE WORK

A performance increase can be obtained with a more specialized system. By utilizing the FPGA strictly as a digital front-end, multiple DSPs can be used as the control platform. For example, a Triple-Body architecture with three DSPs and approximately 95 dB dynamic range analog interfaces can be capable of 1 MHz closed-loop sample rate and a time latency of 1.4 μs for four A/D conversions, a 20th-order filter, a cosine/sine/square root computation, and finally four D/A conversions [3]. A 20th-order filter implemented in LabVIEW FPGA code would require a latency of at least 3.5 μs. The DSP architecture allows more software flexibility with more complex computations, particularly at increasing speeds, and simpler coding. However, this higher performance system dramatically increases hardware complexity, cost, and development time.

ACKNOWLEDGEMENTS

This work was supported by Samsung Electronics Co., Ltd.

REFERENCES

[1] Oppenheim AV, Shafer RW. Discrete Time Signal Processing. Second ed. Prentice Hall, Inc; 1998.

[2] Roberge JK. Operational Amplifiers: Theory and Practice. John Wiley & Sons; 1975.

[3] Lu X. Electromagnetically-driven ultra-fast tool servos for diamond turning [Ph.D. Thesis]. Massachusetts Institute of Technology. Department of Mechanical Engineering; 2005.

INTEGRATED TUNING OF A ROBUST CONTROLLER FOR LINEAR SERVOMECHANISMS

Seong-Hwan Hong[1], Seung-Chul Kim[1] and Sung-Chung Chung[1*]
Hybrid System Design & Control LABoratory
Department of Mechanical Engineering
Hanyang University, Sungdong-Gu, Seoul 133-791, KOREA

ABSTRACT
In order to design a high-performance controller with excellent positioning and tracking performance, an optimal tuning method based on the integrated design concept is studied. DOBs, feedforward controllers and CCC are applied to control the bi-axial linear servomechanism. To derive accurate dynamic models of mechanical subsystems equipped with linear servos for the integrated tuning, system identification processes are conducted through the sine sweeping. An optimal tuning problem with stability, robustness and overshoot constraints is formulated as a nonlinear constrained optimization problem. Optimal gains are obtained through the SQP method. Experimental results confirm that both tracking and contouring errors are significantly reduced by applying the proposed controller and integrated tuning method.

KEYWORDS:cross-coupled control, disturbance observer, feedforward controller, linear motor, integrated tuning

INTRODUCTION
High-speed/precision servomechanisms are widely used in mechatronics, IT, manufacturing and FPD (flat panel display) industries. The positioning and tracking accuracy in high-speed motion is important for the fabrication of feeddrive systems. In the servomechanism with linear motors, the accuracy is affected by dynamic characteristics such as inertia variation, external load, friction, etc. To reduce such errors, feedforward controllers and internal loop compensators are required [1]. To improve the performance of the feedforward controllers, the dynamic characteristics should be precisely identified first. A disturbance observer (DOB) as an internal loop controller has been applied to improve robustness of the control system [1~3]. To improve tracking performance, a cross-coupled control (CCC) system has been used as well [4~6].

In this paper, the optimal tuning of a cross-coupled controller linked with the feedforward controller and the DOB is studied to reduce positioning and tracking errors of linear servos by using the previously developed integrated tuning methods [4,6,7~9]. In this tuning method, parameters of the mechanical subsystem are specified according to the fabricated mechanical subsystem parameters. To derive an accurate dynamic model of the mechanical subsystem of the linear servo, system identification process is conducted by the sine sweeping [10]. A velocity and acceleration feedforward controllers are applied to reduce tracking errors. A multiplicative uncertainty model is used for the DOB [1,3]. The CCC control system for an arbitrary curve, which is combined with the feedforward controller, is formulated by a state-space equation based on a series of linear motion trajectories. Finally, using the results of the optimal tuning, diagonal motion experiments are performed on a bi-axial linear servo (Fig. 1) to verify effectiveness of the proposed optimal tuning procedure. Experimental results confirm that both positioning and tracking errors are significantly reduced by applying the proposed integrated tuning method.

CROSS-COUPLED CONTROL
In coupled control systems, contour errors are increased due to mismatched dynamic variables and loop gains. As the CCC connects orthogonal axes through feedback of contouring errors, better contouring accuracy is obtained than conventional controllers [4~5, 11]. In order to construct the CCC, time varying cross-coupling gains depending on a path trajectory should be clearly identified [4, 11]. In case of

linear motion, contour error is calculated from Eq.(1) [4~5] .

$$\varepsilon_l = -e_x \sin\theta + e_y \cos\theta \quad (1)$$

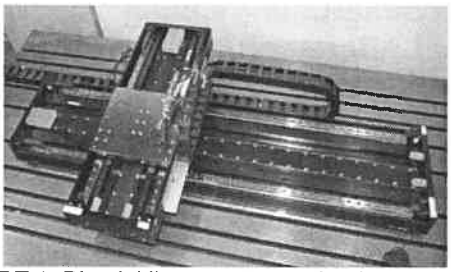

FIGURE 1. Bi-axial linear servomechanism.

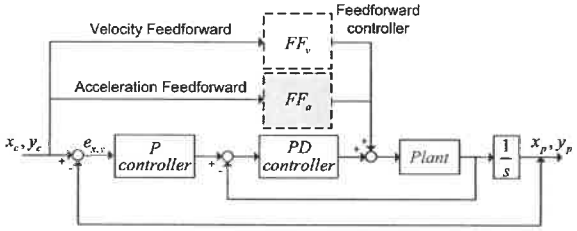

FIGURE 2. Block diagram of the feedforward control.

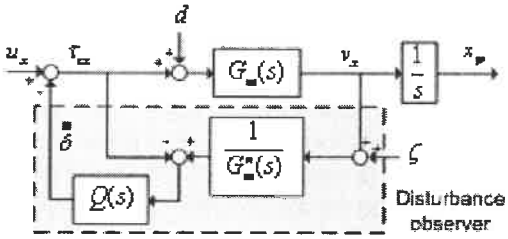

FIGURE 3. Block diagram of the disturbance observer.

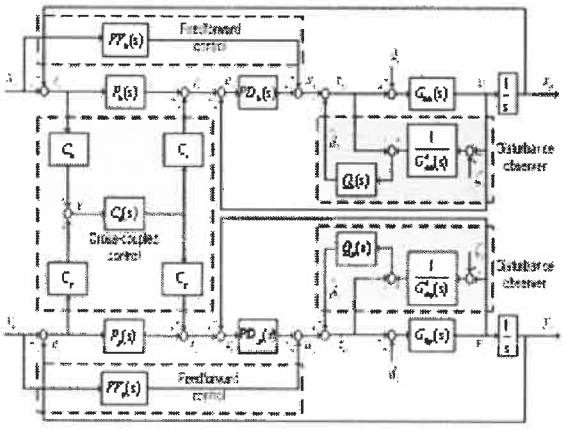

FIGURE 4. Block diagram of the overall system.

FEEDFORWARD CONTROLLER

Fig.2 shows the velocity and acceleration feed forward controllers. It is used to reduce tracking errors related with servo-lag, friction, external load, and so on. This control improves not only bandwidth of the feedback control loop but also tracking performance.

DISTURBANCE OBSERVER

Fig. 3 shows a disturbance observer (DOB) as an internal loop controller. In order to improve robustness of the controller a Q-filter is connected with the DOB. This control structure is simple and robust to compensate for disturbances of the linear servo [1, 3].

Velocity output of the servo v_x is represented by control input *u*, disturbance *d*, and measurement noise ζ as follows:

$$\begin{aligned} v_x &= G_{uv_x}(s)u + G_{dv_x}(s)d + G_{\zeta v_x}(s)\zeta \\ G_{uv_x}(s) &= \frac{G_m(s)G_m^n(s)}{G_m^n(s) + \{G_m(s) - G_m^n(s)\}Q(s)} \\ G_{dv_x}(s) &= \frac{G_m(s)G_m^n(s)\{1 - Q(s)\}}{G_m^n(s) + \{G_m(s) - G_m^n(s)\}Q(s)} \\ G_{\zeta v_x}(s) &= -\frac{G_m(s)Q(s)}{G_m^n(s) + \{G_m(s) - G_m^n(s)\}Q(s)} \end{aligned} \quad (2)$$

If $|Q(j)| = 1$, real system G_m acts like a nominal model G_m^n and disturbances are removed completely. If $|Q(j)| = 0$, measurement noises are removed and robustness is improved. Therefore, Q-filter is proposed as follow:

$$Q(s) = \frac{1 + \sum_{k=1}^{N-r} a_k (\tau s)^k}{1 + \sum_{k=1}^{N} a_k (\tau s)^k} \quad (3)$$

In order to determine the coefficient a_k, following optimization problem is proposed [1]:

$$\min_{a_k} \left[|W_1^{-1}(j\omega) \cdot \{1 - Q(j\omega)\}|^2 + |W_2^{-1}(j\omega) \cdot Q(j\omega)|^2 \right] \quad (4)$$

Where W_1 is the sensitivity function, and W_2 is the complementary sensitivity function. To obtain the optimal solution of Eq. (4), which accounts for the trade-off between the disturbance and noise rejections, the Q-filter is selected as Eq. (5).

$$Q(s) = \frac{4(s\tau) + 1}{(s\tau)^4 + 4(s\tau)^3 + 4(s\tau)^2 + 4(s\tau) + 1} \quad (5)$$

Fig. 4 shows the overall control structure including the CCC and feedforward controllers , and DOBs. $P_{x,y}$ are position controllers, $PD_{x,y}$ velocity controllers, $FF_{ax,ay}$ and $FF_{vx,vy}$ are velocity and acceleration feedforward controllers. C_c is a cross-coupled controller, and $C_{x,y}$ are cross-coupling gains. They are given by

$$P_{x,y}(s) = K_{px,py}$$
$$PD_{x,y}(s) = K_{ppx,ppy} + K_{ddx,ddy}s$$
$$FF_{x,y}(s) = K_{ffvx,ffvy}s + K_{ffax,ffay}s^2$$
$$C_c(s) = K_{pc}\ , \quad C_x = \sin\theta\ , \quad C_y = \cos\theta$$

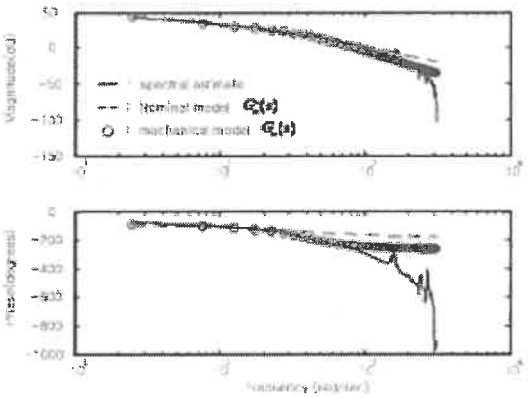

FIGURE 5. Frequency response functions of the mechanical subsystem.

Table 1. Constraints for the optimal tuning system.

Description	Constraints
Relative stability	$g_1 : s_i^{++} < 0,\ s_i^{++} = \{s : P^{++}(s) = 0\},\ i = 1 \sim 20$ $g_2 : s_i^{--} < 0,\ s_i^{--} = \{s : P^{--}(s) = 0\},\ i = 1 \sim 20$ $g_3 : s_i^{+-} < 0,\ s_i^{+-} = \{s : P^{+-}(s) = 0\},\ i = 1 \sim 20$ $g_4 : s_i^{-+} < 0,\ s_i^{-+} = \{s : P^{-+}(s) = 0\},\ i = 1 \sim 20$
Maximum overshoot	$g_5 : M_x(\theta) < 15\%,\quad \text{where } \theta = 80^\circ$ $g_6 : M_y(\theta) < 15\%,\quad \text{where } \theta = 10^\circ$
Robust stability	$g_7 : \lvert Q(s)\rvert_{s=j\omega} < \left\lvert \frac{1}{W(s)} \right\rvert_{s=j\omega}, \forall\, \omega$

IDENTIFICATION OF SERVOMECHANISMS

Identification of the mechanical subsystem is performed to formulate the integrated tuning problem. Sine-sweep method is applied to reduce nonlinear effects of the servo [10]. Linear elements are derived by using the weighted least-square method, which gives weight to particular frequency range. Fig. 5 shows frequency responses obtained from identification processes, and system models are given by

$$G_{mx}(s) = \frac{539553045.8103}{s(s^2 + 470.8727s + 139836.9465)}$$
$$G_{my}(s) = \frac{99838644.669}{s(s^2 + 427.8734s + 130129.9787)}$$
$$G_{mx}^n(s) = \frac{1165363.6706}{s(s + 290.1445)}\ , \qquad G_{my}^n(s) = \frac{111555.4817}{s(s + 128.8477)}$$

Table 2. Optimal tuning results: control gains.

Design variable	Unit	Initial design (uncoupled)	Optimal tuning
$x_1(K_{px})$	V/V	180.000	199.895
$x_2(K_{py})$	V/V	180.100	200.002
$x_3(K_{pc})$	V/V	0.000	200.038
$x_4(K_{ppx})$	V/V	4.000	4.012
$x_5(K_{ddx})$	V/V	0.010	0.0095
$x_6(K_{ppy})$	V/V	10.000	10.003
$x_7(K_{ddy})$	V/V	0.050	0.06
$x_8(K_{ffvx})$	V/V	0.000	0.001
$x_9(K_{ffvy})$	V/V	0.000	0.0004
$x_{10}(K_{ffax})$	V/V	0.000	0.001
$x_{11}(K_{ffay})$	V/V	0.000	0.0005
$x_{12}(\tau_{qx})$	V/V	0.000	0.02
$x_{13}(\tau_{qy})$	V/V	0.000	0.02

OPTIMAL TUNING PROCESS

In this paper, Objectives of the optimal tuning are considered to improve response of the system and contour accuracy. Therefore, optimal tuning of multi-objective function is performed to minimize the settling time and the contour error given by

$$F(\mathbf{x}) = w_1\varepsilon_l + w_2 t_s \qquad (6)$$

w_1 and w_2 are weighting factor of each objective function, ε_l is contour error, t_s is settling time.

There are not only the cross-coupling gains which vary according to the direction of the desired path but also uncertainties in the modeling process. In order to secure stability of the designed system although there are uncertainties, relative stability criteria must be considered in the design process. Kharitonov's theorem [4] is applied to secure relative stability

of the system. In addition, stiffness of system must be guaranteed as a constraint. Since the stiffness and disturbance rejection capability are reduced according to not only the bandwidth increment of Q-filter but also the time constant decrement, robust stability conditions are considered as constraints. To protect the control system from excessive overshoot, maximum overshoot is limited as a constraint as well.

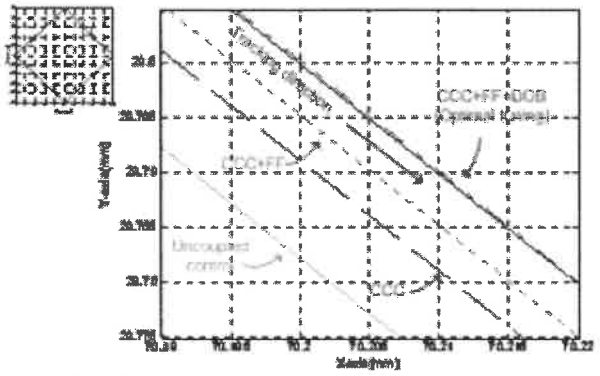

FIGURE 6. Experiment results of the linear motion.

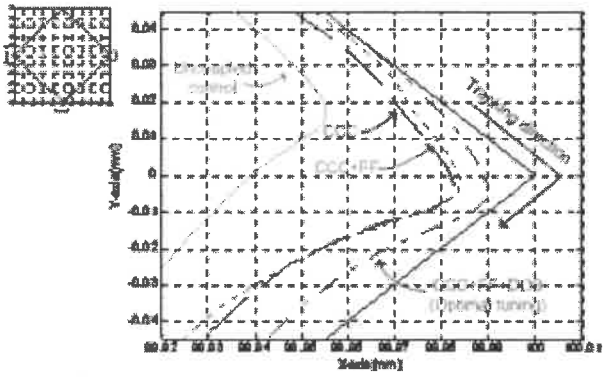

FIGURE 7. Experiment results of the corner motion.

Sequential quadratic programming (SQP) method is applied to solve the optimization problem. Operating conditions are plant uncertainty=±1%, feedrate=1*m/min*, weighting factors of the objective functions $w_{1,2}$=0.5. Table 1 shows constraints.

EXPERIMENTS

Table 2 shows integrated tuning results. To verify the effectiveness and reliability of the tuning, performance tests are conducted on the bi-axial linear stage shown in Fig. 1. Diagonal motion tests are performed with 100mm diagonal length and 1m/min speed. Figs. 6 and 7 show experimental results with better performance than other cases [4, 6].

CONCLUSIONS

In this paper, a cross-coupled controller linked with a feedforward controller and a disturbance observer is applied for improving robustness, positioning accuracy and tracking performance. Reliability of the integrated tuning is confirmed through performance test on the bi-axial linear servomechanism. The controller composed of CCC+FF+DOB approximately has 0.2 μm and 12 μm errors in the linear and corner motion cases. Comparing with other conventional control systems, proposed control structure has better performance.

REFERENCES

[1] Kim, M. S. and Chung, S. C., Integrated Design of Servomechanisms using a Disturbance Observer. Transactions of KSME(A), 2005, 29. 591-599.

[2] Kim, M. S., Sung, C. M. and Chung, S. C., Integrated Design of High-performance Servomechanisms Using a Disturbance Observer. Proceedings of the ASPE 2007 Annual Meeting, 2007, 171-174.

[3] Umeno, T., Kaneko, T. and Hori, Y., Robust Servosystem Design with Two Degrees of Freedom and its Application to Novel Motion Control of Robot manipulators. IEEE Transactions on Industrial Electronics, 1993, 40, 473-485.

[4] Bae, H. K. and Chung, S. C., Optimal Tuning of Biaxial Servomechanisms using a Cross-Coupled Controller. Transactions of NAMRI/SME, 2006, 34. 603-610.

[5] Koren, Y., Cross-Coupled Biaxial Computer Control for Manufacturing Systems. ASME Journal of Dynamic Systems, Measurement and Control, 1980, 102, 265-272.

[6] Sung C.M., Kim K.D., Kim and Chung S.C., Intergrated Tuning of Bi-axial Servomechanisms for Precise Motion Control. Proceedings of the ASPE 2007 Annual Meeting, pp. 183-186.

[7] Kim, M.S. and Chung, S.C., Integrated design methodology of ball-screw driven servomechanisms with discrete controllers. Part I: Modeling and performance analysis. Mechatronics, 2006, Vol. 16, pp. 491–502.

[8] Kim, M.S. and Chung, S.C., Integrated design methodology of ball-screw driven servomechanisms with discrete controllers. Part II: Formulation and synthesis of the integrated design. Mechatronics, 2006, Vol. 16, pp. 503–512.

[9] Kim, M.S. and Chung, S.C., Integrated design methodology for high-precision/speed servo mechanisms. Proc. IMechE, Part C, Journal of Mechanical Engineering Science, 2005, Vol. 219, pp. 843- 852.

[10] Kim, M.S. and Chung, S.C., Friction Identification of Ball-screw Driven Servomechanisms through the Limit Cycle Analysis. Mechatronics, 2006, Vol. 16, pp. 131–140.

[11] Tarng, Y. S., Ghuang, H. Y. and Hsu, W. T., An Optimization Approach to the Contour Error Control of CNC Machine Tools Using Genetic Algorithms. International of Advanced Manufacturing Technology, 1997, 13. 359-366.

PRECISION-LIMIT POSITIONING OF AN ULTRA PRECISION TABLE USING HSMC

Chen Hsieh and Cang-Chin Yang

Institute of Aeronautics and Astronautics
National Cheng Kung University
Tainan, Taiwan, 70101, ROC
chsieh@mail.ncku.edu.tw

ABSTRACT

This paper discusses the application of the higher order sliding mode control (HSMC) to a direct drive system to achieve the so called precision-limit positioning (PLP). By PLP it means that the positioning precision is equal to the limit that is allowed by the system hardware. In this study, a newly developed friction model is used to design the integral gain embedded in the control. Experiment shows that the HSMC system, with a little modification, can really achieve the performance of PLP with expected good robustness as different loads are added. However, the final stage tuning and some other defects still need to be improved.

Keywords: Precision-limit positioning, higher order sliding mode control, friction, linear motor

INTRODUCTION

When it comes to position control, precision-limit positioning (PLP) is a new ultimate performance index. [1] It means that the positioning precision is equal to the limit that is allowed by the system hardware. When a digital position sensor is used in the feedback loop then, under appropriate conditions, it means zero-count steady state error with 100% repeatability. Furthermore, the in-position vibration should also be zero. This is, of course, the limit of the precision that a real system can achieve. In the past, this kind of performance was not considered possible. One of the main difficulties to achieve PLP is to deal with the static friction, which is one of the most unpredictable factors in practical engineering. However, it has been shown by the author in earlier studies that positioning systems can, in fact, benefit from static friction; PLP is achievable with the existence of static friction. More than 4 million positioning tests have been conducted to verify the concept of PLP. [1, 2] Because of its super in-position stability, a system with the performance of PLP is capable of performing count-by-count operations.

In these earlier studies, the control strategies were mainly multi-phase PID controls. These PID controls did exhibit good performance for those cases under which they were designed. However, the robustness under different loads was not satisfying and the design procedures were somewhat tedious.

Conversely, sliding mode control (SMC) [3] is well known for its robustness and systematic design procedures. It is very appropriate for systems with uncertainties. But it has a vital drawback, the chattering phenomenon. To eliminate this drawback, some methods, at the expense of losing steady state error, have been introduced. [3] On the other hand, higher order sliding mode control (HSMC), by introducing an integral term, provides another way to eliminate the chattering effect while maintains zero steady state error. Furthermore, this integral term can easily be modified to perform quasi-integral control at the final stage of positioning to fulfill the requirement needed by PLP. [1] As a result, HSMC has been applied to some positioning systems. [4] However, in these works, the design of the integral gain that is critical to the robustness is lacking. This is mainly because that the bound of the variation of friction is hard to determine. In this research, the friction model introduced in [5] is used to estimate this bound. This model has been proven to match all the important properties in the pre-sliding phase. In the following section, the derivation of HSMC will be described. Section 3 is addressing the way to design the integral gain in the HSMC control. Experimental results and the associated discussions are given in section 4.

CONTROL LAW DESIGN

The motion of a PM DC linear motor can be described by the following equation

$$m\ddot{x} = u - f, \qquad (1)$$

where m is the mass of the slider, u is the applied force, and f is the friction force. It is assumed that m and f are in the range of $[\underline{m}, \overline{m}]$ and $[\underline{f}, \bar{f}]$, respectively. Let x_d be the desired position and $e \equiv x - x_d$ be the position error. By replacing x by e, (1) can be rewritten as

$$\ddot{e} = Bu - F - \ddot{x}_d \tag{2}$$

where $B \equiv m^{-1}$, $F \equiv \frac{f}{m}$. To synthesize the HSMC we define the following sliding surface

$$s \equiv \ddot{e} + p_1\dot{e} + p_2 e = 0 \tag{3}$$

where, p_1 and p_2 are positive scalars. Substituting (2) into (3), it yields

$$s = Bu - F - \ddot{x}_d + p_1\dot{e} + p_2 e = 0$$

Let u_{eq} be the equivalent control.

$$u_{eq} = \ddot{x}_d - p_1\dot{e} - p_2 e + F_0 \tag{4}$$

where $F_0 \equiv \frac{1}{2}\left(\frac{\underline{f}}{\overline{m}} + \frac{\bar{f}}{\underline{m}}\right)$ is the mean value of F.

The control u is then set to be

$$u = B_0^{-1}\left(u_{eq} - W\int_0^t sgn(s)d\tau\right) \tag{5}$$

where $B_0 \equiv (\overline{m}\underline{m})^{-1/2}$ is the geometric mean of B, and W is the integral gain to be determined. Substituting u into s, it turns out that

$$s = \left(BB_0^{-1} - 1\right)u_{eq} - (F - F_0) - BB_0^{-1}W\int_0^t sgn(s)d\tau$$

Taking the derivative of s, it yields

$$\dot{s} = \left(BB_0^{-1} - 1\right)\dot{u}_{eq} - \dot{F} - BB_0^{-1}W\,sgn(s)$$

To be stable, it needs that

$$s\dot{s} = s\left[\left(BB_0^{-1} - 1\right)\dot{u}_{eq} - \dot{F}\right] - BB_0^{-1}W|s| \le -\eta|s|$$

for some $\eta > 0$.

This can be achieved if the control gain W satisfies

$$W \ge \sigma\left[\eta + (\sigma - 1)\left|\dot{u}_{eq}\right|_{max} + \left|\dot{F}\right|_{max}\right] \tag{6}$$

where $\sigma \equiv (\overline{m}/\underline{m})^{1/2}$ and $|\cdot|_{\max}$ is the maximum of $|\cdot|$. It is obvious that to get the equivalent control u_{eq} and integral gain W, we need to know the mean value and the bound of the variation of friction.

ANALYSIS OF THE INTEGRAL GAIN

Basically, friction exhibits a quite complex behavior. It is not only a function of velocity and displacement but also closely related to the pattern of motion. To simplify the problem, we divide the positioning process, according to the friction characteristics, into 4 phases. In this way, the properties of the friction of each phase can be approximated by simple characteristics. The integral gain that satisfies (6) can, hence, be obtained for each phase as described below.

Phase 3

In this phase, the table is sliding and the friction can be expressed as follows.

$$f = c_k\dot{x} + f_k \tag{7}$$

where c_k and f_k are damping coefficient and Coulomb kinetic friction. Suppose these coefficients are bounded in $[\underline{c}_k, \bar{c}_k]$ and $[\underline{f}_k, \bar{f}_k]$, respectively, then (4) becomes

$$u_{eq} = \ddot{x}_d + D_{k0}(\dot{x}_d + \dot{e}) + F_{k0} - p_1\dot{e} - p_2 e \tag{8}$$

where $F_{k0} \equiv \frac{1}{2}\left(\frac{\underline{f}_k}{\overline{m}} + \frac{\bar{f}_k}{\underline{m}}\right)$, $D_{k0} \equiv \frac{1}{2}\left(\frac{\underline{c}_k}{\overline{m}} + \frac{\bar{c}_k}{\underline{m}}\right)$.

Since $\left|\dot{u}_{eq}\right|_{max}$ and $\left|\dot{F}\right|_{max}$ in (6) are also functions of derivatives of x. To obtain a constant but reasonable integral gain W, the derivatives of x embedded in $\left|\dot{u}_{eq}\right|_{max}$ and $\left|\dot{F}\right|_{max}$ are replaced by those of x_d and we have

$$W = \sigma\left[\eta + \tilde{D}_k\left|\dddot{x}_d\right|_{max} + (\sigma - 1)\left|\dddot{x}_d + D_{k0}\ddot{x}_d\right|_{max}\right] \tag{9}$$

where $\tilde{D}_k \equiv 1/2\left(\bar{c}_k/\underline{m} - \underline{c}_k/\overline{m}\right)$.

Phase 2

In this phase, the system is basically sliding[1] but with a slow speed so that the system is in the transition phase between stick and real slipping. The friction force can be approximated by

$$f = f_q(|\dot{x}|)sgn(\dot{x}) \tag{10}$$

where

$$f_q(|\dot{x}|) = \begin{cases} \dfrac{f_k(|\dot{x}| - v_s) + f_s(v_k - |\dot{x}|)}{v_k - v_s}, & v_k \ge |\dot{x}| \ge v_s \\ f_s, & |\dot{x}| < v_s \end{cases} \tag{11}$$

and f_s is the maximum static friction. v_k is the velocity where the cold welding effect starts between the contacting surfaces in the system, and v_s is the largest sliding velocity below which the friction remains to be close to the maximum static friction. Suppose f_s is bounded in $[\underline{f}_s, \bar{f}_s]$. Then the equivalent control and an appropriate integral gain are as follow.

$$u_{eq} = F_{q0}sgn(\dot{x}) + \ddot{x}_d - p_1\dot{e} - p_2 e \tag{12}$$

[1] Sliding is in contrast to vibrating.

$$W = \sigma\left[\eta + (\sigma - 1)\left|\ddot{x}_d\right|_{max} + \frac{\bar{f}_s - \underline{f}_k}{v_k - v_s}\left|\ddot{x}_d\right|_{max}\right] \quad (13)$$

where $F_{q0} \equiv 1/2\left(\underline{f}_k/\underline{m} + \bar{f}_s/\underline{m}\right)$.

Phase 1

In this phase, the system is in the so called pre-sliding stage. It has been shown in [5] that, in this phase, the system demonstrates two kinds of motion - plastic deformation and nonlinear spring deformation. Due to its slow response and work hardening effect, the plastic deformation can be ignored as positioning is concerned. On the other hand, the nonlinear spring deformation shows a phenomenon of Preisach hysteresis and dominates the motion in this phase. The friction force in this phase can be approximated by

$$f = c_s\dot{x} + k_1(x - x_z) + \Delta f_s \quad (14)$$

where c_s is the damping coefficient in this phase, k_1 is the apparent stiffness of the nonlinear spring deformation and x_z is the position when x equals x_z the nonlinear spring is not stretched. Δf_s is the uncertainty of the spring force due to hysteretic behavior, and is bounded by

$$\left|\Delta f_s\right| \le \frac{k_2}{2\beta} \quad (15)$$

where β and k_2 are parameters of the hysteretic behavior as described in [5]. Suppose c_s and k_1 are bounded in $[\underline{c}_s, \bar{c}_s]$ and $[\underline{k}_1, \bar{k}_1]$, respectively. Equations (16) and (17) listed below give an appropriate solution for the equivalent control and the integral gain

$$u_{eq} = \ddot{x}_d + D_{s0}\dot{x} + K_{s0}(x - x_z) - p_1\dot{e} - p_2 e \quad (16)$$

$$W = \sigma\left[\eta + (\sigma - 1)\left|\dot{u}_{eq}\right|_{max} + \tilde{D}_s\left|\ddot{x}\right|_{max} + \tilde{K}_s\left|\dot{x}\right|_{max}\right] \quad (17)$$

where $D_{s0} \equiv \frac{1}{2}\left(\frac{\underline{c}_s}{\bar{m}} + \frac{\bar{c}_s}{\underline{m}}\right)$, $K_{s0} \equiv \frac{1}{2}\left(\frac{\underline{k}_1}{\bar{m}} + \frac{\bar{k}_1}{\underline{m}}\right)$, $\tilde{D}_s \equiv \frac{1}{2}\left(\frac{\bar{c}_s}{\underline{m}} - \frac{\underline{c}_s}{\bar{m}}\right)$ and $\tilde{K}_s \equiv \frac{1}{2}\left(\frac{\underline{k}_1}{\bar{m}} + \frac{\bar{k}_1}{\underline{m}}\right)$.

Phase 0

When the slider is very close to the pre-assigned position with near zero velocity, (14) can be simplified as

$$f = k_1(x - x_z) + \Delta f_s \quad (18)$$

In this phase, the velocity and acceleration of the table cannot be obtained by taking the difference of two consecutive position data. Consequently, the derivatives in u_{eq} and the sliding surface $s = 0$ are ignored. Furthermore, to guarantee zero steady state error, the integral gain should be restricted. [1] We have the following equivalent control and integral gain

$$u_{eq} = K_{s0}(x - x_z) - p_2 e \quad (19)$$

$$W = S_{FT}B_0\frac{k_1\Delta x}{T_s} \quad (20)$$

where S_{FT} is a safety factor, Δx is the sensor resolution, and T_s is the sampling period.

Remark 1

It is clear that the control gains discussed above are designed based on the friction behavior of the phase it belongs to. Following this philosophy, we should identify the status of friction before we can determine which phase of control should be adopted. Unfortunately, it is not possible to identify the friction status by just knowing velocity and position. However, since the positioning of a motion table usually follows a fixed and simple pattern. Taking this into account, we can configure a set of criteria based on the error and velocity of the table to switch the control from one phase to another. Due to space limit, the details of the criteria are omitted.

Remark 2

The saturation problem of HSMC is still an open question. To reduce the possibility of saturation, the motion profile, $x_d(t)$, is preplanned according to the target position, desired cruise speed, appropriate acceleration and current motion states.

VERIFICATION & DISCUSION

The system used for verification is the same as that used in [2]. It is an X-Y table driven by HIWIN linear motors. In this study only y axis is used. The position sensor is the Heidenhein LIP481 linear scale. After electronic interpolation the resolution achieves 2 nm. The table is not protected by any vibration isolator. Both multi-phase PID control and HSMC are tested and compared.

Three kinds of test have been conducted. They are 5 cm long distance positioning, 100nm short distance positioning and count-by-count operation. Each test has been performed for the case when there is no load and the case a load of 7.63 kg is added. Figure 1 to figure 3 show some typical responses of these experiments, and we get the following observations.

1. When it is load free, both control strategies have similar responses on the surface. In all tests, the final error reaches 0 with 1 count in-position vibration due to environmental disturbances. However, the PID control has a small overshoot of about 7 μm in the long distance positioning while HSMC does not. On the other hand, HSMC control takes much longer time to get rid of the residue steady state error. This is because that the way it does integration in phase 0 is to integrate *sign(e)*, it is much slower than the true integration used in the PID control.
2. When load is added, HSMC control keeps about the same performance. Performance of the PID control degrades a little for long distance positioning. But the count-by-count operation tends to be unstable. This is because that the integral gain is approaching the limit for stability in this case.
3. The holding rigidity of HSMC control is weak. This is because that the feed forward term $\ddot{x}_d$ in u_{eq} disappears once the target is reached.

CONCLUSION

Application of the higher order sliding mode control (HSMC) to an ultra precision motion table with the existence of friction has been studied. It shows that this strategy, with some modification, can achieve the performance of the so called precision limit positioning with expected robustness. But the final tuning and holding rigidity are not satisfying. Further improvement is currently under progress.

ACKNOWLEDGEMENTS

This research is jointly supported by NSC grant NSC 96-2221-E-006-224 and MEA grant 95-EC-17-A-05-S1-0014.

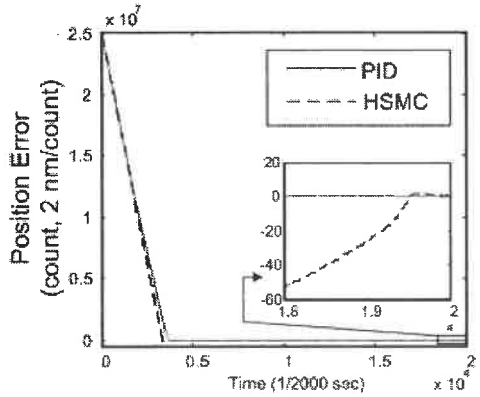

FIGURE 1. 5 cm long distance positioning with 7.63 kg load

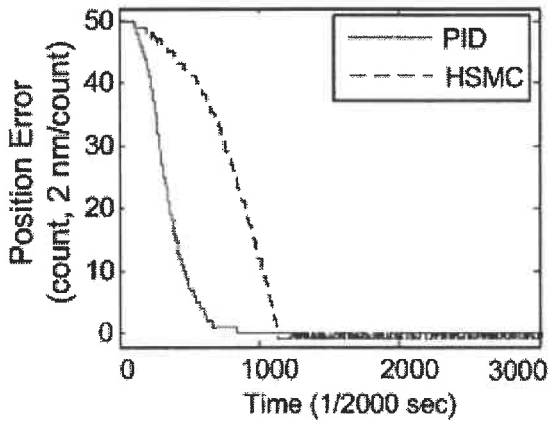

FIGURE 2. 100nm short distance positioning without load

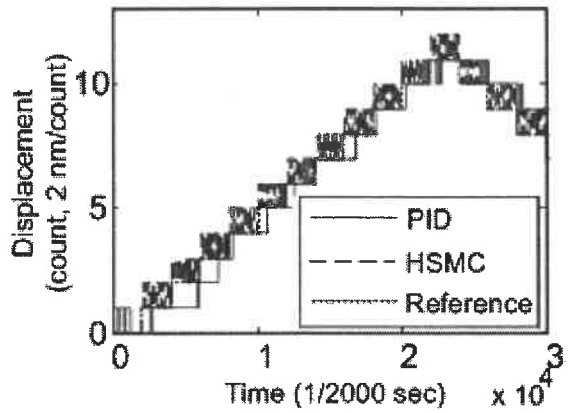

FIGURE 3. Count-by-count motion without load

REFERENCES

[1] T.-Y. Lin, Y.-C. Pan and C. Hsieh, "Precision-limit Positioning of Direct Drive Systems with the Existence of Friction," *Control Engineering Practice*, **11(3)**, 233- 244 (2003).

[2] C. Hsieh, J.-L. Lin, J.-C. Huang and C.-H. Chen, "Precision-limit Positioning of a Linear Motor Nano Drive System," *Material Science Forum*, **505-507**, 1243-1248 (2006).

[3] J. E. Slotin and W. Li, *Applied Nonlinear Control,* Prentice –Hall, Chap. 7 (1991).

[4] C.-L. Chen, M.-J. Jang and K.-C. Lin, "Modeling and high-precision control of a ball-screw-driven stage," *Precision Engineering*, **28**, 483-495 (2004).

[5] C. Hsieh and Y.-C Pan, "Dynamic behavior and modeling of the pre-sliding static friction," *Wear*, **242(1-2)**, 1-17 (2002).

PIEZO DRIVEN XY STAGE WITH NANO-MANIPULATORS FOR SEM OPERATION

Shunsuke Kanegae[1], Chiba Hiroyuki[1], Hisayuki Aoyama[1], Yuka Irie[1], Futoshi Iwata[2], Tatsuo Ushiki[3]
[1]Mechanical Engineering and Intelligent Systems
The University of Electro-Comunications, Chofu, Tokyo, Japan
[2]Faculty of Engineering Shizuoka University
Hamamatsu, Shizuoka, Japan
[3]Graduate School of Medical and Dental Sciences, Niigata University
Niigata, Niigata, Japan

INTRODUCTION

In biotechnology and Micro Electro Mechanical Systems (MEMS), the development of the manipulation system with higher resolution is important for handling a micro-target. In order to observe a small sample such as an animal cell and tissue in a Scanning Electron Microscope (SEM), some special tools that can cut and manipulate the sample in situ are often required. However the conventional XY stages with the lead screw and motor are difficult to install into the small chamber of the SEM because they are too big or adverse effects for SEM imaging.

Therefore this paper discusses that a self-walking small XY stage and manipulation tools with piezo actuator are developed and the performances are checked for the practical application in the SEM.

DESIGN AND DEVELOPMENT OF PIEZO DRIVEN SELF WALKING XY STAGE

For the observation of biological structures (i.e., animal and plant cells and tissues) in the SEM, it is necessary to move manipulation tools from an initial position to the target.

Thus both coarse and fine positioning functions are essential to these stage as well as the size of the stage should be small enough to set up into the small SEM chamber. Figure 1 shows the top view of the newly developed stage.

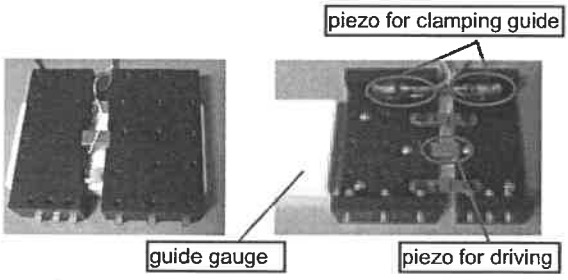

FIGURE 1. Top view and structure of a self walking stage

This stage is composed of three piezo elements. Two piezo elements clamp the guide gauge. The third r piezo element expands and contract. The stage can move along the guide gauge by combination of these piezo movement.

Driving principle

This stage moves using inchworm locomotion. Detail motion is shown as follows.

First, the back is clamped, the front is unclamped, and the middle piezo element is contracted.

Next, the middle piezo element is expanded.

Third, the front piezo element is clamped.

Last, the middle piezo element is contracted. The stage moves by repeating this operation.

Despite such a small displacement of piezo element, this stage is realized coarse motion.

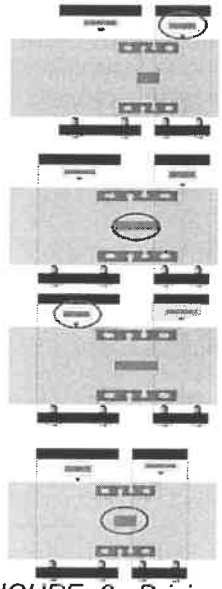

FIGURE 2. Driving principle pattern

Measurement of 1 step displacement

Figure 3 shows the assembled XY stage in which two linear stages were stacked so that positioning in plan can be performed.

We confirmed that this stage can be used as XY stage from experiment of 1step locomotion. The each X stage and Y stage was moved to forward and backward by 1step locomotion. And, we measured the movement using a capacitance gauge.

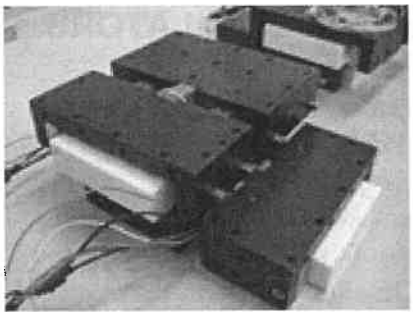

FIGURE 3. Developed XY stage

Figure 4 shows results of our experiments using the XY stage. These graphs show the relationship between stage displacement and applied voltage of piezo for driven.
(a) This graph shows the data of the X stage going forward. (b) This graph shows the data of the X stage going backward. (c) This graph shows the data of the Y stage going forward. (d) This graph shows the data of the Y stage going backward. The each graph shows that displacement is proportional to the piezo applied voltage, indicating that we can control the stage displacement by changing voltage and inchworm movement in this XY stage become successful.

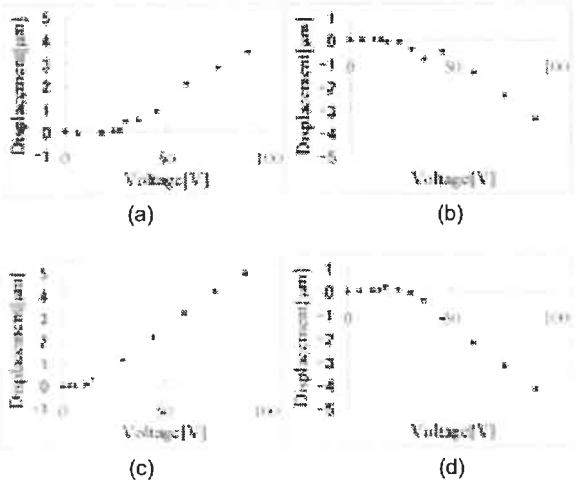

FIGURE 4. Movement performance of XY stage

Minimam displacement of XY stage
Figure 5 shows a reproducible minimum displacement of the XY stage. In this time 6V voltage was applied to the piezo for driven three times. The graph shows the stage moves 2um with three steps and one step displacement is about 0.7um. Our target size of animal cell is 100um. We judged that 0.7um is enough for manipulate these cells.

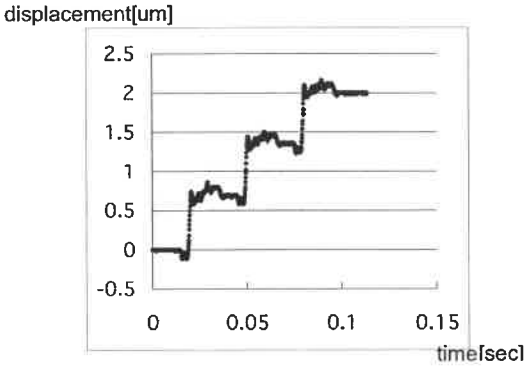

FIGURE 5. Minimum displacement of XY stage

Experiment of withstand load
Experiment of withstand load was performed because some tools should be mounted on the XY stage.
Thus, we examined how the weight changes the behavior of the XY stage. The weights which were increased 0g to 400g by 50g increments ware put on the stage, and the behavior of the XY stage was measured each time.
Figure 6 shows the results of experiments. At the initialize state, the X axis has load of 200g because the Y axis stage is on X axis stage.
(a)This graph shows X axis locomotion. (b)This graph shows Y axis locomotion. Seeing data of the Y axis indicates instability behavior until 100g. This is responsible for accuracy of the assembly, and occurred the stage lifting. After loading 100g constant displacement was recorded. But the stage can be loaded the weight of 400g or less by experiment of withstand load.

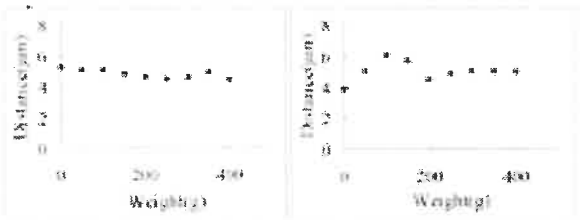

FIGURE 6. Withstand load of XY stage

DEVELOPMENT OF MICRO TOOL TURRET

The tool for the cell manipulation also has been developed as a simple fine tool which can handle biological samples implemented on the XY stage. Because it was necessary to move those tools up and down to do such precise manipulation, the micro tool turret mechanism using 3 piezo elements was developed. Figure 7 shows the isometric view of the micro tool

turret.
The turret rotates by applying the saw-tooth voltage to each piezo elements.

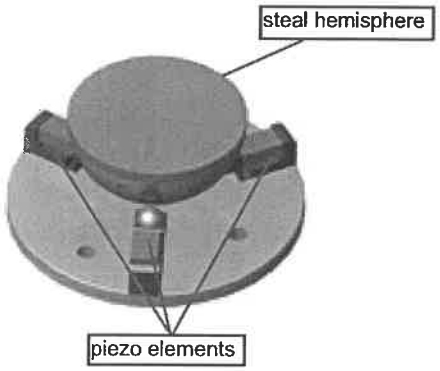

FIGURE 7. Configuration of tilting stage

Experiment of the micro tool turret

We confirmed that the turret can tilt using the autocolimator. Figure 8 shows the result of our experiment. In this time piezo elements are placed like Figure 9. Blue dots are data of tilt down by using the piezo element of ch0. Red dots are data of tilt up by using piezo element of ch1 and ch2. 50 steps saw tooth voltage was applied dots are pointed each 10 steps. When Voltage was applied only to the piezo 0, this stage tilts Y direction 0.33 degrees in 50 steps. X direction is -0.03 degrees. The gap of between Ideal direction and experimental direction is 10%.

It became apparent that the micro tool turret can tilt from this result.

But there is a problem. The problem is the change of the surface condition. Changing of the surface condition makes difficult to adjust tilting of hemisphere. As a future works we have to control the hemisphere by considering the surface condition.

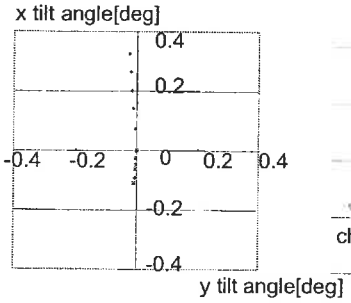

FIGURE 8. Tilting angle of the turret

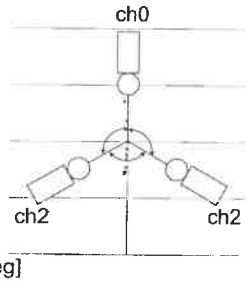

FIGURE 9. Piezo place design

MICRO MANIPULATION TOOL FOR BIOLOGICAL STUDIES IN THE SEM

As a cell manipulation tool, we developed a needle that moved back and forth by using the piezo element. Because the target cell size is about 100um. The developed needle moved the back and forth in a wide range by the width of 33um which is one third of cell size. Because the displacement of the piezo element is low, the displacement amplification mechanism was developed. Figure 10 shows a developed piezo driven needle. It was confirmed that the displacement of piezo element is proportional to applied voltage, and it expands to 30um.

FIGURE 10. Piezo driven needle

Development of piezo driven tweezers

We also developed piezo driven tweezers that is one of cell manipulation tools. Because the size of the target bio-structures is about 100um, we decided to develop piezo driven tweezers that can open 100um. We developed a lever mechanism to amplify displacement again, and made the tweezers. Figure 11 shows new tweezers.

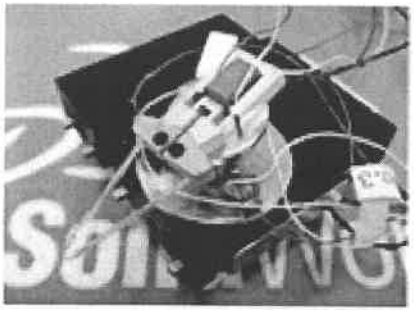

FIGURE 11. Piezo driven tweezers

CONTACT FORCE OF MICRO TOOL

This needle is pasted on thin copper board. If something contacts the needle, the contact force is reach to the copper board and makes strain. The strain of the copper board is measured by the strain gauge.

The needle is pasted on the liner actuator. The actuator downs the needle 20um steps at five times and measures the voltage of the strain gauge.

The result of measurement is shown in Figure 12. We can measure the force which coursed when the needle was pressed 20 micro meters.

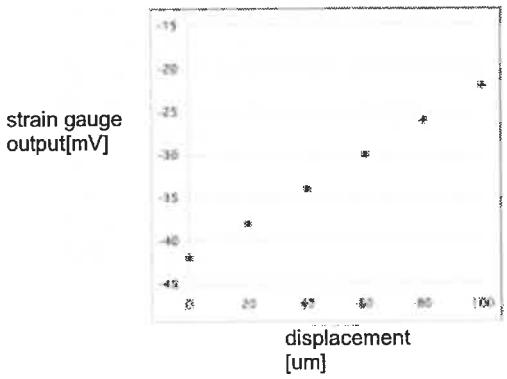

FIGURE 12. Sensitive of strain gauge on the needle

MANIPULATION AND REAL TIME OBSERVATION EXPERIMENT IN SEM

In the SEM chamber there are some bad effects for manipulation such as high vacuum state and electron beam for SEM observation. So that operation in the SEM might not be the same as in the atmosphere.

Figure 13 shows the XY stage in a SEM. We operated the XY stage and the manipulation tool (piezo driven needle) in SEM. We also checked either vibration by clamping that we confirmed in basic experiment makes bad effects for SEM observation or not.

The XY stage and manipulation tools for operation of biological samples were placed in the SEM. The tool is mounted on the stage. The condition in the SEM chamber was ultra vacuum and electron beam was close to the target. Then vibration waveform was inputed to the needle. SEM images are shown in Figure 14. Images shows the top of the needle.

There is no bad effect in SEM images. This clear images indicate that we can operate biological samples with real time observation in this system. The size of the SEM image is 600x500um. (a)This picture shows before moving needle. (b)This picture shows after moving it.

The piezo driven needle is at the top of the sem pictures. AFM needle is found at the bottom. The stage was successfully controlled and The needle was moved forward and backward. This micro movement enabled us to cut the biological soft sample.

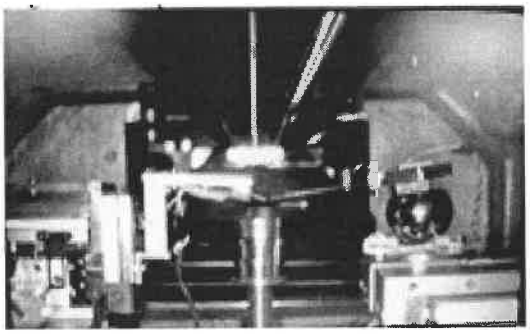

FIGURE 13. Stage with manipulator in SEM

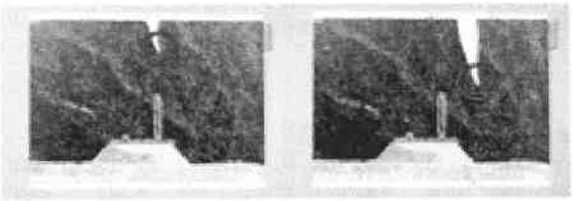

FIGURE 14. Clear picture by SEM observation

CONCLUSION

In this experiment, we successfully designed and fabricated a novel self walking XY stage and fine rotating turret with micro manipulators. The XY stage can move precisely and mount the weight up to 400g. The micro tool turrets rotate finely.

These stage and tools were installed in the SEM, and succeeded in manipulating biological soft samples with this system.

In the future work, improvement will be achieved to make the system more useful for image processing or some sensor and feedback control might be needed.

ACKNOWLEDGEMENT

This research is financially supported by the Leading Project of Ministry of Education,Culture, Sports, Science and Technology, Japan, titled "development of elementary techniques for electron microscope in next generation" .

REFERENCES

[1] M.Jähnisch, H. Hülsen, T. Sievers, S. Fatikow, 2005 "Control System of a Nanohandling Cell within a Scanning Electron Microscope" Proceedings of the 2005 IEEE International Symposium on, Mediterrean Conference on Control and Automation, pp.964-969

NOVEL SWITCHING CONTROL OF THE BALL-SCREW DRIVEN STAGE FOR NANO POSITIONING

Gyu-Ha Kim[1], Sang-Gu Cho[2], Wan-Soo Kim[1], and Sun-Kyu Lee[1]
[1]Department of Mechatronics
Gwangju Institute of Science and Technology (GIST)
Buk-gu, Gwangju, Republic of Korea
[2]Technical Research Center
HYUNDAI STEEL COMPANY
Dangjin-gun, Chungchengnam-do, Republic of Korea

INSTRUCTIONS

A ball-screw driven stage is broadly used because of its simple mechanism, high stiffness and low cost. The ball-screw stage, however, has the limited performance caused by the ball-screw friction that is nonlinear and varies as the position of the stage changes. [1, 2]

Many researchers have proposed methods to resolve the friction problems for precision positioning systems. Generally, precision control of positioning stage requires that accurate model of friction and system identification. [3, 4, 5, 6] These control methods have the difficulty of applying to the industry area because of the complexity of the friction model and the parameter identification. [7]

Other methods to increase the accuracy of the ball-screw stage are the dual stage method [8] and the preload control method [9, 10]. The dual stage method uses the ball screw as a coarse motion actuator and a voice coil or PZT as a fine motion actuator. The preload control method is to control the fine positioning of the stage by the preload change of the ball screw using PZT. These methods satisfy the performance requirements for the stage accuracy. But these also require the cost of additional equipments, and the control system of the stage will be more complicated.

The NCTF (Nominal Characteristic Trajectory Following) control method is the simple control method that needs no complicated mathematical model of friction which was proposed to improve the complex design process and satisfy the requirements such as a fast response and a little overshoot. [7, 11] It satisfies the requirements in the macro dynamic region, and its performance does not satisfy the motion accuracy in the micro dynamic region. In order to overcome the insufficient accuracy in the micro dynamic region, authors proposed a switching control method. This paper presents the dynamic characteristics of the ball-screw stage and the results of the proposed method.

EXPERIMENTAL APPARATUS

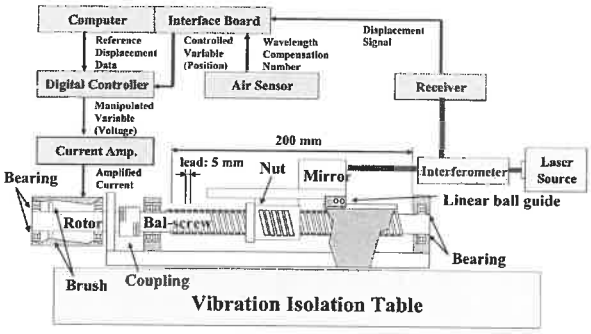

FIGURE 1. Schematic Diagram of Experimental Apparatus

The experimental system, illustrated in Figure 1, consists of the electrical part, the optical metrology and the mechanical part. The electrical part includes a DC brush motor, a motor amplifier, UMAC controller, and a laser interferometer interface board (Agilent N1231A). The stage is driven by the ball screw with the stroke of 200 mm and is measured by the laser interferometer with the resolution of 0.3 nm. The positioning system is installed on the vibration isolating table.

CONCEPT OF NCTF CONTROL

The block diagram of the NCTF control system is presented in Figure 2. The NCTF control system consists of a NCT curve and a PI compensator. The NCT curve is constructed by using the response of the stage that includes the effects of nonlinear characteristics such as friction. Parameters of the PI compensator are calculated by the NCT curve. [7]

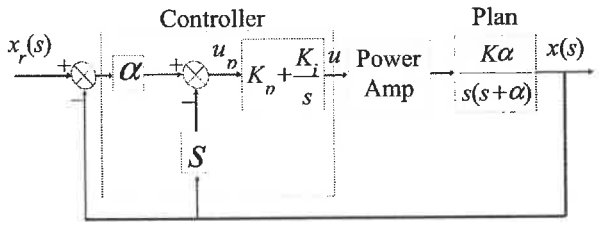

FIGURE 2. Block Diagram of NCTF Control System

The slope of the NCT curve near the origin is related to the parameter α. The NCT Curve shows

$$e = x_r - x \tag{1}$$

$$\dot{e} = \dot{x}_r - \dot{x} = -\dot{x} \tag{2}$$

$$\frac{d\dot{e}}{de} = -\frac{d\dot{x}}{de} = -\alpha \tag{3}$$

where x_r , x , $\dot{x}$, e , and $\dot{e}$ are the object position, the actual position, the actual velocity, the position error, the time derivative of the position error, respectively.

DYNAMIC CHARACTERISTICS OF BALL SCREW DRIVEN STAGE

The effect of friction is considered as a spring in the pre-sliding range. The friction force is proportional to the shear strength of the asperity junction between two contact surfaces. In the pre-sliding region, the movement of stage is caused by the deformation of the asperity junctions of the contact surfaces within several tens of micrometers depending on properties of the roughness of the contract surfaces.

Apart from the pre-sliding range, the effect of friction is neglected or regarded as a constant force in the sliding range. Figure 3 shows both region models, the pre-sliding model and the sliding model.

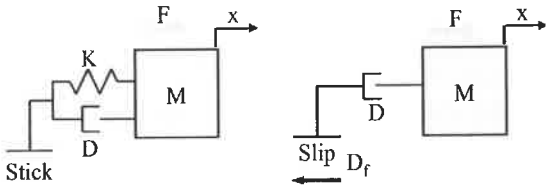

FIGURE 3. Model of Pre-Sliding Region (Left) and Model of Sliding Region (Right)

The transfer function of each region can be expressed as Eq. (4) and Eq. (5) with mass (M), spring constant (K), damping coefficient (D), driving force (F), displacement (x), and kinetic friction force (D_f).

$$\frac{X(s)}{F(s)} = \frac{1}{Ms^2 + Ds + K} \tag{4}$$

$$\frac{X(s)}{F(s)} = \frac{1}{s(Ms + D)} \tag{5}$$

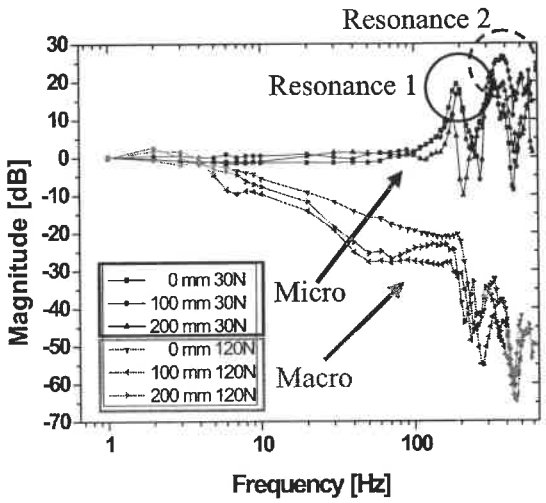

FIGURE 4. Open Loop Frequency Responses of Sine Wave Inputs with 30N/10nm and 120N/110μm

In Figure 4, the open loop frequency responses of the pre-sliding region (solid line) and the sliding region (dash dot line) are illustrated. Two kinds of sinusoidal driving force, amplitude 30N and 120N, were used to verify the difference of characteristics between micro dynamics (the pre-sliding region) and macro dynamics (the sliding region) at the different position (0, 100, 200mm). The frequency range of the input signals was applied from 1Hz to 500Hz. The magnitudes were normalized to 0dB at 1Hz. In Resonance 1, 130Hz is found on micro dynamics range (30N), while 350Hz in Resonance 2. Resonance 1 is driven by the spring-like behavior caused by micro dynamics. The dynamic model is often expressed as a second order system in Eq. (4). In the macro dynamic range, however, a resonance peak is not found, which strongly indicates that the system has different transfer functions in the

micro and the macro dynamic regions. Under this difference, the NCTF control method does not operate properly in the pre-sliding region (micro dynamics) because its plant model is assumed as the macro dynamics model with Eq. (5) as seen in Figure 1. As shown in the Figure 5, the NCTF control method reveals its limitation of resolution.

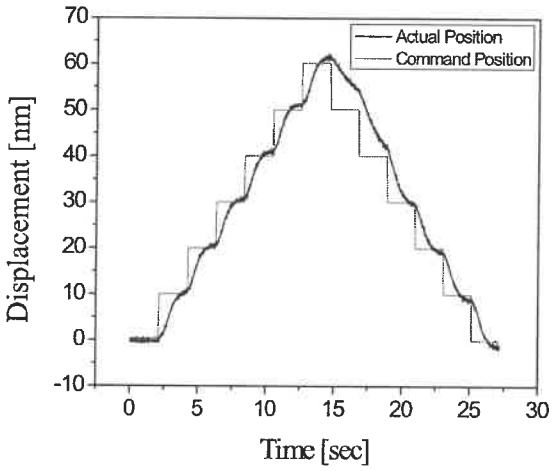

FIGURE 5. 10nm Step Response with NCTF Control

CONCEPT OF SWITCHING CONTROL

Although dual stages use two actuators to achieve fine and coarse motions, ball-screw driven stages using switching control method can be driven with only one actuator. In the existing switching control method, there is the pause time for 50ms to change the coarse control mode to the fine control mode. [12] Although this method has the robust performance, it has the disadvantage of a long response time.

To overcome the limit action of the NCTF control, we designed a switching controller consisting of the NCTF control in the coarse motion control, and the PID control in the fine motion control. To know whether the stage is in the pre-sliding region or in the sliding region, the position error and the velocity of the stage have to be determined. In the proposed switching control, the position error e and the controller output signal u are used to determine whether the stage in the sliding region or in the pre-sliding region. First, in the case of the NCTF control, the error e is only used to detect the entrance into the pre-sliding region because the velocity $\dot{x}$ of the stage is the function with respect to the error e in Eq. (3). Second, to switch the coarse mode to the fine mode correctly, the direction change in the stage input force presented by the controller output signal is also used, which provides the switching time from the coarse mode to the fine mode.

The coarse motion mode can be switched to the fine motion mode by the following procedure.

1. Carry out the NCTF control method as coarse positioning until the stage is within the pre-sliding region.

2. Use the controller output as the detection signal of the transformation from the nonlinear pre-sliding mode to the linear pre-sliding mode. When the sign of the controller output is changed, convert the coarse control mode to the fine control mode.

We conducted several nm-scale and tens mm-scale step response experiments.

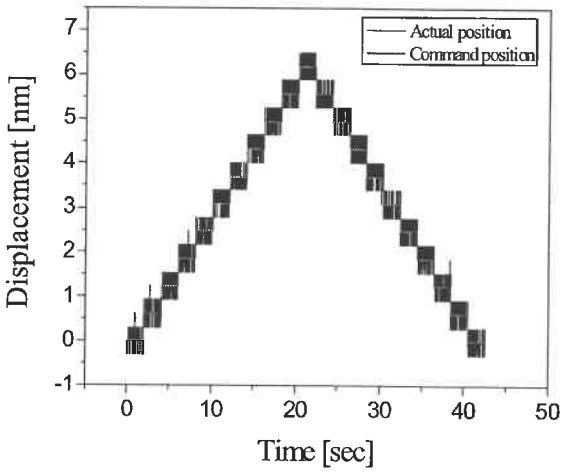

FIGURE 6. 0.6nm Step Response with Switching Control Method

Figure 6 shows that the ball-screw stage can follow the 0.6nm step commands with the period time of 2sec. Figure 7 is the experimental result of 100 mm step response. In the step response using the switching control, it takes 8sec to attenuate the residual motion of the stage caused by the inertial force. After 8sec, the motion error is reduced to about 0.6 nm.

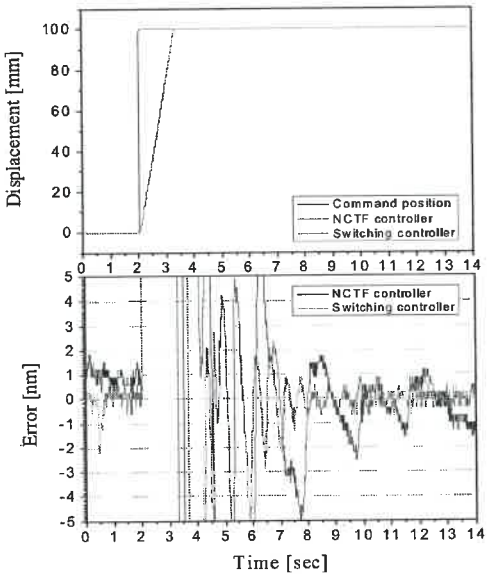

FIGURE 7. 100mm Step Response with Switching Control Method and NCTF Control

CONCLUSION

This paper presents a novel switching control method using the NCTF control as coarse mode, and PID control as fine mode for the ball-screw driven positioning stage. Experiment results show the resolution of the ball-screw stage within nanometer and in 100mm step response, the motion error attenuates to about 0.6nm.

Acknowledgement

This work was supported by the Korea Science and Engineering Foundation (KOSEF) NRL Program grant funded by the Korea government (MEST) (No. R0A-2008-000-10065-0) and Brain Korea 21 (BK 21).

REFERENCES

[1] Chen J S, Chen K C, Lai Z C, Huang Y K. Friction Characterization and Compensation of a Linear Motor Rolling Guide Stage. International Journal of Machine Tools and Manufacture. 2003; 43: 905-915.

[2] Hsieh C, Pan Y C. Dynamic Behavior and Modeling of The Pre-Sliding Static Friction. Wear. 2000; 242: 1-17.

[3] Armstrong-Helouvry B, Dupont P, Canudas De Wit C. A Survey Models, Analysis Tools and Compensation Methods for the Control of Machines with Friction. Automatica. 1994; 30: 1083-1138.

[4] Al-Bender F, Lampaert V, Swevers J. The Generalized Maxwell-Slip Model : A Novel Model for Friction Simulation and Compensation. IEEE Transactions on Automatic Control. 2005; 50: 1883-1887.

[5] Worden K, Wong C X, Parlitz U, Hornstein A, Engster D, Tjahjowidodo T, Al-Bender F, Rizos D D, Fassois S D. Identification of Pre-Sliding and Sliding Friction Dynamics : Grey Box and Black-Box Models. Mechanical Systems and Signal Processing. 2007; 21: 514-534.

[6] Ray L R, Ramasubramanian A, Townsend J. Adaptive Friction Compensation using Extended Kalman-Bucy Filter Friction Estimation. Control Engineering Practice. 2001; 9: 169-179.

[7] Sato K, Wahyudi, Shimokohbe A. Design and Characteristics of Practical Control System for PTP Positioning (in Japanese). Transactions of the Japan Society of Mechanical Engineers Series C. 2001; 67: 3898-3904.

[8] Okazaki Y, Ichikawa S, Otsuka S. A Simple and Compact Hybrid Positioning Stage with 1nm Resolution. Proceedings of the 1st International Conference on Positioning Technology. 2004; 354-355.

[9] Chen J S, Dwang I C. A Ballscrew Drive Mechanism with Piezo-electric Nut for Preload and Motion Control. International Journal of Machine Tools and Manufacture. 2000; 40: 513-526.

[10] Nakehima K, Takafuji K, Tamura Y. Ultra Fine Positioning by Preload Change in Ball Screw Drive. Proceeding of the 1st International Conference on Positioning Technology. 2004; 31-36.

[11] Wahyudi, Sato K, Shimokohbe A. Characteristics of Practical Control for Point-To-Point (PTP) Positioning Systems : Effect of Design Parameters and Actuator Saturation on Positioning Performance. Precision Engineering. 2003; 27: 157-169.

[12] Futami S, Furutani A, Yoshida S. Nanometer Positioning and Its Micro-Dynamics. Nanotechnology. 1990; 1: 31-37.

DEVELOPMENT OF INTELLIGENT ENCODER

Jun Kitawaki, and Chisato Kanamori
Department of Mechanical Engineering and Intelligent Systems
The University of Electro-Communications
Choufu, Tokyo, Japan

INTRODUCTION

This paper discribes an "intelligent encoder. The "intelligent encoder" has encoding function and the fundamental functions of controller. An encoder is device for measureing linear or angular position and displacement.[1] A rotary encoder is for measuring angle, and in this report rotary encoder focused. The encoders are widely used in application such as robots and NC machines for motion control. A rotary encoder is combined with controller device. The controller device computes position or velocity from the rotary encoder output.Then the controller output is determined by the position or velocity or both. Thus for precision motion control, resolution and response-speed of rotary encoders gradually improved. The high resolution encoders' performance are 12-bits(4095 pulses) to 20-bits(1048575 pulses) resolution and 1MHz to 30MHz frequency response.[2] There are such high resolution encoders, but controllers for encoders lack the speed of response for high resolution encoders. To solve these problems, building of new control system using the intelligent encoder is studied in my team.

INTELLIGENT ENCODER

The intelligent encoder is composed high resolution encoder, FPGA and RAM in this report. The encoder is a hybrid of increment and abusolute. The resolution of increment is 15 bits(32767 pulses) and the resolution of absolute is 8 bits(255 pulses.) The maximum scanning frequency is 800[kHz]. The FPGA and RAM are device for computing, which has counting, calculating, judging and commanding components. *F*igure 1 shows the function block-diagram of the intelligent system. Now, because of development term, the encoder, the FPGA and RAM are separated, but finally, to replace the FPGA and RAM by a unique LSI built in the encoder. As a view in the future, the intelligent encoders are going to be used for the joints of the humanoid robot's joints, especially hands, and each encoders of joints determine and reduce the main controller's work. For the experiment of this report, the special equipment is made to check the effectiveness of the intelligent encoder. In order to check the performance of the intelligent encoder's responsibility and the limit of resolution, high speed response at fast rotation is required. Thus a drumming machine is fabricated as the experiment equipment.

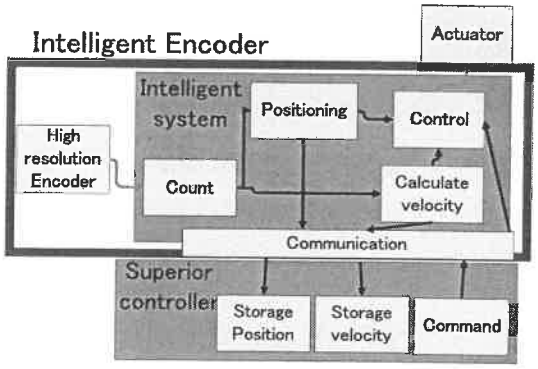

FIGURE 1. The function block diagram of the intelligent system for a intelligent encoder

A DRUMMING MACHINE

The drumming machine is consists of a drum, a stick, a drumming mechanism, an actuator(DC motor), an intelligent encoder(constructed by a high resolution encoder and FPGA board)[3] and a PC, as shown in *Figure*2. The stick is conected with shaft vertically and the encoder senses the rotation of the shaft, as shown in *Figure*3. *Figure*4 shows the arrangement of the stick and the drum. By the arrangement of two, it is defined the comprehensive values of data getting by the experiment. *Figure*5 shows the system diagram of the drumming machine. The commands from the superier controller, such as PC, input the intelligent system, constructed on the FPGA. The intelligent system output PWMs to control the actuator. The mechanism with a stick is behaved by the actuator, and the diplacement of the stick is mesured by the encoder. The encoder output pulses to the intelligent system which count the pulses and calculate to control.

FREE FALL HITTING EXPERIMENT

To search what data could be measured from the drumming machine, with high resolution and high speed sampling intelligent encoder, "free fall hitting experiment" was done. The "free fall hitting experiment" was hitting drum experiment without using actuator,of course without control,but with gravity. It was prospected that the basic characteristics of the data of drumming machine's shaft revolution without actuator was showed. The process of the "free fall experiment" was that

1,Seek origin.
2,Give the stick initial velocity.

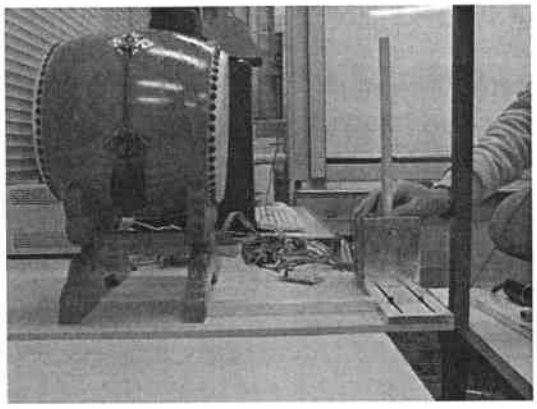

FIGURE 2. Drumming machine overview

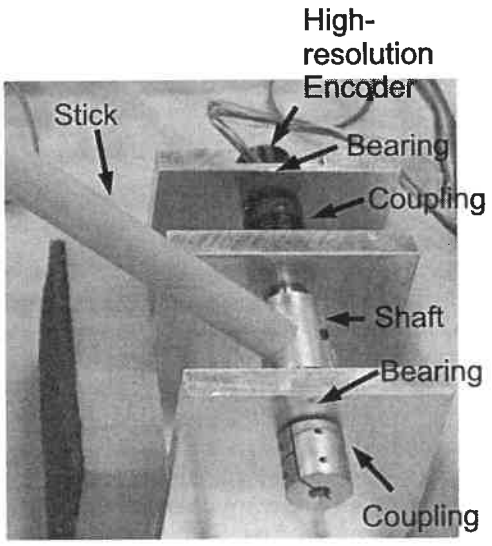

(a) The photo of the mechanism

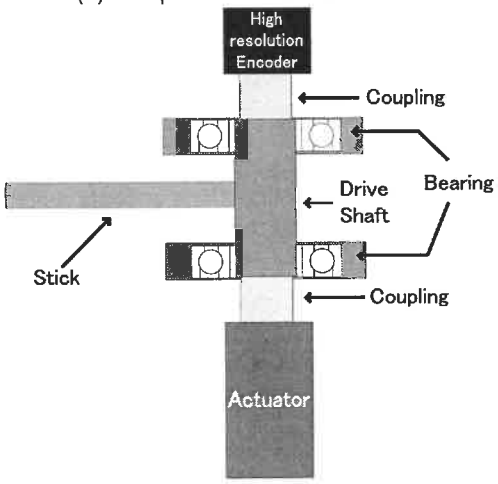

(b) The draw of the mechanism

FIGURE 3. The stick drive mechanism

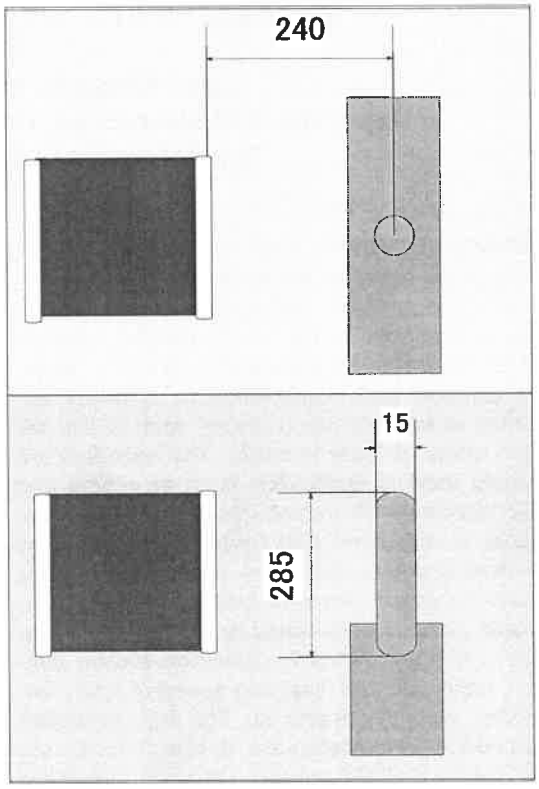

FIGURE 4. The arrangement of the drumming machine's stick and drum

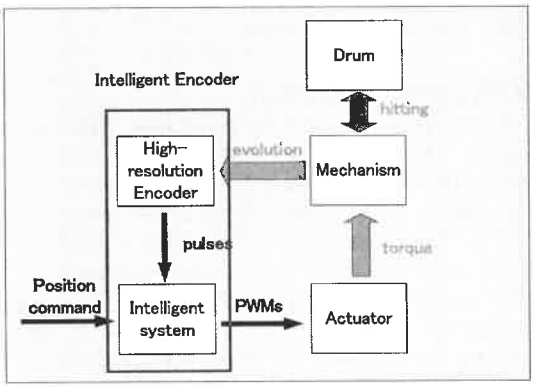

FIGURE 5. System diagram of the drumming machine

3,The stick hit the drum.

4,Measure the stick(shaft) movement from process 2 to process 3.

The sampling rate was about 10[μs]. Three types of speed of hitting drum was done, "fast", "normal" and "slow." It was expected to to be clear by doing the experiment that

1,The displacement data was measured.

2,Change of velocity at the moment of the stick hitting the drum.

3,The differences of movement and vibrations af-

ter hitting in each velocity.

RESULT OF FREE FALL HITTING EXPERIMENT

The experiments' result of three hitting velocities are shown in *Figure*6. The first, to notice normal velocity experiment. The displacement of by "free fall motion" from long range view and the rapid change of velocity and vibrations from the short range view at the around hitting point, as shown in *Figure*7.(a) These data is also shown from fast and slow velocity experiment. The zoom graph at the around hitting of each velocities are shown in *Figure*7.(b) and (c). Peak-peak time and amplitude of vibrations at the after hitting point of each velocities are arranged in a *table*1. To compare the three data of after hitting,it become evident that

1,The amplitude of vibrations of after hitting is propotionate to hittinng velocities.

h *2,The cycle of the vibrations of each hitting velocity are same.*

The displacement and the phenomenon of stick hitting drum can be measured in this experiment. It becomes clear this system brings out enough performance to control the stick precisely.

TABLE 1. The vibrations characteristics in hitting speed

Speed	p-p amplitude[']	p-p time[μs]
slow	0.7	279
normal	1	277
fast	3.5	277

POINT TO POINT CONTROL HITTING EXPERIMENT

To examine what data could be saw when a point to point control was supplied to the drumming machine. In this experiment, the intelligent system control the actuator with feedback using the encoder's signal. The displacement of stick revolution was sent from intelligent system to PC for monitoring. The process of the "step position control hitting drum experiment" was that

1,Set the stick at the vertical point

2,Give the command from to move hitting point

3,The stick moves to the hitting point

4,When the stick hit the drum, the command changes to the vertical point

5,The stick moves to the vertical point

6,hold the stick at the vertical point

From the vibrations, caused by the stick hitting the drum, is measured, as shown in*Figure*9.

CONCLUTION AND FUTURE VIEW

In this report, the intelligent encoder and new control system using the intelligent encoder are proposed. From the experiment with the drumming machine, high resolution angular revolution data can be measured at high speed sampling.

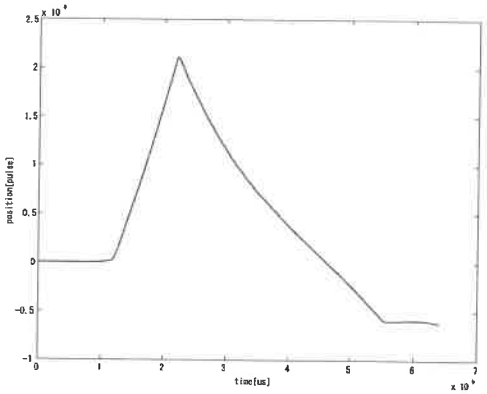

(a) Fast hitting velocity (6.41[deg/μs])

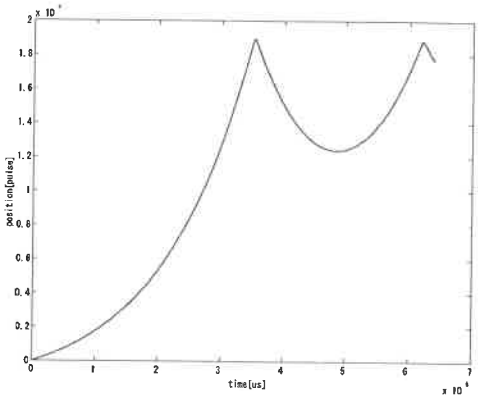

(b) Normal hitting velocity(4.02[deg/μs])

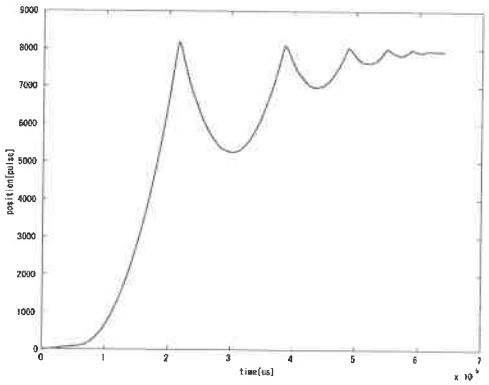

(c) Slow hitting velocity(2.97[deg/μs])

FIGURE 6. position to time graph of the free fall hitting experiment

And also the system can control the actuator by the easy command of superior contoroller. Thus it is demonstrated that the idea of intelligent encoder is available to use for precision way. The next step of the theme of this study is to construct a more preciouse control system and do a search how to coordinate the action with intelligent encoder in a machine as a humanoid robot.

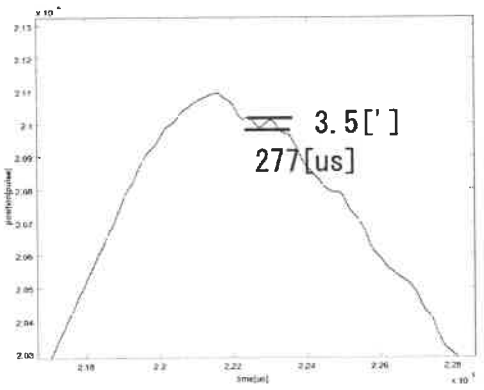

(a) Zoom up at the hitting point of fast hitting velocity

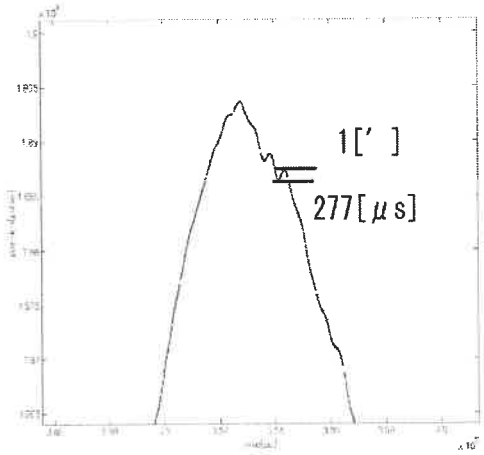

(b) Zoom up at the hitting point of normal hitting velocity

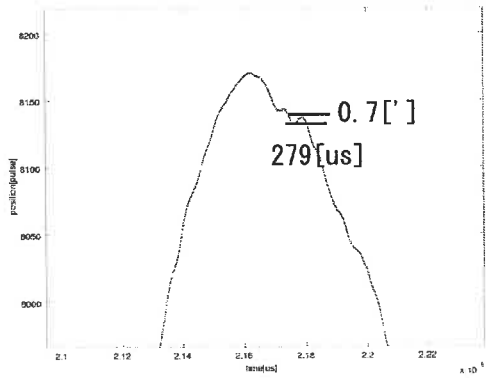

(c) Zoom up at the hitting point of normal hitting velocity

FIGURE 7. Zoom up at the hitting point of the free fall hitting experiment

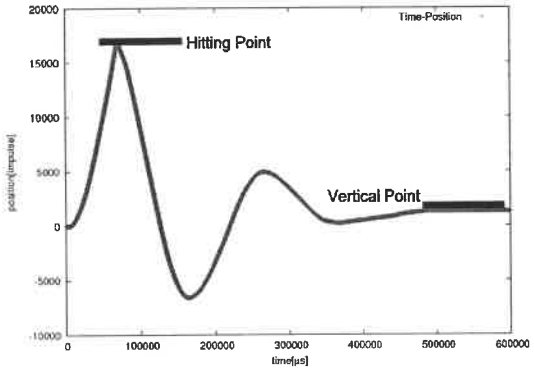

FIGURE 8. Position to time graph of the wave of angular displacement at the hitting the drum by step control

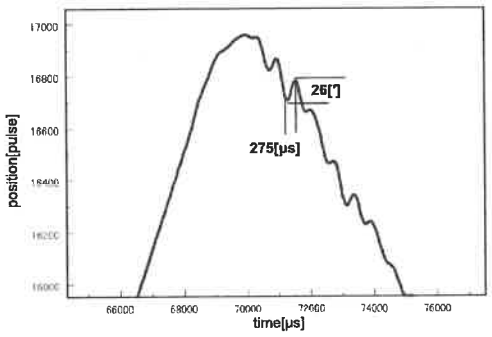

FIGURE 9. Zoom up around the hitting point of Figure8

REFERENCES

[1] W. Bolton,*Mechatronics 3rd edition*,Pearson Education Limited,2003

[2] Tamagawa seiki co.ltd ,*manufactuers catalog of rotary encoders in Tamagawaseiki.co.ltd* ,2007/7 in Japanese http://tamagawa-seiki.com/japan/products/sensor/rotary.html

[3] MTL ,*manufactuers catalog of MTL* ,2007/9

OPTIMIZED PRODUCTION OF COMPLEX SHAPED OPTICAL COMPONENTS VIA PRESICION GLASS MOLDING

Fritz Klocke[1,2], Olaf Dambon[2], Hüsniye Sarikaya[2], Fei Wang[2]
[1]RWTH Aachen University, Laboratory for Machine Tools and Production Engineering, Aachen, Germany
[2]Fraunhofer Institute for Production Technology Aachen, Germany

Instructions

Our everyday life is associated with many leading edge technologies, like automotive industry, laser technology and life science. The key position for the improvement of these technologies is the production of required complex shaped optical components, as spheres, aspheres and arrays, with high accuracy. For example, for the high performance diode laser, fast axis or slow axis collimation lenses with high presicion are required. With this lenses the light beam from the emitter is collimated, thereby the beam divergency is reduced and the beam quality is increased [2,3].

One promising manufacturing process of such components is the presicion glass molding. Different to conventional machining technologies like grinding and polishing, the glass parts are formed in one process step. After heating up the raw parts, the glass is pressed under load into its final shape[1].

Due to different thermal expansion of mold and glass material, the final shape of the glass differs from the mold shape after the molding process.
In this paper, investigations into the with Finite element analysis (FEA) of optimized production of complex shaped optical components will be presented. With the use of the simulation the glass shrinkage can be calculated without any try out molding activities. On the basis of this simulation result, this shrinkage can be directly compensated by mold manufacturing. So the time and cost consuming iteration can be eliminated.

Process Chain for Production of Complex Shaped Optical Components via Presicion Glass Molding

One advantage of the production of complex shaped optical components via presicion glass molding is that, the designated lens is formed to its end shape in one molding cycle. These produced lenses are ready to use so that further time consuming finishing processes are not required. So the production of complex shaped optical components is more efficient compared to the conventional production method, which includes grinding and polishing. Another advantage of this production method is that, complex shaped optical components with high geometrical complexity can be produced with high form accuracy.

The process chain for production of complex shaped optical components consists of four main steps [5] (Fig. 1):

- Design
- Mold making
- Molding
- Measurement

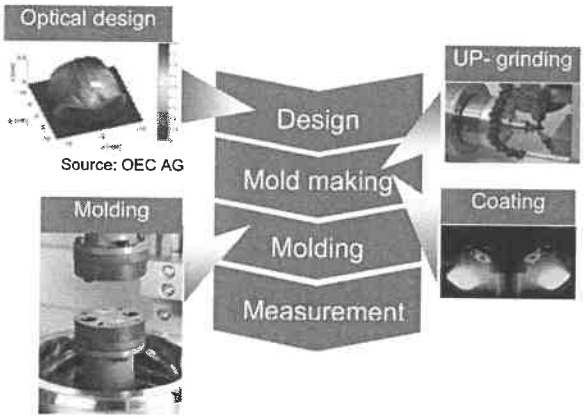

FIGURE 1 Process chain for manufacturing complex shaped optical glass components

The design step includes three sub-steps (Fig. 2). First of all the lens design has to be made. With the lens design the lens dimensions, specifications and quality are defined. After the lens design the glass shrinkage, the actual inserts and glass temperature are calculated by means of finite element analysis. These

calculated data are transported to the next sub-step, insert design. The insert can be finished in consideration of the glass shrinkage, so some pre glass molding steps to determinate the glass shrinkage are not required. Also a reengineering of the insert to achieve high form accuracy by the molded lenses can be eliminated by the usage of the FEA.

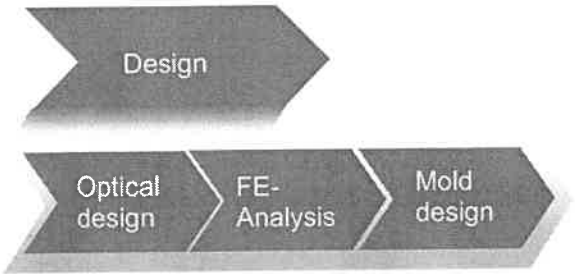

FIGURE 2 Thermal model design step of the process chain for the production of complex shaped optical components via presicion glass molding

In the next sub-step, mold design, the mold and insert dimensions, as well as their quality is defined. In addition to the information transportation from the FEA to the mold design, an inverse information transportation is also required for an effective mold making. The information exchange between FEA and insert design is presented in Figure 3.

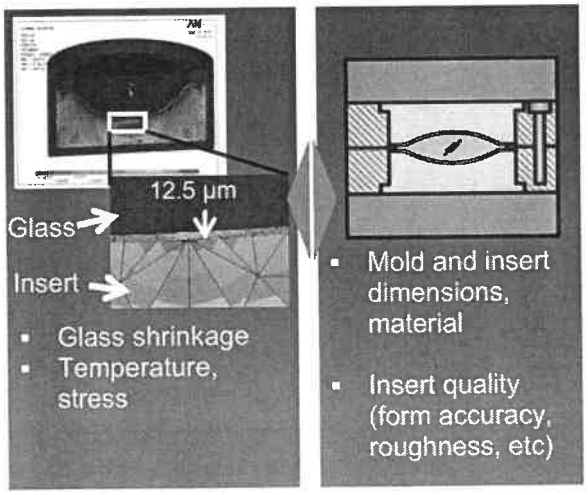

FIGURE 3 Information exchange between FEA and mold design

After design, the next step of the process chain for the manufacturing of complex shaped optical glass components is the mold making. The molds, referred to as insert in precision glass molding, can be finished in many ways. The chosen machining process depends on the insert material of the insert form. As insert material are high temperature and wear resistance, materials such as cemented carbide or silicon nitride are used. The ultra presicion grinding is commonly used for finishing of the cemented carbide inserts. After grinding or turning the molds are coated. The goal of the coating is to increase the wear resistance and the lifetime, respectively, of the inserts.

After the mold making the lens can be molded via presicion glass molding. In this process the insert and also the glass blank are heated up to the molding temperature and the glass blank is pressed to its end shape. After this molding process the ready to use lenses can be installed in optical system.

The final step of the process chain for the manufacturing of complex shaped optical components is the measurement. Two main quality criteria of the inserts and the lenses are the roughness and the form accuracy. Form accuracy can be used to measure the roughness. The form accuracy is checked in many cases with a tactile measurement device.

Finite Element Analysis of Molding Process

The FEA of the presicion glass molding process is accomplished on the basis of three models:

- Thermal model
- Structural model
- Multi-physics model

With the heat model the heat transmission of the molding process is analyzed. Meaning the heat transmissions from infrared lamps to the inserts, to the glass and the heat transport between glass and insert are considered with different heat transfer principles, conduction, convection and radiation. To implement the structural simulation, the boundary conditions are predefined with the structural model. In this model the viscoelastic deformations of the glass at different temperatures are calculated by using the Maxwell model and the Arrhenius shift function; the mold material is treated as a purely elastic material.

Based on the thermal and structural models, a calculation algorithm for the whole process is built up. Which contains three phases, from analogical to the real molding process. First of all, the heating process includes a thermal and a

structural simulation. During the molding process, the structural calculation is divided into many sub steps because of the large deformation in glass. The cooling phase is also simulated in both structural and thermal models, and the calculation is carried out in a program loop which contains different calculation steps with short time intervals.

Conclusions

The verification of a FEA simulation is shown in Figure 5. It is a molding process simulation of a plane-concave lens with an outer diameter of 18 mm and a form accuracy of 2 µm on the non-spherical surface. The insert material is tungsten carbide and the glass is crown glass B 270 of Schott AG. The comparison of the simulated and the measured glass lens geometry shows that a large form deviation up to about 12 µm is achieved in both the measurement and the simulated results, and the difference between these two curves is less than 2 µm. So the FEA simulation can be used for the mold design to reduce the mold making iteration and also to eliminate the pre molding.

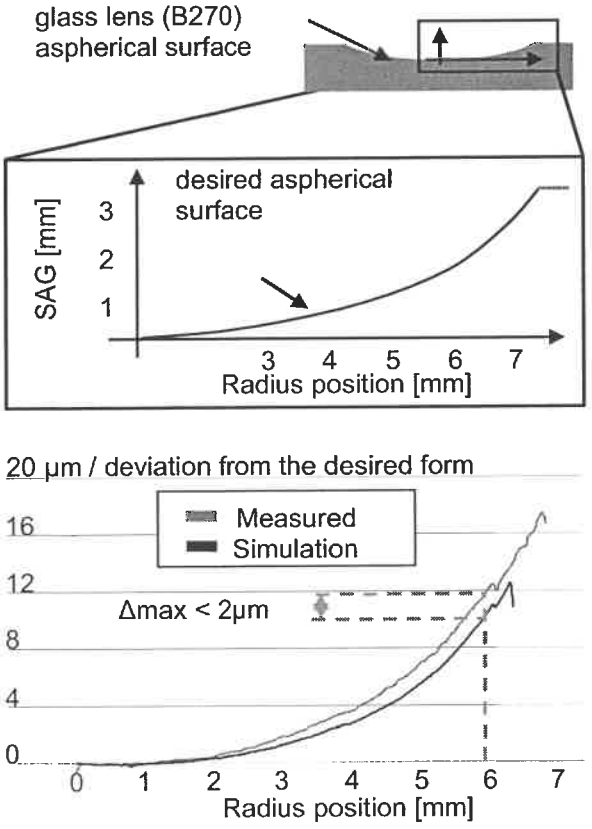

FIGURE 6: Comparison of simulation result to the measurement of the molded lens

Acknowledgment

This work is founded by the German research Association DFG within the Transregional Collaborative Research Center SFB/TR4 "Process chains for the Replication of Complex Optical Components".

References

[1] Katsuki, M.: Glass Molding and Molding Machining for Optical Elements. iMoc International Molded Optics Conference. May 2007, Bremen

[2] Klocke, F.; Bergs, T.; Demmer, A..: Präzisionsblankpressen optischer Gläser. Jahrbuch 2006 . Optik und Feinmechanik, 2004

[3] Klocke, Yi, A.; Bergs, T.; Demmer, A.; Pongs, G.; Chen, Y.: Compression Molding of Presicion Diffractive Glass Optical Components. Proceedings of the 6th euspen International Conference, May 2006, Wien

[4] Klocke, F.; Dambon, O., Pongs, G.: Simulation of Precision Optical Glass Molding. Proceedings of 7th euspen International Conference, May 2008, Zurich

[5] Klocke, F.; Dambon, O., Sarikaya, H.: Investigations to the Molding Accuracy of Complex Shaped Optical Components. 10th euspen Anniversary International Conference, May 2008, Zurich

DETECTION OF MICRO TOOL WEAR IN DIAMOND TURNING OF LARGE AREA MICRO-LENS ARRAY BY IN-PROCESS CUTTING FORCE MEASUREMENT

Young Jin Noh[1], Yoshikazu Arai[1] and Wei Gao[1]
[1] Nano-metrology and Control Laboratory, Department of Nanomechanics, Tohoku University, Sendai, Japan

INTRODUCTION

Diamond turning with fast tool servo (FTS) or fast tool control (FTC) is a promising tool for fabrication of optical components including micro-lens array [1][2]. The micro-lens array is used in various optical communication devices and imaging devices for improvement of the image quality. With the increase of fabrication area of micro-lens array, it is important to monitor the long time fabrication process influenced by tool damage, tool wear, etc. Micro tool wear is easily occurred while the material is being removed from the workpiece because the diamond cutting tool used for fabrication of micro-lens array is fragile with the small nose radius and large clearance angle. Micro tool wear is the reason to reduce both surface finish and accuracy of the micro-lens array. It also increases the cutting force, in turn increase of the tool wear [3]. The most popular method to detect micro tool by direct imaging the tool cutting edge is a scanning electron microscope [4] and an atomic force microscope [5]. However, it takes a long time for the imaging process. It is also necessary to remove the tool from the diamond turning machine for measurement.

The aim of this research is to indirectly detect the micro tool wear by in-process measurement of cutting force. This is based on the fact that the cutting force is increased with the tool wear. Since the change of cutting force caused by tool wear is very small, it is necessary to make the in-process cutting force measurement with a high sensitivity. For this purpose, a stiff but sensitive piezoelectric force sensor is carefully integrated to the FTC unit used for cutting the micro-lens array. To observe the tool wear during the fabrication of micro-lens arrays, it is desired to monitor the generated cutting force at the interface between the cutting tool and the machined surface with the diamond turning process. This paper presents experimental results of detection of cutting tool wear by the FTC unit integrated with a sensitive piezoelectric force sensor, which is designed for in-process measurement of the cutting force.

DESIGN REQUIREMENTS OF FTC UNIT FOR FABRICATION OF MICRO-LENS ARRAY

Figure 1 shows a schematic of the micro-lens array fabricated in the experiment. The micro-lens has a parabolic profile and it is fabricated on the workpiece surface over a large area. The specific parabolic micro-lens designed for the experiment has a length of 190 μm, a width of 90.3 μm and a depth of 5.2 μm. The micro-lenses are fabricated as an array over a Ni-P plating roller surface with a diameter of 55 mm.

Generally speaking, a FTC unit should be designed to satisfy the following requirements for fabrication of micro-lens arrays. First, the length of axial direction (width) of micro-lens is decided by the cutting tool profile. Therefore, for fabrication of a narrow lens, a cutting tool with a small nose radius down to 10 μm should be employed. If the contact between the small sized cutting tool and the workpiece is not well detected, the tool may be broken. Also, the fabrication process is influenced by a lot of factors such as tool damage, tool wear, etc. It is thus desired to detect the initial position of machining and monitoring of the long time fabrication process. Second, the depth along the Z-direction of micro-lens is relatively deep up to tens of micrometers and the maximum stroke of FTC unit should be longer than the depth of micro-lens. Third, because the length along the circumference direction (P_C) of is short, the FTC unit is required a high dynamic characteristic.

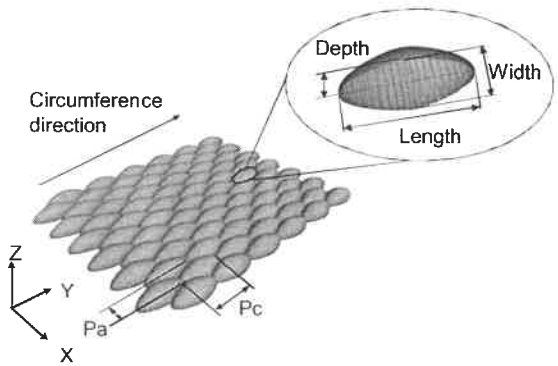

FIGURE 1. Profile of the micro-lens array

DESIGN OVERVIEW OF FTC UNIT

The structure of FTC unit is shown in Figure 2. The hollow-type piezoelectric actuator is installed in the casing under the preload by the spring. The piezoelectric actuator has an outer diameter of 20 mm, an inner diameter of 14 mm and a stiffness of 117.5 N/μm. To get a higher dynamic performance of a piezoelectric actuator, a preload must be introduced in the FTC unit system because the piezoelectric actuator can only generate a pushing force. Generally, a lot of piezoelectric actuators are preloaded against the piezoelectric actuator in order to avoid backlash by alternating load force direction. And preload on the piezoelectric actuator must be higher than any inertial forces of moving parts [6]. In the FTC unit system shown in Figure 2, the piezoelectric actuator is preloaded by adjusting the thickness of spring with a force of 280 N for high dynamic way. The capacitance type displacement sensor with 125 μm range and 12.5 nm resolution is installed in the hollow-type piezoelectric actuator. The bandwidth of the capacitance type displacement is set at 20 kHz. Because the capacitance type displacement sensor is aligned with the axis of the piezoelectric actuator motion, the motion of piezoelectric actuator can be measured by capacitance type displacement without Abbe error.

Experiments are carried out to evaluate the static and dynamic performances of the FTC unit. The input voltage is applied to the piezoelectric actuator and it is magnified by a voltage amplifier. The piezoelectric actuator with the maximum voltage range of 150 V is used. Figure 3 shows the static response when the FTC unit is under the closed loop control. An analog PID controller is employed for servo control of the motion of FTC unit. As can be seen that the static response under the closed loop control become nearly linear. The developed FTC unit has a stroke of 48.3 μm and the linearity error is reduced to approximately 150 nm. The dynamic response is related to mechanical stiffness and mass of moving parts. The dynamic frequency response is measured with a FFT analyzer system. The FTC unit receives the command input signal (swept sine wave) corresponding to a displacement of 500 nm from the function generator. Then, it is compared with the output signal from the capacitance type displacement sensor measuring the position of the head. Figure 4 shows the obtained dynamic response result of the FTC unit along the in-feed direction. The measured resonance frequency in the in-feed direction is approximately 7837 Hz.

The FTC unit is integrated with a piezoelectric force sensor for measurement of cutting force during fabrication process in real time. The high stiffness of the piezoelectric force sensor is demanded in order to reduce the stiffness effect in the fabrication system.

Also, the piezoelectric force sensor which has a high resolution and a high sensitivity is necessary for detecting of small cutting forces due to small removed material chips. For the measurement of cutting force by using the piezoelectric force sensor, a charge amplifier is employed. The piezoelectric force sensor has an outer diameter of 12 mm, an inner diameter of 5 mm, a stiffness of 953.3 N/μm. A piezoelectric force sensor should basically be preloaded in a mounting structure for measurement of process force including tensile force and compression force [7]. The developed FTC unit body has a dimension of ϕ 35×100 mm.

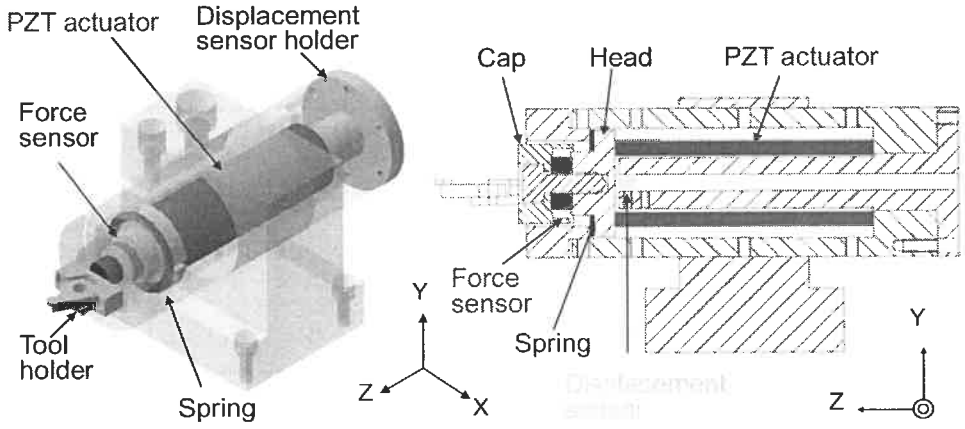

FIGURE 2. Structure of the FTC unit integrated with piezoelectric force sensor

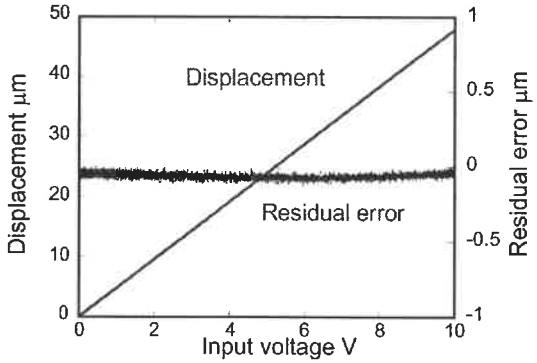

(a) Static response

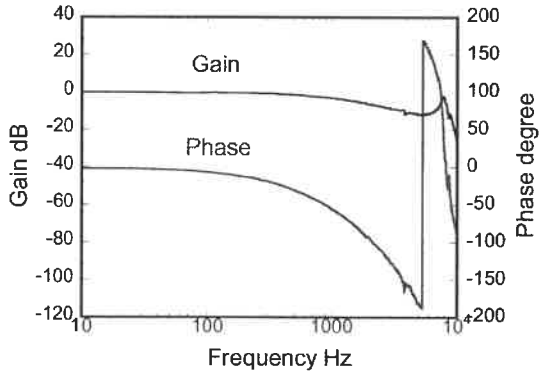

(b) Dynamic response

FIGURE 3. Performance *of FTC unit*

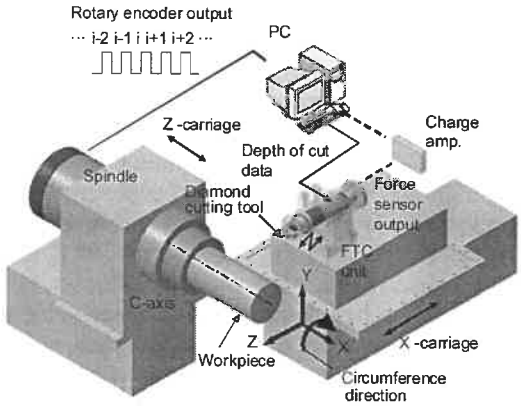

FIGURE 4. In-process measurement system

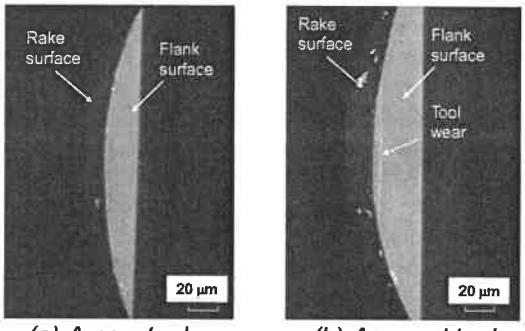

(a) A new tool *(b) An used tool*

FIGURE 5. Microscope image of tool profile

IN-PROCESS DETECTION OF CUTTING FORCE

Figure 4 shows a schematic of the in-process cutting force measurement system. The In-process measurement system consists of a diamond turning machine, the FTC unit and a PC. The PC is used to generate output of depth of cut data and record the output signal of the cutting force from the piezoelectric force sensor.

The FTC unit is mounted on the X-carriage of the diamond turning machine. A roller workpiece is mounted on the spindle. The micro-lens array is fabricated on the roller workpiece surface with a diameter of 55 mm. The fabrication of micro-lens array is started by responding to the trigger signal from the rotary encoder output of spindle. The depth of the micro-lens is controlled by the FTC unit along the Z-direction.

By using the FTC unit integrated with the piezoelectric force sensor, the cutting force can be measured in real time. The generated charge output of the piezoelectric force sensor in the fabrication process is proportional to the force output through the charge amplifier. This output is stored to PC memory through the A/D board.

FABRICATION OF MICRO-LENS ARRAY

First, a pre-cut is carried out to remove the out of roundness of the workpiece by a cutting tool with a 2 mm nose radius. Then the tool is replaced to a cutting tool with a nose radius of 0.2 mm for fabrication of micro-lens array. In order to exhibit the fact that the cutting force change depends on the tool wear, micro-lens arrays are fabricated on the Ni-P plating by a new tool and an used tool with the same nose radius of 0.2 mm, respectively. Figure 5 shows the microscope image of the tools. The contact between the tool and the workpiece is detected by the integrated piezoelectric force sensor. The tool is oscillated by FTC unit with a frequency of 380 Hz and an amplitude of 3 nm so that the piezoelectric force sensor output can be detected with a lock-in amplifier for high sensitivity detection [8]. The contact detection is decided from the output change of the piezoelectric force sensor when the tool is moved by the X-carriage of the diamond turning machine toward the workpiece with a step of 10 nm.

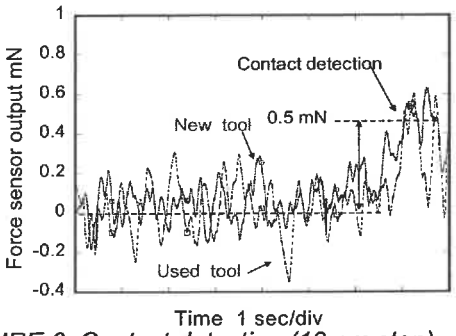

FIGURE 6. Contact detection (10 nm step)

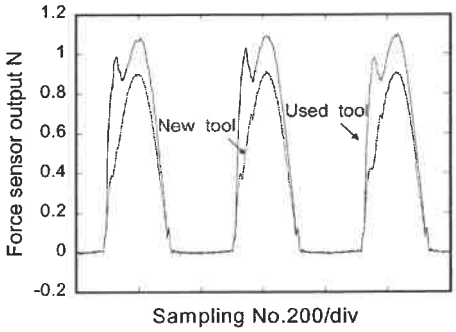

FIGURE 7. The measured cutting force

The piezoelectric force sensor outputs when the contact is detected between the tool and the workpiece by the new tool and the used tool are shown in Figure 6. The initial position of machining can be detected with a resolution of less than 10 nm for both the new tool and the used tool. The micro lenses which have depths of 5.2 μm and pitches of 190 μm, are then fabricated as arrays on the Ni-P plating surface by the two tools, respectively. The measured cutting forces by the FTC unit integrated with the piezoelectric force sensor are shown in Figure 7. The measured cutting forces are 0.9 N and 1.1 N, respectively. It can be seen that the cutting force with the new tool is smaller than that with the used tool. The results have confirmed the fact that the cutting force is increased with the tool wear and it is effective to monitor the tool wear by the piezoelectric force sensor output of the FTC unit. Figure 8 shows photographs and the sectional profiles of the fabricated micro-lens arrays by the two tools, respectively. The surface finish of the micro-lens cut by the new tool is better than that by the used tool.

CONCLUSION

The piezoelectric force sensor-integrated FTC unit has been developed to measure the cutting force in real time. The detection of tool wear can be determined from the monitoring of cutting force.

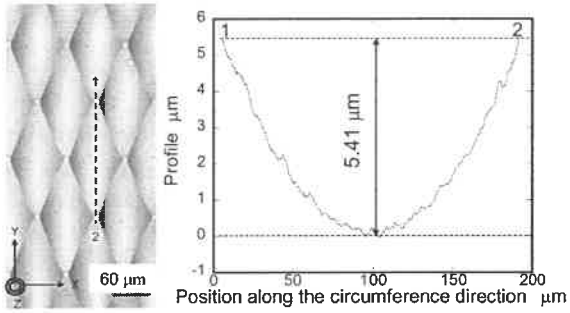

(a) By using a new tool

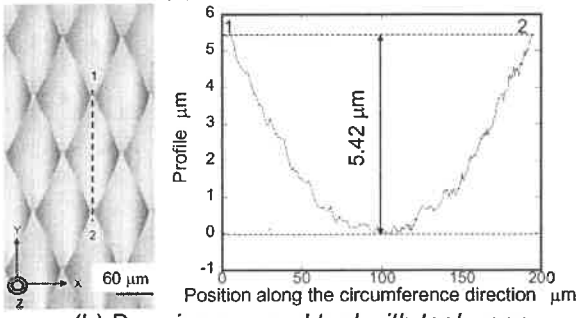

(b) By using an used tool with tool wear

FIGURE 8. Fabricated micro-lens arrays

REFERENCES

[1] W. Gao, T. Araki, S. Kiyono, Y. Okazaki and M. Yamanaka, Precision nano-fabrication and evaluation of a large area sinusoidalgrid surface for a surface encoder. Precision Engineering 2003; 27(3): 289-298.

[2] A. Woronko, J. Huang, Y. Altintas, Piezoelectric tool actuator for precision machining on conventional CNC turning centers. Precision Engineering 2003; 27(4): 335-345.

[3] J. D. Drescher and T. A. Dow, Tool force model development for diamond turning. Precision Engineering 1990; 12(1): 29-35.

[4] S. Asai, Y. Taguchi, K. Horio, and T. Kasai, Measuring the very small cutting edge radius for a diamond cutting tool using a new type of SEM having two detectors. CIRP Annual 1990; 39: 85-88.

[5] W. Gao, T. Motoki, S. Kiyono, Nanometer edge profile measurement of diamond cutting tools by atomic force microscope with optical alignment sensor. Precision Engineering, 2006; 30: 396-405.

[6] http://www.cedrat.com/

[7] http://www.pcb.com/

[8] W. Gao, R. Hocken, J. Patten and D. Lucca, Construction and testing of a nano–machining instrument. Precision Engineering, 2000; 24(4): 320-328.

MOTION CONTROL AND OPTIMIZATION FOR NANO LITHOGRAPHY

Shalom D. Ruben and Tsu-Chin Tsao
Mechanical and Aerospace Department
University of California, Los Angeles
Los Angeles, California

INTRODUCTION

This paper presents some motion control issues that we are addressing in developing a control system for a multi-degree-of-freedom stage designed for nano-imprint-lithography. We describe the motion control software and hardware configuration, and model the coordinate transformation among the spaces of sensors, stage position, and actuators. A characteristic problem that is common to many electric motor driven stages including the one we are working on is the excess number of motors and coils to the stage's kinematic degrees of freedom render a redundant system. To reduce thermal deformation of the work space by the heat generated by the motors, this redundancy is exploited. In minimizing the total electric power of the motors for a given force vector command from the servo controller we derive an interesting result that are general to common systems. Two formulations, one without and one with additional constraint for geometrically symmetric thermal deformation, for total motor heat minimization are considered. We will also present our initial PID servo control experimental result and discuss work in progress to further eliminate the servo errors in the PID loop.

PRECISION STAGE AND CONTROL INTEGRATION

High-precision motion control is a critical element of semiconductor lithography machines. While lithography typically involve planner motion, recent research in precision stages for lithography are designed for all six degrees of freedom mechanical mottion. Some recent designs (as in [1, 2]) use linear permanent magnet motors for actuation and interferometers and capacitance gauges as feedback. The stages are also levitated, with the help of air/fluid bearings, for non-contact motion by the linear motors using Halbach arrays [3]. In these referenced works, the two mappings from a desired force vector to the motor forces and the desired motor(local) force vector, f, to the needed current vector, i, (commutation) are considered separately. Optimization performed for each mapping, separately, does not necessarily represent the system optimization. A multi-degree-of-freedom similar to [2] is under development for nano-imprint lithography (see [1] for extensive design detail). Shown in figure, 1, the stage is in part a 3-DoF mask carrier (structural frame) actuated by piezo-electric actuators and a 6-DoF substrate carrier (platen) actuated by 4 Halbach linear motors. Each motor is capable of producing two orthogonal force. We will focus on the in-plane motion actuated by the Linear motors (x,y,θ_z). The integration of control for the platen is shown some detail in figure 2.

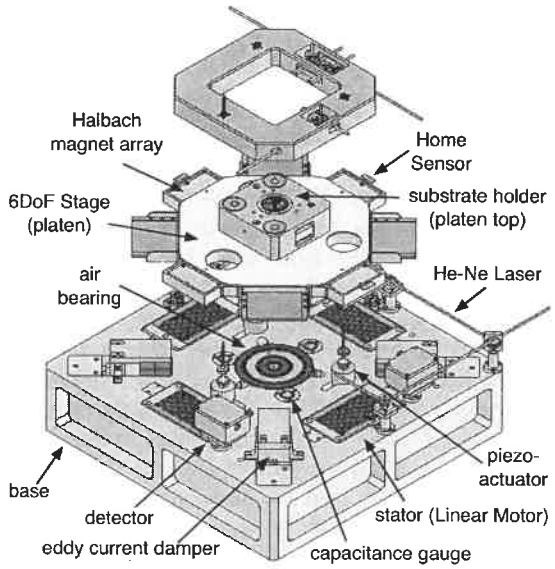

FIGURE 1. exploded view of MAPS stage

A UMAC industrial control system, by Delta Tau Data Systems, Inc, is integrated with the Multi-scale Alignment and Positiong Stage. This control system is composed of a PMAC2 controller and interfacing cards for I/0, A/D conversion, D/A conversion, and 4096X sin/cos quadrature encoder conversion. A PID control algorithm is being used for the initial integration of hardware and software. There is space on the controller for the user to write an advanced control algorithm, but is limited in memory and computational power for more sophisticated schemes, such as those mentioned in this paper. In the future, advanced con-

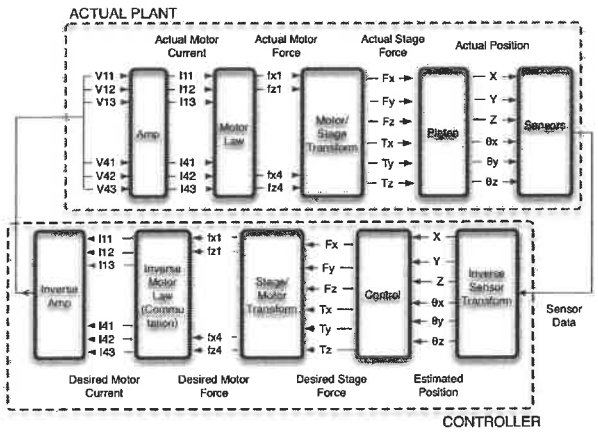

FIGURE 2. detailed block diagram of platen control

trol will be performed on the accompanying PC computer (running windows with a real-time kernel installed, such as INtime from TenAsys Corporation) and data will be read and written into dual-ported RAM to communicate with PMAC in synchronization with the PMAC servo cycle update rate. The commutation for the Halbach motor is user-written. A tranformation on the sensors is performed ,by a user-written code , to convert from the sensors in to platen position. The command from the controller is sent to the user-written commutation. The commutation output is sent the D/A converters which send a desired voltage, proportional to current, to the amplifiers connected to all 12 coils.

DYNAMIC MODELING OF 6 DOF PLATEN

After linearizing the platen model, by assuming that the rotation about each axis (θ_z, θ_x,θ_y) is small and can be used instead of Euler angles, we have a modeled plant G:

$$G: \quad M\ddot{X} + B\dot{X} + KX = F$$

where the state vector X is equal to $[x\ y\ \theta_z\ z\ \theta_x\ \theta_y]^T$ and the global force vector F is defined as $[F_x\ F_y\ T_z\ F_z\ T_x\ T_y]^T$. The relationship between the local forces and the global forces can be seen, by figure 3, to be

$$F = Af$$

where f is defined as $[f_{x1}\ f_{x2}\ f_{x3}\ f_{x4}\ f_{z1}\ f_{z2}\ f_{z3}\ f_{z4}]^T$ and A is defined by:

$$A = \begin{bmatrix} 1 & 0 & -1 & 0 & 0 & 0 & 0 & 0 \\ 0 & 1 & 0 & -1 & 0 & 0 & 0 & 0 \\ R & R & R & R & 0 & 0 & 0 & 0 \\ 0 & 0 & 0 & 0 & 1 & 1 & 1 & 1 \\ 0 & 0 & 0 & 0 & -R & 0 & R & 0 \\ 0 & 0 & 0 & 0 & 0 & -R & 0 & R \end{bmatrix}$$

The current and local force relationship of the 3-

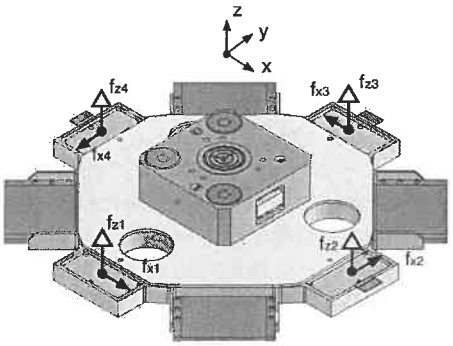

FIGURE 3. local forces acted on the platen

phase Halbach motors is calculated by

$$f = Bi$$

where i is defined as $[i^1\ i^2\ i^3\ i^4]^T$ ($i^k = [i_{1k}\ i_{2k}\ i_{3k}]^T$), and B defines the four Halbach linear motors:

$$f_{xk} = C^x_{1k} i_{1k} + C^x_{2k} i_{2k} + C^x_{3k} i_{3k}$$
$$f_{zk} = C^z_{1k} i_{1k} + C^z_{2k} i_{2k} + C^z_{3k} i_{3k}$$

or in vector form

$$f^k = \begin{bmatrix} f_{xk} \\ f_{zk} \end{bmatrix} = \begin{bmatrix} C^T_{xk} \\ C^T_{zk} \end{bmatrix} i^k$$

Combining the four motors gives B. Where $C^x_{1k}(x_k) = a\cos(Kx_k + P)$, and $C^x_{2k}(x_k)$ and $C^x_{3k}(x_k)$ are shifted by $\frac{2\pi}{3}$. Also $C^z_{1k}(x_k) = a\cos(Kx_k + P + \frac{\pi}{2})$, and $C^z_{2k}(x_k)$ and $C^z_{3k}(x_k)$ are shifted by $\frac{2\pi}{3}$. Combining these two relationships, we have the relationship between the supplied current vector and the global force vector as

$$F = ABi \qquad (1)$$

A controller C is designed so that the pair (G,C) is stable and meet performance requirements using feedback from the sensors. The sensor feedback must be transformed to state feedback. For the platen's in-plane position, the interferometers are used primarily and are measuring positions on the faces of the platen top. The command, from the controller, is a desired global force vector and must be mapped to a current vector to be supplied to the platen. We will define equation 1 as the mapping from i to F and define present the mapping from F to i, commutation, in the following section.

LINEAR MOTOR COMMUTATION

In this section we will show that the assumption of solving minimum power commutation for

each motor ($\min ||i^k||^2$), independent of their relationship to the stage, will actually give the total minimum power ($\min ||i||^2$) is in general incorrect. Although, in the case that of using brushless permanent magnet motors as actuation, the assumption is true (due to the structure of $\boldsymbol{B}$). So the desire to minimize power, and thermal deformation, for systems using Linear motors, can be separated into a kinematic stage and an electromagnetic stage with out loss of the desired goal of minimizing total power. Also, we will propose a novel scheme to minimize thermal deformation by minimizing power subject to the constraints that there is heat symmetry about the center of the platen. Heat symmetry is attained by forcing all the motors to generate the same power ($||i^1||^2 = ||i^2||^2 = ||i^3||^2 = ||i^4||^2 = P$). This is possible, since a current can be supplied, and generate heat, to a linear motor without generating force (when i is in the null space of $\boldsymbol{B}$). It turns out that, again due to the structure of $\boldsymbol{B}$, this problem can also be solved by separating the problem into a kinematic stage and an electromagnetic stage. The important structure of $\boldsymbol{B}$ is that the square matrix $\boldsymbol{B}\boldsymbol{B}^T$ turns out to be equal to a constant times the identity matrix ($= c\boldsymbol{I}$)

Minimum Power Commutation

Given that the platen has 4 motors with 3 coils per motor, solving for the current that produces a desired force is an over-determined problem and has an infinite number of solutions. it is common to solve for the solution that gives minimim power ($\min ||i||^2$ s.t. $F = \boldsymbol{A}\boldsymbol{B}i$) since it is a closed-form solution and easily solved by the pseudo inverse, giving the current vector to be $i = (\boldsymbol{A}\boldsymbol{B})^+F$. Where the solution, using the pseudo-inverse is well known to be equal to solving the following problem:

$$\begin{aligned} &\min ||i||^2 \\ &\text{subject to} \\ &F = \boldsymbol{A}\boldsymbol{B}i \end{aligned} \tag{2}$$

It is possible to attack this problem in two stages, a kinematic stage where the local force vector is $f = \boldsymbol{A}^+F$ and a electro-magnetic stage, where the minimum power current vector is $i = \boldsymbol{B}^+f$ giving us $i = \boldsymbol{B}^+\boldsymbol{A}^+F$. In general these two methods do not give the same solution since $(\boldsymbol{A}\boldsymbol{B})^+ \neq \boldsymbol{B}^+\boldsymbol{A}^+$. In fact, the power solved by the one stage method is less than or equal, and therefore optimal, to the solution of the two stage method ($||(\boldsymbol{A}\boldsymbol{B})^+F|| \leq ||\boldsymbol{B}^+\boldsymbol{A}^+F||$). This tells that, in general, we must not separate the kinematic stage from the electro-magnetic stage when minimizing the power.

Due to the structure of the linear motors, the one stage solution turns out to be equal to the two stage solution ($||(\boldsymbol{A}\boldsymbol{B})^+F|| = ||\boldsymbol{B}^+\boldsymbol{A}^+F||$). In can be shown that the methods are equal by shown that the following equation is true.

$$(\boldsymbol{A}\boldsymbol{B})^+ = \boldsymbol{B}^+\boldsymbol{A}^+$$

The problem described above is a convex optimization problem defined by a quadratic cost function ($||i||^2$) subject to linear constraints ($F = \boldsymbol{A}\boldsymbol{B}i$). It is worth noting that the above results discussed for the Halbach linear motors are also true for the conventional brushless linear motors.

Heat Symmetric Commutation

We propose an adapted problem, by adding the constraints that each motor's power ($||i^k||^2$), separately, is equal to one another:

$$\begin{aligned} &\min ||i||^2 \\ &\text{subject to} \\ &F = \boldsymbol{A}\boldsymbol{B}i \\ &||i^k||^2 = P; \\ &k = \{1, 2, 3, 4\} \end{aligned} \tag{3}$$

This problem is motivated by the temperature gradient, and subsequent non-symmetric deformation of the platen, produced by the motors generating different power profiles. By each motor generating the same power we force heat symmetry on the platen and therefore symmetric deformation about the center of the platen. This problem is non-convex since the added quadratic equality constraints are non-convex [4].

The above stated problem is difficult to solve. We propose to solve this problem by a 3-step method. We will introduce this method and prove that this method is equal to the "exact" solution. The first step of this method (see table 1) involves solving a convex problem that minimizes the maximum power that any of the four motors can have ($\min \max ||i^k||^2$). We set this power, for the motor with the greatest, as P. Finally solving three algebraic equations, for each other motor, gives us the current vectors that will bring their power up to P without changing the local force produced by each motor. We have taken a difficult non-convex optimization problem into a combination of simple problems including a convex optimization problem and an algebraic problem.

The results of a simulated example, where the desired global forces are $F_x = 1, T_z = 1$, and all the rest are zero, are shown in Table 2. Two solutions, a minimum power as in equation 2 and a heat symmetry as in equation 3, are presented. Both solutions produce the same force, while the power output per motor is quite different. The following proves that the solution of the exact heat symmetry problem, in equation 3, and our heat symmetry method, in equation 4, produce the same power for each motor:

Given: desired global force vector F

Step 1: solve convex problem for f

$$\min(\max(||i^k||^2))$$

subject to

$$F = ABi$$

Step 2: set $P = \max_k(||i^k||^2)$ (4)

Step 3: solve for i^k for each motor

$$f^k = \begin{bmatrix} C_{xk}^T \\ C_{zk}^T \end{bmatrix} i^k$$

$$P = ||i^k||^2 = i_{1k}^2 + i_{2k}^2 + i_{3k}^2$$

Output: current vector i

TABLE 1. Heat Symmetry Method

Method	$\|\|i^1\|\|^2$	$\|\|i^2\|\|^2$	$\|\|i^3\|\|^2$	$\|\|i^4\|\|^2$	$\|\|i\|\|^2$
min P	.6	.27	.06	.27	1.2
Heat Sym	.4	.4	.4	.4	1.6

TABLE 2. Solving for i where $F_x = 1; T_z = 4R$

Proof. Let the solution for the problem of equation 3 give P^* for each motor and the solution for the min-max problem of equation 4 be P_{hs}. By the problem in 3, we must have the total power $4P^* \leq 4P_{hs}$. On the other hand, by the problem in 4, $P_{hs} \leq P^*$. Therefore, $P^* = P_{hs}$. □

PRELIMINARY RESULTS AND CONCLUDING REMARKS

The minimum power commutation scheme has been implemented on the PMAC2 controller. Figure 4 shows the experimental results of a PID servo loop tracking trapezoidal profiles for each axis using the interferometer feedback. Work is in progress to implement advanced control, such as iterative learning control, repetitive, and adaptive control [5] to further reduce the repeatable and non-repeatable errors.

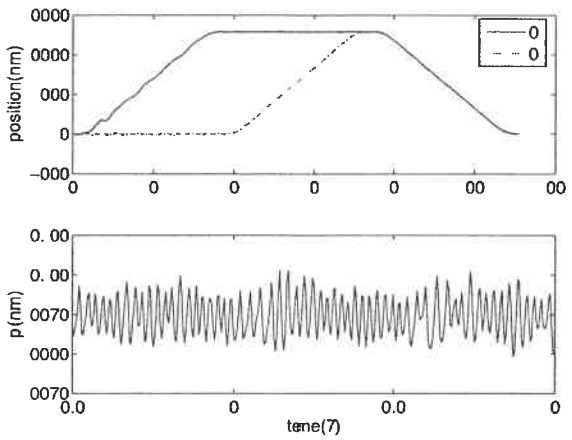

FIGURE 4. platen Trapezoidal trajectory under PID control

ACKNOWLEDGEMENTS

The authors would like to thank Prof. Robert Hocken, Ozkan Ozturk, and other members of the MAPS design team at UNC Charlotte for supporting the integration of the control system, and Delta Tau Data Systems, Inc., for donating the UMAC real-time control hardware and software. This work was supported in part by the National Science Foundation under grant no. DMI 0327077, Nanoscale Science and Engineering Center for Scalable and Integrated NAnomanufacturing (SINAM).

REFERENCES

[1] Ozturk O, Fesperman RR, Hocken RJ. Design of Multi-scale Alignment and Positioning System. In: Proceedings of euspen International Conference; 2008. .

[2] Holmes M, Hocken RJ, Trumper D. The long-range scanning stage: a novel platform for scanned-probe microscopy. Precision Engineering. 2000;24:191–209.

[3] Trumper DL, Kim WJ, Williams ME. Design and Analysis Framework for Linear Permanent Magnet Machines. IEEE Transactions on Industry Applications. 1996;32(2):371–379.

[4] Boyd S, Vandenberghe L. Convex Optimization. Cambridge University Press; 2004.

[5] Lin CY, Tsao TC. adaptive repetitive control of piezoelectric actuators for nano-precision motion control. In: Proceedings of ASPE Annual Meeting; 2007. .

CHARACTERISTICS OF PVAJT TRAJECTORY GENERATOR AND ITS IMPLEMENTATION

Dongwon Shin[1] and Sung-Hyuk Choi[2]
[1]School of Mechanical Engineering
Kumoh National Inst. of Tech.
Gumi, Gyeongbuk, Republic of Korea
[2]Research Center
Ajinextek Co. Ltd.
Daegu, Republic of Korea

INTRODUCTION

This paper presents the new method of generating the trajectory at every cycle using PVAJT data, where P means the position, V the velocity, A the acceleration, J the jerk, and T is the multiplied cycle time. This can reduce the calculation time in the trajectory planner so that it is able to generate more complex trajectory in real time. The cubic spline trajectory generator which can perform complex path of tasks is realized by the PVAJT algorithm as an example of proposed method. As previous studies about spline trajectories,. several researchers have proposed parametric interpolators for Bezier/B-spline and implicit curves [1-2]. And a quintic spline interpolation technique for more improvement of relationship between the parameter to the actual arc-length has been studied [3]. However, all studies deal with PT trajectory generation which has the limitation of calculation if the cycle time of servo controller becomes shorter.

PVAJT TRAJECTORY GENERATOR

The PVAJT means "Position, Velocity, Acceleration, Jerk, Time" of the trajectory. The sets of these 4 values are specified for a given motion at multiple points of trajectory as shown Table 1, where "No" denotes the order of the set and "SegT" the segment time. Segment time means the time interval of the corresponding set and is usually expressed as the multiple number of the cycle time of servo controller. The row of the table represents each PVAJT set.

TABLE 1. The series of PVAJT sets

No	P	V	A	J	SegT
0	P_0	V_0	A_0	J_0	T_0
1	P_1	V_1	A_1	J_1	T_1
...	...	...	...	...	...
j	P_j	V_j	A_j	J_j	T_j
...	...	...	...	...	...
n	P_n	V_n	A_n	J_n	T_n

Let the time at every step of the cycle time T_c be t_k as expressed in Equation (1), where P, V, A and J at some sampling time are given. Then, the command position $P_j^{(k)}$ at each cycle time during the segment time can be generated as following 3rd order interpolation equation.

$$P_j^{(k)} = P_j + V_j t_k + \frac{A_j}{2} t_k^2 + \frac{J_j}{6} t_k^3 \quad (1)$$
$$where\ t_k = T_c k\ (k=0,\cdots, T_j\text{-}1)$$

For example, in case of T_j=3 and T_c=1, $P_j^{(k)}$ from k=0 to k=2 is as below.

$$P_j^{(0)} = P_j$$
$$P_j^{(1)} = P_j + V_j + A_j/2 + J_j/6$$
$$P_j^{(2)} = P_j + 2V_j + 2A_j + 4J_j/3$$

Based on a series of PVAJT set defined as Table 1, the command positions of whole trajectory can be generated at each cycle time. Usually the PVAJT are calculated in the stage of trajectory generator while the interpolated positions are calculated at the front stage of the servo controller. While most trajectory generators calculate only the command position at every cycle time as PT type, the PVAJT trajectory generator calculates all the P, V, A and J at every sampling time larger than the cycle time (i.e. multiple of the cycle time). Thus PVAJT trajectory generator can reduce the burden of calculating the command position at every cycle time.

MOTION PLANNER

Figure 1 shows the structure of the motion planner where PVAJT trajectory generator is included in the lower position. The motion planner receives starting position (usually current position), ending position, path type and velocity profile as the input data. The starting

position is denoted by P_s, and the ending position P_e. There are three kinds of paths which are linear, circular and spline. The velocity profile represents the velocity shape (see Figure 2) along the path with respect to time from the starting position to the ending position, where starting velocity (v_1), acceleration (a_1), maximum velocity (v_m), deceleration (a_2) and ending velocities (v_2) are the parameters of configuring the shape. Using these input data, path length(L) of the given path and time intervals of velocity profile are calculated. The time intervals of velocity profile are accelerating time (t_1), decelerating time (t_2) and total traveling time (T) of the path as shown in Figure 2.

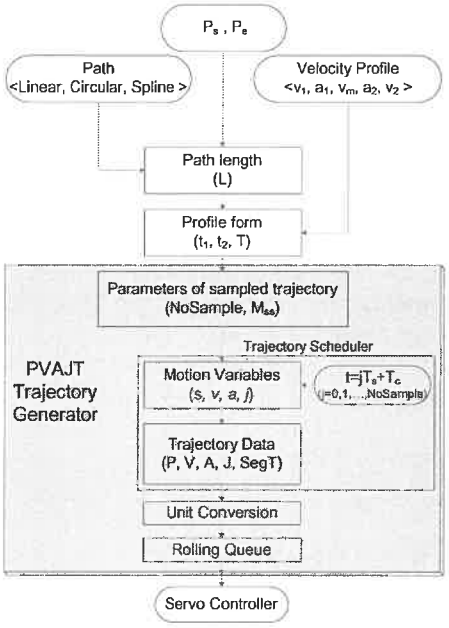

FIGURE 1. Motion planner and PVAJT trajectory generator

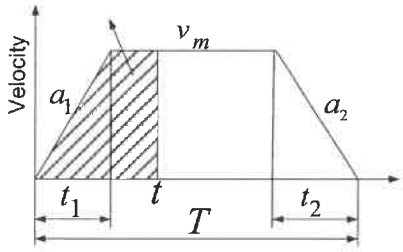

FIGURE 2. Velocity profile and several parameters

After defining the time intervals of the velocity profile, we can go to the next step of the trajectory generation. A few of parameters such as NoSample and M_{ss} are determined before going to the trajectory scheduler. The trajectory scheduler does the repeated task of calculating the scheduling time and the corresponding PVAJT values.

Looking inside of the trajectory scheduler, the values of s, v, a, and j which are respectively position, velocity, acceleration, and jerk variables at the scheduled time on the velocity profile are determined, and subsequently, the values of P, V, A, J and SegT are computed. These values are written in the rolling queue which can be accessed by servo controller. The servo controller fetches the P, V, A, J, SegT from the rolling queue at every sample time, and makes interpolated positions at every cycle time, and finally uses these positions as the reference command positions.

Trajectory Scheduler

The common trajectory generator makes the only P data at every cycle time. However, the PVAJT trajectory generator in this paper makes P, V, A, J data at multiplied cycle time, thus more sophisticated trajectory scheduling is needed. The parameters dealt in the scheduling are as follows.

- Total trajectory time: T
- Cycle time of servo controller: T_c
- Sampling Multiple: M_s
- Sampling time: $T_s=M_s \cdot T_c$
- Number of samples: $N=fix(T/T_s)$
- Residual time: $T_r=T-N \cdot T_s$
- Subsampling multiple: $M_{ss}=round(T_{ss}/T_c)$
- Subsampling time: $T_{ss}= M_{ss} \cdot T_c$
- Digitized trajectory time: $T_n=(N \cdot T_s+M_{ss})T_c$

When T, T_c and M_s are given, the other parameters can be obtained as above equations. In the digital control, the total trajectory time should become the multiple of the cycle time, i.e. T_n. Digitized trajectory time T_n is divided into section of sampling time and subsampling time, where the sampling time is M_s times of the cycle time, the subsampling time is M_{ss} times of the cycle time. We call the motions in the sampling and subsampling time as sampling motion and subsampling motion individually. At every sample, the trajectory information P, V, A, and J are calculated according to scheduling time as expressed as

$$t_j = \sum_{i=0}^{j-1} (SegT)_j T_s + T_c \quad (j = 0, \cdots, n) \qquad (2)$$

where SegT is the multiple number of the cycle time as described in Table 1. The careful point in

the subsampling motion is that the final scheduling time when PVAJ should be calculated does not follow Equation (2), but becomes T due to keeping the ending position continuity while the final segment time in the subsampling motion becomes 1. This final motion in the subsampling motion, we call especially as the ending motion.

For example, we consider the case of T=14.6, T_c=1, M_s=4. Then the other parameters are T_s=4, N=3, T_{ss}=2, M_{ss}=2, T_n=15. The scheduling diagram is illustrated as Figure 3, and SegT values are expressed in Table 2.

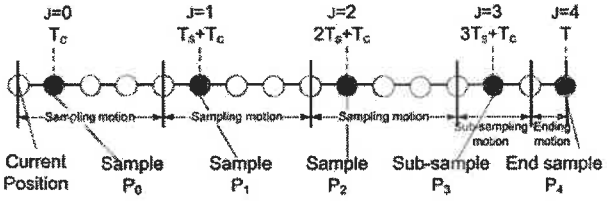

FIGURE 3. Example of trajectory scheduling

TABLE 2. The example of PVAJT sets

No	P	V	A	J	SegT
0	P_0	V_0	A_0	J_0	4
1	P_1	V_1	A_1	J_1	4
2	P_2	V_2	A_2	J_2	4
3	P_3	V_3	A_3	J_3	2
4	P_4	V_4	A_4	J_4	1

The main code of the trajectory generator including the scheduler is as following. The middle part with for-loop is the trajectory scheduler, where the scheduling time, SegT, and PVAJ values according to the selected path are calculated at every step. Next, the basic units of PVAJ, [mm] and [sec] are converted to [count] and [cycle] for the digital servo controller, and the set of [P V A J SegT] is written on the rolling queue from which the servo controller fetches the set.

```
length = length along the path;
[t1,t2,T] = time intervals from velocity profile;
NoSample = fix(T/Ts);
Tss = T-NoSample*Ts;
Mss = ceil(Tss/Tc);
if Mss~=0
   N1 = NoSample;
   N2 = Mss;
else
   N1 = NoSample-1;
   N2 = Ms;
end

for j=0:N1+1
   if j <= N1-1 //Sampling Motion
      t= j*Ts + Tc;
      SegT = Ms;
   elseif j==N1 //Subsampling Motion
      t= N1*Ts + Tc;
      SegT = N2-1; // for ending motion
      if SegT==0, continue, end;
   else
      t= T; %Ending Motion
      SegT = 1;
   end

   [ll,vv,aa,jj]=motion variables from velocity
                 Profile using t;
   P = Position vector of the path;
   V = Velocity vector of the parh;
   A = Acceleration vector of the parh;
   J = Jerk vector of the parh;

   Convert the unit of P,V,A,J
   Writing [P V A J SegT] on the rolling queue.
end
```

CUBIC SPLINE

The proposed method is applied to the cubic spline which can express the complex path, but has difficulty of calculating the trajectory data in short cycle time. The parametric equation of cubic spline is Equation (3) where a_0, a_1, a_2, a_3 are the vector coefficients of the parametric equation. For simplicity, the formulation is presented for only two dimensions (x and y), but it can easily be extended to the three dimensional case.

$$\begin{aligned} \mathrm{P}(u) &= [x(u)\ y(u)] = \mathrm{a}_0 + \mathrm{a}_1 u + \mathrm{a}_2 u^2 + \mathrm{a}_3 u^3 \\ \mathrm{V}(u) &= \mathrm{P}'(u)\frac{du}{dt} = \mathrm{P}'\dot{u} \\ \mathrm{A}(u) &= \mathrm{P}''\dot{u}^2 + \mathrm{P}'\ddot{u} \\ \mathrm{J}(u) &= \mathrm{P}'''\dot{u}^3 + 2\mathrm{P}''\dot{u}\ddot{u} + \mathrm{P}''\dot{u}\ddot{u} + \mathrm{P}'\dddot{u} \end{aligned} \tag{3}$$

The cubic curve has advantage that by varying the magnitude of the tangent vectors the user can modify the interior shape of a curve without changing the position the endpoints.

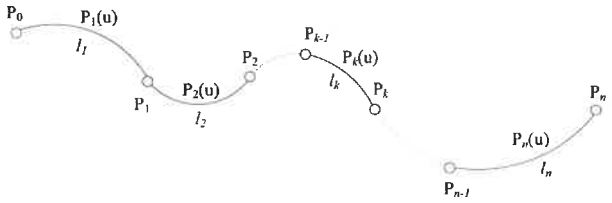

FIGURE 4. Cubic spline interpolating n+1 data points

Relationship between parameter and arc length

In the stage of trajectory scheduling, the arc length s of the curve at every scheduling time can be computed from the velocity profile. The

parameters u in the basic curve such as line and circle are directly proportional to the arc length s, whereas the parameter in the cubic curve is not. Instead, there is a differential relationship between of s and u in the parameterized cubic spline P(u) as follows.

$$ds = |d\mathrm{P}| = \left|\frac{d\mathrm{P}}{du}\right| du = \sqrt{\frac{d\mathrm{P}}{du}\cdot\frac{d\mathrm{P}}{du}}\,du = \sqrt{\mathrm{P}'\cdot\mathrm{P}'}\,du \tag{4}$$

Therefore, the differentials of u with respect to time can be expressed as follows by using $Q(u) = 1/\sqrt{\mathrm{P}'\cdot\mathrm{P}'}$, $v = ds/dt, a = dv/dt, j = da/dt$.

$$\begin{aligned} \dot{u} &= vQ \\ \ddot{u} &= aQ + vQ'\dot{u} \\ \dddot{u} &= jQ + 2aQ'\dot{u} + vQ''\dot{u}^2 + vQ'\ddot{u} \end{aligned} \tag{5}$$

Integrating Equation (4) is expressed as following equations.

$$s = \int_0^u \sqrt{\mathrm{P}'(\mathrm{u})\cdot\mathrm{P}'(\mathrm{u})}\,du \tag{6}$$

Because the value of arc length s at the specified time is obtained from the velocity profile, the parameter u can be evaluated by solving Equation (6). However, solving this equation needs much time in calculating the right integral term, so that it is not fitted well to real time trajectory calculation.
Therefore, the value of parameter u should be estimated by Taylor expansion with the above differential relationship. Because the parameter u is the function of time t, the u_{k+1} can be represented by following Taylor expansion with respect to time.

$$u_{k+1} = u_k + \dot{u}_k\Delta t + \frac{\ddot{u}_k}{2}(\Delta t)^2 + \frac{\dddot{u}_k}{6}(\Delta t)^3 + \cdots \tag{7}$$

where the values of $\dot{u}_k$, $\ddot{u}_k$ and $\dddot{u}_k$ are determined from Equation (5).

For the more accurate value of u, the summation upto higher order term in Equation (7) is required. However, considering the calculation time for real-time motion control, we choose to sum upto the third order term.

CONCLUSION

The design of the PVAJT trajectory planner is presented to reduce the burden of trajectory calculation time at every cycle time. This method is applied to the trajectory generation of complex trajectory such as the spline. Also, we formulated a cubic spline trajectory with arc-length parameter which is estimated as exactly as possible by summing upto the 3rd order in Taylor's expansion.

Figure 5 shows the PVAJ trajectory results for the path of cubic spline, that is, starting position [0 0], ending position [100 -100], tangent vectors [300, 0], [0 -300].

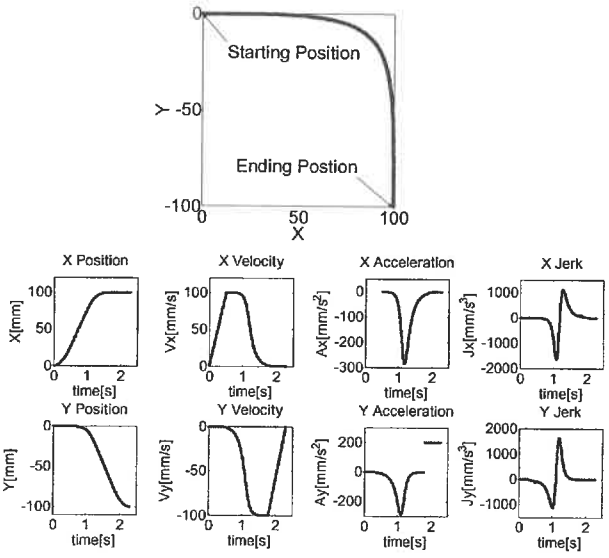

FIGURE 5. Cubic spline path and results of P,V,A,J

ACKNOWLEDGEMENTS

This work was supported by the Short-term Core Technology Development Program funded by the Ministry of Knowledge Econony (MKE, Korea)

REFERENCES

[1] JT Hang, DCH Yang, "A generalized interpolator for command generation of parametric curves in computer controlled machines", Japan/USA Symp Flesible Automat, Vol.1, pp.393-9, 1993.

[2] Y. Koren, C.C. Lo, M. Shpitalni, "CNC interpolators: algorithms and analysis", ASME Manufact Sci Engng, Vol. 64, pp.83-92, 1993.

[3] K. Erkokmaz and Y. Altintas, "High speed CNC systems design. Part 1. Jerk limited trajectory generation and quintic spline interpolation", Int J Mach Tools Manufact , Vol.41, pp.1323-45, 2001.

CONTROL STRATEGIES FOR A DYNAMIC POSITIONING MACHINE AT NANOMETER LEVEL

Raymond H. Yang[1], Chek Sing Teo[2], Eric S. Buice[4], Xianping Liu[3], Weili Wang[3] and Stuart T. Smith[1]

[1]Center for Precision Metrology, The University of North Carolina at Charlotte, Charlotte, NC, USA

[2]Singapore Institute of Manufacturing Technology, Singapore

[3]School of Engineering, University of Warwick, Coventry, UK

[4]PME: Mechatronic System Design, Delft University of Technology, The Netherlands

INTRODUCTION

A dynamic positioning machine for nanoscale engineering has been developed. The system comprises of a 2 DOF long range translation stage carrying a 6 DOF short range stage. The long range stage can traverse an area of 50 mm x 50 mm while the short range stage can provide up to 17 micrometers of linear positioning and 160 x 10^{-6} radians of angular motion to compensate errors generated by the long range stage during traverses. Currently, positioning of the *x*- and *y*-axis along with angular motion about the *z*-axis is monitored by laser interferometers, while positioning of the *z*-axis and angular motion of *x*- and *y-axis* are monitored by 3 capacitance gages. Figure 1 shows the positioning stage and the two different measurement systems.

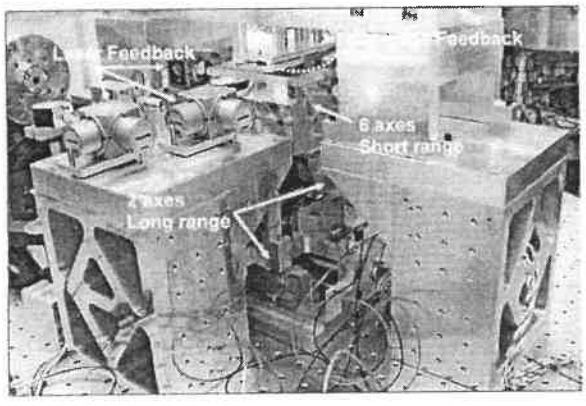

Figure 1: Stage system comprising of a 2 DOF long range stage and a 6 DOF short range flexure-based actuator stage. Current feedbacks include 3 laser positioning signals and a nest of 3 capacitance gages measuring in the vertical plane.

While long range traverse is achieved using a polymeric slideway and feedscrew drive, the fine motion is achieved using a piezoelectrically actuated stage. This design exhibits a number of attributes such as: vacuum compatible assembly, maintains position of long range stage after turning off power, varying load capacity for versatility of applications, nanometer level polymeric bearing noise, low cost components of assembly, high bandwidth scanning for small displacements and low moving mass of the fine motion control. There are, however, a number of challenges associated with the performance characteristics of the actuators and the integration of these two systems having very different dynamic characteristics. This abstract will present current studies to assess these issues. For more details of the stage mechanisms and systems integration, see Buice et al. [1,2,3].

CONTROLLER CONSIDERATION

In past experiments for example, long range stages utilizing sliding contact polymeric bearings, the following characteristics were observed. The frictional component of the slideway bearing is variable during motion. While it may repeat at a specific location the value of the friction coefficient varies with position. Being a stacked system, the motion axes contain a finite coupling in other axes. It has been observed that there is also a micro displacement region that has its own linear dynamic characteristic. In this region, there is a

finite elastic response prior to macroscopic sliding.

For the short range motion controller, dynamic characterization is somewhat simpler due to the fact that this flexure-based actuator can be adequately modeled as a linear system.

CONTROL STRATEGY

The combined stage controller block diagram is shown in Figure 2. At the highest level, the controller is responsible for coordinating fine and coarse motion along with taking images from probe systems associated with the stage.

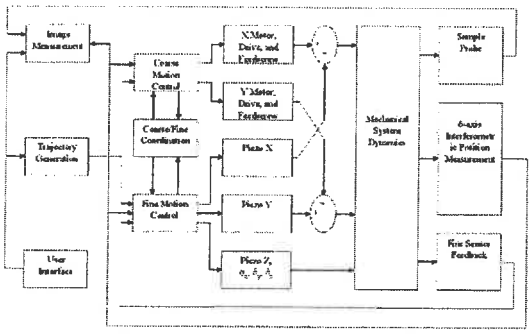

Figure 2: Combined control architecture for dynamic positioning machine.

Fine motion is achieved through a short range stage comprised of six piezoelectric actuators each with a range of 17 micrometers linear motion and up to 160 micro-radians of angular motion. Coarse motion is provided through the long range stage which provides *x*- and *y*-motion up to 50 mm of travel. In the combined controller, the long range stage operates to keep the short range stage in its mid–displacement, while achieving nanometer-scale resolution over the full travel. The short range stage can also be used for fine motion scanning in local targeted areas, while the combined system can serve as a pick-and-place positioning machine.

For a single DOF coarse/fine system of similar design, backlash and lead compensation strategies have been effective for long range traverses responding to sinusoidal demands with controller errors being maintained to within a few 10's of nanometers throughout controlled motions of up to 50 mm [4].

For the multi-DOF system of this study, early studies utilizing simple integral control of the long range stage with lead compensation was not able to maintain a stationary position (short range stage was not operating during these tests). Such operations would be characteristic of the machine operating as a pick-and-place tool. The result of this control strategy is a slow oscillation of the stage during the 'hold' component of the demand. The reason for this is due to the markedly different mechanical characteristics of the system for large and small displacements. For example, when the system is stationary, friction precludes the long range stage from maintaining positioning. This leaves a small residual error between the stationary position of the long range stage that is compensated by the short range platform. While the errors in this instance can be reduced to nanometer levels, this leaves a small error into the integrator of the long range stage controller. The consequence of the stick-slip characteristics of the slideway results in the integrator building up a drive force until sudden sliding motion occurs. The net result is that the system exhibits long time period, duty cycling even when the demand is stationary.

CENTERING METHOD

To overcome the oscillation of the previous controller, experiments (not reported here) have been performed to investigate a switchable controller that deactivates the long range system when the error is within reach of the short range stage during the stationary demand within a pick-and-place operation. However, a more effective controller strategy involves both long and short range stages operating on the demand.

In this case, the long range stage uses feedback from the encoder while the short range stage controller uses the difference between the laser interferometer and the demand to provide an estimate of the positioning error. However, for this system to be capable of reducing the controller error to 'zero', the mid-range deviation of the short range stage is fed into a separate controller that, in turn, provides a second signal that is added to the demand prior to comparison with the encoder position. By driving the short range to its mid-displacement, the combined controller can utilize the full potential of the short range stage actuators to correct for the errors generated by the long range stage during motion. Figure 3 shows a simplified form representing this controller strategy.

The amplifiers used to drive the motors contain a 0.1 V dead-band. This was removed using a deadband compensator to the motor encoder. Currently, the short range stage and mid range positioning is controlled in this new controller using a simple integrator. The long range stage controller comprises dead-band compensation plus a proportional-plus-integral control. Figure 4 shows result for the control of the *y*-axis in pick–and-place operation moving a distance of 3 mm with a stationary time of 20 seconds at each end of the traverse. The data sampling was performed at 1 kHz. Faster sampling intervals up to 10 kHz have been used with little apparent difference in measurement data and system performance. In Figure 4b) it is apparent that there is a considerably larger error

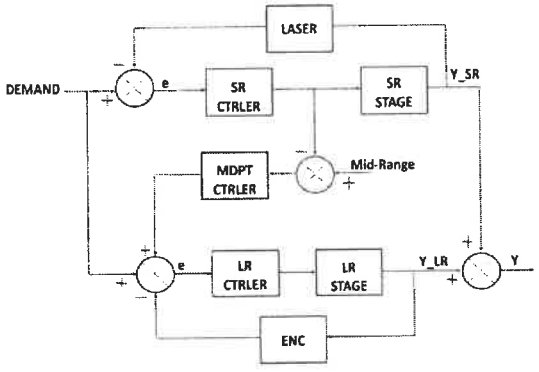

Figure 3: Simplified model of the controller implementing the centering scheme.

(approximately 900 nm rms) during the traverse. By plotting the controller error during the stationary component of the demand trajectory, Figure 4c), the errors reduce to approximately 1.1 nm rms. This is comparable to the noise of the interferometer of approximately 1 nm rms.

For a better understanding of the dynamics, a sinusoidal trajectory was also applied to only the linear y-axis controller and the results of a 5 mm amplitude demand with period of 500 seconds is shown in Figure 5. These four graphs from top to bottom correspond to demand, controller error in the *y-axis*, open loop displacement in the remaining *x*-axis, *z*-axis, and angular displacements about the three axes. Coupling between the *x-axis* and the angular coordinates is apparent from Figure 5. Adding a closed loop control to the 6 DOF fine motion stage enables the displacements in the other 5 DOF to be considerably reduced.

Figure 6 shows results similar to those in Figure 5 for a sinusoidal trajectory of amplitude 15 mm and period 400 seconds. Upon reversal of direction, an angular error of magnitude 0.1 micro radian is apparent. However, during the traverse between changes in direction these angular errors reduce to around 10 nano radians rms. At this stage, the controller errors in the *x*- and *y*-axes are around 0.1 and 1 micrometer

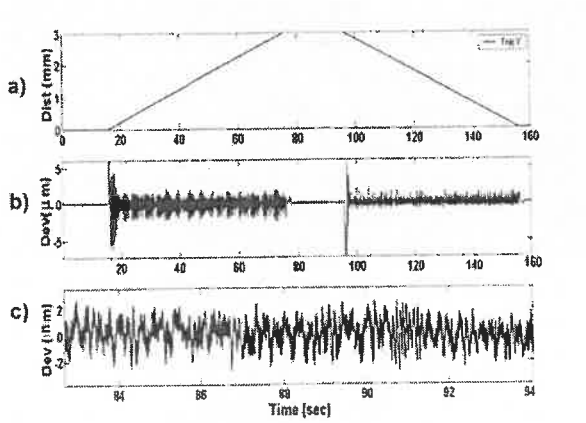

Figure 4: Closed loop control on y-axis trapezoidal trajectory corresponding to a 3 mm traverse, a) Trajectory, b) controller error, c) controller error during stationary component of demand.

respectively. While the traverse rate of 200,000 nm per second is very fast for this system, the error is higher than the target control of better than 10 nm. It is envisaged that correction of some assembly errors in the mechanical system along with further developments in the controller (including smaller sampling intervals) will result in performance improvements.

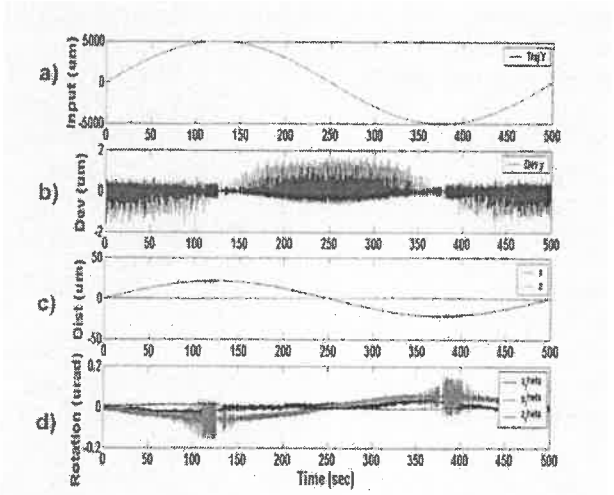

Figure 5: Closed loop control of sinusoidal trajectory of amplitude 5 mm in y direction while all other degrees of freedom are open loop stationary, a) demand, b) controller error, c)linear x and z axes, d) three angular coordinates

Acknowledgements

The authors would like to thank David Trumper and David Otten (MIT) for their valuable contributions. The authors would also like to thank the Center for Precision Metrology (UNCC) and the NSF (DMI-0210543) for financial support of this work. Any opinions, findings, and conclusions or recommendations expressed in this material are those of the author(s) and do not necessarily reflect the views of the National Science Foundation.

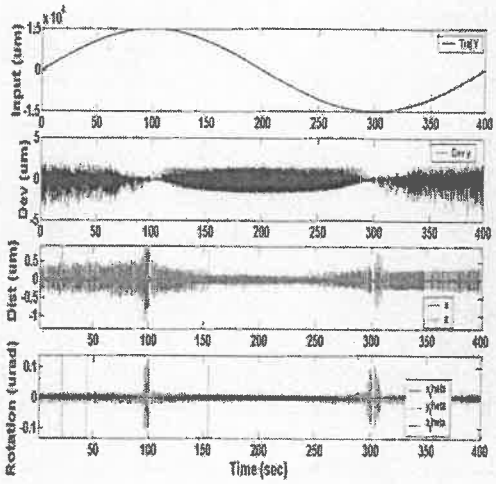

Figure 6: Similar to figure 5 showing closed loop control of a long range sinusoidal motion in the *y* direction of amplitude 15 mm.

REFERENCES

[1] Buice ES, Yang H, Seugling RM, Smith ST, Hocken RJ. Evaluation of a novel UHMWPE bearing for applications in precision slideways. Precision Engineering Journal. 2006; 30 (2): 185 – 191.

[2] Buice ES, Yang H, Smith ST, Hocken RJ, Trumper DL, Otten D, Seugling RM. A comparison of drive mechanisms for precision motion controlled stages. Proceedings of the European Society of Precision Engineering and Nanotechnology. 2006; 6 (1): 321 – 324, ISBN: 0955308208.

[3] Buice ES, Smith ST, Hocken RJ, Trumper DL, Otten D, A versatile, long-range, positioning system for mechanical probe studies, Preceedings of the American Society for Precision Engineering. 2007; 40.

[4] Buice ES, Otten D, Yang H, Smith ST, Hocken RJ, Trumper DL Seugling RM. Control of a 2 DOF long-range and 6 DOF short-range stages for nanometer positioning. Proceedings of the American Society for Precision Engineering. 2006; 37.

IMPROVEMENT OF ADHESIVE STRENGTH FOR TI-DOPED DLC FILMS BY HEAT TREATMENT IN VACUUM

Masao Kohzaki
Department of Mechanical Engineering
Tokai University
1117, Kitakaname, Hiratsuka, Kanagawa 259-1292, Japan

INTRODUCTION

Diamond-like carbon (DLC) films have many excellent properties, such as high hardness, small friction coefficients and low chemical inertness [1,2]. So there is a large amount of industrial interests in developing DLC coating. However, DLC films are limited to the large-scale use because of the weak adhesive strength to substrates. Our attention was focused on improving the adhesive strength of DLC films to substrates by doping of titanium as an active element and subsequent heat treatment in a vacuum.

EXPERIMENTAL

The Ti-doped DLC films have been prepared on monocrystalline silicon substrates by DC magnetron sputtering with carbon and titanium targets in Ar plasma. Figure 1 shows the schematic diagram of DC magnetron sputtering apparatus used for the Ti-doped DLC film preparations. The input target power for carbon was fixed at 400 W. To control the amount of titanium in the film and to investigate influence of titanium contents on chemical bonding states, the target power for titanium varied from 0 to 200 W at a constant substrate temperature of 250 °C. Furthermore, for improving the mechanical properties such as adhesive strength of the thin films, the substrate temperatures ranged between 25 and 350 °C at the target power for titanium of 100 W. The residual pressure in the deposition chamber was 2×10^{-4} Pa. The film depositions were carried out at an Ar gas flow rate of 50 sccm and under a work pressure around 3 Pa. The deposition time was varied to obtain the films with constant thickness. The film thicknesses were measured to be around 1 μm using a surface profilometer (DEKTAK IIA).

After the deposition, the DLC and the Ti-doped DLC films were heated at 500 °C for 10 minutes in a vacuum of 1×10^{-4} Pa. Heating was controlled at rate of 5 °Cmin^{-1}.

The chemical composition and bonding states of the Ti-doped DLC films were investigated by X-ray photoelectron spectroscopy (XPS). In the XPS analyses, the binding energies of C 1s and Ti 2p were measured after Ar^+ ion sputter cleaning. Secondary electron microscopy (SEM) images and transmission electron microscopy (TEM) images were acquired at an operating voltage of 200 kV to investigate the microstructures around the interface between the Ti-doped DLC films and the silicon substrate.

Nano-indentation hardness measurements were carried out with a trigonal (Berkovich) diamond indenter using a commercially available equipment (Nano Indentation Tester ENT-1100a: ELIONIX). Maximum indentation load was 3 mN. Scratch tests for evaluating the adhesion of the films to the silicon substrates were made on a RESCA scratch tester CSR-02 device. The frictional properties of the Ti-doped DLC films were examined using a ball on disk tester in an ambient atmosphere. An AISI52100 ball of 5 mm in diameter was slid against the films at a normal load of 0.5 N and a sliding speed of 30 mm/s.

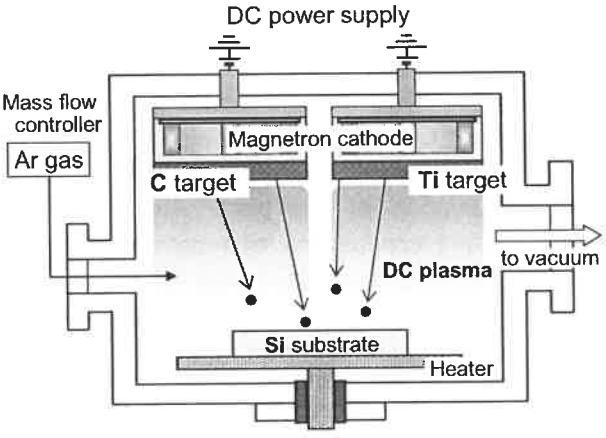

FIGURE 1. Schematic diagram of DC magnetron sputtering apparatus used for the Ti-doped DLC film preparations.

TABLE 1. Chemical composition of the Ti-doped DLC films (at.%).

Deposition Temp. (C)	Input Power to Ti (W)	C	O	Ti
25	100	87	3	10
250	0	100	0	0
250	100	87	3	10
250	200	82	3	15
350	100	87	3	10

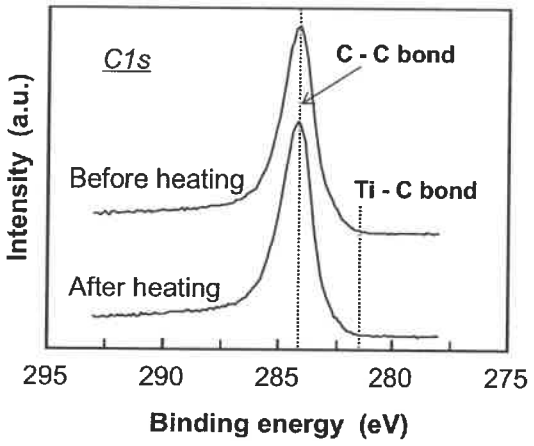

FIGURE 2. C1s spectra of Ti-doped DLC films with Ti content of 15 at.% measured by XPS.

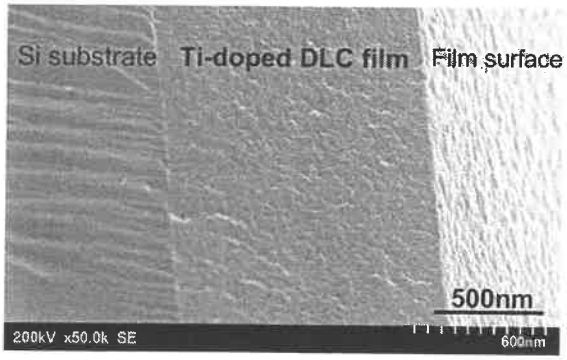

FIGURE 3. Cross sectional secondary electron microscopy image of the Ti-doped DLC film around the interface after the heat treatment.

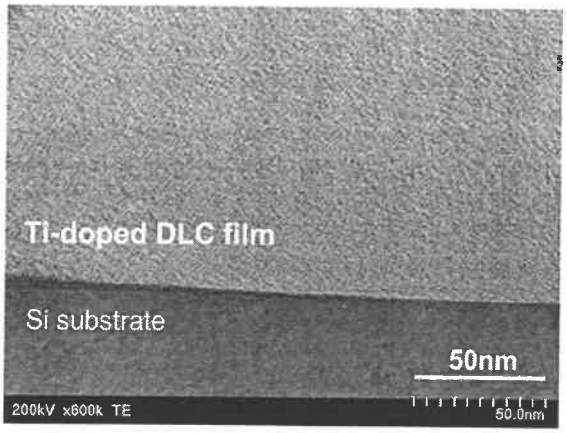

FIGURE 4. Cross sectional transmission electron microscopy image of the Ti-doped DLC film around the interface after the heat treatment.

COMPOSITION AND BONDING STATE

The chemical composition of the Ti-doped DLC films is shown in Table 1. The titanium concentration, measured by X-ray photoelectron spectroscopy, was 10 at.% at a titanium target power of 100 W irrespective of the deposition temperatures. As increasing the target power for titanium, titanium contents in the films increased up to 15 at.%. The XPS analyses revealed that oxygen concentrations in the Ti-doped DLC films were around 3 at.%.

Figure 2 illustrates C 1s peaks in XPS spectra of the films prepared at the titanium target power of 200 W. It should be noted that no significant variations in the C 1s binding energy by the heat treatment were found. As shown in Figure 2, the C 1s peak had only one component at the binding energy of 284.2 eV, which assigned as the C-C bond [3]. The C 1s peak attributed to carbon binding to titanium, which is reported to be 281.5 eV [4], was not observed. Therefore, the Ti-C bond formation is not thought to be promoted by the heat treatment at 500 °C in the vacuum.

MICROSTRUCTURE

Figure 3 shows the cross sectional SEM image of the film prepared at the titanium target power of 200 W and heated at 500 °C in the vacuum. It can be seen from Figure 3 that the surface roughness of the film was small and that the interface between the film and the silicon substrate was clear even after the heat treatment. To investigate the microstructure around the interface in detail, the TEM observation was carried out. However, in the cross sectional TEM image of the film, no mixing of elements was found to occur around the interface as shown in Figure 4.

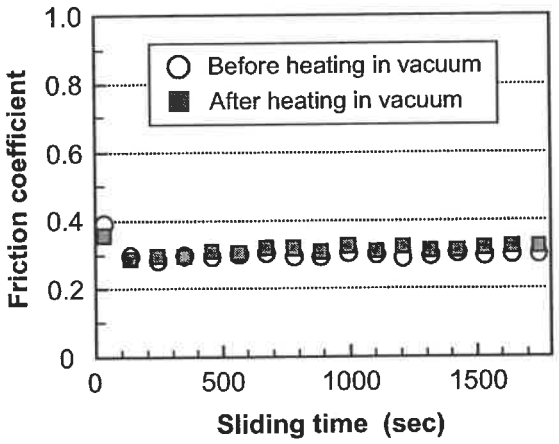

FIGURE 5. Friction coefficients of the Ti-doped DLC films prepared at the titanium target power of 200 W.

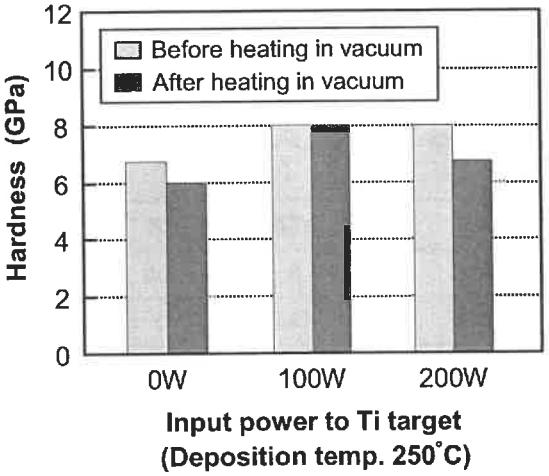

FIGURE 6. Nano-indentation hardness of the Ti-doped DLC films prepared at various target power for titanium.

FRICTIONAL PROPERTY

Figure 5 indicates friction coefficients of the Ti-doped DLC films prepared at the titanium target power of 200 W against a AISI52100 ball. While the friction coefficient of the silicon was around 0.7, those of the films were stable at 0.3. Even after the heating, the Ti-doped DLC films showed the good tribological performance with a low friction coefficient below 0.3 as shown in Figure 5. It should be noted that no measurable wear was observed on the surface of the heat treated films after the friction tests.

NANO-INDENTATION HARDNESS

Nano-indentation hardness of the Ti-doped DLC films prepared at various target powers and at 250 °C is shown in Figure 6. As described before, titanium contents in the film increased with increasing the target power for titanium. However, titanium contents have a small influence on the nano-indentation hardness of the film before heating in the vacuum. In addition, the nano-indentation hardness of the film is almost unchanged by the heat treatment.

Figure 7 indicates the nano-indentation hardness of the Ti-doped DLC films prepared at various deposition temperatures and at the titanium target power of 100 W. As the deposition temperatures increased, the nano-indentation hardness of the films before the heat treatment decreased slightly. On the contrary, apparent dependence of the nano-indentation hardness on the deposition temperatures was not observed after heating in the vacuum.

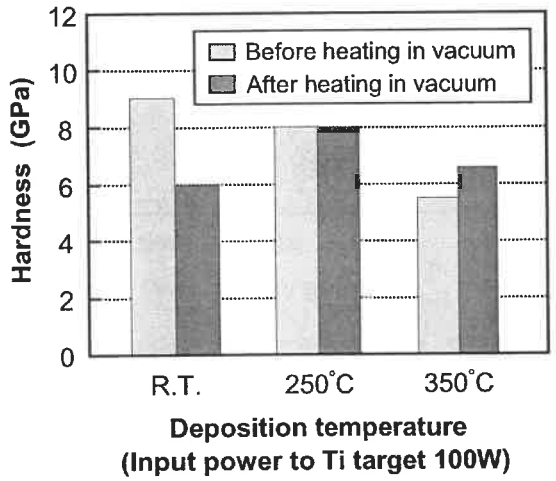

FIGURE 7. Nano-indentation hardness of the Ti-doped DLC films prepared at various deposition temperatures.

ADHESIVE STRENGTH

Figure 8 shows critical loads in scratch tests for the Ti-doped DLC films prepared at various target power for titanium and at 250 °C. The Ti-doped DLC films prepared at 250 °C had almost constant values of the critical loads irrespective of the target power for titanium (of the titanium concentration). By the heat treatment in the vacuum, the adhesion of the Ti-doped DLC film with high titanium concentration was improved effectively and the critical loads of the films containing 15 at.% titanium increased from 180 mN to 400 mN.

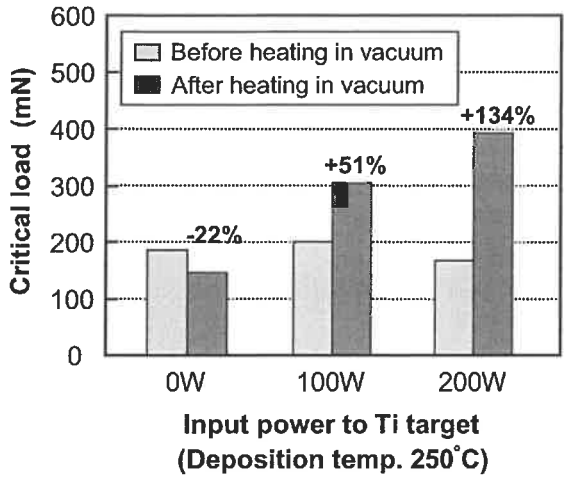

FIGURE 8. Critical loads in scratch tests for the Ti-doped DLC films prepared at various target power for titanium.

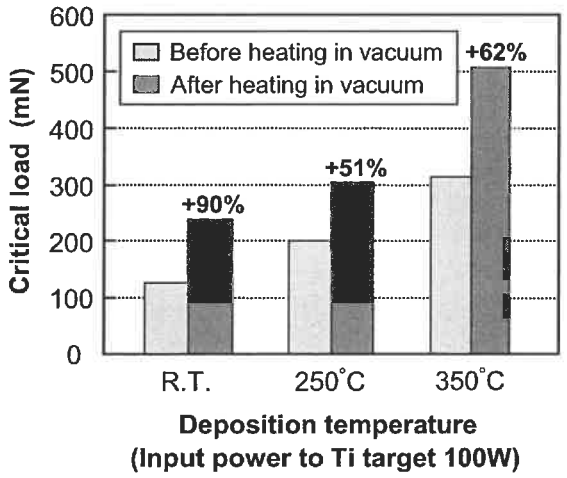

FIGURE 9. Critical loads in scratch tests for the Ti-doped DLC films prepared at various deposition temperatures.

The critical loads in the scratch tests for the Ti-doped DLC films prepared at various deposition temperatures and at the titanium target power of 100 W are shown in Figure 9. The critical loads of the Ti-doped DLC films increased with increasing the deposition temperatures. In addition, the heat treatment in the vacuum was effective for improving the adhesive strength of the film. The heat treated Ti-doped DLC films deposited at 350 °C had the maximum critical load of 500 mN. The apparent increase in the critical loads will be caused by the chemical interaction between titanium in the film and the substrate material.

FUTURE WORK

In this study, an obvious mixing layer was not observed around the interface between the Ti-doped DLC film and the substrate even after the heating at 500 °C for 10 minutes in the vacuum. However, the film formation process mentioned above is thought to be one of the interface design method for improving the adhesion of DLC films and is expected to be rather effective for producing the high adhesion on titanium alloys, which are widely used in the biomedical applications such as the artificial hip joint.

ACKNOWLEDGEMENTS

The author gratefully acknowledges the financial support provided for this research by Osawa Scientific Studies Grant Foundation.

REFERENCES

[1] Tsai H. C, Bogy D.B. Journal of Vacuum Science and Technology. 1987; 5: 3287-3312.
[2] Platon F, Fournier P, Rouxel S. Wear. 2001; 250: 227-236.
[3] Pan W. J, Sun J, Ling H, Xu N, Ying Z. F, Wu J. D. Applied Surface Science. 2003; 218: 297-304.
[4] Schroeder A, Francz G, Bruinink A, Hauert R, Mayer J, Wintermantel E. Biomaterials. 21, 2000; 21: 449-456.

INVESTIGATION ON LASER INTERACTION IN ANNEALING OF AMORPHOUS SILICON FILMS BY PULSED Nd^{3+}:YAG LASER

I. A. Palani [1], Nilesh J. Vasa [2], M. Singaperumal [1]
[1]Precision Engineering and Instrumentation Laboratory
Department of Mechanical Engineering
[2]Department of Engineering Design
Indian Institute of Technology Madras, Chennai 600036, India

INTRODUCTION

Semiconductors such as crystalline silicon play a major role in the application of MEMS devices and photovoltaic application, such as solar cells. Particularly, photovoltaic cells based on silicon are increasingly considered as one of the attractive renewable energy sources. However the resulting cost is high and overall size is limited. Hence an alternative cost-effective approach may be considered by employing laser annealing technique. Laser annealing technique is widely used to repair the defects caused during ion implantation in semiconductor processing [1]. This technique can also be extended to induce crystallization and modify amorphous silicon (a-Si) thin films to produce doped-poly-silicon films.

In this paper frequency tripled pulsed Nd^{3+}:YAG laser (355 nm) is made to interact on amorphous silicon thin films coated on the glass substrate. The surfaces of the treated samples are analyzed through Scanning Electron Microscope (SEM) and Raman spectroscopy to estimate the extent of crystallization and ablation. A one dimensional heat equation model is used to estimate the annealing and the ablation threshold in the laser treatment of a-Si films and to investigate the effect of parameters in annealing of a-Si films. The change in surface morphology in a-Si films due to the laser interaction has been correlated with the experimental and theoretical results to optimize the laser fluence for efficient annealing of a-Si for the production of polysilicon films.

THEORETCIAL INVESTIGATION ON LASER ANNEALING OF SILICON FILMS

Laser annealing is a kinetic process where heating is used to change the microstructure through diffusion. When the laser is made to interact on the surface of a silicon film, it absorbs the energy. This absorbed photon energy makes the atom to vibrate and due to this heat starts to dissipate on to the surface. When the silicon film is irradiated with a laser with incident intensity I, according to Beer Lambert's law, the variation of the intensity (transmitted intensity) with depth is given by $I = I_0 \times \exp(-\alpha x)$. Where I_o is the incident beam intensity (W/m ^{2}), I is the transmitted intensity (W/m^2), x is the depth (m), α is the absorption coefficient (1/m) and R is the reflectivity of the surface. The optical energy ion absorbed by the silicon is converted into the thermal energy which is responsible for increase in a temperature of the film.

In this paper the heat flow on the surface of amorphous-silicon film is considered as one dimensional. The heat balance equation can be derived as,

$$\rho \mathrm{Cp}\ \frac{\partial T}{\partial t} = a \times (1-R) \times I_0 \exp(-a \times x) + k \frac{\partial^2 T}{\partial x^2} \quad \ldots\ldots\ldots 1$$

Where ρ is the density of the material (kg/m^3), C is the specific heat capacity of the material (J/kgK), a is the absorption of silicon, and K is the thermal conductivity of the material (W/mK). The above parabolic heat balance partial differential Eq.1 was solved using linear homogenous transformation system by considering initial and boundary conditions as $T(x,0)=0$; $T(x,t) = 0$ at $x = l$ and $K \neq 0$ [2]. The assumptions considered were: 1)The heat flow is one dimensional and it involves conduction only in one direction, i.e. along the depth; 2) Re-radiation of energy from the surface is negligible; 3) The thermal properties of the absorbing material are independent of the temperature; 4) The intensity and temperatures were calculated for single pulse duration t = 19 ns.

EXPERIMENTAL INVESTIGATION

The laser annealing was performed using a pulsed laser ablation equipment as shown in

Fig. 1. The third harmonic of Nd^{3+}:YAG laser (355 nm) was used with a 10 Hz repetition rate and a pulse width of 19 ns. The laser beam intensity profile was Gaussian and with a beam spot size of 6 mm. Amorphous-Si thin films (400 nm) coated on alkali-free glass wafers (total 0.5 mm thickness) were mounted on an X-Y stage. Laser beam was focused on the a-Si thin film with the focal length of 300 mm and irradiated spot size was approximately 1.5 mm in diameter.

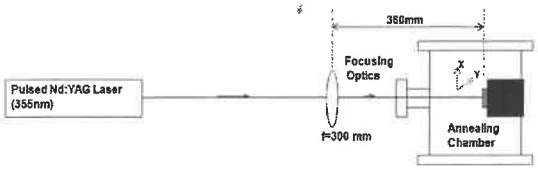

Fig.1 Experimental setup for laser annealing

a-Si coated glass wafers were cut into 15mm × 15mm square pieces and cleaned before mounting on the equipment for annealing. The laser treatment was done in the atmospheric condition. To investigate the influence of the laser fluence on annealing and ablation processes, the a-Si films were treated with different fluence values by altering the laser beam energy. The experimental conditions including sample specifications are described in Table1.

Table 1 Experimental parameters

LASER SPECIFICATION	
Laser	Nd^{3+}:YAG
Wavelength	355 nm
Pulse width	19 ns
Frequency	10 Hz
Energy	20 – 100 mJ
Diameter of the irradiated spot	≅1.5 mm
AMORPHOUS SILICON SPECIFICATION	
Coated substrate	Alkali free glass
Coated thickness	400nm thick
Thickness including the substrate	500μm

RESULTS AND DISCUSSION

A. Crystallization regime and ablation threshold in laser annealing of a-Si films

When high intensity, short pulse-duration laser pulses are made to interact on the surface of the a-Si, the surface temperature reaches above or near to the melting point. As a result Si reaches the liquids temperature and starts getting crystallized as it cools. The crystallization of a-Si starts well above 900 °C and when the temperature exceeds above the melting point 1480 °C [3], it results in an ablation. The effect of the laser fluence value on the corresponding temperature of the irradiated zone was calculated using Eq. (1) and plotted as shown in Fig. 2. Subsequently, the threshold fluence values for the crystallization and the ablation processes were estimated.

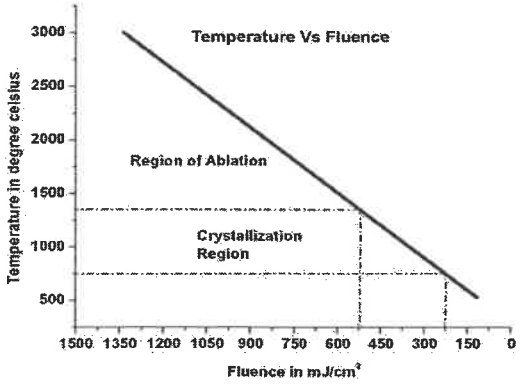

Fig.2 Influence of laser fluence on irradiated surface temperature.

The minimum temperature required for crystallization is 900 °C and the corresponding fluence value was estimated to be around 230 mJ/cm^2. The crystallization regime for a-Si films lies between 750℃ and 1480 °C and the corresponding fluence values are estimated to be between 225mJ/cm^2 and 510 mJ/cm^2. When the films are treated with fluence value higher than the melting fluence (> 520 mJ/cm^2) it results in ablation on the surface. The surface characteristics of a-Si thin films after the laser irradiation were investigated by the scanning electron microscopy technique (SEM) and Raman spectroscopy.

B. Temperature and Recrystallization depth

The amount heat incident on the a-Si thin film was estimated by using Eq. 1 for different laser fluence values. Figure 3 shows the temperature versus annealed depth for different laser fluence values.

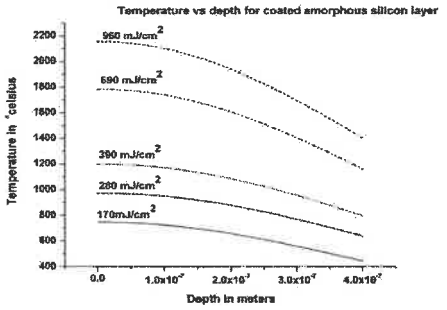

Fig.3 Temperature distribution along the depth of a-Si film

When the laser beam with the fluence of 170 mJ/cm^2 was made to interact on the surface of the a-Si film the corresponding temperature incident on the surface was around 760°C and the temperature was decreased towards the depth of the coated a-Si. When the laser fluence of 280 mJ/cm^2 was made to interact on a-Si the corresponding incident temperature on the surface was estimated to be around 980 °C and the recrystallization depth was estimated to be around 0.1μm depth . When the laser fluence was at 390mJ/cm^2 the incident temperature was expected to be around 1170℃ and the corresponding recrystallization depth was estimated to be around 400 nm. When the laser threshold fluence value was set to 690mJ/cm^2 and at around 960 mJ/cm^2, the temperature was expected to reach above the melting point of a-Si which results in agglomeration and successive ablation of the a-Si films.

C.Surface Characterization of a-Si Films

Laser induced surface modification in silicon was studied through a scanning Electron microscope (SEM) and Raman spectroscopy to investigate the extent the crystallization and to estimate the ablation threshold. Figure 4 shows SEM photographs of a–Si films on glass substrates. Figure 4(a) shows the SEM photograph of the untreated amorphous silicon and no trace of grain or grain boundary was found at high magnification of 6000X. When the amorphous wafers are treated with a fluence of 170mJ/cm^2, a minor modification on the surface was observed at 5000X magnification as shown in Fig. 4(b).

This represented that the laser fluence was not sufficient to start the crystallization but it was sufficient enough to impart a minor structural change. When the laser fluence was increased to 280 mJ/cm^2 the surface was modified as shown in Fig. 4(c). When the laser fluence of 390mJ/cm^2 was made to interact on the surface of a-Si film, grain growth was observed as

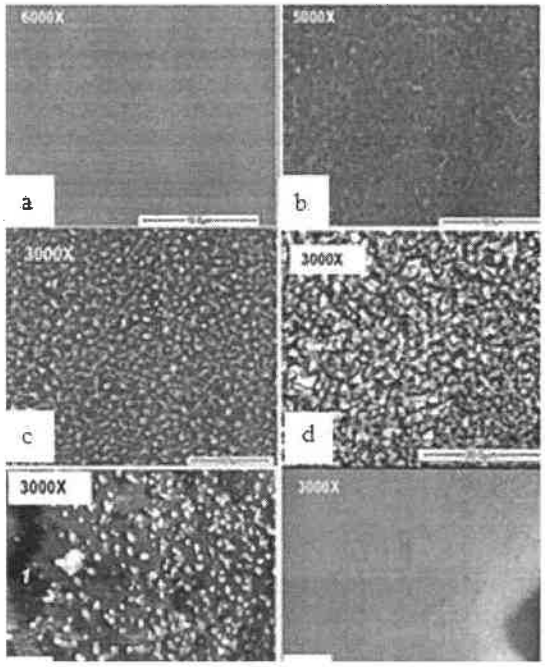

Fig.4 SEM photographs of a-Si films a) untreated b) treated at 170mJ/cm^2 C) 280 mJ/cm^2 d) 390 mJ/cm^2 e) 690 mJ/cm^2 f) 960mJ/cm^2

shown in Fig. 4(d). As compared to the lower fluence values, the grain growth was increased and uniformly distributed with the laser fluence value of around 390mJ/cm^2. When a-Si films were treated with a higher fluence of around 690mJ/cm^2, formation of spherical beads like structure which is termed to as agglomeration [4] was observed accompanied by an ablation as shown in Fig. 4(e). The diameter of the bubbles varied from a few micrometer to few tens of micrometer in size. The agglomeration created holes or spherical beads in the continuous a-Si films resulting into a serious damage. The agglomeration might have been due the boiling of molten Si. During the laser irradiation, outburst of heterogeneously nucleated vapor bubbles might have been promoted by the poor wetting property of a-Si film. When the a-Si films were treated with a fluence of 960mJ/cm^2, a complete ablation was observed and the silicon film was completely removed in the irradiated region and the alkali free glass substrate was observed as shown in Fig. 4(f).

To investigate the extent of crystallinity the laser annealed samples were analyzed by using the Raman spectroscopy technique. Figure 5 shows the typical Raman spectra before and after laser treatment (with different laser fluence values). Crystalline silicon peak is also included to

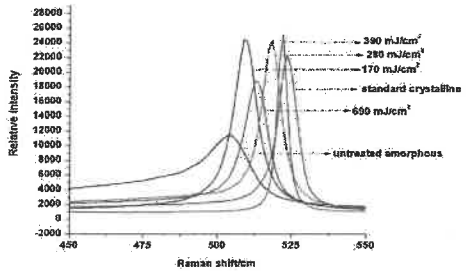

Fig.5 Raman spectra of the laser annealed samples

Investigate the extent of crystallization. As shown in Fig. 5 there is a broadening of peak from 480-520 cm^{-1} for the untreated sample as compared to the other peaks treated at different laser fluence values.

The SEM photographs and the Raman spectra illustrated above can be correlated with the irradiated sample temperature and crystallization. When the laser fluence of 170 mJ/cm^2 was incident on the surface of a-Si the corresponding irradiated zone temperature was theoretically estimated to be around 760 °C which results in minor modification of the surface and this has been confirmed through the SEM photograph and the peak in the Raman spectra for the laser fluence of 170 mJ/cm^2 is also slightly narrower than that of the untreated a-Si sample. When the laser fluence was set at 280 and 390 mJ/cm^2 the corresponding temperature values were estimated to be 980 &1170 ℃, respectively, which is the crystallization regime and this has been confirmed through the SEM photograph and the Raman spectra where the peaks are narrow and lie within the range of standard crystalline peak as can be seen in Fig. 5. When the laser fluence was set at 690 mJ/cm^2 and 960 mJ/cm^2 the corresponding theoretical temperature values were estimated to be around 1800 and 2150℃, respectively, which were well above the melting point. This resulted in agglomeration and ablation of the a-Si film surfaces. This was also confirmed through the SEM photograph. Further, with the laser fluence value of 960 mJ/cm^2, the temperature of the glass substrate was reached above the ductile to brittle transition temperature and crack formation on the surface of the glass was clearly observed as shown in Fig. 4(e). Based on the surface morphology and Raman spectroscopy studies, theoretical estimation of annealing and ablation regime were in good agreement with the experimental observations.

CONCLUSION

The influence of frequency tripled third harmonic pulsed Nd^{3+}:YAG laser of 355nm in annealing of a-Si films has been investigated with different laser fluence values experimentally and theoretically. The films were analyzed using SEM and Raman spectroscopy. The amount of heat incident on the surface was been analyzed theoretically by solving one dimensional heat equation. The depth attained at different fluence was estimated. The theoretically estimated temperature of the irradiated region was highly matching with the results analyzed through SEM photographs and the Raman spectroscopy.

The laser fluence for the efficient production polycrystalline silicon films is estimated to be between 300 mJ/cm^2 and 500 mJ/cm^2 for a thickness of 400 nm of a-Si films coated on glass substrates. The laser fluence for ablation threshold is estimated to be above 525mJ/cm^2. This study can be extended to deposit an a-Si layer on a doped c-Si substrate by using a pulsed laser deposition (PLD) technique and subsequently annealing the same surface to produce a polysilicon surface. Subsequent doping of the polysilicon thin-film can allow fabrication of a hetrojunction layer on Si wafer and photovoltaic devices.

ACKNOWLEDGEMENT

Authors are grateful to Prof. M. S. Ramachandra Rao for allowing the use of the laboratory facility and Maneesh Chandran for assisting in the experiments.

REFERENCES

[1] A. G. Aberle, "Fabrication and characterization of crystalline silicon thin film materials for solar cells," Thin Solid Films, 511-512 (2006) 26 -34

[2] R. Gospavica, M. Sreckovicb, V. Popovc, G. Todorovica, "3D modeling of material heating with the laser beam for cylindrical geometry," Journal of Mathematical and Computer Modeling, 43 (2006),620-631

[3] C.S. Hau-Riege, S. P. Hau-Riege and C. V. Thompson, "Simulation and microstructural evolution induced by scanned laser annealing of metallic interconnects," J. Electronics Materials, 30 (2001) 11 – 16

[4] M. He, R. Ishihara, W. Metselaar, K. Beenakker, "Agglomeration of amorphous silicon films with high energy density excimer laser irradiation" Thin Solid Films, 515 (2007) 2872-2878

SELECTION OF PRECISION ACTUATORS BY NOVEL FUNCTION-STRUCTURE-CORRESPONDENCES

Torsten Erbe[1], József Król[1], Tom Ströhla[2] and René Theska[1]

[1]Dept. Precision Engineering
[2]Dept. Design of Mechatronic Actuators
Faculty of Mechanical Engineering
Technische Universität Ilmenau
Ilmenau, Thuringia, Germany

INTRODUCTION

High precision drive systems are used in manufacturing and measuring machines. They have to fulfil mutually contradictory positioning requirements like high resolution, large positioning range, high stiffness, low friction, self locking and so on. Further on, a high degree of efficiency is required to reduce power loss and heat introduction into the system. In state of the art positioning systems gearless drives are often used in order to eliminate play and friction and to increase stiffness of the positioning system by omitting transmission mechanisms.

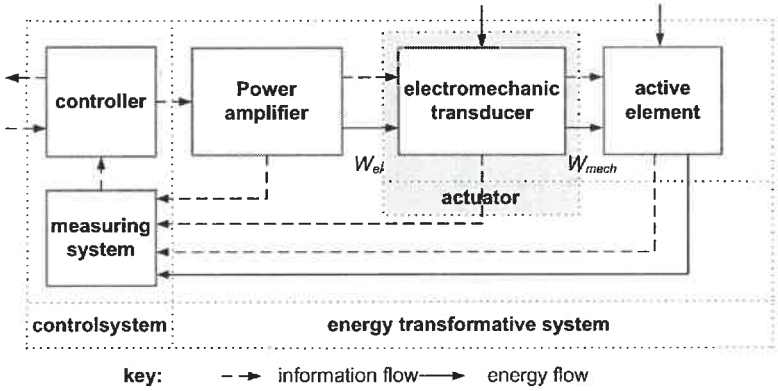

FIGURE 1. Principle of gearless drives

The design of a precision positioning system is a typical example of mechatronic design. While choosing the working principle and actuator fitting best to the positioning task, magnetic, electrical and mechanical properties of all of these principles have to be considered at the same time. The engineer has to be aware of possible actuator principles and has to consider a lot of trade-offs to reach precision requirements of the acquired positioning system. This huge and complex number of dependencies on characteristics and properties is not yet manageable by the engineer on the holistic way.

The aim of the research is to widen up the considered solution space of actuators and working principles. Intention is to help the designing engineer to confine the variety of potential actuators with a software-supported tool. By taking property-correspondences into account, a precision requirement driven actuator selection is possible.

CONTEXT OF ACTUATOR SELECTION

Existing design approaches of heterogeneous systems are limited to domain-specific design methods featuring a general solution plan [1, 2, 3]. They define an overall function to be implemented and assume for this reason so-called function structures, which realise the needed overall function by arrangements and correlation of sub-functions. During this design phase concepts are usually refined by (many) iterations. Figure 1 is an example of a functional structure, a block diagram of a gearless drive.

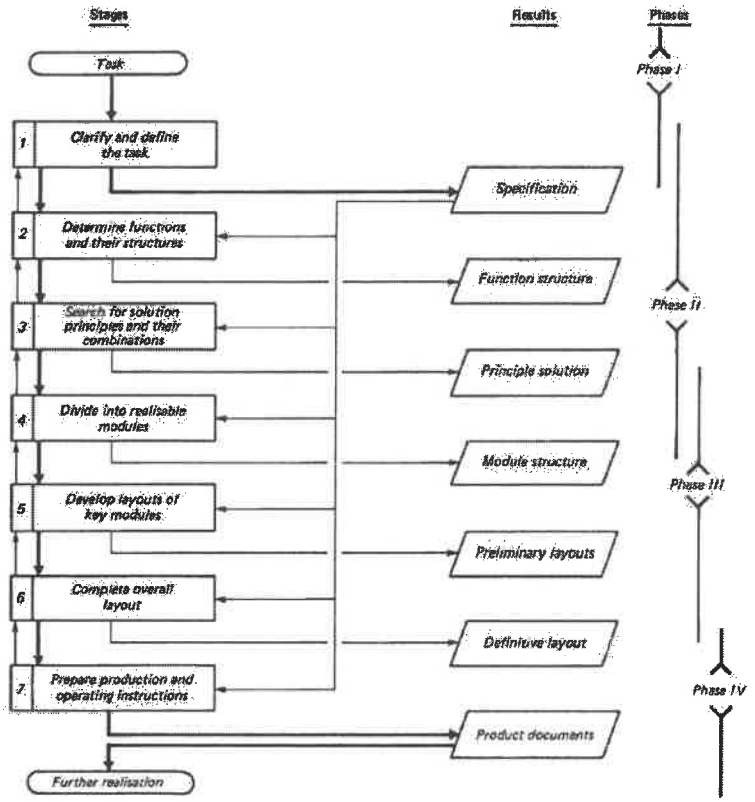

FIGURE 2. Stages of design process [2]

The next step is the transition from the functional description to a structural description. During this transition, in a first step the working principle of the positioning system has to be defined. Thereby most of the properties of the actuator affecting precision are assigned [4]. Defining the working principle of the solution is the crucial issue of the design process and is also ambiguous. Decision on the working principle are followed by embodiment design considerations, usually in several steps before the final solution is defined in all details. Figure 2 shows the stages of the design process with its different design phases and possible iterations.

Until now engineers use established parameters (e. g. power, power density, efficiency factor, etc.) while defining solution principles in the design process. The knowledge of dependencies is based solely on experience of the engineer and only supported by design catalogues. That is why actuators of positioning systems are chosen out of the known, and not of the possible solution space, resulting in a long concept iteration time.

The new function-structure-correspondence tables are a systematic approach applied on gearless drive in the concept stage of the mechatronic design process.

CONCEPT OF ACTUATOR SELECTION

Basic assumptions

Currently used parameters for actuator description represent dependencies of known solutions. These solutions are mostly not comparable, because of differing working principles and nonlinearities. They are able to describe, but not to compare actuators. Figure 3 shows properties and parameters of gearless drives. Those parameters can be single values (e. g. volume, momentum, mass) or combinations (e. g. power, density, efficiency, specific power). Basically only input-, output- and inner parameters of the positioning system can be used as parameters and requirements.

Thereof according to [5] are:

- Properties describe the behaviour of the product (e. g. weight, reliability, robustness, precision). They can not be directly influenced by the designer.
- Characteristics describe the structure, shape

and material consistency of a product (e. g. material, geometry, dimensions, etc.). They can be influenced by the designer.

- Parameters are characteristics and properties given by requirements and their combinations.

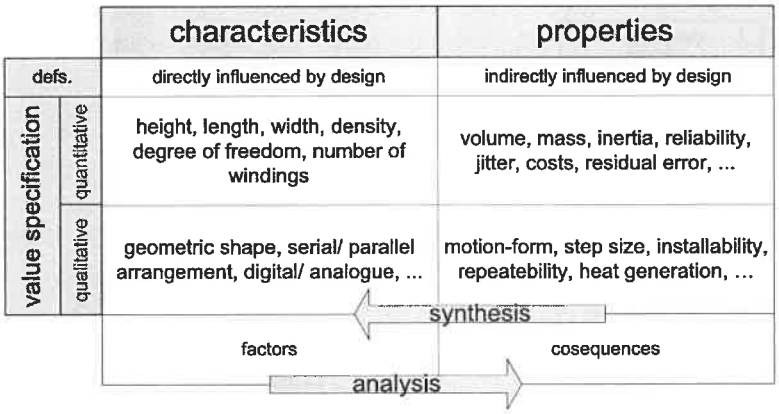

FIGURE 3. Properties and characteristics of gearless drives

Number and type of Actuator Requirements

During the design process the list of requirements of positioning system is specified gradually. While defining the working principle of an actuator, the engineer has to deal with following fundamental problems:

- the number of requirements < decision relevant parameters of structure < number of possible parameters,
- parameters of different working principles are different in quality and quantity,
- parameters of a system mostly depend on multiple characteristics,
- known values of parameters result from layout of actuator and not from working principle itself.

In the function-structure-transition state in the design process many parameters are already defined but not yet usable:

- complete qualitative description of required movement (e. g. degree of freedom, rotary/translatory, limited or unlimited in range),
- all relevant quantitative kinematic and dynamic parameters (velocity, acceleration, momentum, etc.) of required movement,
- generalised quantitative embodiment parameters (generalised volume, width, length, mass,etc.). They can be minima, maxima and value ranges,
- discrete parameters concerning functional restrictions (no magnetic fields, free of sparks, etc.).

Parameters dealing with environment, cost, or machining and manufacturing aspects are determined but can not be taken into account in this early level of the design process.

STRUCTURE OF FUNCTION-STRUCTURE-CORRESPONDENCE-TABLE

The first step of actuator selection is a classification of drives by qualitative movement parameters. The quantitative properties of actuators may be differing, but they can only be compared if their qualitative movement parameters are equal.

According to requirements like kinematics, dynamics, inputs, outputs and embodiment, parameters are correlated. Combinations and unique properties can be taken into account as well. Thereby the engineer is not limited to preassigned values of specific actuators in catalogues and the developing engineer can use every combination of given requirements to choose working principles. The function-structure-correspondences are implemented as a database with characteristic values of known working principles.

Figure 4 shows the principle of the database. The database contains active principles. With values from the specifications solution areas are defined. During the design process the developing engineer specifies more and more values, adapted active principles are chosen from the narrowed solution space and the space of structural shapes, respectively. The user interface is a graphical front end.

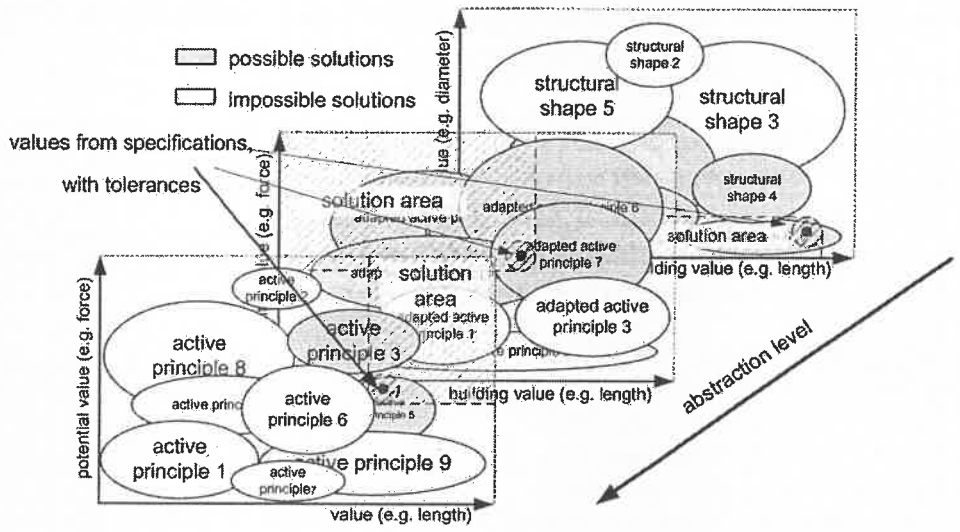

FIGURE 4. Principle of function-structure correspondences table

The existing prototype of the function-structure-correspondence table is a relational database. Query of the database is carried out with user-given parameters in a search screen, with Java-driven background technology. The relational database model and the mathematical description of the known correspondences as a table are programmed in SQL. For future optimisations and modifications the software structure of the database is expandable. The contents of the database can be broadened separately. The actual prototype classifies the driving systems in a database. Presently the content of the database is being extended.

CONCLUSIONS AND FURTHER WORK

Contrary to common abstract design catalogues the information in function-structure-correlation-table:

- it is not classified according to fixed principles, which leads to a new, higher quality of abstraction than a construction catalogue,
- the interdisciplinary and explicit correlations on characteristics and properties are taken into account and
- it is software-based and thus the database is expandable and updatable.

The function-structure-correlation-table is consequently widened up the basis of information like an abstract design catalogue and additionally works as a novel selection assistant for actuator principles. By interlinking interdisciplinary correlations on characteristics and properties, it is for the first time possible to make statements about precision during the concept stage of design and reduce the required number of concept iterations.

ACKNOWLEDGEMENTS

The authors would like to thank the German Federal Ministry for Education and Research (BMBF), Project Management (FZ) Jülich for their support.

REFERENCES

[1] VDI 2206: Design methodology for mechatronic systems [VDI-Guideline]; 2004.

[2] Kallenbach E. Systementwurf – Methoden zum systematischen Entwurf, mechatronischer Produkte des Maschinenbaus. In: VDI/VDE Handbuch Mechatronik-Workshop. VDI-Verlag; 2007. .

[3] VDI 2221: Systematic approach to the development and design of technical systems and products [VDI-Guideline]; 2005.

[4] Hansen F. Konstruktionswissenschaft. Verlag Technik; 1974.

[5] Weber C. CPM/PDD – An extended theoretical approach to modelling products and product development processes. In: Proceedings of the 2nd German-Israeli Symposium on Advances in Methods and Systems for Development of Products and Processes. Fraunhofer-IRB-Verlag; 2005. .

MINERAL CASTING AS MATERIAL FOR MACHINE BASE-FRAMES OF PRECISION MACHINES

Torsten Erbe, József Król, and René Theska
FG Feinwerktechnik/ Precision Engineering
Fakultät für Maschinenbau
Technische Universität Ilmenau
Ilmenau, Thuringia, Germany

OVERVIEW OF BASE-FRAME MATERIALS

In precision engineering the importance of the base-frame on the precision of the machines is often underestimated. Machine base-frames define the position of subsystems like drive systems, measuring systems or machining devices to each other and are often the most expensive single part of a positioning machine. The aim is to achieve low-cost, highly integrated base-frames.

In this article materials for machine base-frames of precision machines are compared and design guidelines for mineral cast are derived. In ultra-precise measuring and machining the base-frame has to guarantee the stable position of all subsystems with high rigidity against static and dynamically changing thermal loads and mechanical forces and torques. The long-term stability is a crucial issue of the base-frame as well.

MINERAL CAST IN MECHANICAL ENGINEERING

Commonly used materials for base-frames are natural stone, cast iron, steel and ceramics. An alternative to these materials is polymer concrete. In this article the compound material will be comprehended as polymer concrete. The machine base-frame made of polymer concrete is called mineral cast. Mineral cast is used as base-frame in e. g. grinding machines or machining centres. However, it is not used commonly in precision positioning machines. The aim of this research is to prove the possibility of the appliance of mineral casting in ultra-precise positioning and measuring.

Composition of polymer concrete

Polymer concrete is a composite material of non-metallic fillers like silica minerals with well-defined grain size and distribution bound in an epoxy resin. The size of the mineral fillers varies from 0,25 mm up to 32 mm [1]. The mechanical properties result from the high-density network of the fillers with direct mineral grain contacts, which is shown in Figure 1 as draft.

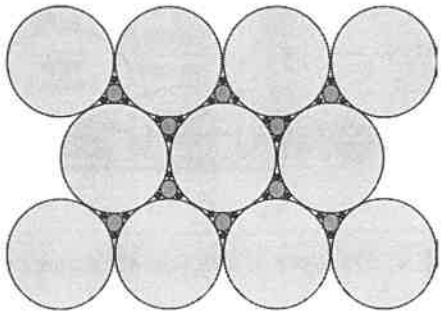

FIGURE 1. Draft of the filler-network with different grain sizes

The epoxy resin is an interlayer, which holds the filler material together. Its volumetric percentage is in applications in mechanical engineering below 12 % [2]. Depending on the chosen resin the chemical reaction of binding takes times from minutes to hours [3]. Several additives are mixed in a low weight percentage to the resin and filler network in order to

- diminish viscosity,
- initiate the polymerisation,
- acceleate/slow down the polymerisation.

Manufacturing of mineral cast

Polymer concrete has to be prepared thoroughly. Filler material has to be dried properly. Grain size fractions of stochiometrical quantities of mineral fillers are mixed with resin and additives. Aim is to achieve full moistening of the mineral fillers and high packing density. To avoid air bubbles in mineral cast, it is possible to mix polymer concrete in vacuum-chambers or to heat the moulding form.

Manufacturing of mineral cast parts is comparable to the technology of iron casting, although curing is based on polyaddition of the resin instead of cooling. During the casting process onto the appropriate moulding form the so called pot-life is of importance. It takes two to six hours in dependence of the complexity of the moulding form [2].

In order to reduce pores and eliminate air from the compound it is densified on shaker plates. For applications in submicrometer-range, during the curing of the resin the moulding form is heated or insulated to receive evenly distributed temperature in the mould and small temperature gradients. Shrinkage during polyaddition is not significant, these factors lead to a low intrinsic tension-level of the mineral casting part.

Depending on the requirements of the achieved precision, tolerances and surface quality of the mineral cast base-frame and the number of castings the utilized moulding forms are made of wood, plastic, steel or cast iron and its combinations. For the use in micrometer-range only cast iron or steel moulding forms are applicable. Nonporous surfaces (functional surfaces) are produced at the bottom of the moulding form.

Function integration in mineral cast

It is possible to integrate other subfunctions than support of measuring or driving subsystems into the mineral cast base-frame by inlets. Figure 2 shows some common inserts with form fit: thread anchors, drilling bars and transport aids. The integration of further functions like lost cores to reduce weight, electrical conductors, channels, heating/cooling pipes with form closure facilitate highly integrated mineral cast base-frames. For applications in precision engineering – to receive better distribution of forces – end-to-end prestressing anchors are used. Monolithical integration of functional surfaces and guideways eliminate or diminish post-processing: up to $10\,\mu m$-resolution it is possible to create functional surfaces with tight tolerances with replication.

Properties of mineral cast

Corresponding to the literature [2, 5] mineral cast has favourable properties:

- outstanding material damping (Figure 3 shows damping curve of mineral casting),
- high thermal capacity,
- low heat conduction,
- low density,
- non-corrosive,
- electrical insulator,
- non-magnetic,
- low water absorption,
- mineral cast is considered as a lightweight construction material.

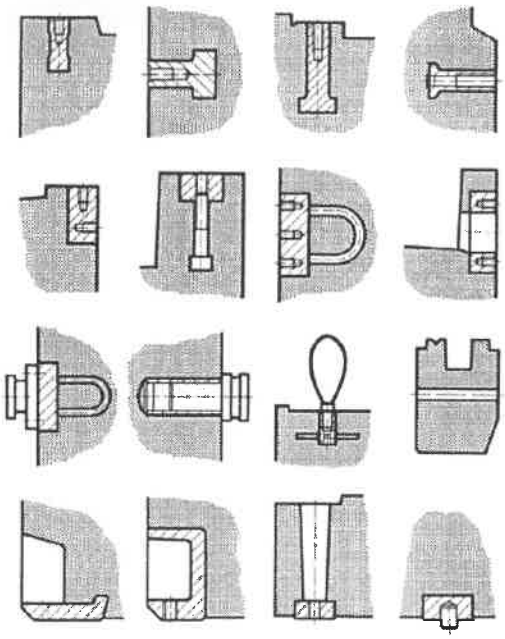

FIGURE 2. Examples of typical inlets [4]

Characterising mineral cast has many difficulties: different fill factors, grain-size distributions and materials, used resins and additives, distributions of natural products influence the properties of the resulting compound. Achieving comparable qualities of different charges is only possible with process control of the applied technology from preparation of the materials until cooling. Anyhow, properties of mineral cast can only be defined in value ranges.

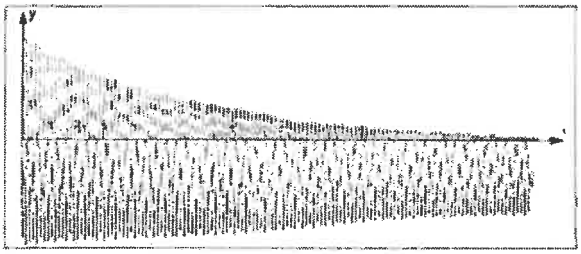

FIGURE 3. Comparison of damping curves of mineral cast (top) and cast iron (bottom) [4]

MINERAL CAST IN PRECISION ENGINEERING

Table 1 compares the properties of mineral cast to cast iron and natural stone. They are evaluated in respect of usage as a base-frame material in measuring machines with submicrometer resolution.

TABLE 1. Comparison of the properties of mineral casting, cast iron and natural stone

	unit	mineral cast	cast iron (GG30)	natural stone
thermal capacity	$[\frac{J}{kgK}]$	0,9- 1,1	0,5	0,85
thermal conductivity	$[\frac{W}{mK}]$	1,5- 2	50	3
thermal expansion	$[\frac{10^{-6}}{K}]$	13- 14	9,2- 11,8	2,1- 9,1
Young's modulus	$[\frac{kN}{mm^2}]$	15	137	60-90
density	$[\frac{g}{cm^3}]$	2,3- 2,4	7,25	2,8-3
tensile strength	$[\frac{N}{mm^2}]$	≤ 10	410- 560	34
compression strength	$[\frac{N}{mm^2}]$	≤ 100	600- 1000	>250

Mechanical properties and dependencies

The following list gives an overview of the mechanical properties relevant in precision engineering.

- Mineral cast has, similarly to cast iron, different strength values on compression and tension. Independent from the used resin the ratio of compression strength to tensile strength is about 9:1 [6].
- Specific stiffness of mineral cast is smaller than the specific stiffnes of natural stone but greater than of cast iron.
- Mechanical material properties of mineral cast are temperature-dependent. Raising the temperature from 20°C to 80°C decreases the compression strength by 50%.
- The fatigue endurance limit of mineral cast is at about 50% of the static load. Fatigue of mineral cast begins at 50% of the nominal compression strength.
- Creeping in submicrometer-range occurs, when mineral cast is exposed to compressive loads $\geq$ 20% of the nominal compressive strength of the polymer concrete.

Thermal properties and dependencies

The relevant thermal properties of mineral cast for applications in submicrometer-range are listed:

- Thermal conductivity of mineral cast is one order below the level of steel or cast iron and comparable to natural stone.
- Thermal capacity of mineral cast is about two times greater than steel or cast iron.
- Thermal expansion is greater than of natural stone, its value is comparable to steel and cast iron.
- The thermal expansion of mineral cast is (in limits) variable in dependence of the resin and its volumetric part.

Conclusions of the properties of mineral cast

The advantage of polymer concrete is the freedom of adjusting thermal expansion at the composition of the compound material. Thermic inertia and the bad thermal conductivity of mineral cast results in comparable values to natural stone. Because high thermal capacity is linked with bad thermal conductivity, the temperature-distribution is not even in mineral cast parts, which leads to hot-spots.

According to the absolute and specific mechanical strength of mineral cast it is not a lightweight construction material in comparison to steel and cast iron. Based on temperature-dependence and creeping, mineral-cast parts are not applicable in base-frames for machines in submicrometer-range.

DESIGN GUIDELINES OF MINERAL CAST IN PRECISION ENGINEERING

Aim of the designing engineer is to create long-term stable base-frames of highly precise measuring machines. Considering the properties of polymer concrete and mineral cast, design guidelines are compiled with special respect of cost-effectiveness, technology and applications. The most important guidelines are listed:

- Technology of mineral casting is similar to iron casting.
- Wall thickness of the moulding form depends on the biggest grains of the grain distribution. Generally the use of wall thickness five to eight times of the largest grain is recommended. Application of smaller fractions result in thinner walls, a multi-mould with differing filler fractions is possible.
- Differing wall thickness in a mineral cast part is due to the low level of intrinsic tension possible, though notching effects have to be considered.
- Mould inclines of approx. 5 degrees is necessary to extract the mineral cast from the moulding form.

- Undercuts are possible. The only restrictions are filling the moulding form and air elimination. Lost cores or filling the moulding form in more steps from multiple directions allow the usage of polymer concrete.
- Inlets should have a wall thickness of three to four times of the largest grain size. Pull-out tension is estimated as 1 MPa.
- Simple and shallow mould form leads to better air elimination and homogenous mineral cast.
- Symmetric design with adequate wall thickness accentuate the positive thermal damping property of mineral cast, though the thermal inertia of the system has to be considered.
- To control the tight tolerated cast-in parts they should be clamped on one (preferably bottom) part.
- Complex geometrical contours of moulding forms are to be avoided.
- Tight tolerances are possible with the use of precise, reuseable steel moulding forms. In a two-step moulding into a second layer of fine-grained material guideways are replicated. Another possibility is the machining of the functional surface.
- With monolthically integrated functional surfaces grinding and post-processing costs are diminished.
- The designer has to aim at a simple and massive form-design without complicated contours, whereas integration of functions in the mineral cast leads to a complex, function-integrated base-frame.
- Machining of the mineral cast base-frame is challengeing in dependency of the mineral fillers.
- Grinding surfaces should be parallel and geometrically separated from other surfaces.
- The designer has to leave enough space between the cast-in parts to permit polymer concrete to fill the room.
- Inlets are always applied form-fitted.
- Casting of defined, tolerated surfaces is cheaper than post-processing (e. g. grinding).
- Use of a safety factor greater four is in dynamically utilised base-frames recommended.
- To avoid creeping in submicrometer-range in shape (after 1000 hours), only 1% of the bending strength is useable.
- Tensile stress and bending strain is to avoid in mineral cast parts, where loads should be transmitted not punctually.

CONCLUSIONS

Polymer concrete is an adequate base-frame material for highly-integrated base-frames produced in series. To diminish production costs replication technology is recommended.

The properties of mineral cast spread statistically. Another issue is creeping under load. They have to be taken into account by the designer with process control and overdimensioned parts with large safety factors. The excellent damping properties of mineral cast are not relevant in measuring machines because dynamic forces and resulting bending and torsion are significant smaller than machining forces with solid-borne vibrations.

To sum up: mineral cast is recommended as base-frame for precision machines with precision $\geq 10\,\mu m$, it is applicable for precision $\geq 1\,\mu m$ and not applicable in submicrometer-range due to uncertain long-term stability.

ACKNOWLEDGEMENTS

The authors would like to thank the German "Bundesministerium für Bildung und Forschung", "Projektträger Jülich" for their support.

REFERENCES

[1] Klaeger S, Bär J. Schlussbericht zum Modyma Teilprojekt 1: FZK: 16 IN 0090; Werkstoffuntersuchungen zur Erarbeitung eines Mineralguss-Werkstoffkataloges für die Konstruktion und Fertigung von Maschinenbauerzeugnissen. Otto-von-Guericke Universität Magdeburg; 2005. electronic ressource.

[2] Jackisch U. Mineralguss für den Maschinenbau. Verlag Moderne Industrie; 2002.

[3] Sahm D. Reaktionsharzbeton für Gestellbauteile spanender Werkzeugmaschinen. RWTH Aachen; 1987.

[4] Fritz Studer AG. GRANITAN-Engineering: Mineralguss GRANITAN;. booklet V. 3.9.

[5] Etmanski B. Zum Eigenschaftsprofil hochgefüllter Reaktionsharzverbundwerkstoffe. Universität Kassel; 1992.

[6] Dey HJ. Das Verformungs- und Bruchverhalten von Reaktionsharzbeton und die Auswirkungen auf Maschinenbauteile. Darmstadt; 1991.

MICRO-POSITIONING FOR PRECISE INK JET DELIVERY

Anthony W. Gatica
M3 Design Inc.
Round Rock, TX, 78681

BACKGROUND

Ink jet delivery systems are integral to many fields, such as paper printing, display creation, and three-dimensional rapid prototyping applications. Printheads are able to dispense picoliter-sized fluid droplets thousands of times per second. Furthermore, the printheads' versatility enables the dispensation of inks, solvents, suspended particles, or biological material. Examples are in the fields of electronics, display technology, and life sciences [1]. By mounting an ink jet delivery system to a moving carriage and passing it over a substrate, fluids can be deposited at precise locations.

Additionally, ink jet printing is an additive process, enabling production processes at the micron level with minimal waste. This can result in low cost and highly accurate products, especially at low volume manufacturing.

While the dispensing precision of the printhead is typically very good, the mechanical tolerances associated with head location are much larger and complex, thus requiring additional setup and adaptive control in order to obtain the most accurate system. Such adjustments are made via a combination of shifting the print heads and varying the print timing.

This paper will investigate methods that can be used to obtain an accurate system of print heads through mechanical adjustment, calibration, and software/hardware control. A successful machine architecture will strike a thoughtful balance among these three categories of compensation. A conceptual embodiment of such a printing system will also be presented and discussed.

CHALLENGES

In a multiple printhead system, there are multiple errors to consider that affect positional accuracy:

- Head-to-head location variability
- Distance from individual printhead to the printing substrate (head gap)
- Individual printhead non-parallelism to the substrate
- Head-to-head nozzle pitch variations
- Exiting drop velocity and trajectory: Nominal variance plus transient effects due to ink temperature
- Orthogonal error of the substrate after loading, relative to the printhead array
- Substrate rotation relative to printhead array as a function of substrate linear position.
- Printhead array rotation relative to substrate as a function of array linear position

Many of these errors can be compensated with mechanical adjustments, calibration, and software control.

MECHANICAL ADJUSTMENTS

The primary method to compensate for non-accurate printhead alignment is to simply adjust the heads in six degrees of freedom. However only three degrees of freedom are necessary: X, Z, and θ_Z as shown in Figure 1. Adjustment X controls head-to-head spacing, Z controls the distance from the printhead to the substrate, and θ_Z controls the apparent nozzle pitch. The Y-axis coincides with the system motion over a substrate to deposit ink, and can be compensated for by pre- and post-firing timing changes per nozzle. Nozzle bow can also be compensated for in this manner. Rotations about the X- and Y-axes can typically be minimized through proper design and datum control principles in a cost-effective manner such that no compensation is required.

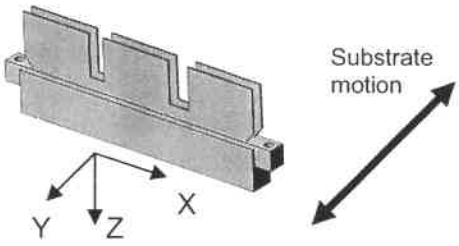

FIGURE 1. Print head coordinate system and axes relative to substrate motion.

Implementation of the adjustments can vary from flexures to mechanical bearings. Friction and hysteresis are the biggest sources of positioning errors. Feedback control must be utilized.

Continuous Print Coverage

No matter how close print heads get to one another there will always be a gap in printed material between adjacent heads. In order to get continuous print coverage, rows of print heads can be offset in the Y-axis to provide mechanical clearance for the printhead size and fine-tuned in the X-axis, as shown in Figure 2, such that the array of print nozzles appears to be continuous.

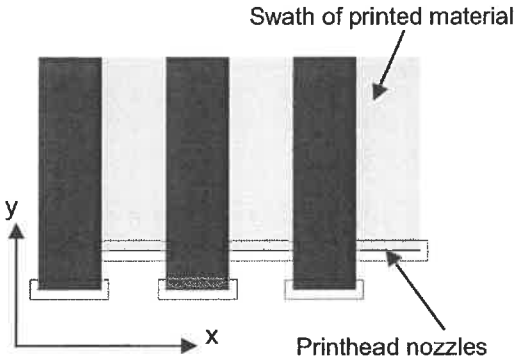

FIGURE 2. Staggering six printheads to get continuous print coverage.

Compensation for Rotation Errors

The source of rotation errors between the substrate and the printhead array may be either θ_z in the X or Y motion stage axes or simply the substrate was not loaded accurately. Three compensation approaches are valid:

- Rotate each head individually and translate as needed.
- Rotate the printhead array as a unit.
- Rotate the substrate precisely at load and during stage motion.

The implementation shown later in this paper utilizes the second approach.

Adjusting Nozzle Pitch

Although the printhead nozzle pitch is fixed, the head can be rotated in θ_Z to reduce the apparent pitch (Figure 3). The apparent pitch is calculated as $P^*\cos\theta_Z$. This allows for denser print coverage or controlling spacing of ink drops. When the printhead rows are rotated to shorten the apparent nozzle pitch, each row needs to translate to maintain a contiguous array of nozzles (Figure 4). Fine adjustment of the print heads is accomplished by the individual X-adjustment and θ_Z adjustment as shown in the print head coordinate system (Figure 1). Sub-micron adjustment can be achieved reliably with miniature motor/gearhead actuators or piezo-electric actuators, coupled to stiction-free bearing assemblies or flexure element bearings.

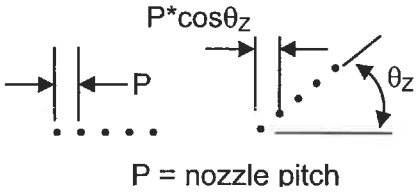

FIGURE 3. Reduction of apparent nozzle pitch by rotating print heads.

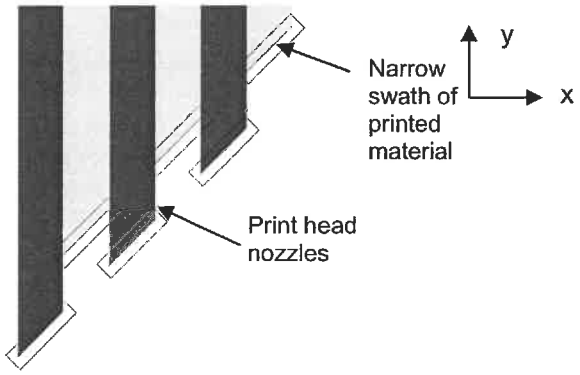

FIGURE 4. Rotating a group of print heads in θ_Z to reduce the apparent nozzle pitch. Note the print head rows have translated relative to one another to obtain continuous print coverage.

SOFTWARE ADJUSTMENTS

Certain print head designs have individually-addressable nozzles. This allows variable timing of each nozzle and can be put to use as described in the next sections. An example of such a print head is the Dimatix Spectra® SX3 with 128 addressable nozzles [2].

TABLE 1. Partial list of Sprectra® SX3 specifications [2].

Specification	*Value*	*Units*
Drop Size	*12*	*Picoliters*
Drop Velocity	*8*	*meters/s*
Drop Velocity Variation	*<2*	*%*
Max Operating Frequency	*10*	*kHz*

Print Head Gap & Parallelism Compensation

Precision ink jet printheads are used in many applications that require extremely small gaps between the print head and substrate. As the gap decreases, the parallelism between the print head and the substrate becomes more sensitive. If the printhead is moved relative to the substrate in the Y-direction (Figure 1) and all nozzles were fired at the same time, the ink drops would strike the substrate at different locations if the head was not parallel to the substrate. Figure 5 presents the equations of motion for a falling ink drop at an initial exit velocity.

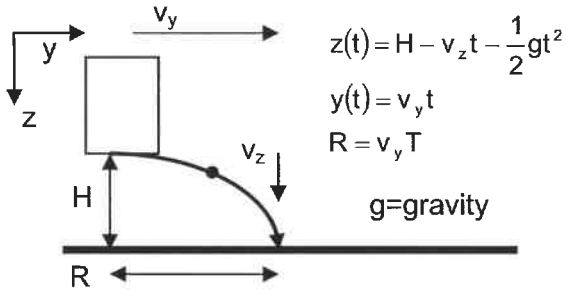

FIGURE 5. Equations of motion governing drop placement during jetting and print head velocity relative to a fixed substrate.

In Figure 5, the value H is the nominal distance between the print head and substrate and T is the nominal time for a drop to strike the substrate after ejected from the print head based on the drop exit velocity and distance H. As an example, let H=0.001m, v_y=1m/s, v_z=8m/s. Setting z(t)=0 and solving the resulting quadratic equation for t, t_1=0.00012499s and t_2= -1.6311137s. Obviously t_1 is the only realistic answer. The resulting distance the drop travels in the y-direction to the substrate is R=0.00012499s * 1m/s = 0.00012499 m or 124.99 microns.

In a multi-printhead system, the necessity to set the working gap of all printheads very close is essential. From the example above a 1% error in nominal working gap between two printheads would result in a 1.25 micron landing error when printing uni-directional. This would double when using bi-directional printing.

If the parallelism of the printhead to the substrate varies by 25 microns from the first nozzle to the last, H=.001025m at the last nozzle. Assuming the other parameters remain the same, the new time to strike the substrate equals 0.00012811s. The resulting value for R is 0.00012811m or 128.11 microns. Thus, a 25 micron parallelism error results in a 3 micron error in drop placement at a relative velocity difference of 1 m/sec.

After the parallelism error is measured or calculated, the timing of firing each nozzle can be adjusted. In the above example, in order to compensate for the parallelism error, the timing on the last nozzle would be advanced so it fired before the first nozzle. If the first nozzle required 0.00012499s for an ejected drop to strike the substrate and the last nozzle required 0.00012811s, the last nozzle should be fired 0.00000312s or 3.12 microseconds sooner.

Adjusting Ink Coverage

For applications that require depositing ink or other material, the amount of material deposited from a given printhead can be controlled in the following manner:

- Vary velocity of print heads relative to the substrate (higher velocity reduces the material dispensed per unit area)
- Vary head jetting frequency (high frequency yields more material dispensed)
- Vary drop spacing by reducing the apparent nozzle pitch (closer spacing of printed drops yields more dispensed material per unit area)
- Vary drop spacing by reducing the number of active jetting nozzles (reduces the dispensed material per unit area)
- Substitute a different printhead to increase or decrease the individual drop volume

Print Head Jetting Calibration

One method to determine the non-parallelism between printhead and substrate is to utilize an optical inspection system to capture images of the ink drops as they exit the print head. Other benefits of the optical system are the ability to measure the exiting drops' trajectory relative to the printhead, and measuring actual drop velocity and volume.

Calculating Parallelism Errors

The optical inspection system can scan along the edge of the print head, monitoring the print head position in the field of view. Thus, the parallelism of the print head relative to the head inspection camera scanning axis can be calculated.

Measuring Ink Drop Velocity

A method to determine ink drop velocity is to strobe a machine vision system multiple times after the ink drop has been ejected from the print head and measure the distance between the drops (assuming the camera's region of interest scale has been calibrated). Figure 6 outlines this graphically.

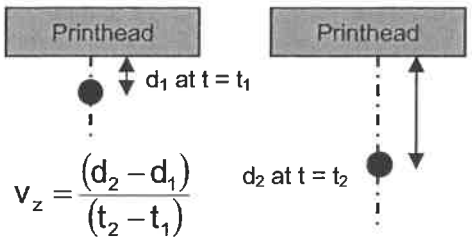

FIGURE 6. Method to calculate ink drop velocity using machine vision.

Ideally t_1 and t_2 would be selected so that the positional midpoint between ink drops represents the chosen working gap for the printhead array.

CONCEPTUAL IMPLEMENTATION

A conceptual implementation of the print head array is shown in Figure 7. This conceptual design has the following features:

- Machined disk containing all print heads
- Air bearing axial support of the disk
- Air bearing radial support of the disk
- Non-contact brushless motor to adjust disk angle
- Groups of printheads ganged together with linear movement of each group
- Individual print head adjustment (3 degrees of freedom) for fine head adjustment

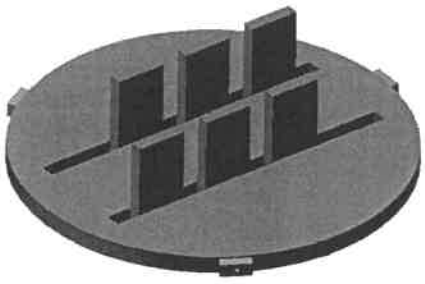

FIGURE 7. Conceptual embodiment of an adjustable print head assembly.

Figure 8 presents how the print heads translate in order to print continuous swaths of material during the disk rotation. As the number of rows of print heads and the number of print heads in each row increase, the disk must become larger. Self deflection of the disk and manufacturing limitations will dictate the maximum size and number of print heads allowable.

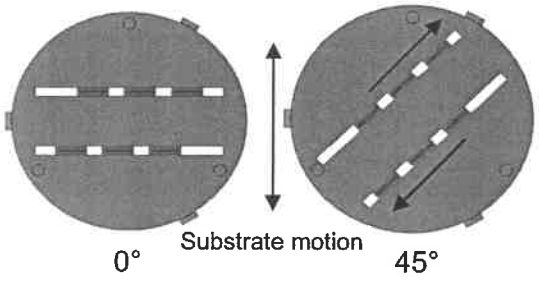

FIGURE 8. Translation of print heads needed to print continuous swaths of material as the disk rotates.

SUMMARY

Ink jet dispensing of inert, organic, or biological materials opens up a wide range of potential applications. Examples are in the fields of electronics, display technology, and life sciences [1]. Furthermore, ink jet is an additive process that doesn't require intermediate masking steps such as photolithography and efficiently uses material without waste.

Commercially available printheads can dispense a wide range of materials with incredible precision. However, assembling them into a usable product requires precise adjustment, calibration, and software control.

Methods that can be utilized to create and calibrate such a printing system have been presented. Additionally a conceptual embodiment of this system has been presented.

REFERENCES

[1] Schloeppler M. New Approaches for Materials Deposition [article on the Internet]. Productronica; 2005, Nov. 17; Munich, Germany; Available from: http://www.dimatix.com/files/productronica_11172005.pdf.

[2] Spectra® SX3 128-Channel Jetting Assembly. [web page on the Internet]. California: FUJIFILM Dimatix, Inc.; 2007, Apr. 05. Available from: http://www.dimatix.com/files/PDS00053_SX3.pdf.

APPLICATION OF PLANAR AIR BEARING CONCEPT FOR PRECISION MACHINE TOOL DESIGN

Jeff Gorniak and Kaan Erkorkmaz
Precision Control Laboratory
University of Waterloo
Waterloo, Ontario, Canada

INTRODUCTION

The North American manufacturing industry has seen a growing demand for precision machined components in recent years. Biomedical devices, micro-optical moulds, and automotive parts are examples of precision manufactured components. Traditional milling practices have reached the limit of the machines' accuracy and cannot achieve high tolerances now demanded in the micro-machining field. New ultra-precision machines have emerged, which incorporate high accuracy positioning and have been developed to meet these new demands [1], [2], [3], [4]. This paper presents a new design which applies the planar air bearing concept to achieve high-speed and high-accuracy positioning over a relatively large work area.

To achieve high accuracy in a precision machine, new designs are required to focus on key sources of error. The influence of environmental changes on positioning is highly prominent, as well as the mechanical design of the drive system and guideways. Flexible components such as ball screws or timing belts limit the positioning accuracy, and require additional compensation techniques to overcome their dynamic limitations [5]. Roller guide ways contribute static and coulomb friction, which requires friction compensation.

A 5-axis ultra-precision machine tool is currently in development, at the University of Waterloo, to answer the new demands from the micro-machining industry. It is capable of high speed, high accuracy movement within a large work volume. The focus of this paper is on the design and fabrication of the planar motion stage for x and y axes. The machine will be driven by direct drive motors, which greatly increases the stiffness and acceleration capabilities. Porous air bearings are used to reduce the effect of static and coulomb friction to a negligible amount. The actuators are secured to the stage using internally cooled couplings, in order to reduce the effect of thermal deformations.

X-Y STAGE DESIGN

Conceptual design of the planar air bearing stage is shown in Figure 1, which consists of a gantry and a work table configuration. Smooth motion is realized by porous carbon air bearings and direct drive linear motors. Previous research in [1] used air bearings and direct drive voice coil actuators to achieve nanometer-level positioning. However, a limitation associated with this design is the relatively short stroke (20 mm) that could be achieved. In the proposed design, standard linear motors were selected to provide 1g acceleration and 1 m/sec peak velocity, for a work volume of 300 x 300 mm^2.

The planar stage consists of a gantry that moves in the y-axis, and a table which moves along x. The (125 kg) mass of the gantry is supported on three ∅80 mm air bearings on a precision ground granite base. Linear motion along the y-axis is achieved with 4 preloaded 75 x 150 mm^2 air bearings, along the sides of the granite guideway. This arrangement provides high stiffness in the y-direction, and also decreases gantry splay. Actuation is provided by two linear motors, supported on both ends of the gantry. The secondary motor, opposite to the guide, is responsible for actively stiffening the free end, in order to avoid excessive bending deflection. Two high resolution linear encoders with 4um sinusoidal signal period provide the feedback. The 35 kg mass of the table is not carried by the gantry, which eliminates unwanted sag. Rather, a 12" x 12" vacuum preloaded (VPL) air bearing situated on the granite base supports the table. The air gap height of the VPL can be controlled by adjusting the vacuum and pressure settings. Preloading the bearing improves the dynamic response and also increases stiffness in the vertical direction. The gantry is made from 304-stainless steel, and serves as the guideway for the x-axis, using an arrangement of four

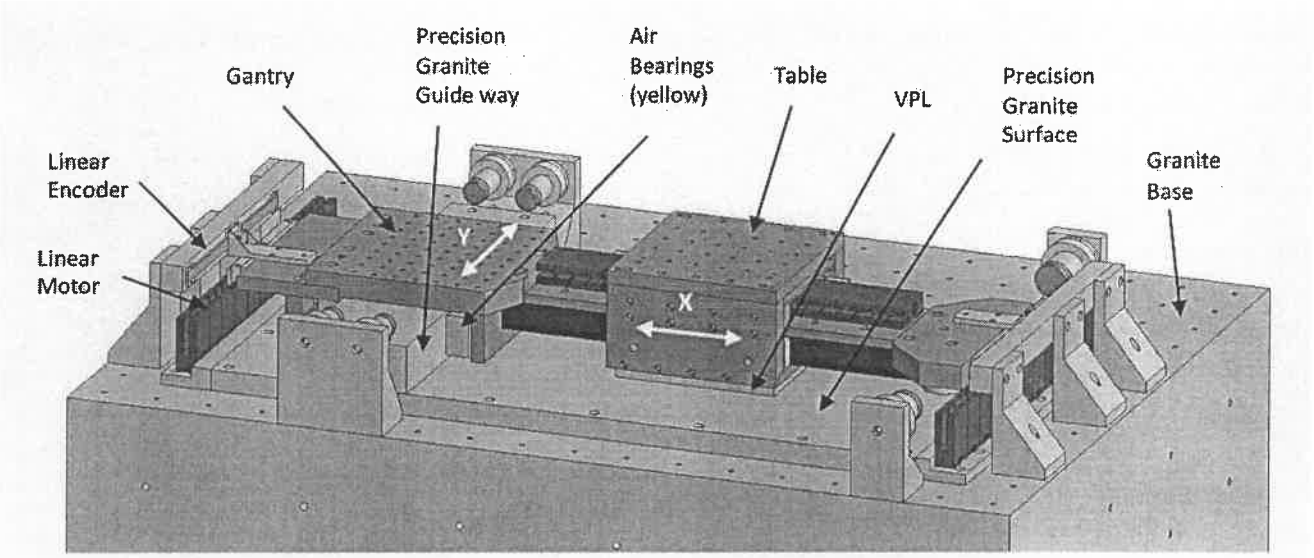

FIGURE 1. Conceptual design of the precision XY stage

50 x 100 mm^2 air bearings. Actuation and measurement is achieved using a linear motor and encoder, mounted on the beam using an aluminum plate.

ERROR BUDGET

An Error Budget is used to outline all major sources of error for the machine. The amount of error contributed by each source is quantified and critical areas can be determined [6], [7]. Efforts can then be made to develop solutions and minimize the overall error. The following error values were not collected experimentally, since the prototype machine is still in fabrication. However, theoretical calculations still provide a good representation of the key sources of error.

Linear Error

The linear error for each axis should be minimal due to the absence of friction from the air bearings and the high resolution of the linear encoders. A measurement resolution of 10 nm is expected, by interpolating the encoder signals at 400x, assuming a reasonable signal-to-noise ratio. The expected servo accuracy is in the order of a few BLU's, resulting in 20-40 nm.

Straightness Error

The granite guide ways were precision ground to a specified tolerance of 2 μm/300mm, in order to accommodate the large VPL. The ride height of the VPL and other preloaded air bearings is 5 μm. These errors cannot be compensated for, unless there is a controlled axis perpendicular to the axis of motion. For example, the horizontal straightness error of the y-axis can be compensated by the x-axis position controller.

Squareness Error

Squareness of the granite y guide block to the global reference frame is critical, as it is the sole reference to the base of the machine. The squareness of the x and y axes will be determined by the manufacturing accuracy of gantry, which has a tolerance of 2 μm/300 mm. Squareness errors, measured after the prototype is built, will be compensated in software.

Angular Error

Angular error values for the stage are difficult to predict, as many factors affect the rotation of the table along the range of the axis such as the topography of the granite surfaces. These errors will need to be determined experimentally and compensated once the prototype is built.

Dynamic Error

Under high acceleration movements along the y-axis, inertial reaction forces from the table will cause the gantry to elastically deformation. As well, the non-linear compression of the air gap of the bearings can cause unwanted flexibility of the stage. For conventional machine tools, this type of loading does not create large enough error to be considered important. However, in our design, it can be a major source of error.

Maximum 1 g acceleration of the table along the y-axis is predicted to deflect the gantry beam by 0.4 μm. Coupled with the deflection is the

compression of the air gaps of the table preloaded air bearings which amounts to 1.5 μm. Hence, an overall error of 1.9 μm is expected in the y-axis during high acceleration movements. This deformation, however, is expected to be repeatable and will be modeled with the intention of applying real-time compensation.

For the peak acceleration of the table in the x-direction, the error in the x-axis is not significantly affected by elongation or compression of the gantry (< 0.2 μm). Mainly, error due to the compression of the air bearings is expected. As these bearings have a higher stiffness than the ones used in the x-axis, they are expected to compress only around 1 um.

Thermal Error

The effect of thermal expansion and contraction is reduced by the design of internally cooled couplings. These couplings are used to attach the linear motors to the stage and will be temperature regulated by a network of internal channels. If the couplings did allow for heat to transfer to the stage, a rise in 1°C would offset the encoder head from the centerline of the gantry by 1.5 μm. Therefore, it is critical that the couplings are used to maintain a constant temperature throughout the stage. To help combat external influences on the machine, the stage will also be located in a controlled environment that regulates the ambient temperature and humidity.

Error Budget Conclusion

The major source of error for the stage is the flexibility of the gantry and compression of the air bearings. However, the potential for the straightness of the guide ways to cause more error is also present, and will be determined through measurements, once the stage is built.

INTERNALLY COOLED COUPLING

The internally cooled couplings are the only components which are in contact with the linear motors. The motors are capable of reaching 130°C during high load situations and at this temperature, severe thermal expansion of the stage can cause reading errors in the linear encoder, as well as table positioning errors. A solution to this problem is to use couplings which remove the heat generated by the motor, by running temperature controlled fluid through a series of channels. Figure 2 shows the internal channels of the coupling, denoted in blue.

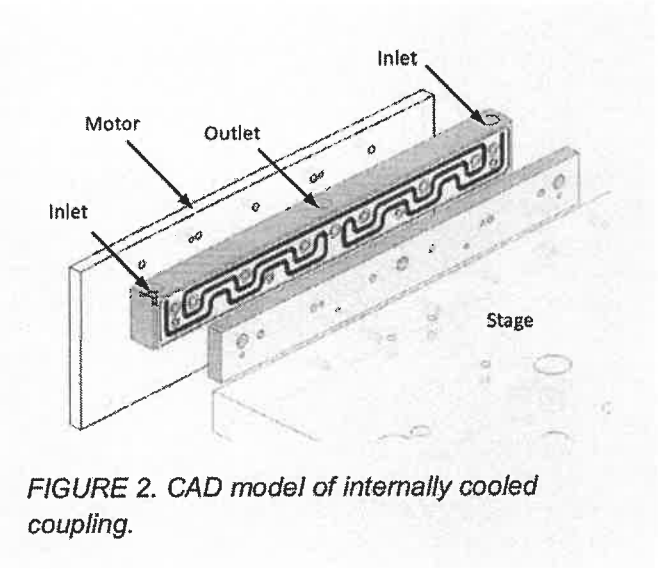

FIGURE 2. CAD model of internally cooled coupling.

A finite element analysis was performed on the coupling to observe the effectiveness of the cooling. The results show that the gantry side of the coupling remains at a constant temperature, even during maximum energy input. This result is crucial as it means that the stage does not directly feel the thermal effect of the motor.

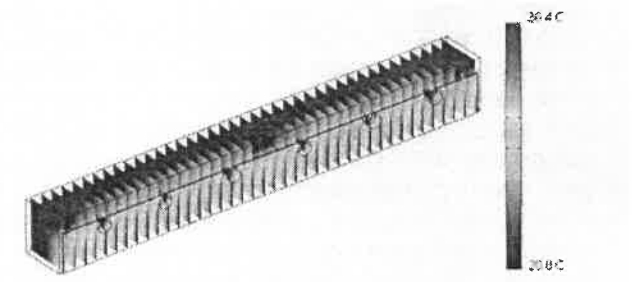

FIGURE 3. Thermal FEA results of coupling under maximum energy input.

ADAPTIVE SLIDING MODE CONTROL

Adaptive sliding mode control (ASMC) theory was developed by Slotine & Li [8], and has successfully been applied in high precision drive controls [5]. The ASMC is designed to maintain the state errors of the system on a sliding surface, which guarantees that the servo errors converge to zero. This is achieved by postulating a Lyapunov function, which formulates a control law that will push the states onto the sliding surface. The equation for the control law consists of the deviation of state errors from the sliding surface (σ), a negative feedback gain K_s, and a parameter-regressor expression $Y(\dot{x}_{ref}, x)\hat{P}$.

$$u_{smc} = K_s \sigma + Y(\dot{x}_{ref}, x)\hat{P} \quad (1)$$

When ASMC is formulated considering rigid body dynamics, and is used to only adapt against unknown disturbances, it assumes the structure of a PID controller with feedforward velocity and acceleration terms. As required, notch filters can be inserted into the loop to avoid exciting the structural resonances. Also, low frequency modes can directly be compensated using ASMC [5]. In our setup, the first resonance frequency, due to the bending mode, is predicted at approximately 800 Hz. Additional sources of flexibility are also anticipated due to the air bearings. Once the stage is built, structural testing will be used to determine the modal frequencies, and to select modes that will be considered in the control law.

CURRENT PROGRESS

To date, one side of the gantry has been built and servo control and metrology tasks are underway. Experimental measurement of volumetric and dynamic errors will be compared against predicted estimates. The remainder of the gantry and table are currently in fabrication.

CONCLUSIONS

This paper has presented a new air bearing design, which is currently being investigated for ultra-precision machine tools. The stage is capable of 1 g acceleration and 1 m/sec velocity within a work volume of 300 x 300 mm^2. An error budget has been presented, which outlines the major sources of error to be due to the elastic deformation of the gantry and variations in the air bearing gap during high acceleration movements. Fabrication of the prototype is currently underway. Following its completion, the position error estimates will be validated experimentally. Repeatable static and dynamic errors sources will also be modeled and compensated in the control law, along with the most significant structural dynamics that limit the achievement of high servo performance.

ACKNOWLEDGMENT

This research is sponsored by NSERC, Auto 21 NCE, and the Ontario MRI in Canada. The authors gratefully acknowledge the industrial collaboration and support provided by New Way Precision, ETEL, Heidenhain, and Rock of Ages.

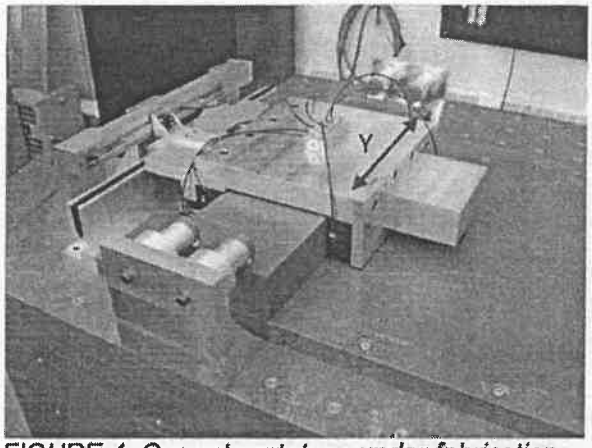

FIGURE 4. Current prototype under fabrication.

REFERENCES

[1] Shinno H, Yoshioka H, Taniguichi K. A Newly Developed Linear Motor-Driven Aerostatic X-Y Planar Motion Table System for Nano-machining. Annals of the CIRP. 2007; 56/1:369-372.

[2] Sriyotha P, Nakamoto K, Sugai M, Yamazaki K. Development of 5-Axis Linear Motor Driven Super-Precision Machine. Annals of the CIRP. 2006; 55/1:381-384.

[3] Van Brussel H., Mechatronic Issues in Machine Tools for High Performance Cutting. Proc. CIRP-HPC'08.

[4] Brecher C., Wenzel C., Klar R., Characterization and optimization of the dynamic tool path of a highly dynamic micro milling machine. Proc. CIRP-HPC'08.

[5] Kamalzadeh A, Erkorkmaz K. Compensation of Axial Vibrations in Ball Screw Drives. Annals of the CIRP. 2007; 56/1:373-378.

[6] Slocum A. Precision Machine Design. Society of Manufacturing Engineers, MI, USA. Prentice Hall: 1992.

[7] Uriarte L, Herrero A, Zatarain M, Santiso G, Lopez de Lacalle LN, Lamikiz A, Albizuri J. Error Budget and stiffness chain assessment in a micromilling machine equipped with tools less than 0.3mm in diameter. Precision Eng. 2007; 31/1-12.

[8] Slotine, J.-J. E., Li, W., Adaptive Manipulator Control: A Case Study. IEEE Transactions on Automatic Control. 1988; 33/11:995-1003.

FABRICATION OF A GREEN CATERPILLAR TYPE IN-PIPE MOBILE INSPECTION MICROROBOT DRIVEN BY PNEUMATIC AND VACUUM PRESSURES

Yukiya GOTO[1], Shigeo KATO[1], Manabu ONO[2] and Toshiaki HAMANO[1]
[1]Nippon Institute of Technology, Saitama, Japan
[2]Tokyo Metropolitan College of Industrial Technology, Tokyo, Japan

INTRODUCTION

We have many small diameter pipes that are gas or water pipes for individual or corporate houses and boilers or hot water pipes for industries. These pipes may be occurred to injure or to corrode by their decrepit. The injury or the corrosion of pipes causes the leak of fluid and links to the accident. So, these pipes must be periodically inspected in order to protect the accident previously. They are settled in the ground or in the narrow spaces and some of them are covered by casings or hard heat insulators. So, it is very difficult to inspect from outside of the pipe. If we can insert a mobile inspection robot into the pipe from the suitable position, we are easy to inspect the pipe. In-pipe mobile robots driven by pneumatic actuator have been proposed by several research groups for same diameter pipes [1], [2]. However, some of these pipes are long and their diameters are different at the place where pipes change from the main to the branch. The diameter of pipes is within 70 mm and 150 mm for example. So, the inspection robot for these pipes must move in different diameter, generating large traction force for the inspection of long distance.

We have fabricated inspection robots applying an earthworm and an inchworm [3], [4]. A braking mechanism which is using cone-shape friction rings for the earthworm type inspection robot is designed for the diameter of 79 mm. Then the inspection robot could not move in pipes whose diameter changes more than 5 mm from 79 mm. The earthworm type inspection robot can not move in pipes that the diameter changes from 70 mm till 150 mm. On the other hand, the inchworm type inspection robot which is using bulging brakes is confirmed to move in pipes whose diameter is 70 mm and 140 mm. However, the traction force of the inchworm type inspection robot changes on the diameter of the pipe. The traction force is 11 N at the 70 mm pipe, but is only 1 N at the 140 mm pipe. The traction force depends on the friction force of the braking mechanism. So, we propose a suction brake for the braking mechanism. The suction brake can stick on the pipe and hold the pipe by the negative pressure supplied from a vacuum pump. The friction force of the suction brake is so larger than those of another braking mechanism and is predicted easily.

Now, we remark the moving motion of a green caterpillar. The green caterpillar sticks a passage such as the leaf by its prolegs. If we can imitate prolegs by the suction brake, we may obtain large traction force. The green caterpillar moves its prolegs by waving its abdomen. This waving motion is imitated by the action of four parallel rubber bellows actuator driven by pneumatic and vacuum pressure. The inspection robot that is imitated the green caterpillar can move at the speed of 20 mm/s in the pipe whose diameters are from 70 mm to 150 mm, generating the traction force of as large as 20 N. We may inspect long and different diameter pipes, because we have obtained large traction force. Besides, the green caterpillar type inspection robot has been confirmed to pass the step more than 5 mm.

GREEN CATERPILLAR

We observed moving motion of the green caterpillar. The moving motion is shown in Figure 1. The green caterpillar consists of a head, a thorax and an abdomen. The thorax has six true legs and the abdomen has five pairs of prolegs. Five pairs of prolegs make three groups that are front two pairs, central two pairs and rear one pair of prolegs. The prolegs of the rear one pair are called as claspers. The prolegs are cylindrical. They are used for walking and clinging as they have microscopic hooks on the base.

The moving of the green caterpillar is as follows.

(a) In the initial condition, the green caterpillar is sticking to the leaf by all of prolegs of the abdomen and is stationary.

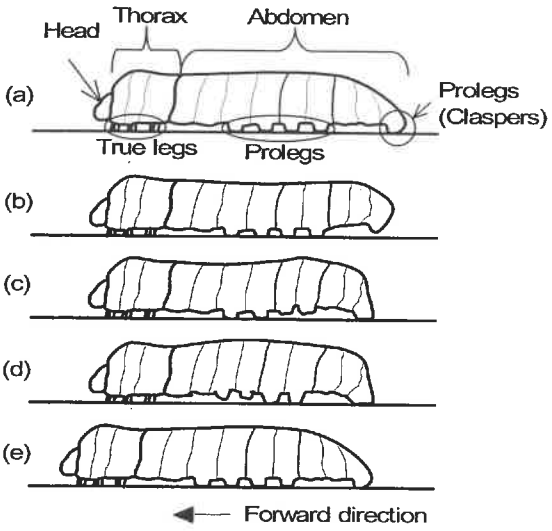

FIGURE 1. Moving Motion of a green caterpillar.

(b) The rear abdomen waves and the rear one pair of prolegs (claspers) are taken off.
(c) The central abdomen waves and the central two pairs of prolegs are taken off and the rear one pair of prolegs land on the leaf that is forward direction from the initial condition.
(d) The front abdomen waves and the front two pairs of prolegs are taken off and the central two pairs of prolegs land on the leaf that is forward direction from the initial condition.
(e) The green caterpillar stops its waving and sticks the all of prolegs to the leaf. Then, the head and the thorax are moved to forward direction. The cycle of moving of the green caterpillar ends.
We understand that the green caterpillar can move to the forward direction by moving of three groups of prolegs in order to the forward direction.

STRUCTURE OF THE ROBOT

A fabricated robot is imitated the abdomen of the green caterpillar. A structure of the robot is shown in Figure 2. The abdomen is imitated by two groups of four parallel rubber bellows actuators which are arranged in the matrix of two rows and two columns. The matrix of two rows and two columns makes a somite of the abdomen. Two parallel rubber bellows in the same row are supplied same pressure by an air feeding tube. The bellows made of Nitrile Butyl Rubber (NBR) is 16 mm in diameter and 76 mm long. A group of prolegs is imitated by a suction brake. The suction brake is a sucker made of NBR and its diameter is 40 mm. The air feeding

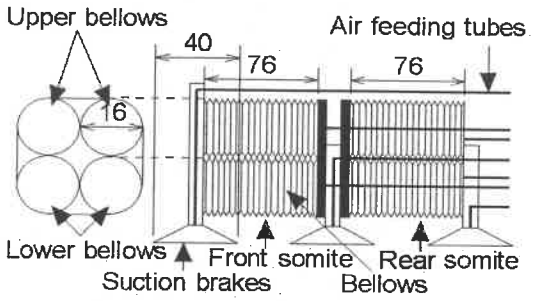

FIGURE 2. Structure of microrobot.

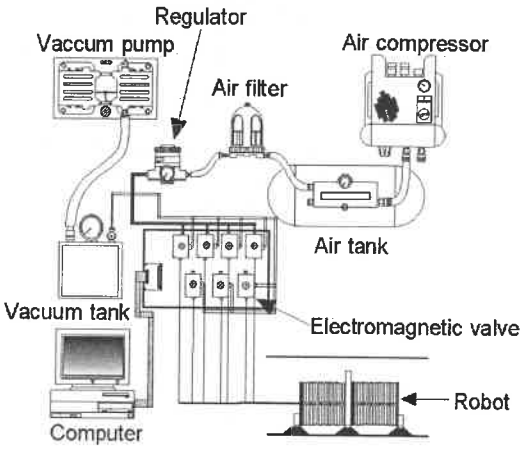

FIGURE 3. Control system of microrobot.

tube for positive and negative pressure is connected in the center of the suction brake. Three suction brakes are arranged at the front, the center and the rear of the two groups of four parallel rubber bellows actuators.

CONTROL SYSTEM OF THE ROBOT

A control system of the robot is shown in Figure 3. The system is constructed by a robot, seven electromagnetic valves, two different (positive and negative) pressure sources, a computer and a valve controller. The positive pressure source is an air compressor and the negative pressure source is a vacuum pump. The moving sequence of the robot is programmed in the computer. The electromagnetic valves are controlled by the computer through the valve controller. The electromagnetic valve has three ports. The electromagnetic valves are connected to the bellows and the suction brakes through the air feeding tubes.

MOVING MOTION OF THE ROBOT

The robot moves in the pipe by stretching and bending motion of two somites and sticking of the suction brakes using positive and negative pressure.

Moving principle of the somite

Moving principle of the somite is shown in Figure 4. The somite consists of bellows. The bellows stretches when positive pressure is supplied and shrinks when negative pressure is supplied. That is, the somite stretches when positive pressure is supplied to the upper and the lower bellows. The somite shrinks when negative pressure is supplied to the upper and the lower bellows. Besides, the somite can bend when different pressure is supplied to the upper and the lower bellows, for example, the somite bends upward, when positive pressure is supplied to the upper and negative pressure is supplied to the lower bellows. The waving motion of the green caterpillar can be imitated by the stretching, shrinking and bending motion of the somite.

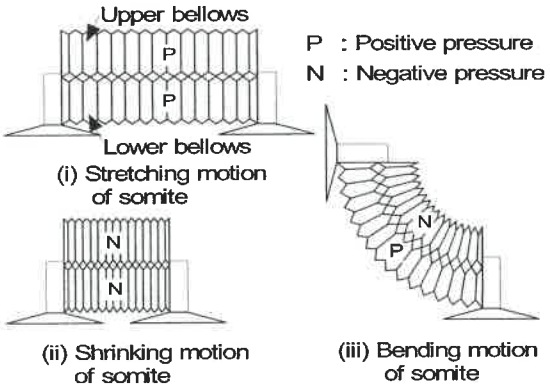

FIGURE 4. Moving principle of somite.

Moving principle of the robot

Moving motions by the pressure changes are shown in Figure 5. The robot moves to the forward direction by moving its three suction brakes in order to the forward direction. The robot waves its front and rear somite to push the suction brake to the wall of the pipe and to lift up the suction brake from the wall of the pipe. The suction brake can stick the wall of the pipe by supplying the negative pressure and release the wall of the pipe by supplying the atmospheric pressure. In Figure 5, black colored suction brake shows that the suction brake sticks the wall of the pipe and white colored suction brake shows that the suction brake releases the wall of the pipe.

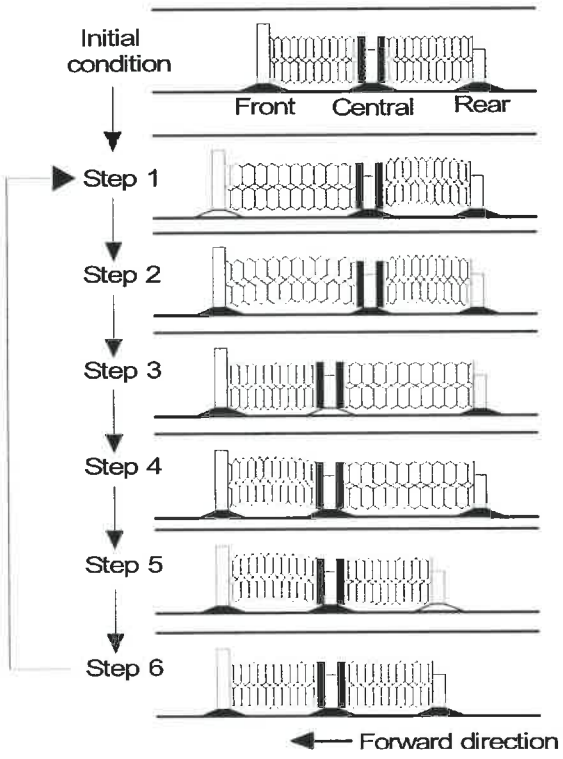

FIGURE 5. Moving principle of microrobot.

In the initial condition, the robot shrinks its front and rear somite and sticks its three suction brakes on the pipe and is in the stationary.
Step 1: The front suction brake releases the wall of the pipe. The front somite stretches to the forward direction. Then, the front suction brake moves to the forward direction.
Step 2: The front suction brake sticks the wall of the pipe.
Step 3: The central suction brake releases the wall of the pipe. In this time, the front somite shrinks. Then, the central suction brake moves to the forward direction.
Step 4: The central suction brake sticks the wall of the pipe.
Step 5: The rear suction brake releases the wall of the pipe. The rear somite shrinks. Then, the rear suction brake moves to the forward direction.
Step 6: The rear suction brake sticks the wall of the pipe.
The robot can move in the pipe by repeating the steps.

MOVING CHARACTERISTICS OF THE ROBOT

The positive pressure of 50 kPa and the negative pressure of -84 kPa are used in the experiment and diameters of pipe made of acrylic are within 70 mm and 150 mm.

Moving speed

Moving speed of the robot is measured in the pipe which is set in horizontal and vertical. The moving speed is shown in Figure 6. Average speed is 20 mm/s in the horizontal case and 23 mm/s in the vertical case. It is confirmed that the moving speed does not depend on the diameters of pipe by the experiment.

Traction force

The experimental traction force is shown in Figure 7. The traction force of 20 N is obtained and does not depend on diameters of the pipe.

Confirmation of passing of the step

The robot is confirmed to pass the step of 5 mm that is made by connecting of pipes whose diameters are 110 mm and 120 mm. The robot can pass the step by its waving motion of the somite.

CONCLUSIONS

1. The green caterpillar can move to the forward direction by moving of three groups of prolegs in order to the forward direction. The green caterpillar moves its prolegs by waving its abdomen.
2. In the fabricated robot, the abdomen of the green caterpillar is imitated by bellows and the prolegs are imitated by the suction brake. The somite structured by four parallel rubber bellows actuators which are arranged in the matrix can imitate the waving motion of the abdomen.
3. The robot that is imitated the motion of the green caterpillar can move pipes whose diameter are more than 70 mm. Average speed is 20 mm/s in the horizontal case and 23 mm/s in the vertical case. The traction force is 20 N and does not depend on the diameter of the pipe. This type inspection robot may move long distance, because it has larger traction force. The robot is confirmed to pass the step of 5 mm.

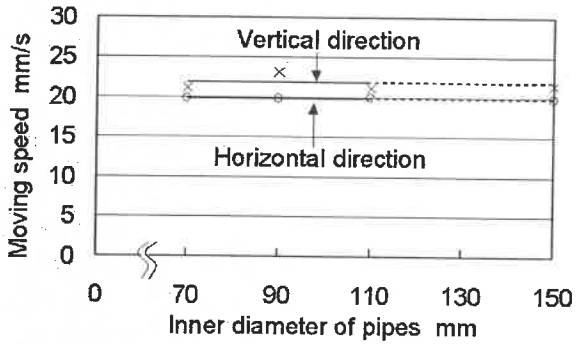

FIGURE 6. Moving speed of microrobot.

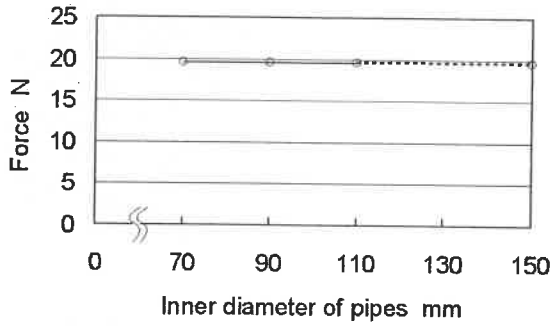

FIGURE 7. The experimental traction force.

REFERENCES

[1] Saga, N., Ueda, S. and Nakamura, T., Development of peristaltic Crawling Robot using Artificial Muscle Actuator, Transaction on The Society of Instrument and Control Engineers, 2005, Vol. 41, No. 12, pp. 1013-1018.

[2] Noritsugu, T. and Kubota, M., Development on In-pipe Mobile Robot using Pneumatic Soft-Actuator, Journal of Robotics Society Japan, 2000, Vol. 18, No. 6, pp. 73-80.

[3] Ono, M. and Kato, S., A Study of an Earthworm type Inspection Robot Movable in Long and Small Diameter Pipes - Development of a Three Somites type Mobile Robot and its Basic Characteristics -, Journal of the Japan Society for Precision Engineering, 2005, Vol. 71, No. 5, pp. 606-612.

[4] Kato, S., Aizawa, Y., Osada, T. and Ono, M., Fabrication of an Inchworm type Mobile Microrobot Movable in Different Diameter Pipes, Proc. of American Society for Precision Engineering 2004 Annual Meeting, pp. 261-264.

A PLATFORM FOR OBSERVING THE BEHAVIOR OF AFM CANTILEVERS DURING QUASI-STATIC LOADING

Lee M. Kumanchik[1], Tony L. Schmitz[1], and Jon R. Pratt[2]
[1]Department of Mechanical and Aerospace Engineering
University of Florida
Gainesville, FL, USA
[2]Manufacturing Engineering Laboratory
National Institute of Standards and Technology
Gaithersburg, MD, USA

INTRODUCTION

This paper describes a platform for studying the bending behavior of ultra-compliant (stiffness less than 1 N/m) atomic force microscope (AFM) cantilevers. The fundamental issue is that a cantilever does not represent an ideal design for precision force measurement due to the parasitic motion of the tip under load. For ultra-compliant cantilevers, the combination of a high adhesive force at the tip and parasitic motion can lead to proportionally substantial lateral (in-plane) forces. In addition, the tip-surface adhesive force can increase the propensity for sticking which is a considerable concern for colloidal probes due to the increased contact surface. These effects can manifest as deviate bending behavior and have been suggested as confounding contact style force calibration/measurement [1] since force is commonly related to tip displacement by an assumed bending model [2].

DESIGN OVERVIEW

The primary components of the apparatus are a scanning white light interferometer (SWLI) and the cantilever positional staging; see Fig. 1. The SWLI collects topographical information via analysis of the interference pattern between the sample and reference surfaces. The inference pattern is varied in a controlled fashion by translating either the sample or reference surface. Since white light has a short coherence length, there is a large variation in absolute interference intensity over a small change in optical path length. This can be related to the position of points on the sample surface; see [3] for a review. The method is non-contact and images through standard microscope objectives. The SWLI is combined with positional staging to provide the relative motion needed for cantilever loading experiments. Naturally, it is required that the staging does not obscure top down viewing of the cantilever system. Detailed specifications of the components in Fig. 1 are provided in Table 1.

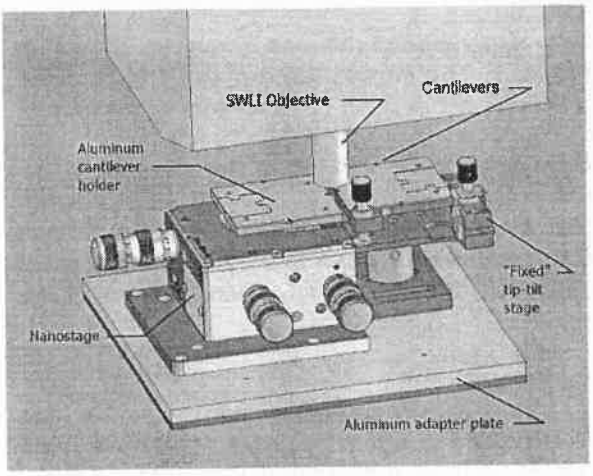

FIGURE 1. Full apparatus: SWLI for topographical measurement, nanostage for translational motion, tip-tilt stage for alignment, and AFM cantilever holders for easy handling.

TABLE 1. List of components, manufacturer, and selected specifications.

SWLI	Zygo NewView 5010	100 mm (Z) z-drive +2/-4 deg (pitch), +/- 4 deg (roll), 150 mm (X/Y) motorized stage 640x480 pixel camera
Nanostage	Thorlabs MAX301	4 mm (X/Y/Z) thumbscrews 20 µm (X/Y/Z) piezos
Tip-tilt stage	Thorlabs AMA501	+/- 4 deg (pitch/roll) thumbscrews
Holders & Adapter	Custom machined Custom polished	Aluminum (no particular grade selected)

SWLI measurements represent a paradigm shift from traditional AFM metrology. Beyond moving from a single point to full, topographical

measurement, there is also the imposition of new constraints. Primarily, a single topographical measurement takes time on the order of seconds, which prevents instantaneous measurement of the cantilever position. The effect is that experiments must be quasi-static, where motion is stopped periodically to perform a measurement. While strobing may provide an alternative, it requires a specific interferometric arrangement and is not discussed here. Secondly, there is a maximum measurable surface angle (off-parallel angle from the objective plane) due to limited lateral resolution and the necessity for sufficient reflected light to return to the detector. The maximum angle varies depending on the objective and system magnification with values ranging from about 1 deg (high magnification) to approximately 34 deg (low magnification). The effect is that two cantilevers cannot be imaged simultaneously if their relative angle is outside the maximum angle. Further, the deflection of a cantilever is limited such that the maximum slope in a profile must fall within the measurement capabilities.

The selected staging provides angular alignment of the cantilevers, a parameter often uncontrolled in traditional AFM platforms. Angular alignment enables different AFM system configurations, such as the standard 12 deg cantilever tilt, to be reproduced. Additionally, it enables the system to be adjusted as closely as possible to the assumed model. Alignment is verified by SWLI measurements, typically using a line or plane fit to the alignment surface. However, one difficulty is that many cantilevers have non-planar profiles due to fabrication-induced internal stresses. Therefore, they do not provide ideal alignment surface candidates. One alternative is to use the cantilever's macroscopic base/chip as the alignment surface since it is flat and nominally parallel to the cantilever. This method is applied here. Using the SWLI to measure this alignment is an iterative process due to the lack of real-time feedback (i.e., it requires a measure, adjust, re-measure sequence).

The holder system consists of flat aluminum plates that adapt to the staging and are large enough to be placed by hand. An important consideration is vertical clearance between the sample and objectives with high magnifications since these objectives typically have short working distances (e.g., a 100x objective may have a working distance of only 0.55 mm). Therefore, in our design, cantilevers are mounted using an adhesive rather than a mechanical clamp to minimize encroachment on the available clearance. As shown in Fig. 2, the mount locations are symmetric, enabling different cantilevers to be rotated into the same work volume with minimal realignment and handling. Since the cantilevers can be aligned to a variety of angles, they are mounted with sufficient overhang to prevent collision with the staging.

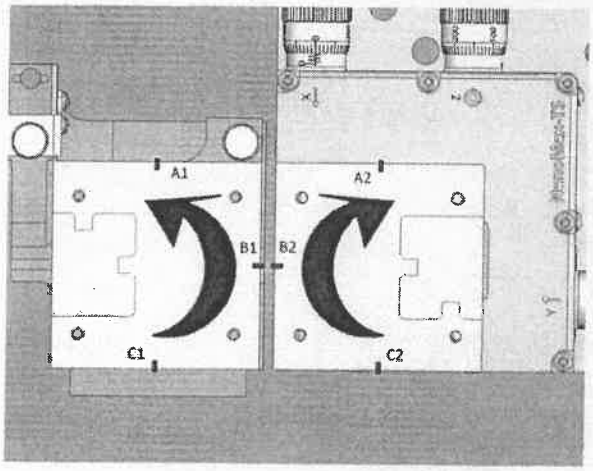

FIGURE 2. Rotating the holders enables rapid reconfiguration. This shows the generically identified chips switching from an experiment between chips B1 and B2 to C1 and C2.

DATA ANALYSIS

Regardless of the type of analysis being performed, there are some cautions worth addressing. First, there is a limited lateral resolution (plan view) of the cantilever which depends on system magnification and the number of pixels in the SWLI camera. For a 10x magnification with a 640x480 pixel camera, for example, the corresponding lateral resolution is 1.18 μm. This places an upper bound on the cantilever length measurement accuracy, which is a sensitive parameter in the Euler-Bernoulli stiffness equation. Next, as previously noted, there is a maximum measurable angle for any given feature by SWLI. Some cantilevers, due to isotropic etching, have sloping edges which cannot be detected by SWLI; see Fig. 3. Not only does this make the cantilever appear shorter, it also affects the ability to locate the tip over a sample. Finally, there is often significant noise in the measured height at sharply inclining edges as shown in Fig. 4. This further complicates data interpretation at the tip and the

base (in some cantilevers). It can also cause problems when there is dust contamination on the cantilever. Keeping the above cautions in mind, the Euler-Bernoulli beam equation is fit to measured cantilever profiles. The procedure used to provide the best fit is described below.

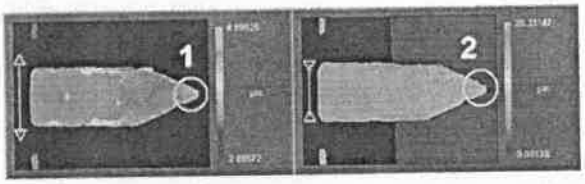

FIGURE 3. Cantilever edge (1) does not register since the feature is too angular. Measurement with a backdrop reveals the edge (2).

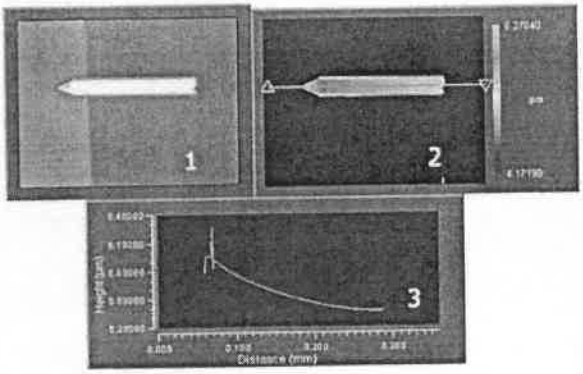

FIGURE 4. Top side of a cantilever as viewed through the objective (1); pyramidal tip is not visible since it resides on the bottom side. A sectional slice (2) shows noise near the edge due to a few specs of dust and the sharp decline of the edge (3).

Profile Extraction

All cantilevers are measured prior to loading and the pre-loaded images subtracted from the loaded images on a per pixel basis to isolate relative motion. This prevents cantilever shape (typically non-planar) from affecting the fit. Lateral drift of the image due to stage settling can occur for long measurement sequences and must be compensated prior to data subtraction using, for example, fiducial monitoring. Next, a slice through the middle of the cantilever is selected in order to reduce the problem to two dimensions, height and length; see Fig. 5.

Profile Smoothing

So that subsequent fitting is performed on a pristine dataset, noise is fenced off using the statistical definition for outliers. If Q_1 and Q_3 are the first and third quartiles and $IQR = (Q_3 - Q_1)$ is the interquartile range, then the outer fence of the data is $Data > Q_3 + 1.5 \cdot IQR$ for mild outliers and $Data > Q_3 + 3 \cdot IQR$ for extreme outliers [4]. The data is iteratively compared for closeness to a polynomial curve fit and outliers are rejected based on the mild outlier criteria. All data, including previous outliers, are re-analyzed for closeness each iteration. The final iteration uses the extreme outlier criteria so that the smallest amount of data is rejected; see Fig. 6.

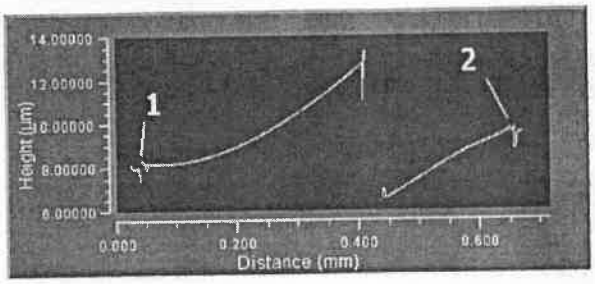

FIGURE 5. A sectional view of two cantilevers. The height gap between levers is occupied by the tip of (1). Noise appears at both the base and edge of (1) and (2).

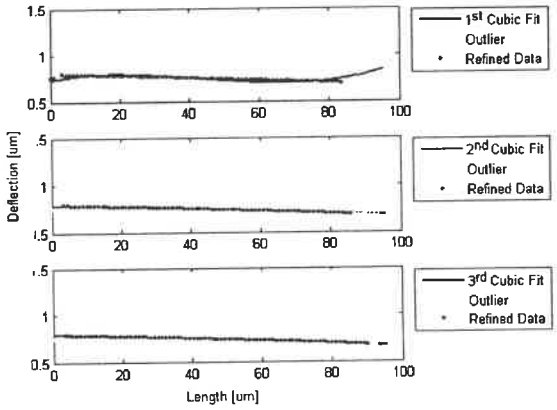

FIGURE 6. A three iteration solution to finding outliers. Since all data is re-analyzed each iteration, only the most extreme outliers are rejected.

Coordinate Transforming

The smoothed data is coordinate transformed into the model space of the Euler-Bernoulli beam bending equation, where the base location is (0, 0). It is common for the cantilever base data to be rejected in the previous step (the base is position invariant during bending and was used as the fiducial). In order to perform the

transformation the base position is extrapolated from the remaining data by a polynomial fit (order 4 is used here); see Fig. 7.

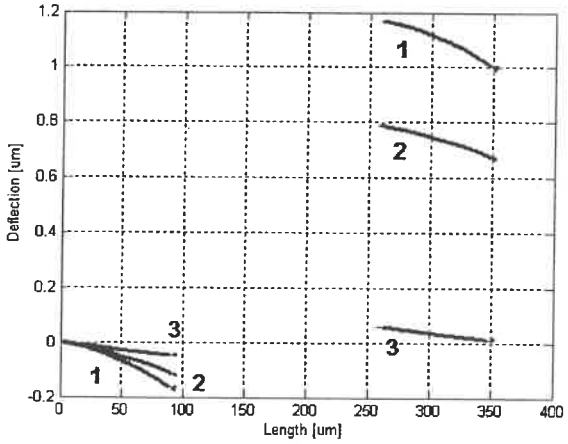

FIGURE 7. Scan-to-scan, data is not guaranteed to be aligned. Coordinate transformation moves each dataset to a common origin. A polynomial fit extrapolates the based position.

Beam Fitting

The Euler-Bernoulli beam equation for a fixed-free beam is compared to the smoothed, coordinate shifted data. The form of the beam equation for tip loading is,

$$y = F\frac{x^2}{6EI}(3L - x)$$

where x is the distance along the length of the beam, y is the beam deflection at x, L is the measured length of the cantilever, $EI = kL^3/3$, k is the stiffness specified by the manufacturer, and F is the force. In a standard AFM, $x = L$, y is measured at a single point, and F is calculated. In this study, there are multiple (x, y) pairs which are used to calculate a least squares fit of F. This fit is plotted on top of the data and compared; see Fig. 8. These results are for 0.027 N/m and 2 N/m cantilevers, respectively, loaded against a rigid surface. The results of the 2 N/m lever show possible deviation from the beam bending model.

ACKNOWLEDGEMENTS

Helpful contributors were John Ziegert, W. Gregory Sawyer, Jerry Bourne, and David Arnold. This research was supported by a grant from the National Institute of Standards and Technology, Gaithersburg, MD.

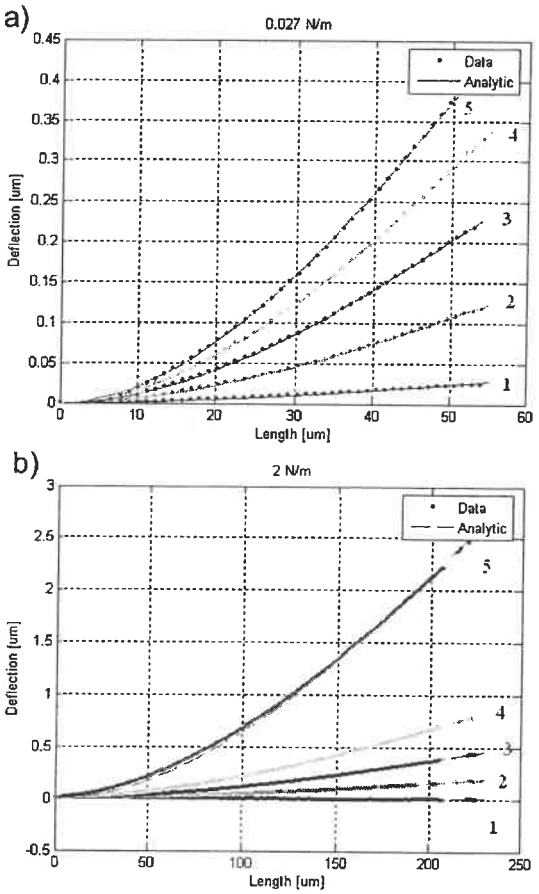

FIGURE 8. Cantilever loaded against a rigid surface. Snapshots (1-5) show the lever from just after contact with the surface to the maximum deflection imposed of about (a) 400 nm, and (b) 2.5 µm.

REFERENCES

[1] Pratt J, Smith D, Newell D, Kramar J. Progress toward Système International d'Unités traceable force metrology for nanomechanics. Journal of Material Research. 2004; 19: 366-379.

[2] Sader J, Chon J, Mulvaney P. Calibration of rectangular atomic force microscope cantilevers. Review of Scientific Instruments. 1999; 70: 3967-3969.

[3] de Groot P, Deck L. Surface profiling by analysis of white-light interferograms in the spatial frequency domain. Journal of Modern Optics. 1995; 42: 389-401.

[4] Renze J. Outlier. Mathworld—A Wolfram Web Resource created by Eric W. Weisstein. 2004; http://mathworld.wolfram.com/Outlier.

A COMPACT, COMPOUND ACTUATOR FOR THE MOLECULAR MEASURING MACHINE

Jing Li[1], Yin-Lin Shen[1], Jaehwa Jeong[2]*, Fredric E. Scire[2], and John A. Kramar[2]
[1]Department of Mechanical and Aerospace Engineering
The George Washington University
Washington DC, USA
[2]Precision Engineering Division
National Institute of Standards and Technology
Gaithersburg, MD, USA
***Current Affiliation: Department of Control and Instrumentation Engineering**
Korea University
Chungnam, Korea

INTRODUCTION

At the National Institute of Standards and Technology, we are developing a large-range, metrology-grade scanning probe microscope (SPM), which we call the Molecular Measuring Machine (M^3). M^3 is uniquely designed to make point-to-point, two-dimensional measurements within a 50 mm by 50 mm measurement area with nanometer-level uncertainties.[1] The instrument uses Michelson interferometers to measure the displacements of the SPM probe relative to the test artifact. Motion in the three orthogonal axes is provided by stacked coarse and fine motion stages that are guided by slide ways and flexure constraints, and driven by piezoceramic linear stepping motors and direct piezoceramic actuators, respectively. The instrument operates in a high vacuum environment, includes multiple stages of vibration isolation, and has temperature control with near millidegree stability at 20 °C.

The machine core is a copper sphere with orthogonal vee and inverted-vee slideways for the upper and lower carriages, which provide the Y and X coarse motion, respectively. The Z-axis motion assembly is suspended from the upper carriage. The design of the Z assembly is particularly challenging because of various competing constraints, especially a limited available volume of only 25 mm in height and 35 mm in diameter, and the need for repeatable motion, and high-resolution position sensors. The coarse-motion stage generates long range motion for the controlled approach of the probe tip to the surface. The fine-motion stage generates guided high-speed motion for servo tracking of the sample height.

In the 20 years since the development of the SPM, many compact actuator designs have been reported. Most of the early designs used piezoelectric steppers as the sample approach element and a piezoelectric tube scanner as the fine motion element. More recently, stage designs have been reported that include metrology capabilities afforded by displacement sensors and motion guides. In exchange, some of the compactness was generally lost. Here, we describe the design, performance, and calibration of a compact, compound Z-motor assembly.

DESIGN

The Z-motor is composed of two motion stages operating in a 25 mm internal diameter stainless steel housing cylinder. The coarse-motion stage is an inchworm-like piezoceramic stepping actuator with a potentiometer-type coarse-motion position sensor. The fine-motion stage is a flexure-guided, piezoceramic-driven actuator with a linear differential capacitance fine-motion position sensor.

Coarse-motion Stage

A cut-away view of the coarse-motion stage is shown in *Figure 1*. The coarse-motion inchworm motor is driven by three multi-stacked piezoelectric ceramic actuators, which are upper brake, pusher, and lower brake. Four-layer stacks are used for the upper and lower brakes, and a six-layer stack for the pusher. Using stacks increases the stroke of the pusher actuator and the radial force of the brakes. The piezoelectric ceramic material for the brakes and pusher is PZT-5H and the thickness of each layer is 0.51 mm. The transverse mode, d_{31}, is used for the brakes and the longitudinal mode,

of the performance of the Halbach linear motors and the eddy current dampers. Aluminum also has light weight, low cost and good thermal conductivity to dissipate the heat generated by the linear motors.

A vacuum preloaded air bearing is embedded into the center of the base to obtain frictionless motion and high stiffness in the z direction. Since the bearing is in a fixed position the umbilical cords for the air and vacuum are eliminated. Four three-phase Halbach linear motors are positioned around the vacuum preloaded air bearing 90 degrees apart from each other so that parallel motors can traverse the platen along their longitudinal directions and if needed, rotate the platen about the z-axis. The Halbach linear motors are also capable of providing force in the z-axis to correct for any roll and pitch. Three capacitance probes positioned around the air bearing will be used to obtain feedback for roll and pitch of the platen as well as displacement of the platen along z-axis. Laser steering optics posts and laser detectors are also positioned on the base. All the wiring, air and vacuum connections are done through the base.

The vacuum preloaded air bearing provides frictionless motion to the platen in the horizontal direction. Eddy current dampers are used for passive mechanical damping to increase the performance of the system. Damping is achieved by using copper plates moving between two magnet arrays [6]. When the copper plate moves in a stationery magnetic field, eddy currents are induced on the copper plate. The induced currents on the copper plate create Lorentz forces impeding the motion.

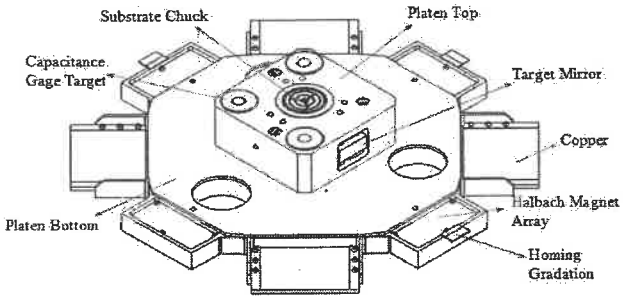

FIGURE 3. Platen

The platen, which glides on the air bearing, consists of two separate parts connected via flexures in order to diminish the effects of thermal gradients. The bottom part carries the Halbach magnet arrays, the copper plates for the eddy current dampers, and the capacitance gage targets. The platen bottom part is made of aluminum and is pocketed to decrease the weight and filled with urethane foam (ISODAMP C-3201 by E-A-R Special Composites) to add more damping to the system. A thin aluminum plate is epoxied on top of the bottom part, in order to increase the natural frequency. The flatness of the bottom surface of the platen is critical to get the platen to float on the air bearing and also to preload it by vacuum. The flatness of the capacitance gage targets is also important for the performance of the sensors. For these reasons the bottom surface was diamond turned together with the capacitance gage targets to make the surface as flat as possible.

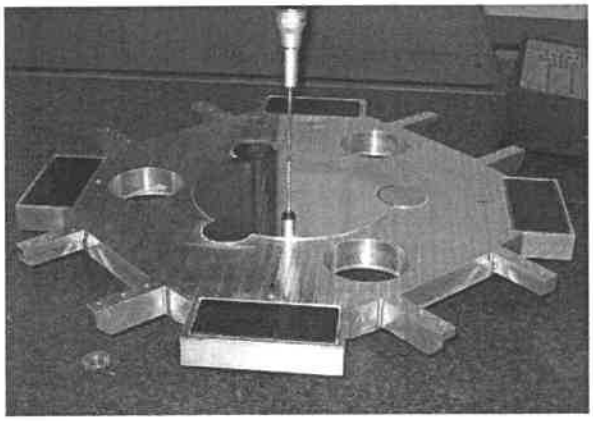

FIGURE 4. Platen bottom on Brown & Sharpe CMM

The top part carries the Zerodur® target mirrors for the interferometers, the chuck for the substrate and the capacitance gage targets. The target mirrors are sliced from a 76.2 mm diameter mirror that has λ/20 flatness. The wafer chuck is currently a temporary chuck which will be replaced with a pin chuck. The two platen parts are connected together by three sets of flexures for thermal growth reasons. The flexures are positioned 120 degrees apart from each other

Since the displacement laser interferometer system can only provide relative feedback, homing sensors are required to start and return the machine to its nominal position. Once the machine is returned to its home position, the reference coordinate system can be defined and

all the axes can be reset to "0". This is important for phasing of the linear motors and for error mapping the machine. Each homing sensor is composed of a scale and a pair of optical interrupters [6]. Three homing sensors are used in MAPS to home the stage in X, Y and θ_z. Two of the sensors are positioned across from each other along the x axis for the rotation about the z axis and the 3rd one is positioned along the y axis.

Interchangeable modules (such as an NIL or AFM head) are supported by the structural frame which also carries the interferometer optics. Spherolinder® semi-kinematic mounts and fine-threaded screws provide coupling between each module and the structural frame. The coupling mechanisms provide 1.5 mm of coarse motion used for compensating variations in substrate and stamp thicknesses. Three PZT actuators coupled to the structural frame via toroidal flexures provide the modules with 40 µm of fine motion travel along the z-axis as well as controlling the pitch and roll motions of the frame/imprint module assembly. Feedback for these motions is provided by using capacitance gages that are referenced to surfaces on the wafer chucks.

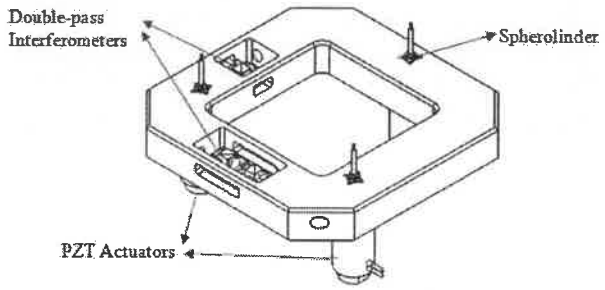

FIGURE 5. Structural Frame on PZT Actuators

The imprinter module consists of a fused silica pin chuck at the center with a seal wrapped around it. The pin chuck was made of optical grade fused silica by wet etching process using hydrofluoric acid with a chrome-gold hard mask to transmit UV light to cure the resist for NIL [7]. The center area is also surrounded by a seal to create a vacuum area for the imprinting process. Three capacitance gages are positioned outside the vacuum area to measure the gap between the imprinter module and the target surfaces on the platen top.

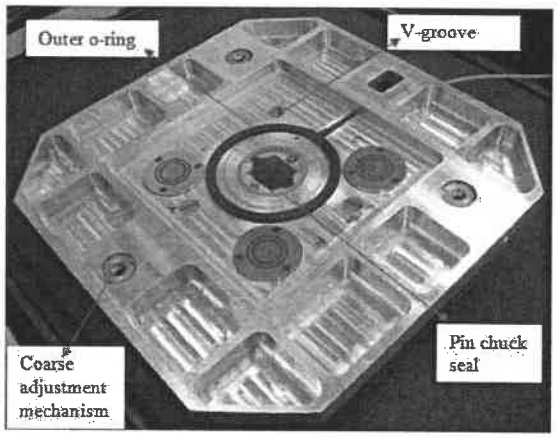

FIGURE 6. Imprinting Module

A moving gantry type bridge was designed and built to hold and locate the optical components required for the moiré fringe alignment and the UV beam steering optics. It consists of left and right columns, the outer spans, the middle span and the gussets. All these components are made of 6061 Aluminum. The bridge translates manually on Hoerbiger ORIGA aluminum guides. All the cables are contained and carried by the chains connected between the columns and the rails. The bridge is manually positioned to the required locations and locked into the positions by a locking mechanism. The first location is the position where the objectives can focus on the moiré fringes for the alignment of the substrate and the stamp. The second position is required for the UV light flooding onto the imprinting area. The bridge is moved to the second position so that the UV light coming from the UV source lens is redirected to the imprinting area by a fold mirror mounted on the bridge.

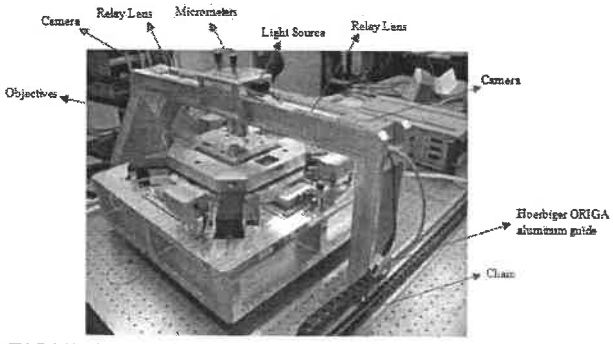

FIGURE 7. Bridge

MAPS also employs a moiré fringe alignment technique to align the substrate and the stamp within sub-10 nm accuracy. The substrate and the stamp both have 2 alignment marks 35.56 mm apart from each other. Each alignment mark

consists of dual linear grating sets having different periods (p_1 & p_2). Period p_1 on the stamp faces period p_2 on the substrate and vise versa.

The error budget of the stage is performed by Fesperman [4] and Ozturk [5] and the error (RSS) is found to be

$$\begin{bmatrix} \Delta X \\ \Delta Y \\ \Delta Z \end{bmatrix}^{(5,5,27)} = \begin{bmatrix} 123.41 \\ 29.69 \\ 0.66 \end{bmatrix} = nm$$

The main sources of error are the temperature variations, the form error of the target mirrors, and the orthogonality of the target mirrors in relation to each other and the capacitance target plates. Another error source is the Abbe offset between the substrate location and the laser interferometers which will have to be compensated. In order to decrease the temperature variations generated by external disturbances and also the internal heat sources in the system, a temperature controlled chamber was modified, tested and proven to be under control within ±0.03 Celsius degrees at a point with gradients of about 0.03 Celsius. The gradients are stable to better than 0.01 Celsius degrees. The critical components such as the structural frame, the platen top, the target mirror holders, and the imprinter module will be replaced with low thermal expansion and high stiffness material to decrease the effect of thermal variations.

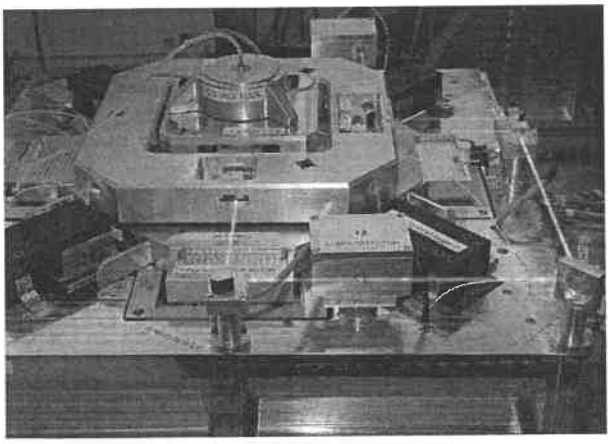

FIGURE 8. Stage under Control with Laser DMI

MAPS is controlled by UMAC industrial control system, which was donated by Delta Tau Data Systems, Inc, to the control (Prof. T.C. Tsao's) group. This control system is composed of a PMAC2 controller and interfacing cards for I/0, A/D conversion, D/A conversion, and 4096X sin/cos quadrature encoder conversion.

CONCLUSION

MAPS was built and assembled at Center for Precision Metrology of Univ. of North Carolina at Charlotte. The stage is under control by using the UMAC controller. The preliminary imprinting tests are performed. The stage is ready to be packed to ship to UCLA to implement advanced control techniques such as iterative learning control, repetitive and adaptive control to reduce the repeatable and non-repeatable errors.

REFERENCES

[1] Harriott L.R., Limits of lithography; Proceedings of the IEEE, Volume 89(3) March 2001 Page(s):366 – 374

[2] Moore G.E., Cramming more components onto integrated circuits, Electronics, Volume 38, Number 8, April 19, 1965

[3] Guo LJ, Nanoimprint Lithography: Methods and Material Requirements, Adv. Mater., 19, 495-513

[4] Fesperman RR, Multi-Scale Alignment Positioning System Ph.D. Dissertation, UNC Charlotte, Mechanical Engineering, 2006

[5] Ozturk O, Multi-Scale Alignment Positioning System Ph.D. Dissertation, UNC Charlotte, Mechanical Engineering, 2008

[6] Ozturk O, Damping and Homing Issues in Nanoimprinting Machine, ASPE Spring Topical Meeting, Precision Mechanical Design & Mechatronics for Sub 50nm Semiconductor Equipment, April 7-8, 2008, Berkeley ,CA

[7] Lemmons TD, Ozturk O, Hocken RJ, Fesperman RR, Fabrication of Fused Silica Optical Quality Pin Chuck Using Wet Etching Process, 23rd ASPE General Meeting, October, 2008, Portland, Oregon

PNEUMATIC SERVO BEARING ACTUATOR FOR ULTRAPRECISE POSITIONING – PART 2: A NEW APPROACH TO ULTRA-PRECISION MOTION CONTROL

Katsumi Sasaki[1], Tomoko Hirayama[2] and Hiroshi Yabe[3]
[1]Pneumatic Servo Controls Ltd.
2266-22 Anagahora, Shimo-Shidami, Moriyama-ku, Nagoya, Aichi, Japan
[2]Dept. of Mechanical Engineering, Doshisha University
1-3 Miyakodani, Tatara, Kyotanabe, Kyoto, Japan
[3]Kyoto University (former affiliation)
Yoshida-honmachi, Sakyo-ku, Kyoto, Japan

INTRODUCTION

Externally pressurized gas-lubricated thrust bearings (aerostatic bearings) keep the bearing clearance constant under a constant supply pressure. We investigated how controlling the supply pressure with an electro-pneumatic servovalve can be used to dynamically adjust the bearing gap height. As a result of our investigation, we developed an electro-pneumatic servo-actuator "pneumatic servo bearing actuator (PSBA)" for position control, force control, and acceleration control.

This paper describes a new approach to ultraprecise positioning that uses PSBAs with multiple-layered thin bearing pads in a tandem arrangement.

The wide range of potential uses of PSBAs requires the use of bearing pads with diameters ranging from small to large, or a bearing with various numbers of the layered pads.

We tested the load capacity of single-pad, 3-layered-pad, 10-layered-pad, and 30-layered-pad PSBAs. We also tested the dynamic response of the ten-layered-pad actuator.

FEATURES OF PNEUMATIC SERVO BEARING ACTUATION SYSTEMS

Pneumatic servo bearing actuation systems have a number of attractive features that form a baseline against which alternate technology systems should be compared.

- simple structure
- simple energy storage and power conversion
- wide temperature capability
- long-term stability
- no EMI or radiation susceptibility
- low hysteresis
- low noise
- high resolution
- high accuracy
- high dynamic response
- high backdrive stiffness(high bearing stiffness)
- slight temperature rise over entire actuation range

SYSTEM COMPONENTS

Servovalve

A three-way, voice-coil-motor-operated nozzle-flapper valve controls the pneumatic flow into and out of the PSBA supply port. Changes in this flow control the pressure of the bearing clearance.

A schematic diagram of servo valve is shown in Figure 1.

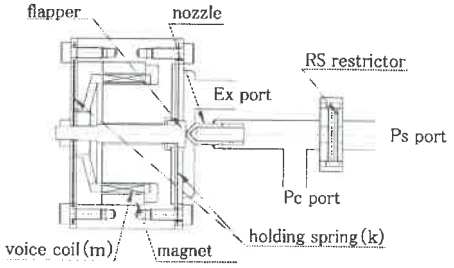

Figure 1. Nozzle-flapper type servo valve.

The nozzle-flapper uses the cylindrical curtain orifice area formed by a flapper (driven by a voice coil motor) moving towards a sharp edged orifice and RS restrictor (fixed orifice).

In a typical application, the bandwidth frequency of the force motor is 200 Hz.

The block diagram in Figure 2 illustrates the system dynamics.

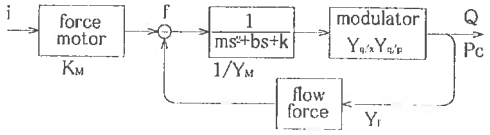

Figure 2. Block diagram for NF type servovalve.

The servovalve specifications are summarized in Table 1.

Table 1. Specifications of servovalve.

Rated Current	1.5A
Operating Pressure	~1MPa
Rated Flow	8 l/min at 0.4MPa
Hysteresis	Less than 0.1%Ir

Bearing actuator

A model of the bearing actuator with the tandemly arranged bearing pads is shown in schematic form in Figure 3.

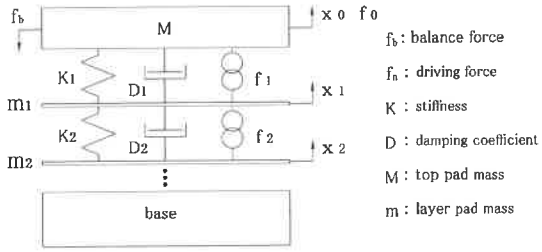

Figure 3. Dynamic model of bearing actuator.

The patterns of grooves on the bearing pad surface is shown schematically in Figure 4.

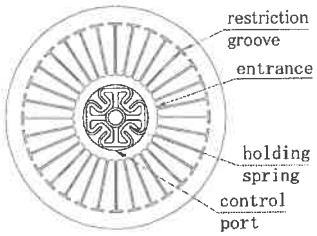

Figure 4. Bearing pad.

The specifications of a typical bearing pad are listed in Table 2.

Table 2. Specifications of bearing pad.

Outer radius of bearing pad	18mm
Radius of inlet port	5mm
Spool mass	350g
Volume, V	3cc

Clearly, a number of simplifying assumptions have been made to arrive at the matrix model.

- the mass of layered pad is negligible (0.6g),
- the performance is modeled for a small stroke at the operating point,
- the gap height between identical configuration pads can be assumed to create the same operation,
- a lumped parameter model is used for the bearing actuator so the admittance matrix can be made linearization

A bearing model with many tandemly arranged pads that was developed for analysis and matching between the bearing and the servovalve or load is shown in Figure 5.

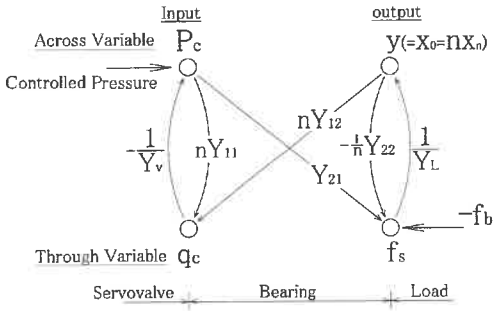

Figure 5. Bearing actuator model.

Five parameters are used in the model.

n : number of bearing pads
Y_{11}: input admittance
Y_{12}: flow gain across bearing
Y_{21}: thrust force gain
Y_{22}: stiffness and damping coefficient

The equations relating the number of pads to the stiffness, damping, and mass of the tandem-layered bearing actuator are:

$$(Ms^2 + \frac{D}{n}s + \frac{K}{n})\Delta y = \Delta f_s \qquad (1)$$

where

$$\Delta f_s = Y_{21}\Delta p_c \qquad \Delta f_s = \Delta f_1 = \Delta f_2 \cdots = \Delta f_n$$

$$Y_{21} = \Delta f / \Delta P_c \qquad \Delta y = n \cdot \Delta x$$

The meanings of the symbols should be referred to Figure 3 and 5. Equation (1) is effectively used to simulate numerically the motion of the top pad.

PSBA SYSTEM MODEL

A PSBA system is constructed of a servo amplifier, a servovalve, a thrust bearing, and position transducer (for closed-loop control).

The PSBA system model depicted in Figure 6 is for two system configurations, an open-loop system without position feedback and a closed-loop system with position feedback.

External disturbances due mainly to servovalve null shift are labeled "E.D.".

The advantages of pressure-generation are combined with the high accuracy and high responsibility of the nozzle-flapper valve operated by the moving coil type force motor.

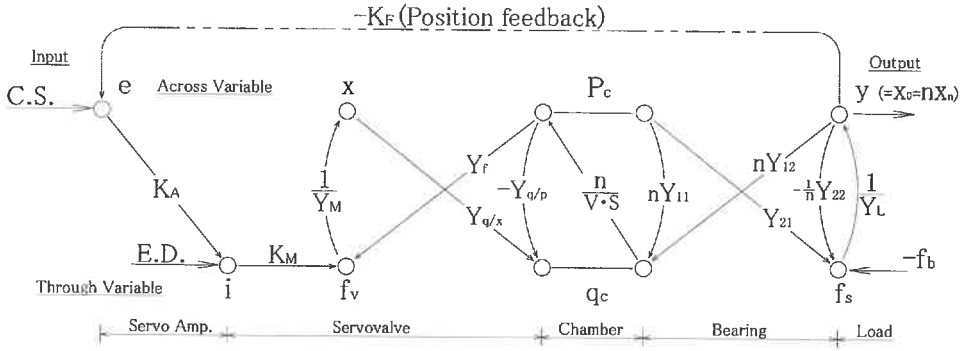

Figure 6. PSBA system model.

The open-loop PSBA system has good time response and high accuracy.

An electrical position feedback PSBA has better linearity, better null stability with external disturbances, (such as supply pressure change, temperature change, and external force change), and higher dynamics, resulting in a higher closed loop gain.

TEST APPARATUS

The static characteristics and dynamic characteristics of the PSBA system were measured using the test apparatus illustrated in Figure 7.

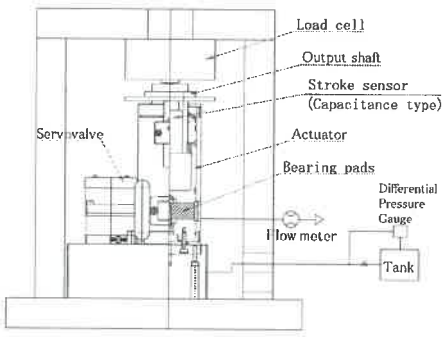

Figure 7. Test apparatus.

A high resolution and high response stroke sensor (ADE Ltd.) was attached to the outside of the actuator to measure the actuator stroke with sub nano resolution.

A single-axis tandem-arranged actuator is diagrammed in Figure 8.

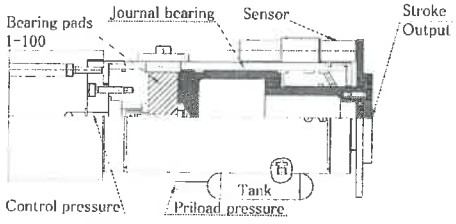

Figure 8. Single-axis actuator.

RESULTS UNDER OPEN-LOOP CONTROL

Static Characteristics

The load capacities for the four types of actuators, (single-pad, 3-layered-pads, 10-layered-pads, and 30-layered-pads) are shown in Figure 9. Note that the bearing stiffness can be obtained by $\Delta f_s / \Delta y$ from the results.

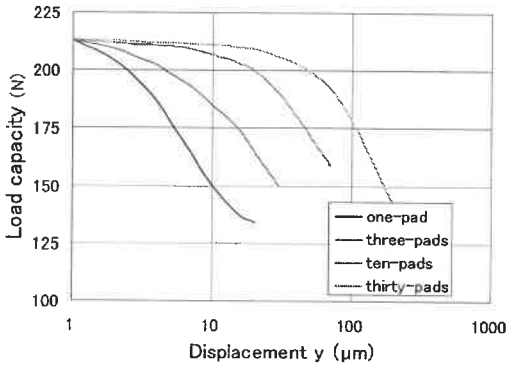

Control pressure (Pc) 0.3MPa

Figure 9. Load capacity.

Response Characteristics

We tested a ten-layered-pads PSBA controlled by a servovalve with precise eight-step input. As shown Figure 10 each step covered about 10 nm, so the PSBA controlled the stroke with a high resolution, high stability, and low noise.

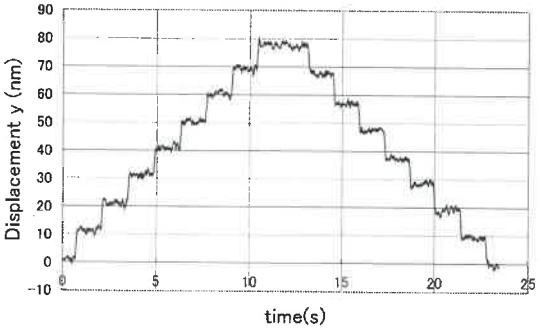

Supply pressure (Ps) 0.3MPa 0-position 20 μm

Figure 10. Eight-step response.

Dynamic Characteristics

The bearing gaps of a ten-layered-pads PSBA were controlled by adjusting the input pressure. The bearing inherent dynamics is represented by the frequency response plots in Figure 11.

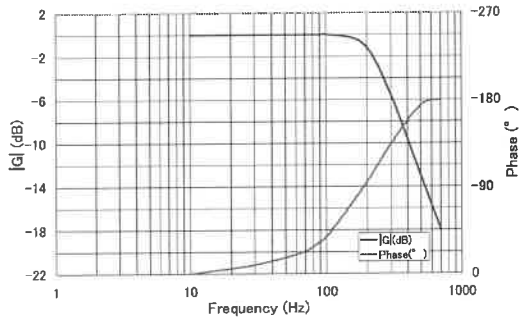

Load capacity 104N, 0-position 20 µm,
6 µm peak-to-peak command amplitude

Figure 11. Inherent frequency response.

Indicate cutoff frequency may be 200 Hz and that damping ratio may be 0.7 assuming a 2nd order system.

The frequency response in the amplifier input versus output stroke of the ten-layered-pad PSBA with open-loop control is shown in Figure 12.

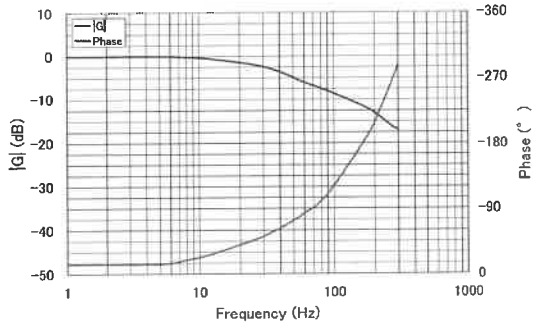

Supply pressure (Ps) 0.3 MPa, 0-position 20 µm,
1 µm peak-to-peak command amplitude

Figure 12. Frequency response (open-loop).

The cutoff frequency may be 22 Hz assuming a 1st order system. In a PSBA in which a small flow-rate servovalve controls flow, the prime cause of attenuation above the cutoff frequency is assumed to be the large air control volume, V of the bearing input chamber.

RESULTS FOR TEN-PAIRED-PAD PSBA WITH CLOSED LOOP CONTROL

Static Characteristics

We tested the load capacity of an electrical position feedback PSBA (closed-loop control) and an open-loop PSBA both with ten-layered-pads. The operating point for both systems (closed-loop and open-loop) was the same, at the 20 µm stroke. As shown in Figure 13.

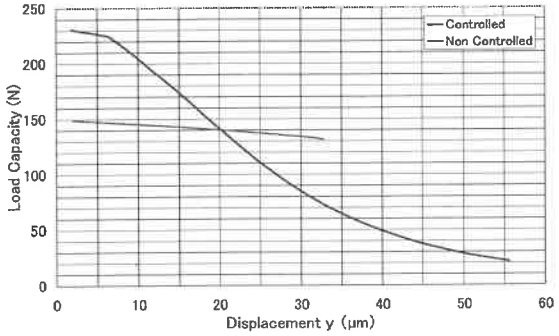

Supply pressure (Ps) 0.3MPa

Figure 13. Load capacity.

The stiffness of the closed-loop PSBA at the operating point was the 12 times larger than that of the open-loop one.

Dynamic Characteristics

The frequency response results are shown in Figure 14. The amplifier gain was adjusted to achieve a loop gain which resulted in a peak amplitude ratio of 1 (0dB).

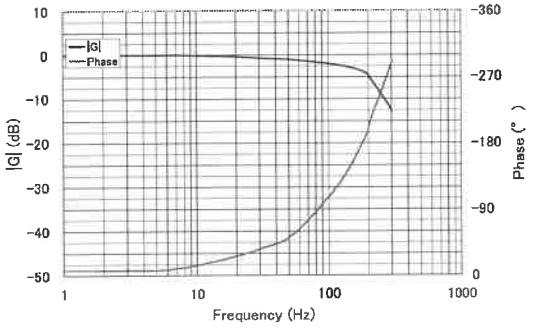

Supply pressure (Ps) 0.3MPa, 0-position 20 µm
1 µm peak-to-peak command amplitude

Figure 14. Frequency response (closed-loop).

CONCLUSION

The excellent performance capabilities of the pneumatic servo bearing actuator mean that it should be directed primarily at applications in the semiconductor industry requiring ultraprecise positioning.

REFERENCES

[1] K. Kogure et al., Bulletin of JSME, Vol. 25, No. 210, (1982) 2039-2045, in Japanese.

[2] J. Blackburn et al., Fluid Power Control, The MIT Press, (1960).

[3] T. Machiyama et al., Bulletin of S.E.R.L. Waseda University, No. 37, (1966) 16-30, in Japanese.

DESIGN OF A HIGH FREQUENCY MEMS SCANNING MIRROR

Herman Soemers[1,2], Krassimir Krastev[3] and Diederik van Lierop[1]
[1]Philips Applied Technologies, Eindhoven, The Netherlands
[2]University of Twente, Enschede, The Netherlands
[3]Yacht, Eindhoven, The Netherlands

INTRODUCTION

The principle of steering laser beam deflection with controlled tilting of (two) mirror surfaces is already widely used in the macro-world for a variety of scanning and processing solutions. The scanning mirror may have controlled rotation around two orthogonal axes, as shown in *FIGURE 1* a) below or two separate 1D scanning mirrors as given in *FIGURE 1* b)

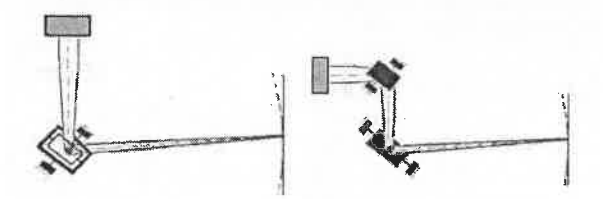

a) b)

FIGURE 1. The principle of scanning surfaces using a) either a 2 DOF tilting mirror or b) two single axis mirrors

Currently micro beamer applications are in development based on laser light sources. These small form-factor beamers may be used as an add-on to a laptop or a mobile phone. The laser beam is focused in such a way that the surface defined by the beam waist has the smallest possible deviation from the screen surface. The image generation is achieved by synchronizing the intensity of the laser light with the mirror scan angles (concept similar to the CRT's). Red, Green and Blue (RGB) laser sources are used for color imaging applications.

Small form-factor beamers with high resolution (typical VGA or SVGA) require small diameter (mm) mirrors moving at high frequency (typical 16 KHz or more). MEMS technology is preferred for manufacturing the mirrors with integrated suspension, actuation and angle sensing. Many demonstrated scanner devices (a number of them is listed in *FIGURE 2*) clearly struggle with the combination of specifications set for the mirror diameter, flatness, rotation angle, dynamics, lifetime, reliability and so on. It poses a tremendous challenge for the designers.

The design proposed in this paper is fundamentally different from the cantilever beam suspended state-of-the-art tilting mirror MEMS devices as currently known. This novel design allows for better dynamics and mirror (dynamic) flatness as well as a low driving voltage.

REQUIREMENTS

To avoid cross-talk between mirrors and to reduce complexity, it was decided to pursue the principle of *FIGURE 1* b). The targeted design specifications for the fast mirror (subject of this paper) are the following:

- Scanning resolution: SVGA 800x600 pixels
- Mirror shape - circular
- Mirror diameter: 1 mm
- Maximum scan angle for SVGA resolution (mechanical): 7.34°
- Operation frequency:18.5 kHz ± 0.3 kHz
- Scanning mode: bi-directional scan, vertical fast scanning axis
- Maximum driving voltage: 100 V
- Maximum mirror surface dynamic deformation: ± 40 nm
- Vertical Comb drive actuation

Now some background is given on the various points of specification.

Resolution

The following formula expresses the relation between the total scan angle and the smallest resolvable spot:

$$N = \frac{\varphi}{\Delta\varphi} = \frac{total\ scan\ angle}{smallest\ resolvable\ spot} = \frac{\varphi \cdot D}{\alpha \cdot \lambda}$$

D = mirror size; λ = wavelength, α= aperture form factor

FIGURE 2 shows that for VGA resolution the θD product need to be larger than 8. The factors α and λ are more or less imposed by the laser source used. This leaves θ and D as design parameters (given a certain oscillation frequency).

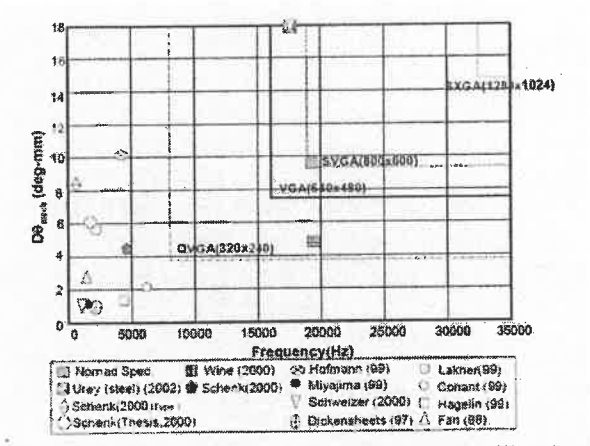

FIGURE 2. Various scanners classification based on the product θD (Taken from [2])

The increase of the mirror size, for example, leads to increase of the mass inertia moment in the oscillator, which affects the dynamic system performance. A rule of thumb states that the total mirror unflatness should be smaller than $\lambda/10$. The dynamic mirror deformation δ is proportional to D^5:

$$\delta_{max} = 0.217 \cdot \frac{\rho f^2 D^5 \theta_{mech}}{Et^2}$$

(ρ = the specific mass, f = tilting frequency, E = Young's modulus, t: mirror thickness)

So it is clear that a bigger mirror diameter affects the mirror dynamic deformation. Increased mirror size also increases the damping in the system. And as a consequence the required actuator torque.

Scanning frequency

The options for the scanning frequency come from the choice of the scanning method (uni- or bi-directional scanning) and from the scanning direction of the high frequency scanner. The bi-directional scanning eases the requirements for the scanning oscillator. Very often vertical high frequency and horizontal low scanning frequency is preferred because the image resolution in the vertical direction is lower than the resolution in the horizontal direction. This leads to further reduction of the operational frequency requirements for the fast scan motion of the scanning mirror.

Higher resolutions require higher scan frequencies which in turn require higher suspension stiffness. Also the damping increases. This becomes increasingly difficult, for greater actuator torque is needed. Also parasitic dynamics may be expected blurring the image.

Actuation and control

It showed that it is most favorable to use electrostatic or electromagnetic driving principle for the fast scanner mirror. Since the electrostatic actuator is more suitable for resonant driving of the micro-mirror it should be considered a good solution for the fast scanner (the one dealt with here).

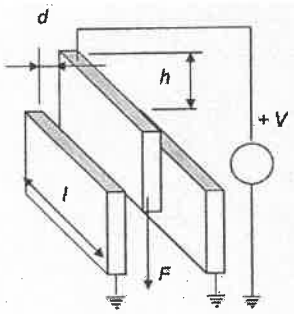

FIGURE 3. Translating capacitive actuator example

The most popular method of bringing torque to a tilting micro- mirror till now is the electrostatic vertical (out-of-plane) comb drive actuator. It produces acceptable energy density and allows larger mirror tilt compared to the parallel plate arrangement.

$$F = \frac{\epsilon_0 \cdot l_p \cdot V^2}{d}$$

(ε = permittivity of air, l_p = length of the comb finger, V= applied voltage and d = gap between the comb fingers).

In principal, an initial offset height is needed between the fixed and the moving plates in order to generate an initial force *F and to control the phase of the oscillation.*,Using additional starting electrodes deposited on top of the fixed set of comb fingers the same effect can be obtained.

We have chosen though to use both the handle and device layer of an SOI (Silicon-on-Insulator) wafer to create the comb-fingers. By controlling the voltage applied to both layers individually, a well defined start-up behavior is guaranteed.

The actuator torque for small angles can be expressed by:

$$T = 2n\frac{\epsilon_0 \cdot l_p \cdot V^2}{d} \cdot w$$

Different types of driving signals for the driving voltage could be used with these comb drive configurations. Here a pulsed driving signal is

used with pulse length = ¼ of the micro-mirror oscillation period. The pulse is synchronized with the oscillation such that it is applied when the moving comb fingers of the mirror are coming towards the fixed comb fingers. When the moveable fingers are moving away from the fixed ones, there is no voltage applied.

Dynamics

The human eye is very sensitive to image irregularities, distortions and jitter caused by the scanning device, which poses very strict requirements for their dynamic performance. Therefore it is preferred to avoid other resonant modes occurring close to the fundamental rotational mode frequency in both scanning directions. It is preferred to have the other mode frequencies much higher than the torsional mode and in such bandwidths that the cross coupling between both orthogonal torsional movements is avoided. This is more difficult to achieve for the fast scanning movement and requires high stiffness constraints of the mirror deflection in all other directions.

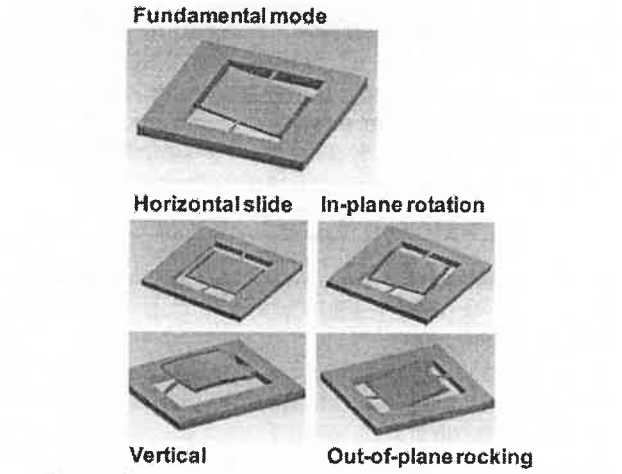

FIGURE 5. Resonance mode shapes of cantilever suspended micro-mirror

CONCEPT DESIGN

The mirror is suspended by torsion beams, but these merely serve as constraints in the y-direction and tilt directions other than the fundamental mode. Four leaf springs with anchor points close to the rotation axis are added to the suspension. At the other end they are connected to mirror support structure (see *FIGURE 6).* The leaf springs add considerable torsional stiffness so that they are dominant in attaining the fundamental mode resonant frequency. This concept gives far greater freedom to realize the desired vibration modes than the traditional cantilever suspension concepts.

Unlike the traditional torsion beam suspended micro-mirror devices that are usually fabricated from the top (device) layer of SOIwafers, the idea for the cantilever beam suspended micro-mirror is that the device is fabricated in both layers. The cross section A-A of the device in *FIGURE 6* shows the positioning of the different device layers in the SOI wafer. The micro-mirror body is divided into two by the BOX (Buried OXide layer), which means that we have two electrically insulated parts of the micro-mirror body.

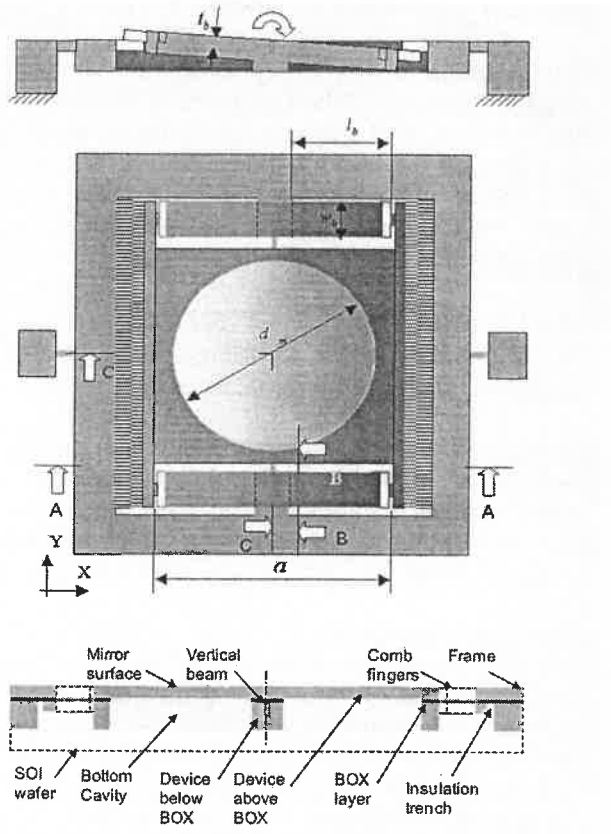

FIGURE 6. Concept top view and cross section A –A in SOI wafer

RESULTS

As shown in *FIGURE 7* the actual design the mirror has a star-shaped support structure to optimize the stiffness of the mirror structure. This structure also connects the comb sections to the mirror and decouples comb deflection from the mirror.

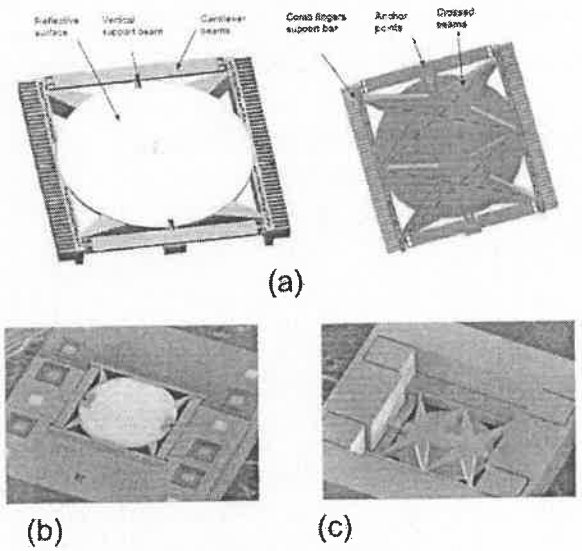

FIGURE 7.(a) Stiffening structure, (b) mounted device with interconnects, (c) back structure (courtesy SILEX)

Preliminary measurements

As the devices became only recently available, mere indicative measurements have been done so far. However they show the great potential of the design presented in this paper. *FIGURE 7* is a screen print obtained with a Polytec dynamic analyzer. It shows the fundamental (tilting) mode that is used for scanning operation. The first device samples have a measured 23.5 kHz fundamental mode frequency with a Q-factor in air around 200, as predicted by our models. Very important however is the pure tilting motion involved with this mode. The first parasitic eigenmode that affects the optical performance of this device is found at 137 kHz.

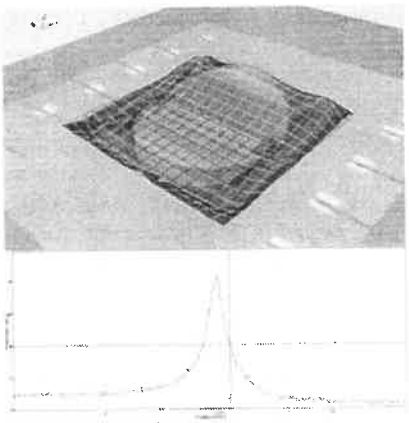

FIGURE 7 The fundamental mode at 23.5 kHz frequency at low amplitudes

Another important characteristic of the mirror actuation system is the tilting amplitude versus the frequency of the actuation signal. *FIGURE 8 clearly* shows the non-linear behavior of the electrostatic actuator (of another sample), which results in a strong asymmetry for large deflections. It also demonstrates that high tilting angles can be achieved, even when an actuation potential has been applied to the device layer only. Larger amplitudes will be obtained when connecting both the handle and device layer, allowing us to easily reach at least the ± 7.34° required for VGA resolution displays, while requiring lower voltages..

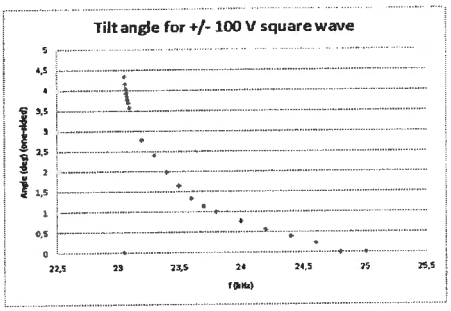

FIGURE 8 (one-sided) tilt angle as a function of the driving frequency at 100 V square wave, using only the device layer.

CONCLUSION

In this paper an alternative to existing MEMS tilting mirror devices is presented which has great potential. Preliminary results indicate the capability to reach SVGA image projection quality with an extremely small form factor. For a complete scanner, a low frequency scanning mirror needs to be added. The real challenge however is the high frequency mirror as presented here. Future work is planned to fully characterize the MEMS mirror and next to build a prototype micro beamer.

REFERENCES

[1] Krastev K, Modeling and Simulation of a 2D Micro-Mirror as a Part of a Scanning System. Graduation Thesis, Heriot Watt University, Edinburgh, 2006

[2] Hakan Urey, Torsional Scanner Design for high-resolution display systems, Optical Scanning II, Proc SPEI vol 4773,pp27-37, Seattle, Washington, July 2002

[3] Schenk H, Dürr P, Kunze D, Kück H, A new driving principle for micromechanical torsional actuators" Micro-electro-mechanical systems (MEMS) 1999., New York,

EFFICIENT EVALUATION OF EARLY MACHINE CONCEPTS IN THE FREQUENCY DOMAIN INCLUDING CONTROL ISSUES

Sascha Weikert, Christian Jaeger, Sergio Bossoni, Konrad Wegener
Institute of Machine Tools and Manufacturing
Swiss Federal Institute of Technology (ETH)
Zurich, Switzerland

INTRODUCTION

For the design of machine tools, a number of optimization tools have been developed in order to optimize these mechatronic systems in regard to their required static, dynamic and thermal behavior. Components and drives are optimized using FEM or simulations in the time domain. The changing requirements concerning productivity and developments in the area of the machine tools changed the focus of the research activities towards optimization of dynamic properties.

In a first step a set of basic properties such as static stiffness and deflections due to inertial and frictional loads can be evaluated using efficient static, quasi-static approaches in order to find appropriate global concepts or configurations. The rigid-body simulation approach can be used for the efficient evaluation of machine tool concepts concerning static and dynamic loads [1].

The properties of the drives themselves can, to a certain extend, be evaluated using 1-D approaches which permit to verify the basic effects in the frequency domain. Investigations in the time-domain are also feasible using models combining control, drives and structure. Here the structure is often represented as additional linearly coupled masses, which allows the phenomenological modeling of significant vibrational properties of the structure.

Afterwards, more detailed information concerning the interaction of the control system drives and structure are needed. At the early stage of the design the allowable control parameters which can be applied for the machine tool are often in the focus. Changing machine configuration parameters influences the allowable values. Therefore these parameters should also be included in the evaluation of the machine tool concept.

In this paper an efficient combination of rigid body models and the representation of controlled drives based on transfer functions is presented. The control properties are reduced to the proportional gains of position and velocity loop, the time constant of the integrator in the velocity loop. The drive properties are represented by the resulting time constant including the current loop parameters and the force constant.

Combining state-space representation of the structure and the linear control/drive model allows the assessment of several transfer functions of the velocity and position loops including behavior at the TCP (Tool Center Point) without using large Finite Element Models.

MACHINE MODEL

The machine tool under investigation is a three axes configuration (see Figure 1). The machine structure is modeled using elastically coupled rigid bodies [2]. The definition of the structure model is done using the IWF Axis Construction Kit (ACK) [3]. This model contains the complete set of stiffness parameters and the mass distribution. Dominating component compliances have been included using automatically segmented beam elements. Drives are represented using single axial linear compliances between the sliders and the body where the fixed bearings are located. This kind of modeling already shows the eigenfrequencies and the corresponding mode shapes of the real machine tool.

ENHANCED MODELING OF DRIVES

In order to include the significant dynamic properties of the drives, its inertias are added using three additional bodies for each axis. On this early stage of modeling the drive's inertia is set equal the driven inertia. Furthermore the drive inertia is then distributed in the ratio of 80, 10 and 10% where the first body represents the DC-motor. The two smaller bodies represent the inertias of the coupling and the gear wheel. These nine bodies are automatically added onto the structure model. These additional bodies are coupled to the driven axis in the corresponding axis of motion with springs, of stiffness k_C

The single axial compliances which were used before are therefore omitted. For the next steps only the axial degrees of motion of the additional bodies are used.

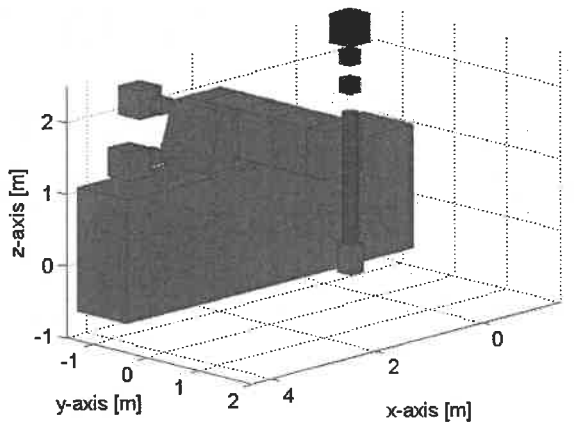

FIGURE 1. Machine tool, completed with nine drive bodies (three per drive direction)

Feed-back variants

In order to permit a wide variety of solutions to be analyzed, semi-closed loop and closed loop feedback configurations can be chosen on demand. For the verification of the resulting TCP behavior the translatory degrees of freedom are used. This offers the possibility to simulate the machine tool using so called "super-closed loop" (TCP position) feed-back configuration also.

CONTROL MODEL

For an early step of design, also the control model has to be kept as basic as possible [4]. For this reason only the following parameters are used here:

- position gain K_V
- velocity gain K_P , integrator time constant T_I
- controlled electrical time constant T_{elc}

This set of parameters is then used in combination with the structure model being completed with the 9 bodies representing the drive components. The most significant output is the relative displacement at the TCP (Tool Centre Point) (Figure 2).

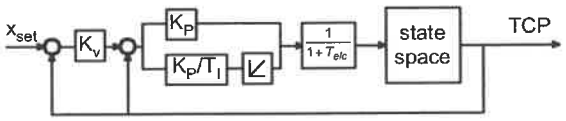

FIGURE 2. Combined control, drive and structure model

One of the major points of interest when discussing new machine tool systems are the control parameter values which can be used without generating position overshoot. Having all the significant parameters of the electromechanical system, the control parameters can be estimated.

Control Parameter Estimation

For the controlled electrical time constant T_{elc} = 1 ms is assumed based on experience.
In the considered example, structural flexibility is the dominant influence on the control loop performance. The controller is commissioned for maximum damping of the dominant mode [5]. For each axis, the inertia ratio λ is derived from the first pole-frequency ω_0 and first zero-frequency ω_N, which leads to the scaled proportional velocity controller gain κ [6].

$$\lambda = \left(\frac{\omega_N}{\omega_0}\right)^2 \qquad \kappa = \omega_0 \cdot \lambda^{\frac{1}{\sqrt{2}}}$$

Based on κ, estimations for the velocity controller integrator time constant T_I and the position gain K_v are obtained:

$$T_I \geq \frac{4}{\kappa} \qquad K_V \leq \begin{cases} \frac{\kappa}{4} & \text{for semi-closed loop} \\ \frac{\kappa \cdot \omega_0}{4 \cdot (\kappa + \omega_0)} & \text{for closed loop} \end{cases}$$

For the velocity gain K_P the total inertia Θ which is about 2500 kg and κ are used:

$$K_P = \Theta \cdot \kappa$$

This scheme for first estimates is now applied for the example and the obtained values are later optimized using the combined model consisting of mechanical structure, drives and control [7].

SIMULATION RESULTS

The transfer function for the x-axis drive obtained from the model is shown in Figure 3. ω_N and ω_0 are clearly visible at 20 and 29 Hz. These values lead to a λ of 0.83 a κ of 25.4 Hz. For the time constant of the integrator gain 0.24 sec and values of 27 1/sec and 17 1/sec are obtained for the position gain K_V for semi-closed and closed loop respectively.

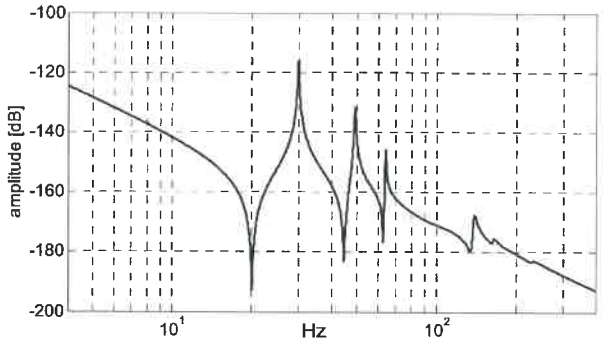

FIGURE 3. Transfer function (force on x-drive to displacement of x-drive), k_c = 100 N/µm

Anti-resonance mode Shape

For illustrative reasons the mode shape for the anti-resonance of the x-axis is shown in Figure 4. While there is no motion at the electric motor, the maximum amplitude is carried out by the body representing the corresponding slider.

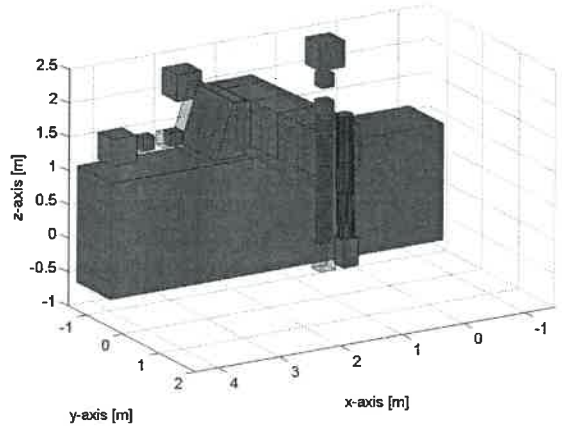

FIGURE 4. Mode-shape for the first anti-resonance of the x-axis at 20 Hz

Semi-closed Loop

Following the system configuration shown in Figure 2, the influence of varying control parameter settings on the transfer function of the controlled system can be evaluated. Figure 5 shows the influence of the position gain when semi-closed position feed-back is applied. In this case, the motion of the body representing the motor is taken as reference: The first assumptive value of 27 1/s can be increased to 52 1/s via iteration without overshoot.

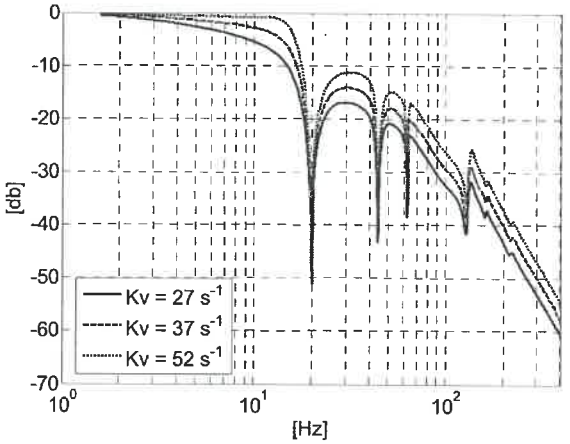

FIGURE 5. Transfer function (position set-point to displacement of x-drive), Semi-closed Loop

Closed Loop

When going to closed loop configuration the well known reduction of the maximum attainable Kv is verified again: The maximum value that avoids overshoot decreases from 52 1/s to 32 1/s (Figure 6).

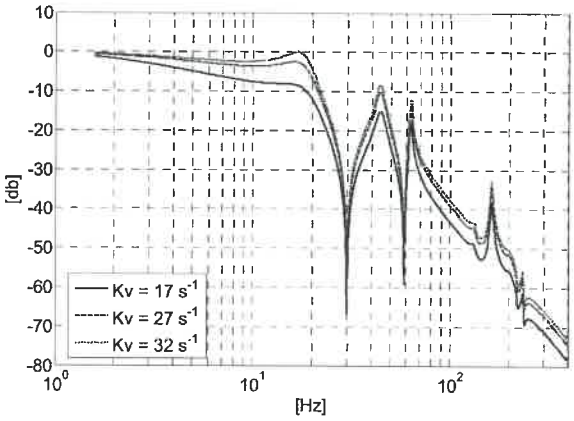

FIGURE 6. Transfer function (position set-point to displacement of x-slider), Closed Loop

Super-closed Loop

Having a look on the hypothetic case of directly measuring of the TCP-movement at the tool tip, the maximum position gain is again reduced.

Cross-talk

The major advantage of spatial machine models is their ability to reveal cross-talk interaction between the directions of motion [1]. Due to drive forces not going through the centre of gravity tilting motions appear which can lead to significant path deviations. For the frequency domain the models used here offer this information also (Figure 7).

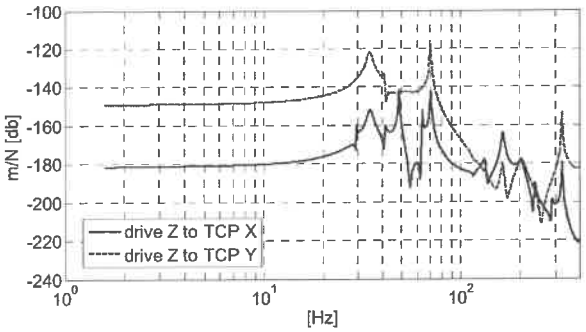

FIGURE 7. Transfer function (force on z-drive to x- and y-displacement of TCP), Open Loop

Motion simulation

When having a model describing the mechanical machine structure and an efficient model of the control, arbitrary movements can be simulated with quite moderate effort.

Figure 8 shows the simulation result of back and forth movements over 100 mm in z-direction with a velocity of 20 m/min, acceleration of 8 m/sec^2 and a jerk of 200 m/sec^3. The significant lateral path deviations at the start and at the end are quite the same as could be measured using a cross-grid measuring device at the real machine (Figure 9).

The differences between measurement and simulation between 15 and 85 mm of the motion are periodic disturbances caused by mechanical drive components (imperfections of the gear e.g.), which were not included in the model. Also, no model parameters such as damping have been adjusted. The values applied here are the same as used for similar machine tools before.

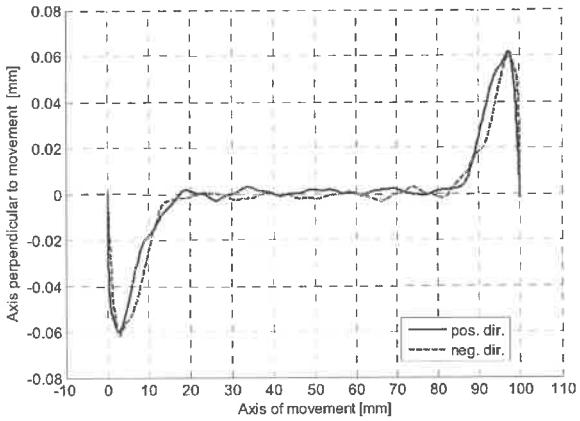

FIGURE 8. Simulation result: positioning motion over 100mm in z-direction, shown in y-z-plane, semi-closed loop

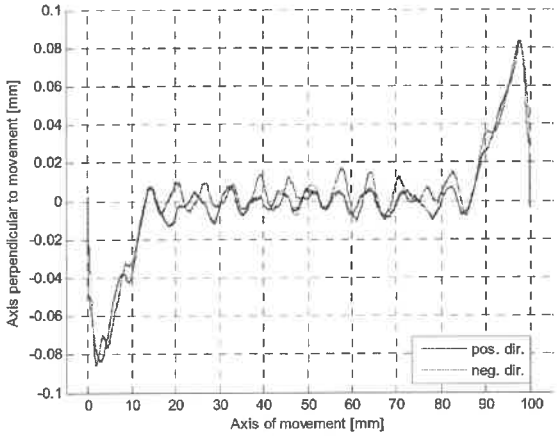

FIGURE 9. Measurement result: positioning motion over 100mm in z-dir., shown in y-z-plane

CONCLUSIONS

Based on elementary design parameters the evaluation of machine tool concepts with regard to their obtainable control parameters is shown. Systematic structural influences of the machine configuration on resulting path deviations are shown via simulation and verified by measurement.

REFERENCES

[1] Rehsteiner F, Weikert S, Rak Z. Accuracy Optimization of Machine Tools under Acceleration Loads for the Demands of High Speed Machining. ASPE Ann. Meeting 98

[2] Zirn O, Weikert S. Modellbildung und Simulation hochdynamischer Fertigungssysteme. Springer Verlag. 2006

[3] Lorenzer Th, Weikert S, Wegener K. Decision-making aid for the Design of Reconfigurable Machine Tools. 2nd Inter. CARV Conf. 2007. Toronto

[4] Nguyen H. Integration regelungstechnischer Modelle für die Konzeptanalyse von Werkzeugmaschinen im Frequenzbereich. Semester Thesis June 2008, IWF-ETHZ

[5] Zirn O. Machine Tool Analysis Modelling, Simulation and Control of Machine Tool Manipulators. Habilitation Thesis. 2007

[6] Batzies E, Schöller T, Welker, V, Zirn O. Optimal Control of Direct Driven Feed Axes with flexible Structural Components. 7th int. Conf. on Power Electronics and Drive Systems, 2007

[7] Skogestad S, Postletwaite I. Multivariable Feedback Control. Wiley. 2005.

MICROSCALE METROLOGY USING STANDING WAVE PROBES

Marcin B. Bauza[1], Shane C. Woody[1], Stuart T. Smith[2], Richard M. Seugling[3]
Ian M. Darnell[3] and Jeffery N. Florando[3]
[1] InsituTec Inc.
Charlotte, NC, USA
[2] UNC Charlotte
Charlotte, NC, USA
[3] Lawrence Livermore National Laboratory
Livermore, CA, USA

INTRODUCTION

Miniaturization has been one of the driving forces in the development of new technologies leading to new products in a variety of industries. As a result, the integration of components over several orders of magnitude on the length scale poses enormous challenges for quality assurance and control [1][2]. Therefore, new solutions are necessary to meet the growing need for more challenging metrology tasks and metrology requirements in nano- and micro-technology. However, with miniaturization, new challenges arise such as the increased influence of adhesion, electrostatic, Van der Waals and meniscus forces that affect the measurement process [3]-[5]. Technical solutions to overcome these micro- and nano-metrology challenges will include the need for traceability, new calibration procedures and calibration artifacts [1][6]. Over the past decade many new metrology tools have been proposed [7][8], however; for contact-based measurements, adhesion between the measurement probe and the specimen still proves to be one of the more difficult challenges to overcome [6]. To address this issue, a new class of tactile sensing probe referred to as standing wave sensor has been developed and was previously presented [9]. Previous work introduced the principle of operation of the standing wave senor. This work presents new measurements showing applications of the standing wave probe as the sensing element in a microscale high aspect ratio profiling system.

EXPERIMENTAL APPARATUS

The instrument used during the experiments presented in this work comprises an engineered gauge head that is rigidly attached to a Moore 1.5 machine frame as shown in Figure 1. The gauge head is composed of a precision spindle and scanning head which are used to position the microscale standing wave probes. The measured components are positioned with an Aerotech™ FiberMax 5 axis positioning platform. A simplified block diagram is provided below to show the reader the instrument with its multi-axis functionality, Figure 2. The *X, Y* and *Z axes* are located on the Moore 1.5 and subsequently used only for coarse alignment. Once the fiber probe and workpiece are positioned within the correct working volume of the FiberMax, the stages on the Moore 1.5 are locked and are not used during the measurement process.

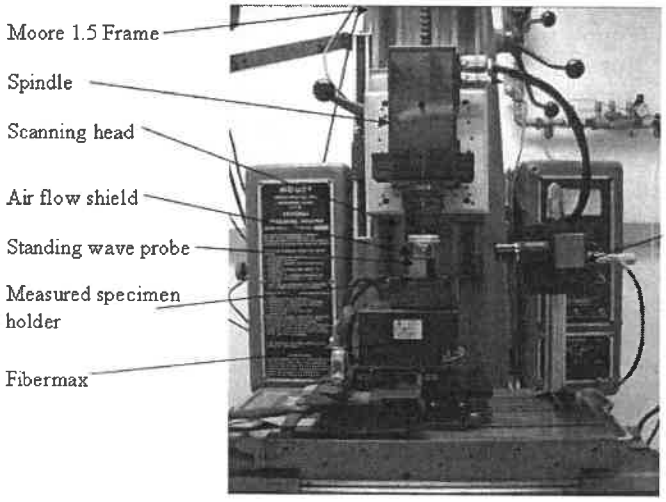

FIGURE 1. Test bed used during experiments.

There are two modes of operation reported for this work. In the first the InsituTec gauge head (configured with the spindle, sub-nanometer servoing head, and fiber probe) is used to perform roundness and cylindricity measurements. For cylindricity measurement, the FiberMax's Z-axis is used to increment the fiber probe along the axis of the hole to perform roundness traces at specified depths. This methodology for roundness scanning has previously been reported for macroscale force probes [10].

The second measurement mode addresses surface profiling for geometries that are conical, concave, and convex as well as flat surfaces. During these measurements, the precision spindle is rotated to align the standing wave probe's sensitive axis normal to the workpiece surface. Both the spindle position and the servoing head are then held at a constant position and not used during the scanning sequence. Instead, the microscale probe is only used in conjunction with the FiberMax alignment stages. During scanning, the *X* axis is translated while the Y-axis is used to control a constant applied force (estimated at 50 μN) between the probe tip and workpiece surface. This method results in a 2D surface plot and may be extended to 3D plots by employing the Z-axis.

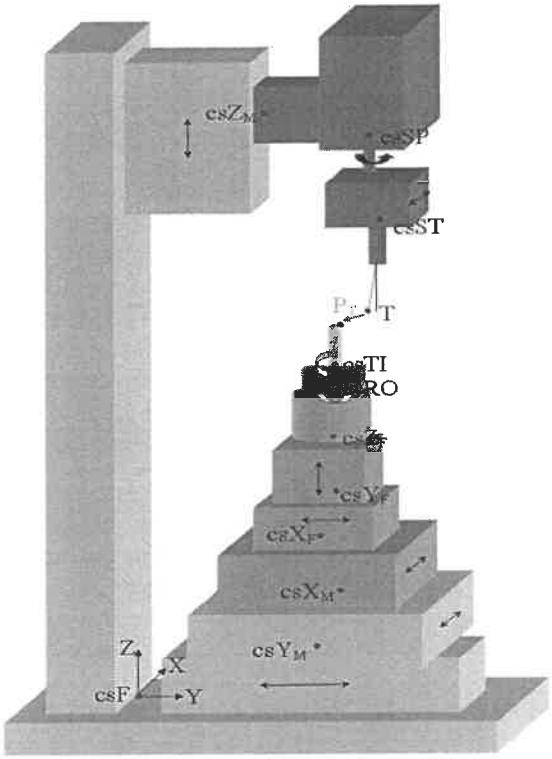

FIGURE 2. Block diagram representation of test bed used during experiments

SYSTEM ERROR MOTION ANALYSIS

To achieve better insight regarding the performance (accuracy and repeatability) of the measuring instrument, a detailed error budget has been derived. Estimates of the magnitude of the error sources are determined using the type A and B methodologies [11], vendor specifications, experimental data, and user experience. All error sources for the test-bed were assumed to be worst case and uncorrelated. In practice the combined error sources will be lower than reported. For example, the 5 axis motion control system supplied by Aerotech generates nanometer level jitter for each axis. This is due to instability in the closed loop control system. The error value given in the error budget assumes each axis oscillates at the maximum specified value at any instant in time. Most likely, all motion components produce a random oscillation which would imply a smaller error source overall. A block diagram of the system is provided in Figure 2 showing the standing wave sensor, scanning head, precision spindle, and Moore machine column and base. To calculate possible errors authors transferred the probe tip (T) from coordinate system csST into the part coordinate system csP using 11 Homogeneous Transform Matrices (HTM). The equation is shown below with values for vector P_T derived for roundness measurements shown in Table 1.

$$\overrightarrow{P_T} = H_P H_{TI} H_{RO} H_{ZF} H_{YF} H_{XF} H_{XM} H_{YM} H_F H_{ZM} H_{SP} \overrightarrow{T_{ST}}$$

TABLE 1. Tabulated error for final vector P_T based upon the system's control instability (table assumes temperature is held constant) and error motions of the axis during roundness scan.

P_{Tx}	P_{Ty}	P_{Tz}
89 nm	107 nm	3 nm

EXPERIMENTAL MEASUREMENTS

Over the past two years various artifacts have been measured including specimens made of glass, steel, aluminum, gold, and silicon. A few examples of these measurements are discussed in the following sections. Additionally, only the raw data is presented to demonstrate the fiber's capability for microscale feature measurements. Further analysis of the data referred to the measured surfaces and shapes is beyond the scope of this paper.

Fuel Injector spray hole

Fuel injectors spray holes represent one of the most challenging features in microscale metrology. Typically, the hole size ranges from 100 to 300 μm in diameter and up to few millimeters in depth. A diesel injector spray hole approximately 180 μm in diameter was selected for this study. Due to positioning limitations, the injector was fixtured to align the spray hole collinear with the fiber probe. A vertical camera with a high magnification is mounted to the gauge head housing, oriented parallel with the

spindle's rotary axis, and offset a known distance from the center axis. During the measurement, the spray hole is located using the camera then the injector is moved by the offset value to the measurement position, Figure 3. The probe is positioning into the hole, locked at a constant applied force (along the hole's side wall) using the nanometer servo stage and the spindle is rotated.

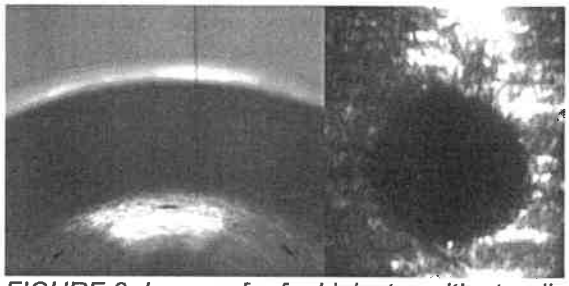

FIGURE 3. Image of a fuel injector with standing wave probe located adjacent to the hole (left), and view of the hole entrance (right).

As the spindle is rotated, the servo stage's position is measured relative to a fixed frame on the end of the spindle, Figure 4. Each circular trace contains 1000 equispaced data points. The 3D plot is obtained by positioning the FiberMax's Z-axis to specified depths and again measuring a circular trace. In this manner, traces equispaced by 50 µm along the depth of the hole are presented below. The data is shown in an unfiltered format with some a cavitation feature indicated in the lower portion of the hole.

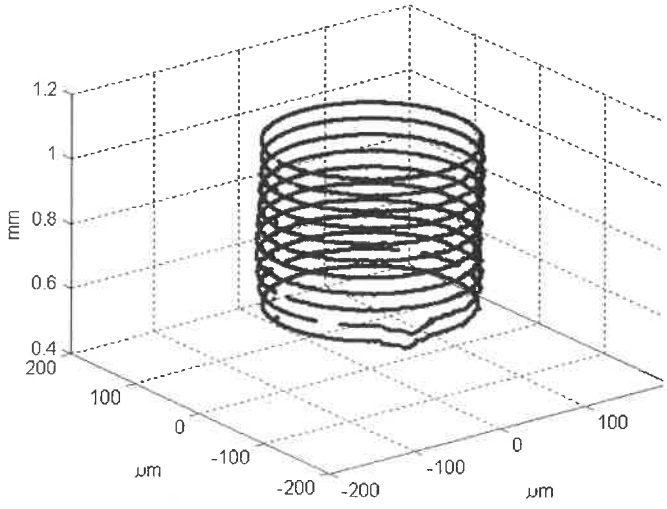

FIGURE 4. 3D representation of the fuel injector spray hole. Notice the cavity present at lower two traces, the depth of the cavity is approximately 30 µm.

Fiber optic glass ferule

Dielectric materials (i.e. glasses certain ceramics) presents another challenge due to high electrostatic forces generated on the workpiece surface. A glass ferrule with a 128 µm thru diameter is manufactured with a larger tapered conical hole on the end. The alignment procedure was similar to that of the fuel injector nozzle. The glass ferrule's hole was scanned twice at different sections. The first scan represents the conically shaped entrance to the thru hole, Figure 5, and the second scan was performed deeper in the thru hole region, Figure 6. Each trace was constructed from 1000 data points and depth measurements were repeated in 10 µm increments using the FiberMax Z-axis. Imperfections of the measured surface can be seen clearly as well as the out of round shape of the ferrule hole.

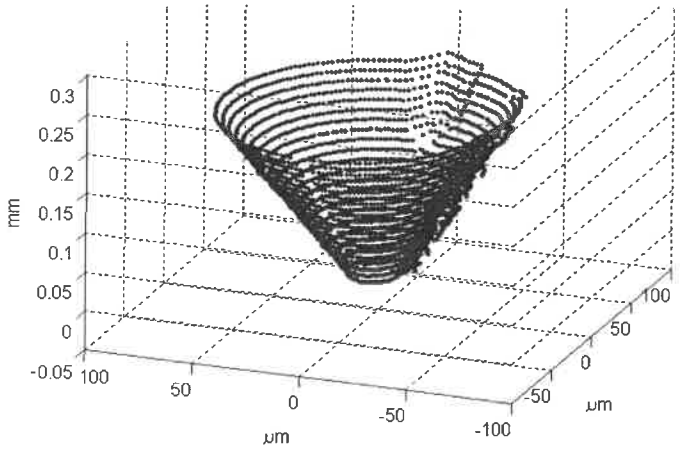

FIGURE 5. 3D representation of a conical tapered entrance to the thru hole of glass ferrule. Notice the chipped surface on the back side which is approximately 20 µm deep.

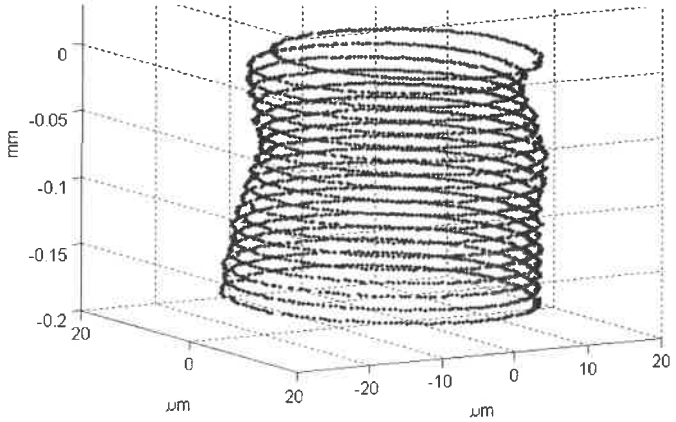

FIGURE 6. 3D representation of the 128 µm glass ferrule where zero in Z corresponds to 100 µm depth.

Concave hemispherical polished surfaces

Highly polished, curved surfaces have proven to be difficult to measure using optical metrology. While specific methods for comparing shapes are available, these are limited to simple geometries and often require manufacture of expensive reference artifacts. More versatile optical instruments are limited by surface reflectance, materials and surface slopes. Also surface profilers and conventional CMM`s are limited due to high contact forces which can lead to scratching and surface damage. On the other hand, standing wave probes introduce low contact forces estimated to be less than 50 μN significantly reducing the risk of scratching. As a case study, a highly polished steel block with a hemispherical concave shape was measured. The dimensions of the hemispherical geometry are approximately 15 mm in diameter and 5 mm deep. The part was fixtured at 45˚ relative to the top of the FiberMax. Using the second mode described earlier, the part was scanned multiple times while changing the vertical height of the *Z*-axis, Figure 7. The data was extracted from the measurement process for each of the 10 traces.

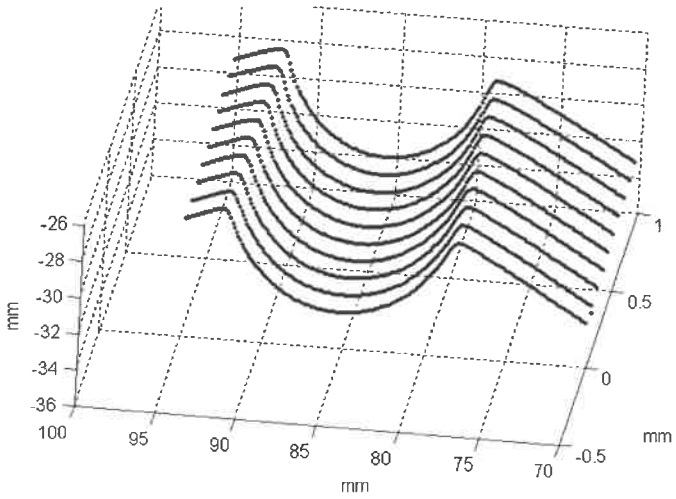

FIGURE 7. 3D representation of part of concave surface with mirror-like surface finish.

The profile is constructed from points which are spaced 2.5 μm apart over 25 mm, and the *Z*-axis is stepped by 25 μm. Due to bandwidth limitations of the *Y*-axis stage which is used to servo control the constant force signal it was not possible to measure surface finish. However, in principle, if a high speed gauge head similar to the one used in previous examples was used then, within the filtering limitations imposed by the fiber tip geometry, surface finish data could be obtained in addition to the surface profile.

ACKNOWLEDGMENTS

This work was performed under the National Institute of Standard and Technology grant number SB134105W0840 and in part under the auspices of the U.S. Department of Energy by Lawrence Livermore National Laboratory under Contract DE-AC52-07NA27344.

REFERENCES

[1] Hansen H.N., Carneiro K., Haitjema H., De Chiffre L., "Dimensional Micro and Nano Metrology" CIRP Annals, 55-2, 721-743 (2006)

[2] Lonardy P.M., Lucca D.A., De Chiffre L., "Emerging Trends in Surface Metrology" CIRP Annals, 51-2, 701-723 (2002)

[3] Yang, F., "Adhesive contact of axisymmetric suspended miniature structure," Sensors and Actuators A104, 44-52 (2003).

[4] Adamson, A.W. and Gast, A.P., "Physical Chemistry of Surfaces, 6th Ed.", Wiley-Interscience, (1997).

[5] Israelachvili, J.N., "Intermolecular and Surface Forces, 2nd Ed." Aca-demic Press, (1992).

[6] Marinello F., Savio E., Carmignato S., De Chiffre L., "Calibration artefact for the microscale with high aspect ratio: The fiber gauge" CIRP Annals – Manuf. Tech. 57, 497–500 (2008)

[7] Danzebrink H.-U., Koenders L., Wilkening G., Yacoot A., Kunzmann H., "Advances in Scanning Force Microscopy for Dimensional Metrology" CIRP Annals 55-2, 841–878 (2006)

[8] Weckenmann A., Peggs G., Hoffmann J., "Probing systems for dimensional micro- and nano-metrology" Meas. Sci. Technol. 17, 504–509, (2006)

[9] Bauza, M.B., Hocken, R.J., Smith, S.T., Woody, S.C., "Development of a virtual probe tip with an application to high aspect ratio microscale features," Rev. Sci. Instrum. 76, 095112 (2005)

[10] Bauza, M.B., Woody, S.C., Smith, S.T., Hocken, R.J., "Development of a Rapid Profilometer with an Application to Roundness Gauging." Precision Engineering. 30 Issue 4; 406-413, (2006)

[11] Taylor B. N., Kuyatt C. E., "Guidelines for Evaluating and Expressing the Uncertainty of NIST Measurement Results." NIST Technical Note 1297, (1994)

Field-of-View Distortion Calibration and Compensation for Ultra-high Accuracy Video-Based Metrology Systems

Yuhua Ding, Joe Tobiason
Micro Encoder Inc.
Kirkland, WA, USA

ABSTRACT

Field-of-View (FOV) distortion affects measurement accuracy by generating location-dependent results in video-based metrology systems. For ultra-high accuracy systems equipped with high-quality lenses, this error can be as small as the uncertainty of obtainable dimensional references. In this research, we develop a method that calibrates the distortion using an uncertified planar artifact. Since the measurement is performed on a plane with a (nominal) constant magnification, we can decouple the calibration for distortion and the calibration for pixel scaling factors, eliminating the need for high-accuracy dimensional references. We first establish a distortion model, and then we solve the model parameters by nonlinear least squares fitting. Furthermore, we find the significant distortion terms by adding them one by one to the model and comparing the fitting residual and convergence. Experimental results of the method on five system configurations show reduced measurement variation across the FOV by up to 80%.

INTRODUCTION

A constant magnification across the Field-Of-View (FOV) is desirable in ultra-high accuracy (UHA) dimensional metrology systems equipped with video-probes and high-quality lenses. Such a system would ideally render true-to-scale images of the 2D object in the object plane, enabling one to apply constant scaling factors in converting pixel dimensions to physical dimensions.

Customers, however, often obtain slightly different measurement results when measuring the same feature in different regions of the FOV. This discrepancy arises from distortion caused by system imperfections such as optical aberrations and non-square sensor elements. In FIGURE 1, for example, the image of an equally spaced grid is no longer true-to-scale because of imaging system distortion. The distortion is nonlinear, which invalidates the assumption of constant magnification, resulting in FOV location-dependent measurement errors.

To maintain a constant scaling factor, we therefore need to calibrate and compensate the nonlinear distortion in order to recover the distortion-free, true-to-scale image of the object. This is a challenging task mainly due to the small magnitude of distortion in UHA systems (often in the sub-micrometer range).

Relation to previous work

Distortion calibration is normally performed as part of camera geometric calibration, where both intrinsic and extrinsic parameters are estimated by measuring features of known physical dimensions ([1,2]). Most artifacts, however, are only accurate to 1μm or 0.1μm, which is not sufficient for calibrating the submicron distortions for UHA systems. The motivation of this research is to develop a calibration method that does not rely on the knowledge of physical dimensions of the artifact.

Contribution of this paper

We exploit the fact that non-linear distortion can be decoupled from scaling factor and develop a method to calibrate the nonlinear FOV distortion using an uncertified planar Chrome-On-Glass (COG) artifact with features whose pixel locations can be measured accurately. Since the artifact does not need to be certified, its cost is greatly reduced. Furthermore, our method does not need a high-accuracy positioning system and is practical for on-site calibration.

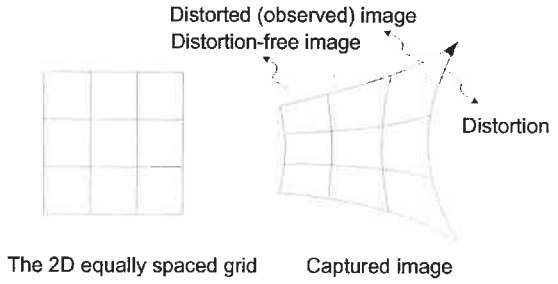

FIGURE 1. FOV distortion.

DISTORTION CALIBRATION

Distortion model

The distortion model for UHA systems can be derived from the general pinhole camera model

by assuming a constant nominal magnification. A general pinhole model consists of four steps ([1,2]):

Step 1: 3D rigid body transformation from the World Coordinate System WCS $[x_w, y_w, z_w]^T$ to the Camera Coordinate System CCS $[x_c, y_c, z_c]^T$

$$\begin{bmatrix} x_c \\ y_c \\ z_c \end{bmatrix} = R_{3\times3}\begin{bmatrix} x_w \\ y_w \\ z_w \end{bmatrix} + T_{3\times1} \quad (1)$$

Step 2: Projection from 3D CCS to undistorted Image Coordinate System ICS (for focal length f)

$$\begin{bmatrix} x_0 \\ y_0 \end{bmatrix} = \frac{f}{z_C}\begin{bmatrix} x_C \\ y_C \end{bmatrix} \quad (2)$$

Step 3: Radial and tangential distortions from undistorted image coordinates to real (distorted) image coordinates in the ICS

$$\begin{bmatrix} x_d \\ y_d \end{bmatrix} = \begin{bmatrix} x_0 \\ y_0 \end{bmatrix} + \begin{bmatrix} D_x \\ D_y \end{bmatrix} \quad (3)$$

where

$$\begin{bmatrix} D_x \\ D_y \end{bmatrix} = (\kappa_1 h_0^{\,2} + \kappa_2 h_0^{\,4} + \kappa_5 h_0^{\,6})\begin{bmatrix} x_0 \\ y_0 \end{bmatrix} + \begin{bmatrix} 2\eta_1 x_0 y_0 + \eta_2 (h_0^{\,2} + 2x_0^{\,2}) \\ \eta_1 (h_0^{\,2} + 2y_0^{\,2}) + 2\eta_2 x_0 y_0 \end{bmatrix},$$

$$h_0^{\,2} = x_0^{\,2} + y_0^{\,2} \quad (4)$$

Step 4: Real image coordinate $[x_d, y_d]^T$ to the column and row $[X_f, Y_f]^T$ in the discretized image

$$\begin{bmatrix} X_f \\ Y_f \end{bmatrix} = \begin{bmatrix} s_x & c_x \\ 0 & s_y \end{bmatrix}\begin{bmatrix} x_d \\ y_d \end{bmatrix} + \begin{bmatrix} O_X \\ O_Y \end{bmatrix} \quad (5)$$

where $[O_X, O_Y]$ is the column and row of the principle point (intersection of the optical axis and the image plane), c_x the shearing (nonperpendicularity) of x and y axes of the sensor, and s_x and s_y the scaling factors (pixels/mm) in x and y, respectively.

In UHA systems, we assume that both the image and object planes are parallel to the focal plane (FIGURE 2). That is, z_c is constant. We normalize WCS and CCS by $f/z_c s_x$ and ICS by $1/s_x$ so that they are in pixel units, use capital letters for the normalized coordinates, and rewrite the four steps above as follows:

Steps 1 and 2 are combined into a 2D rigid body transformation from normalized WCS to normalized distortion-free ICS

$$\begin{bmatrix} X_0 \\ Y_0 \end{bmatrix} = \begin{bmatrix} X_C \\ Y_C \end{bmatrix} = R_{2\times2}\begin{bmatrix} X_w \\ Y_w \end{bmatrix} + \begin{bmatrix} T_x \\ T_y \end{bmatrix} \quad (6)$$

Step 3: Nonlinear distortion in normalized ICS

$$\begin{bmatrix} X_d \\ Y_d \end{bmatrix} = \begin{bmatrix} X_0 \\ Y_0 \end{bmatrix} + \begin{bmatrix} D_X \\ D_Y \end{bmatrix} \quad (7)$$

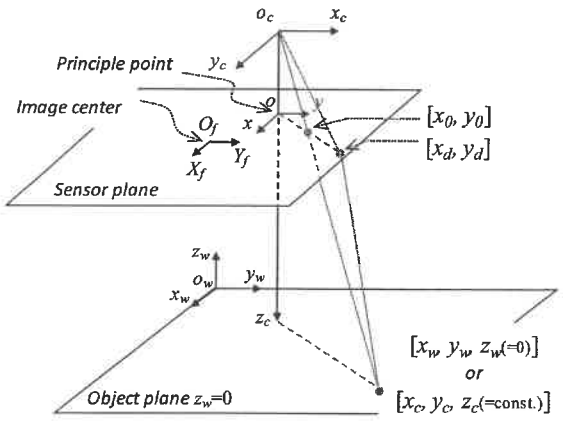

FIGURE 2. Camera model for UHA systems.

where

$$\begin{bmatrix} D_X \\ D_Y \end{bmatrix} = (k_1 H_0^{\,2} + k_2 H_0^{\,4} + k_3 H_0^{\,6})\begin{bmatrix} X_0 \\ Y_0 \end{bmatrix} + \begin{bmatrix} 2p_1 X_0 Y_0 + p_2 (H_0^{\,2} + 2X_0^{\,2}) \\ p_1 (H_0^{\,2} + 2Y_0^{\,2}) + 2p_2 X_0 Y_0 \end{bmatrix},$$

$$k_1 = \frac{\kappa_1}{s_x^{\,2}}, k_2 = \frac{\kappa_2}{s_x^{\,4}}, k_3 = \frac{\kappa_3}{s_x^{\,6}}, p_1 = \frac{\eta_1}{s_x}, p_2 = \frac{\eta_2}{s_x},$$

and $H_0^{\,2} = X_0^{\,2} + Y_0^{\,2}$ (8)

Step 4: Discretization of the image

$$\begin{bmatrix} X_f \\ Y_f \end{bmatrix} = \begin{bmatrix} 1 & C_X \\ 0 & S_Y \end{bmatrix}\begin{bmatrix} X_d \\ Y_d \end{bmatrix} + \begin{bmatrix} O_X \\ O_Y \end{bmatrix} \quad (9)$$

where $C_X = \frac{c_x}{s_x}, S_Y = \frac{s_y}{s_x}$

Since rotation and translation in the combined steps 1 and 2 do not distort the image, steps 3 and 4 define our final distortion model:

$$\begin{bmatrix} X_f \\ Y_f \end{bmatrix} = M_{\{\{k_i\}_{i=1,\ldots,5}, [O_X, O_Y], C_X, S_Y\}}\left(\begin{bmatrix} X_0 \\ Y_0 \end{bmatrix}\right) \quad (10)$$

This model consists of the following terms:

Term	Parameters	
	Symbol	Unit
Principle point	$[O_X, O_Y]$	pixel
Pixel aspect ratio	S_Y	none
Shearing	C_X	none
Radial	k_1	1/pixel^2
	k_2	1/pixel^4
	k_3	1/pixel^6
Tangential	p_1, p_2	1/pixel

Since our model does not involve physical dimensions, distortion calibration is performed entirely in pixel coordinates without requiring certified feature dimensions.

Calibration procedure

The distortion can be calibrated using a planar target with well-defined features such as circles or corners of a checker board pattern on a COG artifact. Calibration is performed in three steps:

- Place the artifact in the object plane (by focusing on the surface).
- Move the set of features to different regions ("pose") of the FOV by in-plane translation and rotation. Measure the pixel location of each feature at each location (FIGURE 3).

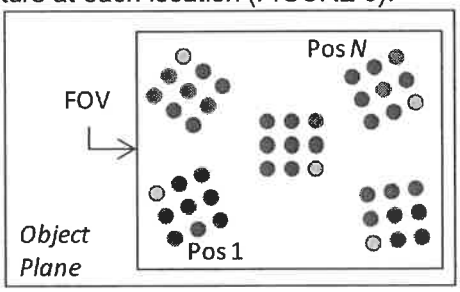

FIGURE 3. Calibrate the FOV distortion using a planar target with circular dots.

- Solve the distortion model using nonlinear Least Squares Fitting (LSF), as shown in FIGURE 4.

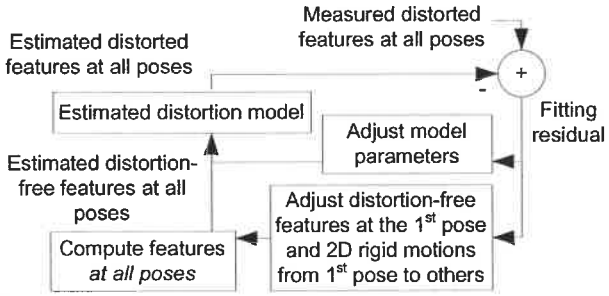
Measured distorted features at all poses
Estimated distorted features at all poses
+
-
Fitting residual
Estimated distortion model
Adjust model parameters
Estimated distortion-free features at all poses
Adjust distortion-free features at the 1st pose and 2D rigid motions from 1st pose to others
Compute features at all poses

FIGURE 4. Solve distortion model parameters using nonlinear least squares fitting.

The fitting procedure solves for three types of variables:

1. The distortion model parameters
2. The distortion-free feature positions at the 1st pose
3. The 2D rigid body transformations of the target from the 1st pose to all other poses

Thus, the total number of fitting variables is:

$$N_{\text{variables}} = N_{\text{model parameters}} + 2N_{\text{feature}} + 3(N_{\text{pose}} - 1) \quad (11)$$

To solve for the fitting variables, we need at least $N_{\text{variables}}$ data points:

$$N_{\text{data}} \geq N_{\text{variables}}. \quad (12)$$

Replacing N_{data} with $2N_{\text{feature}}N_{\text{pose}}$, we get

$$(2N_{\text{feature}} - 3)(N_{\text{pose}} - 1) \geq N_{\text{model parameters}} \quad (13)$$

For example, we can measure as few as 2 features in at least $N_{\text{model parameters}} + 1$ poses or as few as two poses containing at least $(N_{\text{model parameters}} + 3)/2$ features.

Determination of significant terms

Our distortion model in equation (10) captures the common distortion terms reported in the literature. For a specific optical system, however, only a few terms dominate. Many terms do not improve fitting and may in fact increase the sensitivity of the model and decrease the numerical stability of fitting. This is true especially for the higher-order radial and tangential terms ([1]).

To determine the significant distortion terms for a given system, we use different combinations of distortion terms in the model and compare the residual and convergence of the nonlinear LSF. We considered the models listed in TABLE 1. Model M0 is the simplest one, with the pixel aspect ratio term only. Model M0 serves as our baseline for comparison, because this term is already inherent in UHA systems that calibrate separate pixel scaling factors for x and y. Starting from M0, we gradually add radial, shearing, and tangential terms. The 3rd-order radial term (k_1) is added first since it is typically the dominating distortion.

TABLE 1.Distortion models being tested.

Model	$[O_x, O_y]$, k_1	k_2	k_3	p_1, p_2	C_X	S_Y
M0						✓
M1	✓					✓
M2	✓				✓	✓
M3	✓	✓			✓	✓
M4	✓	✓		✓	✓	✓
M5	✓	✓	✓	✓	✓	✓

EXPERIMENTAL RESULTS

Accuracy evaluation on UHA systems is a challenging task due to the small magnitude of the distortion and additional system error sources besides distortion, such as positioning system errors and errors in pixel scaling factors.

A straightforward way to test the accuracy is to measure features of known dimensions. That is, the feature dimensions must be certified to an accuracy of about one magnitude higher than the distortion-related errors. For UHA systems, such an artifact is costly and can be difficult to obtain.

An alternative way of testing the accuracy is to check the measurement variation across the FOV. We choose this way because the goal of our research is to reduce location-dependent variations. The challenge, however, is to isolate

distortion from other error sources. The feature(s) to be measured need to meet two criteria:

1. Distortion-related error can be seen clearly from the measurements.
2. Distortion-related error dominates or can be easily separated from other errors.

For our experiments, we measure the diagonal distance of a square feature on an artifact moved to 9 regions of the FOV and oriented at 0- and 90- degree rotational angles (FIGURE 5). At each location, we extract the corners by a sub-pixel corner detection algorithm, apply distortion compensation, and compute diagonal distances (in pixel values). The Peak-To-Peak variation (P2P) of the 18 measurements represents distortion-related error. For each model M1 to M5, we perform calibration, apply compensation to get the P2P, and compute the improvement with regard to model M0 (FIGURE 6). Models with smaller P2P are considered to be more accurate.

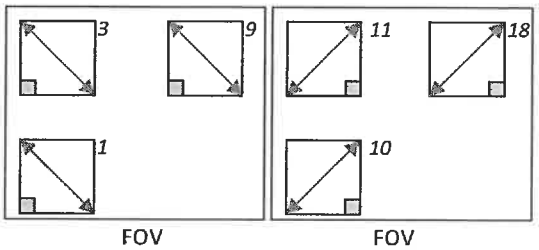

FIGURE 5. Measure diagonal distances of a square in different regions and orientations in the FOV.

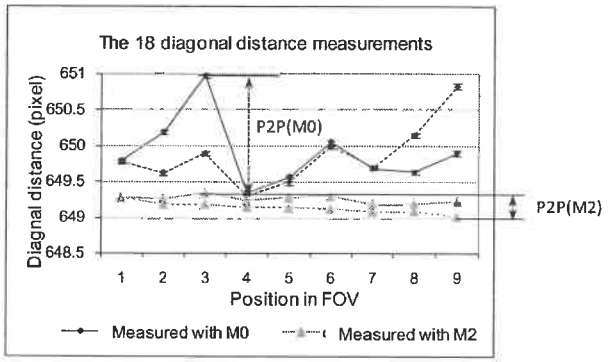

FIGURE 6. Diagonal distance measurements showing the P2P variation.

TABLE 2 lists the configurations we tested and the corresponding improvement of the P2P variation of the diagonal distances.

The test was performed on CNC vision measuring systems equipped with video probes. The magnification is a combination of microscope objectives of 1×, 2.5×, 10× and tube lenses of 1×, 2×, and 6×. The magnitude of distortion depends mainly on lens design and fabrication. It also depends on the size of the sensor. The improvement entries that are grayed out indicate failure of convergence in nonlinear fitting.

For all configurations, model M1 achieved significant improvement, up to 80% smaller measurement variation. There is a slight improvement (except for C#5) from M1 to M2, but no noticeable improvement from M2 on. Therefore, for the systems we tested, terms other than the 3rd-order radial, pixel aspect ratio, and shearing are not necessary.

This test and additional tests show that models M4 and M5 are more likely to fail to converge and are more sensitive to noise. In the test, we also found the method does not completely remove the squareness errors caused by shearing. Further investigation is required.

TABLE 2. Test configurations and improvement on P2P after distortion compensation.

Configurations		C#1	C#2	C#3	C#4	C#5
Nominal magnification		5	1	15	20	2
FOV size (mm)	Width	1.25	6.27	0.42	0.31	3.56
	Height	0.94	4.70	0.31	0.24	2.28
P2P (M0)	(pxl)	0.37	0.69	0.20	0.47	1.66
Improvement on P2P (compared to P2P using M0)	M1	42.8%	69.8%	38.7%	71.1%	80.3%
	M2	47.2%	72.0%	45.7%	75.7%	79.8%
	M3	47.9%	71.3%	45.8%	75.7%	80.1%
	M4	44.8%	71.8%	54.6%	74.7%	80.0%
	M5	49.2%	72.0%	42.2%	74.0%	79.8%

CONCLUSION

We developed a method to calibrate camera distortion for high-accuracy dimensional gauging systems equipped with video probes. The method involves measuring the same set of uncertified but well-defined features on a planar artifact relocated to different regions of the FOV, then solving for the model parameters using nonlinear LSF. Test results of up to 80% smaller measurement variation show that the proposed method is effective in reducing measurement errors caused by camera distortion.

REFERENCES

[1] Tsai, R. Y., A Versatile Camera Calibration Technique for High-Accuracy 3D Machine Vision Metrology Using Off-the-Shelf TV Cameras and Lenses, IEEE Journal of Robotics and Automation, RA-3(4): pp 323-344, 1987.

[2] Zhang, Z., A Flexible New Technique for Camera Calibration, Technical Report MSR-TR-98-71, Microsoft Research, 1998.

PERFORMANCE OF A 2D SPECKLE DISPLACEMENT SENSOR WITH VARIOUS MEASUREMENT SURFACES

Scott A. Harsila[1], Benjamin K. Jones[1] and Karl Masreliez[2]
Micro Encoder, Inc.
[1]Kirkland, WA
[2]Banyuls sur Mer, France

INTRODUCTION

This paper discusses the performance of a 2 dimensional (2D) speckle displacement sensor used with measurement surfaces of various materials and characteristics. The sensor operates by projecting a collimated laser beam onto an optically rough measurement surface. Images of the resulting speckle pattern are acquired via a simple optical system and CMOS sensor. As the underlying measurement surface (and associated speckle pattern) displaces in 2D, measurement images are numerically correlated with an initial reference image to determine the 2D displacement in the plane of the measurement surface. The sensor in its present form is capable of sub-nanometer-position noise, X-Y measurements over a 250 μm X 250 μm measurement range, with update rates of 20-140Hz. The advantage of using a speckle sensor is that the sensor does not need a calibrated scale; the displacement of any optically rough surface may be measured. There are many possible applications for this technology, including but not limited to: monitoring stage drift, nanometer level positioning, monitoring metrology frame deflections, characterizing stage orthogonality/straightness, and (because of absolute measurements) mounting repeatability of measurement target.

Prior work has been conducted in the field of speckle correlation for measurement. Yamaguchi [1] *et al* demonstrated a 1D speckle correlation sensor for linear and rotation measurement with resolution linear and angular resolutions of 1 μm and 0.001°. Shilpiekandula [2] *et al* have discussed a speckle based sensor with resolutions 0.1 μm and 0.00029°

SENSOR CONFIGURATION

We first give an overview of the sensor hardware and computational algorithms. Hardware includes the readhead optical design and custom electronics for position computation. The readhead (FIGURE 1) projects a collimated beam from a laser diode that illuminates the measurement area, an imaging lens, a pinhole aperture and a CMOS camera, all in a telecentric configuration. In a separate enclosure from the sensor readhead are the correlation electronics which include a Digital Signal Processor (DSP) for correlation computation, and hardware for communications between the readhead and PC.

The key algorithm operations are to quickly locate the vicinity of the correlation peak, and then to accurately determine the 2D location of the peak to sub-pixel accuracy via interpolation. Using proprietary curve fitting algorithms, the interpolation achieves a position noise value of better than 1/1000th of a pixel, or ~0.7 nm and an accuracy (defined as the reference position minus the report sensor position) of <±100 nm over the 250 μm 2D range. These algorithms are based on the assumption that the speckle image is uniform – i.e., that the size of the speckle features and level of background intensity are relatively constant over the full field of view. The measurement gap and tolerance of the sensor from the planar measurement surface is 4.5 mm ±0.05 mm. The dimensions of the current sensor prototype are ~40x40x40 mm.

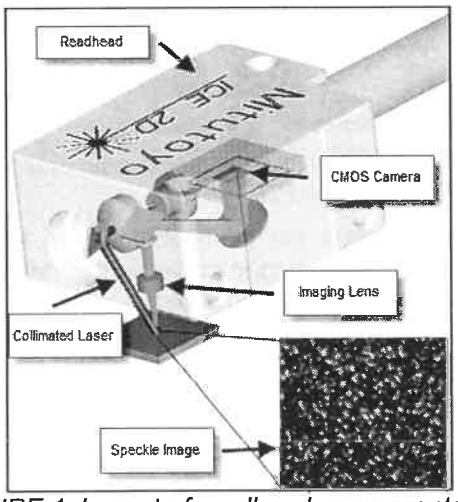

FIGURE 1. Layout of readhead components.

TEST SYSTEM CONFIGURATION

Sensor accuracy testing is conducted on a 2D translational stage with Renishaw RLE10 plane mirror laser interferometers (158 nm signal period, 0.4 nm interpolated digital resolution) simultaneously measuring X and Y position of the stage. The interferometer beam paths are aligned with the sensor measurement axes to minimize Abbe error (FIGURE 2). Burleigh Inchworm piezo actuators are used to displace the Physik Instrumente X-Y magnetically preloaded roller bearing stage. The stage has been qualified with a laser interferometer to have angular deviations of less than 1 arcsecond over the 250 μm X-Y sensor test range. The test system is contained within a thermoelectrically temperature-controlled enclosure that is stable to ±0.03°C over 48 hours, FIGURE 3. The interferometers are compensated for changes in wavelength due to environmental variations using the modified Elden equation [3] (environmental compensation sensor resolutions: 0.01°C, 0.08 mbar, 0.0625% RH). Interferometer dead paths are shielded with clear acrylic tubes to reduce air turbulence.

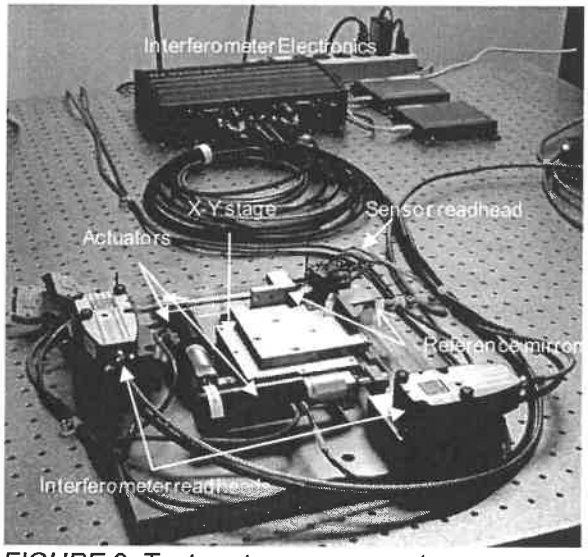

FIGURE 2. Test system components.

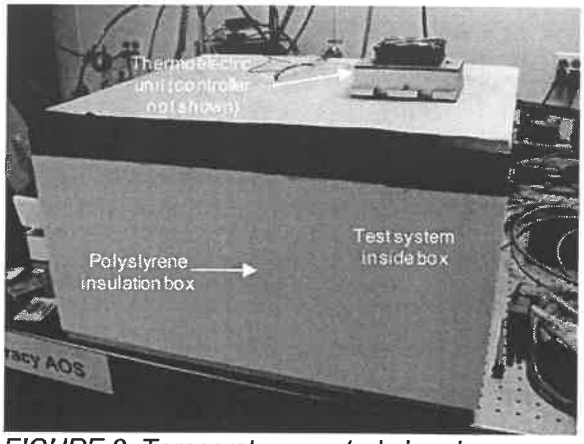

FIGURE 3. Temperature control chamber.

The short term fixed position noise (1σ standard deviation of repeated fixed position measurements) of the test system is shown in FIGURE 4. It has a 1σ value of ~2.2 nm. The long term position drift over 48 hours is ~±33 nm with a 1σ value of ~11 nm, see FIGURE 5.

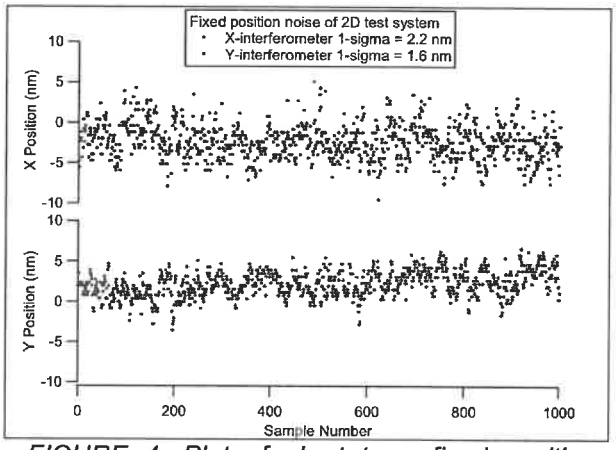

FIGURE 4. Plot of short term fixed position noise of X and Y test system axes. This includes all noise sources in the test system, such as vibrations, thermal drift, air turbulence and electronic noise.

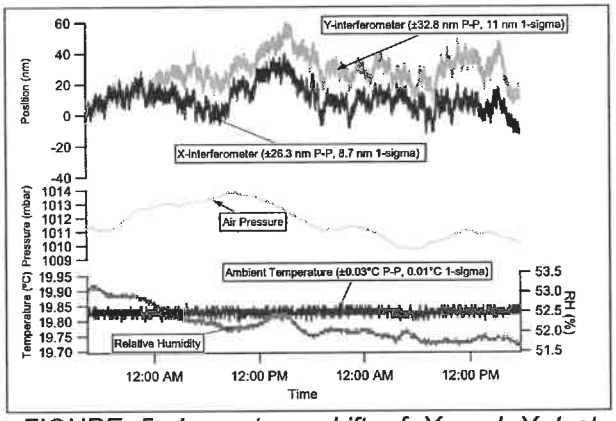

FIGURE 5. Long term drift of X and Y test system axes monitored over 48 hours. Environmental conditions are also shown.

RESULTS

We present our results in terms of a number of performance parameters, including fixed-position noise, accuracy over the full range of travel (250 μm), and reproducibility of the sensor. Accuracy is defined as the difference between the reference interferometer position and the sensor's reported position. Reproducibility is defined as the accuracy of the sensor when tested at different measurement surface locations.

In practice, we find that a number of surface materials, including randomly lapped stainless steels (SST), some ceramics and the backside (unpolished) of processed silicon wafers, yield images that closely match the assumption of speckle uniformity. We present test results for such surfaces showing that the sensor is accurate to within ±100 nm over the full 2D displacement range. Other surfaces, such as ground SST, milled Invar and patterned silicon wafers, yield images with anomalies, distinct directionality or repetitive patterns. Test results show that these surfaces can be successfully measured, although with reduced accuracy. Sample speckle images are shown in FIGURE 6.

The fixed position noise performance of the sensor is displayed in FIGURE 7. Tests have been conducted on lapped stainless steel, ceramic IC package and unpolished silicon wafer. The sensor maintains a fixed position noise 1σ <0.7 nm for these sample surfaces.

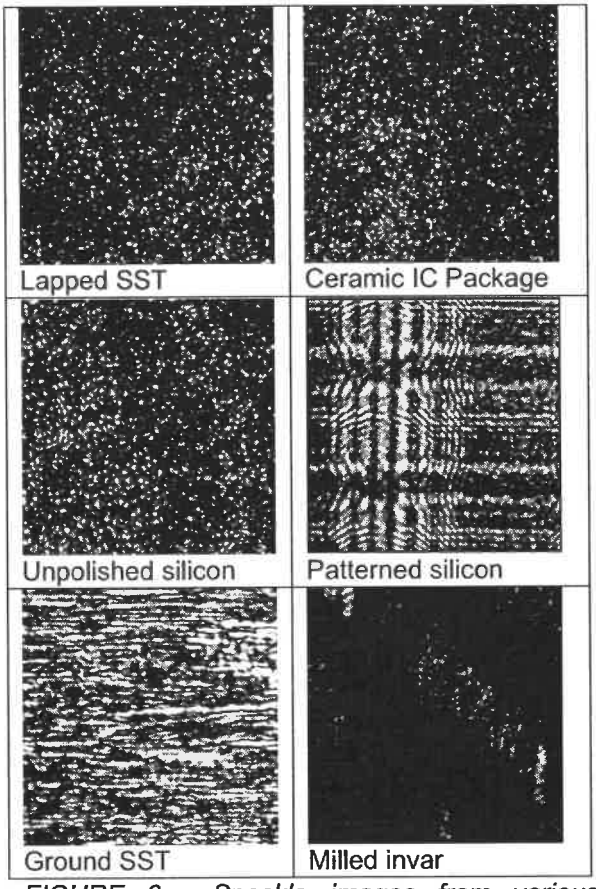

FIGURE 6. Speckle images from various measurement surfaces. Uniform images are shown for lapped SST, ceramic IC package and unpolished silicon. Non-uniform speckle images are shown for patterned silicon, ground SST and milled invar.

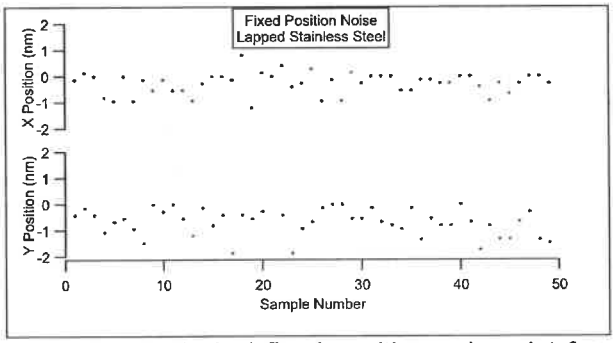

FIGURE 7. Typical fixed position noise plot for lapped SST measurement surface. X and Y position for are plotted. This test was conducted with an update rate of 20Hz, 50 data points were used to calculate standard deviation. Ceramic IC package and unpolished silicon display similar results.

Reproducibility of the sensor on lapped SST is displayed in FIGURE 8. Accuracy tests are conducted by stepping the X-Y test system in a linear fashion in the X, Y and diagonal XY directions. At each step of the test, X and Y position readings are recorded from the sensor and the reference interferometers. The accuracy tests are conducted at a step size of 0.5 μm over the 250 μm range (a typical accuracy test takes ~8 minutes to complete). Test results from four different measurement locations are shown. The sensor accuracy deviation is less than ±100 nm for any of the four accuracy plots.

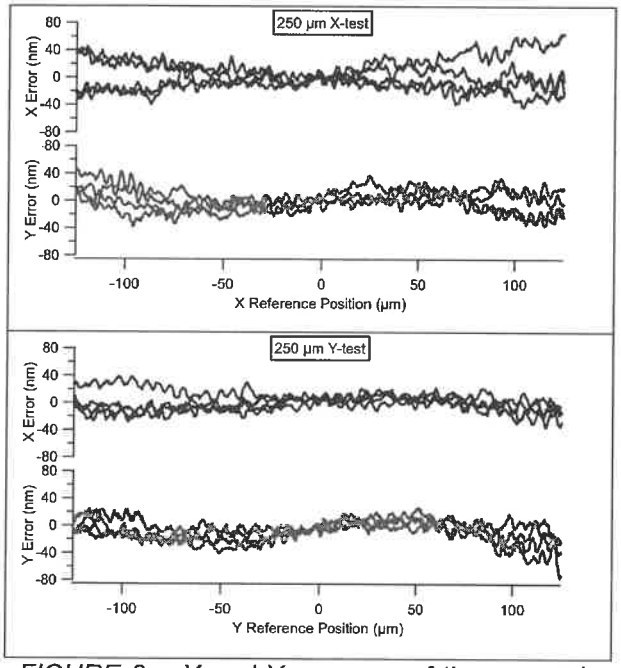

FIGURE 8. X and Y accuracy of the sensor is plotted from four different measurement locations on the same surface of lapped SST. All accuracy plots show less than ±100 nm of error. The top plots are for a test in the X motion axis direction, the bottom plots are for a test in the Y motion axis direction. X and Y accuracy is plotted for each test due to the 2D nature of the sensor.

FIGURE 9 displays the accuracy performance of the sensor when tested using ceramic IC package material and unpolished silicon as measurement surfaces. The peak-to-peak error is less than ±100 nm for these materials.

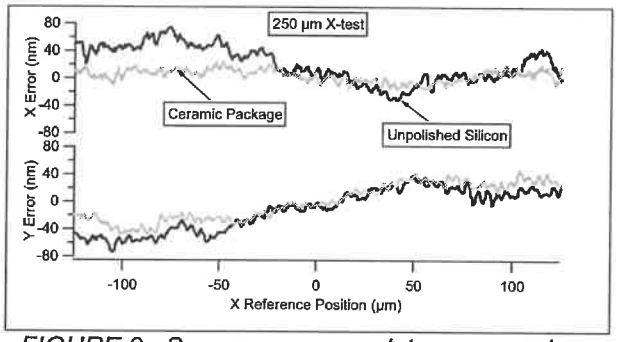

FIGURE 9. Sensor accuracy plots on ceramic IC package and unpolished silicon.

CONCLUSION

We have demonstrated the performance of a 2D speckle based displacement sensor with various measurement materials. The sensor in its present form is capable of <0.7 nm of fixed position noise, and accuracy and reproducibility of <±100 nm over a 250 μm X 250 μm measurement range with various measurement materials. 2D displacement measurements directly on native planar surfaces give this sensor a distinct advantage over other technologies. Trade offs in performance parameters (e.g. range/resolution) can be made to tailor the sensor to various applications.

REFERENCES

[1] Yamaguchi, Ichirou, Fujita, Tadashige. Linear and rotary encoders using electronic speckle correlation. Optical Engineering. 1991; 30(12):1862-1868.

[2] Shilpiekandula, Vijay, Trumper, David L. A laser speckle sensor for compound rotary-linear motion metrology. In: Proceedings of ASPE Annual Meeting 2003.

[3] National Institute of Standards and Technology [homepage on the Internet]. Gaithersburg: Precision Engineering Division; c2001-2007 [updated 2007 April 7; cited 2008 Aug 1]. Index of Refraction of Air; [about 3 screens]. Available from: http://emtoolbox.nist.gov/Wavelength/Abstract.asp

COMPARISON OF FRINGE PATTERN OBTAINED BY SCANNING POLISHED METAL CYLINDERS AND SHARP-EDGED OBJECTS WITH LASER BEAM

Ryszard Jablonski[1], Jerzy Makowski[1]
[1]Faculty of Mechatronics
Warsaw University of Technology
Warsaw, Poland

INTRODUCTION

In laser-scanning measurement of cylindrical objects extremely complex interfering signals occur. They are due to superimposition of reflected, unobstructed and scattered light. The proportions between these components vary in time and also the total intensity distribution changes. The considerations applying Fraunhofer theory are static and fragmentary, and may be concluded that the existing solutions for diffraction of 3D bodies do not fit to engineering applications.

A rigorous diffraction theory is based on Maxwell's equation and the boundary conditions associated with the obstacle [1]. The boundary conditions are used to calculate a field scattered by the obstacle. The origins of this scattered field are currents introduced in the obstacle by the incident field. The scattered field is allowed to interfere with the unobstructed field to produce resultant diffracted field.

Within the Kirchhoff theory of diffraction there are two possible ways of interpretation the diffraction phenomena. The first one, based on so called "edge wave", which refers to T. Young idea was later extended by A. Rubinowicz [1] and the second – Fresnel diffraction model, is based on the "zones concept". T. Young interpreted the diffraction phenomena as a result of interference of the geometrical wave propagating in free space with "the edge wave" [2]. A. Rubinowicz theoretically proved the possibility of division the Kirchhoff diffraction field into two components. One of them has the character of incident wave and the second represents the wave created by interaction between primary field and the edge of object, and this interaction is of reflection type. These mathematical considerations are commonly accepted in the scientific world, but were never proved experimentally.

In the paper the geometrical wave is the undisturbed part of incident wave. The diffracted (or edge) wave is the wave generated by the edge of an object. The obtained results give evidence to the presence of diffraction wave within the undisturbed (free from the other interferences) region.

Having the above in view, the close analysis of detector signal was carried out. The obtained differential intensity characteristics allow determining the important metrological qualities of diffraction field.

MEASURING SET-UP

The outlook of the experimental set-up is presented in Fig.1a. The auxiliary components like: system assuring parallel laser travel, vibration protection set-up, dark chamber, detector electronics, etc, is not shown in the figure.

Fig.1a shows only the main units of the set-up.

The laser (1) beam is transformed by optics (2) and directed to the object (3). The unit (2) contains beam forming optics (beam expander with spatial filter) and scan lens. The intensity distribution pattern is measured by detector unit (4) and detector signal is processed by computer (5). Computer controls the step motors (6) and (7) by means of interface in/out LC-012-1612. The motor (6) scans the laser unit and motor (7) scans the detector worm gear (8). Laser and detector are supplied by separate power sources (9) and (10).

The experiment was limited to the edge effect – it means only to the area located nearby the shadow border line (where the strong diffraction effect is expected).

The scheme of the set-up is presented in Fig. 1b. An object (O), polished steel cylinder, is placed at the focal distance of scan lens (SL). He-Ne laser with beam forming unit, fixed to the X-stage (XS), create the laser head (LH). Scan lens, of the focal length c = 47mm, forms the beam waist $2w_0$=48μm along the Z axis.

In order to avoid the inaccuracies caused by the instabilities of angular deflection, the entire

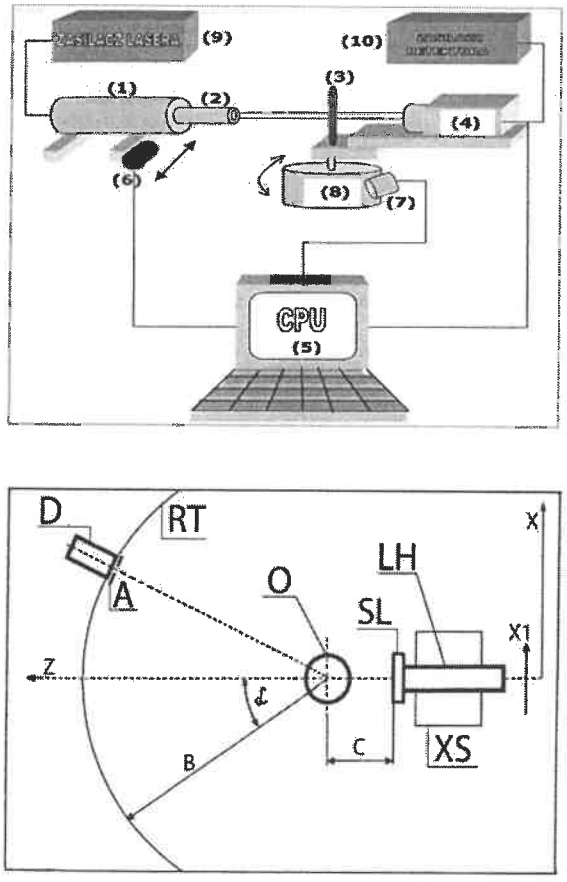

FIGURE.1. Experimental set-up.
a) Outlook (top), b) scheme (bottom)

laser head is scanned across the Z-axis (x1 movement, linear scanning in 2.5μm steps).
The detector unit (fixed to the rotary table (RT), coaxially with object axis) is composed of photodiode (D), aperture (A) 0.3mm and electronic circuit. It was calibrated with the power meter (LaserMate-Q, Coherent) and obtained signal (in V) is proportional to the measured light intensity.

RESULTS

An exemplary plot of diffraction and interference effects originated on the edge of diaphragm (object) is shown in Fig. 2. In general, its course is typical for any shape of object's edge. In order to facilitate the further analysis we defined the particular areas and points on the characteristics [3]:

A - width of undisturbed beam

B - width of diffraction area – segment enclosed between right edge of undisturbed beam and left edge of a partially obstructed beam (by diaphragm). Both widths are measured on the level 1/e.

1 - maximum of intensity of the first interference order (first fringe order).

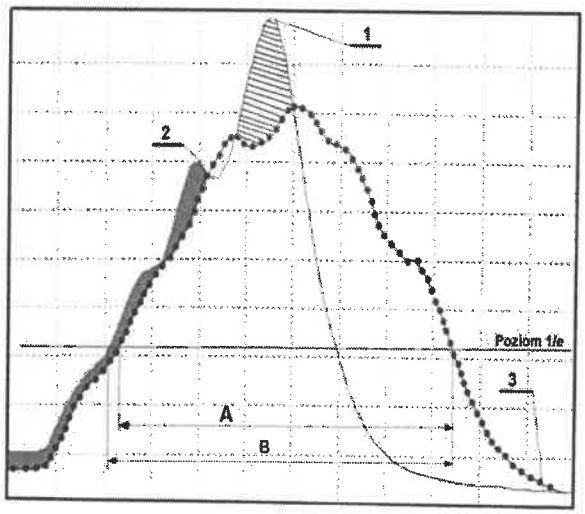

FIGURE 2. Notations used in the paper.

2 - intensity maximum of the second interference order (second fringe order).

3 - behind this point, signal level is considered to be zero.

dotted line – plot of undisturbed wave (the section of the undisturbed beam)

solid line – plot of interference wave (every intensity signal disturbed by obstacle)

border line – shadow border (spreading between points 1 and 3).

gray area – diffraction area (point pattern for which, for constant ordinate, smaller than second interference order level, the difference between abscissas of undisturbed beam and interference course are positive)

shaded area – interference area (point pattern for which the difference between ordinates of undisturbed plot and interference plot are positive and is enclosed between maximum of intensity and zero).

Comparative analysis

The measurements aimed at confirmation the following thesis: the diameter of obstruction (cylinder) influences the position of the first interference order fringe.

The comparative analysis of interference field was performed for sharp edge ≠0.1mm and polished metal cylinder Φ2mm.

As the reference the undisturbed laser beam was taken into account. (theoretically it should have Gaussian shape). Long-term experiments proved, that its course was stable during 10-15 hours (in longer terms these fluctuations did not exceed 3%). Fig. 3 shows the exemplary course taken as reference. Once registered in computer memory was used for comparative and differential analyses.

In this paper we intend to focus on the analysis of the width of diffraction area and the position of interference fringe of first order.

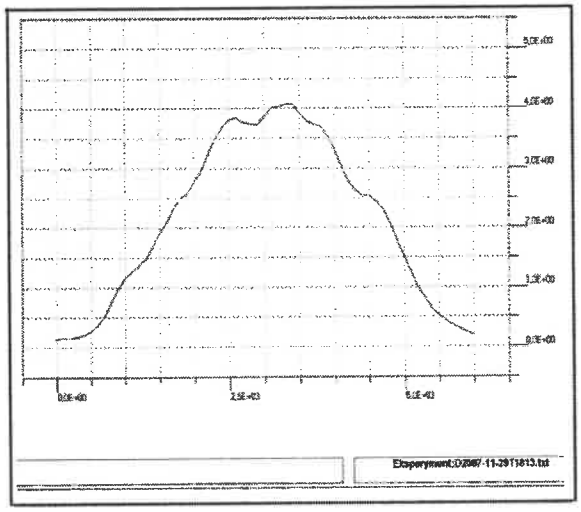

FIGURE 3. The exemplary intensity of undisturbed laser beam used as the reference.

For this purpose we developed the software precisely analyzing the parameters A, B, 1 (see Fig.2).

The results are shown in Fig. 4 and 5. They are performed on the level 1/e. The notation DLT concerns the increment of detector displacement. The values on abscissa (X_{min}, X_{max} and DLT) are given in steps of step motor and the energy values on ordinate in V.

The values indicated in figures show the significant differences in position of shadow border and in the values of interference maximum for sharp edged object and cylindrical object measurements.

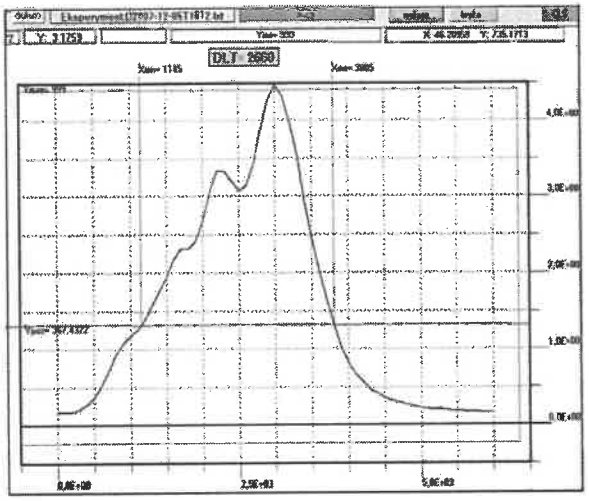

FIGURE 4. Measurement of shadow border and interference maximum for sharp edge ≠0,1mm.

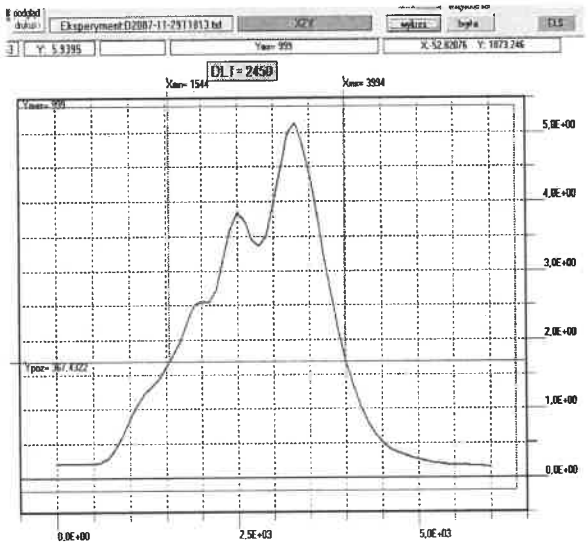

FIGURE 5. Measurement of shadow border and interference maximum for cylindrical object Φ2mm.

This analysis has been extended on the sets of plots (Fig.6 and 7) for sharp edged object and cylindrical object. Figures present 10 plots - starting with intensity of undisturbed laser beam (far right) and followed by successive 9 scans of laser head. These plots reveal the distinct differences in diffraction areas (in interference areas are smaller). These differences are much bigger comparing to undisturbed laser beam fluctuations.

The results are presented in tabular form (Tables 1 and 2). The values are given in steps of step motor driving the detector.

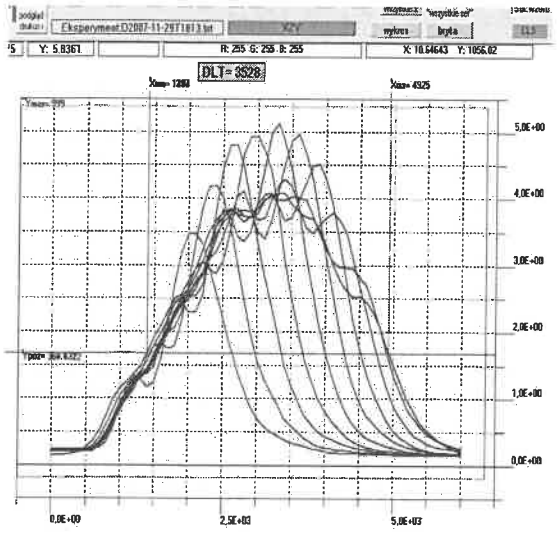

FIGURE 6. Measurement of shadow border and interference maximum for sharp edge ≠0,1mm on set of plots.

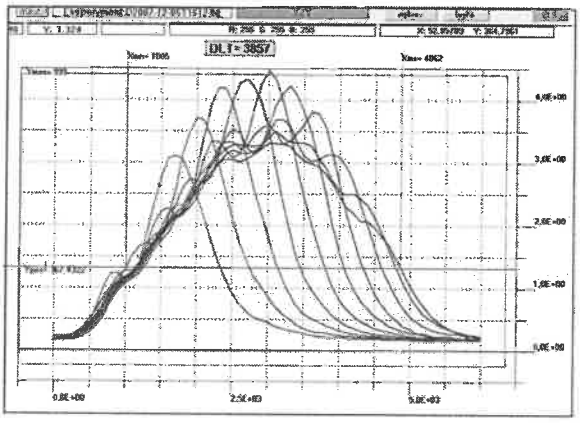

FIGURE 7. Measurement of shadow border and interference maximum for cylindrical object Φ2mm on set of plots.

TABLE 1. Comparison results in ref. to Fig.4, 5

Parameter	≠0,1	Ø2
Undisturbed course		
Beam width	3528	3724
Position of max.	3360	3045
Position of center	3161	3000
Max. intensity course		
Width	2450	2660
Position of max.	3304	3000
Shift of max. in relation to the center of undisturbed course	+143	0

TABLE 2. Comparison results in ref. to Fig.6, 7

Parameter	≠0,1	Ø2mm
Width of undisturbed beam (A)	3528	3724
Width of diffraction area (B)	3528	3857
The difference (B – A)	0	133
The difference in %	0	3,57
Max. energy of undisturbed beam [V] (C)	4,0919	3,3158
Max. of intensity. [V] (D)	5,1384	4,4786
The difference [V] (D-C)	1,0465	1,1628

The comparative analysis of diffraction effects on the sharp edge ≠0.1mm and cylinder Φ2mm shows:

- significant increase of diffraction area for cylindrical object comparing to sharp edged object
- the shift of position of interference maximum in relation to the axis of undisturbed beam only for sharp edged object.

CONCLUSION

The experiments proved the existence of distinct interference maximum. It can be used for determination the position of the edge of an object and also its diameter.

The widths of diffraction area changes differently for sharp edge and cylinder, and it proves that diffraction effects occur also differently.

It was confirmed the dependence between the curvature of an object and position of the first interference fringe. The decay (ratio) decreases with the increase of the radius of curvature.

The investigation of dependences between the measurement signals led to the development of software enabling the calculation and graphic presentation of differential plots. It compensates the influence of the fluctuations of undisturbed laser beam and clearly shows significant differences. The detailed analysis is expected to be in next publication.

REFERENCES

[1] Rubinowicz A., 1966, *Die Beugungswelle n der Kirchhoffschen Teorie der Beugung.* Springer-Verlag, PWN, Warsaw

[2] Born M., Wolf E., 1980, *Principles of optics* - Pergamon Press, Oxford,

[3] Jablonski R., Makowski J., *New Approach to Fringe Pattern Analysis Obtained by Scanning Polished Metal Cylinders with Gaussian Beam.* ISMTII 2007, Sendai, Japan, p.300.

DEVELOPMENT OF THE PRIMARY NANOPARTICLE MEASUREMENT STANDARD BY THE ELECTRO-GRAVITATIONAL AEROSOL BALANCE

Chih-Min Lin, Chao-Jung Chen, Shan-Peng Pan, Han-Fu Weng, and Ta-Chang Yu
Center for Measurement Standards
Industrial Technology Research Institute
Hsinchu, Taiwan, R.O.C.

INTRODUCTION

Nanoparticle characterization has been critical in semiconductor industry, as the feature size of IC continuously shrinks to increase the density of chips in one circuit. The standardization and metrology of nanoparticle characterization are important areas of metrology, though they can be difficult because nanoscale resolution is frequently required. In order to characterize the nanoparticles in nanoscale accuracy, metrology tools are required to detect and analyze these nanoparticles for identifying the sources of the contamination. However, due to lack of calibration standards, inconsistent measurement results are observed for nanoparticle characterizations while different measurement techniques were used [1]. Therefore, in order to accurately and consistently determine the sizes of the nanoparticles, establishments of measurement standards in nanometer range become crucial and necessary.

A primary standard, based on the electro-gravitational aerosol balance (EAB) [2, 3], has been developed at Center for Measurement Standards for nanoparticle sizes ranging from 100 nm to 500 nm in diameter. In this method, charged particles are introduced into the space between horizontally placed planar electrodes. Survival function, defined as the ratio of the number of particles left after holding time to the initial number of particles as a function of the particle mass, is used to evaluate the balance between the electrostatic and gravitational forces exerted on the particles. Based on the evaluation, with known particle mass and particle density, the particle diameter is derived. Since the measurement principle is the simple, this method is expected to achieve high accuracy and low uncertainty. The calibrated or certified particles by this primary standard system with superior uncertainty are used for the calibration of other particle measuring equipment in industry.

THEORY

Two electrodes (stainless steel plates) are placed parallel in a distance H to form a gap to generate an electric field with a voltage V. At initial stage, assuming t = 0, monodispersed particles with electric charge uniformly distribute inside of the two electrodes. As shown in Figure 1, balance can be obtained between the static electric force F_E, assumed in the upward direction, and the gravity force F_G (downward) on a charged particle. After a relaxation time, τ, the particle will move at a constant terminal velocity, v. The terminal velocity, assumed to be in the upward direction, can be represented as:

$$v = \tau[\frac{qeV}{mH} - (1 - \frac{\rho_a}{\rho_p})g] \quad (1)$$

where e is single electric charge, q is the number of static charge on a particle, m is the mass of a single particle, and g is the standard gravitation. In addition, ρ_a and ρ_p are the densities of the air and a particle, respectively.

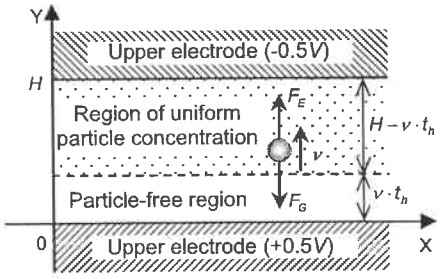

FIGURE 1. Schematic representation of a definite boundary between the uniform particle concentration region and the particle-free region during the sedimentation process.

Furthermore, the relaxation time, τ, is related to the size of the particle, d_p, the density of the particle, ρ_p, and the gas viscosity, η, as shown in below:

$$\tau = \frac{d_p^2 \rho_p}{18\eta} C_c(d_p) \quad (2)$$

where $C_c(d_p)$ is the Cunningham slip correction factor that corrects the non-continuum gas behavior of the drag force for small particles. Due to the terminal velocity, the monodispersed particles move in the upward direction. A portion of the charged particles will stop on the top electrode plate after a holding time, t_h, and a clear space without particles will be formed near the bottom of the electrode plate, as shown in Figure 1. A residual particle ratio can be defined as the numbers of particles at $t = t_h$ to the numbers of particles at $t = 0$. The survival function, $s(m, V)$, is used to describe the ratio as:

$$s(m,\ V) = \begin{cases} 1 - \nu \cdot t_h / H, & \text{If } t_h \le H/\nu \\ 0, & \text{Otherwise} \end{cases} \quad (3)$$

where the $s(m, V)$ is the survival function of the mass of the particle and the charge, V. A slightly distorted isosceles triangle survival function can be obtained according to the mass of the particle, as shown in Figure 2. Three mass numbers mirrored to the 3 poles of the triangle can be used to decide the size of particles: the first two, $m_{\pm}$, are the triangle poles on the base line, and the third one is the top pole of the triangle at point m_0, where the survival function $s(m, V)$ is equal to 1. The m_0 and $m_{\pm}$, can be determined by the following equations as:

$$m_0 = \frac{qeV}{(1 - \rho_a / \rho_p)Hg} \quad (4)$$

$$m_{\pm} = \frac{qeV}{[(1 - \rho_a / \rho_p)g \mp H / t_h \tau]H} \quad (5)$$

The m_0 represents the average mass of the particles. Accordingly, the average size of the particles, d_{p0}, can be calculated by a known average mass, m_0, as:

$$d_{p0} = \left(\frac{6m_0}{\pi \cdot \rho_p}\right)^{1/3}$$

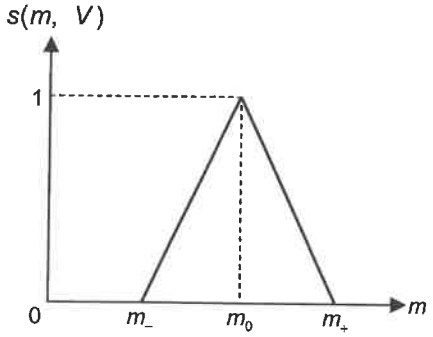

FIGURE 2. Survival function is an isosceles triangle.

MEASUREMENT SYSTEM

The system setup and the measurement procedure in this study are similar to that of Ehara *et al.* [2, 3]. A schematic diagram for the system of the primary standard in this study is shown in Figure 3. The system consists of an aerosol generator, a charge neutralizer, a differential mobility analyzer, a pair of dc voltage sources, a digital multi-meter, a thermometer, a condensation particle counter and homemade electrodes.

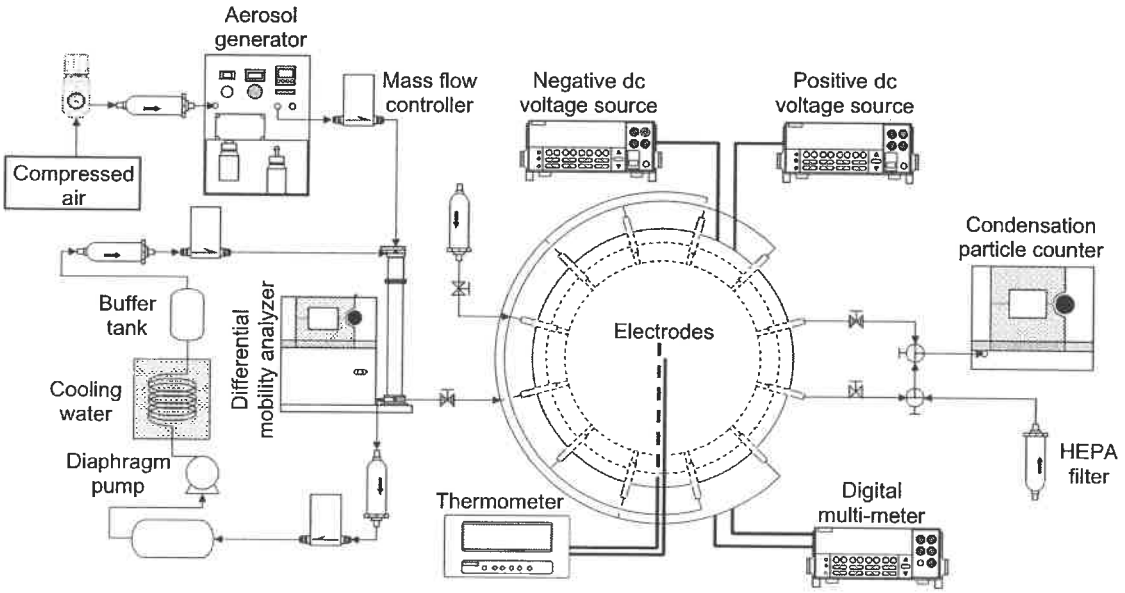

FIGURE 3. Diagrammatic sketch of the electro-gravitational aerosol balance.

The two flat plate electrodes made of stainless steel, 280 mm in diameter and 10 mm in thickness are separated by an alumina annulus. The nominal dimensions of the alumina annulus are 15 mm in height, 210 mm in internal diameter, and 250 mm in external diameter. The volume of the sealed space is, then, 519.54 cm^3. Furthermore, there are twelve openings circumnavigated on the side of the alumina annulus: five of which serve as aerosol inlets, five as clean air inlets, and the remaining two as aerosol outlets. One of the functions for the aerosol outlets is to exhaust the aerosol before the holding time has started, and the other one provides the aerosol to the condensation particle counter after the holding time has elapsed. The flatness of the electrodes and the alumina annulus were evaluated with a computer-generated hologram interferometer, as shown in Figure 4. The PV values of the electrodes and the alumina annulus are less than 2 μm and 4 μm, respectively. The voltage of the electrodes is supplied by the pair of dc voltage sources (Model 2410, Keithley Instruments Inc.), and monitored by the digital multi-meter (Model 2010, Keithley Instruments Inc.). The positively charged particles in the sealed space will be evaluated to determine the sizes of nanoparticles.

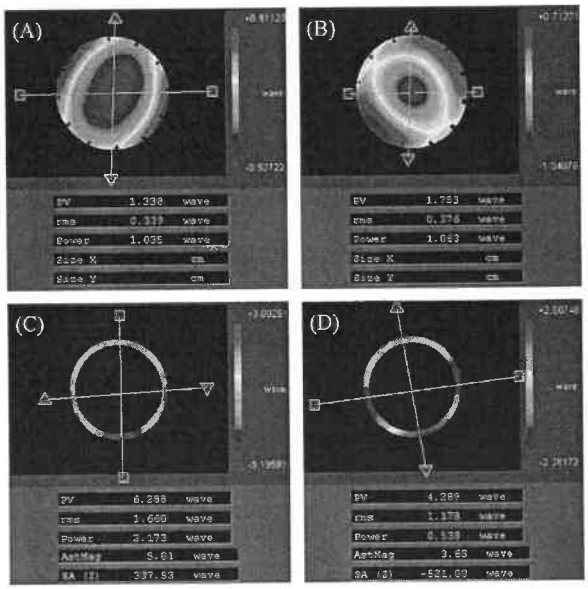

FIGURE 4. Surface flatness measurement: (A) the upper electrode; (B) the lower electrode; (C) and (D) the double sides of the alumina annulus using a computer-generated hologram interferometer with 632.8 nm wavelength.

The liquid suspending particles is first conveyed into the gas phase using the aerosol generator (Aeromaster-V, JSR Corp.). The resulting droplets pass through the Am-241 charge neutralizer where the droplets and charged ions collide to generate charge distributed as a modified Boltzmann distribution. The differential mobility analyzer (Model 3080L, TSI Inc.) is installed on the top of the electrodes in order to filter out the multiply charged particles. As a result, all particles introduced into the space between the parallel plate electrodes are singly charged. After a certainty holding time, particles will be stabilized due to the balance of electrostatic force and the gravitational force. The condensation particle counter (Model 3775, TSI Inc.) counts the number of particles passing through the detector per cubic centimeter of gas flow. In addition, the electrodes are held in an adiabatic vessel to obtain a uniform temperature over the two electrode surfaces, in order to suppress thermophoresis of particles. Consequently, a certain fraction of the particles is deposited on the electrode surfaces from the space between the electrodes. The survival function is used to describe the ratio of the number of particles left after the holding time to the initial number of particles. The particle survival rate, defined as a function of the voltage applied to the electrodes, is used to determine the particle mass. Once the particle density is known, the particle size is calculated and determined.

RESULTS

The specification of the tested sample, JSR SC-048-S, is shown in Table 1. The experimental parameters for employing the differential mobility analyzer are shown in Table 2, and the holding time is set at 45 minutes. The seven measurement data of survival rates is shown in Table 3. The average diameter determined by the primary nanoparticle size standard system is 474 nm, and the best fit survival rate spectrum is shown in Figure 5. The certified diameter provided by the manufacturer is 479 nm, which agrees with the measurement results within 1% difference.

CONCLUSIONS

In order to achieve higher accuracy and lower uncertainty for nanoparticle size measurement, the electro-gravitational aerosol balance method has been used to develop the primary nanoparticle size standard system at Center for Measurement Standards, because of the

simplicity of its principle. The measurements for the particle sizes ranging from 100 nm to 500 nm are currently in progress.

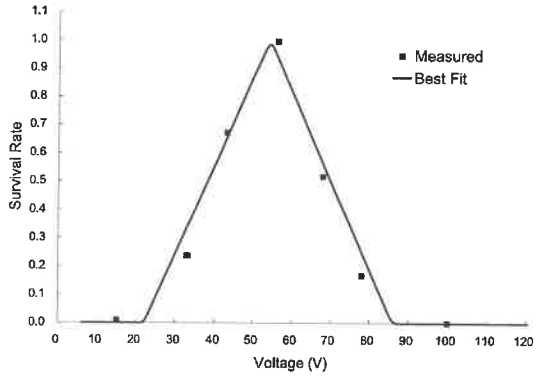

FIGURE 5. Survival rate spectrum obtained for JSR SC-048-S.

Because of the different measurement principles applied in these techniques for nanoparticle size characterizations, the obtained measurement results do not always agree with each other. In some cases, the deviation on the measurements of the same sample is rather significant that would easily lead to the questions of which instrument could be trusted when it comes to determining the sizes of certain nanoparticles and how to translate the difference in measurements among these instruments. Certainly, there are number reasons that would attribute to the disagreement in measurements. It would definitely improve measurement consistency and accuracy if there exist particulate reference standards, international or industrial standards that would sufficiently comprehend details of the measurements. Additionally, measurement consistency and accuracy could be improved, if the nanoscale instruments in the laboratories can be properly evaluated with uncertainty budget, and validated with recognized protocols.

REFERENCES

[1] Wang C Y, Fu W E, Lin H L, Peng G S. Preliminary Study on Nanoparticle Sizes under the APEC Technology Cooperative Framework. Meas. Sci. Tech. 2007; 18: 487-495.

[2] Ehara K, Takahata K, Koike M. Absolute Mass and Size Measurement of Monodisperse Particles Using a Modified Millikan's Method: Part I – Theoretical Framework of the Electro-Gravitational Aerosol Balance. Aerosol Sci. Technol. 2006; 40: 514-520.

[3] Ehara K, Takahata K, Koike M. Absolute Mass and Size Measurement of Monodisperse Particles Using a Modified Millikan' s Method: Part II – Application of Electro-Gravitational Aerosol Balance to Polystyrene Latex Particles of 100 nm to 1 μm in Average Diameter. Aerosol Sci. Technol. 2006; 40: 521-535.

TABLE 1. Attributes of the tested polystyrene latex particles, JSR SC-048-S.

Mean Diameter	Uncertainty (k = 2)	Standard Deviation	CV	Specific Gravity	Number Concentration	Solid Content
479 nm	15 nm	4.79 nm	1.0 %	1.054	1.6×10^{11} #/ml	1 %

TABLE 2. Experimental parameters of the differential mobility analyzer.

Set Voltage	Sheath Air Flow Rate	Main Outlet Flow Rate	Aerosol Flow Rate	Sample Flow Rate	Relative resolution	Trapezoid-city
9905 V	5.40 lpm	6.17 lpm	1.54 lpm	0.77 lpm	0.20	0.33

TABLE 3. Measurement data produced by the primary nanoparticle size standard system.

	1	2	3	4	5	6	7
Voltage (V)	15.052	32.961	42.998	55.984	68.021	78.002	100.006
Survival Rate	0.00872	0.23486	0.67164	0.99365	0.51753	0.16704	0.00004

DEVELOPMENT OF A MEASURING SYSTEM FOR A MICRO HOLE USING AN OPTICAL FIBER PROBE

Hiroshi Murakami[1], Akio Katsuki[2], Hiromichi Onikura[2], and Takao Sajima[2]
[1]Mechanics and Electronics Research Institute
Fukuoka Industrial Technology Center
Kitakyushu, Fukuoka, Japan
[2]Department of Mechanical Engineering, Faculty of Engineering
Kyushu University
Nishi-ku, Fukuoka, Japan

INTRODUCTION

In recent years, there have been increasing demands to measure the accuracy of micro holes of fuel injector nozzles, chemical fiber nozzles, optical fiber ferrules, and so on. It is very difficult to measure precisely the shape of a micro hole with a large length/diameter (L/D) ratio [1-4].

This paper presents a micro hole measuring system using an optical fiber probe. We examine the optimization of design parameters of an optical system using ray tracing. In a trial measuring system, the measuring accuracy is examined in an experiment.

MEASURING PRINCIPLE

Figure 1 shows an illustration of the optical system and a photograph of the fiber probe. Figure 2 shows the measurement principle. An optical fiber of 30 μm diameter with a ball of 50 μm diameter on the end serves as the fiber probe. The system is composed of the fiber probe, two floodlighting fibers(FPX, FPY) and two double-light reception fibers(FX1, FX2, FY1, FY2) in the X and Y directions. The fiber probe is installed between the floodlighting fibers and the light reception fibers in orthogonal positions. The two floodlighting fibers, connected by semiconductor lasers, are used for irradiation of the laser beam around the fiber probe. The stem of the fiber probe is irradiated with a laser beam emitted by the two floodlighting fibers in the X and Y directions. The two double-light reception fibers, connected by four photo diodes, are opposite the floodlighting fibers. The laser beams that transmit the probe are received in the two double-light reception fibers. The intensities, detected by the four photo diodes, are converted into voltage, and are defined as I_{FX1}, I_{FX2}, I_{FY1} and I_{FY2} (V), respectively.

When the fiber probe does not contact a hole surface, the light income of the two double photo

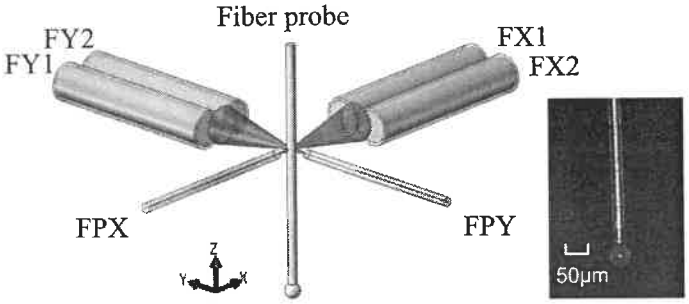

FIGURE 1. Optical system and photograph of fiber probe.

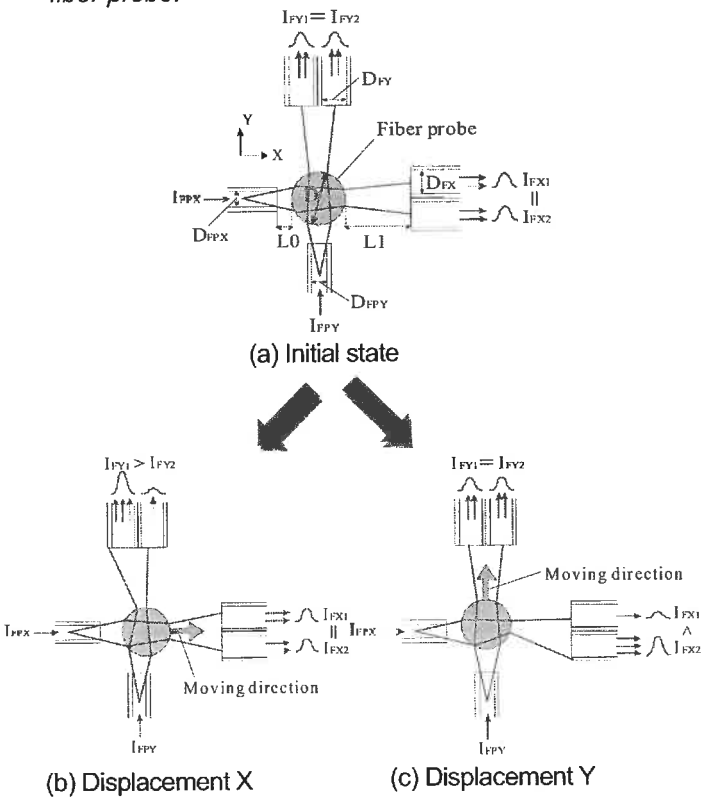

FIGURE 2. Measuring principle.

diodes is equal (I_{FX1}=I_{FX2}, I_{FY1}=I_{FY2}), as shown in Fig2(a). When the fiber probe contacts a hole surface (X direction), the probe is displaced and light income of the two double photo diodes is not equal (I_{FX1}=I_{FX2}, I_{FY1}>I_{FY2}), as shown in Fig.2(b). Consequently, the direction of contact can be obtained. The displacement of the fiber probe is magnified by using the fiber probe as a rod lens. The surface of the micro hole is scanned in the circumferential direction using the precision stage, and the accuracy of micro hole is measured by recording the contact coordinate and displacement of the fiber probe.

An output signal I_X in the X direction using I_{FX1} and I_{FX2} and an output signal I_Y in the Y direction using I_{FY1} and I_{FY2} are defined in Eq.(1) and Eq.(2), respectively.

$$I_X = I_{FX1} - I_{FX2} \quad (1)$$

$$I_Y = I_{FY1} - I_{FY2} \quad (2)$$

OPTICAL ANALYSIS

When the displacement of the fiber probe is detected, the probe sensitivity changes by the distances *L0* between the floodlighting fiber end and fiber probe, the distance *L1* between the fiber probe and light reception fiber end, diameter *D* of the fiber probe and diameters D_{FX}, D_{FY} of the light reception fibers in X and Y directions, respectively. Therefore, we examine the optimization of design parameters of optical system using ray tracing.

In this simulation, the intensities detected by the four photo diodes are defined as the relative light requirement of the incident ray and are expressed as I_X(%), I_Y(%).

First, random numbers of a Gaussian distribution are generated by the Box-Muller method [5] and the ray based on this distribution is radiated from the floodlighting fiber. Then, the rays are traced in the optical system in order, and the coupling efficiency is analyzed at the end of the light reception fiber. Finally, the intensities detected by each photodiode are calculated. In this simulation, the fundamental mode of a single mode fiber for floodlighting is similar to a Gaussian distribution. Table 1 shows the simulation conditions.

ANALYTICAL RESULTS

Figures 3-5 show the simulation results of ray tracing. These figures show the analytical results in the case that the fiber probe is displaced ±5 μm in the X direction.

Figure 3 shows the simulation result of I_X at the distance *L1*=300 μm, 900 μm and 1300 μm. Because I_X changes only slightly, the probe sensitivity of the X direction is low.

Figure 4 shows the simulation result of I_Y at the distance *L1*=300 μm, 900 μm and 1300 μm under the same condition. The rate of change of I_Y becomes a maximum in the case of L1=900 μm, and becomes 0.026 (%/nm) within the range of ±1 μm.

Figure 5 shows the simulation result of I_X and I_Y at the distance L1=900 μm in the case that the direction vector of the probe movement is (1,2). For example, the rate of change of I_X becomes -0.025 (%/nm) within a range between 0～0.5 μm in the X direction, and the rate of change of I_Y becomes 0.013 (%/nm) within the same range. Therefore, it is possible to detect the contact direction by the ratio of the rate of changes of I_X and I_Y.

TABLE 1. Simulation conditions.

Floodlighting fiber (FPX,FPY)	Single mode fiber Core diameter: (D_{FPX}=D_{FPY}=4 μm) Refractive index: 1.463, NA: 0.12
Light reception fiber (FX1,FX2,FY1,FY2)	Multi mode fiber Core diameter: (D_{FX}=D_{FY}=105 μm) Refractive index: 1.457, NA: 0.22
Laser source	Wavelength: 633 nm
D	30 μm
L0	5 μm
L1	300, 900, 1300 μm
Displacement *X*	-5.0～5.0 μm

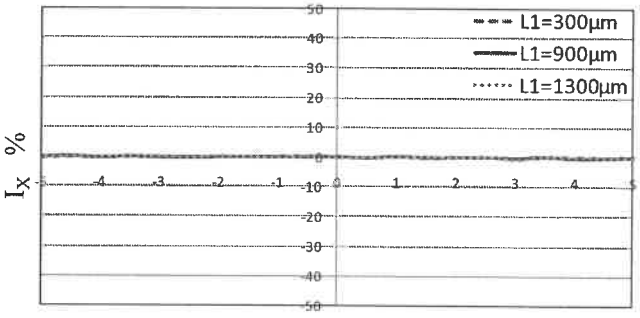

FIGURE 3. Simulation result of I_X at the distance L1=300 μm, 900 μm and 1300 μm (Moving direction of the fiber probe X, D=30 μm).

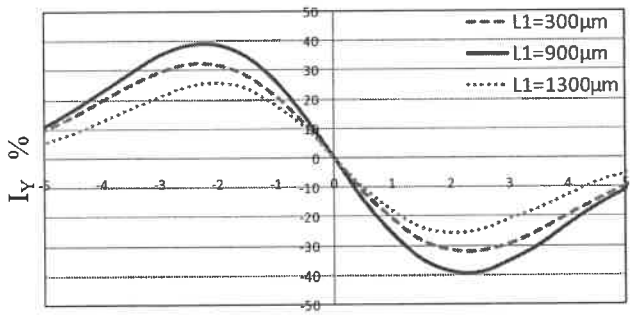

FIGURE 4. Simulation result of I_Y at the distance L1=300 μm, 900 μm and 1300 μm (Moving direction of the fiber probe X, D=30 μm).

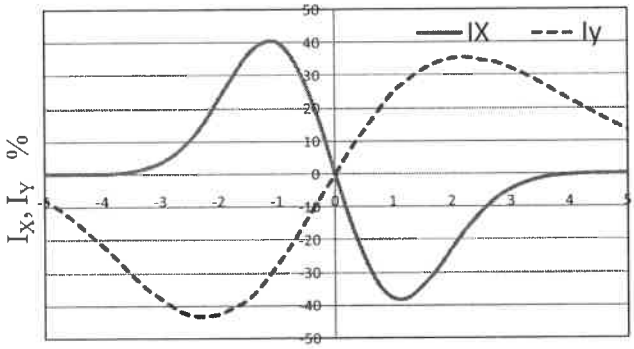

FIGURE 5. Simulation results of I_X and I_Y at the distance L1=900 μm (Direction vector of the probe movement=(1,2), D=30 μm).

EVALUATION OF THE MEASUREMENT RESOLUTION

An experiment is carried out to evaluate the measurement resolution of the fiber probe. The amount of change of an output signal I_Y in the X direction is examined when the probe is displaced by 30 nm in the X direction. Figure 6 shows the experimental apparatus for evaluating the measurement resolution and a photograph taken by a microscope. The probe is displaced in the X direction by the measured surface of the precision piezoelectric stage (P625.2CL, PI Co., Ltd., resolution: 1.4 nm). This stage has a built-in capacitance-type displacement meter.

Figure 7 shows the experimental result. The horizontal axis shows the measuring time, and the vertical axis shows the amount of change of an output signal I_Y in the X direction. The probe sensitivity is calculated with 404nm/V and the dispersion of output voltage caused by various noise is approximately 0.11VP-P. Consequently, the measurement resolution of this fiber probe is

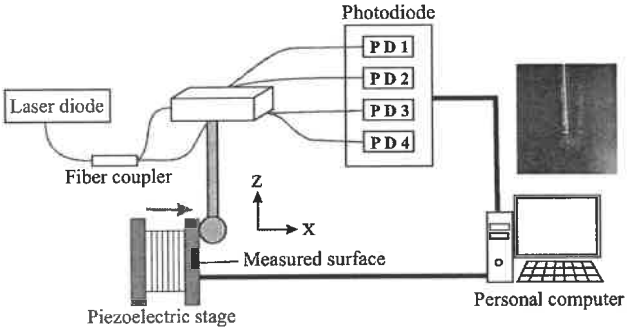

FIGURE 6. Experimental apparatus for evaluating the measurement resolution.

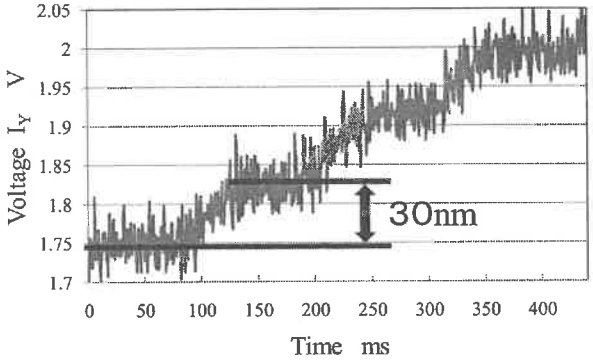

FIGURE 7. Output voltage I_Y of the X-desplacement in the case of step feeding (30 nm) of the stage.

approximately 44nm. In order to improve the measurement resolution, it is necessary to reduce the noise, develop the signal processing method, and use a high-power laser diode.

EFFECT OF THE SURFACE FORCE

In general, When the particle size is less than several 10 μm, the effects of the surface forces for the intermolecular force, electrostatic force and liquid bridge force strengthen to become greater than the force of gravity. Because we use the fiber probe with the 50 μm diameter ball, we find the phenomenon that the measured surface draws the probe closer when the probe approaches the measured surface and when the distance *d* between the probe and the measured plane is less than displacement of 0.35μm. When the probe and the measured surface contact each other, the probe adheres to the measured surface and they can't separate. There is no reproducibility in the adhesion, and it is influenced by the environment (e.g., humidity, temperature) and surface roughness of the measured plane.

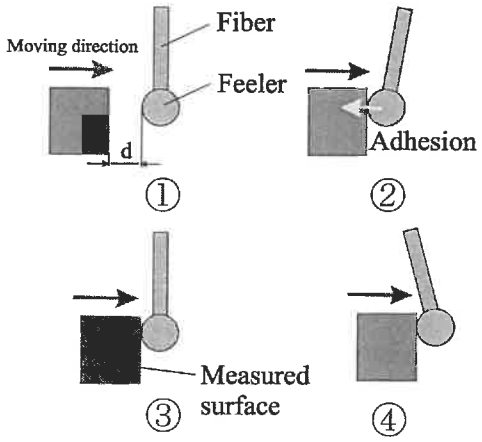

FIGURE 8. Experimental apparatus for evaluating the adhesion force.

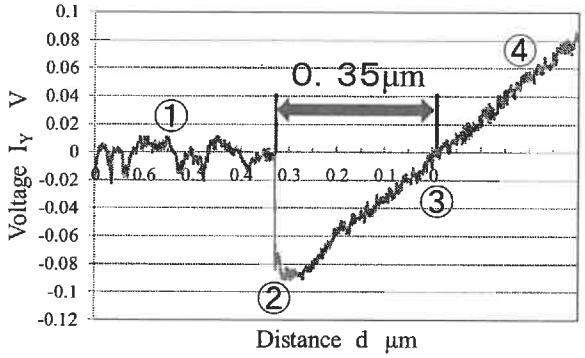

FIGURE 9. Output voltage I_Y of the X-displacement in the case of step feeding (1 nm) of the stage.

So, another experiment is carried out to investigate the effect of the adhesion force.

Figure 8 shows the experimental apparatus for evaluating the adhesion force. The amount of change of an output signal I_Y in the X direction is measured when the measured surface approaches the probe by 1 nm in the X direction. In this experiment, the 100 output voltages for I_Y are acquired every transfer, and the mean value is recorded as output I_Y.

Figure 9 shows the measurement result. ①The output voltage does not change when the distance *d* between the probe and measured surface is more than displacement of 0.35μm. ② The measured surface draws the probe closer and the probe adheres to the measured surface when the probe approaches the measured surface and the distance *d* is less than 0.35μm. The output voltage I_Y expresses a negative value. ③Next, the output voltage I_Y returns to the initial state when distance *d* is 0; this location becomes the contact start point in the initial state. ④Then, output voltage I_Y increases since the probe is displaced in the contact condition. Therefore, the effect of the surface force is not negligible in the measurement of a microstructure. So, we need to select a measuring method with consideration of the surface force. However, a larger force is required to separate the probe adhered to the measured surface from the measured surface.

CONCLUSION

We developed a measuring system for a micro hole using an optical fiber probe. We examined the optimization of the design parameter of this system by ray tracing. Then, after a trial measuring system was manufactured, the measuring accuracy was examined by using basic experimental apparatus. As a result, the following are our result.

1. The design parameters of the optical system are optimized by ray tracing.
2. The resolution of the measuring system is approximately 44 nm.
3. The measured surface draws the probe closer and the probe adheres to the measured plane when the probe approaches the measured surface and distance *d* is less than 0.35 μm.

ACKNOWLEDGMENT

This work was supported by Grant-in-Aid for Young Scientists (B).

REFERENCES

[1] Ji. Guijun, H. Schwenke, E. Trapet. Opto-Tactile Sensor for Measuring Small Structures on Coordinate Measuring Machines. Proc. of ASPE. 1998; 18: 25-28.

[2] U. Brand, S. Cao, W. Hoffmann, T. Kleine-Besten, P. Pornnoppadol, S. Büttgenbach. A Micro-Probing System for Dimensional Metrology on Microsystem Components. Proc.of 2nd euspen International Conference. 2001; 266-269.

[3] M. B. Bauza, S. C. Woody, R. J. Hocken, S. T. Smith. Development of High Aspect Ratio Microscale Force Probe. Proc. of ASPE. 2005; 37: 90-93.

[4] B. Muralikrishnan, J. A. Stone, J. R. Stoup. Fiber deflection probe for small hole metrology. Precision Engineering. 2006; 30: 154-164.

[5] W. H. Press. Numerical Recipes in C. Cambridge University Press. 1988; 216.

PRECISION MEASUREMENT OF MOTION ACCURACY FOR DEVELOPMENT OF MICRO MEASUREMENT CENTER

Ichiro Ogura[1], Yuichi Okazaki[1]
[1] Fine Manufacturing Systems Group
Advanced Manufacturing Research Institute
National Institute of Advanced Industrial Science and Technology (AIST)
Tsukuba, Ibaraki, Japan

INTRODUCTION

We have proposed the microfactory [1] that is a kind of concept, "small manufacturing machines for small mechanical parts". The micro-milling machine, micro lathe, micro press was developed for microfactory system .

To guarantee the profile accuracy of the parts machined by the micro factory, a profile measurement evaluation process is necessary. The concept of micro measurement center (MMC) system [2] is proposed to evaluate profile accuracy machined by the microfctory. The MMC system is an integrated one of micro-CMM [3] and micro cylinder measurement system [2]. The system can change suitable probe unit for measured object, such as general profiles, cylinder profiles and roundness (FIGURE 1). We have developed element technologies of MMC system, such as the micro-CMM and the measurement system for micro cylinder.

Now, we are constructing the integrated system for the prototype of MMC system. To realize this system, we have to valuate accuracy of motion error of stages such as parallelism between each axis strictly. In this report, we propose a new measurement method of evaluating the parallelism between spindle axis (C-axis) and stage axis (z-axis) for producing MMC system. In this method, 2-dimensional angle sensor or dual displacement sensors unit on z-axis measures a master ball that attached z-axis. For the first, we applied the method of using 2-dimensional angle sensors. But it did not perform good result because the reflected light extended. Instead of this method, we applied using dual displacement sensors. Preliminarily experiment is performed to verify this principle. The results show that accurate evaluation of motion is possible.

In addition, we mention about the trial production of a new probe for MMC. The new probe is contact detection type. And it was made from a thin copper plate of 100-microns. The contact detection experiment was tested and it was appeared that the probe detecting ability was less than 50 nm.

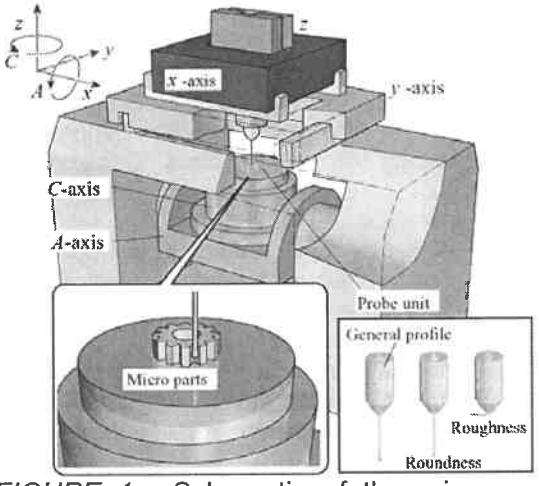

FIGURE 1. Schematic of the micro measurement center

EVALUATING THE PARALLELISM BETWEEN SPINDLE AXIS AND STAGE AXIS

There is already an evaluation method to measure the parallelism between spindle axis and stage axis of 5-axis machining center [4]. FIGURE 2 shows this method. It needs a master ball and a dial gauge. A master ball is attached the main spindle and a dial gage is set to the rotational table.

When the dial gauge measures the master ball at a certain height z_1, there is a certain coordinate (x_1, y_1) that is able to measure the minimum rotational error. At another height z_2, if there is non-parallelism between spindle axis and stage axis, the coordinate (x_2, y_2) should be different than (x_1, x_2). The difference x_2-x_1, y_2-y_1 in z_2-z_1 height changing denotes non-parallelism between two axes.

When we apply this method to MMC by high accuracy, it is necessary to change the dial gauge to the capacitance sensor, because the capacitance sensor has high resolution and measurement accuracy. But in this case, with

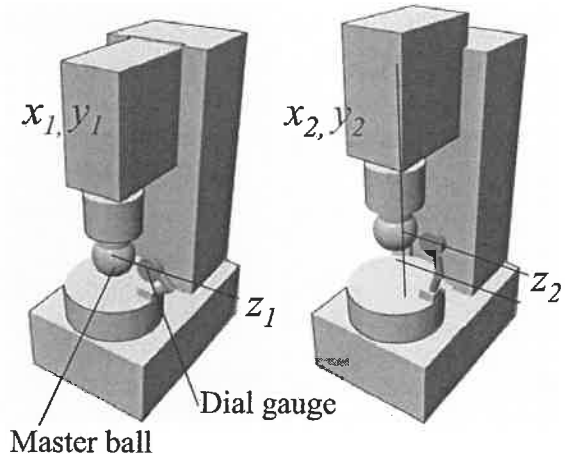

FIGURE 2. Evaluation method to measure the parallelism between spindle axis and stage axis of 5-axis machining center

the rotation of spindle, the cable of this sensor gets twisted easily.

Then, we propose new method in FIGURE 3. This new method also uses master ball and sensor. But master ball is attached to the spindle, and the sensor is set to the main axis. Same as previous method, the parallelism is evaluated by two z-points measurement. But there is a miss-alignment between the center of the spindle rotation and the one of the master ball. There is also an attaching position error between two z-points. Therefore, in this method, the rotational center Q is measured instead of the run-out of rotation.

For the first, we applied 2-dimensional angle sensor to this system. Along the rotation angle ϕ, the two angle outputs (θ_x, θ_y) are denoted by next equations.

$$\sin\theta_x = \frac{R_x}{\sqrt{{R_b}^2 - {R'}^2\cos^2\psi'}}$$

$$\sin\theta_y = \frac{R_y}{\sqrt{{R_b}^2 - {R'}^2\sin^2\psi'}}$$

FIGURE 4 and the following expression show each parameter.

$$\Delta\theta = \tan^{-1}\frac{\Delta y}{\Delta x}$$

$$R'^2 = \left(\xi - \Delta x + R\cos(\Delta\theta - \phi)\right)^2 + \left(\eta - \Delta y + R\sin(\Delta\theta - \phi)\right)^2$$

$$\psi' = \tan^{-1}\frac{\eta - \Delta y + R\sin(\Delta\theta - \phi)}{\xi - \Delta x + R\cos(\Delta\theta - \phi)}$$

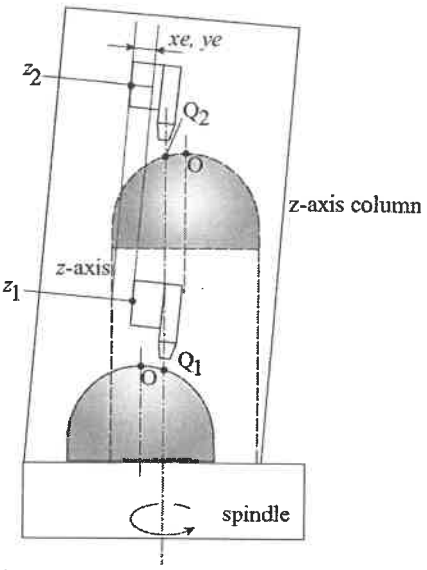

FIGURE 3. Principle of the new evaluation method

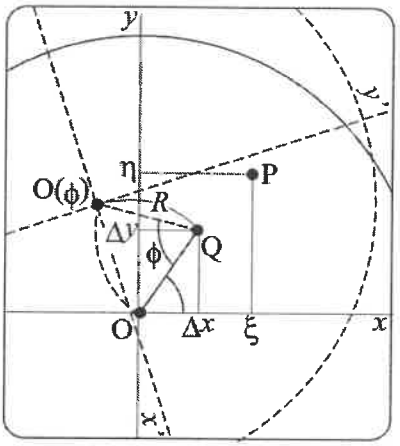

FIGURE 4. Each point of FIG.3

When the measuring point P is same point as rotational center point Q, the variation of the sensor outputs (θ_x, θ_y) becomes the minimum. The reason of using 2-dimensional angle sensor for this system is that the angle change (θ_x, θ_y) according to the rotation of the spindle becomes an indicator that easily discovers the rotation center.

A basic experiment was performed to confirm sensor outputs. A tilted plane mirror is attached to the spindle and the output of 2-dimensional sensor is measured along the spindle rotation. FIGURE 5 shows that result. The x-axis means that the rotation of the spindle and y-axis is the outputs of 2-dimensional angle sensor. Since the measured surface is the tilted plane mirror,

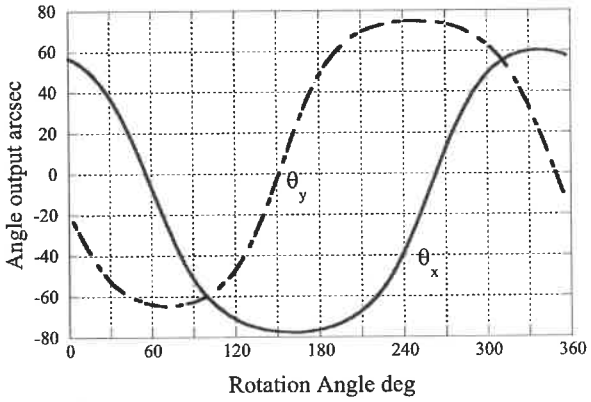

FIGURE 5. Outputs of 2-dimensional angle sensor

the sensor outputs are like almost sinusoidal curve.

We applied this angle sensor to the master ball. Radius of the master ball is 25mm. Although sensitive alignment was executed, the measurement of rotation center point did not perform good result because the reflected light extended. The 2-dimensional angle sensor is original one, which uses auto collimation method. The reflected laser light is detected as a spot on a quadrant photo diode (QPD). Since too much expanded reflected light covers whole area of the QPD, the sensor cannot detect the change of profile angle.

Then, we used not the angle sensor but the two displacement sensors. FIGURE 6 shows a schematic of this method. A jig unit holds two displacement sensors and it is able to rotate around the middle point of sensors. This rotation is less than one times, and then the cables of these sensors do not get twisted. When the displacement sensor measures the master ball in point P, the output becomes in follow equation.

$$m(\phi)=\sqrt{(\xi-\Delta x)^2+(\eta-\Delta y)^2+2R\sin(\phi-\Delta\theta+\alpha)}$$

The parameters are same as FIGURE 4.

There is only one angle ψ, where P-P' line becomes the perpendicular bisector of O-Q line. AT this angle, the outputs of two displacement sensors are same except for the phase. The rotation center exists in the extended line of that middle point. Of course, the rotation center point can be evaluated by one probe scanning on surface, but scanning for the minimum variation of sensor is time consuming. The proposed method is able to detect center point easily just comparing two sensors outputs.

A preliminary experiment is performed for the proposed method. FIGURE 7 shows the result. Before this experiment, the master ball surface is scanned to detect the rotation center. These

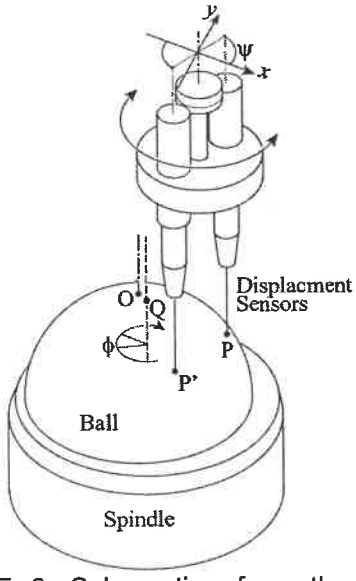

FIGURE 6. Schematic of another method using two displacement sensors

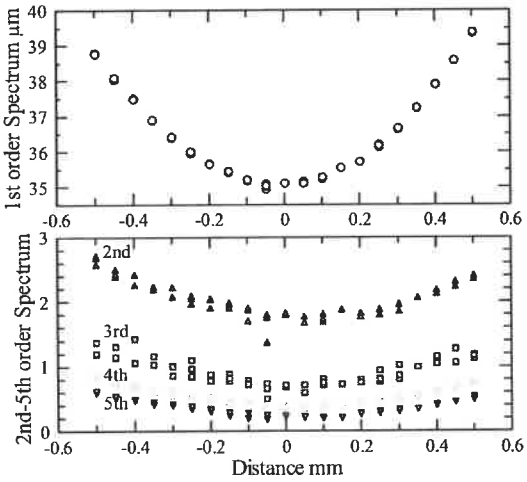

FIGURE 7. Preliminary experiment results for proposed method

graphs mean the outputs of the displacement probe along the x-axis scanning. The distance from rotation center in y direction is 1.0mm. The probe output is converted into the frequency, and until 5th order spectrum is plotted in the graphs. The symmetric spectrum element is obtained along the center position. These results mean that P-P' line becomes the perpendicular bisector of O-Q line.

TRIAL PRODUCTION OF CONTACT PROBE

In our previous study, a contact detecting type probe, which uses piezoelectric gyroscope, is used for micro-CMM [3]. This gyroscope has

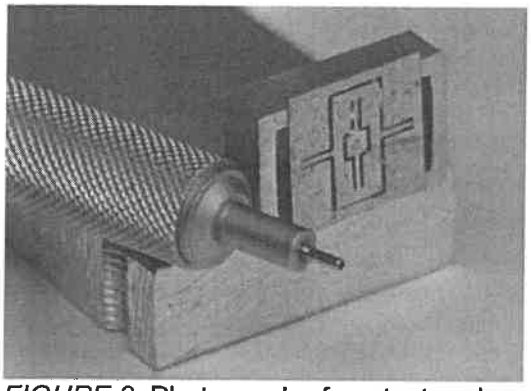

FIGURE 8. Photograph of contact probe

ceramic bimorph structures to detect Coriolis force and we used this sensor as contact detector. This probe has high contact detection less than 50nm, but it cannot detect the contact direction. We developed a contact probe system that can simultaneously detect the contact point and contact direction, using active circular rotation. This system has the validity to measure the 3-dimensional profiles of micro-parts. But when we apply this system to proposed MMC, this probe unit becomes too large to install as assembly. Then, a new contact detection probe is developed as FIGURE 8.

This probe is a kind of cross-beam structure. Copper is used for base plate. The size of this plate is 12mm by 12mm, and the thickness is 100 micron. The length of this beam is 5mm and width is 0.5mm. Using photo lithography method in about 1 hours for the copper plate, the profile of cross-beam is obtained. A contact detection probe and a measurement probe are glued at the face and reverse side of center plate. The probe length is about 8mm and probe ball diameter is 400 microns. When the contact detection probe contacts to measured profile, the beam skews. The measurement probe attached the reverse side of contact one moves opposite side of the contact direction. Optical sensors measure the motion of the measurement probe.

FIGURE 9 shows the output of this probe. In this graph x, y and z direction contact is measured independently. The x-axis of this graph means that the displacement of the contact detection probe motions, and the y-axis denotes optical sensor outputs those measure the motion of the measurement probe. The outputs of this probe are almost linear and the resolution of contact is less than 50nm. The z direction output is small compare with x and y direction. The reason is

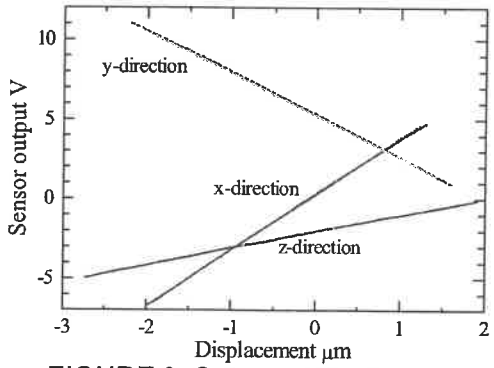

FIGURE 9. Output of the probe.

that the contact movement in the z direction is not skew of the beams but bend of ones.

CONCLUSION

We propose a new measurement method of evaluating the parallelism between spindle axis (C-axis) and stage axis (z-axis) for producing MMC system. Preliminarily experiment was performed and the results show that accurate evaluation of motion is possible. A new contact probe was developed for trial. The contact detection experiments show the less than 50 nm contact detection.

REFERENCES

[1] Kitahara et al.: Microfactory and microlathe, Proc. International Workshop on Microfactoryies (1999)

[2] I. Ogura and Y. Okazaki: Basic Study For Development Of Measurement System For Micro Cylinder, Proc of ASPE annual meeting. (2007).

[3] I. Ogura and Y. Okazaki, Development of micro-CMM Probe detecting contact angle, Proc of ASPE annual meeting. 2004.

[4] S.Ueno, Development of complex machine tools, past, present and future in Japan, International Machine Tool standardization Seminar (2006).

ACKNOWLEDGMENT

Trial production of contact probe is technically supported by Mr. Onishi and AIST NPF (Nano-Processing Facility).

PROFILE MEASUREMENT OF MICRO-ASPHERIC SURFACE BY A SMALL-SCALE MEASURING INSTRUMENT

Atsushi Shibuya, Yoshikazu Arai, Yasuo Yoshikawa and Wei Gao
Department of Nanomechanics
Tohoku University
Sendai, Miyagi, Japan

INTRODUCTION

Along with the miniaturization of optical devices such as medical endoscopes and fiber-optic communication systems, micro-aspheric lenses (1 mm in diameter) have become very important parts [1]. Micro-aspheric lenses are necessary for downsizing and higher image quality. Form accuracy of micro-aspheric lenses is required to be better than 100 nm to make the most of those devises. However, the 100 nm form accuracy is very hard to achieve because aspheric surface profiles are complicated. On the other hand, accurate profile measurement of the aspheric surfaces for realizing on-line assessment is a big challenge. Scanning probe measurement systems with a contact stylus are practical and suitable for profile measurement of aspheric surfaces [2]. We have developed a novel measurement system for micro-aspheric profiles that employs a contact stylus [3]. Contact styli are capable of measuring complicated surfaces that have steep slope such as aspheric surfaces as long as the probe spheres at probe tips contact with the measuring objects. However, lateral resolution of measuring instruments that employ contact styli is restricted by the radius of probe sphere. Most of commercial styli do not have high enough resolution to be employed for micro-aspheric surface scanning. In this research, a micro-stylus, which is composed of a micro-glass-ball and a micro-stylus, is fabricated and it is applied to the micro-aspheric profile measurement system.

DESIGN OF THE MEASUREMENT SYSTEM

The measurement system is schematized in Figure 1. The design is based on a concept: "A small-scale and high precision measuring instrument". The footprint of the machine is 400 mm × 275 mm and the weight of the machine is 57 kg. An aspheric workpiece is mounted on the spindle turntable and a contact-type sensor is mounted on the slide. The aspheric surface is scanned spirally by rotating the spindle and feeding the slide in radial direction of the aspheric workpiece. The surface of a ring artifact surrounding the aspheric workpiece is scanned by two capacitance sensors mounted both sides of the contact-type sensor for the purpose of error motion compensation. Characteristics and specifications of the measurement system are listed below.

Spindle

An air bearing is employed for the spindle. A rotary encoder whose resolution is 0.0038 arc seconds enables positioning accuracy of 1 arc second.

Slide

An air bearing is also employed for the slide. Both the table and the guide are made of ceramics, which is so light and hard that the deflection can be reduced. The stroke of the slide is 70 mm and the resolution of the linear encoder is 0.28 nm. To avoid Abbe error, the scale of the linear encoder is set just below the aspheric workpiece. The vertical and horizontal straightness errors of the slide motion are less than 1 μm within the full stroke.

Contact-type Sensor

A contact-type sensor is employed for the aspheric surface scanning. A shaft of the sensor is fed forward and a ball at the tip of the stylus is pressed to the aspheric object to follow the variation of the surface profile. An air bearing is employed to levitate the shaft so that the shaft can move smoothly. To feed the shaft forward, a technology called inclined self-weight is used [4]. A linear encoder whose resolution is 0.5 nm is attached at the exact center of the shaft to avoid Abbe error.

Vibration Isolation Table and Chamber

The whole measurement system is mounted on a vibration isolation table and covered by a chamber. So it is less affected by vibration and temperature variation.

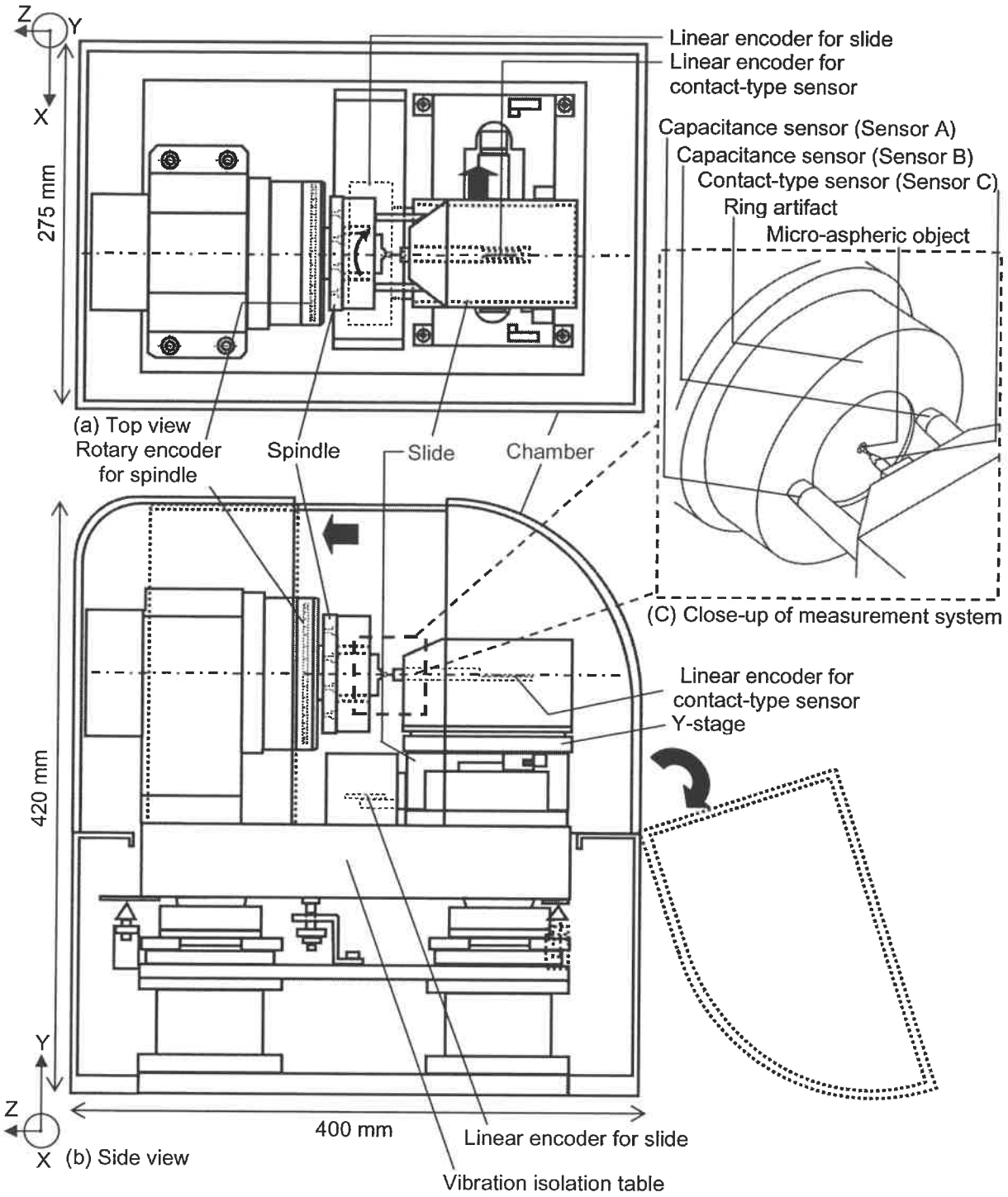

FIGURE 1. Measurement system

ERROR COMPENSATION

For scanning probe measurement system, it is important to compensate error motions of the scanning stage. In this measurement system, the error motions including drifts and vibration between the slide and the spindle can be measured at the same time when the aspheric profile is measured. The error motions are measured by scanning the surface of the ring

artifact by the two capacitance sensors. The output of the contact-type sensor (Sensor C) can be expressed as

$$m_C(x,\theta) = g(x,\theta) + e_{ST}(x,\theta) + e_{CT}(x,\theta) - x(e_{SY}(x,\theta) + e_{CY}(x,\theta)), \quad (1)$$

where $m_C(x,\theta)$, $g(x,\theta)$, $e_{ST}(x,\theta)$, $e_{CT}(x,\theta)$, $e_{SY}(x,\theta)$ and $e_{CY}(x,\theta))$ represent the output of the Sensor C, the aspheric surface profile, axial motion of the spindle, horizontal straightness error of the slide, tilt motion of the spindle and yaw error of the slide respectively. The mean output of the two capacitance sensors (Sensor A and Sensor B) can be expressed as

$$(m_A(x,\theta) + m_B(x,\theta))/2 = (f(d/2 + x,\theta) + f(-d/2 + x,\theta + \pi))/2 + e_{ST}(x,\theta) + e_{CT}(x,\theta) - x(e_{SY}(x,\theta) + e_{CY}(x,\theta)) \quad (2)$$

where $m_A(x,\theta)$, $m_B(x,\theta)$, d and $f(x,\theta)$ represent the output of Sensor A, the output of Sensor B, distance between Sensor A and Sensor B and the surface profile of the ring artifact respectively. By subtracting equation *(2)* from equation (1), the aspheric surface profile can be calculated by using the outputs of the sensors and the surface profile of the ring artifact as follows

$$g(x,\theta) = m_C(x,\theta) - (m_A(x,\theta) + m_B(x,\theta))/2 + (f(d/2 + x,\theta) + f(-d/2 + x,\theta + \pi))/2 \quad (3)$$

The surface profile of the ring artifact can be measured precisely by reversal technique [3].

FABRICATION OF MICRO-STYLUS

Micro-shafts for the micro-styli are made from glass tubes. Glass tubes are stretched to thin the tip of the shaft by heating. Utilizing capillary phenomenon, adhesion bond is filled at the tip of the shaft. Alignment of the probe shaft and micro-glass-ball is conducted by using CCD cameras. The position of the micro-glass-ball is easily set to be centered, because the position is decided by the inner diameter of the micro-stylus. In this paper, two types of the shaft are fabricated for two kinds of diameter of micro-glass-ball (50 μm and 100 μm in diameter) (described as 50 μm-diameter stylus and 100 μm-diameter stylus respectively below). Figures 2(a) and (b) show the photographs of the fabricated micro-styli.

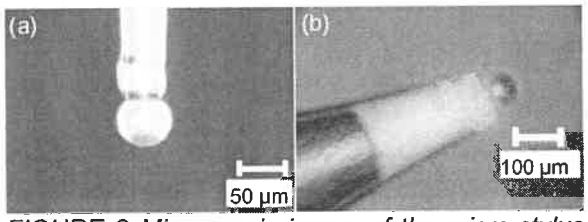

FIGURE 2 Microscopic image of the micro-stylus (a) 50 μm-diameter stylus (b) 100 μm-diameter stylus

EXPERIMENTS

Fabricated micro-styli are attached to the contact-type sensor with a jig and used to scan the micro-aspheric surface. Figure 3 shows the photograph of the measurement system with the micro-stylus. The contact-type sensor with the micro-stylus is mounted on the slide along with the two capacitance sensors. Measurement range of the capacitance sensor is –25 μm to 25 μm which corresponds to –10 V to 10 V. Diameter of the electrode is 1.7 mm. A micro-aspheric object and the ring artifact are mounted on the spindle. The surface of the ring artifact is mirror finished by diamond turning. The micro-aspheric object is mounted on the spindle with a jig which makes it possible to adjust the attitude of the object.

Figure 4 shows the stability of the measurement system. The outputs of the contact-type sensor and the two capacitance sensors are sampled at the same time while the slide and spindle are kept stationary. Left vertical axis represents output of sensors and right represents temperature. 4 lines represent the output of the contact-type sensor, the mean output of the capacitance sensors, differential output between above two outputs which corresponds to equation (3) and temperature. It seems that by applying equation (3) to the sensor outputs displacement variation between the slide and the spindle can be cancelled.

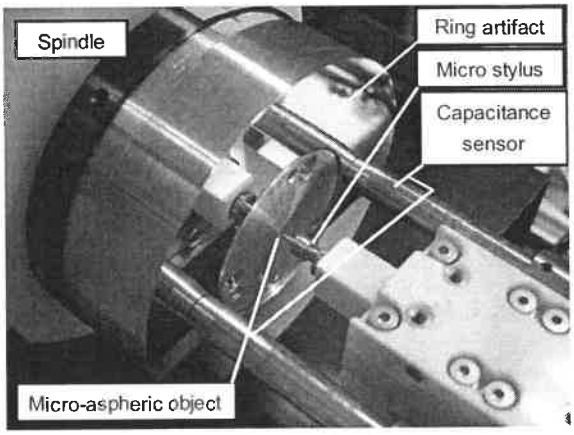

FIGURE 3. Photograph of measurement system

To measure the X-sectional surface profile of the micro-aspheric object, the slide is fed in the X-direction and the micro-aspheric surface is scanned by the contact-type sensor. Traveling speed of the slide is 0.03 mm/s and sampling interval is 10 μm. The profile data is fit to 10th polynomial. Figure 5 shows the measured profile and measurement repeatability. The measurement repeatability is evaluated as standard deviation for 10 times of measurements. Solid line, dashed line and chain line represent measured profile, measurement repeatability with 100 μm-diameter micro-stylus and that of 50 μm-diameter micro-stylus respectively. It would appear that difference of repeatability between 50 μm-diameter and 100 μm-diameter mainly due to the difference of lateral stiffness of the stylus.

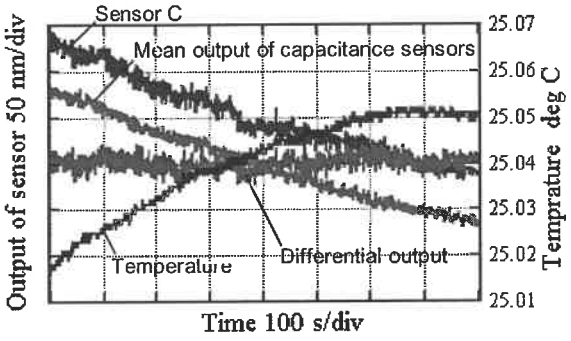

FIGURE 4. Stability of the measurement system

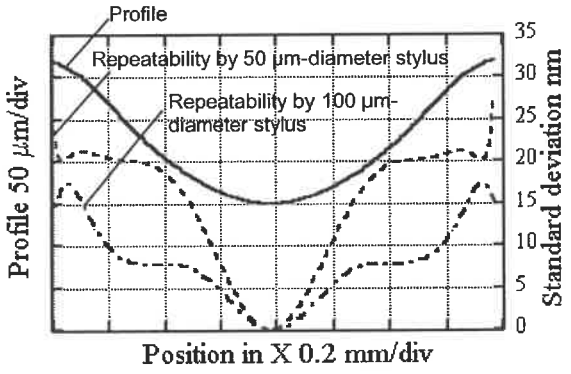

FIGURE 5. X-sectional profile measurement

Finally, 100 μm-diameter stylus is used for spiral scanning of the micro-aspheric surface. Traveling speed of the slide and revolution speed of the spindle are 0.015 mm/s and 10 rpm respectively. The ring artifact was scanned by the capacitance sensors and error motions were compensated. Figure 6 shows the measured profile of the micro-aspheric surface. The measurement repeatability is smaller than ±20 nm all over the surface.

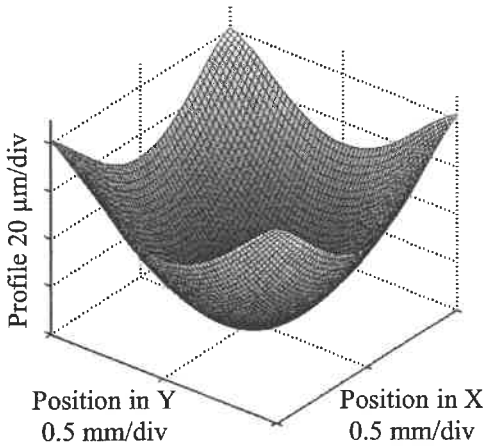

FIGURE 6. Spiral scanning measurement

CONCLUSION

Micro-styli are fabricated for scanning of micro-aspheric surface. X-sectional scanning and spiral scanning with the fabricated micro-styli are conducted for profile measurement of the micro-aspheric object. The measurement repeatability of micro-aspheric X-sectional scanning and spiral scanning by 100 μm-diameter stylus are smaller than ±15 nm and ±20 nm respectively.

ACKNOWLEDGEMENT

This research is supported by a grant-in-aid from JSPS.

REFERENCES

[1] Eric J. Seibel, Mark Fauver, Janet Crossman-Bosworth, Quinn Y. J. Smithwick, and Chris M. Brown, Microfabricated optical fiber with microlens that produces large field of-view, video rate, optical beam scanning for microendoscopy applications. Proceedings of SPIE. 2003; 4957: 46-55.

[2] Chang-Ock Lee, Kilsu Park, Byong Chon Park and Yoon Woo Lee. An algorithm for stylus instruments to measure aspheric surfaces. Measurement Science and Technology. 2005; 16: 1215-1222.

[3] W. Gao, A Shibuya, Y. Yoshikawa, S. Kiyono and C.H. Park. Separation of scanning error motions for surface profile measurement of aspheric miceolens. Int. J. of Manufacturing Research. 2006; 1: 267-282

[4] Y. Nagaike, Y.Nakamura, Y. Ito, W. Gao and T. Kuriyagawa. Ultra-precision On-machine Measurement System for Aspheric Optical Elements. Journal of the Chinese Society of Mechanical Engineers. 2006; 27: 535-540

SUBNANOMETER DISPLACEMENT MEASUREMENT USING COMMON-PATH GRATING INTERFEROMETRY

Chyan-Chyi Wu[1], Cheng-Chih Hsu[1], Ju-Yi Lee[2], and Chao-Jung Chen[1]
[1]Center for Measurement Standards
Industrial Technology Research Institute
Hsinchu 300, Taiwan
[2]Institute of Opto-mechatronics
National Central University
Chung-Li 32054, Taiwan

INSTRUCTIONS

Nanometer-scale positioning devices play an important role and become significant requirement in scientific instruments used for the application of nanotechnology. These devices can be applied to nano-handling, nanomanipulation, and nanofabrication. In addition, they are an essential part of the scanning probe microscopy (SPM) and widely used in many research fields. The precision positioning devices consist of three principle parts, which are the rolling components, the driving system and the position sensor. Piezoelectric actuator is the most popular method for driving system and commercial products have been on the market for a few decades. Therefore, the piezoelectric actuator and the position sensor will play the role of the positioning and the feedback control of the rolling element. To achieve the high resolution positioning, the sensing methods of position sensor become more important and have attracted great attention over the last two decades.

Many position-sensing methods were reported in the past few years and they can be categorized as the heterodyne sensing method [1-3] and the homodyne sensing method [4-6]. W.J. Wu [1] used the synthesis method involved synthesizing higher frequency quadrature signal, mixed with the measurement signals, and added the resultant two signals to the final signal. This final signal had the heterodyne signal form and carried the testing information. This method demonstrated that precise measurement results of the step-motor for a 25 μm step movement could be achieved. F. Demarest [2] proposed a double-passed heterodyne interferometer, which can accomplish high resolution and high-speed measurement. M. Dobosz [4] developed the numerical compensation method to correct the nonlinearity of the laser linear encoder consisting of a laser diode and the reflecting sinusoidal phase grating with 1 μm grating pitch. Y. Jourlin et al. [5] developed the compact displacement sensor consisting of two reflection type gratings with two different grating pitches. This displacement sensor can achieve a compact size with 1×1×3 cm^3 but the resolution is larger than 100 nm because of the packaging tolerance. L. Salbut [6] summarized many articles on grating interferometry for the in-plane displacement sensor. He also proposed five different head types of the waveguide grating interferometer and showed that 20 nm accuracy of the in-plane displacement sensing system can achieve with the fringe pattern analysis technique. However, all of the head types used two different gratings and their parallelism might influence the quality of the interferograms.

In this paper, we propose a common-path optical configuration for subnanometer displacement measurements. According to the optical configuration and heterodyne interferometry technology, it can achieve a displacement measurement with high stability and high resolution. For long-range displacement measurement, the results showed that no significant differences between our method and the comparison instrument. For short-range displacement measurement, our method is able to detect the displacement smaller than 10 nm, while the comparison method could not. Hence, our measurement system can monitor the actual movement behavior of the motorized stage, which is down to subnanometer range. According to our measurement results, the smallest identifiable displacement could be identified to about 6 pm. To our knowledge, it is the first time to realize the identification of the pico-meter displacement variation with heterodyne interferometry in atmosphere condition. If the optical configuration of this method were miniaturized, it might be suitable for use in the movement monitoring system of the motorized stage.

PRINCIPLE

The schematic diagram of this method is shown in *FIGURE 1*. For convenience, the +z axis is chosen to be along the direction of propagation and x- axis is along the horizontal direction. A heterodyne light source [7] is incident onto the beam splitter BS and the light beam is divided into two parts: one is the reference beam that is reflected by the BS and another is the test beam that is passed through the BS and directly incident onto the diffraction grating. Therefore, the reference signal detected by the photodetector D1 has the form:

$$I_r = \frac{1}{2}[1+\cos(\omega t)] \qquad (1)$$

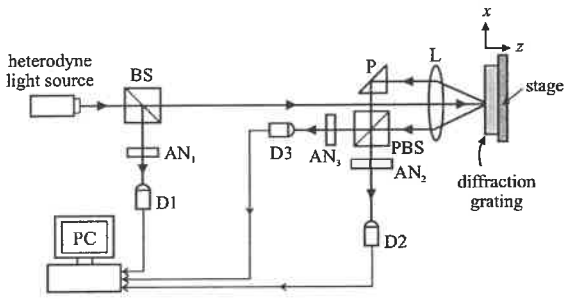

FIGURE 1. The schematic diagram of our laser encoder in 1-D configuration.

The test beam is guided into $\pm 1^{st}$ order diffracted lights and the $+1^{st}$ and -1^{st} order diffracted lights will be collected by a lens L and propagated into two paths: (1) prism P → polarization beam splitter PBS → analyzer AN_2 (45°) → detector D2, (2) polarization beam splitter PBS → analyzer AN_3 (45°) → detector D3. According to the arrangement of the optical configuration, the detector D2 measures the interference signal of *p*- polarization of the $+1^{st}$ order diffracted light and *s*- polarization of the -1^{st} order diffracted light. Similarly, the detector D3 measures the interference signal of *s*- polarization of the $+1^{st}$ order diffracted light and *p*- polarization of the -1^{st} order diffracted light. Hence, the in-plane displacement d can be written as:

$$d = \frac{\Phi d_g}{8\pi m}. \qquad (2)$$

If the diffraction order m, the pitch of the diffraction grating d_g, and the total phase shifting Φ are given, the in-plane displacement d can be obtained simultaneously.

EXPERIMENTS AND RESULTS

A heterodyne light source consisted of a linearly polarized He-Ne laser at 632.8 nm with frequency stabilized control and an electro-optic modulator EOM (model: 4001, New Focus, Inc.) driven by a function generator with 1 kHz sawtooth signal as shown in *FIGURE 1*. The fast axis of EOM was located at 45° to the x-axis and the frequency difference between the *p*- and *s*- polarizations was 1 kHz. The diffraction grating was mounted on the precision stage (model: 8095, New Focus, Inc.). The operated principle of this stage was relied on the static and dynamic frictions, which the stage moved as slow action and fast action respectively. The mechanical structure was consisted of two jaws grasped an 80-pitch screw and a piezoelectric transducer slide in opposite directions [8]. The driver (model: LS-773, New Focus, Inc.) of this stage was designed as an open-loop circuit without feedback control [8]. The grating pitch was 1.6 μm pre-determined by an atomic force microscopy (AFM). The reference and test signals were received by the detectors and sent into the high speed, multi-channel data acquisition card (model: PCI-6143, National Instruments Corporation). Then the phase difference was measured by the pc-based software, which was programmed by the Labview software (version: 7.0, National Instruments Corporation) with the phase-lock technology. The phase resolution of this program can be adjusted manually from 0.1° to smaller than 0.001°.

The experiments dealt with the 1-D displacement measurement using 1-D diffraction grating. The results were compared with commercial precision laser dimensional measuring system (model: HP 5528A and HP 5529A, Hewlett-Packard Development Company) which were calibrated by the primery standard system in National Measurement Laboratory (NML). The sampling-rate of these experiments was kept the same during the whole measurement process and the value was fixed at 128 measured points per second.

We mounted the 1-D grating on the stage and controlled the stage movement discontinuous or continuous. In *FIGURE 2*, we controlled the stage with 10 separated pulses to form the discontinuous movement. It can be seen that each step variation measured by our method was clearer than commercial laser dimensional measuring system. Hence, the actual movement behavior of the stage could not easily observed by commercial laser interferometer. Then we made the stage movement continuous about 120 nm travel range and the results are presented in *FIGURE 3*. *FIGURE 4* represents the displacement response. The diffraction grating

was mounted on a piezoelectric actuator and moved in a sawtooth wave form. These results show that our method has subnanometer sensitivity. We also measured the long-trip in-plane displacement and these results are shown in *FIGURE 5*. The total displacements were about 250 μm and the difference between two measurement methods were 1.403 μm.

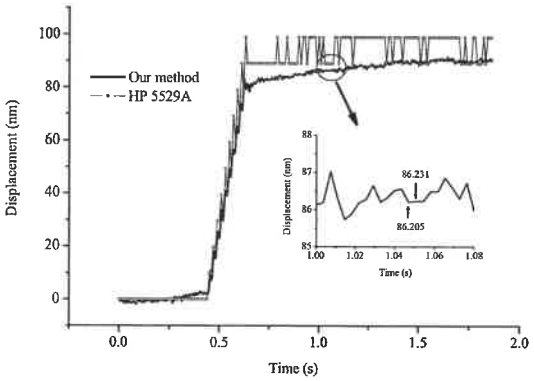

FIGURE 2. The results of the 1-D short-range displacement with 10 discontinuous pulses.

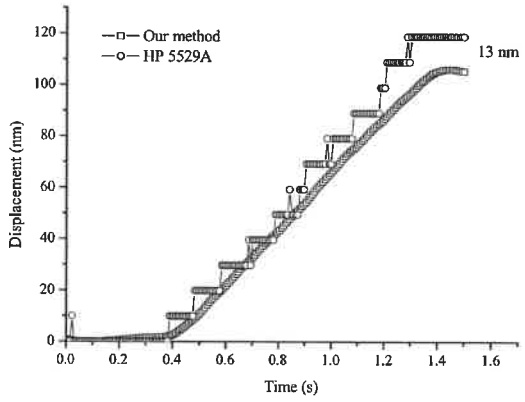

FIGURE 3. The results of 120 nm travel range with continuous movement.

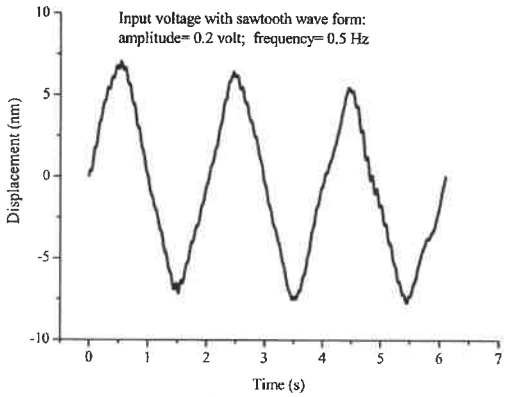

FIGURE 4 The displacement response of a piezoelectric actuator to the input voltage of sawtooth wave form.

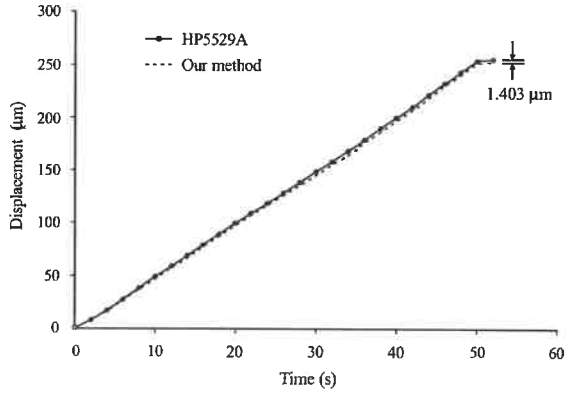

FIGURE 5. The results of the llong-range displacement at the continuous movement of 250 μm.

DISSCUSSION

According to Eq (2), when the phase resolution with 0.001° is considered, the sensitivities are roughly 0.4 pm, 0.7 pm, and 1.1 pm, respectively. It is obvious that the smaller the grating pitch we used, the higher the sensitivity our method achieved. Hence, these theoretical predictions may explain the legitimacy of our measurement results shown in *FIGURE 3*. The phase fluctuation may come from the electrical noise, environment vibration, and the air stream turbulence. The phase fluctuation could be maintained less than 1 degree under well-controlled conditions, such as the active-isolated table, electric isolation system, and the shelter. On the other hand, the smaller grating pitch we used, the lower fluctuation effect of our method can be considered. Therefore, our method may accomplish the pico-meter sensitivity in well-controlled environment by using the commercial grating with micrometer scale of grating pitch. We also consider the system resolution based on the derived theory in prior article [9]. The system resolution will be better than 0.2 nm.

In *FIGURE 2*, the movement behavior of the stage can be observed easily in our measurement results. Clearly, the movements of the stage were move back first and then move forward pulse by pulse. And this situation also found in the *FIGURE 3* which the stage moved continuously. This effect might be caused by reasons such as the expansion and shrinkage of the PZT actuator, driving properties of the motorized stage, and the mechanism structure of the motorized stage. In addition, the fluctuation at the start and the vicinity of the target position caused from total effects on the electronics noise of driven circuit of the motorized stage,

thermal effects coming from the friction of the jaws and screw, and internal noise and software of the HP 5529A. Hence, the response curves are shown tiny difference between them in *FIGURE 2* and *FIGURE 3*. As it can be seen, the quantity of this effect is in nanometer scale or pico-meter scale. That will be a serious problem in ultra-precision positioning. Hence, further experiments are still ongoing to figure out the dominant reason for this effect. Because of the coordinate systems of the motorized stage, commercial apparatus, and the diffracted grating might be not coincidence. The movement directions of these three elements might be different slightly and that will be enlarged as the movement increases. Hence, proper alignment of them will level down the difference of the measurement results by these two measurement methods.

From Wu's analyzes [10], the corresponding maximum error of our method due to the polarization mixing is with a few nanometers for each cycle. The maximum error due to the thermal expansion is about 0.14 nm. And the high frequency noise level due to the electronics is about 0.1 nm. Besides, the misaligned angle between the grating moving axis and the measuring direction is easily near 1°, its corresponding cosine error is about micron scale. Thus we infer that the major cause to the discrepancy in the *FIGURE 2* to *FIGURE 5*. Proper alignment could minimize the discrepancies in the results of our method and HP 5529A.

CONCLUSION

In this paper, we demonstrate 1-D displacement measurement results accomplished with single interferometer. Based on the optical configuration and heterodyne interferometry, this method has some advantages, such as high stability, high resolution, and small uncertainty. From the measurement results, there are no significant differences in displacement measurement between our method and the comparison instrument. And the smallest displacement variation that can be identified is about 6 pm. Moreover, the uncertainty and the sensitivity of our method are better than 5 nm and 1.5 pm, respectively. To compare the theoretical and actual measured results, it was anticipated that the pico-meter resolution might be actualized in our method. These findings lead us to believe that our method can be applied to ultra-precision positioning in controlling the motorized stage movement.

REFERENCES

[1] Wu W.J., Lee C.K., Hsieh C.T. Signal Processing Algorithm For Doppler Effect Based Nanometer Positioning System, Jpn. J. Appl. Phys. 1999; 38: 1725-1729.

[2] Demarest F.C. High-resolution, High-speed, Low Data Age Uncertainty Heterodyne Displacement Measuring Interferometer Electronics, Meas. Sci. Technol. 1998; 9: 1024-1030.

[3] Wu C.M. Heterodyne Interferometer System with Subnanometer Accuracy For Measurement Of Straightness, Appl. Opt. 2004; 43(19): 3812-3816.

[4] Dobosz M. High-resolution Laser Linear Encoder With Numerical Error Compensation, Opt. Eng. 1999; 38: 968- 973.

[5] Jourlin Y., Jay J., Parriaux O. Compact Diffractive Interferometric Displacement Sensor In Reflection, Prec. Eng. 2002; 26: 1-6.

[6] Salbut L. Waveguide Grating (moiré) Microinterferometer For In-plane Displacement/Strain Field Investigation, Opt. Eng. 2002; 41: 626-631.

[7] Chiu M.H., Lee J.Y., Su D.C. Complex Refractive-index Measurement Based on Fresnel's Equations And The Uses Of Heterodyne Interferometry, Appl. Opt. 1999; 38: 4047-4052.

[8] User's guide, Intelligent Picomotor Control Modules: Driver, Controllers, I/O Modules, Joystick, and Hand Terminal, New Focus.

[9] Misumi I., Gonda S. Kurosawa T. Takamasu K., Uncertainty in Pitch Measurement of One-dimensional Grating Standards Using A Nanometrological Atomic Force Microscope, Meas. Sci. Technol. 2003; 14: 463-471.

[10] Wu C M, Lawall J, Deslattes R.D. Heterodyne Interferometer with Subatomic Periodic Nonlinearity," Appl. Opt. 1999; 38: 4089-4094.

PRECISION GRINDING OF SILICON

Mohamed Konneh, and Alao Abdur-Rasheed
Manufacturing and Materials Engineering Department
International Islamic University, Malaysia
P. O. Box 10, 50728 Kuala Lumpur, Malaysia

INTRODUCTION

Silicon constitutes 90% of all semiconductors and it is an important material for making devices in electronics, semi-conducting and optical industries. It is used as optical components in high-resolution thermal imaging systems and also finds applications in micro-electro mechanical systems (MEMS) [1]. Close tolerance and good finishes on the substrate material are essential requirements for these applications. Hence a good finishing technique is required. Nevertheless silicon being a typical hard and brittle material is difficult to machine to a good surface finish. Ductile-mode machining (DMM) is often employed to machine hard and brittle materials. This is a machining technique whereby a brittle material when machined, behaves like a ductile material.

Concerted efforts of researchers [1-6] have shown successes in near 100% ductile machining of hard and brittle materials but using expensive ultra-precision machine tools. Blackley and Scattergood [7] developed an analytical model for single point diamond grinding (SPDT) to explain DMM condition and Kőnig and Sinhoff [8] laid emphasis on grains depth of cut (DOC) as critical a factor for ultra-precision grinding for achieving DMM condition. Obtaining nanometer order surface roughness and minimal subsurface damage is possible with DMM. However the high cost of ultra-precision machines limits exploiting 100% ductile machining concept. Some researchers [9-10] have used a machining technique termed partial-ductile mode machining (PDMM) to machine brittle materials like silicon, germanium and glass using inexpensive conventional CNC machine tools. PDMM assumes machining conditions that generate surfaces between fully fractured and 100% ductile-streaked surfaces.

This paper reports precise partial-ductile grinding of mono-crystalline silicon using an inexpensive NC milling machine. The issues discussed here are ductile streaks and surface roughness parameter. The results are quite satisfactory.

EXPERIMENTAL DETAILS

Work and tools materials

The workpiece materials that were precision ground are mono-crystalline silicon samples precision cut into dimension 15x15x6mm. Tool materials are 5-6mm diameter WINTER (Figure 1) made resin bonded diamond grinding wheels.

FIGURE 1. The grinding pin used in this experiment. Specifications 1A1 W-5-6 D64 K-888 RY C100.

Experimental equipment and instruments

The equipment and instruments that were used for the experimental trials include.

- A 5-axis DMU 35M DECKEL MAHO NC milling with Motor horsepower: 45Kw; Work spindle speed, directly programmable; 5-6300rpm; Linear traverse measuring system resolution, 1µm and coolant flow rate 0-7l/min.
- Ultra-precision High Speed Jig Grinder (NSK PLANET 850), max speed 100,000rpm
- Mitutoyo Surftest (SV-514)
- Jeol (JSM-5600) Scanning Electron Microscope (SEM).

Grinding and the response variables and the experimental designs

Three grinding parameters, viz., DOC (*a*), feed rate (*f*) and spindle speed (*n*) were identified and the responses were the average roughness (R_a) and ductile streaks. The grinding parameters and their levels are shown in Table 1. Both 3-level factorials and the Box-Behnken designs

were used in this study. 3-level factorials were used to study the relationship between the grinding parameters and the response (R_a). They were used also to know the conditions that gave massive ductile surfaces on ground silicon surfaces. Box-Behnken design was used to model the surface roughness (R_a) in terms of the grinding parameters.

TABLE 1. Grinding parameters and their levels.

Grinding parameters	symbols	Levels		
		Low	Middle	High
DOC (μm)	*a*	5	12.5	20
Feed rate (mm/min)	*f*	2.5	6.25	10
Spindle speed (rpm)	*n*	70,000	80,000	90,000

Experimental setup and procedure

Precision grinding experiments were carried out on the vertical 5-axis NC milling whose spindle was upgraded by attaching an ultra-precision high speed jig grinder (Planet 850) to enhance the spindle speed (Figure 2). Pre-grinding was done on each silicon sample to ensure flatness of the workpiece before carrying out any precision grinding trials. Holes drilled in the grinding pin centers by ultrasonic technique prevented zero velocity. Coolant flow rate was maintained at 7litres/min to remove stalling and dragging marks. Before trying out a new grinding condition, a grinding pin was dressed on an alumina dressing stick (Figure 2). After machining trials, surface roughness (R_a) was measured, on a Mitutoyo Surftest (SV-514), using 0.25mm cut-off length and the average reading noted.

RESULTS AND DISCUSSION

3-level full factorials

Table 2 shows the 3 level full factorials and the response R_a. From this table, it can be seen that the highest roughness R_a (150nm)was obtained at condition DOC 5μm, feed rate 10mm/min and spindle speed 80,000rpm (i.e trial 24). This condition also gave fully fractured surface (Figure 3a) while the lowest surface roughness with R_a value of 43nm was found at the condition DOC 20μm, feed rate 6.25mm/min and 70,000rpm (expt. trial 9). This condition also gave the largest amount of ductile streaks. Figure 3 (a-c) depicts the SEM micrographs of a fully fractured surface, partial-ductile streaked surface with deep micro-cracks and abundant ductile streaks with little micro-fracture.

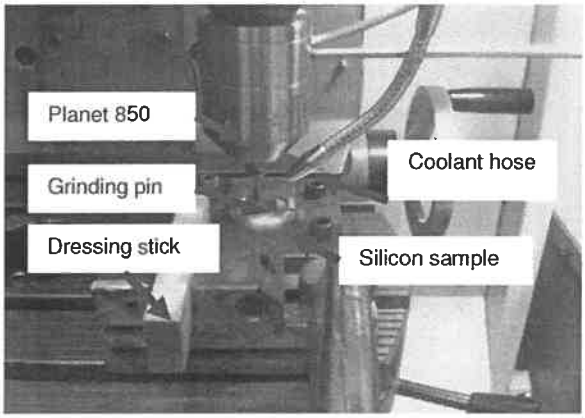

FIGURE 2. The experimental set-up showing a high-speed jig grinder unit attached on NC vertical milling spindle and the Al_2O_3 abrasive stick (grade Nr.2).

TABLE 2. 3-level full factorial experiments conducted with diamond pin of grit size 64μm and the response (R_a).

Expt trials	Controllable factors			Response
	DOC: *a* (μm)	Feed rate: *f* (mm/min)	Spindle speed: *n* (rpm)	R_a (μm)
1	5.0	2.50	80,000	0.093
2	5.0	6.25	70,000	0.057
3	5.0	2.50	90,000	0.090
4	12.5	6.25	70,000	0.063
5	20.0	2.50	90,000	0.105
6	12.5	6.25	90,000	0.060
7	20.0	10.00	90,000	0.078
8	20.0	2.50	80,000	0.100
9	20.0	6.25	70,000	0.043
10	20.0	6.25	90,000	0.070
11	5.0	6.25	90,000	0.087
12	20.0	2.50	70,000	0.065
13	12.5	10.00	90,000	0.080
14	12.5	2.50	80,000	0.047
15	12.5	10.00	80,000	0.080
16	12.5	6.25	80,000	0.107
17	5.0	10.00	90,000	0.115
18	20.0	10.00	80,000	0.105
19	12.5	2.50	90,000	0.057
20	5.0	6.25	80,000	0.057
21	12.5	10.00	70,000	0.060
22	20.0	10.00	70,000	0.093
23	12.5	2.50	70,000	0.047
24	5.0	10.00	80,000	0.150
25	5.0	10.00	70,000	0.060
26	20.0	6.25	80,000	0.083
27	5.0	2.50	70,000	0.063

Main and interactive effects of controllable factors

The main effects plots of DOC, feed rate and spindle speed are shown in Figures 4 (a – c) below.

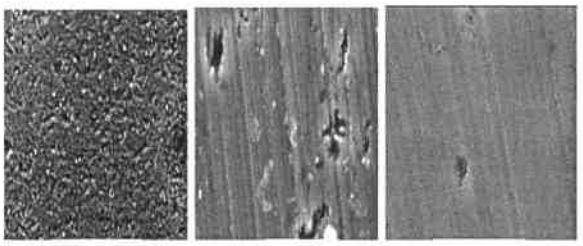

(a) (b) (c)

FIGURE 3. SEM images of ground silicon surface showing (a) fully fractured surface DOC 5µm, feed rate 10mm/min, speed 80,000rpm, (b) massive ductile surface with deep micro-cracks; DOC 20µm, feed rate 6.25mm/min and speed 90,000rpm, (c)abundant ductile streaks with little fracture; DOC 20µm, feed rate 6.25mm/min and speed 70,000rpm.

From the figures, it is shown that DOC, feed rate and spindle speed have non-linear effects on the surface roughness (R_a). The reason for this phenomenon is due to the interaction between the controllable parameters used in the study. Another reason is the second order model developed for R_a in terms of the controllable parameters. Figure 5 shows the DOC- feed rate interaction effect on R_a at spindle speed of 80,000rpm. As can be seen on this figure, there exists strong interaction between DOC and feed rate. This would make the corresponding main effects of DOC and feed rate on R_a to have very little practical meaning. The implication of this is that at 80,000rpm, the effect of DOC on R_a depends on the levels of feed rate.

Box-Behnken experimental result

The mathematical model relating the response variable (R_a) and the grinding parameters is represented by

$$R_a = \phi(a, f, n) \qquad (1)$$

where R_a is the surface roughness, Φ the response function, *a* the DOC, *f*, the feed rate and *n* the spindle speed. In this study Box-Behnken experimental design with three center points was used. Table 3 shows the experimental design based on Box-Behnken and the result obtained for surface roughness (R_a). Second order model was observed to the most suitable to relate surface roughness and the grinding parameters. The procedure for establishing second order model has been well detailed out in Alao's work [11]. The model equation 2 has been developed based on the results obtained in this work.

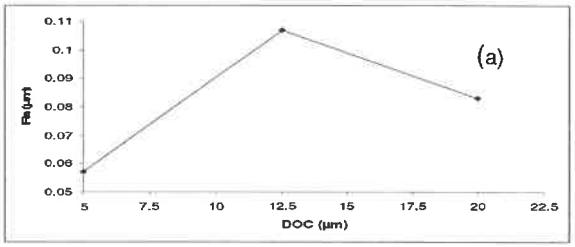

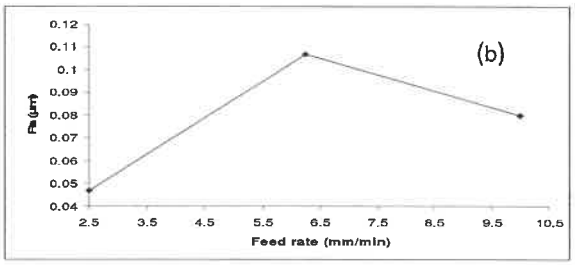

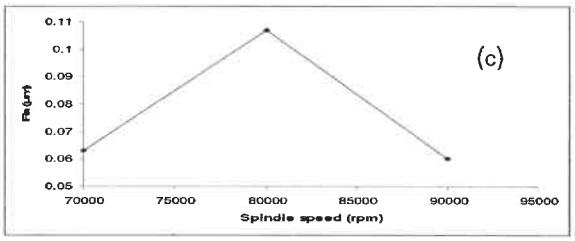

FIGURE 4 (a - c). Main effect plota for surface roughness R_a with (a) DOC, (b) Feed rate and (c) spindle speed.

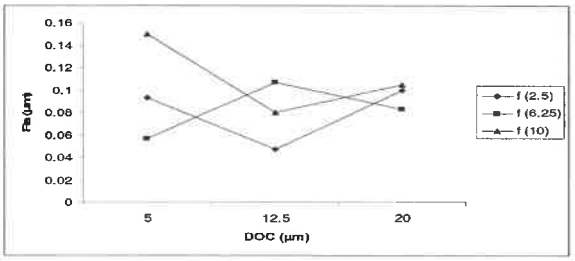

FIGURE 5. Interactive effect of DOC and feed rate on surface roughness R_a.

$$R_a = -3.04 + 1.74\times10^{3}a + 9.0\times10^{3}.f + 7.7\times10^{5}n - 4.6\times10^{4}a\times f - 4.7\times10^{9}n^{2} \qquad (2)$$

Verification of the adequacy of the model is shown in the ANOVA Table 4. The Model F-value of 72.6 implies the model is significant. There is only a 0.01% chance that a "Model F-value" this large could occur due to noise. The adjusted R^2 which is a better statistic than R^2 is found to be 96.24%.

CONCLUSIONS

It has been found in this study that by proper setting of the grinding conditions massive ductile streaks can be achieved on precision ground surfaces of hard and brittle materials. Ductile-streaked surface is desirable to reduce polishing time and improve the surface quality. In this investigation surface roughness as low as 43nm has been obtained. It has also been found that the main effects of all the grinding parameters on surface roughness used in this study exhibit non-linear relationship. Strong interaction was found to exist between DOC and feed rate. Second order model has been established for the roughness in terms of the grinding parameters. The model is capable of navigating the design space.

TABLE 3. Box-Behnken design and the result.

Expt. trial	Controllable factors			Response
	DOC: *a* (μm)	Feed rate: *f* (mm/min)	Spindle speed: n (rpm)	R_a (μm)
1	12.5	2.50	70,000	0.047
2	20.0	6.25	70,000	0.043
3	5.00	2.50	80,000	0.093
4	5.00	6.25	70,000	0.057
5	20.0	6.25	90,000	0.070
6	12.5	6.25	80,000	0.107
7	12.5	10.00	70,000	0.060
8	12.5	2.50	90,000	0.057
9	12.5	6.25	80,000	0.110
10	20.0	2.50	80,000	0.100
11	12.5	10.00	90,000	0.080
12	5.00	10.00	80,000	0.150
13	12.5	6.25	80,000	0.104
14	5.00	6.25	90,000	0.087
15	20.0	10.00	80,000	0.105

TABLE 4. ANOVA table for the R_a model.

Source	Sum of squares	df	Mean square	F val.	P val.
Model	0.012	5	0.0024	72.6	<0.0001
a	0.0006	1	0.0006	18.4	0.002
f	0.0012	1	0.0012	37.1	0.0002
n	0.0009	1	0.0009	29.3	0.0004
af	0.0007	1	0.0007	20.9	0.0013
n^2	0.00833	1	0.0083	258	0.0001
Residuals	0.0003	9	0.0000	-	-
Lack of fit	0.0003	7	0.0000	4.33	0.2003
Pure error	0.00002	2	0.0000	-	-
Cor Total	0.012	14		-	-

ACKNOWLEDGEMENT

The authors are grateful to the Research Management Center of International Islamic University Malaysia for their financial support.

REFERENCES

[1] Fang F Z, Venkatesh V C. Diamond Cutting of Silicon with Nanometric Finish. Annals of CIRP- Manufacturing Technology. 1998; 47(1): 45-49.

[2] Shibata T, Fujii S, Makino E, Ideda M. Ductile-Regime Turning Mechanism of Single-Crystal Silicon. Journal of Precision Engineering. 1996; 18: 129-137.

[3] Venkatesh V C, Fang F, Chee W K. On Mirror Surfaces with and without Polishing. Annals of CIRP- Manufacturing Technology. 1997; 46(1): 505-508.

[4] Bandyopadhyay B P, Ohmori H, Takahashi L. Ductile Regime Finish Grinding of Ceramics with Electrolytic In-Process Dressing (ELID) Grinding. International Journal of Material Manufacturing Process 1996; 11: 789-801.

[5] Fujihara K, Ohshiba K, Komatsu T, Ueno M, Ohmori H, Bandyopadhyay B P. Precision Surface Grinding Characteristics of Ceramic Matrix Composites and Structural Ceramics with ELID. Journal of Machining Science Technology. 1997; 1: 81-94.

[6] Zhang B, Yang F, Wang J, Zhu Z, Monahan, R. Stock Removal Rate and Workpiece Strength in Multi-pass Grinding of Ceramics. Journal of Material Process Technology. 2000; 104: 178-184.

[7] Blackley W S, Scattergood R O. Ductile-Regime Machining Model for Diamond Turning of Brittle Materials. Journal of Precision Engineering. 1991; 13(2): 95-102.

[8] Konig W, Sinhoff V. Ductile grinding of Ultra-precise aspherical optical lenses. SPIE, Lens and Optical Systems Design. 1992; 1780: 778-788.

[9] Zhong Z W. Ductile or Partial Ductile Mode Machining of Brittle Materials. The International Journal of Advanced Manufacturing Technology. 2003; 579-585.

[10] Venkatesh V C, Izman S, Sharif S, Mon T T, Konneh M. Ductile Streaks in Precision Grinding of Hard and brittle Materials. Sadhana. 2003; 28 (5): 915-924.

[11] Alao A R. Precision Micro-scaled Partial Ductile Mode Machining of Silicon. MSc Thesis, International Islamic University, Malaysia. 2007.

DICING PROCESS FOR THE DEVICE SEPARATION OF A SLIDER WITH AN INTEGRATED MICROACTUATOR (SLIM)

S. Cvetkovic, H. Saalfeld, and H.H. Gatzen
Institute for Microtechnology
Center for Production Technology
Leibniz Universität Hannover
Garbsen, Lower Saxony, Germany

ABSTRACT

A Micro Electro-mechanical Systems (MEMS) type Slider with an Integrated Microactuator (SLIM) is capable of moving the read-write element both in vertical direction (adjusting the flying height) and in lateral direction (allowing second stage actuation). Developing this system not only poses substantial challenges in the area of wafer processes, but also in mechanical micromachining for separating the parts. The main challenge is to release a mounting block without breaking the delicate Si leaf springs it is suspended on. This paper describes the process development for separating Si stacks with parts suspended on delicate solid state joints, ultimately intended for being applied to machining the SLIM device. It presents the slicing and dicing experiments conducted and outlines the results.

INTRODUCTION

To increase the recording density of Hard Disc Drives (HDD), a second stage actuator may be integrated in the read/write head to accomplish more accurate and higher frequency track following than possible with existing actuators [1, 2]. One cost competitive approach to achieve this goal is implementing a Slider with an Integrated Microactuator (SLIM) as shown in Fig. 1 [3].

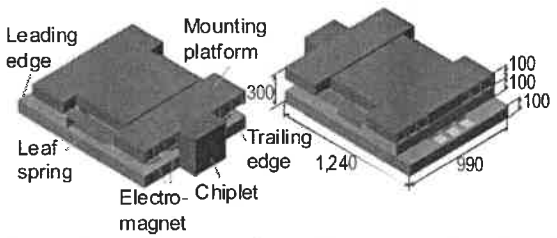

FIGURE 1. Slider with an Integrated Microactuator (SLIM)

An integrated microactuator activates a mounting block to which a chiplet containing the read-write element is attached. The actuator is capable of moving the read-write element on the chiplet both in vertical direction (adjusting the flying height) and in lateral direction (allowing second stage actuation). The mounting block is suspended by a pair of Si leaf springs.

The SLIM is fabricated on two separate wafers. The actuator micro magnetics are located in the bottom part of the device and consist of a pair of active parts. The actuator micro mechanics on top of the micro magnetics part include (1) a base, (2) an actuated mounting platform to which the read/write element (residing on a chiplet) will be mounted, and (3) a pair of Si leaf springs connecting both. A spacer joins the bottom and the top. Each of the three pieces (bottom, top, and spacer) is 100 µm thick; therefore, the whole slider body is a 300 µm thick, stacked structure.

As already mentioned, the SLIM micro magnetics and micro mechanics are fabricated in two separate wafer processes. After their completion, both types of wafers are separated into double row bars. A double row bar consists of two rows of ten slider each, with the sliders joined at their leading edge. The dimensions of either one are 11.89 mm x 2.6 mm x 0.1 mm. The row bars with the mechanics feature anchors for the mounting block at either end. This is necessary for immobilizing the leaf springs until a final slider separation takes place.

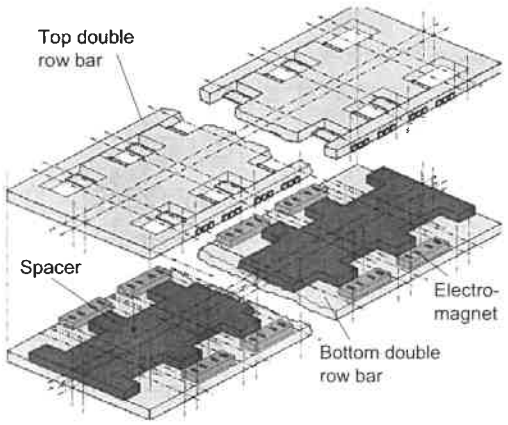

FIGURE 2. Double row bar level stacking (Step 1 and 2)

The fabrication process after dicing the two wafers is as follows. The micro magnetics and micro mechanics double row bars are joined by stacking them with a spacer sandwiched in between (Step 1). After the stacking, the chiplets are attached (Step 2) (Fig. 2). Next, the contact pads at the SLIM leading edges are released by slicing the top of the stacked double row bars (Step 3) (Fig. 3a). After this process step, the double row bar is debonded and remounted topside down. A slicing cut through the double row bar's bottom causes a separation into single row bars (Step 4) (Fig. 3b). However, no debonding occurs at this stage. For separating the sliders, the row bars are sliced (Step 5) (Fig. 3c). A further debonding process releases the single SLIM elements (Step 6). The final two steps are particularly sensitive, since they release the mounting block suspended by the delicate Si leaf springs.

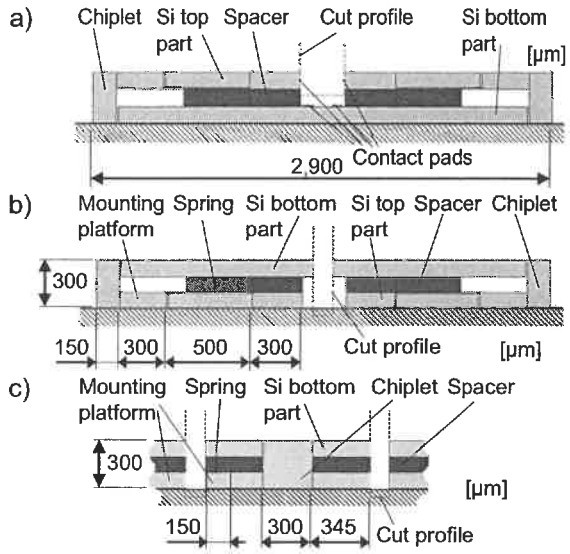

FIGURE 3. Double row bar machining. a) Cut for releasing the contact pads (Step 3); b) Cross cut for creating single row bars (Step 4); and c) dicing cut for slider release (Step 5)

This device poses some interesting machining challenges typical for stacked MEMS devices with cantilever suspended parts released by a dicing process. Besides machining stacked devices without excessive chipping, parts suspended on delicate cantilevers are released by the machining step. This requires a sufficient adhesion of the part during machining, as well as a gentle debonding process to avoid breakage of the delicate cantilevers while the parts are released. The purpose of this paper is to investigate these machining challenges.

EXPERIMENTAL

Starting point for the Si machining tests were studies performed previously [4, 5]. Si can be diced rather easily since it is subject to a metal transition under the pressure conditions occurring during the dicing [6].

Cutting Parameters

Table 1 presents the cutting parameters applied. For the dicing process, four types of dicing wheels were utilized: one with a Ni and the other three with bronze binders of three different hardnesses. The feed rate was varied, and the influence of the coolant supply on both the adhesion of the samples and the integrity on the cantilevers was observed. All parameter combinations were investigated; for each combination, three cuts were made.

TABLE 1. Dicing parameters

Feed rate [mm/min]	1	5	10	-
Binder type	Ni hard	Bronze hard	Bronze medium hard	Bronze soft
Wheel width [µm] (mounting block size)	15	45	100	-
Wheel width [µm] (row bar machining)	100			
Grit size [µm]	4-6			

Dicing was done using a DAC551 dicing machine with a positional accuracy of 0.2 µm and a spindle speed of 30,000 RPM, located in an air conditioned room.

Table 2 provides an overview over the bonding tapes used. Three bonding tapes, differing in the respective adhesive force, were evaluated: a standard "blue tape", a UV-release tape, and thermo-release tape.

TABLE 2. Dicing tape parameters

Dicing tape	Thickness [µm]	Adhesive strength [N/20 mm]	
		Nominal	Releasing
Nitto SWT 20+ (blue tape)	65	0.70	
Nitto UE-111 AJ (UV-tape)	110	8.33	0.20
REXPAN RP3 (thermo-release tape)	211	5.80	0

Mounting Block Size Investigations

Bond issues typically affect the MEMS design, therefore they have to be taken into account appropriately. In our case, the minimal required contact area of the mounting block had to be determined. For avoiding a parts tear-off, the following conditions have to be met: the forces the mounting block is subjected to during the machining process have to be smaller than the adhesive forces exerted by the bonding tape the slider is mounted on. The cutting force exerted is a function of the substrate thickness, the wheel width, and the general cutting parameters. These forces have to be counterbalanced by the tape adhesive force, which is dependent on the tape type and the contact area. Therefore, as a part of a MEMS design process, investigations regarding the contact area required for a save bond have to be conducted.

Double Row Bar Separation Investigations

For simulating MEMS stacks, stacked Si test structures were used (Fig. 4). Two types of Si stacks were applied. Type 1 was a double stack as found in double row bar slicing. Type 2 was a triple stack to simulate slider separation (Step 5).

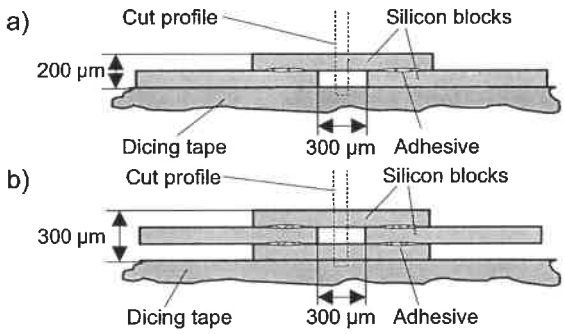

FIGURE 4. Si stacks used in the investigations. a) Si stack to simulate double row bar separation (Type 1); b) Si stack to simulate slider separation (Type 2)

RESULTS

Mounting Block Size Investigations

Table 3 presents the results for the adhesion tests. The test results are shown for two test block footprints: 300 µm x 300 µm and 100 µm x 100 µm. Tests were considered successful (A), if all blocks were still found on the tape after dicing. Tests were considered partly successful (B) if at least 50% of the blocks remained on the tape. Tests failed (C), if less then 50% of the blocks remained on the tape.

TABLE 3. Adhesion results for various blocks

Block footprint [µm]		300 x 300								
Block thickness [µm]		100			300			525		
Wheel width [µm]		15	45	100	15	45	100	15	45	100
Dicing tape	Blue	A	A	B	A	B	B	-	B	B
	UV	A	A	A	A	A	A	-	A	B
	Thermo	A	A	A	A	A	A	-	A	B
Block footprint [µm]		100 x 100								
Block thickness [µm]		100			300			525		
Wheel width [µm]		15	45	100	15	45	100	15	45	100
Dicing tape	Blue	A	B	C	B	B	C	-	B	C
	UV	A	A	B	A	A	B	-	A	B
	Thermo	A	A	B	A	A	B	-	A	B
A: successful; B: partly-successful; C: failed										

The effect of the coolant supply was investigated by covering the substrate with a blue tape. The number of retained parts could thus be enhanced by 10 to 20%.

After the completion of the test series, the actual desired shape of the mounting block was taken into consideration. The smallest block footprint that could be successfully diced was 500 µm x 100 µm (Fig. 5). The usage of UV or thermo-release tapes in combination with a wide wheel yielded the best results.

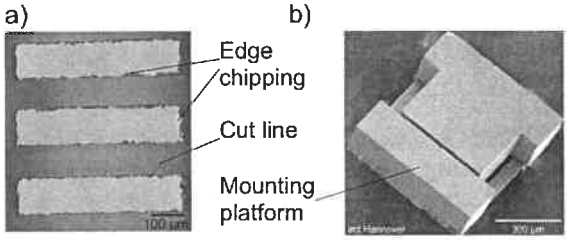

FIGURE 5. Mounting block size results. a) 500 µm x 100 µm blocks; b) 990 µm x 300 µm prototype of mounting platform

To assure that dicing and releasing the parts with free floating thin Si cantilever does not lead to the breakage (simulating Step 5); blocks featuring U-shaped cuts simulating delicate solid state joints were subjected to cutting tests. A thermo-release tape debonding at 140°C proved to be capable of releasing such delicate structures.

Double Row Bar Separation Investigations

Figure 6 depicts the results for the maximal edge chipping, while Fig. 7 shows the achieved cut width. A minimal edge chipping, but also the highest sensitivity to the feed rate was observed using a dicing wheel with a soft bronze binder. The optimal cut width was achieved using the hardest Ni bonded wheel.

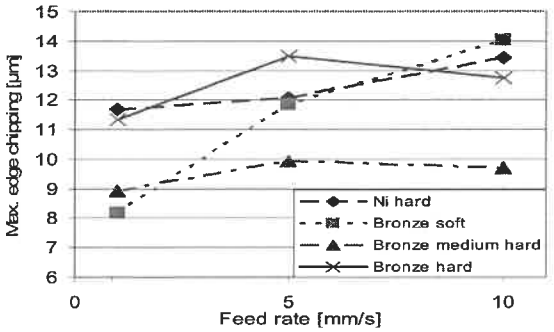

FIGURE 6. Dependence of feed rate and edge chipping for different dicing wheels

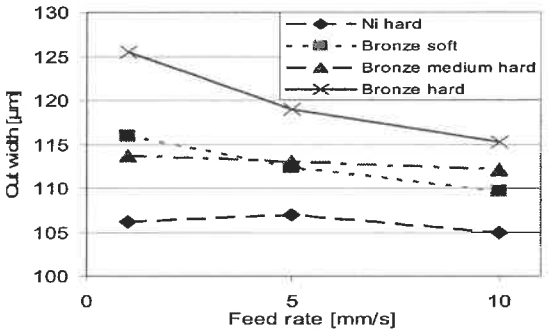

FIGURE 7. Dependence of feed rate and cut width for different dicing wheels

These results indicate that the lowest edge chipping can be achieved using wheels with a soft bond and a low feed rate. On the other hand, wheels with a hard bond are capable of achieving a minimal cut width and are less sensible in regard to the feed rate.

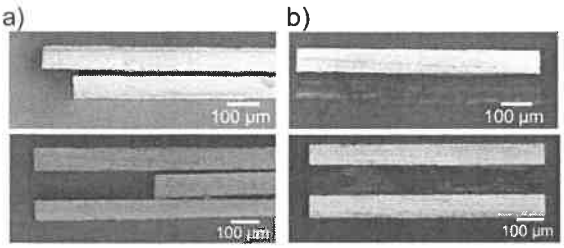

FIGURE 8. Diced and released stacked Si structures: a) side and b) front view

The next task was to find optimal parameters to dice and separate the parts simulating Steps 4 and 5. Using UV and thermo-release tapes, a coolant supply cover and a wheel with 45 µm width as well as a feed rate of 5 mm/s all of the stacked structures could be diced and released from the tape (Fig. 8). All chipping was below critical values, thus not jeopardizing the functionality of the parts (Fig 9).

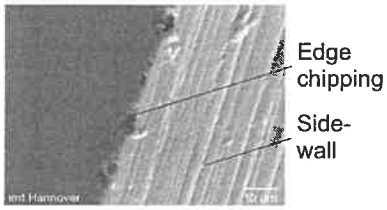

FIGURE 9. SEM-micrograph of edge chipping:

CONCLUSIONS AND OUTLOOK

One particular machining challenge is to separate MEMS stacks, especially if the separation cut includes releasing component parts suspended on delicate cantilevers. With optimal dicing parameters, Si stacks could be diced successfully. A non-destructive debonding of solid state joints could be achieved by using a thermo-release tape. Based on these investigations, a dicing process for stacked SLIM device will be developed and executed.

REFERENCES

[1] L.-S. Fan, et al. "Magnetic Recording Head Positioning at Very High Track Densities Using a Microactuator-Based, Two-stage Servo System", IEEE Trans. Industrial Electronics, 42(3), pp. 222-233, 1995

[2] Y. Lu, et al., „A Silicon Microactuator Using Integrated Microfabrication Technology", IEEE Trans. Mag., 39(5), pp. 2240-2242, 2003

[3] H.H. Gatzen, et al. A Slider with an Integrated Microactuator (SLIM) for Second Stage Actuation in Hard Disc Drives, Intermag, Madrid 2008, Accepted for IEEE Trans. on Magnetics

[4] M. Shikida, et al. Fabrication of Densely Arrayed Micro-Needles with Flow Channels by Mechanical Dicing and Anisotropic Wet Etching, J. Micromech. Microeng., Vol. 16, pp. 1740–1747, 2006

[5] H.H. Gatzen, S. Cvetkovic. Effect of Feed Rate and Grain Concentration on Ductile to Brittle Transition by Silicon Dicing, Proc. Euspen 7th Int. Conf. 2007, Bremen, Germany, Vol. 2, pp. 380-383, 2007

[6] J. Patten et al. Nanoindentation Tests on Diamond-machined Silicon Wafers, App. Phys. Lett. 86, pp. 181913-1-3, 2005

ULTRASONIC ASSISTED GRINDING OF BRITTLE MATERIALS – SURFACE TOPOGRAPHY AND PROCESS FORCES

Berend Denkena[1], Luis de Leon[1], Dennis Hahmann[1]
[1]Institute of Production Engineering and Machine Tools
Leibniz Universität Hannover
Garbsen, Germany

INTRODUCTION

The micromachining of hard and brittle functional components provides high surface qualities and geometrical accuracy. These requirements can only be met by using a grinding process. There are several grinding processes, like peripheral surface grinding [1], peripheral surface grinding with tilted tool [2], ultrasonic assisted peripheral surface grinding [3,4] and reciprocating face grinding [5]. All of them provide different workpiece surface topographies, even if the same grinding wheel or rather the same grain size and grain concentration are applied. Three different peripheral surface grinding processes have been investigated; the results are presented in this paper. A focus is put on ultrasonic assisted peripheral surface grinding. For this purpose, the analyzed peripheral surface grinding processes are performed without and with an ultrasonic assistance of 22 kHz. Furthermore, investigations with a tilted grinding wheel are described. The angle of tilt is set at different levels between 0 and 40 degrees.

PERIPHERAL SURFACE GRINDING

It is known that in peripheral surface grinding, the surface finish is defined by the grinding tool topography and shape. A rough tool surface leads to a worse surface finish on the work piece than a smoother tool surface. Unevennesses of the grinding wheel profile are directly reproduced on the work piece. In reciprocating face grinding, the topography and shape of the work piece mainly depends on the process kinematics. But the contact area in this process is larger than in peripheral surface grinding. The contact area influences the mechanical and thermal load exerted on the work piece. On the one hand, a small contact area leads to lower process forces, which decreases the mechanical load applied on the work piece. On the other hand, a shorter contact length enhances flow of the coolant. Thus the thermal load of the work piece is reduced. One possibility for combining the advantages of both reciprocating face grinding and peripheral surface grinding in one process is to use peripheral surface grinding with a tilted tool. The kinematics of the peripheral surface grinding with tilted grinding wheel is illustrated in FIGURE 1.

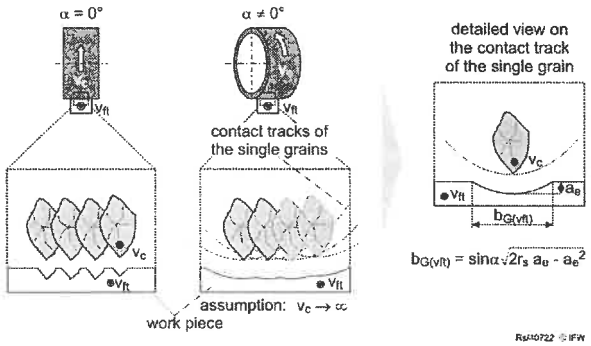
α = 0°
α ≠ 0°
detailed view on the contact track of the single grain
contact tracks of the single grains
assumption: $v_c \rightarrow \infty$
work piece
$b_{G(vft)} = \sin\alpha \sqrt{2r_s a_e - a_e^2}$

FIGURE 1. The effect of the tilt angle on the kinematics in peripheral surface grinding

Due to the tilting, the contact tracks of the single grains are not parallel to the feed rate. This causes an overlapping of the contact tracks. A geometrical analysis of the contact kinematics leads to the assumption that the surface finish improves with a rising tilt angle or diameter of the grinding wheel. This makes clear that the topography and the profile of the work piece mainly depend on the process kinematics. For simplifying the analysis, the elastic and plastic behavior of the material as well as system deflection are not taken into account. Experimental investigations are carried out to validate the theory.

As a set-up for the investigations, a cutting speed v_c of 30 m/s, a feed rate v_{ft} of 100 mm/min and a depth of cut a_e of 1 µm are used (FIGURE 2). The tilt angle between the cutting speed and the feed rate is set at different levels between 0° (peripheral surface grinding) and 40°. With a tilt angle of 0°, the average surface finish is R_a = 95 nm. A tilt angle of 10° already reduces the average surface finish to R_a = 35 nm. A further increase of the tilt angle to 40° reduces the average surface finish slightly

further to R_a = 21 nm. Further experimental investigation shows that this results cannot be transferred directly to lower depth of cut and higher feed rates.

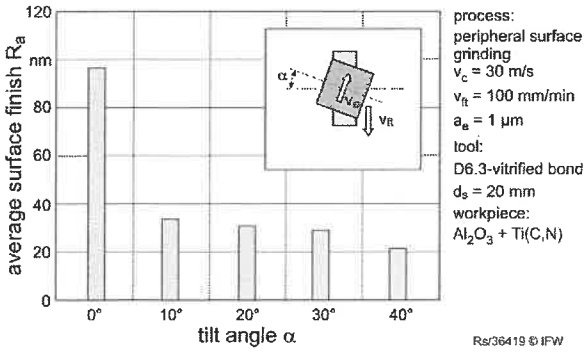

FIGURE 2. The effect of the tilt angle on the average surface finish in peripheral surface grinding

At higher tilt angles, the process becomes instable due to the small contact area at a low depth of cut. Discontinuous chip removal results in dynamic effects and a minor surface quality. In sum, the theory is supported by the experimental investigation. As expected, a tilting of the tool increases the surface quality. But with a low depth of cut and a high feed rate, some effects which have not been taken into account in the theory become more significant.

ULTRASONIC ASSISTED PERIPHERAL SURFACE GRINDING

Another possibility for decreasing the influence of the topography of the grinding tool on the work piece topography in peripheral surface grinding is using ultrasonic assistance. In ultrasonic assisted grinding, the kinematics of peripheral surface grinding are combined with a high frequency sinusoidal oscillation in the axial direction. The resulting speed vector oscillates around the feed direction. To get a first impression of the resulting work piece surface in a theoretical approach, the work piece related movement of a single grain is calculated. For simplification regarding the grain-work piece-contact, it is assumed that the grain penetrates the work piece surface when it reaches the lowest point of the grinding wheel. The work piece related movement of the grain shows that ultrasonic assistance leads to an overlapping of the different contact tracks. Furthermore, it shows that an increase of the cutting speed increases the overlapping of the contact tracks (FIGURE 3). Thus we can assume that a higher surface quality is attained by applying ultrasonic assistance. To proof this, experimental investigations are carried out.

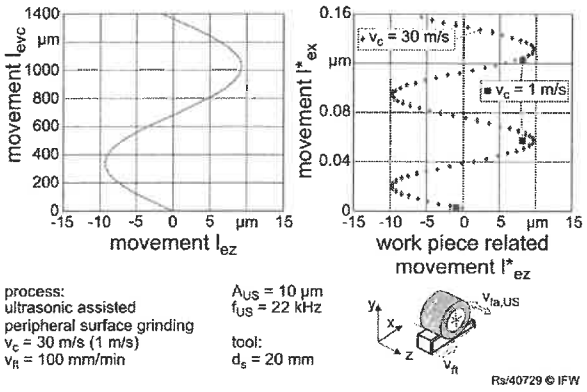

FIGURE 3. The contact point between work piece and tool in ultrasonic assisted grinding

The cutting speed is set to v_c = 30 m/s and the depth of cut to a_e = 0.1 µm. The feed rate is set at different levels between 50 mm/min and 200 mm/min. All experiments are carried out with and without ultrasonic assistance. As shown in FIGURE 4, the feed rate exerts no significant influence on the surface finish both in peripheral surface grinding and ultrasonic assisted grinding.

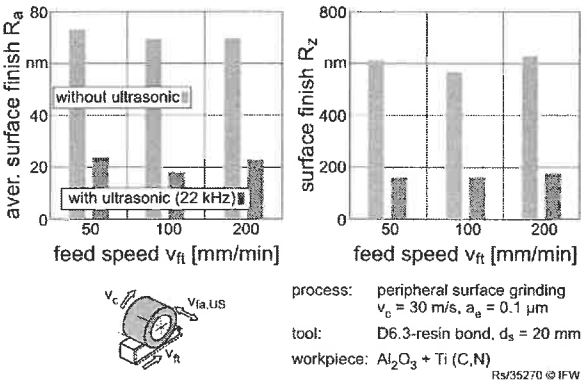
aver. surface finish R_a
surface finish R_z
without ultrasonic
with ultrasonic (22 kHz)
feed speed v_{ft} [mm/min]
process: peripheral surface grinding
v_c = 30 m/s, a_e = 0.1 µm
tool: D6.3-resin bond, d_s = 20 mm
workpiece: Al_2O_3 + Ti (C,N)
Rs/35270 © IFW

FIGURE 4. The effect of ultrasonic vibration on the surface finish in peripheral surface grinding

By peripheral surface grinding, an average surface finish of $R_a \approx 70$ nm, and by ultrasonic assisted grinding an average surface finish of $R_a \approx 20$ nm is attained. It is obvious that ultrasonic assistance has a very significant influence on the surface finish. The roughness is reduced by the factor 3-4 when using ultrasonic assistance. The average surface finish attained by ultrasonic assisted grinding is similar to the roughness which is attained with a tilted grinding

tool. The surfaces of the work pieces were measured 2-dimensionally with an atomic force microscope (AFM) (FIGURE 5).

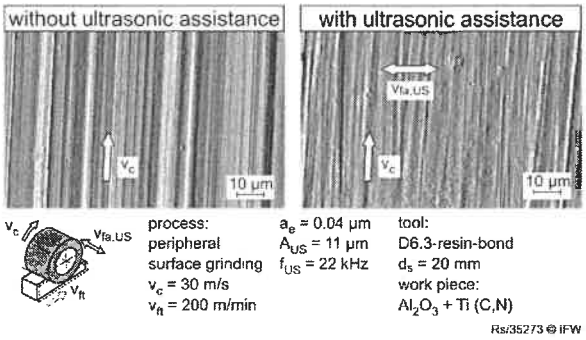

FIGURE 5. Ground surface after peripheral surface grinding and ultrasonic assisted grinding

The effect of ultrasonic assistance is obvious. The grinding grooves which result from peripheral surface grinding without ultrasonic assistance are parallel to the cutting direction and clearly separated from each other. Using ultrasonic assistance, the shape of the grinding grooves is more indistinct. Furthermore, the contact tracks lie at different angles to the cutting direction. The lower roughness and the unparallel contact tracks attained by ultrasonic assisted grinding can be explained by the work piece related movement of the single grain described above.

COMPARISON OF THE GRINDING PROCESSES

In the following, the investigated approaches to enhance the work piece surface quality are directly compared with the results attained by peripheral surface grinding and reciprocating face grinding. Peripheral surface grinding is used as reference. Due to the process kinematics, the shape and topography of the grinding wheel are reproduced on the work piece surface. Both peripheral surface grinding with a tilted grinding wheel and ultrasonic assisted grinding decrease the influence of the tool topography on the work piece surface. This is illustrated by a comparison of the different process results in AFM pictures of the machined work piece surface (FIGURE 6).

It is obvious that the topography of the surface is process-specific. Peripheral surface grinding is characterized by long and straight grinding grooves in the feed direction. After peripheral surface grinding with a tilted grinding wheel, the grinding grooves are in the direction of the tilt angle. Ultrasonic assisted grinding is characterized by overlapped grinding grooves which result from the overlapping of the contact tracks of the single grains.

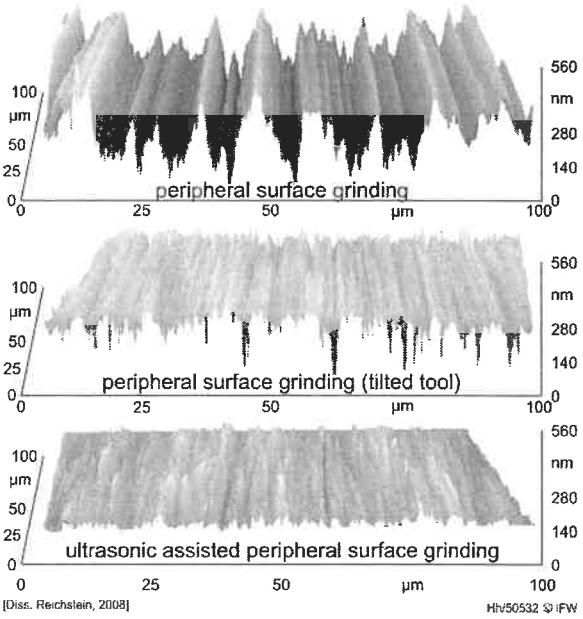
peripheral surface grinding
peripheral surface grinding (tilted tool)
ultrasonic assisted peripheral surface grinding
100 µm 50 25 0
560 nm 280 140 0
0 25 50 µm 100
[Diss. Reichstein, 2008]
Hh/50532 © IFW

FIGURE 6. Ground surface after grinding with tilted, untilted tool und ultrasonic assisted tool

PROCESS FORCES IN ULTRASONIC ASSISTED GRINDING

Beside the surface quality, the process forces play an important role. High mechanical loads during the machining process can especially damage or even destroy small work pieces. It can be assumed that ultrasonic assistance decreases the process forces. A first investigation of the ultrasonic assisted grinding process shows that the minimum achievable workpiece thickness without any breakouts is about three times lower than the thickness attainable by grinding processes without ultrasonic assistance [4]. Commonly used dynamometers are too slow for measuring the dynamic process forces in ultrasonic assisted grinding. Thus a highly dynamical force sensor was used (FIGURE 7).

The investigations are carried out with a cutting speed v_c = 1.88 m/s, a depth of cut a_e = 200 µm and a feed rate v_f = 2.5 mm/min. The frequency of the ultrasonic assistance is 21.5 kHz and the amplitude is set to A_{US} = 10 µm. The force diagrams for the conventional and the ultrasonic assisted grinding processes show significant differences regarding both the absolute force F_n as well as the effective force F_{nRMS} (FIGURE 7).

The absolute forces are up to two times lower in conventional grinding. The detailed force diagram shows that the tool periodically looses contact to the work piece in ultrasonic assisted grinding. This means that material removal only takes place during a half cycle of the ultrasonic vibration.

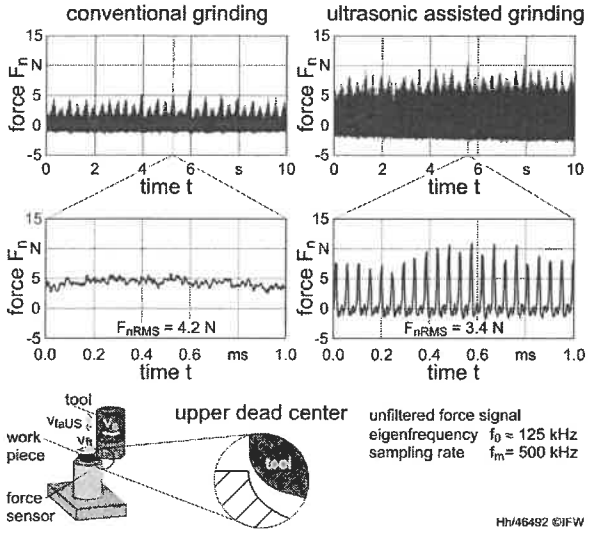

FIGURE 7. Normal forces for conventional and ultrasonic assisted reciprocating face grinding

This result differs from the expected force diagram. The depth of cut is several times higher than the amplitude of the ultrasonic vibration, so a continuous contact between tool and work piece was expected. This would have resulted in a sinusoidal force diagram and a continuous material removal. An explanation for the monitored force diagram is the wear of the grinding tool. A measurement of the tool geometry after the grinding process shows that the radius of the tool corner has the same dimension as the depth of cut. Thus the material removal is not carried out by the tool flank, as expected, but by the corner radius. Under this condition, the amplitude of the ultrasonic assistance enables to lift the tool off.
The effective force in ultrasonic assisted grinding, which is calculated from a period of 1 ms, is about 20% lower than the effective force in conventional grinding.

RESULTS AND CONCLUSIONS

The investigation shows that in peripheral surface grinding, the surface quality of the work piece is limited by the tool geometry and topography. The influence of the tool on the surface of the work piece can be reduced by tilting the grinding wheel. A tilt angle of 10° decreases the surface roughness by the factor three. A further increase of the tilt angle only leads to a small decrease in the surface roughness. It is also possible to lower the influence of the tool on the work piece surface by using ultrasonic assistance. Ultrasonic assistance reduces the surface roughness by the factor 3-4.
High dynamic force measurements show that the absolute force in ultrasonic assisted grinding is three times higher than the absolute force in conventional grinding, although the contact between tool and work piece is interrupted periodically. The effective force calculated from a 1 ms period is about 20% lower for ultrasonic assisted grinding than it is for conventional grinding.
In summary, ultrasonic assisted grinding combines several advantages and should be preferred for the machining of hard and brittle material. The surface quality of the work piece mainly depends on the process kinematics and is significantly better than the one attained by peripheral surface grinding. The thermal load is not increased and the flow of the coolant in the contact zone is enhanced. Furthermore, the process forces are reduced.

ACKNOWLEDGEMENTS

These research works have been conducted in the scope of the collaborative research centre (SFB) 516 "Design and Manufacturing of Active Microsystems" in the particular project B3 "Micromachining".

REFERENCES

[1] Roth, P.: *Abtrennmechanismen beim Schleifen von Aluminiumoxidkeramik*. Dr.-Ing. Dissertation, Universität Hannover, 1994.
[2] Reichstein, M.: *Schleifen miniaturisierter Bauteile*. Dr.-Ing. Dissertation, Leibniz Universität Hannover, 2008.
[3] Daus, N.A.: *Ultraschallunterstütztes Quer-Seiten-Schleifen*. Dr.-Ing. Dissertation, Technische Universität Berlin, 2004.
[4] Denkena, B., Hahmann, D.: *Ultraschallschleifen dünnwandiger Bauteile*. In: wt werkstattstechnik online, Volume 97, H. 11/12, p. 862-867, 2007.
[5] Okana, K.; Waida, T.; Suto, T.; Mizuno, J.; Kobayashi, T.: *Microgrinding of Micromachine Parts*. In: Proceedings of the 1st Int. ABTEC Conference, Seoul, Korea, Nov. 1993, p. 100-105.

NANO-INDENTATION AND SCTRACH TESTS ON OPTICAL FIBER MATERIAL TO DETERMINE DUCTILE MODE CRTICAL DEPTH OF CUT

Yousef A. Gharbia[1], Jayantha Katupitiya[2]
[1] Mechanical Engineering Department
Dhofar University
Salalah, Dhofar, Oman
[2] Mechanical Engineering Department
University of New South Wales
Sydney, NSW, Australia

ABSTRACT

In attempt to use nano-grinding to fabricate micro-lenses on single mode optical fibers to improve light coupling efficiency and also to modify optical fibers tips for use in optical fiber sensors, it was essential to determine the critical depth of cut that would ensure grinding takes place in the ductile mode. This paper presents a study of micro-indentation, nano-indentation and scratch tests carried out to determine forces and depths of cut that would ensure ductile mode material removal. Experiments were conducted using a micro-indenter and an Ultra-Micro Indentation System (UMIS) on samples made from sheets of optical fiber material. The indents were then examined under Scanning Electron Microscope (SEM) and Atomic Force Microscope (AFM). With the scratch attachment, the UMIS was used to make scratches on the same type of sheets. These scratches were made under force control thereby making it possible to determine when cracks would appear. The sheets were later investigated using SEM for a qualitative assessment and then using the AFM to quantify the results. The study revealed the critical depth of cut at which ductile-brittle transition takes place. The results obtained using nano-indenter and scratch tester are consistent. These results were then used to design and build a nano-griding machine that is capable of fabricating micro lenses and other profiles on single mode optical fibers tips.

INTRODUCTION

This research is set out to provide another alternative approach for optical fiber fabrication other than the commonly known techniques, such as chemical etching and, heating and pulling. The recent success in mechanical grinding of brittle and hard materials such as glass, ceramic, and silicon meant that there is a strong potential for this mechanical grinding to be used to grind microlenses on optical fiber endfaces and also to produce other profiles required for the fabrication of optical-fiber sensors. If this technique can be proven to produce mirror-surface finish free from surface and subsurface damages when used on optical fibers, then there is a great potential for it to be successfully implemented to produce the desirable profiles on optical fiber endfaces with high degree of controllability. It has been reported in the literature that in order to grind brittle materials without introducing cracks, the depth of cut would have to be less than 100 nm for most of brittle materials.

The possibility of grinding brittle material in ductile mode was noticed as early as 1954 [1]. It was noted then that during frictional wear of rock salts, the dominant material removal was plastic flow and not fracture. Twenty years later and due to the advancements in precision diamond grinding, Huerta et. al. [2] reported the first reproducible evidence of grinding of brittle material such as glass. The plastic flow they found in grinding corresponds to the plastic deformation prior to crack initiation as reported by Lawn, and Lankford et. al. [3,4]. The first detailed study of grinding ductility was performed using a single grit grinding apparatus [5]. Their study demonstrated that material removal mechanism is directly related to force on the abrasive grain, with lower forces corresponding to increase in grinding ductility. Other studies on various brittle materials including glasses [6] and advanced ceramics [5] showed similar ductile to brittle transition.

The critical depth of cut is useful in determining machining parameters for mechanical machining. Optimizing the machining parameters to improve the throughput and quality of the produced profiles is of extreme

economic importance. The indentation tests were designed to determine the critical depth of cut that can be achieved without causing cracks in the material [7]. In order to mimic the actual grinding process, the scratch test was designed in which the nano-indenter is moved tangentially to the surface of the specimen. This has enabled the visualization of the gradual development of cracks as the depth increased.

Experiments took place in three different set-ups: Micro Indenter, Nano-indenter and nano-scratcher. The aim of micro-indentation test was to determine the range of forces that can be applied without inducing cracks in the material. The determined force range was used in the nano-indenter to study in detail the material deformation regions and the critical depths at which cracks occur. Nano-scratch test helped validate the results in a situation that mimics grinding and gave a good insight into the gradual development of cracks as the depth was increased.

MICRO-INDENTATION TEST

Micro-indentation experiment was conducted using micro-indenter fitted with Vickers indenter. Indentation loads available on the rig were 100, 250, 500, 1000, and 2000mN. Specimens were prepared out of sheets (10x10x2mm) of optical fiber material (fused silica). The sample was coated with a 20 nm of gold prior to indentation. This was to make the indents stand out in comparison with any blemishes that might already exist in the sample material.

All available loads between 250mN and 2000mN were tried. Indents made with loads less than 250mN were not visible. Scanning Electron-Microscope (SEM) examinations were made for indents made by 500, 1000, and 2000mN and are shown in Fig. 2. It reveals that the initial cracks originate at the corners of the prism at the load of 500mN. These cracks grow in size as the load was increased to 1000mN. In addition, new cracks along the sides of the prism started to develop indicating the imminent total failure of the impression area. As the load was increased further to 2000mN cracks have become wider and a total separation of the indent cavity form the surface of specimen was evident. It was concluded from this experiment that the critical load at which brittle-ductile transition takes place is below 500mN and above 250mN for Vickers indenter. It was not possible to narrow down this range using the micro-indenter due to unavailability of loads between 100 and 250mN as well as between 250 and 500mN. However, the aim of this experiment was to roughly identify the range of forces for the given indenter that would demonstrate elastic, plastic and brittle behavior.

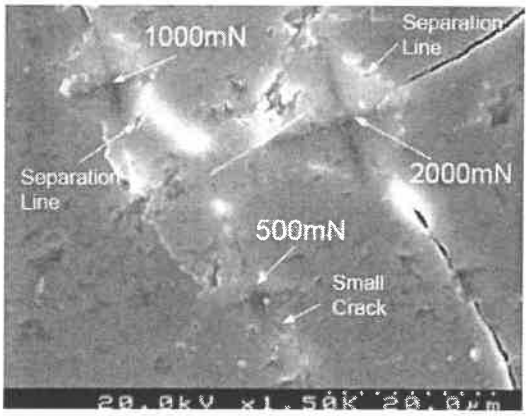

FIGURE 1. Micro indents for 500, 1000, and 2000mN.

NANO-INDENTATION TEST

Nano-indentation was carried out using UMIS (see Fig 2). The nano-indenter provided extremely fine resolution in position measurement (0.05nm) and force control (0.75mN).

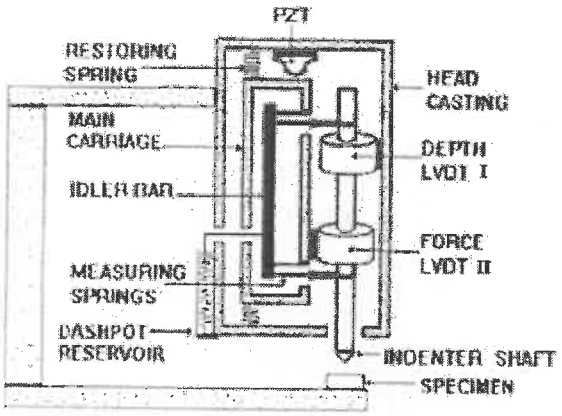

FIGURE 2. Schematic of UMIS (Courtesy of TIP division at CSIRO, Australia).

Samples were prepared in same manner described above. Indentation experiments were carried out using spherical indenter of 5 μm. An array of indents was made with loads ranging from 10mN to 500mN. Loads used were 10mN, 50mN, 100mN, and so on with 100mN increment till 500mN. For each load 5 indentations were made with a separation of 50 μm. The same experiment was repeated for

loads form 100mN to 175mN with 25mN increments.

This experiment is primarily aimed at determining the depth of indentation that can be achieved without causing cracks. It was also intended to help understand the different material deformation regions from elastic to plastic and eventually to brittle under different load conditions.

Pure elastic deformation was evident for loads up to 50mN as shown in Fig. 3 (a). A small noticeable amount of plastic deformation can be seen in Fig. 3 (b). These two graphs indicate that the elastic to plastic transition takes place at a load between 50mN and 100mN.

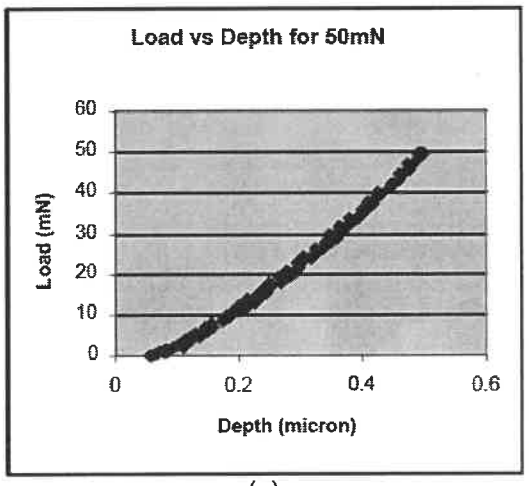

(a)

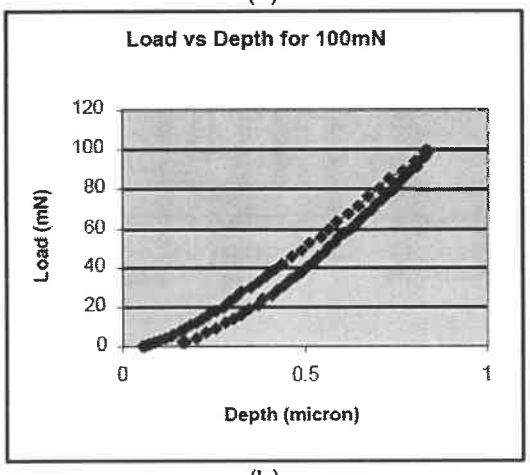

(b)

FIGURE 3. Load vs. depth: (a) for 50mN maximum load, (b) for 100mN maximum load

Although, it is possible to accurately find the point at which elastic-plastic deformation takes place by observing load versus displacement graphs, it was not the case with plastic-brittle transition. There is no clear evidence in these graphs to indicate at which load the plastic-brittle transition takes place. Therefore visual observation using optical microscope and SEM were used to find plastic-brittle transition. Optical microscope photograph taken for an array of indents made by loads of 100, and 200mN are shown in Fig. 4. These tests revealed that initial radial cracks appeared around 200mN.

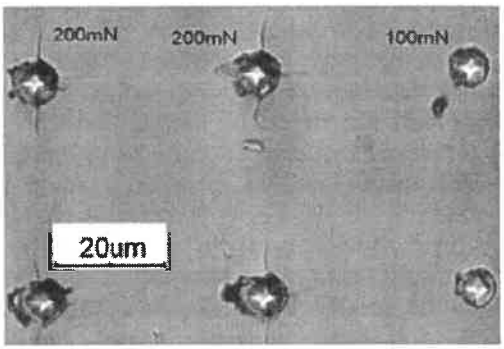

FIGURE 4. Optical microscope photographs of indents made by loads of 100 and 200mN

To study the 100-200mN range another experiment was conducted using loads between 100 and 175mN. Within this range no cracks were visible. Atomic Force Microscope (AFM) was used to measure the maximum depth for the indent made with a force of 175mN, where no cracks were visible. The result shows a maximum depth of 400 nm as shown in Fig. 5 (a). An AFM scan of an indent made with a force of 200mN is shown in Fig. 5 (b). The probe shows a maximum depth of 652nm. The shallow step of 24 nm in the profile is the thickness of the gold coating, just 4 nm higher than the intended thickness.

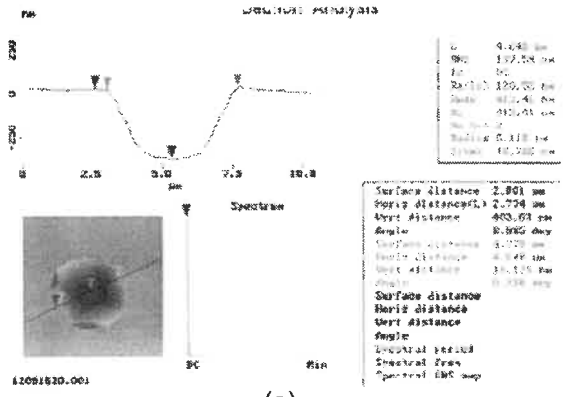

(a)

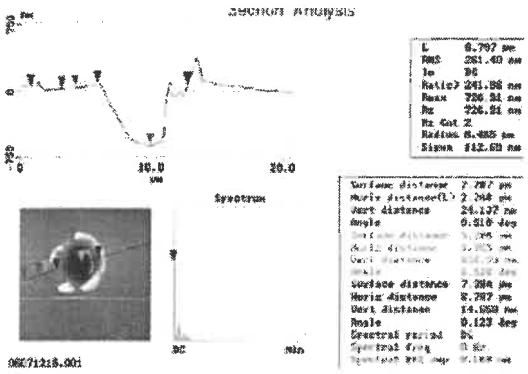

(b)

FIGURE 5. AFM analysis of: (a) 175mN indent, (b) 200mN indent

NANO-SCRATCH TEST

The UMIS can be extended to a nano-scratch tester with an optional attachment. The load is applied to the UMIS indenter shaft in the same manner as in indentation test. The specimen surface was then translated sideways by moving the positioning stage thereby making the indenter tip to produce scratches on the specimen surface. Although the stage velocity could be varied, it was kept constant at 100mm/sec for all the scratches. Series of scratches with maximum loads of 100, 300, and 500 mN were made with indenter. The scratches, 4mm long and 50 μm apart, were repeated 3 times for each load to verify consistency. Loads increased gradually from zero at the start of the scratches until the maximum load is reached somewhere along the scratch after which remained constant throughout.

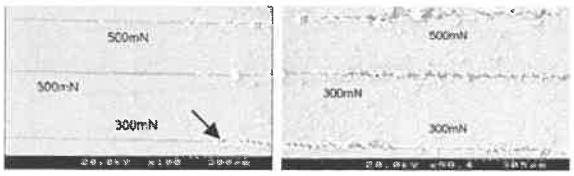

FIGURE 6. SEM pictures of the initial and final sections of scratches made by loads of 300 & 500mN.

Figure 6 shows that scratches start initially smooth and at some distance downstream chipping occurs. The arrow in the figure shows the point at which chipping starts. This point is located at about 1000 μm from the start of the scratch. Figure 7 shows load against lateral displacement for 300 and 500 mN load. The graph shows that the lateral distance of 1000 μm correspondences to a load of 200 mN. AFM analysis conducted at this point revealed that the critical depth of cut is about 440nm.

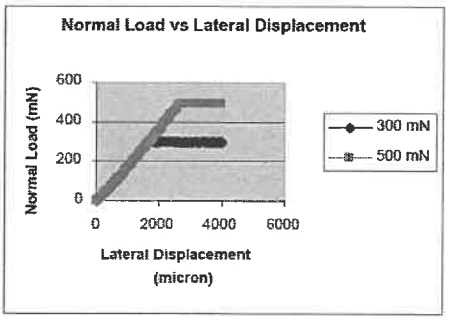

FIGURE 7. Load versus Lateral Displacement for scratches made by 300 and 500mN.

CONCLUSION

It was demonstrated that nano-indentation and nano-scratch tests could be successfully used to identify points of transition from one deformation region to another in optical fiber materials. For the indenter used in this work, the elastic-plastic transition was found to take place at a load between 50mN and 100mN whereas plastic to brittle deformation occurs at about 200mN. The point of transition from plastic to brittle deformation correspond to critical depth of 440 nm based on scratch test, and between 400 nm and 650 nm based on indentation test using the same indenter.

REFERENCES

[1] King R, Tabor D. The Strength Properties and Fractional Behaviors of Brittle Solids. Proc. of the Roy. Soc. London. 1945; A233: 225-238.

[2] Huerta M, Malkin S. Grinding of Glass—Surface Structure and Fracture Strength. J. Eng. For industry. 1976; 89 (2): 459-467.

[3] Lawn B, Wilshaw R. Review Indentation Fracture—Principle and Application. J. of Materials Science. 1975; 10: 1049-1081.

[4] Landkford J, Davidson, DL. Indentation Plasticity Microfracture in Silicon Carbide. J. of Material Science 1979; 14: 1669-1675.

[5] Swain MV. Microfracture about Scratches in Brittle Solids. Proc. Roy. Soc. London 1979; A336: 575-597.

[6] Namba Y, Abe M. Ultra-precision Grinding of Optical Glasses to Produce Super-Smooth Surfaces. Annals of the CIRP 1993; 42: 1; 417.

[7] Fischer-Cripps AC. A review of Analysis Methods for sub-Micron Indentation Testing. Vacuum 2000: 58; 569-585.

MECHANOCHEMICAL DIAMOND STONE CONTAINING $BaSO_4$ ABRASIVE

Masahiro Higuchi[1], Naomichi Furushiro[1], Tomomi Yamaguchi[1], Takashi Sugimoto[1], Noboru Matsumori[2], Hidekazu Ogura[2], and Shoichi Shimada[3]
[1]Kansai University
Suita, Osaka, Japan
[2]Mizuho Co. Ltd
Jyoyo, Kyoto, Japan
[3]Osaka Electro-Communication University
Neyagawa, Osaka, Japan

1. INTRODUCTION

Abrasion machining using bonded abrasives provides rapid material removal and high dimensional accuracy. However, to enhance abrasion machining in surface finishing, it is essential to use it in combination with a secondary erosion process, such as interfacial reaction machining that yields good surface finish and low subsurface damage. A new vitrified-bonded superabrasive stone has been developed to realize such a combined machining process, namely mechanochemical superfinishing [1]. This stone contains cBN grit and the abrasive cerium oxide, CeO_2, which is softer than the bearing steels but reacts chemically with them. Using this stone, it was possible to obtain a smooth surface with negative skewness, which could not be produced using a conventional cBN stone.

A mechanochemical diamond stone that contains the abrasive barium sulfate, $BaSO_4$, has recently been developed. In this paper, the chemical reaction that occurs between $BaSO_4$ and the Fe being machined is investigated theoretically and experimentally, and the performance of diamond stone containing soft and reactive $BaSO_4$ abrasive is evaluated through superfinishing experiments.

2. CHEMICAL REACTION BETWEEN $BaSO_4$ AND Fe

$BaSO_4$ is rarely used as a loose abrasive for polishing. However, it is used as a reactive abrasive for mechanochemical superabrasive stones, since it is softer than steel (Mohs hardness: 3-3.5) and it is almost insoluble in water making it useful as a coolant. In addition, the presence of iron catalyzes the barium [2]. In this study, the interaction of $BaSO_4$ with Fe was analyzed thermodynamically. This analysis reveals that the spontaneous occurrence of the chemical reaction is determined by the change in the Gibbs free energy, ΔG. The energy changes for the reactions were calculated by assuming that the following reactions occur between $BaSO_4$ and Fe.

$$\left.\begin{array}{l} BaSO_4+3Fe=BaS+Fe_3O_4 \\ 3BaSO_4+8Fe=3BaS+4Fe_2O_3 \\ 6BaSO_4+17Fe=6BaS+3Fe_3O_4+4Fe_2O_3 \end{array}\right\} \quad (1)$$

The results shown in Fig. 1 reveal that the changes in the Gibbs free energy have negative values. This implies that $BaSO_4$ oxidizes Fe and forms iron oxides such as Fe_3O_4 and Fe_2O_3. However, it is important to confirm whether the above chemical reactions actually occur.

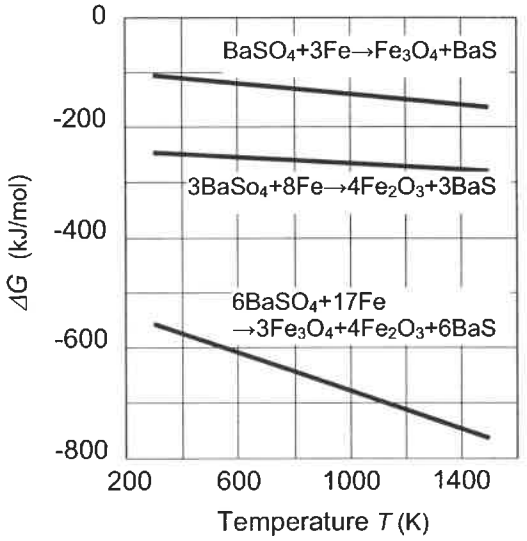

FIGURE 1. Change in Gibbs free energy in oxidation of Fe by $BaSO_4$ as a function of atmospheric temperature.

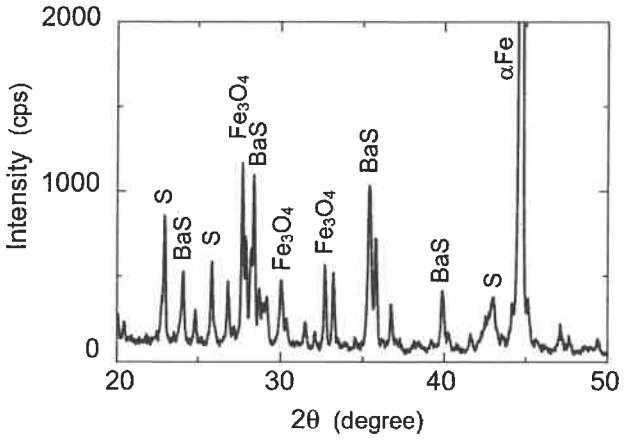

FIGURE 2. X-ray diffraction pattern on surface of SUJ2 specimen embedded in $BaSO_4$ and heated in a vacuum.

Therefore, an experiment investigating Fe oxidation by $BaSO_4$ was performed in the following way.

Two specimens of high-carbon chromium ball-bearing steel SUJ2 were heated at 773 K for 6 h in a high vacuum of 4.2×10^{-3} Pa. One specimen was embedded in $BaSO_4$ abrasives, whereas the other was not. The surface of the latter specimen was hardly damaged on heating; by contrast, the specimen heated inside $BaSO_4$ abrasives was covered with scales. These scales were closely analyzed by X-ray diffractometry and the result is shown in Fig. 2. Peaks due to Fe_3O_4, α-Fe and BaS are observed in the diffraction pattern. It is thus concluded that $BaSO_4$ abrasive in contact with the steel forms a magnetite oxide layer, according to the following reaction.

$$BaSO_4+3Fe\rightarrow BaS+Fe_3O_4 \qquad (2)$$

3. PERFORMANCE OF MECHANOCHEMICAL SUPERABRASIVE STONE

3.1 Test stones

Mechanochemical superabrasive stones were developed for superfinishing of bearing steels. They consisted of $BaSO_4$ of 2000-grit size and synthetic diamond of 4000-grit size with vitrified bond. In this paper, these stones are referred to as SD/$BaSO_4$ stones. In addition, a conventional vitrified SD stone and a vitrified $BaSO_4$ stone that consists of only bonded $BaSO_4$ abrasive were prepared to investigate the effect of the $BaSO_4$ abrasive on the performance of stone.

3.2 Experimental procedures

All tests were performed on a centerless flat surface lapping machine. The workpiece was face-finished by a rotating cup-shaped superabrasive stone with oscillating motion. Table 1 tabulates the superfinishing conditions that were used.

TABLE 1. Superfinishing conditions.

Superfinishing pressure	0.39 MPa
Stone speed	119 m/min
Workpiece speed	99 m/min
Frequency of oscillation	1000 fpm
Amplitude	0.5 mm
Superfinishing fluid	Super fatted emulsifiable oil, 100 x dilution
Workpiece material	SUJ2, HRC60

3.3 Results and discussion

If the $BaSO_4$ abrasive actually reacts on a steel workpiece in the superfinishing process, the material removal rate of the stone containing the $BaSO_4$ abrasive will obey the Arrhenius equation, because of the temperature dependence of chemical reaction rate.

$$\kappa = A\exp\left(-\frac{E_a}{RT}\right) \qquad (3)$$

where κ is the reaction rate, A is the pre-exponential factor, E_a is the activation energy, R is the gas constant and T is the absolute temperature.

The removal rates of the three above-mentioned stones were analyzed based on this empirical law for coolant temperatures from 283 K to 313 K, and their temperature dependences were compared.

Figure 3 shows the Arrhenius plot of the logarithm of the removal rate against the reciprocal of the temperature. The removal rates of the $BaSO_4$ stone and the SD/$BaSO_4$ stone increase almost linearly as the temperature

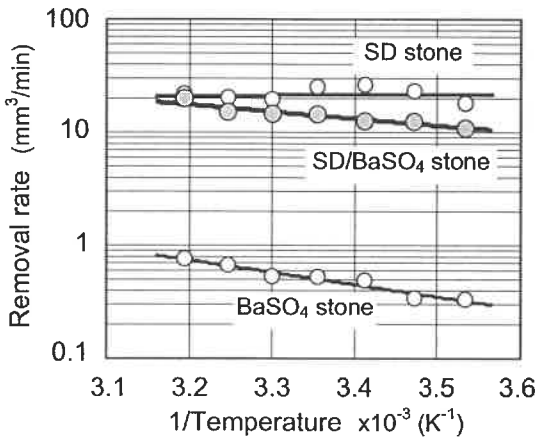

FIGURE 3. Dependence of removal rate on temperature of the superfinishing fluid.

increases. Calculating the apparent activation energy from the slope of the straight line gives 20.7 kJ/mol for the $BaSO_4$ stone and 11.6 kJ/mol for the SD/$BaSO_4$ stone. These correspond to the energies required to oxidize a steel surface, so that both these stones are considered to be able to chemically remove the steel surface. On the other hand, in the case of the SD stone, the removal rate is independent on the temperature, so that the material removal is considered to be due to the scratching action of the SD abrasive only.

These different material removal mechanisms result in substantial variations in the surface integrity of the steel workpiece. Specifically, the addition of the reactive $BaSO_4$ abrasive to a conventional stone resulted in improved surface finish and quality of the surface layer, as described below.

Figure 4 compares the roughness values, R_a, of the surfaces generated by the $BaSO_4$, SD/$BaSO_4$ and SD stones. The $BaSO_4$ abrasive hardly scratches the surface of hardened bearing steel but only rubs it, because of its friability. Nevertheless, when superfinishing with the $BaSO_4$ stone, there is a steady, albeit gradual, improvement in the surface roughness. This is because that the $BaSO_4$ abrasive erodes the tops of the asperities on the steel surface, truncating them to a certain height. Therefore, the SD/$BaSO_4$ stone effectively generates a smoother surface than the SD stone due to the combined effect of the scratching action of the SD abrasive and the rubbing action of the $BaSO_4$ abrasive.

Figure 5 compares the residual stresses induced in the vicinity of the finished surface. As in superfinishing with the SD stone, the superfinishing process invariably leads to compressive residual stresses, because the thermally induced tensile residual stresses are very small in magnitude. However, the residual stress formation is slightly reduced when superfinishing with the SD/$BaSO_4$ stone in place of SD stone. This is probably due to an increase in the tensile stress induced by the heat generated when the $BaSO_4$ abrasive rubs the finished surface. On the other hand, a higher compressive stress value is obtained when the $BaSO_4$ stone is used. This is because that the $BaSO_4$ stone oxidizes the bearing steel. It has been reported that compressive stresses are generated in the oxide film as it forms if the Pilling-Bedworth ratio is greater than 1 [3]. Since the Pilling-Bedworth ratio for steel is estimated to be 1.77, it is considered that higher

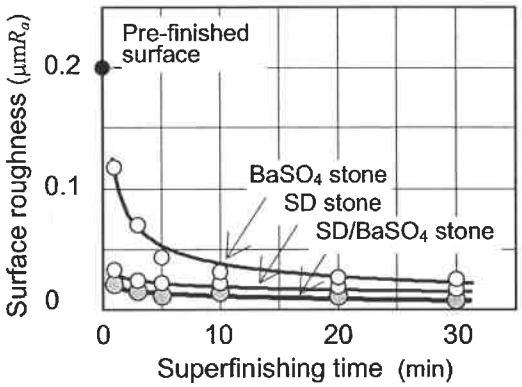

FIGURE 4. Comparison of roughness values of surfaces generated by $BaSO_4$, SD/$BaSO_4$ and SD stones.

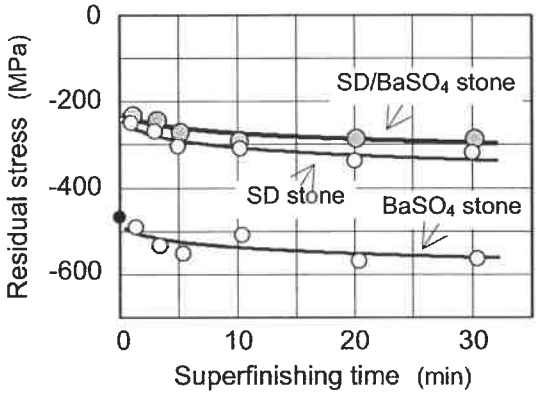

FIGURE 5. Comparison of residual stresses induced by superfinishing with $BaSO_4$, SD/$BaSO_4$ and SD stones.

compressive stresses are induced in it.

Next, to determine the degree of work hardening of the finished surface, the micro-indentation hardness testing was conducted and the change in Vickers hardness with indentation depth was examined. It was found that the hardness decreased with increasing indentation depth at shallow depths and became independent on depth at large depths. The transition depth between these two regions was assumed to be the depth of the hardened layer. The curves shown in Fig. 6 indicate the depths of the hardened layer obtained in such a manner. The depths of the hardened layer are shallower when superfinishing with the $BaSO_4$ stone and the SD/$BaSO_4$ stone than those obtained when superfinishing with the SD stone. In particular, superfinishing with $BaSO_4$ stone results in the shallowest depth of the hardened layer even though it generates the highest compressive residual stress, because chemically removed

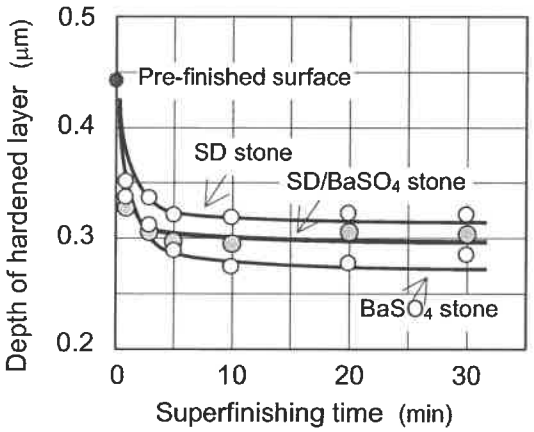

FIGURE 6. Comparison of depths of hardened layer generated by $BaSO_4$, SD/$BaSO_4$ and SD stones.

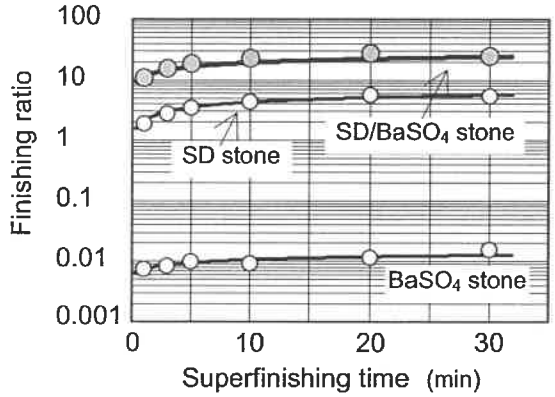

FIGURE 7. Comparison of finishing ratios in superfinishing with $BaSO_4$, SD/$BaSO_4$ and SD stones.

surfaces harden very little. Thus, the $BaSO_4$ stone produces the surface with the distinctive surface integrity.

Figure 7 compares the finishing ratios (i.e., the volume of material removed per unit volume of stone wear) for the three stones. Bearing steel cannot be machined with diamond due to carbon diffusion into the iron causing excessive diamond wear. The SD stone used for superfinishing of bearing steels is no exception to this rule, since it has a finishing ratio of less than 5. However, a finishing ratio of larger than 20 is obtained when using the SD/$BaSO_4$ stone instead of the SD stone; that is, the SD/$BaSO_4$ stone is highly resistant to wear. This is attributed to the formation of an oxide film by the $BaSO_4$ abrasive. If the workpiece surface is coated with an oxide film, it is assumed that the attritious wear of the SD abrasive is due to the deoxidization reaction and not to carbon diffusion, because diamond can deoxidize iron oxide at the temperatures higher than 900 K [4]. Thus, the addition of $BaSO_4$ abrasive to the conventional SD stone improves the finishing ratio as a result of the modification of the wear mechanism.

4. CONCLUSIONS

A mechanochemical diamond stone containing a $BaSO_4$ abrasive was developed and its performance was evaluated through the superfinishing of bearing steels. The $BaSO_4$ abrasive forms a magnetite oxide layer on the steel surface, resulting in the SD/$BaSO_4$ stone exhibiting unique finishing characteristics.

(1) The SD/$BaSO_4$ stone produces a smooth surface suitable for bearing races.

(2) The SD/$BaSO_4$ stone reduces both the hardened layer depth and the compressive residual stress in the finished surfaces.

(3) The SD/$BaSO_4$ stone is highly resistant to wear.

ACKNOWLEDGEMENTS

This research was financially supported by a Grant-in-Aid for Scientific Research from The Japan Society for Promotion of Science (JSPS No. 20560119).

REFERENCES

[1] Higuchi M, Yamaguchi T, Sugimoto T, Shimada S, Matsumori N, Ogura H. Development of Superabrasive Stone for Mechanochemical Superfinishing. Proceedings of ASPE 2007 Annual Meeting. 2007; 473-476.

[2] Dibello P M, Manganaro J L, Aguinaldo E R. Barium Compounds. Kirk-Othner Encyclopedia of Chemical Technology. John Wiley & Sons, Inc. New York: 2004.

[3] William D C Jr. Materials Science and Engineering. John Wiley & Sons, Inc. New York: 2007.

[4] Tanaka H, Shimada S, Ikawa N, Higuchi M, Obata K. Difference in Wear Patterns of Diamond Cutting Tool Depending on Work Materials. Proceedings of 10th ICPE, 2001; 179-183.

ACHIEVEMENT OF HIGH FLATNESS OF LARGE DIAMETER SILICON WAFER IN DOUBLE-SIDED POLISHING -OPTIMIZATION OF POLISHING CONDITIONS BASED ON KINEMATICAL ANALYSIS-

Kenji HIROSE, Toshiyuki ENOMOTO
Department of Mechanical Engineering
Graduate School of Engineering, Osaka University
Suita, Osaka, JAPAN

INTRODUCTION

Semiconductor devices require silicon (Si) wafers as the substrates to be manufactured with very high flatness for miniaturizing the design rule. On the other hand, the size of wafer is increasing for raising the number of device chips per a wafer for reduction of the process cost. Recently, 300 mm diameter wafers are mainly manufactured, and the feasibility study for 450 mm diameter wafers has already started [1].

The double-sided polishing process (Fig. 1) is widely adopted as the finishing process of the Si wafer manufacturing, because wafers with good surface quality and flatness can be obtained economically. Then the next-generation large diameter wafers, that is, 450 mm wafers are considered to be manufactured with the same method as 300 mm diameter wafers, namely, the double-sided polishing machine. However, the double-sided polishing technology has serious problem; it is very difficult to set the appropriate polishing conditions for obtaining the high flatness of the wafer with the pads flat. Then it is pointed out that the present polishing technology cannot meet the requirements in manufacturing of 450 mm wafer.

In the actual manufacturing process, the techniques in which the polishing conditions are changed periodically and the pad surface is conditioned with a diamond dresser are applied to maintain the pad flatness [2]. However, the polishing conditions and parameter modifications are based on experience and skill of the operator, resulting in inferior reproducibility and increased production costs. On the other hand, theoretical optimizing methods of double-sided polishing conditions were already proposed for overcoming the problem [3] [4]; however, the methods did not take the pad flatness or the wafer flatness into consideration.

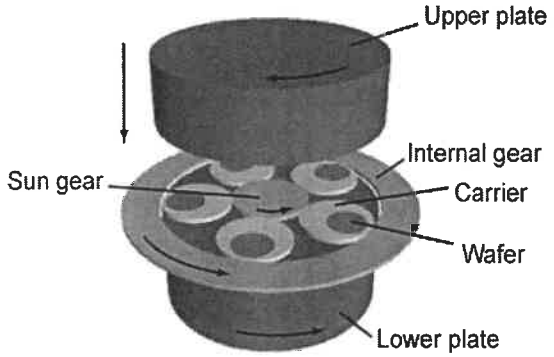

FIGURE 1. Double-sided four-way polishing machine

In this study, the optimization method of double-sided polishing conditions was newly proposed and developed to overcome the problem, namely, achieve high flatness of the Si wafer on maintaining the pad flat.

OPTIMIZATION OF POLISHING CONDITIONS

Modeling of Double-Sided Polishing

As shown in Fig. 2, the double-sided polishing which has five carriers per one batch and one wafer per one carrier (diameter of carrier is about 23 inches) was modeled, considering the size of the polishing machine. The diameter of wafer was set to be 300 mm in the model. Table 1 lists the polishing machine specifications.

Objective Function for Optimization

As a basis, the model of the distribution of material removal on the wafer and the distribution of wear on the pad was developed based on kinematical analysis. The amounts of removal and wear are considered to be followed by the abrasion model and be proportional to the sliding distance between wafer and pads, that is,

the relative velocity between wafer and pads.

First, the relative velocity of the wafer against the pad is calculated on the whole wafer, and then the objective function for the wafer: Jw is obtained as the difference between the maximum value and the minimum value in the calculated relative velocities. Second, the objective functions for pads are obtained from the relative velocities of the pads against the wafer as the almost same way for the wafer. Here, the objective function for the upper pad and the lower pad are described as Jpu and Jpl, respectively. And finally, the multi-objective function: Jwp for wafer and pads is generated with the sum of the weighted each objective function Jw, Jpu and Jpl. The optimization for Jwp brings the optimum polishing conditions of achieving high flatness of wafer and pads.

MULTI-OBJECTIVE OPTIMIZATION OF POLISHING CONDITIONS BY QUASI-NEWTON METHOD

Optimization of Polishing Conditions

The optimization of the polishing conditions, concretely, the rotational speeds of the sun gear (ωsun), internal gear (ωint), and upper (ωpadu) and lower (ωpadl) pads as design variables, was carried out utilizing a quasi-Newton method. Considering the specifications of the commercial polishing machine, the upper and lower limit of rotational speeds of gears and pads were defined as penalty functions. The initial values of four design variables are set to be the values which are commonly used in the actual manufacturing process.

Results of Optimization

Table 2 shows the results about the initial and the optimized design variables and the calculated objective functions. And in the table, the rotation of wafer (ωwaf), the rotation of carrier (ωcrot) and the revolution of carrier (ωcrev) are also shown. Case Ow and case Owp mean the optimized result for only wafer and for wafer and pads, respectively. The distribution of the sliding distance on the wafer and the pads are shown in Fig. 3 and Fig. 4.

As shown in Fig. 3 and Table 2, the distribution of sliding distance on wafer was in the tapered shape and the maximum difference in sliding distance on wafer was very large as 64706 in the initial condition. From Fig. 4, it was found that some distribution variation on both polishing pads exists and the variation value on both pads

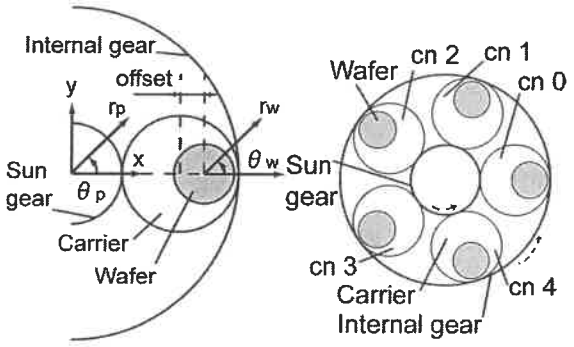

FIGURE 2. Model of double-sided polishing

Table 1. Polishing machine specifications

Internal diameter of pad	550.00 mm
External diameter of pad	1635.00 mm
Diameter of carrier	584.91 mm
Diameter of sun gear	507.59 mm
Diameter of internal gear	1677.41 mm
Distance between centers of carrier and wafer	120.60 mm

Table 2. Multi-objective optimization of polishing conditions

Design variables (Rotation of gears and pads)			
	Initial	Optimized Ow	Optimized Owp
ωsun rpm	11.00	29.19	12.14
ωint rpm	10.00	-10.96	6.75
ωpadu rpm	-10.00	-10.28	-9.93
ωpadl rpm	30.00	30.34	31.89
Objective function (Max. difference in sliding distance on wafer and pads)			
	Initial	Optimized Ow	Optimized Owp
Jw mm	64706	4765	7897
Jpu mm	18244	11906	14900
Jpl mm	17752	36231	24565
Calculated rotation of wafer and carrier			
	Initial	Optimized Ow	Optimized Owp
ωwaf rpm	0.43	38.63	6.73
ωcrot rpm	9.57	-28.38	4.41
ωcrev rpm	10.23	-1.64	8.00

Ow : Optimized for only wafer
Owp : Optimized for wafer and pads

is the same to some extent. The tendency of the increase of the sliding distance at the center of radial direction of polishing pads corresponds well with the actual polishing characteristics [5].

In the case of the optimization for only wafer

(Ow), the distribution variation of the sliding distance on wafer was very small, as compared with that in the initial condition, as Fig. 3 shows. On the other hand, the distribution variation of the sliding distance on the lower pad became large and the difference of the sliding distance on the upper pad and that on the lower pad was also large. This is because only wafer was optimized for in Ow.

The optimization for wafer, and upper and lower pads (Owp) was carried out. As a result, the distribution variation of the sliding distance on wafer was very small, as shown in Table2 and Fig. 3. The difference of the sliding distance on the upper pad and that on the lower pad was a little larger than that in the initial condition, but much smaller than that in Ow. This is owing to being optimized for wafer and pads in Owp.

From Fig. 4, it was found that the sliding distance increased at the center of radial direction of polishing pad in Owp as the same in the initial condition. The reason for this is thought to be that the number of the locus of the wafer on pad is large at the center of radial direction of polishing pad. The deviation of the distribution is considered not to be suppressed by only optimization of the rotational speeds of gears and pads.

OPTIMIZATION OF POLISHING CONDITIONS AND WORKPIECE-HOLE LOCATIONS BY GENETIC ALGORITHM METHOD

In the optimization for wafer and pads (Owp), the distribution variation of sliding distance on wafer was significantly improved and the difference of the sliding distance on two pads was suppressed. However, the maximum difference in sliding distance on lower pad in Owp was larger than that in the initial condition. It is required to develop the optimization which is more effective for minimizing the maximum difference in sliding distance on upper and lower pads.

Workpiece-hole location in carrier is considered to influence strongly to the distribution of sliding distance on pads. Then the optimization considering the workpiece-hole location (OGA) was carried out. Workpiece-hole locations were defined by the difference between centers of carrier and workpiece-hole (lo), and the angle from center of carrier to center of workpiece-hole in static system (θo).

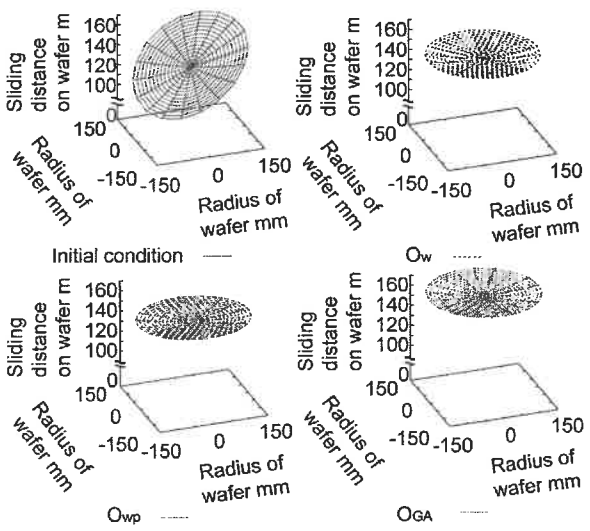

FIGURE 3. Distribution of sliding distance on wafer

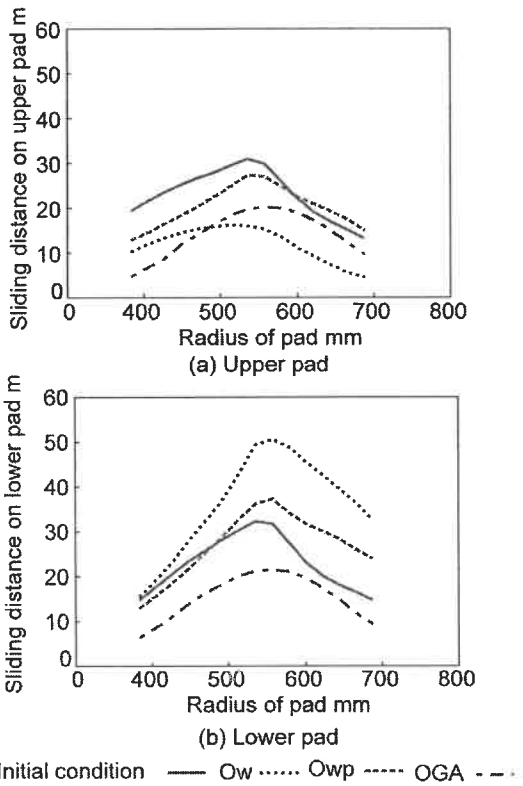

FIGURE 4. Distribution of sliding distance on upper and lower pads

Here, it was difficult to apply the quasi-Newton method as the optimizing method, because of too much design variables, concretely, 14 design variables. Then the genetic algorithm (GA) method was chosen as the method of

optimization, which also has a feature of global searching.

The results of optimization by OGA were shown in Table 3, Table 4, Fig 3 and Fig 4. Carrier numbers in Table 4 were shown in Fig 2 as cn.

From Table 3 and Fig. 3, it was found that the optimization of the polishing conditions including the workpiece-hole locations (OGA) achieved the small distribution variation of the sliding distance on wafer, as compared with other optimization methods (Ow, Owp). The deviations of sliding distances on upper and lower pads were smaller than that by optimization for wafer and pads (Owp), as shown in Fig. 4. Further, the each maximum difference in sliding distances on each pad was smaller than that by the initial condition (Table 3).

Table 3 Optimization of polishing condition

Design variables (Rotation of gears and pads)	
	Optimized OGA
ω_{sun} rpm	-20.68
ω_{int} rpm	4.70
ω_{padu} rpm	-24.02
ω_{padl} rpm	23.66
Objective function (Max.difference in sliding distance on wafer and pads)	
	Optimized OGA
J_w mm	3918
J_{pu} mm	16204
J_{pl} mm	15692
Calculated rotation of wafer and carrier	
	Optimized OGA
ωwaf rpm	-15.92
ωcrot rpm	15.71
ωcrev rpm	-1.19

Table 4 Optimization of workpiece-hole locations

		Carrier number				
		0	1	2	3	4
Initial	l_o mm	120.60	120.60	120.60	120.60	120.60
	θ_o °	0	72	144	216	288
OGA	l_o mm	48.26	116.64	45.22	81.52	102.25
	θ_o °	2	159	282	185	354

CONCLUSIONS

The optimization of double-sided polishing conditions was proposed based on kinematical analysis for achieving high flat large diameter wafer. And it was found that:

(1) In the case of the optimization for only wafer, the distribution variation of the sliding distance on wafer was small, but the difference of the sliding distance on the upper pad and that on the lower pad was very large.
(2) In the case of the optimization for wafer, and upper and lower pads, the distribution variation of sliding distance on wafer was improved, and the difference of sliding distance on the upper pad and that on the lower pad was suppressed.
(3) Optimization of workpiece-hole location in carrier in addition to polishing conditions, namely, the rotation of gears and pads improved the flatness of wafer and pads.

ACKNOWLEDGMENT

The authors express their deepest gratitude to HAMAI CO., LTD.

REFERENCES

[1] International Technology Roadmap for Semiconductors 2007 Edition, Executive Summary Final Draft, (2007-Dec.),p.77.
[2] Arai, H., Planarization Polishing Technique for Large Diameter of Bare Silicon Wafer, Journal of the Japan Society for Precision Engineering, Vol.73, No.7 (2007), pp.756-759. (in Japanese)
[3] Nakagawa, Y., Optimization of Double Sided Polishing Conditions in order to Unify Friction Distance Distribution in a Wafer, Journal of the Japan Society for Precision Engineering, Vol.72, No.5 (2006), pp.641-646. (in Japanese)
[4] Uhlmann, E. and Ardelt, T., Influence of Kinematics on the Face Grinding Process on Lapping Machines, Annals of the CIRP, No.48, No.1 (1999), pp.281-284.
[5] Abe, K., Study for Lapping Technology of 400 mm diameter wafers -3rd report-, Proceedings of Spring Conference of the Japan Society for Precision Engineering , (1998), p.566. (in Japanese)

OPTIMIZATION OF QUALITY OF THE CYLINDRICAL SUPERFINISHED SURFACES

Romeo D. Ionescu[1], Dumitru Amarandei[1]
[1]Faculty of Mechanical Engineering, Mecatronics and Management
"Stefan cel Mare" University
Suceava, Romania

INTRODUCTION

It is a well-known fact that superfinishing is an abrasive process used to achieve micro-finished surfaces, extend product life mainly by increasing the fatigue resistance, reduce the energy loss due to friction and provide the product with superior cosmetic appearance. The process is widely used in the bearing and automotive industries. The procedure can be used in machining processes after any finishing operation, but it is recommended after grinding, if the economic factors are also taken into account [1].

Superfinishing is used as a final process after grinding to remove the ground surface topography and generate a smooth surface with increased loadbearing capacity (ISO 13565-1:1996 and ISO 4287:1997). Most abrasive fine finishing procedures (with the only exception of fine grinding) do not use the abrasive disc (specific to grinding) as a processing tool, but use various other forms of abrasive material concentration bound abrasives in ceramic (stones), abrasive bands, etc. [2].

During superfinishing of cylindrical surfaces, the abrasive stone is pressed against the rotating workpiece while being oscillated in the axial direction. The combined rotational and axial oscillating motions generally result in the intersection of the stone cutting paths during subsequent workpiece revolutions, which is credited with enhancement of stock removal. Axial oscillation of the stone during superfinishing may also promote stone wear and self sharpening of the abrasive, thereby facilitating removal of debris from the cutting zone.

Superfinishing is a complex operation, whose results are influenced significantly by very many factors. The research conducted in various laboratories have demonstrated that working parameters (p, f, v, n...) are important for obtaining the desired surface quality [3], [4]. The process kinematics, suggested by the Supfina company, only in two of the multiple possible variants –one using stone abrasive, and the other using abrasive-impregnated cloth, is presented in Figure 1, [5].

p - the specific pressure force of the abrasive tool on the piece surface
v_w- workpiece rotation velocity
v_t – the tool longitudinal movement velocity
f - axial oscillation frequency

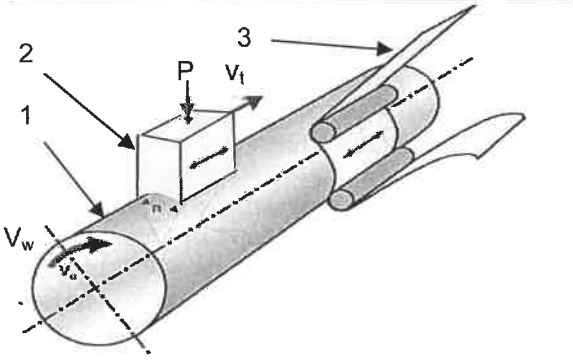

FIGURE 1. The superfinishing principle. Piece 1; Superfinishing tools: stone 2*; band 3.*

The high speed but low amplitude movements of the abrasive grains coating the tool determine the formation of microscopic splinters. This yields very high quality surface, with high load-bearing capacity – Figure 2, [4], in a very short processing time interval.

The situation is further complicated by the wide variety of superfinishing stones having different types of abrasives, grit sizes, hardness grades, and treatments. An especially important stone parameter is the grit size of the abrasive, which significantly affects stock removal and surface roughness.

EXPERIMENT

An experiment was carried out in order to determine the influence of the important factors on the superfinished surface roughness. The researchers used the Taguchi method for the experimental plan and for obtaining the

mathematical model. The obtained matricial model allows an easy identification of the surface roughness values for different combinations of influent factors [3],[4].

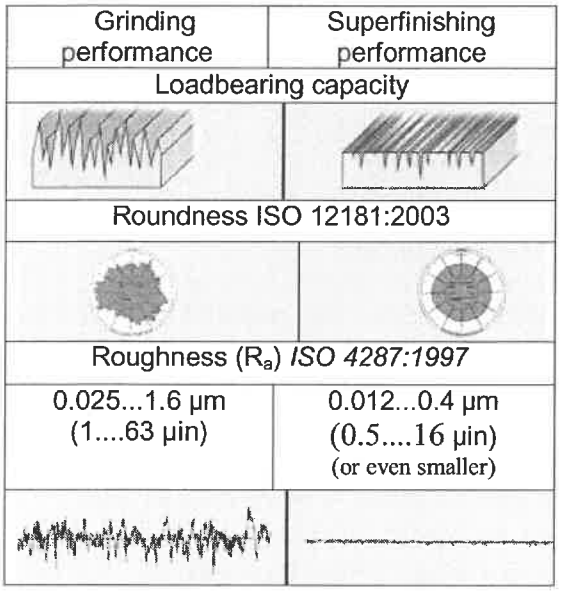

FIGURE 2. Superfinishing performance.

The results of the documentary studies show that because of the multitude and complexity of the phenomena accompanying the technological superfinishing process, these phenomena are not fully elucidated. Several researchers have partially studied the phenomena accompanying the surfinishing and they imposed some simplifying hypothesis even during the experimenting. Exposing the research results, I shall mention some hypotheses that they consider during the experiment, before.

- During an experiment they estimated that the pieces have homogene physical/mechanical characteristics;
- The initial roughness of a piece was considered to be constant for a lot of pieces which are part of the experiment;
- They estimated that only the verifiable parameters had a decisive influence on the processing results, the others factors had aleatory and small influences;
- They considered the working parameters of the superfinishing device as constant on each regulation step during the experiment;
- The measurement of the processing results was made under the same circumstances.

In order to carry out the research, a great number of cylindrical pieces have been processed, as shown in Figure 3. The initial roughnesses were imposed by the grinding process. The pieces were sorted by groups from bigger lots, having roughness R_a as a characteristic. The imposed superfinishing roughness variation accepted for an experimental lot was of maximum one tenth (±0,05 µm).

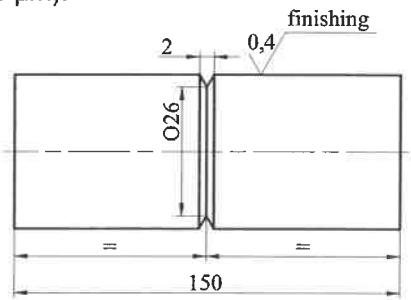

FIGURE 3. Cylindrical pieces used during the experiment. OLC 45 steel, STAS 880-88 *(RO).*

Next, there will be presented diagrams showing the results of some experiments that point out the technological factors that could play a prominent part in the processing result evolution, especially the roughness of the superfinished surface. As a roughness criterion they used the average variation R_a. The aim has been to find the significant progressing range for each factor. The pieces were sorted by groups from bigger lots, having roughness R_a as a characteristic.
The equipment used for measurements is "LINKS 2204" (a product of the Harbin-measuring & Cutting Tool Works) and the estimation parameters in conformity with the romanian standard STAS 5730-85 for

- Ra = the profile arithmetic mean deviation ;
- Rz = the profile irregularities height at ten points;
- Ry = the profile maximum height;
- tp = the profile bearing length percentage; etc.

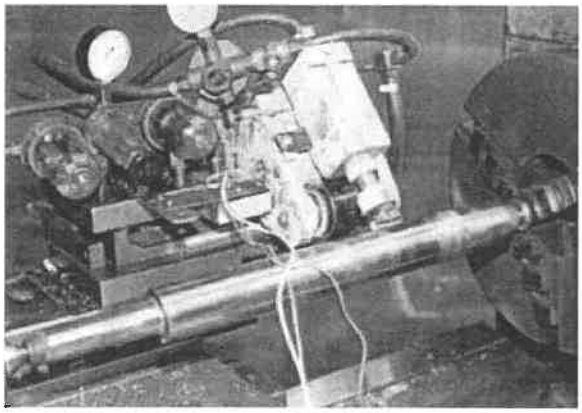

FIGURE 4. Experimental set-up with superfinishing-attachment (Supfina).

The experiments presented in [1], [3] show that certain characteristics of the utilised tool, of the processed material, other than those analysed, and of the cooling-lubricating liquid may modify the process result, Figure 5 and Figure 6.

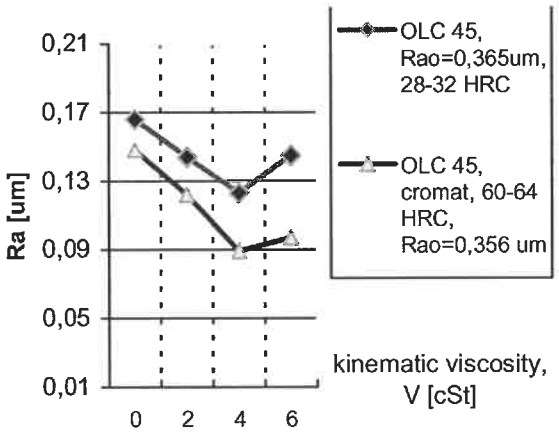

FIGURE 5. Influence of cooling-lubricating liquid on the superfinished surface roughness for OLC 45 steel pieces (28...32 HRC); stone 1=dry; stone 2=kept 4 hours in cooling-lubricating liquid *p=0.2 MPa, f=40 Hz, v=0.365 m/s, s=0.15 mm/rot, EK1 800-05-145 VKHS, L=25 mm, l=15 mm.*

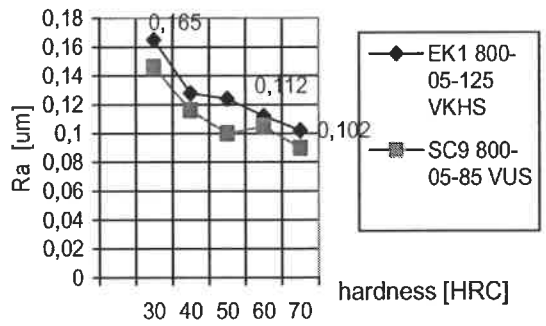

FIGURE 6. Influence of hardness of abrasive stone and steel (OLC 45 and RUL 1) on the superfinished surface roughness.
p=0.3 MPa, f=40 Hz, v=0.365 m/s, s=0.15 mm/rot, L=33 mm, l=15 mm; R_0=0.35...0.38 um.

The pieces have been processed on a lathe machine by means of a Supfina superfinishing device, Figure 4. The following factors have been taken into consideration, all of them on two levels:
- the type of abrasive (ABR) used in the tool's composition: aluminium oxide (noted here as 33A) and silicon carbide (22C0, [2];
- the superfinishing stone hardness (H), [2];
- the superfinishing stone length (L), [2];
- the type of cooling-lubricating liquid (RU) (kinematic viscosity);
- the superfinishing stone preparation (Pr); one level designates the superfinishing stone's preservation for four hours in the cooling liquid, the other refers to the use of the stone abrasive without this preliminary operation;
- the characteristics of the processed material: hardness (HRC) and initial roughness (R_{a0}).

The pieces have been manufactured out of OLC 45 steel, STAS 880-88 (Romanian), with the dimensions presented in Figure 3, in two differently prepared lots: one lot of pieces having the fatigue resistance σ = 850...1000 N/mm^2, the other lot with the hardness 60-64 HRC, obtained by thermal treatment.
The objective of the experiment is to find a relation between the superfinished surface roughness (arithmetic mean R_a) and the factors influencing decisively its value, as well as to find an optimal configuration for the set of analysed factors, configuration expected to yield the smallest roughnesses. The model of the studied system is represented by the relation (1).

$$R_a\sim = M + ABR + H + L + Pr + RU + HRC \times R_{a0} + ABR \times HRC + ABR \times R_{a0} + ABR \times H + H \times R_{a0} + RU \times HRC \quad (1)$$

M = the general mean of responses R_a ;
R_a = the system's response (the experimentally obtained roughness); $R_a\sim$ theoretical results.
There has been devised a Taguchi experiment plan, L_{16} (2^{15}), for the experimental determination of the influence of the mentioned factors on roughness.
The mean medium effects of the main factors are suggestively presented in the diagrams in Figure 7.
As a result of variance analysis (the Fisher/ Snedecor test), the simplified mathematical model can be written, relation (2).

$$R_a\sim = M + ABR + H + L + RU + HRC + R_{a0} + I \quad (2)$$

THE ANALYTIC MODEL OF THE SYSTEM

The final mathematical model of the studied phenomenon receives the matricial form (3). In relation (3), the values in bold type represent the mean effects of the factors leading to the best roughness yielded in the superfinishing process.

$$R_a\sim = 0{,}148 + [+0{,}012 \quad -0{,}012]\,ABR + [+0{,}018 \quad -0{,}018]\,H + [-0{,}015 \quad +0{,}015]\,L + [-0{,}016 \quad +0{,}016]\,RU + [+0{,}019 \quad -0{,}019]\,HRC + [-0{,}034 \quad +0{,}034]\,R_{a0} + \begin{Vmatrix} -0{,}014 & +0{,}014 \\ +0{,}014 & -0{,}014 \end{Vmatrix} ABR \times HRC \quad (3)$$

For the partial description of the process the premise was the fact that the phenomenon

might be described by a relation of the form (4) which takes into account the factors characterising superfinishing [1].

$$R_a = k\, ABR^m\, H^p\, L^q\, Ru^x\, HRC^y\, R_{a0}^z \qquad (4)$$

k is a coefficient which includes the influence of several factors omitted from study, m, p, p, q, x, y, z, exponents which indicate the degree of influence of factors ABR, H, L, RU, HRC and Ra_0 . By looking up the logarythms, equation (4) can be linearized. By changing variables, noting RA=ln R_a, AA= ln ABR, HH = ln H, LL = ln L, UU = ln RU, RR = lnHRC, R0 = ln Ra_0 it obtain the relations (5) si (6).

$$\ln R_a = \ln k + m*\ln ABR + p*\ln H + q \ln L + x*\ln RU + + y*\ln HRC + z*\ln R_{a0} \qquad (5)$$

$$\ln R_a = M+EAA+EHH+ELL+EUU+ERR+ER0 \qquad (6)$$

The mathematical model describing analytically the implication of the considered influent factors in the roughness of the superfinished pieces takes the form (7).
The theoretical values yielded by relation (7) are very close to the experimental values.

$$R_a \approx 0{,}068 ABR^{-0,1} H^{0,49} L^{0,47} RU^{0,22} HRC^{-0,32} R_{a0}^{0,49} \qquad (7)$$

CONCLUSION

The experiment and the subsequent analyses have afforded the selection of significant influent factors. The stone abrasive influences significantly the result of superfinishing by the abrasive material, grain type, and hardness; the dimensional variation of the abrasive stone has turned out to be of lesser importance for the final roughness; if the dimensional variation is accompanied by the change in the stone's pressure on the surface of the piece, then the geometric parameters of the stone abrasive become influent.
The final roughness depends on the characteristics of the processed piece, the most important being the initial roughness and the hardness (thermal and thermo-chemical treatment). Superfinishing is accomplished by means of different abrasives for pieces with different hardnesses (significance of the interaction abrasive–piece hardness).
For industrial practice, the analytic model, in the form of the product of influent factors, is highly important. Such relations, providing information about roughness obtained by superfinishing and taking into account a set of input factors, have not been published in technical literature. The relation can be improved by additional experiments.

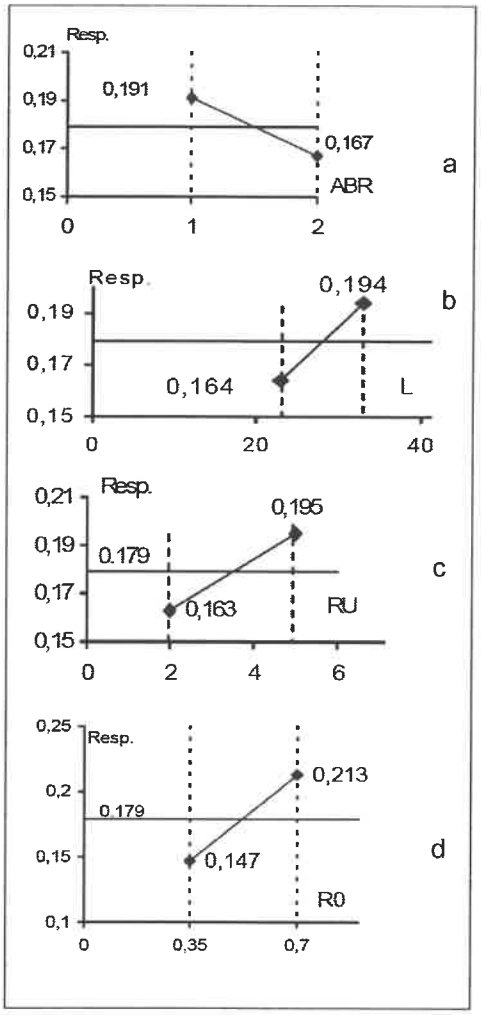

FIGURE 7. Effects plot: the mean medium effects of the main factors. a. type of abrasive (ABR); b. superfinishing stone length (L); c. type of cooling-lubricating liquid (RU); d. initial roughness (R_0).

REFERENCES

[1] Ionescu R., Contribuții la studiul influenței unor factori asupra rugozității suprafețelor superfinisate, Doctoral thesis, Technical University "Gh. Asachi", Iași, 1998.
[2] ATLANTIC, http://www.atlantic-bonn.de/
[3] Ionescu R,, Amarandei D., Influential factors on the superfinished surfaces, Materials Science & Technology 2008 Conference (MS&T '08), Oct. 5-9, 2008, Pittsburgh, Pennsylvania.
[4] Varghese, B, Malkin, S, Selection of optimal superfinishing parameters, Journal of Manufacturing Processes, 2000, http://findarticles.com/p/articles/mi_qa3963/is_200001.
[5] Supfina, http://www.supfina.com/EN/142.htm.

CORRECTIVE POLISHING OF COMPLEX CERAMICS GEOMETRIES

Fritz Klocke[1], Christian Brecher[2], Richard Zunke[1] and Roland Tuecks[2]
[1] Department of Process Technology
Fraunhofer Institute for Production Technology, Aachen, Germany
[2] Department of Production Machines
Fraunhofer Institute for Production Technology, Aachen, Germany

INTRODUCTION

Advanced ceramics are primarily used in adverse environments and applications, due to their high hardness, remarkable corrosion resistance, low thermal expansion, high thermal shock resistance and low weight. Representatives are silicon nitride balls in bearing components and silicon carbide mirrors for astronomical optics devices. Furthermore, these non-oxide ceramics can be used by mold manufacturers for molding complex optics components out of glass. In order to obtain the low roughness requirements of the optical systems, a defect free surface and an accurate form is indispensable. Despite diverse scientific investigations and developments, today's process strategies for computer controlled polishing [1, 2, 3] are still insufficient. The high amount of time and effort needed for the design of robust strategies, especially for small samples and free formed geometries turn out as the biggest deficits.

The main ambition of the ongoing scientific investigations is an efficient design of polishing strategies (process parameters and polishing system) for a computer controlled process (referred to as zonal polishing). This paper presents the methodology which leads to a successful technology transfer from a conventional process (referred to as 2-dimensional) to a zonal polishing process. Important issues are the determination of stable process conditions with reliably high material removal rates (MRR) for the zonal correction of form deviations of complex geometries.

EXPERIMENTAL SETUP

Materials

The transfer of process strategies from "2-dimensional to zonal" is exemplified by processing of hot isostatically pressed silicon nitride as one of the most popular non-oxide ceramics. The specimen were ground by using diamond grinding wheels (2-dimensional) and polished for the investigations of influence functions (zonal), respectively. The default polishing systems use polyurethane foils as tools and ceria slurry based on deionized water.

Methods

Compared to zonal polishing the 2-dimensional process has a number of advantages in terms of relatively simplified process development and scientific investigations, such as high MRR, clearly measurable or even visible effects with respect to technological interactions and straightforward use of metrology of the processing results. Hence, the scientific understanding of process technological aspects can be elaborated with reasonable efforts and used to develop polishing strategies for commonly used materials.

However, this specific process is not capable of polishing free form surfaces which becomes more and more important in a variety of innovative applications. To overcome these limitations, the zonal polishing process can be used. Unfortunately, an apparent lack of understanding and the intricate procedure of investigations hinder the holistic development of polishing strategies for the zonal process. Therefore, the approach of this paper is to use the polishing strategies developed with an established, conventional polishing process (2-dimensional) and transfer these to a zonal polishing machine tool.

Based on theoretical considerations the optimization of the zonal process include practical investigations concerning the formation and stability of the influence function and the so called "foot-print", respectively. For this purpose, experiments with varying process parameters as pressure and relative speed as well as specific zonal process parameters, such as eccentric frequency and radius, were conducted. These preliminary investigations are of vital importance

for establishing a stable correction process of form deviations of complex geometries as former investigations in steel polishing proved [4].

Machine

The presented studies were carried out on a CNC-controlled polishing machine (2-dimensional process) and an adaptable 5-axes polishing module (zonal process) which was developed at Fraunhofer IPT [4, 5]. The required flexibility is ensured by the adaption of the polishing module to a 3-axes machine (FIGURE 1a). Due to the double V-kinematic structure featuring 5 degrees of freedom the module is capable of adjusting its alignment to continuously ensure a perpendicular angle of contact between tool and surface. Furthermore, an individual eccentric movement can be superimposed to the rotating polishing tool at different angles (FIGURE 1b), decisively influencing the characteristic removal profile of the tool. The applied polishing tools (FIGURE 1c) feature a flat plastic base body with a diameter of 12 mm and can be covered with various polishing foils. In addition to the position-controlled mode of the z-axis, the system can change to force-controlled mode in order to permanently assure a steady allocation of pressure in the process zone.

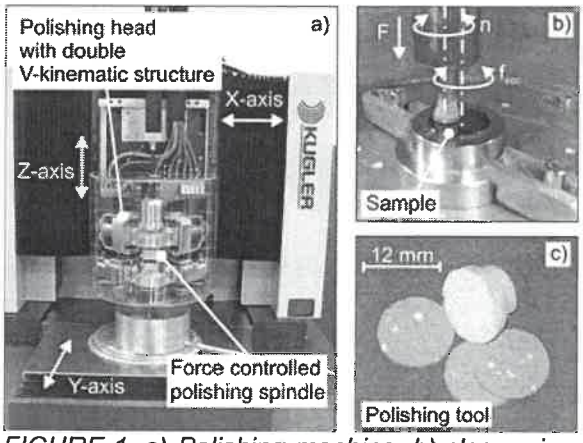

FIGURE 1. a) Polishing machine, b) closer view of process zone, c) tool with polyurethane foil.

In order to realize a corrective zonal polishing process a dwell-time based algorithm is used. As input data for this algorithm, the desired geometry is needed. In addition, a form measurement taken either by tactile or optical metrology is used to determine the local form deviation. The third input is the influence function of the zonal polishing tool which depends on process parameters and polishing system. The subsequent calculation results in a dwell-time controlled path of the polishing tool over the sample and particular process parameters of the polishing process. In order to allow corrections of form deviations on complex geometries a stable, reproducible and deterministically adjustable influence function is of great importance. TABLE 1 shows the parameter range of the polishing module for the design of experiments (DoE).

TABLE 1. Parameter range for the DoE.

Polishing force F	0.5 - 20 N
Force increment	0.2 N
Eccentric frequency f_{ecc}	1 - 10 Hz
Eccentric radius r_{ecc}	0.2 - 4 mm
Spindle revolutions n	500 - 5000 min^{-1}

Metrology

The MRR for developing efficient polishing strategies are quantified by weight measurements of the samples (2-dimensional process) and mathematically estimated by measuring the geometry of the influence function (zonal process), respectively. The latter is realized by using a Form TalySurf (tactical) measurement device. The surface quality was determined by a white light interferometer (optical).

RESULTS AND DISCUSSION

Removal Mechanisms

Former investigations [6] reveal satisfying results using ceria and diamond based slurries in a conventional polishing process of silicon nitride. Achievable MRR are up to 0.3 µm/min. The surface qualities of both polishing processes are highly reproducible and yield to optical surfaces (Ra 1-2 nm, Rt 20-30 nm). However, the use of ceria slurry results in a more efficient process compared to diamond slurry due to less machining efforts. While applying the same applied pressure, less spindle revolutions and certainly less monetary effort are needed. It can be assumed that the advantage of ceria slurry is based on an interaction of chemical and mechanical removal mechanisms as outlined in FIGURE 2. The beneficial process conditions can be explained by hydrolysis of the silicon nitride surface in aqueous solutions in combination with the so called "chemical tooth" ability of ceria [3, 6, 7, 8]. An indicator of the oxidation of silicon nitride by forming sodium hydroxide is shown by an increase of pH (FIGURE 2).

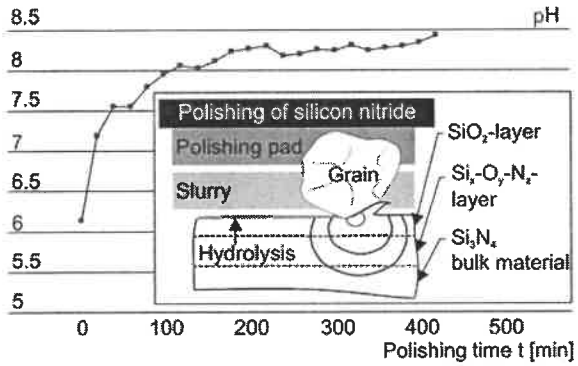

FIGURE 2. Assumed removal mechanisms of polishing silicon nitride with ceria slurry.

Tool Influence Function by Zonal Polishing

The previously identified polishing strategies are used for first experiments regarding the influence function of the zonal process. Taking the Preston Hypothesis for granted (EQUATION 1), a linear increase of the MRR should be realized starting from the center of the rotating tool. FIGURE 3a shows the characteristic W-profile by the adjusted parameters pressure p and relative velocity v_r. The Preston coefficient K_P represents various other influences on the process.

$$MRR = K_P \cdot p \cdot v_r \quad (1)$$

However, the maximum material removal is not found on the outer diameter but at one half to two thirds of the radius of the polishing tool, forming the influence function. Looking further towards the boundary of the influence function, the removal depth declines steadily. This simple trial emphasizes the fact that either an inhomogeneous pressure profile or an influence of the relative velocity in the gap between tool and sample is responsible for the removal profile. The influence function is characterized by depth d_{IF} and radius R_{IF}. Preliminary investigations on steel polishing have shown that R_{IF} can be used for adjusting the eccentricity of the polishing tool movement in order to achieve a Gaussian profile of the influence function [2]. The investigations allowed to determine the ratio of R_{IF} and eccentric radius r_{ecc} to 1:2. By using this value and an experimentally identified value for the eccentric frequency f_{ecc} of 4 Hz the required Gaussian profile can be achieved (FIGURE 3b). The appropriate volume of removed material V_{IF} was computed by importing the 2D-graph of a Form TalySurf in a specially developed Matlab program and amounts to 0.005 mm³ on average (after polishing time of 240 s).

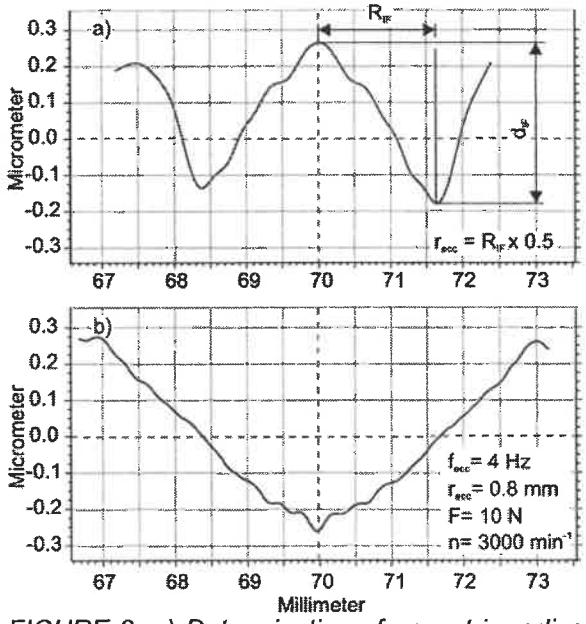

FIGURE 3. a) Determination of eccentric radius as the main parameter for achieving the required (b) Gaussian profile of the influence function.

Investigations of Typical Process Parameters

As the process parameters lead to reproducible Gaussian profiles the time related stability and corresponding MRR are verified. FIGURE 4 shows a slight non-linearity between the removed material V_{IF} after 120 s and 240 s, which can be explained by incomplete saturation of the polishing foil with ceria slurry after a process duration of 120 s.

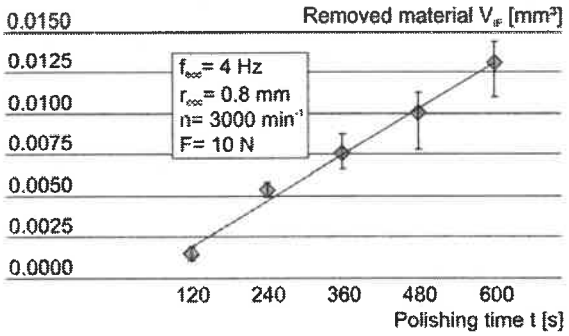

FIGURE 4. Evaluation of process stability.

Therefore, a preparation of the polishing tool before starting the intrinsic polishing process was established. A linear increase of the material removal with increasing dwell-time (FIGURE 4) is a main requirement for a form correction. The overall process stability was proven by up to 3 hours. For further understanding, a variation of the tool revolutions over constant applied pressure and vice versa

have been conducted. Unlike the results of investigations of the steel polishing process [4], the influence of changes of relative velocity on MRR is far more sensitive. Increasing revolutions lead to an increase of the MRR (FIGURE 5a). Furthermore, FIGURE 5b shows that an increase of normal force and applied pressure, respectively, leads to rising MRR. The behavior is approximately linear.

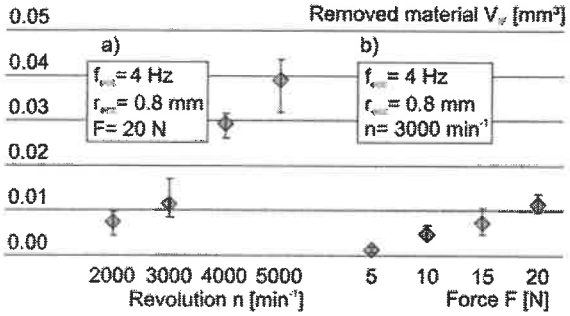

FIGURE 5. Dependency of material removal on (a) relative velocity v_r and (b) process force F.

First Steps Towards Corrective Polishing

Taking advantage of the shown process stability and reproducibility the potential of first steps towards corrective polishing is given. Based on the above mentioned process parameters a stable Gaussian profile of the influence function can be secured. Together with the measured form deviation as well as the desired planar surface the algorithm provides a dwell-time based CNC-program. FIGURE 6 reveals first results of the zonal polishing process of silicon nitride using polyurethane foils and ceria slurry.

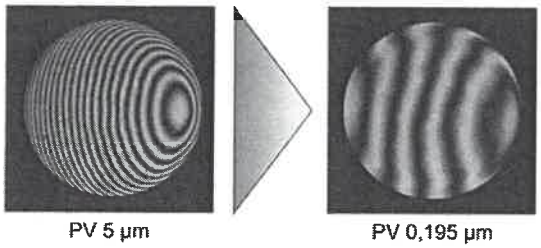

FIGURE 6. Correction of spherical form deviation on a planar workpiece out of silicon nitride by zonal polishing.

CONCLUSION

This paper showed the results of scientific studies with the goal of shortening the development of a stable and reproducible polishing process for corrective machining of complex ceramics samples. The transfer was successful by rendering unnecessary intensive preparatory work on polishing strategies and resulted in satisfying overall results with a high and reproducible MRR and surface quality. In terms of the machine parameters, the eccentric frequency shows only a small impact for the profile formation. However, the eccentric radius, the applied normal force and the relative velocity do have significant impact on the formation of the influence function determining the process efficiency. These technological insights were used to accomplish a first corrective polishing by the zonal process. The ongoing research does include the expanding of geometrical complexity up to free formed surfaces of various advanced ceramics. The results will be presented in future publications.

ACKNOLEDGEMENTS

We sincerely thank the German Research Foundation (DFG) for financial support of the Collaborative Research Center SFB/TR4 (RWTH Aachen and University Bremen (Germany), Oklahoma State University at Stillwater (USA)).

REFERENCES

[1] Bingham, R.G., Walker, D.D., Kim, D.-H., Brooks, D., Freemann, R., Riley, D., 2000, A Novel Automated Process for Aspheric Surfaces, Proc. SPIE, 4093/10:445-450

[2] Yi, A., Hezlep, M., Pol, T., 2004, A Computer Controlled Optical Pin Polishing Machine, J. Materials Processing Technology 146/2:156-162.

[3] Evans, C.J., Paul, E., Dornfeld, D., Lucca, D.A., Byrne, G., Tricard, M., Klocke, F., Dambon, O., Mullany, B.A., 2003, Material Removal Mechanisms in Lapping and Polishing, CIRP Annals, 52/2:611–633.

[4] Brecher, C., Wenzel, C., 2006, Kinematic Influences on the Formation of the Footprint During Local Polishing of Steel, WGP Annals, XIII/1:23-26.

[5] Weck, M., Wenzel, C., 2004, Adaptable 5-axes Polishing Machine-head, Production Engineering, 11/1:95-98.

[6] Klocke, F., Zunke, R., Dambon, O., 2007, Chemo-mechanical Polishing of Silicon Nitride, Proc. euSPEN, 2:356-359.

[7] Jiang, M., Komanduri, R., 1998, On the finishing of Si3N4 Balls for Bearing Applications, Wear, 215/1:267-278.

[8] Hu, Y.Z., Gutmann, R.J., Chow, T.P., 1998, Silicon Nitride Chemical-mechanical Polishing Mechanisms, J. Electrochem. Soc., 145/11: 3919-3925.

POLISHING-GRINDING – AN INNOVATION FOR MANUFACTURING OF HIGH PRECISION OPTICS

F. Klocke[1], A. Gruentzig[1], D. Hollstegge[1], C. Voelker[1], O. Dambon[1], M. Herben[1], B. Bulla[1], D. Czarlay[1], J. Riegel[1]
Fraunhofer Institute for Production Technology
Aachen, Germany

INTRODUCTION

ELID-grinding is mainly used for reproductive components as moulds or single items and prototypes. In this field, several iterating grinding passes with depths of cut of a few micrometers are acceptable. It is hardly found in industrial series manufacturing of components. The application of ELID has been investigated as a method to reduce process time for transmissive optical components, Figure 1. In order to remove a stock height greater than the depth of sub-surface damage of previous grinding steps in a time span which still reduces overall process time, much higher depths of cut than employed at bench-scale are needed. The challenge is here to obtain the desired surface finish as well as the stock removal. Because of this, this paper will give an introduction to the diverse material removal mechanism which occur during the ELID-grinding process in Polishing-Grinding mode.

MATERIAL REMOVAL MECHANISM IN GRINDING

A brittle material, like glass, can be deformed through different mechanisms when machined. If the critical resolved shear stress within the lens exceeds the elastic yield stress, there will be a change from one of reversible energy storage (elastic stretching) to one of irreversible energy dissipation mechanism of deformation (microcrack formation, macroscopic fracture propagation, dislocation motion, etc.).

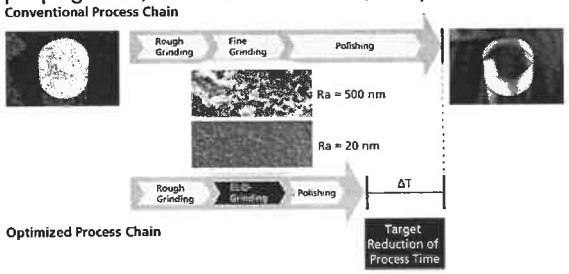

FIGURE 1. Conventional vs. Optimized Process Chain

Ductile regime grinding

In the mechanism of reversible energy storage, also known as ductile-regime grinding, one can clearly identify some advantages when compared to the brittle-regime grinding, like no crack formation, free brittle fracture surface and the reduction of the finishing process through polishing (Klink, 2003). The possibility of utilization of this ductile behaviour, in which the work piece material demands an infeed in sub-micrometer range, is only possible since high precise machine-tools are available. Many authors describe and suggest reference values while choosing process parameters which enable brittle and hard materials to be ground in a ductile-regime mode (Koch, 1991). Through the reduction of the infeed per cutting edge under a critical depth of cut, it is also possible to obtain a surface without cracks in the grinding process. Very sharpened edges and a big infeed per cutting edge lead to brittle fracture, while the cutting velocity doesn't play a role in achieving ductile-regime grinding (Koch, 1991). This transition from brittle to ductile material removal in grinding at small cutting depths can be explained by considerations of material removal energy, and this leads to a critical depth of cut model, presented and discussed by Klink (Klink, 2003).

ELID-GRINDING PROCESS OVERVIEW

The ELID-grinding system is composed of the following components: a metal-bonded diamond wheel, an ELID DC-pulse power source, a commercial grinding fluid (working as an electrolytic agent) and a fixed copper electrode. Figure 2 shows a schematic of the ELID-grinding system. In this system, a copper electrode about 1/6 the area of the grinding wheel is set above the wheel, with a gap between both ranging from 0,1 to 0,3 mm. This ELID DC-pulse power source is used to apply a positive charge to the grinding wheel and negative charge to the electrode; thus the grinding wheel is the anode and the electrode is the cathode. The voltage generated between anode and cathode electrolytically decomposes the grinding fluid,

generating hydroxyl ions. These ions OH- are then attracted to the positive charged component (grinding wheel), being processed and resulting in the formation of a stable oxidized layer there (Ohmori, 2002).

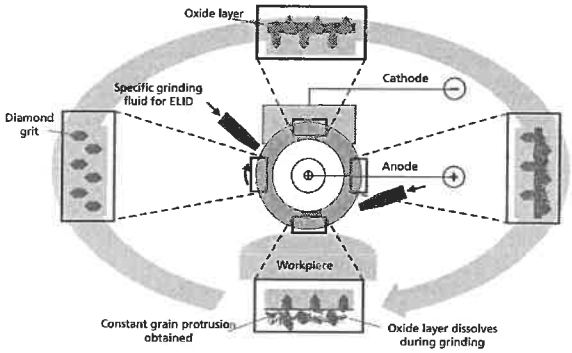

FIGURE 2. Schematic of the ELID-grinding system

This oxidized layer consists Fe_2O_3 and is formed on the grinding wheel surface by the following reactions (Klink, 2003):

$$Fe \Rightarrow Fe^{2+} + 2e^-$$

At the cathode, hydroxyl ions and hydrogen gas are generated:

$$H_2O + 2e^- \Rightarrow H_2 + OH^-$$

Ionized Fe and hydroxyl ions react:

$$Fe^{2+} + 2OH^- \Rightarrow Fe(OH)_2$$

This substance finally changes into oxide at the anode:

$$4Fe(OH)_2 + O_2 \Rightarrow 2Fe_2O_3 + 4H_2O$$

FIGURE 3 shows a schematic of the reactions involved in the process.

Through the formation of this oxidized layer on the anode's surface, the metallic bonding material of the grinding wheel is removed and replaced, leading to the constant formation of protruded grains on the wheel's surface. Due to this effect the ELID-grinding technique is considered a dressing process.

The Moore Nanotech FG500 machine was used for carrying out the experiments. The machine, its specifications and a detailed view of the ELID-system installed in the machine are presented in Figure 4.

MATERIAL REMOVAL IN ELID-GRINDING

It is supposed that the application of ELID alters the material removal mechanisms of the grinding system to a great amount. In abrasive machining processes, it can be differentiated between two- and three-body abrasion.

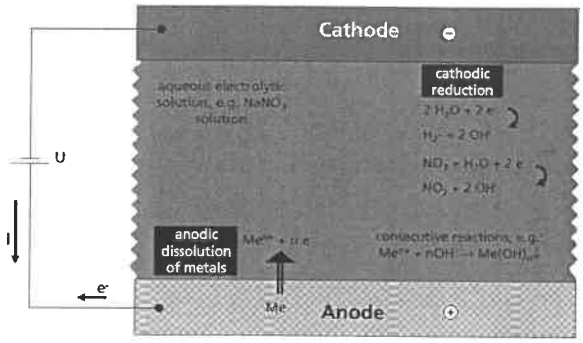

FIGURE 3. Principles of electro chemical machining

Two-body abrasion is caused by bound grains, employed usually in grinding processes, while three-body abrasion is caused by rolling or sliding grains. In polishing and lapping processes both types occur. The ELID-process is classified as a grinding process, but the oxidation of the bond can lead to premature grain breakout (Li, 2005). This reduces the number of grits on the surface and elevates the quantity of loose abrasives in the ELID-process which may have influence on the material removal and wear mechanisms. These influences will be discussed in this section.

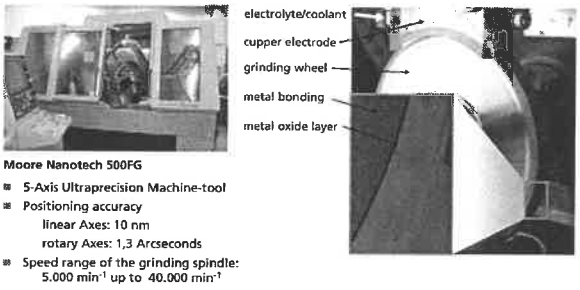

FIGURE 4. Setup of the ELID-system at the Moore Nanotech FG500 Machine

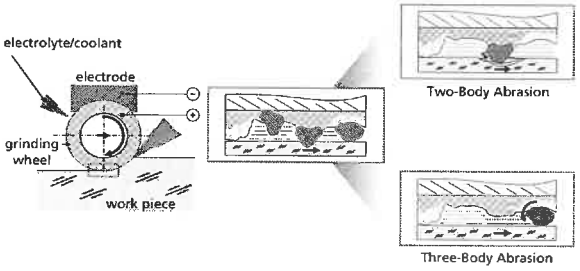

FIGURE 5. Material removal mechanisms in ELID-grinding

Independent from whether two- or three-body abrasion, the interactions between the abrasive grains and the work piece material during the abrasive finishing processes can be grouped into cutting (material removal process), ploughing (material displacement process) and sliding (surface modification process). Crack formation is not only an issue in grinding, but also in three-body abrasion systems. Generally, plastic deformation is favoured when the load applied on the abrasive particle is small, the abrasive grain is blunt or blunts during machining and the ratio of fracture toughness to hardness of the material is high (Marinescu, 2007). Crack formation has a significant influence on the mechanical strength of the work piece. A piece of glass breaks when two conditions coincide. The first is the presence of tensile stress at the surface and the second is the presence of a defect in the region of the tensile stress. The grinding of glass introduces such micro-defects or -cracks to the surfaces, which extend to depths that lie below the common surface roughness. The depths of the micro cracks depend on the grain sizes of the machining tools and are statistically distributed. As a rule of thumb, narrow grain size distributions lead to comparatively narrow strength distributions for ground surfaces. Decreasing grains sizes result in shorter micro cracks and in higher strengths consequently (Schott, 2004).

Chip cutting

In classical grinding, the removal of chips is the main material removal process. Figure 6 illustrates the cutting mechanisms for an anchored grit. The main influence factor is the chip cross sectional area or respectively grit depth of cut. With increasing penetration depth first elastic and then plastic deformation occurs. At further indentation of the grains chip formation takes place. Then micro cracks propagate and lead to fracture, before fracture happens over the complete scratch length.

Loose abrasives

The continuous dressing of the wheel bond facilitates breaking out of abrasive grains or complete bond fragments. As well as in lapping and polishing processes, where the grains get temporarily anchored in the polishing or lapping pad, the above mentioned broken-out particles in the working zone can get anchored again in the wheel surface and cause two-body-abrasion effects, or move with a rolling motion between the moving surfaces, which can be described by three-body abrasion. The machining effect of free abrasive grits in the grinding wheel is comparable to a lapping process.

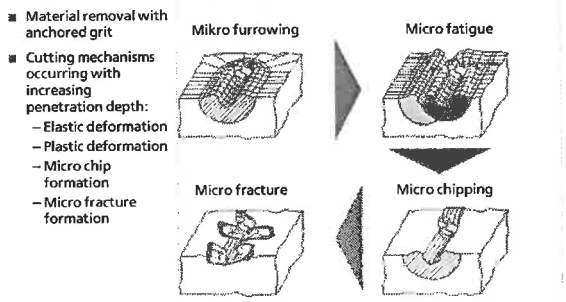

Figure 6. Cutting mechanism in dependence of grit depth of cut (Zum Gahr, 1987)

The similarities are a lapping wheel consisting of cast iron or other metals and a slurry with diamond abrasives. Though, the contact zone is much larger in lapping due to the surface contact, compared to a line or point contact in grinding, resulting in higher contact pressure in the grinding process. The relative speed between tool and work piece is much higher in the grinding process. The abrasive medium concentration is expected to be lower in ELID-Grinding.

When referring to lapping and polishing processes, it has to be taken into account that "wear" not only is used for tool wear, but material removal is often described as a material wear mechanism. Two-body abrasion is considered to produce wear on the work piece rated three times greater than three-body mechanisms using the same loading condition (Marinescu, 2007). Concordantly, Kaller states that the material removal in polishing processes is obtained mainly by embedded grains, that is to say by two-body abrasion (Kaller, 1957). Several researchers have proposed alternative classifications for abrasive grit and workpiece interaction, because this two concepts can create misinterpretations. Gates proposed to take into account the severity of wear from a tribological point of view, derived from a set of factors as particle size, particle shape and contact stress (Gates, 1998). The contact stress is distinguished in high-stress (or grinding) and low-stress (or scratching) abrasion whether the grains are broken during abrasion, as fracturing could create sharp cutting edges and give higher wear rates (Marinescu, 2007). In the case of the rotational grinding process, fracture of loose abrasive grains may have a smaller influence

because the grains leaving the grinding zone will be washed away with the coolant and will not participate in the grinding process. Another group under Trezona and Allsopp proposed the expressions "grooving abrasive wear", in which the same region of the abrasive grain is in contact with the workpiece throughout the process, and "rolling abrasive wear" when the surface of the grain in contact is repeatedly varying (Trezona, 1999). They state that both mechanisms could be produced in a nominally three-body situation by varying the normal load (Marinescu, 2007). Applying this theory to ELID-grinding, grooving abrasion is to be expected for loose abrasives, because the normal load emerging in grinding processes.

TEST RESULTS

The experiments have been carried out with a single-point contact grinding kinematics for asphere production. The influence of the polishing effect with the same grinding wheel used in ELID mode compared to the conventional mode clearly showed a strong advantage in terms of surface roughness. Figure 7 shows an overview of different materials ground in conventional and ELID-grinding mode with a strong influence visible on glass.

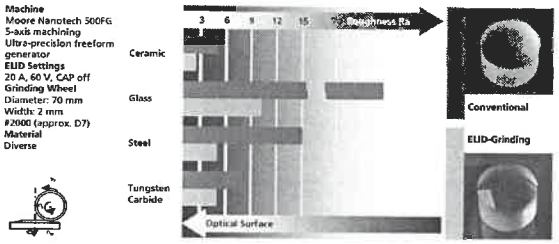

FIGURE 7. ELID-grinding results

The ELID-process is using a pulsed current. The duty ratio can be varied between 0% (no ELID) and 100% (continuous current). The higher the duty ratio the "stronger" the electrochemical wear and oxide layer buildup at the grinding wheel. A thicker oxide layer implies a high rate of loose abrasives bound within the soft surface layer which cause a high level of three-body abrasion, Figure 8. Without ELID or with a low duty ratio of 20 % there is still a brittle-regime grinding mode visible. As soon as the amount of oxide layer production reaches a certain amount, ductile-regime grinding occurs. The higher the duty ratio the higher the influence on the surface of the glass lens.

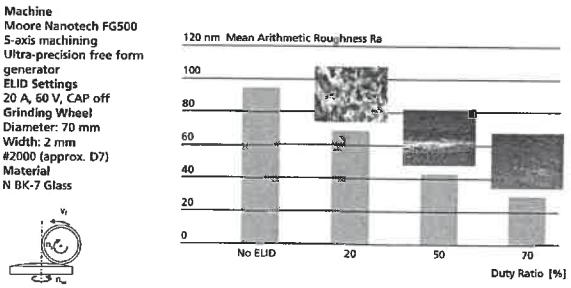

FIGURE 8. Influence of duty ratio over the surface roughness on N-BK7 Glass

CONCLUSION

ELID-Grinding offers a new approach for the grinding technology. It allows the stable employment of grinding wheels with very small grit sizes below 7 µm in diameter. However, material removal mechanism are more diversified than in any other conventional grinding process. It is a combination of many mechanism which can be found in grinding as well as in polishing processes. Within this paper two major mechanically based removal mechanism have been discussed. Still under investigation is the chemically induced influence of ELID on the material removal process. The ELID technology has shown an impact on steel, metal carbides and ceramics. The highest influence however could be seen on optical glass. Future work will focus in particular on the polishing behavior – mechanically and tribo-chemically – of the formed oxide layer within the ELID-process.

REFERENCES

[1] Gates, J.D., 1998, "Two-body and three-body abrasion: a critical discussion", Wear

[2] Kaller, A., 1957, "Der Polierprozess von Glas", Jenaer Jahrbuch

[3] Klink, A., 2003, "Ultra-precision machining of BK7 glass – A comparison between the 5axis Superabrasive Grinding Centre Edgetek and the High Performance 3axis Nanogrinding Machine Tetraform C", Studienarbeit WZL, RWTH Aachen

[4] Koch, E. N., 1991, "Technologie zum Schleifen Asphärischer Optischer Linsen", Dissertation of the RWTH-Aachen, 140p.

[5] Li, J. and Li, J. C. M., 2005, "Mechanisms of sawing of BK7 glass by electrolytic in-process dressing", Journal of Materials Processing Technology

[6] Marinescu, I. D., Uhlmann, E. and Doi, T. K., 2007, "Handbook of Lapping and Polishing", CRC Press

CHARACTERISATION ON THE SURFACE QUALITY AND REMOVAL OF WAFER WITH VARIABLE MACHINING CONDITIONS IN THE WAFER POLISHING SYSTEM

Jung Taik Lee[1], Jong Koo Won[1], and Eun Sang Lee[2]
[1]School of Mechanical Engineering
INHA University
Incheon, Korea
[2]Department of Mechanical Engineering
INHA University
Incheon, Korea

INSTRUCTIONS

Most semiconductors are built on single crystal silicon wafers. The industry has already had several experiences in moving to larger wafer size. Wafer diameter has increased steadily from less than 50mm in the 1970s to 200mm today and possibly to 300mm near future. The number of chips can be produced on a 300mm wafer is roughly 2.5 times that of 200mm wafer[1].

As the starting materials for fabrication of most microchips, silicon wafers must be very flat in order to print circuits on them by lithographic processes. Wafer flatness directly impacts device line-width capability, process latitude, yield, and throughput[2]. The feature sizes of semiconductor devices will continue to decrease and this will demand increasingly flatter wafers[3].

For wafers manufactured by a traditional manufacturing method, only small percentages meet tight flatness specifications. Wafers that do not meet the specifications are often rejected, causing high yield loss. Innovative manufacturing methods are necessary to produce flatter wafers at an affordable cost. Wafer polishing can be optimized by several process parameters such as equipment variables (table and head speed, down force, and slurry flow rate) and consumables (pad, backing film and slurry). Among the consumables for polishing process, especially, pad and slurry play very important roles in the removal rates and within-wafer no uniformity for global planarization ability of polishing process. The pad accomplishes the removal of materials by relative motions between the pad and the wafer chemically attacked by the slurry. Therefore, the pad structure and its material properties are very important in determining polish rate and planarity of a polishing process. Meanwhile, the pad conditioning is used to regenerate the pad surface by breaking up the glazed areas generally using the de-ionized water (DIW) with diamond conditioner.

Therefore, Wafer polishing is very important process concerning a point of view to stabilize wafer finally before executing the device process on the wafer. In this study, the machining conditions which have a major influence on the process of polishing were adapted to temperature. This research investigated the surface characteristic that applies a machining temperature. The temperature on polishing processing is measured by infrared sensor. In this study, the relationship between the surface roughness of Si-wafers and the temperature of polishing processing is analyzed.

WAFER POLISHING SYSTEM

Wafer polishing is process combined mechanical factor with chemical factor. Mechanical factor is a removal machining with the polishing grain within slurry. Chemical factor is a chemical response phenomenon over the wafer surface. Mechanical factors are associated with polishing pad, polishing grain and physical correlation on the wafer surface. Chemical factors are mainly decided by viscosity of slurry, speed of wafer, hardness of grain, characteristics of pad and lubrication characteristic about the wafer curvature. And chemical effect of slurry make surface soften or material removal rate heighten[4].

EXPERIMENT

Concept

FIGURE 1. describes that temperature infrared sensor measure an available temperature in wafer polishing. In variable temperature, there is

a possibility of knowing the change of temperature which it follows in speed and pressure. The experimental set up used the load cell to get the signal of the applied pressure against the polishing pad in real processing. A load cell measuring the normal force is attached between the pneumatic actuator and the member of carrier head and data acquisition system is installed.

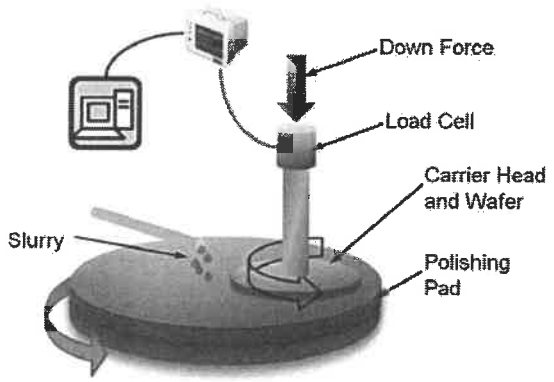

FIGURE 1. Schematic diagram of experiment

Experiment Conditions

During the experiments to determine the surface roughness on applied pressures and working speed, double side polished 300mm wafer was used on a stacked SUBA/IC600 polishing pad. The slurry used is composed of de-ionized wafer, Fujimi 3950.

TABLE 1. The experiment conditions

Speed(rpm)	Applied Pressure (MPa)	Slurry Ratio	Processing Time (sec)
10	0.1	1:10 (Slurry: DI Water)	600
	0.2		
	0.3		
20	0.1		
	0.2		
	0.3		
30	0.1		
	0.2		
	0.3		

This slurry is commercial colloidal silica based slurry with particle size in the 30-40 nm range. Preliminary researchers suggest that the non-uniformity is mainly determined by the ratio between carrier speed and platen speed and the wafer size. For achieving a speed to be closed to each other, the head and platen are rotated with the same or nearly angular speed.

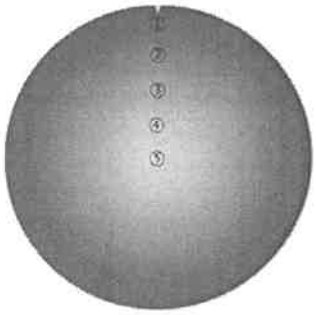

FIGURE 2. Measuring points on the polished 300mm wafer

Experimental parameters are shown in TABLE 1. Surface roughness was measured by non-contact surface profiler, NanoView.
FIGURE 2. shows measuring spots and sequences on the experimental wafer. The average value of five points was adopted as surface roughness.

RESULTS OF EXPERIMENT

FIGURE 3. shows the pressure variation with down force and table speed. When down force is 0.1MPa, the result of FIGURE 3. describe that the measured pressure with load cell kept decrease at the table speed of 20rpm, pressure is increased after 20rpm. In the case of 0.1MPa, pressure was irregularity changed owing to smaller down force.

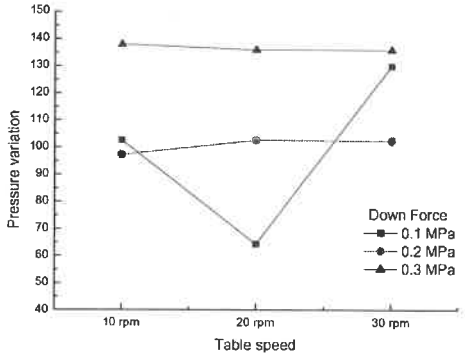

FIGURE 3. The down force variation in the processing time

When down force was fixed to a 0.2MPa and 0.3MPa, the pressure variation is a small variation according to increasing of table speed. In the case of 0.2 MPa and 0.3 MPa, pressure

was a small variation owing to an enough down force. It shows the force evolution with pressure and it is seen that force, does not depend on the table speed when pressure is enough. When down pressure values are too small force depends on table speed, as it can be seen in FIGURE 3.

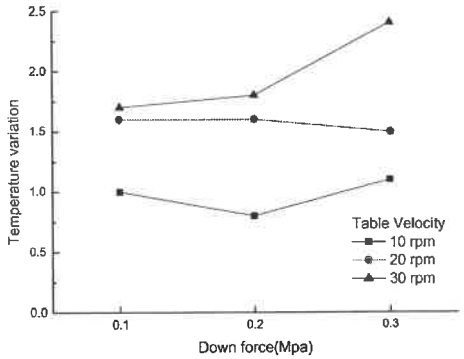

FIGURE 4. The mean value of temperature variation during processing

Temperature variation is the important factor of wafer final polishing. FIGURE 4. shows the temperature variation according to down force. When down force is 0.1MPa in table speed 10rpm, temperature variation is 1 ℃. When down force is 0.3MPa in table speed 10rpm, temperature variation is 1.1 ℃. The temperature variation is effected by down force. The graph shows the temperature variation is effected with down force less than speed.

And FIGURE 5. shows the graph of surface roughness as a function of table speed each down force is measured at five points illustrated FIGURE 2. The surface roughness is measured by NanoView and each point has mean value of five times measurements. The graph of 30rpm speed at 0.1MPa takes the irregular surface roughness distribution as shown FIGURE 5. (c). The value of surface roughness at point 4 is 6.30nm. FIGURE 5. (a), the graph line illustrates slope almost uniform in each speed. Point 2 at 30rpm gets the lowest value which is 1.55nm.

FIGURE 6. shows the results of final polishing experiments with the variation of surface roughness. The surface roughness was increased according to increase of table speed. The reason for this phenomenon is a result of the decreasing temperature variation.

Temperature variation is small and down force is high in the optimum condition. The first important factor is a temperature variation and the second important factor is a down force. This study is accomplished with an ultra-precision surface in wafer final polishing.

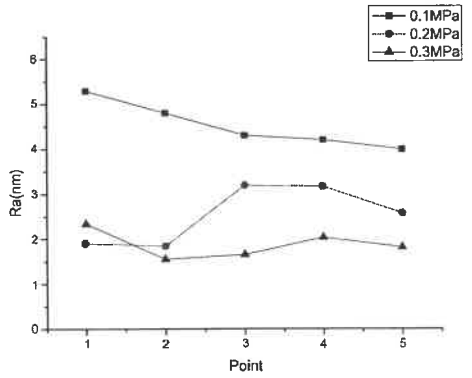

(a) 10 rpm

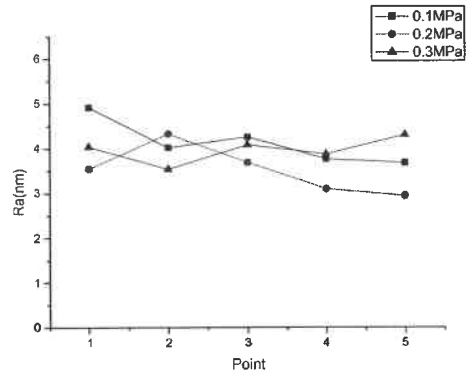

(b) 20 rpm

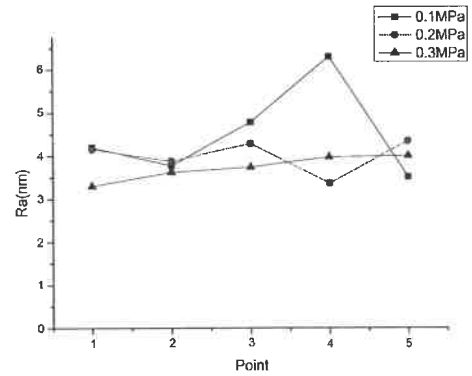

(c) 30 rpm

FIGURE 5. Surface roughness of 5 points as a function table speed

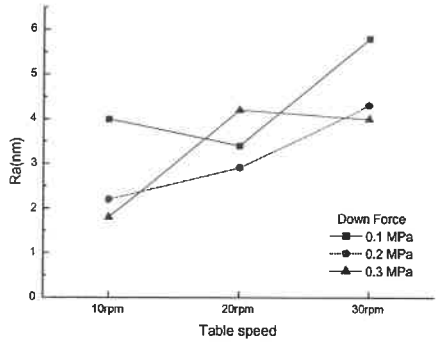

FIGURE 6. Comparison of surface roughness with down force and table speed

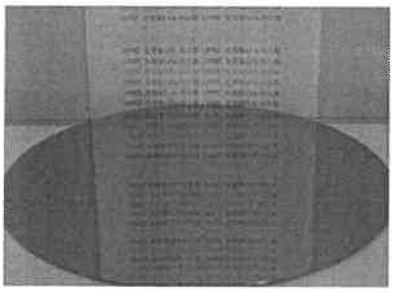

FIGURE 7. Polished Si-wafer after experiments

CONCLUSIONS

Wafer polishing makes the surface planarization to achieve a high-quality. The processing speed and applied down force are an important parameter of polishing process. This study investigated the surface characteristics between the polishing pad and the wafer carrier unit by wafer polishing system.

In several working parameters for 300mm wafer polishing process, especially, the range of the applied pressure, the polishing pad and carrier head speed is investigated very important roles in the surface roughness of polished wafer.

The loadcell is used to get the signal of the down force against the polishing pad in actual processing. The down force variations obtained by loadcell are different from indicated pressures in the gauge of machine at 0.1 MPa, 0.2MPa and 0.3 MPa as variations of speed.

Temperature infrared sensor measures an available temperature in wafer polishing. The surface roughness of experimental workpiece was measured by non-contact surface profiler.

With decreased table speed, surface roughness clearly improved. The result of experiment showed the good surface roughness with decreased table speed. In the wafer final polishing, surface roughness was improved according to decrease of the temperature variation.

The optimum condition is 0.3 MPa, 10 rpm and 10 min, the surface roughness of these conditions is 1.8nm. In this experiment result, the good surface roughness was obtained with a fast rotating speed, a small temperature variation and a high down force. The small variation of temperature makes a superior surface roughness.

ACKNOWLEDGEMENT

This topic of research is by INHA UNIVERSITY Research Grant.

REFERENCES

[1] Z.J. Pei, A Study on Surface Grinding of 300 mm Silicon Wafers, International Journal of Machine Tools & Manufacture. 2002; 42: 385–393

[2] M. Kulkarni, A. Desai, Silicon Wafering Process Flow, US Patent 6,294,469. 2001

[3] R. Vandamme, Y. Xin, Z.J. Pei, Method of Processing Semiconductor Wafers", US Patent 6,114,245. 2000

[4] Y.J. Shin, E. S. Lee, J. H. Kang, Identification of the Mechanical Aspects of Material Removal Mechanisms in CMP, Journal of the Korean society of machine tool engineering. 2000; 5:7-12

INFLUENCE OF POLISHER SURFACE STRUCTURE ON ULTRA-SMOOTHNESS POLISHING CHARACTERISTIC OF MAGNETIC DISK SUBSTRATE

Masataka TAKAGI[1], Heiji YASUI[1], Kouhei KUSABA[1], Noriyuki FUKAKUSA[1]

[1] Graduate School of Science and Technology, Kumamoto University, Kumamoto city, JAPAN

INTRODUCTION

To produce the low cost compact magnetic disk of high storage capacity, the high removal rate and ultra-smoothness polishing technique of the magnetic disk substrate has been strongly required. To build the selecting method of the optimum polishing conditions, for the requirement, is one of the most important matters. The polisher has large influence on the polishing characteristics of magnetic disk substrate[1].

The new polisher used firstly in polishing operation is manufactured by buffing of the new pad which has no pore on the surface just after manufacturing. The polisher reaches its life due to polishing operation. The polisher is refreshed by dressing the surface after reaching the polisher life. In the process of the polishing and dressing operation, the polisher wears. From the results, the polisher surface structure changes because the polisher surface structure can't be manufactured homogeneously in the polisher surface layer. The change of polisher surface structure has the influence on polishing characteristics. As the result, in case the polisher surface structure is not suitable for the required polishing operation, the polisher is exchanged to new polisher by detaching and re-attaching from and to polishing plate. The interval from attaching to detaching influences largely on polishing cost.

From the point of view, in the report, the influence of polisher surface structure on polishing characteristics of magnetic disk substrate is investigated.

MANUFACTURE OF POLISHER

Polisher used is manufactured by buffing the film pad made of wet process method as shown in Fig.1. It is a so-called suede type polisher which is composed of the PET base material with the nap layer. Nap layer is manufactured by wet process method of the polyurethane. The outmost surface just after manufacturing the pad has no pore like skin. This surface is opened pore by buffing with buffing roller. Buffing is done by feeding through the clearance between buffing roller and support roller. Buffing roller has the sandpaper on the roller surface for buffing.

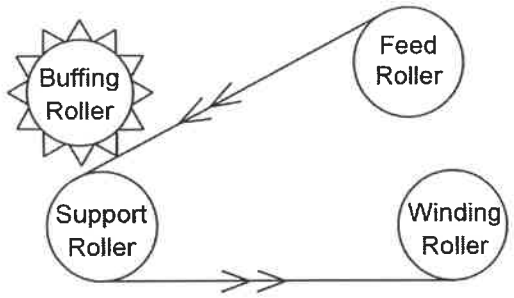

FIGURE 1. Diagram of polisher manufacturing process

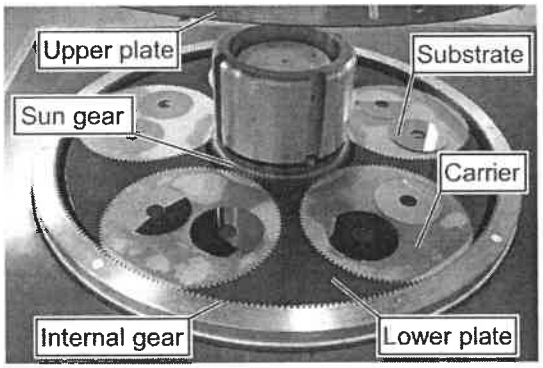

FIGURE 2. Double side polishing machine

In the research, one group of polisher samples is prepared by buffing the same depth using various kinds of the mesh size of sand paper. The other is prepared by changing the buffing depth of cut from the pad surface using the same sand paper. The manufacturing of pad and polisher is made by Fujibo Ehime co., Ltd.

The influence of polisher surface structure on polishing characteristics is investigated by examining the influence of the polisher surface roughness and pore size on the removal rate,

TABLE 1. Experimental conditions

Workpiece	NiP plated aluminum magnetic disk substrate (3.5inch type)
Polisher	Suede type
Polishing fluid	Abrasives : Alumina ϕ 1μm Supply flux *Lg* : 100ml/min
Polishing conditions	Polishing pressure *P* :10kPa Platen rotation : 30rpm

TABLE 2. Physical properties of polisher after buffing of pad

	unit	#180buff	#240buff	#320buff
Thickness	μm	770	770	780
Density	g/cm^3	0.46	0.47	0.46
Compressibility	%	19.6	20.1	18.9
Elasticity	%	94.4	93.2	95.5
Hardness	°	61.5	61.5	62.5
Pore size	μm	40.9	40.5	38.0

polished disk surface waviness and roll-off. However the polishing process of magnetic disk substrate is classified by two stages, that is, the first roughly polishing stage and the second smoothly polishing stage. In the experiment, the characteristics are examined in the first polishing stage.

EXPERIMENTS

The double side polishing machine used in the experiment is manufactured by Speedfam co., Ltd. (9B-5P) . Figure 2 shows the set-up state of substrate on the machine. The formal polishing experiment is done after pre-polishing of about 15 minutes. The main experimental conditions are shown in Table 1. Magnetic disk substrate used is the nickel phosphorus electroless plating aluminum type of 3.5 inches. The alumina abrasive size contained in the polishing fluid used is grain diameter of 1μm. The polishing fluid supply flux is 100ml per minute. The surface waviness of polished substrate is measured with the optical surface roughness measuring instrument (New View 5022 made by the Zygo Corporation).

INFLUENCE OF BUFFING SAND PAPER

The physical properties of polisher buffed by the sand paper of mesh size of #180,240 and 320 are shown in Table 2. The physical properties, that is, thickness, density, compressibility, elasticity, hardness, and pore size are like

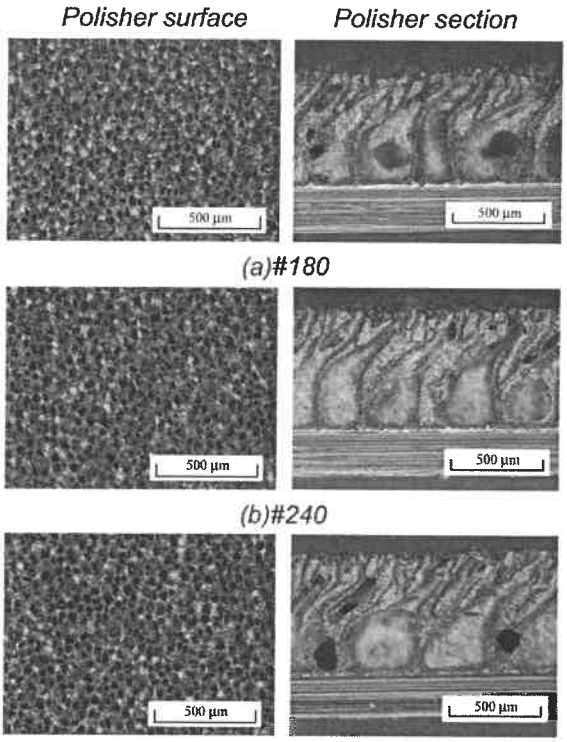

FIGURE 3. SEM picture of pad by different sandpaper number

TABLE 3. Polisher surface roughness after buffing

	#180buff	#240buff	#320buff
Ra μm	6.3	5.4	4.1
Rz μm	29.4	25.3	20.1
Ry μm	40.0	34.8	27.9

almost the same. The reason is considered why the buffed depth of 120μm is considerably thiner than the pad thickness of 770μm.

Figure 3 shows the surface and section of polisher after buffing the pad with the sand paper of mesh size of #180,240 and 320. TABLE 3 shows the surface roughness of polisher as shown in Fig.3 after buffing the pad. From the table, the surface roughness is found to become larger for smaller mesh size of sand paper. The reason is considered why the abrasive grain of sand paper of smaller mesh size is pressed up to deeper surface layer because grain number per unit area in sand paper of small mesh size is less than large size.

Figure 4 shows the relationship between the surface roughness of polished substrate and polisher surface roughness. The polishing time

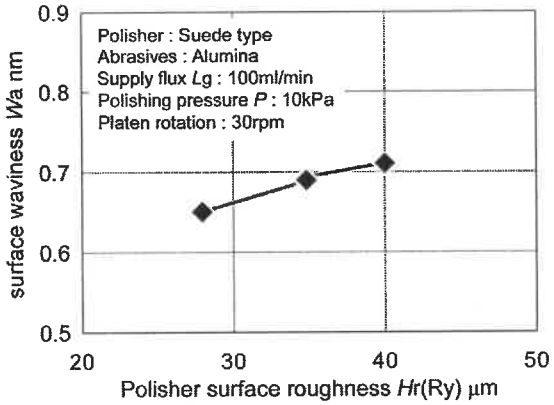

FIGURE 4. Relationship between surface waviness and polisher surface roughness

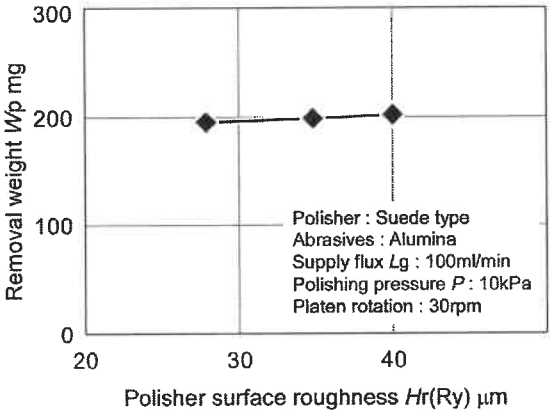

FIGURE 5. Relationship between removal weight and polisher surface roughness

is 5minute. It is clear that the surface roughness is larger for larger surface roughness of polisher. It is considered why the contact pressure of polisher with the substrate in large surface roughness is higher than small surface roughness because the number of contact points in large surface roughness less than small surface roughness

Figure 5 shows the relationship between the substrate removal weight and polisher surface roughness (Ry). It is seen from the figure that polisher surface roughness has little influence on the removal weight. The removal weight is related to the product of contact pressure and number in the contact of polisher with substrate. The result as mentioned above is considered why the product in large surface roughness becomes similar as small surface roughness.

INFLUENCE OF BUFFING THICKNESS

The section of polisher after buffing to various kinds of depths from the pad surface is shown in Fig.6. It is found from the figures that the upper

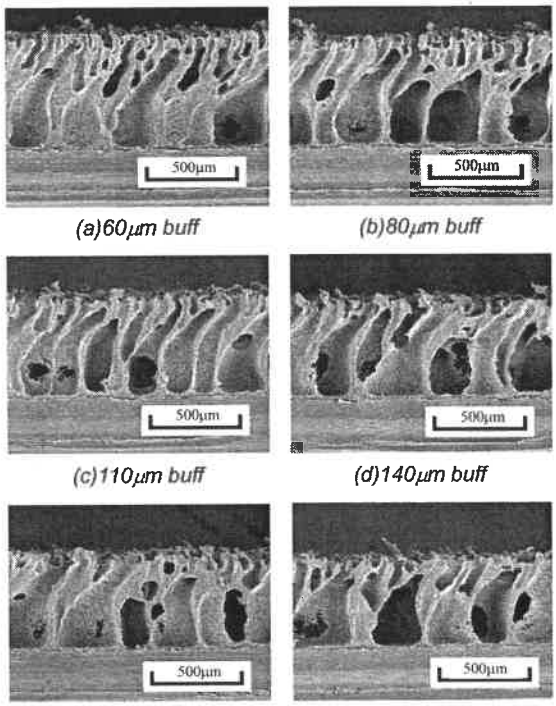

(a)60μm buff (b)80μm buff

(c)110μm buff (d)140μm buff

(e)160μm buff (f)180μm buff

FIGURE 6. Polisher sections manufactured by various kinds of buffing depths

TABLE 4. Physical property of polisher manufactured by various kinds of buffing depths

	0.7mm Nap					
Buffing depth μm	180	160	140	110	80	60
Thickness mm	0.69	0.72	0.74	0.76	0.79	0.81
Density g/cm^3	0.51	0.49	0.47	0.46	0.46	0.45
Hardness ^{o}	65	64	64	63	63	62

layer of polisher is consisted of small pore. In the lower layer, on the other hand, large pore occupies the major of polisher. The manufacturing mechanism of pad is considered to depend on forming the pore shape like the tears drop. Table 4 shows the physical property of polisher manufactured by various kinds of buffing depths. From the table, the buffing depth has slight influence on density and hardness of polisher. The density and hardness of polisher increase somewhat with the increases of buffing depth. The ratio of base thickness of high density to whole polisher layer is considered to become larger for higher buffing depth.

Figure 7 shows the relationship between the pore size formed on the polisher surface and polisher thickness. The pore size becomes for larger polisher thickness, in the other words, smaller buffing depth. It is clear that the section

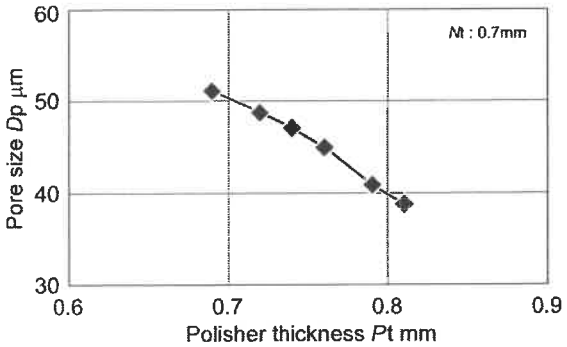

FIGURE 7. Relationship between pore size and polisher thickness

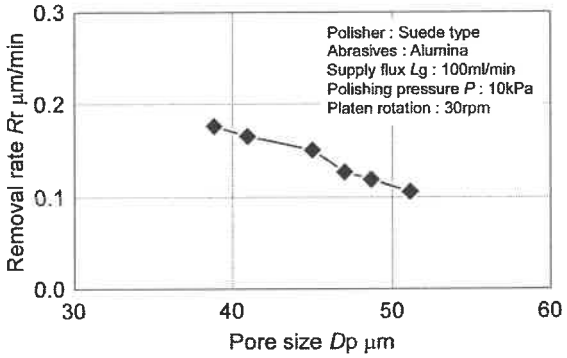
Polisher : Suede type
Abrasives : Alumina
Supply flux Lg : 100ml/min
Polishing pressure P : 10kPa
Platen rotation : 30rpm
Removal rate Rr μm/min
Pore size Dp μm

FIGURE 8. Relationship between removal rate and pore size

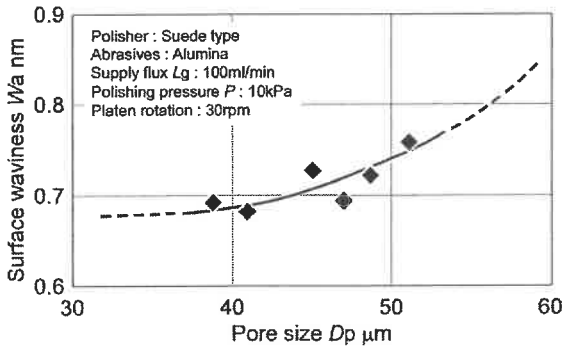
Polisher : Suede type
Abrasives : Alumina
Supply flux Lg : 100ml/min
Polishing pressure P : 10kPa
Platen rotation : 30rpm
Surface waviness Wa nm
Pore size Dp μm

FIGURE 9. Relationship between surface waviness and pore size

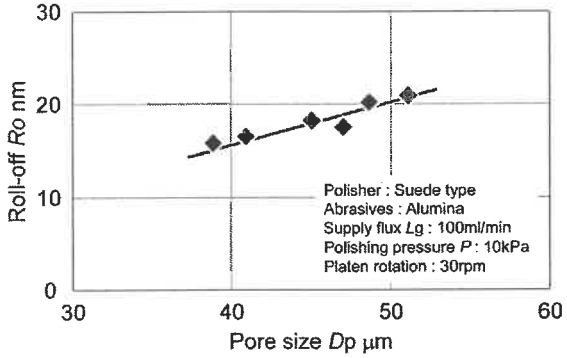
Polisher : Suede type
Abrasives : Alumina
Supply flux Lg : 100ml/min
Polishing pressure P : 10kPa
Platen rotation : 30rpm
Roll-off Ro nm
Pore size Dp μm

FIGURE 10. Relationship between roll-off and pore size

structure of polisher as shown in Fig.6 is related to the result.

The influence of pore size on the removal rate is shown in Fig.8. The removal rate decreases the increase of pore size, in other words, the increase of buffing depth. The reason is inferred why the contact area of polisher with substrate decrease with the increase of pore size.

Figure 9 shows the relationship between surface waviness and pore size. The surface waviness becomes larger for larger pore size, in other words, higher buffing depth. According to the results in Fig.8, the substrate removal rate formed by one abrasive grain is inferred smaller for the polisher of larger pore size. The surface waviness, from the point of view, must become smaller for larger pore size. Nevertheless the experimental result is reverse against the consideration. Thus the formation state of pore in buffing or polishing process is inferred to influence the reverse phenomenon.

Figure 10 shows the relationship between roll-off and pore size. The roll-off becomes larger for larger pore size, in other words, higher buffing depth.

From the results as mentioned above, the removal rate, and the surface waviness and roll-off decrease and deteriorate, respectively as the buffing depth increases. To do the optimum polishing operation, accordingly, the careful consideration must be necessary.

CONCLUSION

The main conclusions obtained are as follows;

1) The pore size on the polisher formed by buffing of the new pad increases with the increase of buffing depth.

2) The removal rate of substrate done in the first polishing stage with alumina abrasives is larger for smaller pore size.

3) The substrate waviness and roll-off formed in the first polishing stage with alumina abrasives become smaller for smaller pore size.

ACKNOWLEGEMENTS

The authors would like to thank FUJIBO EHIME Co., Ltd. for providing polisher.

REFERENCES

[1] K.Yamaguchi, H. Yasui, S. Otsuka, T. Nagata, K.Kusaba: Influence of polisher surface Structure on Polisher Life in Ultra-smoothness Polishing of NiP Plated Aluminum Magnetic Disk Substrate, Proc. ASPE 22th Annual Meeting, pp.481-484

DEVELOPMENT OF NANO-PRECISION SYNERGISTIC FINISHING PROCESS INTEGRATED ELID-GRINDING AND MRF

Ohmori Hitoshi[1], Shaohui Yin [2], Uehara Yoshihiro[3] and Ishida Satoshi[4]
[1]Material Fabrication Laboratory
RIKEN (The Institute of Physical and Chemical Research)
2-1, Hirosawa, Wako-shi, Saitama 351-0198 Japan
[2]National Engineering Research Center for High Efficiency Grinding,
Hunan University
Yuelushan, Changsha, Hunan, 410082, P.R. China
[3]VCAD Fabrication Team,
RIKEN (The Institute of Physical and Chemical Research),
2-1, Hirosawa, Wako-shi, Saitama 351-0198 Japan
[4]The Nexsys Corporation, RIKEN Venture
1-7-13 Kaga, Itabashi-ku, Tokyo, 173-0003, Japan

INTRODUCTION

Automatic and high-efficiency nano-precision manufacturing technique of optical elements surface with sub-nanometer rms surface micro-roughness, λ/10~ λ/20 nm figure accuracy, and damage-free is greatly demanded by advanced optical fields. In conventional grinding process, problems such as wheel loading and glazing can be encountered while grinding optical elements with fine abrasive wheels [1][2]. However, ELID is an efficient method to dress the grinding wheel while performing grinding for a long time. Grinding optical elements using ELID technique is also viable alternative and effective [3][4]. However, in grinding, surface produced by fixed abrasive grinding of these optical materials is characterized by considerable sub-surface damage, micro-crack on the order of the abrasive grain size. This damage [5] should be typically removed by polishing with a friable abrasive such as cerium or aluminum oxide. Therefore, for realizing the extreme precision and surface micro-finish, we considered to seek a best polishing method.

Delighted us is, a revolution finishing method, magneto-rheological finishing (MRF) technology has been invented and developed [6][7][8]. MRF is based on using a MR fluid. It is suggested that MRF is an excellent candidate for polishing optics elements. It is deterministic because the polishing tool removal rate changes little, and the removal function is characterized. If the material removal rate is known accurately, the computer algorithms function to high precision. The polishing tool is easily adjusted, and conforms perfectly to the workpiece surface, enabling aspheric polishing [8][9][10][11].

Therefore, ELID grinding is used as a high-precision and high-efficiency grinding method for hard and brittle materials by using of in-process electrolytic dressing. MRF is a novel precision finishing process for deterministic figure correction and polishing of optical material. In this paper, an ultra-precision synergistic finishing process integrated ELID-grinding and MRF is developed and applied to fabrication of glass lens, SiC, silicon mirror etc. As pre-polishing, in ELID grinding, good surface quality may be obtained in high efficiency, and then, the last high form accuracy and surface roughness may be obtained by MRF. Surface accuracy of the λ/10~ λ/20 nm peak-to-valley and surface micro-roughness less than 10 Angstrom are produced in high efficiency. Research results have shown that this new developed synergistic finishing process may obtain both high efficiency and high quality and may be used to replace conventional optics manufacturing process.

REMOVAL RATE OF MATERIALS BY MRF

Removal Rate of BK7 Glass

When a curvature BK7 glass lens is immersed in the MR suspension for 2 seconds (conditions described in Table 1), the removal "spot" area size is approximately 3.3×2.3 mm. The maximum deep of the spot is 181 nm, the peak removal rate may be calculated to be about 5.43 μm/min

and the volume removal rate is 0.014 mm^3/min.

TABLE 1. MRF conditions of BK glass

MRF machine	Q22Y MRF system (QED)
Finishing mode	Uniform removal & figure correction
Workpiece	Materials: BK7 glass, F.A. 25 *mm*, concave surface, curvature radius 60 *mm*
Delivery system setting	Magnetizing Current: 12*A* Wheel revolution :350 *rpm* Suction pump revolution :110 *rpm* Centrifugal pump revolution: 2800 *rpm*
Delivery system reading	Pressure:7.08 *PSI*; Flow rate:0.2 *l/m*; Viscosity: 38.5 *cP*;
Ribbon parameters	Wheel: 50 *mm*; Ribbon height:1.31 *mm*; Gap: 1.07 *mm*; Depth 0.24 *mm*
MR Fluid	Cerium oxide abrasive

Removal Rate of SiC

A flat SiC part of 30 mm diameter is immersed in the MR suspension for 20 seconds. Conditions are described in Table 2. The mean depth of the removal spot is 303 nm, the peak removal rate and the volume removal rate may be calculated to be about 0.909 μm/min, 0.005 mm^3/min, respectively.

TABLE 2. MRF conditions of SiC plane

Workpiece	1) Materials: SiC, Plano surface 2) Size:Dia.Φ30 *mm*, thickness : 10 *mm* 3) before finishing: 0.95μm*RMS*
Delivery system setting	Magnetizing Current:12*A* Wheel rotation 450*rpm* Suction pump rotation:120*rpm* Centrifugal pump rotation: 3000*rpm*
Delivery system reading	Pressure:7.8*PSI* Flow rate:0.2*l/m* Viscosity: 43.2*cP*
Ribbon parameters	Ribbon height:0.9*mm*; Gap: 0.55*mm*; Depth: 0.35 *mm*
MR Fluid	D10(QED), diamond abrasives
Other condition	Showed in Table 1

Removal Rate of Silicon mirror

A silicon mirror part is immersed in the MR suspension for 3 seconds. Table 3 shows the MRF conditions. The peak removal rate may be calculated to be about 5.04 μm/min and the volume removal rate is 0.036 mm^3/min.

TABLE 3. MRF conditions of silicon

Workpiece	Materials: silicon, Diameter: Φ20 *mm*
Delivery system reading	Pressure 6.6 *PSI*; Flow rate:0.2 *l/m*; Viscosity: 35.5 *cP*;
Ribbon parameters	Wheel: 50 *mm*; Ribbon height:0.97 *mm*; Gap: 0.66 *mm*; Depth 0.33 *mm*
MR Fluid	diamond abrasive
Finishing time	1.19min + 1.13min(2cycle)
Other condition	see Table 1

FINISHING CHARACTERISTICS OF ELID/MRF

To obtain the best polishing quality in a the lowest cost and much less time, we think that using ELID-grinding is a good alternative. On the otherhand, MRF can obtain very good finishing quality. However, its removal rate is lower than grinding, So, pre-finished surface with better surface from accuracy is demanded. Using the nano-precision synergistic finishing process integrated MRF and ELID grinding, high efficiency and higher surface quality of optical materials such as glass, silicon, silicon carbide, can be obtained. In general, Form accuracy of the λ/10~ λ/20 nm peak to valley and surface micro-roughness less than 10 Angstrom are produced in high efficiency.

Form Accuracy of ELID/MRF

Form Accuracy of Curvature BK7 Lens

To verifying obtainable form precision and surface micro-roughness by using the synergistic finishing process, a BK7 glass lens is used to test. At first, ELID grinding is conducted by using #1200 wheel, and glass material is removed mainly in brittle fracture mode. Surface form accuracy λ/5 P-V is obtained. And then, MRF is conducted for 17min (2 cycles), using removal "spot" shown in Figure 2. MRF conditions are shown in Table 1. The finished surface form is measured by Zygo interferometer, and the form accuracy is improved to λ/18 P-V (Figure 1) in a short time.

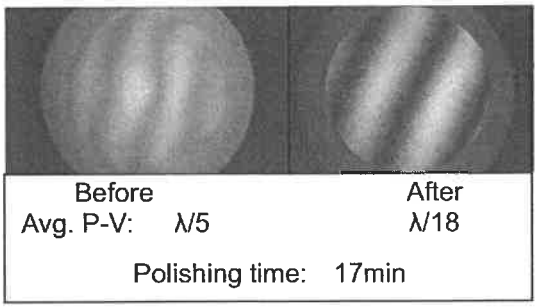

FIGURE 1. Figure accuracies before and after MRF for glass lens

Form Accuracy of SiC Plane Surface

As shown in Figure 2, the P-V of surface produced by #4000, #12000 wheels and MRF (diamond grit size 1.4μm) are 12.7 nm, 2.7 nm, 1.3 nm in order. Although the diamond abrasive grit size in MRF tool is near to that of #12000 grinding wheel, MRF demonstrates smaller cutting depth. This is because that the abrasive removes materials by shear stress in the converging gap and the lateral motion of polishing abrasives across the part surface, not

forces abrasive to cut into the materials as that in fixed abrasive grinding mode. Therefore, MRF may lead a more clean, pit and scratch free surfaces without surface damage.

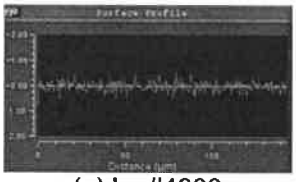

(a) by #4000

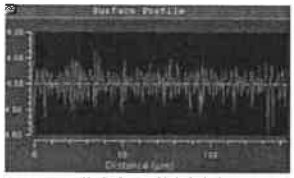

(b) by #12000

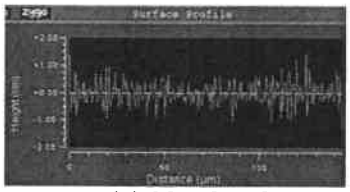

(c) After MRF

FIGURE 2. A comparison of micro-cutting-mark of generated surface. (a) 12.7 nm P-V, (b) 2.7 nm P-V, (c) 1.3 nm P-V.

Form Accuracy of Silicon Mirror

A concave silicon part (Full aperture 40 mm, Clear aperture 35 mm in daimeter, 1800 mm radius of curvature) is generated by ELID grinding using #4000 wheel in an ultra-precision machining system. Before grinding, initial ground surface is measured for calculating the distribution of the form deviation profiles. With these deviation profiles, the NC data is compensated. Form accuracy is 0.311 μm P-V after ELID grinding by #4000 wheel (Figure 3a), and then, it is improved remarkably to 79 nm P-V after MRF (Figure 3b).

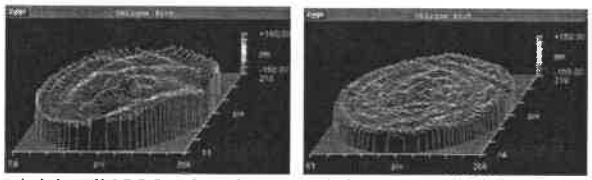

(a) by #4000 wheel (b) after MRF

FIGURE 3. Form map of surface before and after MRF. (a) P-V 311.4 nm, (b) P-V 79 nm.

Micro Surface Roughness of ELID/MRF

Surface Roughness of BK7 Glass Sphere

To verifying obtainable surface micro-roughness by using the synergistic finishing process, the same BK7 glass lens and same conditions are used to test. At first, ELID grinding is conducted by using #1200 wheel, and surface micro-roughness 261 nm rms is obtained in Figure 4a. And then, MRF is conducted for 17 min (2 cycles). As a result, surface micro-roughness 0.56 nm rms is improved considerably in Figure 4b. In a short time, the glass lens surface could be finished to sub-nanometer surface micro- roughness.

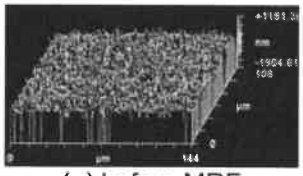

(a) before MRF

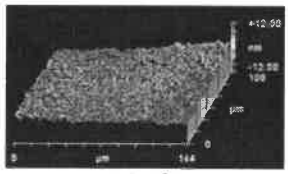

(b) after MRF

FIGURE 4. Optical roughness map of surface before and after MRF. (a) RMS: 261.92 nm, (b) RMS: 0.56 nm

Surface Roughness of CVD-SiC

In this experiment, A same rough surface as in Figure 5a and Figure 5b are ground by #4000, #12000 wheels orderly, and then is finished by MRF in Figure 5c. Those surfaces generated by #4000, #12000 wheels and MR fluid are evaluated comparatively. The obtainable micro-roughness by #4000, #12000 wheels, MR fluid are 5.8 nm, 3.0 nm, 2.5 nm in order, respectively. Compared to #12000 ground surface, the micro-roughness of the finished surface by MR fluid is not improved considerably. The 2-3 nm rms value may be considered to be the limited surface-roughness in this finishing conditions.

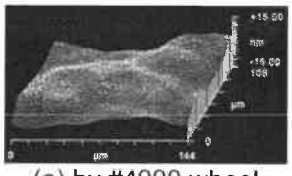

(a) by #4000 wheel

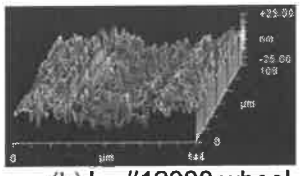

(b) by #12000 wheel

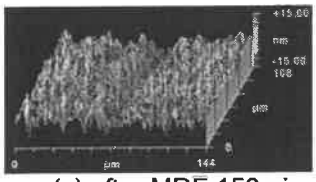

(c) after MRF 150min

FIGURE 5. Comparison of optical roughness map of generated suface. (a) RMS: 5.8 nm, (b) RMS: 3.0 nm, (c) RMS: 2.5 nm.

Surface Roughness of Silicon Wafer

A plano silicon parts were generated by ELID grinding in an ultra-precision machining system. As shown in Figure 6a, ground surface by #4000 wheel, generated in ductile mode, surface micro-roughness less than 4.9 nm rms was obtained. After MRF, the surface roughness was improved to 0.6 nm rms in Figure 6b.

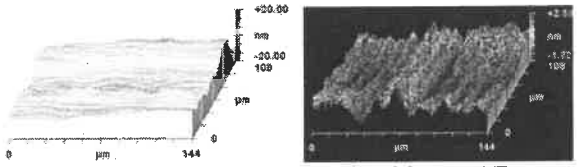

(a) Before MRF (b) After MRF

FIGURE 6. Optical roughness map of surface before and after MRF. (a) RMS: 4.9 nm, (b) RMS: 0.6 nm.

CONCLUSIONS

Owing to lower removal rate of MRF for ultra-hard material, MRF is time-consumable and low efficiency for polishing a rough optical surface. Its pre-finished surfaces should have better figure accuracy and better surface roughness; ELID grinding may meet those needs, so ELID is the best alternative and can decrease finishing time. ELID grinding was conducted before MRF. By applying the ultra-precision synergistic finishing process of ELID grinding and MRF, surface accuracy of the λ/10~ λ/20 nm peak-to-valley and surface micro-roughness less than 10 Angstrom for glass lens were produced in high efficiency. The synergistic technologies may shorten largely finishing time and eliminate the industry's reliance on the specialized skills required to operate today's costly and labor-intensive conventional manufacturing processes. Furthermore, extend the manufacturing state-of-the-art and provide optical manufacturers with the cost effective capability to produce optical elements.

REFERENCES

[1] Johnson J.S, Grobsky K, Bray D.J. Rapid Fabrication of Lightweight Silicon Carbide Mirrors. Proc. SPIE. 2002; 4771: 243-253.

[2] Bifano T, Yi Y, Kahl W.K. Fixed Abrasive Grinding of CVD-SiC Mirrors. Precision Engineering. 1994; 16: 109-116.

[3] Suzuki H, Hirano M, Abe M, Niino Y, Namba Y. Ductile Grinding of Chemical Vapor Deposited Silicon Carbide for X-ray Mirrors. Journal of the JSPE. 1995; 61: 571-575.

[4] Ohmori H, Dai Y, Lin W. Force Characteristics and Deformation Behaviors of Sintered SiC During an ELID Grinding Process. Key Engineering Materials. 2003; 238: 65-70.

[5] Randi J.A, Lambropoulos J.C, Jacobs S.D. Subsurface Damage in Some Single Crystalline Optical Materials. Applied Optics. 2005; 44: 2241-2249.

[6] Prokhorov I.V, Kordonski W. I. New High Precision Magnetorheological Instruments Based Method of Polishing Optics. OSA OF&T Workshop Digest. 1992; 24: 134-136.

[7] Golini D, Kordonski W, Dumas P, Hogan S. Magnetorheological Finishing (MRF) in Commercial Precision Optics Manufacturing. SPIE Proceedings. 1999; 3782: 80-91.

[8] Johnson J.S, Grobsky K, Bray D.J. Rapid Fabrication of Lightweight Silicon Carbide Mirrors. Proc. SPIE. 2002; 4771: 243-253.

[9] Shorey A.B, Jacobs S.D, Kordonski W.I. Experiments and Observations Regarding the Mechanisms of Glass Removal in Magnetorheological Finishing. Applied Optics. 2001; 40: 20-33.

[10] Kordonski W, Golini D. Multiple Application of Magnetorheological Effect in High Precision Finishing. Journal of Intelligent Material Systems and Structures. 2002; 13: 401-404.

[11] Bagnoud V, Guardalben M.J, Puth J. High-energy, High-average-power Laser with Nd: YLF Rods Dorrected by Magnetorheological Finishing. Applied Optics. 2005; 44: 282-288.

ENGINEERING A NEXT GENERATION WATER-BASED GRINDING FLUID

Peter Hug[1], Andrew R. Nelson[2] and Stuart C. Salmon[3]
[1]Recombinant Innovation LLC, Toledo, OH, USA
[2]ARN Engineering LTD, Perrysburg, OH, USA
[3]Next Generation Technology Group Inc., Rossford, OH, US

INTRODUCTION

It has long been said that water alone cools a grinding operation offering little to no lubrication, whereas a straight oil lubricates but with very little cooling. There is a spectrum of grinding fluids with water on one extreme and with straight oil on the other. The question is: As oil is added to water, when does the water begin to exhibit the properties of the oil, and vice versa? Is the relationship linear? Do step changes occur? Previous work has shown that for water-based fluids the relationship between G Ratio and fluid concentration, is not linear, particularly for materials that load grinding wheels, as do soft steels, stainless steels and superalloys [1].

The industrial properties of a grinding fluid fall into two categories: The cutting functions and the non-cutting functions. The non-cutting functions are: Odor, color, fungus, residue, corrosion, foam, mist, filtration, tramp oil rejection, paint stripping, seal swelling, recyclability, bio-degradability, bio-stability and issues with dermatitis. Due to the political and environmental pressures to comply with government regulations and embrace a "green" philosophy, the non-cutting functions have monopolized the R&D programs of many grinding fluid companies. The cutting functions however: Productivity, wheel life, dresser life and workpiece surface integrity; the reason that grinding fluids are used in the first place, have been relegated to a lower priority - until now.

The advent of thin film coatings, in large chip machining processes, like milling and turning, has accelerated the move towards dry and near-dry operations. Grinding and abrasive machining processes however are wet and will be staying wet for some time. With the increasing number of difficult-to-machine materials coming onto the marketplace, both grinding and abrasive machining processes are seeing unprecedented growth. Grinding is a materials driven process. With that realization, the emphasis is beginning to move away from the non-cutting functions of a grinding fluid and more towards the cutting functions. Cooling and lubricity are the two main "cutting function" of a grinding fluid. There are also: pH, conductivity, alkalinity, wetting (surface tension), droplet size for emulsions, extreme pressure additives, detergency and corrosion inhibitors.

A good grinding fluid is not always a good machining fluid and vice versa. The chip formation is vastly different for grinding over machining, along with "tool" geometry (abrasive grains versus inserts), tool materials, tool depths of cut and particularly cutting speeds. A universal metalworking fluid makes neither technical nor economic sense.

In today's world of "continuous improvement" the improvement may have to come from longer wheel life, faster grinding cycles, lower power, better surface finish and lower overall cost. The question for the grinding fluid formulator is what to do to affect those improvements: What to add, what to subtract, where are the synergies and the positive and negative interactions?

The object of this research is to identify some of the component parts and properties of the chemistry of a grinding fluid that influence the cutting functions, with a view to guiding the formulation of a next generation grinding fluid.

THE TESTING SET-UP

It is important, at this stage, to focus on aspects of a grinding fluid that have the most relevance to the industry. It was decided that the initial material to be ground would be a hardened steel. The grinding wheel would be the most popular vitrified grinding wheel grade made by one of the world's largest grinding wheel producers and the process will be reciprocating grinding (small depth of cut and fast feed), the most common grinding method. Having developed and tested a standardized grinding test for grinding fluids [2], the grinding machine was set-up with the following parameters:

Grinding Wheel Specification: Saint-Gobain 32A60 I VBE. 300mm (12") diameter 25mm (1") wide. Wheel speed: 28m/s (5500 sfm) and auto-balanced to less than 0.25 microns (10 micro-inches) amplitude of vibration.

Dressing Cycle: A 'fliese' diamond, 0.89mm (0.035") wide, traversing at 6.35mm/s (15"/min), for 4 overlays, removing 0.025mm (0.001") from the wheel radius, per pass, for three passes.

Grinding Cycle: Table speed: 0.3m/s (60 ft/min). Down feed: 0.012mm (0.0005") per pass, for a total depth of 2.54mm (0.100") per test. Cross feed: Oscillating 0.25mm (0.010") per pass.

Grinding Fluid Conditions: The grinding fluid was applied at 0.73 l/s (11.5 gpm) and 6.89 b (100 psi) via a laminar flow nozzle such that the velocity of the jet of fluid was equal to the surface speed of the grinding wheel. The nozzle position was adjusted to impacting the grinding wheel just prior to entering the arc of cut, after each dress cycle. The fluid was filtered through coarse and fine filters of 20 microns (800 micro-inches) and 10 microns (400 micro-inches) respectively. The system tank holds 190 liters (50 US gallons) of grinding fluid that can be quickly and completely cleaned and changed for rapid turnaround of testing while maintaining the same mechanical set-up for grinding.

Specimen Material: 4140 steel, hardened to Rc55. Each specimen is nominally 150mm (6") long and 20.25 mm (0.800") wide, mounted on a three component piezo-electric dynamometer.

Using proprietary software, the spindle power, normal and tangential forces were synchronously recorded at a scan rate of 1024/sec. The G Ratio was calculated from wheel diameter and part dimension measurements.

The areas to be explored and reported in this paper are: Fluid concentration, surface tension and active sulphur. The object of the testing is to look for step changes, trends and reliable "cause and effect" chemistries that will combine to help formulate a next generation grinding fluid.

RESULTS

The results of the testing will be discussed first with respect to the fluid concentration, then surfactant additives and surface tension and then the addition of active sulphur.

Fluid Concentration A neo-synthetic fluid was used for the concentration experiment. The fluid had performed very well as a grinding fluid in past tests therefore any result, better than those seen at "normal" concentrations, would be significant. Figure 1, below, shows all of the tests run at each concentration from 0 to 50%.

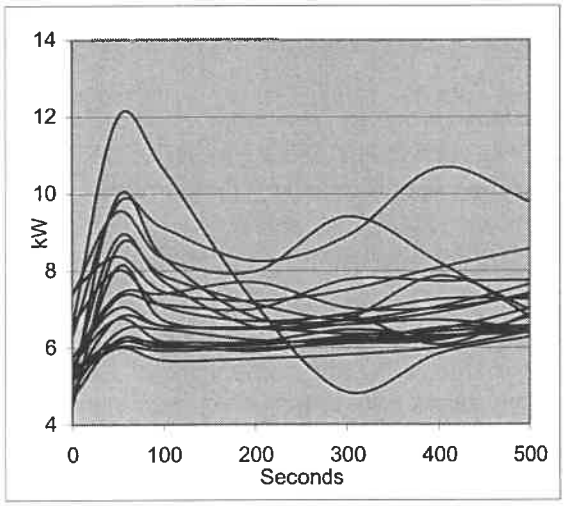

FIGURE 1 (above) shows the relationship of grinding power with respect to time in the grind, for fluid concentrations ranging from 0% to 50%.

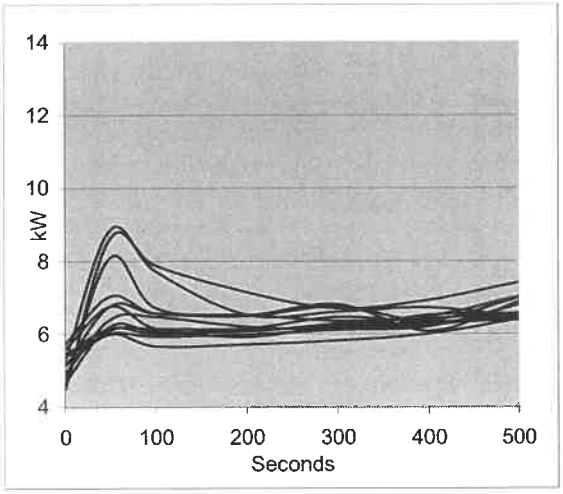

FIGURE 2 (above) is the same chart as figure 1, but with fluid concentrations 0% to 10% omitted.

Interestingly, figure 2 shows that once the 0% to 10% concentration runs are subtracted from figure 1, the pattern of power, versus time, becomes less wild and variable. It would appear that the surface of the grinding wheel was changing significantly at the lower fluid concentrations, such that the surface finish was exceptionally rough (higher than Ra125) until

5% concentration when the surface finish settled down to be in the range Ra35 to Ra 37 for each and every other test thereafter. Notice also that with plain water and no additives, the power takes on a very large swing from the highest power and then the lowest, of all the tests. By observing the normal force, it might appear that the grinding wheel loads up with material in the early stages of the grinding process. The normal force required to penetrate the surface of the material, by both attritiously worn grains and loaded grains, grew to a sufficiently high magnitude to cause the wheel to self-dress and become very sharp and aggressive, hence the very rough surface finish and low G Ratio.

Plotting the G Ratio versus concentration, figure 3 (below), shows that a significant step change occurs around 20% concentration. This is an important result for this particular fluid as its performance, in the conventional range of concentration, was significantly higher than the competitive fluids in the marketplace. The step change in wheel life above 20% concentration is quite remarkable.

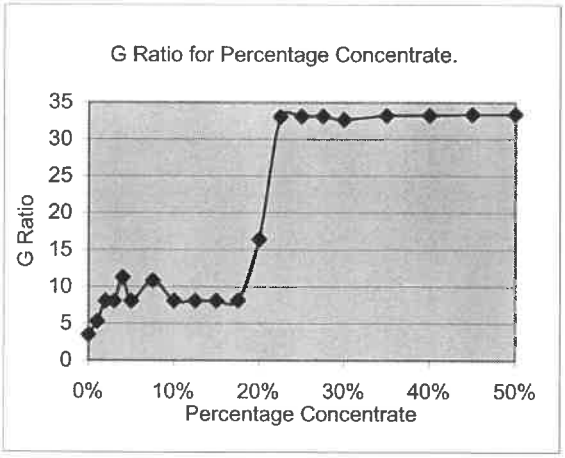

FIGURE 3 (above) shows the G Ratio with respect to the fluid concentration.

Surface Tension Given the step change in G Ratio (shown above) it was decided to observe the effect of surface tension with the addition of a surfactant/wetting agent at the 10% and 25% concentration levels. The side effect of surfactant additions is foam. Surfactant additions were made at two levels: 0.0016% and 0.004% in order to avoid a foaming crisis. There was little to no change in the power with either level of addition of surfactant. The power was consistently higher at the 10% fluid concentration levels (surface tension averaging 37.9 dynes/cm), over the 25% fluid concentration level (averaging 36.8 dynes/cm), by around 17%. The G Ratio remained at around 16.6 for all of the tests except for the 10% fluid concentration level with 0.004% addition of surfactant where the G Ratio climbed to 56. It appears that the surface tension of the grinding fluid is neither a major contributor to the extension of wheel life nor to the reduction in grinding power. Due to its foam generation it is more of a nuisance.

Active Sulphur Sulphur is thought to be a key element in grinding. It is generally used as an EP (Extreme Pressure) additive that reduces the coefficient of friction at the interfacial temperatures (400°C - 750°C) experienced in grinding. The active sulphur compound selected for the testing did not readily dissolve in the neo-synthetic fluid. The sulphur tests were therefore conducted using the active sulphur compound dissolved in water, with a 4% rust inhibitor only, a more rigorous test. Figure 4 shows that the total grinding power decreases with the addition of active sulphur, after a very small percentage addition. The total power, plotted here, is the sum of the power measured at the time intervals of 0, 50, 100, 200, 300, 400 and 500 seconds into the grinding test. Figure 4 shows that the total power does not decrease appreciably above the 2% addition of active sulphur.

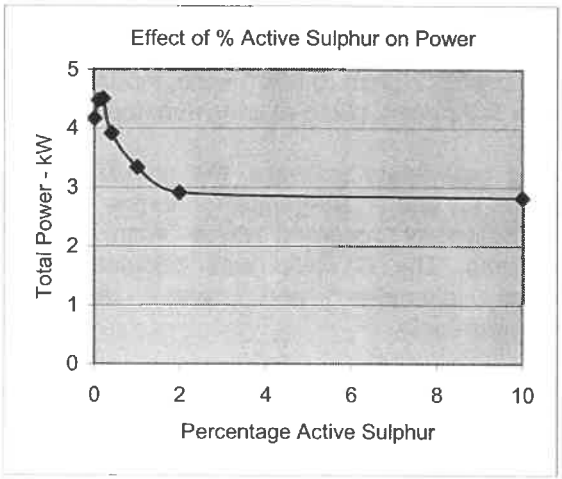

FIGURE 4 (above) shows the effect of active sulphur on grinding power.

Similarly, in figure 5 (below), the G Ratio reaches a maximum benefit at 2% but drops off rapidly thereafter. Any addition of active sulphur above 2% is therefore not beneficial to the grinding operation.

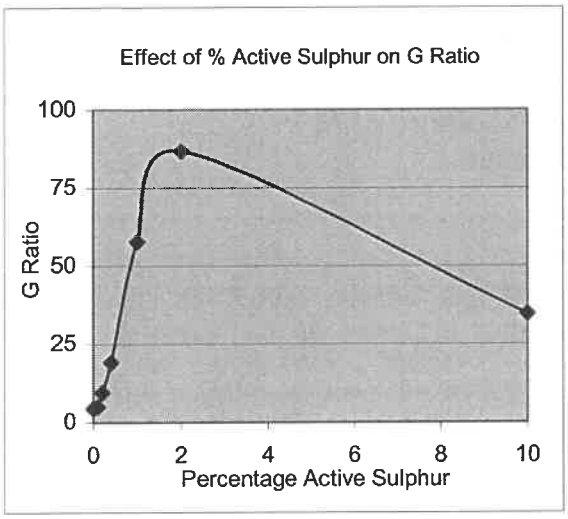

FIGURE 5 (above) shows the effect of the percentage active sulphur on G Ratio.

CONCLUSION

These early observations and initial studies have revealed that the conventional metalworking fluid chemistry, that attempts to maximize lubricity and cooling, is not what constitutes a superior grinding fluid. Though cooling and lubricity are important factors, the one that has become paramount for grinding, based on this program of fluid testing, is detergency. This is the fluid's ability to keep the grinding wheel clean and free from loaded material. Tests that exclude and enhance the oxidation of the ground surface have shown this to be important [3]. Other work has shown that the use of copper, in the presence of ferrous material, prevents the re-welding and build-up of material onto the surface of the grinding wheel [4].

Though surface tension was not significant, the speed of wetting (dynamic surface tension) might show a different result. The pH of a fluid may also influence its detergency. Cleaning fluids were once used [5]. They ground with very low power and yielded a high G Ratio, however the caustic nature of the fluid was such that eye irritation was a major problem for the operator.

The program will go forward to the extent of improving the cutting functions within the bounds of acceptance for the non-cutting functions [6].

FURTHER WORK

The observations and measurements both inside the normal ranges as well as way outside of those ranges will be entered into a neural network [7] to assist in the direction of future work with respect to dynamic surface tension, pH, biocides, fluid stabilizers, oils, emulsifiers and droplet size, for the eventual formulation of an optimized grinding fluid.

ACKNOWLEDGEMENTS

The researchers wish to thank Todd Gearig who programmed the CNC control, ran the grinding machine, then cleaned and changed out the test fluids.

REFERENCES

[1] S.C. Salmon: *Abrasive Lesson Part 2.* (Cutting Tool Engineering. Vol. 53, No.4, 2001). www.ModernGrindingTechnology.com

[2] United States Environmental Protection Agency: *Pollution Prevention Guide To Using Metal Removal Fluids In Machining Operations.* 2002. www.TechSolve.org

[3] E.J. Duwell, I.S. Hong and W.J. McDonald: *The Effect of Oxygen and Water on the Dynamics of Chip Formation During Grinding.* No. 68LC-19. American Society of Lubrication Engineers. Conference, Atlantic City, NJ, USA. October 8-10,1968.

[4] M.F. Frost and P.M.T. Fursdon: Towards Optimum Centreless Grinding. PED Vol 16. Milton C. Shaw Symposium. American Society of Mechanical Engineers Conference Miami, FL, USA. November 17-22,1985.

[5] Nelson, A.R: *Grinding Test Data: Reciprocating.* Master Chemical Corporation, Perrysburg, OH, USA. www.masterchemical.com

[6] P. Hug: *Rapid Enumeration and Viability Determination of Mycobacteria in Metalworking Fluids.* Society for Tribology and Lubrication Engineering Annual Conference, Las Vegas, NV, USA. May 2005.

[7] J. Lawrence, S. Luedeking and J. Fredrickson: *"BrainMaker" Neural Networks and Expert Systems.* California Scientific Software, Nevada City, CA, USA.

Characterization of Pad Materials in Abrasive Profile Polishing

Schulte H., Riemer O., Gläbe R., Brinksmeier E.
Laboratory for Precision Machining LFM
University of Bremen
Germany

INTRODUCTION

Hard and temperature resistant materials are used for mold manufacturing of optical glass lenses. These materials are not machinable by ultra precision diamond milling and turning processes. For example hardened steel or tungsten carbide can be ground in optical quality regarding shape but additional polishing is necessary to guarantee the high requirements for optical surface quality. For finishing of structured surfaces in optical quality industrial processes do not exist. Collimation lenses for high performance diode lasers show as example an increasing industrial application with the requirement for micro structured optics [1]. Due to the growing importance and increasing variety of these structured optics an abrasive polishing process for finishing structured surfaces without degrading the pre-ground high shape accuracy of theses structures was developed by the authors. This paper gives an overview on applicable pad materials for abrasive polishing processes. Polishing experiments in cylindrical groove arrays made from hardened steel show that felt and hardwood cause a clearly better polishing effect compared to plastics.

ABRASIVE PROFILE POLISHING

The requirements of polishing tools for surfaces with micro structures differ considerably from those for polishing continuous surfaces like flats, spheres and aspheres. On the one hand the polishing tool material has to be dimensionally stable in order to guarantee a homogeneous contact area at the workpiece and on the other hand the material must be soft enough in order to enable the polishing effect by carrying abrasives into the contact zone. Furthermore, it must be ensured to machine the pad material by cutting tools into the desired form in-situ on the polishing machine in order to minimize balancing problems by clamping and unclamping of the tool.

The following materials were examined: plastics (PA6/POM), organic felt and laminated hardwood (pear). By applying these materials pre-ground groove structures have been polished to optical surface quality Ra < 10 nm [2]. Polishing experiments on reference workpieces with planar surfaces revealed a clear difference between felt, hardwood and plastic referring to the volume-based material removal. Here the time-dependent material removal is determined by the wear characteristics of the polishing tool.

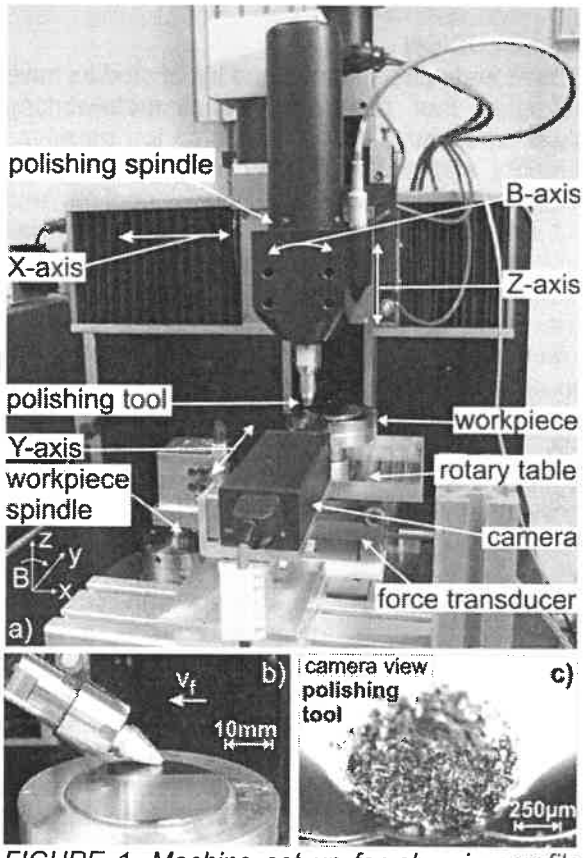

FIGURE 1. Machine set up for abrasive profile polishing of structured surfaces

For abrasive profile polishing of structures an aspheric polishing machine was modified, now incorporating three numerically controlled linear axes (X, Y, Z), a polishing spindle and a workpiece spindle, figure 1a. The polishing spindle mounted on the vertical Z-axis can be

tilted by ±90°, figure 1b. For polishing linear structures the workpiece is aligned to the feed direction by using a manual rotary table. Process forces can be measured by a force transducer placed underneath the workpiece. Furthermore, the polishing tools can be dressed in-situ with a diamond tool to ensure minimal run-out [3]. A camera system with an integrated zoom is used to visualize and control the tool profiling and the polishing process itself. The adjustment of a polishing tool above a groove can be controlled by the camera system, figure 1c. The polishing process can be controlled by monitoring the force components and adjusting the X-, Y- and Z-axis, in order to assure a continuous polishing pressure at the workpiece surface. Compared to conventional polishing processes, the polishing tools for structured surfaces are contacting a much smaller area of the workpiece. The tool material must have a high form stability but must still be soft enough to embed abrasives for ensuring the polishing effect. Preparation of the exact tool shape is realized by diamond turning in-situ on the polishing machine. Hence, the material must also be machinable by cutting operations.

INFLUENCE OF POLISHING PAD MATERIAL

POM/PA6 plastics were originally used because of the high form stability and the good machinability with diamond tools for shaping. But besides these two requirements the polishing effect must also be considered. Figure 2 shows the qualitative properties of these requirements of the determined pad materials. Organic felt material offers a good polishing effect but very low form stability and lowest machinability. Impregnating the material to get carbonized felt enables to diamond turn the tool tip. Laminated hardwood (pear) offers a good polishing effect with high machinability but the form stability requires a very good positioning and adjustment of the polishing pad.

During material removal experiments with these three pad materials the different properties were also dominant. Figure 3 shows the material dependent removal functions ("footprints") in a planar steel workpiece and the corresponding surface topography. The advantages of localized material removal generated by high form stability and additionally a high polishing effect generated by loose embedded abrasives appear at polishing pads made of laminated hardwood. Hence, the advantage of a strong polishing effect with felt material and an accurate contact area due to the high form stability with plastic pads is optimally combined for hardwood pads.

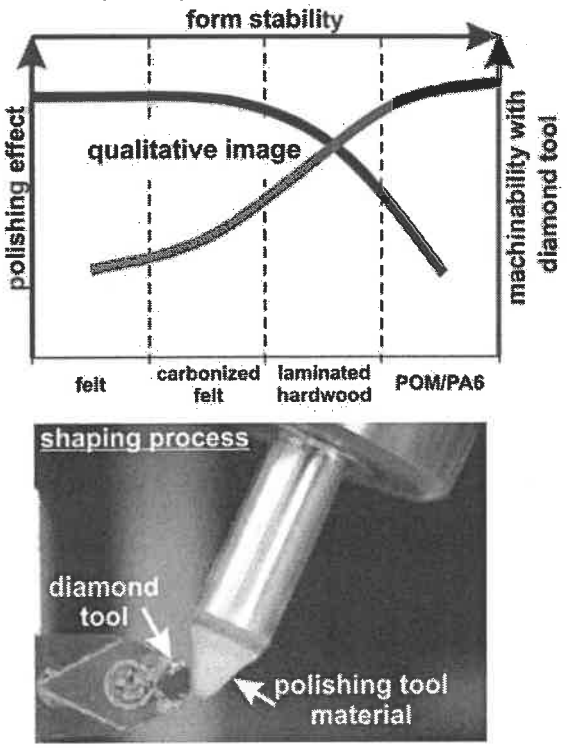

FIGURE 2. Influence of profile polishing tool material on polishing effect and shaping process

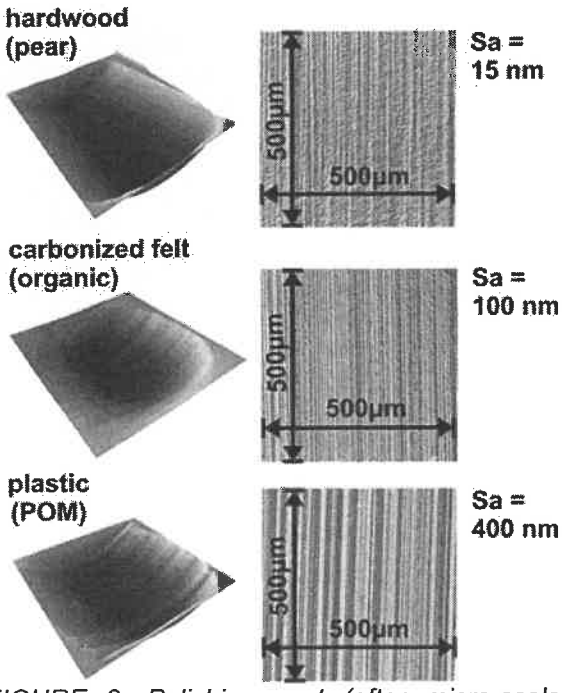

FIGURE 3. Polishing spot (after micro-scale abrasion wear test) depending on pad material with corresponding surface quality at steel workpiece

The surface topographies of the footprints highlight this effect. In spite of directed relative velocity (comparing to profile polishing of structured surfaces) between polishing pad and workpiece during the micro-scale abrasion wear test the hardwood pad material generate roughness is optical quality; the plastic pad and the felt pad perform worse. The footprint measurements by white light interferometry show a significant difference in the surface topography after the micro scale abrasion wear test.

The volume based analysis of the removal functions also show differences between felt, hardwood and plastic. For the evaluation of the experiments the Preston hypothesis was used [4]:

$$\frac{dz}{dt} = k_P \cdot p \cdot v_r$$

Here, the material removal rate dz/dt is calculated from removed volume, contact area and polishing time, the polishing pressure p is calculated from normal polishing force and contact area and the relative velocity v_r is calculated from revolution speed and diameter of the polishing pad. The linear Preston-coefficient k_P incorporates all further influence factors.

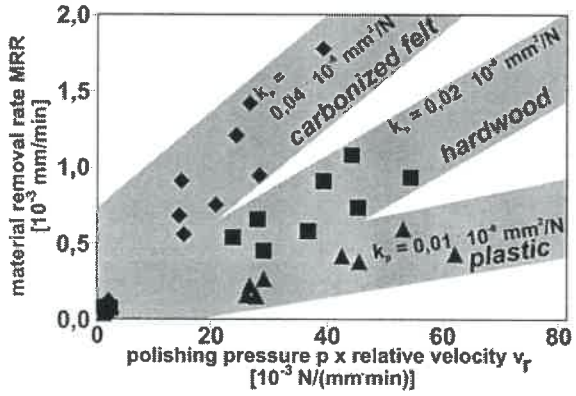

polishing pad: plastic, hardwood, carbonized felt	**work piece:** steel 1.2083
	polishing pressure: p = 0,1 - 3,5 N/mm²
	relative velocity: v_r = 0,25 m/s
abrasive: 3 µm diamond suspension water/oil based	**polishing time:** t = 10 - 20 min
	metrology: profilometer

FIGURE 4. Preston coefficient k_p depending on polishing pad material

Figure 4 shows k_P depending on the applied polishing pad material. With carbonized felt pads the maximum material removal can be realized, pads made of hardwood and plastic achieve lower removal rates. The capability of a polishing process is significantly characterized by the applied polishing pad material. For the newly developed abrasive polishing process the Preston hypothesis is applicable. But compared to conventional polishing processes for continuous surfaces novel pad materials are used which have a strong influence to material removal und polishing effect on the workpiece.

The time dependent material removal is basically characterized by the wear behaviour of the polishing pad. Here, the plastics POM/PA6 fulfil the longest durability as expected. Hardwood bloats after contacting polishing suspensions. Therefore the shape of the polishing pad changes which leads to modification of contact area and polishing pressure and by this to changing material removal behaviour.

At carbonized felt pads single fibers are loosened out of the impregnation which can lead to localised unintentional material removal (e.g. edge rounding). Wear experiments have shown that with applicable pad dressing strategies and continuous process monitoring (polishing pressure, coloration of polishing suspension) constant polishing results are realizable with all analysed pad materials.

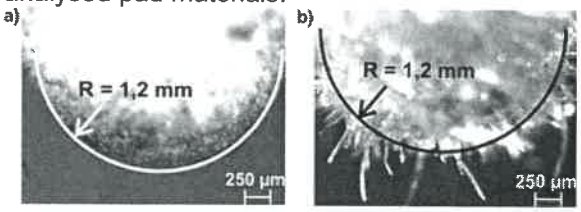

FIGURE 3. Spherical polishing pad made of carbonized feld after dressing (a) and after polishing time t = 5 min (b)

DEFORMATION MODELLING OF POLISHING PADS BY FEM

At groove tips a deformation of the felt material still leads to edge rounding resulting from the compression load during polishing. In previous work the polishing tool deformation has been ignored in experiments, using only very low process forces resulting in negligible deformation.

Thus, the carbonized felt material was characterized by compression experiments giving information about Young's modulus and transversal contraction. These felt material properties and additionally the geometry of the polishing tools is used as input quantities for a FEM deformation model. This model provides

the basis for the calculation of the pressure distribution in the contact area of polishing tool and structured workpiece. A tilted spherical polishing tool was modeled for finishing cylindrical groove structures in tungsten carbide tool inserts. In order to be able to consider in future process designs a larger range of polishing forces adapted polishing tool geometries must be developed, see figure 4.

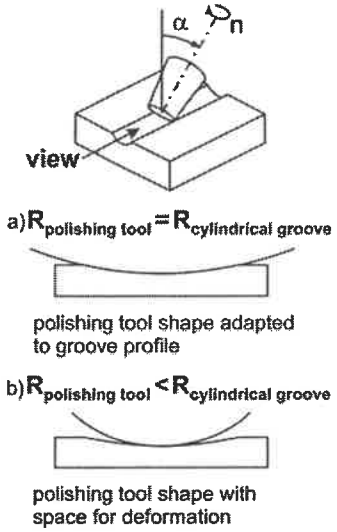
α
n
view
a) $R_{polishing\ tool} = R_{cylindrical\ groove}$
polishing tool shape adapted to groove profile
b) $R_{polishing\ tool} < R_{cylindrical\ groove}$
polishing tool shape with space for deformation

FIGURE 4. Adapted tool shapes during profile polishing of cylindrical grooves

In a first step the FEM model confirms the deformation of the tool during polishing, see figure 5a. The left side shows the first polishing tool contact without load and no deformation. On the right side the deformation under load is visible. A subsequent reduction of the tool radius can avoid the overlap of felt material at adjacent groove areas, see figure 5b. The FEM model shows the required smaller tool diameter depending on polishing force, tool dimension and tool material properties. This adapted tool diameter leads to a homogeneous polishing pressure distribution in the contact area.

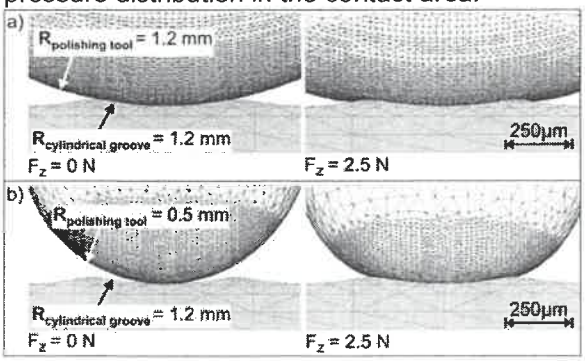

FIGURE 5. FEM-modelling of carbonized felt polishing tool

CONCLUSION

Polishing experiments with adapted tools have verified the FEM model showing a minimized shape deviation at groove transitions after polishing with higher process forces. Advantage of the model based process design is the minimisation of tool shape iteration cycles and the achievement of deterministic polishing processes. Beside material deformation further influencing factors like tool wear and material inhomogeneity lead to local unintentional material removal during polishing which has to be observed for the process design.

By abrasive profile polishing the roughness of micro structured grooves can be improved to optical quality. This polishing process is applicable in optical mould making for quality increase of replicated structured glass lenses.

ACKNOWLEDGEMENT

The work is funded by the German Research Foundation (DFG) within the Transregional Collaborative Research Center SFB/TR4 "Process Chains for the Replication of Complex Optical Elements".

REFERENCES

[1] Evans, C. J.; Bryan, J. B.: "Structured", "Textured" or "Engineered" Surfaces. Annals of the CIRP, Vol. 48/2, 1999, pp. 541-555

[2] Klocke, F.; Brinksmeier, E.; Riemer, O.; Klink, A.; Schulte, H.; Sarikaya, H.: Manufacturing structured tool inserts for precision glass moulding with a combination of diamond grinding and abrasive polishing. IDR Industrial Diamond Review, Vol. 4, 2007, pp. 65-69

[3] Brinksmeier, E.; Riemer, O.; Gessenharter, A.: Finishing of structured surfaces by abrasive polishing. Precision Engineering, Journal of the International Societies for Precision Engineering and Nanotechnology, Vol. 30, 2006, pp. 325-336

[4] Preston, F.W.: The Theory and Design of Plate Glass Polishing Machines. Journal of the Soc. of Glass Technology, Vol. 11, 1927, pp. 214-256

A METROLOGICAL STUDY ON HARDENED STEEL SURFACE FINISHING USING A DIAMOND BURNISHING TOOL

Hidetake Tanaka[1], Hiroaki Tabuto[2], and Kazuhisa Yanagi[1]
[1]Department of Mechanical Engineering
Nagaoka University of Technology
Nagaoka, Niigata, Japan
[2] 3rd Production Engineering Department
Fuji Heavy Industries Ltd
Ota, Gunma, Japan

INTRODUCTION

In recent years, manufacturing process that provides with low cost and high speed as well as accuracy and precision has been increasingly required. The processing techniques, which reduce the environmental load such as grinding sludge and lubricant are also desired in the industry. Today, surface burnishing by a diamond tool is the focus of attention from the industrial field. The burnishing process is one of micro plastic working methods, i.e. a special diamond point tool compresses the metal surface to obtain a mirror-like surface finish as well as to improve its surface hardness like shot-peening. Although, the roller burnishing techniques are applied to surface finishing process of aluminum alloy or stainless steel parts in the industrial field, that is not applicable to hard work materials such as quenched hardened steel. Therefore, a Diamond Burnishing process is proposed as a solution for this instance. However the adequate machining conditions to achieve proper surface finish have not been clarified. In order to evaluate the relationship between burnishing conditions and surface texture, practical burnishing tests were carried out under several machining conditions considering burnishing load and feed rate using an NC lathe.

BURNISHING PROCESS

The burnishing process is one of micro plastic working methods. A special diamond point tool compresses the metal surface to obtain a mirror-like surface finish like as shown in figure 1. Figure 2 shows a practical process while burnishing. Advantage of Burnishing process can be summarized as follows:

- Quick change from a rough surface to a mirror-like surface of Rz 0.1-0.8 μ m.
- Hardening effect and increase of wear resistance.
- Non-machining chip.
- No additional equipment is required except for a NC lathe.

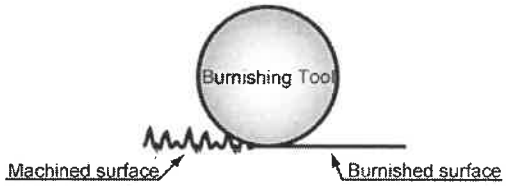

FIGURE 1. Schematic of burnishing process

PROSESS AND MEASUREMENT

Experimental Conditions

In this study, Employed material, work tool and NC machine tool are as follows:

- Workpiece: Cylinder shaped high carbon chromium bearing steel (ISO 100Cr6 Solid-core round bar d20mm L75mm)
- Turning tool: Tungaloy Corporation cBN Sintered compact tool T-cBN BX330
- Burnishing tool: SUGINO MACHINE LTD. Diamond burnishing tool Cat' s EYE
- Machine tool: TAKAMATSU MACHINERY CO., LTD. CNC Precision lathe X-10

Bare and quenched workpieces ware prepared for the experiment. The workpieces are turned before burnishing process as pre processing to satisfy the surface texture of the workpiece to be

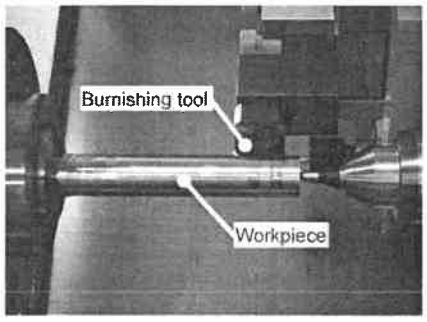

FIGURE 2. Practical burnishing with NC lathe

burnished. The Burnished workpieces were measured by the surface texture and contour measuring instrument (TOKYO SEIMITSU CO. LTD., SURFCOM3000A) and the roundness measurement instrument (Mitsutoyo CO. LTD., ROUND TEST RA-700).Experimental conditions of the burnishing process, which determined considering to the basic experiment are as follows:

- Turning feed rate: 0.16 - 0.22mm/rev
- Burnishing load (Bare material): 120N
- Burnishing load (Quenched material): 300N
- Burnishing feed rate: 0.1 - 0.005mm/rev

Experimental result (surface texture)

The relationship between surface texture and feed rate of the burnished workpieces are graphed out with considering measured result. Figure 3 shows the measured results of the bare material and Figure 4 shows that of quenched material. Figure 3 revealed that in the case of the bare material, excessive small feed rate does not improve the surface texture and the burnished surface is strongly affected by the turned surface. On the other hand, in the case of the quenched material, surface texture is improved with an increase in the burnishing feed rate regardless of the turned surface as shown in Figure 4. This experimental result revealed that the introduced burnishing techniques are significantly effective to make hardened steel surfaces smoother than conventional grinding. However the diamond chip is gradually wearing while using for the burnishing process, the burnished surface texture is significantly affected the worn diamond chip surface texture according to consideration of experimental result.

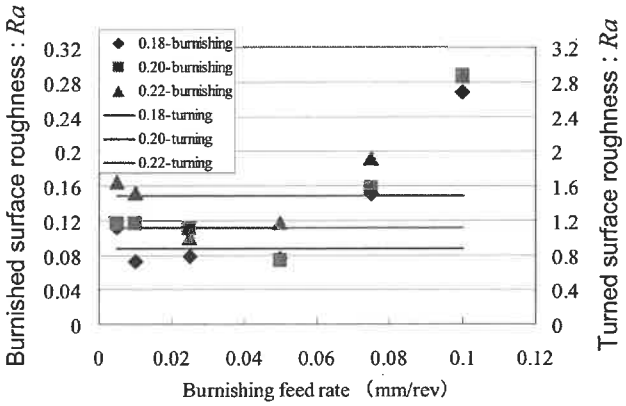

FIGURE 3. Relationship between surface texture and feed rate (Bare material)

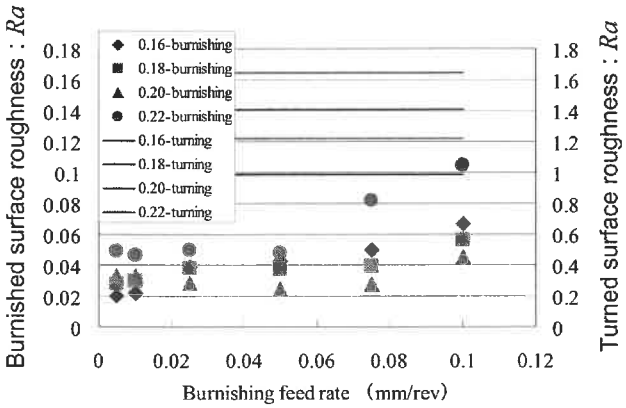

FIGURE 4. Relationship between surface texture and feed rate (Quenched material)

The above result, Figure 5 and Figure 6 show the roughness profiles of the burnished surface of each material. Each roughness profiles are processed in the same condition and these profiles indicate the difference depending on the plastic deformation for the turned surfaces. As shown in Figure 5, plastic deformation by the burnishing tool affects to swelled part around of the hollow. It indicates that excessive small feed rate induces large swelled and hollowed part incrementally while burnishing process and it wreaks spalling surface in the case of bare material.

Experimental result (roundness)

The surface texture of burnished workpiece surface has specific features such that roughness profile in the axial direction is

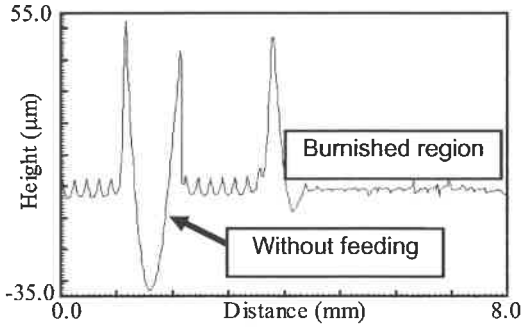

FIGURE 5. Roughness profile (Bare material)

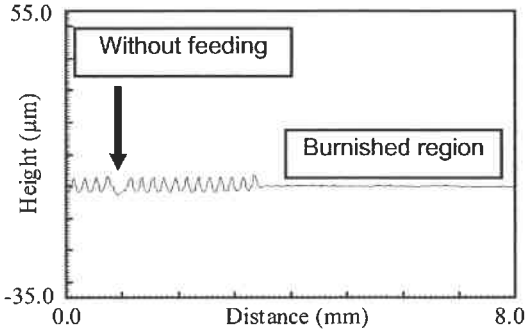

FIGURE 6. Roughness profile (Quenched material)

flattened and while that in the circumferential direction is undulated. Figure 7 shows the roundness measurement results of turned and burnished workpiece. It indicates that burnishing process improves roundness in every condition. However, excessive burnishing load doesn't always improve the surface roughness ether.

Investigation of plastic deformation layer

In order to consider the effectiveness of the burnishing process to the surface layer of the workpiece, cross section of burnished workpiece is observed by SEM (JEOL Ltd. JSM-5600LV). By way of comparison, the ground workpiece, which surface texture improved as same as burnished on is also observed. The burnishing conditions of the observed workpiece are as follows:

- Quenched material
- Turning feed rate: 0.20mm/rev
- Burnishing load: 300N
- Burnishing feed rate: 0.025mm/rev

Figure 8 (a) and (b) show the observed image of burnished and ground workpieces. As shown in Figure 8 (a), when the burnishing tool flattened the surface of the workpiece, plastic deformation of the surface layer is exited to a depth of less than 4μm in the case of the quenched material. Meanwhile, it is expected that intensive residual compressive stress is remained in the surface layer. On the other hand, no plastic deformation of the surface layer is existed in the ground workpiece as shown in Figure8 (b).

APPROXIMATION METHOD FOR CHANGE IN DIAMETER

Previously, the burnished surface textures are appreciated without any consideration for change in diameter. Because prediction of changing in diameter is too difficult due to the burnishing process is application of plastic deformation on the surface of the workpiece including spring back phenomena, not a removal processing. Therefore, in the study the estimation method of change in diameter using algorithm conception of V-parameter deliberated at ISO is suggested and it practically applied considering before and after burnished surface.

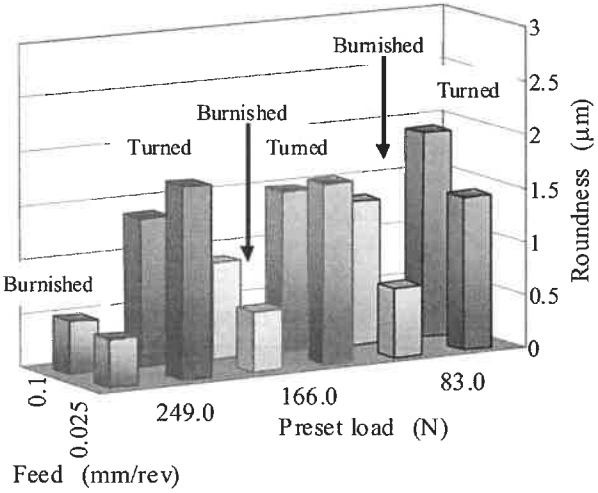

FIGURE 7. Roundness measurement result comparing turning with burnishing

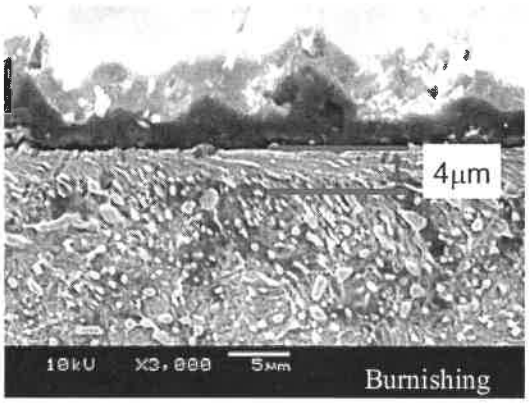

(a) Surface layer by burnishing

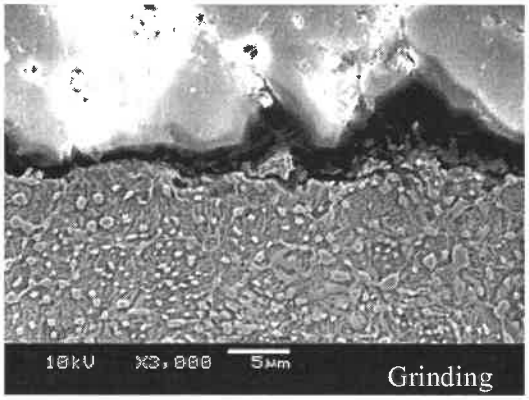

(b) Surface layer by grinding

FIGURE 8. Surface layer images by SEM

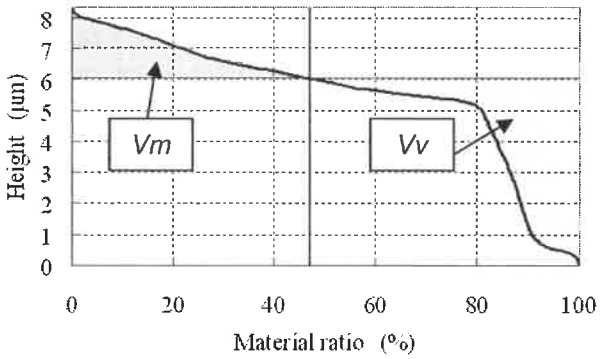

FIGURE 9. Material ratio curve of turned workpiece

Figure 9 indicates calculation result in order of material ratio as *Vm=Vv* from the primary profile of the selected turned part (circled part) as shown in Figure 10 by using of V-parameter. In this case, the material ratio as *Vm=Vv* is 47.1% and it corresponds to 2.2μm lower level from the top of the primly profile. Actually, the change in height is 2.2μm low from the top of the primly profile of turned part in Figure 10.
In the case of the quenched material, the same approximation method for change in diameter is applied considering to the primly profile as shown in Figure 11. From the calculated result, the material ratio as *Vm=Vv* is 43.3% and it corresponds to 3.3μm lower level from the top of the primly profile. In this case, the change in height is 3.3μm low from the top of the primly profile of turned part and the estimation of change in diameter on the burnishing process are demonstrated.

CONCLUSION

We examined the metrological properties of surface finish on cylindrical workpiece using a diamond burnishing tool and obtained the following concluding remarks.
The proposed burnishing process decreases surface roughness by about 10% and also roundness by about 1/30.
Excessive burnishing load doesn't always improve the surface roughness and roundness in this burnishing process.
Plastic deformation of the surface layer by burnishing tool is exited to a depth of less than 4mm in the case of the quenched material.
The estimation method of change in diameter using algorithm conception of V-parameter deliberated at ISO is suggested and it clarified with practically applying considering before and after burnished surface.

REFERENCES

[1] N.S.M. El-Tayeb., K.O. Low and P.V. Brevern, Influence of roller burnishing contact width and burnishing orientation on surface quality and tribological behaviour of Aluminium 6061, Journal of Materials Processing Technology 186 (2007) 272-278

[2] Gyula Varga, Illés Dudás and Balázs Leskó, Examinations of Sliding Burnishing for Finishing Operation of External Cylindrical Surfaces, Proc. of Int. Conf. on Met & Props, April(2000)

[3] Hiroaki TABUTO, Hidetake TANAKA, and Kazuhisa YANAGI, A metrological study on cylindrical surface finishing using a diamond burnishing tool, Proc. of Int. Conf. on Met & Props, July(2007)

[4] ISO 13565-2, Geometrical Product Specification - Surface texture : Profile method; Surfaces having stratified functional properties - Part2: Height characterization using the liner material ratio curve

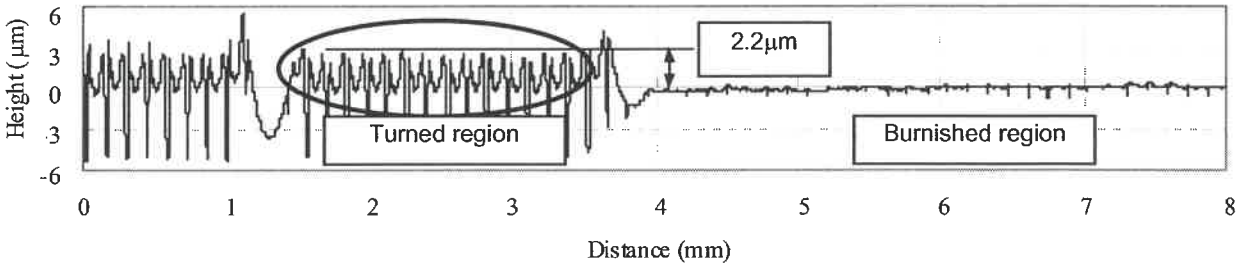

FIGURE 10. Primary profile of turned and burnished work surface (Bare material)

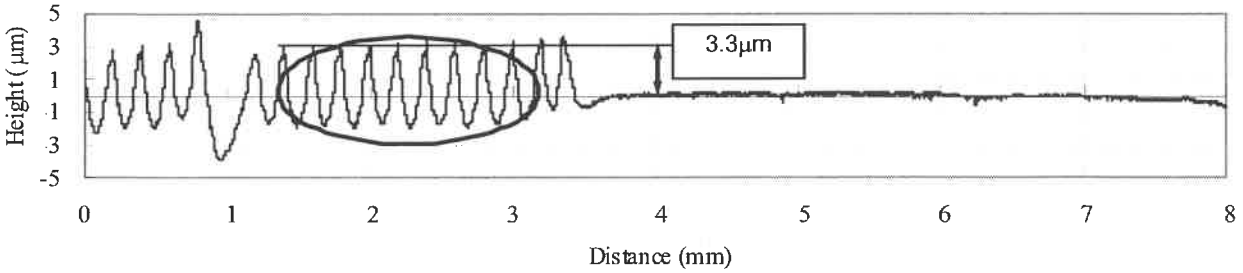

FIGURE 11. Primary profile of turned and burnished work surface (Quenched material)

CONTINUOUS PHASE PLATE POLISHING USING MAGNETORHEOLOGICAL FINISHING

Marc Tricard[1] (2), Paul Dumas[1] , Joe Menapace[2]
[1]QED Technologies®, Rochester, NY USA
[2]Lawrence Livermore National Laboratories, Livermore, CA USA

INTRODUCTION

Magnetorheological Finishing (MRF®) methods and systems have been developed to imprint complex, continuously varying topographical structures onto 430 x 430 millimeter optical surfaces. These optics, known as continuous phase plates (CPPs) are important for kilojoule- and megajoule-class laser systems requiring precise control of beam-shape, energy distribution and wavefront profile. MRF's sub-aperture polishing characteristics make it possible to imprint complex computer generated topographical information at spatial scale-lengths approaching 1 millimeter and surface peak-to-valleys as high as 22 millimeters to within 30 nanometers of design specifications.

High-powered laser systems utilized for inertial confinement fusion research, such as the National Ignition Facility (NIF) at Lawrence Livermore National Laboratory (LLNL), Laser MegaJoule (CEA) near Bordeaux, France, and OMEGA at the Laboratory for Laser Energetics require precise characterization and control of the laser beam illumination at the target plane. A major portion of this work centers upon developing and engaging state-of-the-art technology to set the stage for creating nuclear fusion in a laboratory setting. Continuous phase plates (CPPs) form the vital and enabling portion of the optics chain used in these kilojoule- and megajoule-class laser systems because they make it possible to manipulate and control laser beam-shapes, energy distributions, and wavefront profiles [1, 2]. This prescribed beam characteristic control is made possible via manipulation of the incoming wavefront by the CPPs. CPPs function in combination with a focusing element to define the size and shape of the beam at focus, the wavefront characteristics (uniformity) at the focal plane, and the intensity of the beam within the focal spot.

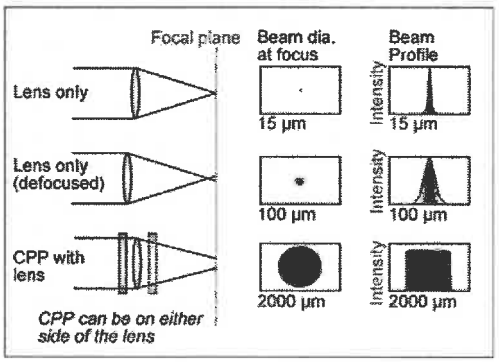

FIGURE 1. Focal plane characteristics with a lens focused to diffraction limit (top), with a lens moved from focus (middle), and with a lens and CPP combination set at focus (bottom). The CPP allows the focal plane to be sized and shaped while maintaining a high level of uniformity across the far-field spot.

As illustrated in Figure 1, a focusing element such as a lens results in laser light focused to a diffraction limited far-field spot of about 15 µm in diameter at the focal plane (about a 30,000 times reduction in size). Even though the focused beam possesses high intensity, it is too small to use for illumination of large areas (about 1 mm in size) with high intensity coherent light. Additionally, it has a highly non-uniform intensity profile due to the limitations of the focusing element and light diffraction, which result in non-uniform illumination. Attempting to increase the spot size to about 100 µm by defocusing the lens, which one would think could be a course of action, does make the far-field spot larger, but its shape and intensity profile remain ill-conditioned. Introduction of a CPP into the optics chain that is specifically designed to yield the required far-field spot size and intensity uniformity in the focal plane solves the problem. CPPs fall into the category of diffractive optics where we take advantage of the apparent bending of light waves in response to small topographical changes on an optical surface. CPPs are made by imprinting a continuously varying phase profile onto an optical surface, as shown in Figure 2.

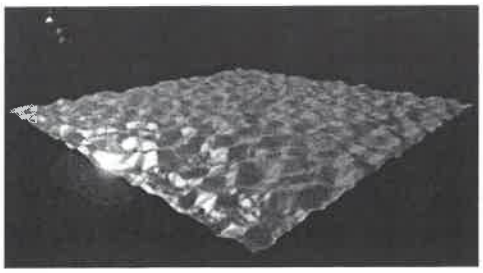

FIGURE 2. Continuously varying topographical CPP pattern with an 8.6 µm peak-to-valley imprinted onto a 430 x 430 x 10 mm fused silica substrate using MRF.

MANUFACTURING CPPs

Manufacture of CPPs to the extreme tolerances required for use in high-power laser systems demands state-of-the-art technology for topographical imprinting. Magnetorheological Finishing (MRF®) polishing technology is a highly versatile and precise process for polishing surface topography into optical surfaces. MRF is a deterministic polishing process; that is, the end result can be predicted and repeatedly achieved. MRF greatly enhances product quality and repeatability while providing a quantum leap in throughput, productivity, yield, and cost effectiveness by replacing the art of optic polishing with science and technology. [3]

MRF is an advanced optical finishing process combining interferometry, precision equipment, and computer control [4]. It utilizes a sub-aperture polishing tool, or removal function, generated by the interaction of a magnetic field and an iron-based Magnetorheological fluid containing microscopic abrasive particles such as ceria or nano-diamonds as shown schematically in Figure 3.

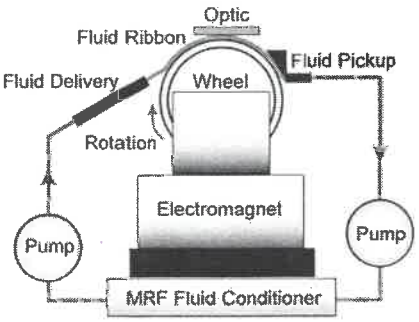

FIGURE 3. MRF polishes optics by creating a sub-aperture polishing tool using magnetic media and an electromagnet. Material is removed in the area where the optic is immersed into the fluid ribbon. Surface polishing is accomplished by rastering or rotating the optic over the ribbon. The fluid is continuously recycled.

A MRF tool removes material from an optical surface when the optic is positioned at a fixed distance from a moving spherical wheel. An electromagnet located below the wheel surface generates a magnetic field in the gap between the wheel and optic. When the MR fluid is delivered to the wheel, it is pulled against the wheel surface by the magnetic field gradient and becomes a sub-aperture polishing tool. A sophisticated computer program determines a schedule for varying the translation velocity of the optic as it sweeps through the polishing zone, in a raster pattern. Because the removal function is interferometrically characterized and highly stable, the system can efficiently deliver high precision parts. Other advantages are that the polishing tool is easily adjusted, and conforms perfectly to the optical surface, enabling topographical polishing. The deterministic nature of the MRF process makes it possible to correct optical figure over a large area using a small controllable removal function. In its normal operating configuration, MRF uses the removal function and dwell time to differentially remove material from areas of an optic so that the desired surface or wavefront properties are obtained. Imprinting of surface topography onto an optical surface such as that required for CPPs is a non-traditional application of this technology. The distinct difference is that instead of removing the waviness or imperfections from the optical surface, MRF is applying surface structure in a deterministic fashion. For short spatial periods, one can think of the process as imprinting or correcting a number of small geometric errors, or lenses, present on a large piece of glass. Here, the size of the removal function becomes important in attaining the desired topographical fidelity. The MRF system software provides the mechanism to perform this task by using a solving algorithm that performs a deconvolution of the removal function shape and the incoming surface structure measured via interferometry or mathematically supplied by the user. In a typical raster-polishing application, the MRF software uses the existing surface figure as a starting point and a flat surface as the desired end-point. The algorithm attempts to converge to a solution that minimizes the rms of the surface via the removal function/existing surface deconvolution. For imprinting, the process must be inverted. It must start with an existing surface figure and end with a surface possessing desired topography. This is

accomplished by adding the height-inverted topographical imprint map (negative image) to the starting metrology. The solving algorithm converges this virtual surface towards flatness. This results in the proper removal of material from the initial optical surface even though the software output is a plano surface. The process is shown in Figure 4.

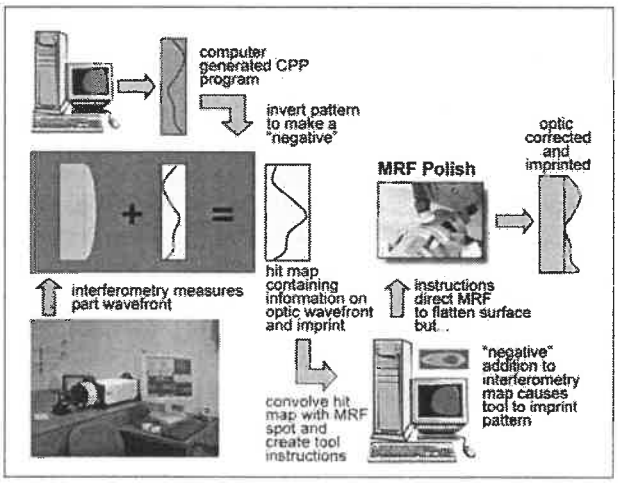
computer generated CPP program
invert pattern to make a "negative"
optic corrected and imprinted
MRF Polish
interferometry measures part wavefront
hit map containing information on optic wavefront and imprint
instructions direct MRF to flatten surface but...
"negative" addition to interferometry map causes tool to imprint pattern
convolve hit map with MRF spot and create tool instructions

FIGURE 4. The MRF imprinting process integrates interferometry, computer generated prescriptions, and custom-designed software to create machine instructions to deterministically enable topographical imprinting on CPPs.

Imprinting large-aperture CPPs requires specialized MRF instruments capable of imprinting topographies on large-aperture optics. An integral part of our efforts for making CPPs a reality involved a large-aperture MRF tool. This machine is used to perform final finishing on CPP substrates and to imprint the necessary topography to manufacture a CPP. The large-aperture MRF system uses two wheels for efficiency, one large (370 mm diameter) and the other small (50 mm diameter), with optimized computer algorithms that together provide a greatly increased range of finishing options and range of topographical feature sizes that can be imprinted. The MRF process provides for a high level of versatility and speed in CPP manufacture as topographical polishing can be conducted by combining computer generated CPP and/or interferometric profiles with large MRF volumetric removal rates (~1 mm^3/min). Additionally, the process seamlessly fits into the advanced manufacturing process technology for production of large-aperture optical components possessing high-ultraviolet damage resistance. [5]

CPP imprinting of large-aperture optics typically utilizes both the large and the small wheels to take advantage of the different material removal functions sizes (bandwidth). The imprinting utilizes a multi-pass approach to obtain the desired topographical fidelity using superposition to provide for process breakpoints necessary for testing. To start the process, computer generated hitmaps containing the CPP topographical pattern and the existing wavefront in the substrate are introduced to the MRF machine. The initial passes during the MRF imprinting process use the 370 mm wheel and large MRF removal functions to imprint long spatial period features into the optical surface. Iterative raster scans are used with smaller removal functions to imprint smaller spatial period features into the optic and to refine the gradients present in the pattern. These passes begin with the 370 mm wheel and moderately sized removal functions and end with the 50 mm wheel and small removal functions. This strategy maximizes material removal over the topographical frequencies being imprinted. Each iteration is conducted using the CPPs measured transmitted wavefront from each MRF pass. This in-process interferometry is used to track imprinting progress and to optimize phase front corrections in the CPPs topography. The iterative process is complete when the optic transmitted wavefront converges to the required specification. We routinely attain 20-30 nm rms difference between the CPP prescription presented to the MRF and the final optic transmitted wavefront. With over a total of 82 large-aperture CPPs imprinted, we have only found 1 MRF related artifact that was of concern. This artifact was a polished localized lenslet on the optic surface arising from a drop of MR fluid that was not cleaned off during the imprinting process. Additionally, we have shown that CPPs can be manufactured for use in the ultraviolet (351 nm) portions of a laser system at fluences up to 14 J/cm^2 at 3 nsec pulse length by extending our capability of manufacturing laser damage resistant optics using MRF to CPP imprinting. [5] This is due to the fact that MRF polishing removes subsurface damage, which is a major source responsible for initiating damage in optics at high laser fluences. [6]

The MRF imprinting process is the only proven process that can make ultra-precise large-aperture CPPs. From the size standpoint, this process can routinely manufacture high performance plates up to 1000 x 750 mm in size.

MRF is also very efficient with respect to the fabrication time required to complete a CPP imprint. For a 430 x 430 mm CPP, MRF can complete an imprint in 56 hrs. This puts MRF imprinting into a high-throughput manufacturing category where plates can be manufactured at rates 3 to 7 times faster than other technologies.

RESULTS

In March 2006, we imprinted a 134 mm diameter CPP for the JANUS laser system at LLNL for high-powered short-pulse laser experiments, Figure 7. The JANUS laser has produced the highest irradiance (power per unit area) ever recorded: two sextillion (2×10^{21}) watts per square centimeter.

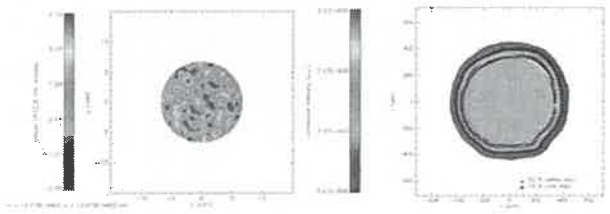

FIGURE 7. Near-field interferogram (left) for a 135 mm diameter CPP fabricated for use on the JANUS laser system imprinted using MRF with a peak-to-valley of 11.7 μm. The resulting far-field spot (right) has a 710 μm diameter at 95% encircled energy. The far-field spot is uniform to within 4%.

We are currently using large-aperture MRF polishing to manufacture ultraviolet laser damage resistant main debris shields and CPP substrates for use on the NIF laser system at a rate of 10 optics per month. In addition to imprinting CPPs, we developed MRF polishing techniques to a point where we routinely use it to manufacture large-aperture 430 x 430 mm plano fused silica optics to less than 125 nm peak-to-valley flatness that can withstand laser fluences of greater than 14 J/cm^2 at 351 nm, 3 nsec pulse width without damage.

Over the past year, our team has engaged large-aperture MRF polishing on 940 mm and 800 mm diameter BK-7 grating substrates for use on the OMEGA, VULCAN (Great Britain), TITAN, and NIF ARC petawatt-class laser systems and laser system upgrade projects. The extreme precision of the MRF tool enables us to polish these substrates to less that 100 nm peak-to-valley flatness over the entire optical surface so that high-efficiency gratings can be subsequently applied. These optics are used as laser beam pulse compressors.

SUMMARY

Manufacture of CPPs to the extreme tolerances required for use in high-power laser systems demands state-of-the-art imprinting technology to be successful. To meet this challenge, we engaged in the development of Magnetorheological Finishing (MRF) technology to arrive at a highly versatile and precise process for polishing surface topography into optical surfaces. MRF is an advanced optical finishing process combining interferometry, precision equipment and computer control, has brought the optics fabrication industry to new levels of precision in recent years.

REFERENCES

[1] Menapace, J., Davis, P., Steele, W., Hachkowski, M.R., Nelson, A., Xin, K., 2006, MRF applications: on the road to making large-aperture ultraviolet laser resistant continuous phase plates for high-power lasers, Proc. SPIE 6403, 64030N.

[2] Menapace, J., Dixit, S., Génin, F., Brocious, W., 2004, MRF for imprinting continuous phase plate structures onto optical surfaces, Proc. SPIE 5273, 220.

[3] Golini, D., Kordonski, W.I., Dumas, P., Hogan, S., 1999, Magnetorheological finishing (MRF) in commercial precision optics manufacturing, Proc. SPIE 3782, 80.

[4] Evans, C.J., Paul, E., Dornfeld, D., Lucca, D.A., Byrne, G., Tricard, M., Klocke, F., Dambon, O., Mullany, B.A., 2003, Material Removal Mechanisms in Lapping and Polishing, Annals of the CIRP, 52/2: 611.

[5] Menapace, J., Penetrante, B., Golini, D., Slomba, A., Miller, P., Parham, T., Nichols, M., Peterson, J., 2002, Combined advanced finishing and UV-laser conditioning for producing UV-damage-resistant fused-silica optics, Proc. SPIE 4679, 56.

[6] Kordonski W.I., Golini D., 1999, Fundamentals of magnetorheological fluid utilization in high precision finishing. Journal of Intelligent Material Systems & Structures, 10/9, 683-9.

CHARACTERIZING QUANTUM DOTS FOR USE IN DETECTING SUBSURFACE DAMAGE

Wesley B. Williams[1], Brigid A. Mullany[1], Patrick J.Moyer[2], Wesley C Parker[2] and Mark H. Randles[3]
[1]Department of Mechanical Engineering and Engineering Science
University of North Carolina Charlotte
Charlotte, NC, USA
[2]Department of Physics and Optical Science
University of North Carolina Charlotte
Charlotte, NC, USA
[3]Northrop Grumman Synoptics
Charlotte, NC, USA

SUMMARY

Polishing, lapping and grinding are finishing processes used to achieve critical surface parameters in a variety of precision applications including optical and electronic components. As these processes remove aberrations on the surface through mechanical and chemical interactions they may induce a stressed layer of cracks below the surface. This subsurface damage can degrade the performance of a final product by creating optical aberrations due to diffraction, premature failure in oscillating components and a reduction in the laser damage threshold of high energy optics [1]. These defects are typically detected by etching or dimpling the surface to expose the underlying damage, both of which are destructive tests.

The authors propose a non-destructive method for assessing subsurface damage in a polished or lapped glass sample. The method consists of tagging the abrasive slurry with quantum dots (nanometer scale semiconductors that fluoresce at a given wavelength when subject to laser excitation) and using a confocal microscope to map the depth of fluorescence signal in the sample. The quantum dots are believed to be sufficiently small (with diameters of 2-5nm) [2] that they will be able to travel into sample defects if they are open to the surface during the polishing process.

Prior to polishing samples with quantum dot tagged slurries, it is important to characterize the performance of the confocal microscope and the expected fluorescent response in the samples. Toward this end, glass samples were exposed to high concentration solutions of quantum dots for varying times before being cleaned. It was found that samples exposed for the longest duration (270 minutes) had high localized levels of fluorescent response, indicating that quantum dots had been adsorbed onto the surface.

BACKGROUND

Subsurface Damage

Subsurface damage (SSD) is a layer of defects and stressed material that exists beneath an apparently smooth surface that provides no indication of the damage that lies beneath. These defects can negatively impact the performance of optical components by introducing optical aberrations, if aggravated they can propagate to the surface [1], or by reducing the laser induced damage threshold (LIDT), a measure of how much energy can be passed through an optical component without risking catastrophic failure [3].

Subsurface damage is seen to correlate with the rate of material removal [4]. As such, one theory is that localized compressive stress fields in the region of the traveling abrasive particle can cause brittle fractures which are further aggravated by the tensile stress fields that trail the abrasive particle. These fractures may be covered up by mechanisms such as material flow [5] or redeposition [6] or they may simply not be open to the surface in the absence of localized stresses.

Without visual indications of the damage at surface, SSD is difficult to detect. Traditionally it has been assessed by etching to remove the topmost layer of the surface, exposing the defects that lie beneath [7], as well as a related technique of dimpling [1]. While relatively simple

to perform, both tests are destructive and subject to the lateral resolution limitations of optical microscopy in assessing the subsurface damage.

Confocal Microscopy

Confocal microscopy, pioneered by Minsky, consists of a setup where light from outside the focal plane is largely prevented from reaching the light detector [8]. This rejection of light outside the focal plane, coupled with exclusion of light from points adjacent to the focal point reduces haze and increases the sharpness of the image [9]. By scanning and assembling an array of these points, a 2-D image can be formed and a series of these 2-D images (or optical slices) can be stacked to form a 3-D representation of the subject. Confocal microscopy is utilized for its ability to image planes beneath the surface of a sample [10] which lends it to biological imaging applications where it is used to acquire optical sections of living specimens which have been treated with fluorescent dyes. The lateral resolution improvements over conventional microscopes as well as the ability to focus beneath a sample surface lead to its use in the inspection of surface topographies for semiconductors and subsurface integrity of transparent materials [11] [12].

Quantum Dots

Quantum dots are nanoscale semiconductors that fluoresce when subject to excitation. They have been designed to restrict the motion of conduction band electrons by carefully controlling the particle size [13]. By restricting the size of the particle the conduction band electrons are forced into discrete energy states when excited, versus the bulk material which allows for a multitude of energy states. This restriction results in more narrow energy emission spectra when the semiconductors are excited.

These dots offer several advantages over organic fluorescent dyes such as rhodamine, the most important of which are; broad excitation spectra, more intense fluorescence, narrower emission spectra, and increased resistance to photobleaching (diminishing of the fluorescent response in successive excitations) [14].

EXPERIMENTAL SETUP

The confocal microscope used consists of three main components; the excitation source, the photon detector and the sample stage which interact as shown in Figure 1 below.

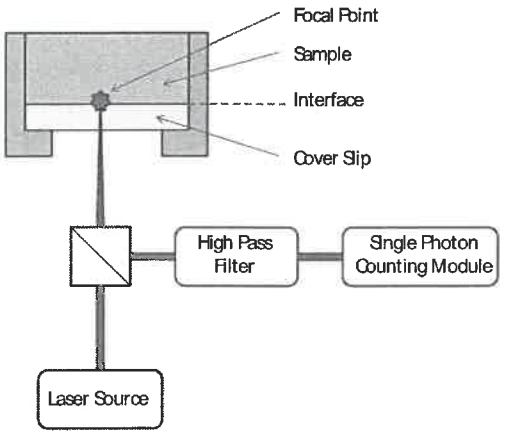

FIGURE 1. Arrangment of key components in the confocal microscope.

Excitation is provided at 470 nm wavelength by a PicoQuant PDL 800 diode laser driver pulsed at 10 MHz. The light illuminates the sample causing fluorescent material that is present to fluoresce. The light from the fluorescence is reflected through a corner cube to a long pass filter. The 538 nm long-pass filter is used to reject any reflected light from the laser. Finally, the small aperture of the EG&G SPCM single-photon avalanche diode acts as the pinhole in a traditional confocal microscope to reject fluorescence outside of the focal plane.

The sample stage is a flexure based design that keeps the optics stationary while moving sample during the scan [15]. The sample stage accommodates samples which can fit on a 25 mm × 25 mm glass cover slip (used to prevent contaminating the optics with fluorescent material) and provides motion in x, y and z directions with ranges of 64.5 µm, 49.7 µm and 31.5 µm respectively [15].

PROCEDURE

A quantum dots solution was prepared consisting of "Aloe Green" EviDots from Evident Technologies diluted with toluene and acetone to a concentration of 0.4 nmol/mL. These dots are cadmium-selenium cores with a zinc-sulfide shell and have a diameter of approximately 2.5 nm [2] with absorption and emission peaks at 540 nm and 553 nm respectively.

Samples of Corning 0215 glass were cleaned with isopropyl alcohol (IPA) moistened tissues

before 2 drops of quantum dot solution were placed on the surface. The samples were then divided into 4 groups. The first was cleaned after 15 minutes with IPA moistened tissues. The second group was cleaned in the same manner after 75 minutes while the third group as cleaned after 270 minutes. The final group was left uncleaned. Each sample surface was covered with a glass coverslip to prevent contamination.

The samples were then scanned on the confocal microscope at 3 locations and multiple focal planes into each sample. The first scan was taken at the interface between the sample and the coverslip at each location, then additional images were taken at 5 μm intervals into the cover slip (up to 10 μm) and 2 μm intervals into the sample (up to 10 μm) by finely adjusting the sample stage with piezoelectric actuators. At each focal plane, the fluorescent response was measured over a 40 μm×40 μm area with a total of 256×256 data points.

RESULTS

The fluorescent response data from each focal plane was analyzed in a MATLAB program that normalized the data with respect to the maximum fluorescent response measured on a glass sample without exposure to quantum dots. A representative scan of fluorescent response is shown below in Figure 2.

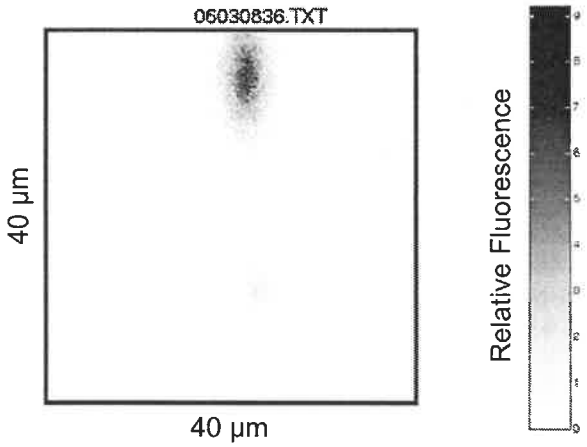

FIGURE 2. Image from the confocal microscope showing fluorescence in a sample exposed to quantum dots for 270 minutes prior to cleaning. The relative fluorescence scale is established with the maximum signal in a control sample (untreated by quantum dots) being equal to a value of one.

The fluorescent values below the normalized value of 1 were discarded as fluctuations were within the measurement noise of the sample. The remaining data was then examined to look for the maximum value and mean value of data points above the threshold as well as the percentage of the data points in the total scan that exceeded the threshold. The average values (across the 3 locations and multiple focal planes on the samples) and associated deviations are listed in Table 1.

TABLE 1. Normalized fluorescent response in glass samples exposed to quantum dot solution.

Sample	Maximum above threshold	Mean above threshold	% data above threshold
Cleaned after 15 minutes	1.4 (σ=0.2)	1.2 (σ=0.1)	0.01% (σ=.008%)
Cleaned after 75 minutes	1.9 (σ=0.9)	1.4 (σ=0.2)	0.03% (σ=.03%)
Cleaned after 270 minutes	12.0 (σ=17.7)	2.4 (σ=1.4)	0.9% (σ=1.2%)
Sample Not Cleaned	10.1 (σ=6.4)	2.3 (σ=0.6)	5.7% (σ=5.4%)

Samples with a fluorescent response above the threshold were then analyzed to see how the fluorescence varied with the position of the focal plane. Examples of the fluorescent response for samples cleaned after 75 and 270 minutes are shown in Figure 3 below.

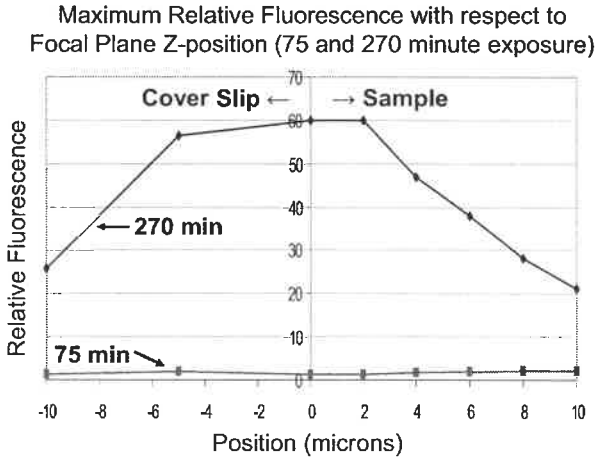

FIGURE 3. Relative Fluorescence with Respect to Position in the Sample. Negative values denote focal planes in the coverslip, while positive values are in the glass sample.

In the case of the sample exposed for 270 minutes, there is a peak in the fluorescent response near the interface. This value decreases as the focal plane is moved into the cover slip (negative values, moving left) and as the focal plane is moved into the sample (positive values, moving right). Such a decrease indicates that the fluorescent material is no longer in the plane of focus and its fluorescence is increasingly prevented from reaching the photon counting module.

DISCUSSION

The samples cleaned after 15 and 75 minutes showed minor increases in fluorescent response over the control samples and only in a small percentage of the data points. The samples cleaned after 270 minutes showed an extreme increase in the fluorescent response, but once again only in a small percentage of points.

The results of these tests illustrate the expected behavior of glass samples exposed to quantum dots in solution, independent of a polishing process. Exposure to quantum dots for less than 75 minutes prior to being wiped clean should not result in an appreciable adsorption of quantum dots onto the surface. Thus if significant number of quantum dots are retained in sample that was polished with a quantum dot tagged slurry for 75 minutes or less, the retention of quantum dots can reasonably be attributed to the influence of polishing mechanics. Polishing with quantum dot tagged slurries is underway.

ACKNOWLEDGEMENTS

This material is based upon the work supported by the Nation Science Foundation under Grant No. 0620783. Any opinions, findings and conclusions or recommendations expressed in this material are those of the authors and do not necessarily reflect the views of the National Science Foundation. Northrop Grumman, Synoptics has been an invaluable industrial partner with Bryan Stanley, Kevin Stevens and Adam Dittli making notable contributions to this work.

REFERENCES

[1] Lindquist, A., S.D. Jacobs, and A. Feltz. *Surface Preparations for Rapid Measurement of Sub-surface Damage Depth*. in *Science of Optical Finishing Topical Meeting*. 1990. Monterey, Calif.

[2] *Quantum Dots Features*. Quantum Dots Explained 2008 [cited 2008 April 14]; Available from: http://www.evidenttech.com/quantum-dots-explained/quantum-dot-features.html.

[3] Genin, F.Y., et al., *Role of light intensitification by cracks in optical breakdown on surfaces*. J. Opt. Soc. Am. A, 2001. **18**(10): p. 2607-2616.

[4] Lambropoulos, J.C., et al., *Non-contact estimate of grinding-induced subsurface damage*, in *Optical manufacturing and testing III*. 1999: Denver, Colorado. p. 41-50.

[5] Bowden, F.P. and T.P. Hugher, *Physical Properties of Surfaces IV-Polishing, Surface Flow and the Formation of the Beilby Layer*. Proceedings of the Royal Society of London. Series A, Mathematical and Physical Sciences, 1937. **160**(903): p. 575-587.

[6] Adam, N.K., *The Polishing of Surfaces*. Nature, 1927. **119**(2987): p. 162-163.

[7] Beilby, G.T., *Aggregation and Flow of Solids*. 1921, London: Macmillan and Company Limited.

[8] Minsky, M., *Microscopy Apparatus*, U.S.P. Office, Editor. 1961: USA.

[9] Semwogerere, D. and E.R. Weeks, *Confocal Microscopy*, in *Encyclopedia of Biomaterials and Biomedical Engineering*. 2005, Taylor & Francis.

[10] Hocken, R., N. Chakraborty, and C. Brown, *Optical Metrology of Surfaces*. CIRP annals, 2005. **54**(2): p. 705-719.

[11] Winn, A.J., et al., *Examination of microhardness indentation-induced subsurface damage in alumina platelet reinforced borosilicate glass using confocal scanning laser microscopy*. Journal of Microscopy, 1997. **186**(1): p. 35-40.

[12] Fine, K.R., et al., *Non-destructive, real time direct measurement of subsurface damage*. Proceedings of SPIE, 2005. **5799**: p. 105-110.

[13] Reed, M.A., *Quantum Dots*, in *Scientific American*. 1993. p. 118-123.

[14] *Nanomaterials catalog Vol 7*. 2005, Evident Technologies.

[15] Elliott, K., *Development of a Versatile Scanning System for Multi-Probe Biomedical Measurements*, in *Department of Mechanical Engineering and Engineering Science*. 2008, University of North Carolina at Charlotte: Charlotte, NC.

CONTACT STIFFNESS OF VITRIFIED AND RESINOID GRINDING WHEELS TAKING INTO ACCOUNT OF THE DRESSING CONDITION

T. Yamada[1], H.-S. Lee[1] and K. Takemoto[1]
[1]Department of Mechanical Engineering, College of Science and Technology, Nihon University, Tokyo, JAPAN

INTRODUCTION

The stiffness of a grinding system consists of the stiffness of a grinding wheel support system, the stiffness of a workpiece support system and the contact stiffness between a grinding wheel and a workpiece. In a grinding system, elastic deformation occurs as a result of the action of normal grinding forces. These elastic deformations induce not only residual stock removal from the workpiece, but also machining errors.

In these stiffnesses of the grinding system, the stiffness of the grinding wheel support system and the stiffness of the workpiece support system are determined depending on the construction of each grinding machine. On the other hand, the contact stiffness between the grinding wheel and the workpiece varies the difference of the dressing lead or of the grinding condition. Therefore, the quantitative estimation of the contact stiffness is difficult. And, in the conventional grinding operation, vitrified grinding wheel and resinoid grinding wheel are applied as well known. However, the difference of the contact stiffness of vitrified grinding wheels and resinoid grinding wheels have never been investigated. And, contact stiffness taking into account of dressing condition has never also been investigated.

From such a viewpoint, this paper aims to quantify the contact stiffness of vitrified grinding wheels and resinoid grinding wheels, taking into account of the dressing condition. The contact stiffnesses of grinding wheel under the dressing leads are 0, 0.25, 0.5 and 1.0 mm/rev are measured. And, the contact stiffnesses of both wheels are compared.

CONTACT STIFFNESS BETWEEN GRINDING WHEEL AND WORKPIECE

Contact stiffness is the stiffness in contact area between a grinding wheel and a workpiece. And, the elastic deformation of the grinding wheel occurs as a result of the action of normal grinding force in this contact area.

Figure 1 shows a schematic diagram of a horizontal grinding system. In order to calculate the contact stiffness of the grinding wheel, the elastic deformation of the wheel and the acting normal grinding force have to be measured. Normal grinding force F can be directly measured by a force sensor. However, an

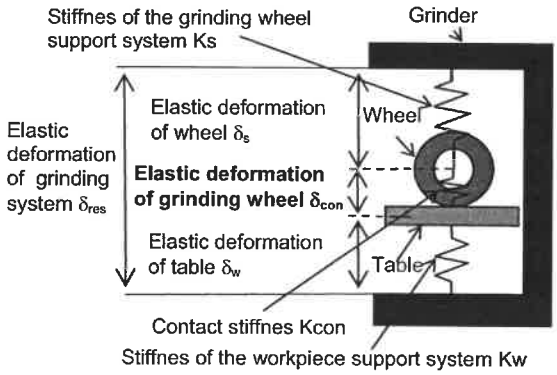
Stiffnes of the grinding wheel support system Ks
Grinder
Elastic deformation of wheel δ_s
Wheel
Elastic deformation of grinding system δ_{res}
Elastic deformation of grinding wheel δ_{con}
Elastic deformation of table δ_w
Table
Contact stiffnes Kcon
Stiffnes of the workpiece support system Kw

FIGURE 1. Schematic diagram of horizontal grinding system

elastic deformation of the grinding wheel in the contact area cannot be immediately measured. Here, elastic deformation of the grinding operation system δ_{res} includes a deformation of the grinding wheel support system δ_s, a deformation of the workpiece support system δ_w and the deformation of the grinding wheel δ_{con}, as shown in Figure 1. So, if deformations of δ_{res}, δ_s and δ_w could be measured and/or calculated, the elastic deformation δ_{con} could also be calculated by subtracting δ_s and δ_w from δ_{res}. Here, δ_{res} can be measured, however, δ_s and δ_w cannot be measured. Therefore, as the first step, in order to obtain δ_s and δ_w, stiffness of a grinder is measured.

STIFFNESS OF THE GRINDER AND FROATING AMOUNT OF THE TABLE

Stiffness of a grinding wheel support system Ks and stiffness of a workpiece support system Kw indicating stiffness of a horizontal grinder, as

shown in Figure 1, cannot be directly obtained. So, separating the stiffness between table and spindle head, and the stiffness between spindle head and spindle tip, these stiffnesses were

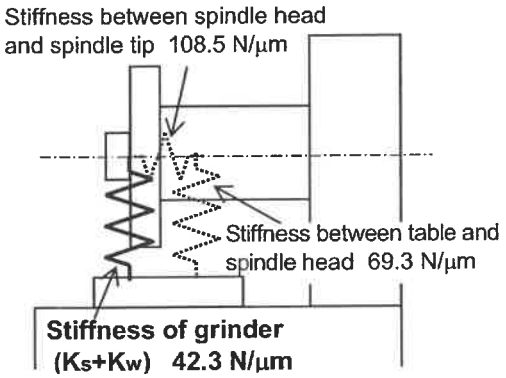

FIGURE 2. Measured results of stiffness of horizontal grinder

individually measured. Figure 2 shows measured results of both stiffnesses. The stiffness between table and spindle head was 69.3 N/μm, and the stiffness of spindle head and spindle tip was 108.5 N/μm. Since these stifnesses are connected in series, the stiffness of horizontal grinder can be calculated as 42.3 N/μm. Therefore, from this stiffness and normal grinding force, the elastic deformation between table and spindle tip $\delta s+\delta w$ can be calculatedly obtained by Hooke's law.

On the other hand, structure of table consists of sliding guide faces of V-flat shapes, where lubricating oil is applied. Here, grinder's table is floated by the lubricating oil when table is moving. Therefore, in grinding operation, certain depth of cut is settled, however, actual depth of cut is larger than settled depth of cut by influence of the floating amount of the table. In order to obtain actual depth of cut, the floating amount of the table has to be measured before experiment.

Figure 3 shows measured results of relation among the acted force in the table, the table feed speed and the floating amount of the table. From this figure, it is known that, in case that the table feed speed is 4.2 m/min, the table floats 2.6 μm when the acted force is 0 N, and the table floats 1.4 μm when the acted force is 80 N. From this result, it is known that the floating amount of the table varies with the normal grinding force. In this experiment, since the table

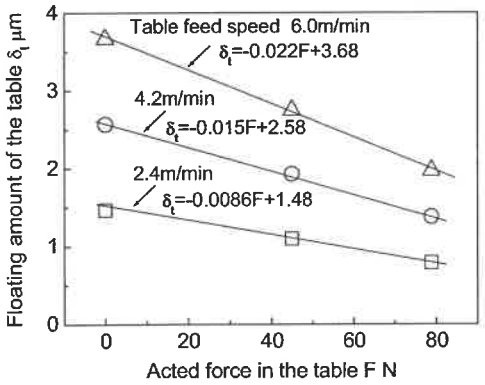

FIGURE 3. Relation between acted force in the table and floating amount of the table

feed speed is operated 4.2 m/min, the floating amount of the table δt is calculated by the following equation.

$$\delta_t = -0.015F + 2.58 \quad (1)$$

MEASURING METHOD OF CONTACT STIFFNESS

In order to obtain the elastic deformation of grinding wheel between a grinding wheel and a workpiece, the elastic deformation of total grinding system δres was measured at first. Table 1 shows grinding condition. Used grinding wheels were vitrified wheels and resinoid wheels, and were dressed by the dressing leads 0, 0.25, 0.5 and 1.0 mm/rev. In grinding operation, the peripheral peed was 1800 m/min, the settled depth of cut was about 10 μm. Normal grinding force was measured by a force sensor located below the workpiece. Since one path grinding was carried out, a grooves with wheel width is generated on the workpiece surface. After grinding, in order to obtain the stock removal of workpiece, ground groove shape was measured by a contour measuring device.

TABLE 1. The grinding condition

Grinding w heel	WA60K6V WA60J6B
Peripheral speed	1800m/min
Table feed speed	4.2m/min
Dressing lead	0, 0.25, 0.5, 1.0mm/rev
Dressing depth of cut	50μm
Settled depth of cut	10μm
Workpiece	SS400

MEASUERED RESULTS OF THE ELASTIC DEFORMATION OF GRINDING WHEEL

Figure 4 shows a measured result of ground surface of workpiece in case that dressing lead is 0.0 mm/rev for vitrified wheel. From this figure, it is known that ground surface is formed for wheel width. Here, in this figure, the actual depth

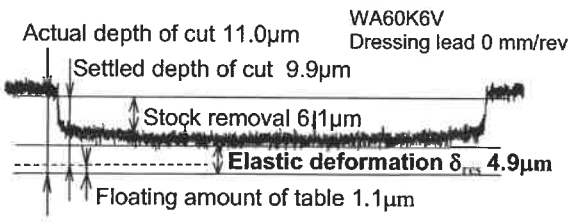

FIGURE 4. Measured results of elastic deformation of grinding wheel

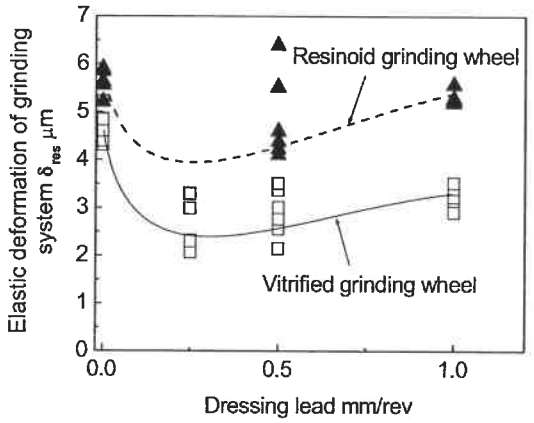
Elastic deformation of grinding system δres μm
Resinoid grinding wheel
Vitrified grinding wheel
Dressing lead mm/rev

FIGURE 5. Relation between dressing lead and elastic deformation of grinding system

of cut indicates the sum of the settled depth of cut and the floating amount of the table. The settled depth of cut can be measured by an electrical micrometer in operation. The floating amount of the table can be calculated by substituting measured normal force to equation (1). Therefore, from subtracting the stock removal of workpiece from the actual depth of cut, the elastic deformation of grinding system δ_{res} can be obtained. As shown in Figure 4, since the actual depth of cut is 11.0 μm, and the stock removal is 6.1 μm, the elastic deformation of grinding system δ_{res} is calculated as 4.9 μm. In such a same way, other condition's elastic deformations of grinding system are measured, and measured results are shown in Figure 5.

As shown in Figure 1, the elastic deformation of grinding wheel in contact area δ_{con} can be

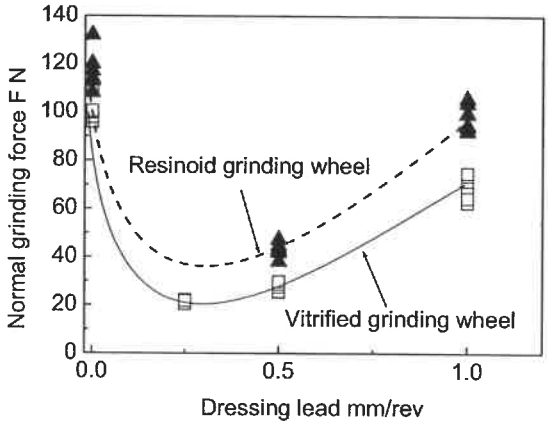

FIGURE 6. Relation between dressing lead and normal grinding force

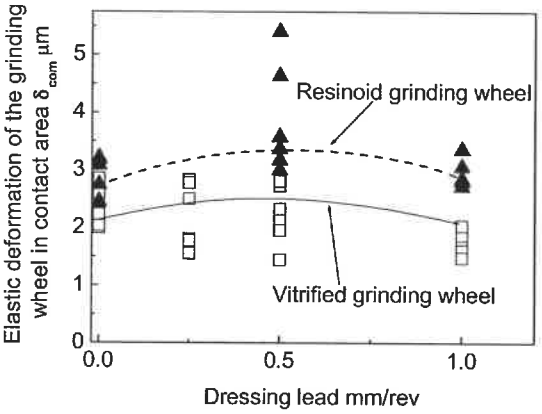
Elastic deformation of the grinding wheel in contact area δcon μm
Resinoid grinding wheel
Vitrified grinding wheel
Dressing lead mm/rev

FIGURE 7. Relation between dressing lead and elastic deformation of the grinding wheel area

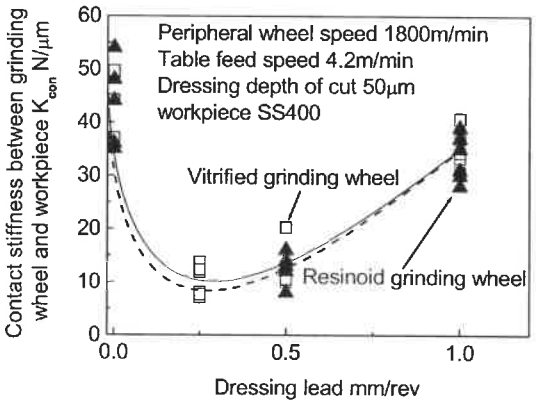
Contact stiffness between grinding wheel and workpiece Kcon N/μm
Peripheral wheel speed 1800m/min
Table feed speed 4.2m/min
Dressing depth of cut 50μm
workpiece SS400
Vitrified grinding wheel
Resinoid grinding wheel
Dressing lead mm/rev

FIGURE 8. Relation between dressing lead and contact stiffness

obtained by subtracting the elastic deformation between spindle and table $\delta_s+\delta_w$ from the total elastic deformation of grinding system δ_{res}.

Here, $\delta s+\delta w$ can be calculated by dividing the normal grinding force F shown in Figure 6 by the stiffness between spindle and table $Ks+Kw$ shown in Figure 2. Therefore, by subtracting $\delta s+\delta w$ from δres, the elastic deformation of the grinding wheel δcon can be obtained, as shown in Figure 7.

CALCULATED RESULTS OF THE CONTACT STIFFNESS OF GRINDING WHEEL

Figure 8 shows calculated results of the contact stiffness of grinding wheel $Kcon$ that is obtained by dividing the normal grinding force F shown in Figure 6 by the elastic deformation δcon shown in Figure 7. From this figure, it is known that the contact stiffness is greatest when the lead is 0.0 mm/rev, and smallest when the lead is 0.25 mm/rev. It is considered that the contact stiffness closely correlates with the number of abrasive grains on the grinding wheel surface [1] [2]. In this consideration, it is also known that, as shown in Figure 6, the normal grinding force is smallest when the lead is 0.25 mm/rev that regards as smallest number of grains on the wheel surface.

On the other hand, from results of the elastic deformation of grinding wheel shown in Figure 7, especially for vitrified wheels, it is known that the influence of the dressing lead variation is not large for the elastic deformation of grinding wheel. From this result, it can be considered that the residual stock removal of a workpiece is not affected by the difference of dressing lead.

CONTACT STIFFNESS FOR DIFFERENCE OF BOND

Comparing the contact stiffness of vitrified wheel with one of resinoid wheel, difference of the contact stiffness for both wheels is small. It is considered that this cause is that the contact stiffness of wheel $Kcon$ varies with depending on the normal grinding force. Figure 9 shows relation between the normal grinding force and the contact stiffness when dressing lead is 1.0 mm/rev for vitrified and resinoid grinding wheels. From this figure, it is known that contact stiffness varies with the normal grinding force. Here, difference of contact stiffness for both wheels is not seen in Figure 8. However, as shown in Figure 9, it is known that the contact stiffness for both bonds vary. As shown in Figure 6, in case of the dressing lead 1.0 mm/rev, the normal grinding force for vitrified wheel was 60 N, and the normal grinding force for resinoid wheel

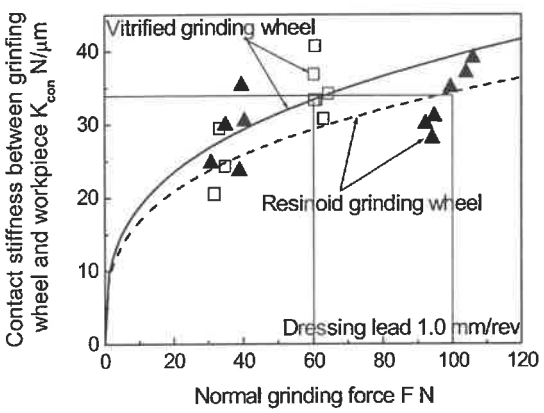

FIGURE 9. Relation between normal grinding force and contact stiffness between grinding wheel and workpiece

was 100 N. Comparing contact stiffnesses for each normal force in Figure 9, it is known that both contact stiffness corresponds with at 34 N/μm. From above, since contact stiffness varies with normal grinding force, it can be considered that difference of contact stiffness for both grinding wheels shown in Figure 8 is not occurred in this area.

CONCLUSIONS

Contact stiffnesses of grinding wheel for vitrified and resinoid wheel were measured for different dressing lead. Results obtained in this study are summarized as follows;

- It is known that the contact stiffness depends on the number of abrasive grains on the wheel surface, and is smallest when dressing lead is 0.25 mm/rev.
- It is found that difference of the contact stiffnesses of vitrified wheel and resinoid wheel is small. However, it is caused by that contact stiffness varies with the normal grinding force.

REFERENCES

[1] Takazo Y, Hwa-Soo L, Hironori M. Study on the Contact Stiffness of Grinding Wheels Due to the Difference of Dressing Condition. Proceedings from ASPE Annual Meeting. 2006; 10: CD-ROM.

[2] Takazo Y, Hwa-Soo L. Effect of Dressing Condition on the Contact Stiffness of Vitrified Grinding Wheels. Advances in Abrasive Technology X. 2007; 639-645.

INFLUENCE OF NORMAL FEED ON SURFACE ROUGHNESS IN NEWLY DEVELOPED ULTRA-SMOOTHNESS GRINDING METHOD

Heiji YASUI[1], Ryushiro SAKAMOTO[1], Yusuke TANAKA[1], and Takuro YOSHIMURA[1]
[1]Graduate School of Science and Technology
Kumamoto univeristy
Kumamoto city, Kumamoto Japan

INTRODUCTION

With the increase of demand of high quality components, the ultra-smoothness grinding technique with high productivity has been strongly required. From the point of view, in our previous researches, the ultra-smoothness grinding method based on the new concept in which the ground surface roughness is near that formed by polishing is developed [1].

The investigation on the optimum ultra-smoothness grinding conditions is necessary for the most useful utilization of the new grinding method. It is important for the resolution of subject that the influence of grinding parameters such as wheel speed, normal feed, parallel step feed and depth of cut is investigated.

To build the selecting method of the optimum conditions in the ultra-smoothness grinding method, in the research, the influence of normal feed on the surface roughness is examined.

GEOMETRICSL INFLUENCE OF NORMAL FEED ON SURFACE ROUGHNESS

The ultra-smoothness grinding method is shown schematically in Fig.1. First of all, the workpiece, in the method, is ground by feeding the workpiece at normal feed f_{Gn} toward the direction normal to grinding direction. The normal feed f_{Gn} must be smaller than the wear length w_n of cutting edge normal to grinding direction. After the workpiece is slightly step-fed a small length f_p parallel to grinding direction, the workpiece is ground again by feeding opposite direction. Whole surface of workpiece is finished by repeating such a grinding procedure. Using the method, the surface roughness of various kinds of ground materials such as cemented carbide, glass, fine ceramics and so on is found roughly to attain below 50nm (R_z) in three dimensional measuring of 256 micro-meters square.

In case of $f_{Gn}<w_n$, the geometrical chip formation is shown schematically in Fig.2. As seen in the ground surface is formed by transcription of extremely flat wear surface of

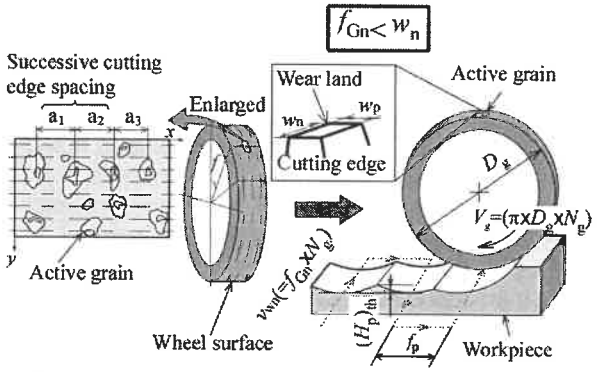

FIGURE 1. Surface roughness formed by ultra-smoothness grinding method

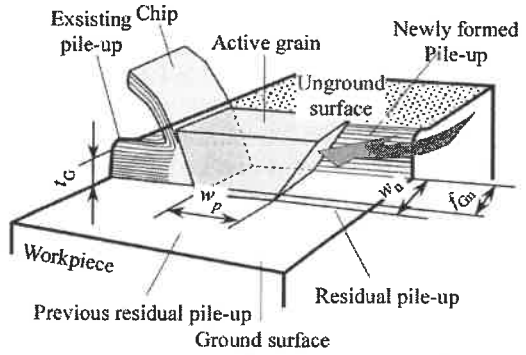

FIGURE 2. Image model of ground surface formed by cutting edge in case of $f_{Gn}<w_n$

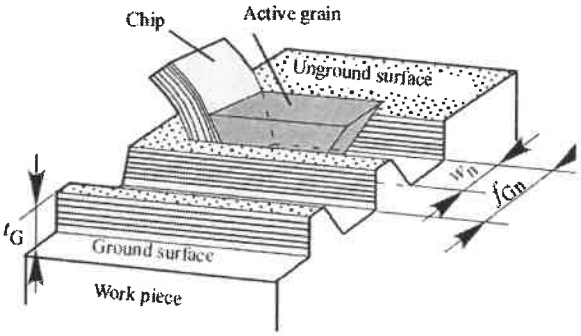

FIGURE 3. Image model of ground surface formed by cutting edge in case of $f_{Gn}>w_n$

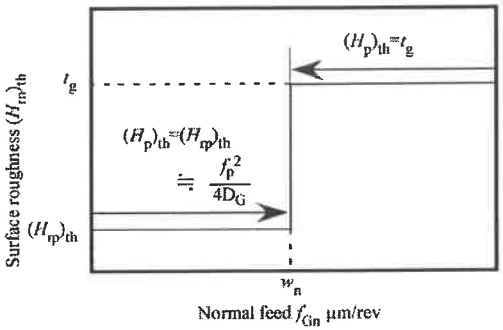

FIGURE 4. Diagram of the relationship between geometrical surface roughness and normal feed

cutting edge. The grinding grooves do not occur on the ground surface.

In case of $f_{Gn}>w_n$, on the contrary, the geometrical chip formation is shown schematically in Fig.3 From the figure, grinding grooves occurs on the ground surface because the uncut part of workpiece is formed on the workpiece surface. In case the ground surface is formed by one cutting edge as shown in Fig.3, the depth of grinding groove and surface roughness become equal to wheel depth of cut t_G. The actual surface roughness, however, becomes remarkably smaller than the wheel depth of cut because a lot of cutting edges exist in practice on the wheel surface. Thus the step formed by the difference between the outmost cutting edge and other cutting edge is considered to be t_g as shown in Fig.4. FIGURE 4 shows diagrammatically the relationship between geometrical surface roughness and normal feed. As understood from the figure, in ultra-smoothness grinding method, the surface roughness increases suddenly in just becoming $f_{Gn}>w_n$.

EXPERIMENTS

Appearance of experimental system is shown in Fig.5. The each axis of horizontal grinder can be moved below 100 nanometer accuracy by NC controller in design. Experimental conditions are shown in Table1. To compare the grinding characteristics of brittle material with ductile material, Hot-Pressing Silicon Carbide ceramic (HPSC ceramic) and cemented carbide are used as the workpiece. The metal bonded diamond wheel used is coarse grain size type of #140. The wheel speed is V_g=12m/s. Normal feed per a wheel revolution f_{Gn} ranges from f_{Gn}=10 μm/rev to f_{Gn}=80 μm/rev. Soluble type of grinding fluid of 1/10 dilution is supplied to the grinding point with the flow rate of 12L/min. The observation and roughness measurement of the ground surface

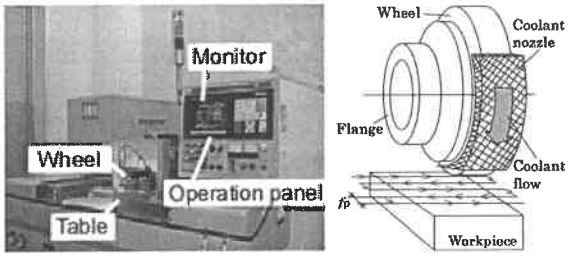

FIGURE 5. Appearance of experimental system

TABLE 1. Experimental conditions

Workpiece	Hot-pressed Silicon Carbide (HPSC), Cemented carbide (P20),
Wheel	SD140Q50M, D_GxB_GxD_i:100mmx6mmx25mm
Wheel speed	V_G : 12 m/s
Normal table	v_{wn} : 0.38 – 3.04 mm/s
Normal feed	f_{Gn} : 10 – 80 μm/rev
Parallel step feed	f_P : 5 – 10 μm/pass
Depth of cut	t_G : 5μm
Grinding fluid	Soluble type (1/10)
Flow rate	12 *L*/min

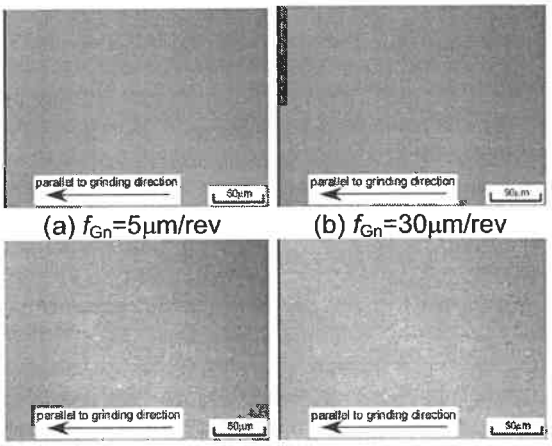

(a) f_{Gn}=5μm/rev (b) f_{Gn}=30μm/rev

(c) f_{Gn}=50μm/rev (d) f_{Gn}=80μm/rev

FIGURE 6. Change of ground HPSC surface with normal feed

[SD140Q50M, V_G=12m/s, t_G=5μm, f_p=10μm/pass, Soluble type(1/10)]

are done with a microscope and a surface interferometer, respectively.

RESULTS AND DISCUSSIONS

Fig.6 shows the HPSC ceramic surface ground by ultra-smoothness grinding method for four kinds of normal feeds. In the small normal feed of f_{Gn}=5μm/rev, from the figure, no grinding grooves and micro-cracks are observed on the ground surface. In the normal feed of f_{Gn}=30μm/rev, small micro-cracks occurs a little on the surface. The micro-cracks increases somewhat in f_{Gn}=50μm/rev. In the largest

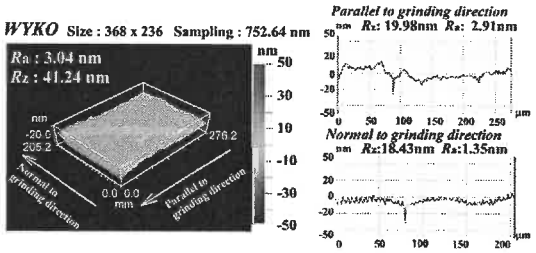
WYKO Size : 368 x 236 Sampling : 752.64 nm
Ra : 3.04 nm
Rz : 41.24 nm
Parallel to grinding direction
Rz: 19.98nm Ra: 2.91nm
Normal to grinding direction
Rz:18.43nm Ra:1.35nm

(a) f_{Gn}=5μm/rev

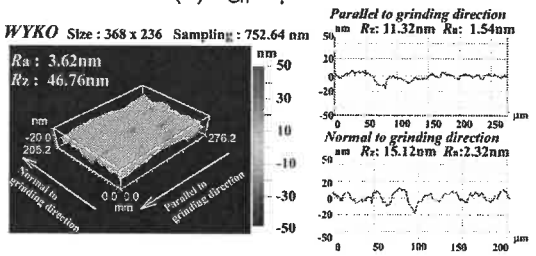
WYKO Size : 368 x 236 Sampling : 752.64 nm
Ra : 3.62nm
Rz : 46.76nm
Parallel to grinding direction
Rz: 11.32nm Ra: 1.54nm
Normal to grinding direction
Rz: 15.12nm Ra:2.32nm

(b) f_{Gn}=30μm/rev

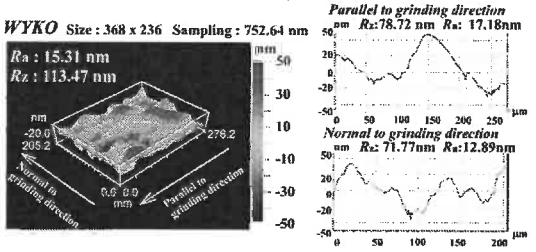
WYKO Size : 368 x 236 Sampling : 752.64 nm
Ra : 15.31 nm
Rz : 113.47 nm
Parallel to grinding direction
Rz:78.72 nm Ra: 17.18nm
Normal to grinding direction
Rz: 71.77nm Ra:12.89nm

(c) f_{Gn}=50μm/rev

FIGURE 7. Change of surface roughness with normal feed in case of HPSC
[SD140Q50M, V_G=12m/s, t_G=5μm, f_p=10μm/pass, Soluble type (1/10)]

normal feed of f_{Gn}=80μm/rev in the experiment, a lot of large cracks appear on the surface.

The surface roughness of ground HPSC ceramic are shown in Fig.7. In the small normal feed of f_{Gn}=5μm/rev, three dimensional surface roughness is H_{r3D}=41.2nm(R_z). In the normal feed of f_{Gn}=30μm/rev, the surface roughness becomes 46.7nm which is slightly larger than f_{Gn}=5μm/rev. In the normal feed of f_{Gn}=50μm/rev, however, the surface roughness becomes steeply larger than below the normal feed of f_{Gn}=30μm/rev. The reason is why large micro-cracks occur on the ground surface.

By the way, in Fig.7(a) and Fig.7(b), two dimensional surface roughness normal to grinding direction is found to be consisted of the profile equal to the frequency of normal feed per a wheel revolution. Considering the geometrical formation mechanism of surface roughness as mentioned above, it is considered difficult that the profile occurs due to the frequent step formed by the difference between the outmost

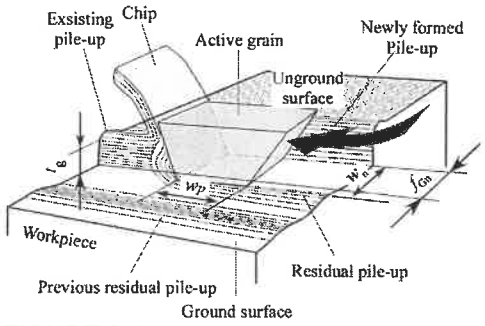

FIGURE 8. Image model of the workpiece flow to cutting edge side in the condition of ultra-smoothness grinding

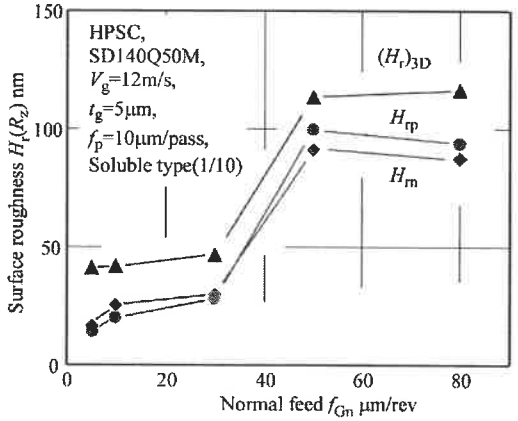

FIGURE 9. Relationship between surface roughness and normal feed in case of HPSC

cutting edge and other cutting edge in the condition of $f_{Gn}>w_n$ because the surface roughness is too small to be the step. The formation mechanism of the profile equal to the frequency of normal feed per a wheel revolution is inferred, as shown in Fig.8, to be dependent of the workpiece side flow from rake face of cutting edge.

Fig.9. shows the relationship between the surface roughness of ground HPSC ceramic and normal feed. Below f_{Gn}=30μm/rev, from the figure, the surface roughness becomes gradually large with the increase of normal feed. Over the critical normal feed of f_{Gn}=30μm/rev, the surface roughness deteriorates steeply with the small increase of normal feed. The reason is considered why large and deep micro-cracks begin to occurs. Beyond f_{Gn}=50μm/rev, furthermore, the surface roughness becomes gradually large with the increase of normal feed again. At near f_{Gn}=50μm/rev, from the results, the step phenomenon as shown in Fig.4 is considered to occur.

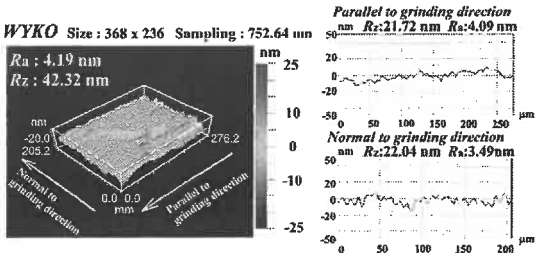
WYKO Size : 368 x 236 Sampling : 752.64 nm
Ra : 4.19 nm
Rz : 42.32 nm
Parallel to grinding direction
Rz:21.72 nm Ra:4.09 nm
Normal to grinding direction
Rz:22.04 nm Ra:3.49nm

(a) f_{Gn}=10μm/rev

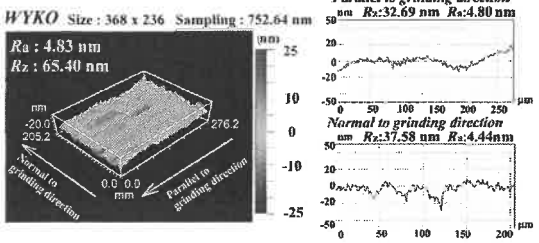
WYKO Size : 368 x 236 Sampling : 752.64 nm
Ra : 4.83 nm
Rz : 65.40 nm
Parallel to grinding direction
Rz:32.69 nm Ra:4.80 nm
Normal to grinding direction
Rz:37.58 nm Ra:4.44nm

(b) f_{Gn}=40μm/rev

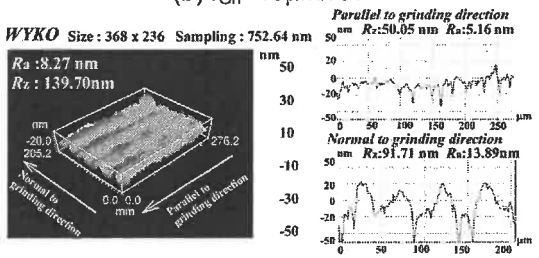
WYKO Size : 368 x 236 Sampling : 752.64 nm
Ra :8.27 nm
Rz : 139.70nm
Parallel to grinding direction
Rz:50.05 nm Ra:5.16 nm
Normal to grinding direction
Rz:91.71 nm Ra:13.89nm

(c) f_{Gn}=50μm/rev

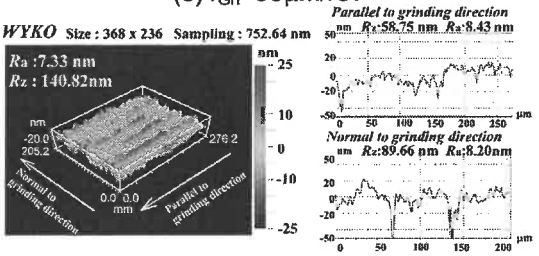
WYKO Size : 368 x 236 Sampling : 752.64 nm
Ra :7.33 nm
Rz : 140.82nm
Parallel to grinding direction
Rz:58.75 nm Ra:8.43 nm
Normal to grinding direction
Rz:89.66 nm Ra:8.20nm

(d) f_{Gn}=80μm/rev

FIGURE 10. Change of surface roughness with normal feed in case of cemented carbide

[SD140Q50M, V_G=12m/s, t_G=5μm, f_n=10μm/pass, Soluble type (1/10)]

Fig.10 shows the surface roughness of cemented carbide ground at three kinds of normal feeds. In the normal feed of f_{Gn}=10μm/rev, from the figure, the surface roughness is about H_{r3D}=42.3nm(R_z). In the normal feed of f_{Gn}=40μm/rev, the surface roughness becomes H_{r3D}=65.4nm of somewhat larger than f_{Gn}=10μm/rev. In f_{Gn}=40μm/rev, the surface is formed similar as f_{Gn}=10μm/rev. Beyond f_{Gn}=40μm/rev, however, the surface roughness deteriorates steeply and is H_{r3D}=139.7nm(R_z) at f_{Gn}=50μm/rev. The frequency of grinding grooves equal to the normal feed of f_{Gn}=50μm/rev is found clearly on the ground surface. In the f_{Gn}=80μm/rev,

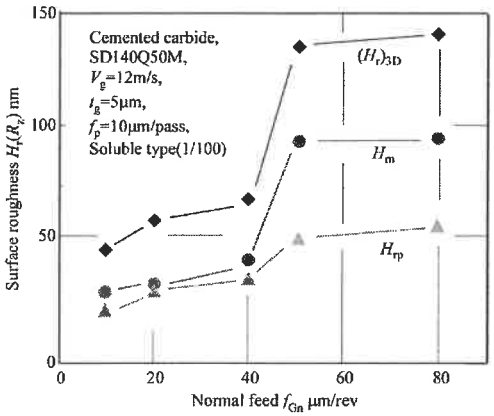

FIGURE 11. Relationship between surface roughness and normal feed in case of cemented carbide

furthermore, the surface roughness is almost the same as f_{Gn}=50μm/rev.

In case of cemented carbide, the relationship between the surface roughness and normal feed is shown in Fig.11. Below f_{Gn}=40μm/rev, the surface roughness becomes gradually larger with the increase of normal feed. Beyond the critical normal feed of f_{Gn}=40μm/rev, however, the surface roughness deteriorates steeply with the small increase of normal feed. From f_{Gn}=50μm/rev, furthermore, the surface roughness becomes gradually large with the increase of normal feed again. At near f_{Gn}=50μm/rev, from the results, the step phenomenon as shown in Fig.4 is considered to occur. Namely the wear length w_n of cutting edge normal to grinding direction is referred to be about 50μm.

SUMMARY

The main conclusions obtained are as follows:
(1)Below the critical normal feed, the surface roughness of ground silicon carbide ceramic and cemented carbide becomes below $H_{r(3D)}$=60nm (Rz).
(2) Beyond the critical normal feed, the surface roughness begins to deteriorate steeply to a certain value in both cases of ground cemented carbide and silicon carbide ceramic.
(3) Beyond the critical normal feed, grinding grooves or cracks begins to occur on the ground surface of cemented carbide or silicon carbide ceramic.

REFERENCES

[1] H.YASUI et al.; Influence of Fluid Supply on Ultra-smoothness Grinding of Silicon Nitride Ceramic with #140 Metal Bond Diamond Wheel, Proc. ASPE 19th Annual Meeting, (2004) pp.566-569

AN INVESTIGATION ON IN-PROCESS DRESSING METHOD DEVELOPED FOR NEW ULTRA-SMOOTHNESS GRINDING METHOD USING SUPER ABRASIVE WHEEL

Heiji YASUI[1], Yusuke TANAKA[1], Ryushirou SAKAMOTO[1] and Kiyoshi MATSUDA[1]
[1]Graduate School of Science and Technology, Kumamoto University Kumamoto city, JAPAN

INTRODUCTIONS

With the increase of the demand of high quality components, the high productive and ultra-smoothness grinding technique has been strongly required. For the requirement, the ultra-smoothness grinding method in our previous researches is newly developed[1)]. In the method, long grinding time is necessary until finishing a grinding operation. Thus the wheel life occurs often until finishing an operation though the high quality of super abrasive wheel is used. Specially, the wheel life is easy to occur in the grinding of easy-to-loading materials such as aluminum alloy, titanium alloy and so on. To recover the wheel performance, the wheel has to be dressed repeatedly. In such a grinding operation, the in-process dressing is considered useful.

From the point of view, the new in-process dressing method is developed previously in our research[2)]. In the method, the rectangle vitrified alumina stick is pressed to the wheel as similar as the popular dressing method. In addition, the dressing fluid which contains loose abrasives in the grinding fluid is circulated between the wheel-stick contact zone. Loose abrasives act to remove loading and the depth of increase chip pocket. Dressing system based on the device is manufactured on trial and ascertained useful previously for in-process dressing in grinding of aluminum alloy.

In the report, following the previous research, the dressing characteristics in the new in-process dressing method are investigated.

STICK AIDED FLUID-CONTAINING-ABRASIVES CIRCULATION DRESSING METHOD (SAFAC DRESSING METHOD)

The newly developed in-process dressing method which is denoted by stick aided fluid-containing-abrasives circulation dressing method (SAFAC dressing method) is shown in Fig.1. As seen in the figure, the rectangle vitrified alumina stick which is manufactured by

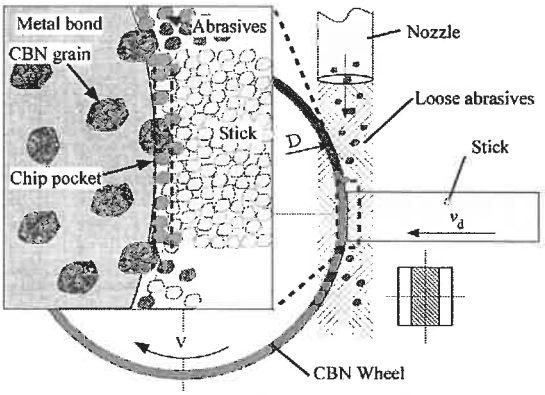

Figure 1. Schematic of stick aided fluid-containing-abrasives circulation dressing method (SAFAC dressing method)

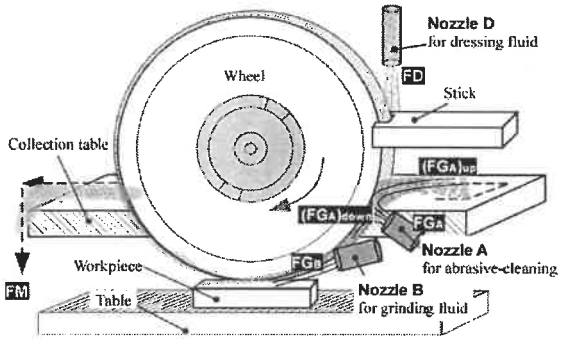

Figure 2. Schematic of dressing-fluid circulation dressing method

the similar method as the grinding wheel is pressed to the wheel. The rectangle vitrified silicon carbide stick can be used also. Simultaneously, the fluid-containing-abrasives which is denoted by "dressing fluid" is supplied between the wheel-stick contact zone. The supply is done by the circulation of dressing fluid. Loose abrasives in the fluid act to remove loading and increase chip pocket. The dressing fluid flows down from the stick-wheel contact zone. If the loose abrasives in dressing fluid flows into the wheel-workpiece contact zone, that is, grinding point, the workpiece surface is scratched by the loose abrasives and as a result, the ground surface deteriorates largely. Thus it is necessary to protect the entering of abrasives

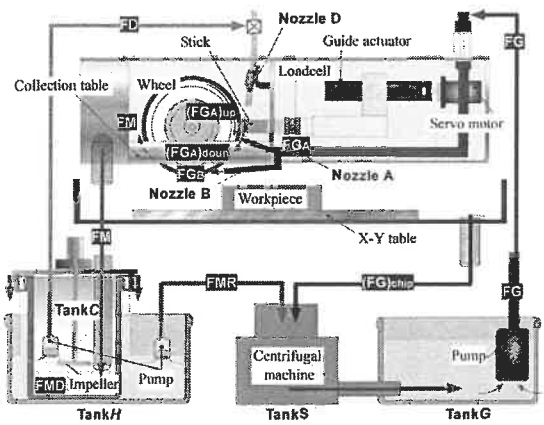

FIGURE 3. Circulation system of dressing fluid and grinding fluid

Table 1. Experimental conditions

Common conditions	
Wheel	CBN140Q100M Do×B×Di:ϕ200×12×ϕ50 mm
Grinding fluid	Soluble(1/50,1/100),Flow rate:12*l*/min
Wheel speed	V_G=30m/s
Grinding conditions	
Grinding method	Ultra Smoothness method
Workpiece	Aluminum alloy (JIS A5025)
Depth of cut	t_G=5μm
Vertical feed	f_{Gn}=50μm/rev
Parallel feed	f_p=50μm/pass
Dressing conditions	
Dressing fluid	Loose abrasives:WA#320 Containt of abrasives:10-30*wt*% Flow rate:0.5, 7.5*l*/min
Cleaning fluid	Soluble(1/100) Flow rate:7*l*/min (48*l*/sec)
Stick	WA#180 Stickfeed: v_D=50,350nm/rev Breadth×Thickness×Length : 25mm×30mm×103mm
Pause time	T_{ps} = 0,5,10 sec

to the wheel-workpiece contact zone before the dressing fluid flows into the wheel-workpiece contact zone. As the protecting method, the abrasive-cleaning method as shown in Fig.2 is devised. The protection in the method is done by flowing the grinding fluid at high pressure to wheel surface.

EXPERIMENTS

Figure 3 shows the diagram of experimental system with circulation system of dressing and grinding fluids. The dressing fluid is supplied to wheel-stick contact zone from the upper side of stick. The fluid flowing down from the contact zone is stored in the collection tank through different path from grinding fluid. A part of the stored fluid is used again as dressing fluid. After grinding fluid is separated from the rest of the stored dressing fluid by centrifugal machine, the

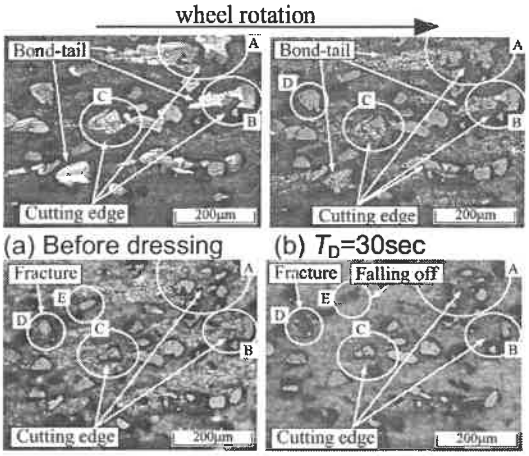

FIGURE 4. Behavior of wheel surface in SAFAC dressing process

【CBN140Q100M, Soluble(1/50),V_G=30m/s, WA loose abrasive #320,WA Stick #180, v_D=350nm/rev】

separated grinding fluid is used again as grinding fluid. The experimental conditions are listed in Table 1. The wheel used is metal bonded CBN wheel of grain size of #140 and concentration of 100. The workpiece and grinding fluid used are an aluminum alloy and soluble type. Depth of chip pocket, cutting edge ratio, cutting edge density and successive cutting edge spacing are obtained by digital processing the date measured with stylus profilometer and microphotograph attached on the cover of wheel. However cutting edge ratio means the ratio of total wear area of cutting edge to measuring area.

BEHAVIOR OF WHEEL SURFACE IN SAFAC DRESSING PROCESS

Figure 4 shows the change of wheel surface with SAFAC dressing process. The wheel surface before dressing, on which loading is observed is formed by plunge grinding of aluminum alloy of 50mm long. Grinding passes are the number of 500. By SAFAC dressing for 30 sec, the loading together with bond is removed considerably. After SAFAC dressing of 300 sec, the bond is removed additionally. The bond tail behind the cutting edge is diminished largely. After dressing time of 1200 sec, the bond is removed largely and as a result, the chip pocket becomes deep. Due to the large difference between cutting edge surface and bond surface, the simultaneously focusing of those can't be done with the object lens of ten magnifications attached to microscope. On the other hand, the fracture or falling-off of cutting edge occurs a little.

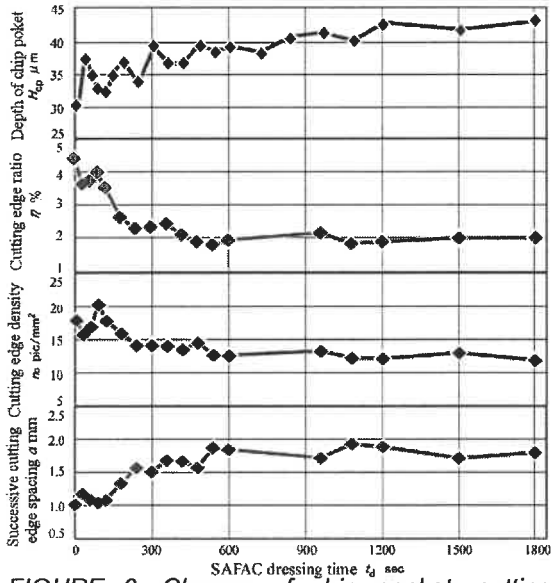
Depth of chip poket H_{cp} μm
Cutting edge ratio η %
Cutting edge density n_e pic/mm²
Successive cutting edge spacing a mm
SAFAC dressing time t_d sec

FIGURE 6. Change of chip pocket, cutting edge ratio, cutting edge density and successive cutting edge spacing with SAFAC dressing time
【CBN140Q100M, Soluble (1/50), V_G=30m/s, WA loose abrasive #320,WA stick #180, v_D=350nm/rev】

Change of depth of chip pocket, cutting edge ratio, cutting edge density and successive cutting edge spacing with SAFAC dressing time is shown in Fig.5. Up to dressing time of 1200 sec, the depth of chip pocket increases approximately linear with dressing time though the rate of increase of chip pocket tends to decrease a little as dressing time increases. The cutting edge ratio decreases steeply until a critical SAFAC dressing time, in other words, in initial dressing process. After the critical dressing process, it tends to change little. The cutting edge density decreases with comparably gentle slope until the critical dressing time. After the critical dressing time, it tends to change little as similar as cutting edge ratio. From the results, the steep decrease of cutting edge ratio in initial dressing process is considered dependent on both occurrence of falling-off and fracture of cutting edge. Successive cutting edge in initial dressing process becomes long steeply as dressing time increases. However after the initial dressing process it tends to change little.

INTERMITTENT TYPE OF IN-PROCESS SAFAC DRESSING

In the continuous SAFAC dressing method, the consumption of dressing stick, dressing equipment and electric power becomes large. Thus the intermittent type of in-process dressing is examined. The experimental method of

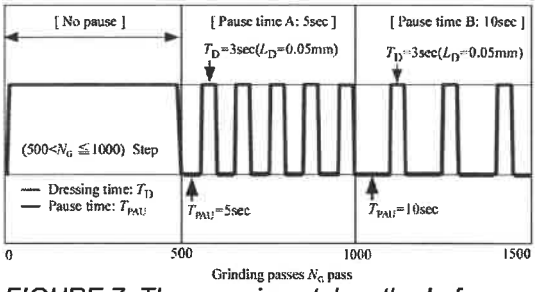

FIGURE 7. The experimental method of intermittent *type of in-process dressing*

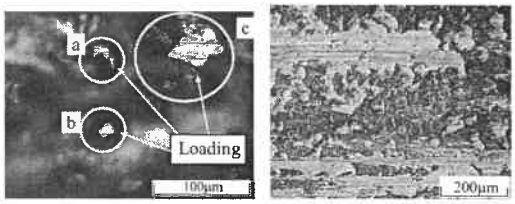

(a) Wheel surface (b) Workpiece surface

FIGURE 8. Wheel surface and workpiece surface after grinding of aluminum alloy without using in-process SAFAC dressing
【CBN140Q100M,Al(A5052,*L*w x *B*w=50x10), Soluble(1/50), V_G=30m/s, v_w=5m/min, t_G=5μm/pass】

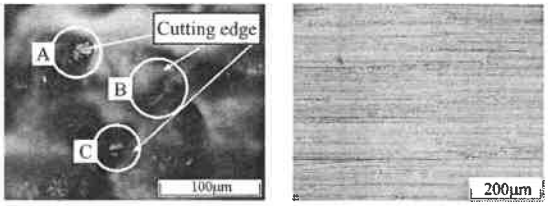

(a) Wheel surface (b) Workpiece surface

FIGURE 9. Influence of dressing pause time on wheel surface and workpiece surface in in-process SAFAC dressing during plunge grinding of aluminium alloy
【CBN140Q100M,Al(A5052,*L*w x *B*w=50x10), Soluble(1/50), V_G=30m/s, v_w=5m/min, t_G=5mm/pass, WA loose abrasive #320, WA stick #180, v_D=35nm/rev, T_{pus}=10sec】

intermittent type of in-process dressing is shown in Fig.7. Under the continuous in-process SAFAC dressing, grinding of aluminum alloy is done firstly. Grinding passes are 500. Secondly, under the intermittent type of in-process SAFAC dressing in which the five seconds in every three seconds of in-process SAFAC dressing is paused, grinding of aluminum is done. Finally under the intermittent type of in-process SAFAC dressing for the pause time of ten seconds grinding of aluminum is done.

Figure 8 shows the wheel surface and workpiece surface after 500 passes of plunge grinding of aluminum alloy without using in-process SAFAC dressing. In the figure, loading and adhesive trace are observed. on the wheel

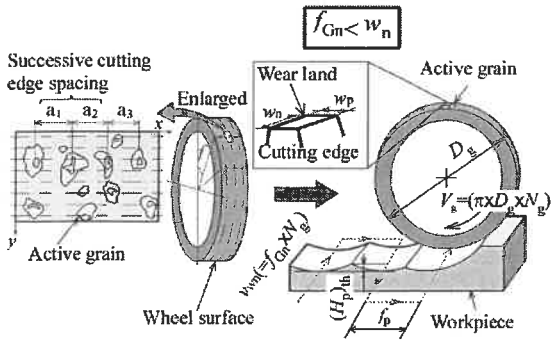

FIGURE 10. Surface roughness formed by ultra-smoothness grinding method

surface and ground workpiece surface, respectively. It is clear that large area of aluminum alloy is difficult to be ground smoothly without dressing operation.

Figure 9 shows, by using in-process SAFAC dressing, the wheel surface and workpiece surface obtained after grinding process as shown in Fig.7. It is clear from the figure that loading and adhesive trace can't be found on the wheel surface and ground workpiece surface. In case of intermittent type of in-process dressing, accordingly, SAFAC dressing effects large for grinding of aluminum alloy.

APPLICATION TO ULTRA-SMOOTHNESS GRINDING

The schematic diagram of ultra-smoothness grinding method[1] developed previously in our research is shown in Fig.10. First of all, in the method, the contact width of workpiece-wheel is ground by feeding the workpiece toward the direction normal to grinding direction. Secondly, the workpiece is slightly step-fed a small length toward the direction parallel to grinding direction. After the parallel step-feed, thirdly, the workpiece-wheel contact width is ground again by feeding reversely the workpiece toward the direction normal to grinding direction. The whole surface of workpiece is finished by repeating such grinding procedure.

Figure 11 shows the surface and its roughness of aluminum alloy ground by ultra-smoothness grinding method with in-process SAFAC dressing. However the workpiece surface of right side is ground by ultra-smoothness grinding. According to measuring results in Fig.11(c), the surface is found to be smooth and consisted of the regular grinding grooves of 50μm equal to the normal feed of workpiece per a wheel revolution. It is considered from the results that the in-process SAFAC dressing method is useful for ultra-smoothness grinding method.

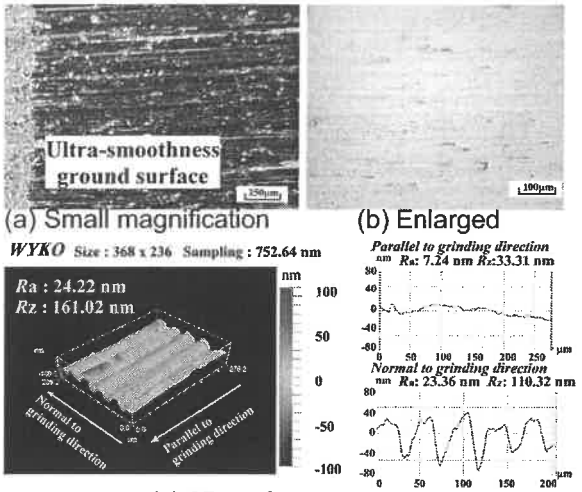
Ultra-smoothness ground surface
(a) Small magnification
(b) Enlarged
WYKO Size : 368 x 236 Sampling : 752.64 nm
Ra : 24.22 nm
Rz : 161.02 nm
Normal to grinding direction
Parallel to grinding direction
Parallel to grinding direction Ra: 7.24 nm Rz:33.31 nm
Normal to grinding direction Ra: 23.36 nm Rz: 110.32 nm

(c) 3D surface roughness

Figure 12. With SAFAC dressing

【CBN140Q100M,Al(A5052),Soluble(1/100), V_G=30m/s,t_G=5μm/pass, f_P=50μm/pass, f_{Gn}=50μm/rev,WA loose abrasive #320, WA stick #180,v_D=50nm/rev】

SUMMARY

The main conclusions obtained are as follows;

(1) The newly developed in-process SAFAC dressing method is available for the efficient chip pocket formation under a little breakage and falling-off of cutting edge on CBN wheel surface.

(2) The bond tail formed rear the cutting edge can be small by using the new in-process dressing method.

(3) The loading occurring easy in the ordinal grinding of aluminum alloy is found little for long grinding time by using the new in-process dressing method.

(4) In-process SAFAC dressing method is useful for ultra-smoothness grinding.

ACKNOWLEDGEMENT

The authors would like to thank Noritake Super Abrasive Industries Co. Ltd. and Yushiro Chemical Industry Co. Ltd. for providing grinding wheels, and grinding fluids.

REFERENCES

[1]H.YASUI et al.; Influence of Fluid Supply on Ultra-smoothness Grinding of Silicon Nitride Ceramic with #140 Metal Bond Diamond Wheel, Proc. ASPE 19th Annual Meeting, (2004) pp.566-569

[2]H.YASUI et al.; An Investigation on In-process Dressing Method of Super Abrasive Wheel for Newly Developed Ultra-Smoothness Grinding Method Proceedings of the euspen International Conference, Zurich May(2008) pp.92-95

MACHINE VISION WITH SPINDLE METROLOGY USING A CCD CAMERA

Theodore R.S. Deakyne[1], Eric R. Marsh[1], and John Lehman[2], Brent Bartlett[2]
[1]Machine Dynamics Research Laboratory
The Pennsylvania State University
21 Reber Building, University Park, PA 16802, USA
[2]Vision and Optical Sensing Systems
Confero Solutions
780 5th Avenue, King of Prussia, PA 19406, USA

INTRODUCTION

This paper examines the feasibility of a Machine Vision system for spindle metrology integrated into milling and lathe machines for smarter more automated machines. A gigabit ethernet CCD camera is used to collect images of a rotating cylindrical artifact. The artifact is mounted to a motorized 4R air bearing spindle. The images from the camera are synced to the orientation of the spindle through a Heidenhain encoder. A PC utilizes both LABVIEW and MATLAB to compile and process the data. The setup is mounted on top of a Moore base. The camera is mounted to the xy-stage to help with focusing and picking up edges of the artifact. The camera can also be mounted perpendicular to the cylindrical artifact to collect additional new information for the measurements as shown in Figure 1. The motorized spindle is mounted on the table of the Moore base and aligned to the camera using capacitance sensors. The benefits of a camera system compared to traditional touch probes and capacitance probes are larger working distances, runout measurements of the cutting tools, identification of tools, properly seated collets and etc. [1, 2]. The system will eventually be able to check for damaged and worn tools as well. The current

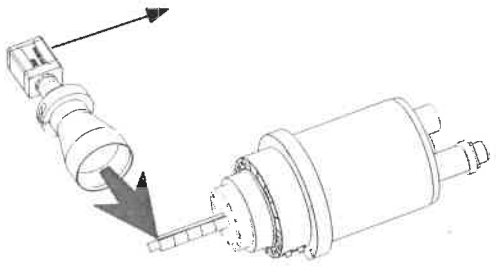

FIGURE 1. Gigabit ethernet camera taking a perpendicular measurement of the cylindrical artifact mounted on the air bearing spindle.

camera supports a TTL logic external triggering event, which allows it to be synced to the rotation of the spindle through the encoder. The camera's features and imaging formats are completely configurable. The exposure and pixel matrix have been decreased resulting in a frame rate of 530fps. Higher frame rates with small exposure time allows for faster spindle rotation. These adjustments also help to alleviate image blurring and the loss of high frequencies in the image (details). Long exposure times with fast spindle speeds lead to blurring in an image by capturing the motion; objects within the image have moved to a new set of pixels before the exposure has ended. The diameter, D, of the rotating artifact must also be considered. With constant angular speed, ω, the velocity increases from zero at the center to $\omega * D/2$ at the end of the artifact.

The encoder is mounted on a shaft at the back of the spindle. An on-board circuit converts the analog data to TTL square waves, low/high signals/pulses, that can be utilized by hardware and software. For a single rotation of the spindle, the encoder outputs three square waves, two with 512 low/high pulses (phase A and B), and one with 1 low/high pulses (index). At the beginning of the run the user inputs the number of images per revolution, based on multiplies of the phase A and B signals, and the number of revolutions to be collected. LABVIEW then programs the hardware, which waits to be triggered by the index. The camera is then triggered externally via hardware and dumps the images to RAM. At the end of the cycle the images are then saved to the hard drive. To account for trigger latency, exposure time, time between pulses and readout time, the data presented in this paper is based on 16 images per revolution for 6 revolutions at spindle speeds of 180-360RPMs.

IMAGING

There is a variety of different objects that may be setup in milling and lathe machines that the vision system will be required to measure. Both the environment of the machine and features of the objects can either help or hinder those measurements. The work demonstrated in this paper simplified both the environment and objects measured. Two objects were measured which are shown in Figure 2. The first, (a), is the front face of a two flute endmill and the second, (b), is the edge of the front face to the cylindrical artifact. The cylindrical artifact was made using a Twin mount air bearing grinder and was measured to have a radial and axial runout below 0.0001in and less than 0.001in over a 3.55in length of the shaft.

The accuracy and precision of the vision measurements comes down to software, pixel size, and magnification of the lens. The 4R air bearing is highly repeatable with radial and axial error motions below a microinch and a tilt error less than 0.1 microradians. The mounted cylindrical artifact is also repeatable. For a simulated radial runout of a tool on the axis of rotation the cylindrical artifact is dialed 0.004in off the 4R's axis of rotation using a mechanical thousandths increment indictor. To measure this 0.004in offset with the vision system the edge of the object will be found and compared through a series of images. Finding the actual edge is crucial in order to have precise and accurate measurements. The camera resolution is 0.00094in using a telecentric lens with a magnification of 0.31. This resolution can be seen when zooming in on image (b) as shown in Figure 2 (c). In the figure, the edge is not a sharp line but a gradient of pixels. MATLAB software processes the images first by creating a binary image from the grayscale using thresholding. Thresholding depends on the lighting used and is optimized through trial and error. All pixels above a certain threshold are lumped into the object. Starting at the upper left corner the software searches for the transition in the binary image. The transition point is considered the edge. The first located transition pixel is marked with an 'X' and the following ones are marked with 'O's' as shown in (c). There is a total of 145points chosen per edge which are compared from image to image. The edge location acquired in the images represent a length of about 0.14in.

MEASUREMENTS

After all of the data has been collected the software locates the image number and pixel edge. Marking all the pixels over the entire set and plotting pixels vs. images the graph looks like Figure 3. The patterns that start to emerge in the graph depends on the amount of images per revolution acquired. Like other data acquisition procedures it is critical to have enough samples to avoid aliasing. It was found that 16 images or greater produced enough information to recognize patterns.

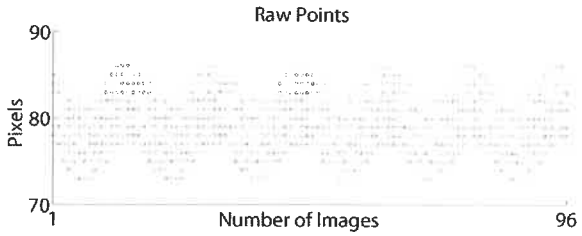

FIGURE 3. Each of the circles mark the pixel and image number of a found edge. The pattern is sinusoidal because the imaged edge is wobbling on the axis of rotation.

The raw points are mean-subtracted, and a calibration factor is multiplied to the pixels, converting them to measurements of length. Comparing all of the measurements, the average runout of the tool's edge from the spindle axis can be plotted as shown in the top graph of Figure 4. It should be noted that this is the combined runout of the object compared to the spindle axis of rotation, a combination of radial, axial, tilt, and form error of the part. These error motions are well documented and defined and can usually be separated [3, 4]. Sampling images that are perpendicular to the artifact will help separate these.

The bottom graph shown in Figure 4 represents image averaging. Image triggering from the orientation of the spindle leads to 6 duplicate sets of images in the data. The 16 images in each set are averaged together which reduces the image noise and removes the asynchronous error. Usually in images some of the pixels will represent noise. This noise may create a missed location of the edge which is minimized by the averaging. Next, data points between subsequent images were estimated using spline fits of order five. This processing resulted in a vision runout measurement closer to the mechanical indictor runout

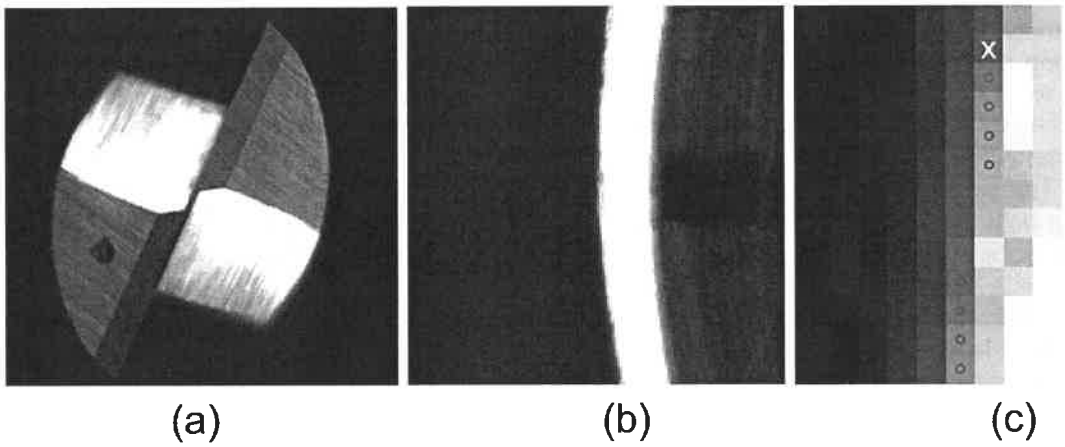

FIGURE 2. Images of the objects used with the machine vision system. From left to right; (a) Face of a straight, two flute endmill used for tool wear, (b) Face of the ground cylindrical artifact used for tool of axial measurement simulations, (c) Zoom view of cylindrical artifact with edge detection marked by 'O's'.

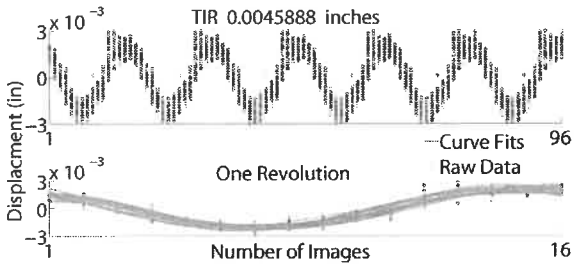

FIGURE 4. Calibrated results of the imaged edge. The top graph shows six revolutions of data with a total runout measurement, combination of radial, axial, tilt, and form error. The bottom graph shows the results of averaging images to reduce noise and spline fits to estimate measurements between images in the series.

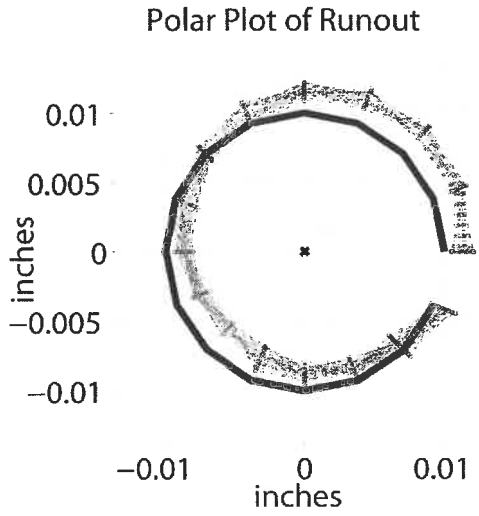

FIGURE 5. The orientation of the collected images are known from the encoder triggering of the camera. This makes it easy to create polar plots.

measurement.

The end result is a polar plot of the measurements seen in Figure 5. It clearly shows the total runout of the artifact compared to axis of rotation of the air bearing spindle. At this stage either the control system or operator would have to make corrections in order to fix the runout of the tool.

ENVIRONMENT

The environment of the Vision Systems can greatly effect the measurements. In real machining operations there is coolant, chips, airflow and non-uniform light which can result in false edge detection. Figure 6 shows what can happen to measurements using non-unform lighting. Originally this data was believed to be showing a defect in the edge of the artifact. The once around was removed from the data showing more clearly that the spikes were very repeatable as shown in Figure 7, in which the spike occurred every sixteenth image starting after the twelfth image. Multiple measurements produced the same results. There appeared to be no difference looking at the image by eye, but the intensity matrix revealed

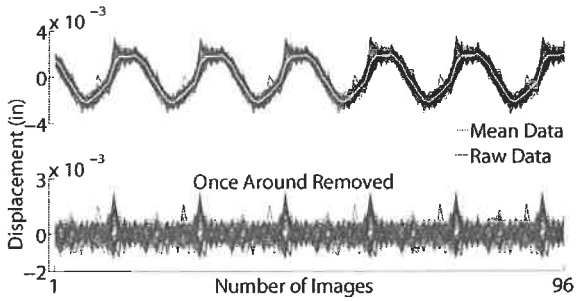

FIGURE 6. Sinusoidal pattern with higher frequencies combined. Higher frequencies could be asynchronous error, form error of the part, or spindle error. In this case it turned out to be error caused by non-uniform lighting.

that a group of pixels along the bottom of the image was the culprit. Adjusting the LED ring light solved this problem. Repeated tests using the same exact parameters as before produced the results in Figure 8. The total measured runout decrease from 0.0046in to 0.0044in.

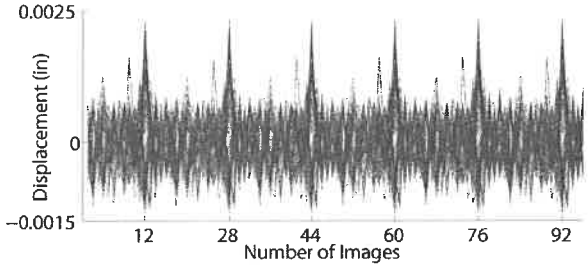

FIGURE 7. The low frequency sinusoidal once around has been removed revealing the error. At this stage the images and pixels can be re-examined to look for defect in the edge of the artifact.

CONCLUSIONS

The advantages of a vision system on a CNC machine would allow higher precision parts, and less mistakes in machining operations. As shown by this work the tool runout from the axis of rotation of the spindle can be measured. Averaging duplicate frames and spline fitting helped to remove random noise and increased the accuracy of the runout measurements. However, more work on the edge detection is necessary to improve the accuracy and precision of the runout measurements. It was also shown that the edge is a gradient of pixels. Improving the detection of the actual edge for the object in the image will require better algorithms.

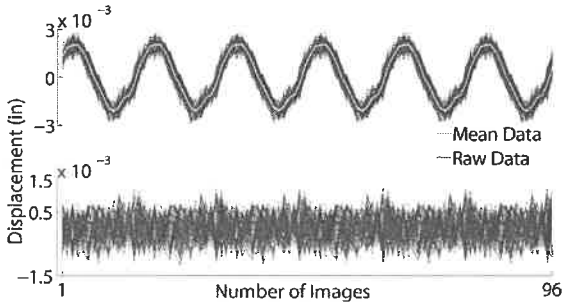

FIGURE 8. More uniform sinusoidal pattern without the previous spikes. Results of corrected the non-uniform lighting.

The next stage of this research involves upgrading the vision system. The second generation will have more resolution, smaller pixels, faster frame rates and a higher lens magnification. This is crucial in order to see micron level spindle error motion and form errors. Also multi temporal imaging and motion image filtering will be researched to improve the measurements of the vision system. Environmental factors will also have to be addresses such as air blowers to remove chips and coolant, better lighting, or through software.

REFERENCES

[1] Huang J, Bi C, Jiang Q, Tan C, Lim C. Performance Analysis of the Vision Measuring Machine for Spindle Motor. Instrumentation and Measurement Technology Conference. 2006;(5).

[2] Aronson RB. Small-Part Metrology. Manufacturing Engineering. 2008;140(1).

[3] Grejda RD. Investigation of a Master Axes of Rotation for Use in Spindle Metrology. The Pennsylvania State University; 1999.

[4] Marsh RE. Precision Spindle Metrology. 2nd ed. DEStech Publications, Inc.; 2007.

MEASUREMENT AND COMPENSATION OF A 4 AXIS ULTRA-PRECISION MACHINE TOOL FOR GENERATING MICRO PATTERNS ON THE LARGE SURFACES

Jooho Hwang[1], YoungChan Song[1], Chang-Kyu[1] Song and Chun-Hong Park[1]
[1]Intelligent Manufacturing system division
Korea Institute of Machinery and Materials
Daejeon, South Korea

INSTRUCTIONS

This paper describes a method to measure and compensate a 4 axes ultra-precision machine tool that generates micro patterns on the large surfaces. The grooving machine is usually used for making a micro mold for many electrical parts such as a light guide plate for LCD and fuel cells. The ultra precision machine tool has three linear axes and one rotational table. Shaping is usually used to generate micro patterns. In the case of 50 μm pitch and 25 μm height pyramid pattern machining with a 90□wedge angle bite, one of linear axis is used for long stroke motion for high cutting speed and other linear axis are used for feeding. The triangular patterns can be generated with many times of long stroke of one axis. Then 90□rotation of work piece is needed to make pyramid patterns with superposition of machined two triangular patterns.

To make a two dimensional positioning error, straightness of two axes in out of plane, squareness between the each axis are important. Positioning errors, straightness and squarness were measured by laser interferometer system. Those were compensated and confirmed by ISO230-6. One of difficult problem to measure the error motions is squareness or parallelism of axis between the rotational table and linear axis. It was investigated by self-cutting of turning against each moving axis and calculated by waveness data from surface roughness tester. This error was compensated by command of Z-axis motion.

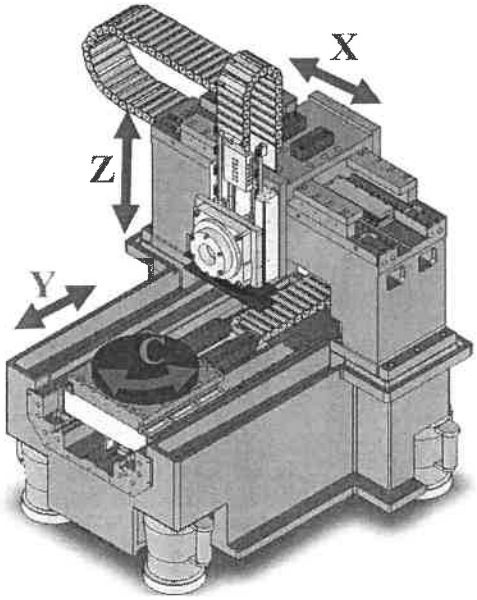

FIGURE 1. Configuration of the 4 axis ultra precision machine

CONFIGURATIONS OF THE MACHINE TOOL

Figure 1 shows the basic configurations of the ultra-precision 4 axis machine tools. It has 3 linear axes and 1 rotational axis to be used in shaping, milling and turning process. The hydrostatic oil bearings are used for the guide of all the 4 axes, regarding compactness and high stiffness of the machine tools. To maintain non-contact state, the coreless linear motors are used for actuators of 3 linear axes and a frameless rotating motor is inserted in a rotating table.

The machining volume of the machine tool is 500 mm × 500 mm × 150 mm and the rotating axis (c-axis) is inserted in Y axis. The base of the machine tools is made from cast iron and supported by four air-springs vibration mount. The vertically moving axis (Z-axis) weighs 70.8 kg and wiring with an another 70.8 kg counter mass and mounted on the X axis. The position sensor of the each linear axes is a hologram precise optical scales, which has 650 μm precise grating and the resolution is changeable from 300 nm to 1 nm.

EVALUATION AND COMPENSATION OF THE LINEAR AXES

The error of the z axis; small moving axis; is relatively smaller than X and Y axes, because the machine tool is used for generating micro

patterns Therefore, the 2-dimensional position errors are main errors to be compensated. The two dimensional (2D) errors are occurred owing to relative motion of the two axes. The 2D position errors on the XY plane are mainly affected by straightness, pitch, yaw and perpendicular errors of the each axis. In the case of machining micro patterns on the plane, the change of height along to Z axis is less than 100 μm and effect of yaw error can be simplified by assuming tool point is on the center. Therefore, the measured 1D position error can replace the errors owing to yaw and pitch errors and can be expressed by

$$\begin{bmatrix} \delta P_x(i,j) \\ \delta P_y(i,j) \end{bmatrix} = \begin{bmatrix} \delta P_{x1D}(i) + \delta_x(j) \\ \delta P_{y1D}(j) + a_x(i)\theta_{xy} + \delta_y(i) \end{bmatrix} \quad (1)$$

Where, $\delta p_x(i,j)$ and $\delta p_y(i,j)$ are x direction error and y direction error according to position of x and y, respectively; $\delta p_{x1D}(i)$ is 1D position of X axis and ; $\delta_x(j)$ and $\delta_y(j)$ represent horizontal motion errors at machining point in the X and Y directions; θxy is perpendicular error between X and Y and ax is moving distance from origin of X axis.

The position and motion errors in equation (1) was measured by laser interferometer and used as inputs. Figure 2 shows the estimated 2D position errors. The maximum deviations of 2D position errors are 11.59 μm for x-axis and 12.33 μm for y-axis, respectively. The estimated position errors are compared with diagonal measurement shown in figure. 3. As shown in the figure 3 a steering mirror is located in front of the beam splitter and it turns angle of beams to 45 ° and the reflector is fixed on the corner of the tables. The height of the beam path is maintained at 120mm, which is average height of the machining point. The measured results are analyzed by ISO 230-6 standard and shown in figure 4. The estimated error laser interferometer measured data along two diagonals, (400,400) to (0,0) and (0,400) to (400,0) are compared with in the figure 4. As shown in the figure the estimated errors are similar in shape and magnitude. It shows that the error model of the equation (1) is efficient to estimate 2D models.

The 1D position error was measured in center of the table and compensated each X and Y axis.

The perpendicular error (θ_{12}) affects the position error $\delta p_y(i,j)$ as indicated by equation (1). It is possible to measure the perpendicular error

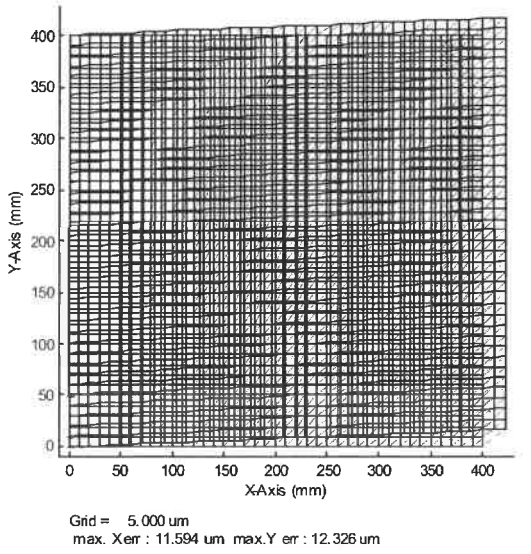

FIGURE 2. Estimated 2D position errors on the XY plane

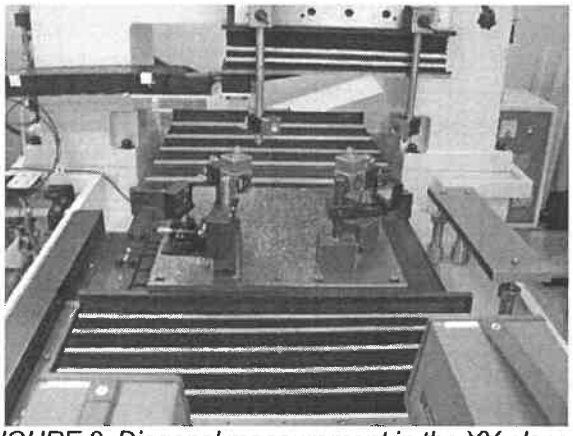

FIGURE 3. Diagonal measurement in the XY plane

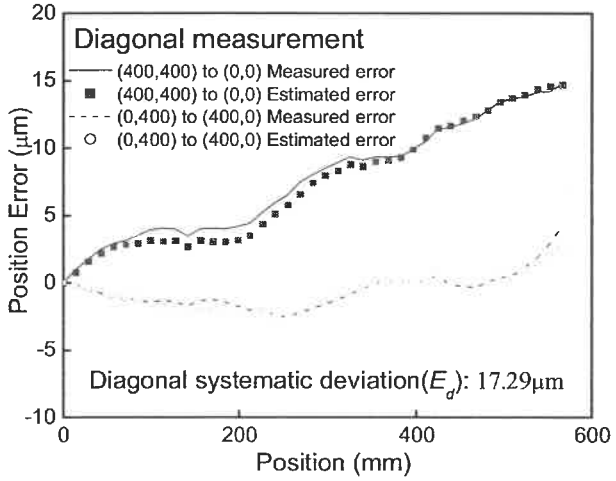

FIGURE 4. Diagonal measurement results before compensation

using two different methods. One could calculate the error directly from the diagonal measurements using equation (2),

$$\theta_{12} = \cos^{-1}\frac{P_d^{\,2} - P_x^{\,2} - P_y^{\,2}}{2P_xP_y} \qquad (2)$$

where P_d is the measured position along the diagonal direction, P_x is the measured position along the X-axis, and P_y is the measured position along the Y-axis. This is easy to measure and requires only one step of the diagonal measurement process without changing the interferometer system optics.

To compensate 2D errors in XY plane, each errors were corrected by re-shaped command signal. The horizontal motion error was eliminated by small shift of the cross-axis.

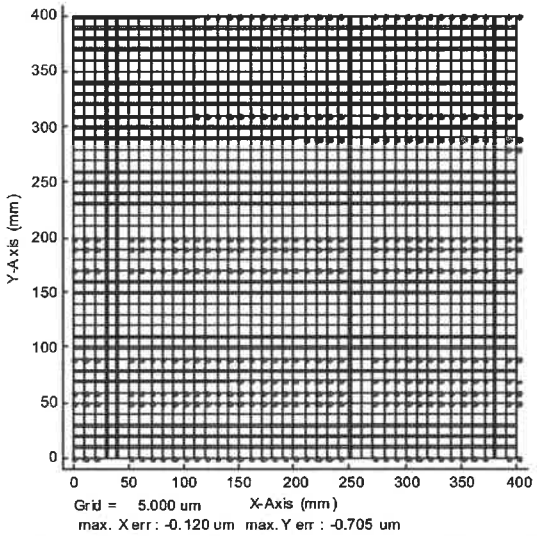

FIGURE 5. Estimated 2D position errors after compensation

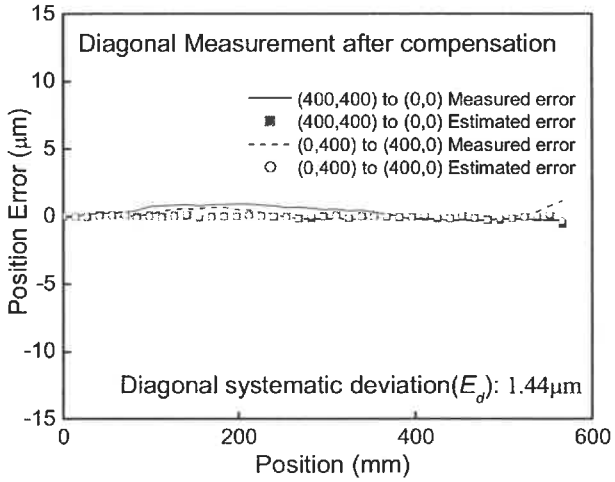
Diagonal Measurement after compensation
(400,400) to (0,0) Measured error
(400,400) to (0,0) Estimated error
(0,400) to (400,0) Measured error
(0,400) to (400,0) Estimated error
Diagonal systematic deviation(E_d): 1.44μm
Position Error (μm)
Position (mm)

FIGURE 6. Diagonal measurement results after compensation

Figure 5 shows the estimated 2D position errors when all the errors describing in equation (1) are compensated. The estimated maximum errors are 0.12 μm and 0.71 μm in X-axis and Y-axis, respectively.

The diagonal measurement errors are shown in figure 6. As shown in figure, the diagonal systematic errors are decreased from 17.3 μm to 1.44 μm from the effect of compensation. The comparison between estimated and measured errors are shown in figure 6. The motion errors, those are used as input of the estimation, were measured in center position of the table but, the diagonal errors were measured in the corner of the table as shown in figure 3. Those could be the main reason of difference between the estimated and measured data. The amount and shapes of difference shown in both figures 4 and 6 are very similar.

ERRORS OF THE ROTATIONAL AXIS

One of main application of the micro patterns on the large surface is making pyramid patterns. To make the pyramid, the triangular prism pattern is grooved firstly along X axis then patterned material is rotated 90° by C axis and same triangular prism is grooved cross of the previous pattern.

During 90° rotating, the height change in the surface are occurred owing to perpendicular errors between C, X and Y axis. The measuring method about this problem is not reported.

To measure the angle between linear and rotational table, the face cut turning was performed as shown in figure 7. The C axis was used as spindle and X axis was used as feeding axis.

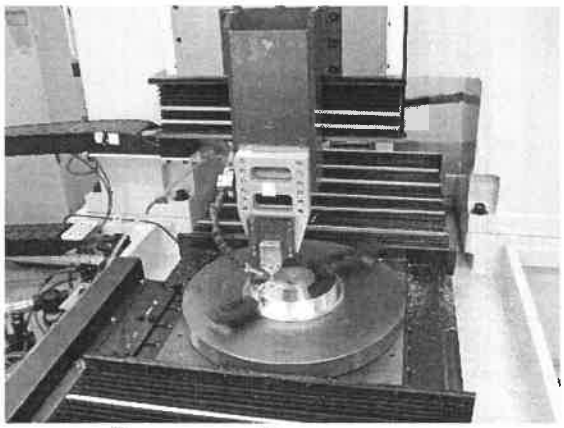

FIGURE 7. Turning to measure perpendicular errors between C and X axes

FIGURE 8. Waveness measurement using surface roughness tester

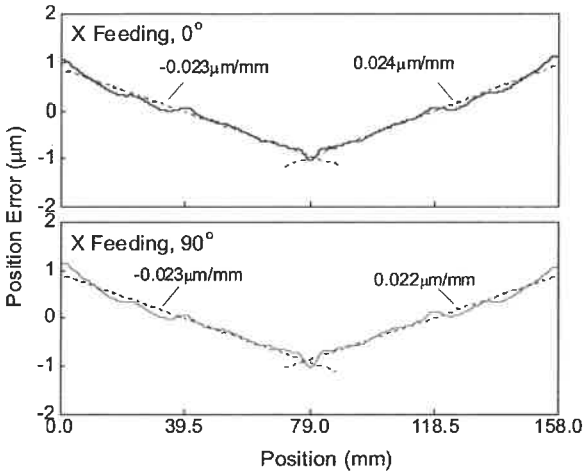

FIGURE 9. Perpendicular error between C and X axes

The waveness of machined surface was measured by surface roughness tester (Taylor Hobson, Form Talysurf) along a radial directions and after rotating specimen 90°. Because the turning surface is axisymmetric, the slope in Fig. 9 should be same. As shown in figure 9, the least square fitting slope is almost same within 0.023 ± 0.001 μm/mm. The slope indicates that perpendicular error between rotational axis of C and X axis is 0.023 μm/mm which means when rotate 90°, the height difference may be occurred about 9.2 μm in 400mm distance along Y axis.

Figure 10 shows the perpendicular error between Y and C axis. As shown in figure 10, the average of the four slope is 0.001 μm/mm , which indicate only 0.4 μm in 400mm distance. C axis is mounted on Y axis but the X axis is on the column of the bed, which seems main reason of the perpendicular errors. This error can be corrected by height of Z axis along the X axis. This correction will be performed in the further works

CONCLUSIONS

This paper describes a method to measure and compensate a 4 axes ultra-precision machine tool that generates micro patterns on the large surfaces. To make a two dimensional positioning error, straightness of two axes in out of plane, squareness between the each axis are important. Positioning errors, straightness and squarness were measured by laser interferometer system. One of difficult problem to measure the error motions is squareness or parallelism of axis between the rotational table and linear axis. It was investigated by self-cutting of turning against each moving axis and calculated by waveness data from surface roughness tester. This error was compensated by command of Z-axis motion.

REFERENCES

[1] A.C. Okafor, Y.M. Ertekin, Derivation of machine tool error models and error compensation procedure for three axes vertical machining. International Journal of Machine Tools and Manufacture. 2000; 40; 1199–1213.

[2] C. Raksiri,M. Parnichkun, Geometric and force errors compensation in a 3-axis CNC milling machine, International Journal of Machine Tools and Manufacture. 2005; 44 ; 1283–1291.

[3] A.H. Slocum, Precision Machine Design, Prentice Hall, Englewood Cliffs, NJ, 1992.

[4] ISO230-6, Test Code for Machine Tools-Part 6: Determination of Positioning Accuracy on Body and Face Diagonals (Diagonal Displacement Tests) 2002.

[5] M.A.V. Chapman, Limitations of laser diagonal measurements, Precision Engineering; 2003; 27 ; 401–406.

[6] Hwang, J., Park, C., Lee, C. and Kim, C., "Estimation and correction method for the two-dimensional position errors of a planar XY stage based on motion error measurements," International Journal of Machine Tools and Manufacture, 46, pp. 801-810, 2006.

DETECTION OF ORIENTATION-DEPENDENT, SINGLE-CRYSTAL DIAMOND TOOL EDGE WEAR USING CUTTING FORCE SENSORS, WHILE SPIN-TURNING SILICON

Eric R. Marsh[1], George A. Kim[2], and James A. Simonson[2]
[1]**Pennsylvania State University**
University Park, PA, USA
[2]**Edge Technologies, Inc.**
Indianapolis, IN, USA

Introduction

The purpose of this project is to experimentally determine the benefits of spin-turning infrared materials known to cause relatively rapid wear of single-crystal, synthetic diamond cutting tools. The testing explores the specific issues of non-uniform workpiece properties (single crystal silicon), non-uniform cutting tool properties, and machining parameters. This work includes a description of a precision spindle-based tool holder that provides high stiffness and accurate rotation for turning optical-grade surfaces.

Precision diamond turning of infrared crystals such as silicon is based on the theory that ductile regime machining requires very shallow depths of cut [1, 2]. However, it may be possible to remove material faster and with improved surface finish if compression-strain heating and high pressure phase transformation phenomena are recognized and developed as part of the machining process [3].

Silicon's high pressure phase transformation under loading has been shown in a number of nanoindenting, scribing, and cutting experiments [4, 5, 6]. Raman spectroscopy has also been used to demonstrate the occurrence of a high pressure phase transformation in which silicon's atomic structure changes from diamond face centered cubic to other, metallic-like phases including β-tin [7]. Yan et al. have shown that upon release of the hydrostatic stress of a cutting tool the silicon returns to an amorphous state with more favorable microplasticity [8].

When we seek to reconcile these experiments with the manufacture of infrared optics three significant obstacles remain. First, it is well known that single point diamond turned surfaces often show three or four-fold regions (sectors) of distressed crystal. Furthermore, the surface finish of the optic often degrades towards the center of the optic, where the cutting velocity is lowest. Finally, silicon causes relatively fast deterioration of diamond cutting tools by both chemical wear and graphitization.

It would seem that the three or four-fold sectors of distressed crystal are indicative of brittle-fracture machining characteristics interspersed with ductile machining characteristics on the octahedral (111) and cubic (100) crystal planes, respectively. Harder crystals and harder machining directions on those planes require more compression-strain-heating to complete phase transformation in those distressed crystal sectors.

We suggest that the phase transformation generated in a turning process is a function of the material removal rate (MRR), set by the turning parameters of cutting velocity; feed rate and depth of cut; and rake angle and the crystal's material properties. Higher MRR and negative rake angles generate more energy in the uncut chip region for phase transformation to occur. As the center of the optic is approached the MRR goes to zero, ductile machining goes to brittle-fracture machining and surface finish degrades.

The challenge is that increased MRR and negative rakes, which enable the desirable phase transformation, also cause the diamond tool edge to get hotter and therefore wear out faster. This is a result of the fcc (diamond) carbon oxidizing and graphitizing at the resulting higher temperatures. The rates of these chemical reactions rise exponentially with the temperature of uncut chip region and turning conditions. Flood cooling is recommended, and water, with ten times the heat carrying capacity, may be preferred over oil.

This work seeks to make use of the phase transformation in the uncut chip region while avoiding

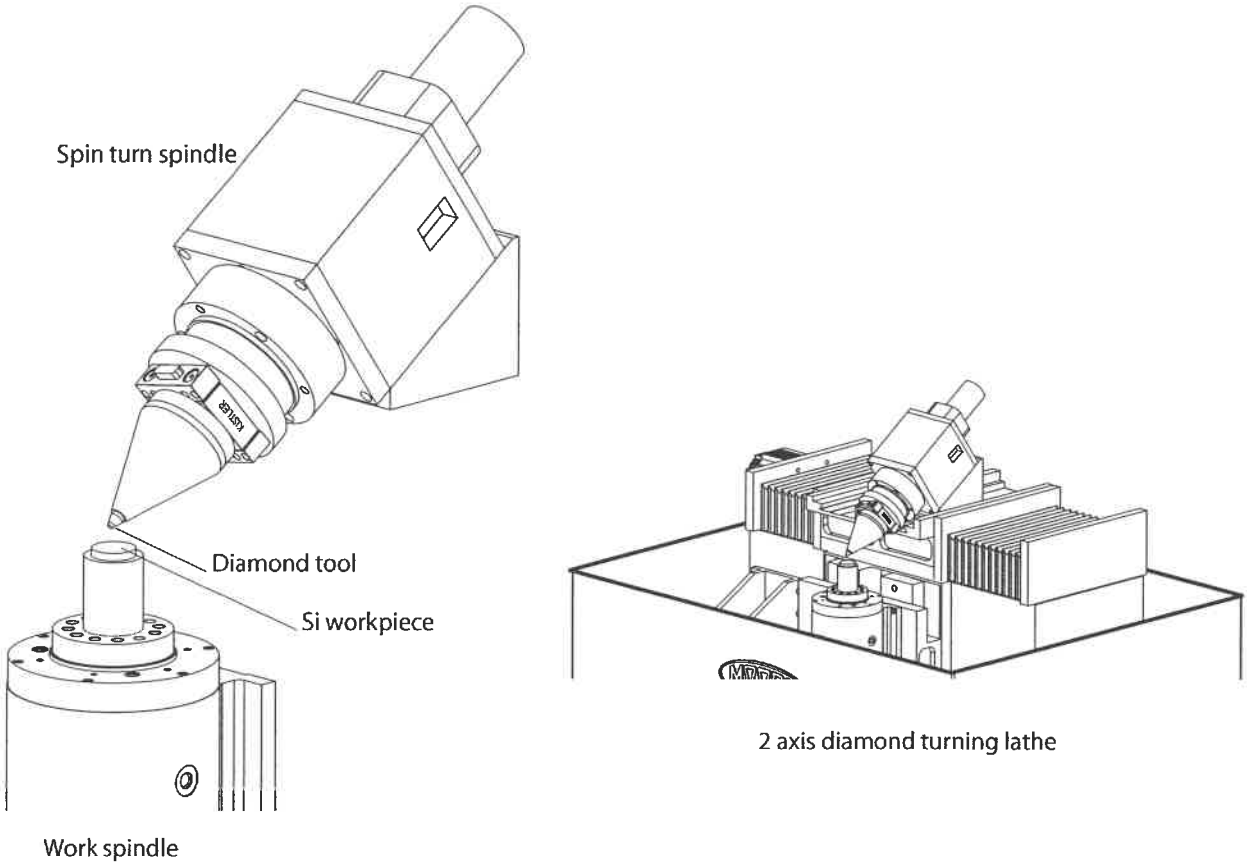

FIGURE 1. Machine configuration for spin turning silicon optics. The tool spindle is rotated 125° from the work spindle and the tool has an additional 10° crown for a total effective rake angle of -45°.

the rapid degradation of the diamond tool by constantly providing a fresh cutting edge. This is achieved with a spin-turning mechanism, similar in concept to Shaw's rotary cutting tool, originally proposed in 1952 and later revisited by several others [9, 10, 11].

Spin turning with diamond cutting tools

Figure 1 shows one implementation of spin turning with diamond tools. This configuration is particularly helpful in establishing the negative tool rakes used in turning brittle materials. The workpiece will rotate in the usual range of speeds, which is dictated by workpiece size, material, and geometry. The cutting tool will generally rotate at a much lower speed, or even remain stationary with occasional brief indexes in angular position.

It is clear that the spin turn spindle and tool face challenging geometric constraints in order to maintain accurate form in the finished workpiece. Both tool eccentricity as well as spindle error motion will lead to workpiece errors, unless explicitly mapped out using careful metrology. These challenges led to Ezugwu's comments summarizing the challenge of cutting with rotary tools [12]:

- likelihood of errors in profile
- likelihood of chatter due to large tool radius and reduced stiffness
- difficulty of producing stepped components.

These concerns are addressed in the work that follows so that silicon and other brittle materials may be machined with single point diamond tools. Although the spin turning approach is not likely to match the accuracy of turning with stationary tools, the avoidance of accelerated wear in aggressive materials such as silicon will justify its use in many demanding applications.

Errors in profile result from three sources of geometric error. The first is eccentricity in the cutting tool, which may originate in the mounting of the tool on the toolholder, or the toolholder on the spin turning spindle. Second, the cutting tool may not be round, which will lead to a mapping of tool shape errors in the workpiece. In general, the sharpening of the edge of a diamond is a challenging task that is further frustrated by anisotropy of the single crystal. Finally, error motion in the spin turning spindle will lead to undesired motion of the cutting tool with respect to the workpiece.

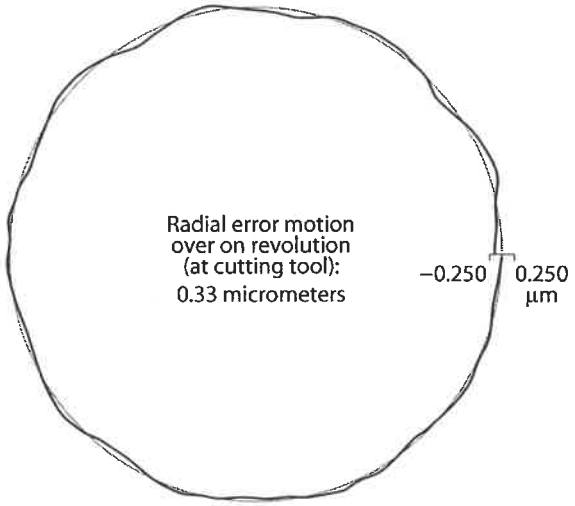

FIGURE 2. Spindle error motion over one complete revolution.

These three error sources may be mitigated by a combination of careful engineering and CNC compensation. In our approach, the diamond tools are sharpened on interchangeable spindles that are used for both tool prep and the actual cutting. Once sharpened, the tool remains on the spindle so that the eccentricity of the cutting edge is automatically minimized. Alternatively, the cutting tool could be carefully centered on a spin-turning spindle using an indicating band with any remaining eccentricity programmed into the CNC controller for compensation.

The anisotropy of diamond leads to some out-of-roundness during the sharpening of the cutting edge. In the work shown here, the cutting edge is prepared with a chemo-mechanical process that minimizes, but does not completely eliminate this effect. We chose not to map this error out because of the difficulty of adequate characterizing the tool edge profile error, although this has been successfully demonstrated.

The spindle error motion and compliance presents the final challenge to maintain workpiece form accuracy. In the work shown here, two different spin turning spindles were used. The first was an air bearing spindle with error motion of less than 25 nm in the sensitive direction. This spindle is so good that the error motion is virtually negligible. Like any tool holder, there will be some deflection due to compliance in the spin turning structure, which will tend to change as the tool encounters the angle-dependent hardness of the rotating silicon workpiece. In a second round of

testing, a tapered roller bearing spindle was used to achieve much higher stiffness, but with 100 nm of error motion in the sensitive direction. The tapered roller bearing spindle's error motion is repeatable and mappable, provided that the spindle rotations are accounted for and reset between cuts. No attempt was made to perform this mapping in this preliminary work.

Experimental setup

The remainder of this work describes cutting experiments that compare silicon turning with stationary and spinning tools.

coolant	deionized water
spindle speed	1000 RPM
feed	1 micrometers/rev
depth of cut	5 micrometers
workpiece	(100) Si

Ongoing work

The spin turning concept is expected to be well-suited to laser-assisted diamond turning. Laser heating of the uncut chip region greatly improves ductility of the chip with the unfortunate side effect of enhancing oxidation and graphitization of the diamond cutting edge [13]. Given that spin turning likely reduces spot-heating and prolongs edge life, they appear to be naturally suited for each other. A next step is research to apply the spin turning method to rough-machining a difficult material such as silicon carbide mirrors.

REFERENCES

[1] Bifano T, Dow T, Scattergood R. Ductile-regime grinding of brittle materials: experimental results and development of a model. In: Proceedings of the SPIE: Advances in Fabrication and Metrology for Optics and Large Optics. vol. 966; 1988. p. 108–115.

[2] Blaedel K, Taylor J, Evans C. Ductile-Regime Grinding of Brittle Materials. In: Jahanmir S, editor. Machining of Ceramics and Composites. Marcel Dekker; 1999. p. 139–176.

[3] Abdel-Aal HA, Reyes Y, Patten JA, Dong L. Extending electrical resistivity measurements in micro-scratching of silicon to determine thermal conductivity of the metallic phase Si-II. Materials Characterization. 2006;57(4-5):281–289.

[4] Leung TP, Lee WB, Lu XM. Diamond turning of silicon substrates in ductile-regime. Journal of Materials Processing Technology. 1998;73(1-3):42–48.

[5] Pharr GM, Oliver WC, Clarke DR. Mechanical behavior of silicon during small-scale indentation. Journal of Electronic Materials. 1990;19(9):881–887.

[6] Vodenitcharova T, Zhang LC. A mechanics prediction of the behaviour of monocrystalline silicon under nano-indentation. International Journal of Solids and Structures. 2003;40(12):2989–2998.

[7] Kovalchenko A, Gogotsi Y, Domnich V, Erdemir A. Phase transformations in silicon under dry and lubricated sliding. Tribology Transactions. 2002;45(3):372–380.

[8] Yan J, Takahashi H, Tamaki J, Gai X, Harada H, Patten J. Nanoindentation tests on diamond-machined silicon wafers. Applied Physics Letters. 2005;86(18):181913.

[9] Shaw MC, Smith PA, Cook NH. Rotary cutting tool. American Society of Mechanical Engineers – Transactions. 1952;74(6):1065–1073.

[10] Kishawy HA, Wilcox J. Tool wear and chip formation during hard turning with self-propelled rotary tools. International Journal of Machine Tools and Manufacture. 2003;43(4):433–439.

[11] Li L, Kishawy HA. A model for cutting forces generated during machining with self-propelled rotary tools. International Journal of Machine Tools and Manufacture. 2006;46(12-13):1388–1394.

[12] Ezugwu EO, Bonney J, Yamane Y. An overview of the machinability of aeroengine alloys. Journal of Materials Processing Technology. 2003;134(2):233–253.

[13] Rozzi JC, Pfefferkorn FE, Shin YC, Incropera FP. Experimental Evaluation of the Laser Assisted Machining of Silicon Nitride Ceramics. Journal of Manufacturing Science and Engineering. 2000;122(4):666–670.

THERMISTOR BRIDGE PERFORMANCE IN THE 10^{-4} TO 1 HZ RANGE AND ITS APPLICATIONS IN GRAVITATIONAL WAVE DETECTION PROJECTS

Sei Higuchi[1], Daniel E. Clark[2], Brian Lantz[3] and Daniel B. DeBra[1]
[1]Department of Aeronautics & Astronautics, Stanford University, Stanford, CA, U.S.A.
[2]Department or Mechanical Engineering, Stanford University, Stanford, CA, U.S.A.
[3]Edward L. Ginzton Laboratory, Stanford University, Stanford, CA, U.S.A

INTRODUCTION

The design and characterization of thermistors as a temperature sensing device that enables microkelvin temperature resolution is driven by the science requirements of the LISA (Laser Interferometer Space Antenna) project and also for the LIGO (Laser Interferometer Gravitational-wave Observatory) seismic isolation projects. Past research has been conducted for long term stability over several years (Patterson et al [1, 2]) but does not include performance data of interest to LISA and LIGO in the frequency spectrum of noise and performance of 10^{-4} to 1 Hz. Their data primarily focused on $f \ll 10^{-4}$ Hz. Particularly for the LISA thermal requirement, the temperature fluctuations across the gravitational reference sensor (GRS) has to be regulated as low as $30\ \mu K/\sqrt{Hz}$ for 0.1 mHz to 1 Hz. Thus, it calls for a temperature sensor that is capable of measuring as precise as microkelvin resolution.

The use of the op-amp (regular or chopper-stabilized), thermistor bridge nominal resistance value, bridge drive level and feedback resistance are optimized using a cost function that takes into account the noise sources and their relation to the overall thermistor accuracy. The principal noise sources of interest include resistor / thermistor Johnson noise, voltage noise in the op-amp(s), current noise in the op-amp(s), self-heat of the thermistor element, dSPACE ADC noise, and noise in the bridge drive circuit. Finally, the preliminarily experimental result of relative spectral noise of thermistor is demonstrated.

Thermistors have been chosen as our best candidate for temperature control applications because of their high sensitivity, availability, cost, and compactness. Patterson and et al [1, 2] conducted long-term stability of thermistors for nearly four years. However, there has been no experimental work on "mid-term" spectral stability of thermistors, yet. Hammond and Benjaminson [3, 4] demonstrated a resolution of $0.0001\ ^oC$ with linear quartz thermometer and the similar level of resolutions were claimed by some past research [5, 6]. However, the quartz thermometer doesn't have fast enough bandwidth for our applications. Meanwhile, RTDs are considered for our temperature sensor candidate. They lack sensitivity to small temperature change and have a slower response time than thermistors.

EXPERIMENTAL SYSTEM

A schematic figure of the experimental system is shown in Figure 1. Four thermistor bridges,

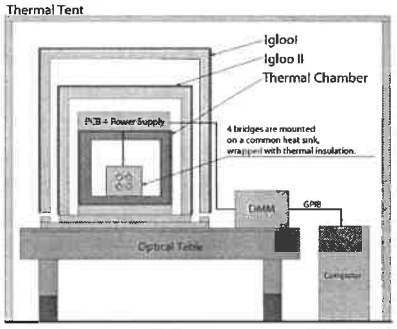

FIGURE 1. Experimental apparatus for thermistor bridge circuit tests

mounted on a common heat sink (see Figure 2) and wrapped with an air-bubble sheet, are placed in the center of a double walled thin metal thermal enclosure. A thermocouple monitors the bridges with ($< 100\ \mu K/\sqrt{Hz}$) noise. The enclosure is wrapped in flexible insulation, and wrapped again with copper foil. This copper foil surface equalize the temperature distributions around the enclosure, and the inside temperature could be controlled to high-precision by a heating-pad/thermocouple feedback system. Surrounding the enclosures are 2 in. (5 cm) of foil-covered polystyrene foam insulation, labeled Igloo I and Igloo II, to create sealed control volumes. A PCB and a power supply are placed on top of the thermal chamber and inside of Igloo I. This setup

will minimize the unwanted effect of heat generation from the power supply to the bridges and also temperature variations at the PCB could be smaller. Experimental data is acquired through a 20-channel, 20-bit digital multimeter and logged on a desktop computer. Finally, the entire system is placed within a clear plastic thermal tent, primarily to cut down on air drafts. The nominal value for the bridges was chosen through the optimization method introduced in later section. One of the optimal values, which minimizes circuit noise and self-heat generation, is 293 $k\Omega$. 200 $k\Omega$ is used for our baseline bridge because the closest available glass-bead thermistor on the market was 200 $k\Omega$. We also test 10 $k\Omega$ and 300 Ω-bridges.

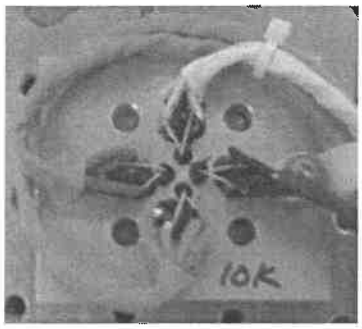

FIGURE 2. Thermistor bridges nested on an aluminum heat sink

Figure 3 depicts the electric circuit that is used for the tests. We use a chopper stabilized op-amps, LTC-1250, as our baseline design in order to avoid $1/f$ noise at the low frequency range. The voltage reference, LT-1021, is shared with all four bridges so that the common mode can be canceled out. The output voltage, V_{out}, is amplified at another stage with a gain of 10, which is not shown in the figure. The op-amps could be swapped to non-chopper stabilized op-amps to compare the noise performances.

DATA PROCESSING

Resistance of thermistors is modeled as

$$R_{th,i} = R_0 e^{\alpha_i (T_i - T_0)} \simeq R_0 + R_0 \alpha \Delta T_i \quad (1)$$

where $\Delta T_i = T_i - T_0$.; R_0 is the nominal value of thermistor at T_0 that is typically 25 ^oC; i is the bridge number, or $1, 2, \cdots, 4$. This expression is valid as long as the temperature change at a thermistor is small enough and we assume that the resistance is a linear function of temperature change. We take the first R_0 term as the bias and the second $R_0\alpha$ is the scale factor. For each bridge, temperature difference, $\Delta T_i(t)$, is computed by dividing the measured voltage, v_i, by circuit transfer function, β, that is derived from the circuit in Figure 3. The transfer function looks like

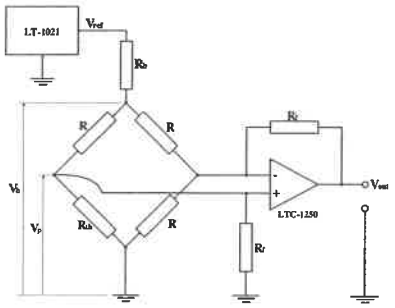

FIGURE 3. Thermistor bridge circuit

$$\beta = \frac{V_{out}}{\Delta T} = \frac{1}{2}\alpha R_f \left(\frac{V_{ref}}{R_b}\right) \quad (2)$$

The bridge circuit output, $v_i(t)$, can be modeled as

$$v_i(t) = b_i + s_i \Delta T_i(t) + n_i(t) \quad (3)$$

Then, the constant bias, b_i, and the scale factor, s_i, need to be matched as closely as possible in order to estimate the noise term, n_i. One can fit b_i and s_i such that a cost function, J_i for each of bridges, is minimized.

$$J_i = [\bar{v}(t) - (b_i + s_i \Delta T_i(t))] \quad (4)$$

$$\bar{v} = \frac{1}{N}\sum_{i=1}^{N} v_i(t) \quad (5)$$

where $N = 4$; $\bar{v}$ is a reference voltage, which is the average of four measurements. The solution, $p_i = [b_i, s_i]^T$, is given by solving a set of linear equations. Then, we get the relative residual of the fit:

$$n_i(t) = \bar{v}(t) - (b_i + s_i \Delta T_i(t)) \quad (6)$$

In terms of equivalent temperature noise,

$$n_{t,i}(t) = \beta^{-1} n_i(t) \quad (7)$$

CIRCUIT DESIGN METHODOLOGY USING COST FUNCTION MINIMIZATION

We have developed a design methodology for thermistor bridge circuit. In essence, we would

like to formulate an optimization problem that is:

$$\begin{aligned} \text{minimize:} \quad & J(\vec{x}) \\ \text{with respect to:} \quad & \vec{x} = [R, R_b, R_f]^T \\ \text{subject to:} \quad & c(\vec{x}) \preceq 0 \\ & \vec{x}_{lb} \preceq \vec{x} \preceq \vec{x}_{ub} \end{aligned}$$

so that we can get optimal solutions for each application by solving the optimization problem. The following three quantities are chosen as the design variables: R, bridge resistance, R_b, bias resistance (excitation resistance), R_f, feedback resistance, and $V_{ref} = 10\ V$ for voltage reference. The cost function $J(\vec{x})$ and the constraints $c(\vec{x})$ are different by applications. Typically, the cost function is composed of circuit noise level, self heat generation by thermistors, and circuit transfer function.

The total output of the circuit in terms of amplitude spectral density, $e_o\ V/\sqrt{Hz}$, can be expressed by the following equation:

$$e_o = \sqrt{e_1^2(f) + e_2^2(f) + e_3^2(f)} \qquad (8)$$

where $e_1\ V/\sqrt{Hz}$ is op-amp output due the the temperature variations at the heat sink where thermistor is attached. This quantity is what we are interested in measuring.; $e_2\ V/\sqrt{Hz}$ is op-amp output due to the self-heating of thermistor, which is a systematic phenomena. The e_2 term accounts for only the noise from the voltage reference. The constant component of self-heating is expressed as $e_b\ V$.; $e_3\ V/\sqrt{Hz}$ is the op-amp output due to the electric circuit noise including the op-amp current noise, the op-amp voltage noise, and Johnson noise from electrical resistances.

Figure 4 shows various circuit noise, circuit transfer function and self-heating temperature as functions of design variables. Each circuit noise is expressed in terms of equivalent temperature, namely divided by the circuit transfer function β. Each design variable is normalized as $\bar{x}_i = (x_i - x_{lb})/(x_{ub} - x_{lb})$ where x_{ub} and x_{lb} are the upper/lower bounds of the design variables respectively. In order to maximize the sensitivity of the temperature circuit, we want to minimize the circuit noise as well as self-heat temperature. To reduce the circuit noise, a higher value of bridge resistance and lower values of feedback/bias resistances are desired. However, the combination of a high bridge resistance and a low bias resistance results in larger self-heat generation. For this reason, bridge test experiments are conducted with

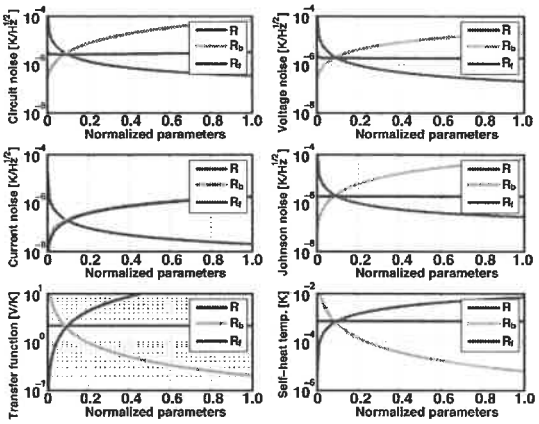

FIGURE 4. Performance curves as a function of design variables: total circuit noise (top-left), voltage noise (top-right), current noise (middle-left), Johnson noise (middle-right), circuit transfer function (bottom-left), self-heating temperature (bottom-right).

two separate scenarios: (1) neglect the self heat effect so that the self heat temperature can be canceled out as a common mode. (2) minimize self-heat effect while maximizing the sensitivity of the bridge. If multiple bridges are mounted on the common heat sink, relatively close to each other, the temperature variations at the bridges are going to be common. Thus, the self heating effect will also be a common noise source. The first scenario minimizes the total circuit noise integrated over the frequency range of interest, $f = [f_{min}, f_{max}]$, and is subjected to some noise level. γ is a relaxation constant (< 1). Note that $\Delta f = f_{max} - f_{min}$.

$$\begin{aligned} \text{minimize:} \quad & E_3 = \int_f e_3^2(\vec{x}) df \\ \text{with respect to:} \quad & \vec{x} = [R, R_b, R_f]^T \\ \text{subject to:} \quad & \frac{\sqrt{\int_f e_3^2(\vec{x})}}{\beta(\vec{x})\sqrt{\Delta f}} \leq \gamma \Delta T_{hs} \\ & \vec{x}_{lb} \preceq \vec{x} \preceq \vec{x}_{ub} \end{aligned}$$

The solution is: $R^* = 293.626\ k\Omega$, $R_b^* = 442.029\ k\Omega$, $R_f^* = 1.00008\ M\Omega$, $I_b = 22.6229\ \mu A$, $\Delta T_{th} = 0.923447\ mK$, $E_3 = 0.452845\ \mu V_{rms}$. Because self-heating doesn't appear in the problem formulation, the optimizer chooses relatively higher bridge resistance value while the feedback resistance becomes smaller for a lower op-amp voltage noise. We use 300 and $10k\ \Omega$-thermistors

in order to check if the noise performance is improved for a higher bridge impedance. In this scenario, one is able to estimate the fundamental noise limitation of a thermistor.

The second scenario takes into account all possible noise sources. Self-heat dissipations is desired to be a minimum. The optimizer minimizes the self-heating temperature rise $\Delta T_{th}(\vec{x})$, which is relatively constant. Then, the electronics noise is constrained to be less than some fraction of the op-amp output associated with the heat sink temperature variation, ΔT_{hs}, which is set to 1 $\mu K/\sqrt{Hz}$.

$$\begin{aligned} \text{minimize:} \quad & \Delta T_{th}(\vec{x}) \\ \text{with respect to:} \quad & \vec{x} = [R, R_b, R_f]^T \\ \text{subject to:} \quad & \frac{\sqrt{\int_f e_3^2(\vec{x})df}}{\beta(\vec{x})\sqrt{\Delta f}} \leq \gamma \Delta T_{hs} \\ & \vec{x}_{lb} \preceq \vec{x} \preceq \vec{x}_{ub} \end{aligned}$$

The solution is: $R^* = 8.81082\ k\Omega$, $R_b^* = 15.9971\ k\Omega$, $R_f^* = 4.99961\ M\Omega$, $I_b = 625.14\ \mu A$, $\Delta T_{th} = 21.157\ mK$, $E_3 = 30.2994\ \mu V_{rms}$.

PRELIMINARILY EXPERIMENTAL RESULTS

Figure 5 shows noise data processed by following the method introduced previously. The top chart is the time history over nearly 10 hours and the bottom chart is the amplitude spectral density (ASD) estimate of the noise data. In the ASD chart, MATLAB simulation results and calculated values based on Patterson et al's experimental data [1] are also compared. We fitted their data with second-order Fourier series and estimated its ASD. In addition, the LISA thermal requirement, $30\ \mu K/\sqrt{Hz}$ for $0.1\ mHz < f < 1\ Hz$, is shown with dashed lines.

CONCLUDING REMARKS

In this article we have successfully demonstrated the fundamental spectral noise limitation of thermistors by estimating the amplitude spectral density. The experimental result shows very reasonable agreement with the simulation results and implies a potential of microkelvin precision temperature measurement for the gravitational wave detection missions, which requires $30\ \mu K/\sqrt{Hz}$.

ACKNOWLEDGMENTS

Authors would like to acknowledge YSI Inc. for providing precision thermistors.

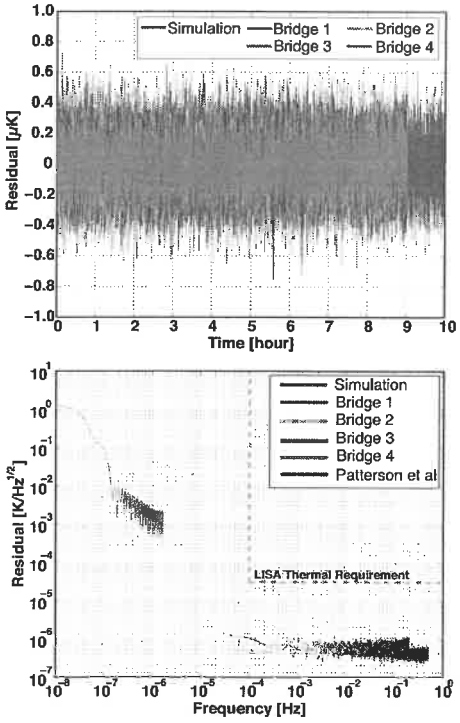

FIGURE 5. Noise of $10\ k\Omega$ *thermistor bridges*

REFERENCES

[1] Lawton KM, Patterson SR. Long-term relative stability of thermistors. Journal of the International Societies for Precision Engineering and Nanotechonology. 2000;25:24–28.

[2] Lawton KM, Patterson SR. Long-term relative stability of thermistors: Part 2. Journal of the International Societies for Precision Engineering and Nanotechonology. 2002;26:340–345.

[3] Hammond DL, Benjaminson A. The Linear Quartz Themometer - a New Tool for Measuring Absolute and Difference Temperatures. Hewlett-Packard Journal. 1965;16(7):1–7.

[4] Hammond DL, Benjaminson A. The crystal resonator - a digital transducer. IEEE spectrum. 1969;p. 53–58.

[5] Wade WH, Slutsky LJ. Quartz Crystal Thermometer. The Review of Scientific Instruments. 1961;33(2):212–213.

[6] Smith WL, Spencer WJ. Quartz Crystal Thermometer for Measuring Temperature Deviations. The Review of Scientific Instruments. 1963;34(3):268–270.

TEST UNCERTAINTY & TEST UNCERTAINTY RATIO (TUR)

Samira A Khanam[1], Edward Morse[1]
Department of Mechanical Engineering and Engineering Science
The University of North Carolina at Charlotte
Charlotte, NC 28223, USA

Measurement is a process to determine the value or physical quantity of a measurand. The measurand is the particular quantity subject to measurement [1]. Each test of dimensional measurement contains one or more measurement steps. These steps contain inaccuracies or errors. To describe these errors the term "Uncertainty" is used. The ISO International Vocabulary of Basic and General Terms in Metrology (VIM) define uncertainties as "a parameter, associated with the result of a measurement that characterizes the dispersion of the values that could be reasonably attributed to the measurand (VIM 3.9)." In general, different measurements may have different uncertainty statements, even if they are measured with the same instrument [2]. Elimination of uncertainty is not the focus for measurement only the reduction of it is possible. The most common dimensional measurand is associated with the work piece. The example can be the measurand when measuring the diameter of the hole by using micrometer or any other instrument. The uncertainty associated with this kind of measurand is known as "*Task specific* uncertainty". The uncertainty associated when testing a piece of equipment is a new concept in this field. As a result this discussion focuses on this new type of uncertainty which is known as "*Test uncertainty*". The example can be to calibrate micrometer by using a gauge block or to calibrate CMM by using a step gauge. The uncertainty associated with this kind of measurand which is the "error of the instruments" is known as "Test Uncertainty". This is mentioned in ISO 23165 in which test uncertainty is characterized for CMM.

As stated above error is associated with the measurement process. The term error and the uncertainty are not exactly same. Error is the difference between the result and the true value. In practice, no one can know the true value. So the measured value is compared with the reference value. The reference value gives a point of reference with an uncertainty which is commonly accepted to compare an indicator. If calibrated at NIST the true value is inside that reference value. In [2] S.D Phillips *et al* states, "The relationship between the measured or indicated values and those of the reference values is a key issue with regards to calibration...all calibration must include the statement about the accuracy of the instrument or artifact as required by traceability." We interpret this to mean test uncertainty in this discussion. Any calibration result showed the error or the deviation of the measurand with respect to the reference value and uncertainty associated with this error. There are different kinds of measurand for different kinds of measurement process. Consequently the uncertainty will be different also. A clear description of different kinds of uncertainty associated with different kind of measurand is explained in table-1.

TABLE 1.

Measurand/ Quantity	Activity	Uncertainty (U)
Some characteristics of the work piece	Measuring a work piece to conform to specific value or tolerance	Task specific U
The length of the artifact	Calibrating the material standard size. (Diameter of a sphere)	Calibration U
The error of the instrument (E-value)	Calibrating an instrument	Test U

Table 2 is showing the uncertainty contributors for different kinds of Uncertainty.

TABLE 2.

Contributor	Task Specific Uncertainty	Test Uncertainty
Environment 1)Temperature 2)Work Piece	1) If instrument does not compensate with temperature it has effect on TSU 2) The temp. difference between W/P and room temp.	1) Any error introduced by the instrument is not the part of TU 2) If artifact is compensate with temperature of instrument, then it is part of instrument, not include in TU
Reference element of measurement equipment	Resolution of the main scale (analogue or digital)	Does not apply (Part of the instrument)
Measurement setup (Probe selection, tip size etc.)	Form deviation of tip, Offset, extension	Usually specified by std. Poor setup may influence TU.
Software and calculations	Rounding/Quantification Sampling Algorithms	Well defined in the standard, may be eliminated
Metrologist	Experience, training, knowledge (precision)	Reproducibility
Measurement object , work piece or measuring instrument characteristics	Surface roughness, form deviation of the w/p	Form error of artifact, uncertainty for the length of artifact
Measuring procedure	Alignment, Clamping fixturing, Number of measurement etc. example: Due to the measurement process of w/p like repeatability	Alignment, Clamping fixturing , number of measurement etc. example: Instrument repeatability error is not the part of TU, but the repeatability error for tester is the part of TU.

Example of "Task specific uncertainty" & "Test uncertainty"

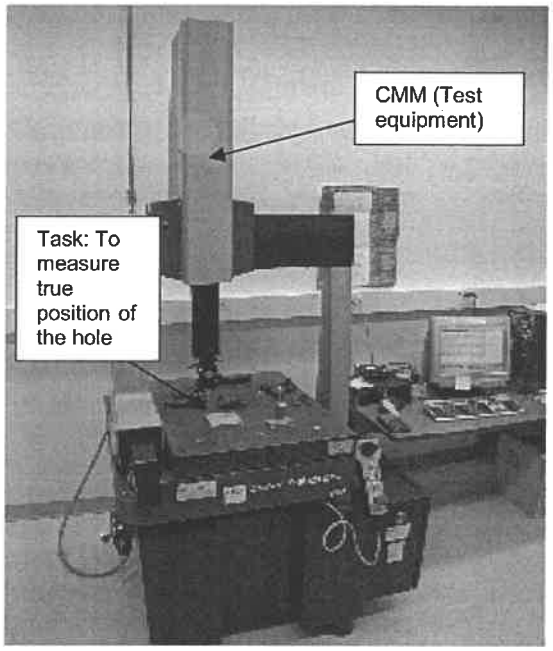

FIGURE 1. CMM is measuring the true position of the hole of a block (Task specific uncertainty)

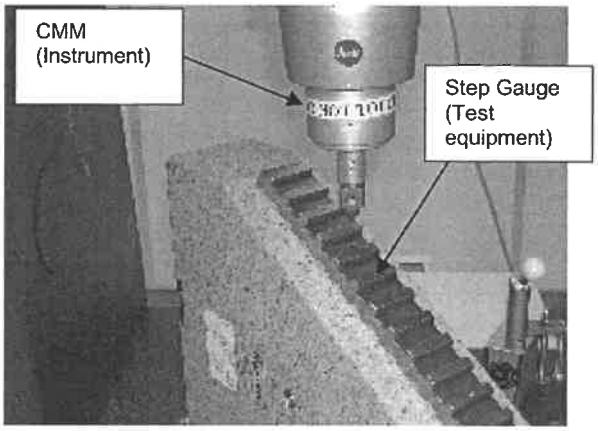

FIGURE 2. CMM is calibrating by using a step gauge (Test uncertainty)

Test uncertainty depends on significantly test equipment, test procedure (which should be well recognized) and the influence of the human operator. When calculating the test uncertainty all these factors should be reasonably estimated to ensure that the result does not give any wrong impression of uncertainty. Test uncertainty is only

the indication of the quality of the test, it is not the machine performance. By defining the test, how well test is performed, the influence of the operator, selection and placement of test instrument test uncertainty can be decreased and consequently increasing the precision and usefulness of the test.

Another topic, *Test Uncertainty Ratio* (TUR) is a measure of the ability of a particular measurement instrument and/or process to evaluate conformance to specification. TUR is the ratio between the tolerance or specification and the uncertainty present in the test of this tolerance or specification. Historically, the rule of thumb for an appropriate ratio was that the TUR must be at least 10:1. The higher the ratio, the better the performance of the test. Currently, a ratio of 4:1 or even 3:1 is considered acceptable. This is due mostly to the better performance of manufacturing equipment, and the tighter and tighter specifications on manufactured components. In many cases, test equipment with an uncertainty small enough for a 10:1 TUR does not exist, or is prohibitively expensive for the application. There are two main applications of the TUR: the first is in the calibration of measuring instruments and equipment, the second is in the inspection of manufactured components. The focus of this document is the second application – *how do we determine the Test Uncertainty Ratio for a part that we need to measure using a particular gage?* The list below gives some of the important things to consider.

1. The uncertainty statement in the gage's product literature might **not** be the uncertainty needed to calculate TUR.
2. The result of the gage's most recent calibration is *almost certainly* **not** the uncertainty needed to calculate TUR.
3. The tolerance value on the part drawing is – if interpreted correctly – going to be needed to calculate TUR.
4. There will be more than one TUR calculation for a part if there is more than one tolerance that must be inspected.

To preview what will be covered in this paper, the *task-specific measurement uncertainty* must be estimated *for the measurand in question* for each tolerance. This is the "1" value. The range of allowable values for the measurand in question (this is usually the tolerance) must be known, and is compared to "4".

$$\mathrm{TUR} = \frac{Tolerance\ for\ the\ measurand}{Task \cdot specific.uncertainty}$$

As is easily inferred from the equation above, the TUR ratio compares the allowable variation for the measurand (the numerator) with the variability associated with finding the measurand (the denominator).

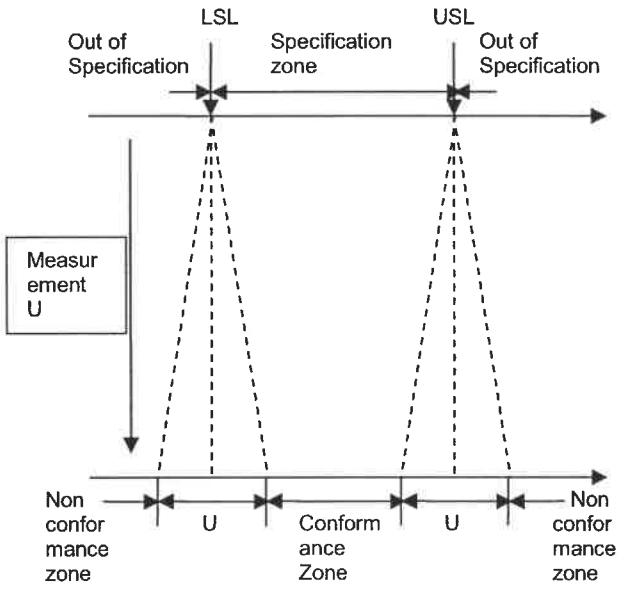

FIGURE 3. Relationship between Specification Zone and Conformance Zone

One function of industrial measurement is to determine whether a particular part *measurand* (length, form, location, etc.) conforms to the specification given on the part drawing or model. The difference between the specification zone and the conformance zone for a measurand is explained with the aid of *FIGURE* 3, taken from ISO 14253-1:1998(E). The upper horizontal line of the figure shows the specification zone, which is bounded by the lower specification limit (LSL) and the upper specification limit (USL). If the "true value" of the measurand is within the specification zone, then the specification is satisfied, otherwise the measurand is out of specification. However, we can never know the "true value" of the measurand. In order to state whether we believe that the measurand is in or out of specification, we have to acknowledge the existence of uncertainty in the measurement process. This is shown in the lower horizontal line in *FIGURE 3.* If the measurand is in conformance zone, we are suitably confident

that the true value is in specification. Similarly, if the measurand is in the non-conformance zone, we are confident that the true value is out of specification. For the uncertainty region shown between conformance and non-conformance, we need to apply the "Decision rules." A decision rule is a method – agreed on by two parties – to decide whether to accept or reject a part when the measurement value lies in this uncertainty region.

One common decision rule used in industry is **"Simple Acceptance and Rejection Using an N:1 Decision Rule"** as defined in ASME B89.7.3.1-2001. Using this decision rule, the measured value is compared directly to the specification zone (i.e. the conformance zone and the specification zone are identical). This rule has the effect of dividing the risk for accepting bad parts and rejecting good parts between the supplier and customer. In order to limit this risk, the requirement of N:1 is placed on the test uncertainty ratio (N is often 4, as mentioned already). In *FIGURE 4* below, taken from the B89.7.3.1 document, the acceptance and rejection zones are shown to be identical to the specification zones.

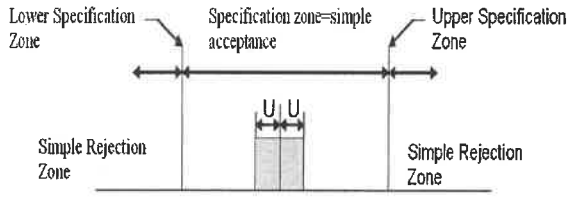

FIGURE 4. Schematic view of Simple acceptance/rejection with a 4:1 uncertainty requirement

The measurement uncertainty interval is of width 2U, where U is expanded uncertainty, and the uncertainty interval is no larger than one-fourth the product's specification zone for N = 4. [B 89.7.3.1-2001] For the simple acceptance rule with a 4:1 ratio means that the tolerance range is at least 4 times the uncertainty interval.

REFERENCES

[1] http://www.measurementuncertainty.org/mu/guide/uncertainty.html

[2] S.D Phillips et al. A Careful Consideration of the Calibration Concept. Journal of Research of the National Institute of Standards and Technology. 2001; 106:371-379.

[3] Adams M. A2LA Guide for the Estimation of the Measurement Uncertainty in Testing. American Association of Laboratory Accreditation Manual, 2002.

[4] http://en.wikipedia.org/wiki/Measurements.

[5] Guidance Uncertainty of Measurement concept in European Standards.

BAYESIAN UPDATING OF STABILITY BELIEFS

Raúl E. Zapata[1], Michael G. Traverso[2], Ali E. Abbas[2], Tony L. Schmitz[1]
[1]Department of Mechanical and Aerospace Engineering
University of Florida
Gainesville, FL, USA
[2]Department of Industrial and Enterprise Systems Engineering
University of Illinois at Urbana-Champaign
Urbana, IL, USA

INTRODUCTION

Research since the 1960s has shown that machining stability is dependent on the selected operating parameters, the tool and material combination, and the dynamic properties of the system. Pre-process stability calculations [1-2] require knowledge of the force model (based on the tool and work material) and the tool point frequency response function, or complex frequency dependent ratio of the tool displacement to the excitation force. The frequency response function, FRF, can be measured using modal testing or predicted via system models (analytical or finite element) [3]. Both experiments and models have associated costs due to the necessary equipment and the time for dedicated engineering personnel to carry out the tests and/or analyses. Because the force model and tool point FRF vary with setup (new workpiece material or tool geometry, for example), the data is case specific and can be time-consuming to collect. These technical and economic complications lead to reduced application of pre-process stability predictions.

An alternative to the predictive methods is to perform a limited number of test cuts using the selected material/ tool combination to improve knowledge regarding suitable operating conditions. In our previous work, we incorporated uncertainty into pre-process stability calculations by allowing the input variables to take on random instead of deterministic values [4]. However, this still required advanced knowledge of the force model and tool point FRF.

In this paper, we describe the application of Bayesian updating to modify beliefs about whether a cut will be stable or unstable based only on the results of experimental cuts and some general mathematical assumptions. Convergence of these beliefs to the well-known stability lobe diagram (Fig. 1) is demonstrated.

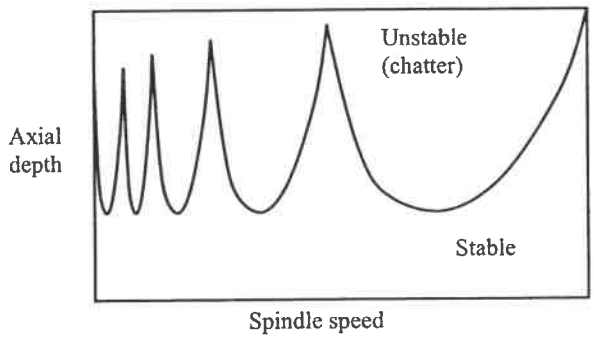

FIGURE 1. Sample stability lobe diagram

BAYESIAN UPDATING

Bayesian analysis is a rigorous and rational method of updating one's beliefs about an uncertain variable after observing evidence or receiving new information. Specifically, it requires a prior distribution f_{pri} that represents the belief prior to experimentation, a likelihood function f_{like} that relates the results of an experiment to the information gained from the experiment, and results in a posterior distribution f_{post} that takes into account both the prior beliefs and the results of the experiment. This posterior distribution is determined by

$$f_{post}=c\cdot f_{like}\cdot f_{pri}$$

where the constant c is determined through normalization. The posterior distribution can then be treated as a prior distribution for another experiment. This updating process can be repeated for any number of experiments.

Initial Prior Distribution

Let d denote the axial depth of cut, s denote spindle speed, and b(s) denote the stability boundary. In this sample analysis, the domain is restricted to the interval $s \in [5\ \text{krpm}, 20\ \text{krpm}]$. The prior distribution was chosen to be

$$f_{pri,s}(d) \sim U(0 \text{ mm}, 2 \text{ mm}) \text{ for all } s$$

where $\sim U(a_1,a_2)$ denotes a uniform distribution from a_1 to a_2. This uniform distribution indicates our belief that the possibility for chatter increases linearly with depth of cut, but we do not have any knowledge about the spindle speed dependence. The uniform distribution is demonstrated in Fig. 2, where white denotes a high probability of stability and black denotes a low probability of stability.

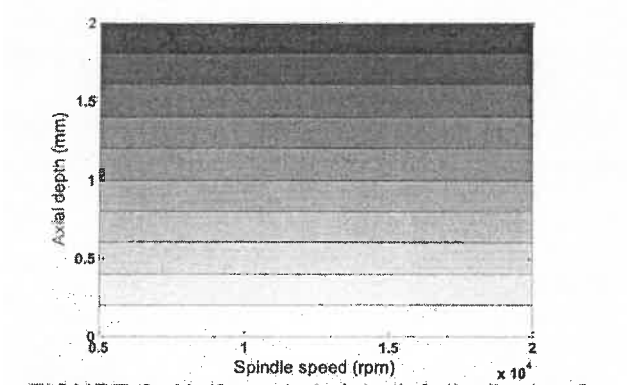

FIGURE 2. Uniform (prior) belief distribution for selected domain.

Likelihood Function

For a test cut at spindle speed s_0 and axial depth d_0, the likelihood function at s_0 is given by [4]:

$$f_{like}(s_0,d|s_0,d_0 \text{ stable}) \sim U(d_0, 2 \text{ mm}) \quad (1A)$$

$$f_{like}(s_0,d|s_0,d_0 \text{ unstable}) \sim U(0 \text{ mm}, d_0) \quad (1B)$$

To determine the likelihood function at other spindle speeds, b(s) was treated as a "random walk" from s_0. Since the expectation over all random walks is given by the solution to the diffusion equation [5], the likelihood function is given by the solution to the initial value problem:

$$\frac{\partial f_{like}}{\partial s}(||s-s_0||,d) = k\frac{\partial^2 f_{like}}{\partial d^2}(||s-s_0||,d)$$

with initial conditions determined by Eq. 1A or 1B, depending on the outcome of the experiment. The diffusion coefficient k is assignable and should be chosen such that:

$$k = E\left[\left(\frac{\delta b(s)}{\delta s}\right)^2\right] \cdot 0.5$$

However, because the speed dependent stability boundary is unknown, we cannot apply this equation. Instead, k should be chosen to reflect one's best guess of its value. Since this value can depend on tool geometry and cutting parameters, as well as the domain and units chosen for s and d, it is a case specific quantity and must be selected separately for each analysis.

Additionally, since a bounded distribution is being used in this case, boundary conditions must be imposed. In this case, reflective boundary conditions were used since absorbing boundary conditions result in an information gain infinitely far from the tested spindle speed.

NUMERICAL STUDY

To test the effectiveness of this updating scheme, simulated experiments were performed against a reference stability lobe generated using the algorithm derived in [2]. The tool geometry and cutting parameters used in the algorithm are summarized in Table 1.

TABLE 1. Parameters used for numerical examples throughout the paper.

Property	Value	Units
Tangential cutting coefficient	2395	N/m^2
Radial cutting coefficient	719	N/m^2
Number of teeth	4	teeth
Tool diameter	10	mm
Radial depth of cut	5	mm
Tool stiffness	$5x10^6$	N/m
Damping ratio	0.05	-
Tool natural frequency	2.4	kHz

The first step was to choose a parameter k consistent with our beliefs. Sample updates for k values of 0.0005 and 0.0001 are shown in Figs. 3 and 4.

Based on our general knowledge of stability lobe diagrams, k was chosen to be 0.0005. Preliminary numerical tests were performed to validate the stable and unstable updating effects as shown in Figs. 3 and 5.

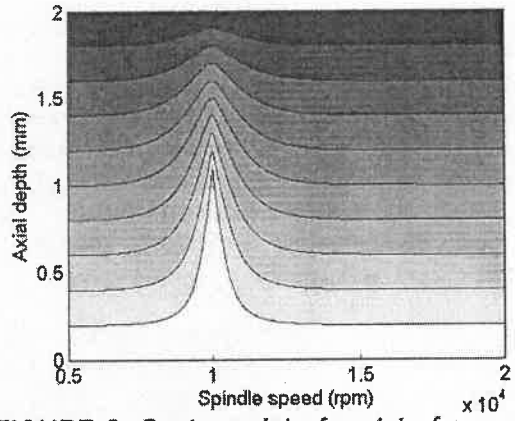

FIGURE 3. Contour plot of update for a stable test at s=10000 rpm, d = 1 mm, and k = 0.0005.

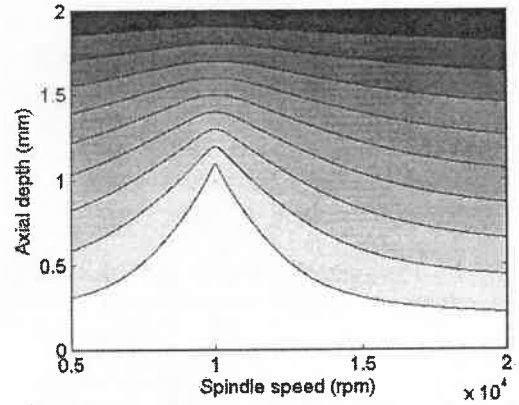

FIGURE 4. Contour plot of update for a stable test at s = 10000 rpm, d = 1 mm, and k = 0.0001.

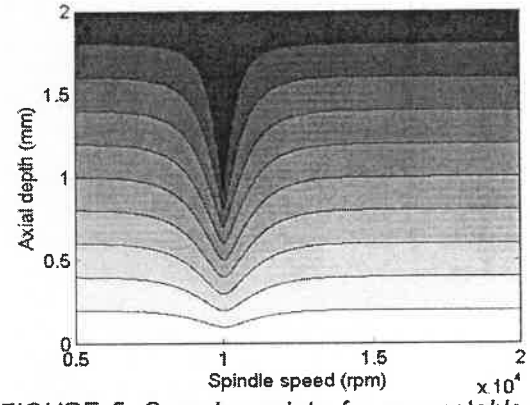

FIGURE 5. Sample update for an unstable test performed at s = 10000 rpm, d = 1 mm and k = 0.0005.

Next a series of tests were performed in order to evaluate this updating scheme's convergence to a calculated stability lobe boundary. A grid of 105 points consisting of 21 spindle speeds and 5 axial depths were selected as shown in Fig. 6.

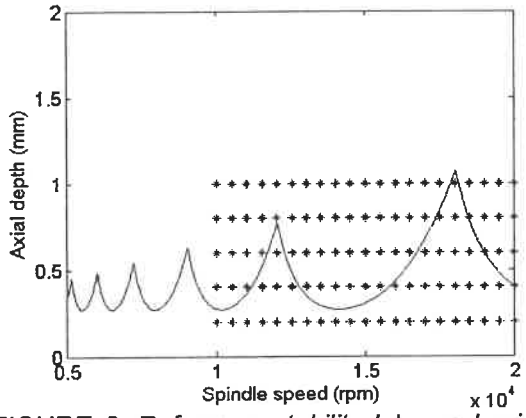

FIGURE 6. Reference stability lobe and grid of test points.

To simulate the experiments, each test point was compared to the calculated stability boundary to determine whether it was stable or unstable. The updating procedure was then performed on a point by point basis. Note that this is in no way representative of an optimal testing policy and was used solely for demonstration. The final posterior distribution after all testing is shown in Fig. 9. Note the strong similarity to Fig. 6 within the test range. In addition, several intermediate steps are also shown to illustrate the progression of convergence (Figs. 7 and 8).

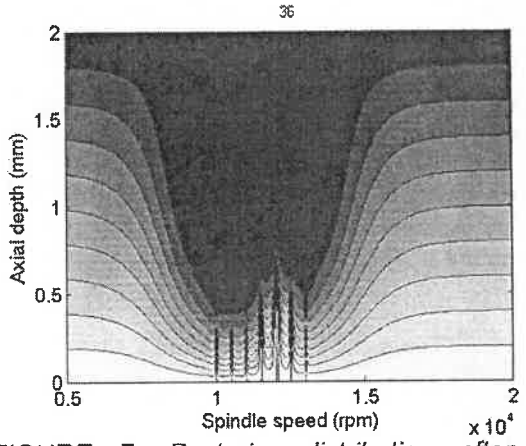

FIGURE 7. Posterior distribution after 35 experiments.

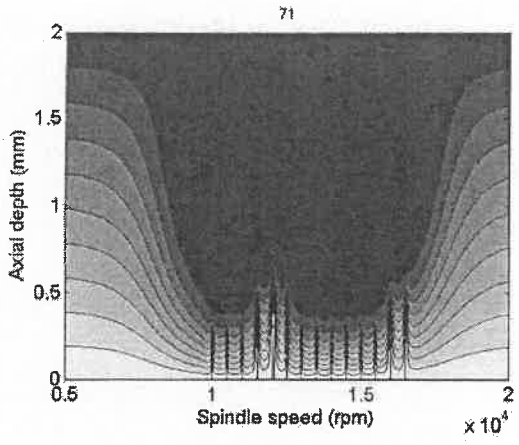

FIGURE 8. Posterior distribution after 70 experiments.

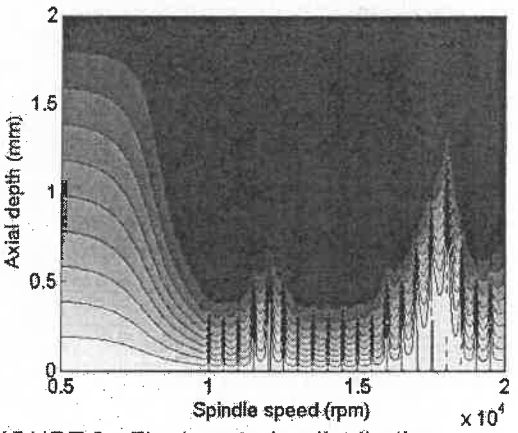

FIGURE 9. Final posterior distribution.

CONCLUSION

It is common practice to perform cutting tests on a particular machine setup to determine usable parameter combinations for machining. However, it is difficult to infer how each test affects our knowledge of the surrounding milling parameter space. This paper presented a method to use the most basic information (stability or instability) to update beliefs (knowledge) of the parameter options surrounding our test points. The important variables of the procedure and its basic methodology were explained here. In addition, convergence to the well known stability lobe diagram [2] was shown.

Future work regarding this method will include finding a testing policy that optimizes the value of experimentation as well as incorporating more complex information concerning the location of the stability boundary that can be gathered using in process metrology, such as a microphone or force dynamometer. Implementing this information will enable the user to gain more knowledge from each experiment and the overall value/effectiveness of this method will increase. Another goal is to implement guidelines for selecting a k value based on the domain size and cutting conditions. This may be achieved using a look up table or, given adequate patterns, an empirical equation.

Acknowledgements

The authors gratefully acknowledge financial support for this work from the National Science Foundation (DMI-0642569 and DMI-0641827). Any opinions, findings, and conclusions or recommendations expressed in this material are those of the authors and do not necessarily reflect the views of the NSF. They also wish to thank G. Hazelrigg for numerous helpful discussions.

REFERENCES

[1] Tlusty J, Zaton W, Ismail F. 1983, Stability Lobes in Milling, Annals of the CIRP. 1983; 32/1: 309-313.

[2] Altintas Y, Budak E. Analytical Prediction of Stability Lobes in Milling. Annals of the CIRP. 1995; 44/1: 357-362.

[3] Schmitz T, Duncan GS. Three-Component Receptance Coupling Substructure Analysis for Tool Point Dynamics Prediction. Journal of Manufacturing Science and Engineering. 2005; 127/4: 781-790.

[4] Abbas A, Yang L, Zapata R, Schmitz T. 2007, Application of Decision Analysis to Milling Profit Maximization: An Introduction. International Journal of Materials and Product Technology, (to appear).

[5] Nagasawa M. 1993, Schrodinger Equations and Diffusion Theory. Basel: Birkhauser Verlag.

THE DESIGN AND OPTIMIZATION OF CASCADED CHEVRON FLEXURES AND ACTUATORS FOR PRECISION MOTION GUIDANCE

Shih-Chi Chen[1,2] and Martin L. Culpepper[2]
[1]Wellman Center for Photomedicine
Massachusetts General Hospital, Harvard Medical School
Boston, MA
[2]Department of Mechanical Engineering
Massachusetts Institute of Technology
Cambridge, MA

ABSTRACT
This paper presents modeling and optimization procedures for optimizing the stiffness and transmission ratio of cascaded chevron flexures that are used as actuators and/or transmissions in small-scale precision machines. The principle of mechanical impedance matching is used to optimize the mechanical performance of the chevrons. This opens the way to optimization of electrical and thermal characteristics of chevron actuators. The utility of this approach is demonstrated in the context of a microactuator for a micro-optical scanning system.

INTRODUCTION
Chevron flexures are used as transmissions [1-4] that either (i) transform the output of high-force, low-stroke actuators (*e.g.* piezoelectric actuators) to a different force-stroke combination or (ii) serve as the transducing and transmission of strain-based actuators (*e.g.* thermomechanical actuators). A conventional chevron flexure is shown at the top of Figure 1A, and several design parameters are shown in Figure 1B.

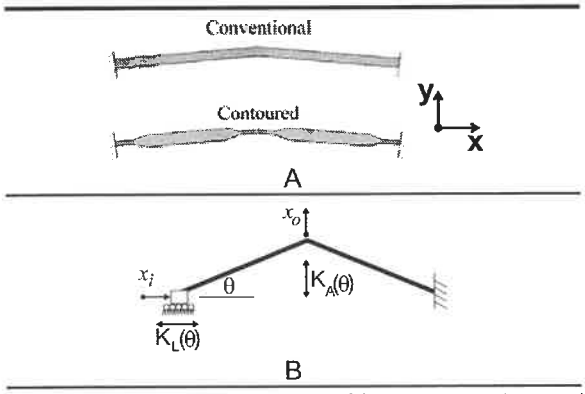

FIGURE 1: Chevron with constant and contoured cross sections (A) and design parameters (B)

Chevrons are commonly used with piezoelectric and μ–thermomechanical actuators (μ–TMAs). In the former case, the piezo actuator drives the input of the chevron, x_i, to achieve larger output stroke, x_O. In the later, x_i is fixed and a current is passed through the beam so as to yield an output displacement.

The transmission ratio ($T_r = x_o/x_i$), axial stiffness (K_A) and lateral stiffness (K_L) of a chevron flexure are a function of the chevron's side angle, θ. As θ increases from zero (i) the T_r and the lateral stiffness decrease sharply and (ii) the axial stiffness increases gradually. In many applications, one desires to place multiple chevrons that are cascaded, *i.e.* in series, with the first chevron driving the input of a second chevron and so on. This results in sequential amplification of the input motion at the expense of stiffness. In this paper we provide a parametric model that may be used to manage the tradeoff between T_r and stiffness for chevrons in series. The demonstration of the modeling and its application are presented in the context of designing a μ–optical scanner.

MICRO SCANNER LAYOUT
Figure 2 shows the scanner layout. The scanner is designed to route a laser and scan its focal point across a plane by translating a graded index (GRIN) lens and rotating a prism. The GRIN lens and prism actuator should possess a stroke of 100 μm and 2° respectively. Figures 2A and 2B show that sets of chevron TMAs 1-2 and 4-5 serve as the transducing elements. The output of TMA sets 1-2 are amplified by chevron flexure 3. The output of TMA sets 4-5 are amplified via set 6 chevron flexures. The TMAs are contoured as shown at the bottom of Figure 1A to enhance their thermal and mechanical performance [1].

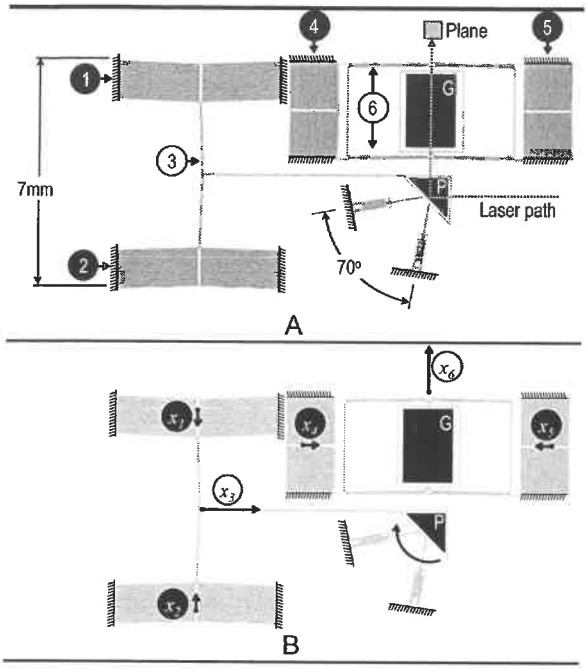

FIGURE 2: μ–scanner layout showing banks of parallel chevron actuators 1-2-4-5 and amplifying chevrons 3-6 (A) and actuator displacements that are amplified by the chevrons and resulting motion of the GRIN lens (G) and prism (P) (B)

MODELING AND DESIGN

The optimization of energy transfer through cascaded compliant machine elements may be achieved by matching their mechanical impedance, *i.e.* designing the chevron flexures so that the axial stiffness of the first chevron (K_{A1}) and lateral stiffness of the second chevron (K_{L2}) are equal. There are two ways to achieve equivalent stiffness values: (1) adjust θ_1 and θ_2 that are defined in Figure 3. This approach is best suited for applications wherein the chevrons are used as transmissions. (2) place N of the first chevrons in parallel so that their combined axial stiffness equals the lateral stiffness of the second chevron. The dotted lines in Figure 3 indicate where additional chevrons could be added. This approach is best used when the first chevron serves as a transmission and actuator. For example a TMA.

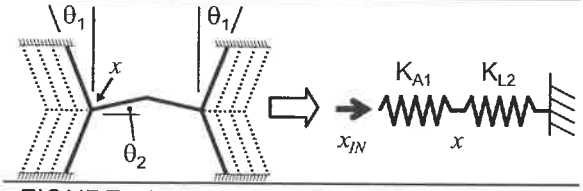

FIGURE 3: A two–spring model for the cascaded chevron mechanism.

The relationship between the side angles and number of chevrons is plotted in Figure 4.

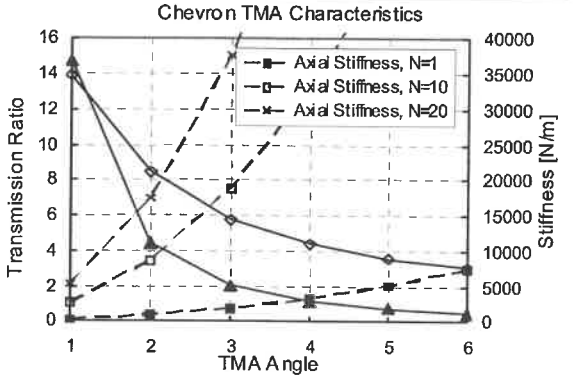

FIGURE 4: Transmission ratio, axial, lateral stiffness of a chevron mechanism as a function of angle. The axial stiffness may be increased by adding multiple chevron TMAs in parallel.

Cascaded chevron mechanism may be modeled as a two–spring system in Figure 3. The variable X_{IN} represents the displacement of a chevron TMA (first chevron mechanism), and X is the output displacement of the cascaded system. The relationship between X and X_{IN} is shown in Equation (1). The overall T_r of the cascaded mechanism is shown in Equation (2). The stroke of cascaded system is the product of the input displacement and the system's T_r, as shown in Equation (3).

$$X = \frac{1}{1 + K_{L2}(\theta_2)/K_{A1}(\theta_1)} \cdot X_{IN} \quad (1)$$

$$T_{TRANSMISSION} = T_{R1}(\theta_1) \cdot \left[\frac{1}{1 + K_{L2}(\theta_2)/K_{A1}(\theta_1)}\right] \cdot T_{R2}(\theta_2) \quad (2)$$

$$S_{STROKE} = T_{R1}(\theta_1) \cdot \left[\frac{1}{1 + K_{L2}(\theta_2)/K_{A1}(\theta_1)}\right] \cdot T_{R2}(\theta_2) \cdot X_{IN} \quad (3)$$

These equations replace intuition and iterative FEA as the common means of optimizing performance. This has been shown to yield a factor of 10X improvement [2-4] in the performance of cascaded chevrons.

Equation (2) was used to set a T_r as a function of θ_1 and θ_2. A plot of the optimal T_r for a given number of the TMAs was also obtained and the results are plotted in Figure 5.

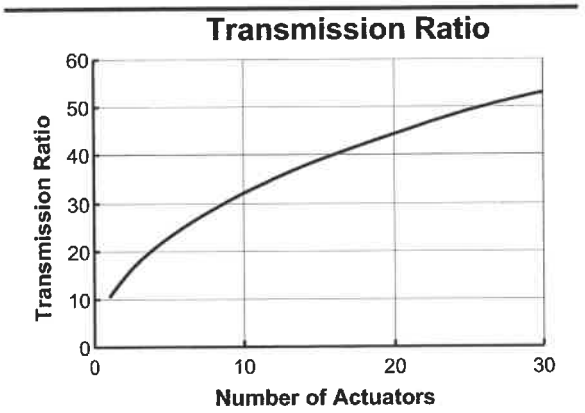

A

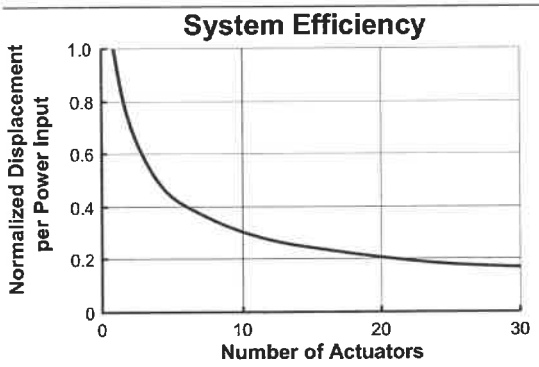

B

FIGURE 5: GRIN actuator performance as a function of design parameters.

Figure 5 shows that more parallel TMAs lead to a larger T_r. It would be tempting to simply increase the number of actuators bounded only by actuator footprint, but designers must understand that the preceding approach by itself only optimizes the mechanical characteristics of the chevrons. Unfortunately, there is a decrease in power efficiency with an increase in the number of actuators. This would point to a need to minimize the number of TMAs if the optimization objective is to minimize power consumption. In the case where chevrons are used as actuators, mechanical optimization must be accompanied by temperature and power optimization. Following is a general design approach that is applicable for different design/optimization objectives:

Step 1: Determine the required stroke (S) from functional requirements.
Step 2: Determine the required displacement (d) of an individual TMA.
Step 3: Determine the required optimal T_r by dividing the system stroke by the individual TMA's displacement ($T_r = S/d$).

Step 4: Obtain the corresponding values for θ_1 and θ_2 for the optimal T_r from the transmission equation.

Based on the preceding approach, the following demonstrates the procedures that were used to engineer the GRIN lens actuators for: (1) lowest temperature, and (2) minimum driving power. The design processes for the prism actuator is identical and will not be described.

Design for temperature minimization

The design process is: (1) determine the TMA's maximum operating temperature from functional requirements, *e.g.*, 150°C, (2) optimize the TMA's performance, *e.g.* stroke, at the specified temperature by the geometric contouring method [1], and (3) obtain the required number of TMAs and the relative optimal T_r from the surface plots that are shown in Figure 6. The surface plots were generated using Equation (2). The results are shown in Figure 6 and indicate that the optimal T_r increases as (i) the number of TMAs increases and (ii) the values of θ_1 and θ_2 decrease. Accordingly, the required stroke and temperature may be achieved by selecting N = 20 TMAs and θ_1 = 2.0° and θ_2 =2.0°, where the optimal T_r is 45.

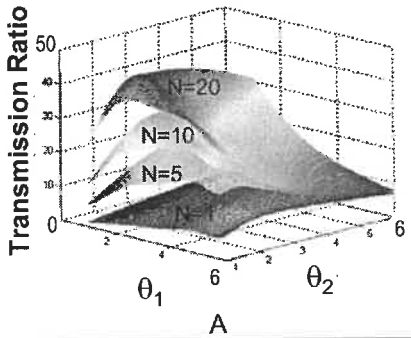

A

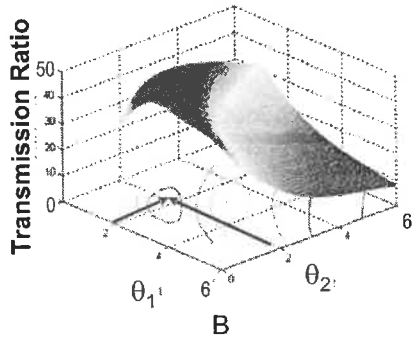

B

FIGURE 6: GRIN actuator performance

Design for power minimization

As TMAs operate more efficiently at high temperature, the required displacement is achieved when a large portion of a TMA's material operates at the highest safe operating temperature for silicon, *e.g.* 1200°K.

This example uses only two parallel TMAs to achieve a 100 µm output displacement with 125 mW power consumption, where the optimal T_r is 28, for θ_1 = 2.5°, and θ_2 =3.6°. Note N = 2 was selected so the required stroke may be achieved without exceeding 1200 °K. The T_r surface plots of the GRIN lens actuator design are presented in Fig 7. These surface plots were obtained using Equation (2). In the contour maps of Fig 7B, the flat region corresponds to the optimal angles of the T_r, therefore the optimal T_r is moderately insensitive to variations in θ_1 and θ_2.

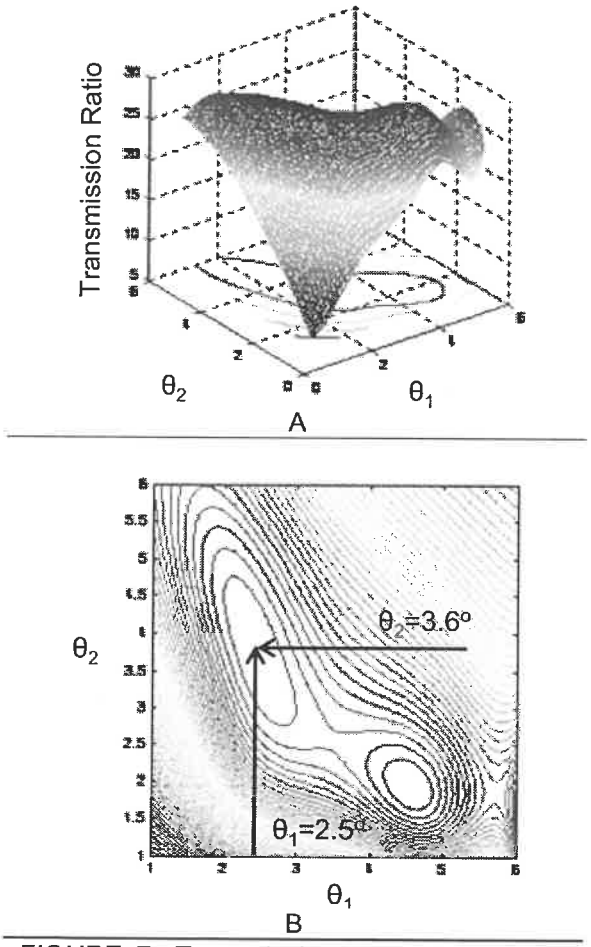

FIGURE 7: Transmission ratio of the GRIN lens actuator for a low power objective

The design parameters and simulated performance of the GRIN lens and prism actuators are summarized in Table 1.

TABLE 1. Design parameters and performance

GRIN		
	Temp Min.	Power Min.
T_r	45.1	28.1
θ_1	2.0°	2.5°
θ_2	2.0°	3.6°
Stroke	100 µm	100 µm
Power	700 mW	125 mW
Prism		
	Temp Min.	Power Min.
T_r	42.5	11.4
θ_1	2.0°	5.0°
θ_2	2.5°	5.5°
Stroke	2.0°	4.0°
Power	500 mW	50 mW

CONCLUSION

In this paper, we have presented a parametric model and the general design steps that may be used to design and optimize cascaded chevron flexures. These results enable designers to systematically obtain the optimal mechanical design for their applications. The results may be used within the overall optimization procedure of thermomechanical chevron actuators.

REFERENCES

[1] Chen, S and Culpepper, M L. Design of Contoured Microscale Thermomechanical Actuators. J. MEMS. 2006; 15(5): 1226-34.

[2] Park, J-S, Chu, L L, Oliver, A D and Gianchandani, Y B. Bent-beam electrothermal actuators—Part II: Linear and rotary microengines. J. of MEMS. 2001; 10(2): 255–262.

[3] Que, L, Park, J-S and Gianchandani, Y B. Bent-beam electrothermal actuators: I. Single beam and cascaded devices. J. of MEMS. 2001; 10: 247–54

[4] Hubbard, N B and Howell, L. Design and characterization of a dual-stage, thermally actuated nanopositioner. J. of Micromech. Microeng. 2005; 15: 1482-1493.

DESIGN AND FABRICATION OF A MICROROBOT MOVABLE IN HUMAN'S LARGE INTESTINE MODEL

Shigeo Kato[1], Manabu Ono[2], Yukiya Goto[1] and Toshiaki Hamano[1]
[1]Department of Systems Engineering
Nippon Institute of Technology
Miyashiro, Saitama 345-8501, Japan
[2]Department of Mechanical System Engineering
Tokyo Metropolitan College of Industrial Technology
Shinagawa, Tokyo 140-0011, Japan

INTRODUCTION

An inspection of the large intestine is very effective in order to prevent the large intestine cancer. A fiberscope is excellent for the inspection of the large intestine. However, the inspection by the fiberscope often attends many pains and injuring of the large intestine. We are hoping the inspecting method for the large intestine with no pain and no injuring of the large intestine before the operation by the fiberscope. Many microrobots that can move in the large intestine have been proposed by several research groups [1], [2]. However, the sure moving in the large intestine has not been confirmed, because the actual large intestine in our human body is flexible and has very severe bending curve at the sigmoid colon, the splenic flexure and heptatic flexure. Then the mobile moving in the large intestine is very difficult.

Now, we propose a new microrobot that can surely move in the large intestine in the human body. We need a holding work to the radius direction of the flexible large intestine and a driving work to longitudinal direction of the large intestine using the friction force by the holding of the large intestine, in order to move surely in the flexible and severely curved large intestine, for example, that is a sigmoid colon. We use seven rubber bellows in series. Two outer rubber bellows are supplied six bulging rubber sheets. These are called as the braking mechanism. The braking mechanism works as a brake of the microrobot. The second rubber bellows from the front rubber bellows is called a moving mechanism. The moving mechanism moves the microrobot by stretching and shrinking. Four rubber bellows are arranged after the moving mechanism in a matrix condition. These are called as the bending mechanism. The bending mechanism can bend the microrobot more than 100 degrees by its bending motion. The microrobot can pass the sigmoid colon. When the rubber bellows of the braking mechanism shrinks, six bulging rubber sheets spread to the radius direction and touch the large intestine. Then the spread bulging rubber sheets surely hold the large intestine. When the rubber bellows of the braking mechanism stretches, spreading to the radius direction of the six bulging rubber sheets and touching to the large intestine are canceled. In this condition, the microrobot can be inserted into the anus. The rubber bellows are stretched by pneumatic pressure and shrank by vacuum pressure. The stretching, shrinking and bending motion of the rubber bellows are controlled by a computer and electromagnetic valves.

The microrobot has been confirmed to move from the anus to the transverse colon through the sigmoid colon in the artificial human's large intestine model for the freshman doctor's inspection training using the fiberscope.

ARTIFICIAL HUMAN'S LARGE INTESTINE MODEL

An artificial human's large intestine model is shown in Figure 1. The numbers in the figure are the diameter of the large intestine model. The large intestine model is made of rubber. We see the anus downward of the figure. There exists the rectum following the anus. The sigmoid colon, the descending colon, transverse colon and the ascending colon follow the rectum. The cecum follows the colons. The large intestine consists of the rectum, the sigmoid colon, the descending colon, transverse colon, the ascending colon and the cecum.

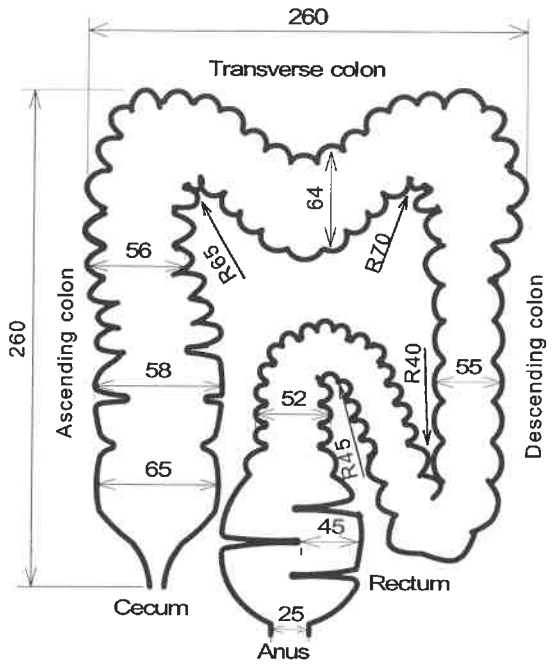

FIGURE 1. An artificial human's large intestine model.

STRUCTURE OF THE FABRICATED MICROROBOT

Structure of the fabricated microrobot is shown in Figure 2. The microrobot consists of two braking mechanisms, a driving mechanism and a bending mechanism. The two braking mechanisms and driving mechanism are driven by bellows which are 16 mm in outer diameter, 35 mm long and made of nytrile butyl rubber (NBR). The bending mechanism is driven by four bellows which are arranged as matrix and are 8 mm in outer diameter, 60 mm long and made of NBR. Each bellows is an independent vessel. Seven air feeding tubes that are 1.25 mm in outer diameter, 0.65 mm in inner diameter and 1 m long are connected to the two braking mechanisms, the moving mechanism and the bending mechanism. The bulging rubber sheets for two braking mechanisms are 7 mm wide, 2 mm thick, 36 mm long and made of NBR. The bulging rubber sheets are reinforced by plastic sheets. The rubber bellows are stretched by pneumatic pressure (positive pressure) and shrank by vacuum pressure (negative pressure). The stretching, shrinking and bending of the rubber bellows are controlled by a computer and electromagnetic valves.

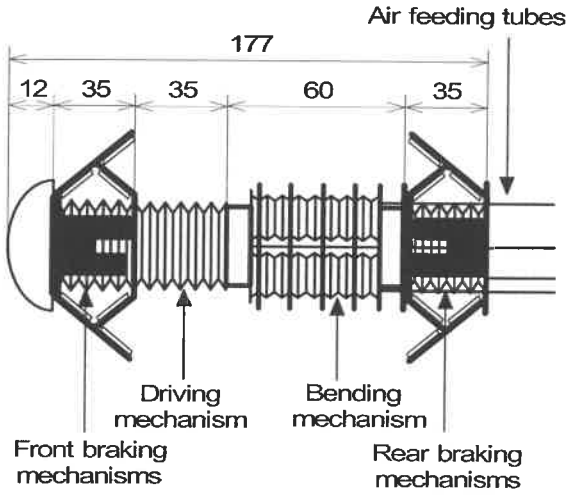

FIGURE 2. Structure of the fabricated microrobot.

EXPERIMENTAL APPARATUS

An experimental apparatus for measuring the characteristics of the microrobot is shown in Figure 3. A computer controls seven electromagnetic valves through a valve controller. Seven air feeding tubes are connected from the electromagnetic valves to the two braking mechanisms, the driving mechanism and the bending mechanism of the microrobot. An air compressor is connected to the entrance port of the electromagnetic valves and feeds the positive pressure in order to stretch the bellows. A vacuum pump is connected to the exit port of the electromagnetic valves and feeds the negative pressure in order to shrink the bellows.

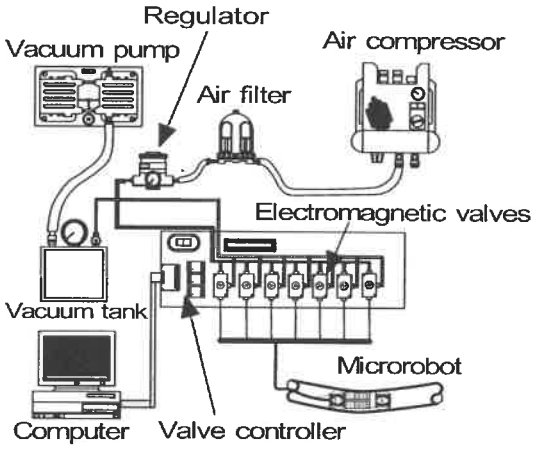

FIGURE 3. Experimental apparatus.

MOVING PRINCIPLE OF THE MICRORBOT AT THE SIGMOID COLON

The moving principle of the microrobot at the sigmoid colon is shown in Figure 4.

Step 1: At initial, all the bellows are shrinking by the negative pressure. The bulging sheets of the front and rear braking mechanisms are at the condition of the braking and hold the rectum.

Step 2: The positive pressure is supplied to the front braking mechanism and the braking is canceled.

Step 3: The positive pressure is supplied to the moving mechanism and the two outer bellows of the bending mechanism. The bending mechanism bends more than 100 degrees to inside direction, because the two outer bellows stretch. Then, the driving mechanism can move into the sigmoid colon.

Step 4: The negative pressure is supplied to the front braking mechanism. The front braking mechanism is in the condition of the braking and holds the sigmoid colon. At that time, the positive pressure is supplied to the rear braking mechanism and the braking is canceled.

Step 5: The negative pressure is supplied to the driving mechanism and the two outer bellows of the bending mechanism. The rear part of the microrobot can move to the front direction, because bellows of the driving mechanism and the two outer bellows of the bending mechanism shrink.

Step 6: The negative pressure is supplied to the rear braking mechanism. The rear braking mechanism is in the condition of the braking and holds the sigmoid colon. It is same as the initial condition and one cycle is over. The microrobot can pass the sigmoid colon and the splenic flexure by this series of the step.

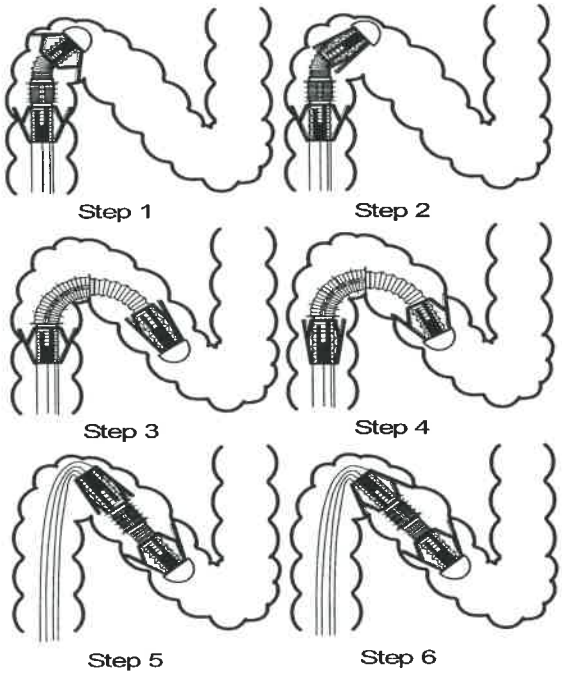

FIGURE 4. The moving principle of the microrobot at the sigmoid colon.

EXPERIMENT

Bending characteristics of the bending mechanism

Characteristics of the bending mechanism are measured. Different pressures are supplied to the outer and the inner bellows. The relationship between the difference of pressure and the bending angle is shown in Figure 5. The bending angle is confirmed to be same, if the difference of pressure is positive or negative.

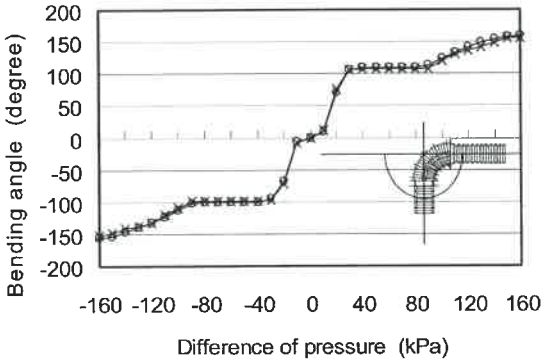

FIGURE 5. The relationship between the difference of pressure and the bending angle.

The bending angle of 110 degrees is obtained at the difference of pressure is 30kPa. The relationship between the feeding time of the difference of pressure and the bending angle is shown in Figure 6. The bending action is confirmed to be done at about 1 second.

Diameter of the bulging braking sheet

The relationship between the pressure in the braking mechanism and the diameter of the bulging braking sheet is shown in Figure 7. The diameter of the bulging sheet is less than 25 mm at the pressure more than 20 kPa. Then, the braking mechanism can pass the anus, because the diameter of the anus is 25 mm.

Moving experiment

Silicon oil is splayed inner wall of the large intestine model. The microrobot is inserted into the anus of the large intestine model. The microrobot can move to the hepatic flexure through the rectum, the sigmoid colon, the descending colon and the transverse colon.

CONCLUSION

(1) We fabricated a new microrobot that can move in an artificial human's large intestine model for the freshman doctor's inspection training using the fiberscope. The microrobot consists of two braking mechanism, a moving mechanism and a bending mechanism. The braking mechanism has a bulging brake which consists of six bulging rubber sheets.

(2) We confirmed by the experiment that the fabricated microrobot can move to the hepatic flexure through the rectum, the sigmoid colon, the descending colon and the transverse colon

(3) This microrobot may be used to the inspection mobile microrobot for the human's large intestine, because the artificial human's large intestine model is very similar to the human's large intestine.

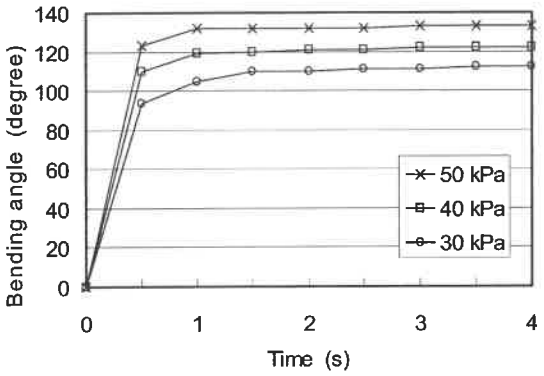

FIGURE 6. The relationship between the feeding time of the difference of pressure and the bending angle.

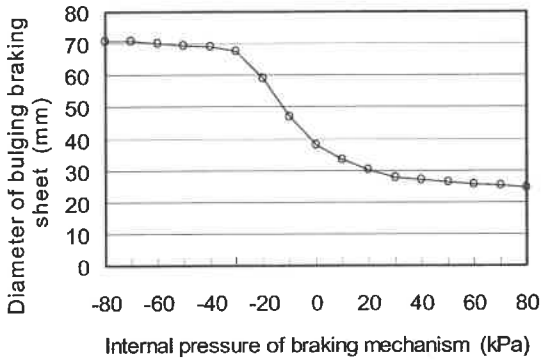

FIGURE 7. The relationship between the pressure in the braking mechanism and the diameter of the bulging braking sheet.

REFERENCES

[1] L. Phee, C. Stefanini, A. Arena, D. Accoto, A. Menciassi, G. Pernorio, M. Boccadore, P. Dario: "Mechanical Clamping Mechanism for Locomotion in the Gastrointestinal Tract", Proceedings of the 2nd International Conference of EUSPEN, pp. 770- 773.

[2] M. Ono, E. Arakawa, S. Kyoumine, S. Kato: " Fabrication of a Microrobot Movable in a Freely Held Pig's Small Intestine", Proceedings of the 2nd International Conference of EUSPEN, pp. 806- 809.

COMPARISONS OF ANCHOR DESIGNS FOR MEMS RESONANT MASS SENSORS

Chengzhang Li and Michele H. Miller
Department of Mechanical Engineering-Engineering Mechanics
Michigan Technological University
Houghton, Michigan, USA

ABSTRACT

The anchor design for resonant mass sensor cantilevers has an important effect on structural dynamic behavior. We investigated five anchor designs and determined their effect on static deflection as well as resonant frequency. The first two designs are the simplest and most commonly used. The third and fourth designs, observed in the literature, add material to the anchor pillar by encapsulating sacrificial material. The fifth design, one of our own, adds two "feet" that extend alongside the cantilever. Static deflection under an applied uniform pressure was predicted using finite element analysis. Resonant frequencies for the first several vibration modes were also predicted. The results suggest that the anchor rigidity has a significant effect on static deflection. The most effective design had a static deflection approximately one half of that for the simplest design. The effect on resonant frequency is slightly more modest but still significant.

INTRODUCTION

A MEMS resonant mass sensor consists of a micromachined cantilever beam coated with a substance that binds to a chemical vapor of interest. Binding to the cantilever increases its mass and reduces its natural frequency. Detection of resonant frequency change has proven to be a highly sensitive approach to chemical vapor sensing. The cantilevers can be fabricated in an array, and the coatings varied to improve reliability and selectivity. Sensitivity improves as stiffness increases, mass decreases, and damping decreases. Our goal is to develop optimal cantilever designs that lead to an order-of-magnitude improvement in sensitivity.

A micromechanical anchor is the support structure that joins the microstructure with the substrate. Because the anchor is typically made up of one film layer, its rigidity is very low. However, when modeled, the anchor is usually assumed to be a fixed boundary condition. As a result, micromechanical device performance may differ significantly from model prediction.

Several variations on anchor design have been previously analyzed and tested [1,2]. Available fabrication processes limit the number of possible designs. In this paper we propose a new anchor design and compare its performance to previously studied anchor designs.

ANCHOR GEOMETRIES

Figure 1 illustrates three types of anchor structures that have been used for cantilevers. Geometry A would be created by depositing polysilicon over a sacrificial layer (located in the space below the cantilever) and then etching away polysilicon beyond the fixed end and free end of the cantilever. Finally, the sacrificial layer under the cantilever would be etched away. Geometry B is created with the same process except the etch boundary near the fixed end of the polysilicon is moved farther to the left.

Geometry C has a thicker anchor structure. It could be created by depositing material of the sacrificial layer in the anchor region (as well as under the cantilever) and then encapsulating it with polysilicon. The conformal deposition of polysilicon leaves a small dimple. As in the first two designs, the polysilicon is etched to its final geometry. The exposed sacrificial material under the cantilever is then removed while the encapsulated sacrificial material remains.

Figures 2-5 show the meshes for the three anchor designs introduced in Figure 1. Note that geometry C has two versions. All cantilevers are 100 μm long, 10 μm wide and 3 μm thick.

Diameter of the bulging braking sheet

The relationship between the pressure in the braking mechanism and the diameter of the bulging braking sheet is shown in Figure 7. The diameter of the bulging sheet is less than 25 mm at the pressure more than 20 kPa. Then, the braking mechanism can pass the anus, because the diameter of the anus is 25 mm.

Moving experiment

Silicon oil is splayed inner wall of the large intestine model. The microrobot is inserted into the anus of the large intestine model. The microrobot can move to the hepatic flexure through the rectum, the sigmoid colon, the descending colon and the transverse colon.

CONCLUSION

(1) We fabricated a new microrobot that can move in an artificial human's large intestine model for the freshman doctor's inspection training using the fiberscope. The microrobot consists of two braking mechanism, a moving mechanism and a bending mechanism. The braking mechanism has a bulging brake which consists of six bulging rubber sheets.

(2) We confirmed by the experiment that the fabricated microrobot can move to the hepatic flexure through the rectum, the sigmoid colon, the descending colon and the transverse colon

(3) This microrobot may be used to the inspection mobile microrobot for the human's large intestine, because the artificial human's large intestine model is very similar to the human's large intestine.

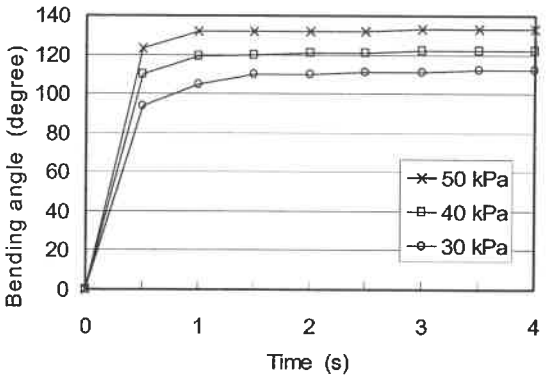

FIGURE 6. The relationship between the feeding time of the difference of pressure and the bending angle.

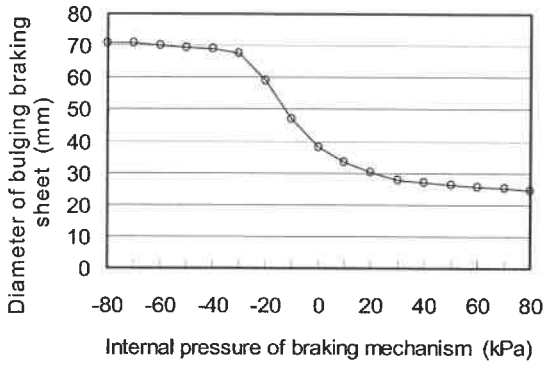

FIGURE 7. The relationship between the pressure in the braking mechanism and the diameter of the bulging braking sheet.

REFERENCES

[1] L. Phee, C. Stefanini, A. Arena, D. Accoto, A. Menciassi, G. Pernorio, M. Boccadore, P. Dario: "Mechanical Clamping Mechanism for Locomotion in the Gastrointestinal Tract", Proceedings of the 2nd International Conference of EUSPEN, pp. 770- 773.

[2] M. Ono, E. Arakawa, S. Kyoumine, S. Kato: " Fabrication of a Microrobot Movable in a Freely Held Pig's Small Intestine", Proceedings of the 2nd International Conference of EUSPEN, pp. 806- 809.

COMPARISONS OF ANCHOR DESIGNS FOR MEMS RESONANT MASS SENSORS

Chengzhang Li and Michele H. Miller
Department of Mechanical Engineering-Engineering Mechanics
Michigan Technological University
Houghton, Michigan, USA

ABSTRACT

The anchor design for resonant mass sensor cantilevers has an important effect on structural dynamic behavior. We investigated five anchor designs and determined their effect on static deflection as well as resonant frequency. The first two designs are the simplest and most commonly used. The third and fourth designs, observed in the literature, add material to the anchor pillar by encapsulating sacrificial material. The fifth design, one of our own, adds two "feet" that extend alongside the cantilever. Static deflection under an applied uniform pressure was predicted using finite element analysis. Resonant frequencies for the first several vibration modes were also predicted. The results suggest that the anchor rigidity has a significant effect on static deflection. The most effective design had a static deflection approximately one half of that for the simplest design. The effect on resonant frequency is slightly more modest but still significant.

INTRODUCTION

A MEMS resonant mass sensor consists of a micromachined cantilever beam coated with a substance that binds to a chemical vapor of interest. Binding to the cantilever increases its mass and reduces its natural frequency. Detection of resonant frequency change has proven to be a highly sensitive approach to chemical vapor sensing. The cantilevers can be fabricated in an array, and the coatings varied to improve reliability and selectivity. Sensitivity improves as stiffness increases, mass decreases, and damping decreases. Our goal is to develop optimal cantilever designs that lead to an order-of-magnitude improvement in sensitivity.

A micromechanical anchor is the support structure that joins the microstructure with the substrate. Because the anchor is typically made up of one film layer, its rigidity is very low. However, when modeled, the anchor is usually assumed to be a fixed boundary condition. As a result, micromechanical device performance may differ significantly from model prediction.

Several variations on anchor design have been previously analyzed and tested [1,2]. Available fabrication processes limit the number of possible designs. In this paper we propose a new anchor design and compare its performance to previously studied anchor designs.

ANCHOR GEOMETRIES

Figure 1 illustrates three types of anchor structures that have been used for cantilevers. Geometry A would be created by depositing polysilicon over a sacrificial layer (located in the space below the cantilever) and then etching away polysilicon beyond the fixed end and free end of the cantilever. Finally, the sacrificial layer under the cantilever would be etched away. Geometry B is created with the same process except the etch boundary near the fixed end of the polysilicon is moved farther to the left.

Geometry C has a thicker anchor structure. It could be created by depositing material of the sacrificial layer in the anchor region (as well as under the cantilever) and then encapsulating it with polysilicon. The conformal deposition of polysilicon leaves a small dimple. As in the first two designs, the polysilicon is etched to its final geometry. The exposed sacrificial material under the cantilever is then removed while the encapsulated sacrificial material remains.

Figures 2-5 show the meshes for the three anchor designs introduced in Figure 1. Note that geometry C has two versions. All cantilevers are 100 μm long, 10 μm wide and 3 μm thick.

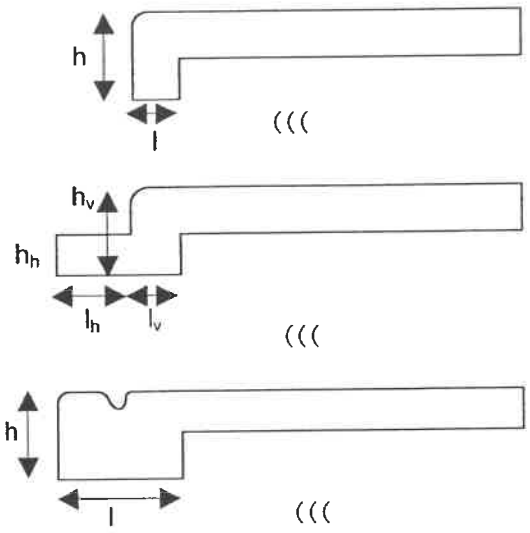

FIGURE 1. Three anchor designs observed in the literature.

A new anchor geometry is proposed as shown in Figure 6. The design is similar to C2 with the addition of two feet to the sides of the cantilever. Like geometries C1 and C2, the thick anchor structure could be created by encapsulating material from the sacrificial layer.

Finite element analysis of these five designs (A, B, C1, C2, and D) was carried out using ANSYS software. Solid, triangular elements were used. The software automatically chose the appropriate mesh unit size. Shell elements could not be used because the section thickness of the structure is not uniform. Instead we chose the element type of solid 45 for its accuracy. The following properties of polysilicon were assumed: Young's modulus = 130 GPa, Poisson's ratio = 0.278, and density =2330 kg/m^3.

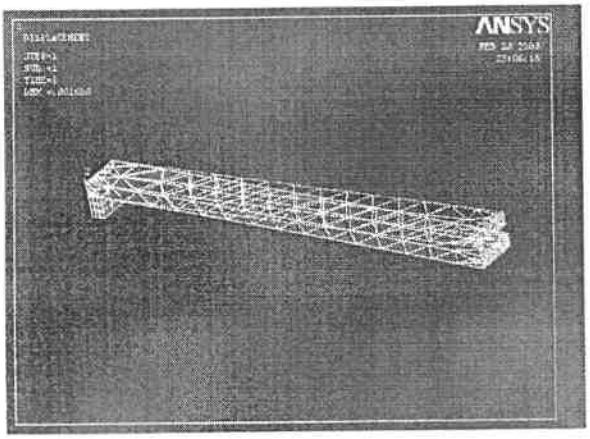

FIGURE 2. Mesh for geometry A; anchor width w is 10 μm, length l is 3, and height h is 8 μm.

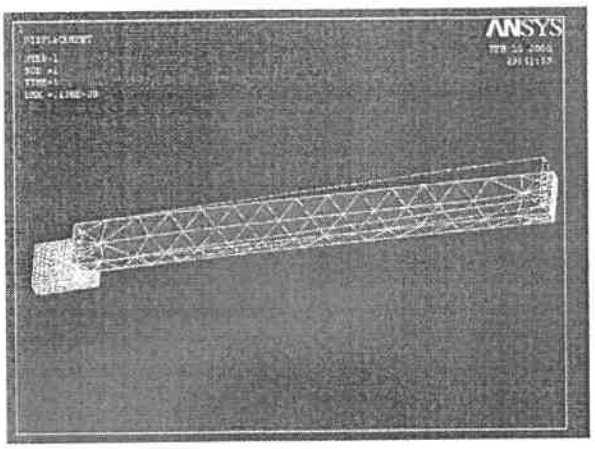

FIGURE 3. Mesh for Geometry B; w = 10 μm; vertical part of anchor has length l_v of 3 μm and height h_v of 8 μm; horizontal part of anchor has length l_h of 20 μm and height h_h of 3 μm.

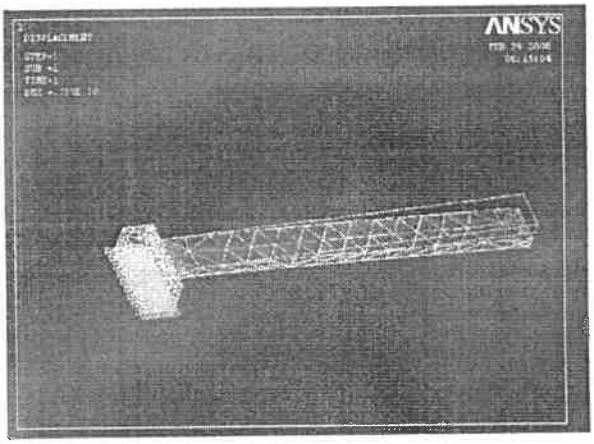

FIGURE 4. Mesh for Geometry C version 1; w = 20 μm, l = 8 μm and h = 8 μm.

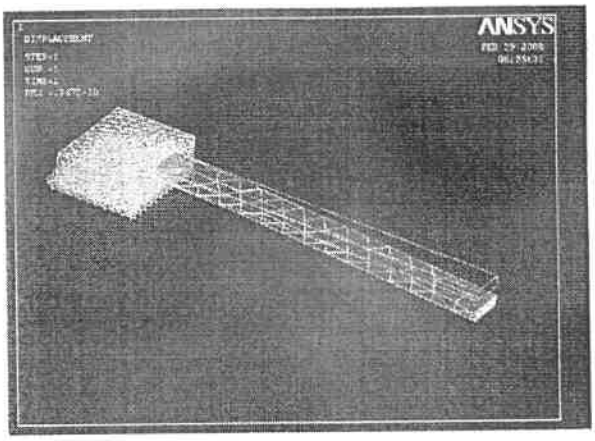

FIGURE 5. Mesh for Geometry C, version 2; w = 30 μm, l = 23 μm and h = 8 μm.

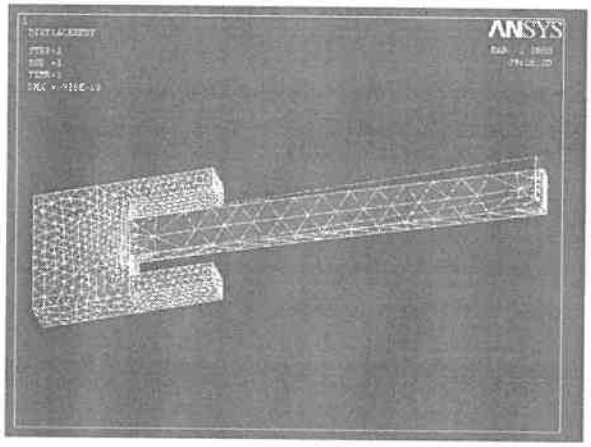

FIGURE 6. Mesh for new geometry D; large rectangular part of anchor is 23 μm long, 30 μm wide and 8 μm tall; each foot is 20 μm long, 5 μm wide and 8 μm tall.

SIMULATION RESULTS

Static displacement and resonant frequencies were determined for each of the five designs. Note that all five designs have the same cantilever dimensions.

Displacement

A uniform pressure of 1000 Pa was applied to the top of the cantilever and the tip displacement was calculated. Table 1 summarizes the tip displacements for the five designs.

TABLE 1. Maximum displacement due to applied pressure of 1000 Pa.

Design	Displacement, nm
A	15.0
B	13.7
C1	7.54
C2	7.47
D	7.16

The results clearly show the dramatic effect that anchor design has on rigidity. Anchor B has higher rigidity than anchor A because its pillar area is larger. Design C1 produces a significant improvement over designs A and B. The larger pillar area of C2 produces negligible improvement over C1. The rigidity of the new design D is slightly better than the two C designs.

Resonant Frequency

The finite element models were then used to predict the resonant frequencies of the first several vibration modes for each of the cantilever designs. Figures 7-10 illustrate four vibration modes for design D.

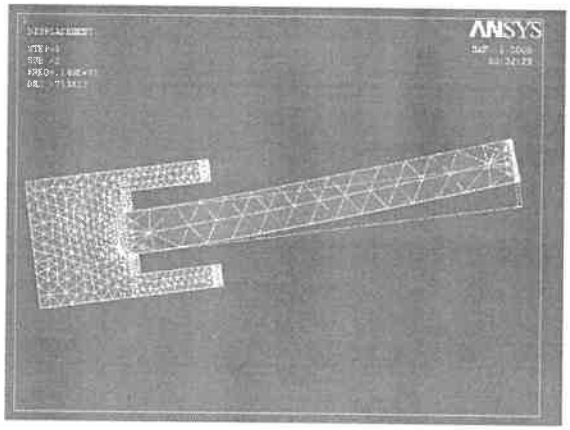

FIGURE 7. Second vibration mode of design D.

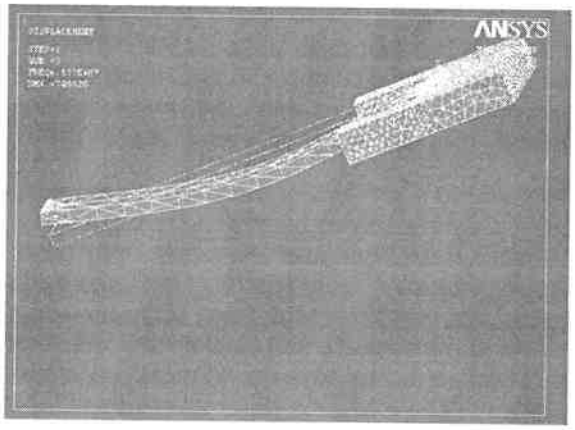

FIGURE 8. Third vibration mode of design D.

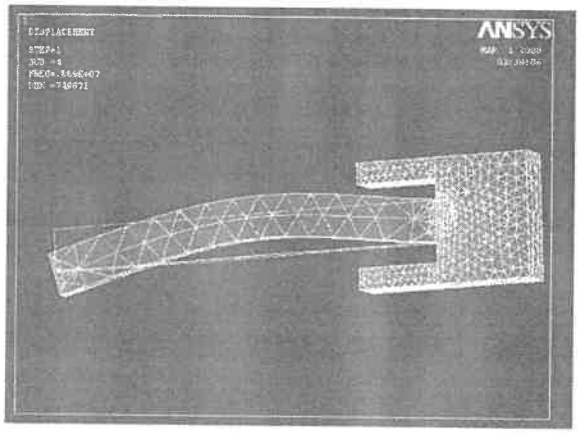

FIGURE 9. Fourth vibration mode of design D.

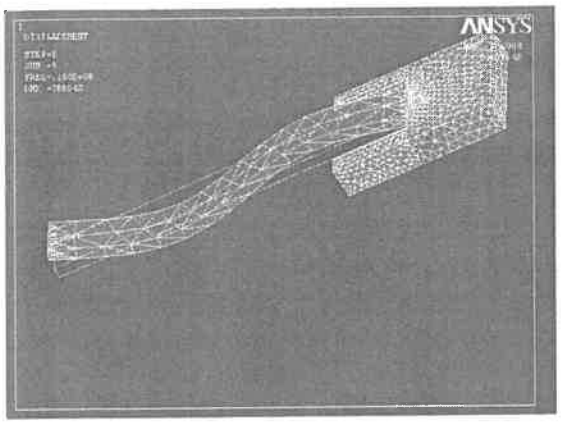

FIGURE 10. Fifth vibration mode of design D.

Figure 11 shows the frequency response function for design D. The first four resonant peaks are at approximately 0.8 MHz, 1.5 MHz (damped and not visible), 5.8 MHz, and 8.9 MHz (barely visible).

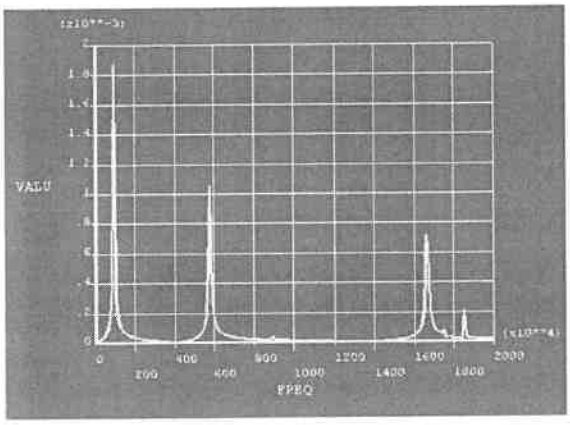

FIGURE 11. Frequency response for design D.

Figure 12 compares the resonant frequencies of the first four modes for the five designs. The resonant frequencies are noticeably higher for the last three designs, as expected from the static deflection results. Keep in mind that the actual devices will behave somewhat differently as this simulation did not take damping into consideration.

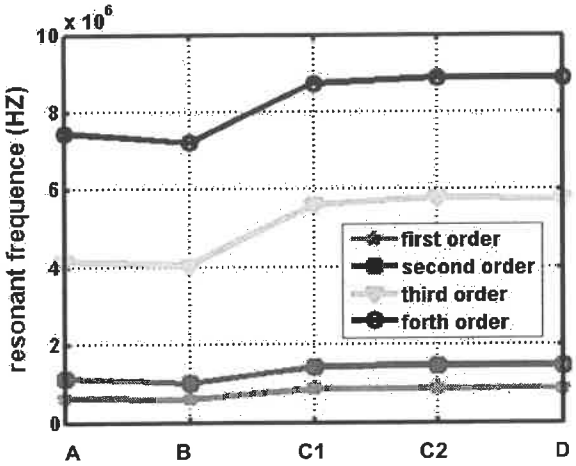

FIGURE 12. Comparison of resonant frequencies for the five anchor designs.

CONCLUSIONS

High stiffness and resonant frequency are desirable for many MEMS devices including resonant mass sensors. During the design process, the anchor is often assumed to be perfectly rigid, and this leads to inaccurate predictions of device performance. With finite element analysis of five designs we have shown that anchor design has a significant effect on static displacement. The most effective design had a static displacement of approximately one half of that for the simplest design. The effect on resonant frequency is slightly more modest but still significant. One way to produce the larger, thicker anchors that give the best performance is to encapsulate material from the sacrificial layer.

ACKNOWLEDGMENTS

This work was supported in part by the State of Michigan 21st Century Jobs Fund project number 06-1-P1-0283.

REFERENCES

[1] Lishchynska, M., N. Cordero and O. Slattery, "State of the Art in Prediction of Mechanical Behaviour of Microsystems," 5th. Int. Conf. on Thermal and Mechanical Simulation and Experiments in Micro-electronics and Micro-Systems, EuroSimE2004, pp. 287-293.

[2] Gill, J. J.-Y., L. V. Ngo, P. R. Nelson and C.-J. Kim. "Elimination of Extra Spring Effect at the Step-Up Anchor of Surface-Micromachined Structure," *Journal of Microelectromechanical Systems*, Vol.7, No.1, March 1998, pp. 114-121.

INVESTIGATION OF AIR DAMPING AND Q IN A MEMS RESONANT MASS SENSOR

Chengzhang Li, Michele H. Miller
Department of Mechanical Engineering-Engineering Mechanics
Michigan Technological University
Houghton, Michigan, USA

INTRODUCTION

For a resonant mass sensor, one definition of sensitivity is the ratio of resonant frequency change to mass change. This is not the complete story, however, as the change in resonant frequency needs to be detectable. Thus, the resonator's Q factor (which is inversely related to damping ratio) is an important characteristic of the resonator. A low Q factor corresponds to a broad resonance peak whose exact peak frequency is more uncertain.

Several approaches have been taken to compensate for the deleterious effect of air damping. Resonators packaged in near-vacuum have significantly higher Q factors than those operating at atmospheric pressure. A commercially available liquid density meter solves the problem of damping by using a U shaped hollow cantilever through which the liquid under test flows [1]. In this way, the resonator has the benefit of being surrounded by a vacuum environment while its resonant frequency is still influenced by the density (mass) of the liquid inside it. Another approach to reducing air damping is to put holes in the cantilever. Still another approach is to make the gap between the cantilever and surrounding surfaces large. In this paper we investigate the interactions between air pressure, gap, cantilever geometry, and Q factor.

DAMPING MECHANISMS

Microcantilevers can be influenced by various damping mechanisms, including internal friction, energy loss in support structures or coatings, molecular damping, airflow damping, and squeeze film damping [2]. This paper focuses on vibration-airflow damping and squeeze film damping.

Airflow damping results from vibration of the cantilever in air; it can be modeled using hydrokinetics [2]. The presence of a thin gap below the cantilever increases the amount of damping considerably. When the cantilever moves, it squeezes the gap and the gas flows out from its edges. The narrow pathway restricts the flow causing the gas pressure to increase and the plates to decelerate. Air damping is described by the Reynolds equation [3]:

$$\frac{\partial P}{\partial x}\left(\rho\frac{h^3}{\mu}\frac{\partial P}{\partial x}\right)+\frac{\partial P}{\partial y}\left(\rho\frac{h^3}{\mu}\frac{\partial P}{\partial y}\right)=12\frac{\partial(\rho h)}{\partial t} \quad (1)$$

where P is the air pressure (and a function of the lateral coordinates x and y), ρ is the air density; μ is the air viscosity, and h is the gap (which changes as the cantilever moves up and down). Many approximations for the effective air viscosity based on Knudsen number have been proposed. Squeeze film damping becomes the dominant form of damping when the air gap is much smaller than the width of the cantilever.

SIMULATION GEOMETRY

Figure 1 illustrates a micromechanical cantilever surrounded by air. The cantilever in our simulation is made of silicon and is 300 μm × 30 μm × 3 μm with a gap of 4 μm. The applied load is a uniform pressure to the top surface of the cantilever.

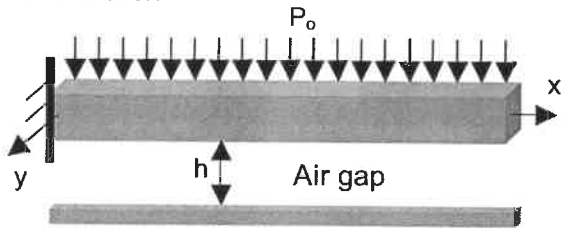

FIGURE 1. Microcantilever geometry.

HOMOGENEOUS CANTILEVERS

Simulations were performed for solid cantilevers by applying a pressure load and recording the time response. Both step and sinusoidal loads were applied. Variables of interest were the applied load, air pressure, and gap size.

Effect of Applied Load

The first type of simulation is a step response to an applied load. The air pressure surrounding

the cantilever was set to 300 Pa. Figure 2 shows the step response for applied loads ranging from 50 Pa to 400 Pa. Note that the oscillations are slowly decreasing in amplitude and that the steady-state displacement will be proportional to applied load.

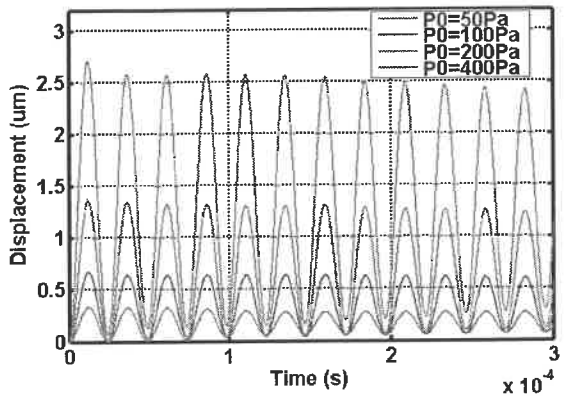

FIGURE 2. Step responses to four different applied loads.

Effect of Air Pressure

Next, the applied pressure was kept constant, and the surrounding air pressure was varied. Figure 3 shows the step response for air pressures ranging from 150 Pa (0.0015 atm or 1.1 Torr) to 9600 Pa (0.095 atm or 72 Torr).

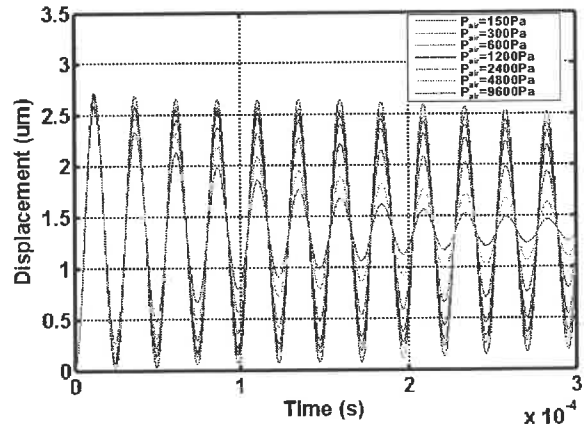

FIGURE 3. Step responses in different air pressures

The damping coefficient and quality factor (Q) can be extracted from the step responses. For a second order system, the damping ratio can be found from the logarithmic decrement between the 1st and *m*th peak of the step response as follows:

$$\zeta = \frac{1}{2\pi m} \ln\left(\frac{x_1}{x_{m+1}}\right) \qquad (2)$$

where x is the height of a peak in the sinusoidal response. The quality factor is related to the damping ratio according to:

$$Q \simeq \frac{1}{2\zeta} \qquad (3)$$

Q values were found for the underdamped responses in Figure 3. The results are plotted in Figure 4.

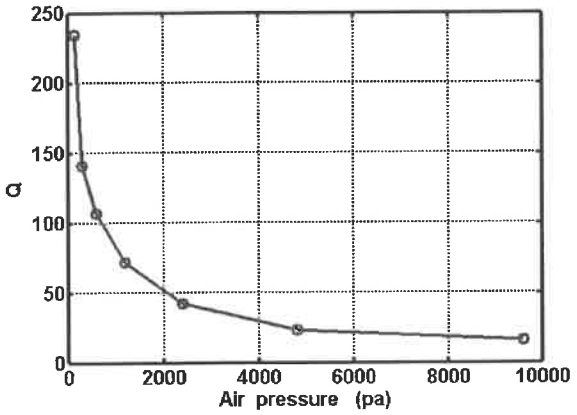

FIGURE 4. Q factors at different air pressures.

Effect of Gap Size

The effect of gap size was investigated by holding the applied pressure and surrounding air pressure constant while testing different gap sizes. Figure 5 shows the step responses for an applied pressure of 400 Pa, an air pressure of 300 Pa, and gap sizes ranging from 1 μm to 8 μm.

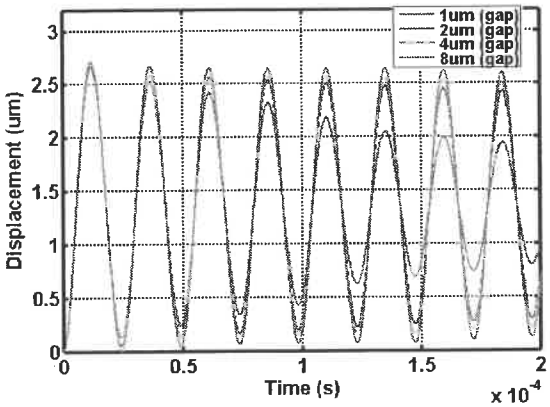

FIGURE 5. Step responses with different gap sizes.

Again, the step responses were used to estimate Q factors. Figure 6 shows that gap has a strong effect on Q factor.

The frequency response for the microcantilevers can be found using the brute force approach of applying a sinusoidal pressure, recording the

amplitude of the time response, and forming the ratio of dynamic output amplitude over static deflection. Figure 7 shows an example of the time response to a sinusoidal input of applied pressure ranging from +5 Pa to -5 Pa. The air pressure was 300 Pa. The steady-state has not been reached for the 2, 4 and 8 μm gap cases in the amount of time shown. For the 8 μm gap case, the steady-state is reached after 2.2 x 10^{-3} seconds with an amplitude of 3.18 μm.

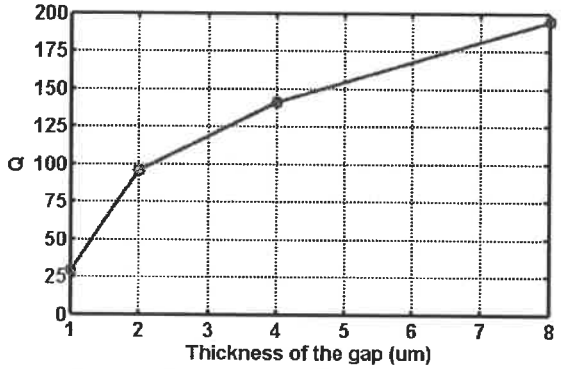

FIGURE 6. Q factors for different air gaps.

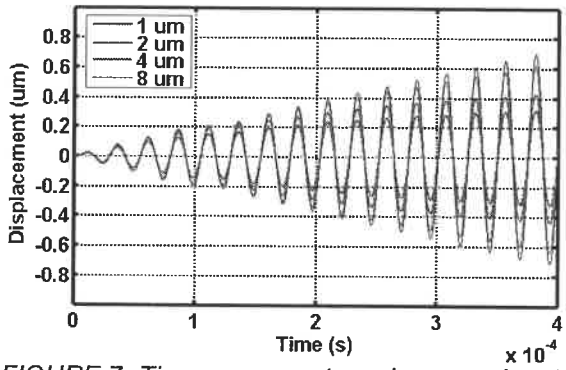

FIGURE 7. Time response to a sine wave input.

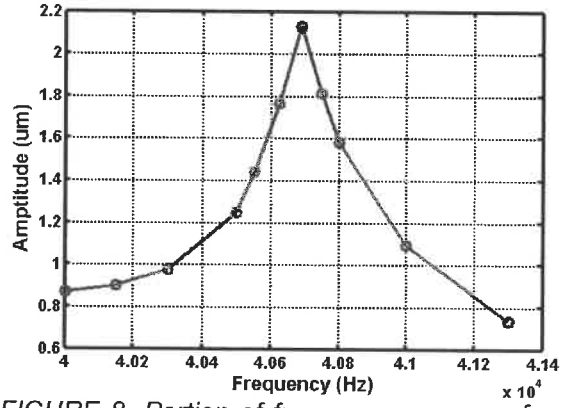

FIGURE 8. Portion of frequency response for 4 μm gap case.

The frequency response provides another way to obtain Q. Figure 8 shows a portion of the frequency response for the 4 μm gap case, focusing on the frequencies near resonance. If we divide the frequency where the largest amplitude is achieved by the difference between the two frequencies where $1/\sqrt{2}$ of the largest amplitude is achieved, we get the value of Q=150. This is close to the Q of 141 shown in Figure 6 for the 4 μm case. Keep in mind that the system is not an ideal second order system.

CANTILEVERS WITH HOLES

Silicon plates perforated with small holes are becoming popular for micromechanical transducers and actuators. In addition to providing access for etch chemicals, the holes reduce squeeze film damping. The holes make modeling more complicated, requiring that the Reynolds' equation (Equation 1) be modified by adding a term that represents the damping effect of air-flow in the holes.

Effect of Number of Holes

Using finite elements we tested three kinds of hole structures for their effect on damping. The "large hole" cantilever has three holes; the "medium hole" cantilever has 12 holes; and the "small hole" cantilever has 48 holes. The outside cantilever dimensions remain the same as before. All three cantilevers have the same total hole area of 3000 μm^2. In all cases, the applied pressure was 400 Pa, the surrounding air pressure was 300 Pa, and the gap was 4 μm. Figures 9 and 10 show the large and medium hole cantilevers deflected under a static applied load.

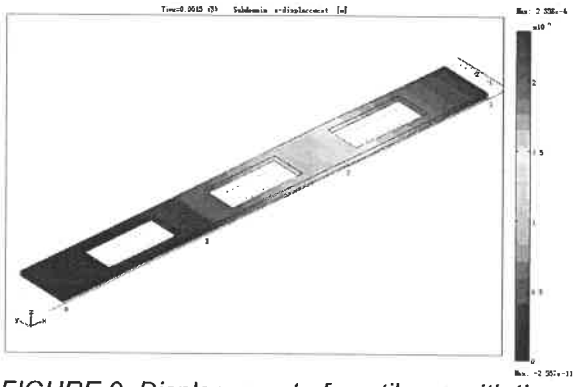

FIGURE 9. Displacement of cantilever with three large holes (20 μm x 50 μm each).

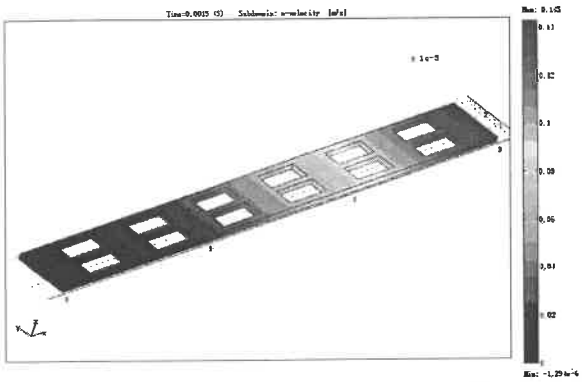

FIGURE 10. Displacement of cantilever with 12 medium holes (10 μm x 25 μm each).

Figure 11 shows the step responses for the three types of cantilevers. The large holed cantilever has the most damping: although the initial amplitude is large, the exponential decay is fastest. Based on the step responses, Q factors for the large, medium, and small holes are: 110, 271, and 168, respectively. These compare with a Q of 141 for no holes. These results are somewhat unexpected and indicate the complexity of the phenomenon. Because energy is lost at the edges of the holes, the case of many small holes (with large total perimeter length) was expected to produce the most damping. However, adding holes changes the area moment of inertia and makes it vary along the length of the cantilever. While the hole area is the same for the three beams, they have different stiffnesses. Q will be affected by both damping and stiffness. Also, it appears as if the location of the holes is important. Making the hole areas coincide with the largest cantilever motions would seem to reduce damping. More investigation is needed to sort out the various effects.

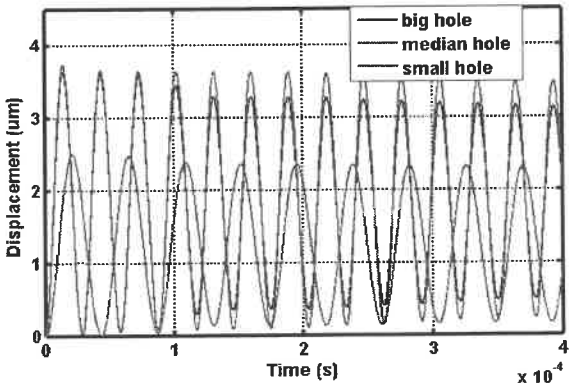

FIGURE 11. Step response of cantilevers with different numbers of holes (same total hole area).

Effect of Total Hole Area

Additional simulations were run using the 12 hole design but varying the individual hole area from 0 to 250 μm^2. Figure 12 shows the Q factors that were determined from the step responses. The Q factor steadily increases with hole area.

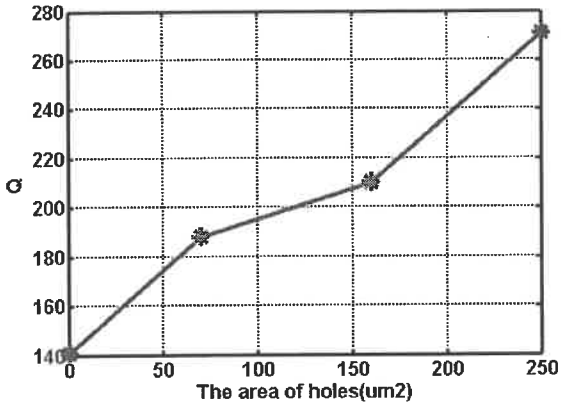

FIGURE 12. Effect of hole size on Q factor.

CONCLUSION

Squeeze film damping can have a deleterious effect on resonator device performance. This paper has shown how air pressure, gap, and holes in the cantilever affect the resonator's Q factor. When it is impractical to package a resonating device in vacuum, gap size and hole size and placement may be designed to improve performance. There will be limits to increasing the gap and increasing the hole area. Both would increase the actuation voltage in an electrostatically actuated device. Also, greater hole area reduces the surface area available for binding to chemicals of interest.

ACKNOWLEDGMENTS

This work was supported in part by the State of Michigan 21st Century Jobs Fund project number 06-1-P1-0283.

REFERENCES

[1] Zhang, Y., S. Tadigadapa and N. Najafi, "A Micromachined Coriolis-Force-Based Mass Flowmeter for Direct Mass Flow and Fluid Density Measurement," *Proceedings of Transducers '01, Eurosensors XV*, Munich, Germany, 2001.

[2] Hosaka H, K. Itao, S. Kuroda, "Damping characteristics of beam-shaped micro-oscillators," *Sensors and Actuators A*, Vol. 49, 1995, pp. 87-95.

[3] M. Bao, H. Yang, Y. Sun, and P. J. French. "Modified Reynolds' equation and analytical analysis of squeeze-film air damping of perforated structures," *J. Micromech. Microeng.*, Vol. 13, 2008, pp. 795-800.

NANOMETER-SCALE ULTRASONIC CUTTER USING AN ATOMIC FORCE MICROSCOPE CONTROLLED BY A HAPTIC DEVICE

Futoshi IWATA[1], Kouhei OHARA[1], Shinsuke KAWANISHI[1], Hisayuki AOYAMA[2] and Tatsuo USHIKI[3]

[1]Department of Mechanical Engineering, Faculty of Engineering, Shizuoka University, Hamamatsu, Shizuoka, Japan

[2]Department of Mechanical Engineering and Intelligent Systems, University of Electro-Communications, Chofu, Tokyo, Japan

[3]Division of Microscopic Anatomy, Graduate School of Medical and Dental Scinences, Niigata University, Niigata, Japan

INTRODUCTION

Scanning probe microscopes (SPMs) are well known as surface imaging tools at nanometer-scale resolution. SPMs can be used not only for surface observation but also for local surface fabrication. The typical fabrication technique using an SPM is to directly scratch on surfaces with the probe. The contact between the probe and the surface can be maintained at a constant force, thus allowing reliable fabrication by scratching on the surface.[1-7] However, some polymeric materials and biological samples exhibit complicated scratched behavior, such as bundle formation, due to the sliding interaction between the AFM probe and the viscoelastic surfaces,[6,7] making it difficult to cut the polymer surfaces smoothly for nanometer-scale fabrication. Furthermore, it is challenging to control the surface cutting in the case of inhomogeneous materials such as polymer blends and biological samples, due to their inhomogeneous stiffness. As a result, other force feedback techniques are needed to realize flexible control of scratching forces.

In the realm of force feedback control, haptic technology refers to technology that supplies an interface between the operator and the machine via the operator's sense of touch while applying forces. By combining ultrasonic scratching with haptic technology, we hope to develop a nanometer-scale ultrasonic cutter that will be a very effective tool in the fields of nanometer-scale engineering, biology and anatomy.

In this paper, we describe a nanometer-scale fabrication technique for use on surfaces based on ultrasonic oscillation scratching to realize smooth cutting of viscoelastic materials such as polymers and biological samples. The AFM fabrication technique was coupled with a haptic device consisting of a pen type handle. By handling the pen of the device, operator can directly move the AFM probe to scratch the surface for nano fabrication with fine human sensomobility. The cutting properties of polymer and biological sample are discussed in comparison with conventional scratching in contact mode.

EXPERIMENTAL PROCEDURE

Ultrasonic Scratching

Figure 1 is a drawing of the AT-cut quartz crystal resonator (QCR) used as a sample substrate for the ultrasonic cutting fabrication. The direction of the crystal oscillation depends on the crystallographic orientation. The AT-cut QCR provided mechanical shear oscillation. The shear deformations of the QCR are parallel to the surface of the crystal plate. The sample was prepared on the surface of the QCR. Polished QCR was employed (Nihon Dempa Kogyo Co., Ltd.) as the AFM sample substrate. The wafer plate was 8.5 mm in diameter and 0.33 mm thick. The resonance frequency of the QCR was 9 MHz.

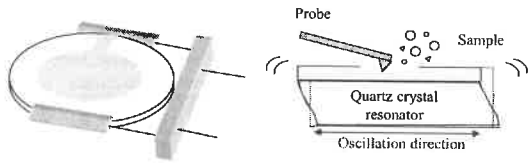

FIGURE 1. AT-cut quartz crystal resonator. The shear deformations of the AT-cut QCR are parallel to the surface of the crystal plate. The QCR oscillates at its resonance frequency of 9 MHz with an amplitude of a few nanometres. The samples are prepared on the wafer of the QCR. The oscillating sample surfaces are scratched with the AFM probe for ultrasonic cutting.

In these experiments, we used polymer and biological samples to test the ultrasonic cutting performance. Polycarbonate films were prepared as a polymer sample. The polymer solution, (2 mg/mL in 1,2-dichloromethane), was cast by spin-coating the solution onto QCR wafers at 2000 rpm for 5 s. For biological samples, collagen fibrils, taken from rat tail tendons, were adsorbed on the wafer plate of the QCR using tweezers and then dried with a stream of dry air. The details of the preparation of the suspension of collagen fibrils and the incubation method are described elsewhere.[13)]

Prepared QCR wafers were put on the AFM sample holder, which was located on a piezoelectric tube scanner, as shown in Fig. 2. The cantilever employed in the experiments was a commercial one designed for contact mode operation (Olympus OMCL-TR800PSA). The spring constant of the cantilever was 0.57 N/m. The piezoelectric tube scanner was used for loading the force and moving the sample against the tip. With respect to the tip scratching the surface, the sample surface was moved in *x-y* directions by the tube scanner with QCR oscillation under applied loading force. In this paper, we refer to scratching on the surface with QCR oscillation as ultrasonic scratching.

Haptic Device Human Interface

Figure 2 shows a schematic diagram of the nano fabrication system based on the AFM controlled by the haptic device. We employed a commercial haptic device that has a pen type handle with a serial rink mechanism (PHANTOM Omni; SensAble Technologies) was employed. A homemade system consisting of an AFM, controller[8)] and software was modified to include the haptic device for the control of ultrasonic cutting. With respect to lateral movement in the *x* and *y* directions, the signal from the haptic device is sent to the personal computer, and then the signal is sent to the PZT drive circuit passing through a digital to analog converter. In our experiments, 1 mm in the lateral displacement of the pen handle corresponds to 15 nm in movement of the AFM probe. The topographical signal detected in the AFM controller is fed to the personal computer, and then the signal is converted to the displacement in the *z* direction of the pen handle of the haptic device. Using this process, the nanometer-scale topographical information detected by the AFM can be scaled up to millimeter movements of the pen handle of the haptic device, and the nanometer-scale topography on the surface can

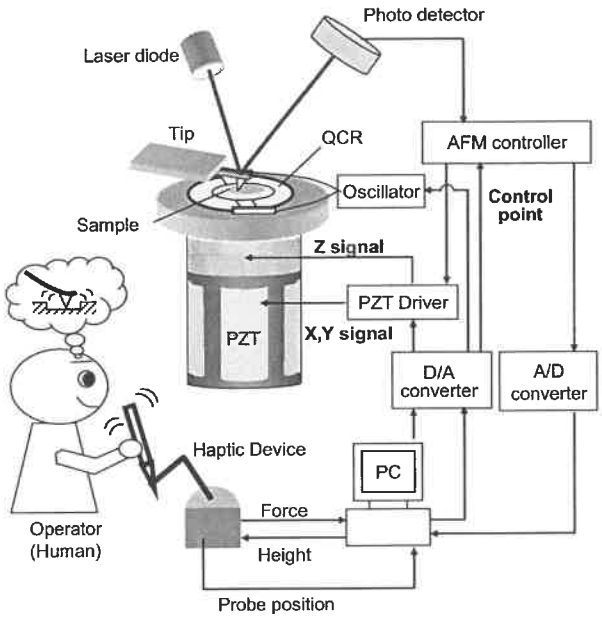

FIGURE 2. Schematic diagram of the experimental setup of an AFM for an ultrasonic nano cutter. The AFM was coupled with a haptic device, so the operator could feel the reaction from the sample during scratching.

be felt in the operator's fingers holding the pen handle. In our system, the surface roughness of 1 nm corresponds to 3 mm in movement of the pen handle of the haptic device. During the manipulation, if the operator pushes the pen handle of the haptic devices against the reaction, a signal is sent to the personal computer to calculate and convert the force feedback signal, and then the converted signal is sent to the feedback controller to change the setting point of the feedback control. The system changes the force between the probe and the surface in response to the pushing reaction by the operator. By this sequential process, the operator can change the applying force between the probe and the surface by feeling the force reaction from the surface via the haptic device.

The AFM fabrication process proceeds as follows. First, the surface topography is ascertained just before the fabrication by the AFM, and then the topographical image is displayed on a screen in front of the operator. After observing the image on the screen, the operator moves the AFM probe using the haptic device to scratch the surface. During the process, the operator can recognize the probe position as a cursor indicated on the AFM image.

During the scratching fabrication, the trajectory lines of the probe movement are drawn on the AFM image. In the haptic device, the pen handle has a button to turn on the oscillator of the QCR for ultrasonic scratching. Thus the operator can start and stop ultrasonic scratching at any position on the surface while feeling the reaction from the surface. After the fabrication, the scratched surface is sequentially obtained by the normal AFM operation.

EXPERIMENTAL RESULTS

Figure 3 shows the topographies of polycarbonate (PC) surfaces scratched by the AFM. Figure 3(a) shows the PC surface scratched without QCR oscillation, which means normal AFM scratching in contact mode. In this image, four scratched lines are barely visible. The scratched loading forces were changed from 100 nN to 160 nN. The number of the reciprocating stroke is one time. Even with the lines scratched with high loading force over 100 nN, it is difficult to recognize the lines due to structures that are too shallow. Figure 3(b) shows the line scratched 10 times at a loading force of 120 nN. In this image, the scratched line can be clearly seen. However, the cross-sectional profiles taken along the line indicate periodical bumps, as shown in Fig. 3(c). Such periodical bumps appearing on scratched surfaces are generated by the interaction between the probe and the viscoelastic polymer surfaces.[7] A polymer surface during bundle formation behaves more like a material exhibiting rubber elasticity than a material in a glassy state. The macromolecules at the surface possess an extra degree of freedom of motion and so need just a little pulling to be separated from the bulk. The macromolecules are laterally stretched by the AFM tip, which might induce surface distortion such as the formation of bundles. Consequently, it is difficult to control the cutting of polymer surfaces using conventional scratching in contact mode.On the other hand, Fig. 3(d) shows the cut lines scratched with QCR oscillation at different loading forces. The number of the reciprocating stroke is one time. In this image, five lines are clearly recognized. Figure 3(e) shows the cross-sectional profile taken along the line scratched with a loading force of 160 nm. The profile of the line bottom is very flat in comparison with that of the line scratched by conventional scratching. Figure 4 shows the relationship between the loading force and the mean depth of the scratched lines.

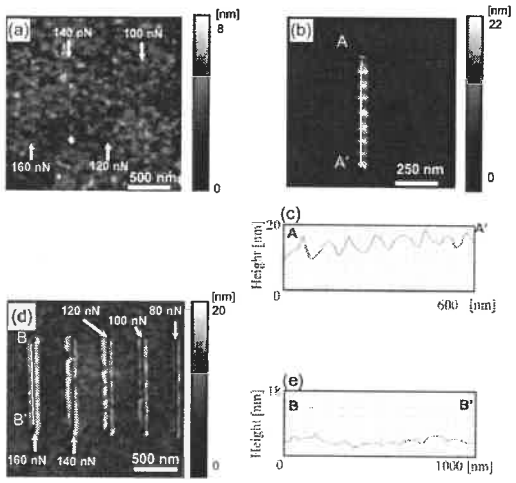

FIGURE 3. AFM images of a polycarbonate surface scratched by AFM probe at constant force. (a) Lines on the PC surface scratched without QCR oscillation. (b) Line on the PC surface scratched 10 times back and forth at a loading force of 120 nN. (c) Cross-sectional profiles taken along the scratched line in image (b). (d) Lines on the PC surface scratched without QCR oscillation. (e) Cross-sectional profiles taken along the line scratched at the loading force of 160 nN in image (d).

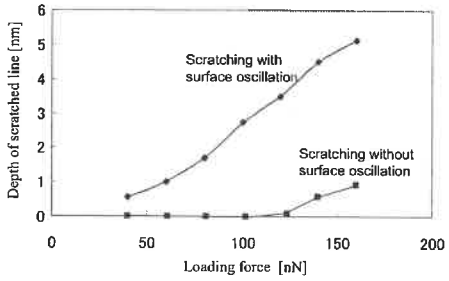

FIGURE 4. The relationship between the depth of the scratched lines and the loading force..

As shown in this figure, the depth of the conventional scratched lines increases with increasing loading force. The depth of the ultrasonic scratched lines also increases with increasing loading force. However, the mean depth of the ultrasonic scratched lines is several times deeper than that of the conventional scratched lines. In particular, although the depths of the conventional scratched lines are almost zero when the loading force is below 100 nN, the ultrasonic scratched grooves are significantly deeper.

With respect to the ultrasonic scratch, the surface is oscillated laterally with an ultrasonic

frequency of 9 MHz, which generates high-speed repetitive scratch with an amplitude of a few nanometer. The speedy-small scratch can cut the polymer surface, due to a reduction in the viscous damping properties of polymers. Consequently, the ultrasonic scratch progresses deeply and smoothly in comparison with the conventional scratch.

Finally, we applied the system to a biological sample. Figures 5 show the collagen fibrils taken from a rat tail tendon. In the AFM image, the collagen fibrils had a semi-cylindrical profile. They have periodic transverse grooves and ridges on their surfaces, which is known as D-periodicity.[9] We cut the gap position of the collagen fibrils by AFM scratching using the haptic device. The direction of the long axis of the cantilever was parallel to the vertical axis of the AFM images. In the case of normal AFM scratching without QCR oscillation, it was very hard to cut the collagen because the structure consists of fibrils and subfibrils. However, using ultrasonic scratching with the haptic device, it was relatively easy to cut the fibers. Figure 5(b) shows the collagen fibrils successfully cut by the system. The direction of the QCR oscillation was parallel to the vertical axis of the AFM image. During the cutting, we recognized the topographical change in the collagen by feeling the response of the haptic device. It was very useful to predict the result. By feeling the result with the haptic device, we could adjust the appropriate parameters such as loading force and moving speed to achieve certain results. As a consequence, the collagen fibrils could be successfully cut by ultrasonic scratching by applying a force above 200 nN at a speed of 100 nm/s. Therefore, using this system, we can realize a nanometer-scale ultrasonic cutter that may be an effective tool in the fields of nanometer-scale machining of synthetic and biological materials.

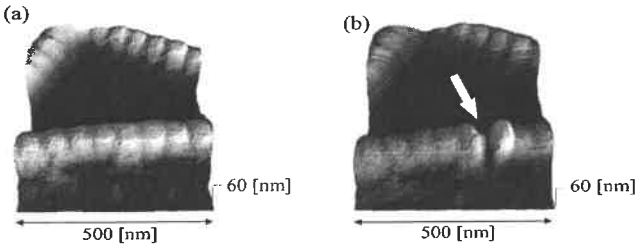

FIGURE5. Collagen fibrils taken from a rat tail tendon. (a) Topographic image of the collagen fibrils before scratching. (b) Topographic image of the collagen fibrils after scratching.

CONCLUSION

Novel scratching of local surfaces was performed using an atomic force microscope coupled with a haptic device. The operator can feel the force reaction during the fabrication process. To test the system, polycarbonate surfaces were successfully fabricated. In contact mode scratching, the surface was not carved smoothly, and the cutting force during the fabrication was also felt as an irregular reaction in the haptic device. On the other hand, the surface could be smoothly carved in the case of ultrasonic scratching. At that time, the cutting force during the fabrication could be felt as a smooth cutting reaction in the haptic device. Using biological samples, collagen fibrils were also successfully cut by ultrasonic scratching. The fabrication system might be very useful for many applications, especially in the fields of nanometer-scale engineering and biological manipulation.

ACKNOWLEDGMENTS

It is gratefully acknowledged that this work has been supported by the Leading Project of Ministry of Education, Sports, Science and Technology "Development of elementary techniques for electron microscope in next generation".

REFERENCES

[1] Ogino T., Nishimura S. and Shirakashi J., Jpn. J. Appl. Phys. 2007; 46: 6908.
[2] Iwata F., Matsumoto T. and Sasaki A., Nanotechnology 2000;11: 10.
[3] Gregor M., Plecenik T., Praščák M., Mičunek R., Kubinec M., Gašparík V., Grajcar M., Kúš, P. and Plecenik A., Appl. Phys. Lett. 2007; 91: 122502.
[4] Iwata F., Matsumoto T., Ogawa R. and Sasaki A., J. Vac. Sci. Technol. B, 1999;17: 2452.
[5] Iwata F., Yamaguchi M. and Sasaki A., Wear 2003; 254: 1050.
[6] Meyers G. F., Dekoven, B. M. and Seitz, J. T., Langmuir 1992; 8: 2330.
[7] Leung, O. M. and Goh, M. C., Science 1992; 255: 64.
[8] Sasaki A., Iwata F., Katsumata A. and Fujiyasu J., Rev. Sci. Instrum. 1997; 68: 1296.
[9] Yamamoto S., Hashizume H., Hitomi J., Shigeno M., Sawaguchi S., Abe, H. and Ushiki T., Arch. Histol. Cytol. 2000; 63: 127.

THE DISECRETE POLYSTYLENE-GOLD CORE-SHELL NANOPARTICLES ARRAY AND THEIR SURFACE PLASMONIC PROPERTIES

Nobuyuki Zettsu, Shuhei Uchida, and Kazuya Yamamura
Research Center for Ultra Precision Science and Technology, Osaka University
2-1 Yamadaoka Suita, Osaka, Japan

INSTRUCTIONS

Nanoshells, concentric nanoparticles consisting of a dielectric core and a metallic shell, are simple spherical nanostructures with unique, geometrically tunable optical resonances. As with all metallic nanostructures, their optical properties are controlled by the collective electronic resonance, or plasmon resonance, of the constituent metal, typically silver or gold. In striking contrast to the resonant properties of solid metallic nanostructures, which exhibit only a weak tunability with size or aspect ratio, the optical resonance of a nanoshell is extraordinarily sensitive to the inner and outer dimensions of the metallic shell layer.

The underlying reason for this lies beyond classical electromagnetic theory, where plasmon-resonant nanoparticles follow a mesoscale analogue of molecular orbital theory, hybridizing in precisely the same manner as the individual atomic wave functions in simple molecules. This plasmon hybridization picture provides an essential "design rule" for metallic nanostructures that can allow us to effectively predict their optical resonant properties. Such a systematic control of the far-field optical resonances of metallic nanostructures is accomplished simultaneously with control of the field at the surface of the nanostructure.

The nanoshell geometry is ideal for tuning and optimizing the near-field response as a stand-alone surface-enhanced Raman spectroscopy (SERS) nanosensor substrate and as a surface-plasmon-resonant nanosensor. Tuning the plasmon resonance of nanoshells into the near-infrared region of the spectrum has enabled a variety of biomedical applications that exploit the strong optical contrast available with nanoshells in a spectral region where blood and tissue are optimally transparent.

Unfortunately, these important applications have been greatly impeded. Prior to the realization of these resonant properties, methods to synthesize monodisperse nanoshell particles and to isolate (non close-packed assembly) them in a controlled environment are two obstacles that must be overcome. Only close-packed assemblies are available through most of available bottom-up self-assembled approaches. Furthermore, attaining high throughput and large area fabrication continues to be a major challenge.

In this work, we demonstrated facile fabrication of large-sized two-dimensional discrete polystyrene@gold (PS@Au) core-shell nanoparticles array with tunable their structural parameters, including both nanoshell geometry and interparticles distances, as well as their localized surface plasmon resonance (LSPR) properties, and explored the LSPR sensitivity to bulk refractive index changes.

EXPERIMENTAL SECTIONS

For all of the experiments, Si (100) wafers were cut into pieces of 50×50mm^2, and cleaned with H_2SO_4/H_2O_2 (7:3) solution. Hexagonal close-packed (hcp) polystyrene (PS) nanoparticles monolayer was prepared by spin-coating from 50μL of 10wt% mono-dispersed PS nanosphere suspension (ϕ:260nm) diluted with mixture solution containing both equal mass of deionized water and ethanol.

Subsequent atmospheric pressure helium (He) plasma treatment to the hcp-structured PS nanoparticles monolayer at designated time, providing non close-packed assembly with controllable their diameters and interparticle distances. The glow discharge was produced at an applied frequency of 13.56 MHz, an applying power of 15W. The gap distance was adjusted to ca.1mm. After He plasma treatment, thin gold film was deposited on the discrete PS nanoparticle film using thermal vacuum evaporation, resulting in the discrete PS@Au core-shell nanoparticles array. The structural

parameters and the LSPR properties were measured by scanning electron microscopy and ultraviolet-visible-near infrared (UV-Vis-NIR) spectroscopy. Furthermore, to explore the LSPR sensitivity to bulk refractive index changes, the nanoparticles arrays were exposed to various solvents with different dielectric constant.

RESULTS AND DISCUSSION

Relationship between plasma treatment time and the structural parameters in the PS nanoparticle array, including diameter and interparticle distance, is shown in Figure 1. Those parameters were proportionally changed against to the treatment time. Scanning electron microscopy also revealed such trend that the spherical shape of the parent PS nanoparticles was well preserved during the plasma treatment. These results strongly indicated that plasma-physical etching isotropically progressed for the PS nanoparticles, and should allow the preparation of discrete PS nanoparticles array with different structure parameters by controlling the plasma treatment time.

Figure 2 depicts that the changes in the scattering spectra taken from the PS@Au core/shell nanoparticles array with different structure parameter. Two major intense scattering peaks, related to propagation of localized surface plasmon in the PS@Au nanoparticles arrays, were observed at NIR and visible regions. The LSPR line could be well-tuned from to 600 to 1050 nm by changing the structural parameters. Theoretical calculation revealed that those were contributed to the dipole plasmon resonance of the discrete PS@Au core/shell nanoparticles and large polarization generated from plasmonic interactions at the interface between PS@Au core/shell nanoparticles and the Si substrate large polarization, respectively.

And we have examined the dependence of the peak wavelength on the refractive index of solvents above the nanoparticles array to study the NIR-sensing performance. We saw a linear dependence that was similar to what has been seen earlier in studies of other nanoparticles. The refractive index unit (RIU) reached by up to 160 nm RIU^{-1}, which was larger level than that of well studied Ag triangular nanostructured array as a LSPR bio-sensor.[1]

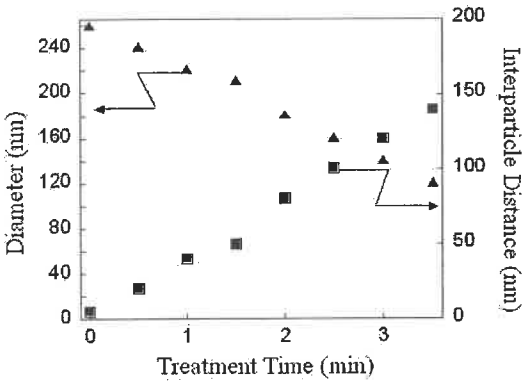

Figure 1. The changes in shape variations of the discrete PS nanoparticles array under atmospheric He pressure plasma treatment with applying power of 15W.

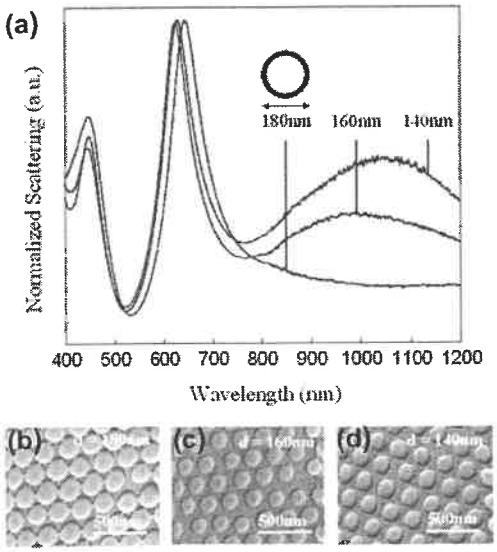

Figure 2. The changes in extinction spectra (a) and the SEM images (b)-(d) taken from the PS@Au core/shell nanoparticles array with different plasma treatment time.

REFERENCES

[1] Haes A, Zou S, Schatz G, Van Duyne P. A Nanoscle Optical Biosensor: The Long Range Distance Dependence of the Localized Surface Plasmon Resonance of Noble Metal Nanoparticles. Journal of Physical Chemistry B. 2004; 108; 109-116.

EXPERIMENTAL STUDY OF MICRO ULTRASONIC MACHINING PROCESS

Sreenidhi Cherku, Murali M Sundaram, and K P Rajurkar
Center for Nontraditional Manufacturing Research
University of Nebraska-Lincoln
Lincoln, Nebraska, USA

INTRODUCTION

Micro ultrasonic machining (micro USM), is one of the efficient material removal processes especially suitable for the micromachining of hard and brittle materials. The principle of micro USM is shown in Figure 1. In micro USM workpiece which is placed on the workpiece table vibrates at ultrasonic frequency (40 KHz). Abrasive slurry is injected on the top of the workpiece. There is a rotating tool which hits the abrasive particles in the slurry which in turn hit the workpiece and chip away the material from it. The vibrations given to the workpiece aid in refreshing the slurry so that fresh abrasive particles are in contact with the workpiece and also in removing the debris from the tool workpiece gap [1-4].

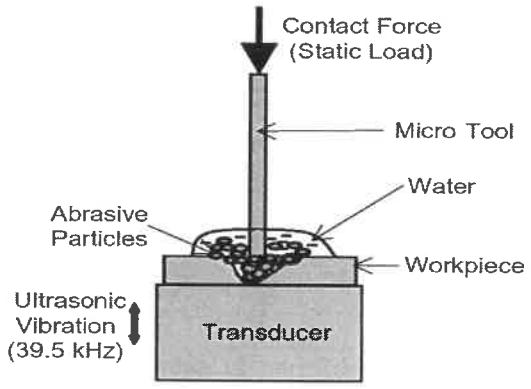

FIGURE 1. Principle of USM

The abrasive slurry acts as lubricating agent as well as coolant in reducing the frictional heat generated due to the movement of the abrasive particles on the workpiece and heat generated by the vibrations due to the transducer. The slurry also collects the debris from the machined area. In general micro USM is carried out with water as the medium due to its properties of excellent coolant, easy removal of debris from machining zone due to low viscosity, low cost and easy availability.

In many conventional machining processes like grinding, milling and broaching processes oil has been successfully used as cutting fluid. These oils can be used either as straight oils, which are pure petroleum based oils or emulsifiers which are water based oils. Use of straight oils have excellent lubricating properties and are used especially for machining process involving low speeds, low clearance requiring high quality surface finish. These oils have more viscosity and good lubricating properties than water and causes less tool wear. Hence, it may be prudent to use oil based slurry in micro USM. This paper reports the experimental inverstigation of the same.

SYSTEM DESIGN

An in-house built experimental micro USM system based on the design concept of "vibration on work piece [5,6]" is schematically shown in Figure 2.

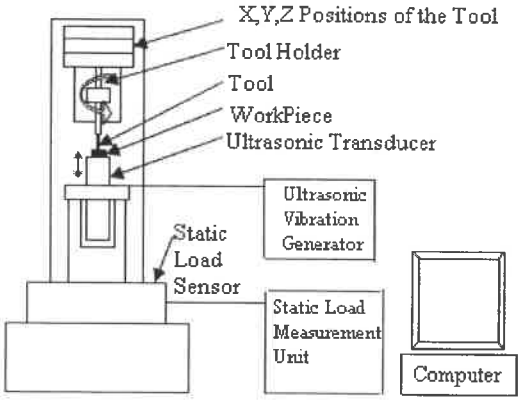

FIGURE 2. Schematic of in-house built Micro USM

A micro tool, attached to a mandrel rested on V-shaped block is rotated by a DC motor and is free to move in X, Y and Z directions with six degrees of freedom. Micro tools with different diameters are prepared by wire Electrical Discharge Grinding (WEDG). The micro tool is

sensitive to elastic bending, vibration, and breakage. Therefore, the contact force between tool and workpiece needs to be controlled and limited to a certain level during machining. This is achieved by implementing a close-loop control strategy with force feedback. Key system components such as electronic balance and three-axis stage have high resolution (0.1 mg and 25 nm, respectively) to meet the demand of accuracy in micro machining.

EXPERIMENTAL RESULTS & DISCUSSION

The machining parameters used in the study are listed in Table 1.

TABLE 1. Machining parameters

Control Variable	Setting
Applied Load	3 g
Vibration amplitude	1 µm
Rotational Speed	1000RPM
Abrasive Particle Size	0~0.5, 1~3, 3~5
Abrasive concentration	0.5%,1%,3%
Medium of the slurry	Water, Oil
Tool Diameter	180 µm
Vibration amplitude	1 µm
Tool Material	Tungsten
Work Piece Material	Silicon Wafer
Abrasive Material	Poly Crystalline Diamond

Holes with drill depth of 30 µm are drilled on the silicon wafer. Each of these experiments are repeated thrice and the averaged to analyze the results.

Material removal rate (MRR)

In machining with fine sized grains as shown in Figure 3, the MRR increases with the increase in the abrasive particles due to increase in the number of particles involved in the machining. MRR is more when machining with the water as oil is more viscous than water hampers the process of debris removal in the processing of machining thus accounting for less MRR.

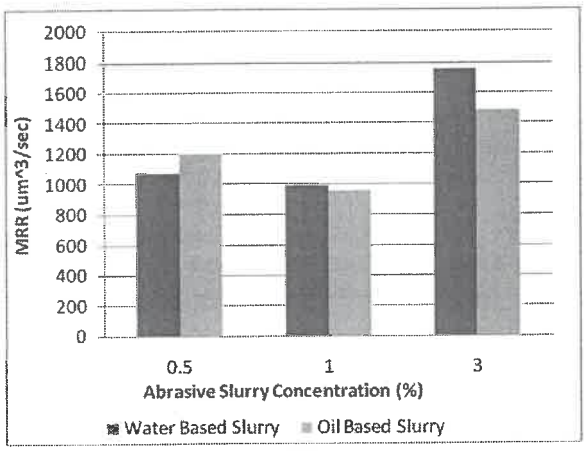

FIGURE 3. MRR vs Concentration for particle size 0~0.5

Using medium sized particles as shown in Figure 4, MRR increases with the increase in the concentration as there are cutting edges for a given volume of abrasive slurry. The MRR is more when machined with oil compared to water as shows the comparison of MRR between water based and oil based slurry with respect to the varying abrasive slurry concentrations for the particle size of 1~3.

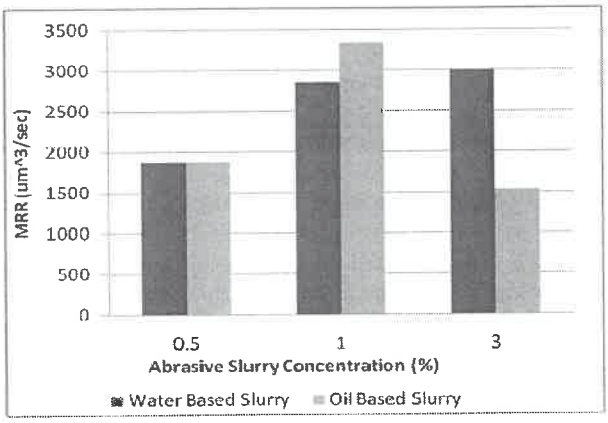

FIGURE 4. MRR vs Concentration for particle size 1~3

When machining with coarser grains as shown in Figure 5, the MRR is more when machined in aqueous medium compared to oil. As the grains become coarser the grain boundaries try to interlock reducing the number if cutting edges. Oil possessing more viscous property interlocks these grains strongly compared to water thus contributing to less MRR.

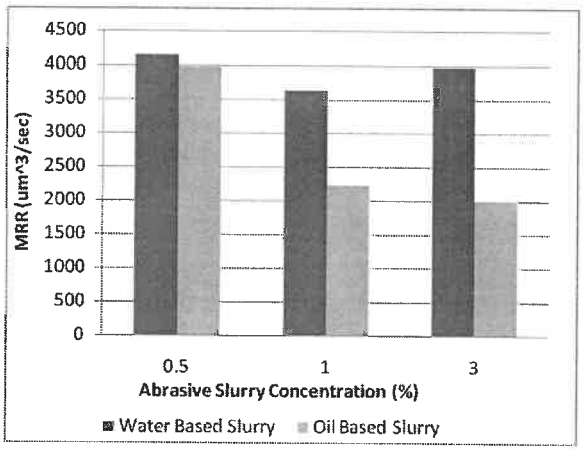

FIGURE 5. MRR vs Concentration for particle size 3~5

It is observed that machining with water based slurry is more suitable for finer particles sizes with higher concentration or medium particles sizes with medium concentration or coarser particle sizes with lower particles where as machining with oil based slurry is always suitable for all the particle sizes with low concentration.

Surface Roughness

When machining with finer grains the surface shown in Figure 6, finer grains having constant cutting edges hit the workpiece repeatedly. Further the debris is added in the process of material removal increasing the frictional heat making the surface rougher with the increase in the concentration. However oil acting as coolant reduces the surface roughness to some extent. Thus producing good surface finish compared to machining in water medium.

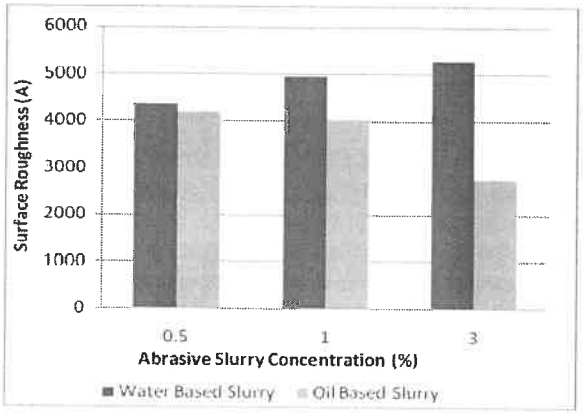

FIGURE 6. Surface Roughness vs Concentration for Particle Size 0~0.5

Using medium sized abrasives the surface roughness shown in Figure 7, with the increase in the concentration the particle size decreases in the process of machining, indicating more number of particles to absorb the heat generated during the process which eventually reduces the surface roughness. However surface roughness for oil is less compared to water since water acting as coolant absorbs the generated heat.

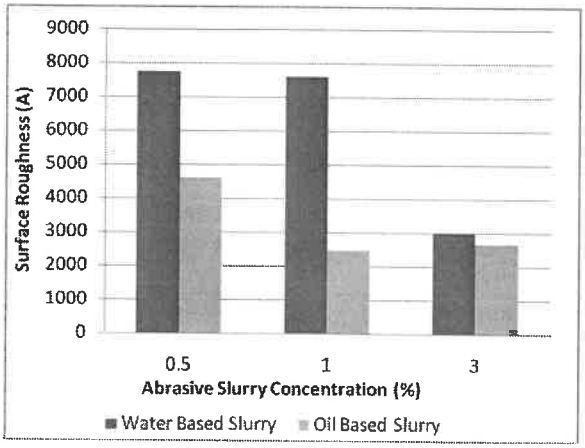

FIGURE 7. Surface Roughness vs Concentration for Particle Size 1~3

When machining with coarser size grains as shown in Figure 8, as the concentration increases there are more coarser particles hitting the work surface thus making it rougher. Since oil acts as better coolant than water thus giving better surface finish.

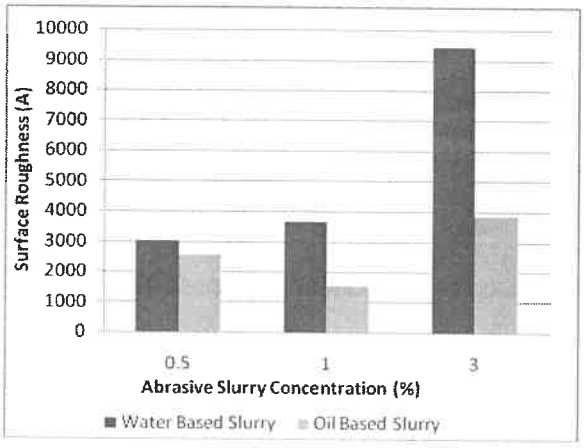

FIGURE 8. Surface Roughness vs Concentration for Particle Size 3~5

Finally it is observed that machining with oil based slurry gives good surface finish compared

to the water based slurry. Furthermore good surface finish is given by machining with the finer particles whereas machining with coarser grains gives poor surface finish.

Machining Mode in Oil Based and Water Based Slurry

It is evident from the SEM images of the holes drilled that brittle machining mode occurs when machining with oil where as ductile machining occurs when machining with water. Oil possessing the property of more viscosity acts as good lubricant displacing the particles in the machining zone without indenting the surface and just scratching it thus machining in the brittle mode. However the particles in the machining zone are constant without being displaced when water is used, particles protruding into the surface of the workpiece indenting it thus machining in ductile mode.

The ductile and brittle machining mode can be differentiated according to the particle size used in machining [7]. Use of smaller particle size results in ductile machining mode as there are number or particles in the machining zone, distributing the applied static load in machining among many small particles and reducing the net force applied per particle, just scratching the surface leading to ductile machining mode. Machining with larger particles involves more static load per particle as there are less particles thus indenting the surface leading to brittle machining mode.

SUMMARY

This paper presents the results of micro ultrasonic machining using oil based abrasive slurry. An in-house built experimental setup was used to conduct designed experiments. The influence of process parameters such as slurry medium, slurry concentration, and abrasive particle size on the performance of micro USM Material Removal Rate (MRR) and Surface Roughness (SR) is reported. It is evident from the experimental study that machining with water based slurry is suitable only for finer particles sizes with higher concentration or medium particles sizes with medium concentration or coarser particle sizes with lower particles where as machining with oil based slurry is always suitable for all the particle sizes with low concentration. Further the study reveals that machining with oil based slurry gives good surface finish compared to the water based slurry. Good surface finish is given by machining with the finer particles whereas machining with coarser grains gives poor surface finish.

ACKNOWLEDGEMENTS

The financial support from the NSF under grant number CMMI – 0728294 and DMI – 0355380 is acknowledged.

REFERENCES

[1] T.B.Thoe, D.K.Aspinwall, M.L.H.Wise. Review on Ultrasonic Machining. International Journal of Machine Tools & Manufacturing. Vol.38; pp.239-355; 1998.

[2] Z.Yu, K.P.Rajurkar, A.Tandon. Study of 3D Micro-Ultrasonic Machining. Journal of Manufacturing Science and Engineering. Vol.126; 2004.

[3] X.Hu, Z.Yu, K.P.Rajurkar. State of the art investigation and research issues in micro ultra sonic machining. ASME International Conference on Manufacturing Science and Engineering. 2006.

[4] Z.Yu, X.Hu, K.P.Rajurkar. Influence of debris accumulation on material removal and surface roughness in micro ultrasonic machining of silicon. Annals of CIRP. Vol.55; pp. 201-204; 2006.

[5] K. Egashira, T. Masuzawa, M.Fujino, X.Q.Sun. Applications of USM to Micromachining by On-the –machine Tool Fabrication. International Journal of Electrical Machining. Vol.2; pp.31-36; 1997.

[6] K. Egashira, T. Masuzawa. Micro Ultrasonic Machining by the Application of Work Piece Vibration. Annals of CIRP.Vol.48; pp.131-134; 1999.

[7] M.M.Sundaram, C.Sreenidhi, K.P.Rajurkar. Micro Ultrasonic Machining Using Oil based Abrasive Slurry. Accepted for Publication in the Proceedings of the 2008 International Manufacturing Science and Engineering Conference. Oct 7-10; 2008.

COMBINATION MACHINING OF WIRE-SAWING WITH ELECTRO-CHEMICAL DISCHARGE MACHINING

Katsushi Furutani[1], and Michiaki Tomoto[1,2]
[1]Department of Advanced Science and Technology
Toyota Technological Institute
Nagoya 468-8511 Japan
[2]Toray Engineering Co., Ltd. at present

INTRODUCTION

In recent years, high performance devices are demanded in electronics, optical and medical apparatus in which glass and fine ceramics are often used. They are hard to machine and crack on their surface during cutting and grinding because of their brittleness and hardness.

Electro-chemical discharge machining (ECDM) has been studied for machining such insulating materials [1][2]. Figure 1 shows the principle of the conventional ECDM. An insulating workpiece is dipped in electrolyte as working fluid and a tool electrode is pressed on a surface with a small load. When the negative voltage is applied to the tool electrode, it is covered with bubbles and discharges occur in the bubbles. Then the chemical reaction between the electrolyte and the workpiece is accelerated and the heat by the discharge gradually removes the surface. However, many cracks were observed in the glass machining. The accumulation of the heat by discharge causes the cracks. An electrode motion is good for decreasing the cracks because fresh working fluid takes away the heat accumulation. Because the discharge heat accelerates also the chemical reaction between Si and Na components, a rigid bond Si-O-Si is replaced with a softer bond Si-O-Na. Then this reaction diffuses on the surface and the sodium ions encroach other bonds. The bond Na-O is much weaker than the siloxane bond Si-O in glass. Na_2O-SiO_2 containing the bond Na-O has low viscosity and its structure is fragile and soluble in water. Na^+ ion assists the glass removal and the increasing Na_2O composition makes the surface softer. Therefore, the surface of the glass is easily removed. [3]. A travelling wire is sometimes used [4]. An ECDM process with a rotating abrasive impregnated tool has been studied to increase the removal rate of glass and alumina [5]. Although its peripheral speed was 0.5 mm/s, the removal rate of the glass was improved about 20%.

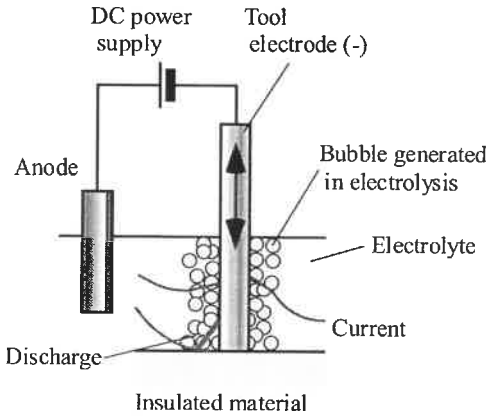

Figure 1. Principle of electro-chemical discharge machining.

On the other hand, a method for wire saw fabrication by electrical discharge machining (EDM) has been proposed with a green compact of WC-Co powder [6]. The electrode is crumbled by the discharge and the powders are supplied from the electrode into the gap during the deposition process. The main component WC is melted by the discharge heat and deposited on the workpiece after reacting with the cracked carbon from the working oil. Then the wire saw was covered with WC layer as shown in Figure 2.

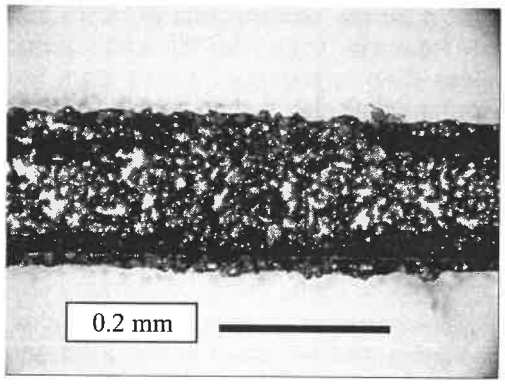

Figure 2. Wire saw with WC deposition.

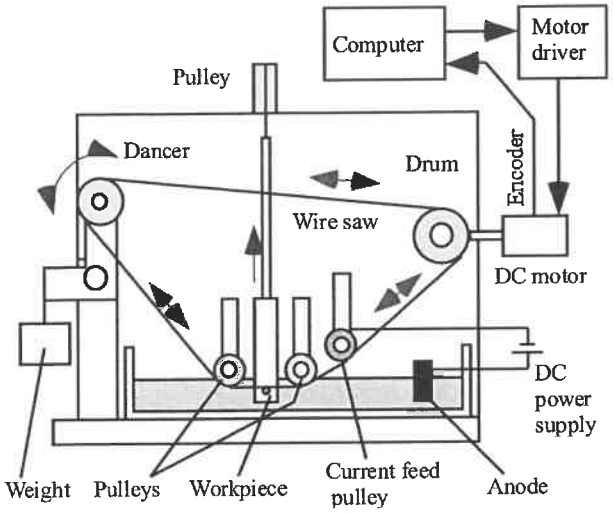

Figure 2. Configuration of cutting machine.

Brittle materials such as glass and basalt could be cut with the wire saw as well as metals.

In this paper, slicing with the WC-coated wire saw is combined with ECDM to improve the machining performance.

EXPERIMENTAL SETUP

Figure 3 shows a prototype of a cutting machine. It consists of a set of drums to feed and wind a wire or wire saw, a motor, a guide unit, a dancer to adjust the wire tension with a dead weight of 410 g and a DC power supply. It measures 360 mm × 308 mm × 256 mm. The drum measures 60 mm in diameter. Because the OH^- ion increases with the progress of machining, most parts were made from stainless steel or PTFE to prevent from the erosion by the electrolyte. The anode made of graphite was dipped into electrolyte (10 wt% $NaNO_3$ solution) and the voltage applied.

A 3-m stainless steel wire with a diameter of 0.2mm was reciprocated by alternating the rotating direction of the drum. The cutting machine was controlled by a PI compensator written in LabVIEW. It was stringed between two pulleys made of PTFE with an interval of 50 mm. The WC layer with a thickness of 20 μm was deposited by EDM [6]. The current density should be large to generate enough bubbles around the cutting portion. The wire except the cutting portion about 2-3 mm was covered with insulated tubes to minimize the exposure length of the wire to the electrolyte.

Table 1. Machining Conditions.

	ECDM	Grinding	Combination
Wire tool	SUS304 ϕ0.2 mm	SUS304 ϕ0.2 mm with WC coat	
Applied voltage V	70 V	0 V	70 V
Cutting load N	0.6		
Tension weight g	410		
Wire feed rate m/s	0	Increasing from 0 to 0.8 in 3.4 s	
Machining time min.	10		

ECDM: Electro-chemical discharge machining

Table 1 shows machining conditions. A silica glass rod with a diameter of 5 mm was used for a workpiece. A cutting load of 0.6 N was applied with a weight for the upward gravity-feed. The wire was stationary in ECDM not to stir the electrolyte. The wire feeding speed was increased to 0.8 m/s with a constant acceleration in grinding and the combination machining. A voltage of 70 V, determined by some preliminary experiments, was applied in ECDM and the combined machining.

After 10-minute machining, the grooves were observed with an optical microscope from the above to measure their width and depth. Their side walls and bottoms were observed a scanning electron microscope. The depth was defined as the distance between the surface and the deepest part of the groove. The width included cracks at the groove edges. The average of cutting depth and width was calculated in 5-time machining.

EXPERIMENTS

The machining performance of ECDM, wire sawing and their combination was compared. All machining methods were tested in the electrolyte.

Figure 4 shows results of machining. The surface of the side walls was removed by heat or chemical reaction by ECDM. Parallel streaks to the wire feeding direction were observed on the bottom, and vertical ones, on the side walls. The bubble flow caused them. Scratches were observed both the surface of the bottom and

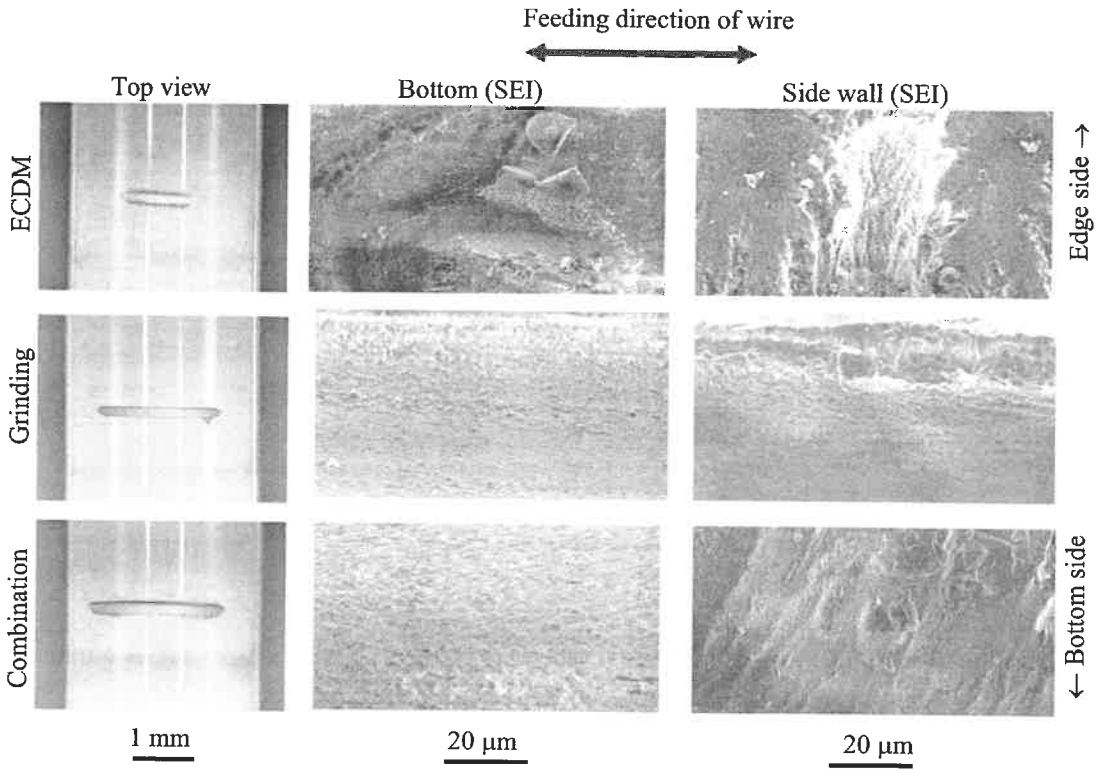

Figure 4. Results of machining.

side walls by grinding. The removal by heat or chemical reaction and vertical streaks were observed on the side walls and the scratches and some speckles, on the bottom by the combination machining. Cracks were seldom observed in all cases because of a small cutting load of 0.6 N.

Figure 5 shows the comparisons of the groove depth and width. The removal rate of the combination machining is larger than that of individual use of ECDM or grinding. The groove width by grinding was smaller than the others. The nonuniform WC deposition caused the variations of the depth and width by grinding. Because the surface of the workpiece was softened by the chemical reaction, the variations by ECDM and the combination machining was small. The groove bottom was mainly removed by grinding. However, the side walls were also removed by the others because the bubbles were generated on the side of the wire tool more easily than its bottom. A long residence time of the wire saw in ECDM and the combination machining, which means a low machining speed, causes the removal of the side walls in the horizontal direction. Consequently, the groove

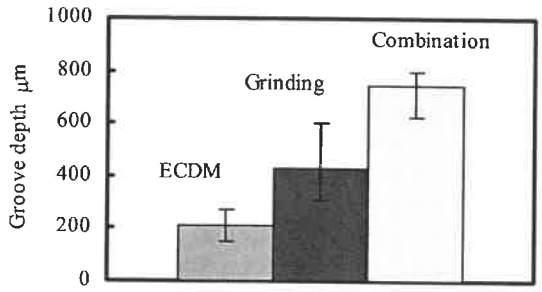

(a) Groove depth.

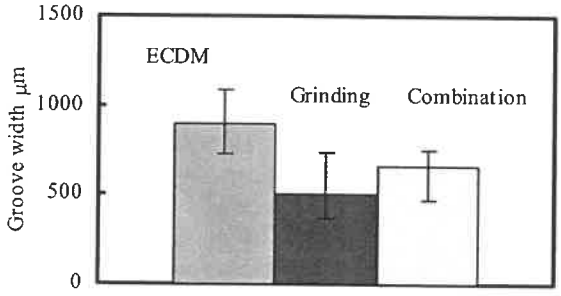

(b) Groove width.

Figure 5. Dimensions of grooves.

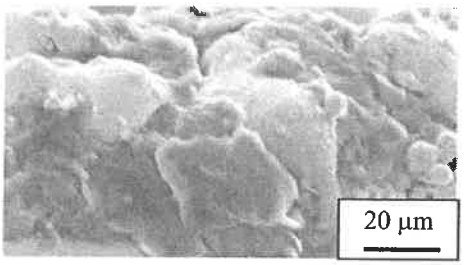

(a) Before machining

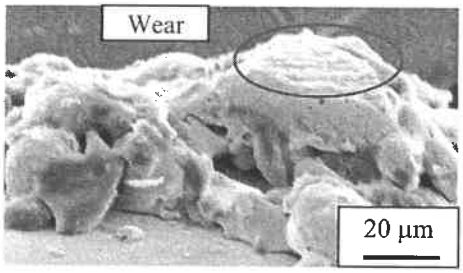

(b) After machining (load: 0.6 N)

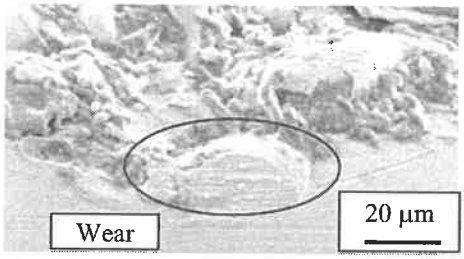

(c) After machining (load: 2.1 N)
Figure 6. Wear of WC deposition.

width by ECDM was wider than that by the combination machining. The wire saw feeding helped to drag the working fluid and flush the sludge. Providing the fresh working fluid also assisted to disperse the discharge and decrease the cracks. The synergy effect of grinding with ECDM was obtained.

Figure 6 shows WC deposition before and after machining. Because the cutting load was small, higher parts of the deposition wore little. No damage by the discharge, erosion and scaling off was observed on the deposition surface. Because a large current of several amperes in average flowed through the wire saw in ECDM and the combination machining, the wire saw discolored due to the Joule heat.

CONCLUSIONS

In this paper, a combination machining of grinding with ECDM was experimentally investigated to improve the machining performance. Conclusions can be drawn as follows.

(1) The machined groove by the combination machining was deeper than that by independently applying grinding or ECDM.

(2) The cracks were seldom observed on the bottom and side walls under a small cutting load.

The authors would like to thank Prof. Kazuyoshi Kondo of Toyota Technological Institute and Dr. Masayuki Suzuki of Sansyu Engineering Service for their valuable advice, and Mr. Kenji Muramatsu of Shinkikai Giken for their helpful cooperation. This study was supported by Industrial Technology Research Grant Program in 2005 from New Energy and Industrial Technology Development Organization (NEDO) of Japan.

REFERENCES

[1] Kurafuji H, Suda K. Electrical Discharge Drilling of Glass I. Annals of CIRP. 1968; 16: 415-419.

[2] Wüthrich R, Fascio V. Machining of Non-conducting Materials Using Electrochemical Discharge Phenomenon – An Overview. Int. J. Mach. Tool. Manuf. 2005; 45: 1095-1108.

[3] Furutani K, Maeda H. Machining glass rod with lathe type electro-chemical discharge machine. J. Micromech. Microeng. 2008; 18(6): 065006, 1-8.

[4] Peng W Y, Liao Y S. Study of electrochemical discharge machining technology for slicing non-conductive brittle materials. J. Mater. Process. Technol. 2004; 149: 363-369.

[5] Jain V K, Choudhury S K, Ramesh K M. On the machining of alumina and glass. Int. J. Mach. Tool. Manuf. 2002; 42(11): 1269-1276.

[6] Furutani K, Suzuki K. A Prototype of Electrical Discharge Coater for Wire Saw. Proc. 40th CIRP Int. Seminar Manuf. Syst., Liverpool, UK. 2007; PT-7/1-6.

NEW APPROACHES OF BEVEL SHAPE GENERATION FOR QUARTZ CRYSTAL

Ken-ichiro Horio[1], Jun-ichi Kaneko[1], and Tsugio Yamazaki[1]
[1]Mechanical Engineering Department
Saitama University
Saitama, JAPAN

INTRODUCTION

A crystal of quartz, which is properly cut and polished, is used for wristwatches, clocks, radios, TVs, computers, cell phones and digital cameras as the oscillators, the electric filters or the optical filters. More than two billion crystals are manufactured annually.

The shape of the crystal of quartz has so called bevel shape. That means edges or corners of the device are a few micrometers thinner than center region of that as Figure 1. The bevel shape is effective to reduce spurious and its temperature dependent. The spurious may appear some tens of kilohertz above the wanted series resonance.

The bevel shape has been attained by the barrel polishing technique which is needed long time (more than 200 hours) and result low yielding rate.

The size of the device is continuing smaller. The latest one is a size of less than a millimeter even along long sides of a rectangle. It becomes very hard to manufacture the bevel shape of a small quartz device by the barrel polishing because the weight of device is too light to rotate effectively in the barrel.

We tried new approaches to realize the bevel shape. One is chemical etching technology and the other is spherical lapping technology.

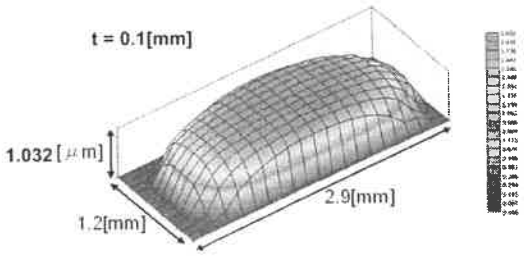

FIGURE 1. The bevel shape

CHEMICAL ETCHING TECHNOLOGY

In chemical etching technology we have investigated about chemical solution, etching conditions, mask materials and masking process.

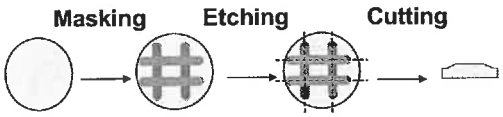

FIGURE 2. Bevel shape formation by chemical etching

Chemical Solution and Etching Conditions

We investigated both hydrofluoric acid and ammonium fluoride as the chemical solution of the process with changing working temperature. We conclude that the hydrofluoric acid is better than the ammonium fluoride as etching rate of the latter was too small to apply it to the process.

Mask Materials and Masking Process

Commercially available photo resist material for the silicon process was used as the mask material in the hydrofluoric acid etching. As bonding strength of the photo resist to the quartz surface is weaker than to the silicon wafer, the mask was easily peeled off or got crinkled even within five minutes.

We have developed several improvements on the masking process, for example, surface treatment on the quartz surface prior to spin coating of photo resists or repetition of the spin coating to get thick resist. Finally we could have 0.1 micrometer height difference derived by etching of 20 minutes.

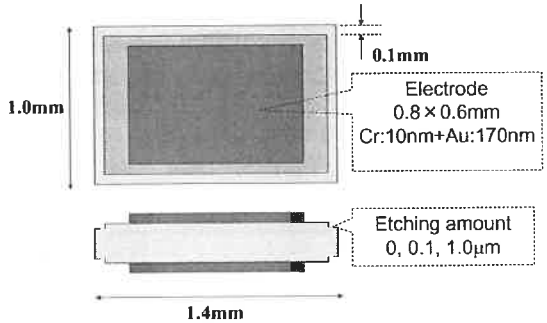

FIGURE 3. Simulation model for revealing the etching amount for the bevel shape

In order to assess the 0.1 micrometer height, we conducted the numerical simulation. The simulator was commercially available one and the size of the model was a practical one (1.4 x 1.0 x 0.03-0.04 mm; Figure 3.) with changing the bevel amount 0, 0.1, 1 micrometer respectively. It is cleared in Figure 4 that the simulation result of the 0.1 micrometer step height is much closer to the result of 1 micrometer height.

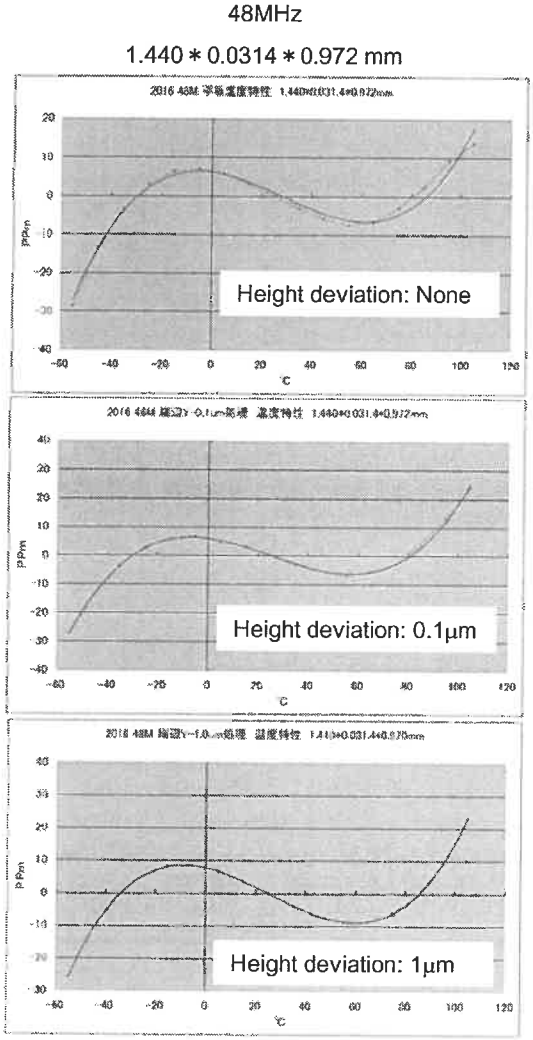

FIGURE 4. Simulation results (temperature dependent). The result of 0.1- micrometer deviation is very similar to that of 1-micrometer deviation.

SPHERICAL LAPPING TECHNOLOGY

We have also tried to apply spherical lapping technology for reducing sides of a specimen. In the spherical lapping technology, both the Oscar type lapping (Figure 5) and the conditioning ring type lapping (Figure 6) have tried.

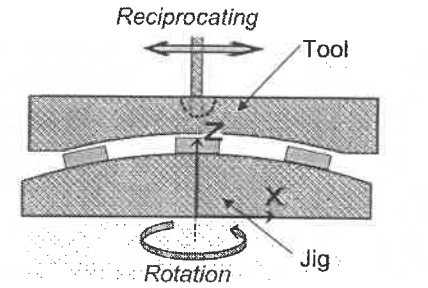

FIGURE 5. Oscar-type process for spherical form generation

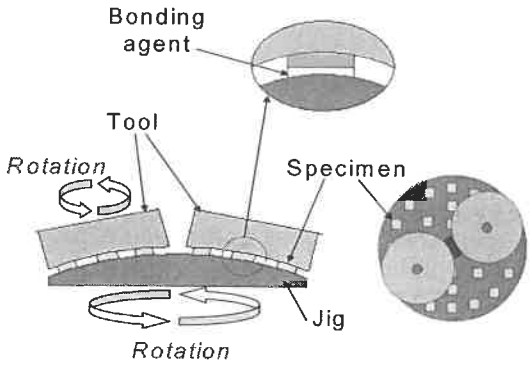

FIGURE 6. Conditioning ring type process for spherical form generation

In both technologies, combination of concave tool and convex jig (specimens holder) is used. After the specimens are glued on the surface of the jig, supply of the slurry and relative motion between the tool and the jig generate bevel shape on the edges of those within a few hours. If you put a lot of specimens on the jig, you can get bevel shaped specimens as much. The yielding rate is expected too much higher than that in the barrel polishing.

One of the differences between the two processes is the relative motion. In the Oscar type, they are rotation and linear reciprocating. In the conditioning ring type process, there are only rotations. The other difference is the size of the tool. The tool for the Oscar type is almost as large as that of the jig. The tool for the conditioning ring type is much smaller than the jig (Figure 6).

Lapping Conditions

We have revealed the influences of the process conditions to manufacturing process. Examined parameters are listed below.

1a. Rotation or reciprocating speed
1b. Range of reciprocation

1c. Slurry concentration
1d. Lapping pressure
1e. Figure accuracy of tool or jig
We have revealed that the yielding rate of the process really depends on the shape accuracy of the tool or the jig.

Bonding Conditions

One of the key technologies of these processes is bonding specimens to the tool. The bonding process consists of bonding agent supply, pre-heating, pressurization and keeping (with pressure). Examined parameters during our bonding trials are listed below.
2a. Consumption of bonding agent (for each specimen)
2b. Processing temperature
2c. Bonding pressure
2d. Duration of keeping
In order to arrange all the specimens normal to the surface of the jigs (specimen holders), we developed a smoother to be used during the bonding process (Figure 7).

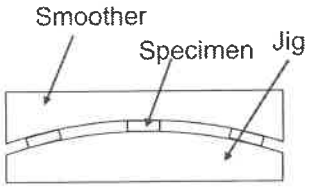

FIGURE 7. Arrangement of a smoother used during the bonding process

Effect of Elastic Deformation

The specimens for this study are very thin up to around 30 micrometers. The elastic deformations during the whole process are not negligible. The transition is thought to be listed below.
The surface of the specimen before the bevel generation process is flat as in Figure 8. After the bonding process the surface of the specimen has some curvature which is a little bit larger than the curvature of the tool. The 'a' indicates the deviation from the ideal flat surface at the end of the specimen.
After the lapping/polishing process the curvature of the specimen usually changes to the curvature of the tool. The 'b' also indicates the deviation from the ideal flat surface at the end of the specimen.
When the specimen is removed from the jig (specimen holder) by, for example, heating, the deformation changes like the spring back in the

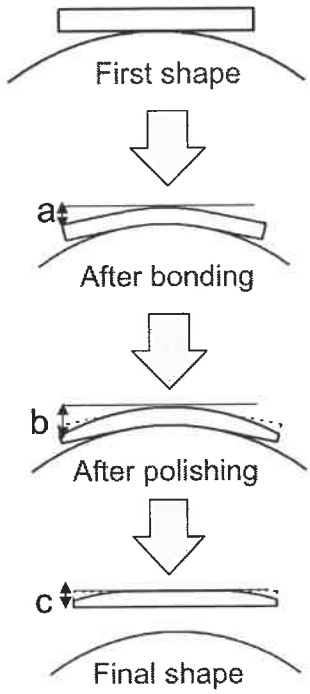

FIGURE 8. Transition model of deformed shape of the specimen during the whole process

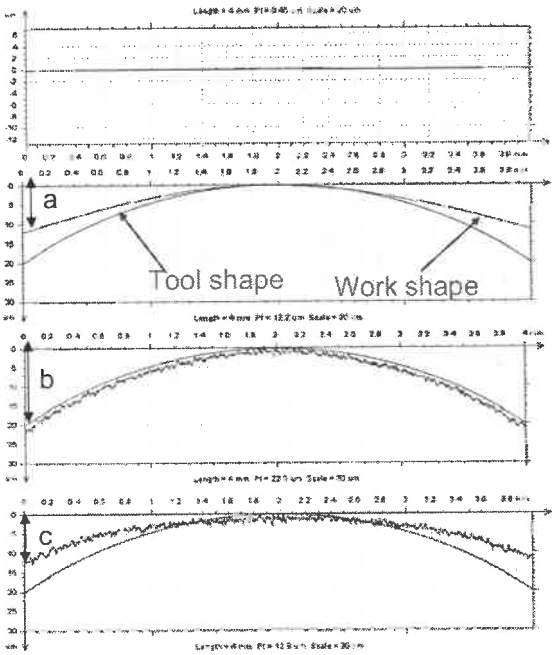

FIGURE 9. Transition of surface profile along the whole process

plastic deformation process. The 'c' also indicates the deviation from the ideal flat surface at the end of the specimen.

Experimental results

Figure 9. shows experimental results of these deformations. The 'a' to 'c' indicate same symbols as in Figure 8.

Discussions

The issue here is how the relation between these three kinds of deformation is.

Figure 10 shows the relation between the 'a' and the 'c' in the various specimens. Figure 10 indicates that the 'c', the final shape of the process, strongly depends on the 'a', deformation during bonding process.

The relation can express a+c=b+3. The 'b' is very constant because it is almost same as the curvature of the tool.

So we can derive the following thing. If you can reduce the deviation of the deformation during bonding process on the specimens upon the jig, you can get very stable bevel shape. That means that you can expect very high yielding rate on bevel generating process.

CONCLUSIONS

0.1 micrometer step for the bevel shape of quartz crystal is enough to reduce spurious and its temperature dependent.

The chemical etching process is applicable to generate the bevel shape.

The spherical lapping technology is also applicable to generate the bevel shape.

The elastic deformation of the specimen during bonding has strong relation to the spring back amount in releasing from the jig after the spherical lapping.

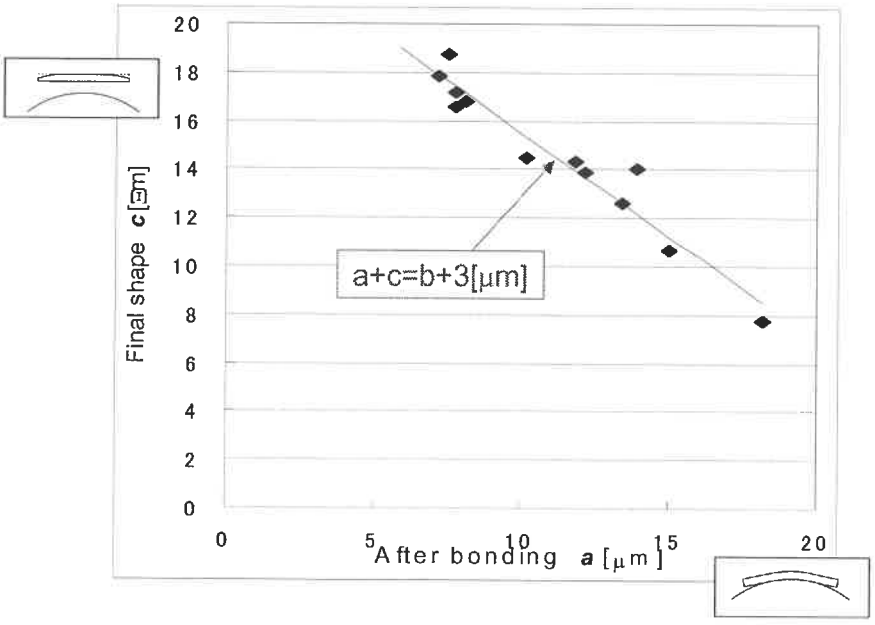

FIGURE 10.Relation between the three kinds of deformation

LOCAL SYNTHESIS OF CARBON NANOTUBES BY ELECTRON BEAM-HEATING CHEMICAL VAPOR DEPOSITION

Hirotoshi Kaito[1], Keisuke Nagato[1], Keigo Kasuya[2], Kensuke Tsuchiya[3], Tetsuya Hamaguchi[1] and Masayuki Nakao[1]
[1]Department of Engineering Synthesis, The University of Tokyo, Tokyo, Japan
[2]Central Research Laboratory, Hitachi Ltd., Tokyo, Japan
[3]Insutitute of Industrial Science, The University of Tokyo, Tokyo, Japan

INTRODUCTION

Carbon nanotubes [1] (CNTs) have many excellent properties, such as nanometer-order thinness, various electric conductivities, good thermal conductivities and high tensile strengths. Figure 1 shows a transmission electron microscopy (TEM) image of single-walled CNTs. Many research studies on the applications of CNTs, such as field-effect transistors, field emitters, gas sensors and composite materials, are carried out. One barrier for these applications is uncontrollability in the growth process. It is difficult to control their position, length, direction and properties.

CNTs can be synthesized by mainly three processes: arc discharge, laser vaporization and thermal chemical vapor deposition (CVD). We focused on CVD because it enables the synthesis of CNTs directly on a substrate. In a conventional CVD process, catalysts on substrates are set in a heating furnace and then hydrocarbon or alcohol gases [2] are introduced in the furnace. These gases, catalysts and heat are essential in growing CNTs. Catalyst patterning has been achieved for the position control of CNT synthesis [3][4]. On the other hand, heat localization is another method for the position control. One of the merits is damage minimization to substrates by heat. Other is that it enables to change the irradiation condition along the position.

Our group has already succeeded in the local synthesis of CNTs with a diameter of 1.5 μm, using a focused Nd:YAG laser (λ =1064 nm) [5]. However, light has a concentration limit due to the diffraction limit. Thus, we use electron beams (EBs) to focus the energy and localize heated regions more precisely.

An electron of an accelerated EB has a very large energy (~ 10 keV) compared with a photon of the laser (~ 1 eV). EBs are used to induce chemical reactions, such as polymerization of resists used for EB lithography and EB-CVD for fabricating nanostructures [6]. However, high-energy EBs can cause defects, such as crystal defects of target substrate. In this study, we determine the conditions of CVD assisted by EB heating (EBH-CVD).

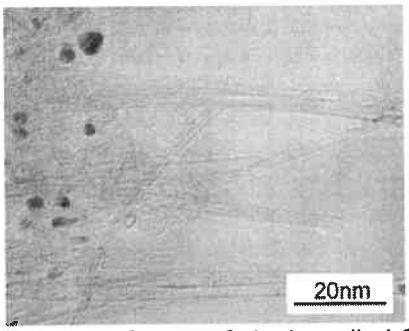

FIGURE 1. TEM image of single walled CNTs

EXPERIMENTAL SETTING

We used an electron beam evaporation system (ULVAC, Inc., EGK-3M) as an EB source. The system has a sufficient power for heating up to the CNT growth temperature. Substrates are set on the evaporation hearth. The temperature of the substrates is measured using a noncontact infrared ray (IR) thermometer. The IR thermometer is calibrated using a ceramic heater and a thermocouple. The experimental setting is shown in figure 2.

PRELIMINARY EXPERIMENT

As a preliminary experiment, we irradiated EBs against CNTs and catalysts at a high vacuum (~ 10^{-2} Pa) to determine whether EBs damage CNTs and catalysts. The acceleration voltage of EBs was 4 kV. The scanning electron

microscopy (SEM) image of CNTs and Raman spectra did not change after EB irradiation up to 900 °C. Defects were observed above 1000 °C. Also, catalysts were not damaged by EBs up to 900 °C, rather CNTs were more synthesized from catalysts irradiated with EBs. Catalysts heated above 1000 °C could not induce a marked CNT synthesis. Both defects were probably produced by overheating. These results indicate that EBs we used had no negative effect on CNTs and catalysts.

EBH-CVD CONDITIONS

CVD requires hydrocarbon or alcohol gas (> 10 Pa), but EB emission requires a high vacuum (~ 10^{-2} Pa). Thus, it is essential to appropriately set the gas pressure to meet both requirements. We set the substrate in a cavity and introduced the gas with a thin nozzle (internal diameter of 0.58 mm) to maintain the gas pressure. With this system, the gas pressure around the substrate was maintained sufficiently high for CNT growth and sufficiently low around the EB emitter. Figure 3 shows the nozzle and substrate arrangement. To validate the gas condition, CVD was conducted using a ceramic heater instead of EBs. Catalysts were Fe/Co nanoparticles supported on zeolite. The chamber was vacuumed to 2.7 $\times 10^{-2}$ Pa with a turbomolecular pump and ethanol was introduced with the nozzle at 4 sccm. Then the substrate was heated at 800 °C for 5 min. Synthesized CNTs were observed by SEM.

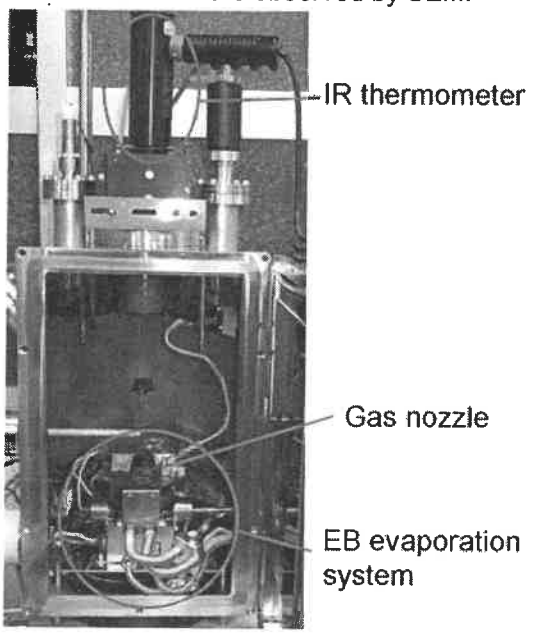

FIGURE 2. EB evaporation system (below) and thermometer (upper) used in this experiment

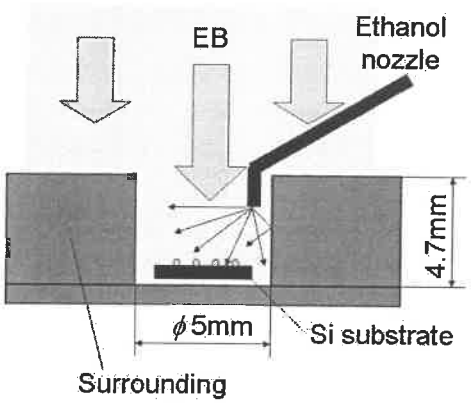

FIGURE 3. Nozzle and substrate arrangement

EXPERIMENT 1

Next, we conducted CVD using EBs as a heat source. Fe/Co nanoparticles supported on zeolite were put on a Si substrate, and the substrate was set on an evaporation hearth surrounded by a metal cavity. The chamber was vacuumed by a turbomolecular pump. When the chamber was vacuumed to 2.7 × 10^{-2} Pa, ethanol vapor was supplied by the thin nozzle at 4 sccm. The entire ethanol flow pipe was heated up to 50 °C in order to stabilize ethanol vapor. Then, EBs were irradiated with an acceleration voltage of 4 kV. The heating temperature was varied to 600, 700, 800, 900, and 1000 °C. The surface temperature was maintained for 5 min and then the EB system was turned off. SEM images of the substrate are shown in figure 4. CNTs were observed from 700 to 1000 °C. CNTs were observed more likely at the edge of the substrate than at the center. Raman spectra are shown in figure 5. The excitation wavelength was 488 nm. The G-band (1590 cm^{-1}) originating from the graphite structure was sharper from 700 to 900 °C. The desirable temperature ranged from 700 to 900 °C. This tendency is similar to CVD conducted in the furnace (alcohol catalytic (AC) -CVD). The G-band compared with the D-band (about 1350 cm^{-1}) originating from amorphous carbon or crystal defects was more distinct at the edge of the substrate than at the center. The D*-band (1610 cm^{-1}) also originating from crystal defects was observed at the center of the substrate. The radial breathing mode (RBM: about 150 to 300 cm^{-1}) detected only at the edge of the substrate indicates the presence of single-walled CNTs. These results indicate that the CNT growth condition was better at the edge than at the center. Because the edge of the substrate was potentially blocked from EBs by the cavity wall, EBs might have disturbed the growth of CNTs.

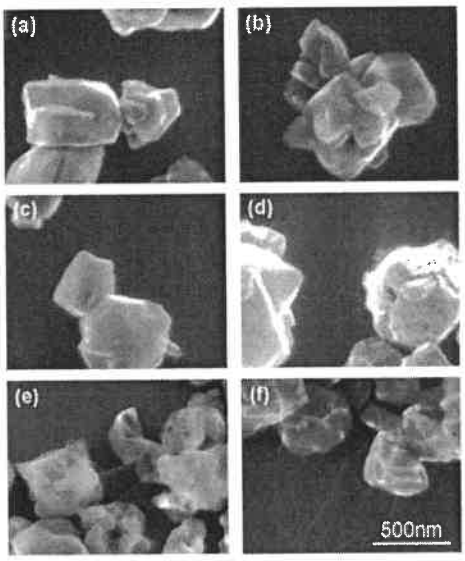

FIGURE 4. SEM image of CNTs synthesized by EBH-CVD at different temperatures and positions. (left: center of substrate; right: edge, (a),(b); 600 °C, (c),(d); 800 °C, (e),(f); 1000 °C)

EXPERIMENT 2

Then, we attempted EBH-CVD with sputtered Co catalysts because zeolite may have covered catalysts from EB irradiation. We sputtered Co to a SiO_2 thermally oxidized Si substrate by radio frequency magnetron sputtering. The Co film thickness was less than 1 nm. We conducted EBH-CVD as described previously. The heating temperature was varied to 700, 800, and 900 °C. CNT-like substances were synthesized only at 800 °C. Figure 6 shows the surface of the substrate. Raman spectra were too weak to detect CNTs. CNT synthesis might be disturbed by EBs and growth rate might be positive only at 800 °C.

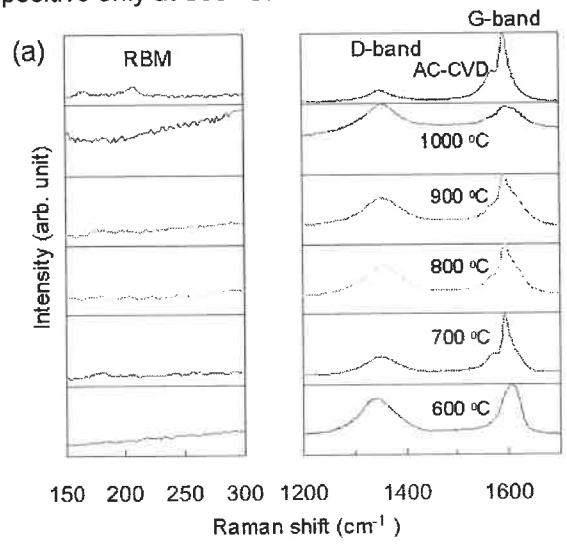

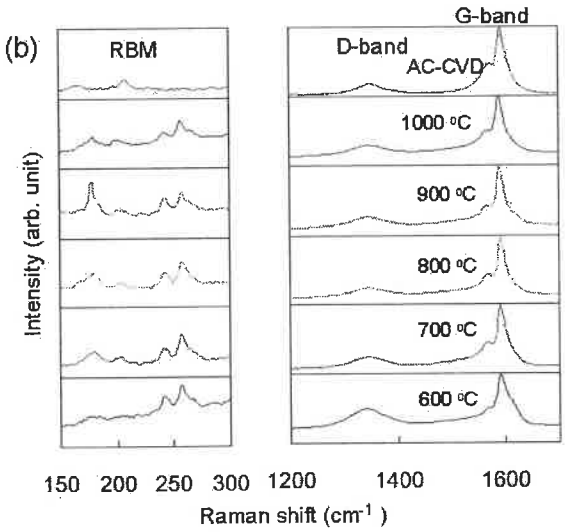

FIGURE 5. Raman spectra from specimen (a) center of substrate, (b) edge

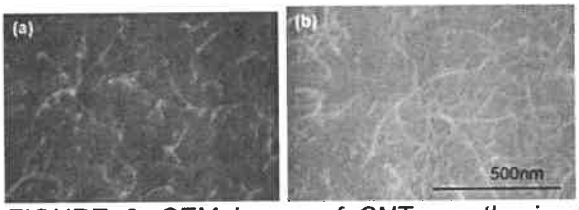

FIGURE 6. SEM image of CNTs synthesized from sputtered Co. (a) EBH-CVD at 800 °C and (b) CVD in furnace at 900 °C, 1 kPa ethanol

ESTIMATION OF HEAT LOCALIZATIOIN

In this study, we used EBs with a spot diameter of 5 mm. We calculated the possibility of heat localization using focused EBs. As a starting point, we estimated heat transfer properties. We set simple boundary conditions: the generation of heat is constant at the area of half sphere, the temperature of infinite distance is fixed, heat radiation is ignored and a steady state is assumed. With such approximation, we could use one-dimensional spherical symmetry, and thus the heat transfer equation became

$$\lambda \frac{1}{r^2}\frac{\partial}{\partial r}\left(r^2 \frac{\partial T}{\partial r}\right) + w = 0 ,$$

where T: temperature, r : distance from the center, λ: thermal conductivity, w : heat generation per unit volume.

This equation can be analytically solved.

$$T = T_\infty + \frac{w r_b^2}{6\lambda}\left\{3 - \left(\frac{r}{r_b}\right)^2\right\} \qquad (0 \le r \le r_b)$$

$$T = T_\infty + \frac{wr_b^3}{3\lambda r} \qquad (r_b \le r \le r_\infty)$$

where T_∞ : temperature at infinite distance,

r_b : boundary distance of heat generation area

From this solution, thermal conductivity affects largely to heating temperature. One limiting factor for focusing EBs is the space charge effect. If the current density of EBs increases and the distance between electrons decreases sufficiently, the beam diameter increases. To reduce this effect, one may support heating by a heater and reduce beam current or accelerate electrons at a higher voltage. However, if the acceleration voltage increases, EBs penetrate the substrate more deeply and heating area increases. One example is that a 10 keV electron penetrates Si about 1 μm. To avoid EB penetration, one may use a material with a large atom number. Still, the fundamental solution is to use a lower acceleration voltage. However, if the acceleration voltage is too low, the EB density attenuates instantly through CVD gas atmosphere. From this viewpoint, the realistic acceleration voltage is around 10 kV.

As far as one-dimensional spherical symmetry is true, our estimated EB heating conditions are as follows: an acceleration voltage of 10 kV, a beam diameter of 200 nm, a beam current of 2.7 μA, a thermal conductivity of 23.0 $W/m \cdot K$ (material model is Hf) and 300 K at infinite distance. Under these conditions, the central temperature may be 700 °C and the area higher than 600 °C is about 150 nm in diameter. The temperature distribution is shown in figure 8.

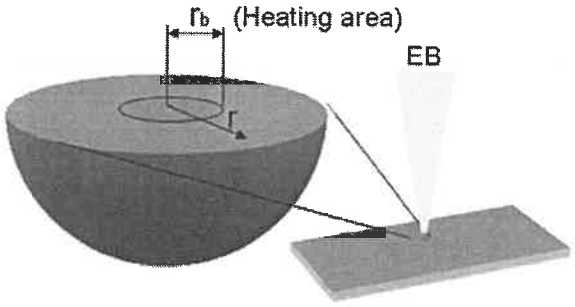

FIGURE 7. Calculation model for heat transfer

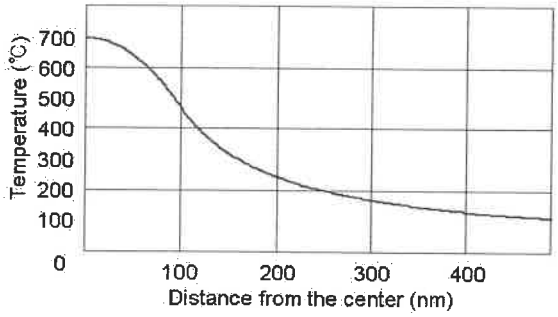

FIGURE 8. Calculated temperature distribution

CONCLUSION

We have successfully synthesized CNTs by EBH-CVD. We confirmed that the optimum temperature of EBH-CVD does not differ from that of standard thermal CVD. Thus, the energy from EBs may not assist chemical reactions, rather EBs with an acceleration voltage of 4 kV may negatively affect on the synthesis of CNTs. The EBs used in this study were not focused and we calculated the temperature distribution when EBs were focused on the nanoscale.

ACKNOWLEDGEMENT

Catalysts supported on zeolite and a Raman spectrum analyzer were provided by Maruyama Lab. at The University of Tokyo. We would like to thank Prof. S. Maruyama and Ms. Z. Zhang.

REFERENCES

[1] Iijima S. Helical microtubules of graphitic carbon. Nature. 1991; 354: 56-58

[2] Maruyama S et al. Low-temperature synthesis of high-purity single-walled carbon nanotubes from alcohol. Chemical Physics Letters. 2002; 360: 229-234

[3] Wei B Q et al. Organized assembly of carbon nanotubes. Nature. 2002; 416: 495-496

[4] Ishida M et al. Diameter-controlled carbon nanotubes grown from lithographically defined nanoparticles. Japanese Journal of Applied Physics. 2004; 43: 1356-1358

[5] Kasuya K et al. Rapid and localized synthesis of single-walled carbon nanotubes on flat surface by laser-assisted chemical vapor deposition. Japanese Journal of Applied Physics. 2007; 46: 333-335

[6] Matsui S, Mito M. Si deposition by electron beam induced surface reaction. 1988; 53: 1492-1494

DEVELOPMENT OF A PRECISE AND QUICK RESPONSE PNEUMATIC PRESSURE REGULATOR AND ITS APPLICATION TO PNEUMATIC VIBRATION ISOLATOR

Tomonori KATO[1], Kotaro Tadano[2], Kenji Kawashima[2], Nobuaki Yamamoto[3], and Toshiharu Kagawa[2]

[1]Tokyo Metropolitan College of Industrial Technology, 1-10-40 Higashi-oi, Shinagawa, Tokyo, Japan

[2]Tokyo Institute of Technology, 4259 Nagatsuta-cho, Midori-ku, Yokohama, Kanagawa, Japan

[3]Tokyo Meter Co., LTD, 461 Imai-Minamicho, Nakahara-ku, Kawasaki, Kanagawa, Japan

INTRODUCTION

Pneumatic vibration isolators are widely used to isolate precision machinery. The air-springs which are usually employed can support a high pay load using relatively low energy[1].

Regulators are an essential component of pneumatic systems. In order to control the pressure of flammable gases, where leakage must be prevented, gas governors are used. However, as leakage is acceptable in most other pneumatic systems, relief type pressure regulators are widely used[2]. In order to control the supply pressure to vibration isolators, standard commercial precision pressure regulators are often used. However, the response of most of these is relatively slow. For regulators for ultra-precision applications, the need for quick response and accuracy must be addressed. The standard approach to negate the deficiencies of commercially available regulators is to install an accumulator tank between the regulator and the isolator servo valve. However, even this is largely inadequate. Herein, a new type of pneumatic pressure regulator is proposed which exhibits high precision and quick response. The regulator consists of an isothermal chamber, a spool type servo valve (SP valve), a pressure sensor, a quick response laminar flow sensor (QFS), and a pressure differential sensor (PD sensor) as developed by the authors.

In this paper, the structure and design of the proposed pressure regulator are explained. Secondly, performance tests on a fabricated prototype are conducted. Thirdly, to evaluate the effectiveness of the regulator, it is applied to the control of the supply pressure to an actively controlled pneumatic vibration isolator.

DEVELOPMENT OF A PRECISE AND QUICK RESPONSE PNUEMATIC PRESSURE REGULATOR

Structure of The Proposed Pressure Regulator

A schematic and photograph of the proposed pressure regulator are shown in Figs. 1 and 2, respectively. It is composed of a SP valve (FESTO MPYE-5-M5-SA), a QFS, an isothermal chamber, a PD sensor and a pressure sensor (TOYODA PD-64S500K). Though the SP valve had 5 ports, the valve was used as a 3 port servo valve, i.e. supply, control and exhaust ports. The unused ports were plugged.

The 'Isothermal Chamber' is the result of previous research[3]. This is filled with metal wool which leads to a nearly isothermal state change in the chamber. The isothermal chamber used herein has a volume V of 1.0×10^{-3} m^3. A QFS is a differential pressure type flow sensor and its dynamic characteristics were calibrated using an "unsteady flow generator" in previous research[4]. The 'PD sensor' measures the pneumatic pressure differential with high precision and a quick response[5]. The resolution of the PD sensor used in this research is about 200 Pa/s, and the break point frequency of the sensor is about 190 Hz.

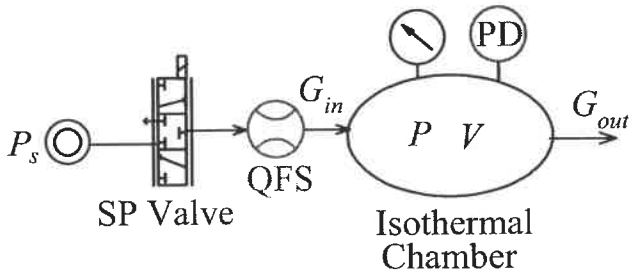

Figure 1: Regulator schematic

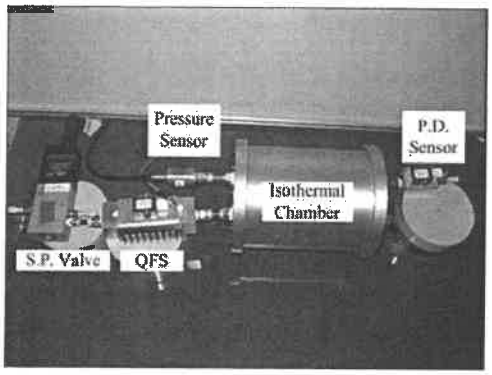

Figure 2: Photograph of the regulator

Controller Design

The purpose of the pressure regulator developed herein is to maintain the pressure in the isothermal chamber at a set value. The component to be supplied, i.e. the pneumatic vibration isolator, is connected downstream of the isothermal chamber. The important point is that, irrespective of upstream or downstream disturbances, the pressure in the isothermal chamber should be maintained. A block diagram of the proposed pressure regulator is shown in Fig. 3. The SP valve characteristics are approximated to the linear constant *Kv*. There is one main loop and two minor loops. The main loop is a pressure feed back loop. One of the minor loops, "Minor Loop 1", is a flow rate control loop which compensates for the nonlinear characteristics of the SP valve and can also reduce the affects of supply pressure variation[6]. The other minor loop, "Minor Loop 2", estimates and compensates the output flow rate Gout (an upstream disturbance for pressure control).Noting the isothermal conditions, total differentiation of the state equation for the air leads to:

$$G_{in} - G_{out} = \frac{V}{R\theta}\frac{dP}{dt} \tag{1}$$

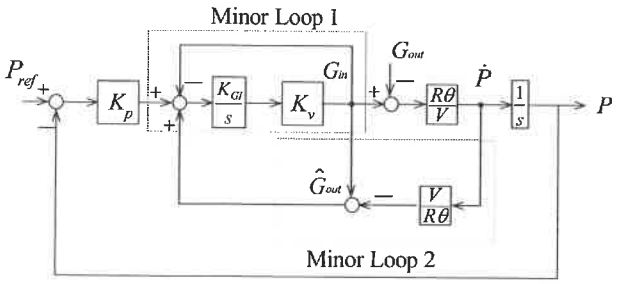

Figure 3: Block diagram of the proposed pressure regulator

Therefore, by measuring Gin using the QFS and measuring dP/dt using the PD sensor, $\hat{G}_{out}$, which is the estimated value of *Gout* can be calculated:

$$\hat{G}_{out} = G_{in} - \frac{V}{R\theta}\frac{dP}{dt} \tag{2}$$

By positively feeding $\hat{G}_{out}$ back to the flow rate controller, when a disturbance occurs downstream of the isothermal chamber, the pressure *P* recovers immediately.

With reference to Fig. 3, assuming that the time constants of the minor loops are much shorter than that of the main loop, the transfer function of the main loop can be expressed:

$$\frac{P}{P_{ref}} = \frac{1}{1+T_p s} = \frac{1}{1+\frac{V}{K_p R\theta}s} \tag{3}$$

In order to make T_p=0.1 s, the proportional controller gain K_p is set at 1.19×10^{-7} kg/(Pa s). Suppose the flow rate loop (Minor Loop 1) has a reference value of G_{ref} and an integral controller gain of K_{gi}, the transfer function can be written:

$$\frac{G_{in}}{G_{ref}} = \frac{1}{1+T_G s} = \frac{1}{1+\frac{1}{K_v K_{g_i}}s} \tag{4}$$

Here, to be accurate, K_v is nonlinear. In this research, the SP valve (FESTO MPYE-5-M5-SA) is subject to the conditions that the pressure at the supply port is 500 kPa [abs] and the pressure at the control port is about 300 kPa [abs]. For these conditions, K_v can be approximated to 2.155×10^{-4} kg/(s V). As mentioned above, the time constant T_G of Minor Loop 1 should be much smaller than T_p. K_{gi} is set to 6.19×10^{5} (s^2 V)/kg which leads to a value of T_G of about 0.0075 s. Consequently, T_p:T_G=15:1. The sampling time of the controller is 0.1 μs.

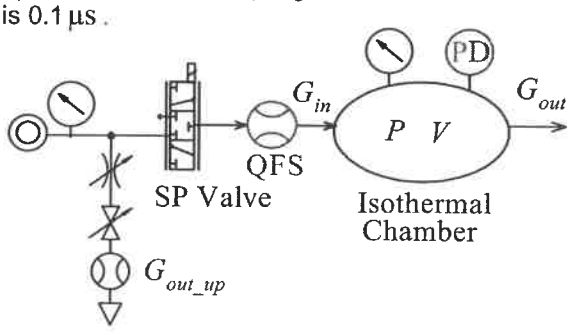

Figure 4: Experimental apparatus to test the affection of the supply pressure change

PERFORMANCE TEST OF THE REGULATOR

Experimental Setup

To test the performance of the proposed pressure regulator, the apparatuses shown in Fig. 4 was conceived. With reference to Fig. 4, in order to create an upstream disturbance, a diverging flow channel, a hand valve operated variable restriction, and a rotor type flow meter were employed. As a basis for comparison, the same experiments were conducted on a commercially available precision regulator.

Upstream Disturbance

Using the experimental apparatus shown in Fig. 4, P_{sv} is first set to 300 kPa [abs]. At t=30 s, after the pressure P settles, the hand valve is opened. The experimental results for P_s and P are given in Figs. 5 and 6, respectively. Fig. 6 clearly shows that the proposed regulator maintains the desired pressure very accurately and the disturbance at t=30 s has no discernable effect. In contrast, the commercially available precision regulator exhibits a steady state error of about 500 Pa which increases further subsequent to the disturbance.

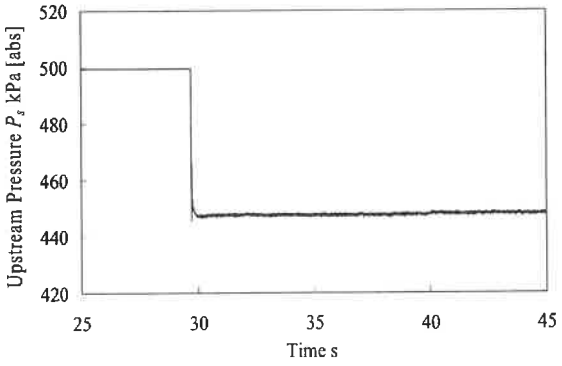

Figure 5: Response of P_s to an upstream disturbance

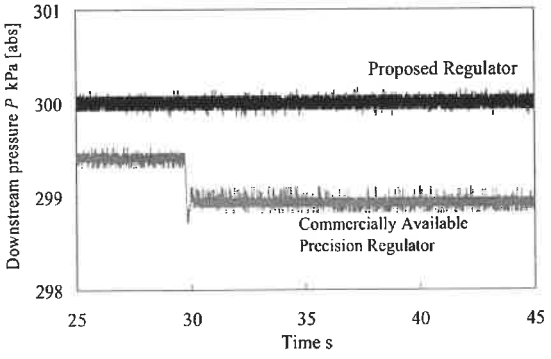

Figure 6: Response of P to an upstream disturbance

APPLICATION OF THE DEVELOPED REGULATOR TO AN PNUEMATIC VIBRATION ISPLATOR

Air Spring System

In this chapter, the proposed pressure regulator is applied to the supply pressure control of an actively controlled pneumatic vibration isolator for precision machinery. An actively controlled pneumatic isolation table consists primarily of a payload, air-springs, nozzle flapper type servo valves, displacement sensors, acceleration sensors and a controller. To demonstrate the effectiveness of the proposed method, experiments were conducted using the simple apparatus shown in Fig. 7. The payload is supported by 8 air-springs (4 vertical, 4 horizontal) . Fig. 8 shows a block diagram of the active control system for the vibration isolator. The relative position and absolute acceleration of the table are fed back. The characteristics of the nozzle flapper type servo valve (NF valve) can be represented using a lagged pressure integrator. The resolutions of the displacement and acceleration sensors are 1 μm and 9.8×10^{-6} m/s^2, respectively.

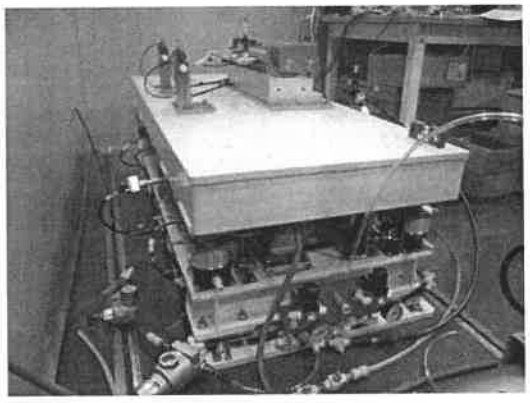

Figure 7: Picture of the pneumatic vibration isolator employed herein

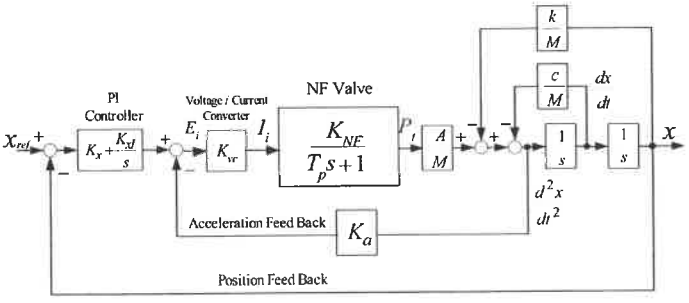

Fig. 8 Block diagram of the active control system for the vibration isolator

Experimental Procedure

As shown in Figs. 9, the proposed pressure regulator is attached upstream of the NF valve. The supply pressure is about 700 kPa [abs]. Firstly, the displacement of the table was set to a reference value of x_{sv}=3.48 mm. At t=5 s, the hand valve was opened and a disturbance created. The disturbance flow rate was about 6.47×10^{-3} kg/s. At t=20 s, the hand valve was closed. This type of disturbance imitates the usage of other machinery in a factory which causes supply pressure reduction and flow pulsation. For comparison, the experiment was repeated with the commercially available precision regulator installed in place of the proposed regulator. The displacement and the acceleration of the table were recorded in both experiments.

Experimental Results

The experimental result for displacement is shown in Fig. 10. In the case of the commercially available precision regulator; soon after the hand valve was opened, the displacement changed by about 3 μm.

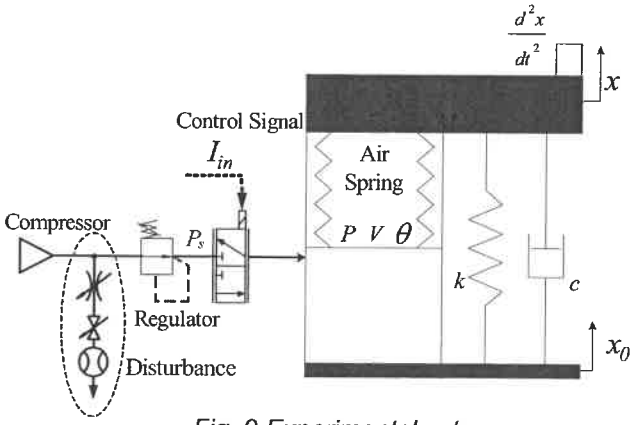

Fig. 9 Experimental setup

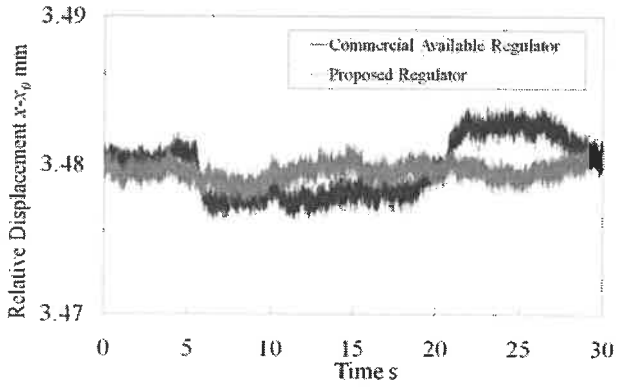

Fig. 10 Experimental results (Displacement)

This indicates that the upstream pressure reduction leads to a downstream pressure reduction. In contrast, for the proposed regulator, the displacement shows little discernable affects from the disturbance.

CONCLUSION

Herein, a new type of pneumatic pressure regulator, composed of an isothermal chamber, a spool type servo valve, a quick response laminar flow sensor, and a pressure differentiator was proposed and tested. After the performance of a prototype pressure regulator was confirmed through testing, it was applied to the supply pressure control for an actively controlled pneumatic vibration isolator. Compared with a commercially available precision pressure regulator, the superiority of the proposed regulator was clearly visible, especially in terms of avoiding affects from disturbances upstream or downstream of the regulator.

REFERENCES

[1] Snowdon, J. C., "Vibration Isolation: Use and Characterization", J. Acoustical Soc. Am., 1979, 66, pp. 1245-1279.

[2] Blain, W., "The Analysis and Design of Pneumatics Systems", Wiley, 1967.

[3] Kawashima K., Kagawa T., Fujita T., "Instantaneous flow rate measurement of ideal gases", Trans. ASME, J. Dyn. Syst. Meas. Control, 2000, 122, pp. 174-178.

[4] Kawashima K., Kagawa T., "Unsteady flow generator for gases using an isothermal chamber", Measurement, 2003, 33, pp. 333-340.

[5] Kawashima K., Kato T., Yamazaki Y., Yanagisawa M., Kagawa T., "Development of slit type pressure differentiator using an isothermal chamber", Meas. Science and Technology, 2005, 16, pp. 1150-1156.

[6] Kato T., Funaki T., Kawashima K., Kagawa T., "Active Control of Vibration Isolation Table with Quick Flow Sensor", Proc. of International Fluid Power Conference (IFK2006), Vol.1, pp. 109-120

MULTISECTIONAL SYNTHESIS OF TUNGSTEN OXIDE NANOWIRES USING MICROPATTERNED LAYER FOR FIELD-EMISSION DISPLAYS

Hiroki Moritani[1], Keisuke Nagato[1], Yusuke Kojima[1], Masaki Furubayashi[1], Keigo Kasuya[2], Tetsuya Hamaguchi[1], and Masayuki Nakao[1],
[1]Department of Engineering Synthesis,
The University of Tokyo,
Tokyo, Japan
[2]Central Research Laboratory,
Hitachi Ltd.,
Tokyo, Japan

INTRODUCTION

Tungsten oxide nanowires (Figure 1(a)) are one-dimensional nanostructures, with diameters of 10-100 nm and a length of about 1 μm. The nanowires are spontaneously grown by the simple annealing of pure tungsten materials up to about 800 °C. Since the nanowires have high aspect ratios and are easily fabricated, they have attracted considerable attention as promising materials for field emitters of field-emission displays (FEDs) [1-3]. However, since the nanowires grow randomly, field emission is not uniform in a pixel (Figure 1(b)) [4]. Therefore, it is necessary to control the growth section in order to utilize the nanowires for FEDs. Moreover, heating the entire system for the synthesis of the nanowires may damage the system. To resolve these problems, multisectional heating has been attracting considerable attention. We proposed a new multisectional heating process using a micropatterned layer and local current heating (Figure 2).

MULTISECTIONAL HEATING USING MICROPATTERNED LAYER AND LOCAL CURRENT HEATING

We used W/Cr films sputtered with thicknesses of 200/50 nm on Si substrates covered with an oxide layer (SiO_2) as samples. The thickness of the SiO_2 layer was 1 μm. These films were deposited by standard radio frequency magnetron sputtering. The Cr film prevented the W film from detaching from the Si substrates. Ar was used as sputtering gas. The base pressure of the sputtering chamber was 1×10^{-2} Pa and the sputtering pressure was 5×10^{-1} Pa. The deposition rate of tungsten was 13 nm/min. After deposition, we covered each sample with a positive photoresist (AZ-1500 (20cP), AZ Electronic Materials) using a spin coater. The thickness of the photoresist was 1 μm. Each sample was exposed to ultraviolet light through a photomask with the pattern of the micropatterned layer. The photoresist exposed was removed using a photoresist developer and the W/Cr film was etched using etchants. After etching, the photoresist that remained on the pattern was removed using a photoresist remover.

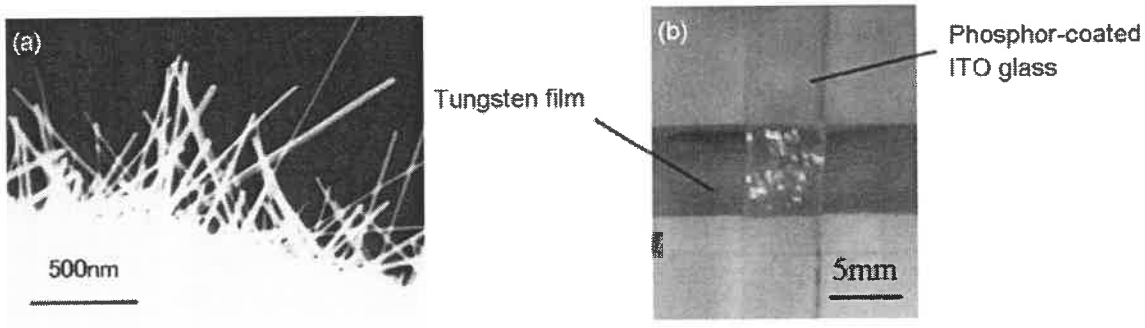

FIGURE 1. (a) SEM image of tungsten oxide nanowires.
(b) Fluorescence image of field emission through phosphor-coated ITO glass and tungsten film with tungsten oxide nanowires.

To date, we have successfully synthesized tungsten oxide nanowires simultaneously on a regular 20 by 20 array of narrow sections with a pitch of 15 μm using the micropatterned layer (Figures 3(a-d)) [5]. This synthesis required a voltage of 19 V and a current of 0.49 A. The vacuum chamber maintained an oxygen atmosphere of 4×10^{-2} Pa.

Figure 4 shows a schematic of the application of the multisectional synthesis of tungsten oxide nanowires for manufacturing FEDs. The regions of the nanowires are controlled in a pixel by the micropatterned layer. Moreover, by using the micropatterned layer as the lower electrode of a display, wiring systems are not required.

RELATIONSHIP BETWEEN DISPERSION DEGREE OF TUNGSTEN OXIDE NANOWIRES AND FIELD-EMISSION PROPERTIES

Generally, the dispersion degree of the emitters significantly affects their field-emission properties for the concentration of the electric field (Figures 5(a-b)) [6, 7]. To realize FEDs with nanowires synthesized using local current heating, the dispersion of the synthesis sections must be optimized. As a preliminary experiment, we studied the relationship between the dispersion degree of the nanowires and the field-emission properties.

In this study, we developed islandlike patterns of W/Cr films to disperse the nanowires deliberately (Figure 6). We varied the dispersion degree of the nanowires by varying the pitch of the patterns. We synthesized the nanowires on each pattern using a vacuum furnace and investigated the conversion of their field-emission properties.

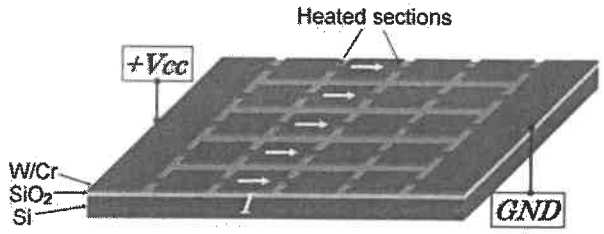

FIGURE 2. Schematic of micropatterned layer and local current heating.

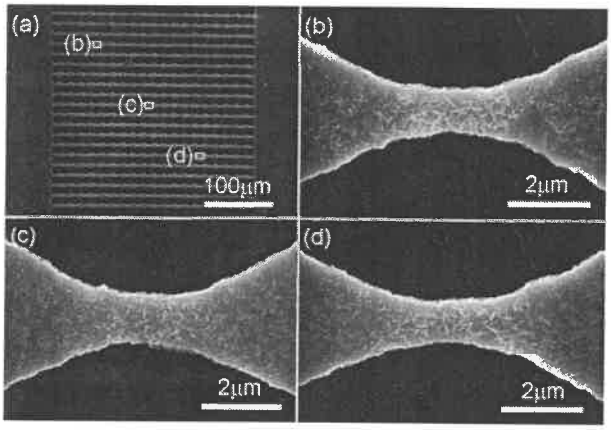

FIGURE 3. SEM images of regular array of tungsten oxide nanowires (20 by 20 array with pitch of 15 μm). (a) Entire image of micropatterned layer and (b-d) magnified images of synthesized regions.

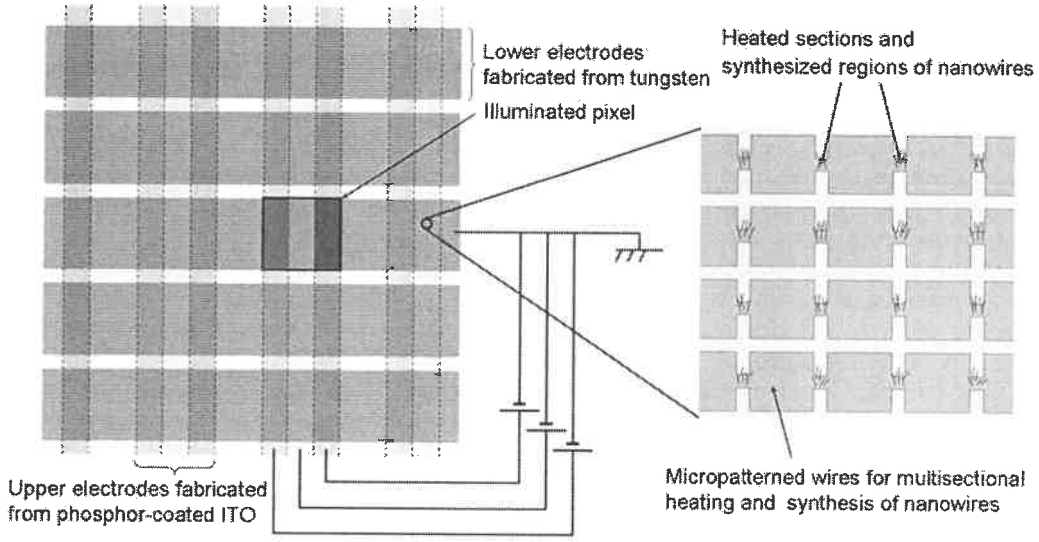
Lower electrodes fabricated from tungsten
Illuminated pixel
Heated sections and synthesized regions of nanowires
Upper electrodes fabricated from phosphor-coated ITO
Micropatterned wires for multisectional heating and synthesis of nanowires

FIGURE 4. Application of multisectional synthesis of tungsten oxide nanowires for manufacturing FEDs.

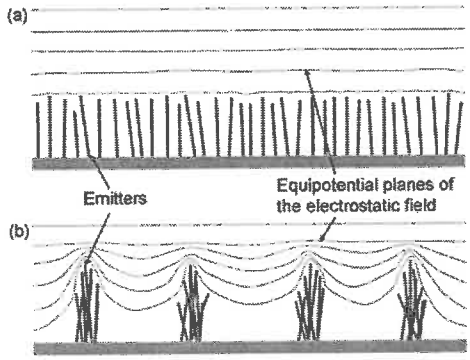

FIGURE 5. Schematic of effect of dispersion degree of emitters on concentration of electric field. Emitters exist (a) uniformly and (b) dispersively.

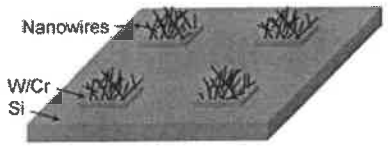

FIGURE 6. Schematic of tungsten oxide nanowires synthesized on islandlike patterns of W/Cr films.

EXPERIMENTAL

We fabricated patterns of W/Cr films using a lift-off process. We covered a Si wafer with a positive electron beam (EB) resist (ZEP-520A, ZEON Corporation). The thickness of the resist was 400 nm. The wafer was exposed to EBs with a program to write the micropatterned layer. The EB resist exposed was removed using an EB resist developer. We sputtered W/Cr films on the wafer. The sputtering conditions were the same as those in the experiment using local current heating, except the deposition rate of 6 nm/min. After deposition, we lifted off the W/Cr films using toluene and a supersonic cleaner.

We developed four patterns in this experiment (Figures 7(a-d)). The pitches of 1 × 1 μm^2 squares were (a) 2, (b) 5, (c) 10, and (d) 15 μm. The patterned area was 5 × 5 mm^2. We annealed the samples in the vacuum furnace at a temperature of 560 °C by infrared heating, while controlling the oxygen pressure to 4 × 10^{-2} Pa by introducing oxygen gas. The base pressure of the vacuum furnace was 3 × 10^{-3} Pa. To investigate the field-emission properties, the samples were set in a vacuum chamber through ITO glass and connected with a high voltage power supply (Figure 8). The gap of the samples and ITO glass was 50 μm. The base pressure of the vacuum chamber was 2 × 10^{-3} Pa.

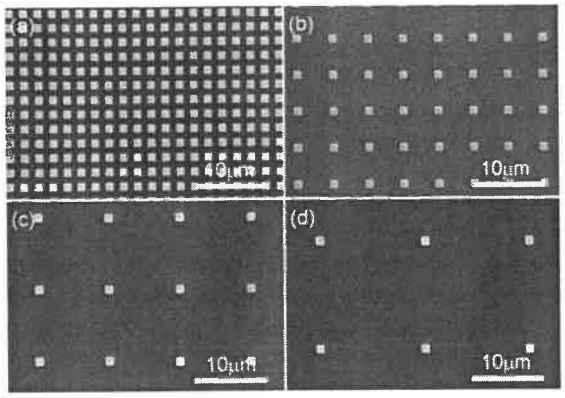

FIGURE 7. SEM images of 1 × 1 μm^2 square patterns with pitches of (a) 2, (b) 5, (c) 10, and (d) 15 μm.

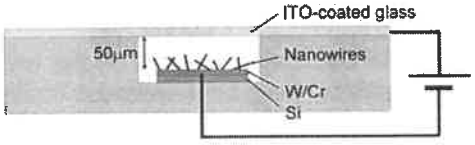

FIGURE 8. Schematic of field-emission experiment.

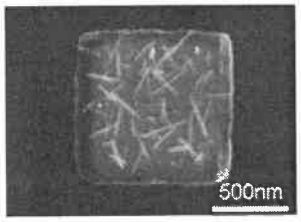

FIGURE 9. SEM image of one of square patterns after annealing.

RESULTS AND DISCUSSION

Figure 9 shows the SEM image of one of the square patterns after annealing. Tungsten oxide nanowires were synthesized on the square patterns. The length of the nanowires was 100-500 nm, and the number of nanowires on one square was 60-80. Figure 10 shows the current density versus electric field (I-V) plot and Fowler-Nordheim (F-N) plot of the samples. In the sample with a pitch of 5 μm, current was first detected at an electric field of about 35 V/μm. In the samples with pitches of 10 and 15 μm, current was first detected at an electric field of 20-30 V/μm. The maximum current densities obtained immediately before discharging were 22 μA/cm^2 with a 5 μm pitch, 65 μA/cm^2 with a 10 μm pitch, and 82 μA/cm^2 with a 15 μm pitch. Generally, the longer the pitch, the better the field-emission properties. This tendency agrees with the general relationship

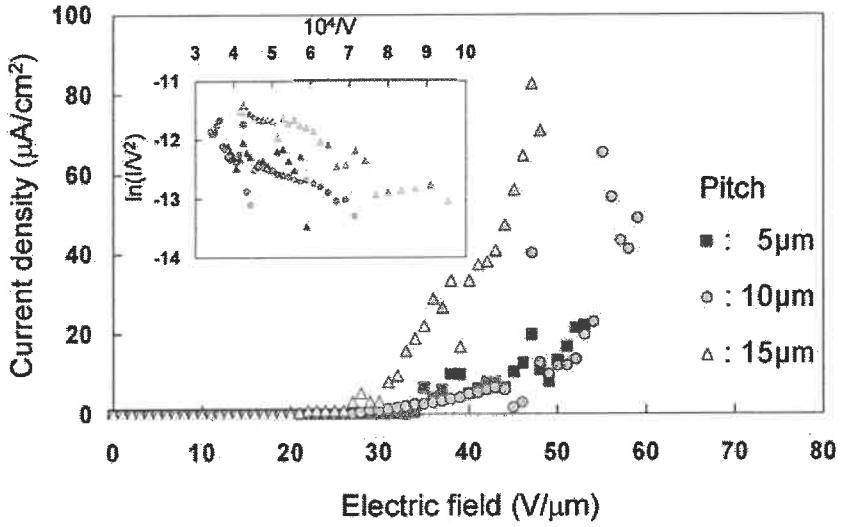

FIGURE 10. Current density versus electric field (I-V) plots of samples. The inset shows Fowler-Nordheim (F-N) plots of samples.

between the dispersion degree of the emitters and field-emission properties. If we use a pattern with a longer pitch, field-emission properties will become better. In the sample with a 2 μm pitch, electric discharging was observed before field emission.

CONCLUSION

We studied the relationship between the dispersion degree of tungsten oxide nanowires and field-emission properties. We used the nanowires synthesized on the patterns of W/Cr films as the samples. By varying the pitch of the patterns, we varied the dispersion degree of the nanowires. We observed that the sample with a long pitch resulted in better field-emission properties. In this technique, we can optimize the dispersion of the synthesis sections for local current heating.

ACKNOWLEDGEMENT

The EB lithography for a lift-off process was carried out using The University of Tokyo VLSI Design and Education Center (VDEC)'s EB writer (F5112+VD01) donated by ADVANTEST Corporation.

REFERENCES

[1] J. Zhou, L. Gong, S. Z. Deng, J. Chen, J. C. She, N. S. Xu, R. Yang, and Z. L. Wang: "Growth and field-emission property of tungsten oxide nanotip arrays", Appl. Phys. Lett. 87 (2005) 223108.

[2] J. Zhou, Y. Ding, S. Z. Deng, L. Gong, N. S. Xu, and Z. L. Wang: "Three-dimensional tunsten oxide nanowire networks", Adv. Mater. 17 (2005) 2107.

[3] R. Seelaboyina, J. Huang, J. Park, D. H. Kang, and W. B. Choi: "Multistage field enhancement of tungsten oxide nanowires and its field emission in various vacuum conditions", Nanotechnology 17 (2006) 4840.

[4] Y. Kojima, K. Kasuya, T. Ooi, K. Nagato, K. Takayama, and M. Nakao: "Effects of oxidation during synthesis on structure and field-emission property of tungsten oxide nanowires", Jpn. J. Appl. Phys. 46 (2007) 6250.

[5] K. Nagato, Y. Kojima, K. Kasuya, H. Moritani, T. Hamaguchi, and M. Nakao: "Local synthesis of tungsten oxide nanowires by current heating of designed micropatterned wires", Appl. Phys. Express 1 (2008) 014005.

[6] L. Nilsson, O. Groening, C. Emmenegger, O. Kuettel, E. Schaller, L. Schlapbach, H. Kind, J.-M. Bonard, and K. Kern: "Scanning field emission from patterned carbon nanotube films", Appl. Phys. Lett. 76 (2000) 2071.

[7] M. W. Geis, J. C. Twichell, and T. M. Lyszcyarz: "Diamond emitters fabrication and theory", J. Vac. Sci. Technol. B 14 (1996) 2060.

MICRO AND NANO ASSEMBLY TOOLS UTILIZING STANDING WAVE TECHNOLOGY

Bartosz K. Nowakowski[1], Stuart T. Smith[1], Shane C. Woody[2],
[1]Center for Precision Metrology
University of North Carolina at Charlotte
Charlotte, North Carolina, USA
[2]Insitutec Inc.,
Charlotte, North Carolina, USA

INTRODUCTION

This paper will present some observations drawn from our ongoing investigations into the use of standing wave probes for micro-manipulation tools. Generally, a manipulation system will comprise one or more probes that can be maneuvered, like fingers, to pick up and place small components. Such multi-probe devices are often referred to as grippers and/or tweezers. FIGURE 1 is a schematic diagram indicating the major components the tweezers being used to grip a specimen on a substrate. The tweezers is shown in this case as two fibers. The contact forces between components are indicated with the subscripts *G* referring to the tweezers (fingers 1 or 2) and specimen, *S* between specimen and substrate and *n* and *t* discriminating normal or tangential forces respectively. In this work, the fingers of the tweezers are built from a tuning fork crystal resonator and a 3 mm long 7 µm diameter carbon fiber, see FIGURE 2. Performance and details of operation can be found in [1] while the use of these probes for tweezers applications is discussed in [2].

Over the last two years a number of studies have been undertaken to better understand the issues and develop solutions for assembly of micro-scale systems in ambient environments. Some issues that are addressed by this research and will be presented at the conference include

- Meniscus dominated, single fiber and specimen interactions.
- Adhesion forces between probe/specimen and specimen/substrate.
- Effects of substrate material, ambient conditions and surface roughness on adhesion forces.
- Two probe tweezer studies for picking and placing glass micro spheres.
- Optimization of probes for grip and release.

Technologies to facilitate micro and nano assembly represent a tool for building structures from individual parts from components manufactured by multiple processes to enable assembly of systems. To achieve this, an assembly system must incorporate many functions such as force sensing, object detection, metrology, manipulation, modification and energy delivery. In the world dominated by

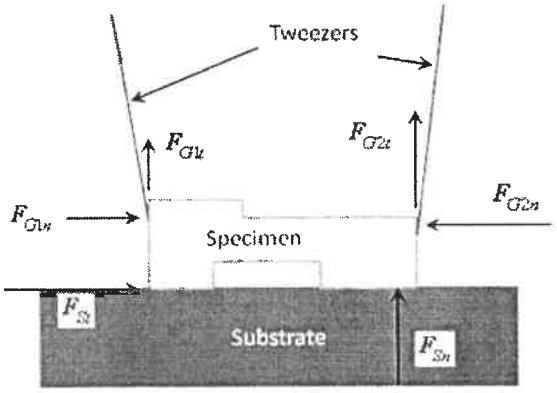

Figure 1. Block diagram indicating components of a generalized tweezers as part of an assembly tool

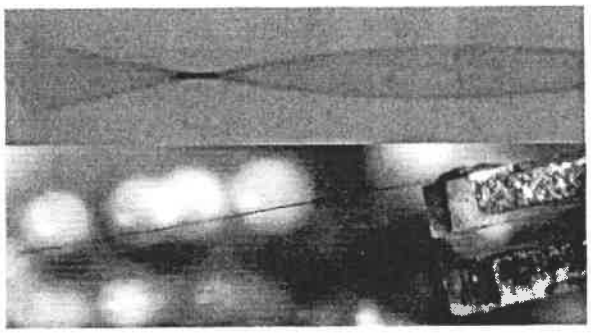

FIGURE 2. Images of the standing wave probe. Oscillating fiber (above), oscillating fiber attached to the tuning fork crystal oscillator shown on the right (below).

intermolecular forces it is not possible to rely on gravity for releasing and holding components in place. Consequently, it is necessary to amass new knowledge of methods for assembly of functional devices.

The aim of current efforts is to develop an automated, multi-axis, micro tweezers station based on standing wave probe 'fingers'. The self sensing of these probes will enable force control during pick and place operations as well as dimensional metrology of micrometer and sub micrometer features.

EXPERIMENTAL ASSESSMENT

The following sections provide a brief overview of these experimental studies.

Static pull-off force measurements

A series of static pull-off measurements have been performed to determine forces needed to pick up an object from a given substrate and the forces bonding an object to the fiber. Adhesion force between the specimen and substrate was measured by bringing a 150 µm glass sphere that was attached to the probe fiber into contact with a specimen and then retracting the probe until contact was broken, see FIGURE 3. From the displacement of the fiber when the probe was retracted, as well as its geometry and material properties, the force could be calculated using beam bending theory. In other similar experiments force has been measured between a probe fiber and a number of different glass spheres. This work revealed that the substrate adhesion forces could be comparable or greater

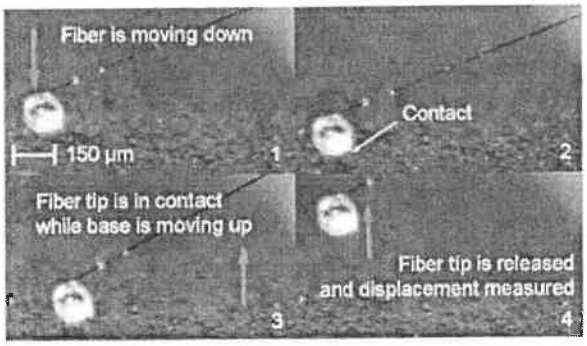

FIGURE 3. Photographs showing adhesion measurements in which a sphere, attached to the free end of a fiber, is contacted with a substrate and then retracted while monitoring the fiber deflection. In another experiment the fiber is contact directly onto a sphere to measure contact force between the fiber and sphere.

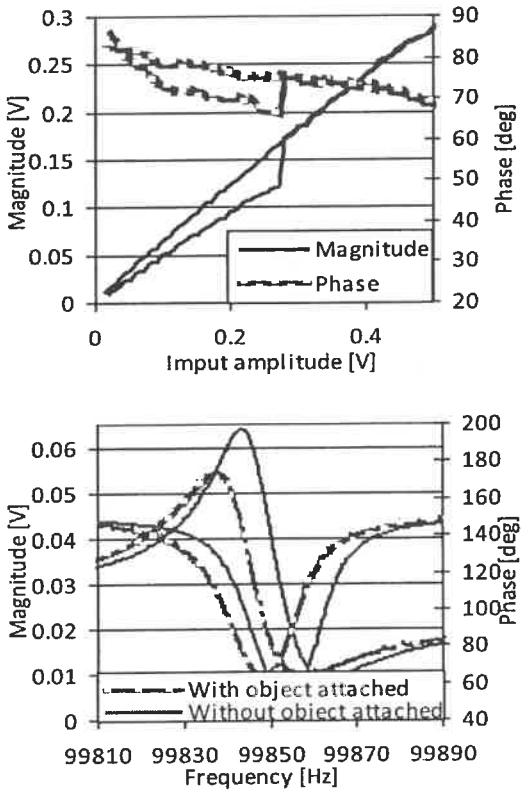

FIGURE 4. Measurements of the release of a 100 µm sphere attached to a carbon fiber by a meniscus film. Upper graph plots the measured magnitude and phase signals from the fiber sensor as the drive amplitude is ramped with the signal jump when object is released. The lower graph shows frequency response of the probe before and after release

than those between the fiber and specimen, typically in the range 0.1 to 1 µN. Application of hydrophilic coatings could reduce these forces to levels below our resolution of around 50 nN.

Self-sensing

A key attribute of the probe is that the sensor signal may be used to monitor probe to specimen interactions during manipulation of the micro-scale object. This will be crucial in applications requiring knowledge of what is happening during manipulation as well as detecting when the object has been successfully picked up or released. FIGURE 4 shows the sensor signal from a probe that has a 100 µm glass sphere attached near to its free end using meniscus forces. In experiments, the glass sphere was first attached to the fiber when not energized and therefore not oscillating. The fiber was then excited near to its natural frequency

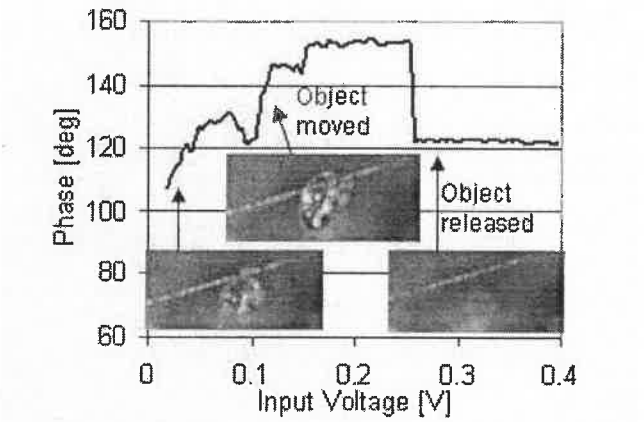

FIGURE 5. Sensor signal from a probe to which a glass sphere is adhered by meniscus forces. Photographs inset shows frames from a movie and corresponding times at which the sensor signal is recorded [2]

with linearly increasing amplitude and a movie of the subsequent motion recorded simultaneously with the data collection. During these experiments a number of dynamic interactions are often observed. In the experiment represented in FIGURE 5 two rather interesting phenomena were visually observed that also resulted in measurable signal changes. The first of these is motion of the sphere relative to the fiber. This motion could be either along the axis of the probe shank, rotation of the sphere about its own axis (rather like that of a Harlem Globe Trotter spinning a basket ball on his finger) or the sphere rotating about the fiber. Finally, when the amplitude goes above a threshold value the sphere is ejected.

A number of experiments were performed to estimate repeatability of release amplitudes using the same specimen. Again, using a single fiber, the same object was picked up from a surface a number of times relying on adhesion forces. The oscillation amplitude was then increase linearly similar to the previous discussion. Both the magnitude and phase of the probe output were recorded to determine maximum input amplitude needed to release the object. In these early experiments there was considerably variability of the release amplitude mainly because it was not possible to attach the object at the same location along the fiber length. Both phase and amplitude signals can be used to provide a clear measure of the release event. From these measurements, it was possible to determine amplitudes that would result in a high probability of release. It was observed that the natural frequency of the probe would generally increase after release of the sphere.

Temperature influence on probe resonance

Using a calibrated temperature chamber, environmental effects on the tuning fork resonator have been assessed. FIGURE 6 shows experiment results from three separate experiments in which the tuning fork was placed in the chamber that was set to -10 degree Celsius and stepped at 1 degree increments. At each temperature the tuning fork frequency response was measured and the value of the frequency at peak amplitude recorded. Deviations from the value recorded at -10 Celsius were then plotted as a function of temperature.

It was found that when tuning fork oscillator is removed from its hermetically sealed environment the resonant frequency can shift by as much as 60 Hz throughout this 30°C range. Again, this is a small extract from a substantially more detailed study. The large temperature variations shown here are reduced if the temperature does not go below that of the dew point. This indicates a significant influence with both temperature and humidity. Interestingly, there is also a small jump of around 2 Hz in the resonant peak at a temperature a little below 0 C for the tuning forks in air. It is thought that this is due to the freezing of thin water films on the tuning fork surface.

Multi-fiber tweezers

Multi-fiber probe systems are also likely to find

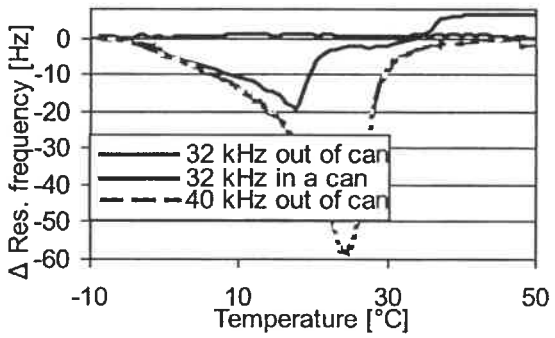

FIGURE 6. Experiments indicating variation from peak frequency response as a function of temperature for three different resonators, a tuning fork in a can (black line), a 32 (blue line) and 40 (red line) kHz fork exposed in air.

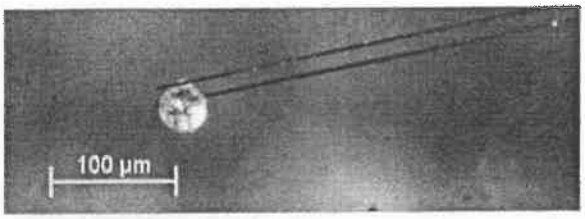

FIGURE 7. Microscope image showing a two probe resonator with a sphere attached near to the free end

application in micro and nano assembly processes. FIGURE 7 shows a microscope image of a two fiber probe in which both fibers are attached to a single resonator beam. This indicates just one of many concepts that are currently being manufactured and characterized. In this example it is possible to use one tuning fork crystal oscillator with two fibers attached and a probe second with one fiber to create a 3-point gripper. Clearly, many combinations of such an approach are possible, many of which are currently being studied.

Finally, a semi-automated gripper station has been built to investigate micro-manipulation and assembly techniques using two probes that can be moved towards and away from each other to create a tweezing action. Objects ranging in size from 10 to 200 µm have successfully picked up and released using standing waves, see FIGURE 8. This system can be operated using joysticks that operate both the tweezers and a three axis motion control stage. Currently, feedback is provided by two high magnification, long range objective camera systems. This system has also been used for simple assemblies.

FUTURE WORK

Different design concepts including three and more finger grippers to be able to pick submicron object as well as larger up to around 500 µm are to be implemented in the near future. In the longer term a complete robotic system capable of automatic assembly based on known position of assembly parts and with ability to find needed parts at unknown position (vision system with shape recognition) will be built and tested. This system will also be equipped with force sensing technology as well as functions making this tweezers system a full dimensional metrology machine (micro CMM). Finally, there is a substantial ongoing effort to design and manufacture probes with reduced dimensional

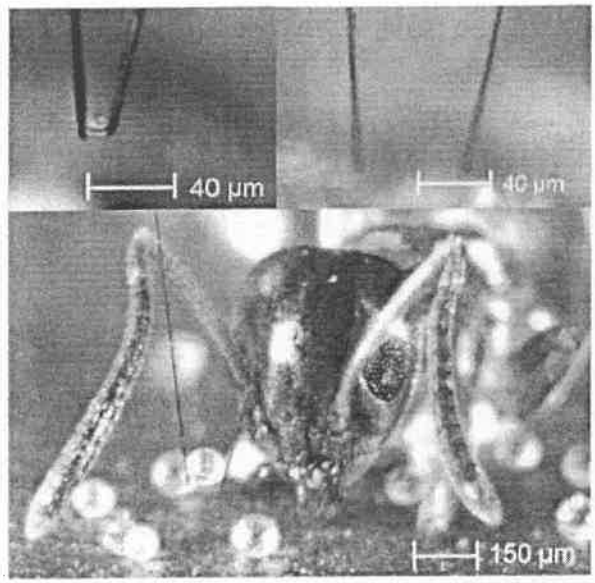

FIGURE 8. Photographs showing the automated gripper system in operation to pick up a 10 µm sphere (top left) and release using standing wave (top right) and a larger sphere located in front of a 'small' Ant .

scales operating at higher frequencies. A times ten per year scaling and frequency increase is the goal of this sub-program.

ACKNOWLEDGEMENTS

The authors wish to acknowledge Dr. Marcin Bauza of Insitutec Inc., NC, and Dr. Richard Seugling of Lawrence Livermore National Laboratory, CA, for their input to, and support of, this work. This work was supported by the National Science Foundation grant 0637422. Any opinions, findings, and conclusions or recommendations expressed in this material are those of the author(s) and do not necessarily reflect the views of the National Science Foundation. Part of this work was performed under the auspices of the U.S. Department of Energy by Lawrence Livermore National Laboratory under Contract DE-AC52-07NA27344.

REFERENCES

[1] Bauza M., Woody S.C., Hocken R.J, and Smith S.T., 2005, Development of a virtual probe tip with an application to high aspect ratio microscale features, *Rev. Sci. Instrum.*, **76**(9), 095112(8 pages).

[2] Woody S.C., Nowakowski B., Bauza M. and Smith S.T., 2008, Standing wave probes for micro-assembly, *Rev. Sci. Instrum.*, at press.

DEVELOPMENT OF MULTI-WIRE EDM SLICING METHOD FOR SILICON INGOT

Yasuhiro Okamoto[1], Yoshiyuki Uno[1], Akira Okada[1], Satoru Ohshita[1], Tameyoshi Hirano[2] and Shiro Takata[3]
[1]Graduate School of Natural Science and Technology, Okayama University, Okayama, Japan
[2]Toyo Advanced Technologies Corporation, Hiroshima, Japan
[3] Makino Milling Machine Corporation, Kanagawa, Japan

INSTRUCTIONS

The diameter of silicon wafer becomes larger in order to increase the number of chips per one wafer. For such a larger diameter silicon ingot is mainly sliced by using multi-wire method, in which a long thin wire is used with slurry. In this method, several hundreds of wafers could be sliced at the same time. However there are still problems remained, such as large cracks, slurry treatment, contamination and so on. Therefore, we proposed a new slicing method of mono-crystalline silicon ingot using wire electrical discharge machining (wire-EDM), and showed the possibility of wire EDM slicing for mono-crystalline silicon ingot [1]. However, the efficiency of wafer slicing by the commercially-available wire-EDM compared to multi-wire saw method is very low, because the number of sliced wafer was only one per one process in the conventional wire-EDM method. Therefore, a multi-wire EDM slicing equipment was newly developed with a single wire and a multi-EDM power supply unit in order to increase the efficiency of wafer slicing [2-4]. In this report, machining characteristics for mono-crystalline silicon ingot using this newly developed multi-wire EDM slicing equipment was discussed. Besides, the possibility of applying this technique to silicon ingot for solar cell was also investigated.

EXPERIMENTAL SETUP

The newly developed multi-wire EDM slicing equipment is schematically shown in Figure 1. The electrode wire is wound spirally on wire guides many times along the wire guide pitch. The wire is fed reciprocally by reversing the feed direction, when the wire comes to the end of set travel length. The silicon ingot is sliced by moving the workpiece in the downward direction. The wire sub guide is prepared at the nearest side to workpiece in order to stabilize the wire position. Three sets of conductivity piece for supplying discharge pulse to the wire electrode were placed at the position between wire guides and wire sub guides. In this experiment, the wire pitch is set to 1.1 mm, and the maximum number of machinable wire electrode is limited to three according to the number of the multi-power supply unit, which can generate three discharge pulses at the same time.

Main machining conditions are listed in Table 1. Molybdenum wire of 180 μm in diameter was used as a wire electrode with polarity (-). Two kinds of mono-crystalline silicon with different specific resistance were used as a workpiece. One is 10^{-2} Ω·cm for semiconductor wafers, and another is 2-3 Ω·cm for solar cells. A multi-power supply unit was newly developed, which can generate lower and longer discharge pulse compared to the normal commercial wire-EDM equipment. This power supply unit was composed of high-voltage circuit and low-voltage one. The high-voltage circuit plays a significant role of ignition for electrical discharge, while the low-voltage circuit keeps the discharge voltage during the set pulse duration. In this paper, open circuit voltages of high-voltage and low-voltage circuit are described as uiH and uiL

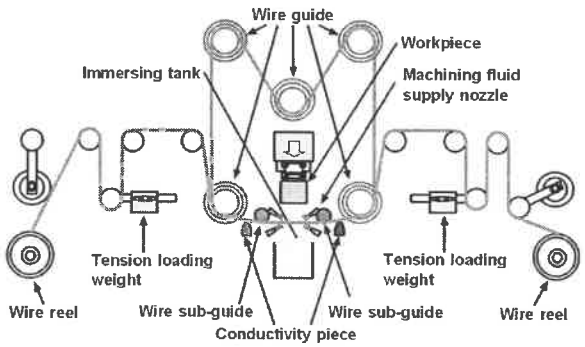

FIGURE 1. Schematic diagram of multi-wire EDM equipment.

TABLE 1. Machining conditions.

Electrode	Mo(-) ϕ80, 120, 180 μm
Specific resistance of workpiece	$\rho_s = 10^{-2}$ Ω·cm ρ_s = 2-3 Ω·cm
Wire tension	F = 15 N
Wire speed	W_s = 100-600 m/min
Open circuit voltage	ui_H = 300 V ui_L = 100-120 V
Discharge current	i_e= 3-8 A
Discharge duration	t_e= 5, 20 μs
Duty factor	τ = 20-30 %
Dielectric working fluid	Deionized water
Specific resistance of dielectric working fluid	ρ_w = 10k-300k Ω·cm
Temperature of dielectric working fluid	θ_f = 20 °C

respectively. In slicing of silicon for semiconductor wafers, only low-voltage circuit was used. On the other hand, the both discharge circuits were used in slicing of silicon for solar cells.

SLICING OF LOW RESISTANCE SILICON INGOT

Supply method of working fluid

In this newly developed slicing equipment, since many wire electrodes are arranged at the same plane with a narrow pitch, an individual nozzle could not be prepared for each wire electrode. In order to supply working fluid to working point, two kinds of supply method were investigated. One is the nozzle supplying method, and another is an immersion method. Figure 2 shows the difference of kerf shapes for two supply methods of working fluid. When the working fluid was supplied by nozzle, the pitch of kerf was greatly changed from place to place due to the surface tension of working fluid generated between wire electrodes. On the other hand, constant kerf pitch of 1.1 mm in setting value could be obtained by immersion method. Therefore, this immersion method was used hereafter.

Influence of wire speed

Figure 3 shows the displacement of workpiece for various wire speeds, where the slicing distance was set to 10 mm. The machining rate of wire speed for 400 and 500 m/min decrease around 10 minutes. On the other hand, the displacement of wire speed 600 m/min increases proportional to machining time. Then, the machining time becomes shorter with increasing the wire speed.

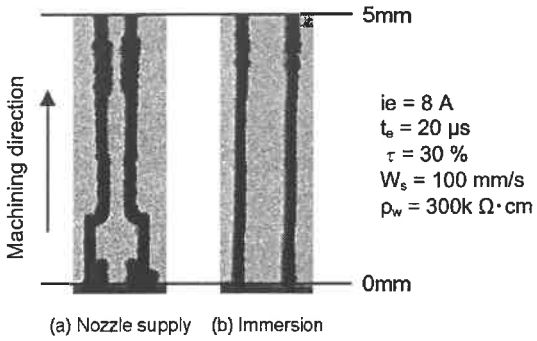

FIGURE 2. Difference of kerf shape by working fluid supply method, where mono-crystalline silicon ($\rho_s = 10^{-2}$ Ω·cm) of 80 mm in thickness was sliced by two wire electrodes of 180 μm in diameter.

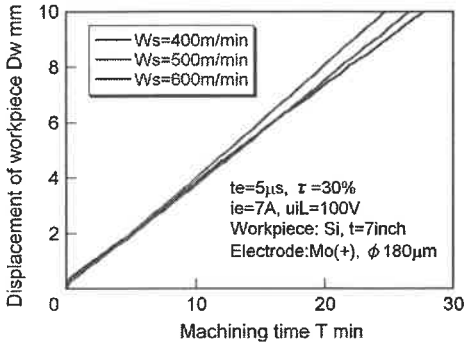

FIGURE 3. Displacement of workpiece for various wire speeds, where mono-crystalline silicon ($\rho_s = 10^{-2}$ Ω·cm) of 7-inch in thickness was sliced by single wire electrode of 180 μm in diameter.

Figure 4 shows the kerf shapes for various wire speeds. L or R means the side of workpiece from the front side of slicing equipment. The difference of kerf shape is not recognized at each side, and the straight kerf shape can be obtained for every wire speed. On the other hand, the width of kerf was different by wire speed as shown in Table 2. Maximum and minimum kerf width decreased with increasing the wire speed, and difference of kerf width between maximum and minimum value also becomes smaller in higher wire speed.

Judging from these results, it is considered that higher wire speed can improve the removal function of debris from the kerf. In general, normal commercial wire-EDM equipment removes debris from the kerf by the flushing of working fluid from the nozzles. However, when the pitch of wire electrode becomes smaller than 1.1 mm, and much narrower pitch will be

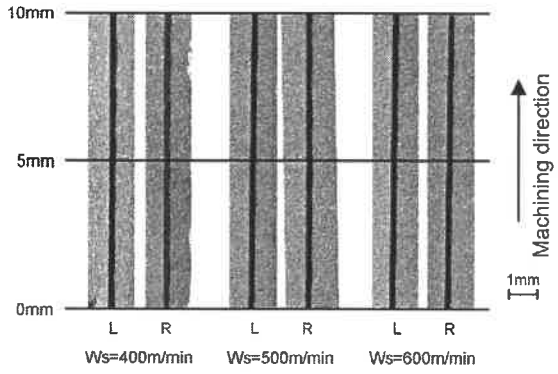

FIGURE 4. Kerf shape for various wire speed, where mono-crystalline silicon (ρ_s = 10^{-2} Ω·cm) of 7-inch in thickness was sliced by single wire electrode of 180 μm in diameter under the machining conditions: i_e = 8 A, t_e = 20 μs, τ = 30 %, ρ_w = 300k Ω·cm.

TABLE 2. Kerf width for various wire speed, where mono-crystalline silicon (ρ_s = 10^{-2} Ω·cm) of 7-inch in thickness was sliced by single wire electrode of 180 μm in diameter under the machining conditions: i_e = 8 A, t_e = 20 μs, τ = 30 %, ρ_w = 300k Ω·cm.

Wire speed (m/min)	Min. kerf width (μm)	Max. kerf width (μm)
400	212.6	258.9
500	208.4	236.8
600	204.2	229.5

required in order to reduce the kerf loss.
The narrow kerf and thinner wafer thickness were investigated under the suitable machining conditions as shown in Figure 5. The wire electrode of 80 μm can perform the kerf loss less than 100 μm, and the wafer of 100 μm in thickness can be obtained by stable machining conditions with the wire electrode of 180 μm.

SLICING OF SILICON INGOT FOR SOLAR CELLS

The slicing of high resistance silicon for solar cell was investigated by changing the specific resistance of dielectric working fluid in order to improve the slicing performance.
Figure 6 shows the variations of removal rate and surface roughness with specific resistance of dielectric working fluid, where the slicing distance and thickness were 10 mm and 80 mm respectively. As shown in this figure, surface roughness was kept almost constant value for every specific resistance of dielectric working

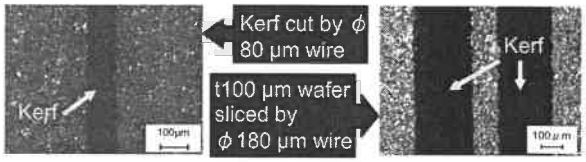

FIGURE 5. Reduction of kerf width and wafer thickness for mono-crystalline silicon (ρ_s = 10^{-2} Ω·cm) of 80 mm in thickness.

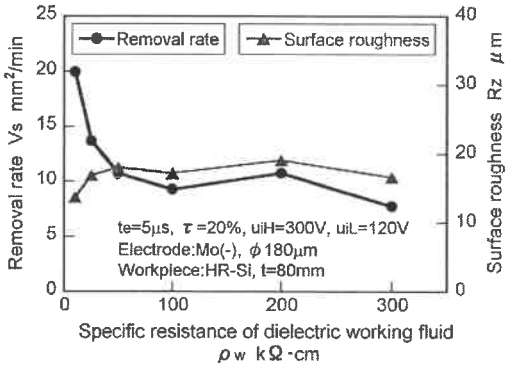

FIGURE 6. Removal rate and surface roughness for various specific resistance of working fluid, where mono-crystalline silicon (ρ_s = 2-3 Ω·cm) of 80 mm in thickness was sliced by single wire electrode of 180 μm in diameter.

fluid, while the removal rate increased with decreasing specific resistance. From the measurement of discharge pulse, it was cleared that discharge voltage decreased with decreasing the specific resistance of dielectric working fluid, while the discharge current increased with decreasing specific resistance. Therefore, it is considered that the removal rate increased with decreasing the specific resistance of dielectric working fluid.
Figure 7 shows the variations of kerf width and crack depth with specific resistance of dielectric working fluid. Here, the crack depth was measured from micrograph of the angle cut workpiece surface after both polishing and reactive ion etching. The kerf width decreased with decreasing the specific resistance except for 300 kΩ·cm. Especially, the kerf width was less than 200 μm at 10 kΩ·cm in specific resistance of dielectric working fluid, which was narrower than the result of silicon of 10^{-2} Ω·cm for semiconductor wafers [1]. On the other hand, the crack depth decreased with decreasing the specific resistance of dielectric working fluid except for 300 kΩ·cm. Especially at less than 50 kΩ·cm in specific resistance of dielectric working fluid, the crack depth is smaller than 13

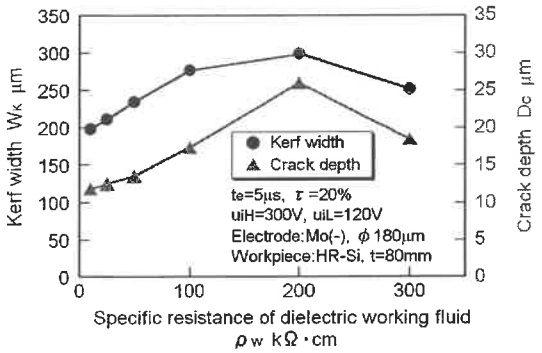

FIGURE 7. Kerf width and crack depth for various specific resistance of working fluid, where mono-crystalline silicon (ρ_s = 2-3 Ω·cm) of 80 mm in thickness was sliced by single wire electrode of 180 μm in diameter.

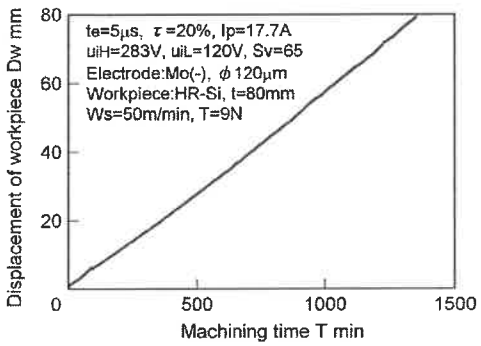

FIGURE 8. Slicing of poly-crystalline silicon ingot, where workpiece (ρ_s = 2-3 Ω·cm) of 80 mm in thickness was sliced by single wire electrode of 120 μm in diameter.

μm. Although the open circuit voltage is three times higher than the slicing of 10^{-2} Ω·cm silicon ingot, the crack depth of high resistance silicon of 2-3 Ω·cm was almost equal to that of slicing the silicon ingot for semiconductor devices. The control of specific resistance of dielectric working fluid leads to the improvement of slicing performance.

In solar cells, the poly-crystalline silicon ingot was widely used because of its high cost performance. Then, the slicing of poly-crystalline silicon ingot of 80 mm square was carried out as shown in Figure 8. The displacement of workpiece relatively increases proportional to machining time. The kerf width was less than 150 μm, and stable slicing of poly-crystalline silicon ingot was also accomplished by this technique.

This newly developed multi-wire EDM slicing equipment can slice even high resistance silicon ingot, and it is assumed that this technique has the potential as a new slicing method of silicon ingot for both semiconductor wafers and solar cells.

CONCLUSIONS

A new slicing method of silicon ingot with multi-wire EDM was proposed, and the possibility of applying this technique to silicon ingot for semiconductor wafers and solar cells were experimentally investigated. Main conclusions obtained are as follows;

(1) The slicing result in immersion method is superior than that in nozzle supply method, because the machining state is stable.

(2) In slicing of mono-crystalline silicon ingot of 10^{-2} Ω·cm, the removal rate increases and the kerf width decreases with increasing the wire speed. The thinner wafer of 100 μm in thickness and narrow kerf loss less than 100 μm can be obtained.

(3) It is possible to slice the high-resistance mono-crystalline silicon ingot of 2-3 Ω·cm by using this multi-wire EDM slicing equipment. The kerf width and the crack depth decrease with decreasing specific resistance of dielectric working fluid, while the removal rate increases.

(4) The slicing of poly-crystalline of 2-3 Ω·cm can be performed by using the new multi-wire EDM slicing equipment.

ACKNOWLEDGMENTS

The authors would like to express their sincere thanks to Sin-Etsu Handotai Co.,Ltd for supplying expensive mono-crystalline silicon ingot.

This work was partly supported by New Energy and Industrial Technology Development Organization (NEDO), Grant No. 06990701-0.

REFERENCES

[1] Uno Y, Okada A, Okamoto Y, Hirano T. A New Slicing Method of Monocrystalline Silicon Ingot by Wire EDM. International Journal of Electrical Machining. 2003; 8: 21-26.

[2] Uno Y, Okada A, Okamoto Y, Suzuki K. Hirota S, Hirano T, Takata S, Ishikawa K. Proceedings of International Conference on Leading Edge Manufacturing in 21st Century. 2005; 783-786.

[3] Hirota S, Uno Y, Okada A, Okamoto Y, Hirano T, Takata S. Proceedings of 2005 Takamatu Conference of Chugoku Shikoku Branch, JSPE. 2006; 81-82 (in Japanese).

A CUTTING TOOL WITH NANO/MICRO-TEXTURED SURFACE FOR HIGH ANTI-ADHESIVE EFFECTS

Tatsuya SUGIHARA, Toshiyuki ENOMOTO
Department of Mechanical Engineering,
Graduate School of Engineering, Osaka University
Suita, Osaka, Japan.

INTRODUCTION

Aluminum alloys have several advantages such as a high ratio of strength to its mass, good corrosion resistance, and so on. Hence the demand for aluminum alloy is rapidly increasing especially in the transport industry as lightweight composite materials. Generally it is considered that aluminum alloys are easy-to-cut materials due to their low hardness compared with steel material. However, it is noted that some serious problems exist. Since aluminum alloys have a low melting point and a high ductility, aluminum chip adheres strongly to the cutting edge of the tool, which leads to the tool breakage. Then many cutting technologies concerning about cutting fluid, fluid supply method, surface coating of cutting tool and surface finishing of cutting tool have been developed. In particular, diamond-like carbon (DLC) coated tool having extremely low frictional surface is applied to a dry cutting for aluminum alloy. However, aluminum chip adheres to the DLC coated tool in actual [1] and hence cutting fluid must be used in cutting of aluminum in practical use. Furthermore, the tool breakage occurs frequently in cutting processes such as deep-hole drilling, milling and tapping, in which a cutting fluid is difficult to be directly supplied to cutting point.

To solve this problem, we proposed a cutting tool with micro-textured surface to investigate the role of the textured surfaces play in a) retaining cutting fluid, and b) reducing the actual contact area between the tool and chip [2]. These effects lead to increase lubricity and promote anti-adhesive effects at the tool-chip interface. A cutting tool with a segment-structured diamond-like carbon (DLC), as shown in Fig. 1, was developed in our previous research [2], and it is revealed that the cutting tool maintains good lubricity in wet conditions from the evaluations of the shear angle, the cutting force, the friction coefficient of rake face, and so on. However, the evaluation of adhesion was not carried out in our previous research.

In this paper, the anti-adhesive effect of the previous developed tool with micro-textured surface is discussed. And, the cutting tool with nano/micro-textured surface is proposed in order to achieve excellent anti-adhesive effect. The cutting performance is also evaluated.

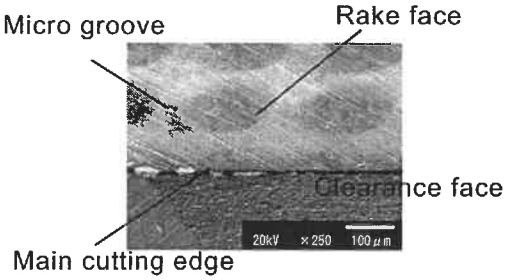

FIGURE 1. Previous developed tool with micro-textured surface

CUTTING PERFORMANCES OF A CUTTING TOOL WITH MICRO-TEXTURED SURFACE

Cutting experiments were conducted using a vertical machining center (YAMAZAKI MAZAK Corp., AJV-18), as illustrated in Fig. 2. Figure 3 shows the geometry of the cutting tool, in which a cutter has single insert. The center of the cutter was set on the center line of the workpiece. Table 1 lists the cutting conditions.

As an experimental result, the cutting force of the tool with micro-textured surface was decreased 15-20 % compared with a conventional DLC coated tool. Moreover, it was revealed that the developed tool maintains good lubricity in wet conditions from the evaluations of the shear angle. Figure 4 shows a SEM (Scanning Electron Microscope, JOEL JSM-5800A) image of the rake face of the tool with micro-textured surface after wet cutting (cutting distance 900m). As shown in this Figure,

aluminum adhesion occurred in tool rake face and the grooves were buried by the adhesion.

Here, the calculated theoretical contact length between the tool rake face and chips [3] was about 180 μm. So, it is considered that there were only 1 or 2 grooves in the contact area between the tool rake face and chips. And the width of grooves were so wide, from Fig. 4, that the adhesion entered easily into the bottom of grooves. From the above-mentioned considerations, it was found that ultra-fine, namely, nano/micro scale grooves must be generated on tool surface for improving anti-adhesion effect.

DEVELOPMENT OF A CUTTING TOOL WITH NANO/MICRO-TEXTURED SURFACE

Femto second laser technology was adopted to generate nano/micro periodic grooves on rake face of a cemented carbide tool [4] [5]. Precise periodic structure like grooves can be generated with a linear polarized femto second laser of energies nearby ablation threshold, and space of the periodic structures is about the same as the laser wavelength [4]. Applying this method, the nano/micro scale grooves with 100-150 nm depth and 700 nm pitch were periodically generated on the rake face of cemented carbide cutting tool by the laser (Canon Machinery Inc., Model Surfbeat R; peak wavelength 800 nm, pulse duration 150 fs, cyclic frequency 1 kHz, pulse energy 300 μJ). Figure 5 shows a SEM image and AFM (Atomic Force Microscope, Nanotechnology Nano-R2; Pacific) image of the rake face of the newly developed tool. As can be seen in Fig. 5, the shapes of these grooves are like a sine wave, which is thought to make the contact area between tool surface and chip small. Before the laser irradiation, the tool surface was polished with diamond slurry to be surface roughness P-V 40 nm. After grooving, DLC film (by plasma-CVD method) was coated on the textured surface for improving anti-adhesive effect. The coating caused the depth of grooves to be decreased about 10-20 nm.

CUTTING PERFORMANCES OF A CUTTING TOOL WITH NANO/MICRO-TEXTURED SURFACE

The cutting experiment was carried out with newly developed cutting tool under the conditions listed in Table 1. SEM (Hitachi High-Technologies Corp., S-3400NX) images and EDX (Energy Dispersive X-ray Spectrometry) analyses of aluminum of rake face after wet

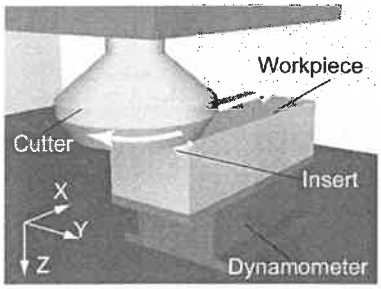

FIGURE 2. Experimental setup of face milling tests

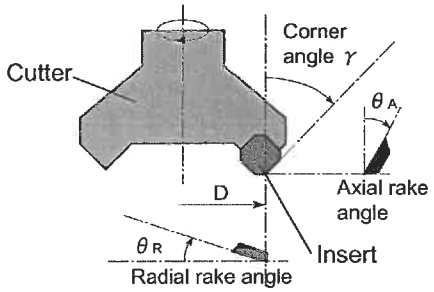

FIGURE 3. Geometry of cutting tool

Table 1 Cutting conditions

Workpiece	A5052 W 75 mm - L 210 mm	
Tool (Insert)	Cemented carbide K10 SEKN42M, Sumitomo Electric Hardmetal	
Tool geometries	Axial rake angle θ_A	20°
	Radial rake angle θ_R	-3°
	True rake angle α	12.4°
	Corner angle γ	45°
	Cutter diameter D	80 mm
Cutting speed	380 m/min (1500 rpm)	
Depth of cut	3 mm	
Feed rate	0.12 mm/rev.	
Cutting fluid	Emulsion type (JIS A1) Finecut CFS-100, NEOS	
Supply rate	12.6 L/min	

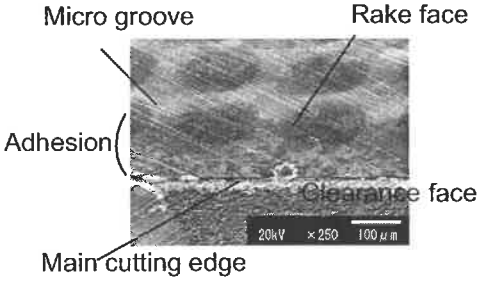

FIGURE 4. Previous developed cutting tool with micro-textured surface after cutting

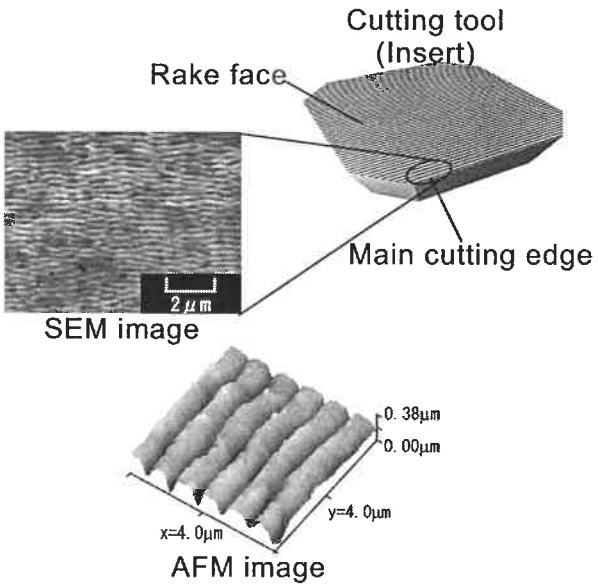

FIGURE 5. Newly developed cutting tool with nano/micro-textured surface

cutting (cutting distance at 1800 m) are shown in Fig.6. Figure 6 (a), (b) and (c) show the tool with polished surface, the tool with nano/micro grooves in the parallel direction against the cutting edge and the tool with nano/micro grooves in the orthogonal direction against the cutting edge, respectively. Figure 7 shows the concentration of aluminum atom on the rake face. Figure 8 (a), (b) and (c) show the optical microscope (KEYENCE Corp., VF-7500) images and the profile curves of the orthogonal direction against the main cutting edge after cutting (cutting distance at 1800 m).

From these results, it was confirmed that the adhesion occurred strongly on the rake face of the conventional DLC-coated tool, namely the polished tool. In contrast, it was found that nano/micro texture, particularly, nano/micro scale grooves in the parallel direction against the main cutting edge significantly improved the anti-adhesive effects for the tool surface. Then the enlarged SEM image of the rake face of developed tool after cutting (cutting distance at 1800m) is shown in Fig.9. From this figure, it was confirmed that the nano/micro grooves was not buried with the adhesion after cutting.

As cutting performances, a cutting shear angle and a cutting force were evaluated. Figure 10 shows the change of the cutting shear angle with the rotational angle of insert. As shown in Fig. 10, the shear angle obtained with the

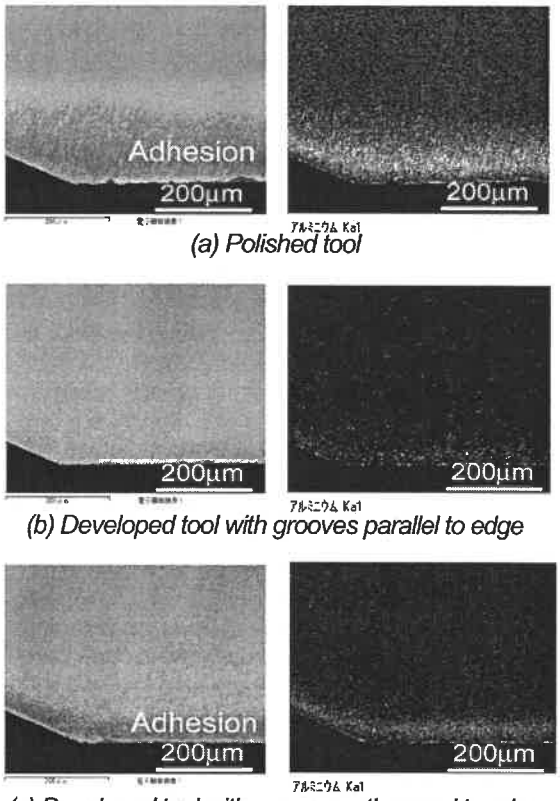

FIGURE 6. Rake face of DLC coated tool with nano/micro-texture after cutting (Left: SEM image, Right: EDX-Al image)

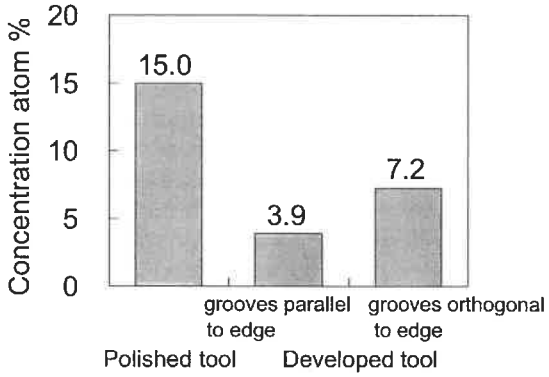

FIGURE 7. Concentration of aluminum atom on rake face

developed tool was larger than that of the polished tool. Figure 11 shows the coefficient of friction on the rake face of the cutting tool calculated by the measured cutting forces. The result also indicates that the nano/micro-texture significantly improved the lubricity on the tool surface. Moreover, it was confirmed that the low friction coefficient was maintained constant in milling experiment.

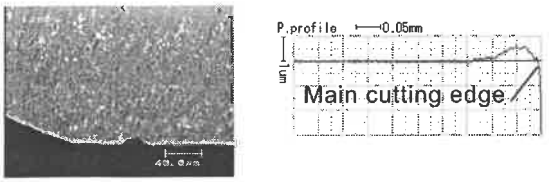

(a) Polished tool

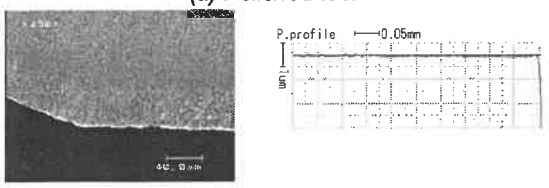

(b) Developed tool with grooves parallel to edge

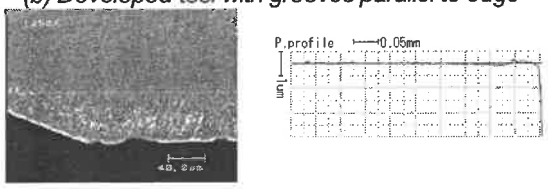

(c) Developed tool with grooves orthogonal to edge

FIGURE 8. Rake face of DLC coated tool with nano/micro-texture after cutting (Left: Optical image, Right: Sectional profile).

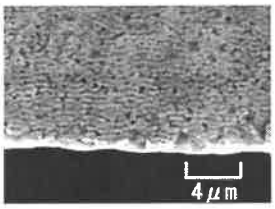

FIGURE 9. Rake face of developed tool with nano/micro-grooves parallel to cutting edge after cutting

CONCLUSION

A cutting tool with nano/micro-textured surface was developed for improving the anti-adhesive effect in cutting of aluminum alloy. And it was found that:

(1) A cutting tool with nano/micro-textured surface was developed by femto second laser.
(2) Nano/micro textures on the surface of cutting tool significantly decreased the adhesion.
(3) Excellent anti-adhesive effect was brought when the grooves were generated in the parallel direction against the main cutting edge.

ACKNOWLEDGEMENTS

The authors would like to express their deepest gratitude to Canon Machinery Inc., Nippon ITF Inc. and NEOS CO., LTD.

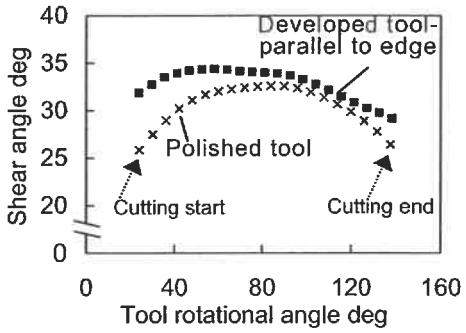

FIGURE 10. Shear angle in cutting

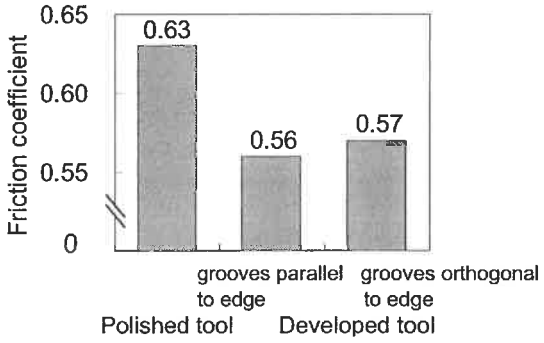

FIGURE 11. Coefficient of friction

REFERENCE

[1] Yoshimura H. et al., Study of generation and growth of adhesion mechanism in near-dry cutting of aluminum alloys. Journal of the Japan Society for Abrasive Technology 2007; 51 (7); 416-421.

[2] Enomoto T. et al., Development of a cutting tool with micro structured surface. Transactions of the Japan Society of Mechanical Engineers Series C 2007; 73 (729); 1560-1565.

[3] Sato, K. et al., Study on the Mechanism of Metal Cutting (Part1) –On the Tool-Chip Contact Length-, Journal of the Japan Society for Precision Engineering, Vol.25, No.289 (1959), pp.50-56. (in Japanese)

[4] Sawada H. et al., Precise periodic structuring with femtosecond-laser. Journal of the Japan Society for Precision Engineering 2003; 69 (4); 554-558.

[5] Sawada H, et al., Effect of precise periodic structures with femtosecond-laser on tribological characteristics under sliding tests. Journal of the Japan Society for Precision Engineering 2004; 70 (1); 133-137.

IMPROVEMENT OF THICKNESS UNIFORMITY OF SILICON AND SOI WAFER BY NUMERICALLY CONTROLLED LOCAL WET ETCHING

Kazuya Yamamura, Takuro Mitani and Nobuyuki Zettsu
Research Center for Ultra-Precision Science and Technology
Osaka University
Suita, Osaka, Japan

INTRODUCTION

Silicon on insulator (SOI) wafers are promising semiconductor material. The applying of the SOI substrate realizes high speed LSIs and low power consumption electronic devices by the reduction of parasitic junction capacitance [1]. Furthermore, the occurrence probability of a soft error caused by exposure to radiation and neutrons can be reduced because the device layer is completely insulated from the substrate by the buried oxide (BOX) layer. In the next generation's specifications, required thickness and its uniformity of the SOI layer to fabricate the fully depleted metal oxide semiconductor transistor are 13-15 nm and ±5 %, respectively [2].

However, in conventional machining process, the accuracy of machining strongly depends on stiffness of the machining equipment, and also is affected by external disturbances, such as the vibration or thermal deformation of the workpiece and the machine, because of the contact-removal mechanism, so that it is very difficult to fabricate thin SOI layer having nanometer level thickness and uniformity with high reproducibility. Furthermore, a crystallographically subsurface damage layer, which degrades the performance of the electronic device, is inevitably generated on the processed surface because plastic deformation or brittle fracture is utilized as a removal mechanism.

To solve these issues, some novel machining methods, such as plasma assisted chemical etching (PACE) [3], plasma chemical vaporization machining (PCVM) [4-6] and magnetorheological finishing (MRF) [7] have been developed. In the case of applying the PCVM, thickness was thinned from 200 nm to 13 nm, and thickness distribution was improved from ±4.2 nm to ±2.0 nm. However, these methods need expensive equipments, especially in the case of the plasma process, it needs process chamber, vacuum pump, gas supply unit, etc.

We had developed numerically controlled local wet etching (NC-LWE) as a novel deterministic subaperture figuring and finishing method, which is suitable for fabricating various optical components and finishing functional materials [8]. The LWE method utilizes a chemical reaction between the etchant and the surface of the workpiece as a removal mechanism, so that there is no degradation of the physical properties of the workpiece material. Furthermore, the machining properties of NC-LWE are insensitive to external disturbances, such as the vibration or thermal deformation of the workpiece or the machine, because of its noncontact removal mechanism. Therefore, although the cost of introduction is very low, the ultraprecision machining properties are achieved more easily compared with other conventional machining methods. By applying the NC-LWE process, flatness of the 6 inches size synthesized quartz glass substrate for the photomask has been improved from 192 nm to 56 nm peak-to-valley (p-v) in the evaluation area of 142×142 mm^2, so that we proposed NC-LWE as a novel finishing method for improving the thickness distribution of silicon and SOI wafer.

EXPERIMENTAL APPARATUS

Figure 1 shows the schematic diagram of the NC-LWE system. This system is constructed from a workpiece holder, an xy-table driven by stepping motors, an etchant nozzle head, and an etchant circulation unit. In the case of the Si or SOI wafer, the wafer is held by the vacuum chuck. The nozzle head consists of an etchant supply part and a suction part, which are arranged coaxially, and the removal area is limited to inside of the suction slit. There is no etchant solution, which causes excessive etching beyond intended removal depth, on the surface of a workpiece after the nozzle has passed, because both the amount of supplied etchant and the suctioned etchant are properly balanced. Therefore, the rinsing by water to stop the etching reaction is not necessary in the LWE process. Furthermore, outer slit of the nozzle head suctions not only the liquid etchant but also the ambient air, so that forcedly suctioning

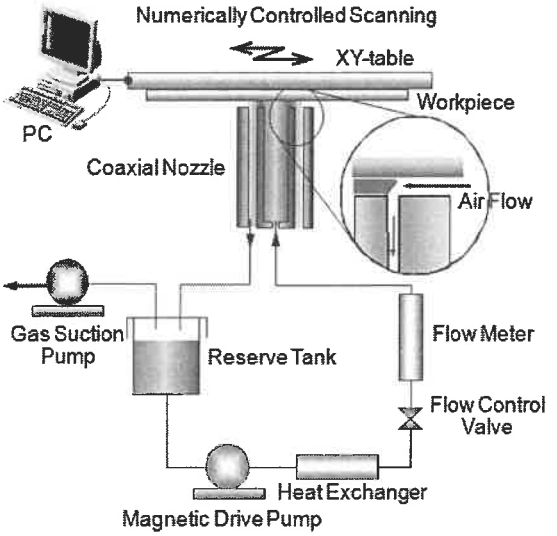

FIGURE 1. Schematic diagram of the LWE system.

prevents the processed surface roughness from degrading by absorbing the etchant vapour diffused from the nozzle head.

RESULTS AND DISCUSSION

Machining Characteristics

Figure 2 shows a removal footprint formed by using a circular coaxial nozzle head having diameter of 15 mm, and in this paper, all machining parameters are same as shown in Table 1. We applied HF/HNO_3 mixtures to etch the silicon, because that etchant has isotropic etching characteristic and does not contain alkaline metal which cause operation error in the silicon electronic device. In the case of the etching of the quartz glass by supplying hydrofluoric acid from a coaxial nozzle, the shape of the removal footprint becomes the simple columnar shape [8]. However, in the case of the etching of the silicon applying the HF/HNO_3 mixtures, cross-section of the removal footprint shows concave shape as shown in Fig. 2(b) by being affected of the distribution of flow velocity, because etching mechanism, which consists of silicon oxidation process by nitric acid and subsequent dissolution process of silicon dioxide by hydrofluoric acid, is very complicated [9].

Figure 3 shows the relationship between the inverse scanning speed of the worktable, which means dwelling time of the etchant supply nozzle, and the maximum removal depth of the etched trench. The removal volume of the silicon precisely increases in proportion to increase of

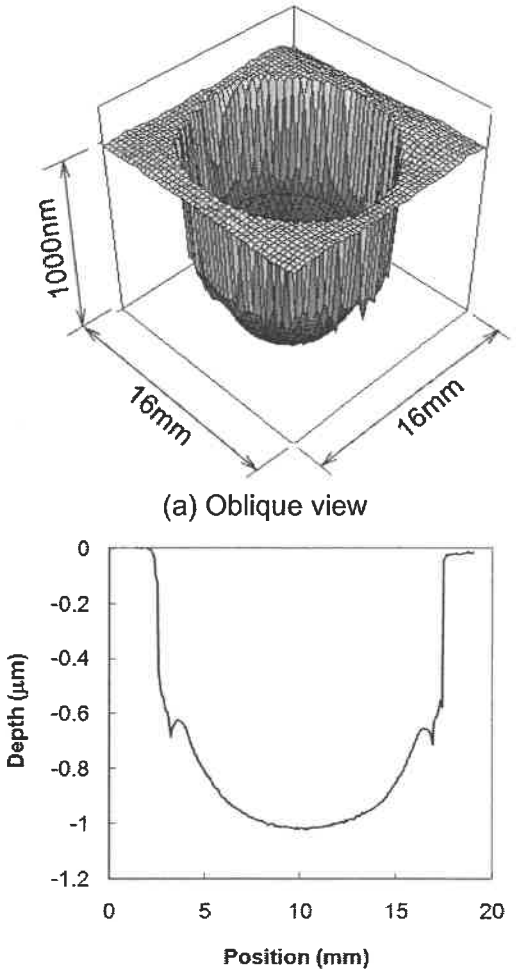

FIGURE 2. Shape of the removal footprint. (Dwelling time : 10s, Removal rate : 0.82 mm^3/min)

the dwelling time. Therefore, the uniformity of the thickness of the silicon wafer is improved only by controlling of the scanning speed of the worktable.

TABLE 1. Machining parameters.

Etchant Composition Temperature Flow rate	 HNO_3 57 wt%, HF 2.5 wt% 25 °C 50 L/h
Nozzle diameter	Φ15 mm
Gap distance	250 μm

Figure 4 shows the relationship between the elapsed time and the etch rate ratio. The elapsed time and the etch rate ratio mean circulation time of the etchant and the ratio of

current etch rate to the initial etch rate, respectively. The forced suction of the etchant in the LWE system gradually changes composition of the etchant by evaporation with an elapsed time, and as a result, the etch rate of the silicon decreases to about 70 % of the initial value after two hours passed from the beginning of the process as shown with square symbol in Fig. 4. To keep an etch rate constant, hydrofluoric acid of 50 wt% was added to the etchant at the rate of 2 g every 15 minutes. Then fluctuation of the etch rate was kept in constant within ±2.5 % for over 120 minutes as shown with diamond symbol in Fig. 4. The etch rate of the silicon was kept by addition only for hydrofluoric acid. Therefore, it is thought that the evaporation rate of the hydrofluoric acid is greater than that of the nitric acid.

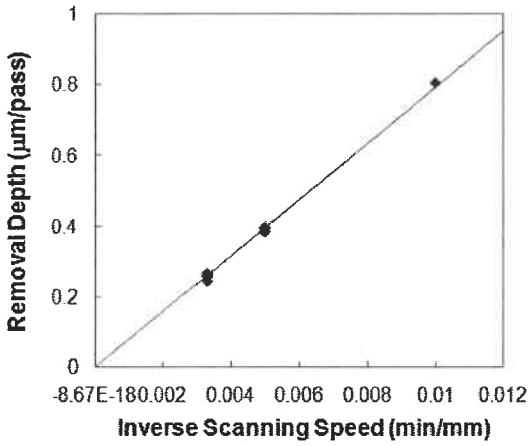

FIGURE 3. Relationship between inverse scanning speed of the worktable and the maximum removal depth of the etched trench.

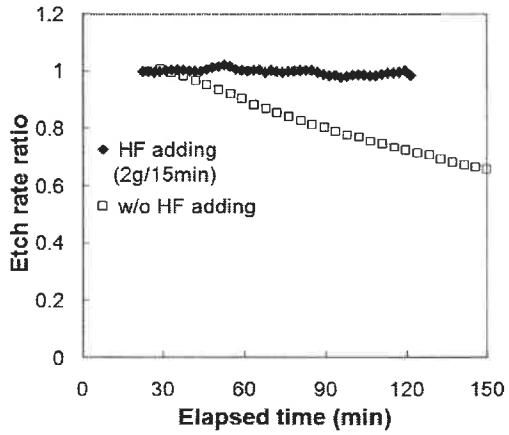

FIGURE 4. Relationship between elapsed time and etch rate ratio.

Correcting of the Thickness Distribution of Bulk Silicon Wafer

We tried to improve the thickness distribution of the bulk silicon wafer by applying the local wet etching. The diameter, orientation, average thickness and specific resistance of the bulk silicon wafer used in this experiment were 200 mm, p-type (100), 725 μm and 7-12 Ω·cm, respectively. The objective wafer was held by vacuum chuck to the worktable, and numerically controlled raster scanning was performed with feed pitch of 2 mm.

Figure 5 shows the thickness distribution of the silicon wafer before and after correcting. The thickness distribution was measured by UltraGage 9700 (ADE corporation). In this result, average thickness of the wafer was thinned from 723.4 μm to 722.9 μm, and thickness uniformity was improved from 650 nm (p-v) to 400 nm (p-v) in the evaluation area of Φ180 mm. And the processing time was 55 minutes. Figure 6 shows the histogram of the thickness deviation to the average thickness of the silicon wafers. The standard deviation of the thickness was improved from 128.6 nm to 47.5 nm.

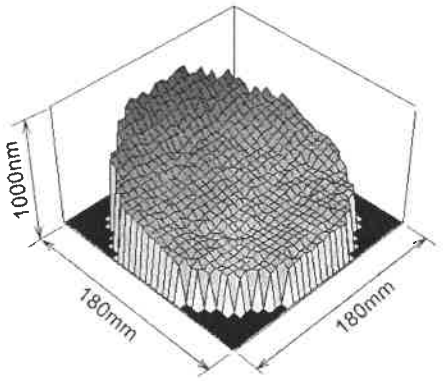

(a) Before correction

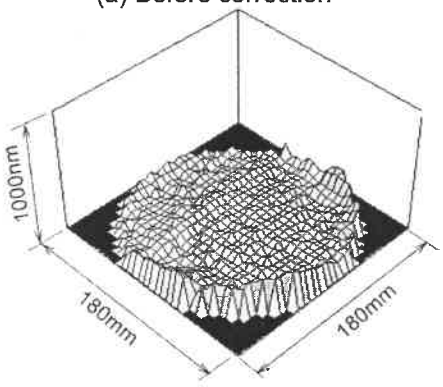

(b) After correction

FIGURE 5. Improvement of thickness uniformity of a bulk silicon wafer. (Φ180 mm area)

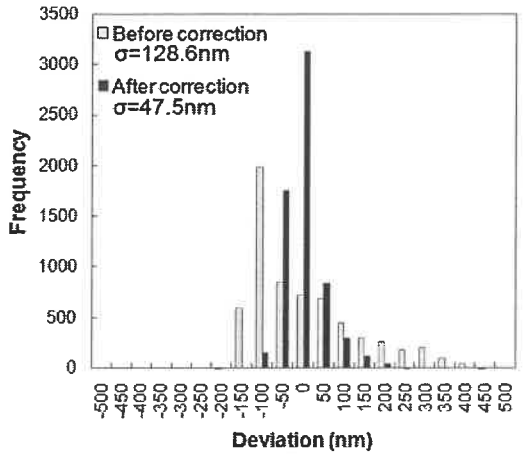

FIGURE 6. Histogram of thickness deviation to the average thickness of the silicon wafers. (Φ180 mm area)

In the evaluation area within a diameter of 140 mm except the peripheral edge of the wafer, the uniformity and the standard deviation of the thickness were improved from 420 nm (p-v) to 150 nm (p-v) and from 90 nm to 28 nm, respectively. The actual removal volume was less than the setting removal volume in the peripheral edge of the wafer. It is thought that the difference of the height and/or wettability between the silicon wafer and the wafer holder caused unstable contact state of the etchant. Therefore, we will accomplish improvement to enlarge a correctable area of the wafer and an application to the SOI wafer of this thickness correcting method.

CONCLUSIONS

A novel ultra-precision figuring process named LWE, which utilizes chemical removal reaction between a liquid etchant and the workpiece surface, was developed for figuring the ultra-precision optical components, correcting the thickness distribution of the bulk silicon and SOI wafer, and so on. In the LWE process, removal footprint is localized by using a coaxial etchant supply and suction nozzle head, and removal volume is proportional to the dwelling time of the nozzle head on the workpiece surface. Therefore, this process enables deterministic figuring by only controlling the scanning speed distribution of the nozzle head. The machining characteristics of the silicon which were applied HF/HNO_3 mixtures were investigated, and it was found that adequate addition of the hydrofluoric acid keeps the etching rate constant within ±2.5 % during the machining operation. Thickness uniformity of the Φ200 mm bulk silicon wafer was improved from 420 nm (p-v) to 150 nm (p-v) in the Φ140 mm area.

ACKNOWLEDGEMENTS

This work was partially supported by the Industrial Technology Research Grant Program in 2005 from the New Energy and Industrial Technology Development Organization (NEDO) of Japan and a Grant-in-Aid for 21st Century COE Research (H12) from the Ministry of Education, Culture, Sports, Science and Technology, Japan.

REFERENCES

[1] Yamaguchi Y, Ishibashi A, Shimizu M, Nishimura T, Horie K, Akasaka Y. A high speed 0.6-μm 16 K CMOS gate array on a thin SIMOX film. IEEE. Trans. Electron Devices. 1993; 40: 179-186.

[2] The International Technology Roadmap for Semiconductors 2006 update, Front End Process.

[3] Mumola P. B, Gardopee G. J, Ferg T, Ledger A. M, Clapis P. J, Miller P. E. Plasma-thinned silicon-on-insulator bonded wafers. Proceedings of the Second International Symposium on Semiconductor Wafer Bonding Science, Technology, and Applications. 1993: 410-422.

[4] Mori Y, Yamauchi K, Yamamura K, Sano Y. Development of Plasma Chemical Vaporization Machining. Rev. Sci. Instrum. 2000; 71: 4627-4632.

[5] Mori Y, Yamamura K, Sano Y. Development of the Machine for the X-ray Mirror Fabrication. Rev. Sci. Instrum. 2000; 71: 4620-4626.

[6] Mori Y, Yamamura K, Sano Y. Thinning of silicon-on-insulator wafers by numerically controlled plasma chemical vaporization machining. Rev. Sci. Instrum. 2004; 75: 942-946.

[7] Tricard M, Dumas P. R, Golini D, Mooney J. T. SOI Wafer Polishing with Magnetorheological Finishing (MRF). Proceedings of the IEEE SOI Conference 2003: 127-129.

[8] Yamamura K. Fabrication of Ultra Precision Optics by Numerically Controlled Local Wet Etching. Annals of the CIRP. 2007; 56: 541-544.

[9] Yamamura K, Mitani T. Etching characteristic of local wet etching of silicon in HF/HNO_3 mixtures. Surf. Interface Anal. 2008; 40: 1011-1013.

MANUFACTURE AND MEASUREMENT OF A PRECISION MILLI-SCALE GERMANIUM OPTICAL ARRAY FOR NOVEL THERMAL IMAGING SYSTEMS

Matthew A. Davies[1], Brian S. Dutterer[1], Thomas Suleski[2], and Michael L. Barkman[1]
[1]Department of Mechanical Engineering and Engineering Science
[2]Department of Physics and Optical Science
The University of North Carolina at Charlotte
Charlotte, North Carolina, USA

INTRODUCTION

Micro-optics is one of the foremost technologies enabling the production of compact optoelectronic and micro electro-optical mechanical systems for a wide range of industries (e.g., biomedical, surveillance, telecommunications, and many others). Photolithographic techniques are the dominant method of manufacturing many types of micro-optics due mainly to the success of similar techniques in the electronics industry for manufacturing and integration. However, lithographic methods face limitations that can restrict their applicability including the accuracy of lens prescriptions, the primarily 2-dimensional nature of the process and the amount of material that can be cost effectively removed. Five axis diamond machining can extend the capability and functionality of micro-optic components but providing a platform on which structures ranging from many centimeters to sub-micrometer level can be incorporated in the same component. Kinematic alignment features and true 3-dimensional structures -- important particularly in the performance of optical components - can also be manufactured on the same component. Thus packaging/assembly features and performance features can be manufactured in a single set-up. These approaches may provide a cost-effective alternative that meets the strict requirements of micro-optics production, while also serving as an enabling technology for new types of micro-optical components and systems [1].

In this work, we apply these ideas to the manufacture of a germanium multi-lens array aimed at credit-card-thin thermal imagers. The multiple lenses are of an aspheric meniscus-type with millimeter-scale apertures and are designed to work with a single thermal sensor array. There is a continued drive for miniaturization of optical imaging systems, ranging from military applications to cell phone cameras. One approach to reducing the thickness of imaging systems is to replace one large lens with an array of smaller lenses; then, though image processing, reconstruct a single high-resolution image from the lower resolution images generated by the lens array (see, for example, [2-6]). This paper discusses one of the first attempts to apply this technology to thermal imaging systems in Germanium using diamond machining.

DESIGN OF THE OPTIC

The optic discussed here is a dual-sided aspheric lens array fabricated in germanium for integration into a compact multi-aperture long wavelength infrared (LWIR) imaging system for the 8-12 micrometer band, as illustrated in Figure 1. The germanium element contains an array of aspheric convex lenses (diameter 4.93 mm and sag 538 microns) on one side, and an array of aspheric concave lenses (diameter 4.00 mm and sag 292 microns) on the opposite side. The target center-to-center (distances between maxima/minima) accuracy of the lens components on a single side was ±1 micrometer. The target side-to-side alignment of the maxima and minima of each lens was ±5 micrometers, and the target surface finish was 5 nm R_a.

For this example, the design requirements push the lens specifications (particularly lens sag) outside the realm of conventional microlens fabrication techniques, which are typically based on lithographic patterning (e.g., thermal reflow, laser direct-write, grayscale lithography) and transfer etching [7]. Diamond turning [8, 9] has the capability to fabricate lenses on the necessary size scales, but standard diamond turning systems are not conducive to fabrication of arrays of lenses, particularly with high placement accuracy. The lens arrays in this

system must be integrated with other optical components fabricated through lithographic methods; thus, whatever technique is finally chosen to fabricate the germanium lens arrays must be compatible with on-wafer fabrication, and must also provide placement precision comparable to lithographic techniques.

MANUFACTURING ARRANGEMENT

The machining of the aspheric micro optics array in germanium was performed on a Moore Nanotechnology 350 FG 5-axis nano-solid freeform generator. The machine has three linear axes (X-Y-Z) with a feedback resolution of 1 nm and a stated linear positioning accuracy better than 10 nm. All of the axes have a straightness of better than 0.5 µm across the full range of travel of the machine (350 mm by 300 mm by 150 mm). The machine has an air-bearing main spindle that can be used for turning at speeds up to 10,000 RPM or as a coordinated (C-axis) with an angular positioning accuracy of ±2.0 arc seconds. It also has an 110,000 RPM high-speed spindle and an oil-hydrostatic rotary axis (B-axis). The machine also has an integrated 100X digital microscope for tool inspection. For expediency in manufacturing this prototype a turning rather than milling approach was taken; however for production of multiple components (20 per wafer) a milling approach is being considered.

The lens arrays were machined on a 2 mm thick, 150 mm diameter germanium wafer. A precision grid of gold fiducial lines had already been lithographically patterned on both sides of the wafer. Since the lens locations are referenced to the gold fiducial lines, a custom kinematic mount for the on-machine microscope was constructed so that the wafer surface could be viewed from along the spindle axis. Since the entire lens array is off-center, a custom vacuum system was interfaced with the spindle. The balance was adjusted using an on-machine radial error motion to 2 nm – 3 nm at a 500 RPM spindle speed with the wafer mounted in the desired positions.

To determine the position of the origin of the lens array, the on-machine microscope was mounted to view the gold cross-line origin on the wafer: the origin of the first lens array. The wafer and the spindle were rotated in 180° first horizontally and then vertically. The position was corrected using the machine x-y axes in conjunction with the three pin system until

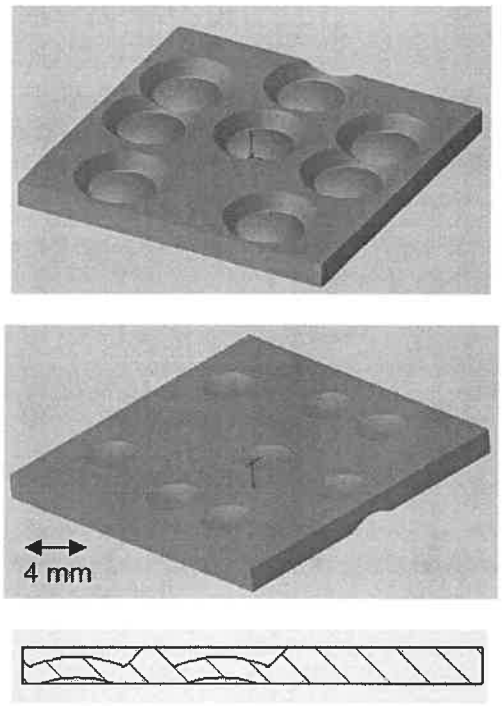

FIGURE 1: Two-sided Germanium lens array having eight meniscus-type aspheric optics.

rotations indicated that the gold line origin was centered on the spindle axis to better than ± 1 micrometer. The wafer was removed and replaced more than ten times to ensure that the pin-system was repeatable; also ruling tests were conducted in cupra-nickel 706 to test the repeatability of the positioning system. Next the tool was centered first using the on machine microscope mounted on the y-axis (normal tool centering location) and then cutting tests and the on-machine microscope again mounted onto view the part was used to center the tool in x

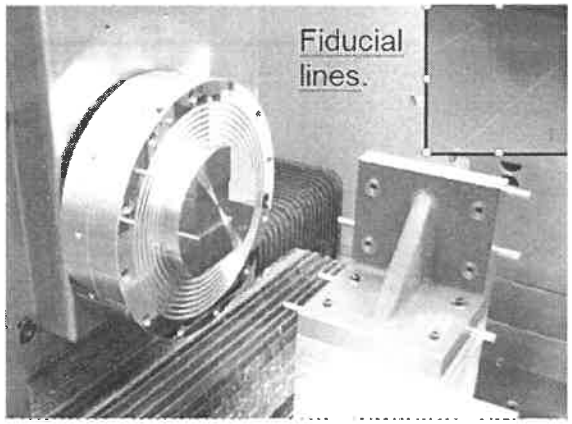

FIGURE 2: Three pin positioning system and cupra-nickel test wafer used to check positioning repeatability by ruling tests.

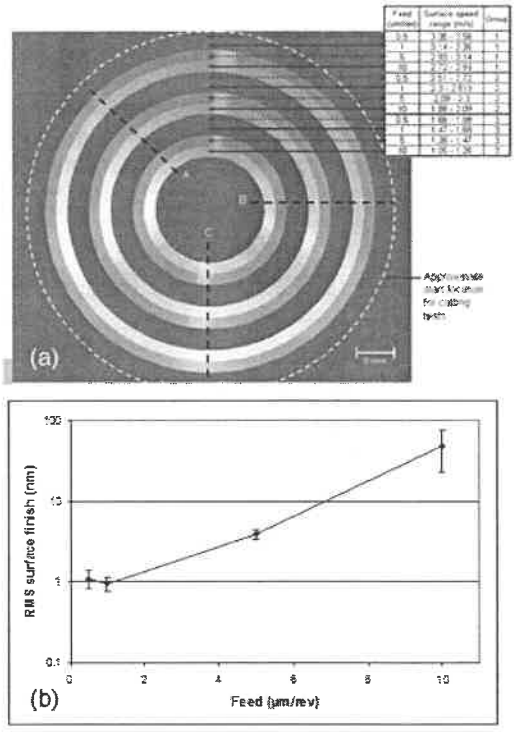

FIGURE 3: (a) shows a set of cutting tests made on a single wafer in different parameter regimes; and (b) shows the variation of surface finish with federate.

and y to better than ± 1 micrometer. Now the wafer position coordinate system could be used to place the wafer for turning by the tool for each lens. The wafer could also be "flipped" and repositioned using a corresponding gold fidicial cross-line set on the opposite side; thus side-to-side positioning accuracy was in part limited by the lithographic process to lay out the locating features.

MACHINING PARAMETER DEVELOPMENT

Single crystal diamond tools with -25° and -45° rake angles were confirmed to enable ductile-regime cutting. It was also confirmed that combinations of depths of cut ranging from 1 µm to 10 µm and feedrates ranging from 0.5 µm/rev to 10 µm/rev produced ductile-regime cutting. Surface speeds ranged from 1 m/s to 3.5 m/s. Shown in Figure 3 (a) are three bands cut with a -25° rake angle with a 381 micrometer nose radius tool and a depth of cut of 2 µm. Also shown in Figure 3(b) is the change in surface finish (measured on a white light interferometer) for all parameter values and at the three different crystal orientations A, B, and C and for the three groups of parameters. Feedrate which was by far the most sensitive variable for determining finish as has been previously shown in the literature [10-12].

RESULTS

The lens arrays were machines with a -45° rake angle and a constant spindle speed of 500 RPM. Programming of the aspheric surface was done with a commercial software package specialized for machining optics. Both sides (compare to Figure 1) of the lens array are shown in Figure 4. For reference the gold fiducial grid is approximately 26 mm on a side.

Both a micro Twyman-Green interferometer configuration and scanning white light interferometry (SWLI) were used to perform an initial assessment of the form accuracy and surface finish of the lens arrays. While it was not possible to measure the entire lens surfaces with available equipment, the results obtained suggest that the lenses are well within design tolerance. Using the micro Twyman-Green configuration, the base radii of curvature were measured to match the design values to within the measurement uncertainty of the interferometer setup (~1%), with a form accuracy better than λ/10 at 632.8 nm

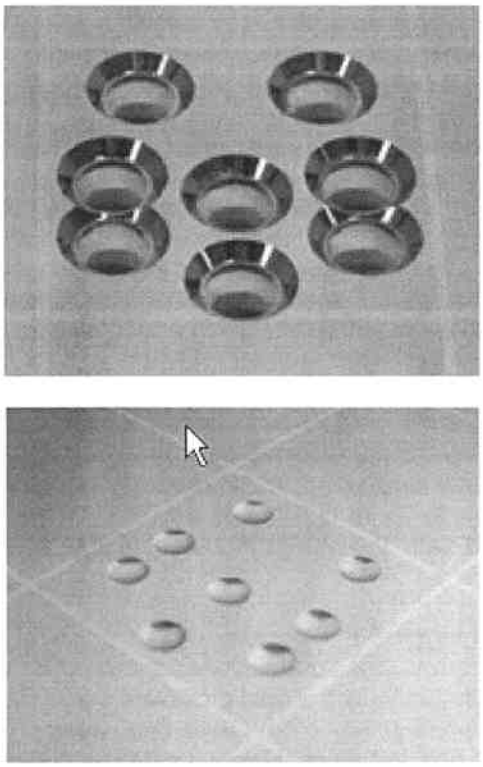

FIGURE 4: Refractive lens array fabricated in Germanium for infrared imaging system.

(measurements performed over a central patch with a 0.09 NA objective).

Similarly, SWLI measurements were performed to assess the surface finish of the germanium lenses. As before, it was not possible to measure the entire lens surfaces, but measurements around the apex of the lenses again showed excellent quality, with an estimated surface finish of ~ 2nm RMS. It is interesting to note the small circular features at the apex of the lenses (~10-15 nm high) which are likely due to motor pole print-through in the system but are not large enough to affect the performance of the optic.

In conclusion, we have demonstrated the fabrication of a precision, dual-sided microlens array in germanium for integration into a compact, LWIR multi-aperture imaging system. Sample cutting parameters for germanium were discussed, and characterization of the devices demonstrates that lens arrays outside the capability of standard lens array fabrication techniques can be realized through free-form micromachining with near lithographic precision, with excellent form accuracy and surface finish. Integration and testing of the assembled system is ongoing. Future work is aimed at utilizing micro-milling and/or ruling to improve and/or change the performance of the germanium optics. The techniques proposed here are not limited to germanium but are also directly applicable to any diamond turnable material (metals, plastics) and can be used to manufacture optics or molds for optics.

REFERENCES

[1] M. A. Davies, C. J. Evans, S. R. Patterson, R. Vohra, and B. C. Bergner, Application of Precision Diamond Machining to the Manufacture of Micro-photonics Components, Proc. SPIE 5183, 2003, 5183:94-108.

[2] A. Ashok and M. A. Neifeld Recent progress on multidomain optimization for ultrathin cameras, 2006, Proc. SPIE 6232, 62320N.

[3] D. J. Brady, M. Feldman, N. Pitsianis, J. P. Guo, A. Portnoy, and M. Fiddy, Compressive optical MONTAGE photography, Proc. SPIE 5907, 2005, 590708.

[4] Y. Kitamura, R. Shogenji, K. Yamada, S. Miyatake, M. Miyamoto, T. Morimoto, Y. Masaki, N. Kondou, D. Miyazaki, J. Tanida, and Y. Ichioka Reconstruction of a High-Resolution Image on a Compound-Eye Image-Capturing System, Appl. Opt., 2004 43(8):1719-1727.

[5] N. P. Pitsianis, D. J. Brady, A. Portnoy, X. Sun, T. Suleski, M. A. Fiddy, M. R. Feldman, and R. D. TeKolste, Compressive imaging sensors, Proc. SPIE 6232, 2006 62320A.

[6] J. Tanida, T. Kumagai, K. Yamada, S. Miyatake, K. Ishida, T. Morimoto, N. Kondou, D. Miyazaki, and Y. Ichioka, Thin Observation Module by Bound Optics (TOMBO): Concept and Experimental Verification" Appl. Opt., 2001, 40(11):1806-1813.

[7] D. Daly, Microlens Arrays. New York: Taylor & Francis Inc., 2001.

[8] E. Brinksmeier and W. Preub, "Fabrication of Precision Molds," 1st International Conference and General Meeting of the European Society for Precision Engineering and Nanotechnology (euspen), 1999, 187-190.

[9] M. Weck and S. Fischer, "Manufacturing of Microstructures Surfaces using Ultraprecision Turning, Milling and Shaping," 1st International Conference and General Meeting of the European Society for Precision Engineering and Nanotechnology (euspen), 1999, 420-423 (1999).

[10] P. N. Blake and R. O. Scattergood, "Ductile-Regime Machining of Germanium and Silicon" Journal of the American Ceramic Society, 73(4), 949-957 (1990).

[11] J. Yan, K. Maekawa, J. Tamaki, and A. Kubo, "Experimental Study on the Ultraprecision Ductile Machinability of Single-Crystal Germanium" JSME International Journal, Series C, 47(1), 29-36 (2004).

[12] W. S. Blackley and R. O. Scattergood, "Chip topography for ductile-regime machining of germanium" Journal of Engineering for Industry, Transactions of the ASME, 116(2), 263-266 (1994).

MANUFACTURE OF LARGE OPTICS: MATERIALS AND PROCESSES

David Brooks and Anthony E Gee
Department of Physics and Astronomy
University College London
Gower Street, London, England WC1E 6BT

1 HISTORY

1.1 Glass, Lenses, Spectacles and Mirrors

By 1500BC, in the E Mediterranean, colourless glass was being produced, (including water-filled blown spheres which could focus) and quartz crystal was also available [1,2]. In 212BC Archimedes defended Syracuse from the attacking Roman fleet using 'a burning glass' [3] (a translation error for polished metal shields?).

In 11thC Alexandria, scholar Abu Al Hasan of Baghdad, (also referred to as 'Al-Hazen') recorded geometrical theory of concave mirror focusing [2]. This was followed in the late 13thC by ophthalmic correction lenses (spectacles) due to English cleric-inventor Roger Bacon [2] and soon 'opticians' were making them across Europe. However, rough grinding and fine polishing of small glass optics to spherical form and fine finish (to 10s of nm) remained more accepted than understood.

1.2 The Telescope

The first utility telescope using two lenses is credited to Lippershey, a Dutch spectacle maker, in 1608. Hearing of it, Galileo in Padua made a telescope for the merchants of nearby Venice (to give advance knowledge of ships arriving).

In 1668, Newton [5] constructed the first reflecting telescope using a 34 mm (1.33 ins) diameter primary mirror of focal length 155 mm (6 ins) made from 'bell metal' (bronze). Being brittle, the established artisan spectacle-makers' glass-working techniques obtained its intrinsic metallic reflection. Not suffering the chromatic aberration of contemporary refractor telescopes, the instrument had much shorter focal length and so was considerably more compact with higher resolution.

Newton pioneered use of a pitch-polisher tool charged with abrasive, ('putty' in his case: finely powdered calcium carbonate and linseed oil)[5]. The mirror was made from the brittle bronze eutectic comprising 67% copper and 33% tin with an added doping of arsenic to 'whiten' the metal [2]. Known as 'speculum' in optical sciences, this alloy readily tarnishes, requiring re-polishing to maintain adequate reflectivity (63%). It was used in ever larger telescope mirrors over the next two hundred years, taking diameters to 1.8m.

1.3 Mirrors vs Lenses

It is worth comparing the lens and mirror as primary focusing elements.

In a reflecting telescope, the secondary mirror causes obstruction but there is little resulting loss in light or resolution.

A lens requires two surfaces coaxially aligned on a single blank which demand precision manufacture, including their mutual orientation in four degrees of freedom. Being effectively a 'curved prism', the single lens *disperses* colours (wavelengths) differentially to foci along the optical axis. To reduce the effects, telescopes were made with (ungainly) long foci and tubes until the advent of the two-lens (doublet) 'achromat' in the 18thC which brought the foci for two colours (blue and red) into coincidence. However, the two extra surfaces add considerably to manufacturing costs.

Definitively, a mirror requires only one surface, involving no transmission, refractivity or dispersion. However, an error e in its surface causes a reflected (air) path error $2e$. In a refracting glass surface the error e is desensitised by a factor of 3 as the resulting path change involves exchange of glass (index 1.5) with air (index 1.0). This applies to both surfaces (or all four in an achromatic doublet. However, form errors in a doublet can be offset to some extent by mutual rotation.

Glass transparencies (>90%) considerably exceed reflectivities of most metals and a lens does not tarnish. However, larger lens thicknesses (proportional to aperture) incur temperature-gradient stress and refractivity problems resulting in index-differences, scatter and micro-cracking. Metal mirrors suffer fewer thermal problems and are considerably more rugged. Thermal defocus is the main disadvantage with advantages of improved mirror 'micro-seeing' and thermal emissivity.

2 LARGER APERTURE OPTICS

2.1 Needs

There are two fundamental drivers for increasing the aperture of objective focusing elements:

1. Finer image resolution, which is directly proportional to wavelength and inversely proportional to aperture diameter,
2. Increased light flux energy, ie brightness at the focus (proportional to the area of the optic, and diameter squared).

2.2 The 48 inch (1.2m) Mirror of Sir Wm Herschel (1738-1822)

William Herschel [4,6] was a musician-tutor in Bath when he took up astronomy. Unable to obtain satisfactory mirrors, he set about making them himself, including casting speculum blanks (at some personal risk) and learning to grind and polish their surfaces. Soon he produced mirrors considerably superior to those of the established instrument makers (enabling him to resolve objects hitherto unseen).

Herschel experimented with the alloy ratio, the grinding and polishing abrasives and the pitch materials. For rough form grinding, he used Naxos emery with iron or brass tools; they were then cleaned to become the backing for polishing pitch charged with rouge abrasive. For larger mirrors, he developed a series of polishing machines with crank-handle drives and ratchet and pawl systems to rotate the mirror and tool at preset differential intervals and rates with figure of eight motion.

Herschel undertook the first systematic observations of the night sky and in 1781 discovered Uranus. Appointed personal astronomer to King George III, he moved to Slough (to be near Windsor Castle for royal astronomical soirees). There he progressed mirror-making capability to a diameter of 1.22 m (48 in) and 12.2m (40ft) focal length.

2.3 The 72 inch (1.8m) Mirror of William Parsons, 3rd Earl of Rosse (1800-1867)

At Birr Castle, Co Offaly, Ireland, Lord Rosse investigated production of cast speculum mirrors [3,4]. He also investigated lightweight mirrors comprised of a thin-walled backing structure soldered to a faceplate could detect no optical differences between this blank and a monolith cast disc. However, for unspecified reasons, he reverted to the monolith casting for his telescopes.

His work culminated in a telescope 1.83m in diameter and 16m long which remained the world's largest from 1845 to 1917. The 150 mm (6 in) thick primary mirror (weighing 3.5 tonnes) took eight casting attempts. Twyman [2] reports that Rosse polished it with a pitch tool using rouge with ammonia soap and water (the ammonia retarded and removed tarnishing). The instrument has been rebuilt in recent years (see 5.3).

2.4 Chemical and Electrolytical Enhancement of Ablation, (Henry Draper 1837-1882)

Draper produced speculum mirrors, based on alloy proportions obtained on a visit to Lord Rosse [3,4]. He perfected techniques of figuring with acid and experimented with electrolytic action for figuring, (making the speculum the positive pole of a voltaic circuit with acidulated water as electrolyte). Such techniques are currently employed in the semiconductor industry to speed the polishing of sawn wafers.

3. REFRACTOR VS REFLECTOR

By the end of the 19thC, lens apertures approached a plateau culminating in 40 inches (1.01m) for the objective of the Yerkes Observatory refractor designed by G E Hale [3,4]. As chemical silvering had become available [4], on moving to Mt Wilson Observatory, he redirected his efforts toward larger glass mirrors: first a 50 inch instrument followed by the 100 inch (2.5m) Hooker Telescope of 1917 and then the 200 inch (5m) completed on Mt Palomar in 1948. This work set the scene for a number of 4m aperture instruments using glass or glass-ceramic mirrors.

Doublings in aperture require proportionate scaling of required associated technologies. During chemical silvering, the 3 tonne 100 inch mirror was agitated successfully but, when the 25 tonne 200 inch mirror was attempted, the building agitated instead. Fortunately, at Harvard Observatory Lab., John Strong presciently demonstrated the viability of aluminium vapour deposition [3] which now sees extensive use for reflecting optics, multiple thin film filters and VLSI microelectronics fabrication.

Monolith glass mirror technology continued to 8m apertures based on the rotating furnace [13] which considerably reduced roughing requirements for faster aperture ratios in more compact instruments. These offered improved performance and the considerable economies of shorter tube length (to the cube of which, the building volume is proportional).

4 PRODUCTION OF LARGE ASPHERIC OPTICS

4.1 Special Issues in Polishing Aspherics

The well-tried techniques of convergent (spherical) optical polishing for spectacle manufacture requires the polishing tool and optical surface to 'nest' throughout ie maintaining close contact for all overlapping (shearing) mutual positions when subjected to the relevant two degrees of translational freedom and one of rotation [7]. A spherical optic is 'stigmatic' (ie yields best focus) only for auto-focussing a point source.

Alternate conic sections of rotation apply to other required optical geometries: the paraboloid focuses collimated parallel light (including from a point source at infinity), the ellipsoid focuses light diverging from a point source at one of its foci so as to converge at the other and the hyperboloid will refocus an already convergent light beam to a different focus (and reciprocity applies).

In aspherics, radius of curvature varies with radial position so the polishing lap must either be small enough or sufficiently flexible not to impose unacceptable departure from the required form; even so, force and dwell must be carefully controlled to achieve the required local ablation. For aperture ratios >10, the difference between spherical and requisite aspheric form is deemed negligible and the lap can be full size. As the aperture ratio reduces below this value, then so must the lap-size unless it is has form-adaptable capability.

4.2 Machining to Form plus Fine Polishing

A novel process for aspheric optics' manufacture was devised by Dr Reason pre 1950 at the Taylor Hobson Company, Leicester [1]. The form was generated with a diamond tool (either single point or high speed rotating burr) on an ultra-precision machine tool to within *the requisite aspheric form error specification* whilst accepting (grey) surface finish equivalent to traditional free abrasive roughing. With a soft bag-polisher, the time is established for removing subsurface damage and the resulting induced ('parasitic') spherising error measured. Production of the required aspheric then requires machining of the prepolished form so as to include a correction-term for the unwanted spherisation incurred in polishing.

Horne [1] describes a similar approach employed contemporarily by the Bell and Howell Co, Chicago. These facilities were used to produce aspheric aerial camera and projection lenses of up to 175mm (7 inch) aperture and Schmidt correctors to 275mm (11 inches).

4.2 Ion Beam and Magnetorheological Finishing

Over the last thirty years, new processes such as ion beam ablation and magnetorheological polishing have been developed. For new telescope designs requiring very fast (short focus) optics, traditional methods of production cannot produce the required surface quality for the optical performance necessary. With the aid of computer control, production techniques have been developed to produce the latest generation of large telescopes [12].

4.3 Metrology

At apertures below about 0.4m, standard interferometric wavefront metrology and other full aperture tests can be employed using commercial instrumentation. Traditional tests, such as Foucault's arrangement [2] amenable to larger apertures, are restricted to the stigmatic focusing condition. In the case of perfect spherical mirror, a point source at its centre of curvature will return a stigmatically focused beam there.

However, for paraboloidal objectives used in most astronomical telescopes, stigmatic focusing requires a (bright) point test source at infinity or a full-aperture well-collimated input source light beam which in turn requires a collimator optic of the same or greater aperture. An alternative is a 'contrived null' test based on an appropriately (conjugally) distorted source wavefront from a conjugate focal point, the nominated 'centre' of curvature in the case of a mirror. Using this, a perfect test-optic shows stigmatic focus but the Hubble Large Space Telescope illustrated difficulties incurred in this approach.

Other tests for large apertures include the Shack-Hartmann point source array test [1-3] which is particularly suited to electronic areal image detectors and can be enhanced using Foucault's test [1]. The Ronchi test [1] can be modified by predistorting the line pattern either optically or by computer generation.

Testing large convex secondary mirrors is particularly troublesome at full aperture as it is difficult to access a focus other than in a completed instrument.

5 DEVELOPMENTS

5.1 Large Arrays and High Volume Production

With current conceptions of large telescopes employing primary focusing elements with apertures in the 20m+ range and areas of 100s of m^2, the manufacture of tessellated multi-mirror arrays is encouraging further interest in metal optics. During production, storage and installation, of such large numbers of (1-2m) optics, ruggedness during handling becomes an issue. An accident with a malleable metal mirror will usually result in some minor damage but the optic will be still repairable and usable. However a glass (or brittle metal) optic is very susceptible to fracture rendering it unusable. In the last few decades, around 6% of large optics produced have been lost through accidents during handling [14].

Development of beryllium, silicon carbide and aluminium lightweight substrates enables construction of adaptive and active metal optics with low inertia characteristics, capable of withstanding high momentary loads [11]. They also enable rapid tilting accelerations for infra-red astronomy and high frequency-response in adaptive secondary mirrors. However, there are (different) issues of manufacturing process costs and handling for both beryllium and silicon carbide.

Soft metals like aluminium and beryllium cannot themselves be optically polished due to factors including their anamorphous grain structure. Since 1944, the development of electroless autocatalytic 'Kanigen' nickel-phosphide coating [1] has enabled a regular hard layer of nickel to be deposited on such metallic substrates. Although it offers only 63% intrinsic reflectivity, it can be polished using classical (glass-working) techniques to take a vapour deposited aluminium coating [1].

5.2 Aluminium Mirrors

As a result of the development of high precision externally pressurized gas and liquid bearings over recent decades, single-point diamond lathe turning enables aluminium mirrors to be machined to form (_/4) and to near-finishes (2nm R_a) for astronomical telescope mirrors.

Aluminium has merits of ease of casting, machining and ruggedness of handling which makes it attractive in competing with other materials such as glasses, glass ceramics, beryllium and silicon carbide.

The Euroxpean Southern Observatory (ESO) investigated constructing the primary mirror of their 'New Technology Telescope' (NTT) from aluminium although it was eventually made from zero expansion

glass. This in turn led to the 'Large Active Mirrors for Astronomy' (LAMA) programme, which examined the possibility of manufacturing the 'Very Large Telescope' (VLT) primary mirrors from aluminium. The LAMA programme concluded with the construction of two 1.8 meter diameter nickel coated aluminium mirrors [8]. A 23 feet diameter aluminium collimating mirror was made for the JPL Solar Space simulator [9] in 1967. It was highly polished to 1200 inch radius of curvature but did not require astronomical form quality.

5.3 Reconstruction of the Rosse 1.8m Telescope at Birr Castle

In 1996, funding was obtained through various sources to rebuild the Rosse 1.8m telescope at Birr Castle [10]. The original speculum mirror, (on exhibition at the Science Museum, S Kensington, London) was deemed too fragile so it was decided to make the required replacement of aluminium with a nickel coating to be polished to optical quality [11] and overcoated with a vapour deposited aluminium layer. The Optical Science Lab., University College London, undertook the work to reconstruct the optics. This included supplying the paraboloidal primary and flat secondary aluminum mirrors, two eyepieces and their mounts, the mounting trolley with whiffle tree support system for the primary and support leg mount for the secondary. These were successfully installed on the telescope in 1999 [11].

6 SUMMARY

Current plans for new larger telescopes extend demands beyond previous manufacturing capabilities in terms of scale, materials and processes. Reviews of these indicate that metal mirrors (in particular, aluminium) may provide for the way forward.

7 REFERENCES

[1] Horne D. F., *Optical Production Technology* Adam Hilger, London, 1972 (or 2nd edn Adam Hilger, Bristol 1983).

[2] Twyman F., *Prism and Lens Making*, Hilger and Watts, London, 2nd ed 1952; (republished Adam Hilger/IOP , Bristol, 1988).

[3] King H. C., *The History of the Telescope*, Griffin, London, 1955.

[4] Learner, R., *Astronomy Through the Telescope,* Van Nostrand Rheinhold, New York NY, 1981.

[5] Newton I, *Opticks,* Dover, New York NY,1979 (orig.pub. 1704).

[6] Herschel Sir Wm. *Personal Archive*, Royal Astronomical Society, Burlington House, London W1V 0NL.

[7] Gee A. E., *Modeling the Mechanics of Free Particulate Abrasive Polishing from the Viewpoint of the Single Point Process*, Proc SPIE, Vol 2775, p 611-618, 1996.

[8] Rozelot J. P., *Why Choose a Primary in Aluminium: Traps or Fashion?* Proc International Workshop on Mirror Substrate Alternatives, pp3-17, CRNS-NSO, Grasse, France, 1995.

[9] Eddy R. P. *Fabrication of the 23ft Collimating Mirror for the JPL 25ft Space Simulator*. NASA Technical Report 32-1214, Jet Propulsion Lab., Pasadena CA, 1967.

[10] **http://www.birrcastle.com/telescopeRestoration.asp**

[11] Brooks D. PhD Thesis, University College London, 2001.

[12] Wilson R. N., *Reflecting Telescope Optics 2*, pp33-37 Springer, Berlin, Germany, 1999.

[13] **http://mirrorlab.as.arizona.edu/SOMLBrochure.pdf**

[14] Walker D. D. & Bingham R. G., The Choice of Material for Adaptive Secondary Mirrors. Proc International Workshop on Mirror Substrate Alternatives, pp19-28 CRNS-NSO, Grasse, France, 1995.

A TWO-DEGREE-OF-FREEDOM LINEAR ENCODER FOR MEASUREMENT OF POSITION AND STRAIGHTNESS

Akihide Kimura[1], Yoshikazu Arai[1] and Wei Gao[1]
[1]Department of Nanomechanics
Tohoku University
Sendai, Miyagi, Japan

INTRODUCTION

Displacement measurement is an essential technique in the field of precision metrology and precision manufacturing. The linear encoder is the most popular displacement sensor for measurement of the position of a moving stage along the axis of motion. Many commercially available linear encoders, whose principles are based on interference and diffraction, can achieve nanometer-level accuracy and sub-nanometer level resolution over the range of more than tens of millimeters [1]. Compared with laser interferometers, linear encoders are more robust to influences of air pressure, air temperature and relative humidity because of the short optical length in the sensor system.

In addition to position measurement, straightness measurement, which is defined as the displacement along the axis vertical to the axis of motion, is also an essential task for a precision stage [2]. Conventionally, it is necessary to employ a different sensor, such as the straightness measurement kit of a laser interferometer or the combination of a capacitance-type displacement sensors and a straightedge, to accomplish the straightness measurement. This makes the measurement system complicated and expensive.

To solve these problems, we propose a two-degree-of-freedom (two-DOF) linear encoder that can measure not only the X-directional position but also the Z-directional straightness of a linear stage. In this paper, principle of the two-DOF encoder and a prototype encoder are introduced. Basic performances of the prototype encoder are also reported.

PRINCIPLE

Figure 1 shows a schematic of the two-DOF linear encoder. The encoder is composed of a refractive scale grating with a pitch of P, and an optical sensor head. The scale grating is the same as that used in a conventional linear encoder. Differing from the conventional linear encoder, a reference grating is employed in the sensor head. The reference grating is identical to the scale grating except the scale length. The reference grating is set perpendicular to the scale grating like the mirrors of a Michelson interferometer.

The optical sensor head consists of a laser diode (LD), a collimating lens, four prisms, a non-polarizing beam splitter (BS), a reference grating and a detector unit. The detector unit is composed of two photo-detectors (PDs), PD X+1 and PD X-1. A laser with a wavelength of λ, which is emitted from the LD, is collimated by the collimating lens. The collimated laser is divided into the two beams by the BS. Each beam is projected onto the scale grating and the reference grating. The prisms bend X-directional ±1 order diffracted beams to make them parallel to the collimated laser.

In the optical sensor head, X-directional ±1 order diffracted beams from the two gratings are superimposed to generate interference signals. Assume that $Us_{X\pm1}$ and $Ur_{X\pm1}$ represent the wavefront functions of the X-directional ±1 order diffracted beams from the scale grating and the reference grating respectively. $Us_{X\pm1}$ and $Ur_{X\pm1}$ can be obtained as

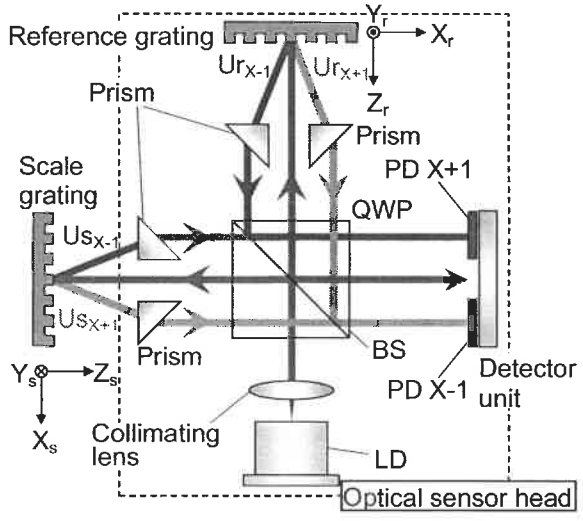

Figure 1. Schematic of the two-DOF linear encoder.

$$Us_{X+1} = U_0 \exp(iK\Delta x) \cdot \exp\{iv(1+\cos\theta)\Delta z\} \quad (1)$$

$$Ur_{X+1} = U_0 \quad (2)$$

$$Us_{X-1} = U_0 \exp(-iK\Delta x) \cdot \exp\{iv(1+\cos\theta)\Delta z\} \quad (3)$$

$$Ur_{X-1} = U_0 \quad (4)$$

where $K=2\pi/P$, $v=2\pi/\lambda$, θ is the first-order diffraction angle, U_0 is the amplitude of the wave. The first term of Us_{X+1} is produced by the phase shifting effect of the scale grating displacement along the X-direction. The second term is produced by the optical path difference caused by the scale grating displacement along the Z-direction.

Then, Us_{X+1} and Ur_{X+1} generate the X-directional +1 order interference wave U_{X+1}.

$$U_{X+1} = Us_{X+1} + Ur_{X+1} \quad (5)$$

Similarly, the X-directional -1 order interference wave U_{X-1} is given by

$$U_{X-1} = Us_{X-1} + Ur_{X-1} \quad (6)$$

The interference signals $I_{X\pm1}$, which are detected at PD X±1 respectively, can be calculated as the conjugated complex multiplication of interference waves.

$$\begin{aligned} I_{X+1} &= U_{X+1} \cdot \overline{U_{X+1}} \\ &= 2U_0^{\,2}\left[1+\cos\{K\Delta x + v(1+\cos\theta)\Delta z\}\right] \end{aligned} \quad (7)$$

$$\begin{aligned} I_{X-1} &= U_{X-1} \cdot \overline{U_{X-1}} \\ &= 2U_0^{\,2}\left[1+\cos\{-K\Delta x + v(1+\cos\theta)\Delta z\}\right] \end{aligned} \quad (8)$$

Since equations (7)(8) are functions of Δx and Δz, XZ-directional displacements can be calculated from these interference signals basically. However, the interference signals are influenced by the variation of U_0, which is proportional to the intensity of the laser. Moreover, the moving directions of the scale grating cannot be distinguished from equations (7)(8) because of the nature of the cosine function.

ARRANGEMENT OF THE OPTICAL SENSOR HEAD

To solve above problems, layout of the optical sensor head is arranged as *Figure 2*. An incident beam from the LD is divided into two beam components (p- and s-polarizations) at a polarizing beam splitter (PBS). Each beam passes through quarter wave plates (QWPs) whose fast axis is set 45 degree from the p-direction of the incident beam and diffracted beams return back through the prisms and the QWPs. Polarization states of diffracted beams are translated into perpendicular directions by passing through the QWPs twice, so superimposed diffracted beams go to the BS. Then, the superimposed diffracted beams are divided into four paths by the BS and the two PBSs. Four divided waves go to four detector units each other and interference signals are detected at each detector unit.

In the optical paths between the BS and PBSs, three QWPs are inserted as *Figure 2*. The fast axes of the QWPs are also shown. These QWPs control phases and polarization directions of four divided waves. As a result, the interference signals detected at each detector unit have 0°, 180°, 90° and 270° phase-differences. Finally, four two-phase output signals S_α and S'_α (α=X+1, X-1) can be obtained by processing these interference signals.

$$\begin{aligned} S_{X+1} &= \frac{I_{X+1}(0^\circ) - I_{X+1}(180^\circ)}{I_{X+1}(0^\circ) + I_{X+1}(180^\circ)} \\ &= \sin\{K\Delta x + v(1+\cos\theta)\Delta z\} \end{aligned} \quad (9)$$

$$\begin{aligned} S'_{X+1} &= \frac{I_{X+1}(90^\circ) - I_{X+1}(270^\circ)}{I_{X+1}(90^\circ) + I_{X+1}(270^\circ)} \\ &= \cos\{K\Delta x + v(1+\cos\theta)\Delta z\} \end{aligned} \quad (10)$$

$$\begin{aligned} S_{X-1} &= \frac{I_{X-1}(0^\circ) - I_{X-1}(180^\circ)}{I_{X-1}(0^\circ) + I_{X-1}(180^\circ)} \\ &= \sin\{-K\Delta x + v(1+\cos\theta)\Delta z\} \end{aligned} \quad (11)$$

$$\begin{aligned} S'_{X-1} &= \frac{I_{X-1}(90^\circ) - I_{X-1}(270^\circ)}{I_{X-1}(90^\circ) + I_{X-1}(270^\circ)} \\ &= \cos\{-K\Delta x + v(1+\cos\theta)\Delta z\} \end{aligned} \quad (12)$$

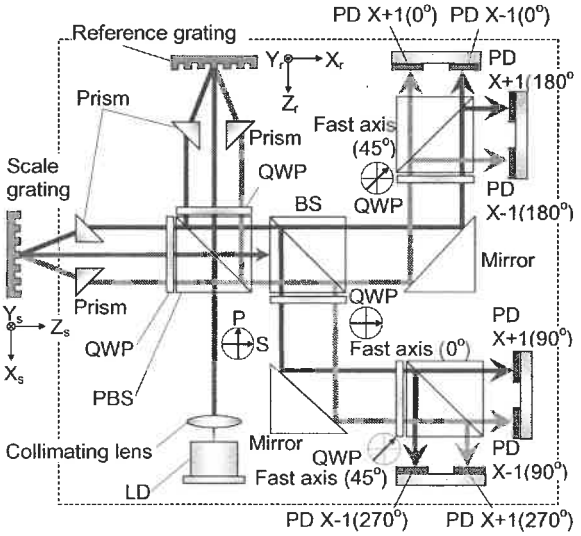

Figure 2. Arranged layout of the optical sensor head.

As can be seen, influence of U_0 is removed from equations (9)-(12). In addition, the moving directions of the scale grating can be judged from phase-relationships between two-phase output signals. From equations (9)-(12), XZ-directional displacements are calculated as

$$\Delta x = \frac{1}{2K} \cdot \left\{ \arctan\left(\frac{S_{X+1}}{S'_{X+1}}\right) - \arctan\left(\frac{S_{X-1}}{S'_{X-1}}\right) \right\} \quad (13)$$

$$\Delta z = \frac{1}{2v} \cdot \frac{1}{1+\cos\theta} \cdot \left\{ \arctan\left(\frac{S_{X+1}}{S'_{X+1}}\right) + \arctan\left(\frac{S_{X-1}}{S'_{X-1}}\right) \right\} \quad (14)$$

BASIC PERORMANCES OF THE TWO-DOF LINEAR ENCODER

Figure 3 is a photograph of a prototype two-DOF linear encoder. The size of the optical sensor head is about 50(X) x 50(Y) x 30(Z) mm^3. The LD with a wavelength of 685 nm is used in the optical sensor head. Diameter of the collimated laser is approximately 1 mm. The commercial gratings with a pitch of 1.6 μm are employed as the scale grating and the reference grating. The length of the scale grating is 12.7 mm, which determines the measurement range of the X-directional position. Detectors include two PD cells per one package.

Current signals from PDs are converted to voltage signals by IV converter circuits. After gains and offsets of the voltage signals are adjusted electrically, output signals expressed as equations (9)-(12) are produced by analog devices. In addition, residual gain and offset errors and phase-deviations between two-phase output signals are compensated by software. XZ-displacements are calculated from output signals processed above.

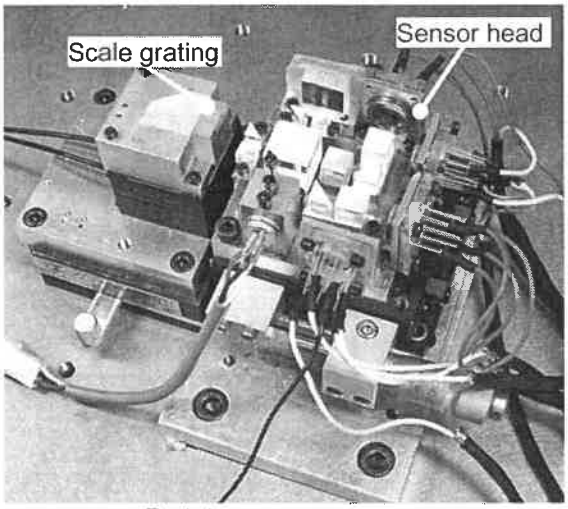

Figure 3. Prototype of the two-DOF linear encoder.

A working distance between the scale grating and the optical sensor head is about 5 mm, where the amplitudes of the output signals become largest. *Figure 4* indicates normalized peak-to-peak values of the output signals when the working distance is changed near 5 mm. It can be seen that peak-to-peak values of the output signals is kept half compared to max value within the working distance of ± 300 μm.

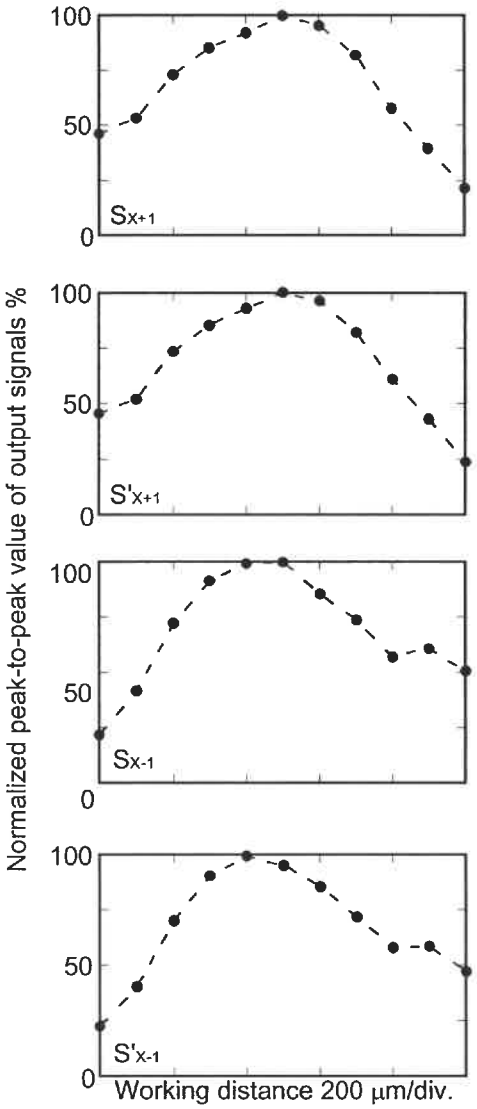

Figure 4. Normalized peak-to-peak values of the output signals with respect to the working distance.

Figure 5 shows processed two-phase output signals when the scale grating is moved by a piezo stage (PI, P-620. 2CL with linearity of ±0.02 % within stroke of 25 μm) along the Z-direction. A capacitive sensor is integrated inside the piezo stage for the feedback control. Interpolation errors are evaluated as a difference between Z output from the two-DOF linear encoder and the sensor inside piezo stage. The amplitudes of the interpolation errors are ±1 % with respect to displacement of one signal period. This value is equal to approximately ±16 nm and ±3 nm as X- and Z-displacements respectively. These errors can be caused by the polarization mixing effect, imperfection of the electrical circuit.

Figure 6 shows the X- and Z-directional output from the two-DOF linear encoder under condition the piezo stage is settled stationary. An interferometer (Canon, DS-80 with resolution of 0.08 nm) monitors the stability of the piezo stage and its output is also plotted in *Figure 6*. Sampling frequency is 100 kHz. Both sensors detect approximately 400 Hz vibration component, whose amplitude is maximum of 0.5 nm. It can be said that the two-DOF linear encoder has a resolution under 0.5 nm in the X- and Z- directions.

SUMMARY

A new displacement sensor, the two-DOF linear encoder, is proposed to measure not only the X-directional position but also the Z-directional straightness of a linear stage. The prototype of the two-DOF linear encoder is developed experiments are carried out to evaluate basic performances of the sensor. The working distance is approximately 5 mm. Interpolation error is about ±1 %, which is equal to approximately ±16 nm and ±3 nm as X- and Z-displacements respectively. Resolution is under 0.5 nm in the X- and Z- directions.

Future work is measuring of the X-directional position and the Z-directional straightness of the precision linear stage.

ACKNOWLEDGEMENT

This research is supported by a grant-in-aid from JSPS.

REFERENCES

[1] A. Teimel, Technology and applications of grating interferometers in high-precision measurement, Precision Engineering, 14-3, 147-154, 1992.

[2] Wei Gao, Yoshikazu Arai, Atsushi Shibuya, Satoshi Kiyono, Chun Hong Park, Measurement of multi-degree-of-freedom error motions of a precision linear air-bearing stage, Precision Engineering, 30-1, 96-103, 2006.

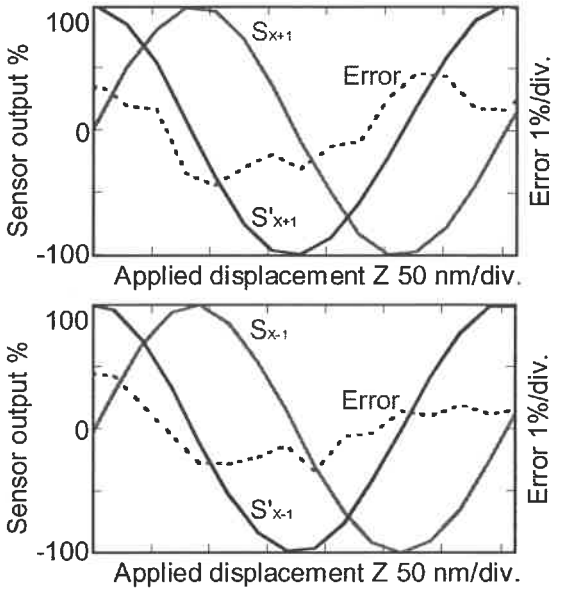

Figure 5. Two-phase output signals S_α and S'_α ($\alpha = X+1, X-1$) and interpolation errors.

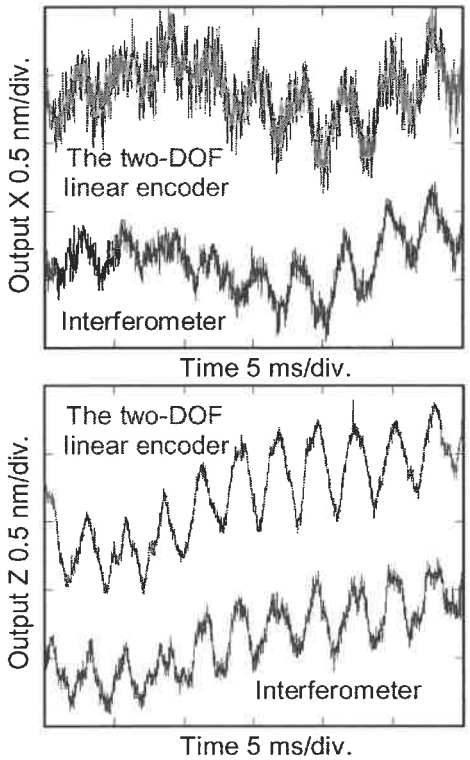

Figure 6. Resolution of the two-DOF linear encoder.

DEVELOPMENT OF A SENSITIVE 3-AXIS ANGLE SENSOR BASED ON LASER AUTOCOLLIMATION

Yusuke Saito[1], Yoshikazu Arai[1] and Wei Gao[1]
[1]Nano-Metrology and Control Lab, Department of Nanomechanics
Graduate School of Engineering, Tohoku University
Sendai, Miyagi, Japan

INTRODUCTION

Two-axis angular displacement errors such as pitch and yaw of a flat mirror target can be detected by the laser autocollimation method [1]. This optical angle-detective method based on optical lever is easily satisfied the key requirements for applying to the ultra-precision profile measurement such as flatness measurement of large silicon wafers [2-3], or measuring a dynamic angle motion errors such as precision stage movements, since the system has advantage of its high sensitivity and quick response. However, roll-directional angle error can't be detected by simply applying this method. In this paper, we describe simultaneous measurement about three-axis angle detection. This method improves the laser autocollimation method from two-axis measurement to three-axis measurement by using a diffraction grating as the target mirror. Two prototypes (Prototype I, Prototype II) of the three-axis angle sensor were designed and fabricated. In Prototype I, the three-axis angular measurement of the target was carried out by sensing the displacements of the 0^{th}-order and $\pm1^{st}$-order diffraction beam spots on the focal plane of the objective lenses. The 3-axis angle measurement methods were categorized into three types according to the behavior of the spots on the focal plane and each of them has been evaluated by the experiment.

Prototype II was used only the $\pm1^{st}$-order diffracted beam spots for the three-axis angle detection, which reduced the number of optical components and the dimension of the sensor. To improve the diffraction efficiency of the $\pm1^{st}$-order diffracted beams, a one-axis rectangular grid was employed as the target mirror. The experimental results about measurement ranges and resolutions were also carried out.

PRINCIPLE OF THREE-AXIS ANGLE MEASUREMENT METHOD

The conventional method for simultaneous two-axis angle measurement is proposed by laser autocollimation [2-3]. The system is a combination of a thin laser beam as a light source and a quadrant photo diode (QPD) as its detector. A plane mirror is often used as the target reflector of this optical system. When the target mirror has inclination $\Delta\theta_Y$, the spot displacement is occurred on the focal plane of the objective lens, simultaneously. The relationship between the incident angle $\Delta\theta_Y$ and the corresponding displacement $\Delta d_{V\_\theta Y}$ is expressed by the following equation:

$$\Delta\theta_Y = \arctan\left(\frac{\Delta d_{V\_\theta Y}}{2f}\right) \fallingdotseq \frac{\Delta d_{V\_\theta Y}}{2f} \quad (1)$$

Where f is the focal length of the objective lens, the $\Delta\theta_Y$ and the $\Delta d_{V\_\theta Y}$ are assumed to be very small in this equation. It is possible to calculate the change of the tilt motion of the target mirror just by detecting the change of the spot position $\Delta d_{V\_\theta Y}$ on the focal plane. Since this system has high sensitivity, quick response and fine horizontal resolution, it has been widely applied to ultra precision shape measurements [3].

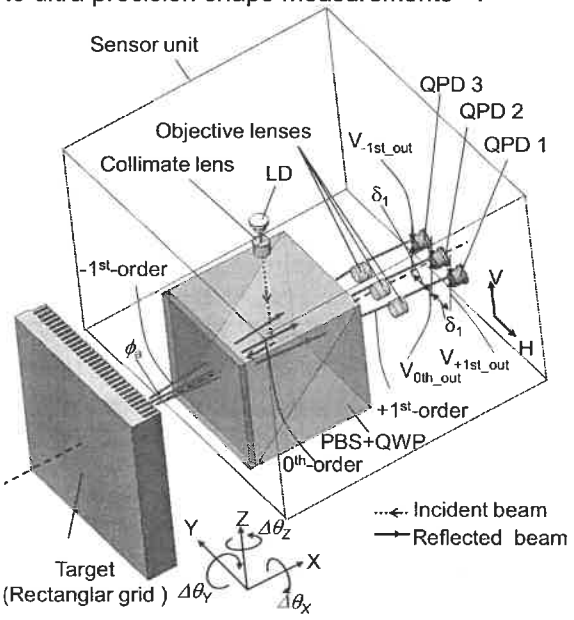

FIGURE 1. Principle of three-axis angle detection

The laser autocollimation method is able to measure two-axis angular displacements: such as $\Delta\theta_Y$ and the $\Delta\theta_Z$ directions simultaneously, by detecting the spot displacements along with V and H-axis of the detector, while this method can't measure the $\Delta\theta_X$ directional angle displacement. To realize simultaneous three-axis angle measurement, using a diffraction grating as a target instead of the plane mirror. Figure 1 shows schematic diagram for three-axis angle detection method with diffraction grating. Laser beam is projected by laser diode (LD). A rectangular grid is chosen as a target, because the diffraction efficiency of the odd numbers is higher than that of the even numbers.

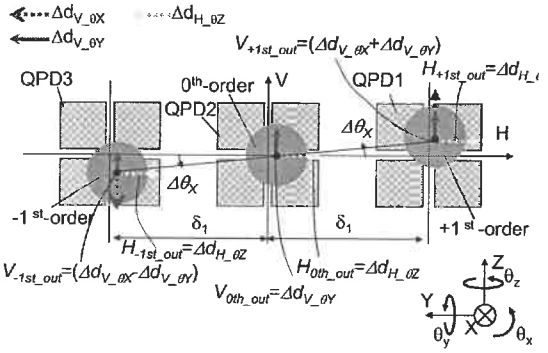

FIGURE 2. Linear spot displacements on the Quadrand Photo Diodes (QPDs)

In the three-axis angle detection, the linear displacements of the 0th-order and the ±1st-order diffracted beam's spots are used as in the case of the two-axis angle detection. The diffraction angle ϕ_a of the ±1st-order diffraction beams can be expressed as $\phi_a \approx \lambda/p$, where p is the pitch of the diffraction grating and λ is the wavelength of the laser beam. The focusing position of the ±1st-order diffraction beams is determined as $\delta_1 \approx f\lambda/p$, calculated from equation (1) and ϕ_a. Figure 2 shows the schematics of the linear displacements of the spot when target has three-axis angle inclination. The spots of the ±1st-order diffraction beam keep the distance $|\delta_1|$ from the 0th-order beam spot. When the target has inclination of the $\Delta\theta_X$ direction, each of the ±1st-order's optical spots on the focal plane rotates to the opposite direction around the 0th-order beam spot with the radius $|\delta_1|$. Assuming that this rotational displacement is very small, the linear displacement $\Delta d_{V\_\theta X}$ of the optical spot can be expressed by the following equation:

$$\Delta d_{V\_\theta X} \approx \delta_1 \Delta\theta_X \tag{2}$$

The influence of the displacement $\Delta d_{V\_\theta Y}$ corresponding inclination $\Delta\theta_Y$ can be removed by using two displacements of each ±1st-order's optical spots as follows:

$$V_{\theta X} \approx \frac{(\Delta d_{V\_\theta Y} + \Delta d_{V\_\theta X}) - (\Delta d_{V\_\theta Y} - \Delta d_{V\_\theta X})}{2} = \frac{V_{+1st\_out} - V_{-1st\_out}}{2} \tag{3}$$

In equation (3), the lower capital such as +1st_out and -1st_out are expressed the outputs from QPD1 and QPD3 using +1st or -1st order dffraction beam. It should be noted that the working distance of the sensor is limited because of the use of the ±1st-order diffraction beams for $\Delta\theta_X$ detection. In addition, another method for detecting the $\Delta\theta_X$ angle is proposed by using two outputs from +1st order (or -1st order) and 0th order beam spot movements:

$$V_{\theta X} \approx \frac{(\Delta d_{V\_\theta Y} + \Delta d_{V\_\theta X}) - \Delta d_{V\_\theta X}}{2} = \frac{V_{+1st\_out} - V_{0th\_out}}{2} \tag{4}$$

The angle $\Delta\theta_Y$ and $\Delta\theta_Z$ are measured by detecting the spot movement of $V_{0th\_out}=\Delta d_{V\_\theta Y}$ and $H_{0th\_out}=\Delta d_{H\_\theta Z}$, respectively according to the movement of the 0th-order diffraction beam. These angles are also able to detect by using two outputs from QPD1 and QPD3 as follows:

$$V_{\theta Y} \approx \frac{(\Delta d_{V\_\theta Y} + \Delta d_{V\_\theta X}) + (\Delta d_{V\_\theta Y} - \Delta d_{V\_\theta X})}{2} = \frac{V_{+1st\_out} + V_{-1st\_out}}{2} \tag{5}$$

$$H_{\theta Z} \approx \frac{H_{+1st\_out} + H_{-1st\_out}}{2} \tag{6}$$

The three-axis angles can be obtained simultaneously by detecting the linear displacements expressed in equations (1)-(6). Then the proposed method for three-axis angle detection can be categorized as three measurement types shown in Table 1.

TABLE 1. Three-axis angle measurement method

Angle	Method 1	Method 2	Method 3
$\Delta\theta_X$	$(V_{+1st\_out} - V_{-1st\_out}) / 2$	$(V_{+1st\_out} - V_{-1st\_out}) / 2$	V_{+1st_out} (or V_{-1st_out}) - V_{0th_out}
$\Delta\theta_Y$	V_{0th_out}	$(V_{+1st\_out} + V_{-1st\_out}) / 2$	V_{0th_out}
$\Delta\theta_Z$	H_{0th_out}	$(H_{+1st\_out} + H_{-1st\_out}) / 2$	H_{0th_out}

DESIGN AND EXPERIMENT ABOUT THREE-AXIS ANGLE SENSOR (PROTOTYPE I)

To evaluate the three types of measurement methods indicated in Table 1, the prototype three-axis angle sensor was designed and fabricated as shown in Figure 3. This optical system uses 2-axis rectangular grid with 5.5 μm pitch as the target reflector. The laser beam was collimated by the lens and bended perpendicular by the prism. It shaped by the ϕ2 mm aperture and displayed onto the target reflector. The reflected 0^{th}-order and $\pm1^{st}$-order diffraction beams went through each objective lens and were focused to be small optical spots on the QPDs to detect the corresponding displacements as the laser autocollimation. The dimension of the three-axis angle sensor was 86.0 mm × 56.3 mm × 59.0 mm (W × L × H).

The experimental setup for evaluating the $\Delta\theta_X$ and the $\Delta\theta_Z$ angle directional output about Prototype I was simply used a two-axis PZT-driven tilt stage for generating the inclination of the target rectangular grid that was mounted on the stage. A plane mirror was also mounted orthogonal direction toward the target. The certain directional movements of the target rectangular grid had been calibrated by using the commercial autocollimator. The commercial autocollimator has an angle resolution of 0.01 arc-seconds, accuracy of 0.5 arc-seconds and measuring range of 60 arc-seconds. Then the output from the Prototype I was compared with the calibration result. The evaluation of $\Delta\theta_Y$ angle direction was also carried out.

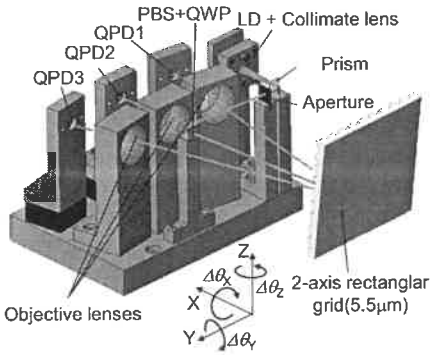

FIGURE 3. Optical design of three-axis angle sensor (Prototype I)

EXPERIMENTAL RESULTS OF SENSOR OUTPUT CURVES

Figure 4 shows the sensor output curves of the Prototype I in $\Delta\theta_X$ directional output by Method 2. In this experiment, sinusoidal voltage was applied to the two-axis PZT-driven tilt stage with amplitude of about ±20 arc-seconds. The horizontal axis in the figure is the applied angle, and left vertical axis shows the output from the Prototype I. The residual from a linear fitting of the output curve is also plotted as right axis in the figure. Then the $\Delta\theta_Y$ and $\Delta\theta_Z$ directional outputs were also carried out in the same condition. The linearity in the $\Delta\theta_X$, $\Delta\theta_Y$ and $\Delta\theta_Z$-directions were evaluated to be 4.33 arc-seconds, 1.40 arc-seconds and 1.42 arc-seconds over measurement ranges of ±20 arc-seconds, respectively. The other measurement methods were also carried out. Table 2 shows the evaluating results. From the point of view of the linearity in the output curve, the Method 2 shows the best result.

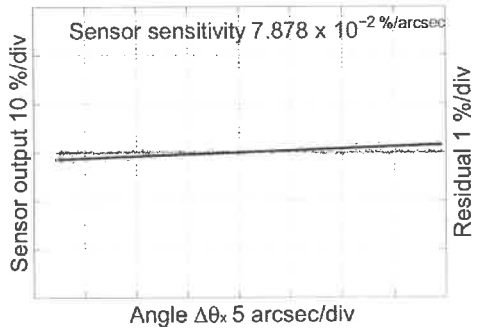

FIGURE 4. Sensor output curves about $\Delta\theta_X$ directional output (Measurement method 2, Prototype I)

TABLE 2. Experimental results of residual in the output curve

Angle	Method 1	Method 2	Method 3
$\Delta\theta_X$	0.13 %	0.13 %	0.24 %
$\Delta\theta_Y$	1.70 %	1.28 %	1.70 %
$\Delta\theta_Z$	1.71 %	0.71 %	1.71 %

TABLE 3. Experimental results of resolution test

Angle	Method 1	Method 2	Method 3
$\Delta\theta_X$	1.78 "	1.78 "	2.78 "
$\Delta\theta_Y$	0.09 "	0.11 "	0.09 "
$\Delta\theta_Z$	0.09 "	0.15 "	0.09 "

The resolutions of the Prototype I was also carried out by evaluating the short period stability (8 seconds) and resolution of the three methods was estimated from S/N ratio. Table 3 shows the evaluating results about the three methods. According to result of the Table 3, the Method 1 shows the best result.

SIMPLIFICATION OF THE OPTICAL SYSTEM

The results of table 2 and table 3 indicate that the Method 1 or the Method 2 is suitable for three-axis angle detection. Furthermore, Method 2 is profitable measurement method for miniaturization of an angle sensor. Then we fabricated the new type of three-axis angle sensor in Method 2 (Prototype II). Figure 5 shows the photograph of the sensor. The target reflector was a one-axis rectangular grid with 4 μm grating pitch. The size of the sensor is 64.0 mm × 65.0 mm × 59.0 mm (W × L × H). Experiment for evaluating the sensor output curves was also carried out. The linearity in each directional output curves about $\Delta\theta_X$, $\Delta\theta_Y$ and $\Delta\theta_Z$ were estimated to be 13.8 arc-seconds, 0.88 arc-seconds and 0.63 arc-seconds over measurement ranges of about ±200 arc-seconds, ±20 arc-seconds and ±20 arc-seconds, respectively. Figure 6 shows the results of resolution test. A sinusoidal signal with a frequency of 1 Hz was applied to the tilt stage. Prototype II could detect small tilt angle of the target up to about ±0.1 arc-seconds in $\Delta\theta_X$ direction and ±0.02 arc-seconds in $\Delta\theta_Y$ and $\Delta\theta_Z$ directions in cut-off frequency of a sensor amplifier is 20 kHz.

FIGURE 5. Photograph of Prototype II

CONCLUSION

The following conclusions are drawn from this study:

[i] A measurement method for simultaneous three-axis angular displacements based on laser autocollimation has been proposed.

[ii] Three-types of measurement methods for simultaneous three-axis angle have been proposed. To estimate these measurement methods, prototype I was developed. The dimension of the Prototype I was 86.0 mm × 56.3 mm × 59.0 mm (W × L × H).

[iii] The new type of three-axis angle sensor called Prototype II was also developed in Method 2. The dimension of this sensor was 64.0 mm × 65.0 mm × 59.0 mm (W × L × H). The resolutions/ranges of the sensor in $\Delta\theta_X$, $\Delta\theta_Y$ and $\Delta\theta_Z$-directions were ±0.1 arc-seconds/±200 arc-seconds, ±0.02 arc-seconds/±20 arc-seconds and ±0.02 arc-seconds/±20 arc-seconds, respectively.

The future work might deal with evaluating the accuracy of the three-axis angle sensor.

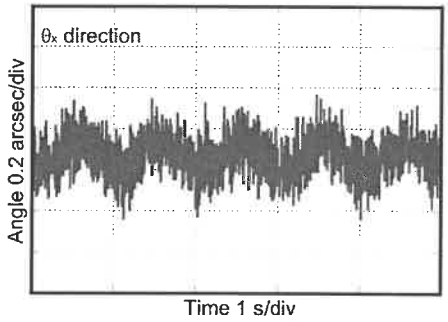

(a) $\Delta\theta_X$ directional output

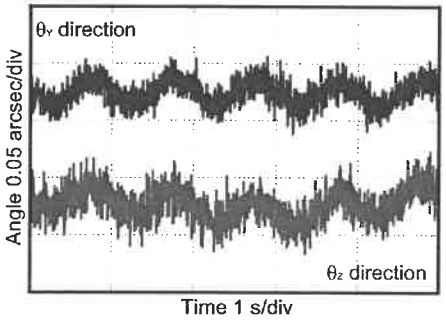

(b) $\Delta\theta_Y$ and $\Delta\theta_Z$ directional outputs

FIGURE 6. The resolution test results of Prototype II

ACKNOWLEDGEMEN

This research is supported by a grant-in-aid from JSPS.

REFERENCES

[1] W. R. Moore: Foundations of Mechanical Accuracy: The Moore Special Tool Company, 1970; Chapter 3.

[2] A.E. Ennos and M.S. Virdee: High accuracy profile measurement of quasi-conical mirror surfaces by laser autocollimation, Precision Engineering, 1982; 4(1), 5-8.

[3] W. Gao, P. S. Huang, T. Yamada and S. Kiyono: A compact and sensitive two-dimensional angle probe for flatness measurement of large silicon wafers, Precision Engineering, 2002; 26(4), 396-404.

DESIGN, FABRICATION AND TESTING OF KINOFORM LENSES

Kenneth Garrard, Alex Sohn and Thomas Dow
Precision Engineering Center
North Carolina State University
Raleigh, NC USA

INTRODUCTION

Fresnel lenses are a type of lens that eliminates the bulk of a conventional lens by collapsing the lens thickness while retaining the curvature necessary for focusing. Figure 1 shows the Fresnel lens equivalent of a conventional lens. For a rotationally symmetric lens, the discontinuities or grooves formed when collapsing the lens are annular. This produces a much thinner lens, particularly for large apertures.

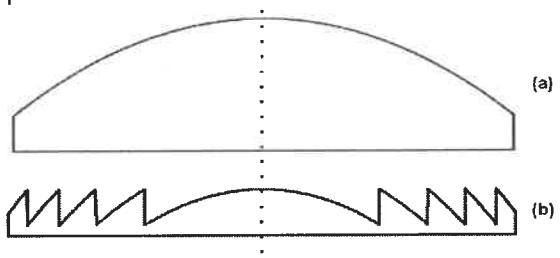

FIGURE 1. A Fresnel lens (b) is a collapsed version of a conventional lens (a).

The advantages of a Fresnel lens are that more light is transmitted due to lower absorption and dispersion. With more uniform thickness a Fresnel lens is typically easier to replicate by molding. For these reasons Fresnel lenses are being considered for improved laser scanning systems.

Fresnel lenses are intended as purely refractive lenses. A kinoform lens combines refractive and diffractive properties of Fresnel lenses and zone plates to produce an efficient diffractive lens that can focus as well as cancel chromatic aberration.

PHASE MATCHED KINOFORM DESIGN

The lens system for a scanner should focus the source laser beam into a small spot on the image plane. The ideal spot location is a linear function of scan angle (i.e., the F-theta condition). The size and shape of the spot is determined by both refraction and diffraction. Even if the lens surfaces are designed so that all rays converge at the same location on the image plane, the spot size will not be zero due to diffraction. The best possible case for a circular aperture is an intensity cross-section with 95% of the light energy concentrated within an area of angular diameter 1.22 λ/A, where A is the aperture diameter and λ is the wavelength. Each zone of a Fresnel lens both redirects incident light toward a focal point and produces a diffraction pattern due to the discontinuous boundaries with adjacent zones. However, the light from the various zones is not necessarily in phase at the focal point. The result is a complex pattern of interference pattern with multiple peaks.

It is possible for the diffraction peaks to all be directed to the same point on the image plane. This is done by varying the width and depth of the zones to ensure that the optical path length from the center of each zone is an integer multiple of the incident light wavelength. This apodization process (i.e., aperture tuning), matches the phase of the refracted light so that the location of constructive interference can be controlled.

Kinoform Lens

The resulting lens is known as a kinoform lens and may be designed using Equation 1 to select the radial distance, R_j, from the center of the aperture to the boundary of each Fresnel zone [1].

$$R_j^2 = 2 j M_j \lambda L \qquad (1)$$

The wavelength is λ, L is the distance to the focal point as measured parallel to the optic axis, j is the zone number and M_j is the phase match order for the j^{th} zone. The phase match order specifies how many integer multiples of wavelength there are in the difference between the optical path lengths for zone j and zone j-1. Equation 1 is approximate and valid only in the paraxial case, that is, when L >> R. However, it is simple to find an exact relation for the radial separation of adjacent Fresnel zones such that light at the focus from all zones is in phase.

Exact Phase Matching

Figure 2 illustrates the kinoform phase matching concept for two adjacent zones of a conical Fresnel lens. Light rays incident at heights R_1 and R_2 will be in phase when they reach the focus if the optical paths D_1 and D_2 differ by an integer multiple (the phase match order, M) of the wavelength.

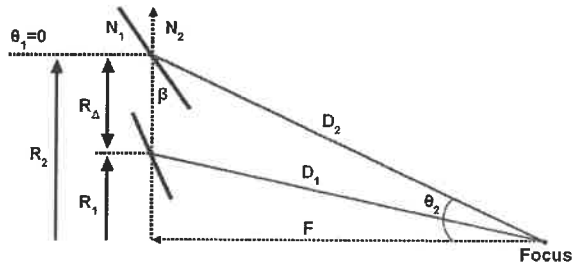

FIGURE 2. Kinoform phase matching concept.

Equation 2 relates the optical path length for adjacent zones with the matched phase difference of light waves reaching the focus from those Fresnel zones.

$$M\lambda = D_2 - D_1 = \sqrt{F^2 + R_2^2} - \sqrt{F^2 + R_1^2} \qquad (2)$$

This equation is easily solved for R_1 or R_2 given any F, M and λ and the other R. The zone centers larger and smaller than any given radial distance R are found with Equation 3,

$$R^{\pm} = \sqrt{R^2 + M^2\lambda^2 \pm 2M\lambda\sqrt{F^2 + R^2}} \qquad (3)$$

Kinoform Lens Design Code

Matlab code that iteratively designs a kinoform Fresnel lens to focus a collimated beam of light to a point has been written. It first calculates the locations of the Fresnel zones for the desired focal length, aperture, wavelength, refractive index and phase match order. Then equation 4 is then used to find the slope of the lens surface at the center of each zone that will refract an incident ray to the focus. The geometry associated with Equation 4 is that of Figure 2. η is the ratio of the refractive indices on opposite sides of the aperture.

$$\tan\beta = \frac{\sin\theta_1 + \sin\theta_2}{\sqrt{\eta^2 - \sin^2\theta_1} - \cos\theta_2} \qquad (4)$$

Multiple rays are traced to the focal point through each zone. The diffraction pattern at the image plane is calculated directly from the Fresnel-Kirchhoff diffraction integral [2] by summing the magnitude and phase of light from each ray – lens intersection to every point on the image plane [3].

Figure 3 shows a plot from the kinoform design software for a 200 mm focusing lens with a phase match order of 7. The plot shows the lens aperture, the incident beam, the diffraction pattern at the image plane and a ray trace from the lens to the focus. Output vectors containing (x,y,z) coordinates of the aperture, surface slopes, zone boundary locations and depths, ray surface intersections, and the diffraction intensity distribution are also produced. The plot information includes both the refraction spot location and width at the image plane and the diffraction peak center location and size (full width at half max).

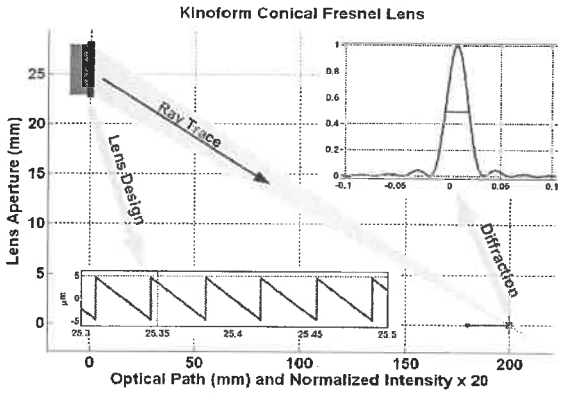

FIGURE 3. Kinoform lens design, ray trace and diffraction analysis.

Zooming into the plot in Figure 3 reveals the structure of the conical kinoform lens surface as seen in the lower left inset (with traced rays removed for clarity). Five complete zones near the center of the aperture are shown. The difference in zone depth and width is very small and is not apparent in the plot because the wavelength (650 nm) is relatively small and the focal length is relatively large (200 mm), requiring a very small change in zone spacing to produce phase matched optical path lengths from the central ray of each zone. For this lens there are 140 zones over a 5 mm aperture that range in depth from 9.13 to 9.19 μm and in width from 32.92 to 40.01 μm. The conical slopes range from 12.92° to 15.5° and are calculated with Equation 4 so that the central rays converge exactly at the focus. Rays are traced past the image plane to show the spread of refracted light that result from using a conical instead of aspheric zone profile.

The diffraction pattern as observed at the image plane is shown in the upper right inset of Figure 3. By matching the phase of refracted rays from the lens to the image, the maximum intensity from each zone occurs at the same location, very close to the focus. The plot shows the diffraction distribution with a marker at its peak (7.66 µm from the focus) and a bar indicating its width (23.37 µm) at half the maximum value. The ray trace intersection with the image plane near the focus is also shown in Figure 3. Since the slope of each zone is constant, rays that are not incident at the center of the zone do not converge exactly at the focus. The width of the region of the image plane where the rays cross the image plane is 39.95 µm and the geometric center of this region is 17 nm from the intended focal point.

KINOFORM FABRICATION

The surface of a kinoform lens cannot be contoured with a round-nosed tool as in single-point turning. The side of the dead sharp tool forms the flat refractive portion of the lens and must be rotated at each plunge to change the angle as the groove radius is changed.

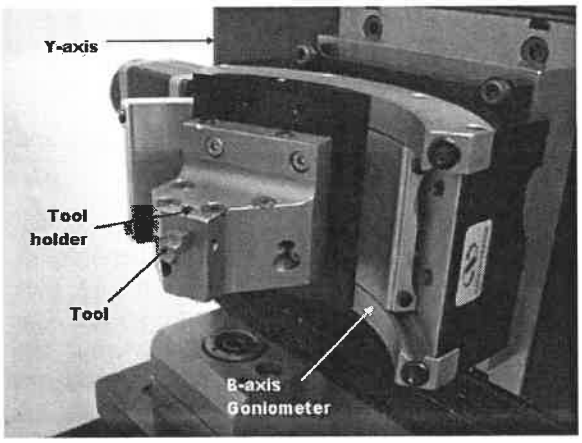

FIGURE 4. Newport Goniometer mounted on y-axis of diamond turning machine

A ball-bearing goniometer B-axis is used to rotate the tool and fabricate varying groove angles. The B-axis is mounted to the Nanoform 600's Y-axis and the tool is held securely via a non-adjustable tool holder as shown in Figure 4.

Cuts were performed both from the inside to the outside of the part and vice versa as shown in Figure 5. This change in cutting direction produces a significantly different chip, as shown in Figure 6 although the material removed is the same. This is thought to have a significant impact on the cutting mechanics and the final result of the cut. The SEM micrographs in Figure 7 show a distinct difference between the surfaces as a result of the two different cutting directions. It appears that while the outside-to-inside cut produced grooves that are relatively free of burring, the inside-to-outside cuts produced large "curtain" like burrs that were firmly attached to the tips of the grooves. This is believed to be caused by the chip remaining attached at the tip of the groove because the tip of the previously cut groove is now unsupported and can easily deform above the cutting edge of the tool.

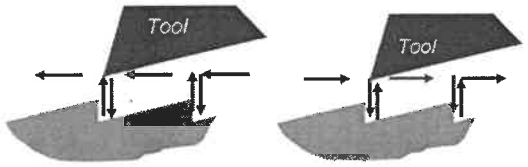

(a) (b)

FIGURE 5. Preliminary cutting tests shown with different cutting direction a) outside-to-inside and b) inside-to-outside.

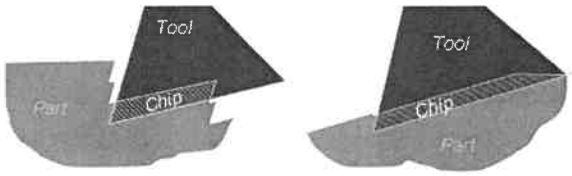

(a) (b)

FIGURE 6. The chip cross section differs significantly for a) outside-to-inside and b) inside-to-outside cutting

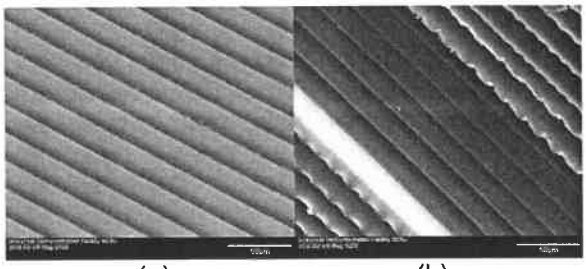

(a) (b)

FIGURE 7. The chip cross section differs significantly for a) outside to inside and b) inside to outside cutting.

Metrology

The surface finish and flatness of the kinoform lens facets is excellent. Figure 8 shows the surface finish of one facet of the lens. It is about 28 µm wide and is flat to 19 nm over this width; that is, about one part in a thousand. The

surface finish is also exceptional - 2.7 nm RMS. Some of the facets had high frequency features from plastic shearing during machining, but in general, the surface illustrated in Figure 8 reflects the quality of the machined features.

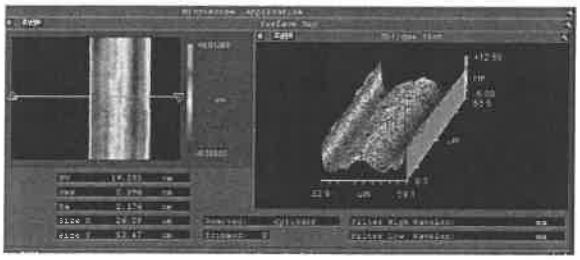

FIGURE 8. Surface finish of a kinoform focusing lens facet. The facet face is flat to 19 nm over a width of 28 µm. Surface finish is 2.7 nm RMS.

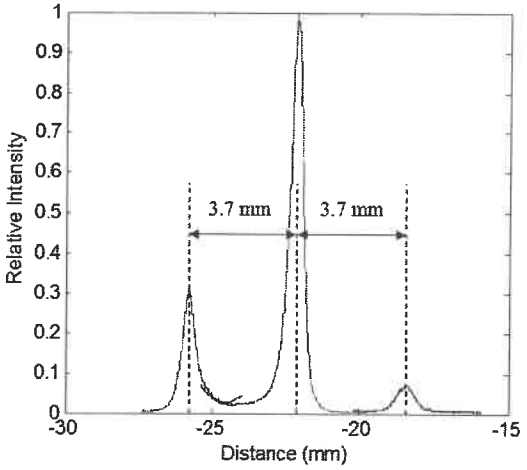

FIGURE 9. Kinoform Relative Intensity Plot, FWHM spot size at the central peak is 480 µm.

KINOFORM PERFORMANCE

Digital Camera

A monochrome Epix 5M10 camera with the higher resolution was used to measure the lens spot size. This camera has 2592 x 1944 array of photocells spaced 2.2 µm apart. The overall size of the array is 5.7 mm wide by 4.28 mm high. It has a sensitivity of 1.4 V/lux-sec at 550 nm illumination. The camera interleaves signals from the sensors to a pair of A/D converters to increase throughput to the video board in a PC. Unfortunately, each of these converters has a slightly different gain and as a result adjacent pixels have an offset value. Average 2x2 pixel blocks resolves this issue and the resulting horizontal and vertical resolution is 4.4 µm.

Spot Size Measurement

To measure the spot size, the beam from a 650 nm solid state laser source with adjustable collimating optics was directed into the kinoform lens (grooves away from source) and the camera was located near the designed 200 mm focal length. The diameter of the beam was approximately 4 mm. The spot consisted of a bright spot surrounded by a circle of lower intensity (~20%) with a radius of 3.7 mm. The FWHM size of the central spot was 480 µm. The measurement shown in Figure 9 was created by moving the camera to make 3 images with the same exposure. Stitching them together provides a wider field of view than possible with the 4.5 mm focal array width. The variation of the magnitude of the secondary peaks is probably caused by the alignment of the lens and camera.

The spot size was also measured using a 150 mm diameter collimated HeNe laser on a Zygo GPI interferometer. The entire 50 mm annular segment of the lens can be illuminated with this technique and by placing the lens on the GPI's part stage; the image can be viewed while moving through focus. The size of the spot was disappointingly large – nearly 500 µm. While large, this is about half the size of a commercial conical Fresnel lens (885 µm) that was also measured.

Additional work related to the fabrication technique (the ball bearing stage is a potential problem) and lens design sensitivity studies should identify reasons for the measured performance.

ACKNOWLEDGEMENT

Funding for this research was provided by Lexmark International, Inc., monitored by P. Heink.

REFERENCES

[1] Rossi. M., R. Kunz and H. Herzig. Refractive and diffractive properties of planar micro-optical elements. Applied Optics, 34, 26, 5996-6007, (1995).

[2] Born M. and E. Wolf. Principles of Optics, 7th Ed. Cambridge University Press, (1999).

[3] Dow, T., K. Garrard and A. Sohn. Final Report – Phase I, Fresnel Scanning Lens Design. Precision Engineering Center, North Carolina State University (2007).

THE DEVELOPMENT OF AN OFFSET-LOCKED FREQUENCY STABILIZED HETERODYNE LASER SOURCE FOR PRECISION METROLOGY

Charles G. Stroup, Jr., Jerald L. Overcash, Robert J. Hocken
Center for Precision Metrology
University of North Carolina at Charlotte
Charlotte, NC, USA

ABSTRACT

An offset locked frequency stabilized helium neon laser (FSL) featuring a 20 MHz heterodyne split has been developed at the University at North Carolina at Charlotte for use on the Sub Atomic Measuring Machine's (SAMM) X, Y, and θ_z positional feedback interferometers. The FSL will replace the current Zygo 7702 series laser head. It will provide twice the intensity at greater than 1.0mW and more than two orders of magnitude greater frequency stability at approximately 7 parts in 10^{11}. The FSL utilizes a sealed cavity helium neon laser offset locked to a commercially available iodine stabilized offset locked helium neon laser. A thermofoil heater provides the necessary actuation for closed loop frequency control. A sealed chamber houses the offset locked laser, providing passive environmental stability.

INTRODUCTION

Previously, the laser delivery system for the Sub Atomic Measuring Machine's (SAMM) X, Y, and θ_z positional feedback interferometers consisted of a Zygo 7702 laser head. The Zygo 7702 proved to be adequate given the measurement demands of the system. However, better frequency stability, more beam intensity, and direct traceability to the definition of the meter are needed to support the recent upgrades of the SAMM [1].

A frequency stabilized offset locked helium neon laser system (FSL) has been developed to meet the new specifications mandated for the upgraded SAMM. Our FSL consists of a internal mirror helium neon (He Ne) laser tube (working laser) offset locked to a iodine-stabilized offset locked He Ne laser (reference laser) [2,3]. Our reference laser provides direct traceability to the definition of the meter and a stable platform for which to base our system.

It is important to note the behavior of a laser tube. The frequency of the light being emitted by a He Ne laser is directly related to the distance between its resonant mirrors. We have chosen an internal mirror He Ne laser similar to that in figure 1. Therefore, any expansion or contraction of the glass body related to pressure changes or thermal expansion results in a change in distance between its mirrors and a change in frequency of the emitted light. This is both the basis of our control scheme and the source of our errors.

FIGURE 1. Picture of a laser tube similar in size and the same in construction as the one used as our working laser.

SYSTEM DESIGN

A thermofoil heater is wrapped around the circumference of the working laser tube and provides a means of frequency tuning for closed loop control. The working laser is enclosed in a sealed cylindrical decoupling chamber and constrained by two silicone rings. This chamber provides isolation of our working laser from pressure variations in the ambient environment as small as 0.05mmHg, rapid changes in temperature, or air current effects. Of these sources, pressure was found to be the most significant. The two beams of the working laser, one 2.5mw and the other 0.1mw, exit through two glass windows located on each end while all electrical signals needed for laser operation and frequency control are passed into the decoupling chamber with vacuum compatible feed through connectors.

The reference laser is piped via optical fiber to the working laser assembly and recollimated with a fiber coupler. The less intense beam of the working laser is mixed with the reference laser beam using a cube polarizing beam splitter. The resulting signal contains two linear, orthogonal polarizations representing the reference and working lasers. The two polarizations states are combined by a Glan Thompson polarizer before the interference signal falls on an amplified avalanche photo detector.

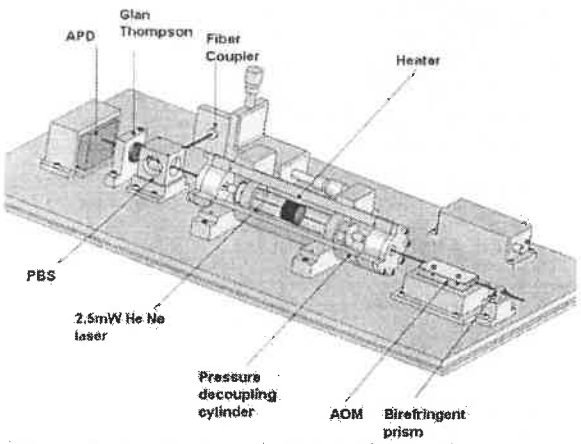

FIGURE 2. Diagram of the FSL's components (not including the reference laser). APD: avalanche photo detector. PBS: polarizing beam splitter. AOM: acousto-optic modulator.

The SAMM utilizes heterodyne interferometry therefore the high intensity signal from the working laser must be conditioned according to the application. The unaltered 2.5 mW signal consists of a single, linear polarization state rotated 45° with respect to the horizontal plane. The signal first passes through an acousto-optic modulator (AOM) operating at 20 MHz. With the AOM properly aligned, three diffracted beams of significant intensity are produced parallel to the horizontal plane of the AOM; the 0^{th} order beam remains unaltered while the two 1^{st} order beams are shifted in frequency by plus and minus 20MHz. The 1^{st} order beams diverge from the 0^{th} order beam in opposite directions at the separation angle of the AOM (~2° for our AOM). Each beam's polarization is unchanged at this point. The three beams then pass through a birefringent prism which combines the vertical component of the 0^{th} order beam with the horizontal component of the down shifted 1^{st} order beam and combines the horizontal component of the 0^{th} order beam with the vertical component of the up shifted 1^{st} order beam. In essence, four beams are produced, two of which are capable of heterodyne interferometry. One of the two heterodyne signals is passed through an aperture and enters the SAMM for use on its positional feedback interferometers. See figure 3 for a visual description of the heterodyne signal process.

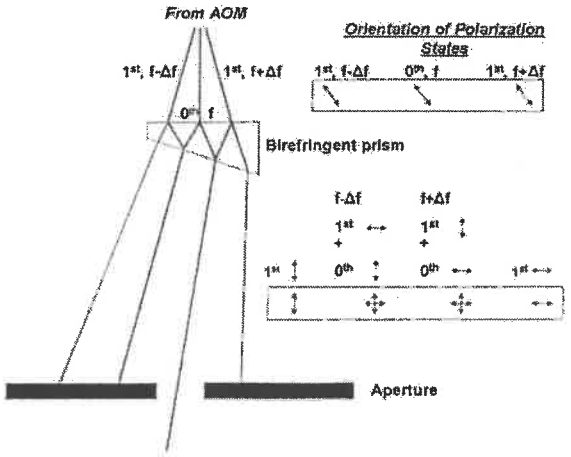

FIGURE 3. Diagram of diffracted beams before and after the birefringent prism. The orientation of the polarization states are relative to cross sectional views of each beam.

Control Scheme

The signal from the avalanche detector is sent to a frequency counter which generates a numerical value for the frequency difference (beat frequency) between the working laser and reference laser. A dedicated control computer running Labview® software monitors the frequency over a General Purpose Information Bus (GPIB). The beat frequency is subtracted from a user defined offset frequency creating an error signal. The error signal is sent to a digital PID controller which generates a digital correction voltage for the heater. A DC offset is constantly applied to the heater such that the laser tube expands and contracts equally given a negative or positive change in voltage, respectively. The correction voltage is added to the DC offset in software and is outputted from the control computer through a digital-to-analog converter (DAC). The signal is amplified before passing to the thermofoil heater that tunes the frequency of the laser. We have been able to achieve update rates as fast as 35 ms, however, a much slower rate on the order of 300 ms proves more ideal given the slower response of our system.

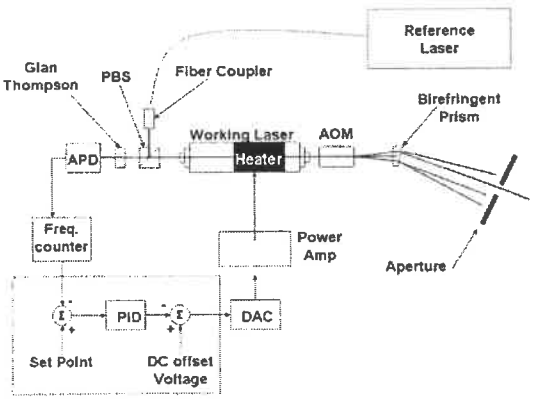

FIGURE 4. Simplified block diagram of offset locking scheme and electronics. APD: avalanche photo detector. PBS: polarizing beam splitter. AOM: acousto-optic modulator. DAC: digital to analog converter. PID: proportional, integral, derivative.

Key Design Features

Affixing a heater radially to the laser tube has several characteristics that are conducive to a highly stable system. The slower response of a thermally controlled scheme provides good mechanical averaging, thus eliminating any effects from electrical noise associated with our correction signal. It has also given us the ability increase the gate time of our counter and update our control loop at a more deliberate rate, giving time to further average any noise associated with the beat frequency between the reference and working laser. Once under control, we have been able to increase the gate time to as much as 300 ms with a control loop update rate of approximately 350 ms while still maintaining lock status. Such a slow update rate is only possible through the use of our environmentally decoupled chamber. Otherwise, small pressure changes or slight air currents would cause the frequency to slip well out of the stable zone between update points.

DATA PRESENTATION

The motivation behind the design and construction of our decoupling chamber was to eliminate frequency instability resulting from rapid pressure changes. Our FSL is housed in an over-pressurized metrology lab. Consequently, the opening and closing of our lab door, or any door in the metrology suite, causes fast changes in ambient pressure ranging from 0.05 to 0.15mmHg, more than enough to cause an error in frequency stability. Before the utilization of the decoupling chamber, we saw frequency variations of approximately 0.4MHz peak to peak resulting from the fore mentioned pressure spikes. The beat frequency between the reference and working lasers and pressure data were taken simultaneously to illustrate the error resulting from the pressure changes, see figure 5.

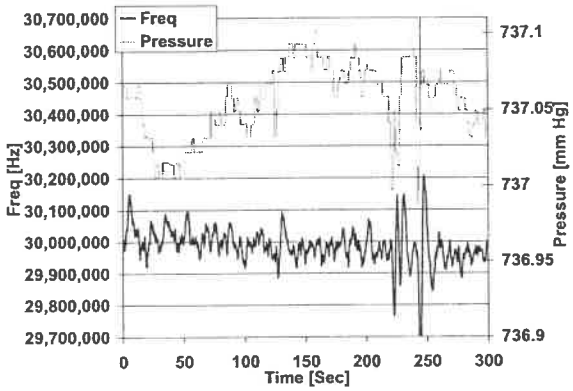

FIGURE 5. Data showing the relation between pressure and the beat frequency between our working and reference lasers.

The lab door was opened and closed at times of approximately 225 and 250 seconds in figure 5. These fast pressure variations are uncontrollable while the slow pressure drift of nearly equal amplitude that occurs between 10 and 150 seconds is compensated by the controller. The frequency data contains changes from both the reference and working laser. However, the reference laser utilizes PZT frequency tuning allowing sufficient control bandwidth to compensate for the fast pressure variations [3].

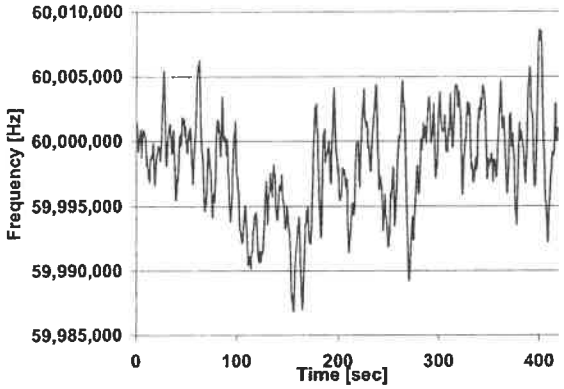

FIGURE 6. Short sample of data representing the frequency difference between the working laser and reference laser with a frequency counter gate time of 150ms. A counter gate time of 300ms has produced better stability of which has been observed but not recorded.

SUMMARY AND CONCLUSION

The use of a heater as frequency control and the unique design of our environmentally decoupled chamber have allowed us to reach the level of stability necessary for the precision metrology applications for which our FSL is intended. With a gate time of 150ms, the stability of our FSL is approximately 7 parts in 10^{11} (including the instability of the reference laser at 2.5 parts in 10^{11}) [3]. Figure 6 shows a short sample of data representing the stability we have achieved. A higher level of stability has been observed with the counter gate time set at 300ms, but no data has been recorded with the prototype system. The final assembly is in development and is soon to be integrated with the SAMM.

Acknowledgements

This research is funded by the National Science Foundation under award number 0506898 and carried out in the Center for Precision Metrology. Any opinions, findings, and conclusions or recommendations expressed in this material are those of the author(s) and do not necessarily reflect the views of the National Science Foundation.

REFERENCES

[1] J. Overcash, C. Stroup, R. Hocken, "Resolution Considerations in Interferometer Based Ultra-Precision Machines," Proc. Euspen, Switzerland, May 2008.

[2] J. Lawall and J.M. Pedulla, "Ultrastable laser array at 633nm for real-time dimensional metrology," Rev. Sci. Inst., 72-7, July 2001.

[3] Winters Electro-Optics, Inc., Model 200 Offset-Locked Iodine-Stabilized He-Ne Laser.

AUTOMATED PART CENTERING THROUGH IMPULSE ACTUATION

Stephen Furst, Thomas Dow, Alex Sohn, and Ken Garrard
Precision Engineering Center
North Carolina State University
Raleigh, North Carolina, USA

INTRODUCTION

The task of aligning a part on a spindle is part of many machining operations. For example, when a part is manually placed on a holding chuck it must be aligned prior to machining. Also, when machining a two-sided part such as a hemishell, one side is machined first; then the part must be transferred from the first holding fixture (typically a vacuum chuck) to another fixture that is suited for machining side two. If during this transfer the part becomes misaligned, features on side two will not be properly related to features on side one.

Typically, precision part-centering is a manual operation that requires an operator to measure the part runout with a displacement gage and manually tap the high side of the part until it is centered. This paper describes a method that will automate this centering task. To make the technique applicable to a variety of machines and processes, it was assumed that the initial magnitude of the radial runout was up to 2.5 mm and the final value must be within 5 µm.

Transfer of a Two-Sided Part

The centering task discussed here is part of a part transfer process that will allow a two-sided part to be machined without operator intervention as shown in Figure 1. The tasks required for this transfer are: 1) locate the part, 2) locate the receiving chuck in the same coordinate system, 3) determine if part and receiving chuck dimensions are compatible and the part is centered, 4) determine the motion needed to implement the transfer, 5) move the part to the chuck and transfer vacuum.

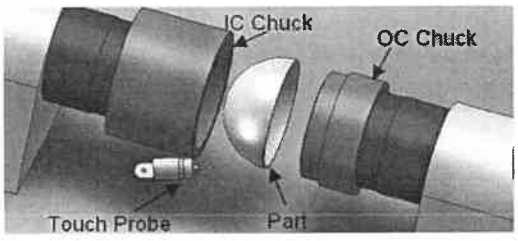

FIGURE 1. Exploded hemishell transfer.

A touch probe is used to locate the part and chuck and to measure any runout. This probe is assumed to be part of the machine and can be moved to touch the part or chuck at any linear or angular position. It is also part of the machine controller and thus can be read axes positions and perform calculations based on multiple readings to find best fit circles, runout magnitude, distances, etc.

To transfer a part from IC (Inner Contour) to OC (Outer Contour) chuck, the probe touches three different points: the face of part, its inner radius and the inner pole. The probe is referenced to radial and axial fiducial features on the chucks. Based on the measurements of the part and fiducial locations, the controller can tell whether the part is appropriately sized for the receiving chuck and the distance to move in the axial direction for part transfer. Because the OC of the part must be smaller than the chuck, some radial misalignment can occur during transfer.

PART REALIGNMENT

The emphasis of this paper is automated centering of the part. The radial runout that occurs from automated transfer or manual placement of the part must be corrected before machining can proceed. For a part on a vacuum chuck this entails first measuring the magnitude and direction of the misalignment, then centering the part against the force of friction.

Runout Measurement

For manual centering, part runout is typically measured using an LVDT or electronic gage head. However, a touch probe is used here to automate the process. To measure the runout of a hemispherical part, the part is touched at a number of points as the part is rotated through 360 degrees. A best fit sine wave is then calculated, with the amplitude representing the magnitude of the runout and the phase indicating the location of the high spot. However, the form errors of the part and the repeatability of the probe measurement cause uncertainty in the runout value. An example is

shown in Figure 2 where the assumed form error of the part ($2\sigma \pm 12.5$ μm) and repeatability of the probe ($2\sigma \pm 0.3$ μm) cause each touch point to be offset from the nominal part radius. These errors result in uncertainty in the measurement of the runout. At least 3 points are needed to calculate a single best fit sine wave but more points reduce this uncertainty, as shown in Figure 2. For the runout goal of this effort (5 μm), at least 5 points will be needed.

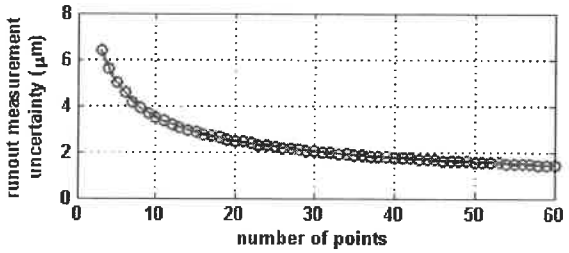

FIGURE 2. Runout measurement uncertainty.

Actuation against Friction

Once the magnitude and direction of the runout is measured, the part must be actuated in the presence of friction. Substantial work has been done to characterize the highly non-linear phenomenon of friction [1]. In the simplest models, friction force is computed as the product of a friction coefficient, μ, and normal force, N, as in Equation (1).

$$F_f = \mu N \tag{1}$$

In reality, friction force is much more complicated than this simple relation because the friction coefficient is not constant. For example, static friction is typically higher than dynamic or Coulomb friction. On small scales the transition between static and dynamic friction is of interest.

Stribeck, Coulomb, and Viscous Friction

Stribeck friction attempts to describe the behavior of the friction force as a function of velocity, particularly in the transition between static and dynamic friction. Figure 3 shows the different types of friction forcing phenomenon.

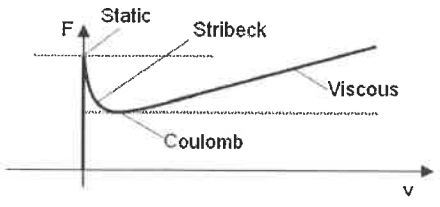

FIGURE 3. Combined model of friction force as a function of velocity.

For the purpose of precision part alignment, the relative velocity between the two sliding surfaces—the part and the vacuum chuck face—is small (~10 mm/s). As a result, the effects of viscous friction can be ignored.

Stick-Slip Behavior

Stick-slip behavior results when a part is pushed across a friction interface by an actuator with some compliance, as diagramed in Figure 4.

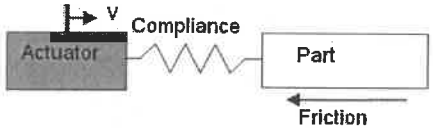

FIGURE 4. Stick slip model diagram.

As the actuator moves toward the part at constant velocity, the spring compresses and the force the actuator exerts increases linearly. As long as this force is less than the static friction limit, the friction force increases to exactly counter the spring force. Once the static friction limit is reached, the part begins to move. Then the friction force decreases rapidly, as described by Stribeck friction, and Equation (2).

$$F(v) = N\left(\frac{A}{\exp(bv)} + B\right) \tag{2}$$

where A is the difference between the static and dynamic friction coefficients, B is the dynamic friction coefficient, and b is a chosen constant representing the rate of decay of the Stribeck friction curve.

The built up spring force propels the part ahead until eventually friction can slow and stop the part completely. The resulting behavior is described as stick-slip. Since tests verified that once a force exceeds the static friction limit the friction force decreases and the part slips, the stick-slip phenomenon must be considered in the design of the actuator.

ACTUATION METHOD

A number of methods were considered to overcome friction and move the part on a vacuum chuck. The chosen method should be the one that satisfies the following criteria:

- Best position control
- Most repeatable
- Lowest risk of part damage
- Fastest realignment
- Easiest to implement

The methods considered included pushing the part with one of the machine axes, tapping the part to mimic the process currently used by skilled operators, vibrating the chuck in an attempt to reduce the friction coefficient and pulsing the vacuum to reduce the normal force.

Tapping as an Actuation Method

For any actuation method, moving the part will require applying a force that is greater than static friction. However, once the part starts to slip and the friction force decreases, the part will accelerate rapidly under the same applied actuation force. Therefore, the best positioning control will likely come from force that exceeds the static friction limit for a short period of time before being removed. This forcing behavior is best realized with a tap, which has a force profile such as shown in Figure 4.

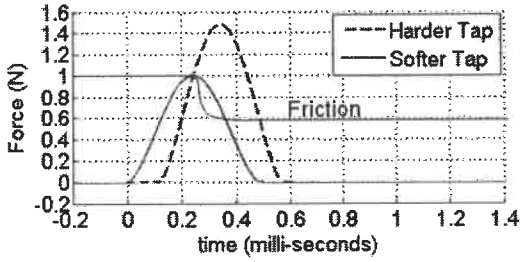

FIGURE 4. The force profiles of two separate hammer taps superimposed on an approximation of the friction force.

Error! Reference source not found.Once a tap force exceeds the static friction limit, the friction force will drop and the difference between the input tap force and the retarding friction force will accelerate the part. The area between the tap force profile and the friction force profile is proportional to the momentum imparted on the part. Even when the peak of the tap force barely exceeds the static friction limit, as in the case of the solid line in Figure 4, there is a non-zero amount of work done on the part. This suggests that there is a minimum distance a part can be moved against the non-linear friction force.

TAPPER DESIGN AND IMPACT MODELING

An actuator has been designed to apply a peak force of 250 N (56 lbs) to a part without damaging it. A part made out of aluminum has been assumed in the analysis. The tapper is designed based on the impact dynamics, which result from the Hertzian deflection of the plunger head and the part.

Hertzian Deflection

The Hertzian deflection of the tapper head and the aluminum part surface causes a tap to produce force a profile similar to those in Figure 4. The deflection of the impacting bodies creates a finite collision time and limits the peak force. The behavior of the two impacting spheres during a tap can be calculated using the Hertzian equations for elastic deformation [2].

As a Hertzian impact progresses, the centers of the two impacting spheres approach each other and the force between them builds according to Equation (3).

$$P = \left(\frac{y}{1.040}\right)^{\frac{3}{2}} \left(\frac{K_D}{C_E^{\,2}}\right)^{\frac{1}{2}} \tag{3}$$

where C_E and K_D relate to the material properties and diameters of the two impacting bodies as in Equation (4).

$$C_E = \frac{1-\nu_1^{\,2}}{E_1} + \frac{1-\nu_2^{\,2}}{E_2} \quad \text{and} \quad K_D = \frac{D_1 D_2}{D_1 + D_2} \tag{4}$$

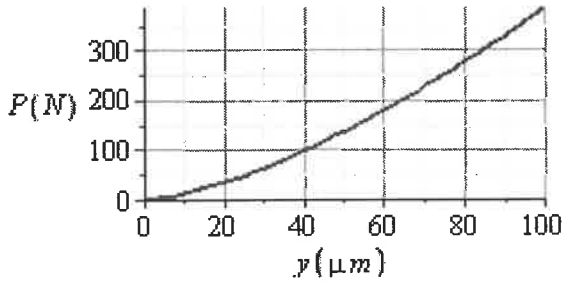

FIGURE 5. Variation of impact stroke, y, with applied force.

Figure 5 shows that a peak force of 250 N will develop an impact deflection of about 75 μm. When the impact starts, the tapper head has depth, y, of zero. As the impact progresses the force that the tapper is exerting on the part increases. The initial energy of the tapper's translating element required to generate an impact stroke of 75 μm and peak force of 250 N can be found from Equation (5).

$$E_0 = \int_{y=0}^{y=75} P(y)dy \tag{5}$$

This equation represents the area under the curve in Figure 5. Substituting Equation (3) for P(y), Equation (5) can be solved for the initial kinetic energy required to produce a peak impact force, P.

$$E_0 = \frac{2*1.040^{\frac{3}{2}}}{5} * \frac{C_E^{\frac{2}{3}}}{K_D^{\frac{1}{3}}} P^{\frac{5}{3}} \qquad (6)$$

Equation (6) is plotted in Figure 7 below.

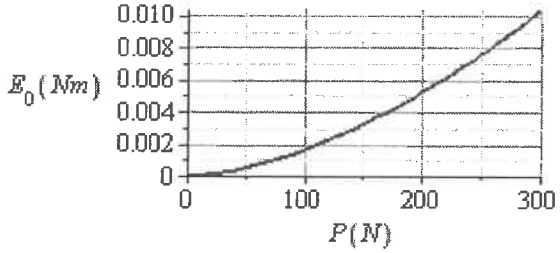

FIGURE 7. Initial kinetic energy required to produce a peak impact force

Actuation Simulation

A friction model is combined with the impact model to simulate the response of a part on a vacuum chuck to a controlled tap. The displacement of an aluminum hemishell with an outer radius of 76.2 mm and inner radius of 69.9 mm is predicted. The simulations are run with an initial energy of 0.009 Nm. The static friction coefficient is taken as 0.25, the dynamic friction coefficient as 0.15, and the normal force from vacuum is 1000 N.

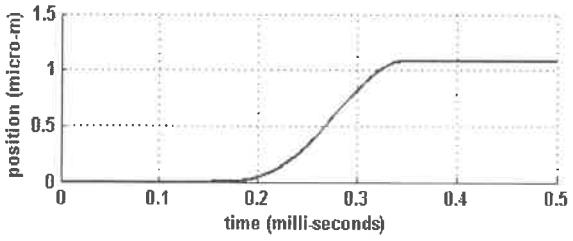

FIGURE 8. Part displacement due to impact.

Figure 8 shows that the part begins to accelerate at 0.15 ms, immediately after the impact force exceeds the friction force.

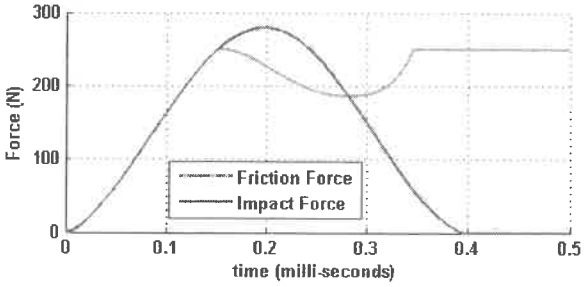

FIGURE 9. Simulation of actuation forces

Figure 9 shows how the motion of the part reduces the friction force. The area between the friction and impact force lines in Figure 9 is the momentum transferred to the part. The model was calibrated through testing and the energy of the actuating tap applied is calibrated based on the magnitude of part runout.

REALIGNEMENT ACTUATOR

A voice coil motor actuator has been designed to accelerate a translating core to the desired impact velocity and hold the core at that velocity until the impacts the part and produces the desired actuation force profile. The core is supported on a linear ball bushing, as shown in Figure 10.

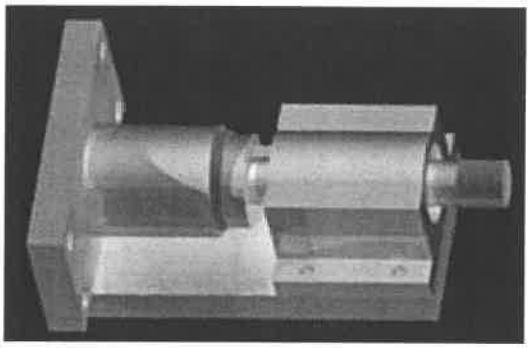

FIGURE 10. Model of tapping actuator.

Actuator Design and Fabrication

The realignment actuator has been assembled and tested. It is capable of applying a repeatable tap over a 4 mm range which allows it to align a part that has runout up to 4 mm.

SUMMARY

A method has been developed to correct the misalignment a part on a spindle that results from either the transfer of a two-sided part or manually placing a part on a vacuum chuck. An actuator has been designed, fabricated and tested that is capable of runout misalignments of up to 4 mm.

REFERENCES

[1] Olsson, H. et. al. "Friction Models and Friction Compensation." European Journal of Control (1998) 4: 176-195.

[2] Roark, R., Young, C. K., "Formulas for Stress and Strain." McGraw Hill, 1975.

ACKNOWLEDGEMENT

This project was supported by B & W Technical Services Y-12.

FABRICATION OF MICRO ASPHERICAL LENS ARRAY USING FAST TOOL SERVO WITH TOOL PATH COMPENSATION

Wei-Yao Hsu, Fong-Zhi Chen, Ching-Hsiang Kuo, Yuan-Chieh Cheng, and Wen-Lung Lin
Instrument Technology Research Center
National Applied Research Laboratories
Hsinchu, Taiwan, ROC

INTRODUCTION

The optical components with micro structure have been extremely developing and applied to optoelectronic devices for the past decade [1-3], such as light uniform for micro projectors and the light guide plate for liquid crystal display (LCD). The most used structures are one or multi-direction V-groove and micro lens array. The processes for manufacturing of such micro structures could be categorized into micro-system technologies and micro-engineering technologies [2]. To get high three-dimensional form accuracy, micro-engineering technologies such as fly-cutting, micro milling, grooving, and fast tool servo (FTS) are more suitable for micro optical structure fabrication. In this study we focus on the micro lens array fabrication using FTS. In general, the micro lens array consists of spherical lenses and could be fabricated by diamond turning with FTS. It performs high efficiency and high surface quality. With FTS, diamond tool could have a small and fast motion during the turning processes. Since the diamond tool radius needs to be taken into account for the diamond tool path generation, it is very difficult to get an analytic solution for micro aspherical lens array machining. In this study we use the over cutting depth compensation to approach the diamond tool path of FTS machining for micro aspherical lens array. In following sections we introduce the tool path generation of FTS for micro aspherical lens array fabrication in detail; for verification, a micro lens array with parabolic surface was cut and measured by the ultra precision machining machine (FF705XG, from Precitech) and ultrahigh accurate 3-D profilometer (UA3P-4, from Panasonic) respectively.

FTS AND ITS TOOL PATH GENERATION

FTS machining configuration is shown in FIGURE 1: the FTS controller receives the X-position and working spindle angle from the diamond turning machine, and calculates the FTS actuator stroke. The algorithm of FTS stroke is defined by the micro lens array specifications and diamond tool radius, and then written in C-language and complied in the SOP interface software. SOP is the software name abbreviated in German and means the controlling system for high precision manufacturing of surfaces [5].

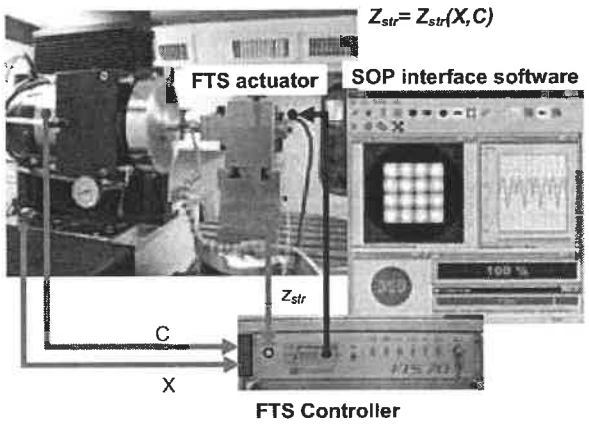

FIGURE 1. FTS MACHINING CONFIGURATION

In general the micro lens array is designated by the reference frame located in the workpiece, i.e. the location and surface profile of each lens is determined by x and y. While the local coordinate system could be represented by polar coordinate system as:

$$x = r \cdot \cos\theta$$
$$y = r \cdot \sin\theta \qquad (1),$$

where r is cutting position of the X-axis (relative to rotation center of the working spindle) and θ is the rotational angle of the working spindle.

For rectangular lens array, the location of each lens could be defined by the pitch along x- and y-direction respectively (Xp and Yp). Each lens has its serial numbers as $Xcol$ and $Yrow$, and could be described as:

$$Xcol = floor(\frac{x}{Xp} + 0.5)$$
$$Yrow = floor(\frac{y}{Yp} + 0.5) \quad (2).$$

Then the lens center position could be found as:

$$Xcen = Xcol \cdot Xp$$
$$Ycen = Yrow \cdot Yp \quad (3).$$

As shown in FIGURE. 2, e and f are the distance between the cutting point and lens center along the cutting concentric direction and radial direction respectively, and r_s is the distance between the lens center and working spindle center along the cutting radial direction. These geometric parameters could be calculated as follow:

$$e = \begin{bmatrix}\cos(\theta + \pi/2) & \sin(\theta + \pi/2)\end{bmatrix} \cdot \begin{bmatrix}Xcen \\ Ycen\end{bmatrix} \quad (4),$$

$$r_s = \begin{bmatrix}\cos\theta & \sin\theta\end{bmatrix} \cdot \begin{bmatrix}Xcen \\ Ycen\end{bmatrix} \quad (5),$$

$$f = r - r_s \quad (6).$$

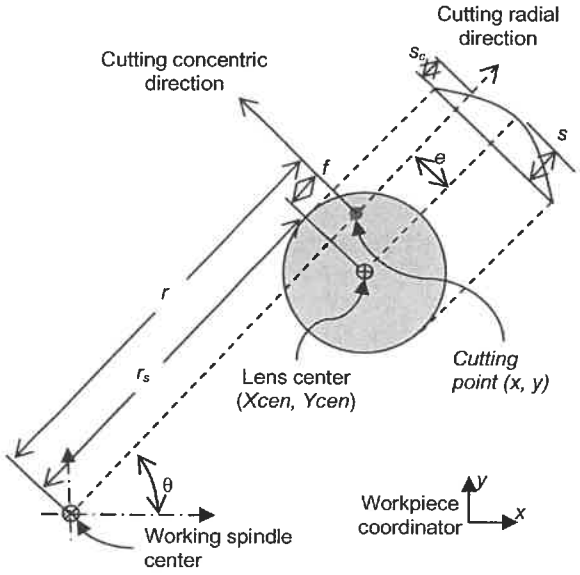

FIGURE 2. Relationship between micro lens and cutting point

To get the correct lens surface profile, the diamond tool radius needs to be taken into account. For spherical lens surface, the diamond tool path with tool radius compensation is always circular path with radius as $R_{ls}+r_t$ and $R_{ls}-r_t$ for convex and concave spherical lens respectively. R_{ls} is the radius of the cross section of the lens surface of cutting radial direction and r_t is the diamond tool radius. Since cross sections without lens center have different aspherical surface profile, micro lens array with aspherical lens surface profile is very difficult to generate diamond tool path with tool radius compensation. If the diamond tool path follows the aspherical surface profile without tool radius consideration, the surface would have over cutting problem. As shown in FIGURE 3, the over cutting depth E_z approximates to $(1/\cos\alpha - 1)r_t$, where α is the tangential slope of the aspherical profile at the cutting point. In this study we develop the diamond tool path of FTS for micro aspherical lens array, and the diamond tool radius compensation is set as $(1/\cos\alpha - 1)r_t$. The tangential slope of the aspherical profile at the cutting point could be gotten by partial differential to the standard aspherical surface equation with respect to the offset along the cutting radial direction.

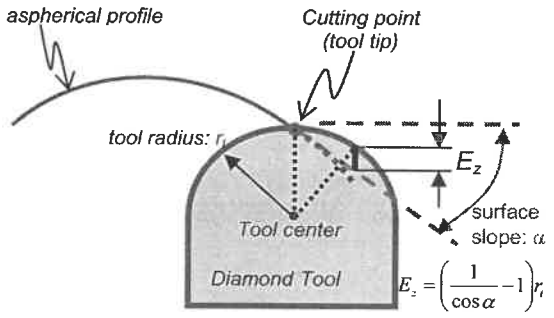

FIGURE 3. Diamond tool path follow the surface profile.

In general, an aspherical lens surface profile has a standard formulation as:

$$Z = Z(h) = \frac{ch^2}{1 + \left[1 - (1+k)c^2h^2\right]^{1/2}} + \sum_{i=2}^{n} A_{2i}h^{2i} \quad (8),$$

where h is the lateral distance from the lens center and has relationship with e and f as:

$$h^2 = e^2 + f^2 \quad (9).$$

Substituting equation (9) to equation (8), we can

get:

$$Z(e,f)=\frac{c\cdot\left(e^2+f^2\right)}{1+\left[1-(1+k)\cdot c^2\cdot\left(e^2+f^2\right)\right]^{1/2}}+\sum_{i=2}^{n}A_{2i}\cdot\left(e^2+f^2\right)^i \quad (10).$$

It is the function of e and f to describe the surface profile. If the diamond tool path follows the lens surface profile without diamond tool radius compensation, there would be surface height error in cutting radial section as:

$$E_z=\left(\frac{1}{\cos\alpha}-1\right)\cdot r_t=\left[\left(1+\tan^2\alpha\right)^{1/2}-1\right]\cdot r_t \quad (11).$$

Eq. (11) shows that the surface height error depending on cutting radial slope and diamond tool radius. Cutting radial slope could be found by partial differential with respect to f, as shown in following,

$$\begin{aligned}\tan\alpha&=\frac{\partial Z}{\partial f}\\&=2\cdot c\cdot f\left(1+\left[1-(1+k)\cdot c^2\cdot\left(e^2+f^2\right)\right]^{1/2}\right)^{-1}\\&+(1+k)\cdot c^3\cdot f\cdot\left(e^2+f^2\right)\cdot\\&\left(1+\left[1-(1+k)\cdot c^2\cdot\left(e^2+f^2\right)\right]^{1/2}\right)^{-2}\cdot\\&\left[1-(1+k)\cdot c^2\cdot\left(e^2+f^2\right)\right]^{-1/2}\\&+\sum_{i=2}^{n}2\cdot i\cdot A_{2i}\cdot f\cdot\left(e^2+f^2\right)^{i-1}\end{aligned} \quad (12).$$

Finally, the fast tool servo stroke with tool radius compensation can be represented as:

$$\begin{aligned}&Z_{str}=S-Z(e,f)-E_z\\&if\ S-Z(e,f)-E_z\le 0,\ \ Z_{str}=0\end{aligned} \quad (13),$$

where S is the sag of lens center relative to the lens edge.

Theoretically, one should use a small radius diamond tool to reduce the form error due to the tool over cutting as shown in Eq. (11). But the disadvantages are the worse surface roughness and poor cutting efficiency. To reduce cutting remained concentric groove, it is better to use a bigger radius diamond tool. For this reason we develop the diamond tool path with over cutting depth compensation.

Cutting and measurement of micro parabolic lens array

To verify the above method of tool path planning, a rectangular micro parabolic lens array was cut and measured. The optical parameters of the micro parabolic lens array are: vertex curvature c = 1/30mm^{-1} (concave), conic coefficient k = -1, center sag S = 60μm lens pitch Xp = Yp= 4.5mm, and the diamond tool radius is 0.5mm. We wrote a C-language program based on given parameters and above equations, then complied it using SOP software. Figure 4 shows the compiled and simulated result.

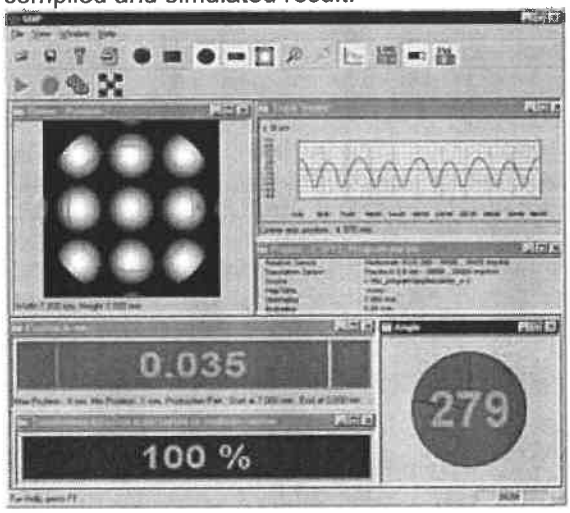

FIGURE 4. Tool path compiled and simulated result using SOP software.

After all the preparation process, we used the ultra-precision machining machine FF705XG equipped with fast tool servo FTS 70 to cut the micro parabolic lens array and the ultrahigh accuracy 3-D profilometer UA3P-4 to measure its form accuracy. Figure 5 shows the form accuracy of the center lens, and it is 0.3055μm. Figure 6 and 7 show the form accuracy of upper and right lens, and they are 0.2998μm and 0.2880μm respectively. As shown in Figure 5, there exists rotational symmetric form error of the center lens and it is due to the FTS stroke gain error. While the asymmetric form errors of the other lenses as shown in Figure 6 and 7 are due the complicated cutting system problems. We don't need to calibrate the FTS stroke gain error anymore, because reducing the center lens form error by stroke gain adjustment would increase the form errors of other lenses.

The results show that the FTS diamond tool path with over cutting depth compensation could reduce the form error in aspherical lens array cutting effectively.

CONCLUSION

In this study the micro aspherical lens array with 60μm sag, 30mm basic radius and -1 conic

coefficient was cut by Precitech FF705XG diamond turning machine with fast tool servo and measured by Panasonic UA3P-4. The measurement results show that the micro aspherical lens array fabrication using FTS with over cutting depth compensation could get acceptable form accuracy less than 0.3μm. It means the micro lens design will be more flexible on just the spherical surface.

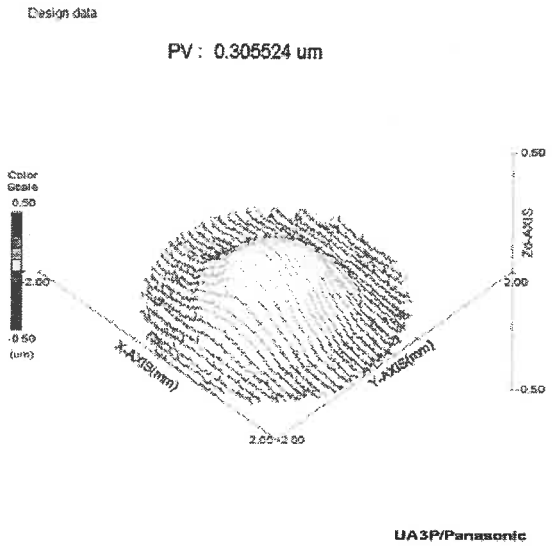

FIGURE 5. Form accuracy of the center lens

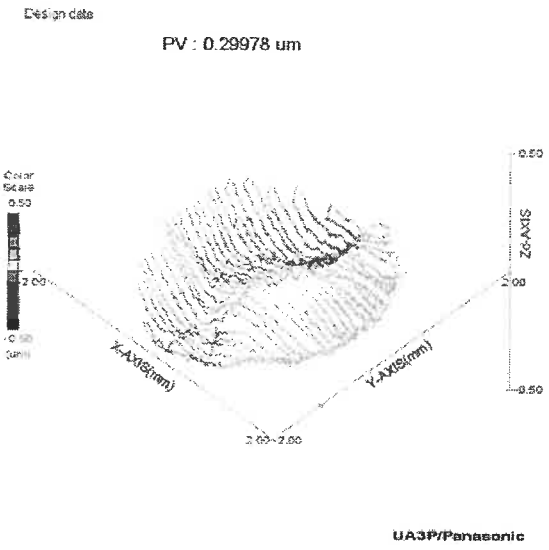

FIGURE 6. Form accuracy of the upper lens

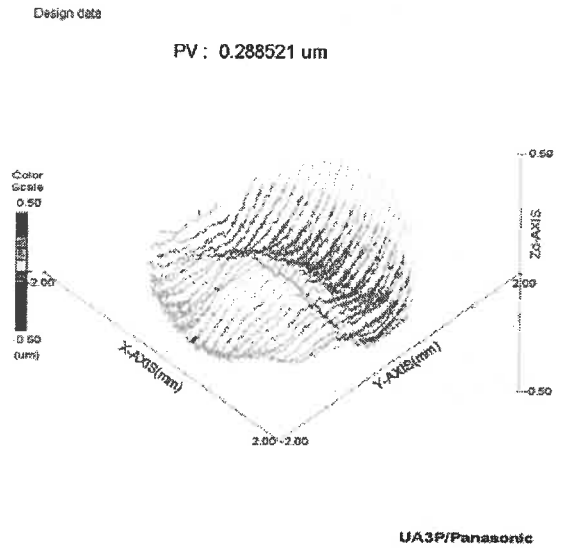

FIGURE 7. Form accuracy of the right lens

Acknowledgement

This work was supported by the National Science Council of the Executive Yuan, Republic of China under grant no. NSC 96-2221-E-492-009.

REFERENCES

[1] Oltmann Riemer. A Review on Machining of Micro-Structured Optical Molds. Key Engineering Materials 2008; Vols364-366 pp 13-18.

[2] M. A. Davies, C. J. Evans, S.R. Patterson, R. Vohra, B. C. Bergner. Application of precision diamond machining to the manufacture of micro-photonics components. Proc. of SPIE 2003; Vol. 5183 Lithographic and Micromachining Techniques for Optical Component Fabrication II, pp94-108.

[3] Jui-Wen Pan, Chih-Ming Wang, Hsiao-Chin Lan, We-shin Sun, and Jenq-Yang Chang. Homogenized LED-illumination using microlens arrays for a pocket-sized projector. OPTICS EXPRESS. 2007; Vol. 15 No. 17: 10483-10491.

[4] Spectral process, SOP manual, Handbuch, Stand 17.10.03.

EXPERIMENTAL STUDY ON MICROASSEMBLY BY USING LIQUID SURFACE TENSION

Yasuhiro KATO, Takeshi MIZUNO, Hiroshi TAKAGI, Yuji ISHINO, and Masaya TAKASAKI
Graduate School of Science and Engineering
Saitama University, JAPAN.

INTRODUCTION

Recent developments in the electronic industries have been promoting the miniaturization of electronic devices, which makes electronic components assembled on the substrate more minute and closely. In manufacturing process of small electronic devices, surface-mounting machines commonly pick up chips by using vacuum (negative pressure). In the future, surface mount devices will be more miniaturizing, which increases difficulty in picking up or manipulating objects.

One of the methods of overcoming such a problem is to use liquid for the manipulation of objects. Sato *et al.* [1] have studied the principle and characteristics of microparts self-alignment using liquid surface tension. Obata *et al.* [2] have proposed micromanipulation based on capillary force. In this method, the capillary force between a spherical object and the concave probe-tip accomplishes picking it up. However, wetting the stage is necessary for placing the object.

The authors have proposed a method of picking up an object by using liquid surface tension in combination with vacuum suction [3]. The feasibility of the proposed method has been demonstrated experimentally. In the experiments, however, the volume of liquid was not controlled, and only one object was treated. This paper clarifies the relationship between the formed drop size and liquid volume stored into the nozzle. In addition, the proposed method is also applied to spherical objects.

PRINCIPLES OF PICKING UP

The conventional method using vacuum is shown in Figure 1. The object is picked up by using negative pressure generated by vacuum and placed by breaking the vacuum. However, the misalignment between the center of the handling part of the machine causes failing in picking the object. Figure 2 shows a schematic illustration of the picking up procedure using a drop [3]. This process is explained as follows: (1) the nozzle is positioned above a chip, (2) a drop is formed on the nozzle's top, (3) the nozzle approaches to the chip for the drop to contact, (4) just after the contact, the chip moves on the surface of the drop to the bottom of the drop due to gravity, (5) the drop is sucked by making the pressure negative in the nozzle so that the chip is fixed on the center of the top of the nozzle.

The proposed method can align the center of an object with the center of the nozzle automatically even if there is a deflection between them initially. It is called as self-centering effect [3].

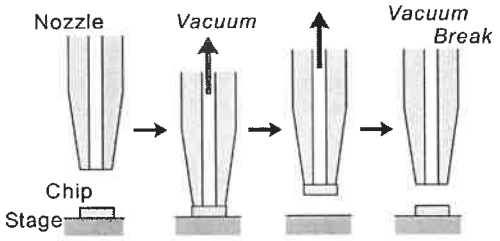

FIGURE 1. Schematic illustration of picking up procedure by conventional method.

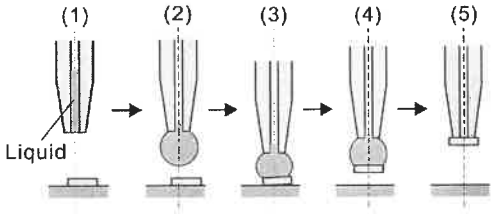

FIGURE 2. Schematic illustration of picking up procedure: (1) Positioning, (2) forming, (3) lowering, (4) picking up, and (5) sucking.

EXPERIMENTAL APPARATUS

Figure 3 shows an experimental system. Compressed air is passed through the ejector unit into the nozzle. The ejector unit controls pressure in the nozzle with three electronic switches. This research pay attention to the liquid volume stored in the nozzle.

A triaxial stage has a *X-Y* slider and a vertical positioner. The nozzle unit is attached to the positioner for up-down movement. Objects to be picked up are placed on the *X-Y* slider. The microscope is used to observe the process of picking up an object and to measure the size of drops or the deflection between the center of an object and the center of the nozzle. Ultrapure water is used as liquid to avoid the ill effects of contaminations.

DROP SIZE CONTROL

Process of storing water into the nozzle

Figure 4 shows the process of storing liquid to the nozzle. First, the nozzle approaches a tank storing water. After the nozzle touches the water surface, water is sucked into the nozzle by decreasing pressure in the nozzle for a preset time. The nozzle is raised from the water surface, and increases pressure for forming a drop on its top.

The decreased pressure P and the time T_S for sucking water into the nozzle are parameters determining the size of formed drops on its top.

Measurement of drop sizes

The sizes of formed drops on nozzle's top were measured. Figure 5 shows the results when T_S was set to be 0ms to 60ms and P=-0.5, -1.0 and -1.5 kPa (gauge pressure).

In T_S < 10 ms, drops with curvature larger than the nozzle's external diameter are formed as shown in Figure 6 (a). These drops evaporated soon after forming or were blown off due to the pressure fluctuation of inside the nozzle. Thus, these drops are inadequate for picking up with self-centering effect.

In 10 < T_S < 20 ms, drops were formed in a hemispherical shape on the nozzle's top as shown in Figure 6 (b). It was observed that the curvatures of the formed drops were constant independently of P or T_S, but depended on the external diameter of the nozzle's top. The drops kept its sizes due to capillarity in spite of evaporation.

In T_S > 20 ms, water formed spherical drops on the nozzle's top as shown in Figure 6 (c). As the P and T_S become larger, the curvatures of these drops tend to increase in proportion. The drop was stable on the nozzle's top, and its form was kept during picking up although the drop evaporated gradually or the pressure fluctuated.

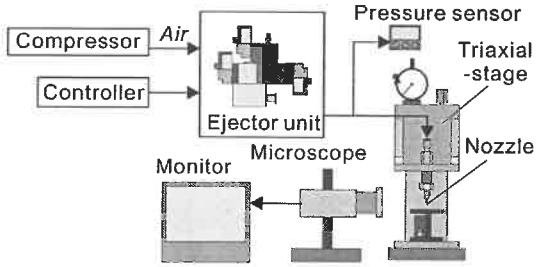

FIGURE 3. Schematic illustration of the experimental system.

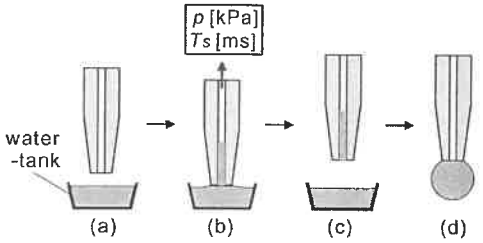

FIGURE 4. Schematic illustration of store/form procedure: (a) lowering, (b) sucking, (c) upping, and (d) forming by applying positive pressure.

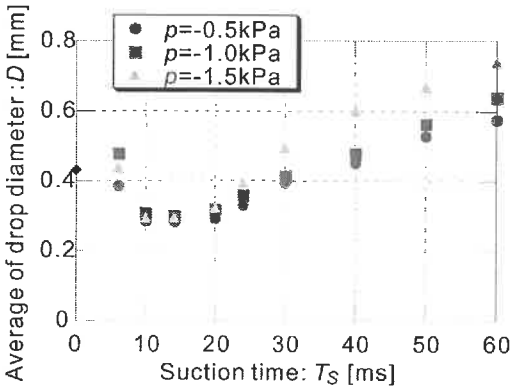

FIGURE 5. Relation between the average of drop diameter and the suction time T_S. The mark ◆ represents the result when the nozzle raised just after it contact water without negative pressure.

However, when the time T_S was too long, a drop was sometimes formed in the side of nozzle as shown in Figure 6 (d). Two types phenomenon were observed in this case. One is that the formed drop moved to side of the nozzle, which must be caused by pressure fluctuation inside the nozzle. The other is that the drop moved during increasing its size, and then the drop was formed. This must be caused by moisture on the nozzle's side face. These two kinds of phenomenon were often observed for large P and T_S.

Hemispherical drops are, therefore, used in following experiments to avoid the above problem that the drop is formed in the side of the nozzle.

PICKING UP WITH A HEMISPHERICAL DROP

Figure 7 show the results of picking up a chip resistance whose size is 0.4 x 0.2 x 0.1 mm. It is an industrial component called as "0402". Chips are placed in the stage with a prescribed deflection. Hemispherical drop sizes depend on the nozzle's external diameter, so three differential nozzles were used. Misalignment was given in the X-direction in Figure 7 (a) and in the longitudinal direction (Y-direction) in Figure 7 (b).

The results were classified into three patterns as follows shown in Figure 8:

Success: Picking up a chip with self-centering effect.

Failure 1: With a large misalignment, the drop touched the chip and the stage at the same time. When nozzle was raised, the chip remained on the stage.

Failure 2: The drop touched the electrode so that the chip was picked up with gradient.

The lines in Figure 7 are the maximum deflection defined in Figure 9 where a drop contacts with both the chip and the stage at the same time. From the geometrical relation it is given by:

$$L_{max} = \sqrt{\frac{D^2}{4} - \left(\frac{D}{2} - h\right)^2} + \frac{l}{2} \qquad (1)$$

The parameter l is the depth and the width of the chip in Figure 7 (a) and (b), respectively.

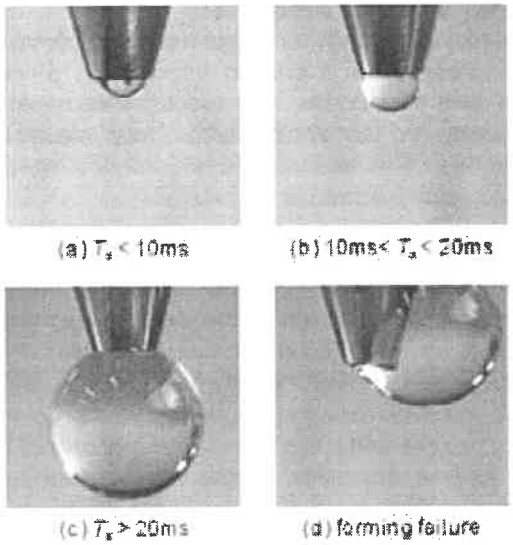

FIGURE 6. Classification of drop configuration. The case of (d) often occurred when the water stored in the nozzle was more than the condition of (c).

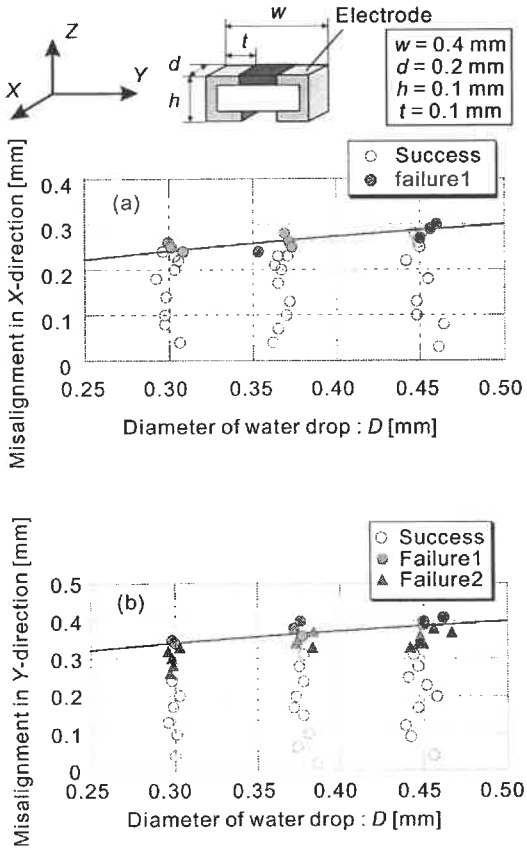

FIGURE 7. Relation between the diameter of the hemispherical drop and the misalignment for picking up a chip shown above: *(a) X-direction; (b) Y-direction.*

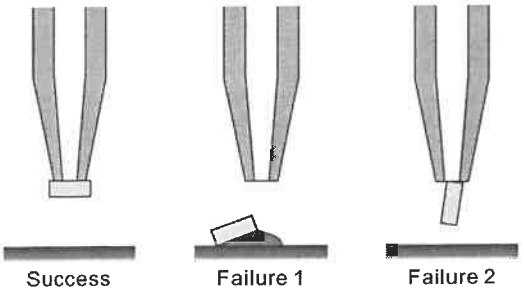

FIGURE 8. Classification of results for picking up a chip resistance.

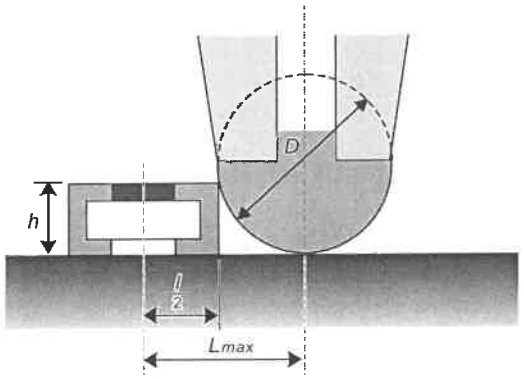

FIGURE 9. Definition of maximum deflection L_{max}.

Roughly speaking, a chip can be successfully picked up with misalignment less than 65% of L_{max}. Failure 2 was not observed for X-direction misalignment. Because the drop does not touch the electrode part of the chip.

PICKING UP SPHERICAL OBJECTS

Four kinds of zirconium balls whose diameter are 0.3, 0.4, 0.5 and 0.6 mm were used as objects to be picked up. They are placed in the stage with a prescribed deflection. Figure 10 shows the results of picking up a ball with one of three nozzles. It was observed that the formed drop curvature was almost equal to the external diameter of the nozzle.

The results were classified into two patterns that had been observed by the experiment to the chip, Success and Failure 1. The line in Figure 10 is the maximum deflection where a drop contacts with both the ball and the stage at the same time.

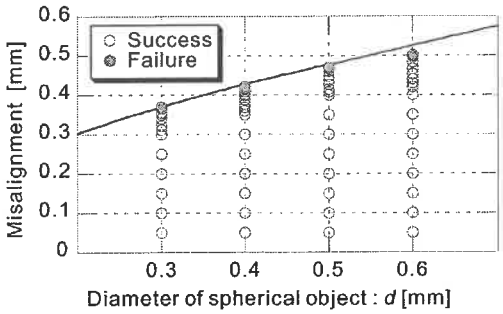

FIGURE 10. Relation between the sizes of spheres and misalignment.

From the geometrical relation, it is given by:

$$\begin{aligned} d < D: \quad & L_{max} = \sqrt{dD}, \\ d > D: \quad & L_{max} = \frac{1}{2}(d + D), \end{aligned} \tag{2}$$

where d: diameter of the sphere, D: diameter of the drop. A sphere can be successfully picked up with misalignment in less than 95% of L_{max}.

CONCLUSION

Microassembly using water drop was studied experimentally. The relation between the drop sizes and the water volume stored inside the nozzle was examined. The conditions in which the formed drops become hemispherical have been clarified. In picking up with a hemispherical drop, misalignment allowable for successful picking up was 65% of the geometrical limit L_{max} in the case of the chip resistance "0402", and 95% of L_{max} in the case of spherical object.

REFERENCES

[1] Sato K, Seki T, Hata S, Shimokohbe A. Principle and Characteristics of Microparts Self-alignment using Liquid Surface Tension. Journal of the Japan Society of Precision Engineering 2000; 2: 282-286.

[2] Obata K, Motokado T, Saito S, Takahashi K. A scheme for micro-manipulation based on capillary force. J. Fluid Mech. 2004; 498, 113-121.

[3] Takagi H, Takasaki M, Ishino Y, Mizuno T. Microassembly using Surface Tension. Dynamics & Design Conference 2007; 424.

RAPID SHAPE COMPARISON METHOD FOR 3D VIRTUAL MANUFACTURING SYSTEMS

In-Ho Song[1] , Won-Seck Lee[1] and Sung-Chong Chung[1*]
[1]Hybrid System Design & Control LABoratory
Department of Mechanical Engineering
Hanyang University, Sungdong-Gu, Seoul 133-791, KOREA

ABSTRACT
Digital manufacturing system (DMS) is widely used for virtual manufacturing in the car industry. Larger scale 3D simulation environment is required for precision manufacturing. This requires memory optimization of the DMS for rapid visualization and analysis. This paper proposes a shape comparison method for large scale simulation of 3D digital manufacturing systems. Proposed method finds redundant data during CAD data conversion for reference processing to save memory in proportion to the redundant data. In addition, a unique ID of GUID is used in the reference processing so that the results are sustained when the files are saved. Performance of the proposed algorithm is confirmed through case studies.

KEYWORDS
Digital Manufacturing System, Memory Optimization, Precision Assembly, Shape Comparison, Virtual Manufacturing System.

INTRODUCTION
DMS called virtual manufacturing system (VMS) is indispensable to construct a car assembly plant [1]. One of implementation bottlenecks of the 3D DMS is hardware memory. It is difficult not only to upload large scale 3D factory data at once but also to verify the entire factory in three dimensions. One of the most effective means to overcome the problem is removing redundant data of the assembly factory. This requires redundancy check of each part. However, CAD systems generally resolve the problem by referencing identical parts, and then convert CAD system data and load them to the DMS. This recognition procedure of each part delays 3D simulation on the VMS.

There have been many studies for comparing part configurations such as a comparison based on part histogram calculation [2], manufacturing feature recognition-based technique [3], B-rep graph [4], and product information-based technique [5]. There is also a research regarding the status of these studies [6]. However, most studies use degrees of similarity for comparisons, which requires more computation than the approach taken in this paper to confirm complete matches.

In order to design a lightweight VMS for the rapid and accurate simulation of the assembly job in the auto industry, this paper propose a rapid shape comparison method. It recognizes identical parts of the 3D manufacturing data to optimize memory of the 3D DMS. The model signature graph method proposed by Peabody [4] is applied to extract identical parts. A text-based signature graph is also proposed to construct an algorithm for comparing parts efficiently. Finally, performance of the devised algorithm is evaluated by measuring the time required for finding redundant parts of a station model in the automobile factory.

SHAPE RECOGNITION METHODS
In this paper, model signature graphs (MSG) [4] is modified and applied to build the 3D part comparison method. ACIS kernel is used to extract geometric and topological data from CAD data [7, 8]. Instead of constructing a graph, the geometry of ACIS kernel [9] of Fig. 1 and the corresponding text symbol of the selected geometry information are transmitted to the DMS.

Followings are the shape recognition procedures: First, a symbol indicating the curve type included in a surface is provided with the radius for ellipse, and the length for intcurve and straight line. The ellipse entity in ACIS kernel also includes circle, arc and the ellipse itself. Since the method is constructed based on texts,

it is called as the text-based model signature graph (TMSG). This approach does not create characteristic values of configuration based on computation, but the data conversion time is necessary for generating geometry information. Although it is difficult to determine similar part, it is easy to extract identical parts through the TMSG. Since identical parts should be extracted to save memory, it is an adequate approach for the DMS.

Fig. 2(a) shows a simple part to describe the developed TMSG. The cylinder consists of four faces A, B, C and D. TMSGs of them are shown in Fig. 2(b). The sixth row as the total TMSG is compared when the part is requested the comparison. Fig. 3 shows the procedure to execute the TMSG algorithm.

First, translator [7,8] converts input data from CAD data to ACIS data. They are translated to TMSGs according to solid units. And each solid is assigned to its GUID, a unique identification number. When the conversion is accomplished, recognition procedure to distinguish identical parts is conducted. As one to one comparison of each string of TMSGs of solids takes a lot of time, numbers of characters of the TMSGs are compared first. When the size of characters is the same, comparisons of the TMSGs are conducted to determine whether parts are same. When both parts are recognized as the same solids, copy GUID of the original solid to the identified solid. And assign relative location between the solids through the homogeneous transformation matrix. Repeat the above procedures up to the final solid and end the recognition process.

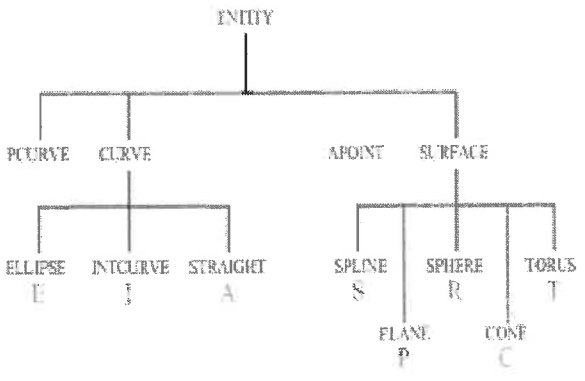

FIGURE 1. Geometry of ACIS kernel.

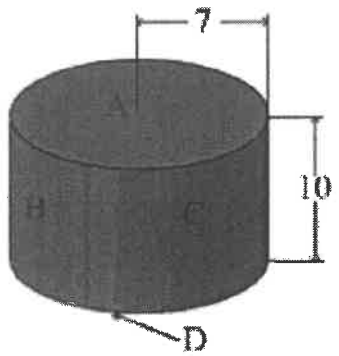

(a) A cylinder

Face	TMSG
A	PE7E7
B	TCE7A10E7A10
C	TCE7A10E7A10
D	PE7E7
Total TMSG	PE7E7TCE7A10E7A10 TCE7A10E7A10 PE7E7

(b) TMSG

FIGURE 2. A cylinder and its TMSG.

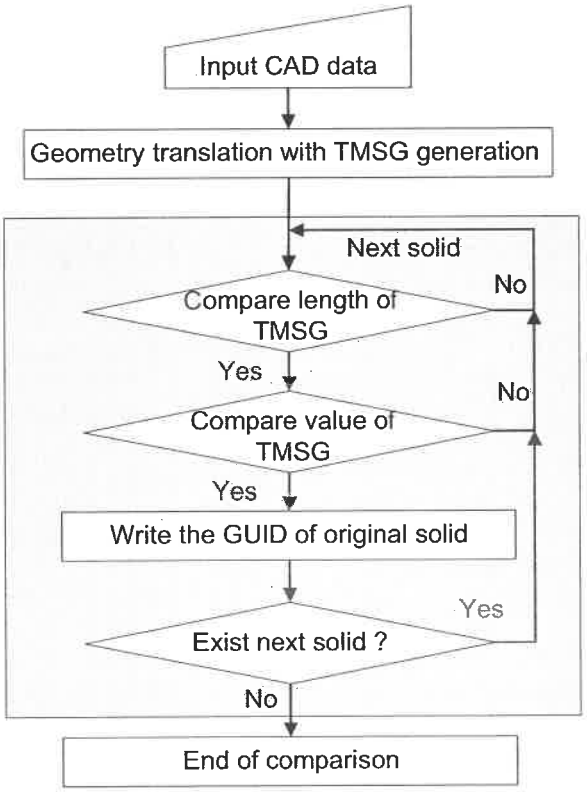

FIGURE 3. TMSG comparison algorithm.

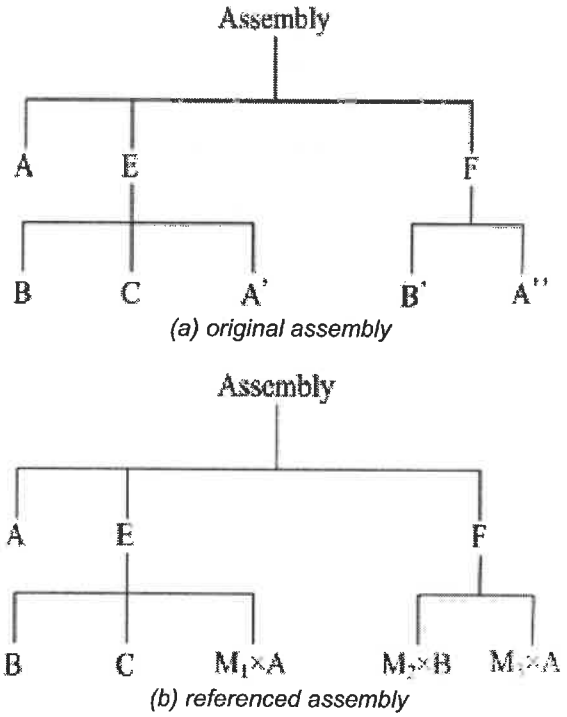

FIGURE 4. Structure of an assembly.

For example, Fig. 4(a) shows a CAD assembly data structure including several A and B parts. A' and A" are A parts in different locations. B' is another B in different location referencing the original B solid. Using the devised TMSG method, identical parts positioned in different locations A' and A" are recognized as $M_1 \times A$ and $M_3 \times A$, respectively. Where M_1 and M_3 are homogeneous transformation matrices representing relative positions of them in the world coordinates. B' is recognized as $M_2 \times B$ as well. Fig. 4(b) assembly structure reduces memory space and expedites the loading procedure of solids on the VMS.

GENERATION OF THE UNIQUE ID FOR PART COMPARISON

After parts are recognized, original parts have to be linked with the referenced parts. When the original and reference parts are on the same program, address values are used for the referencing. However, a unique ID is required to link the original part to the referenced part when the assembly data are not only saved as a file for reconfiguration but also transferred to another system.

Microsoft creates and uses GUID as a unique ID. It is applicable to calling various components [10]. JT format from UGS PLM also uses GUID to reference parts [11]. GUID is a 128-bit integer created through combining the MAC address, which is the computer network ID, and the duration time from the reference time in milliseconds. This always yields a unique ID value. This approach is adopted to develop the rapid shape comparison system in this paper. Original part's GUID and corresponding positioning data including rotation and translation information of the original part are stored for the next usage.

CASE STUDY

In order to test the performance of the developed shape comparison algorithm, the automobile factory station parts and the station assembly shown in Fig. 5 and 6 are used, respectively. There are 109 station parts, as listed in Table 1, and 38 of them (34.86%) are original parts. It takes 0.094 seconds to recognize reference parts through the proposed comparison algorithm. The second station assembly consists of 1756 parts, as shown on the third column of Table 1, and 151 of them (19.99%) are original parts. It takes 3.516 seconds to search for reference parts by comparing them with the proposed method. Table 2 describes specifications of the test computer used in this case study. As an assembly usually consists of less than 2000 parts, the results confirm rapidness of the developed algorithm. It is applicable to the VMS.

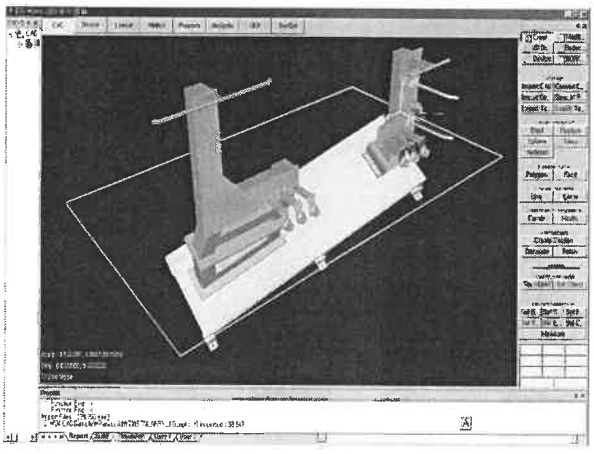

FIGURE 5. Automobile factory station parts for the comparison test.

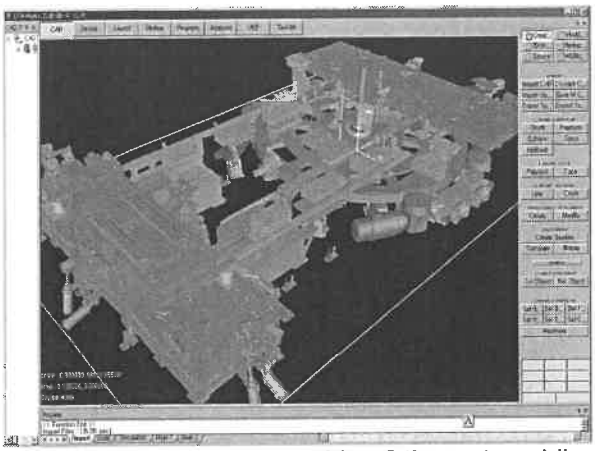

FIGURE 6. Station assembly of the automobile factory.

TABLE 1. Specifications and results of the test data.

	Example 1	Example 2
Total parts	109	1756
Original parts	38	151
Original ratio	34.86%	19.99%
Comparison time	0.094 sec	3.516 sec

TABLE 2. Specifications of the test computer.

Item	Specification
CPU	Intel Core 2 2.00GHz
RAM	2.00 GB
OS	Windows XP Professional

CONCLUSIONS

Applying the TMSG comparison algorithm, a rapid shape comparison method for 3D digital manufacturing system has been devised. Following conclusions are obtained:

(1) TMSG algorithm does not calculate the characteristic equation, developed comparison method is faster and more efficient than others.

(2) Using the proposed method in a 3D DMS, memory space is saved in proportion to the number of redundant parts.

(3) As the original parts include feature data, and the referenced parts include ID of the original parts and positional information, CAD data are loaded and managed very efficiently on the VMS.

(4) Validity and effectiveness of the proposed methodology have been verified through case studies.

REFERENCES

[1] Kim Y S, Yang J S, Han S H. A Multichannel Visualization Module for Virtual Manufacturing. Computers in Industry. 2006; 57: 653-662.

[2] Ankerst M, Kastenmuller G, Kriegel H P, Seidl T. 3D Shape Histograms for Similarity Search and Classification in Spatial Databases. Lecture Notes in Computer Science. 1999; 1651: 207-226.

[3] Ramesh M, Yip-Hoi D, Dutta D. Feature based Shape Similarity Measurement for Mechanical Parts. ASME Journal Computer Information Science. 2001; 1 : 245-256.

[4] Kalyanapasupathy V, Lin E, Minis I. Group Technology Code Generation Over the Internet. ASME Design Engineering Technical Conferences. 1997; 14-17.

[5] Peabody M, Regli W C. Clustering Techniques for Databases of CAD Models. Technical Report DU-MCS-01-0, PA: Department of Mathematical and Computer Science. Drexel University. 2001.

[6] Iyer N, Jayanti S, Lou K, Kalyanaraman Y, Ramani K. Three-dimensional Shape Searching: State-of-The-Art Review and Future Trends. Computer-Aided Design. 2005; 37: 509-530.

[7] Song I H, Chung S, Chung S C. Precision Design Verification System of Injection Molds using Web-based 3D Viewing Technology. Proceeding of the ASPE. 2006; 21: 451-454.

[8] Song I H, Chung S C. Synthesis of the Digital Mock-Up System for Heterogeneous CAD Assembly. Transactions of the North American Manufacturing Research Institution of SME. 2007; 35: 777-785.

[9] Corney J, Lim T. 3D Modeling with ACIS. Saxe-Coburg Publications. UK: 2001.

[10] http://msdn.microsoft.com/en-us/library/system.guid.aspx

[11] JTOpen. http://www.jtopen.com

HIGH-SCAN RATE POSITIONER FOR SCANNED PROBE MICROSCOPY

R. Ian MacKenzie, Aaron J. Gawlik, and David L. Trumper
Mechanical Engineering Dept.
Massachusetts Institute of Technology
Cambridge, MA, U.S.A.

INTRODUCTION

In recent years, high-speed atomic force microscopy (AFM) has been the subject of new focus [1, 2, 3]. The high resolution capability makes AFMs a promising technology for dimensional metrology of artifacts such as semiconductor integrated circuits and photomasks. Further, to allow cost-effective use of an AFM in on-line measurement processes, it is necessary to achieve high imaging rates, and thereby high scan rates of the AFM tip. We report here on an initial design effort and prototype of a novel two degree of freedom (2 DOF) scanner for the fast scan (x-axis) and vertical (z-axis) for a high-speed, high-accuracy AFM. Our ultimate design goal is to scan a 50 μm × 50 μm area of 10^6 pixels with a 10 μm vertical range at a 1 Hz rate. The desired sensor noise is 1 nm in the horizontal scan axes, and 0.2 nm in the vertical surface-following axis. The scanner is intended for imaging targets such as selected areas on semiconductor wafers. The relatively large mass of such targets requires that the approximately 200g accelerations of the fast scan axis be allocated to the tip scanning mechanism. We also allocate the vertical height-following function to the scanner vertical axis due to its potentially achievable high bandwidth.

Two prototypes were designed, fabricated, and tested. Neither incorporates an AFM tip, and therefore has no imaging mechanism. The main purpose of these prototypes is to illustrate the feasibility of the novel 2 DOF scanner design. Actuation is remote from the proposed tip location, which allows metrology to easily access the tip. The actuator used is a 2 DOF Lorentz motor with a moving-magnet/stationary-coil design. Flexures allow movement in the x- and z-directions. The x-axis scanning is implemented at the system's resonant frequency while the z-axis is positioned in a conventional random access fashion. The use of resonant scanning allows high speed while dissipating very low power.

This paper focuses on the results of the second prototype. We present the mechanical and actuator design, the scanner control, the metrology noise performance, and the experimental results confirming the design feasibility.

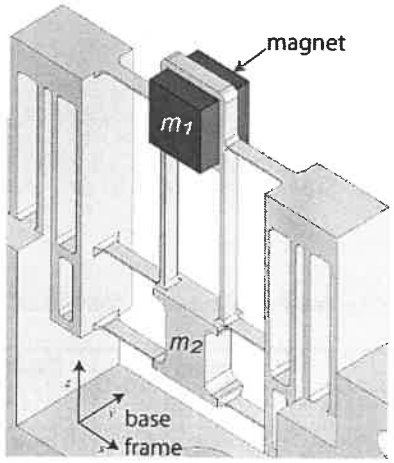

FIGURE 1. The CAD model shows the mechanical flexure design.

SCANNER MECHANICAL DESIGN

The scanner's 2 DOF are designed into a monolithic structure that allows each DOF to operate essentially independently. This imposes design considerations and constraints relating to structure design, actuation technology, and position sensing. Flexures are the primary structure element in part because they can be designed to allow single DOF movement without friction, can be readily manufactured, and can be scaled to small ranges of motion.

Figure 1 shows the second scanner prototype without actuators or sensors. There was no intention that this prototype incorporate a tip, so the surface that the tip would be mounted to in a traditional AFM (the bottom surface of m_2) is obstructed by sensors. Two sets of vertical flexures allow x-axis motion (one set consists of the four outermost flexures that are attached to the base and the the other set consists of the six in-

nermost flexures that are free of the base) and six horizontal flexures allow z-axis motion.

Mode Design

For motion in the x-axis, the flexure design shown in Figure 1 can be modeled as a 2-stage spring-mass-damper system. The actuation force is applied to m_1, and the resultant motion is sensed on m_2, which will ultimately carry the AFM tip. Under the simplifying assumption of no damping, which is valid for this lightly-damped flexure mechanism, the equations of motion can be written as

$$\begin{bmatrix} m_1 & 0 \\ 0 & m_2 \end{bmatrix} \begin{bmatrix} \ddot{x}_1 \\ \ddot{x}_2 \end{bmatrix} + \begin{bmatrix} k_1 + k_2 & -k_2 \\ -k_2 & k_2 \end{bmatrix} \begin{bmatrix} x_1 \\ x_2 \end{bmatrix} = \begin{bmatrix} f \\ 0 \end{bmatrix} \quad (1)$$

where k_1 and k_2 are the x-direction stiffnesses associated with the outer and inner vertical flexure sets (see Figure 1), respectively, x_1 and x_2 are the motions associated with m_1 and m_2, respectively, and f is the forcing function applied at m_1. Solving this in the unforced case gives two modal frequencies ω_1 and ω_2. These frequencies are associated with modes in which the masses move in-phase and in anti-phase, respectively. The desired scan mode is the in-phase mode.

The first mode shape must also be in the ratio $\begin{bmatrix} 1 & 2 \end{bmatrix}^T$. This requirement is present so that the two vertical flexure sets have equal x-axis deflections, and thus have z-axis deflections which cancel.

Actuator Design

Electromagnetic shear-mode actuators drive the scanner. The configuration is a stacked-coil design, which allows for the same type of coil to be used for both x- and z-direction actuation, and, to first-order, decouples the forces.

The top pair of coils in Figure 2 generates a Lorentz force in the z-direction. Current flows in the x-direction where the two coils meet in the center, and interacts with the y-directed B-field from the magnet (not shown) to produce a force in the z-direction. Similarly, the bottom pair of coils is oriented such that force is generated in the x-direction. A complementary actuator assembly is located on the opposite side of the magnet and completes the magnetic circuit through the steel backing, balances the forces about the center of mass of m_1, and generates higher total forces.

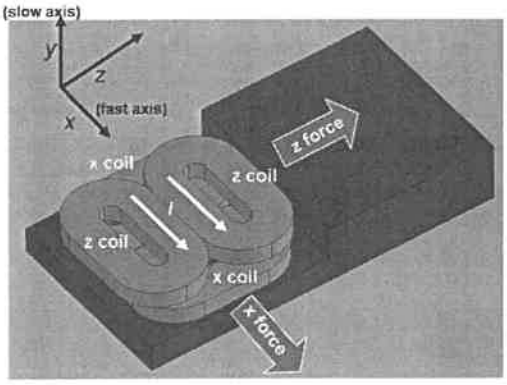

FIGURE 2. The CAD model of the actuator half shows how the Lorentz forces are generated.

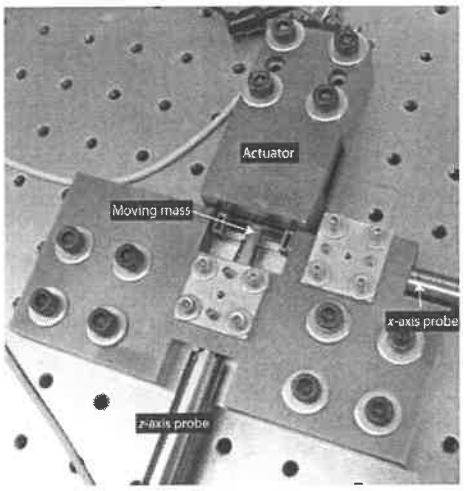

FIGURE 3. The flexure-based scanner is shown with actuator and metrology system.

Figure 3 shows the fully assembled second scanner prototype.

Separate actuators were designed and built for each prototype. This allowed each prototype to be optimized for efficiency. However, the first prototype actuators were used when testing the second prototype flexure suspension because the second prototype actuators had not arrived at the time of testing.

CONTROL

Control of z-axis

Control of the z-axis is achieved via conventional loop-shaping methods. The controller is designed around the z-axis open loop frequency response. A triple-lead controller is used to obtain the desired phase margin at a 1.5 kHz crossover fre-

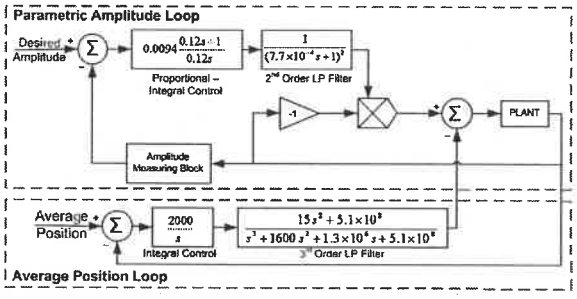

FIGURE 4. The block diagram of the x-axis controller shows a parametric amplitude control loop and an average position loop.

quency. The z-axis will achieve higher bandwidth (~5 kHz) upon completion of a high resolution A/D converter and data acquisition system in parallel development [4]. A proportional-integral controller is used to obtain zero steady-state error.

Control of x-axis

The goal of the x-axis control is to implement a self-sustaining oscillation that resonates at the frequency of the first mode ω_1 with a 50 μm p-p amplitude. This amplitude control of the x-axis is achieved by parameter variation of loop gain. Figure 4 shows a block diagram of the x-axis control. To achieve self-sustaining oscillation in which the amplitude is constant, the closed-loop system poles must lie on the imaginary axis of the s-plane.

The parametric amplitude control is a conventional loop except for one key difference: the gain block (multiplication block in Figure 4) can change value. This gain block is thereby dynamically adjusted to make the loop marginally stable. The amplitude of the output is measured in the amplitude measuring block and then compared to the desired amplitude. The parametric amplitude controller (the PI block and 2^{nd} order LP filter block) then drives this error to zero by changing the value fed into the multiplication block, thereby changing the loop gain.

The crossover frequency of this amplitude loop is estimated to be about 5-10 Hz using modeling techniques presented in [5]. A proportional-integral controller is used to remove any steady-state error between the desired and measured amplitude. The 2^{nd} order low-pass filter is included to attenuate the effect of any spurious error signal at the frequency of oscillation or its harmonics.

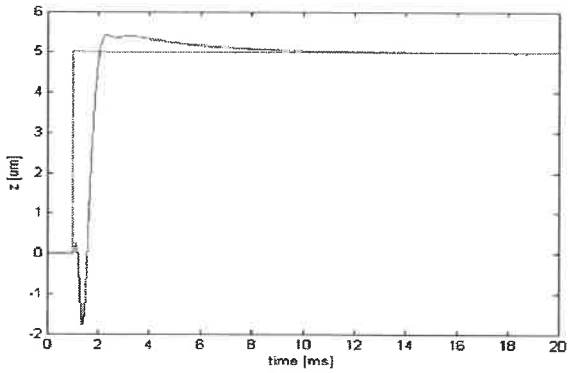

FIGURE 5. The z-axis position response to a 5 μm step demand is shown.

The other half of the x-axis controller is the average position loop, also shown in Figure 4. This conventional loop keeps the average position of the x-axis at zero during scanning because the amplitude controller operates independently of the average position. This controller is designed around the open-loop dynamics of the x-axis. Integral control is used to eliminate steady-state error, and a 3^{rd} order Chebyshev filter is used to keep the loop magnitude at the first mode well below unity and thus keep the oscillation from affecting the average position loop.

EXPERIMENTAL RESULTS

Control Results

Figure 5 shows a 5 μm z-axis closed-loop step response. As expected, the response exhibits zero steady-state error and indicates that the z-axis can achieve a 10 μm displacement range (±5 μm). The step response initially moves in the opposite direction of the command. This is due to the controller output saturating through the digital-to-analog convertor (DAC), a nonlinear effect. This problem of saturation can be counteracted by contouring the reference trajectory appropriately.

Figure 6 shows the x-axis steady-state output of the amplitude control loop for a 50 μm p-p amplitude demand. As desired, the frequency of oscillation is 1025-1026 Hz, which is the frequency of the first mode.

Power consumption

The maximum steady-state power dissipation in the z-axis was calculated by measuring the voltage and current required for a 5 μm step. The voltage output reaches a steady-state value of 1.8

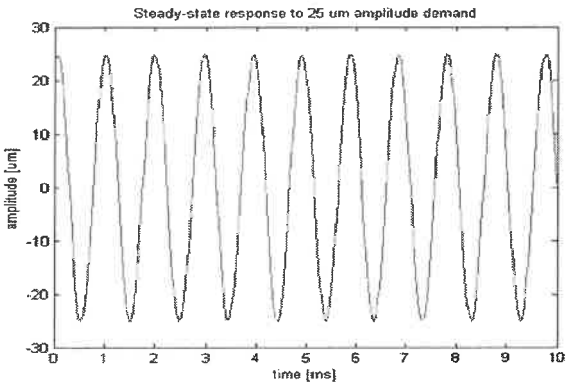

FIGURE 6. The x-axis amplitude controller response is shown in steady-state.

V and the current reaches a steady-state value of 150 mA. These values indicate that the steady-state power dissipation is 260 mW.

Voltage and current readings were also recorded during a 50 μm p-p scan on the x-axis. The peak voltage is 2.01 V and the peak current is 78 mA. The current lags the voltage by 67°. Using these values, the RMS dissipative power is 44 mW (63 mW peak) and the RMS reactive power is 107 mW (151 mW peak). These very low power values are the result of driving at resonance and the high Q of this system resonance.

Power consumption is expected to decrease appreciably upon implementation of the the actuators sized for the second prototype.

Capacitance sensor noise

The noise of the capacitance sensors was tested by interfacing them with a Tektronix AM502 differential amplifier and capturing the differential amplifier output data on an oscilliscope. The bandwidth of the differential amplifier output was varied between 10 kHz and 100 kHz. The noise results for each probe and for each filter bandwidth setting are shown in Table 1. The x-axis probe meets the target specification. The z-axis probe meets the target specification when the probe is used with a 10 kHz bandwidth filter setting.

CONCLUSION

The prototype presented herein demonstrated a novel 2 DOF resonance scanner. The mechanical flexure design allowed the 2 DOF to be essentially decoupled from each other. The actuator design illustrated the capability of utilizing only one magnet to provide forces in 2 DOF. Commensurate with the flexure design, the actuator permits low power consumption required to drive each axis. Resonant control of the x-axis was shown to be feasible. Capacitance probes demonstrated low noise characteristics while permitting high-bandwidth control. Bandwidth and noise however, are limited overall by the dSPACE data acquisition system bandwidth and resolution.

TABLE 1. Capacitance sensor RMS noise results for 100 kHz and 10 kHz bandwidth settings.

Probe	Target noise [nm]	100 kHz [nm]	10 kHz [nm]
x probe	1.0	0.65	0.15
z probe	0.2	0.33	0.08

To address these issues, we have been developing an FPGA-based control solution which will use 24-bit analog-to-digital converters. The high-speed data acquisition will be implemented on a high-speed FPGA system with control loops running at their required loop rates [4]. Although challenging areas of investigation remain, this initial study demonstrates a feasible baseline for continuing development.

ACKNOWLEDGMENTS

This work was supported by Samsung Electronics Co., Ltd.

REFERENCES

[1] Ando T, Kodera N, Naito Y, Kinoshita T, Furata K, Toyoshima Y. A high-speed atomic force microscope for studying biological macromolecules in action. Chem Phys Chem. 2003;4:1196–1202.

[2] Fantner G, Schitter G, Kindt H, Ivanov T, Ivanova K, Patel R, et al. Components for high speed atomic force microscopy. Ultramicroscopy. 2006;106:881–887.

[3] Humphris A, Miles M, Hobbs J. A mechanical microscope: high-speed atomic force microscopy. Applied Physics Letters. 2005;86:034106–1–034106–3.

[4] Gawlik A. Applied high resolution digital control for universal precision systems [Master's thesis]. Massachusetts Institute of Technology. Department of Mechanical Engineering; 2008.

[5] Roberge J. Operational amplifiers: theory and practice. New York, U.S.A: John Wiley & Sons; 1975.

PERFORMANCE IMPROVEMENTS IN THE MEASUREMENTS OF A LARGE RANGE SCANNING PROBE MICROSCOPE

Prem Rachakonda, John Kramar
Manufacturing Engineering Laboratory
National Institute of Standards & Technology,
Gaithersburg, Maryland, USA

ABSTRACT

The Molecular Measuring Machine (M^3) is a three-dimensional metrology instrument designed to measure feature positions over an area of 50 mm x 50 mm with a combined uncertainty of one nanometer. The probing device is a scanning probe microscope and the metrics are Michelson interferometers. Achieving sub-nanometer scale metrology over such large areas requires customized instrument design to deal with challenges like thermal stability, machine stiffness, noise in control electronics, etc. In the past few years, M^3 has been moved to our new Advanced Measurement Laboratory (AML), into an underground, class 100 room, with ± 0.01 K temperature control and floating-slab vibration isolation.

Since then, M^3 has been undergoing an overhaul to achieve its performance goals. The changes include tuning the viscous damping of the fine motion stages to achieve a lower Q-factor; new optics to replace the existing ones that had damaged coatings; realignment of the motion generation stages; and a new in-vacuum fiber optic beam delivery system for interferometer system to negate the effects air turbulence. The improvement in the Q-factor of the motion stages was around 51.8 % and the loss in the motion due to viscous damping was about 6.25 %, which is an acceptable value. The new beam delivery system for the interferometers reduced the noise level from about 300 pm to 180 pm. This beam delivery system is expected to improve the interferometer-guided closed-loop controlled imaging. Each of these improvements contributes towards our ambitious goal of achieving a 1 nm uncertainty.

One of the motivations for developing M^3 is to be able to explore the use of atomic crystal lattices as intrinsic length standards. To use a crystal lattice in this way as a metric, the lattice dimensions must be characterized and validated by means of SI traceable measurements. The immediate goal of this work is to report initial M^3 interferometric measurements of the lattice constants of one of the simplest materials for SPM imaging, graphite. These results are expected to corroborate graphite lattice constant measurements by other means, e.g., x-ray diffraction, and conversely will also serve as a means of validating the measurements performed by M^3.

CHARACTERIZATION OF MICROSTRUCTURE FREEFORM SURFACES USING A PATTERN MATCHING ANALYSIS

C.F. Cheung*, L.B. Kong, W.B. Lee and S. To
Advanced Optics Manufacturing Centre, The Hong Kong Polytechnic University, Hung Hom, Kowloon, Hong Kong

Microstructure freeform surface is a type of freeform surfaces which is widely used in optical-mechanical-electronic components with increasing high precision requirement. This paper presents the characterization of structured freeform surfaces based on a pattern matching analysis method. The method employed rough matching by micro-structure features and then precise matching based on least squared criteria to optimize matching results. The capability of the proposed method is realized through a trial implementation of a prototype surface characterization system。With the successful development of the pattern matching analysis method, the accuracy and the efficiency of the characterization of the microstructure freeform surfaces such as micro-lens array can be significantly increased.

Keywords: Microstructure freeform Surfaces, Microlens array, Surface characterization, Pattern matching, Form error, Fast tool servo machinin

1. INTRODUCTION

The history of microlens fabrication can be traced to over 300 years ago when Robert Hook first melted rods of Venetian glass to form small lenses. There has been an upsurge of interest in microlens as the benefits of photonics over electronics have been realized since the late 1980s [1].

Nowadays, micro-structured freeform surfaces are widely used in various applications since they can produce unique or particular optical performance. Generally, micro-structured freeform surfaces are small scale topologies are classified as micro-grooves, micro-lens arrays, pyramids, etc. They are widely used for photoelectrical parts such as light guide for display device, micro-lens scanners [2], or micro-lens arrays for Flat-Panel Devices, and are applicable for optical communications, optical data storage, digital displays, and laser beam shaping [3]. A microlens array is composed of many microlenses which are arranged in a particular pattern, and there are differences in the radii of microlenses among rows. With the use of microlens array, fewer LED light sources may be used to achieve a uniform distribution of light. Microlens arrays are mainly used in Liquid Crystal Displays (LCDs) and the applications include mobile phones, hand-held palm pilots and TVs, etc.

During the past decade, some research work on microlens characterization can be found in the available literature. Nussbaum et al [4] characterized the surface profile and the wave aberrations besides the surface roughness. The research emphasized geometrical features and functional performance of microlens array product. In the research by Liu, et al [5], the optical performance was tested such as the spot uniformity, the spot sizes, and the positions of the focused spots at various accessible locations, which is an indirect characterization for microlens array quality. Some parameters such as microlens pitch, fill factor, surface quality, wave front quality and so on have been examined for lens-let array for astronomical spectroscopy by Lee and Haynes [6]. Ottevaere et al [7] measured the geometrical dimensions, the sag and the surface roughness of the microlenses, as well as the optical characteristics such as wavefront aberrations and the focal lengths. Gu, et al [8] measured microlens profile and some optical parameters such as focal length and spot size by a laser scanning reflection/transmission confocal microscopy. Micro-lens arrays are traditionally fabricated by hot-embossing and photoresist re-flow methods, followed by Inductively Coupled Plasma (ICP) etching, the surface quality of single lens in terms of surface roughness and optical properties are characterized [9]. For single lens profile analysis, surface roughness of microlens array on bulk metallic glass is analysed [10]. Gao et al [11] proposed an on-line measurement and profile characterization of micro-structure surfaces.

Based on the overview of the literature, most of research is either focused on single lens characterization, or the optical performance, relativelyvery little research has been conducted to study pattern of the microlens array and the relationship with the machining mechanism. In this paper, a pattern matching analysis method is presented for microlens array is characterized by both of single microlens quality and the array parameters such as lattice dislocation. The metrology of microlens array is presented including the data acquisition process, data processing, micro-lens array parameters exploration, etc. The data of the microlens array is obtained by non-contact optical methods, e.g., Wyko NT 8000 and TalySurf CCI 3000, which provide a high precision solution for measuring the microlens array data. Microlens Lattice Dislocation parameters have been developed in the present study. The proposed lattice parameters are useful for studying the microlens array accuracy and can also be meaningful and helpful for the relationship built-up with the machining mechanism and machining process. Case studies have been conducted and the experimental results further verify the validity and efficiency of the proposed method. Some suggestions on micro-structures characterization are recommended in this paper, a pattern matching analysis method is presented for the characterization of structured freeform surfaces. The method is preliminarily evaluated through a preliminary experiment.

2. A FRAMEWORK OF THE PATTERN MATCHING ANALYSIS METHOD

FIGURE.1 shows schematic diagram of the proposed pattern matching analysis method。It starts from the construction of the normal template of the microlens array based on a geometrical model which takes into consideration of the geometrical parameter such as no. of lens, size of the lens, radius of the lens, etc. As shown in FIGURE.2, the normal template of the micro-structure array surface can be divided into two groups, namely structured surface (SS) and base surface (BS). The structured surfaces are arrayed in a certain pattern such as tessellation array format, to achieve some specific optical performance or other functional requirement.

In the structure array, one single structured surface can be expressed as follows:

$$\begin{cases} S_s = f_{i,j}(x,y) \\ (x,y) \in D_{i,j} \end{cases} \quad (1)$$

Where, $D_{i,j}(i=m, j=n)$ is the structured surface area in an m×n format.

The base surface can be presented as

$$\begin{cases} S_b = f_b(x,y) \\ (x,y) \in D_b \end{cases} \quad (2)$$

Where, D_b is the base plane area.

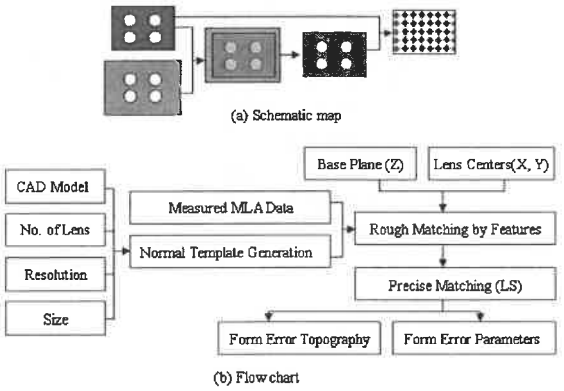

FIGURE 1. Schematic diagram of the pattern matching analysis method.

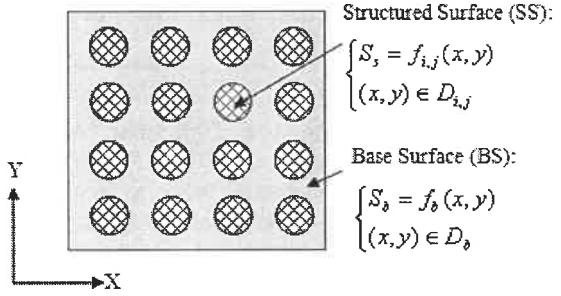

FIGURE 2. Illustration map of micro-structured surface.

The surface data of the microlens array are measured by a 3D surface profile measurement system such Wyko NT8000 or CCI from Taylor Hobson Co. The measured microlens array surfaces are reconstructed from the measured data based on Bi-Cubic B-spline surface interpolation [12]. Bi-Cubic B-spline surface interpolation for corresponding point searching process is shown in FIGURE 3.

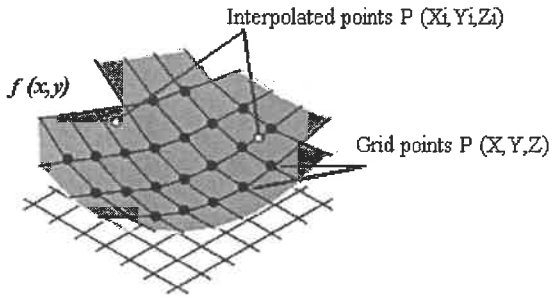

FIGURE 3. Bi-Cubic B-spline surface interpolation.

The measured surface for the microlens array is given by:

$$f(x,y)=\sum_{i=0}^{n}\sum_{j=0}^{m}d_{i,j}N_{i,3}(u)N_{j,3}(v) \qquad (3)$$

Where, $d_{i,j}$ is the control knot, $N_{i,3}(u)$ and $N_{j,3}(v)$ are normalized B-spline basis function of order 3 in u and v direction respectively. For each slice surface of uniform cubic B-spline, the basis function can be expressed as

$$N_3(u)=\frac{1}{3}\begin{bmatrix}-1 & 3 & -2 & 1\\ 3 & -6 & 0 & 4\\ -3 & 2 & 3 & 1\\ 1 & 0 & 0 & 0\end{bmatrix}\begin{bmatrix}u^3\\ u^2\\ u\\ 1\end{bmatrix} \qquad (4)$$

$N_3(v)$ can be expressed similarly.

The measured surface and the normal template of the design surface are going through a rough matching based on the micro-structure features of the micro-lens array and then precise matching based on least squared criteria [12] to optimize matching results. The proposed method characterizes the pattern of microstructure surface as an integral part. This is different from the traditional characterization methods which usually evaluate the form error of microstructure freeform surface as a single structure surface.

3. IMPLEMENTATION AND PRELIMINARY EXPERIMENTAL WORK

In the present study, a prototype surface characterization system has been built based on the pattern matching analysis method. The prototype is developed using Matlab. A cutting experiment has been conducted to produce a microlens array using a 2-axis ultra-precision machine incorporated with Fast Tool Servo (FTS) technology (Nanoform 200 from Precitech in US). The machined surface was measured by a WYKO NT8000 3D surface profiler system. The measured are measured by the surface characterization system. The results are shown in FIGURE 4.

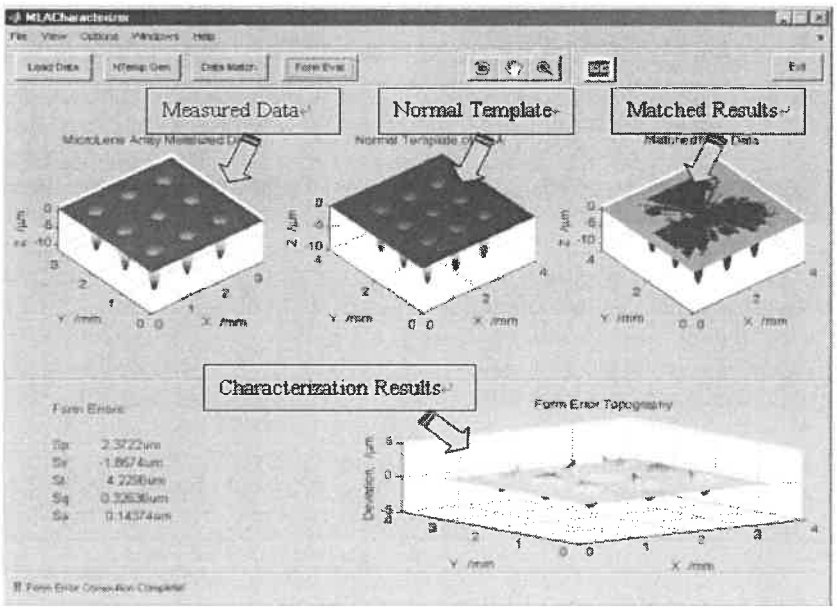

FIGURE 4. Results of the characterization of a FTS machined microlens array by the prototype surface characterization system developed based on the pattern matching analysis method.

4. CONCLUSION

Microstructure freeform surface is a type of freeform surfaces which is widely used in optical-mechanical-electronic components with increasing high precision requirement. Most of the previous research work has either been based on single surface characterization or the evaluation of the optical performance. Relatively little research has been conducted to study pattern of the micro-structure freeform surface array. This paper presents a new characterization method for microstructure surfaces based on a pattern matching analysis method. The method is composed of the data acquisition process, data processing, pattern matching and analysis, respectively. The method employs rough matching by microstructure features and then precise matching based on least squared criteria so as to optimize matching results. After matching the measured data to the computer-aided design (CAD) model, the deviation from the measured data to the design model is then calculated and subsequent form errors of the measured micro-structure freeform surface are obtained. This is different from the traditional characterization methods which usually evaluate the form error of microstructure freeform surface as a single structure surface. The proposed method characterizes the pattern of microstructure surface as an integral part. Preliminary experiment has been conducted on a micro-lens array workpiece fabricated by Fast Tool Servo (FTS) machining and the results indicate that the method is capable of improving the accuracy and the efficiency of the characterization of the microstructure freeform surfaces such as micro-lens array.

ACKNOWLEDGEMENT

The authors would like to express their sincere thanks to the Research Grants Council of the Government of the Hong Kong Special Administrative Region of the People's Republic of China for financial support of the research work under the project no. PolyU 5140/05E

REFERENCES

[1] Dan Daly, Microlens Arrays, Taylor&Francis Inc, 2001

[2] Minoru Kobayashi, Katsumasa Fujita, Tomoyuki Kaneko, Tetsuro Takamatsu, Osamu Nakamura, and Satoshi Kawata, Second-harmonic-generation microscope with a microlens array scanner, Optics Letters, 27(15), 1324-1326

[3] A. Saitoh and K. Tanaka, Self-developing aspherical chalcogenide-glass microlenses for semiconductor lasers, Applied Physics Letters, 83(9), 2003, 1725-1727

[4] Ph Nussbaum, R. Völkel, H.P. Herzig, M. Eisner and S. Haselbeck, Design, fabrication and testing of microlens arrays for sensors and Microsystems, Pure Appl. Opt. 6 ,1997, 617–636.

[5] Y. Liu, B. Robertson, G. C. Boisset, M. H. Ayliffe, R. Iyer, and D.V. Plant, Design, implementation, and characterization of a hybrid optical interconnect for a four-stage free-space optical backplane demonstrator, Applied Optics, 37(14), 1998, 2895-2914

[6] D. Lee and R. Haynes, Characterization of Lenslet Arrays for Astronomical Spectroscopy, PUBLICATIONS OF THE ASTRONOMICAL SOCIETY OF THE PACIFIC, 113: 1406-1419, 2001 November.

[7] H. Ottevaere, B. Volckaerts, J. Lamprecht, J. Schwider, A. Hermanne, I. Veretennicoff and H Thienpont, Two-dimensional plastic microlens arrays by deep lithography with protons: fabrication and characterization, J. Opt. A: Pure Appl. Opt. 4, 2002, S22–S28

[8] E. Gu, H. W. Choi, C. Liu, C. Griffin, J. M. Girkin, I. M. Watson, M. D. Dawson, G. McConnell and A. M. Gurney, Reflection/transmission confocal microscopy characterization of single-crystal diamond microlens arrays, Applied Physics Letters, 84(15), 2004, 2754-2756

[9] C.L. Lee, H.W. Choi, E. Gu, M.D. Dawson, H. Murphy, Fabrication and characterization of diamond micro-optics, Diamond & Related Materials, 15 (2006) 725-728

[10] C.T. Pan, TT. Wu, F.F. Chen, Y.C. Chang, C.J. Lee and J.C. Huang, Hot embossing of micro-lens array on bulk metallic glass, Sens. Actuators A: Phys. (2007), doi:10.1016/j.sna.2007.10.040

[11] Wei Gao, Makoto Tano, Shinji Sato, Satoshi Kiyono, On-machine measurement of a cylindrical surface with sinusoidal micro-structures by an optical slope sensor, Precision Engineering, 30 (2006), 274–279

[12] Cheung, C.F., Li, H.F., Lee, W.B., To, S. and Kong, L.B. " An Integrated Form Characterization Method for Measuring Ultra-precision Freeform Surfaces " , International Journal of Machine Tools and Manufacture, Vol.47, No. 1, p.81-91 (2007).

ANALYSIS OF SURFACE ACCURACY BY END MILLING

Naoto IKEDA[1], Yoshikazu KOBAYASHI[1], Kenji SHIRAI[1], and Kouichi TOZAWA[2]
[1]Department of Computer Science
College of Engineering, Nihon University
Tamura-machi, Koriyama, Japan, 963-8642
[2]Nissan Motor Co., Ltd.
Zama, Kanagawa, Japan, 228-8502

1. INTRODUCTION

Over the recent years, micrometer order accuracy is increasingly required in parts such as automobile and digital equipment. For this reason, research and development on improving machining accuracy is being actively carried out using end mill. [1] Although surface texture is often focused on, accuracy improvement by end milling is important for realizing visual value added and function improvement. Setup errors can be reduced by continuously machining on one machine without performing datum level grinding, resulting in high-precision surface texture. In this study, evaluations were carried out for achieving high precision grinding of work material at the datum level. First, level difference and roughness were measured and evaluated in the machining of the work material at the datum level. Next, level difference patterns were determined by acquiring the cutting load from the main spindle, and measuring machining level difference at the datum level of the work material. From these results, the correlation between cutting load and machining level difference was clarified.

2. OUTLINE OF SYSTEM

Figure 1 shows the basic configuration of the system. This system consists of a micro-machining unit and a computer which controls it. It has three axes, X, Y, Z, and the rotational speed of the main spindle is controlled by the main spindle controller. [2] The PC (Personal Computer) used for control has programs for cutting load monitoring and machining. The load voltage of the main spindle is acquired from the machine spindle controller by the cutting load monitoring program via the A/D (Analog/Digital) converter. This load voltage is taken to be the cutting load. The program for machining inputs the various machining conditions based on preset operation data, and sends control signals to the motor controller via the GP-IB (General Purpose Interface Bus).

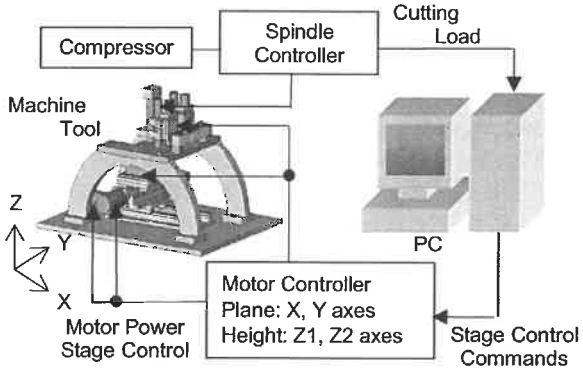

FIGURE 1. SYSTEM CONFIGURATION

3. CUTTING CONDITIONS

Figure 2 shows the work material shape used in this study, and Table 1 shows the cutting conditions.

The workpiece measured 18 mm x 18 mm and was made of carbon steel S50C. It was cut in a straight line in the cutting experiments. The spindle speed was 30000min^{-1}, the feed rate was 30mm/min, and cutting depth was 5 μm. The tool used was a square end mill with a diameter of 0.9mm, tool length of 38mm, and teeth number of 2. Experiments were conducted varying the L/D (tool protrusion length/tool diameter) at 22.5, 13.5, and 5.04. The cutting fluid used was MSMTP420 (MISUMI Corporation) which is effective for difficult machining.

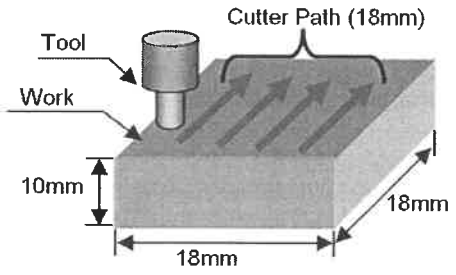

FIGURE 2. WORK PIECE

4. MEASURING AND EVALUATION METHODS

Figures 3 show the measuring method and evaluation method. The machining level difference measured using a scanning white light interferometer was a distance of 3mm from A to B shown in Figure 3, and surface roughness of 7 μm from C to D. The machining level difference was measured at five places, to obtain the difference between the maximum and minimum values of the machined cross section for the scanned area A to B shown at the bottom of Figure 3. These maximum, minimum and mean values were adopted. [3] The measured width of one level difference was made to correspond to a cutting pitch at 630 μm. The surface roughness was scanned from feed direction C to D, and evaluated using the arithmetic mean roughness Ra. [3]

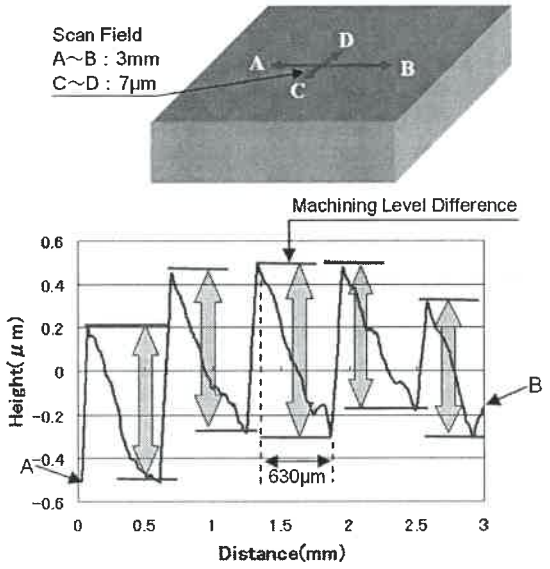

FIGURE 3. MEASUIRING AND EVALUATION METHODS

5. ANALYSIS OF MACHINING LEVEL DIFFERENCE

Figure 4 shows the machining level difference at the L/D value of 25 and indicates that the level difference changes to a saw shape. This is due to the tilting of the tool caused by cutting resistance. Figure 5 shows the machining level difference at each L/D value. The tendency in which the machining level difference decreases with decreasing L/D value can be seen. This indicates that the grinding undercut of the tool is small compared to the machined surface. Consequently, in the case of flat machining, the L/D value should be made smaller to achieve smaller machining level difference.

TABLE 1. CUTTING CONDITIONS

Work	Carbon Steel(S50C)
Cutting Size	18×18[mm]
Spindle Speed	30000[min^{-1}]
Feed Rate	30[mm/min]
Cutting Depth	5[μm]
Cutting Pitch	0.63[mm]
Tool	Square End Mill
Tool Diameter	φ 0.9[mm]
Tool Length	38mm
Teeth Number	2
Tool Protrusion Length	22.5, 13.5, 5.04[mm]

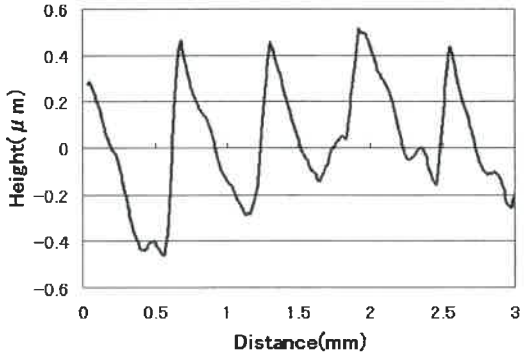

FIGURE 4. MACHINING LEVEL DIFFERENCE AT L/D VALUE OF 25

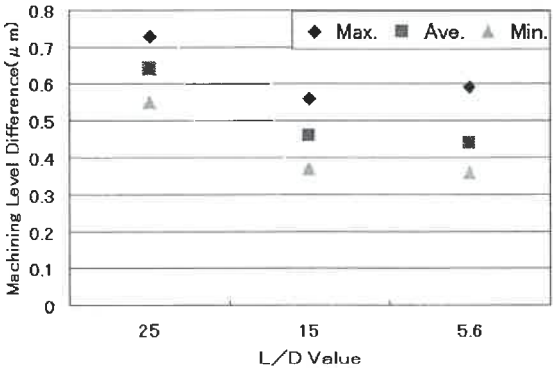

	L/D:25	L/D:15	L/D:5.6
Max.	0.73μm	0.56μm	0.59μm
Ave.	0.64μm	0.46μm	0.44μm
Min.	0.55μm	0.37μm	0.36μm

FIGURE 5. MACHINIING LEVEL DIFFERENCE AT EACH L/D VALUE

6. ANALYSIS OF A MACHINED SURFACE

6.1 ANALYSIS OF A CUTTER MARK

Surface roughness was analyzed from C to D shown at the top of Figure 3, which is the feed direction of the machined surface. First, the width of the cutter mark was calculated from the cutting condition. The width of the cutter mark is the feed per revolution per edge, and it can be calculated from the spindle speed, feed rate, and teeth number. In this example, it is 0.5 μm per edge, so the width of the cutter mark is 0.5 μm. The machined surface was analyzed based on this value.

Figure 6 shows the condition of the machined surface at the L/D value of 25. The cutter mark is seen to be greatly projected from the photograph of Figure 6. Looking at the graph in Figure 6, a cutter mark of about 4 μm can be seen projected, and this is eight times larger than that calculated. The protrusion of the tool is long due to the rotation of the tool.

Figure 7 shows the condition of the machined surface at the L/D value of 5.6. The cutter mark appears small as shown in Figure 7. Looking at this in the graph, a cutter mark of about 1 μm is being projected, which is twice larger than the calculated value. Compared to the L/D value of 25, this value is closer to the calculated value due to the small rotation of the tool.

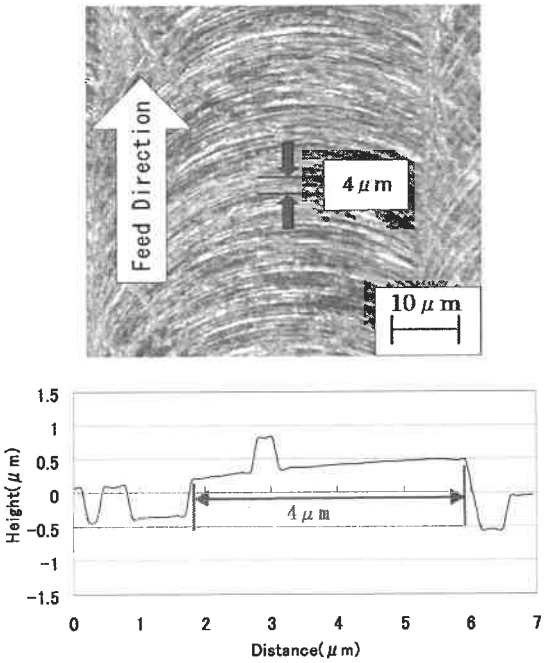

FIGURE 6. CONDITION OF MACHINED SURFACE AT L/D VALUE OF 25

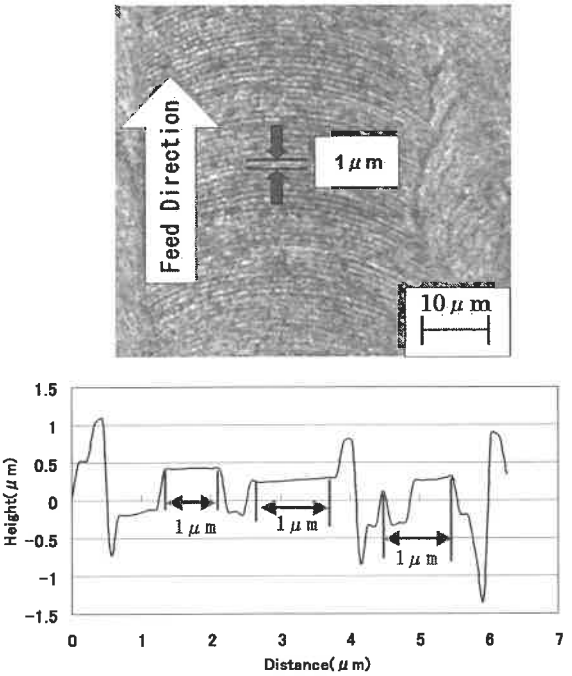

FIGURE 7. CONDITION OF MACHINED SURFACE AT L/D VALUE OF 5.6

6.2 ANALYSIS OF SURFACE ROUGHNESS

Surface roughness was also analyzed in the feed direction of the machined surface. Figure 8 shows the graph of the surface roughness at each L/D value. Surface roughness decreases with decreasing L/D value. Analysis of the machined surface roughness indicates that when the rotation of the tool is large (e.g.: L/D value of 25), the cutter mark increases, and the surface roughness increases in proportion to this. On the other hand, the surface roughness decreases when the rotation of the tool is small (e.g.: L/D value of 5.6 due to the small cutter mark.

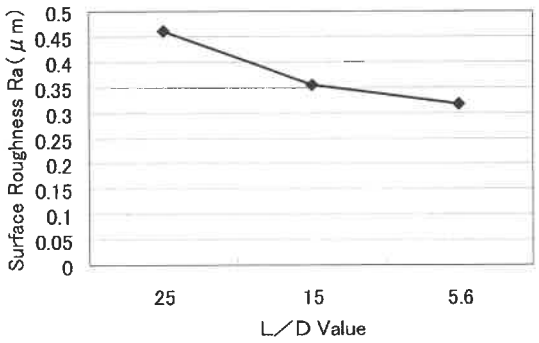

FIGURE 8. SURFACE ROUGHNESS ACCORDING TO CHANGES IN L/D VALUE

7. GRADIENT OF MACHINED SURFACE

The authors have been conducting fluctuation measurements of the machining load using a small diameter end mill tool at this laboratory, but in this study, the machining load is acquired by measuring the fluctuation of the voltage value from the spindle. Applying this, the correlation between the machining load and level difference patterns was analyzed.

Cutting load was acquired by using the cutting conditions shown in Table 1, but the parameters shown in Table 2 were varied. First, the machining level difference a-b and feed per revolution c at the datum level of the work material were calculated (Figure 9). Next, $\theta=\tan^{-1}((a-b)/c)$ is obtained. This was done by extracting part of the machined cross-section as shown in Figure 9, and then combining the cutting load with the calculated θ. As a result, as shown in Figure 10, the gradient of the machined surface increased as the cutting load increases. However, the cutting load is found to decrease at one place, and the causes shall be studied in the future.

8. CONCLUSIONS

Roughness and machining level difference were measured for evaluations to achieve high precision machining of the datum level of work material. The following conclusions were obtained by acquiring the cutting load from the main spindle, and measuring the machining level difference of the datum level of the work material to determine level difference patterns.

(1) Based on the size of the L/D value, the machining level difference varied between 0.63 μm (maximum), 0.43 μm (minimum), and average 0.51 μm.

(2) Due to rotation of the tool, difference in the cutter mark was seen, the greatest being by eight times.

(3) The cutting load and gradient of the machined surface were proportional, and it was found that the gradient increased as the cutting load increased.

9. FUTURE TASKS

In future studies, further improvement in the precision of datum level machining and correction of the machined surface gradient will be aimed at. However, because the current machine tool has three axes, it is mechanically difficult to correct machined surface gradient. Correction will therefore be attempted by using a 5-axis machine tool and tilting the table.

TABLE 2. CHANGED PARAMETERS

Cutting Pitch	0.36, 0.45, 0.54, 0.63, 0.72[mm]
Tool Protrusion Length	5.04[mm]

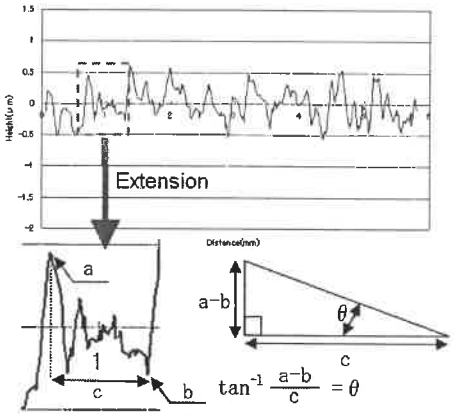

FIGURE 9. CALCULATION METHOD OF MACHINED SURFACE GRADIENT

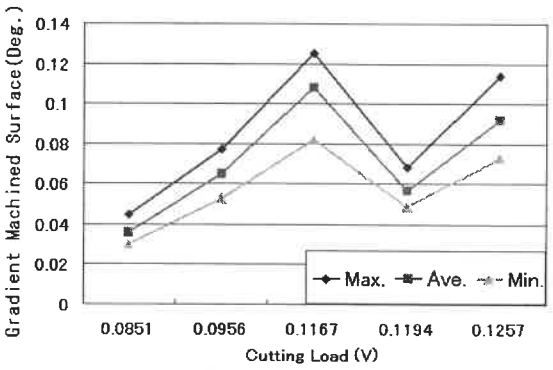

FIGURE 10. GRADIENT OF MACHINED SURFACE

REFERENCES

[1] N.Ikeda, Y.Kobayashi, K.Shirai, K.Tozawa: Study on Flatness Evaluation of Surface Texture by End Mill Machining, JSPE 2008 Spring Annual Meeting, Kanagawa, Japan, March, 2008

[2] Y.Kobayashi, K.Shirai, M.Sato, K. Tozawa: Development of Surface Texturing System by Mechanical Machining, ASPE 2004 Annual Meeting, Orland, Florida, USA, October, 2004

[3] N.Ikeda, Y.Kobayashi, K.Shirai, K.Tozawa: Research on Accuracy Evaluation of Flat Milling by Square End Mill Tool, Proceedings of 2008 CONFERENCE on DIE and MOULD TECHNOLOGY, Tokyo, Japan, June, 2008

MODELLING OF CYLINDER SURFACE TOPOGRAPHY

Pawel Pawlus[1], and Rafal Reizer[2]
[1]Department of Manufacturing Processes and Production Organisation
Rzeszow University of Technology,
Rzeszow, Poland
[2]Institute of Technology
University of Rzeszow
Rzeszow, Poland

INTRODUCTION

Most engineering surfaces have height distributions similar to Gaussian. Multi-process texture is more important from functional point of view. Plateau honed cylinder surface is the typical example. It consists of smooth wear-resistant and load-bearing plateaux with intersecting deep valleys working as oil reservoirs and debris trap. The tribological behaviour of engineering surfaces, such as hydrodynamic and elastohydrodynamic lubrication, wear or contact problems can be predicted numerically. The solution of these problems involves input of surface data, which can be obtained either from digital input from profilometer or from numerical simulation of the rough surfaces. Randomly generating surface roughness by numerical means is simpler and offers some advantages. The hardware and software requirements can be eliminated. Furthermore, the simulation of surface forming during manufacturing and operating processes ensures decrease of cost and time of experimental investigation. Today reference software and reference data are needed in order to check accuracy of the algorithms and output parameters from the software.

The time series model of rough surface [1, 2, 3, 4] was applied to surface topograhy numerical generation.
Fast Fourier Transform is also popular in generating surfaces [5, 6, 7]. In majority of presented above papers the surfaces of Gaussian normal ordinate distribution were generated. Usually non-Gaussian random surfaces with the desired skewness and kurtosis were obtained by transforming the surface of normal ordinate distribution using the Johnson translatory system [8, 9]. This profile is characterised by variance, correlation length, skewness and kurtosis. The other possibility is creation of two Gaussian profiles PP (plateau) and PV (valley) with correlation lengths and variances as parameters characterizing them. Then the points of smaller ordinates were selected [10]. The special procedure was done in order to obtain required values of parameters.

In this paper three methods of simulation of multi-process profile were compared and the best of them recommended. The extension of the finest method was used in order to model 3D surface topography. The examples of using this method for the simulation of plateau-honed cylinder surface topography are given.

CALCULATION PROCEDURES

The methods proposed in References [6, 9] based on FFT approach are set preserve the skweness, kurtosis together with auto-correlation function or spectral density of surfaces.
A digital filter was employed by Hu and Tonder [6] to generate an output sequence of known auto-correlation function by a linear transformation system. For generation of profiles of non-Gaussian ordinate distribution, the gaussain input sequence was transformed to an input sequence with appropriate skewness and kurtosis by using Johnson translatory system of distribution [11].
The amplitude part was constructed by Wu [9] from given spectral density or auto-correlation function. The phase part was obtained by using Johnson translator system. By iteration and adjusting the input skewness and kurtosis, the required non-Gaussian surfaces can be generated.
The parameters describing surface after 2 processes can be calculated from the probability plot of material ratio curve. The slopes of each straight lines (Pqp and Pvq) give the Pq roughness of the corresponding process. The intersection point on normal probability graph of

abscissa Pmq defines the separation of plateau and base textures. The proposed plateau roughness Rpq, valley roughness Rvq and Rmq are three parameters characterising plateau honed surface (ISO 13565-3 standard). Also the transition characteristic (plateau depth Pd) from one to another process can be estimated. There is a connection between Ppq, Pvq, Pmq and Pd:

$$Pd = Pmq\ (Ppq-Pvq) \qquad (1)$$

The following procedure ought to be done in order to simulate two-process profile:
1. Creation two Gaussian profiles PP (plateau) and PV (valley) with correlation lengths and variances as parameters characterizing them.
2. The choice of the distance (Pd) between the mean lines of the profiles (the centre of the distributions).
3. For all the points "i" of two distributions (profiles): If PP(i) > PV(i) then RP(i) (resulting profile after two processes) = PV(i), else RP(i) = PP(i).

We used FFT to generate Gaussian profiles according do Reference [7]. Each profile was completely characterised by two parameters: the standard deviation height parameter (Pqp, Pqv) and horizontal parameter derived from the autocorrelation function of exponential shape (correlation length CL – the distance, at which auto-correlation function slowly decays to 0.1 value).
The special procedure was developed in order to obtain prescribed values of skewness Psk and correlation length CL of the modelled profile (in addition to Pqp, Pqv and Pmq parameters). So, Pq, CL, Pqp, Pqv and Pmq (Pd) were input parameters of the model.
Firstly the group of profiles of given values of given standard height deviation as well as different correlation length were generated. Then, profiles of standard deviation Pqp and Pqv were superimposed using described procedure. In next step, correlation length of the resulting profile was calculated, if difference between CL of modelled and measured profile was smaller than δCL next step was done. If not, the other pair of profiles was superimposed until the profile with prescribed correlation length was obtained. In next step, skewness of resulting profile was calculated. When the difference between Psk parameters of modelled and measured profiles was smaller than limiting value δPsk the calculation was finished. In other cases, two new profiles of Gaussian ordinate distribution were superimposed.
As the result of initial investigations the limiting values (tolerance) of skewness and correlation length were set (δCL = 1μm, δPsk = 0.5).

THE RESULTS OF 2D PROFILE ANALYSIS

About 20 plateau honed cylinder surafces were analysed. Hu and Tonder method was called M1, Wu method – M2, but method of profile imposition – IM.
The unfiltered levelled profile parameters were compared. Digital filtration was not used. Asssessment length was 4 mm. Profile measurement gauge without skid was applied.
The average absolute relative errors of Pa parameter computation were 34.78% after using M1 method, 15.95% M2 and 4.35% IM. The errors of Pq parameter computation were smaller and amounted to, respectively: 11.05%, 10.05% and 3.21%. The small parameter distortion after using IM method is interesting, because in this case Pq was not input parameter. The biggest errors of Pt parameter computation were obtained after using M2 method (55%), they were smaller after M1 (38.43%) and IM method application (6.7%). Generally the errors of statistical parameters computation were smaller than those of maximum amplitude parameters. The application of IM metod caused the smallest errors.
Parameters included in ISO 13565-2 standard were analysed. When M1 method was applied, average errors of Pk parameter were 64.33%, Ppk 24.53%, Pvk 25.89%, Pmr1 38.69% and Pmr2 7.28%. After M2 method application these errors were: for Pk 139%, Ppk 257.53% Pvk 29.37%, Pmr1 57.16% and Pmr2 13.6%, but after IM method usage: for Pk 10.17%, Ppk 8.77% Pvk 24.36%, Pmr1 22.41% and Pmr2 8.05%. The distortions of Rk family parameters were the biggest after using M2 method and the smallest IM procedure.
Parameters included in ISO 13565-3 standard were input parameters for IM modelling method. Therefore their average errors were smaller than 5% (maximum deviations were smaller than 10%). When M1 method was used, the average errors of parameters were: for Ppq 59%, Pvq 138.12% and Pmq 24.1%. After M2 method application, the errors were greater and amounted respectively: for Ppq 196.33%, Pvq 248.65% and Pmq 31.15%. Values of Ppq and Pvq parameters of modelled profiles were larger than those of measured profiles when M1 and M2 methods were applied.

The mean errors of PSm parameter computation after using M1, M2 and IM methods amounted respectively to: 25.1%, 33% and 15.7%. Application of M2 method caused the biggest errors, however then deviations of correlation length computation were the greatest after using M1 method. When M1 and M2 methods were applied, the PSm parameters of modelled profiles were smaller than those of measured profiles.

Rms. slopes of modelled profiles were bigger than of measured profiles. The errors amounted to: 62.22% after using M1 method, 101% - M2 and 10.03% - IM.

The average absolute errors of Psk parameter computation were 38% after using M1 method, 17.95% M2 and 5.4% IM. The errors of obtaining Pku parameter are, respectively 103.82%, 89% and 15.1%. The small errors obtained after using IM method deserves attention because Pku parameter was not input parameter in this model.

Generally IM methods was superior to M1 and M2 methods with regard to simulate plateau-honed cylinder profiles.

Figure 1 presents example of measured and modelled profile. The parameter values are also given.

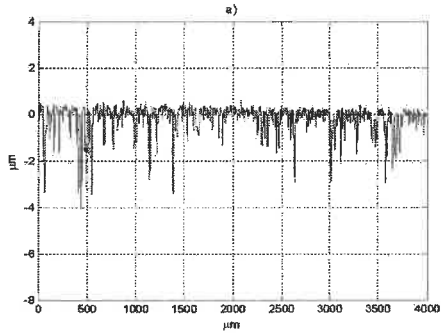

Pq = 0.656 μm, PSm = 0.018 mm, PΔq = 7.65°, Psk = -3.48, Pku = 16.94, Ppq = 0.18 μm, Pvq = 1.78 μm, Pmq = 79%

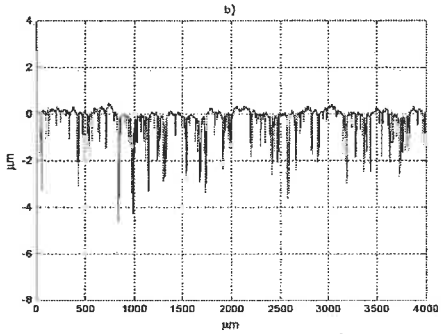

Pq = 0.69 μm, PSm = 0.02 mm, PΔq = 6.98°, Psk = -3.28, Pku = 14.27, Ppq = 0.172 μm, Pvq = 1.773 μm, Pmq = 77.6%

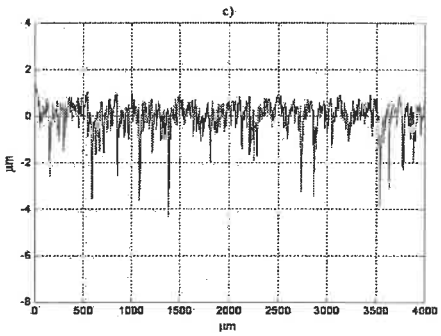

Pq = 0.677 μm, PSm = 0.02 mm, PΔq = 9.18°, Psk = -2.98, Pku = 11.47, Ppq = 0.32 μm, Pvq = 1.4 μm, Pmq = 80.2%

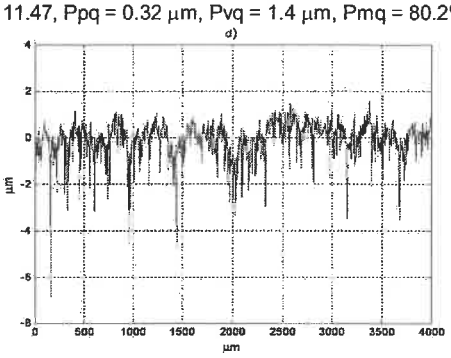

Pq = 0.74 μm, PSm = 0.019 mm, PΔq = 11.01°, Psk = -3.1, Pku = 13.42, Ppq = 0.45 μm, Pvq = 1.85 μm, Pmq = 85.4%

FIGURE 1. a) measured profile, b) profile modelled by IM method, c) profile modelled by M1 method, d) profile modelled by M2 method

THE RESULTS OF 3D SURFACE TOPOGRAPHY ANALYSIS

IM method was extended into 3 dimensions. The special procedure was used in order to obtain the honing angle and parametrs decsribing plateau honed cylinder surface topography.

Firstly, the oriented two-directional structures characterised by Sq parameter equalled to Sqv of plateau-honed surface were formed. Then 2 structures rotated by ϕ angle and 180 - ϕ angle were superimposed. Similar procedure was done for surface topography of Sq parameter equal to Sqp of resulting surface. Then the obtained valley and plateau surfaces were superimposed similarly to profiles. This procedure was repeated for various correlation lengths of two-dimensional structures (before rotation) and surafce the most similar to measured surafce was selected.

Average error of Sq parameter was 6.9%, Sa 1.5%, St 19.2%, Sz 14.45%, Sp 14.83% and Sv 25.4%. It was confirmed that the deeviations of parameters describimg maximum heigh were greater than those characterising average height. Errors of Spq determination was on

average 2.5%, Svq 5.7%, Smq 2.5%, Sk 8.65%, Svk 12%, Spk 11.2%, Sr1 15%, Sr2 8%. The mean errors od Ssk and Sku parameters determination were larger and amounted to 20.1% and 25.1%, respectively. The average errors of spatial parameters were: for Sds 25.2%, Sal 21.1%, Str 19.2%. Average deviation of SΔq parameter determination was small (4%) but of Ssc larger (13.6%).

Figure 2 presents isotropic views of measured and modelled surface. Selected parameters values are also given.

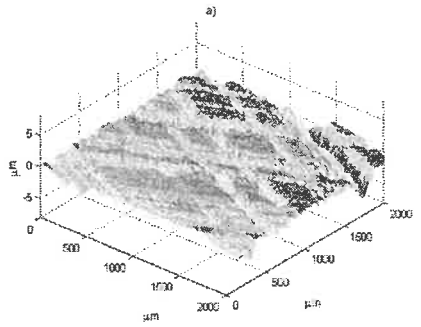

Sq = 0.713 μm, Sz=4.75 μm, SΔq = 0.089, Spq = 0.307μm, Svq = 1.148 μm, Smq = 69.4%, Str = 0.066, Std = 26.5°

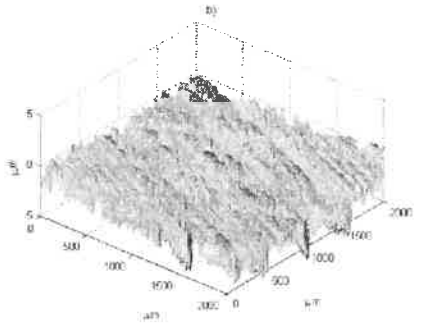

Sq = 0.721 μm, Sz = 4.02 μm, SΔq = 0.089, Spq = 0.304 μm, Svq = 1.348 μm, Smq = 64.3%, Str = 0.08, Std = 26.4°

FIGURE 2. a) measured surface topography, b) modelled surface topography of plateau honed cylinder

CONCLUSIONS

Two-process surface can be modelled by imposition of random plateau Gaussian structure on base (valley) structure. This method is better than other methods of non-Gaussian surfaces modelling presented in literature. It is possible to obtain parameters of modelled profile similar to those of measured profile using iterative procedure. The height, horizontal as well as parameters describing the shape of the profile ordinate distribution can be well modelled. This procedure can be extented into 3 dimensions after modification. It was found that simulation method can be properly used for plateau honed cylinder surface.

REFERENCES

[1] Watson W, King T G, Spedding T A, Stout K J. The machined surface – time series modelling. Wear. 1979; 57: 195-205.

[2] Whitehouse D J. The generation of two dimensional random surfaces having a specified function. CIRP Annals. 1983; 32/1: 495-498.

[3] Gu X, Huang Y. The modelling and simulation of rough surface. Wear. 1990; 137: 275-285.

[4] Uichidate M, Shimizu T, Iwabuchi A, Yanagi K. Generation of reference data of 3-D surface texture using the non-casual 2-D AR model. 9th International Conference on Metrology and Properties of Engineering Surfaces. Halmstad, Sweden. 2004; 67-76.

[5] Newland D E. An introduction to random vibration and spectral analysis. 2nd edition, Longman. London: 1984.

[6] Hu Y Z, Tonder K. Simulation of 3-D random surface by 2-D digital filter and Fourier analysis. Int. J. of Mach. Tools Manufact. 1992; 32: 82-90.

[7] Wu J -J. Simulation of rough surfaces with FFT. Tribology International. 2000; 33: 47-58.

[8] Watson W, Spedding T A. The time series modelling of non-gaussian engineering processes. Wear. 1982; 83: 215-231.

[9] Wu J -J. Simulation of non-Gaussian surfaces with FFT. Tribology International. 2004; 37: 339 –346.

[10] Pawlus P. Simulation of stratified surface topographies. Wear. 2008; 264: 457-463.

[11] Hill I D, Hill R, Holder R L. Fitting Johnson curves by moments. Applied Statistics. 1976; 25: 149-176.

OPTIMIZING A GAUSSIAN FILTER LONG WAVELENGTH CUTOFF FOR IMPROVING 3D BALLISTICS SIGNATURE CORRELATIONS

John Song, Li Ma*, Theodore Vorburger, and Susan Ballou
National Institute of Standards and Technology (NIST)
Gaithersburg, MD 20899
***Guest Researcher, Kent State University, Kent, OH 44242**

1. TOPOGRAPHY MEASUREMENTS FOR BALLISTICS IDENTIFICATION

When bullets and casings are fired or ejected from a gun, both the macro- and the micro-topographies on the gun parts leave striation or impression marks on the fired bullets or the ejected casings, and thus form the characteristic features on their surface. The macro-topography features include the number, shape, size, direction and twist angle of the rifling ridges in the gun barrel. These features shape the striation topography of the fired bullets. The macro-topography also includes the size and form of the firing pin, breech face and ejector which impact with the casing during firing, and form the impression topography on the ejected casings. Macro-topography features therefore represent the common characteristics of a group of guns manufactured from the same design, manufacturer and tooling process. When the macro-topography features leave striation or impression marks on the surface of the bullets or casings, their common characteristics form the "Class Characteristics" on the bullets or casings [1]. The "Class Characteristics" are similar between bullets or between casings fired from guns manufactured from the same production line. In forensic science, "Class Characteristics" are used for the identification of the type and manufacturer of a weapon [1].

On the other hand, the micro-topography or surface roughness [2] of the gun parts represents, in addition to stochastic differences, unique characteristics of the gun. The micro-topographies can be unique for different guns even manufactured from the same production line one after another. When the micro-topographies of the gun parts leave striation or impression marks on the surface of the bullets or casings, its unique characteristics can cause "Individual Characteristics" on the bullets and casings. In forensic science, "Individual Characteristics" are used for the identification of an individual firearm and to link the fired bullets or ejected casings to a suspect firearm [1].

2. EXTRACTING "INDIVIDUAL CHARACTERISTICS" FROM "CLASS CHARACTERISTICS" USING GAUSSIAN FILTERS

Surface topography includes a wide range of spatial wavelength components, from the form deviation features, which are comparable to the size of the part, through surface waviness to surface roughness in the extreme short wavelength domain [2]. However, for many topographic measurements and correlations to establish individual characteristics of bullets and casings, the surface roughness carries the most interest. A "clear" extraction of the surface roughness from waviness and form deviation therefore plays a key role in topography measurements and correlations. High-pass Gaussian filter characterized by the long wavelength cutoff λc can be used for this purpose [2]. Therefore, optimal selection of λc has particular importance for an unambiguous extraction of "Individual Characteristics" from the "Class Characteristics". A poorly chosen λc might result in the "Class Characteristics" being inappropriately included in the "Individual Characteristics", resulting in a sub-optimum correlation.

The NIST Standard Reference Materials (SRMs) 2460 Standard Bullets and 2461 Standard Casings are developed for establishing ballistics measurement traceability and quality assurance in the United States [3]. The NIST 2D and 3D Topography Measurement System is developed for topography measurements of the SRM bullets and casings [3, 4]. This system can be generally used for 2D and 3D topographic measurements and comparisons in other areas [5]. For the measurements of the SRM bullets and casings, a standard long wavelength cutoff λc = 0.25 mm [2] is used and has shown good correlation results [3 - 5]. However, when using this system for ballistics correlation of real bullets and casings, it is found that the 0.25 mm standard long wavelength cutoff may not be optimum [6]. It is necessary to develop an

approach to optimizing the Gaussian filter long wavelength cutoff λc for improving the ballistics signature correlations, particularly for the firing pin topographies whose curvature form must be filtered out before the signature correlations.

3. AN APPROACH TO OPTIMIZING GAUSSIAN FILTER LONG WAVELENGTH CUTOFF λc

A set of designed experiments using two groups of fired casings is presented for optimizing the Gaussian filter long wavelength cutoff λc for firing pin signature correlations. Group 1 includes 20 pairs of matched casings, i.e., both fired from the same guns; the Group 2 includes 20 pairs of casings all fired from different guns. These casings were selected from our previous study for the feasibility assessment of a National Ballistics Imaging Database [7], in which 70 casings were chosen from a collection of test fires by De Kinder et al. [8] and 108 casings were fired at NIST. The two groups of 40 pairs of casings were randomly selected from the De Kinder test fires in which ten 9 mm pistols were used, each fired seven casings. These casings were previously imaged by an optical confocal microscope [7]. The 3D topography images are used in this study for correlation tests using a Gaussian regression filter [9] with a long wavelength cutoff λc ranging from 0.15 mm to 0.65 mm. No short wavelength cutoff λs [2] is used. The correlation level is quantified by the value of the cross-correlation function maximum, CCF_{max}, which is defined as the value of the cross-correlation function (CCF) when these two correlated topographies are registered at their maximum correlation position [3 - 5]. At this position, a parameter called the topography difference, D_s, may also be calculated. The D_s value is given by the rms roughness Sq [2] of the topography difference of the two correlated topographies. When $D_s = 0$, the two correlated topographies must be exactly the same (point by point). Detailed information can be found in Ref. [3 - 5].

Figure 1a shows the average CCF_{max} values for two groups of casings, CCF_{max1} and CCF_{max2} as a function of different long wavelength cutoff values λc. The error bars represent the standard deviation of the mean. It can be seen that for both groups of casings, the average CCF_{max} values increase with the increase of λc, because more curvature form components on the firing pin surface are included for topography correlations. Their common "Class Characteristics" features (curvature form) increase the correlation value CCF_{max}. Furthermore, the Group 1 casings fired from the same guns show higher correlation value (CCF_{max1}) than that of the Group 2 casings fired from different guns (CCF_{max2}), because the similar "Individual Characteristics" of the casings fired from the same guns contribute to the higher CCF_{max} values in Group 1.

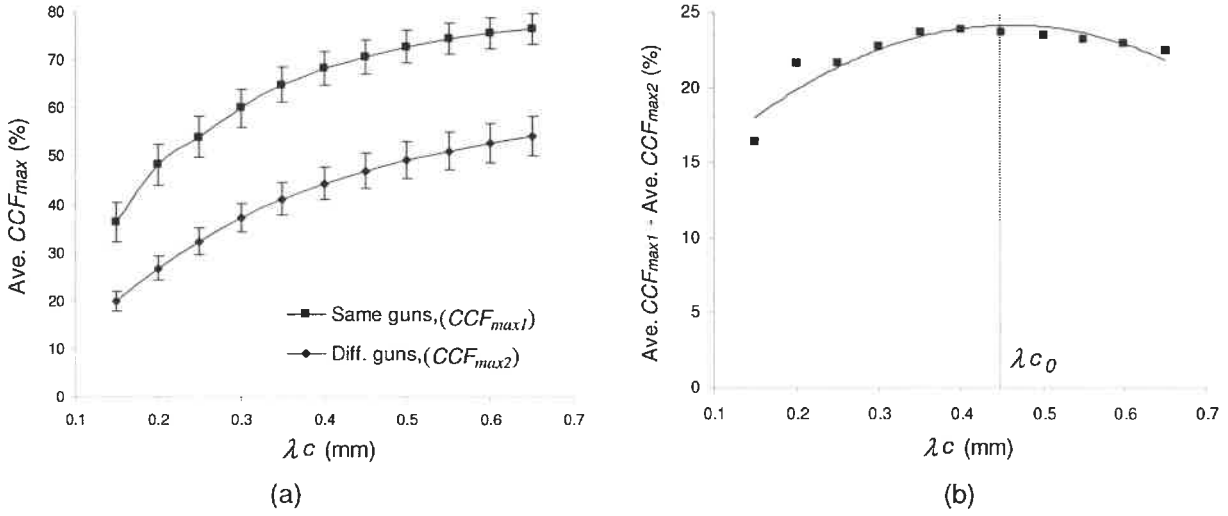

Fig. 1. a) The average correlation values of 20 pair of casings fired from the same guns, CCF_{max1}, and 20 pairs of casings fired from different guns, CCF_{max2}, as a function of the Gaussian regression filter long wavelength cutoff λc. The error bars represent the standard deviation of the mean. b) The maximum difference of the correlation values, $CCF_{max(1-2)} = (CCF_{max1}) - (CCF_{max2})$ occurs at $\lambda c_0 \approx 0.45$ mm.

Figure 1b shows the difference of the average CCF_{max} values between the two groups of casings $CCF_{max(1-2)} = CCF_{max1} - CCF_{max2}$ as a function of different long wavelength cutoffs λc. It can be seen that the maximum difference occurs at $\lambda c_0 \approx 0.45$ mm. It is therefore suggested that $\lambda c_0 \approx 0.45$ mm be considered as the optimal long wavelength cutoff for distinguishing the "individual characteristics" from the "class characteristics" for topography correlations of the firing pin signatures.

4. CORRELATION TEST RESULTS

The set of 70 De Kinder casings is used for a correlation test. These casings were imaged in our previous study [7] using an optical confocal microscope. Image problems including center-shifting, outliers and dropouts are found on some images, which may affect the accuracy of the topography correlation tests. As a result, ten casing images with these problems are removed from the correlation test. The remaining 60 casing images are correlated using the Gaussian regression filter with a long wavelength cutoff $\lambda c_0 = 0.45$ mm, and compared with the correlation results using the IAI (Intelligent Automation Inc.) filter in our previous study [7]. The IAI filter represents essentially a moving average series with a finite number of terms tapered by a Gaussian weighting function. The effective cutoff is limited either by the number of terms in the series or the sharpness of the taper. The net effect is that the short wavelength cutoff is about 4 μm and the long wavelength cutoff is about 40 μm for the firing pin impression data [7].

A summary for the top ten correlation results are shown in Table 1. This is a list of the ten other entries in the database that have the highest correlation scores with respect to a reference entry [7]. Among the 60 test casings, most have six matched casings fired from the same pistol. However, some casings have less than six matched casings because ten casings had been removed from the tests. As a result, there are only a total of 314, instead of 360, marching pairs for the 60 casings. The actual matching pairs and matching rate for the IAI filter are 208 pairs or 66.2 % in matching rate, i.e., 66.2 % of the 314 matching pairs appear in the top ten list. It increases to 76.8 % when using the optimal long wavelength cutoff $\lambda c_0 = 0.45$ mm. This rate can be improved further by adding in other criteria for topography matches notably, the rms roughness Sq and the topography difference parameter D_s. First the Sq value of the filtered topography is used as a second discrimination parameter. If the ratio of the Sq of the two correlated topographies is higher than 3 or lower than 1/3, the casings are considered as a non-match and are removed from the top ten list. With this added criterion, the fraction of matching casings appearing in the top ten list is increased to 79.9 %. This fraction can be further improved by considering the topography difference D_s [3 - 5]. If $D_s \geq 300$ % is considered as a non-match, the correlation rate is increased to 80.6 % (see Table 1).

Table 1. Top ten list results for the IAI filter and the optimized Gaussian filter cutoff $\lambda c_0 = 0.45$ mm.

	IAI Filter	Optimized Gaussian Filter ($\lambda c_0 = 0.45$ mm)		
			$1 < \lvert SqA/SqB \rvert < 3$ $1/3 < \lvert SqA/SqB \rvert < 1$	$D_s < 300$ %
Casing No. Ideal Match Pairs	60 314			
Correct Match Pairs	208	240	250	252
Ave. Match (max. = 6)	3.5	4.00	4.17	4.20
Match (%)	66.2	76.8	79.9	80.6

5. SUMMARY AND FUTURE WORK

The Gaussian filter long wavelength cutoff λc plays an important role in distinguishing the "Individual Characteristics" of firing pin signatures in ballistics identifications. The optimized Gaussian filter long wavelength cutoff can be determined from the maximum difference of the average CCF_{max} values between casings fired from the same guns and those from the different guns. In our study, the matching rate increases by about 10 % by using the optimized cutoff of $\lambda c_0 = 0.45$ mm comparing with the use

of the previous IAI filter. More work can be done to study the effect of the Gaussian filter short wavelength cutoff λc, and the effects of different makes of guns and ammunition on the accuracy of ballistics correlations.

ACKNOWLEDGEMENTS

The funding for this research was provided by the National Institute of Justice (NIJ) through the Office of Law Enforcement Standards (OLES) at NIST. The authors are grateful to T.B. Renegar, A. Zheng, E. Whitenton and D. Kelley of NIST, and to M. Ols of the Bureau of Alcohol, Tobacco, Firearms and Explosives (ATF) for their contributions in the development the NIST SRM 2460/2461 Standard Bullets and Casings, and to B. Bochbach of Intelligent Automation Inc. (IAI) for cooperation in the NIST project of Feasibility Assessment of a National Ballistics Imaging Database.

REFERENCES

[1] Moenssens, A.A., Starrs, J.E., Henderson, C.E. and Inbau, F.E. *Scientific Evidence in Civil and Criminal Cases*, Foundation Press, NY, 1995, pp327-336.

[2] ASME B46.1-2002, *Surface Texture (Surface Roughness Waviness and Lay),* ASME, New York, 2003.

[3] Song, J., Whitenton, E., Kelley, D., Clary, R., Ma, L. and Ballou, S., "SRM 2460/2461 standard bullets and casings project," *J. Res. Natl. Inst. Stand. Technol.* **109**, 6, November 2004, pp533-542.

[4] Ma, L., Song, J., Whitenton, E., Zheng, A. and Vorburger, T., "NIST bullet signature measurement system for SRM (standard reference material) 2460 standard bullets," *Journal of Forensic Sciences,* **49**, 4, 2004, pp649-659.

[5] Song, J. and Vorburger, T., "Topography measurement and applications" in the *Proceedings of the 2006 International Symposium on Precision Mechanical Measurements (ISPMM)*, August 2006, Urumqi, China.

[6] Song, J., Ma, L. and Vorburger, T., "The effect of Gaussian filter long wavelength cutoff λc in topography comparisons and measurements," in the *Proceedings of 2006 ASPE*, October 2006, Monterey, CA.

[7] Vorburger, T., Yen, J., Bachrach, B., Renegar, T., Filliben, J., Ma, L., Rhee, H., Zheng, A., Song, J., Riley, M., Foreman, C. and Ballou, S., "Surface Topography Analysis for a Feasibility Assessment of a National Ballistics Imaging Database", *NISTIR 7362*, NIST, May, 2007.

[8] De Kinder, J., Tulleners, F. and Thiebaut, H., "Reference ballistic imaging database performance," *Forensic Sci. Int.* **140**, 207, 2004.

[9] Blunt, L. and Jiang, X., "Advanced Techniques for Assessment Surface Topography", *Kogan Page Science*, 2003.

STUDY OF AN INTERPOLATION OF FLATNESS DATA MEASURED BY SUCCESSIVE DIFFERENTIAL LASER AUTO-COLLIMATION

Yutaka Uda[1], Shoichi Shimada[1], and Yasuyuki Go[2]
[1]Department of Mechanical Engineering
Osaka Electro-communication University
Neyagawa, Osaka, Japan
[2]Machine Design Division
Nagase Integrex Co., Ltd.
Seki, Gifu, Japan

INSTRUCTIONS

Demands for long mechanical and optical parts which have high straightness or flatness are increasing. Examples are seen in a flat panel for liquid crystal display, a throttle die for thin film production and machine elements of semiconductor equipments. Although the length of the parts exceeds 1 m, the requirement for their figure accuracy is higher than 0.1μm. However, there is no useful method to evaluate precisely the figure accuracy of the long parts. The reasons are inevitable difficulties in manufacturing long tangible datum and in prevention of deformation due to gravity and environment. Therefore, developing the ultra-precision measuring machine for long parts is an urgent need.

In the last paper, a new concept of straightness measuring machine based on differential laser auto-collimation (DLAC) is proposed. By DLAC method, the difference in inclination angle is successively measured between two probing points along a straight line on a surface to be measured as a discrete data at every probing distance. The probing distance depends on the distance between angle sensors. In the successive measuring, the relatively shorter spatial-wavelength components of surface figure are eliminated than a certain value determined by the probing distance. To measure surface profile in more detail, the sensors must be set up closer. However, the measuring time increases as the probing distance decreases. The longer measuring time causes the larger measuring error due to a thermal drift of the sensors. Therefore, there is a limitation in the probing distance. However, high-frequency components of surface figure cannot be measured correctly by the sensors with the longer probing distance.

In this paper, to increase the number of data points, an interpolation method is proposed of figure data between the probe points measured by successive differential laser auto-collimation.

IN-SITU SELF CALIBRATION LASER DIFFERENTIAL AUTO-COLLIMATION

A schematic drawing of in-situ self calibration DLAC is shown in Figure1. To eliminate the alignment error of laser beams and angle detectors, the system consists of two angle detectors (AD_a, AD_b), which simultaneously detect the angles in inclination of the surface at two measuring points on the surface to be measured, two laser diodes (LD_a, LD_b) and a rotary table with two polarization beam-splitters (PBS_a, PBS_b) and two quarter-wave plates (QWP_3, QWP_4). In Figure 1, the inclination angles of the reflected laser beam $T(x_1)$ and $T(x_2)$ from the points x_1 and x_2 on the surface $S(x)$ are simultaneously detected by the angle detectors AD_a and AD_b, respectively. d is the distance between x_1 and x_2 (probing distance).

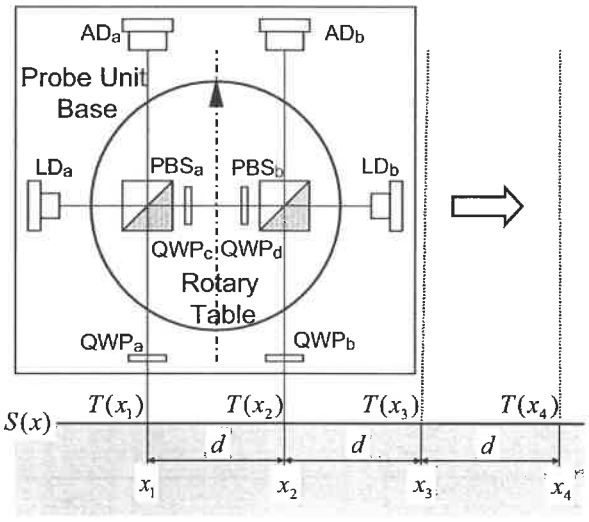

FIGURE 1. In-situ self calibration Differential Laser Auto-Collimation

The new DLAC method proposed can detect the difference in inclination, $T(x_1)$-$T(x_2)$, by eliminating not only error motion in the scanning but also the alignment errors of the devices in the system.

INTERPOLATION METHOD PROPOSED

The differential output signal measured by in-situ DLAC is expressed by Eq(1).

$$Ds\ (x_i) = T(x_{i-1}) - T(x_i) \quad (1)$$

Assuming that the surface inclination and offset distance of the probes at $x_1=0$ is zero, the inclination angle at x_i is expressed by Eq(2).

$$T(x_i) = -\sum Ds(x_{i-1}) \quad (2)$$

The estimated figure profile $f(x)$, which approximately represents the figure profile, is calculated from $T(x_i)$ using Eq(3). (Fig.2)

$$f(x_i + \frac{d}{2}) = d \times \sum T(x_i) \quad (3)$$

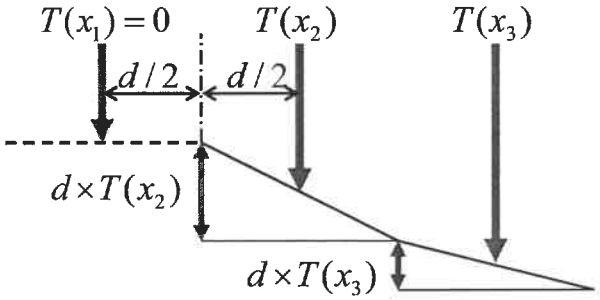

FIGURE 2. The figure profile f(x) estimated from $T(x_i)$

As the inclination $T(x_1)$ is assumed to be zero, estimated figure profile $f(x)$ includes a base line inclination error which is corresponding to the true inclination in $S(x_1)$. The inclination error and offset distance can be compensated at the last step of calculation.

The procedures of interpolation method are described in the following six steps as shown in Figure 3.

Step 1 Correcting the differential output signals, $Ds(x_i)$ at every step of d/n, where n is an integer. By the procedure, n data groups can be obtained by shifting the starting point of scanning d/n.

Step 2 Estimation of figure profiles $f_j(x_i+d/2)$ for each data groups. $j = 0,1,2,\Lambda\ ,n$.

Step 3 Preparation of temporary standard for surface figure by linear interpolation of the distance data $f_0(x)$ as shown in Figure 4.

Step 4 Estimation of difference, $E_j(x_i+d/2)$, between the temporary standard and $f_j(x)$. $E_j(x_i+d/2)$ is expressed by Eq(4).

$$E_j(x_i + d/2) = f_1(x_{i-j} + d/2) - f_j(x_i + d/2) + \frac{f_1(x_{n+i-j} + d/2) - f_1(x_{i-j} + d/2)}{n} \times j \quad (4)$$

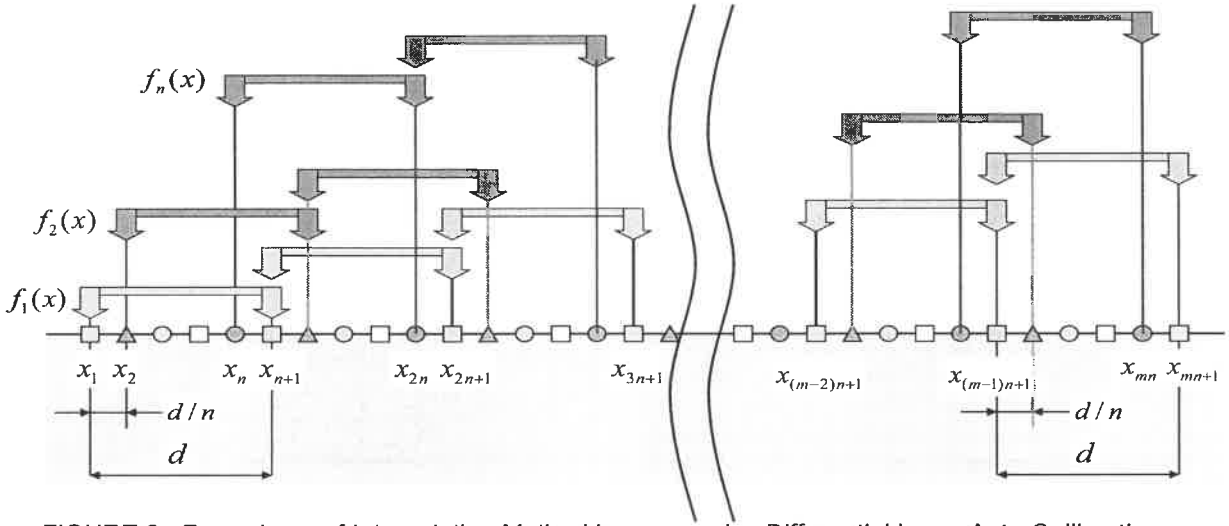

FIGURE 3. Procedures of Interpolation Method by successive Differential Laser Auto-Collimation

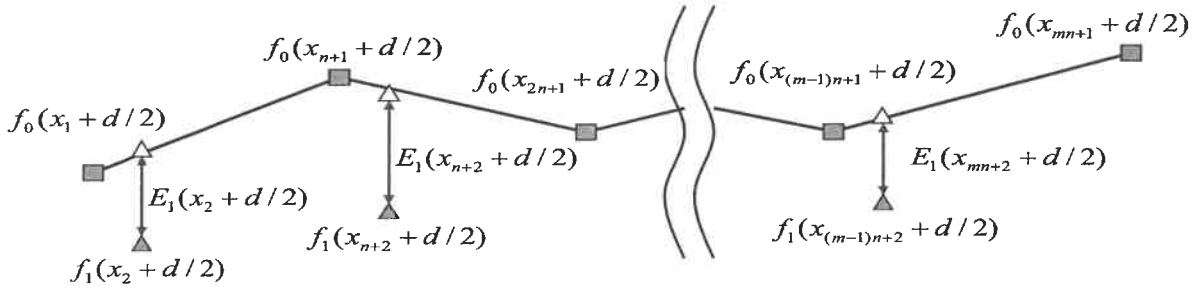

FIGURE 4. Estimation of $E_j(x_i+d/2)$ using a straight-line approximation

Step 5 Supposing that $f_j(x)$ is expressed as $f_0(x)+a_jx+b_j$, calculate the correlation coefficients a_j and offset b_j by a least square method. $f_j(x)$ is expressed by Eq(5).

$$f_j(x) = f_0(x) + a_j x + b_j \qquad (5)$$

Step 6 The calculated surface profile data is combined.

Step 7 Finally, to compensate the inclination and the offset of the combined profile, the base line of the surface is estimated.

SIMULATION RESULTS

To confirm the effectiveness of the proposed interpolation method, numerical simulation is carried out under n=10. The figure to be measured is a sinusoidal wave the amplitude of which is 2. The wavelength is longer than 4 times of probing distance. In general, the sinusoidal wave profile cannot be reconstructed from the discrete profile data the sampling distance of which is longer than 1/4 of the wavelength. Figure 5 are the calculated results in the case of $f_0(x_i+d/2)$ and $f_5(x_i+d/2)$.

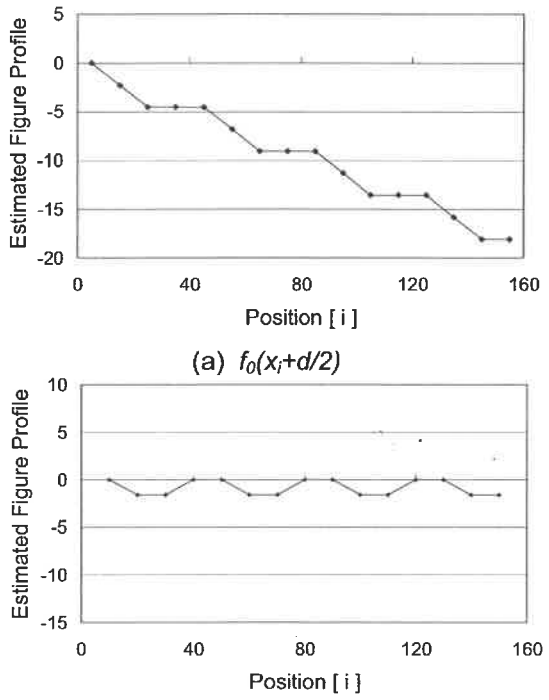

FIGURE 5. Simulation results of $f_0(x_i+d/2)$ and $f_5(x_i+d/2)$

The combined surface profile is shown in Figure 6. After compensate the inclination and the offset, the surface profile estimated is shown in Figure 7. The result suggests the validity of the interpolation method proposed. However the amplitude of the wave is a little bit bigger than that of the true profile because of the effect of transfer gain depending on wavelength. Figure 8 shows the calculated transfer gain. X-axis is the ratio between the probing distance and the wave length. If the starting point of scan is shifted, the inclination error $f_j(x_i+d/2)$ changes due to phase shift of sinusoidal wave. However, by a proper compensation corresponding to the phase shift, estimated surface figure can be obtained correctly.

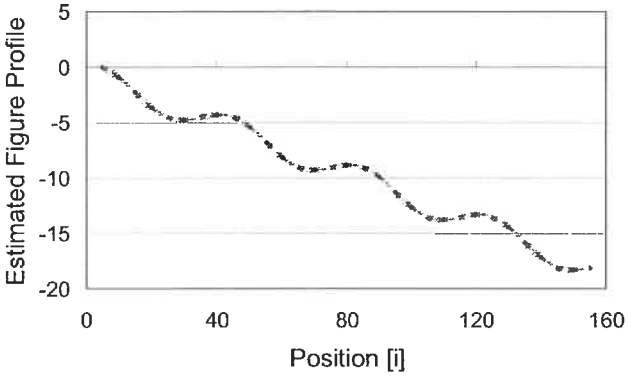

FIGURE 6. Results of combined surface profile

Figure 9 shows the result of simulation for a surface profile including two waves with different wavelength as shown in Table 1. Solid line is a figure profile compensated by transfer gain. All discrete data are almost on the correct figure profile. The results suggest that the interpolation method proposed is useful one for the data processing in DLAC method.

Table 1. Simulation Parameter of two waves

	Wavelength	Amplitude	Gain
No.1	*8d*	*4*	*1.026*
No.2	*4d*	*2*	*1.111*

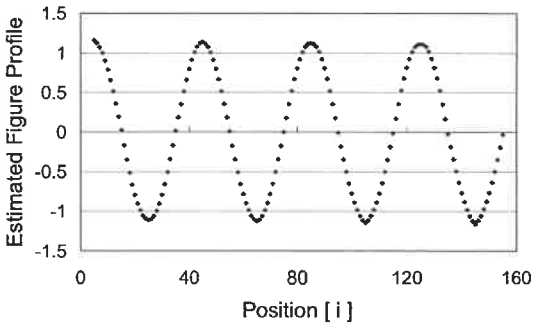

FIGURE 7. Result of estimated surface profile

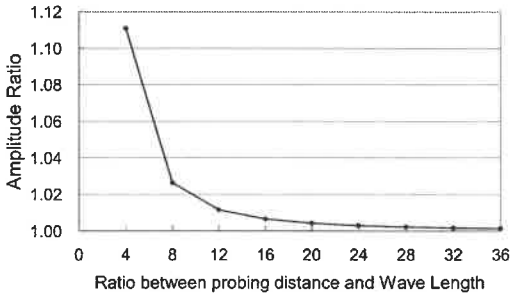

FIGURE 8. Transfer gain

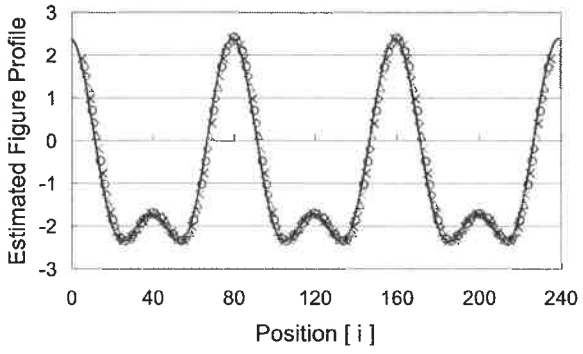

FIGURE 9. Result of Surface Profile with two waves

SUMMERY

The new concept of interpolation method for DLAC is proposed. To confirm an effectiveness of the method proposed, a numerical simulation is carried out.

(1) The new proposed method can interpolates the profile data between the discrete data obtained by two angle sensors.

(2) In the case that multiple frequency components are include in surface figure, calculated data must be compensated with a transfer gain corresponding to each wavelength. Using this method, the shortest measurable wave length is 4 times longer than the probing distance.

(3) The interpolation method is not be influenced by the shift of starting point.

ACKNOWLEDGMENT

This work was supported by the Grant-in-Aid for Scientific Research (Start-up), (18860079) of the Ministry of Education, Science, Sports and Culture, Japan. The authors express their thanks to Professor S. Kiyono for his useful suggestions and advices.

REFERENCES

[1] Kiyono S, Fukaya N, Kume T. "Differential Laser Autocollimation Method (1st Report)". J.S.P.E. 1989; Vol.55 No.2; 412-417

[2] Kiyono S, Kume T, Asakawa Y, Kamada O. "Differential Laser Autocollimation Method (2nd Report)". J.S.P.E. 1991; Vol.57 No.4; 652-657

[3] Uda Y, Shimada S, Go Y. "Development of Straightness Measuring Machine for Long Parts using In-Situ Self Calibration Laser Differntial Auto-Collimation –Influence of Probe Assemble Error-". 2007; Proc. 22-ASPE Annual Meeting; 359-362

ULTRA FINE TOOL SERVO SYSTEM

Gan Sze Wei[1], M. Rahman[1], Lim Han Seok[2]
[1]Department of Mechanical Engineering
National University of Singapore
10 Kent Ridge Crescent, Singapore 119260
[2] Mikrotools Pte. Ltd.
Block 51, #01-06/07
Ayer Rajah Crescent, Singapore 139948

INTRODUCTION

The strong demand for ultraprecision components with sub-micrometer accuracy and nanometer surface finish in today's industries has gradually delivered focus in the research area of nano-machining technology. Diamond turning is one of the most effective processes for nano-machining due to the nanometric edge sharpness of the tool, form reproducibility and wear resistance [1]. Since mid-1980's, an active device called Fast Tool Servo (FTS) has been introduced for diamond turning [2]. Initially, the FTS was implemented in order to compensate the systematic error on the machine tool during turning [3]. As soon as the FTS was established, researchers started to make greater efforts to employ the FTS to machine non-symmetrical and micro-feature surfaces [4-6]. Mainly, the FTS system is specially designed with local position measurement or global position measurement [7] for feedback and control purpose. Another approach of FTS system is the force measurement which is essential for monitoring the dynamic cutting force [8]. Recently, Gao et al have developed an instrument for measuring the cutting force and thrust force in nanomachining [9]. It is clear that understanding the machining force can directly reflect the actual machining phenomenon.

This paper presents a newly developed fine position tool servo or so called ultra Fine Tool Servo (FTS) with the cutting force measurement system. The ultra FTS system is targeted to achieve high resolution, high accuracy and repeatability, and subsequently a sufficient bandwidth and stiffness to machine micro-features and non-symmetrical surfaces.

ULTRA FINE TOOL SERVO DESIGN

The ultra Fine Tool Servo (FTS) is designed and installed on a T-base miniature ultraprecision lathe. A piezoelectric actuator which is the driving element is placed in the center of the flexure structure as shown in Figure 1. The piezoelectric actuator moves the tool tip to feed in the desired distance according to the applied voltage. In order to avoid the Abbe error, the miniature force sensor is also installed in-line with the piezoelectric actuator and the capacitance sensor as well. The interesting part in the design of ultra FTS is the flexure structure. It is designed by considering both local position measurement and force measurement ability and will the details are given in the following section.

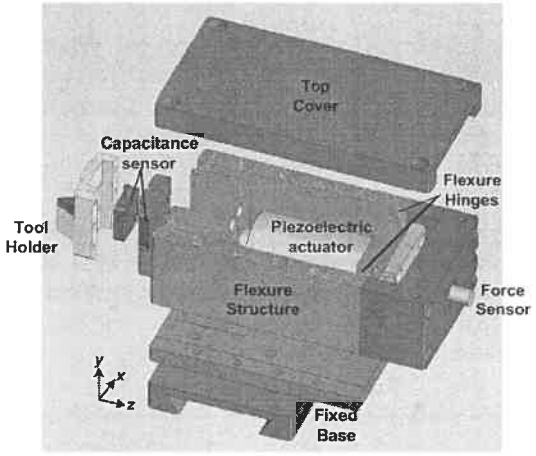

FIGURE 1. Ultra Fine Tool Servo

Flexure Structure Mechanism

A new flexure mechanism is introduced for the ultra FTS which is allowed the force measurement and the piezoelectric actuator movement to operate simultaneously. A free-body diagram is provided in Figure 2 to describe the flexure mechanism of the ultra FTS. The linkage between the bars is assumed to be well jointed and elastically deformable. When an external load, F_D such as cutting force is applied, the whole structure gets translated in the axial direction. In order to feed the tool tip in the desired position as commanded through programming, the piezoelectric actuator extends

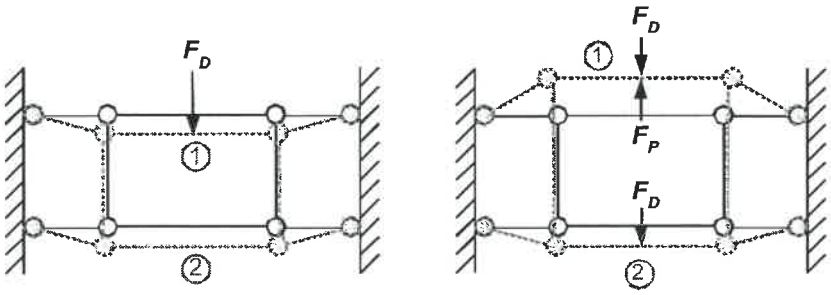

FIGURE 2. Flexure structure

and generates the element (1) to move against the F_D direction. However, the element (2) gets displaced in the direction where F_D is applied. The force F_P is greater than force F_D which means that the displacement of element (1) is larger than element (2). Generally, the translation of the piezoelectric actuator is guided by a flexure mechanism element. In micro-precision machinery, a flexure mechanism with the notched hinges is a good choice in designing a micro-positioner system. One effective design is a parallel and symmetric design. When the piezoelectric actuator is pushing the guiding system, a minor force from the piezoelectric actuator, F_m may be acting on the force sensor as shown in Figure 3. Therefore, the sensor output, F_S is considered as a superposition of F_D and F_m. It is essential to determine the relationship between the displacement of the FTS and the force acting from the piezoelectric actuator to the force sensor without the machining process.

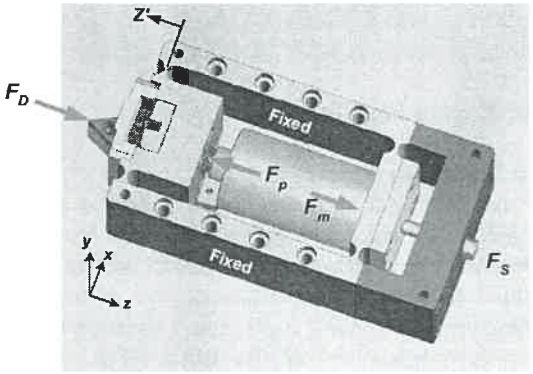

FIGURE 3. Assembled flexure structure

Mechanical Characteristics

The resonance frequency of an open-loop ultra FTS system is approximately 5.5 kHz, and a sufficient dynamic response is up to 2 kHz as shown in Figure 4. For a closed-loop response of the ultra FTS system, a sinusoidal voltage is applied to the piezoelectric actuator with the frequency of 1 Hz. As shown in Figure 5, it can be observed that a displacement resolution of 1 nm can be achieved. However, a dynamic displacement of 5 nm only can be obtained up to 300 Hz in the closed-loop system. Table 1 shows the mechanical properties of the ultra FTS that is obtained from experimental testing.

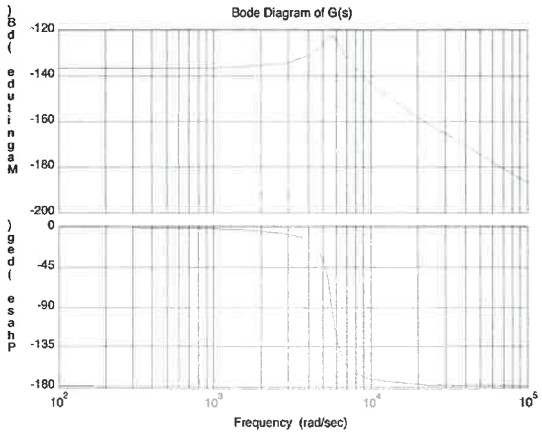

FIGURE 4. Frequency response for open-loop system

Force Measurement System

From the calibration result, it is clear that the output of the miniature force sensor is directly proportional to the applied load and the result shows that the force sensor is able to work in stable condition. Besides, the linear relation between the force and the displacement of the piezoelectric actuator can be obtained as shown in Figure 6. However, careful attention still needs to be paid in order to determine the actual thrust force (F_t).

TABLE 1. The Mechanical Properties of ultra Fine Tool Servo

Mass (kg)	0.22
Stiffness (N/μm)	7.1813
Damping coefficient (kg/s)	240.326
Natural frequency (kHz)	2

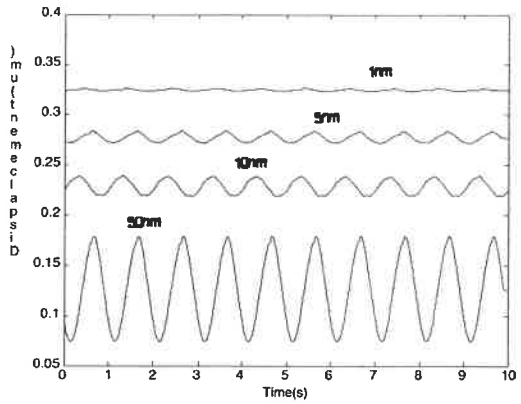

FIGURE 5. Dynamic displacement

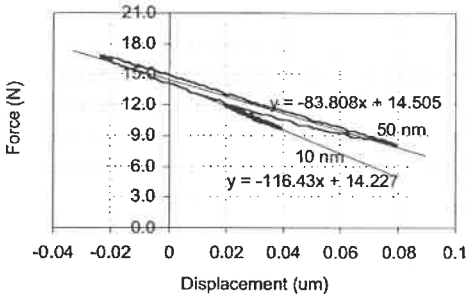

FIGURE 6.Relationship between force and displacement for the ultra FTS

SYSTEM INTEGRATION AND CONTROL

Figure 7 shows the T-base miniature ultraprecision lathe and the ultra FTS system. The axes are clearly illustrated: translational stages as *x*- and *z*-axis, spindle revolution as *c*-axis, and ultra FTS as *w*-axis. All the axes are controlled by a high speed motion controller called UMAC in order to achieve the integration as illustrated in Figure 8. The ultra FTS system consists of a high voltage amplifier with a capacitance driver, and a charge amplifier of the force sensor. For the control of ultra FTS system, the actual displacement is fed back to the motion controller and the positioning error is controlled by the PID and feedforward controller in order to minimize the following error. The main concern of the integration system is to achieve the synchronized motion between the machine axes and the ultra FTS.

EXPERIMENTAL DETAILS AND RESULTS

In the machining experiment, a polycrystalline diamond (PCD) insert with 0.1 mm tool nose radius was used. An aluminium alloy workpiece has been used and tested in the experiment. The aim of this experiment was to investigate the capability of the ultra FTS system in machining a micro-feature surface during face turning. Besides, it is also interesting to analyse the micro-features machining phenomenon with the ultra FTS system by monitoring the thrust force. In this study, only a micro-level amplitude pulse-type waveform was machined by using the ultra FTS system. The cutting conditions that were used in this study were 15000 rpm cutting speed, 0.3 mm/s feed rate, and cutting was performed under dry condition.

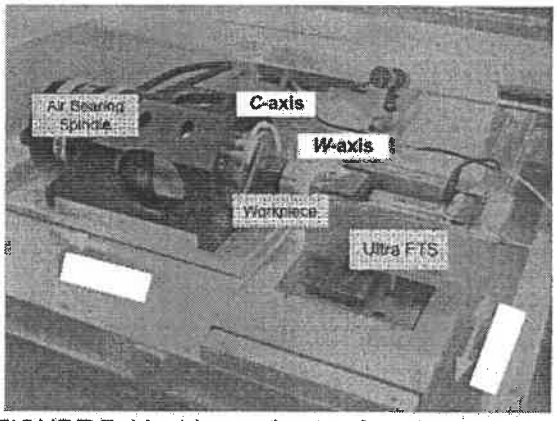

FIGURE 7. Machine tool setup for ultra FTS

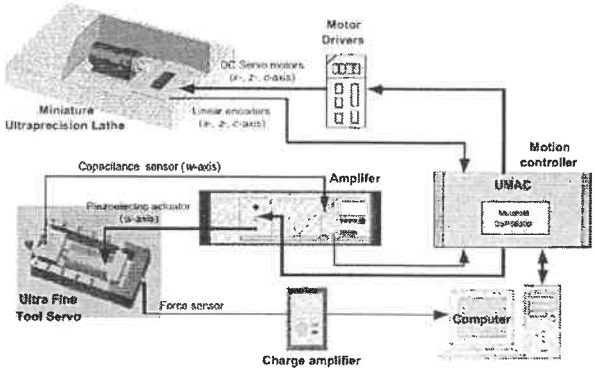

FIGURE 8. Block diagram of the ultra FTS integration system

In order to investigate the performance of the ultra FTS system, a pulse-type waveform with micrometer amplitude was machined on the

aluminium alloy workpiece. Figure 9 shows the effect of thrust force and the surface roughness of the machined surface during the ultra FTS system implementation. Obviously, it was found that the waveform profile of the machine surface is almost identical to the generated signal from the ultra FTS system. This phenomenon can be adequately explained by the good tracking performance of the ultra FTS system during turning process. The roughness of the machined surface is less than 10 nm which is considered as a great achievement of this study. Thrust force measurement demonstrates that it is decreasing when the tool tip of ultra FTS system moved to the peak of the waveform amplitude, and vice versa. Also, it can be observed that the overall magnitude of thrust force is slightly decreased between the cutting distance from 0 to 2 mm. This might have happened because the *x*-axis translational slide is tilted in certain angle and causes the inaccuracy of the machined surface. This problem can be solved by implementing the global error measurement system in the ultra FTS as discussed by [7].

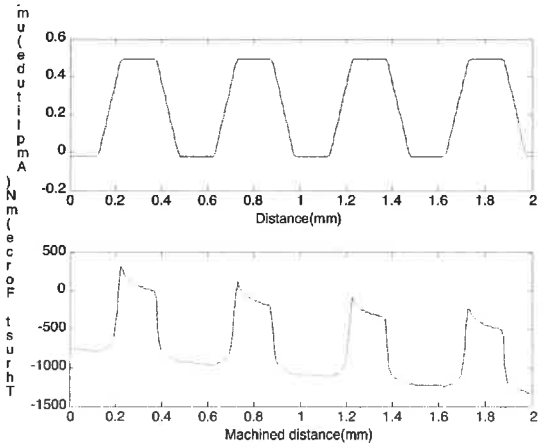

FIGURE 9. Effect of thrust force and actual displacement during the ultra FTS system implementation

CONCLUSIONS

The main objective of this paper is to develop an innovative piezoelectric-based ultra Fine Tool Servo (FTS) system for a miniature ultraprecision lathe. The FTS system was designed for generating micro-feature surfaces on small-sized workpieces and for measuring the thrust force along the in-feed direction by a built-in force sensor during diamond turning process. The developed ultra FTS systems established the new concept of the flexure structure design comprising the actuator with capability of measuring the micro-Newton thrust force. The flexure structure design is totally different from the design of fast tool servo that is found in the literature.

From the experimental results, the ultra FTS system is found to be able to machine the commanded waveform profile accurately and with good surface roughness of less than 10 nm. Besides, the thrust force can effectively illustrate the machining phenomenon during the machining process.

REFERENCES

[1] N. Ikawa, R.R. Donaldson, R. Komandur, W. Konig, T.H. Aachen, P.A. McKeown, "Ultra-precision metal cutting – the past, the present and the future", Ann. of the CIRP, vol.40, no.1, 1991, 587-594.

[2] Patterson, S.R., and Magrab, E.B., "The design and testing of a fast tool servo for diamond turning", Precision Engineering, vol.7, no.3, 1985, 123-128.

[3] E. Kouno, "A fast response piezoelectric actuator for servo correction of symmetric errors in precision machining," Ann. of the CIRP, vol.33, no.1, 1984, 369-372.

[4] Dow, T.A., Miller, M.H., and Falter, P.J., "Application of a fast tool servo for diamond turning of nonrotationally symmetric surfaces", Precision Engineering, vol.13, no.4, 1991, 243-250.

[5] T. A. Dow, M. H. Miller, P. J. Falter, "Application of a fast tool servo for diamond turning of nonrotationally symmetric surfaces", Precision Engineering, vol.13, no.4, 1991, 243-250.

[6] D. Wu, K. Chen, X.K. Wang, "Tracking control and active disturbance rejection with application to noncircular machining", International Journal of Machine Tools & Manufacture, vol.47, 2007, 2207-2217.

[7] S.W. Gan, H.S. Lim, M. Rahman, F. Watt, "A fine tool servo system for global position error compensation for a miniature ultra-precision lathe," International Journal of Machine Tools & Manufacture, vol.47, 2007, 1302-1310.

[8] J.A. Abler, "Process modeling and correction of dynamic errors in diamond turning," Ph.D. Thesis, North Carolina State University, 1994.

[9] W. Gao, R.J. Hocken, J.A. Patten, J. Lovingood and D.A. Lucca, "Construction and testing of a nanomachining instrument," Precision Engineering, vol.24, 2000, 320-328.

MACHINING TECHNOLOGY OF MICRO WAVED V-PATTERN USING SHAPING PROCESS

Te-Jin Je[1], Doo-Sun Choi[1], Kang-Won Lee[1], Kyung-Tak Park[1], Kyung-Hyun Whang[1]
[1]Korea Institute of Machinery & Materials (KIMM), Daejon, Korea

INTRODUCTION

Recently, high-function, high-efficiency, compact and low-cost are demanded in LCD display industry.

Optical films which are used in BLU are trying to enhanced efficiency and low-cost through minuteness, complex and large-area. Research for micro complex pattern which used in optical film is active [1][2][3].

In generally, shaping process or planning process is applied to manufacture mold for light guide panel(LGP) and optical film which has micro pattern [4][5][6][7]. Moreover roll mold machining technology for large-area film is studying and is applied in various fields [8].

In this paper, plane micro complex pattern machining was realized.

Micro waved V-pattern which is application of basic V prism pattern was tried to form. Its pattern is estimated to decrease optical interference effect such moiré [9]. It's basic machining experiment only with using shaping system control. This paper represents that how small micro waved V-pattern can be made and analyze effect of tool feeding direction, tool relief angle and tool material.

MICRO WAVED V-PATTERN SHAPE

Figure 1 shows specification shape of micro waved V-pattern. Keeping specific height(H), this pattern consists of plural structure which has alternate amplitude of left and right along the feeding direction .

Its shape is depended on pitch(P), amplitude (W) and period(T).

EXPERIMENTAL SYSTEM AND MACHINING METHOD

Figure 2 shows experimental apparatus diagram for micro waved V-pattern machining. This machine has 3-axes of driving system such as X, Y and Z axes. X and Y axes have the air static pressure bearing in driving system. Z axes is operated by servo motor. X and Y axis motion determines amplitude of left and right on machining path, position of X, Y axis. Z axis motion determines vertical position.

The each cutting force of 3-axes can be measured in real time because dynamometer is attached to the Z axis.

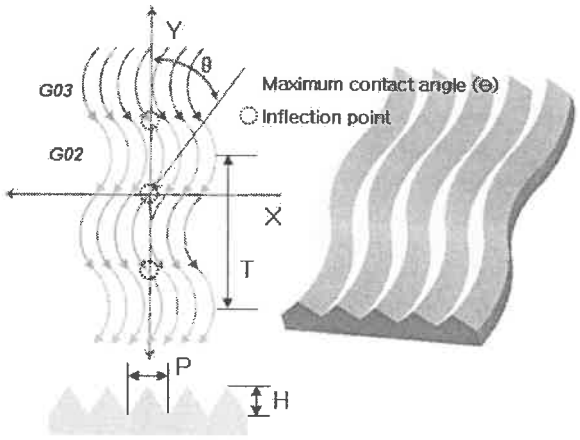

FIGURE 1. Shape of micro waved V-pattern and main configuration parameters

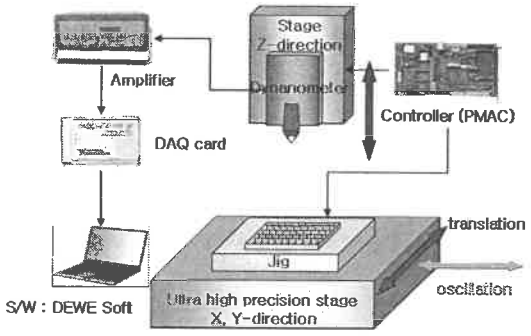

FIGURE 2. Schematic of experimental setup

Machining path is made using EdgeCAM software through arranging G02 and G03 NC code on alternation for designed period(T), amplitude(W) and pitch(P).

As diamond tool follows designed path, waved shaping process is operated through system motion control.

PCD and SCD tool are used. Shape angle is 90° and relief angle is 3°, 10°.

Cutting depth is 5_/pass and total depth is 25_ through fifth processing.

TABLE 1. Experimental conditions

Items	Conditions
machining method	shaping process
workpiece	6:4 brass
machining tool	material : PCD, SCD shape angle : 90° relief angle : 3°, 10°
shape of pattern	micro waved V-pattern
pattern pitch	50_
cutting depth	5_/pass
cutting speed	100mm/min

TOOL FEEDING DIRECTION, TOOL RELIEF ANGLE AND TOOL MATERIAL EFFECT ANALYSIS

On machining micro waved V-pattern using fixed tool, the shape and size of pattern has several limitation because of the interference of the relief face of tool is occurred for the amplitude and period of pattern. The relief angle has to be considered when tools are designed because the interference is differently occurred by amount of relief angle. Tool motion of micro waved V-pattern can be considered to linear shaping path with continuous changed tangent slope as Figure 3. On the machining path, tangent slope has biggest angle for Y-axis of feeding direction in inflection point and its point is maximum contact angle.

The effect of interference between tool relief face and workpiece can be estimated by feeding the tool in cutting path obtained by the maximum contact angle occurred for the change of amplitude and period.

Table 2 shows maximum contact angles as main configuration parameter of micro waved V-pattern. Maximum contact angle increases for decreasing of pattern period on fixed amplitude.

Linear shaping experiment was carried out for obtained maximum contact angle as Fig 3.

TABLE 2. Maximum cutting angle of each micro waved V-pattern

Contents		Aamplitude (w)		
		50_	25_	15_
Period (T)	1,000_	11°	5.72°	3.44°
	500_	22°	11°	6.87°
	300_	36°	18.92°	11°

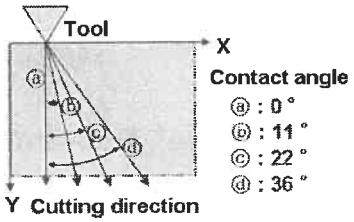

FIGURE 3. Maximum cutting angle of micro waved V-pattern

Figure 4 shows result surface of linear shaping experimental. It is more difficult to form pattern as maximum contact angle increases because interference of tool relief face breaks down machined pattern.

And the interference of relief angle 3° is bigger than the one of relief angle 10°

On machining micro waved V-pattern, it is necessary to design proper pattern shape and to consider tool relief angle for minimizing interference effect of tool relief face.

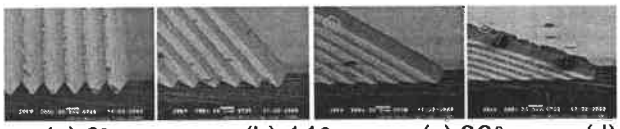

(a) 0° (b) 11° (c) 22° (d) 36°

tool relief angle 3°

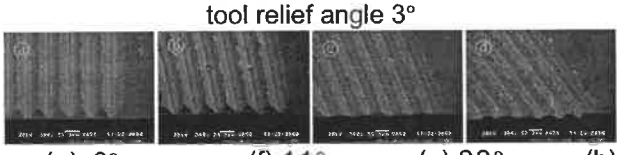

(e) 0° (f) 11° (g) 22° (h) 36°

tool relief angle 10°

FIGURE 4. Comparison of machined surface for maximum cutting angles

Figure 5 shows the result of machined surface of micro waved V-pattern using PCD tool with relief angle 3° on pattern shape designed as table 2.

Formation of pattern is bad as maximum contact angle increases more and more due to inference of tool relief face on machining micro waved V-pattern in Figure 5(a), 5(b) and 5(c).

Addition experiment with maximum contact angle 11° for each period carried out.

Although the results of machined surface can not be quantitatively compared, they are nearly similar as Figure 5(d), 5(e) and 5(f).

Figure 6 shows cutting force diagram which was measured on fifth pass

Sampling time which is horizontal axis is equal .

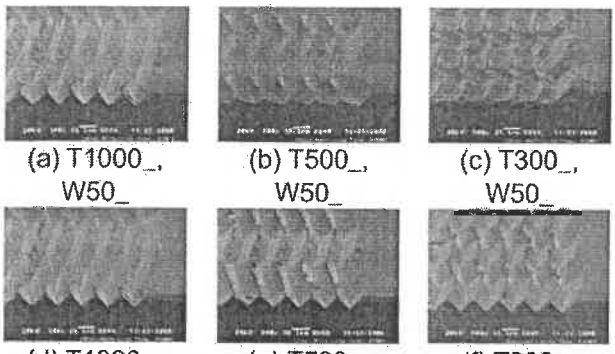

FIGURE 5. Comparison of machined surface by PCD tool with relief angle 3°

Cutting force of X axis and Z axis are much bigger than major cutting force of Y axis.
And each of cutting force has periodicity because tool motion operates by periods. They alternate value within specified range and show sine waved shape. At inflection point, inference of tool relief face was greatly occurred.
Although maximum contact angle increases, cutting force decreases because of decreasing of cutting section area which was due to inference of tool relief face.

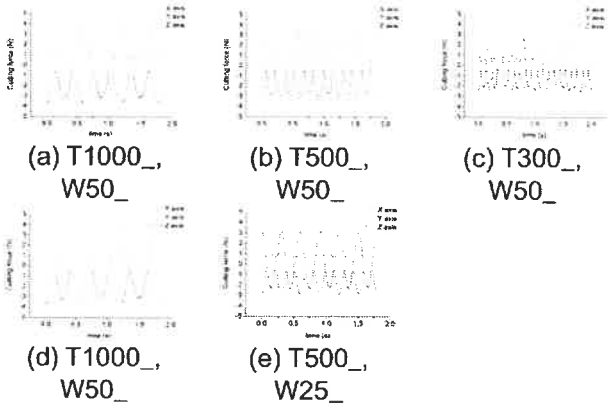

FIGURE 6. Comparison of cutting force by PCD tool with relief angle 3° on fifth path

Micro waved V-pattern experimental using PCD and SCD with relief angle 10° was carried out on same condition.

Figure 7 shows different of machined surface according to the kind of tool type. The result of tool relief angle 10° is good comparing with Figure 5 machined result of tool relief angle 3°. The machined surface by PCD tool is rough and have scratch and burrs but the surface by SCD tool is clear and does not have any scratch and burr.

In this experiment, micro waved V-pattern which has 300_ of period and 15_ of amplitude was realized.

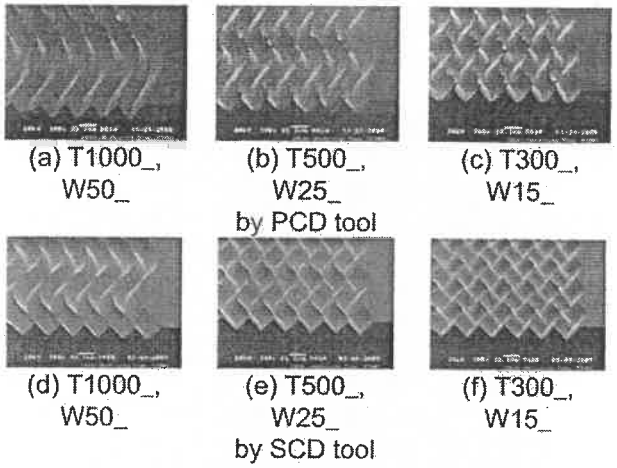

FIGURE 7. Comparison of machined surface according to tool material with relief angle 10°

Figure 8 shows the shape of cutting chip formed in micro waved V-pattern mold that machined by using SCD tool with relief angle 10°. On the whole flow type chip was formed but the chip was regularly damaged on the right and left of cutting chip in same pitch. Interference of tool relief face was most greatly occurred at the near inflection point.

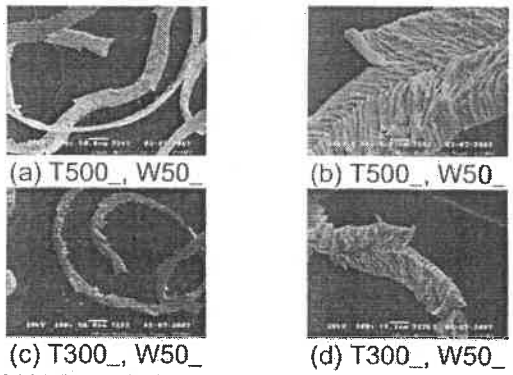

FIGURE 8. Chip formation damaged by relief surface of SCD tool with relief angle 10°

Figure 9 shows cutting force diagram in micro waved V-pattern mold on machining by tool relief angle 10°. The cutting force of X axis in amplitude direction and Z axis in vertical direction are smaller than the one of Y axis in moving direction of tool. The reason is decreasing of interference effect for increased tool relief angle between tool relief face and workpiece on same conditions.

Cutting force measured by SCD tool is smaller than the one of PCD tool on same condition.

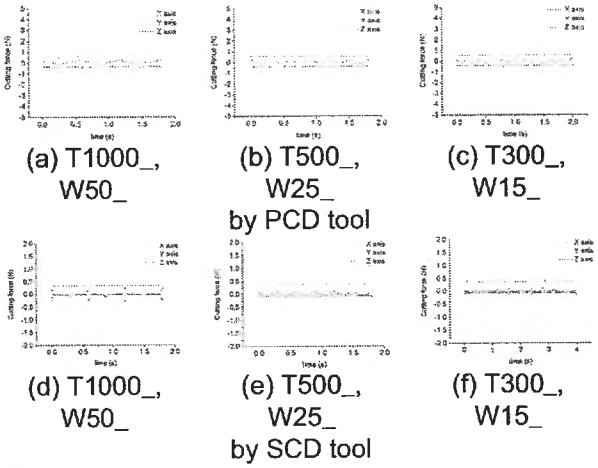

(a) T1000_, W50_ (b) T500_, W25_ (c) T300_, W15_ by PCD tool

(d) T1000_, W50_ (e) T500_, W25_ (f) T300_, W15_ by SCD tool

FIGURE 9. Comparison of cutting force according to tool material with relief angle 10°

CONCLUSIONS

1. Basic machining experimental of micro waved V-pattern was carried out using system motion control on high precision shaping process and micro machining technology of micro waved V-pattern with period 300_ and amplitude 15_ was founded.
2. On machining micro waved V-pattern using fixed tool, it is necessary to design range of amplitude within tool relief angle for minimizing interference effect of tool relief face.
3. Maximum interference of tool relief face occurs near inflection point and deviation of machined surface is greatest in this point
4. It's necessary to decrease interference effect of tool relief face for machining wide amplitude micro waved V-pattern.
5. Machined surface and patterned shape of SCD tool is better than it of PCD tool on same machining condition

REFERENCES

[1] D. Lee. Topics of BLU & Optical Films for BLU. Display Industrial Forum. Displaybank, KOREA, 2007.

[2] United States Patent. Optical film. No. US 6,354,709.

[3] Fumio Ide. The optical films for flat panel displays. CMC, ISBN4-88231-430-4, C3054. 2004.

[4] K. Sawada, T. Kawai, H. Terashima. Ultra-high Precision Machining Technology of Micro Structure. The Sixth International Micro-machine Symposium. pp.199-202. 2000.

[5] Moriwaki T., Okuda K. Machinability of copper in ultraprecision micro diamond cutting. Annals of the CIRP, Vol. 38, No. 1. pp.115. 1989.

[6] Y. E. Yoo, S. M. Hong, T. J. Je, D. S. Choi. Mechanical machining of prism pattern. Transactions of Materials Processing. Vol. 15, No. 1. pp.71~75. 2006.

[7] T.J. Je, E.S. Lee, D.S. Choi, J.C. Lee, H. Choi. Development of a Mechanical Micro Machining System and its Applications. Proceedings of the KSMPE. pp.220-204. 2003.

[8] D. S. Choi, T. J. Je, Y. E. Yoo. J. S. Yoon. A Study on the High Aspect Ratio Pattern Roll Mold Fabrication Technologies. EUSPEN, Vol. 1. pp.396-400. 2006.

[9] Y. C. Park, The Principle and Applications of Moire Phenomenon. J. of KSPE. Vol. 17, No. 6. pp.25-31. 2000.

FACTORS AFFECTING CHANGES IN REMOVAL RATE OF ELASTIC EMISSION MACHINING

Masahiko Kanaoka[1], Hideo Takino[1], Kazushi Nomura[1]
Hidekazu Mimura[2], Kazuto Yamauchi[2, 3], Yuzo Mori[3]

[1]Lens Engineering Development Department
Nikon Corporation
Sagamihara, Kanagawa, Japan

[2]Department of Precision Science and Technology
[3]Research Center for Ultra-Precision Science and Technology
Osaka University
Suita, Osaka, Japan

INTRODUCTION

Extreme ultraviolet (EUV) lithography is expected and currently being developed as a future chip-printing technology suitable for the features at design scales smaller than 40 nm.
To focus the EUV light at a wavelength of 13.5 nm, high-precision optical mirrors with a surface roughness of 0.1 nmRMS are required. In addition, mirror substrates must be low-thermal-expansion materials because EUV light is easily absorbed in matter and subsequently converted to heat. ULE (Corning Inc.) and Zerodur (SCHOTT AG) are well-known examples of such materials. A smoothing technique that can satisfy those specifications is strongly required.

Elastic emission machining (EEM) is expected as one of the adequate techniques. EEM has been successfully developed for the fabrication of hard-X-ray mirrors, by which sub-30nm focusing was established under diffraction-limited conditions at the wavelength of 0.08 nm [1][2]. In this achievement, the material of the mirror surface was single-crystal silicon, on which EEM is known to realize an atomically well-ordered surface [3].

It has already been demonstrated that EEM is effective for smoothing surfaces of low-thermal-expansion materials [4]. In this study, relationships between machining conditions and removal rate were examined, and furthermore, changes in removal rate were discussed on the basis of the results of the analysis of powder particle behavior in machining slurry.

PRINCIPLE OF EEM

EEM is a non-contact machining process, differing from conventional polishing, which uses an abrasive pad. The removal process in EEM solely depends on the contact between powder particles and the workpiece surface.

Fine powder particles are brought to the workpiece surface by a flow of pure water, and the chemical reaction between the surfaces of the workpiece and the particles results in the removal of surface atoms from the workpiece, as shown in Figure 1.
Therefore, atomic-order smoothness without crystallographic damage can be achieved.

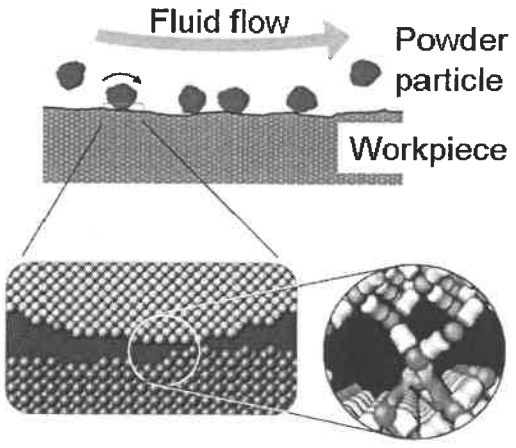

FIGURE 1. Schematic representation of atom removal process in EEM.

MACHINING HEAD FOR PARTICLE SUPPLY

In this study, a rotating sphere made of elastomeric material is utilized as a tool for generating fluid flow. Stable fluid flow is obtained using the state of elastohydrodynamic lubrication between the surfaces of the rotating sphere and workpiece, which can maintain a non-contact state at the machining point during EEM. A continuous particle supply to the workpiece surface can be achieved by this stable fluid flow.

The thickness and fluid flow velocity of a lubrication film depend on machining conditions of load, rotation speed and concentration of powder particles.

Figure 2 shows a schematic representation of the rotating sphere during machining. The lubrication state is numerically calculated, and the conditions under which the lubrication film thickness becomes approximately 1 μm are applied to machining. The surface of the rotating sphere becomes approximately parallel to the workpiece surface across the lubrication film at the machining point, which results in an approximately linear velocity gradient in the film.

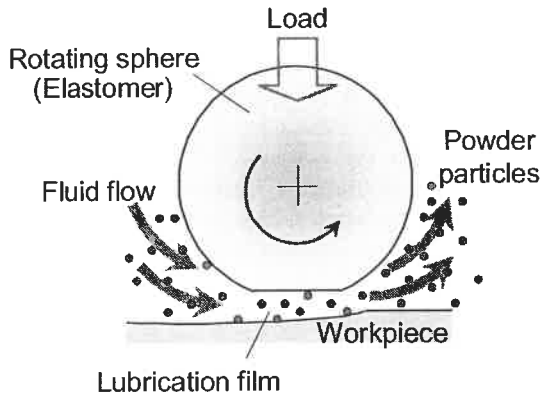

FIGURE 2. Schematic representation of particle supply to workpiece surface using rotating sphere.

EEM APPARATUS

Figure 3 shows a schematic of the EEM system. This system consists of a three-axis control system, which makes it possible to process any desired area on a workpiece surface. A work spindle with a rotating-sphere head is suspended by a cross spring, similar to a pendulum, and the head is immersed in a tank of fluid mixture. The load acting on the rotating sphere is generated by applying a load to the work spindle.

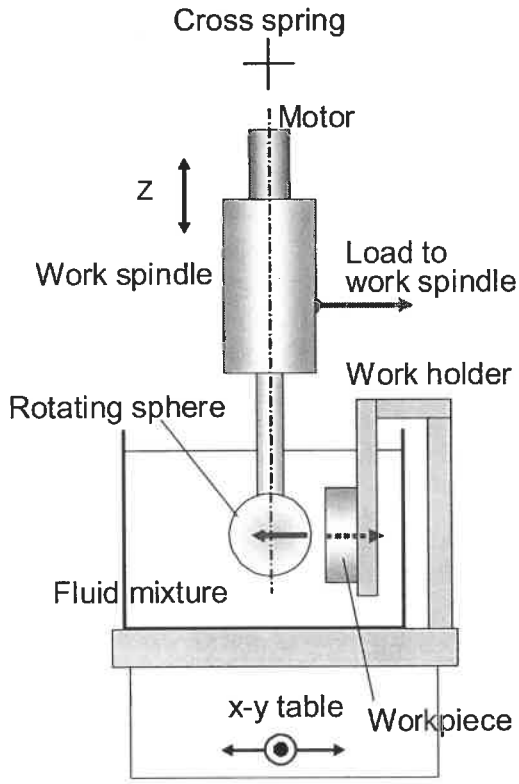

FIGURE 3. Schematic of EEM apparatus.

EXPERIMENTAL

Two different relationships were examined. One is between the removal rate and the rotation speed of the rotating-sphere head, and the other is between the removal rate and the concentration of particles in machining slurry.

Removal rate was evaluated by measuring the unit removal mark on a flat Zerodur surface processed for 1 min using a three-dimensional optical profiler (NewView, ZYGO). Powder particles are spherical, 80 nm in diameter and made of SiO_2.

Experimental results are shown in figure 4. In the examination of the relationship between removal rate and head rotation speed, removal rate is observed to be negatively correlated with rotation speed. Moreover, in the examination of the relationship between removal rate and particle concentration, removal rate is observed to rapidly decrease after peaking at 15 %.

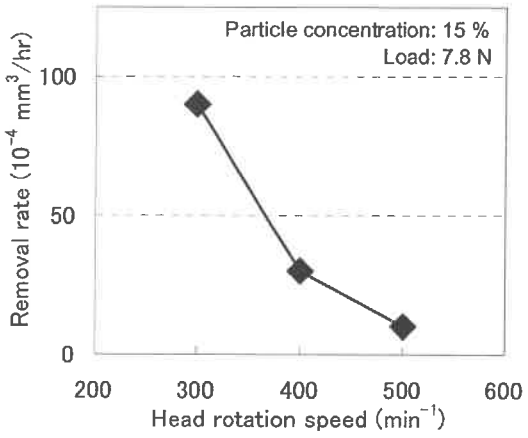

(a) Removal rate vs head rotation speed

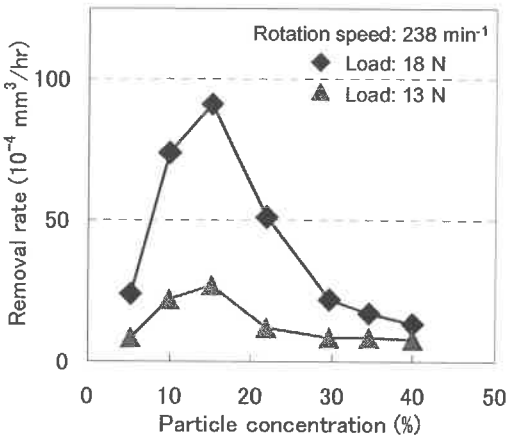

(b) Removal rate vs particle concentration

FIGURE 4. Changes in removal rate with increasing rotation speed of rotating sphere (a) and particle concentration of machining slurry (b).

DISCUSSION ON REMOVAL RATE

As mentioned above, the removal process depends on powder particles supplied to the workpiece surface. Assuming that the volumes removed by each particle are all equivalent, changes in removal rate can be considered to correspond to those in the number of particles supplied to the workpiece surface per unit time. This indicates that changes in removal rate can be estimated by tracing particle behavior and counting the number of particles supplied to the workpiece surface.

Increases in rotation speed and particle concentration cause an increase in the number of particles passing through the lubrication film per unit time. However, the number of particles supplied to the workpiece surface per unit time, or removal rate, does not simply increase. This may be due to the presence of forces preventing particles from being supplied to the workpiece surface. These forces can be considered to increase when the fluid flow velocity and the concentration of particles in the lubrication film increase.

ANALYSIS OF PARTICLE BEHAVIOR

To investigate the fact that removal rate is not positively correlated with the increase in the number of particles passing through the lubrication film per unit time, particle behavior is analyzed by taking forces acting on particles into consideration.

Figure 5 shows the forces acting on a particle passing through a lubrication film. F_{Dx} and F_{Dz} are the Stokes drag forces in the x and z directions, and F_G and F_B are the gravity and buoyant forces, respectively. F_L is the lift force generated in fluid flow with a velocity gradient, which is known as the Suffman force [5]. F_{Fx} and F_{Fz} are the forces generated by a mutual interaction of particles in the x and z directions, acting on a particle to hinder it from moving forward.

Particle behavior can be traced by solving equations of motion expressed with these forces.

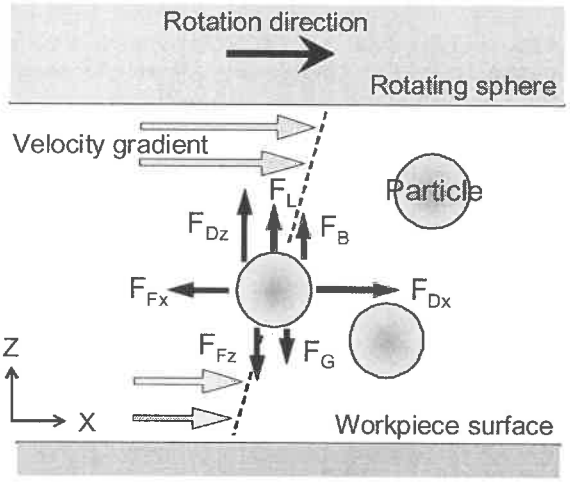

FIGURE 5. Schematic representation of forces acting on particle passing through lubrication film.

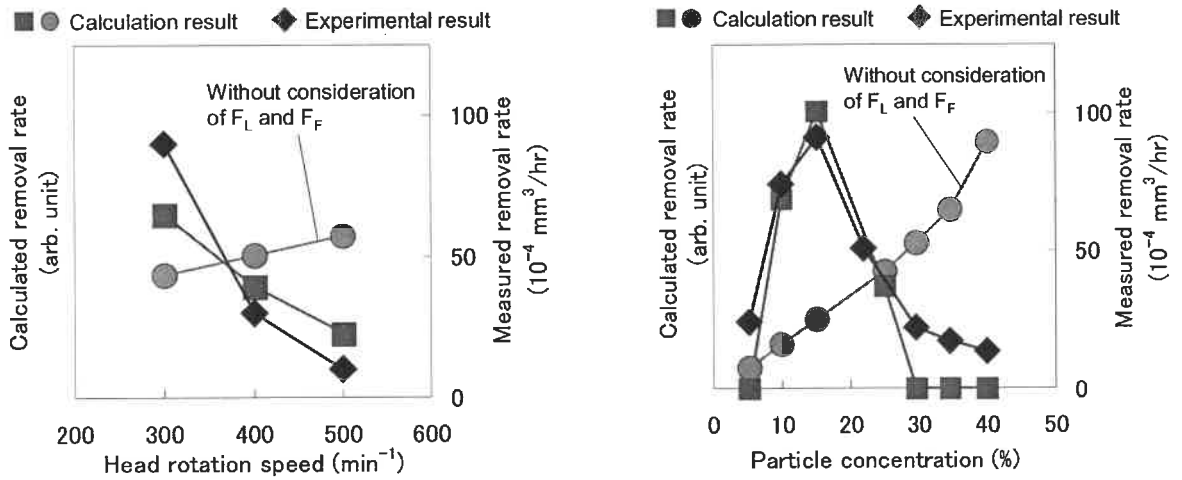

(a) Removal rate vs head rotation speed *(b) Removal rate vs particle concentration*

FIGURE 6. Comparisons of changes in removal rate between calculation and experimental results.

Figure 6 shows comparisons of changes in removal rate between the analysis and experimental results obtained in two experiments.

Three different curves are represented in each graph: one is an experimental result and the other two are calculation results. One of the calculation results is obtained by solving the equations of motion without considering F_L, F_{Fx} and F_{Fz}.

When the forces F_L, F_{Fx} and F_{Fz} do not act on particles, the calculated value is positively correlated with the increase in head rotation speed or particle concentration, completely differing from the measured value. However, when all forces are taken into consideration in the calculations, the calculation curve reasonably agrees with the experimental curve. This indicates that the forces F_L and F_F strongly affect changes in removal rate.

CONCLUSIONS

Removal rate does not simply increase with an increase in the rotation speed of the rotating-sphere head or the concentration of particles in machining slurry.

In the examination of the relationship between removal rate and head rotation speed, removal rate is observed to be negatively correlated with rotation speed.

Moreover, in the examination of the relationship between removal rate and particle concentration, removal rate rapidly decreases after peaking at 15 % (maximal concentration: 40 %).

The causes of these findings were clarified by analyzing the behavior of powder particles at the machining point. Particle behavior is strongly affected by forces acting on a particle generated by a velocity gradient of fluid flow and by a mutual interaction of particles, which results in changes in removal rate.

REFERENCES

[1] K. Yamauchi, K. Yamamura, H. Mimura, Y. Sano, A. Saito, K. Endo, A. Souvorov, M. Yabashi, K. Tamasaku, T. Ishikawa and Y. Mori; Jpn. J. Appl. Phys. Vol. 42, 7129-7134 (2003).

[2] H. Mimura, S. Matsuyama, H. Yumoto, H. Hara, K. Yamamura, Y. Sano, M. Shibahara, K. Endo, Y. Mori, Y. Nishino, K. Tamasaku, M. Yabashi, T. Ishikawa, K. Yamauchi; Jpn. J. Appl. Phys. Vol.44, No. 18, 2005, L539-L542.

[3] K. Arima, A. Kubota, H. Mimura, K. Inagaki, K. Endo, Y. Mori, K. Yamauchi; Surf. Sci. 600, 185 (2006).

[4] M. Kanaoka, C. Liu, K. Nomura, M. Ando, H. Takino, Y. Fukuda, Y. Mori, H. Mumura, K. Yamauchi; J. Vac. Sci. Technol. B 25(6), Nov/Dec 2007, 2110.

[5] P. G. Suffman; J. Fluid Mech. ,22 (1965) 385.

ULTRA PRECISION MACHINE INTEGRATED MEASUREMENT OF SPHERES AND ASPHERES WITH A TWYMAN-GREEN INTERFEROMETER

E. Uhlmann[1], M. Kurz[1], T. Bluemel[2], R. Neubert[2], D. Oberschmidt[1]
[1]Institute for Machine Tools and Factory Management
Technical University Berlin
Berlin, Germany
[2]FISBA OPTIK GmbH
Berlin, Germany

ABSTRACT
The paper discusses the approach and the possibilities of integrating a state of the art, commercially available, Twyman-Green interferometer into an ultra precision lathe, focusing on hardware and software conditions.

INTRODUCTION
Workpieces machined on ultra precision machines with diamond tools have a very low surface roughness of less than *Ra* = 10 nm and the high geometry accuracy, which is generally assumed to be better than 1 µm. Nevertheless, in order to ensure such a high standard, numerous measurements and following corrections are often necessary. There are two established ways of measuring and correcting:
Firstly, there is the machine-integrated measurement via a stylus-based tactile probe, which is delivered with the machine tool from the original equipment manufacturer. Hereby the sensor scans a specific line of the workpiece passing the rotation center. Advantages of the tactile probe are the available machine-integration including suitable software and the robust design, which is appropriate for a harsh manufacturing environment. Disadvantages are the facts that the workpiece has to be rotation-symmetric, the surface is being compromised during measurement, and, due to the use of the machine axes, motion errors caused e.g. by the guidance system are not considered and thus not identifiable.
Secondly, machine external standard tactile or optical measurement systems are utilized. Advantages are the installation in a calm measurement environment, a better efficiency because the device can be used for more than one machine tool, and additionally, even irregularities caused by the machine tool can be captured, and in the case of an optical measurement the surface is not being destroyed. Disadvantageous are the loss in time and positioning accuracy due to the removing and eventual remounting of the workpiece.
Regardless of the type of the used device, after the measurement the result usually can be used to generate a correction NC-program. For this purpose the actual form is compared with the target form by an application (e.g. WEC – workpiece error compensation by Moore Nanotechnology Systems, LLC, USA), which generates a suitable correction NC-program to compensate workpiece errors. These errors are caused in the case of tactile machine-integrated measurement mainly by tool irregularities.

In order to overcome the limitations of tactile, respectively, off-machine measurement and to expand the field of application, the Institute of Machine Tools and Factory Management (IWF) of the Technical University Berlin and FISBA OPTIK GmbH are working together to integrate a state of the art interferometer (FISBA OPTIK µPhase®2) including an adapted correction loop into an 5-axes ultra precision machining system (Nanotech® 350 FG by Moore Nanotechnology Systems, LLC, USA) available at the IWF. The following paragraphes outline the measurement set up, the correction loop realised, a test structure and the first results of a corrected spherical mirror.

SET UP ON THE MACHINE
Interferometers are often seen as lab instruments requiring environment-controlled rooms, skilled operators and enough space for the instrument. Nevertheless, ultra precision machines with their stiff machine bed, hydrostatic oil respectively airostatic bearings and guidance systems with linear motor drives, and high resolution scales are an adequate base for interferometrical measurements regarding vibration, temperature control or positioning. A

prototypical carrier, which is easy to use and rapidly mounted respectively demounted, was designed and built out of standard optic elements to fit on an ultra precision system equipped with a rotary axis (B-axis on the 350 FG) on which both the tool and the interferometer are mounted together (see Figure 1). In order to bring the interferometer into measurement position, the existing machine axes are used. Only the horizontal tilt has to be adjusted manually after mounting due to the nonexisting A-axis.

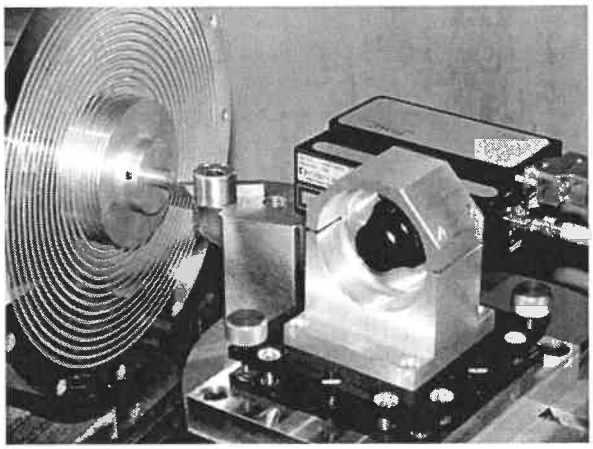

FIGURE 1. Diamond tool and μPhase® interferometer mounted on B-Axis

Switching between processing of the workpiece and measurement is done by simply rotating the B-axis. During the machining of the part, the interferometer remains on the machine. And the lens is protected by a cover to avoid damages and contamination by loose chips. Cables had to be suspended to avoid drawback.

CORRECTION LOOP

When integrating an interferometer directly on an ultra precision machine, besides using it for fast lateral tool adjustment, the next logical step is to use the measurement results to establish a direct in-line correction of the workpiece. With the latter, loss of accuracy can be avoided, which is otherwise inevitable after taking the sample off and placing it again on the machine after an offline measurement. In order to establish a whole correction loop (see Figure 2), the measured 3-dimensional surface has to be transformed into a correction NC-program. This is done by specifically designed algorithms for calculating the deviation between target and actual surface and for generating the tool path.

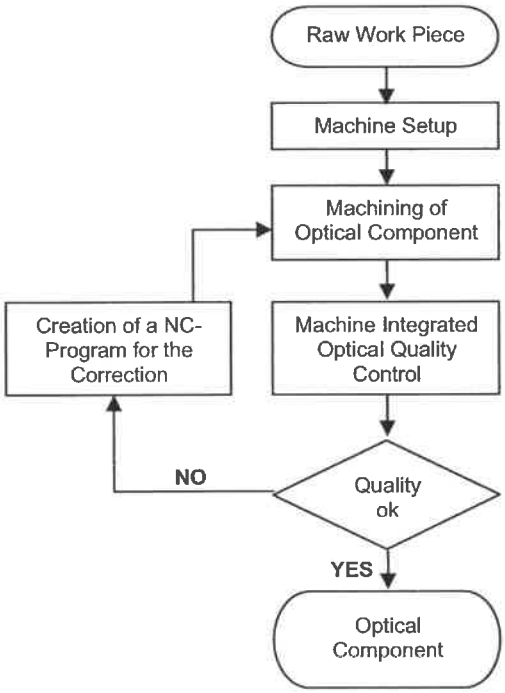

FIGURE 2. Correction loop realized with μPhase® interferometer on Nanotech® 350 FG

TEST STRUCTURE

The FISBA μPhase®2 interferometer uses a spherical coordinate system for measurement. The machine tool operates with the Cartesian coordinate system. To check the correct transformation between the coordinate system of the measurement device and that of the machine tool, an aspheric test structure with measurable and distinguishing rotation-symmetric marks of known shape was designed. Using an uncontrolled diamond tool with a radius of about $r_\varepsilon = 1.5$ mm and a cutting edge waviness of $w_{ce} < 2$ μm, a spherical brazen part with diameter $D = 8$ mm and curvature $R = 15$ mm was superimposed with rotation-symmetrical radial sinus waves with peak-to-valley amplitudes of $PV = 1$ μm and wave lengths of $\lambda = 1$ mm. Immediately after the machining process the sample was measured by the FISBA OPTIK μPhase®2 Interferometer, which returns a 3-dimensional measurement of the whole sphere. This surface topography was used to compute the 2-dimensional surface deviation shown in Figure 3.

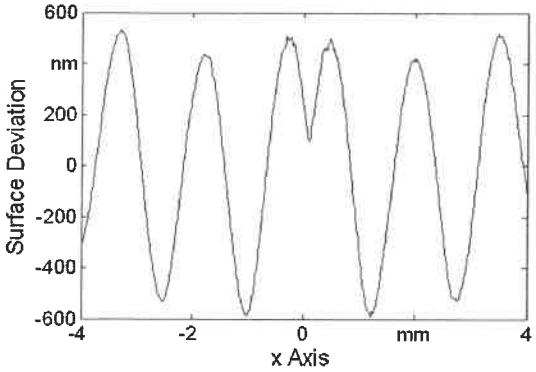

FIGURE 3. Measurement result of a test sphere with superimposed sine waves.

Using this result and the sphere without the sinus waves as target form, the deviation between target and actual form was calculated. Therewith the tool path for the correction run was generated. With the resultant NC-program the part was remachined remaining on the vacuum chuck of the machine during the whole procedure. Figure 4 shows the calculated 2-dimensional measuring result of the corrected workpiece. Outcome is a peak to valley value well below PV = 200 nm, which was found to be acceptable for further measurements.

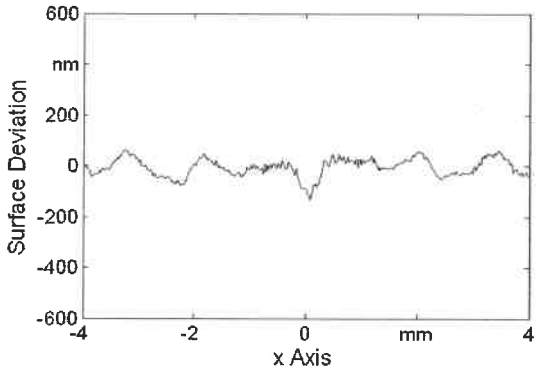

FIGURE 4. Measurement result of the corrected asphere from Figure 3.

OPTICAL MEASUREMENT ON THE MACHINE

The test part with a diameter of D = 8 mm is rather small. In order to show the feasibility of the correction loop a larger sphere with a diameter of D = 100 mm was chosen and machined, measured and corrected with the same means as in the test part procedure. Figure 5 shows the initial measurement result with a surface deviation of more than 400 nm.

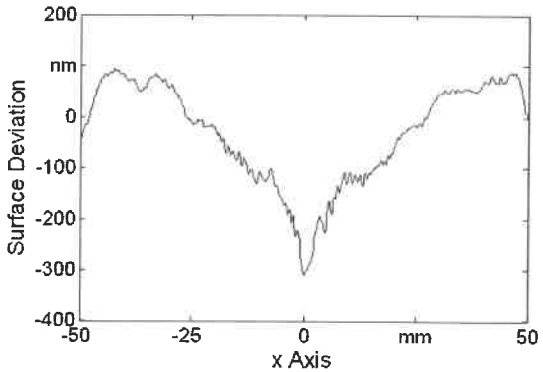

FIGURE 5. Measurement result of a sphere (D = 100 mm, R = 160 mm)

After the correction run the surface deviation has been diminished down to 100 nm shown in Figure 6.

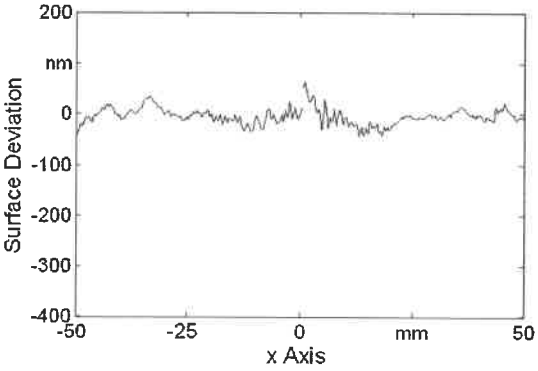

FIGURE 6. Measurement result of the sphere from Figure 5 after the correction run.

CONCLUSION

Optical measurements with a state of the art and commercially available interferometer directly on an ultra precision machining system are possible. The realized correction loop has shown significant improvement regarding the surface deviation compared to an uncorrected asphere respectively sphere. The benefits of an integrated optical measurement device are a faster tool adjustment in lateral direction and the establishment of a correction loop with the possiblilty to measure rapidly, 3-dimensionally, non-destructively, and without moving the workpiece.

ACKNOWLEGEMENT

This research work was sponsored by the German government, Bundesministerium für Wirtschaft und Arbeit, under the PRO INNO II program, project „MeTAsO“ (KF0084101WM4).

ULTRA PRECISION MACHINING DISTURBANCE FREQUENCY EXTRACTION FROM FINISHED SURFACE METROLOGY

Paula A. Meyer[1], Stephen C. Veldhuis[1], and Mohamed A. Elbestawi[1]
[1]Department of Mechanical Engineering
McMaster Manufacturing Research Institute (MMRI)
McMaster University
Hamilton, Ontario, Canada.

1. INTRODUCTION

Diamond face turning is a type of ultra precision machining, a special branch of machining which includes micrometric form accuracy and nanometric surface finish [1]. To achieve these requirements, any unwanted movement between the cutting tool and workpiece must be addressed, and its impact on the finished surface mitigated or eliminated. This movement includes small amplitude vibration. Determining vibration frequency from a measured workpiece presents a powerful tool to identify and correct process disturbances.

This extended abstract studies the effect of harmonic relative tool / workpiece vibration on a diamond face turned surface, and demonstrates via simulation how a disturbance frequency can be extracted from a measured surface topography. A model is derived that uses available metrology equipment such as a Zygo Newview 5000 white light interferometry system. Simulation studies show that the frequency of vibration can be discerned from the waviness pattern on a machined surface in the feed direction.

2. THE SURFACE METROLOGY SYSTEM

Waviness is a surface finish error with wavelength greater than surface roughness (feed) and less than form error. On a diamond face turned workpiece waviness is the dominant type of surface error. In-situ displacement measurements of relative tool / workpiece movement in the in-feed direction is a challenge due to the nanometric levels associated with ultra precision machining, and the potential for broadband disturbances. However, the Zygo provides the opportunity to make such determinations post-machining.

Face turning is a continuous cutting process. The machined workpiece surface resembles a spiral. This surface contains the history of the relative tool / workpiece motion in the in-feed direction. If the spiral were uncurled, a time series of motion would be produced. This concept is illustrated in Figure 1.

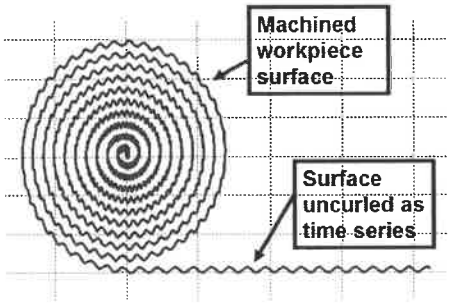

FIGURE 1. Spiral created on face turned surface and uncurled spiral with in-feed cutting information as a time series.

2.1 Surface Metrology Challenges

Resolution and Field of View

The Zygo measures a very precise topography of planar data in the in-feed direction, however the number of pixels is limited to 640x480 in this case. If a larger workpiece area is sought, the resolution is compromised. Thus while accurate, the Zygo image only samples a small portion of the surface. The result is a sparsely sampled time series as illustrated in Figure 2.

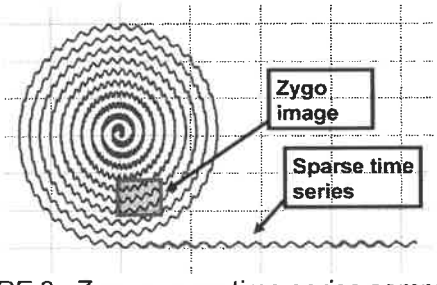

FIGURE 2. Zygo sparse time series sampling

With respect to the Zygo image size, a 6061 aluminum workpiece with 100 mm outer diameter is considered. For finish turning conditions, a spindle speed of 1000 RPM and feed rate of 2 μm/rev is employed. According to [2] with respect to interferometric microscopy, the shortest wavelength is measurable with 5 pixels. In the feed direction, the shortest expected wavelength is the feed at 2 μm. Thus the largest recommended resolution is 0.4 μm. The most appropriate available Zygo zoom for these requirements is 800 times, with resolution of 0.28 μm. The resulting image size is 180 μm by 140 μm. If the y-axis is the feed direction, then the maximum observable feed direction wavelength is 140 μm with this particular zoom and resolution.

Constantly Changing Cutting Speed and Time Interval

Further complications arise from the fact that the feed rate and spindle speed used are constant. This means that the effective cutting speed changes constantly during face turning. A Zygo image has fixed spatial sampling, and thus the corresponding time interval in the sparsely sampled time series is not constant.

3. DERIVATION OF EQUATIONS

Relative tool / workpiece motion in the in-feed direction, z(t), is assumed to be harmonic with disturbance frequency ω_d and constant amplitude z_{amp} as described in equation (1). By superposition, if other harmonic motion exists, then the values can be summed together.

$$z(t) = z_{amp} \sin(\omega_d t) \tag{1}$$

3.1 Derivation to Accommodate Surface Metrology System

Re-expressing equation (1) in polar coordinates in the feed direction addresses some of the issues identified in the previous section like a sparsely sampled time series, and a variable time interval. In equation (2) angle θ is the rotation of the workpiece, and is a function of time and spindle speed.

$$z(\theta) = z_{amp} \sin\left(\frac{60\omega_d \theta}{2\pi N}\right) \tag{2}$$

Next consider a workpiece that is discretized radially as shown in Figure 3, where each spoke is called θ_{1p}. Subsequent rotations add 2π radians to each θ_1 value. For any given spoke p, equation (3) applies, where m is an integer representing the number of rotations.

$$z(\theta_{mp}) = z_{amp} \sin\left[\frac{60\omega_d}{2\pi N}\left(2\pi m + \theta_{1p}\right)\right] \tag{3}$$

This derivation is similar to that found in [3], [4], [5] and [6]. Details on the tool geometry are not included in this simulation.

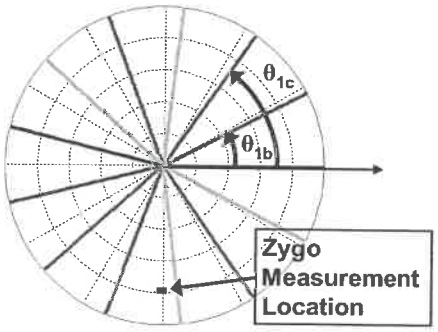

FIGURE 3. Radial discretization of workpiece with Zygo measurement location noted.

Equation (3) is in the classical configuration of an angular velocity and phase angle. Here angular velocity is in radians per rotation as expressed in equation (4), and phase angle is in radians as expressed in equation (5).

$$\Omega = \frac{60\omega_d}{N}\left(\frac{radians}{revolution}\right) \tag{4}$$

$$\phi(p) = \frac{60\omega_d \theta_{1p}}{2\pi N}\left(radians\right) \tag{5}$$

Equation (4) indicates that regardless of the spoke in question, θ_{1p}, for constant spindle speed and disturbance frequency, the spatial frequency in the feed direction is always the same.

Thus, if a spatial Fast Fourier Transform (FFT) is performed on a Zygo image of feed lines, then all feed lines should yield the same magnitude information. However, due to the cyclical nature of the sine wave, various disturbance frequencies for a given spindle speed will yield the same spatial frequency magnitude results. However, from equation (5) it is also evident that the phase angle for each spoke is unique.

From equation (5) an expression to find the unique disturbance frequency for a dominant

spatial waviness pattern can be found from a Zygo image. Subscripts a and b in equation (6) represent spoke indices for closely spaced feed lines in the Zygo image.

$$\omega_d = \frac{60\left|\theta_{1b} - \theta_{1a}\right|}{2\pi N\left|\phi_{1b} - \phi_{1a}\right|} \qquad (6)$$

4. SIMULATION AND RESULTS

A Zygo measured surface is simulated in Matlab with a known disturbance frequency ω_d and amplitude z_{amp}. The disturbance frequency used is from an experimental data set. Then from the simulated surface, without knowing it a priori, the disturbance frequency is extracted via equation (6). Following this a comparison is made between the actual and estimated disturbance frequency.

4.1 Experimental Data Used in Simulation

In-situ vibration measurements have been made on an ASG 2500 diamond turning machine using a Kistler 8702B50 accelerometer and a 8702B25 accelerometer at the tool and spindle locations respectively. Signals are analogue anti-alias filtered, and sampled synchronously with a NI PCI-6023E. In Matlab the signals are differenced for relative acceleration, and an FFT is then performed to see the dominant disturbance frequencies. For the cutting conditions described in Section 2, the power spectrum in Figure 4 is produced. A dominant observed disturbance frequency of 4928.2 Hz is used in simulation.

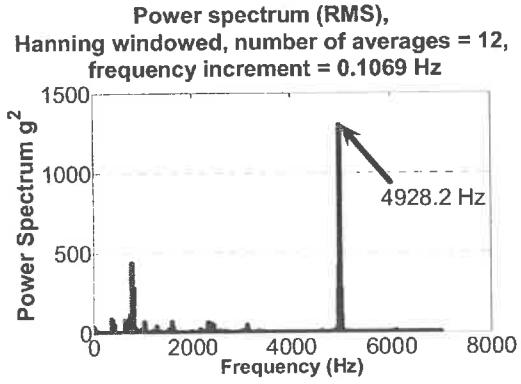

FIGURE 4. Power spectrum of relative tool / workpiece acceleration on ASG 250

For simulation, the workpiece surface is assumed to be measured at a radius of 40 mm with feed direction along the y-axis, and the cutting direction along the x-axis. Using the orientation shown in Figure 3, the median image θ_1 is $\frac{3\pi}{2}$ radians.

4.2 Simulation Results

With the dominant disturbance frequency of 4982.2 Hz observed in Figure 4, the resulting wavelength in the feed direction is 29.43 µm and observable in the 800 times zoom field of view according to [2]. The amplitude z_{amp} used in simulation is 1 nm. The simulated Zygo image is shown in Figure 5. The x and y axis values are the workpiece coordinates which have their origin at the workpiece center.

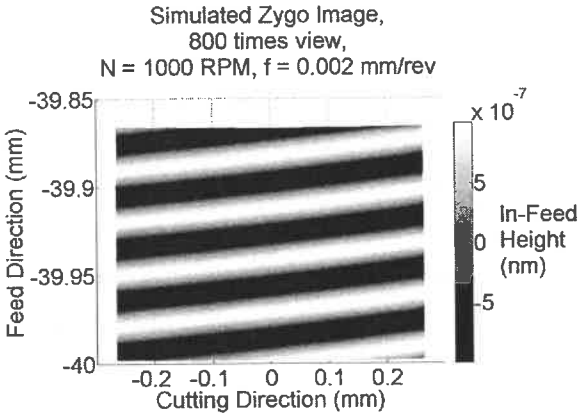

FIGURE 5. Simulated Zygo image with disturbance frequency of 4928.2 Hz.

In Figure 6, five equally spaced feed lines are plotted. Here the phase angle shift is observable. For illustration purposes, the feed line spacing that is depicted in Figure 6 is larger than the image θ_1 resolution of 0.0016 degrees, and is still within the bounds of the Zygo image.

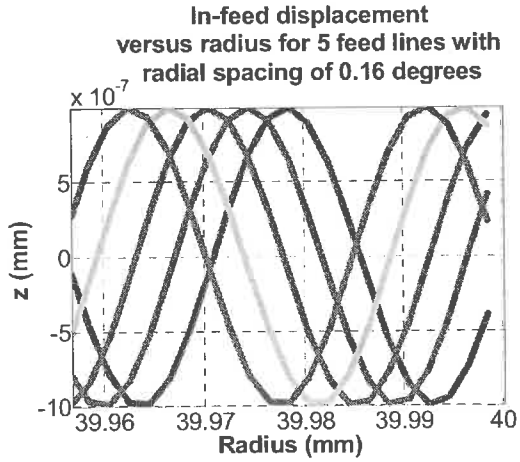

FIGURE 6. Five equally spaced feed lines demonstrating change in phase angle.

In Figure 7 the magnitude and wrapped phase angle for the spatial FFT of each feed line are depicted. Data is first Hanning windowed. The peak magnitude is observed at a spatial frequency of 33.95 1/mm, which is equivalent to a wavelength of 29.5 μm. As previously noted, this wavelength value could be associated with a number of different disturbance frequencies.

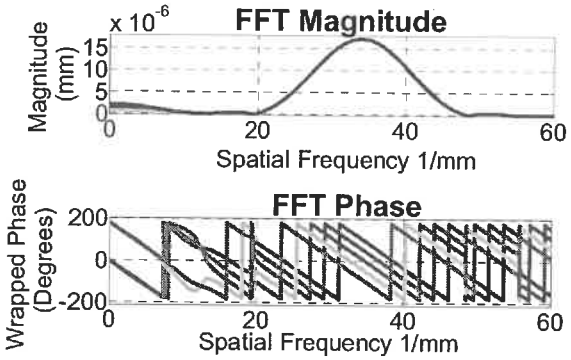

FIGURE 7. Spatial FFT for each feed line.

Effectiveness of Finding Disturbance Frequency in Simulated Zygo Image

The wrapped phase angles for each feed line at the spatial frequency associated with a peak magnitude are shown in Figure 8. The radial and phase angles in conjunction with the spindle speed are used in equation (6) to find the disturbance frequency ω_d.

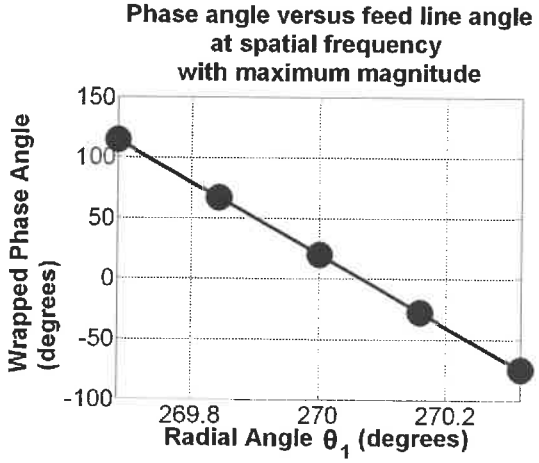

FIGURE 8. Phase angle for each feed line at peak FFT magnitude frequency.

Finally, in Table 1 the disturbance frequency estimates found via simulation and equation (6) are shown along with per cent error for each adjacent feed line pair. The error is significantly less than 1 per cent.

TABLE 1. Disturbance Frequency found with phase angle and per cent error.

f_d estimate (Hz)	% Error
4977.7	0.090
4981.0	0.024
4986.9	0.094
4982.6	0.008

5. CONCLUSION

For diamond face turning, it has been demonstrated with simulation that disturbance frequency causing a waviness error can be discerned from a surface measured via a Zygo image using spatial FFT information in the feed direction. This methodology presents the potential to understand and correct disturbances responsible for creating unwanted waviness patterns on diamond face turned surfaces.

ACKNOWLEDGEMENT

The authors wish to acknowledge the support of the Ontario Centre of Excellence, the Natural Sciences and Engineering Research Council of Canada, and B-Con Engineering.

REFERENCES

[1] Ikawa N, Donaldson R, Komanduri R, König W, McKeown P, Moriwaki T, Stowers I. Ultraprecision Metal Cutting - The Past, The Present and the Future. Annals of the CIRP. 1991; 40(2): 587-594.

[2] The American Society of Mechanical Engineers (ASME). ASME B46.1-2002 Surface Texture (Surface Roughness, Waviness, and Lay) An American National Standard. New York; 2002.

[3] Takasu S, Masuda M, Nighiguchi T. Influence of Study Vibration with Small Amplitude Upon Surface Roughness in Diamond Machining. Annals of the CIRP. 1985; 34(1): 463-467.

[4] Cheung C, Lee W. A Multi-Spectrum Analysis of Surface Roughness Formation in Ultra-Precision Machining. Precision Engineering. 2000; 24: 77-87.

[5] Cheung C, Lee W. Modelling and Simulation of Surface Topography in Ultraprecision Diamond Turning. Proceedings of the Institution of Mechanical Engineers, Part B: Journal of Engineering Manufacture. 2000; 214: 463-480.

[6] Cheung C, Lee W. Characterisation of Nanosurface Generation in Single-Point Diamond Turning. International Journal of Machine Tools & Manufacture. 2001; 41: 851-875.

DEVELOPMENT OF CAPP/CAM SYSTEM FOR ULTRAPRECISION MICROMACHINING

Takanobu Oba[1], Tohru Ishida[1], Yoshimi Takeuchi[1]
[1]Department of Mechanical Engineering
Osaka University
Yamadaoka 2-1, Suita, Osaka 565-0871, Japan

INTRODUCTION

In recent years, miniaturization draws attention to integrate electronics device, optical and optoelectroc instruments. This proceeds the sophistication and miniaturization of parts constructing these device and instruments. Complicated 3-D microparts can be created by the development of multi-axis control ultraprecision machining centers [1]. Multi-axis control machining has several advantages, i.e. to be able to use short tools and to avoid the resetting of workpieces. 3-D CAD/CAM systems for multi-axis control micromachining are also developed to save time and labor in preparing numerical control data. However, operators consume a long time in process planning since there are few computer systems that help process planning for micromachining. Therefore, operators have to make the process plan, based on empirical knowledge and intuition. In the near future, the demand for microparts will grow further, and the reduction in machining lead-time will be requested, too. It is vital to develop CAPP (Computer Aided Process Planning) system for 3-D ultraprecision micromachining in response to these demands.

The study deals with the development of fundamental CAPP/CAM system for multi-axis control 3-D micromachining. Miniaturization of cutting tools causes the stiffness degradation, thus resulting in the unstable machining condition. Therefore, operators have to decide processing strategy, while taking it into consideration. The system developed in the study can decide tool posture in 5-axis control machining automatically, considering the above matter. The strategy of deciding the tool posture is in the following manner. Firstly, tool collision between tool and workpiece must be avoided. In 5-axis control machining, it is difficult for operators to estimate the movement of tool and workpiece before machining. Therefore, CAM system has to provide the collision check function. Secondly, the system aims at reducing the tool posture change in multi-axis control machining, because the accuracy of rotational axes affects the machining accuracy. Thirdly, the important thing is to use a shorter tool. In 5-axis control machining, it is more difficult to estimate tool length than 3-axis control machining because various tool postures are allowed. The use of short and high stiffness tool enables stable machining. Conventional CAM system for 5-axis control machining places an emphasis on tool collision avoidance. The tool length and the amount of tool posture change are not necessarily considered. In the study, tool entrance face concept [2] is used to realize this strategy. Tool attitude is decided by optimizing shape and position of tool entrance face.

TOOL ENTRANCE FACE CONCEPT

Figure 1 shows concept of tool entrance face concept. Tool entrance face is the surface which defines tool posture to machining a surface. The tool path generation method that uses tool entrance face is as follows. A tool center point is generated, based on a point on offset surface. A tool axis vector is obtained by connecting a point on the offset surface with a point on the tool entrance face, as illustrated in Figure 1(b). The two surface are represented with u-v parameters. So, a point on the surface is determined by a pointing a set of u-v parameter. Thus, a tool center point and a tool axis vector are determined almost at the same time. In addition, continuously changing tool path can be generated by changing parameters continuously, for instance, changing parameters along isoparametric curve.

The procedure of the tool entrance face generation is as follows. In the first step, the offset surface is generated, which is the surface being offset in the

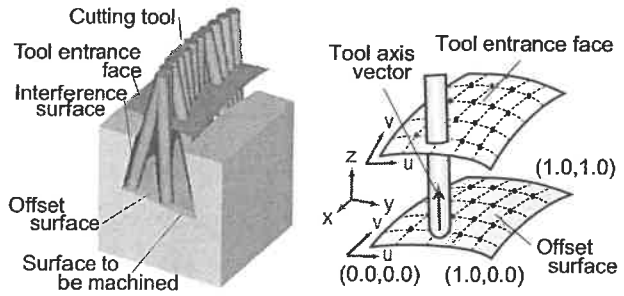

(a) Tool pass for deep groove. (b) Relationship between tool entrance face and tool axis vector.

FIGURE 1. Tool entrance face concept.

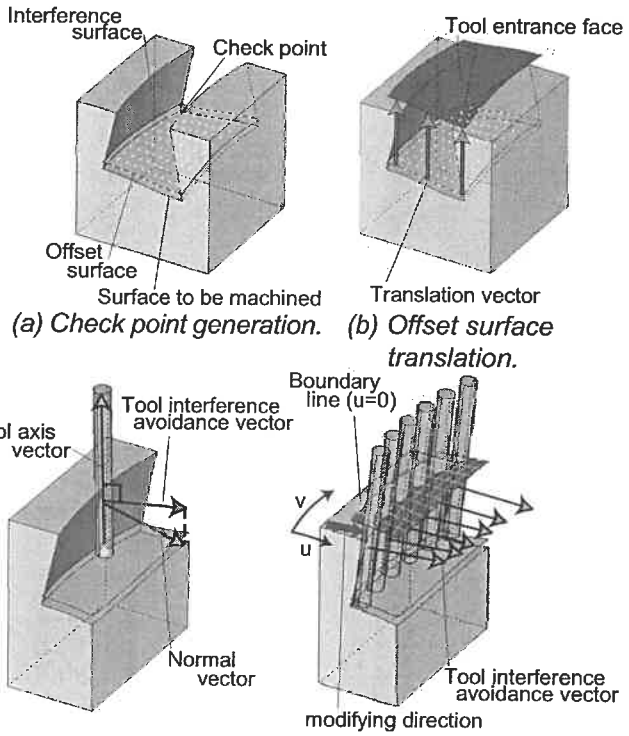

(a) Check point generation. (b) Offset surface translation.

(c) Tool interference avoidance vector calculation. (d) Relationship between tool interference avoidance vector and modifying direction.

FIGURE 2. Tool entrance face generation.

normal direction by a tool radius. On the offset surface, check point is generated by dividing the offset surface parametrically, as shown in Figure 2(a). In the next step, tool entrance surface is generated by translating offset surface, as illustrated in Figure 2(b). Tool axis is determined by connecting a check point and a point on tool entrance face which is represented by the same parameters. Then tool collision is checked. If the tool which is determined by the tool entrance face and check point interferes with workpiece model, boundary of tool entrance face is modified. This operation is repeated until cutting tool does not interfere with workpiece.

The entrance face is modified by a shrinking method. This method assumes that the surface to be machined is quadrilateral one. Therefore there are four boundary lines which are moved to modify tool entrance surface. Which boudary line is moved is decided by the following manner.Firstly, all check points, where the tool interferes with workpiece, are selected. Secondly, the normal vector in the region which interferes with tool is calculated. The component of the normal vector, orthogonal to the tool axis vector, is set as tool interference avoidance vector, as illustrated in Figure 2(c). Thirdly, to which isoparametric direction of tool entrance face the tool interference avoidance vector points is examined. There are four isoparametric directions.+u, -u, +v and -v. In this figure, the tool interference avoidance vector points to +u direction. The direction to which the most tool interference avoidance vectors point is set as modifying direction. The boundary line which crosses modifying direction is moved in modifying direction. In Figure 2(d), all tool avoidance vector point to +u direction, therefore the boundary line on which u=0 is moved in the direction of +u. By this method it becomes possible to modify tool entrance face, considering the state of tool interference on the entire surface.

SEARCH FOR TOOL ENTRANCE FACE GENERATING DIRECTION

The way of generating tool entrance face allows various directions. The direction of generating tool entrance face affects the entire tool posture on surface to be machined. The search for the tool entrance face generation direction optimizes tool posture so that shorter tool can be used and tool posture change in machining can be reduced.

The tool length is estimated by accessible cone [3]. The top of the cone is set on a check point and the center axis of the cone is equal to tool center axis, as illustrated in Figure 3. The apex angle of accessible cone is set so that the conic surface can contact with workpiece model. The tool which is inside of the cone does not interferes with workpiece model. The lareger apex angle is, the shorter tool can be used. Accessible cone is calculated at all collision check points. The smallest apex angle among them is selected.

Tool posture change in machining is evaluated by

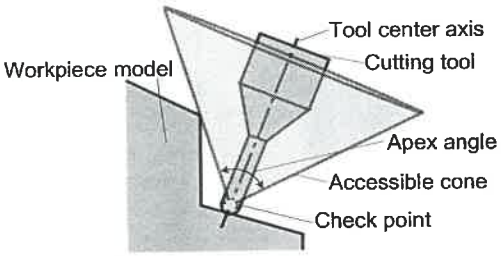

FIGURE 3. Accessible cone.

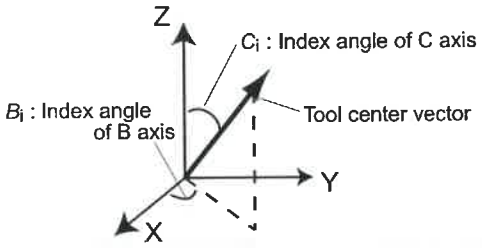

FIGURE 4. The way of calculating an index angle.

estimating travel distance of machine tool. The system assumes the use of 5-axis control machining center which is equipped with three translational axes (X, Y, Z) and two rotational axes (B, C).Tool position is set by translational axes and tool posture is set by rotational axes. The system evaluates travel distance of rotational axes. Figure 4 shows the way of calculating index angle, based on tool axis vector. The travel distance of rotational axes d is obtained by the following equation (1).

$$d=\sqrt{\sum_{i=1}^{n-1}\left\{(B_i-B_{i+1})^2+(C_i-C_{i+1})^2\right\}} \qquad (1)$$

In this study, lexicographic comparison is used to evaluate the direction of generating tool entrance face. The priority of evaluation is set in order of the travel distance of rotational axes and the apex angle of accessible cone. In other words, the travel distances of rotational axes that is calculated from each tool entrance face are compared first. Next, if they are equaly small, the apex angles of accessible cone are compared.

The area where tool entrance face can be generated is limited. So the system roughly searches the direction from which the surface to be machined is visible. At first, the faces of workpiece model are approximated by triangle polygons, as illudtrated in Figure 5. The line of sight direction is discretized and represented by two angles θ and ϕ, which are divided into equal interval $d\theta$ and $d\phi$. θ and ϕ correspond to the index angle of C and B axes respectively. Then, the number of visible facet of surface to be machined is counted on each line of sight direction and set to n_i. Maximum n_i is set to n_max. The line of sight

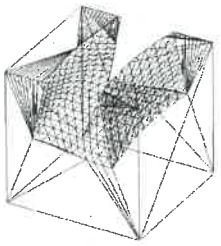

FIGURE 5. Workpiece model approximated by triangle polygons.

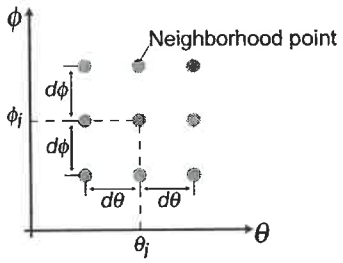

FIGURE 6. The way of generating neighborhood points.

direction on which α percent of n_max or more facet is visible are set to start point of the next local search.

Next, local search is conducted to generate tool entrance face. The procedure is as follows:

1: Tool entrance face is generated by translating offset surfece in the direction of translational vector $\mathbf{Tr}_i$. The translational vector $\mathbf{Tr}_i$ is obtained by following equation (2). D represents the distance of translation.

$$\mathbf{Tr}_i=\left(D\sin\theta_i\cos\phi_i \quad D\sin\theta_i\sin\phi_i \quad D\cos\theta_i\right) \qquad (2)$$

2: Calculating apex angle of accessible cone, ap_i, and travel distance of rotational axis, d_i, for each tool entrance face.

3: Sorting the list of tool entrance face generating direction $\mathbf{Tr}_i$ by lexicographic comparison.

4: Selecting rank in the top β % of the list as the start points of next local search.

5: Generating neighborhood points, as illustrated in Figure 6, and renewing the list of tool entrance face generating direction. Rank in top β % of the list and 8 neighborhood points are newly set to the list.

6: Shrinking the search area by following equation (3). If $d\theta$ and $d\phi$ are less than ε, local search is end. If not so, return to 1:.

$$d\theta=\gamma\times d\theta \qquad d\phi=\gamma\times d\phi \qquad (3)$$

ROUGH CUTTING USING TOOL ENTRANCE FACE

Tool entrance face concept is effective in finish cutting because workpiece shape is almost same as target shape. However, it is difficult to apply tool entrance face concept for rough cutting. Our previous study [4] proposes a method that helps decision of tool posture for 3+2 axis control rough cutting. However, the method does not consider finish cutting. The system developed in this study uses tool postures obtained from tool entrance

face for deciding index angle of 3+2 axis control rough cutting.

Tool posture is set at each check point by tool entrance face concept. The use of these tool postures as the index angle enables 3+2 rough cutting. However, there are some index angles that is not indispensable. Our previous study proposes a method picking out the minimal index angle by multi-stage decision process. The sysytem developped in the study also uses accessible cone concept to decide index angles. The accessible cone required for finish cutting is already obtained. To use shorter tool also in rough cutting, the apex angle of accessible cone must be larger than that for finish cutting. The procedure considering this matter is as follws:

1: Calculating machining possibility matrix. Machinability of each tool posture is checked at each check point. Machinability is judged in terms of tool interference and apex angle of accessible cone. If an apex angle of accessible cone is smaller than that of finish cutting, the combination of the tool posture and collision check point is not machinable.
2: Calculating accesible cone list. Accessible cones that is required to machine all machinable collision checkpoint in each tool posture is set to the list.
3: Choosing the check point that cannot be machined by the tool posture that is chosen before referring to machining possibility matrix. The check point with the least number of tool posture which can machine the point is selected from among those interference check points. One of the tool posture which can machine the point is chosen. This operation is repeated until all points can be machined.
4: Tool posture sequence with least number of tool posture change and maximum accessible cone is selected as the best tool posture sequence.

According to the process above mentioned, tool posture sequence for rough cutting with less possibility of tool interference and less tool posture change is obtained.

SIMULATION

To confirm the proposed method, the simulation is conducted by using CAD workpiece model. Figure 7 shows a CAD model of impeller. Figure 8 shows the tool posture that is obtained by proposed method. The parameters for search is as follows. $d\theta$=5, $d\phi$=5, α=80, β=10, γ=0.5,D=30, ε=0.6. Table 1 lists the index angle for rough cutting

FIGURE 7. Target shape. *FIGURE 8. Tool pass.*

TABLE 1. Index angles for rough cutting.

Tool posture	Index angle [degree]	
	B axis	C axis
1	220.8	46.8
2	228.0	39.1

that is obtained by the method above mentioned.

CONCLUSION

To carry 3-D micromachining automatically, the study develops fundamental CAPP/CAM system for micromachining. The study develops tool posture decison method in multi-axis control machining, considering tool length and distance of tool posture change. The potential of realizing CAPP/CAM function for micromachining is confirmed by simulation.

REFERENCES

[1] Y. Takeuchi, H. Yonekura, K. Sawada, Creation of 3-D tiny status by 5-axis control ultraprecision machining. Computer-Aided Design, 2003; 35: 403-409.

[2] Takehiro INOUE, Tohru ISHIDA and Yoshimi TAKEUCHI, Rapid 5-Axis Control Tool Path Generation by Means of Interference-free Space Concept. Proceedings of the 4th International Conference on Leadinf Edge Manufacturing in 21st Century, 2007; 489-494.

[3] Kunimori Morimoto and Masatomo Inui, Study on Computer-Aided Process Planning of Mold Part Machining - An Algorithm for Determing the Optimal cutting Direction for Deep mold Machining -. Journal of the Japan Society for Precision Engineering (in Japanese), 2007; 73: 286-290.

[4] UMEHARA Takeshi, ISHIDA Tohru, TERAMOTO Koji, TAKEUCHI Yoshimi, Effective Tool Pass Generation Method for Roughing in Multi-axis Control Machining (Machine Elements and Manufacturing). Transactions of the Japan Society of Mechanical Engineers. C (in Japanese), 2007; 73: 2387-2393

HISTORICAL NOTE ON DYNAMIC STRAIN MEASUREMENTS

Richard L. Rhorer
Manufacturing Process Metrology Group
Manufacturing Metrology Division
National Institute of Standards and Technology
Gaithersburg, Maryland, USA

INTRODUCTION

Starting in the 1950s, Dr. James F. Bell, Professor of Solid Mechanics at the Johns Hopkins University, started experimenting with high-strain rate measurements using a diffraction grating strain gage apparatus. He used this type of apparatus for a number of years and published many related papers and books reporting on this work, including his book [1] which presents a large amount of data on the dynamic properties for many different metals.

The Bell diffraction grating approach for dynamic material properties is not used today. The almost universal approach is to use a Split Hopkinson Pressure Bar, also called the Kolsky Bar after Professor H. Kolsky of Brown University, to determine the dynamic stress-strain curves for metals. This apparatus does not require the production of a diffraction grating. In the Kolsky bar the strain in the sample is calculated by using variable-resistance electrical gages that measure the elastic strain in a long high strength steel bar that carries the stress wave that deforms the sample. The construction and operation of the Kolsky bar apparatus is well described in the ASM Handbook [2], and a Kolsky bar apparatus has been built at NIST. Since 2002 the NIST Pulse Heated Kolsky Bar Apparatus has been used to determine dynamic mechanical properties [3].

The modern digital image correlation (DIC) techniques of measuring dynamic strain may prove to be a valuable improvement to the traditional Kolsky bar. The work summarized in this ASPE presentation is part of an effort to investigate techniques for calibrating DIC in highly dynamic situations, as well as a comparison study of the Kolsky bar method with Bell's classical diffraction grating approach.

STRAIN AND DIFFRACTION GRATINGS

A normal reflective diffraction grating is a series of closely spaced parallel grooves. Many commercial gratings are replicas of a master grating produced on a precision ruling machine. When a monochromatic beam of light is directed at a grating, as shown schematically in Fig. 1, the angle of the diffracted light beam can be determined if the line spacing, a, and the wavelength of the light, λ, are known. The simple grating equation is:

$$\sin\theta = \frac{n \cdot \lambda}{a} \qquad (1.1)$$

where n is the order of the diffracted beam.

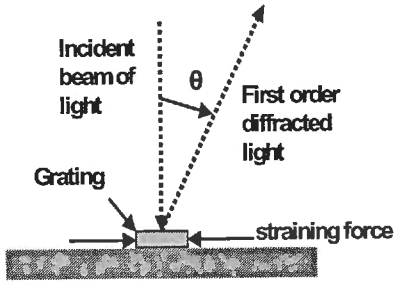

FIGURE 1. Diffraction grating geometry.

When the grating is either attached to a test specimen or ruled directly on the specimen, any strain in the specimen causes a very slight change in the groove spacing. An experimental apparatus that can accurately measure the angle of the diffracted light can then be used to measure the strain in the sample. The strain can be expressed as:

$$\varepsilon = \frac{(a - a_0)}{a_0} \qquad (1.2)$$

where a_0 is the initial line spacing and $(a - a_0)$ is the change in line spacing caused by strain ε. The strain in terms of the diffraction angle is then, using equation (1.1):

$$\varepsilon = 1 - \frac{\sin\theta_0}{\sin\theta} \qquad (1.3)$$

where θ_0 is the angle measured prior to straining the specimen. A more general expression of the grating equation can be written that involves the case where the grating is

tipped from the normal direction which may occur in a real application.

BELL'S STRAIN GAGE

Professor Bell developed the grating strain gage as a sophisticated apparatus that measured the diffraction angle with very high time resolution using photomultiplier tubes and oscilloscope recorders. The apparatus used by Professor Bell is shown in Fig. 2. This system allowed the strain-time history of the sample to be recorded during an impact of the sample by a projectile fired from an air gun. The diffraction gratings on Bell's cylindrical samples were machined using a specially built ruling engine based on a small commercial lathe. The Bell lathe/ruling engine could rule 35,000 lines per inch (1378 lines per mm) for short distances, usually a 0.005 inch (125 μm) long gage section, on the approximately 25 mm diameter cylindrical samples. The Bell lathe was apparently used to make thousands of samples over a number of years. We would judge this machine as a truly ultra-precision machine tool even by modern standards.

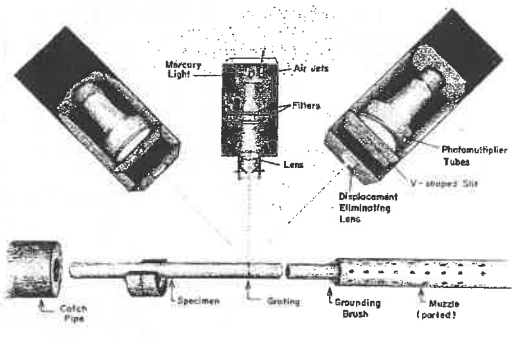

FIGURE 2. Bell's diffraction grating based measuring apparatus (copied from Bell [1], page 12.)

Professor Bell states that the design of the Bell lathe was influenced by the tradition of making gratings at Johns Hopkins University [4], in particular the making of precise screws for ruling engines. The production of astronomical diffraction gratings at Johns Hopkins by Professors Rowland, Anderson, Wood, and Strong from the 1880s up through the 1950s is well documented by Strong [5] and others. Chris Evans in his book on the history of precision engineering refers to the work at Johns Hopkins University on ruling engines and their influence on precision engineering [6].

DISCUSSION

The apparatus used by Professor Bell has several advantages. The strain gage is an integral part of the sample and will not come off—even at very high strains and strain rates—during an impact experiment, for example. The precision engineering question is: can a grating on a cylindrical sample, like those produced by Professor Bell in the 1950s, be produced using a modern diamond turning machine? An interesting project would be to not only answer this question but also conduct an experiment in our Kolsky bar with a sample that has a grating machined on it. The results of such an experiment would allow a direct comparison between the Kolsky Bar approach and the grating strain gage.It appears possible to use modern ultra-precision machining capabilities to produce gratings on samples quickly and cost effectively. Using a dead-sharp diamond tool and a feed of 0.725 μm per revolution a grating could be produced with the same number of lines per mm that was produced on the Bell lathe. In Bell's gratings the tool used was not an actual cutting tool, but a "boat" shaped diamond tool that raises a small ridge as it produces the groove. The diamond tool was weighted slightly and followed the surface of the cylinder. We are proposing to try an actual cutting tool to produce a grating on an aluminum sample. We can then dynamically test the sample with the grating machined on its surface in our Kolsky bar.

REFERENCES

[1] Bell, James F., *The Physics of Large Deformation of a Crystalline Solids*, Springer Tracts in Natural Philosophy, Vol.14, Springer-Verlag, NY, 1968.

[2] Gray, G.T. III, Classic Split-Hopkinson Pressure Bar Testing, *Vol.8, ASM Handbook 10th Ed,* American Society of Metals, p. 462-469, 1998.

[3] Rhorer, R.L., Dynamic Material Properties for Machining Simulation using the NIST Pulse-Heated Kolsky Bar, ASPE Proc., Portland, 2003.

[4] Bell, J. F., Diffraction Grating Strain Gauge, Soc. Exp. Stress Analysis Proc. Vol. 17-2, pg. 51 -64, 1959.

[5] Strong, J., The John Hopkins University and Diffraction Gratings, J. of the Optical Soc. of Am., Vol. 50, No.12, pg 1148-1152, 1960.

[6] Evans, C.J., *Precision Engineering: An Evolutionary View*, Cranfield, 1989.

APPLICATION OF MAGNETORHEOLOGICAL JET (MR JET®) IN PRECISION FINISHING

Aric B. Shorey[1], Justin P. Tracy[1], and William I. Kordonski[1]
[1]QED Technologies
Rochester, NY, USA

INTRODUCTION

Abrasive jets provide a useful tool in machining operations for fabricating challenging designs. However, applying this technology for fabrication of precision optical components introduces a number of technical challenges. A fundamental property of a fluid jet is that it will begin to lose its coherence once it exits the nozzle. This instability results in an unpredictable removal rate of the fluid jet, which makes it unsuitable for use in a deterministic finishing process. This can be avoided by using a magnetorheological (MR) fluid and applying a magnetic field where it flows from the nozzle exit. The success of this approach has been demonstrated and implemented into the Magnetorheological Jet (MR Jet) finishing process. The magnetically stabilized jet of MR polishing fluid produces a stable and reproducible material removal function (polishing spot) at a distance of several tens of centimeters from the nozzle making MR Jet an attractive technology for the finishing of complex shapes such as free form optics, steep concaves, cavities and molds. Recent results show diverse application of this technology that includes precision finishing of optical designs that range from flats and spheres to aspheres and even conformal shapes. This includes the ability to deterministically finish optics < 1 mm in size to high precision and work with materials such as glass, metals, and ceramics such as sapphire.

MAGNETORHEOLOGICAL JET (MR JET®) FINISHING

Jet Stabilization

In contrast to conventional abrasive jet polishing methods where material removal relies on the kinetic energy of impacting particles, the technique discussed in this paper is based on an assumption that the energy required for polishing may be supplied by the radial spread of a liquid jet over a surface to be polished. [1-6] Such fluid flow may generate sufficient surface stress to provide the regime of material removal, which is characteristic of polishing. As mentioned above, a typical liquid jet breaks down at a very short distance from the nozzle (a few nozzle diameters), making regular, jet-based polishing techniques highly sensitive to the nozzle-offset distance. This limits polishing configurations to those in which the removal function is stable, significantly restricting the finishing of complex shapes.

A method of jet stabilization has been proposed, developed, and demonstrated whereby the round jet of magnetorheological fluid is magnetized by an axial magnetic field when it flows out of the nozzle [1-6]. This local magnetic field induces a structure within the fluid [7] and high apparent viscosity [8] within the portion of the jet that is adjacent to the nozzle, resulting in the suppression of all of the most dangerous initial disturbances. As a result, the MR fluid ejected from the nozzle defines a highly collimated, coherent jet. The stabilizing structure induced by the magnetic field within the jet gradually begins to decay as the jet passes beyond the field. However, the remnant structure still suppresses disturbances and, thus, consequent stabilization of the jet can persist for a sufficient time that it may travel up to several meters (depending on the jet diameter) without significant spreading or loss of structure. For nozzle sizes on the order of 1 mm in diameter coherent jets of 0.5 meters are routinely achieved.

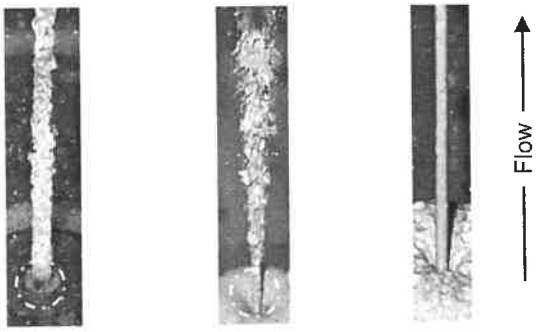

a. Water b. MR Fluid Field off c. MR Fluid Field on

FIGURE 1. Jet snapshot images

This is illustrated in Figure 1. In the case of water, the jet remains stable only for ~ 2 nozzle diameters (note transparent section inside dashed circle at the outlet of Figure 1a). MR fluid has higher viscosity and therefore, the coherent part of the jet extends on ~ 7 - 8 diameters. Initial disturbances (visible in the form of ripples on the surface of the coherent part of the jet in Figure 1b) eventually result in the jet breaking down and rapid spreading. However, when magnetized at the outlet, the jet of MR fluid remains coherent for more than 200 diameters (i.e. ~ 0.4 meters for the case shown in Figure 1c).

Experimental Set Up

A MR Jet finishing system, a portion of which is shown in Figure 2, has been constructed using a 5-axis CNC platform and polishing control software. The delivery system comprises a mixing vessel to disperse the solids in the MR fluid, a pump, means to maintain temperature and viscosity of the fluid and pressure and flow sensors to monitor the system conditions. A magnetic field optimized for the properties of the MR fluid is located beneath the spindle of the CNC platform and stabilizes the jet. With the magnet activated, a collimated jet is directed vertically upwards to the workpiece held by the spindle. Used fluid is collected and recirculated.

FIGURE 2. Experimental set-up.

Removal Function

Figure 3 shows a model of the fluid flow as the jet impinges normal to the workpiece surface. One of the benefits of working with a collimated jet is that as the jet meets the surface, the fluid flows radially outward as opposed to simply bombarding the surface with kinetic energy. It is this radial shear flow that leads to the material removal. [9] As indicated in Fig. 3, there is no removal in the center, where the jet impinges the surface, but instead the bulk of the removal occurs outside of the area of impingement as the fluid radiates outward. Additional unique attributes of using a collimated jet is that it provides a stable and predictable removal function. This is true whether the jet impinges normal to the surface or at angle and provides a great deal of flexibility in the applications that MR Jet can address.

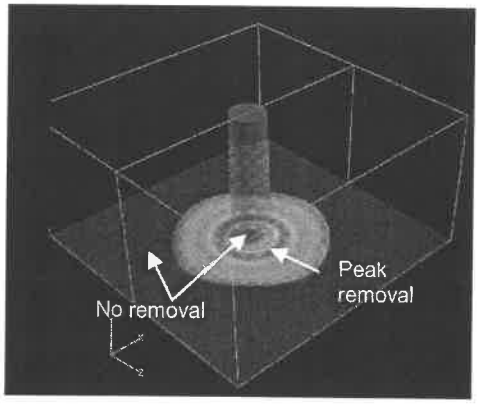

FIGURE 3. Model of the flow as the MR Jet impinges on the workpiece surface.

Results on Novel Geometries

Cavities

MR Jet has been demonstrated to achieve extremely high precision on a wide range of applications, from flats to spheres, aspheres and spherical domes [1,5,6]. In addition to these shapes, jet finishing has been applied to novel geometries described below.

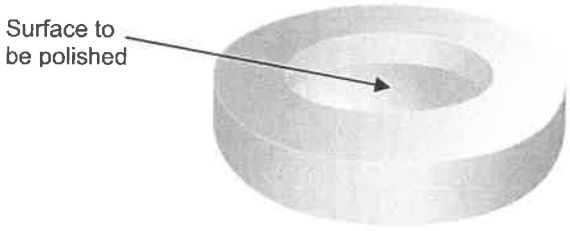

FIGURE 4. Schematic of a cavity that was finished with MR Jet.

One unique geometry that has been finished with MR Jet is shown in Fig. 4. In this case, a flat optical surface at the bottom of a ~10 mm deep cavity was polished, which is nearly impossible to accomplish with most finishing techniques. The results are shown in Figs. 5a and 5b. MR Jet was able to finish this surface to improve the figure from >73 nm rms to ~6 nm rms.

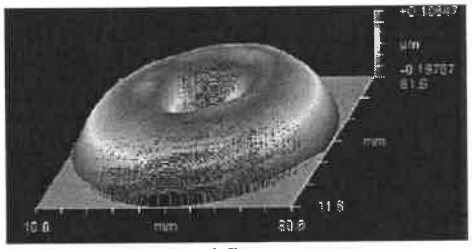

5a Initial figure error
PV = 304 nm
rms = 73.4 nm

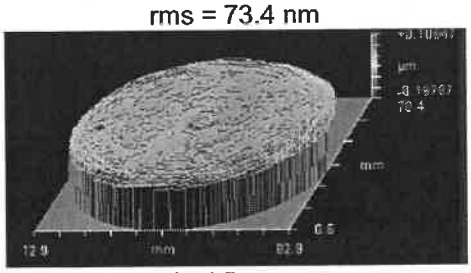

5b Final figure error
PV = 47 nm
rms = 6 nm

FIGURE 5. The initial figure error (5a) and final figure error (5b) after polishing the bottom of a cavity in Fig. 4 with MR Jet.

Millimeter-Sized Optics

Another unique attribute of jet finishing technology is that it can be scaled to address millimeter-sized apertures (like the lens shown in Fig. 6). There was an objective to print an aspheric shape with only a 1.3 mm diameter and ~2.5 um of aspheric departure into a flat glass surface. The blue line in Fig. 7 shows the desired final shape of the surface, and the magenta line shows the result of printing the figure into the surface. The agreement between the Desired and Actual profiles demonstrates the ability of the system to reliably polish such complex shapes into extremely small aperture sizes. Clear apertures as small as 0.8 mm have been polished to within 25 nm P-V of the target shape.

FIGURE 6. Jet finishing can be scaled to address optics with millimeter-sized apertures.

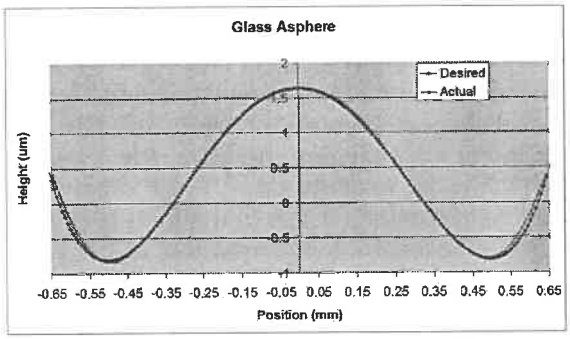

FIGURE 7. - Comparison of the profiles of the Desired (blue) and Actual (magenta) profiles of the asphere printed in over only a 1.3 mm diameter aperture.

Conformal Shapes

The unique attributes of MR Jet provide a great deal of flexibility in the geometries that can be finished and the ability to correct a conformal dome shape (see Fig. 8) has recently been demonstrated. The radius of curvature varies from ~200 mm to ~10 mm across the surface, increasing the degree of difficulty of this job. The MR Jet process has been developed to account for these difficult challenges.

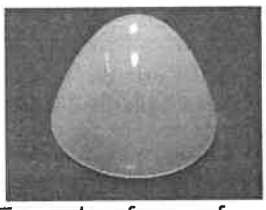

FIGURE 8. Example of a conformal dome that was polished using the MR Jet process.

The initial figure error of the exterior of the dome profile is shown in Fig. 9a [10] (28 um P-V and 8.9 um rms) and the figure error after correcting with MR Jet is shown in Fig. 9b (3.4 um P-V and 1.1 um rms). The figure was improved from 8.9 um rms to 1.1 um rms. This shows that the conformability and stability of the MR Jet provides the means to account for such a wildly changing surface and correct the figure in a deterministic fashion. This result is an important milestone in the precision manufacture of conformal shapes and opens up numerous possibilities to the optical designer for incorporating increasingly complex designs in their systems.

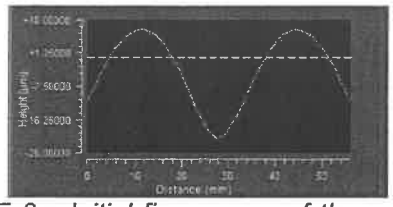

FIGURE 9a. Initial figure error of the outside of the conformal dome. 28 um P-V and 8.9 um rms

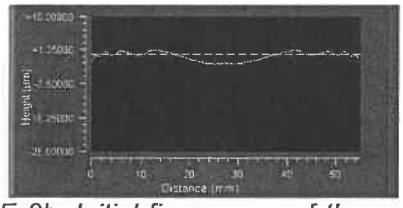

FIGURE 9b. Initial figure error of the outside of the conformal dome. 3.4 um P-V and 1.1 um rms

Summary

It has been demonstrated that impingement of a magnetically stabilized, collimated jet of MR fluid induces radial surface flow, which results in generation of the stable, predictable polishing tool. The scalability of jet finishing provides a tool to deterministically correct the figure of optics smaller than 1 mm in size. Due to the insensitivity to the offset distance, MR Jet provides a versatile tool for finishing complex shapes to high precision, ranging from conventional geometries such as flats, spheres and aspheres to increasingly complex shapes like conformal domes.

Acknowledgements

Authors appreciate valuable inputs from Don Golini, Arpad Sekeres, Justin Tracy and other colleagues at QED. In addition, we acknowledge the contributions of Prof. S. Gracewski from University of Rochester Department of Mechanical Engineering and the Center for Optics Manufacturing.

Portions of the research reported in this presentation were performed in connection with contract DAAD17-03-C-0055 with the U.S. Army Research Laboratory (Aberdeen, MD) and contract No. N68936-05-C-0003 from Naval Air Warfare Center Weapons Division (China Lake, CA). The views and conclusions contained in this document are those of the authors and should not be interpreted as presenting the official policies or position, either expressed or implied, of the U.S. ARL, the NAWCW Division, or the U.S. Government unless so designated by other authorized documents. Citation of manufacturer's or trade names does not constitute an official endorsement or approval of the use thereof. The U.S. Government is authorized to reproduce and distribute reprints for Government purposes notwithstanding any copyright notation hereon.

REFERENCES

[1] William Kordonski, Aric B. Shorey, and Arpad Sekeres, "New magnetically assisted finishing method: material removal with magnetorheological fluid jet", *Proceedings SPIE*, **5180**: 107-114.

[2] Kordonski W., Golini D., Hogan S., and Sekeres A. "System for abrasive jet shaping and polishing of surface using magnetorheological fluid", US Patent #5,971,835, 1999

[3] Kordonski W. " Apparatus and method for abrasive jet finishing of deeply concave surfaces using magnetorheological fluid", US Patent # 6,561, 874, 2003

[4] W.I. Kordonski, A.B. Shorey, and M. Tricard, "Magnetorheological Jet (MR Jet™) Finishing Technology",*Journal of Fluids Engineering* ***128(1):20-26 (2006).***

[5] William Kordonski, Aric Shorey, and Marc Tricard, "Jet-induced high-precision finishing of challenging optics", *Proceedings SPIE*, **5869** :44-51, (2005).

[6] A. Shorey, W. Kordonski, M. Tricard, "Deterministic precision finishing of domes and conformal optics", Proceedings SPIE, 5786: 310-318 (2005).

[7] Y. Graselli, G. Bossis and E. Lemaire, "Field-induced structure in magnetorheological suspensions", *Prog. Colloid Polym. Sci.* ***93, 175-177 (1993).***

[8] A.B. Shorey, W.I. Kordonski, S.R. Gorodkin, S.D. Jacobs, R.F. Gans, K.M. Kwong, C.H. Farny, "Design and testing of a new magnetorheometer:, *Review of Scientific Instruments* **70**(11): 4200-4206 (1999).

[9] W. Kordonski and A. Shorey, "Magnetorheological (MR) Jet Finishing Technology", *Journal of Intelligent Material Systems and Structures,* ***18,*** (2007).

[10] Figure was characterized using the PGI 1250A from Taylor Hobson.

SURFACE GENERATION IN ULTRA PRECISION SINGLE POINT DIAMOND TURNING OF ALUMINUM

Mohammed Tauhiduzzaman and Stephen C. Veldhuis
Mechanical Engineering Department
McMaster University
Hamilton, ON, Canada

INTRODUCTION

Ultra precision single point diamond turning is a very promising tool based manufacturing technology because of its reliability, productivity and wide range of applications. However, with the reduction in cutting dimensions compared to traditional precision machining, the process physics differs substantially. This is largely because of size effects and increased surface finish expectations. In this study, an effort will be made to better understand the effect that material micro-structure plays on the machining process and to explain the physics of surface generation in ultra precision machining of aluminum alloys. In machining studies the surface roughness is observed to decrease with a decrease in the undeformed chip thickness (feed) but it is consistently higher than the theoretically predicted value. To explain and understand this fly-cutting tests have been performed with various undeformed chip thicknesses. The cutting tools were studied under the SEM before and after machining to ensure that the tool wear was minimal. Chips were also studied under an SEM and a strong presence of ploughing action (Serrated chip) was observed near the valley where the undeformed chip thickness is very small.

Efforts have been made to describe this phenomenon using geometry and discrete dislocation theory. Finally, the cutting forces in all three directions have been measured while performing the fly cutting tests and will be used in the explanation of the cutting process.

ANALYSIS OF DIAMOND CUTTING

Cutting depths of 1-10 μm versus 0.1-1mm and cutting edge radiuses for single crystal diamond tool of 60~100 nm [1] versus conventional TiN coated tungsten carbide tools of 8~10 μm [2] highlight the differences between ultra precision and precision machining. Moreover, a typical precision CNC machine tool has a positional accuracy of ±0.1 μm [2] where as diamond turning machine tools have feedback in the nanometer range. These differences are often used to highlight the "size or scaling effect".

Cutting physics and surface generation

Figure 1 provides a schematic diagram showing the rake face of the tool having a nose radius (R_n), feed rate (f) and uncut chip thickness (t) [3-5] of a turning operation. Figure 1 also shows the change in cutting behavior along the cutting edge. With the reduction in uncut chip thickness (t) not only does the tool effectively behave as a rounded edge but the material properties also functionally change. The rounded edge causes an increase in thrust force over the cutting force that promotes ploughing during cutting. Again, from the theory of plasticity applied to metal cutting it is known that for plastic deformation to occur there has to be some defects in the form of "voids" *viz.* dislocations, inclusions etc. [6, 7]. However, there are at least five scale lengths to describe plasticity *viz.* atomistic, discrete dislocations, sub-grain dislocation substructures, grain or crystal and macro-scale as shown in Figure 2 [7].

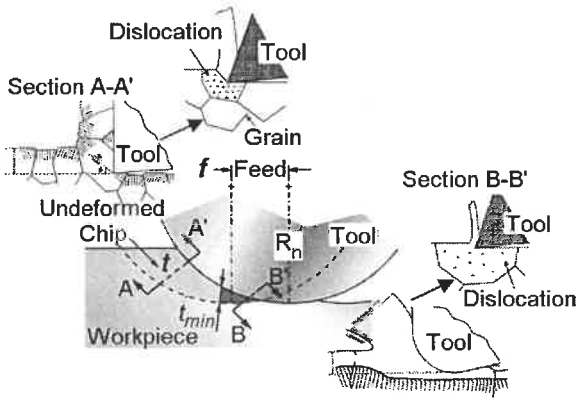

FIGURE 1. Change in cutting behavior along the cutting edge [3-5].

Again, according to the literature [8], a heavily deformed metal can have a dislocation density from 1,000 to 10,000 μm^{-2}. However, when there is a material with no defects, for example a metal "whisker", that is loaded in bending it

shows no plastic flow and the material behaves elastically to the point of fracture *i.e.* they are perfectly brittle (yield strain ≥ fracture strain) [9]. Finally, it can be concluded that the reason for ploughing action, material side flow and elastic recovery is probably because of the combined effect of discrete dislocation distribution and a "metal whisker" effect.

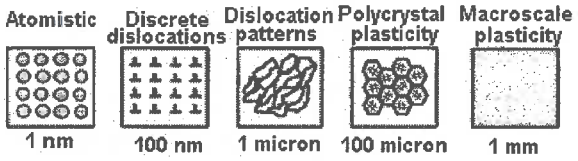

FIGURE 2. Five scale lengths of plasticity [7].

Analytical uncut chip area

Figure 3 shows three successive positions of the tool with a nose radius of R_n and feed (t) in a Cartesian 2D coordinate system. From Figure 3, the allowable step size (t) and tool - workpiece contact length (BEC) for Single Point Diamond Cutting, SPDC (L_{SPDC}) can be estimated as shown in Equations 1 and 2. The side cutting edge has been intentionally neglected in equation 1 as for standard cutting tools [10] with a nose radius of 1.5 mm and 0.5 mm, the extreme values of step size t are found to be 2,819 µm and 939 µm which are too high for real life applications. Similarly, the expression (Equation 3) used in conventional machining for tool - workpiece contact length (L) [9] is not feasible for diamond cutting where, C_s is the side cutting edge angle. Moreover, the term $t/2$ in equation 3 is an approximation where most of the ploughing is occurring and has great importance in diamond cutting as can be seen from Figure 3.

$$t = 2R_n \sin\theta_s = 2R_n \sin\left\{\cos^{-1}\left(1-\frac{d}{R_n}\right)\right\} \quad (1)$$

$$L_{SPDC} = (\theta_s + \theta_e)^c \times R_n \quad (2)$$

$$L = \frac{d - R_n(1-\sin C_s)}{\cos C_s} + \frac{90 - C_s}{180}\pi R_n + \frac{t}{2} \quad (3)$$

Again, the aggregated chip area along the X-Axis has been determined as can be seen from Figure 4 which gives very good insight on the surface generation physics of the process. This can be used to help approximate the plastic deformation scale boundaries. Total analytical uncut chip area *and* contact length (L) has also been determined as shown in Figure 5.

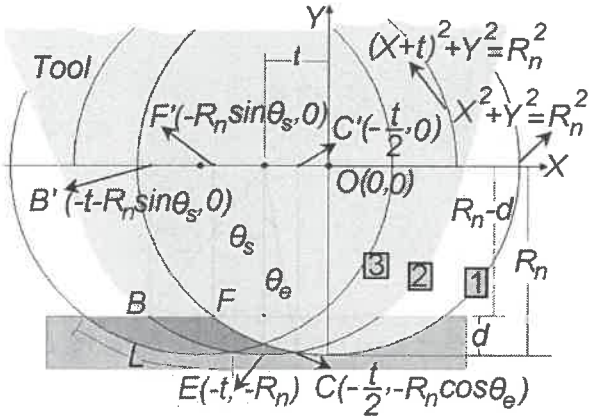

FIGURE 3. Theoretical chip area and tool - workpiece contact length L.

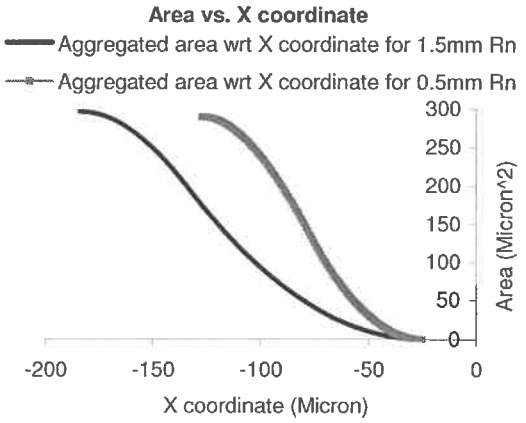

FIGURE 4. Aggregated uncut chip area with respect to X axis for t= 50 µm and d= 6 µm

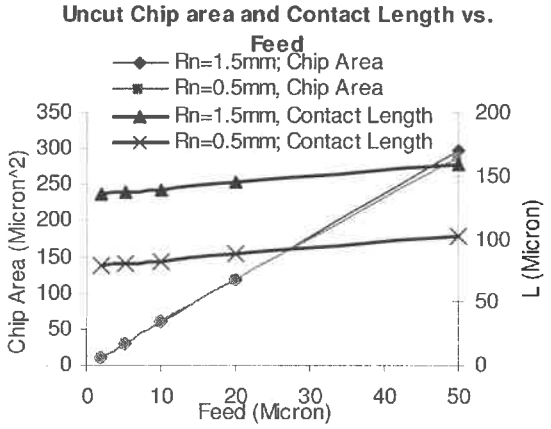

FIGURE 5. Theoretical uncut chip area and contact length L for 6 µm depth of cut.

EXPERIMENTAL SETUP

The experiments are conducted on a Precitech Freefrom 700G five axis CNC machining centre. Fine grained sample of Aluminum 6061,

annealed 6061 Aluminum and 99.99 wt% pure Aluminum have been turned with Single Crystal Diamond tools having a cutting nose radius of 1.50 mm and 0.5mm, 0^{o} Rake and 7^{o} clearance angle. A Kistler dynamometer (Type 9256B1) was used to collect the three components of the cutting force through the Dual mode amplifier (Kistler type 5010) to the computer. A "Zygo" white light interferometer is used to measure the surface profile. Mist coolant is used for lubrication and chip evacuation. A number of fly-cutting tests have also been done on a commercially available 6061 Aluminum alloy. The cutting conditions for fly cutting are: 300 rpm (50.71 m/min), uncut chip thicknesses of 2, 5, 10, 20 and 50 µm, depth of cut: ~6 µm and feed in the raster direction of 2mm/min and nose radius: 1.50 mm and 0.50 mm.

SURFACE ANALYSIS

Diamond turned surfaces are shown in Figure 6 where the average surface roughness values are less than 10 nm. However, the P-V (R_{th}) values for fine grained 6061 Al is 38.5 nm; Annealed 6061 Al is 45.582 nm and 99.99% pure Al is 54.3 nm where the theoretical P-V value is 0.3357nm for 2µm/rev feed rate. One reason for this behavior is because of the material induced vibration as shown in Figure 7.

FIGURE 6. Mirror finish achieved at 500rpm, R_n=1.5mm, 1mm/min feed and 6µm Depth of cut

It has also been observed that cutting speed does not have any dominant affect on the surface roughness of the machined part. Finally, based on these observations the authors have performed Fly-cutting tests to investigate if there is any other factor that affects surface roughness. The surface roughness results of the fly-cutting tests are shown in Figure 8 and are compared with the theoretical values. Tool wear is studied after all tests and it did not show any wear (Figure 9). The main finding of this work is that it is the ploughing action of the material that is playing a significant role in causing material side flow. The observations that enabled the authors to conclude this are shown in Figures 10 and 11 for a 50 µm feed. Figure 10 shows clearly the pileup of material between the feed marks and Figure 11 which shows a chip further supports this phenomenon with the presence of a serrated edge on one end (left) and a smooth edge on the other side.

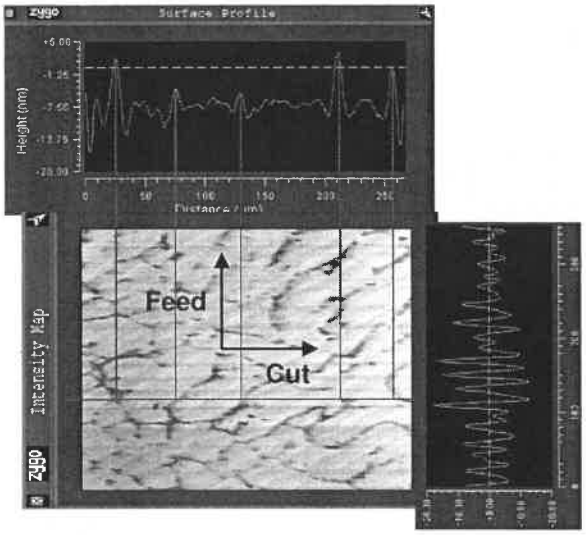

FIGURE 7. Material induced vibration in cutting direction

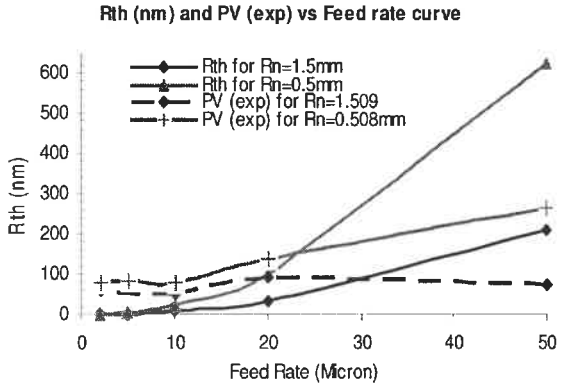

FIGURE 8. Surface Roughness in Fly-cutting at 300 rpm and depth of cut: ~6 µm

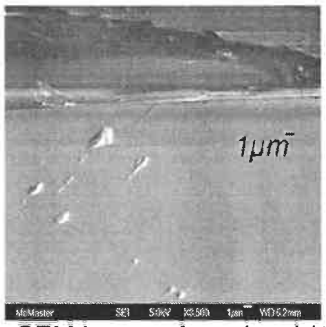

FIGURE 9. SEM image of used tool (1.5mm R_n)

CUTTING FORCE ANALYSIS

Cutting forces have been measured and it has been repeatedly observed that the feed force

and thrust force increases and the cutting force decreases with a decrease in feed (Figure 12).

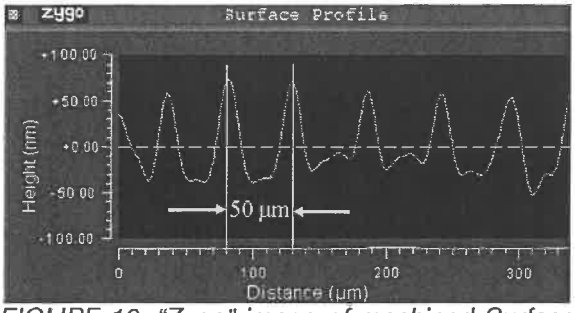

FIGURE 10. "Zygo" image of machined Surface at 300 rpm and depth of cut: ~6 µm, feed= 50 µm, nose radius: a. R_n= 1.509 mm in feed direction (200X)

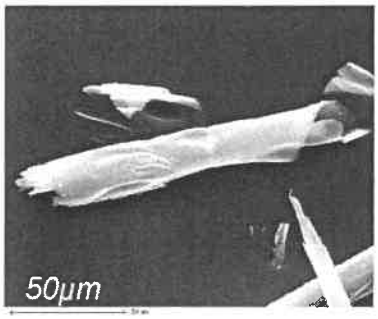

FIGURE 11. SEM image of chip (300 rpm, d: ~6 µm, feed= 50 µm)

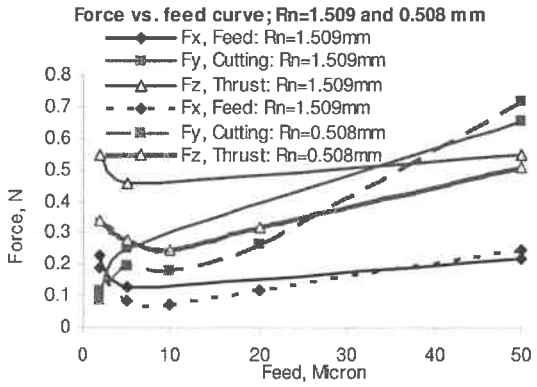

FIGURE 12. Forces vs. Feed for DOC= ~6 µm.

CONCLUSION AND FUTURE WORK

Understanding the surface generation of aluminum alloys under Single point diamond turning and fly cutting have been done. Material induced vibration resulting from hard grain boundaries has been found to have a significant influence on surface roughness. Again, with the reduction in uncut chip area, the probability of encountering any defect (*viz.* dislocation) is reduced and the material starts to behave consistent with materials deforming at the atomistic scale. However, because of the applied force (or stress), the material tears and deforms from the bulk material and produces a serrated form of chip (ploughing) at the thin edge with the rest of it springing back. Unfortunately, this portion of the material leaves a signature on the machined surface. However the author believes that there is a strong possibility of brittle failure of the ductile Aluminum where the uncut chip area tends to "Zero". The author also believes that incorporating defects in the material is desirable as this will reduce the ploughing action. Finally, a tool with the smaller nose radius would result in less ploughing as it removes more material at a certain position of the tool.

REFERENCES

[1] Ng, Chee Keong, Sreyes, Melkote N., Rahman, M., Kumar, A. Senthil, Experimental study of micro-and nano-scale cutting of aluminum, IJMTM, 46 (2006) 929–936

[2] Simoneau A., Ng E. and Elbestawi M.A., Surface defects during microcutting, IJMTM, 46 (2006) 1378-1387.

[3] Knuefermann, M. M. W.; A Model for Surface Roughness in Ultraprecision Hard Turning; CIRP; Vol. 35; Issue1; 2004; pp99-102

[4] Moriwaki T. and Okuda K., Machinability of copper in ultra-precision micro diamond cutting, CIRP Vol. 38/1/1989; pp 115-118

[5] Sugita Tahaaki, Ueda Kanji, and Inana Toyojiro. Fundamental of Machining (In Japanese). KOURITU Book Publication. Japan, 1984.

[6] Gurson, A.L., 1977. Continuum theory of ductile rupture by void nucleation and growth: Part I Ð yield criteria and flow rules for porous ductile media. ASME J. Engng. Mater. Techn. 99, 2-15.

[7] McDowell, David L.; Modeling and experiments in plasticity; International Journal of Solids and Structures 37 (2000) 293-309

[8] Callister, William D.; Material Science and Engineering An Introduction; Fourth Edition; John Wiley & Sons, Inc.; 1997.

[9] Shaw, M. C.; Metal Cutting Principles; Second Edition; Oxford University Press; 2005.

[10] K & Y Diamond [http://www.kydiamond.ca/: visited July 21, 2008]

ACKNOWLEDGEMENT

The authors wish to acknowledge the support of the Ontario Centre of Excellence and B-Con Engineering.

MACHINING OF GLASS LENS MOLD WITH MINUTE STRUCTURES BY GRINDING AND CUTTING

Shingo Yamamoto[1], Taichi Fujii[1], Minoru Hirano[2], Tetsuro Shibukawa[3], Tohru Ishida[1], Yoshimi Takeuchi[1]
[1]Dept. of Mechanical Engneering, Graduate School of Engneering
Osaka University
Yamadaoka 2-1, Suita, Osaka 560-0871, JAPAN
[2]Dept. of Machine Tool R&D, Research&Development Center
JTEKT Corporation
Asahi-machi 1-1, Kariya, Aichi 448-8652, JAPAN
[3]Product Planning Dept.
Mitsui Seiki Kogyo Co., Ltd.
Hachiman 6-13, Kawajima-machi, Hiki, Saitama 350-0193, JAPAN

INTRODUCTION

In optical devices, the demand of lenses with complicated shapes like Fresnel shape is recently growing up[1]. Fresnel shape has some sharp edges on curved surfaces. These lenses are generally composed of polymer due to the easiness of machining die with a single crystal diamond cutting tool. In recent years, it is strongly required to make these lenses by glass in terms of improving its optical performances. Brittle materials such as cemented tungsten carbide are used for glass molding. Thus, it is expected to develop a high precision machining method to fabricate minute structures on brittle materials, difficult to machine.

Concerning such a demand, the two-axes turning method with disk type resinoid bonded diamond grinding wheel or polycrystalline diamond milling tool, as shown in Figure 1, is proposed to machine glass lens mold die with Fresnel shape[2]. As these tools are composed of diamomd grains, it is difficult to form tool edge sharply. It causes the deterioration of form accuracy of sharp edges. In addition, the tool sharp edge may cause the increase in tool wear and the deterioration of surface roughness. Therefore, it is expected to apply a single crystal diamond cutting tool with a very sharp edge for high precision machining of glass molding die with Fresnel shape.

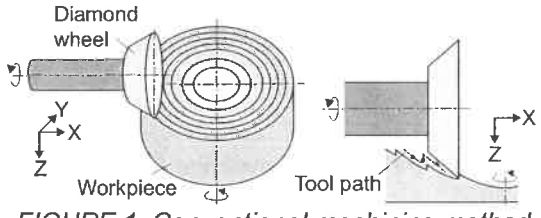

FIGURE 1. Conventional machining method.

The study proposes a new machining process for the brittle material molding die with Fresnel shape shown in Figure 2, aiming at high precision machining. In the proposed process, the curved surfaces except for sharp edges are machined by the conventional grinding method with the disk type metal bonded diamond grinding wheel. Then, ultra precision cutting with a very sharp single crystal diamond cutting tool is applied to create the sharp edges. The ultraprecision machining center, AHN®05 by JTEKT Corporation, is used for experiments. The machine has three translational axes, X, Y, and Z and has a rotational axis, B. The resolution of translational axes are 1nm, and rotational axis is 0.0001 degree.

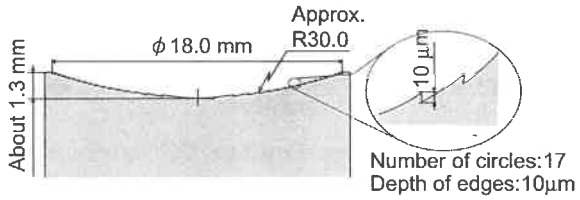

FIGURE 2. Target shape to be machined.

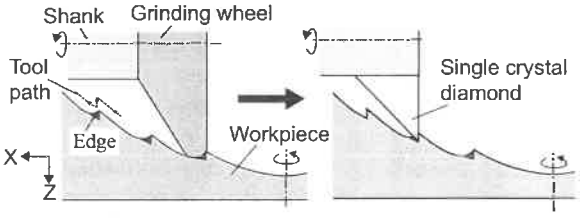

FIGURE 3. Complex machining.

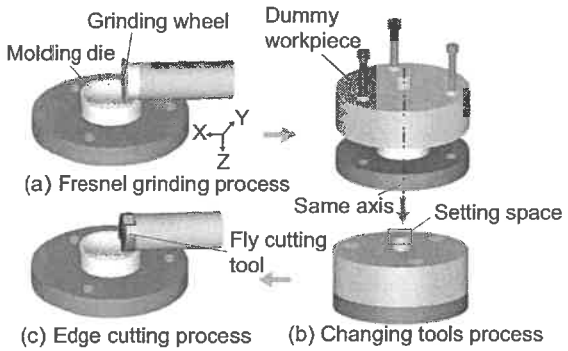

FIGURE 4. Proposed machining method.

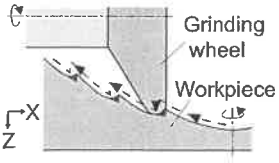

FIGURE 5. Grinding method.

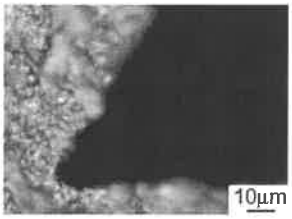

FIGURE 6. Carbon ground by trued wheel.

TABLE 1. Grinding conditions

Workpiece	Binderless tungsten carbide J05
Rotational number	200rpm
Wheel	SD3000J75M
Diameter	ϕ25mm
Rotational number	12000rpm
Depth of cut (Rough cut)	0.5μm
Depth of cut (Finish cut)	0.2μm×2 0.1μm×1 0μm×1
Feed rate	0.2mm/min
Grinding fluid	Oil mist (BLuebe LB10)

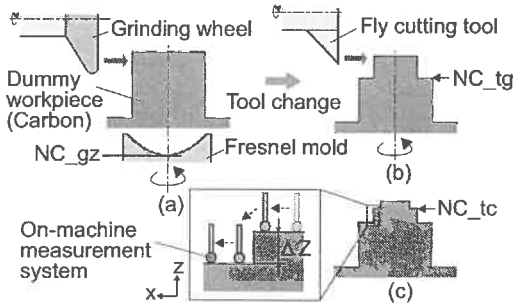

FIGURE 7. Z-direction positioning process.

THE PROPOSED MACHINING METHOD

The proposed machining method is shown in Figure 3. At first, the curved surfaces except for sharp edges are machined by grinding method with the disk type diamond grinding wheel. Then, fly cutting method is applied to create the sharp edges. However, the tool original point alignment is necessary when the grinding wheel is exchanged for fly cutting tool. The tool exchange process illustrated in Figure 4. The alignment is done by installing a new workpiece, called the dummy work, which is set on the machined workpiece, and machining it.

The details of the complex machining method proposed by this research are explained in the following.

CURVED SURFACE GRINDING PROCESS

The area except the edge section is machined with a knife edge grinding wheel. Fresnel shape is machined by moving a knife edge grinding wheel along the section curve in the simultaneous two axes (X and Z axis) control, while rotating the workpiece set in the main axis, as shown in Figure 5. In this research, a metal bonded grinding wheel that has high binding strength and small deformation volume is used to decrease the contact point error by the elastic deformation of the grinding wheel as much as possible.

The truing of diamond grinding wheel by WA cup truer is experimented. The grinding wheel is attached to an air turbin spindle, and WA cup truer is attached to the main axis. The end surface of grinding wheel is at first trued. Then, grinding wheel is tilted 30 degree, and the side surface of grinding wheel is trued. The shape of trued wheel edge is observed by grinding a carbon plate. Figure 6 shows the microphotograph of ground carbon plate. The radius of wheel edge is about 5μm.Then, the NC data is made, based on this radius of the wheel edge, and the first grinding of the Fresnel shape is done. Table 1 shows grinding conditions.

The profile of machined shape is observed with a 3D profilometer, UA3P by Matsushita Electric Industrial Co.,Ltd.. The NC data is corrected, based on the shape error. The correction machining is done.

TOOL EXCHANGE PROCESS

THE ORIGINAL POINT POSITIONING OF CUTTING DIRECTION (Z-DIRECTION)

The positioning method of the original point of cutting direction is shown in Figure 7. It aims to obtain Z-axis coordinates where the tool contact positions are equal before and after tool exchange. Z-axis coordinates at the final grinding of the molding die center are set to be NC_gz, and the dummy work made of the carbon is installed on the molding die. At the beginning, the end section of the dummy work is plain ground at the Z-axis position of NC_tg, as shown in Figure 7(a). Then, the grinding wheel is exchanged for the fly cutting

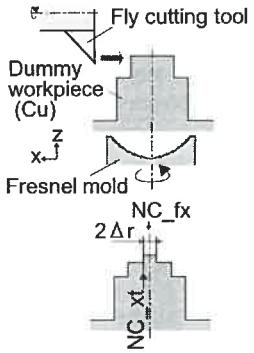

FIGURE 8. X-direction positioning process.

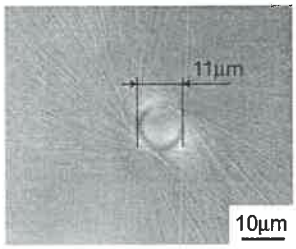

FIGURE 9. Micrograph of Cu dummy workpiece.

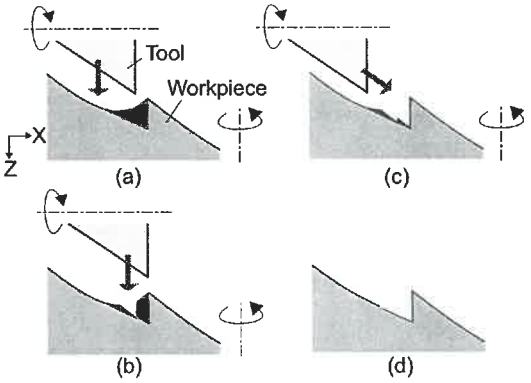

FIGURE 10. Edge cutting process.

tool, as shown in Figure 7(b), to perform plain cutting of dummy work at the Z-axis position of NC_tc. Difference (ΔZ) of height is measured with an on-machine contact profilometer (The stylus radius: 0.25mm), as shown in Figure 7(c). Z-axis original point coordinates (NC_fz) can be obtained, as shown by Expression (1).

$$NC\_fz = NC\_tc - \Delta Z - (NC\_tg - NC\_gz) \quad (1)$$

THE ORIGINAL POINT POSITIONING OF FEED DIRECTION (X-DIRECTION)

Figure 8 shows the positioning method of the original point of feed direction. At first, the dummy work is installed on the molding die. Then, the dummy work is plain cut with fly cutting tool at NC_xt located near the center point. X-axis original point coordinates are assumed to be NC_fx, which are set to the molding die center point in the grinding process. When the diameter of the remaining circular cylindrical shape is assumed to be Δr, NC_fx is presented by Expression (2). Consequently, X-axis original point coordinates are obtained.

$$NC\_fx = NC\_xt - \Delta r \quad (2)$$

In this instance, the remaining circular cylindrical shape is observed with the microscope, as shown in Figure 9. The diameter is derived from analyzing the image. From the figure, Δr is obtained as 5.5μm, which enables to determine X-axis original point coordinates.

EDGE SECTION CUTTING PROCESS

After the original point coordinates of the fly cutting tool are determined according to the above mentioned tool exchange process, the edge section is cut. Figure 10 shows the tool path in the edge section cutting process, where the tool is fed in the Z direction, as shown in Figure 10(a) and (b). The most of part in the edge section is removed. The remaining part is cut two or more times along the section curve, as shown in Figure 10(c). The workpiece is cut from the center to the outside in sequence by this tool path. Table 2 shows cutting conditions.

TABLE 2. Cutting conditions in edge cutting process

Rotational number of workpiece	50rpm
Rotational numeber of tool	12000rpm
Cutting direction	Down cutting
Vertical feed rate	0.00018~ 0.00071mm/min
Cutting depth of oblique feed	0.1μm
Oblique feed rate	0.005mm/min
Cutting fluid	Oil mist (BLuebe LB10)

VERIFICATION OF PROPOSED METHOD

The machining of glass molding die with Fresnel shape is conducted by using the proposed method. The cutting time of edge section is about 52 hours. Figure 11 shows the whole view of machined molding die. Figure 12 shows the SEM observation result of the center of the molding die. Figure 13 shows the Nomarski microphotograph of ground surface, where mirror surface is obtained by ductile mode grinding. The surface roughness of ground surface is measured with a 3D optical profiler, New View 5022 by Zygo Co.,Ltd., and is about 18nmRy. The profile of machined shape is observed with UA3P. Figure 14 shows the deviation of machined shape except for neighborhood of edge sections. The shape accuracy of molding die is 0.14μm(PV). Figure 15 shows the profile of Fresnel shape removing the aspheric shape from the whole machined shape. The measured depth of edge is 10.13μm(PV), approximately equal with design value 10μm.

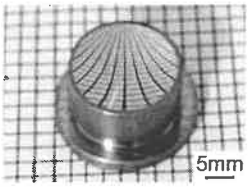

FIGURE 11. Whole view of workpiece.

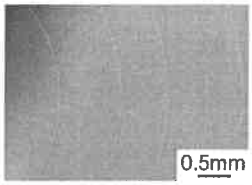

FIGURE 12. SEM image of workpiece.

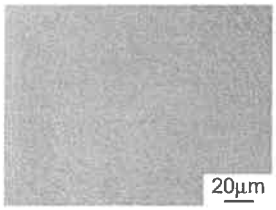

FIGURE 13. Micrograph of center of workpiece.

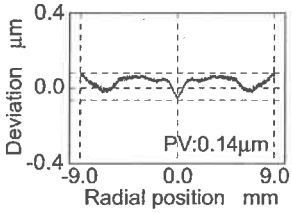

FIGURE 14. Shape accuracy (Reference:Base line).

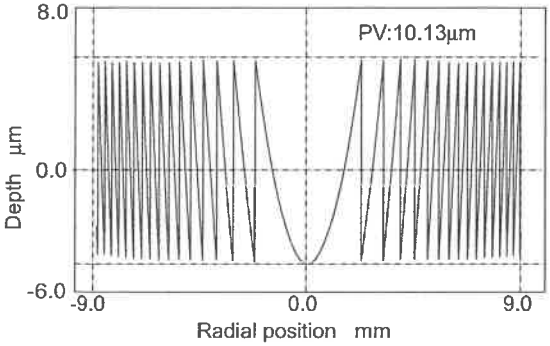

FIGURE 15. Profile of Fresnel shape (Reference:Aspheric).

The edge section of the molding die machined by the proposed complex machining is compared to one of a molding die machined by only grinding process. The SEM observation result of the 1st edge from the molding die center is shown in Figure 16. Very steep edge shape is obtained in the complex process, while rounded edge shape in only grinding process. Figure 17 shows the measured result of edge section with UA3P. It is confirmed that the complex process can create steep edge shape although the part near edge section cannot be measured accurately according to the diameter of the stylus. Figure 18 shows the observation result in the edge section machined by proposed method with SEM. The SEM observation result of 15th edge from the center of the workpiece is shown in Figure 19, together with the measured result by UA3P shown in Figure 20. It is seen that very steep edge shape is obtained in the complex machining as well as the 1st edge, thus showing the effectiveness of the proposed method.

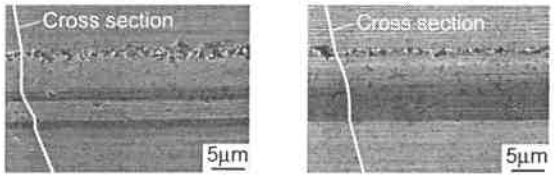

(a) Complex machining (b) Grinding

FIGURE 16. SEM images of 1st edge.

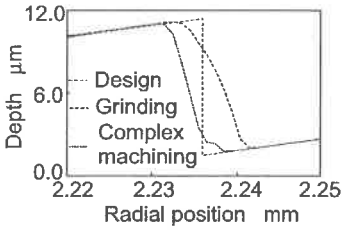

FIGURE 17. Profile of 1st edge (UA3P).

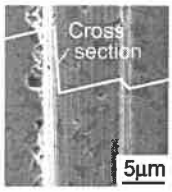

FIGURE 18. Top view of complex machined edge.

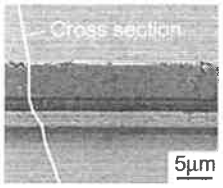

FIGURE 19. SEM image of 15th edge.

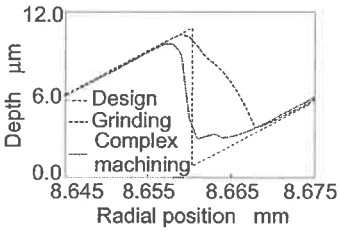

FIGURE 20. Profile of 15th edge (UA3P).

CONCLUSION

In this research, the complex machining method is proposed that uses the grinding process with a knife edge grinding wheel for the curved surface part and the fly cutting for the edge part so that the glass lens molding die with Fresnel shape can be accurately machined.

Very steep edge shape can be obtained in machining a cemented tungsten carbide molding die with Fresnel shape compared with only grinding process. As the result, the usefulness of the proposed method is shown.

REFERENCES

[1] Y. Ono. Recent Advances in Diffractive Optical Elements: From Diffractive Optics towards Periodic Structure Optics. Japanese Journal of Optics (in Japanese). 2003; 32: 468-475

[2] Y. Yamamoto, H. Suzuki, T. Moriwaki, T. Okino, T. Higuchi. Precision Grinding of Micro Fresnel Lens Molding Die (2nd Report). Journal of the Japan Society for Precision Engineering (in Japanaese). 2007; 73: 688-692

INFLUENCE OF CUTTING SPEED ON ULTRA-PRECISION CUTTING CHARACTERISTICS OF STAINLESS STEEL WITH COATED-CEMENTED-CARBIDE TOOL

Heiji YASUI[1], Takeharu KAWABAYASHI[1], Akira TOYAMA[1], Hirohumi HAYASHI[1], Akira SHINOZAKI[2]

[1] **Graduate School of Science and Technology, Kumamoto University, Kumamoto city, JAPAN**

[2] **Ariake National College of Technology, Omuta city, JAPAN**

INTRODUCTION

Difficult-to-cut materials such as stainless steels, titanium metals and so on, have excellent mechanical and chemical properties. Thus, with the increase of demand of high quality components, the high level of ultra-precision cutting technique of difficult-to-cut materials has been strongly required. The diamond tool used generally for soft materials such as aluminum, copper and so on, however, is applied difficult for difficult-to-cut materials because the diamond tool wears huge at the short cutting length. From the point of view, in our previous researches, various kinds of tool materials are examined. From the results, the coated-cemented-carbide tool is found so effective for the ultra-precision cutting of the difficult-to-cut materials [1-2]. The surface roughness formed by ultra-precision cutting of difficult-to-cut materials with coated-cemented-carbide tool is ascertained roughly to attain below 100nm (*Rz*) in two dimensional measurement. The influence of cutting parameters on the ultra-precision characteristics of difficult-to-cut materials with coated-cemented-carbide tool is necessary to be cleared for utilizing optimally the coated-cemented-carbide tool.

To build the selecting method of optimum conditions in the ultra-precision cutting method, in the report, the influence of cutting speed on the surface roughness and tool wear in ultra-precision cutting of stainless steel with coated-cemented-carbide tool is investigated.

EXPERIMENTS

The experiments are executed by face-turning stainless steel SUS316 (in JIS) with coated-cemented-carbide tool set on the ultra-precision turning machine as shown in Fig.1. Main experimental conditions are summarized in Table 1. Cutting speeds are used in the ranges of *Vc*=9.6m/min-10.5 m/min of low cutting speed, *Vc*=56-62 m/min of middle cutting speed, and *Vc*=113-125 m/min and *Vc*=141-157m/min of high cutting speed. Soluble type of cutting fluid

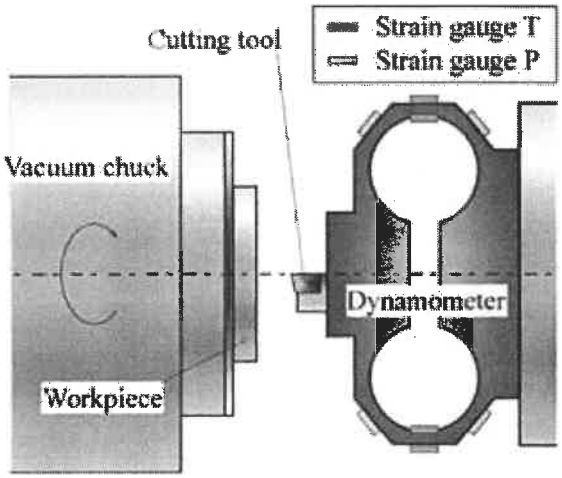

FIGURE 1. Set-up of ultra-precision face-turning experimental system

Table 1 Experimental conditions

Machine tool : Ultra-precision lathe ULC-100A Toshuiba Machine CO.,LTD
Cutting tool: Disk type tool (Formed Coated) Nose radius: 8.0 mm, Rake angle: 0 deg. Relief angle: 7 deg
Workpiece material: SUS316 (18Cr-10Ni-2Mo)
Cutting fluid: Solution type cutting fluid
Cutting conditions: Feed rate: f = 2 μm/rev Depth of cut: d = 5 μm Cutting speed: Vc = 9.6-157 m/m Cutting length: l = 119 m

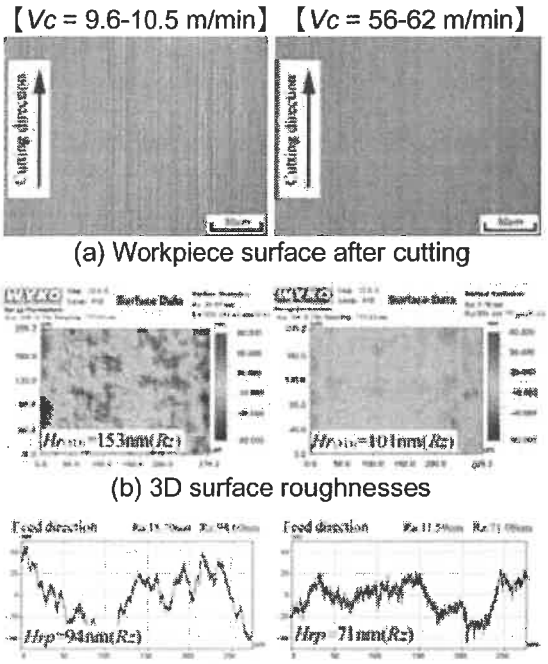

FIGURE 2. Comparison of SUS316 surfaces face-turned at low cutting speed with middle cutting speed [f=2micro-meters/min,d=5micro-meters, L=119mm, Water-immiscible type cutting fluid]

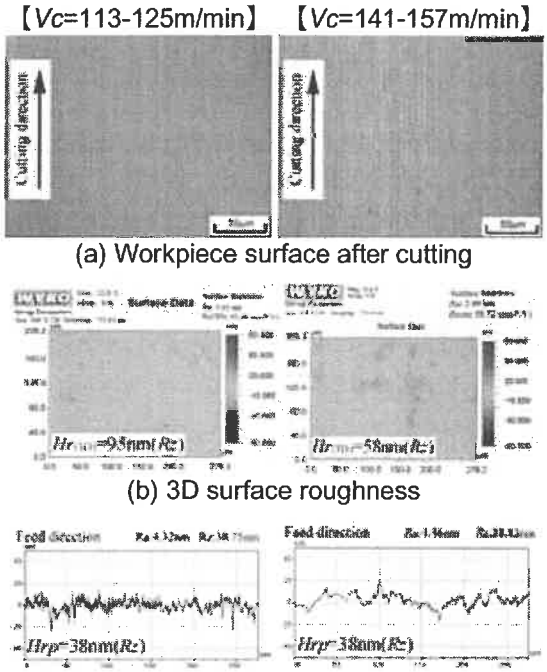

FIGURE 3. Comparison of SUS316 surfaces face-turned at two kinds of cutting speed [f=2micro-meters/min,d=5micro-meters, L=119mm, Water-immiscible type cutting fluid]

is directly supplied to cutting point with compressed air. The face-turned stainless steel surface is differential interference microscope .Its surface roughness measured with surface interferometer (WYKO 3D). The wear of cutting tool is also observed with Scanning Electron Microscope (SEM). Cutting force is measured by octagonal elastic ring attached to the lathe as shown in Fig.1.

RESULTS AND DISCUSSIONS

Figure 2 shows the workpiece surfaces after cutting at low and middle cutting speed of *Vc*=9.6-10.5 m/min and *Vc*=56-62 m/min with coated-cemented-carbide tool. On the surfaces formed by both cutting speed, deep and irregular cutting grooves, scratches and cracks in addition to the regular cutting grooves equal to the frequency of tool feed is observed partially on the cut surface. The 3D surface roughness formed at *Vc*=9.6-10.5 m/min and *Vc*=42-60 m/min is approximately $Hr_{(3D)}$=153nm (*Rz*) and $Hr_{(3D)}$=101nm (*Rz*), respectively. The 2D surface roughness in feed direction at *Vc* =9.6-105 m/min and *Vc*=56-62 m/min are

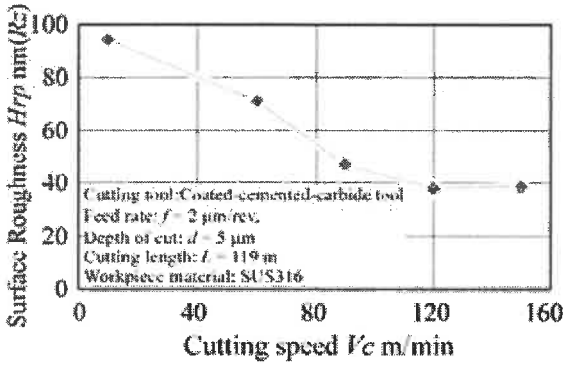

FIGURE 4 Influence of cutting speed on surface roughnes

Hrp=94 nm(*Rz*) and *Hrp*=71 nm(*Rz*), respectively. The large undulation is found to influence on the surface roughness.

Figure 3 shows the workpiece surfaces after cutting at high cutting speed of *Vc*=113-125 m/min and *Vc*=141-157 m/min with coated-cemented-carbide tool. On the sarfeces formed by both cutting speed, regular cutting grooves corresponding to tool feed is observed clearly. Though the small micro-cracks are

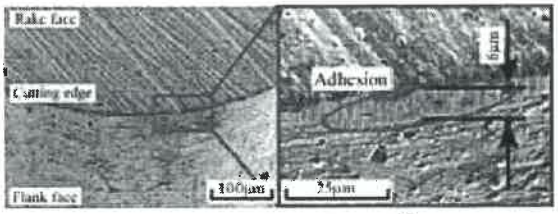

(a) V_c = 9.6-10.5 m/min

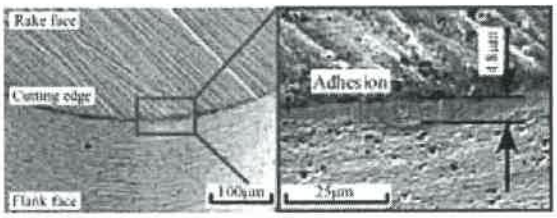

(b) V_c = 56-63 m/min

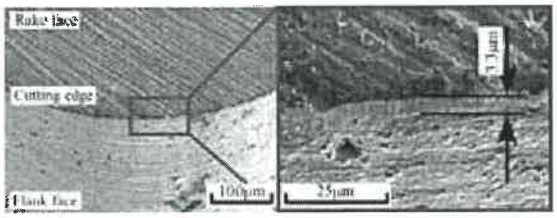

(c) V_c =115-125m/min

FIGURE 5 Comparison of flank wear face-turned at three kinds of cutting speed [f=2micro-meters/min,d=5micro-meters, L=119mm, Water-immiscible type cutting fluid]

partially observed, those are considerably small.The 3D surface roughness formed at Vc=113-125 m/min

and Vc=141-157 m/min are $Hr_{(3D)}$=95nm (Rz) and $Hr_{(3D)}$=58 nm(Rz), respectively. Both of the 2D surface roughness in feed direction at Vc=113-125 m/min and Vc=141-157 m/min are about Hrp=38nm (Rz). The undulation in high speed cutting becomes remarkably smaller than low speed cutting. The surface roughness in high speed cutting, from the results, is considered outstandingly better than cutting speed.

Figure 4 shows the change of the surface roughness with cutting speed. Up to Vc=90m/min, the surface roughness is found to become steeply smaller as cutting speed is higher. Over Vc=90m/min, however, the surface roughness is almost the same value of $Hr_{(3D)}$=40nm. Accordingly higher cutting speed is referred for getting better surface roughness in ultra-precision of stainless steel with coated-cemented-carbide rool.

The flank wears of cutting edge after cutting of

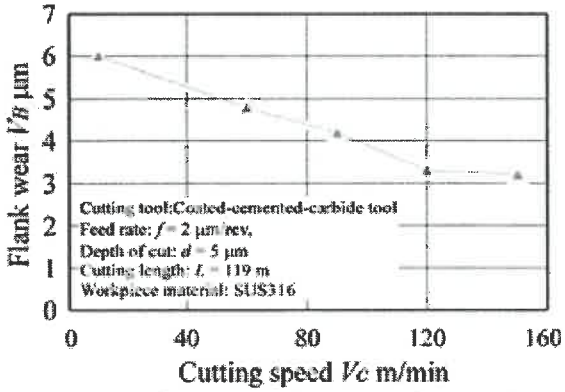

FIGURE 6 Influence of cutting speed on the flank face wear

SUS316 at various kinds of cutting speed are shown in Figure 5. In both of low and middle cutting speed of Vc=9.6-10.5m/min and Vc=42-60 m/min, the adhesion of stainless steel to flank face is observed. In high cutting speed of V_c =115-125m/min, on the other hand, the adhesion can not be found on the flank face. The wear breadths of flank face in Vc=9.6-10.5m/min, Vc=42-60 m/min and V_c=115-125m/min are V_B=6μm, V_B=4.8μm and V_B=3.3μm, respectively. Higher cutting speed becomes for lower flank wear.

FIGURE 6 shows the change of the wear breadth of flank face with cutting speed. The relationship is similar to the relationship as shown in Fig.4 between surface roughness and cutting speed. That is, up to Vc=120m/min, the wear breadth of flank face becomes steeply smaller as cutting speed is higher. Over Vc=120m/min, however, the surface roughness is almost the same value.

In the results as mentioned above, the large flank wear rate in low and middle cutting speed is considered due to the occurrence of adhesion to flank face. The surface roughness is considered also influenced by the adhesion. In high speed cutting, the adhesion occurs little on the flank face. As the result, the flank wear rate becomes small. Thus the smooth surface roughness is considered to be formed.

The cutting forces of cutting edge after cutting of SUS316 at various kinds of cutting speed are shown in Figure 7. In case of all cutting speeds, thrust force becomes larger than principal force. In normal cutting operation like large depth of cut of 1mm, thrust force becomes generally smaller than principal force. From the point of

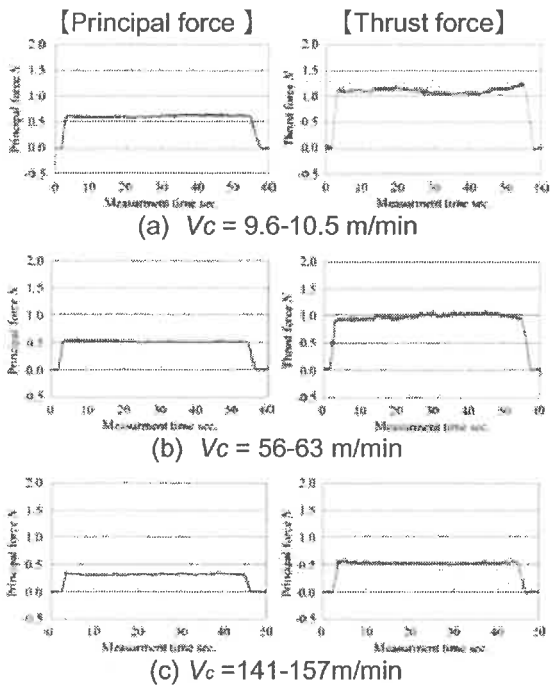

FIGURE 7 Comparison of cutting force at three kinds of cutting speed [f=2micro-meters/min, d=5micro-meters, L=119mm, Water-immiscible type cutting fluid]

view, the reverse phenomenon in the ultra-precision cutting is considered why the dull edge shape beyond the edge roundness of 1μm at least influences on the cutting mechanism. Namely the Influence of round cutting edge on practical ultra-precision cutting mechanism is considered. However the difference between the thrust force and principal force tends to be shrunk. From the result, the influence of cutting speed on the cutting mechanism is inferred to be related to the reverse phenomenon in the ultra-precision cutting.

Figure 8 shows the relationship between cutting force and cutting speed. Both of principal force and thrust force decreases as cutting speed is higher. The rate of decrease in thrust force tends to be somewhat larger than principal force. Thrust force and principal force in low cutting speed of *Vc*=9.6-10.5 m/min is 1.1N and 0.58N. Thrust force and principal force in high cutting speed of *Vc*=141-157 m/min, on the contrary, is 0.52N and 0.31N. The ratio of principal force to thrust force in *Vc*=141-157 m/min and *Vc*=9.6-10.5 m/min is about a 0.6 and 0.53. The reason is considered why the wear breadth of flank face

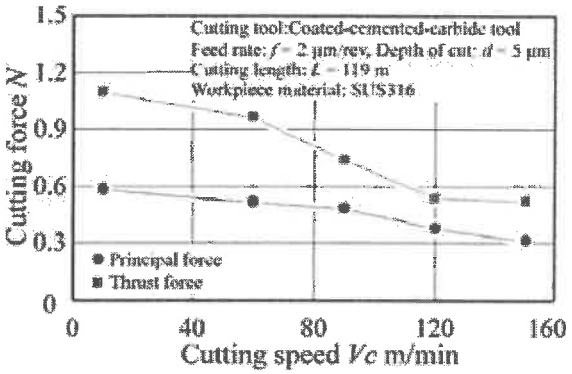

FIGURE 8 Influence of cutting speed on the cutting force

in low cutting speed, as seen in Fig.5, becomes larger than low cutting speed.

SUMMARY

The main conclusions obtained are as followed:

(1) The surface roughness of stainless steel formed by ultra-precision cutting with coated-cemented-carbide tool is improved better for higher cutting speed. The irregular cutting grooves are observed on the stainless steel surface formed at low cutting speed.

(2) The wear rate of cutting edge of coated-cemented-carbide tool in ultra-precision cutting of stainless steel is lower for higher cutting speed. The adhesion to cutting edge occurs at low cutting speed.

(3) The best surface roughness obtained in the experiments is *Hr*=39nm (*Rz*) in two dimensional measurement of 256 micro-meters.

ACKNOWLEGEMENTS

The authors would like to thank Sanyo Special Steel Co., Ltd. for providing workpiece materials.

REFERENCES

[1] H. Yasui, S.Sakamoto, M.Kawada, S.Kondo and A.Hosokawa, "Ultra-precision Cutting of Beta Titanium Alloy" Proc. of the ASPE 2000 Annual Meeting, pp.70-73(2000).

[2]S.Sakamoto, H.Yasui, A.Fujimori and S.Kondo, "Ultra-Precision Cutting of Stainless Steel by Using Coated Carbide Bite", Proceedings of the ASPE 2002 Annual Meeting, pp.597-600(2002).

Authors Index

Abbas, Ali E. . . . 476
Aketagawa, Masato . . . 132
Alao, Abdur-Rasheed . . . 376
Alger, Ethan T. . . . 15
Amarandei, Dumitru . . . 176, 400
Aoyama, Hisayuki . . . 249, 496
Arai, Yoshikazu . . . 264, 368, 550, 554
Ashida, Kiwamu . . . 61
Badami, Vivek G. . . . 144
Ballou, Susan . . . 599
Bamberg, Eberhard . . . 192
Barkman, Michael L. . . . 542
Bartlett, Brent . . . 456
Bauza, Marcin B. . . . 120, 340
Beckwith, John F. . . . 136
Blackburn, Travis Lee . . . 31
Bluemel, Thomas . . . 619
Boehnke, David . . . 43
Boltryk, Peter . . . 124
Bossoni, Sergio . . . 336
Brecher, Christian . . . 404
Brinksmeier, Ekkard . . . 35, 65, 92, 428
Brooks, David . . . 546
Buice, Eric S. . . . 276
Bulla, Benjamin . . . 88, 408
Butler, David Lee . . . 31
Butler, Hans . . . 79*
Cacace, Lennino . . . 27
Carrillo, Manuel A. . . . 15
Caskey, Gregory W. . . . 324
Castro, Carlos . . . 15
Chaikool, Patamaporn . . . 132
Chen, Chao-Jung . . . 356, 372
Chen, Fong-Zhi . . . 570
Chen, Qunyi . . . 100
Chen, Shih-Chi . . . 480
Cheng, Yuan-Chieh . . . 570
Cherku, Sreenidhi . . . 502
Cheung, Chi-Fai . . . 587
Cho, Sang-Gu . . . 253
Choi, Doo-Sun . . . 611
Choi, Sung-Hyuk . . . 272
Chung, Sung-Chong . . . 188, 212, 241, 578
Clark, Daniel E. . . . 468
Culpepper, Martin Luther . . . 480
Cvetkovic, Srecko . . . 380
Czarlay, Dirk . . . 408
Dambon, Olaf . . . 88, 261, 408
Danjyo, Hiroki . . . 39
Dankwart, Collin . . . 35
Danyluk, Steven . . . 31
Darnell, Ian M. . . . 120, 340
Davidson, Stuart . . . 116
Davies, Angela D. . . . 152
Davies, Matthew A. . . . 542
de Leon, Luis . . . 384
Deakyne, Theodore Roy . . . 456
DeBra, Daniel B. . . . 468
Deck, Leslie L. . . . 144
DeMarco, Christopher . . . 80
Denkena, Berend . . . 43, 384
Ding, Yuhua . . . 344
Dong, Jingyan . . . 156
Dow, Thomas A. . . . 100, 164, 558, 566
Drabarek, Pawel . . . 148
Dumas, Paul R. . . . 436
Dutterer, Brian S. . . . 542
Dzenitis, Elizabeth G. . . . 15
Eischen, Jeffrey W. . . . 164
Elbestawi, Mohamed A. . . . 622
Ellis, Jonathan D. . . . 140
Enomoto, Toshiyuki . . . 396, 534
Erbe, Torsten . . . 288, 292
Erkorkmaz, Kaan . . . 300
Ess, Markus . . . 168
Falldorf, Claas . . . 35
Farahi, Faramarz . . . 152
Ferreira, Placid M. . . . 156
Fesperman Jr., Ronnie R. . . . 216, 324
Fleischer, Matthias . . . 148
Florando, Jeffery N. . . . 120, 340
Flucke, Christian . . . 92
Fujii, Taichi . . . 640
Fujisaki, Kazuhiro . . . 180
Fujiwara, Kunihiko . . . 200
Fukakusa, Noriyuki . . . 416
Furst, Stephen J. . . . 566
Furubayashi, Masaki . . . 522
Furumoto, Tatsuaki . . . 221, 229
Furushiro, Naomichi . . . 180, 392
Furutani, Katsushi . . . 506
Gan, Sze Wei . . . 607
Gao, Wei . . . 264, 368, 550, 554
Garrard, Kenneth P. . . . 100, 558, 566
Gatica, Anthony W. . . . 296
Gatzen, Hans H. . . . 380
Gawlik, Aaron J. . . . 237, 582
Gee, Anthony E. . . . 546
Gharbia, Yousef A. . . . 388
Gläbe, Ralf . . . 35, 92, 428
Gnausch, Tobias . . . 148
Go, Yasuyuki . . . 603

*Extended abstract unavailable at press time

Gorniak, Jeff 300
Goto, Yukiya 304, 316, 484
Grüntzig, Alexander 408
Hahmann, Dennis 384
Hamaguchi, Tetsuya 514, 522
Hamano, Toshiaki 184, 304, 316, 484
Harsila, Scott A. 348
Hauer, Glenn 104
Hayashi, Hirofumi 644
Henselmans, Rens 27
Herben, Maurice 408
Heselhaus, Michael 88
Higuchi, Masahiro 392
Higuchi, Sei 468
Higuchi, Toshiro 180
Himeno, Ryutaro 180
Hirano, Minoru 640
Hirano, Tameyoshi 530
Hirayama, Tomoko 39, 328
Hirose, Kenji 396
Hiroyuki, Chiba 249
Hocken, Robert J. 108, 216, 320, 324, 562
Hollstegge, Daniel 408
Holzapfel, Wolfgang 71
Hong, Seung-Hwan 188, 241
Horio, Ken'ichiro 510
Horita, Kouichi 204
Horiuchi, Takeji 204
Hosokawa, Akira 221, 229
Howe, Matthew 192
Hsieh, Chen 245
Hsu, Cheng-Chih 372
Hsu, Wei-Yao 570
Hug, Peter 424
Hwang, Jooho 460
Ikeda, Naoto 591
Inoue, Katsumi 233
Ionescu, Romeo 176, 400
Irie, Yuka 249
Ishida, Satoshi 420
Ishida, Tohru 626, 640
Ishino, Yuji 574
Ito, Shuzo 316
Iwata, Futosh 249, 496
Jablonski, Ryszard T. 352
Jäger, Christian 336
Jansen, Ger L. M. 172
Je, Tae-Jin 611
Jeong, Jaehwa 312
Jones, Benjamin K. 348
Jones, Christopher W. 116
Joo, Ki-Nam 140
Kadotani, Masato 39
Kagawa, Toshiharu 518
Kaito, Hirotoshi 514
Kanamori, Chisato 257
Kanaoka, Masahiko 615
Kaneeda, Toshiaki 196, 200
Kanegae, Shunsuke 249
Kaneko, Jun-ichi 510
Kasuya, Keigo 514, 522
Kato, Shigeo 184, 304, 316, 484
Kato, Tomonori 518
Kato, Yasuhiro 574
Katsuki, Akio 204, 360
Katupitiya, Jayantha 388
Kawabayashi, Takeharu 644
Kawanishi, Shinsuke 496
Kawashima, Kenji 518
Kent, Robert A. 15
Khanam, Samira Akter 472
Kim, George A. 464
Kim, Gyu Ha 253
Kim, Hyo Soo 136
Kim, Seung-Chul 241
Kim, Wan-Soo 253
Kimura, Akihide 550
Kinugawa, Kohei 196
Kitagawa, Takakazu 39
Kitawaki, Jun 257
Klingmann, Jeffrey L. 15
Klocke, Fritz 88, 261, 404, 408
Kobayashi, Yoshikazu 591
Kohzaki, Masao 280
Kojima, Yusuke 522
Kokubo, Mitsunori 180
Kondoh, Shinzuke 61
Kong, L. B. 587
Konneh, Mohamed 376
Kordonski, William I. 632
Kosmowski, Mark T. 160
Kramar, John A. 116, 312, 586*
Krastev, Krassimir 332
Król, József 288, 292
Kumanchik, Lee 308
Kunieda, Masanori 55
Kuo, Ching-Hsiang 570
Kuriyagawa, Tsunemoto 51
Kurz, Martin 619
Kusaba, Kouhei 416
Kusano, Takahiko 229
Lantz, Brian T. 468
Leach, Richard K. 116
Leang, Kam 128
Lee, Eun Sang 412
Lee, Hwa-Soo 208, 444
Lee, Ju-Yi 372
Lee, Jung Taik 412
Lee, Kang-Won 611
Lee, Kwang-Jo 188

*Extended abstract unavailable at press time

Lee, Sun-Kyu . . . 253
Lee, Wing-Bun . . . 587
Lee, Won-Seck . . . 212, 578
Lehman, John . . . 456
Lemmons, Tiffany Dawn . . . 216
Leo, Cheng Seng . . . 31
Levasier, Leon . . . 79*
Li, Chengzhang . . . 488, 492
Li, Jing . . . 312
Lim, Han Seok . . . 607
Lin, Chih-Min . . . 356
Lin, Wen-Lung . . . 570
Lin, Yongchuan . . . 229
Liu, Xian Ping . . . 276
Ljubicic, Dean Marko . . . 108
Loopstra, Erik R. . . . 79*
Lu, Xiaodong . . . 19
Ludwick, Stephen J. . . . 104
Lünemann, Björn . . . 35
Ma, Li . . . 599
MacKenzie, Ross Ian . . . 237, 582
Makinouchi, Akitake . . . 180
Markowski, Jerzy . . . 352
Marsh, Eric R. . . . 456, 464
Maser, Jorg . . . 23
Masreliez, Karl . . . 348
Masui, Keijiro . . . 61
Matsuda, Kiyoshi . . . 452
Matsumori, Noboru . . . 392
Matsuoka, Takashi . . . 39
Mayr, Josef . . . 168
McBride, John W. . . . 124
McGlauflin, Michael L. . . . 112
Menapace, Joe . . . 436
Meyer, Paula . . . 622
Mikami, Hirofumi . . . 208
Miller, George L. . . . 15
Miller, Michele H. . . . 488, 492
Mimura, Hidekazu . . . 615
Mishima, Nozomu . . . 61
Mitani, Takuro . . . 538
Miyata, Yoshiaki . . . 200
Mizuno, Takeshi . . . 574
Montesanti, Richard C. . . . 15
Morantz, Paul . . . 84
Mori, Yuzo . . . 615
Moritani, Hiroki . . . 522
Morse, Edward P. . . . 472
Morton, Roger K. . . . 220*
Moyer, Patrick J. . . . 440
Moylan, Shawn P. . . . 112
Mukhopadhyay, Deepkishore . . . 156
Mullany, Brigid A. . . . 440
Munnig Schmidt, Robert-Han . . . 140
Murakami, Hiroshi . . . 360
Nagato, Keisuke . . . 514, 522
Nakano, Shizuka . . . 61
Nakao, Masayuki . . . 514, 522
Nelson, Andrew . . . 424
Nelson, Jerry E.**
Neubert, Ralf . . . 619
Ng, Sum Huan . . . 31
Noh, Young Jin . . . 264
Nomura, Kazushi . . . 615
Nowakowski, Bartosz K. . . . 526
Oba, Takanobu . . . 626
Oberschmidt, Dirk . . . 96, 619
Ockwell, David C. . . . 79*
Ogura, Hidekazu . . . 392
Ogura, Ichiro . . . 364
Ohara, Kouhei . . . 496
Ohmori, Hitoshi . . . 420
Ohshita, Satoru . . . 530
Okada, Akira . . . 530
Okamoto, Yasuhiro . . . 530
Okazaki, Yuichi . . . 364
Okuyama, Eiki . . . 132
Onikura, Hiromichi . . . 204, 360
Ono, Manabu . . . 184, 304, 316, 484
Otten, David . . . 237
Overcash, Jerald Lee . . . 108, 320, 562
Ozawa, Masahito . . . 221
Ozturk, Ozkan . . . 216, 324
Palani, Anand Iyamperumal . . . 284
Pan, Shan-Peng . . . 356
Paone, Matthew . . . 19
Park, Chun Hong . . . 460
Park, Kyung-Tak . . . 611
Parker, Wesley C. . . . 440
Pawlus, Pawel . . . 595
Pengwang , Eakkachai . . . 156
Petrariu, Viorel . . . 176
Pratt, Jon R. . . . 116, 308
Rachakonda, Prem Kumar . . . 586*
Rahman, Mustafizur . . . 607
Rajurkar, Kamlakar P. . . . 502
Randles, Mark H. . . . 440
Reizer, Rafal . . . 595
Reynolds, Jack L. . . . 15
Rhorer, Richard L. . . . 630
Richardson, Derek . . . 100
Riegel, Joachim . . . 408
Riemer, Oltmann . . . 428
Rosielle, P. C. J. N. . . . 27
Ruben, Shalom . . . 268
Rueff, Matthew C. . . . 136
Saalfeld, Henry . . . 380
Sahin Nomaler, Funda . . . 172
Saito, Yusuke . . . 554
Sajima, Takao . . . 360

*Extended abstract unavailable at press time
**No abstract available

Sakamoto, Ryushiro 448, 452
Salmon, Stuart C. 424
Sarikaya, Hüsniye 261
Sasaki, Katsumi 39, 328
Schmitz, Tony L. 80, 136, 308, 476
Schulte, Heiko 428
Scire, Fredric E. 312
Selberg, Lars A. 144
Seugling, Richard M. 15, 120, 340
Shen, Yin-Lin 312
Shibukawa, Tetsuro 640
Shibuya, Atsushi 368
Shilpiekandula, Vijay 225
Shimada, Shoichi 392, 603
Shin, Dongwon 272
Shinozaki, Akira 644
Shirai, Kenji 591
Shore, Paul 75, 84
Shorey, Aric B. 632
Shu, Deming 23
Simonson, James A. 464
Singaperumal, Makaram 284
Slocum, Alexander H. 19
Smith, Stuart T. 120, 276, 340, 526
Soemers, Herman M. J. R. 332
Sohn, Alex 100, 558, 566
Song, Chang-Kyu 460
Song, In-Ho 212, 578
Song, Jun-Feng John 599
Song, Young-Chan 460
Spaan, Henny A. M. 65
Spiewak, Swavik A. 104
Spronck, Jo W. 140
Steinbuch, Maarten 27
Ströhla, Tom 288
Stroup Jr., Charles G. 320, 562
Sugihara, Tatsuya 534
Sugimoto, Keigo 233
Sugimoto, Takashi 392
Suleski, Thomas J. 542
Sundaram, Murali M. 502
Suratkar, Amit Ravindra 152
Tabuto, Hiroaki 432
Tadano, Kotaro 518
Takagi, Hiroshi 574
Takagi, Masataka 416
Takasaki, Masaya 574
Takata, Shiro 530
Takemoto, Kenji 444
Takeuchi, Yoshimi 49, 626, 640
Takino, Hideo 615
Tanaka, Hidetake 432
Tanaka, Ryutaro 221, 229
Tanaka, Yusuke 448, 452
Tauhiduzzaman, Mohammed 636
Taylor, Curtis R. 128
Teo, Check Sing 276
Theska, René 288, 292
To, Suet S. 587
Tobiason, Joseph D. 344
Tomoto, Michiaki 506
Tonnellier, Xavier 84
Toyama, Akira 644
Tozawa, Koichi 591
Tracey, Justin P. 632
Traverso, Michael G. 476
Tricard, Marc 436
Trumper, David L. 108, 237, 582
Tsao, Tsu-Chin 268
Tsuchiya, Kensuke 514
Tuecks, Roland 404
Uchida, Shuhei 500
Uda, Yutaka 603
Ueda, Takashi 221, 229
Uehara, Yoshihiro 420
Uhlmann, Eckart 96, 619
Uno, Yoshiyuki 530
Ushiki, Tatsuo 249, 496
Usman, Irfan 19
Van Brussel, Hendrik 65
van Eijk, Jan 65
van Lierop, Diederik 332
Vasa, Nilesh Jayantilal 284
Veldhuis, Stephen C. 622, 636
Verlaan, Ad 140
Völker, Carola 408
von Kopylow, Christoph 35
Vorburger, Theodore V. 599
Wang, Bo 43
Wang, Fei 261
Wang, Wei Li 276
Wegener, Konrad 168, 336
Weikert, Sascha 168, 336
Weng, Han-Fu 356
Whang, Kyung Hyun 611
Williams, Wesley B. 440
Won, Jong Koo 412
Woody, Shane C. 120, 340, 526
Wu, Chyan-Chyi 372
Yabe, Hiroshi 39, 328
Yamada, Takazo 208, 444
Yamagata, Yutaka 180
Yamaguchi, Tomomi 392
Yamamoto, Nobuaki 518
Yamamoto, Shingo 640
Yamamura, Kazuya 500, 538
Yamanaka, Masashi 233
Yamauchi, Kazuto 615
Yamazaki, Tsugio 510
Yanagi, Kazuhisa 432

Yang, Cang-Chin 245
Yang, Chun 31
Yang, Raymond Hua 276
Yasui, Heiji 416, 448, 452, 644
Yin, Shaohui 420
Yokota, Hideo 180
Yoshihara, Nobuhito 51
Yoshikawa, Yasuo 368
Yoshimura, Takuro 448
Youcef-Toumi, Kamal 225
Yu, Ta-Chang 356
Yui, Akinori 19
Zapata, Raúl E. 80, 476
Zdanowicz, Erik M. 164
Zettsu, Nobuyuki 500, 538
Zhao, Zijun 124
Zunke, Richard 404